NASA/TM—2008– 215633

Terrestrial Environment (Climatic) Criteria Guidelines for Use in Aerospace Vehicle Development, 2008 Revision

D.L. Johnson, Editor
Marshall Space Flight Center, Marshall Space Flight Center, Alabama

December 2008

The NASA STI Program…in Profile

Since its founding, NASA has been dedicated to the advancement of aeronautics and space science. The NASA Scientific and Technical Information (STI) Program Office plays a key part in helping NASA maintain this important role.

The NASA STI program operates under the auspices of the Agency Chief Information Officer. It collects, organizes, provides for archiving, and disseminates NASA's STI. The NASA STI program provides access to the NASA Aeronautics and Space Database and its public interface, the NASA Technical Report Server, thus providing one of the largest collections of aeronautical and space science STI in the world. Results are published in both non-NASA channels and by NASA in the NASA STI Report Series, which includes the following report types:

- TECHNICAL PUBLICATION. Reports of completed research or a major significant phase of research that present the results of NASA programs and include extensive data or theoretical analysis. Includes compilations of significant scientific and technical data and information deemed to be of continuing reference value. NASA's counterpart of peer-reviewed formal professional papers but has less stringent limitations on manuscript length and extent of graphic presentations.

- TECHNICAL MEMORANDUM. Scientific and technical findings that are preliminary or of specialized interest, e.g., quick release reports, working papers, and bibliographies that contain minimal annotation. Does not contain extensive analysis.

- CONTRACTOR REPORT. Scientific and technical findings by NASA-sponsored contractors and grantees.

- CONFERENCE PUBLICATION. Collected papers from scientific and technical conferences, symposia, seminars, or other meetings sponsored or cosponsored by NASA.

- SPECIAL PUBLICATION. Scientific, technical, or historical information from NASA programs, projects, and missions, often concerned with subjects having substantial public interest.

- TECHNICAL TRANSLATION. English-language translations of foreign scientific and technical material pertinent to NASA's mission.

Specialized services also include creating custom thesauri, building customized databases, and organizing and publishing research results.

For more information about the NASA STI program, see the following:

- Access the NASA STI program home page at <http://www.sti.nasa.gov>

- E-mail your question via the Internet to <help@sti.nasa.gov>

- Fax your question to the NASA STI Help Desk at 301–621–0134

- Phone the NASA STI Help Desk at 301–621–0390

- Write to:
  NASA STI Help Desk
  NASA Center for AeroSpace Information
  7115 Standard Drive
  Hanover, MD 21076–1320

NASA/TM—2008–215633

Terrestrial Environment (Climatic) Criteria Guidelines for Use in Aerospace Vehicle Development, 2008 Revision

D.L. Johnson, Editor
Marshall Space Flight Center, Marshall Space Flight Center, Alabama

National Aeronautics and
Space Administration

Marshall Space Flight Center • MSFC, Alabama 35812

December 2008

Acknowledgments

This document is dedicated to the memory of the late Glenn E. Daniels, who passed away in 2004. Mr. Daniels was the originator and technical compiler of this terrestrial document when it was first published in the early 1960s. He continued updating this document until his retirement from NASA Marshall Space Flight Center (MSFC) in 1974. Others, in the early years, who have contributed a large technical influence to this document include Dr. William W. Vaughan, G. Wade Batts, and the late Dr. George H. Fichtl, Orvel E. Smith, and Sayre Clark Brown.

The editor wishes to acknowledge and thank a large number of aerospace engineers and personnel in varying scientific fields that have technically contributed and assisted in the preparation of this document. The following personnel were principal contributors for the technical sections identified:

Section	Title	Contributor and Responsible Persons
1.	Introduction	Dale Johnson and William W. Vaughan
2.	Winds	Stanley Adelfang, Orvel E. Smith, and William W. Vaughan
3.	Atmospheric Thermodynamic Properties and Models	Dale Johnson and William W. Vaughan
4.	Solar and Thermal Radiation	C.G. Justus and James Luers
5.	United States and World Surface Extremes	Lee Burns, Gregory Hammer, and Dale Johnson
6.	Humidity	Dale Johnson and William W. Vaughan
7.	Precipitation, Fog, and Icing	James Luers, Dale Johnson, and Vernon Keller
8.	Cloud Phenomena and Cloud Cover Models	Gary Thomas, Dale Johnson, and Vernon Keller
9.	Atmospheric Electricity and Thunderstorms	William Koshak, Frank Leahy, and Dale Johnson
10.	Atmospheric Constituents	Kirk Fuller and Dale Johnson
11.	Aerospace Vehicle Exhaust, Toxic Chemical Release, and Accoustic Propagation	Dale Johnson and Paul Rosati
12.	Occurrences of Tornadoes, Hurricanes, and Related Severe Weather	Dale Johnson and Frank Tatom
13.	Geologic Hazards, Earth Properties, and Aerospace Vehicle Implications	Dale Johnson
14.	Sea State	Ian Young, Vernon Keller, and Dale Johnson

Available from:

NASA Center for AeroSpace Information
7115 Standard Drive
Hanover, MD 21076–1320
301–621–0390

This report is also available in electronic form at
<https://www2.sti.nasa.gov>

Acknowledgments (Continued)

Section	Title	Contributor and Responsible Persons
15.	Mission Analysis, Prelaunch Monitoring, and Flight Evaluation	William W. Vaughan, Stewart Deaton, and Dale Johnson
16.	Conversion Units	William W. Vaughan, Gregory Hammer, and Dale Johnson

The editor wishes to thank the following people for their technical review or assistance which offered valuable suggestions used to enhance this document: John Sharp (MSFC), the late Harold L. Crutcher (NOAA), Vernon Keller (MSFC), Richard McNider (UAH), Gerald Wieczorek (USGS), David Perkins (USGS), Jennifer Bosch (Rutgers), Richard Wegrich (MSFC), Steven Hudson (MSFC), Andrew Hodges (MSFC), Kevin Knupp (UAH), Kris White (NOAA), Bill McCaul (UAH), John Madura (KSC), Frank Merceret (KSC), Stanley Changnon (ISWS/UIUC), Michael Pidwirny (Okanagan U.), Mike Newchurch (UAH), Sam McCown (NOAA), Sofia Caires (KNMI), Andreas Sterl (KNMI), Burton Summerfield (KSC), Amber Armstrong (USAF), Paul Rosati (USAF), Tony Clark (MSFC), Chuck Doswell (CIMMS), Luz Marina Calle (KSC), Brian Blake (CUSEC), C.G. Justus (MSFC), Ryan Decher (MSFC), B. Jeff Anderson (MSFC), E. Philip Krider (University of Arizona), Michael Stevens (NRL), and the many others that we may have unintentionally left off this listing.

Special acknowledgments are given to Paul Gill (NASA Technical Standards Program Office), to Nelson Parker (MSFC, Safety and Mission Assurance), to David Edwards (MSFC, Natural Environments Branch Chief), to B. Glenn Overby (MSFC, Propulsion Systems Engineering and Integration Office), and to Michael Ryschkewitsch (NASA Chief Engineer) for their guidance and support which led to the completion of this document.

Special thanks go to Dr. Henry E. Fuelberg of the Florida State University, Meteorology Department, for his complete technical review of the entire draft document. Also to Dr. John R. Mecikalski of The University of Alabama in Huntsville for his indepth technical review of the final document.

Extra special thanks go to Dr. William W. Vaughn for his steadfast assistance in both the technical and the logistical preparation of this document, along with his very extensive reviews of each draft section.

Also, thanks go to MSFC's Betty Fowler, Kim Narmore, Buddie Martin (Pace & Waite), Mary Chou (STI), Beth Merrell (STI), Susan Burrer (STI), and others for coordinating, proofing, final typing, assembly, and printing this document. Without their contributions, this document would not exist.

Dale L. Johnson (MSFC), Editor
and William W. Vaughan (UAH), Technical Assistant

FOREWORD

These guidelines provide updated information regarding the natural environment for altitudes between the surface of the Earth and 90 km altitude for the principal NASA aerospace vehicle development, operational, and launch locations and associated local and worldwide geographical areas.

These guidelines supersede all editions of *NASA Technical Memorandum 4511* entitled, "Terrestrial Environment (Climatic) Criteria Guidelines for Use in Aerospace Vehicle Development" dated August 1993. It is recommended for use in the development of design requirements and specifications for aerospace vehicles and associated equipment. The origin of this Terrestrial Environment (Climatic) Criteria Guidelines dates to the early 1960s. It was originally conceived and the early editions prepared under the direction of Glenn E. Daniels of the NASA Marshall Space Flight Center's Aerospace Environment Division. This report has also been provided to the NASA Technical Standards Program for publication as NASA-HDBK-1001A.

The information presented in these guidelines is based on data and models considered to be accurate. However, in those design applications that indicate a critical environment interface, the user should consult an environmental specialist to ensure application of the most current information and scientific engineering interpretations.

Various NASA programs have provided resources required for the preparation of these guidelines. Major support came from NASA Headquarters Office of Safety and Mission Assurance, Space Operations Mission, Exploration Systems Mission, and NASA Chief Engineer.

Many references, including key documents such as: (1) *NASA/TM—2008–215581*, "The NASA MSFC Earth Global Reference Atmospheric Model–2007 Version (GRAM–07)," (2) *NASA CR—1998–208859*, "A Compendium of Wind Statistics and Models for the NASA Space Shuttle and Other Aerospace Vehicle Programs," and (3) *NASA TM—2000–21–131*, "Analysis and Assessment of Peak Lightning Current Probabilities at the NASA Kennedy Space Center," have been included in this guideline revision as an update to the original *NASA Technical Memorandum 4511* published in August 1993.

Requests for technical information, corrections, or additions to this document should be directed to the Chief, Natural Environments Branch, NASA Marshall Space Flight Center, Marshall Space Flight Center, AL 35812. Requests for general information concerning the contents of these guidelines should also be sent to the Chief, Natural Environments Branch, NASA Marshall Space Flight Center, Marshall Space Flight Center, AL 35812. This document may also be viewed and downloaded as *NASA/TM—2008–215633*, free of additional charge, from the NASA Scientific and Technical Information Web site at <https://www2.sti.nasa.gov>.

TABLE OF CONTENTS

TABLE OF CONTENTS (Continued)

TABLE OF CONTENTS (Continued)

TABLE OF CONTENTS (Continued)

TABLE OF CONTENTS (Continued)

TABLE OF CONTENTS (Continued)

TABLE OF CONTENTS (Continued)

TABLE OF CONTENTS (Continued)

TABLE OF CONTENTS (Continued)

TABLE OF CONTENTS (Continued)

TABLE OF CONTENTS (Continued)

Terrestrial Environment (Climatic) Criteria Guidelines for Use in Aerospace Vehicle Development, 2008 Revision

NASA/TM—2008–215633
December 2008

D.L. Johnson, Editor

Section 1: Introduction

TABLE OF CONTENTS

LIST OF FIGURES

LIST OF TABLES

TECHNICAL MEMORANDUM

TERRESTRIAL ENVIRONMENT (CLIMATIC) CRITERIA GUIDELINES FOR USE IN AEROSPACE VEHICLE DEVELOPMENT, 2008 REVISION

1. INTRODUCTION

1.1 General

Atmospheric phenomena play a significant role in the design and operation of aerospace vehicles and in the integrity of aerospace systems and elements. The terrestrial environment design criteria guidelines given in this handbook are based on statistics and models of atmospheric and climatic phenomena relative to various aerospace design, development, and operational issues. This revision contains new and updated material in most sections.

Aerospace vehicle design guidelines are provided for the following environmental phenomena: winds; atmospheric models and thermodynamic properties; thermal radiation; U.S. and world surface extremes; humidity; precipitation, fog, and icing; cloud phenomena and cloud cover models; atmospheric electricity; atmospheric constituents; aerospace vehicle exhaust and toxic chemical release; tornadoes and hurricanes; geologic hazards; and sea state. Sections 15 and 16 include information on mission analysis, prelaunch monitoring, flight evaluation, physical constants, and metric/English unit conversion factors.

In general, this document does not specify how the designer should use the data in regard to a specific aerospace vehicle design. Such specifications may be established only through the analysis and study of a particular design problem. Although of operational significance, descriptions of some atmospheric conditions have been omitted since they are not of direct concern for an aerospace vehicle system's design, the primary emphasis of this document. Induced environments (vehicle caused) may be more critical than the natural environment for certain vehicle operational situations. In some cases, the combination of natural and induced environments will be more severe than either environment alone. Induced environments are considered in other aerospace vehicle design criteria documents, which should be consulted for such information.

The natural environment criteria guidelines presented in this document were formulated based on discussions with, and requests from, engineers involved in aerospace vehicle development and operations. Therefore, they represent responses to actual engineering problems and not just a general compilation of environmental data. NASA Centers, various other Government agencies, and their associated contractors responsible for the design, mission planning, and operational studies use this document extensively. The *Glossary of Meteorology* and *Glossary of Weather and Climate*, published by the American Meteorological Society, 45 Beacon Street, Boston, MA 02108, should be consulted for the definitions of environment terms not otherwise defined in this handbook.

This document also does not include information on the natural environment above 90 km. A recently issued document sponsored by the European Space Agency (ESA), ECSS-E-ST-10-04C, "Space Engineering—Space Environment," provides an excellent summary from the engineering application viewpoint on all aspects of the space environment. It may be downloaded from the European Cooperation for Space Standardization Web site <http://www.esa.nl>. Also, the NASA Marshall Solar Activity monthly document that provides current and future estimates of 13-mo Zurich smoothed solar and geomagnetic activity may be downloaded from <http://sail.msfc.nasa.gov/>.

1.2 Engineering Importance

It is important to recognize the need to define the terrestrial environment very early in the design and development cycle of any aerospace vehicle. The bibliography for section 1 provides a number of documents that address this subject. This need is especially true for a new configuration such as the new Constellation Ares I and Ares V vehicles (see fig. 1-1), or any other future launch vehicle. Using the desired operational capabilities, launch locations, and flight profiles for the vehicle, specific definitions of the terrestrial environment can be provided which, if the aerospace vehicle is designed to accommodate, will ensure the desired operational capability within the defined design risk level. It is very important that those responsible for the terrestrial environment definitions for the design of an aerospace vehicle have a close working relationship with program management and design engineers. This will ensure that the desired operational capabilities are reflected in the terrestrial environment requirements specified for design of the vehicle.

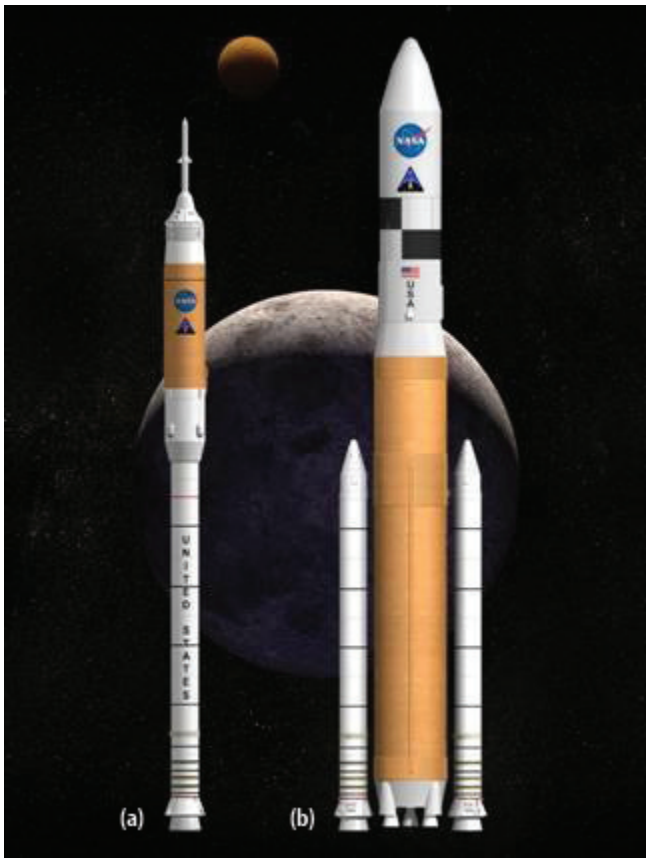

Figure 1-1. NASA's proposed launch vehicles: Constellation (a) Ares I and (b) Ares V.

An aerospace vehicle's response to terrestrial environment design criteria must be carefully evaluated to ensure an acceptable design relative to desired operational requirements. The choice of criteria depends on the specific launch and landing location(s), vehicle configuration, and expected mission(s). Vehicle design, operation, and flight procedures can be separated into particular categories for proper assessment of environmental influences and impact on the life history of each vehicle and all associated systems. These include categories such as (1) purpose and concept of the vehicle, (2) preliminary engineering design, (3) structural design, (4) control system design, (5) flight mechanics, orbital mechanics, and performance (trajectory shaping), (6) optimization of design limits regarding the various natural environmental factors, and (7) final assessment of the natural environmental capability for launch and flight operations.

Another important matter that must be recognized is the necessity for having a coordinated and consistent set of terrestrial environment requirements for use in a new aerospace vehicle's design and development. This is particularly important when diverse groups are involved in the development, and is of utmost importance for any international endeavor. A "central control point" having responsibility for the definition and interpretation of the terrestrial environment inputs is critical to the successful design and operation of any new aerospace vehicle. Without this control, different terrestrial environment values or models can be used with costly results in terms of money, time, and vehicle performance. This central control point should also include responsibility for mission analysis, test support requirements, flight evaluation, and operational support relative to terrestrial environment requirements.

During the early stages of a new aerospace vehicle's design and development, tradeoff studies to establish the sensitivities of various terrestrial environment-forcing functions are important. Feedback from these studies is key to establishing the necessary terrestrial environment requirements for the vehicle's final design. A single source (central control point) responsible for the terrestrial environment inputs and their interpretation is important. This will preclude a multitude of problems in the final design and development process, and will enable terrestrial environment requirements to be established with a minimum amount of communications problems and misunderstanding of design issues.

The close association between the design and test engineering groups and those responsible (central control point) for the terrestrial environment inputs is key to the success of the vehicle's development process. This procedure has been followed in many NASA aerospace vehicle developments and is of particular importance for any new aerospace vehicle. Figure 1-2 illustrates necessary interactions relative to terrestrial environment definition and engineering application. Feedback is critical to the vehicle development process relative to terrestrial environment requirements and thus the ability to produce a viable vehicle design and operational capability.

Finally, although often not considered to be significant, it is very important that all new aerospace vehicle design review meetings include a representative from the terrestrial environment group (central control point) assigned to support the program. This will ensure good understanding of design requirements and timely opportunity to incorporate terrestrial environment inputs and interpretations, which are tailored to the desired operational objectives, into the design process. It is also necessary that any proposed deviations from the specified terrestrial environment requirements, including those used in preliminary design tradeoff studies, be approved by the responsible terrestrial environment central control point to ensure that all program elements are using the same baseline inputs. This will also help the program manager understand the operational impact of any change in terrestrial environment requirements before implementation into the design. Otherwise, gross errors and deficiencies in design can result from using different inputs selected from various diverse sources by those involved in design and other performance studies.

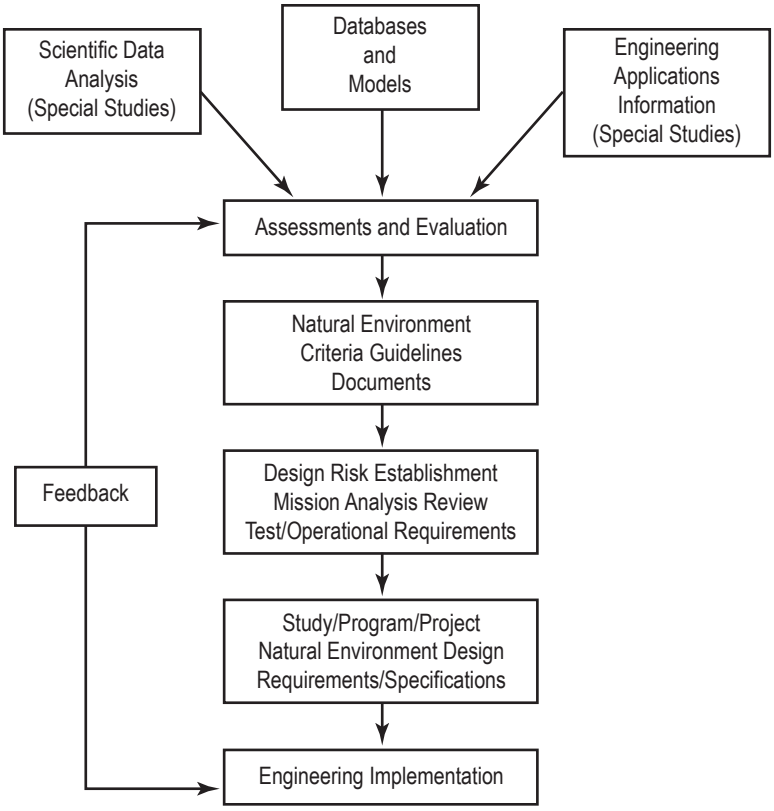

Figure 1-2. Natural terrestrial environment definition and analysis for aerospace vehicle engineering application.

One must remember that the flight profile of any aerospace vehicle includes the terrestrial environment. Terrestrial environment definitions are usually limited to information below ≈90 km (≈295,000 ft). Thus, an aerospace vehicle's operations will always be influenced to some degree by the terrestrial environment with which it interacts. As a result, the definition of the terrestrial environment and its interpretation is one of the key aerospace vehicle design and development inputs. This definition plays significant roles; e.g., in the areas of structures, control systems, trajectory shaping (performance), aerodynamic heating, and takeoff/landing capabilities. The aerospace vehicle's capabilities which result from the design, in turn, determine the constraints and flight opportunities for tests and operations.

1.3 Terrestrial Environment Issues

Experience gained from developing terrestrial environment design criteria for previous aerospace vehicle programs has proven that, to be most effective, the terrestrial environment design criteria for a new vehicle should:

(1) Be available at the inception of the program and developed to ensure the desired operational performance of the aerospace vehicle.

(2) Be issued under the signature of the program manager and be part of the controlled program definition and requirements documentation.

(3) Specify in the design criteria document the terrestrial environment for all phases of activity including prelaunch, launch, ascent, on-orbit, descent, and landing.

For extremes in the terrestrial environments, there generally is no known physical upper or lower bound. However, wind speed does have a strict physical lower bound of zero. Essentially all observed extreme conditions have a finite probability of being exceeded. Consequently, terrestrial environment extremes used for design must be accepted with the knowledge that there is some risk of the values being exceeded. The measurement of many environmental parameters is not as accurate as desired. In some cases, theoretical model estimates are believed to be more useful for design use than those indicated by empirical distributions from short periods of record. Therefore, theoretical values have been given considerable weight in selecting the extreme values for some parameters; e.g., peak surface winds. Criteria guidelines are presented for various percentiles based on the available data. Caution should be exercised in the interpretation of these percentiles in aerospace vehicle studies to ensure consistency with physical reality and the specific design and operational problems of concern.

Aerospace vehicles are not normally designed for launch and flight in severe weather conditions such as hurricanes, thunderstorms, ice storms, and squalls. Environmental parameters associated with severe weather that may be hazardous to aerospace vehicles and associated ground support equipment include strong ground and in-flight winds, strong wind shears and gusts, turbulence, icing conditions, and electrical activity. Terrestrial environment guidelines provide information relative to those severe weather characteristics that should be included in design requirements and specifications if required to meet the program's mission operational requirements.

Knowledge of the terrestrial environment is also necessary to establish test requirements for aerospace vehicles and in design of associated support equipment. Such data are required to define the fabrication, storage, transportation, test, and preflight design condition and should be considered for both the whole vehicle system and the components which comprise the system.

The group having the central control point responsibility and authority for defining and interpreting terrestrial environment design requirements must also be in a position to pursue environment input-related applied research studies and engineering assessments and updates. This is necessary to ensure accurate and timely terrestrial environment inputs tailored to the program's needs. Design engineers and program managers who assume they can simply draw on the vast statistical databases and numerous models of the terrestrial environment currently available in the literature, without interpretation and tailoring to specific vehicle design needs, can prove to be a major deterrent to the successful development and operation of an aerospace vehicle.

Although a vehicle design ideally should accommodate all expected operational environment conditions, it is neither economically nor technically feasible to design an aerospace vehicle to withstand all terrestrial environment extremes. For this reason, consideration should be given to protecting vehicles from some extremes. This can be achieved by using support equipment and specialized forecast personnel to advise on the expected occurrence of critical terrestrial environment conditions. The services of specialized forecast personnel may be very economical compared to the more expensive vehicle designs that would be required to cope with all terrestrial environment possibilities.

The terrestrial environment is a major environmental driver for an aerospace vehicle's design and is the focus of this document. However, the natural environment above 90 km must also be considered for aerospace vehicles. The orbital operating phase of an aerospace vehicle includes exposure to the space environment, including atomic oxygen, atmospheric density, ionizing radiation, plasma, magnetic fields, meteoroids, etc., plus a few

manmade environments, such as orbital debris. Specific aerospace vehicle terrestrial and space environments design requirements are normally specified in the appropriate vehicle design criteria documentation.

Good engineering judgment must be exercised in applying terrestrial environment requirements to an aerospace vehicle's design analysis. Consideration must be given to the overall vehicle mission and system performance requirements. Knowledge is still lacking on relationships between some of the terrestrial environment parameters that are required as inputs to the design of aerospace vehicles. Also, interrelationships between vehicle parameters and terrestrial environment variables cannot always be clearly defined. Therefore, a close working relationship and team philosophy must exist between the design and operational engineer and the respective organization's terrestrial environment central control point specialists.

1.4 Vehicle and Terrestrial Environment Areas of Concern

As noted, it is important that the need for defining of the ground, ascent, on-orbit, and descent aerospace vehicle operational terrestrial environments be recognized early in the design and development phase of the vehicle program. Engineering technology is constantly changing. In some cases, the current trends in engineering design have increased a vehicle's susceptibility to terrestrial environment factors. Based on past experience, the earlier the terrestrial environment central control point specialists become involved in the design process, the less the potential for negative environmental impacts on the program downstream through redesign, operational workaround, etc.

In many cases, it is impossible to clearly define the limiting extreme values for a particular terrestrial environment parameter that may occur during the desired operational lifetime of the vehicle. It may not be technically nor economically feasible to design a vehicle to withstand an extreme environment value. However, a lower value may be defined such that the probability is small that the lower value will occur during the desired operational lifetime of the vehicle. Additional launch delay risks may also be acceptable versus the expense of additional design considerations. Because of these and other considerations, a value less than the extreme may be a more appropriate design requirement. The terrestrial environment specialist has the responsibility to provide the program manager and chief engineer with pertinent information so they can determine the highest risk value that is feasible for the program in that particular environment area. Therefore, it is very important that the aerospace vehicle program manager and the chief engineer have a good understanding of the operational risks due to the selected design terrestrial environment.

Table 1-1 provides a reference guide for the terrestrial environment specialist, program managers, design engineers, and others on the development team for a new aerospace vehicle program. This information summarizes potential terrestrial environment areas of engineering concern when first surveying a vehicle project. As the table indicates, terrestrial environment phenomena may significantly affect multiple areas of an aerospace vehicle's design, and thus operational capabilities, including areas involving structure, control, trajectory shaping (performance), heating, takeoff and landing capabilities, materials, etc.

1.5 Environmental Test Procedures

This document does not address the subject of environmental test procedures. Reference should be made to MIL-STD-810F, "Department of Defense Test Method Standard for Environmental Engineering Consideration and Laboratory Tests," January 1, 2000, available from the Defense Automation and Production Service, 700 Robbins Avenue, Philadelphia, PA 19111–5094. This standard may also be downloaded from the

Table 1-1. Key terrestrial environment parameters needed versus engineering systems (X) and mission phase (P).

X	Terrestrial Environment Parameter																								P
Launch Vehicle Systems (sub-)	Winds and Gusts		Atmospheric Thermody-namics		Atmospheric Constituents		Solar/ Thermal Radiation		Atmospheric Electricity		Clouds and Fog		Humidity		Precipitation or Hail		Sea State		Severe Weather		Geologic Hazards		Mission Phase
System	X	P	X	P	X	P	X	P	X	P	X	P	X	P	X	P	X	P	X	P	X		Mission analysis
Propulsion/ engine sizing	X		X	P		P			X				X	P					X				Manufacturing
Structures/ airframe	X	P	X	P			X		X	P				P	X	P	X		X	P		P	Testing
Performance/ trajectory/G&N	X	P	X	P		P		P	X	P		P		P		P		P		P		P	Transport and ground hdl
Aerodynamics	X	P	X	P		P		P		P				P		P		P		P			Rollout/ On-pad
Thermal loads/ aerodynamics heat	X	P	X	P		P	X	P		P		P		P		P		P		P			Prelaunch DOL count down
Control	X	P	X	P		P		P	X	P		P		P		P			X	P			Lift-off/ ascent
Loads	X	P	X	P						P		P				P	X	P	X	P			Stages recovery
Avionics		P		P	X		X		X	P		P	X			P			X	P			Flight
Materials	X		X	P	X	P	X	P	X				X		X		X		X				Orbital
Electrical power		P		P	X				X	P	X				X	P				P			Desent
Optics		P	X	P		P	X			P	X	P		P	X	P		P		P			Landing
Thermal control		P	X	P	X	P	X	P		P				P	X	P		P		P			Post-land
Telemetry, tracking, and communication		P	X	P	X	P		P	X	P	X	P		P	X	P		P	X	P		P	Ferry/ transport
		P								P				P		P				P		P	Facil/spt Equip
		P		P		P				P				P		P						P	Refurbishment
Mission operations	X	P	X	P	X	P	X	P	X	P	X		X	P	X	P	X		X	P	X	P	Storage

DoD via <http://assist.daps.dla.mil/>. MIL-STD-810F covers procedures for low pressure (high altitudes), high and low temperatures, temperature shock, temperature altitude and temperature-humidity altitude, solar radiation, rain, humidity, fungus, salt fog, dust (fine sand), and space simulations (unmanned test). An excellent comparison of the various international environmental testing standards may be found in the *Journal of Environmental Sciences*, Vol. XXIV, No. 2, March/April 1981.

1.6 Some Lessons Learned

The Marshall Space Flight Center Natural Environments Branch and its predecessor organizations have over 50 yr of experience in the development and interpretation of terrestrial environment requirements for use in the design and operation of aerospace vehicles. During this period, a large number of "lessons learned" have formed the basis for the contents of this handbook. A few of these lessons learned are summarized in the following list:

(1) Title: Wind Vectors Versus Engineering Vector Conventions

- Background. Flight mechanics use of wind vectors versus conventional meteorological usage. In the case of flight mechanics, the vector is stated relative to direction that force is being applied. However, in meteorology, the wind vector is stated relative to direction from which wind force is coming.

- Lesson. The proper interpretation and application of wind vectors is important to avoid a 180º error in structural loads and control system response calculations.

(2) Title: Design Requirements, Not Climatology

- Background. While based on climatology and models, both physical and statistical, natural environment requirements are part of the overall vehicle design effort necessary to ensure that mission operational requirements are met. Thus, they must be selected and defined on this basis. Simply making reference to climatological on databases will not produce the desired vehicle performance.
- Lesson. Members of the natural environments group assigned as the control point for inputs to a program must also be part of the vehicle design team and participate in all reviews, etc. to ensure proper interpretation and application of natural environment definitions/requirements relative to overall vehicle design needs.

(3) Title: Early Input of Natural Environment Requirements Based on Interpretation of Mission Purpose and Operational Expectations

- Background. One needs to develop the natural environment definitions and requirements for a program as soon as possible after one has the level one requirements for the program's mission. Thus, all concerned with the development will have a common base with associated control on changes made to natural environment definitions/requirements and associated vehicle operational impacts.
- Lesson. The definition of the natural environment requirements for a vehicle that are necessary to meet the mission requirements is important for all concerned with the program. This provides visibility to all, especially the program manager and systems engineers, relative to the impact on the operation of the vehicle and to natural environment design requirements on the program's mission.

(4) Title: Consistent Input for all Users More Important for Tradeoff and Design Studies Than Different Inputs on Natural Environment Topic

- Background. The natural environment is one of the key drivers for much of the design efforts on an aerospace vehicle's thermal, structural, and materials control. Differences in the natural environment inputs used by different design groups can mask critical engineering design inputs if not avoided by consistent and coordinated natural environmental inputs and interpretations for engineering applications.
- Lesson. The need for a focused natural environment group which provides coordinated and consistent environment definitions/requirements/interpretations is key to having all concerned direct their efforts toward the same inputs, thus contributing to engineering applications that can readily be interpreted from a common base.

(5) Title: Ability to Test New or Changes in Natural Environment Requirements Versus Results Important Before Implementing Them as Formal Requirements

- Background. Preliminary assessment of natural environments definitions and requirements first must be accomplished in collaboration with a responsible engineering group in order to identify design drives versus mission requirements. Based on this information, the appropriate natural environment definitions and requirements can be implemented and controlled accordingly.
- Lesson. To avoid problems with the engineering interpretation of natural environment definitions and requirements, the natural environments group responsible first must interact directly with an appropriate engineering group to ensure proper use and interpretation when formally implemented as part of the overall program requirements.

(6) Title: Need to Maintain Natural Environment Requirements for Design and Operation of Vehicle as Base From Which Other Requirements are Related

- Background. Taking this action provides a viable and robust operational vehicle capability that will meet the vehicle's mission operational natural environment requirements. Otherwise, a vehicle will be produced that will have a lower operational capability based on natural environment conditions. The natural environment operational requirements can be monitored and decisions made regarding launch operations, etc., or, in case monitoring is not practical or in an emergency, the vehicle will be functional relative to probable natural environment conditions established on the basis of past records and mission requirements.
- Lesson. Do not design an aerospace vehicle with the required natural environment design requirements incorporated as one of the nonnominal inputs and RSS in the final vehicle design decision.

(7) Title: Natural Environment Elements That Cannot be Monitored Prior to Operational Decision Must be Minimum Risk Level Possible Consistent With Mission Capability Requirements

- Background. For an aerospace vehicle launch, most natural environment elements can be monitored and thus taken into account before making a launch decision. The same is true for some on-orbit and deep-space spacecraft operational requirements. In such cases, lower probability occurrence environments may be considered, consistent with mission requirements, along with subsequent savings on design. Vehicle ascent winds through max Q versus reentry winds is an example of lower probability (higher risk of occurrence) versus higher probability (lower risk of occurrence) natural environment design requirements for a vehicle. However, for minimum risk of occurrence, natural environment requirements must be used for design to ensure operational capability when natural environments cannot be measured or monitored.
- Lesson. It is necessary to carefully analyze the mission requirements relative to vehicle operations and provide the natural environment definitions and requirements accordingly in collaboration with the vehicle program manager to ensure understanding of the implications of environments provided for design.

(8) Title: Maintain Natural Environment Requirements for Design as a Separate Document but Integral to Overall Mission Requirements for Vehicle

- Background. The natural environment definitions and requirements for the Space Shuttle and Space Station were provided so they could be controlled and available in separate program documents as part of the overall design requirements documentation. This not only provided direct access for all concerned with use of natural environment inputs into design and mission planning but also provided an easy control of inputs. Changes, where required, were readily possible with the change of one document that had application for all natural environment inputs to the program.
- Lesson. Each vehicle development program should have only one natural environment definition and requirements document. It should be an integral part of the overall mission requirements for the vehicle design, development, and operations, and be controlled accordingly.

(9) Title: Atmospheric and Space Parameter Analysis Model

- Background. The ability for a program manager to easily access information on the operational impact of a vehicle design change relative to the natural environment is an important tool for decision making. In addition, such a tool provides additional insight into mission planning activities, including launch and landing delay probabilities.
- Lesson. Knowledge by mission managers, chief engineers, mission planners, etc. on the availability of an Atmospheric and Space Parameter Analysis Model is a valuable decision-making tool and should be utilized in making the tradeoff decision when the desired operational natural environment is a factor.

(10) Title: Reference Period for Design Statements of Natural Environment Definitions and Requirements Relative to Launch and On-Orbit Operations

- Background. For launch statements on natural environment definitions and requirements, the worst reference month should be used. This provides an operational capability relative to the natural environment that ensures that for any given month, the desired operational capability will be met. Thus, for the worst month reference period, the minimum risk of launch delay due to the natural environment will occur with all other months having less probabilities of launch delay. The same situation exists for natural environments associated with on-orbit operational capability, and deep-space operations. In other words, for these cases, the anticipated lifetime in these operational conditions must be taken into account along with the acceptable risk for comprising the mission relative to natural environment conditions exceeding the design requirements.
- Lesson. All launch natural environment definitions and requirements for the design of a vehicle must be made less with respect to a worst month reference period. For natural environments associated with on-orbit and deep-space operations, the anticipated lifetime in these operational conditions must be taken into account along with acceptable risks for operations.

(11) Title: Life-Cycle Cost Estimates and Natural Environment Operational Constraints of Vehicle

- Background. Once a vehicle has been developed, the constraints relative to operations in the natural environment should be assessed based on the resulting capability of the vehicle. This is the case for launch, on-orbit, and deep-space aspects of the mission. An Atmospheric and Space Environment Parameter Analysis Model can be especially helpful in this regard. The resulting information should be incorporated into the development of the full life-cycle cost estimates and model for the vehicle program.
- Lesson. Consideration needs to be given to the natural environmental constraints on launch and spacecraft operations when developing full life-cycle cost estimates and models.

(12) Title: Accelerated Schedule Without the Infrastructure

- Background. The decision to accelerate a program development schedule needs to be made in light of in-place competences, resources, and management operations. A number of factors can affect this decision, including recognizing the issues and necessary work involved, availability of natural environment skills within the contractor community and interaction between the NASA program offices interfacing with contractors, and isolation of natural environments skills from systems engineering teams working the program.
- Lesson. Program systems engineering offices should have a “skills checklist” and routinely review government and contractor capabilities to ensure that all necessary expertise is available and tied in appropriately relative to natural environment and other engineering activities.

(13) Title: Lessons Learned—Design Process

- Background: The design process is a blend of classical procedures and evolving philosophical principles and practices in the ever-changing and challenging environments of customer expectations, new technologies, and constraining economics. An engineering product builds on those consistent and proven practices and philosophies selected in the design process.
- Lesson: Engineering reports such as Ryan et al. (1996) and Blair et al. (2001) endeavor to identify and illuminate a few recurring design process lessons learned and principles published, experienced, and observed that lead to the design of successful aerospace launch vehicle products that operate within the terrestrial environment.

BIBLIOGRAPHY

Blair, J.C.; Ryan, R.S.; Schutzenhofer, L.A.; and Humphries, W.R.: "Launch Vehicle Design Process: Characterization, Technical Integration and Lessons Learned," *NASA/TP—2001–210992*, NASA Marshall Space Flight Center, AL, May 2001.

Johnson, D.L.; and Anderson, B.J.: "The Role of the Natural Environment in Launch Vehicle Development," Chapter 7, Space Launch and Transportation Systems: Design and Operations, Vol. 1, 2005, unpublished.

Johnson, D.L.; Hill, C.K.; Vaughan, W.W.; Brown, S.C.; and Batts, G.W.: "Natural Environment Requirements Definition and Significance for Aerospace Plane Development," *AIAA Paper No. 93–5074*, AIAA/DGLR Fifth International Aerospace Planes and Hypersonic Technologies Conference, November 30–December 3, 1993, Munich, Germany, American Institute of Aeronautics and Astronautics, Reston, VA.

Pearson, S.D.; Vaughan, W.W.; Batts, G.W.; and Jasper, G.L.: "Importance of the Natural Terrestrial Environment With Regard to Advanced Launch Vehicle Design and Development," *NASA TM 108511*, NASA Marshall Space Flight Center, AL, June 1996.

Ryan, R.; Blair, J.; Townsend, J.; and Verderaime, V.: "Working on the Boundaries: Philosophies and Practices of the Design Process," *NASA TP-3642*, Marshall Space Flight Center, AL, July 1996.

Vaughan, W.W.; and Brown, S.C.: "Natural Environment Considerations for Space Shuttle System Development Support," *Journal of Spacecraft and Rockets*, Vol. 22, No. 3, pp. 355–360, 1985.

Vaughan, W.W.; Johnson, D.L.; Pearson, S.D.; and Batts G.W.: "The Role of Aerospace Meteorology in the Design, Development and Operation of New Advance Launch Vehicles," *Proceedings of the Seventh Conference on Aviation, Range and Aerospace Meteorology*, American Meteorological Society, Boston, MA, February 1997.

Terrestrial Environment (Climatic) Criteria Guidelines for Use in Aerospace Vehicle Development, 2008 Revision

NASA/TM—2008–215633
December 2008

D.L. Johnson, Editor

Section 2: Winds

TABLE OF CONTENTS

TABLE OF CONTENTS (Continued)

TABLE OF CONTENTS (Continued)

LIST OF FIGURES

LIST OF FIGURES (Continued)

LIST OF FIGURES (Continued)

LIST OF FIGURES (Continued)

LIST OF TABLES

LIST OF TABLES (Continued)

LIST OF TABLES (Continued)

LIST OF TABLES (Continued)

LIST OF TABLES (Continued)

LIST OF TABLES (Continued)

LIST OF ACRONYMS AND SYMBOLS

AGL	above ground level
APRA	atmospheric parametric risk analysis
ASTM	American Society for Testing and Materials
$BaSO_4$	barium sulfate
BNpdf	bivariate normal probability density function
CAT	clear-air turbulence
CIRA	COSPAR International Reference Atmosphere
CMDL	Climate Monitoring and Diagnostics Laboratory
CO_2	carbon dioxide
DOE	Department of Energy
DOL	day of launch
DRWP	Doppler radar wind profiler
DSF	daily statistics file
EAFB	Edwards Air Force Base
ERA	Edwards Reference Atmosphere
FAA	Federal Aviation Administration
GGUAS	Global Girded Upper Air Statistics
GRAM	Global Reference Atmospheric Model
GSFC	Goddard Space Flight Center
GUACA	Global Upper Air Climatic Atlas
HBCU	Historically Black Colleges and Universities

LIST OF ACRONYMS AND SYMBOLS (Continued)

Hg	mercury
ICAO	International Civil Aviation Organization
IP	in-plane
IR	infrared
ISO	International Standardization Organization
JSC	Johnson Space Center
KSC	Kennedy Space Center
LB	land breeze
lox	liquid oxygen
L.S.	large scale
LST	local standard time
MAP	Middle Atmospheric Program
MET	Marshall Engineering Thermosphere
MFFG	median filter/first guess
MG	Meteorology Group
MIL-SPEC	military specification
MKS	meter-kilogram-second
MSFC	Marshall Space Flight Center
MSL	mean sea level
NASP	National Aero-Space Plane
NIAM	NASP Integrated Atmospheric Model
NLS	National Launch System

NOAA	National Oceanic and Atmospheric Administration
NREL	National Renewable Energy Laboratory
OP	out-of-plane
PRA	Patrick Reference Atmosphere
PSD	power spectrum density
PW	precipitable water
RCC	Range Commanders Council
R&D	research and development
RD	relative deviation
RF	radio frequency
RMS	root mean square
RRA	Range Reference Atmosphere
SB	sea breeze
SI	International System of Units
SRB	solid rocket booster
SSC	Stennis Space Center
SSE	Surface meteorology and Solar Energy
SSP	Space Shuttle Program
STAR	solar and thermal atmospheric radiation
STD	standard deviation
TCL	trailing convergence line
TMY2	typical meteorological year, version 2

UV	ultraviolet
VAFB	Vandenberg Air Force Base
VRA	Vandenberg Reference Atmosphere
VWM	vector wind model
WMO	World Meteorological Organization
WRC	World Radiation Center
WRR	World Radiometric Reference
WSMR	White Sands Missile Range

NOMENCLATURE

A	gust amplitude; positive constant
a	vehicle flight azimuth; von Karman constant
b	standard deviation
C	cospectrum
CV	coefficients of variation
c	parameter
c_i	dimensionless constant
D	percentage
d	distance
d_m	gust half-width
E	spectral density; emittance of surface; irradiance
E_i	emittance of object
F_p	failure probability
f	function
f_w	correction for wind speed
G	gust factor
H	height; scales of distance
H_b	height of the base of the gust
h	shear intervals
I	solar radiation
I_{DH}	direct horizontal solar radiation
I_{dH}	diffuse scattered radiation
I_{DN}	direct normal incident solar radiation
I_{TH}	horizontal solar radiation
I_{TN}	total normal solar radiation
I_{TS}	total radiation received at surface
I_i	blackbody with several radiation sources
K	magnitude of wave number vector
k	shape parameter
k_z	vertical wave number
L	scale length; standard deviation of turbulence; gust length
M	molecular weight; multiplication factor

m	air mass
m_w	parameter
N	desired lifetime (years)
P	probability; pressure
p	percentile level constant
p_e	probability reference ellipse
Q	quadrature spectrum
q	aerodynamic pressure
R	nondimensional quantity; universal gas constant
r	conditional probability density function for wind speed; correlation coefficients
S	spectrum; solar constant
s_U	standard deviation
s_V	standard deviation
$\mathcal{T}$	transmittance
T	number of flight hours; design lifetime; total time; dimensionless time step; temperature
T_A	air temperature
T_D	design return period
T_R	blackbody temperature
T_S	surface temperature
T_V	virtual temperature
t	time
t_i	amount of time spent in the *i*th flight regime
$t_N{}^*$	dimensional time
U	calculated risk; zonal wind component
u	peak wind speed; longitudinal component of turbulence (subscript)
$u^*{}_0$	surface friction velocity
u_g	gust
u_I	peak instantaneous vertical average wind speed
u_i	dimensionless gust
u_P	vertical average peak wind speed
u_r	reference level wind speed
$u(z)$	steady-state wind profile
$u(z_r)$	quasi-steady wind speed at height z
V	meridional wind component; gust model; volume

NOMENCLATURE (Continued)

V_d	discrete gust
V_m	gust magnitude; maximum velocity
v	meridional wind component; lateral component of turbulence (subscript)
W	wind speed
W_D	design speed
w	mixing ratio of water vapor to dry air; Wien's displacement constant; wind speed; vertical component of turbulence (subscript)
w^*	gust velocity
X	reduced variable for wind shear
x	variable
Y	reduced variable for wind speed
y	variable; load quantity
y_1	head wind component
y_2	cross wind component
Z	required height
z	height; altitude above mean sea level
z_0	surface roughness length
z_r	reference height
α	angle of attack parameter; azimuth
β	angle of sideslip parameter; tilt angle
γ	parameter; nondimensional quantity
Δ	angle between the wind vectors
ΔT_{BS}	surface temperature differential resulting in a change in blackbody temperature
Δ_t	dimensional time step
δ	optical depth
δ_c	cloud optical depth
θ	zenith angle; wind direction
λ	wavelength; gust thickness parameter
(λ)	vertical scale of motion
λ_e	bivariate normal probability ellipse
$\lambda_{\max}$	wavelength of maximum radiation intensity for the blackbody
μ	parameter
ξ	respective means parameter
ρ	linear correlation coefficient; mass density

NOMENCLATURE (Continued)

ρ_S	atmospheric density at sea level
σ	Stefan-Boltzmann constant
σ^2	variance of turbulence
σ_x	standard deviation
σ_y	standard deviation
σ_η	standard deviation
τ	nondimensional quantity; average period of length in time
Φ_{ii}	three-dimensional gust spectrum
Φ_{jj}	three-dimensional gust gradient spectrum
Φ_w	spectra lateral component of turbulence
ϕ	phase angle
Ψ	parameter (depends on stability)
Ω	wave number
ω	frequency

2. WINDS

2.1 Introduction

An aerospace vehicle's response to atmospheric disturbances, especially wind, must be carefully evaluated to ensure that the design will meet its operational requirements. The choice of criteria depends on the specific launch location(s), vehicle configuration, and mission. The vehicle's design, operation, and flight procedures must be separated into phases for proper assessment of environmental influences and impacts upon its life history. These phases include (1) the initial purpose and concept of the vehicle, (2) its preliminary engineering design for flight, (3) its structural design, (4) its guidance and flight control design, (5) optimizations of its design limits, and (6) the final assessment of its capability for launch and operations.

Because the wind environment significantly affects the design and operation of aerospace vehicles, it is necessary to use good technical judgment and apply sound engineering principles in preparing wind criteria that are descriptive and representative. Although wind criteria guidelines contained in this document were especially prepared for application to aerospace vehicle programs, the information is applicable to other areas such as aeronautical engineering, architecture, atmospheric diffusion, wind and solar energy conversion research, and many others. The proper selection, analysis, and interpretation of wind information are responsibilities of the atmospheric scientists working in collaboration with the design engineers.

The information given in section 2 covers wind models and criteria guidelines applicable to various design problems. The risk level selected for the design depends upon the design philosophy used by management for the aerospace vehicle development effort. To maximize vehicle performance flexibility, it is considered best to utilize those wind data associated with the minimum acceptable risk levels. In addition, the critical mission-related parameters, such as exposure time of the vehicle being affected by the natural environment quantities, launch windows, reentry periods, launch turnaround periods, etc. should be considered carefully. Initial design work using unbiased (with respect to wind) trajectories based on nondirectional ground or in-flight winds may be used unless the vehicle and its mission are well known and the exact launch azimuth and time(s) are established and adhered to throughout the program. In designs that use wind-biased trajectories and directional wind criteria, rather severe wind constraints can result if the vehicle is used for other missions, different flight azimuths, or if other vehicle configurations are developed. Therefore, caution must be exercised in using wind criteria models to ensure consistency with the physical interpretation of each specific vehicle design problem relative to the overall design philosophy for the vehicle. Several references are cited that discuss special and specific problems related to the development and specification of wind environments for aerospace vehicle programs.

A comprehensive historical account of wind models and studies used to support design analyses for various NASA aerospace vehicles, including the Space Shuttle, is documented in *NASA/CR—1998–208859*, "A Compendium of Wind Statistics and Models for the NASA Space Shuttle and Other Aerospace Vehicle Programs" (ref. 2-1). In addition, section 2.4 "Historical Ascent Flight Wind Profile Information" contains additional material on this subject.

A listing of other wind-related subsectional locations within this document is given on p. 2-144 (sec. 2.6).

2.2 Ground Wind (<150 m)

2.2.1 Introduction

Ground winds for aerospace vehicle development applications are defined to be those winds in the lowest 150 m (492 ft) of the atmosphere. The winds in this layer of the atmosphere are characterized by very complicated three-dimensional flow patterns with rapid variations in magnitude and direction in space and time. An engineering requirement exists for models that define the structure of wind in this layer because of the complicated and possibly critical manner in which a vehicle might respond to certain aspects of the flow, both when the vehicle is stationary on the launch pad and during the first few seconds after the launch. The forces generated by von Karman vortex shedding are an example of the effect of wind on aerospace vehicles. These forces can result in base bending moments while the vehicle is on the launch pad and pitch and yaw plane angular accelerations and vehicle drift during lift-off. Other equally important examples can be cited. The basic treatment of the ground wind problem relative to vertically oriented vehicles on-pad and during lift-off has been to estimate the risk of encountering crucial aspects of wind along the vertical. It should be noted that, in addition to the engineering requirements for on-pad and launch winds for vertically ascending vehicles, a requirement for ground wind models also exists for horizontally flying vehicles for takeoff and landing. This aspect of the natural wind environment is discussed in sections 2.3.12 through 2.3.15.

Because ground wind data are applied by aerospace vehicle engineers in numerous ways, depending on the specific problem, various viewpoints and kinds of analytical techniques were used to obtain the environmental models presented here. Program planning, for instance, requires considerable climatological insight to determine the frequency and persistence distributions for wind speeds and wind directions. However, for design purposes, the aerospace vehicle must withstand certain unique predetermined structural loads that are generated from exposure to known peak ground wind conditions. Ground wind profiles and the ground wind turbulence spectra contribute to the development of the design ground wind models. Surface roughness, launch site structures, thermal environment, and various transient local and large-scale meteorological systems influence the ground wind environment for each launch site. The Cape Canaveral sea/land breeze conditions encompass both the ground and inflight wind regions >3,000 ft. If one considers the return flow aloft, this may occur above 3,000 ft. The characteristics of these winds and associated meteorological characteristics are described in section 2.5, Cape Canaveral (KSC) Sea/Land Breeze Winds. Surface winds including mountain-influenced winds such as mistral, foehn, Santa Ana, and Chinook winds are discussed in section 5.2.2.5 under surface wind.

2.2.2 Considerations in Ground Wind Design Criteria Development

To establish the ground wind design criteria for aerospace vehicles, several important factors must be considered:

(1) Where is the vehicle to operate?
(2) What is the launch location?
(3) What are the proposed vehicle missions?
(4) How many hours, days, or months will the vehicle be exposed to ground winds?
(5) What are the consequences of operational constraints that may be imposed on the vehicle because of wind constraints?
(6) What are the consequences if the vehicle is destroyed or damaged by ground winds?
(7) What are the cost and engineering practicalities for designing a functional vehicle to meet the desired mission requirements?
(8) What is the risk that the vehicle will be destroyed or damaged by excessive wind loading?

In view of this list of questions, or any similar list that a design group may enumerate, it becomes obvious that the establishment of ground wind environment design criteria for an aerospace vehicle requires an interdisciplinary approach involving several engineering and scientific disciplines. Furthermore, the process is an iterative one. To begin the iterative process, specific information on ground winds is required.

2.2.3 Introduction to Exposure Periods Analysis

Valid, quantitative answers to such questions as the following are of primary concern in the design, mission planning, and operation of aerospace vehicles:

(1) What is the probability that the peak ground wind at some specified reference height will exceed (or not exceed) a given magnitude in some specified time period?
(2) Given a design wind profile in terms of peak wind speed versus height from 10 to 150 m, what is the probability that the design wind profile will be exceeded in some specified time period?

Given a statistical sample of peak wind measurements for a specific location, the first question can be answered in as much detail as a statistical analyst finds necessary and sufficient. This first question has been thoroughly analyzed for Kennedy Space Center (KSC), partially for Vandenberg Air Force Base (VAFB), and to a lesser degree for other locations of interest.

The analysis becomes considerably more complex in answering the second question. A wind profile is required, and to develop the model, measurements of the wind profiles by properly instrumented ground wind towers are required as well as a program for scheduling the measurements and data reduction. Every instantaneous wind profile is unique; similarity is a matter of degree. Given the peak wind speed at one height, there is a whole family of possible profiles extending from the specified wind at that height. Thus, for each specified wind speed at a given height, there is a statistical distribution of wind profiles. Recommended profile shapes for KSC and other locations are given in the following sections. The analysis needed to answer the second question is not complete, but we can assume that, given a period of time, the design wind profile shape will occur for a specified wind speed at a given height. For example, in the event that a thunderstorm passes over the vehicle, it is logical to assume that the design wind profile shape will occur and that the chance of the design wind profile being exceeded is the same as the probability that the peak wind (gust) during the passage of the thunderstorm (see sec. 9.4.2) will strike the vehicle or point of interest (ref. 2-2).

2.2.4 Development of Extreme Value Concept

It has been estimated from wind tunnel tests that only a few seconds are required for the wind to produce near steady-state drag loads on a launch vehicle in an exposed condition on the launch pad. For this and other reasons, the peak wind speed has been adopted as the fundamental measurement of wind for use in design studies. Equally important, when the engineering applications of winds can be made in terms of peak wind speeds, it is possible to obtain an appropriate statistical sample that conforms to the fundamental principles of extreme value theory. One hour is a convenient and physically meaningful minimum time interval from which to select the peak wind. An hourly peak wind speed sample has been established for KSC from wind information recorded on continuous-recording charts. Representative peak wind samples for VAFB have been derived from hourly steady-state wind measurements using statistical and physical principles. From the hourly peak wind records, the daily and monthly peak wind records can be computed. An extreme value probability function is used to summarize these statistics.

2.2.4.1 Envelope of Distributions. In the development of statistics for peak winds, it was recognized that the probability of hourly, daily, and monthly peak winds exceeding (or not exceeding) specified values varied with time of day and from month to month. The Gumbel extreme value probability distribution (ref. 2-3) is an excellent fit to the samples of hourly, daily, monthly, bimonthly (in two combinations), and trimonthly (in three combinations) periods taken over the complete period of record, thereby justifying the use of this distribution. However, in establishing vehicle wind design criteria for the peak winds versus exposure time, it is desired to present a set of wind statistics in such a manner that every reference period and exposure time would not have to be examined to determine the probability that the largest peak wind during the exposure time would exceed some specified magnitude. To accomplish this objective, envelopes of the distributions of the largest peak winds for various time increments for the various reference periods were constructed. For example, to obtain the envelope distribution of hourly peak winds for the month of March, the largest peak wind was selected at each percentage point from the 24 peak wind distributions (one for each hour). For a 365-day exposure, the distribution for the extreme largest yearly peak wind data sample is used.

Selected wind profile envelopes of distributions are given in section 2.2.5.5. It is recommended that these envelopes of distributions be used for vehicle wind design considerations. This recommendation is made under the assumption that it is not known what time of day or season of year critical vehicle operations are to be conducted. Furthermore, it is not desirable to design a vehicle to operate only during selected hours or months. Should all other design alternatives fail to lead to a functionally engineered vehicle with an acceptable risk of not being compromised by wind loads, then distributions for peak winds by time of day for monthly reference periods may be considered for limited missions. For vehicle operations, detailed statistics of peak winds for specific missions are meaningful for management decisions, in planning missions, and in establishing mission rules and alternatives for the operational procedures. To present the wind statistics for all these purposes is beyond the scope of this document. Each space mission has many facets that make it difficult to generalize and to present all the available statistics in brief form.

2.2.5 Design Ground Wind Profiles for Aerospace Vehicles

Specific information about the wind profile is required to calculate ground wind loads on aerospace vehicles. The Earth's surface is a rigid boundary that exerts a frictional force on the lowest layers of the atmosphere, causing the wind to approach zero velocity at the ground. In addition, the characteristic length and velocity scales of the mean (steady-state) flow in the first ≈150 m (boundary layer) of the atmosphere combine to yield extremely high Reynolds numbers with values that range between approximately 10^6 and 10^8, so that for most conditions (wind speeds >1 m/s) the flow is fully turbulent. The lower boundary condition, the thermal and dynamic stability properties of the boundary layer, the distributions of the large-scale pressure, the Coriolis force, and the structure of the turbulence combine to yield an infinite number of wind profiles.

Data on basic wind speed profiles given in this section are for use in vehicle design studies. With respect to design practices, the application of peak winds and the associated turbulence spectra and discrete gusts should be considered. The maximum response obtained for the selected risk levels for each physically realistic combination of conditions should be employed in the design. Care should be exercised so that wind inputs are not taken into account more than once. For example, the discrete gust and spectrum (a discrete bandwidth of energy in the turbulent spectrum) of turbulence are representations of the same thing, namely atmospheric turbulence. Thus, one should not calculate the responses of a vehicle due to the discrete gust and spectrum and then combine the results by addition, root-sum-square, or any other procedure since these inputs represent the same thing. Rather, the responses should be calculated with each input and then enveloped.

2.2.5.1 Peak Wind Concept. An example of a peak wind speed for an hourly time period is given in figure 2-1. Peak wind statistics have three advantages over mean wind statistics:

(1) Peak wind statistics do not depend on an averaging operation as do mean wind statistics.

(2) To construct a mean wind sample, a chart reader or weather observer must perform an "eyeball" or electronic average of the wind data, causing the averaging process to vary from day to day according to the mood of the observer, and from observer to observer, and to the integration technique used. Hourly peak wind speed readings avoid this subjective averaging process.

(3) To monitor winds during the countdown phase of an aerospace vehicle launch, it is much easier to monitor peak wind speed than the mean wind speed. However, with today's modern electronic computational techniques, monitoring a mean wind speed over any given time interval is not as serious a problem.

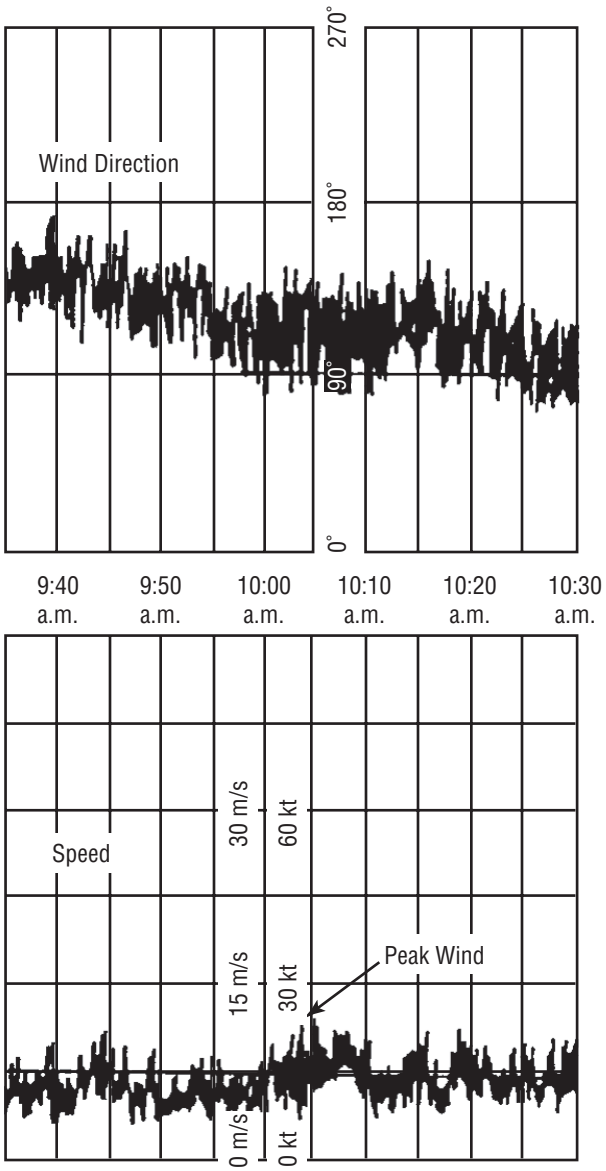

Figure 2-1. Example of an hourly peak wind speed and associated direction record.

Smith et al. (ref. 2-4) have performed extensive statistical analyses with peak wind speed samples measured at the 10-m level. In the course of the work, the concept of exposure period probabilities was introduced into the design and operation of aerospace vehicles. By determining the distribution functions of peak wind speeds for various periods of exposure (hour, day, month, year, etc.), it is possible to determine the probability of a certain peak wind speed magnitude occurring during a prescribed period of exposure. Thus, if an operation requires, for example, 1 hr to complete, and if the critical wind loads on the aerospace vehicle can be defined in terms of the peak wind speed, then it is the probability of occurrence of the peak wind speed during a 1-hr period that gives a measure of the risk of the occurrence of structural failure. Similarly, if an operation requires 1 day to complete, then it is the probability of occurrence of the peak wind speed during a 1-day period that gives a measure of the risk of structural failure.

These peak wind statistics are usually transformed to the 18.3-m (60-ft) reference level for design purposes, or sometimes to higher levels for operational applications. However, to perform loading and response calculations resulting from steady-state and random turbulence drag loads and von Karman vortex shedding loads, the engineer requires information about the vertical variation of the mean wind and the structure and turbulence in the atmospheric boundary layer. The philosophy is to extrapolate the peak wind statistics up in height via a peak wind profile, and the associated steady-state or mean wind profile is obtained by applying a gust factor that is a function of wind speed and height.

2.2.5.2 Peak Wind Profile Shapes. To develop a peak wind profile model, ≈6,000 hourly peak wind speed profiles measured at NASA's ground wind tower facility at KSC were analyzed. The sample, composed of profiles of hourly peak wind speeds measured at the 18-, 30-, 60-, 90-, 120-, and 150-m levels, showed that the variation of the peak wind speed in the vertical, below 150 m, for engineering purposes, could be described with a power law relationship given by

$$u(z) = u_{18.3}\left(\frac{z}{18.3}\right)^{k} \quad , \tag{2.1}$$

where $u(z)$ is the peak wind speed (m/s) at height z in meters above the natural grade and $u_{18.3}$ is a known peak wind speed at z = 18.3 m. The peak wind is referenced to the 18.3-m (60-ft) level because this level has been selected as the standard reference for the KSC launch area. A reference level should always be stated when discussing ground winds to avoid confusion in interpretation of risk statements and structural load calculations.

A statistical analysis of the peak wind speed profile data revealed that, for engineering purposes, k is distributed normally for any particular value of the peak wind speed at the 18.3-m level. Thus, for a given percentile level of occurrence, k is approximately equal to a constant for $u_{18.3} \leq 2$ m/s. For $u_{18.3} > 2$ m/s,

$$k = c\left(u_{18.3}\right)^{-3/4} \quad , \tag{2.2}$$

where $u_{18.3}$ has the units of meters per second. The parameter, c, for engineering purposes, is distributed normally with mean value 0.52 and standard deviation 0.36 and has units of $(\text{m/s})^{3/4}$. The distribution of k as a function of $u_{18.3}$ is depicted in figure 2-2. The $\bar{k}+3\sigma$ values are used in design studies.

2.2.5.3 Instantaneous Extreme Wind Profiles. The probability that the hourly peak wind speeds will occur (within the boundary layer ≤150 m) simultaneously is small. Accordingly, the practice of using peak wind profiles introduces some conservatism into the design criteria; however, the probability is relatively large that when the hourly peak wind occurs at the 18.3-m level, the winds at the other levels will almost take on the hourly peak values.

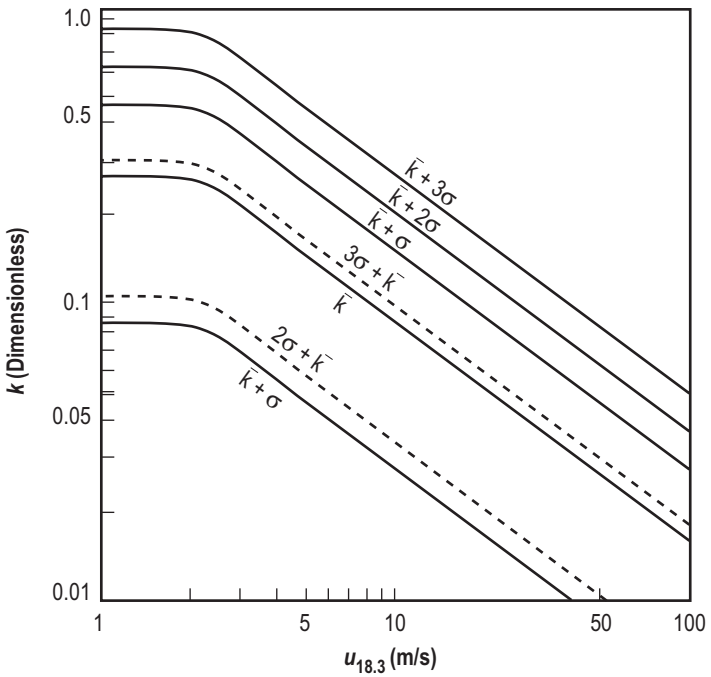

Figure 2-2. Distribution of the peak wind profile parameter *k* for various peak wind speeds at the 18.3-m (60-ft) reference level for KSC.

To gain some insight into this question, ≈35 hr of digitized magnetic tape data were analyzed. The data were digitized at 0.2-s intervals and partitioned into 0.5-, 2-, 5-, and 10-min samples. The vertical average peak wind speed, u_P, and the 18.3-m mean wind speed, $\bar{u}_{18.3}$, were calculated for each sample. In addition, the instantaneous vertical average wind speed time history at 0.2-s intervals was calculated for each sample, and the peak instantaneous vertical average wind speed, u_I, was selected for each sample. The quantity $\bar{u}_I / \bar{u}_P$ was then interpreted to be a measure of how well the peak wind profile approximated the instantaneous extreme wind profile.

Figure 2-3 is a plot of $\bar{u}_I / \bar{u}_P$ as a function of $\bar{u}_{18.3}$. The data points tend to scatter about a mean value of $\bar{u}_I / \bar{u}_P$ 0.93; however, some of the data points have values equal to 0.98. These results justify the use of peak wind profiles for engineering design purposes.

2.2.5.4 Peak Wind Profile Shapes for Other Test Ranges and Sites. Detailed analyses of ground wind profile statistics are not available for test ranges and sites other than KSC. The exponent *k* in equation (2.1) is a function of wind speed, surface roughness, etc. For moderate surface roughness conditions, the extreme value of *k* is usually ≤0.2 during high winds (>15 m/s). For design and planning purposes for test ranges and sites other than KSC, it is recommended that the values of *k* given in table 2-1 be used. These values of *k* are the only values specified in this document for sites other than KSC and represent estimates for the 99.87 percentile, or 3σ (0.13-percent risk), values for the peak wind speed profile shape. A recent study resulted in $k = 0.085$ for Edwards Air Force Base (EAFB), with associated peak wind speeds corresponding to an altitude of 4 m (13 ft).

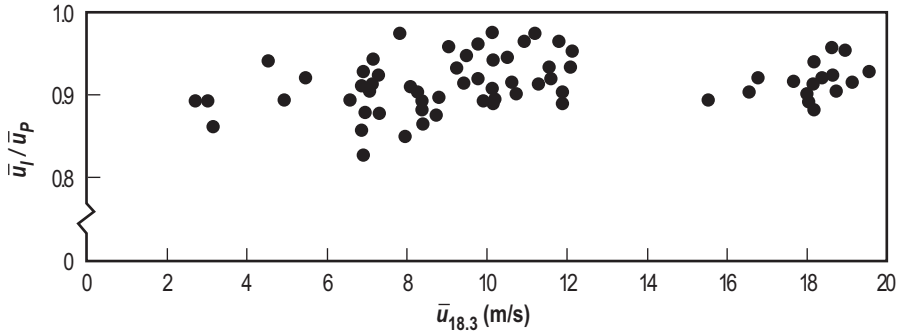

Figure 2-3. The ratio $\bar{u}_I / \bar{u}_P$ as a function of the 18.3-m (60-ft) reference level mean wind speed $\bar{u}_{18.3}$ for a 10-min sampling period.

Table 2-1. Values of *k* to use for test ranges other than KSC.

k Value	18.3-m Reference Level Peak Wind Speed (m/s)
$k = 0.2$	$7 \leq u_{18.3} < 22$
$k = 0.14$	$22 \leq u_{18.3}$

2.2.5.5 Aerospace Vehicle Design Wind Profiles. The data presented in this section provide basic peak wind speed profile (envelope) information for test, free-standing, launch, and lift-off conditions to ensure satisfactory performance of an aerospace vehicle. To establish vehicle responses, the peak design surface winds are assumed to act normal to the longitudinal axis of the vehicle on the launch pad and to be from the most critical direction.

2.2.5.5.1 Design Wind Profiles for Kennedy Space Center. Peak wind profiles are characterized by two parameters: (1) The peak wind speed at the 18.3-m reference level and (2) the shape parameter *k*. Once these two quantities are defined, the peak wind speed profile envelope is completely specified. Accordingly, to construct a peak wind profile for KSC, in the context of launch vehicle loading and response calculations, two pieces of information are required. First, the risk of exceeding the design wind peak speed at the reference level for a given period must be specified. Once this quantity is given, the design peak wind speed at the reference level is automatically specified (fig. 2-4). Second, the risk associated with compromising the structural integrity of the vehicle once the reference level design wind occurs must be specified. This second quantity and the reference level peak wind speed will determine the value of *k* that is to be used in equation (2.1).

It is recommended that the $\bar{k} + 3\sigma$ value of *k* be used for the design of aerospace vehicles. Thus, if an aerospace vehicle designed to withstand a particular value of peak wind speed at the 18.3-m reference level is exposed to that peak wind speed, the vehicle has at least a 99.865-percent chance of withstanding possible peak wind profile conditions. See table 2-56 for standarized normal (univariate) distribution for percentiles and interpercentile ranges.

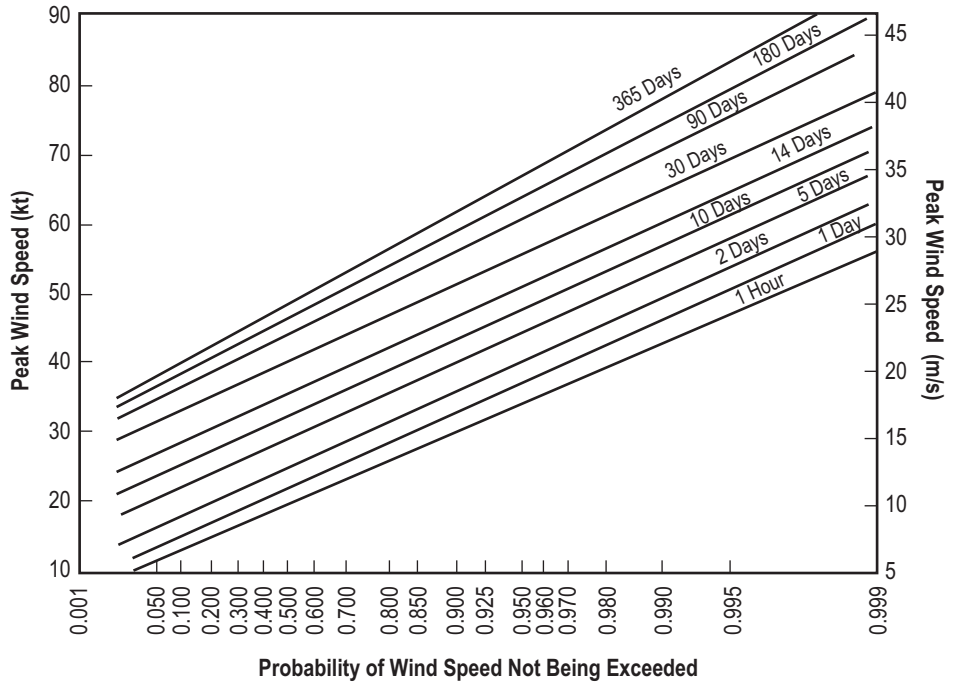

Figure 2-4. Reference level of 18.3 m (60 ft); KSC peak wind speed for windiest reference period versus probability for several exposure periods applicable to vehicle design criteria development.

Operational ground wind constraints for established vehicles should be determined for a reference level (above natural grade) near the top of the vehicle while on the launch pad. The profile may be calculated using equations (2.1) and (2.2) with a value of $k = \bar{k} + 3\sigma$. This will produce a peak wind profile envelope associated with an upper reference level ground wind constraint.

Table 2-2 contains peak wind speed profiles for various envelope values of peak wind speed at the 10-m (33-ft) level for fixed values of risk for the worst monthly-hourly reference periods of the year for a 1-hr exposure. To construct these profiles, the 1-hr exposure period statistics for each hour in each month were constructed. This exercise yielded 288 distribution functions (12 mo times 24 hr), which were enveloped to yield the largest or "worst" 10-m-level peak wind speed associated with a given level of risk for all monthly-hourly reference periods. Thus, for example, according to table 2-2 there is at most a 10-percent risk that the peak wind speed will exceed 13.9 m/s (27 kt) during any particular hour in any particular month at the 10-m level; and, if a peak wind speed equal to 13.9 m/s (27 kt) should occur at the 10-m level, then there is only a 0.135-percent chance that the peak wind speed will exceed 24.1 m/s (46.8 kt) at the 152.4-m (500 ft) level or the corresponding values given at the other heights.

Table 2-2. Peak wind speed profile envelopes for various values of risk of exceeding the 10-m- (33-ft-) level peak wind speed for 1-hr exposure (hourly-monthly reference period) for KSC.

Height		Risk (%)									
		20		10		5		1		0.1	
(m)	(ft)	(m/s)	(kt)	(m/s)	(kt)	(m/s)	(kt)	(m/s)	(kt)	(m/s)	(kt)
10.0	33	11.8	22.9	13.9	27.0	15.8	30.8	20.3	39.5	26.7	51.9
18.3	60	13.5	26.3	15.7	30.5	17.7	34.4	22.3	43.4	28.8	56.0
30.5	100	15.2	29.5	17.4	33.8	19.5	37.9	24.2	47.0	30.8	59.8
61.0	200	17.8	34.5	20.0	38.9	22.1	43.0	26.9	52.3	33.6	65.5
91.4	300	19.5	37.8	21.7	42.2	23.9	46.4	28.7	55.7	35.4	68.9
121.9	400	20.8	40.4	23.0	44.7	25.2	48.9	30.0	58.3	36.8	71.5
152.4	500	21.9	42.5	24.1	46.8	26.2	51.0	31.0	60.3	37.8	73.6

Tables 2-3 through 2-5 contain peak wind speed profile envelopes for various values of peak wind speed at the 10-m (33-ft) level and fixed values of risk for various exposure periods. The 1-day exposure values of peak wind speed were obtained by constructing the daily peak wind statistics for each month and then enveloping these distributions to yield the worst 1-day exposure, 10-m-level peak wind speed for a specified value of risk (daily-monthly reference period). The 30-day exposure envelope peak wind speeds were obtained by constructing the monthly peak wind statistics for each month and then constructing the envelope of the distributions (monthly-annual reference period). The 10-day exposure statistics were obtained by interpolating between the 1- and 30-day exposure period results. The envelopes of the 90-day exposure period statistics are the 90-day exposure statistics associated with the 12 trimonthly periods (January-February-March, February-March-April, March-April-May, etc.) (90-day annual reference period). Finally, the 365-day exposure period statistics were calculated with the annual peak wind sample (17 data points) to yield one distribution. Tables 2-3 through 2-5 contain the largest or "worst" 10-m-level peak wind speed associated with a given level of risk for the stated exposure periods.

Table 2-3. Peak wind speed envelopes for a 10-percent risk value of exceeding the 10-m- (33-ft-) level peak wind speed for various reference periods of exposure for KSC.

Height		Exposure (Days)									
		1		10		30		90		365	
(m)	(ft)	(m/s)	(kt)	(m/s)	(kt)	(m/s)	(kt)	(m/s)	(kt)	(m/s)	(kt)
10.0	33	15.2	29.6	20.5	39.8	24.3	47.1	26.8	52.0	29.5	57.4
18.3	60	17.1	33.2	22.5	43.7	26.4	51.2	28.9	56.2	31.8	61.7
30.5	100	18.8	36.6	24.3	47.3	28.3	54.9	30.9	60.0	33.8	65.6
61.0	200	21.5	41.8	27.1	52.7	31.1	60.4	33.8	65.6	36.7	71.3
91.4	300	23.2	45.1	28.9	56.1	32.9	63.9	35.6	69.1	38.5	74.8
121.9	400	24.5	47.6	30.2	58.6	34.2	66.5	36.9	71.7	39.8	77.4
152.4	500	25.6	49.7	31.2	60.7	35.3	68.5	38.0	73.8	40.9	79.5

Table 2-4. Peak wind speed profile envelopes for a 5-percent risk value of exceeding the 10-m- (33-ft-) level peak wind speed for various reference periods of exposure for KSC.

Height		Exposure (days)									
		1		10		30		90		365	
(m)	(ft)	(m/s)	(kt)	(m/s)	(kt)	(m/s)	(kt)	(m/s)	(kt)	(m/s)	(kt)
10.0	33	17.3	33.7	22.6	43.9	26.4	51.2	29.0	56.4	32.1	62.3
18.3	60	19.3	37.4	24.7	47.9	28.5	55.4	31.2	60.7	34.3	66.7
30.5	100	21.0	40.9	26.5	51.6	30.5	59.2	33.2	64.6	36.4	70.7
61.0	200	23.7	46.1	29.3	57.0	33.3	64.8	36.2	70.2	39.3	76.4
91.4	300	25.5	49.5	31.1	60.4	35.1	68.2	38.0	73.7	41.2	80.0
121.9	400	26.8	52.0	32.4	63.0	36.5	70.8	39.3	76.4	42.5	82.6
152.4	500	27.8	54.1	33.5	65.1	37.5	72.9	40.4	78.5	43.6	84.7

Table 2-5. Peak wind speed profile envelopes for a 1-percent risk value of exceeding the 10-m- (33-ft-) level peak wind speed for various reference periods of exposure for KSC.

Height		Exposure (days)									
		1		10		30		90		365	
(m)	(ft)	(m/s)	(kt)	(m/s)	(kt)	(m/s)	(kt)	(m/s)	(kt)	(m/s)	(kt)
10.0	33	22.1	43.0	27.4	53.3	31.2	60.6	34.2	66.5	37.8	73.4
18.3	60	24.2	47.0	29.6	57.5	33.5	65.0	36.6	71.0	40.2	78.0
30.5	100	26.1	50.7	31.6	61.3	35.5	68.9	38.6	75.0	42.3	82.1
61.0	200	28.9	56.1	34.5	66.9	38.4	74.7	41.6	80.8	45.3	88.0
91.4	300	30.6	59.5	36.3	70.4	40.3	78.2	43.5	84.4	47.2	91.7
121.9	400	32.0	62.1	37.6	73.0	41.6	80.8	44.8	87.1	48.6	94.3
152.4	500	33.0	64.1	38.7	75.1	42.7	82.9	45.9	89.2	49.7	96.5

It is recommended that the data in tables 2-2 through 2-5 be used as the basis for aerospace vehicle design for KSC operations. Wind profile statistics for the design of permanent ground support equipment are discussed in section 2.2.10.

Mean wind profiles or steady-state wind profiles can be obtained from the peak wind profiles by dividing the peak wind by the appropriate gust factor (sec. 2.2.7). It is recommended that the 10-min gust factors be used for structural design purposes. Application of the 10-min gust factors to the peak wind profile corresponds to averaging the wind speed over a 10-min period. This averaging period appears to result in a stable mean value of the wind speed. Within the range of variation of the data, the 1-hr and 10-min gust factors are approximately equal for sufficiently high wind speed. This occurs because the spectrum of the horizontal wind speed near the ground is characterized by a broad energy gap centered at a frequency $\cong 0.000278$ Hz (1 cycle/hr) and typically extends over the frequency domain 0.000139 Hz (0.5 cycle/hr) $< \omega <$ 0.0014 Hz (5 cycles/hr). The Fourier spectral components associated with frequencies <0.000278 Hz (1 cycle/hr) correspond to the meso- and synoptic-scale atmospheric motions, while the remaining high-frequency spectral components correspond to mechanically and thermally-produced turbulence. Thus, a statistically stable estimate of the mean or steady-state wind speed can be obtained

by averaging over a period in the range from 10 min to 1 hr. Since this period is far longer than any natural period of structural vibration, it assures that effects caused by the mean wind properly represent steady-state, non-transient effects. The steady-state wind profiles, calculated with the 10-min gust factors, that correspond to those in tables 2-2 through 2-5 are given in tables 2-6 through 2-9.

Table 2-6. 10-min mean wind speed profile envelopes for various values of risk of exceeding the 10-m- (33-ft-) level mean wind speed for a 1-hr exposure (hourly-monthly reference period) for KSC.

Height		Risk (%)									
		20		10		5		1		0.1	
(m)	(ft)	(m/s)	(kt)	(m/s)	(kt)	(m/s)	(kt)	(m/s)	(kt)	(m/s)	(kt)
10.0	33	7.2	14.1	8.6	16.6	9.8	19.1	12.7	24.6	16.7	32.4
18.3	60	8.8	17.1	10.3	19.9	11.7	22.6	14.8	28.7	19.1	37.2
30.5	100	10.3	20.0	11.9	23.1	13.4	26.0	16.8	32.6	21.4	41.6
61.0	200	12.7	24.7	14.5	28.1	16.1	31.3	19.7	38.3	24.7	48.1
91.4	300	14.3	27.8	16.1	31.3	17.9	34.7	21.6	42.0	26.8	52.1
121.9	400	15.6	30.3	17.4	33.9	19.2	37.3	23.0	44.8	28.3	55.1
152.4	500	16.6	32.3	18.5	35.9	20.3	39.4	24.2	47.0	29.6	57.5

Table 2-7. 10-min mean wind speed profile envelopes for a 10-percent risk value of exceeding the 10-m- (33-ft-) level mean wind speed for various reference periods of exposure for KSC.

Height		Exposure (days)									
		1		10		30		90		365	
(m)	(ft)	(m/s)	(kt)	(m/s)	(kt)	(m/s)	(kt)	(m/s)	(kt)	(m/s)	(kt)
10.0	33	9.4	18.3	12.8	24.8	15.1	29.4	16.7	32.5	18.5	35.9
18.3	60	11.2	21.8	14.9	28.9	17.5	34.0	19.2	37.3	21.1	41.0
30.5	100	12.9	25.2	16.9	32.8	19.6	38.1	21.5	41.7	23.5	45.6
61.0	200	15.6	30.3	19.9	38.6	22.8	44.3	24.8	48.2	27.0	52.4
91.4	300	17.3	33.7	21.8	42.3	24.8	48.3	26.9	52.2	29.1	56.6
121.9	400	18.7	36.3	23.2	45.0	26.3	51.2	28.4	55.2	30.7	59.7
152.4	500	19.7	38.4	24.3	47.3	27.6	53.5	29.7	57.6	32.0	62.2

2.2.5.5.2 Design Ground Wind Profiles for Other Locations. Tables 2-10 through 2-17 contain recommended design ground wind profiles for several different risks of exceeding the 10-m- (33-ft-) level peak wind speed and 10-min mean wind speed for a 1-hr exposure period. These tables are based on the same philosophy as tables 2-2 and 2-6 for KSC. The locations for which data are provided include Stennis Space Center (SSC), MS; VAFB, CA; White Sands Missile Range (WSMR), NM; and EAFB, CA.

Table 2-8. 10-min mean wind speed profile envelopes for a 5-percent risk value of exceeding the 10-m- (33-ft-) level mean wind speed for various reference periods of exposure for KSC.

Height		Exposure (days)									
		1		10		30		90		365	
(m)	(ft)	(m/s)	(kt)	(m/s)	(kt)	(m/s)	(kt)	(m/s)	(kt)	(m/s)	(kt)
10.0	33	10.8	20.9	14.1	27.4	16.5	32.0	18.2	35.3	20.1	39.0
18.3	60	12.7	24.7	16.3	31.8	18.9	36.8	20.7	40.3	22.8	44.3
30.5	100	14.5	28.2	18.4	35.8	21.2	41.1	23.1	44.9	25.3	49.1
61.0	200	17.3	33.6	21.5	41.8	24.5	47.6	26.6	51.6	28.9	56.2
91.4	300	19.1	37.1	23.5	45.6	26.6	51.6	28.7	55.8	31.2	60.5
121.9	400	20.5	39.8	25.0	48.5	28.1	54.6	30.3	58.9	32.8	63.7
152.4	500	21.6	42.0	26.1	50.8	29.3	57.0	31.6	61.4	34.1	66.3

Table 2-9. 10-min mean wind speed profile envelopes for a 1-percent risk value of exceeding the 10-m- (33-ft-) level mean wind speed for various reference periods of exposure for KSC.

Height		Exposure (days)									
		1		10		30		90		365	
(m)	(ft)	(m/s)	(kt)	(m/s)	(kt)	(m/s)	(kt)	(m/s)	(kt)	(m/s)	(kt)
10.0	33	13.8	26.8	17.1	33.3	19.5	37.9	21.4	41.6	23.6	45.9
18.3	60	16.0	31.1	19.7	38.2	22.2	43.2	24.3	47.2	26.7	51.8
30.5	100	18.1	35.1	21.9	42.6	24.7	47.9	26.9	52.2	29.4	57.1
61.0	200	21.2	41.1	25.3	49.2	28.3	54.9	30.6	59.4	33.2	64.7
91.4	300	23.1	44.9	27.4	53.3	30.5	59.2	32.9	63.9	35.7	69.4
121.9	400	24.6	47.7	29.0	56.3	32.1	62.4	34.6	67.2	37.5	72.8
152.4	500	25.8	50.0	30.2	58.7	33.4	64.9	35.9	69.8	38.9	75.5

Table 2-10. Surface peak wind speed profile envelopes for various values of risk of exceeding the 10-m- (33-ft-) level peak wind speed for 1-hr exposure (hourly-monthly reference period) for the SSC area.

Height		Risk (%)									
		20		10		5		1		0.1	
(m)	(ft)	(m/s)	(kt)	(m/s)	(kt)	(m/s)	(kt)	(m/s)	(kt)	(m/s)	(kt)
10.0	33	10.2	19.8	12.3	23.9	14.2	27.6	19.1	37.2	27.3	53.0
18.3	60	11.5	22.4	13.9	27.0	16.0	31.2	21.5	42.0	29.7	57.7
30.5	100	12.8	24.8	15.4	29.9	17.8	34.5	23.9	46.5	31.8	61.9
61.0	200	14.6	28.4	17.7	34.3	20.4	39.6	27.4	53.4	35.1	68.1
91.4	300	15.9	30.8	19.2	37.2	22.1	43.0	29.8	57.9	37.2	72.2
121.9	400	16.8	32.7	20.3	39.4	23.4	45.5	31.5	61.4	38.7	75.2
152.4	500	17.6	34.2	21.3	41.3	24.5	47.7	33.0	64.3	39.9	77.5

Table 2-11. Surface mean wind speed profile envelopes for various values of risk of exceeding the 10-m- (33-ft-) level, 10-min mean wind speed for 1-hr exposure (hourly-monthly reference period) for SSC area.

Height		Risk (%)									
		20		10		5		1		0.1	
(m)	(ft)	(m/s)	(kt)	(m/s)	(kt)	(m/s)	(kt)	(m/s)	(kt)	(m/s)	(kt)
10.0	33	7.3	14.1	8.8	17.1	10.1	19.7	13.7	26.6	19.5	37.9
18.3	60	8.2	16.0	9.9	19.3	11.4	22.3	15.4	30.0	21.2	41.2
30.5	100	9.1	17.7	11.0	21.4	12.7	24.7	17.1	33.2	22.8	44.2
61.0	200	10.5	20.3	12.6	24.5	14.6	28.3	19.6	38.2	25.0	48.6
91.4	300	11.3	22.0	13.7	26.6	15.8	30.7	21.3	41.4	26.6	51.0
121.9	400	12.0	23.3	14.5	28.2	16.7	32.5	22.5	43.8	27.7	53.7
152.4	500	12.6	24.4	15.2	29.5	17.5	34.1	23.6	45.9	28.5	55.4

Table 2-12. Surface peak wind speed profile envelopes for various values of risk of exceeding the 10-m- (33-ft-) level peak wind speed for 1-hr exposure (hourly-monthly reference period) for VAFB.

Height		Risk (%)									
		20		10		5		1		0.1	
(m)	(ft)	(m/s)	(kt)	(m/s)	(kt)	(m/s)	(kt)	(m/s)	(kt)	(m/s)	(kt)
10.0	33	10.3	20.0	12.3	23.8	14.2	27.5	18.4	35.8	24.3	47.3
18.3	60	11.6	22.5	13.8	26.8	16.0	31.0	20.8	40.3	26.5	51.4
30.5	100	12.9	25.0	15.3	29.7	17.7	34.3	23.0	44.7	28.5	55.2
61.0	200	14.8	28.7	17.6	34.1	20.3	39.4	26.4	51.3	31.3	60.9
91.4	300	16.0	31.1	19.0	37.0	22.0	42.8	28.7	56.7	33.2	64.4
121.9	400	16.9	32.9	20.2	39.2	23.3	45.3	30.4	59.0	34.5	67.1
152.4	500	17.7	34.4	21.1	41.0	24.4	47.4	31.7	61.7	35.6	69.2

Table 2-13. Surface mean wind speed profile envelopes for various values of risk of exceeding the 10-m- (33-ft-) level, 10-min mean wind speed for 1-hr exposure (hourly-monthly reference period) for VAFB.

Height		Risk (%)									
		20		10		5		1		0.1	
(m)	(ft)	(m/s)	(kt)	(m/s)	(kt)	(m/s)	(kt)	(m/s)	(kt)	(m/s)	(kt)
10.0	33	7.4	14.3	8.9	17.0	10.1	19.6	13.1	25.6	17.4	33.8
18.3	60	8.3	16.1	9.9	19.2	11.4	22.1	14.8	28.8	18.9	36.7
30.5	100	9.2	17.8	10.9	21.2	12.6	24.5	16.4	31.9	20.3	39.5
61.0	200	10.5	20.5	12.6	24.4	14.5	28.1	18.9	36.7	22.4	43.5
91.4	300	11.4	22.2	13.6	26.4	15.7	30.5	20.5	39.8	23.7	46.0
121.9	400	12.1	23.5	14.4	28.0	16.7	32.3	21.7	42.1	24.7	17.9
152.4	500	12.7	24.6	15.1	29.3	17.4	33.8	22.7	44.0	25.5	49.4

Table 2-14. Surface peak wind speed profile envelopes for various values of risk of exceeding the 10-m- (33-ft-) level peak wind speed for 1-hr exposure (hourly-monthly reference period) for WSMR.

Height		Risk (%)									
		20		10		5		1		0.1	
(m)	(ft)	(m/s)	(kt)	(m/s)	(kt)	(m/s)	(kt)	(m/s)	(kt)	(m/s)	(kt)
10.0	33	7.9	15.3	10.7	20.9	12.7	24.7	17.7	34.3	26.8	52.1
18.3	60	8.9	17.3	12.1	23.6	14.3	27.9	20.0	38.8	29.2	56.7
30.5	100	9.9	19.1	13.4	26.1	15.9	30.9	22.1	42.9	31.3	60.9
61.0	200	11.3	22.0	15.4	30.0	18.2	35.5	25.4	49.3	34.4	66.9
91.4	300	12.3	23.8	16.7	32.6	19.8	38.5	27.6	53.4	36.5	71.0
121.9	400	13.0	25.2	17.7	34.5	21.0	40.8	29.2	56.6	38.0	73.9
152.4	500	13.7	26.4	18.5	36.1	22.0	42.7	30.6	59.3	39.2	76.2

Table 2-15. Surface mean wind speed profile envelopes for various values of risk of exceeding the 10-m- (33-ft-) level, 10-min mean wind speed for 1-hr exposure (hourly-monthly reference period) for WSMR.

Height		Risk (%)									
		20		10		5		1		0.1	
(m)	(ft)	(m/s)	(kt)	(m/s)	(kt)	(m/s)	(kt)	(m/s)	(kt)	(m/s)	(kt)
10.0	33	5.6	10.9	7.7	14.9	9.1	17.6	12.6	24.5	19.2	37.2
18.3	60	6.4	12.3	8.6	16.9	10.2	19.9	14.3	27.7	20.8	40.5
30.5	100	7.1	13.7	9.6	18.7	11.3	22.1	15.8	30.7	22.4	43.4
61.0	200	8.1	15.7	11.0	21.4	13.0	25.3	18.2	35.2	24.6	47.8
91.4	300	8.8	17.0	11.9	23.3	14.1	27.5	19.7	38.2	26.1	50.7
121.9	400	9.3	18.0	12.6	24.6	15.0	29.1	20.9	40.4	27.1	52.8
152.4	500	9.8	18.9	13.2	25.8	15.7	30.5	21.9	42.3	28.0	54.4

Table 2-16. Surface peak wind speed profile envelopes for various values of risk of exceeding the 10-m- (33-ft-) level peak wind speed for 1-hr exposure (hourly-monthly reference period) for EAFB.

Height		Risk (%)									
		20		10		5		1		0.1	
(m)	(ft)	(m/s)	(kt)	(m/s)	(kt)	(m/s)	(kt)	(m/s)	(kt)	(m/s)	(kt)
10.0	33	10.1	19.6	12.7	24.6	15.4	30.0	21.3	41.4	29.8	57.9
18.3	60	10.8	21.1	13.6	26.4	16.5	32.1	22.7	44.1	31.6	61.5
30.5	100	11.5	22.4	14.4	28.0	17.5	34.0	23.9	46.5	33.3	64.7
61.0	200	12.5	24.2	15.6	30.3	18.9	36.7	25.7	50.0	35.6	69.2
91.4	300	13.1	25.4	16.3	31.7	19.7	38.4	26.8	52.2	37.0	72.0
121.9	400	13.5	26.2	16.8	32.7	20.4	39.6	27.6	53.7	38.1	74.0
152.4	500	13.8	26.9	17.2	33.5	20.9	40.5	28.3	55.0	38.9	75.6

Table 2-17. Surface mean wind speed profile envelopes for various values of risk of exceeding the 10-m- (33-ft-) level, 10-min mean wind speed for 1-hr exposure (hourly-monthly reference period) for EAFB.

Height		Risk (%)									
		20		10		5		1		0.1	
(m)	(ft)	(m/s)	(kt)	(m/s)	(kt)	(m/s)	(kt)	(m/s)	(kt)	(m/s)	(kt)
10.0	33	10.1	19.6	12.7	24.6	15.4	30.0	21.3	41.4	29.8	57.9
18.3	60	10.8	21.1	13.6	26.4	16.5	32.1	22.7	44.1	31.6	61.5
30.5	100	11.5	22.4	14.4	28.0	17.5	34.0	23.9	46.5	33.3	64.7
61.0	200	12.5	24.2	15.6	30.3	18.9	36.7	25.7	50.0	35.6	69.2
91.4	300	13.1	25.4	16.3	31.7	19.7	38.4	26.8	52.2	37.0	72.0
121.9	400	13.5	26.2	16.8	32.7	20.4	39.6	27.6	53.7	38.1	74.0
152.4	500	13.8	26.9	17.2	33.5	20.9	40.5	28.3	55.0	38.9	75.6

The peak/mean wind profiles were constructed with a 1.4 gust factor and mean 3σ value of k, as given in section 2.2.5.4. Some additional general ground wind data are given in references 2-5 and 2-6 for several other locations.

2.2.5.5.3 Frequency of Reported Calm Winds. Generally, aerospace vehicle design criteria wind problems are concerned with high wind speeds, but a condition of calm or very low speeds (generally <0.5 mps (<1 kt)) may also be important. For example, with no wind to disperse venting vapors such as liquid oxygen (lox), a poor visibility situation could develop around the vehicle. Calm wind conditions can also have significant implications relative to the atmospheric diffusion of vehicle exhaust clouds (see sec. 11). In addition, calm wind in conjunction with high solar heating can result in significantly high vehicle compartment temperatures. Table 2-18 shows the frequency of calm winds at the 10-m (33-ft) level for KSC as a function of time of day and month. The maximum percentage of calm winds appears in the summer and during the early morning hours, with the minimum percentage appearing throughout the year during the afternoon. Similar tables for other locations can be generated upon request.

2.2.6 Spectral Ground Wind Turbulence Model

Under most conditions, ground winds are fully developed turbulent flows. This is particularly true when the wind speed is greater than a few meters per second or the atmosphere is unstable, and especially when both conditions exist. During nighttime conditions when the wind speed is typically low and the stratification is stable, the intensity of turbulence is small, if not nil. Spectral methods are a particularly useful way of representing the turbulent portion of the ground wind environment for launch vehicle design purposes, as well as for use in diffusion calculations of toxic fuels and atmospheric pollutants.

2.2.6.1 Introduction. At a fixed point in the atmospheric boundary layer, the instantaneous wind vector from the quasi-steady wind vector is the horizontal vector component of turbulence. This vector departure can be represented by two components, the longitudinal and the lateral components of turbulence, which are parallel and perpendicular to the steady-state wind vector in the horizontal plane (fig. 2-5). The model contained herein is a spectral representation of the characteristics of the longitudinal and lateral components of turbulence. The model analytically defines the spectra of these components of turbulence for the first 200 m of the boundary layer. In addition, it defines the longitudinal and lateral cospectra, quadrature spectra, and corresponding coherence functions associated with any pair of levels in the boundary space. Details concerning the model can be found in references 2-7 through 2-10.

Table 2-18. Frequency (percent) of reported calm wind at the 10-m (33-ft) level for KSC.

Hour	Month												
(EST)	Jan	Feb	Mar	Apr	May	June	July	Aug	Sep	Oct	Nov	Dec	Ann.
00	4.8	4.0	3.6	1.3	7.3	9.2	11.7	13.7	6.3	6.9	6.3	6.0	6.8
01	2.8	1.3	2.4	1.7	8.9	8.3	10.9	14.1	7.1	4.8	6.3	6.5	6.3
02	4.8	2.2	3.6	2.9	7.7	10.0	11.7	13.7	10.4	7.3	5.4	4.0	7.0
03	5.2	3.1	2.0	3.8	8.5	12.1	11.3	17.3	12.1	5.2	2.9	3.2	7.3
04	2.8	4.4	2.4	3.8	5.2	13.8	14.5	13.7	10.8	5.2	4.6	2.8	7.0
05	4.4	4.0	3.2	2.9	9.7	16.3	15.3	18.5	13.3	3.6	4.6	4.4	8.4
06	4.4	4.0	4.4	2.9	8.9	16.3	19.8	19.0	13.3	3.2	5.0	5.2	8.9
07	3.6	4.4	4.8	6.3	10.5	16.7	18.1	19.4	15.8	4.4	5.4	5.6	9.6
08	3.6	6.6	6.5	2.9	2.4	5.4	6.0	6.9	4.6	4.0	8.8	4.4	5.2
09	3.6	1.8	2.0	2.1	2.8	3.8	4.8	1.6	4.2	0.8	4.6	5.6	3.1
10	0.4	1.8	1.6	1.7	0.4	3.8	4.0	2.8	2.1	_	1.3	2.4	1.8
11	0.4	1.3	1.2	1.7	0.8	1.3	2.4	0.8	2.9	0.8	1.7	0.8	1.3
12	1.6	0.4	_	_	_	0.8	0.8	0.4	1.3	0.4	2.1	1.2	0.8
13	2.0	0.4	_	_	0.4	1.3	0.4	1.6	0.8	0.4	1.7	0.4	0.8
14	0.8	4.0	0.8	0.4	0.4	0.8	1.2	1.6	1.3	0.8	_	0.4	0.7
15	0.4	1.3	_	_	_	0.8	0.4	1.6	2.5	0.4	0.4	0.4	0.7
16	0.4	0.4	0.4	_	0.8	0.4	0.8	0.4	1.3	0.8	–	0.8	0.5
17	1.6	0.4	_	0.4	0.4	2.1	0.8	3.2	2.1	1.6	1.7	2.0	1.4
18	4.0	1.8	0.8	0.4	1.6	2.5	3.2	4.0	2.9	1.2	5.0	7.7	2.9
19	2.8	3.5	2.0	_	1.6	5.0	2.8	5.2	4.6	1.2	7.1	6.5	3.5
20	4.4	3.5	2.8	1.7	3.2	6.7	5.6	8.5	7.5	1.6	6.3	6.0	4.8
21	5.2	4.0	3.2	1.3	4.8	7.5	10.5	8.9	8.3	4.4	5.0	6.0	5.8
22	3.6	2.2	2.4	1.7	6.0	7.5	7.7	12.9	7.9	4.8	6.3	5.2	5.7
23	5.6	3.5	4.8	0.8	6.5	8.3	10.5	15.3	10.0	5.6	4.6	5.2	6.8
All Hours	3.1	2.5	2.3	1.7	4.1	6.7	7.3	8.6	6.4	2.9	4.0	3.9	4.5

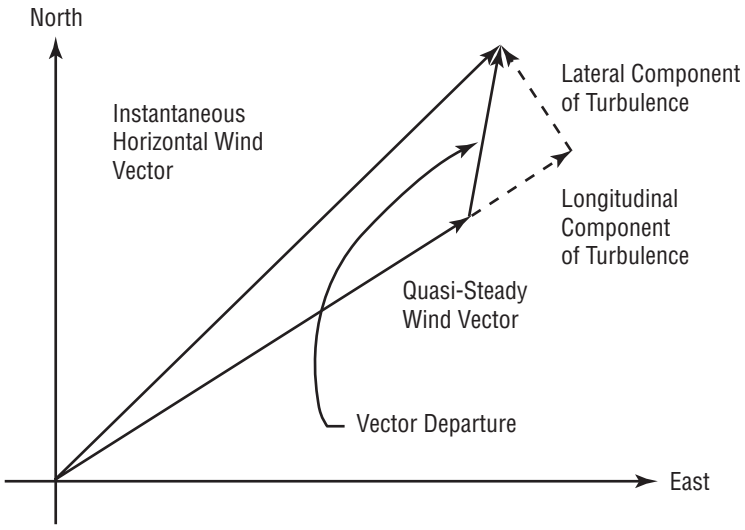

Figure 2-5. The relationship between the quasi-steady state and the horizontal instantaneous wind vectors and the longitudinal and lateral components of turbulence.

2.2.6.2 Turbulence Spectra. The longitudinal and lateral spectra of turbulence at frequency, ω, and height, z, can be represented by a dimensionless function of the form

$$\frac{\omega S(\omega)}{\beta u_*^2} = \frac{c_1 f / f_m}{\left[1 + 1.5\left(f / f_m\right)^{c_2}\right]^{5/3 c_2}} \ , \tag{2.3}$$

where

$$f = \frac{\omega z}{\bar{u}(z)} \ , \tag{2.4}$$

$$f_m = c_3 \left(\frac{z}{z_r}\right)^{c_4} \ , \tag{2.5}$$

$$\beta = \left(\frac{z}{z_r}\right)^{c_5} \ , \tag{2.6}$$

and

$$u_* = c_6 \bar{u}\left(z_r\right) \ . \tag{2.7}$$

In these equations, z_r is a reference height equal to 18.3 m (60 ft); $u(z_r)$ is the quasi-steady wind speed at height z; and the quantities c_i (i = 1,2,3,4,5) are dimensionless constants that depend upon the site and the atmospheric stability. The frequency, ω, in units of cycles per unit time, is defined with respect to a structure or vehicle at rest relative to the Earth. These equations and variables are further described and explained in reference 2-7. The reader is referred to sections 2.3.12 and 2.3.13 for the definition of turbulence spectral inputs for application to the takeoff and landing of conventional aeronautical systems and the landing of the Space Shuttle orbiter vehicle. The spectrum $S(\omega)$ is defined so that integration over the domain $0 \le \omega \le \infty$ yields the variance of the turbulence. Engineering values of c_i are given in table 2-19 for the longitudinal spectrum and in table 2-20 for the lateral spectrum. The ground wind spectral model is only valid to heights at and above the 18.3-m level.

Table 2-19. Dimensionless constants (c_i) for the longitudinal spectrum of turbulence for KSC.

Conditions	c_1	c_2	c_3	c_4	c_5
Light wind daytime conditions	2.905	1.235	0.04	0.87	–0.14
Strong winds	6.198	0.845	0.03	1.0	–0.63

Table 2-20. Dimensionless constants (c_i) for the lateral spectrum of turbulence for KSC.

Conditions	c_1	c_2	c_3	c_4	c_5
Light wind daytime conditions	4.599	1.144	0.03	0.72	–0.04
Strong winds	3.954	0.781	0.1	0.58	–0.35

The constant c_6 to input into equation (2.7) can be estimated with the equation

$$c_6 = \frac{0.4}{\ln\left(\frac{z_r}{z_0}\right) - \Psi} \ , \tag{2.8}$$

where z_0 is the surface roughness length of the site and Ψ is a parameter that depends upon the stability. If z_0 is not available for a particular site, then an estimate of z_0 can be obtained by taking 10 percent of the typical height of the surface obstructions (grass, shrubs, trees, rocks, etc.). The typical height is determined over a fetch (the distance the wind blows over a surface) equal to ≈1,500 m (≈4,900 ft). The parameter Ψ vanishes for strong wind conditions and is of order unity for light wind, unstable daytime conditions at KSC. Typical values of z_0 for various surfaces are given in table 2-21.

Table 2-21. Typical values of surface roughness length (z_0) for various types of surfaces.

Type of Surface	z_0 (m)	z_0 (ft)
Mud flats, ice	10^{-5}–$3x10^{-5}$	$3x10^{-5}$–10^{-4}
Smooth sea	$2x10^{-4}$–$3x10^{-4}$	$7x10^{-4}$–10^{-3}
Sand	10^{-4}–10^{-3}	$3x10^{-4}$–$3x10^{-3}$
Snow surface	10^{-3}–$6x10^{-3}$	$3x10^{-4}$–$2x10^{-2}$
Mown grass (~0.01 m)	10^{-3}–10^{-2}	$3x10^{-3}$–$3x10^{-2}$
Low grass, steppe	10^{-2}–$4x10^{-2}$	$3x10^{-2}$–10^{-1}
Fallow field	$2x10^{-2}$–$3x10^{-2}$	$6x10^{-2}$–10^{-1}
High grass	$4x10^{-2}$–10^{-1}	10^{-1}–$3x10^{-1}$
Palmetto	10^{-1}–$3x10^{-1}$	$3x10^{-1}$–1
Suburbia	1–2	3–6
City	1–4	3–13

The function given by equation (2.3) is depicted in figures 2-6 and 2-7. Upon prescribing the steady-state wind profile $u(z)$ and the site (z_0), the longitudinal and lateral spectra are completely specified functions of height, z, and frequency, ω. A discussion of the units of the various parameters mentioned previously is given in section 2.2.6.4.

2.2.6.3 The Cospectrum and Quadrature Spectrum. The cospectrum (C) and the quadrature spectrum (Q) associated with either the longitudinal or lateral components of turbulence at levels z_1 and z_2 can be represented by the following:

$$C(\omega, z_1, z_2) = \sqrt{S_1 S_2}\, \exp\left(-0.3465 \frac{\Delta f}{\Delta f_{0.5}}\right) \cos\left(2\pi \gamma \Delta f\right) \ , \tag{2.9}$$

$$Q(\omega, z_1, z_2) = \sqrt{S_1 S_2}\, \exp\left(-0.3465 \frac{\Delta f}{\Delta f_{0.5}}\right) \sin\left(2\pi \gamma \Delta f\right) \ , \tag{2.10}$$

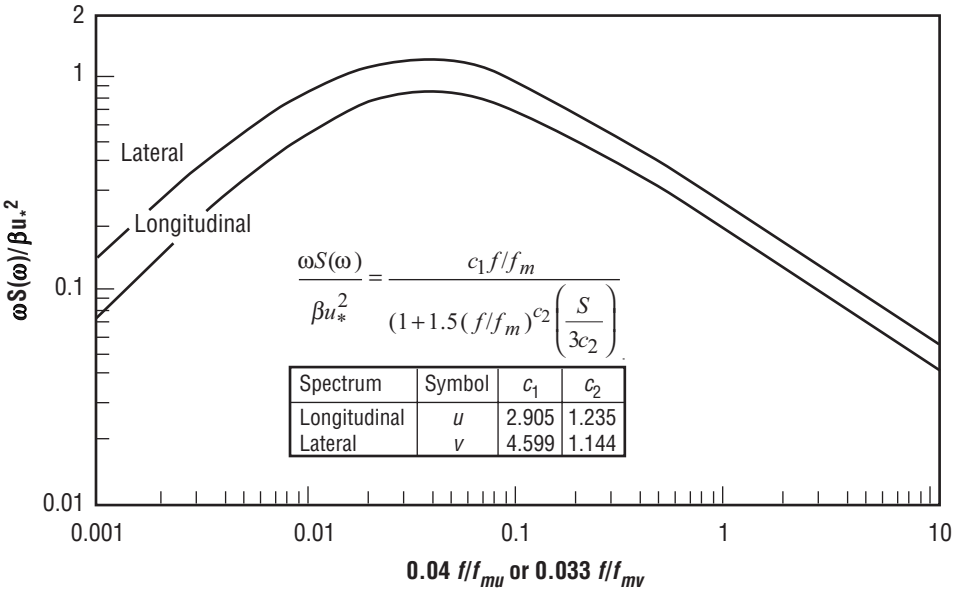

Figure 2-6. $\omega S(\omega)/\beta u_*^2$ versus 0.04 f/f_m (longitudinal) and 0.033 f/f_m (lateral) for light wind daytime conditions.

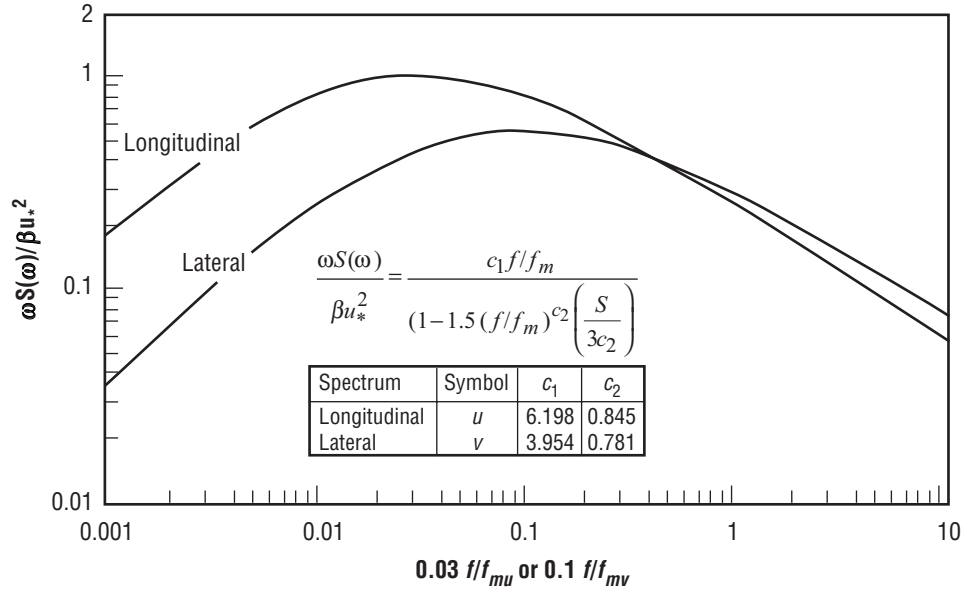

Figure 2-7. $\omega S(\omega)/\beta u_*^2$ versus 0.03 f/f_m (longitudinal) and 0.1 f/f_m (lateral) for strong wind conditions.

where

$$\Delta f = \frac{\omega z_2}{\bar{u}(z_2)} - \frac{\omega z_1}{\bar{u}(z_1)} \ . \tag{2.11}$$

The quantities S_1 and S_2 are the longitudinal or lateral spectra at levels z_1 and z_2, respectively, and $u(z_1)$ and $u(z_2)$ are the steady-state wind speeds at levels z_1 and z_2. The quantity $\Delta f_{0.5}$ is a nondimensional function of stability, where $\Delta f_{0.5}$ is that value for which the coherence (coh) is equal to 0.5, and values of this parameter for KSC are given in table 2-22. The nondimensional quantity, γ, should depend upon height and stability. However, it has only been possible to detect a dependence on height at KSC. Based upon analysis of turbulence data measured at the 150-m (492-ft) Ground Wind Tower facility at KSC, the values of γ in table 2-23 are suggested for KSC. The quantity $\Delta f_{0.5}$ can be interpreted by constructing the coherence function, which is defined to be

$$\mathrm{coh}(\omega, z_1, z_2) = \frac{C^2 + Q^2}{S_1 S_2} \ . \tag{2.12}$$

Table 2-22. Values of $f_{0.5}$ for KSC.

Turbulence Component	Light Wind Daytime Conditions	Strong Winds
Longitudinal	0.04	0.036
Lateral	0.06	0.045

Table 2-23. Values of γ for KSC.

Turbulence Component	$(z_1+z_2)/2 \leq 100$ m	$(z_1+z_2)/2 > 100$ m
Longitudinal	0.7	0.3
Lateral	1.4	0.5

Substituting equations (2.9) and (2.10) into equation (2.12) yields

$$\mathrm{coh}\,(\omega, z_1, z_2) = \exp\left(-0.693 \frac{\Delta f}{\Delta f_{0.5}}\right) . \tag{2.13}$$

2.2.6.4 Units. The spectral model of turbulence presented in sections 2.2.6.2 and 2.2.6.3 is a dimensionless model. Accordingly, the user is free to select the system of units desired, except that ω must have the units of cycles per unit time. Table 2-24 gives the appropriate metric and U.S. customary units for the various quantities in the model.

Table 2-24. Metric and U.S. customary units of various quantities in the turbulence model.

Quantity	Metric Units	U.S. Customary Units
ω	Hz	Hz
$S(\omega)$, $Q(\omega)$, $C(\omega)$	$m^2\ s^{-2}/Hz$	$ft^2\ s^{-2}/Hz$
f, f_m, Δf, $\Delta f_{0.5}$	Dimensionless	Dimensionless
z, s_r, z_0	m	ft
u, u_*	m/s	ft/s
β	Dimensionless	Dimensionless
Coh	Dimensionless	Dimensionless
γ	Dimensionless	Dimensionless
Ψ	Dimensionless	Dimensionless

2.2.7 Ground Wind Gust Factors

The gust factor, G, is defined to be

$$G = \frac{u}{\overline{u}} \ , \tag{2.14}$$

where

$u =$ maximum wind speed at height z within an average period of length in time, τ
$\overline{u} =$ mean wind speed associated with the average period τ, given by

$$\overline{u} = \frac{1}{\tau}\int_0^{\tau} u_i(t)\,dt \ , \tag{2.15}$$

$u_i(t) =$ instantaneous wind speed at time, t
t = time reckoned from the beginning of the averaging period.

If $\tau = 0$, then $\overline{u} = u$ according to equation (2.15), and it follows from equation (2.14) that $G = 1$. As τ increases, $\overline{u}$ departs from u, and $\overline{u} \le u$, and $G > 1$. Also, as τ increases, the probability of finding a maximum wind of a given magnitude increases. In other words, the maximum wind speed increases as τ increases. In the case of $\overline{u} \ge 0$ and $u \ge 0$ ($\overline{u} = 0$ might correspond to windless free convection), $G \ge \infty$. As $\overline{u}$ or u increases, G tends to decrease for fixed $\tau > 0$; while, for very high wind speeds, G tends to approach a constant value for given values of z and τ. Finally, as z increases, G decreases. Thus, the gust factor is a function of the averaging time, τ, over which the mean wind speed is calculated, the height, z, and wind speed (mean or maximum).

2.2.7.1 Gust Factor as a Function of Peak Wind Speed ($u_{18.3}$) at Reference Height for KSC. Investigations (ref. 2-10) of gust factor data have revealed that the vertical variation of the gust factor can be described with the following relationship:

$$G = 1 + \frac{1}{g_0}\left(\frac{18.3}{z}\right)^p \ , \tag{2.16}$$

where z is the height in meters above natural grade. The parameter, p, a function of the 18.3-m (60-ft) reference height peak wind speed in meters per second, is given by

$$p = 0.283 - 0.435 e^{-0.2 u_{18.3}} \quad . \tag{2.17}$$

The parameter g_0 depends on the averaging time and the 18.3-m peak wind speed and is given by

$$g_0 = 0.085 \left(\ln \frac{\tau}{10} \right)^2 = 0.329 \left(\ln \frac{t}{10} \right) + 1.98 - 1.887 e^{-0.2 u_{18.3}} \quad , \tag{2.18}$$

where τ is given in minutes and $u_{18.3}$ in meters per second.

These relationships are valid for $u_{18.3} \geq 4$ m/s and $\tau \leq 10$ min. In the interval 10 min $\leq \tau \leq 60$ min, G is a slowly increasing monotonic function of τ, and for all engineering purposes, the 10-min gust factor ($\tau = 10$ min) can be used as an estimate of the gust factors associated with averaging times >10 min and <60 min (10 min $\leq \tau \leq 60$ min).

The calculated mean gust factors for 10 min for values of $u_{18.3}$ in the interval 4.63 m/s $\leq u_{18.3} \leq \infty$ are presented in table 2-25 in both the U.S. customary and metric units for $u_{18.3}$ and z. As an example, the gust factor profile for $\tau = 10$ min and $u_{18.3} = 9.27$ m/s (18 kt) is given in table 2-26. Since the basic wind statistics are given in terms of hourly peak wind, use the $\tau = 10$-min gust factors to convert the peak winds to mean winds by dividing by G. All gust factors in these sections are expected values for any particular set of values for u, τ, and z.

2.2.7.2 Gust Factors for Other Locations. For design purposes, the gust factor value of 1.4 (ref. 2-9) should be used over all heights of the ground wind profile at other test ranges. This gust factor should correspond to an approximate 10-min averaging period.

Table 2-25. 10-min gust factors for KSC.

Reference Height 18.3-m (60-ft) Peak Wind		Height Above Natural Grade in Meters (ft)						
m/s	kt	10 (33)	18.3 (60)	30.5 (100)	61 (200)	91.4 (300)	121.9 (400)	152.4 (500)
4.63	9	1.868	1.812	1.767	1.710	1.679	1.658	1.642
5.15	10	1.828	1.766	1.718	1.657	1.624	1.602	1.585
5.66	11	1.795	1.729	1.678	1.614	1.580	1.556	1.539
6.18	12	1.768	1.699	1.645	1.579	1.544	1.520	1.502
6.69	13	1.746	1.674	1.618	1.552	1.514	1.489	1.471
7.21	14	1.727	1.652	1.595	1.525	1.488	1.464	1.446
7.72	15	1.712	1.634	1.576	1.505	1.467	1.442	1.424
8.24	16	1.698	1.619	1.559	1.487	1.449	1.424	1.409
8.75	17	1.686	1.606	1.545	1.472	1.424	1.409	1.390
9.27	18	1.676	1.594	1.532	1.459	1.421	1.395	1.377
9.78	19	1.668	1.584	1.522	1.447	1.409	1.384	1.365
10.30	20	1.660	1.575	1.512	1.437	1.399	1.374	1.355
12.90	25	1.634	1.545	1.480	1.403	1.365	1.339	1.321
15.40	30	1.619	1.528	1.462	1.385	1.346	1.321	1.302
≥17.96	≥35	1.599	1.505	1.437	1.359	1.320	1.295	1.277

Table 2-26. Gust factor profile for $\tau = 10$ min and $u_{18.3} = 9.27$ m/s (18 kt).

Height		Gust Factors
(m)	(ft)	(G)
10.0	33	1.676
18.3	60	1.594
30.5	100	1.532
61.0	200	1.459
91.4	300	1.421
121.9	400	1.395
152.4	500	1.377

2.2.8 Ground Wind Shear

Wind shear near the surface—for design purposes—is a shear that acts on an aerospace vehicle, free-standing on the pad, or at time of lift-off. For overturning moment calculations, the wind shear should be computed by first subtracting the 10-min mean wind speed at the height corresponding to the base of the vehicle from the peak wind speed at the height corresponding to the top of the vehicle (see sec. 2.2.5.5 for mean and peak wind profiles) and then dividing the difference by the height of the vehicle. The reader should consult references 2-11 through 2-19 for a detailed discussion of the statistical properties of wind shear near the ground for engineering applications.

2.2.9 Ground Wind Direction Characteristics

Figure 2-1 (sec. 2.2.5.1) shows an example of an hourly time trace of wind direction (section of a wind direction recording chart). This wind direction trace may be visualized as being composed of a mean wind direction plus fluctuations about the mean. An accurate measure of ambient wind direction near the ground is difficult to obtain sometimes because of the interference of the structure that supports the instrumentation and other obstacles in the vicinity of the measurement location (ref. 2-20). This is particularly true for launch pads; therefore, care must be exercised in locating wind sensors in order to obtain representative measurements of the ambient wind direction.

General information, such as the following, is available and may be used to specify conditions for particular engineering studies. For instance, the variation of wind direction as a function of mean wind speed and height from analysis of the 150-m (492-ft) Ground Winds Tower Facility data at KSC is discussed in reference 2-4. A graph is shown in reference 2-4 that gives values of the standard deviation of the wind direction σ_θ as a function of height for a sampling time of ≈5 min.

2.2.10 Design Winds for Facilities and Ground Support Equipment

2.2.10.1 Introduction. In this section, the important relationships between desired lifetime, N (years); calculated risk, U (%÷100); design return period, T_D (years); and design wind, W_D (m/s or kt) will be described for use in facilities design for several locations.

The desired lifetime, N, is expressed in years, and preliminary estimates must be made as to how many years the proposed facility is to be used.

The calculated risk, U, is a probability expressed either as a percentage or as a decimal fraction. Calculated risk, sometimes referred to as design risk, is a probability measure of the risk the designer is willing to accept that the facility will be destroyed by wind loading in less time than the desired lifetime.

The design return period, T_D, is expressed in years and is a function of desired lifetime and calculated risk.

The design wind, W_D, is a function of the desired lifetime and calculated risk and is derived from the design return period and a probability distribution function of yearly peak winds.

2.2.10.2 Development of Relationships. From the theory of repeated trial probability, the following expression can be derived:

$$N = \frac{\ln(1-U)}{\ln\left(1-\frac{1}{T_D}\right)} \ . \tag{2.19}$$

Equation (2.19) gives the important relationships for the three variables—calculated risk, U (%+100); design return period, T_D (years); and desired lifetime, N (years). If estimates for any two variables are available, the third can be determined from this equation.

Design return period, T_D, calculated with equation (2.19) for various values of desired lifetime, N, and design risk are given in table 2-27. The table presents the exact and adopted values for design return period versus desired lifetime for various design risks. The adopted values for T_D are in some cases greatly oversized to facilitate a convenient use of the tabulated probabilities for distributions of yearly peak winds.

Table 2-27. Exact (Ex) and adopted values for design return period (T_D, yr) versus desired lifetime (N, yr) for various design risks (U).

N (yr)	Design Return Period (yr)									
	U = 0.5 (50%)		U = 0.2 (20%)		U = 0.1 (10%)		U = 0.05 (5%)		U = 0.01 (1%)	
	Ex	Adopt	Ex	Adopt	Ex	Adopt	Ex	Adopt	Ex	Adopt
1	2	2	15	5	10	10	20	20	100	100
10	15	15	45	50	95	100	196	200	996	1,000
20	29	30	90	100	190	200	390	400	1,991	2,000
25	37	40	113	125	238	250	488	500	–	–
30	44	50	135	150	285	300	585	600	–	–
50	73	100	225	250	475	500	975	1,000	–	–
100	145	150	449	500	950	1,000	1,950	2,000	–	–

2.2.10.3 Design Winds for Facilities. To obtain the design wind, the wind speed corresponding to the design return period must be determined. Since the design return period is a function of risk, either of two procedures can be used to determine the design wind: (1) Through a graphical or numerical interpolation procedure or (2) based on an analytical function. A knowledge of the distribution of yearly peak winds is required for both

procedures. For the greatest statistical efficiency in arriving at the probability that the peak winds will be less than or equal to some specified value of yearly peak winds, an appropriate probability distribution function must be selected and the parameters for the function estimated from the sample of yearly peak winds. The Gumbel distribution (ref. 2-3) is an excellent fit for the yearly peak ground wind speed at the 10-m (33-ft) level for KSC. The distribution of yearly peak wind speed (10-m level), as obtained by the Gumbel distribution, is tabulated for various percentiles together with the corresponding return periods in table 2-28. The values for the parameters α and μ for this distribution are also given in this table.

Table 2-28. Gumbel distribution for yearly peak wind speed, 10-m (33-ft) reference level, including hurricane winds for KSC.

Return Period (yr)	Probability	y	m/s	kt
2	0.50	0.36651	25.45	49.47
5	0.80	1.49994	31.79	61.79
10	0.90	2.25037	35.98	69.95
15	0.933	2.66859	38.33	74.50
20	0.95	2.97020	40.01	77.77
30	0.967	3.39452	42.38	82.39
45	0.978	3.80561	44.68	86.86
50	0.98	3.90191	45.22	87.90
90	0.9889	4.49523	48.54	94.35
100	0.99	4.60015	49.12	95.49
150	0.9933	5.00229	51.37	99.86
200	0.995	5.29581	53.01	103.05
250	0.996	5.51946	54.26	105.48
300	0.9967	5.71218	55.34	107.58
400	0.9975	5.99021	56.90	110.60
500	0.9980	6.21361	58.14	113.02
600	0.9983	6.37628	58.75	114.20
1,000	0.9990	6.90726	62.02	120.56
10,000	0.9999	9.21029	74.90	145.60

α^{-1} = 5.5917 m/s (10.87 kt) μ = 23.4 m/s (45.49 kt)
$\Phi = \exp(-\exp(-y))$, where $y = \alpha(x-\mu)$
Φ = probability distribution function of the reduced variate, y.

The design wind speed can now be determined by choosing a desired lifetime, design risk, by taking the design return period from table 2-27 and looking up the wind speed corresponding to the return periods in table 2-28. For combinations not tabulated in tables 2-27 and 2-28, the design return period can be interpolated.

2.2.10.4 Procedure to Determine Design Winds for Facilities. The design wind, W_D, as a function of desired lifetime, N, and calculated risk, U, for the Gumbel distribution of peak winds at the 10-m (33-ft) reference level, can be derived as

$$W_D = \frac{1}{\alpha}\left[-\ln\left[-\ln(1-U)\right]+\ln N\right]+\mu \ , \tag{2.20}$$

where α and μ are estimated from the sample of yearly peak wind.

Taking the values for α^{-1} = 5.59 m/s (10.87 kt) and for μ = 23.4 m/s (45.49 kt) from table 2-28 and evaluating equation (2.20) for selected values of N and U yields the data in table 2-29.

Design wind speed versus desired lifetime is plotted in figure 2-8 where the slopes of the lines are equal.

Table 2-29. Facility design wind, $W_{D_{10}}$, with respect to the 10-m (33-ft) reference level peak wind speed for various lifetimes (N) for KSC.

Design Risk			Design Wind ($W_{D_{10}}$) for Various Lifetimes (N)*							
			N = 1		N = 10		N = 30		N = 100	
(U)	$1-U$	$-\ln(-\ln(1-U))$	(m/s)	(kt)	(m/s)	(kt)	(m/s)	(kt)	(m/s)	(kt)
0.63212	0.36788	0	23.40	45.49	36.28	70.52	42.42	82.46	49.15	95.55
0.50	0.50	0.37	25.45	49.47	38.33	74.50	44.47	86.44	51.20	99.53
0.4296	0.5704	0.58	26.62	51.76	39.50	76.79	45.65	88.73	52.38	101.82
0.40	0.60	0.67	27.16	52.79	40.03	77.82	46.18	89.76	52.92	102.85
0.30	0.70	1.03	29.17	56.70	42.04	81.72	48.19	93.67	54.92	106.75
0.20	0.80	1.50	31.79	61.79	44.66	86.82	50.81	98.76	57.54	111.85
0.10	0.90	2.25	35.99	69.95	48.86	94.98	55.00	106.92	61.74	120.01
0.05	0.95	2.97	40.01	77.77	52.88	102.80	59.03	114.74	65.76	127.83
0.01	0.99	4.60	49.12	95.49	62.00	120.52	68.14	132.46	74.88	145.55

*Values of N are given in years.

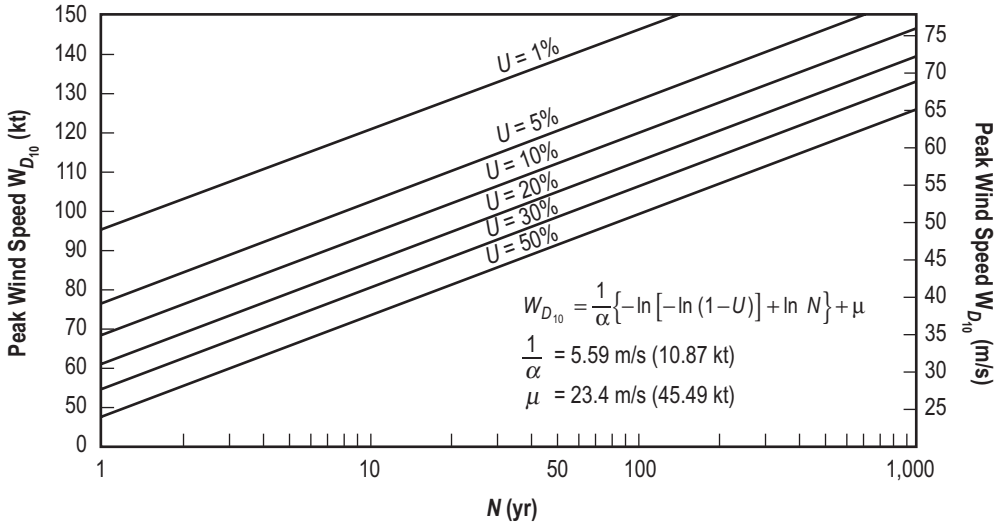

Figure 2-8. Facility design wind, $W_{D_{10}}$, with respect to the 10-m (33-ft) reference level peak wind speed for various lifetimes (N) for KSC.

2.2.10.5 Wind Load Calculations. The design wind for a structure cannot be determined solely by wind statistics at a particular height. The design engineer is most interested in designing a structure that satisfies the user's requirements for utility, which will have a small risk of failure within the desired lifetime of the structure, and which can carry a sufficiently large wind load and be constructed at a sufficiently low cost.

The total wind loading on a structure is composed of two interrelated components—steady-state drag wind loads and dynamic wind loads (time-dependent drag loads, vortex shedding forces, etc.). The time required for a structure to respond to the drag wind loads dictates the averaging time for the design wind profile. In general, the structure response time depends upon the shape of the structure. The natural frequency of the structure and its components are important in estimating the dynamic wind load. It is conceivable that a structure could be designed to withstand very high peak wind speeds without structural failure and still oscillate in moderate steady-state wind speeds. If such a structure, for example, is to be used to support a precision tracking radar, then there may be little danger of overloading the structure by high peak winds; but, the structure might be useless for its intended purpose if it were to oscillate in a moderate steady-state wind. Also, a building may have panels or small members that could respond to dynamic loading in such a way that long-term vibrations could cause failure without any structural failure of the main supporting members.

Since dynamic wind loading requires an intricate knowledge of the particular facility and its components, no attempt is made here to state generalized design criteria for dynamic wind loading. The emphasis in this section is on winds for estimating drag wind loads in establishing design wind criteria for structures. Reference is made to sections 2.2.5.5 and 2.2.6 for information appropriate to dynamic wind loads.

2.2.10.6 Wind Profile Construction. Given the peak wind at the 10-m (33-ft) level, the peak wind profile can be constructed with the peak wind profile law from section 2.2.5.5. Steady-state wind profiles can be obtained by using appropriate gust factors which are discussed in section 2.2.7.

To illustrate the procedures and operations in deriving the wind profile and the application of the gust factor, three examples are worked out for KSC. Peak wind speeds at the 10-m level of 36, 49, and 62 m/s (70, 95, and 120 kt) have been selected for these examples. These three wind speeds were selected because they correspond to a return period of 10, 100, and 1,000 yr for a peak wind at the 10-m level at KSC. Table 2-30 contains the risks of exceeding these peak winds for various values of desired lifetime. Table 2-31 gives the peak design wind profiles corresponding to the desired lifetimes and calculated risks presented in table 2-30. These profiles were calculated using equation (2.22).

Table 2-30. Calculated risk (U) versus desired lifetime (N, yr) for assigned design winds related to peak winds at the 10-m (33-ft) reference level for KSC.

N (yr)	$W_{D_{10}}$ = 36 m/s (70 kt) T_D = 10 yr U(%)	$W_{D_{10}}$ = 49 m/s (95 kt) T_D = 100 yr U(%)	$W_{D_{10}}$ = 62 m/s (120 kt) T_D = 1,000 yr U(%)
1	10	1.0	0.1
10	65	10	1
20	88	18	2
25	93	22	2.5
30	95.8	26	3
50	99.5	39.5	5
100	99.997	63.397	10

T_D =Design return period

Table 2-31. Design peak wind profiles for design wind relative to the 10-m (33-ft) reference level for KSC.

Height		$W_{D_{10}}$ = 36 m/s (70 kt)		$W_{D_{10}}$ = 49 m/s (95 kt)		$W_{D_{10}}$ = 62 m/s (120 kt)	
(m)	(ft)	(m/s)	(kt)	(m/s)	(kt)	(m/s)	(kt)
10.0	33	36.0	70.0	48.9	95.0	61.8	120.0
18.3	60	38.4	74.5	51.4	99.9	64.5	125.2
30.5	100	40.0	78.6	53.7	104.2	66.8	129.8
61.0	200	43.4	84.4	56.8	110.4	70.1	136.2
91.4	300	45.3	88.0	58.8	114.2	72.2	140.2
121.9	400	46.7	90.7	60.2	117.0	73.6	143.0
152.4	500	47.8	92.8	61.3	119.1	74.8	145.3

2.2.10.7 Use of Gust Factors Versus Height. In estimating the drag load on a particular structure, it may be determined that wind force of a given magnitude must act on the structure for some period (e.g., 1 min) to produce a critical drag load. To obtain the wind profile corresponding to a time-averaged wind, the peak wind profile values are divided by the required gust factors. The gust factors for winds >15 m/s (29 kt) versus height given in table 2-32 are taken from section 2.2.7. This operation may seem strange to someone who is accustomed to multiplying the given wind by a gust factor in establishing the design wind. This is because most literature on this subject gives the reference wind as averaged over some time increment (e.g., 1, 2, or 5 min) or in terms of the "fastest mile" of wind that has a variable averaging time, depending upon the wind speed. The design wind profiles for the three examples, peak winds of 36, 49, and 62 m/s (70, 95, and 120 kt) at the 10-m (33-ft) level for various averaging times, τ, given in minutes, are illustrated in tables 2-33 through 2-35. Following the procedures presented herein, the design engineer can objectively derive several important design parameters that can be used in designing a facility that will (1) meet the requirements for utility and desired lifetime, (2) withstand a sufficiently large wind loading with a known calculated risk of failure due to wind loads, and (3) allow the design engineer to proceed with tradeoff studies between the design parameters and to estimate the cost of building the structure to best meet these design objectives.

Table 2-32. Gust factors for various averaging times (τ) for peak winds >15 m/s (>29 kt) at the 10-m (33-ft) reference level versus height for KSC.

Height		Various Averaging Times, τ (min)				
(m)	(ft)	τ = 0.5	τ = 1	τ = 2	τ = 5	τ = 10
10.0	33	1.318	1.372	1.528	1.599	1.599
18.3	60	1.268	1.314	1.445	1.505	1.505
30.5	100	1.232	1.271	1.385	1.437	1.437
61.0	200	1.191	1.223	1.316	1.359	1.359
91.4	300	1.170	1.199	1.282	1.320	1.320
121.9	400	1.157	1.183	1.260	1.295	1.295
152.4	500	1.147	1.172	1.244	1.277	1.277

Table 2-33. Design wind profiles for various averaging times (τ) for peak design wind of 36 m/s (70 kt) relative to the 10-m (33-ft) reference level for KSC.

		Design Wind Profiles for Various Averaging Times, τ (min)											
		τ = 0		τ = 0.5		τ = 1		τ = 2		τ = 5		τ = 10	
(m)	(ft)	(m/s)	(kt)	(m/s)	(kt)	(m/s)	(kt)	(m/s)	(kt)	(m/s)	(kt)	(m/s)	(kt)
10.0	33	36.0	70.0	27.3	53.1	26.2	51.0	25.1	48.8	23.6	45.8	22.5	43.8
18.3	60	38.3	74.5	30.2	58.8	29.2	56.7	28.0	54.5	26.5	51.6	25.5	49.5
30.5	100	40.4	78.6	32.8	63.8	31.8	61.8	30.7	59.7	29.2	56.8	28.1	54.7
61.0	200	43.4	84.4	36.5	70.9	35.5	69.0	34.4	66.9	33.0	64.1	31.9	62.1
91.4	300	45.3	88.0	38.7	75.2	37.8	73.4	36.7	71.4	35.3	68.6	34.3	66.7
121.9	400	46.7	90.7	40.3	78.4	39.5	76.7	38.4	74.7	37.0	72.0	36.0	70.0
152.4	500	47.7	92.8	41.6	80.9	40.7	79.2	39.8	77.3	38.4	74.6	37.4	72.7

Table 2-34. Design wind profiles for various averaging times (τ) for peak design wind of 49 m/s (95 kt) relative to the 10-m (33-ft) reference level for KSC.

		Design Wind Profiles for Various Averaging Times, τ (min)											
		τ = 0		τ = 0.5		τ = 1		τ = 2		τ = 5		τ = 10	
(m)	(ft)	(m/s)	(kt)	(m/s)	(kt)	(m/s)	(kt)	(m/s)	(kt)	(m/s)	(kt)	(m/s)	(kt)
10.0	33	48.9	95.0	37.1	72.1	35.6	69.2	34.1	66.2	32.0	62.2	30.6	59.4
18.3	60	51.4	99.9	40.5	78.8	39.1	76.0	37.6	73.1	35.5	69.1	34.2	66.4
30.5	100	53.6	104.2	43.5	84.6	42.2	82.0	40.7	79.1	38.7	75.2	37.3	72.5
61.0	200	56.8	110.4	47.7	92.7	46.5	90.3	45.0	87.5	43.2	83.9	41.8	81.2
91.4	300	58.7	114.2	50.2	97.6	49.0	95.2	47.7	92.7	45.8	89.1	44.5	86.5
121.9	400	60.2	117.0	52.0	101.1	50.9	98.9	49.6	96.4	47.8	92.9	46.5	90.3
152.4	500	61.3	119.1	53.4	103.8	52.3	101.6	51.0	99.2	49.2	95.7	48.0	93.3

Table 2-35. Design wind profiles for various averaging times (τ) for peak design wind of 62 m/s (120 kt) relative to the 10-m (33-ft) reference level for KSC.

		Design Wind Profiles for Various Averaging Times, τ (min)											
		τ = 0		τ = 0.5		τ = 1		τ = 2		τ = 5		τ = 10	
(m)	(ft)	(m/s)	(kt)	(m/s)	(kt)	(m/s)	(kt)	(m/s)	(kt)	(m/s)	(kt)	(m/s)	(kt)
10.0	33	61.7	120.0	46.8	91.0	45.0	87.5	43.0	83.6	40.4	78.5	38.6	75.0
18.3	60	64.4	125.2	50.8	98.7	49.0	95.3	47.2	91.7	44.6	86.6	42.8	83.2
30.5	100	66.8	129.8	54.2	105.4	52.5	102.1	50.7	98.6	48.2	93.7	46.5	90.3
61.0	200	70.1	136.2	58.9	114.4	57.3	111.4	55.6	108.0	53.2	103.5	51.5	100.2
91.4	300	72.1	140.2	61.6	119.8	60.1	116.9	58.5	113.8	56.3	109.4	54.6	106.2
121.9	400	73.6	143.0	63.6	123.6	62.2	120.9	60.6	117.8	58.4	113.5	56.8	110.4
152.4	500	74.7	145.3	65.2	126.7	63.8	124.0	62.2	121.0	60.1	116.8	58.5	113.8

2.2.10.8 Recommended Design Risk Versus Desired Lifetime. Unfortunately, there is not a clear-cut precedent from building codes to follow in recommending design risk for a given desired lifetime of a structure. Conceivably, a value analysis in terms of original investment cost, replacement cost, safety of property and human life, loss of national prestige, and many other factors should be made to give a measure of the consequences of the loss of a particular structure in arriving at a decision as to what risk management is willing to accept for the loss within the desired lifetime of the structure. If the structure is an isolated shed, then obviously its loss is not as great as a structure that would house many people or a structure that is critical to the mission of a large organization, nor is it as potentially unsafe as the loss of a nuclear power plant or storage facility for explosives or highly radioactive materials. To give a starting point for design studies aimed at meeting the design objectives, it is recommended that a design risk of 10 percent for the desired lifetime be used in determining the wind loading on structures that have a high replacement cost. Should the loss of the structure be extremely hazardous to life or property, or critical to the mission of a large organization, then a design risk of 5 percent or less for the desired lifetime is recommended. These are subjective recommendations involving arbitrary assumptions about the design objectives. Note that the longer the desired lifetime, the greater the design risk is for a given wind speed (or wind loading); therefore, realistic appraisals should be made for desired lifetimes.

2.2.10.9 Design Winds for Facilities at VAFB, WSMR, EAFB, and SSC.

2.2.10.9.1 Wind Statistics. The basic wind statistics for these four locations are taken from reference 2-21, which presents isotach maps for the United States for the 50-, 98-, and 99-percentile values for the yearly maximum "fastest mile" of wind at the ≈10-m (≈33-ft) reference height above natural grade. By definition, the fastest mile is the fastest wind speed in miles per hour of any mile of wind flow past an anemometer during a specified period (usually taken as the 24-hr observational day), and the largest of these in a year for the period of record constitutes the statistical sample of yearly fastest mile. From this definition, it is noted that the fastest mile as a measure of wind speed has a variable averaging time; e.g., if the wind speed is 60 mph, the averaging time for the fastest mile of wind is 1 min. For a wind speed of 120 mph, the averaging time for the fastest mile of wind is 0.5 min. Thom (ref. 2-21) reports that the Frechet probability distribution function fits his samples of fastest mile very well. The Frechet probability distribution function is given as

$$F(x) = e^{-\left(\frac{x}{\beta}\right)^{-\gamma}}, \tag{2.21}$$

where the two parameters β and γ are estimated from the sample by the maximum likelihood method. From Thom's maps of the 50, 98, and 99 percentiles of fastest mile of wind for yearly extremals, we have estimated (interpolated) for these percentiles for the four locations and calculated the values for the parameters β and γ for the Frechet distribution function and computed several additional percentiles, as shown in table 2-36. To have units consistent with the other sections of this document, the percentiles and the parameters β and γ have been converted from miles per hour to meters per second and knots. Thus, table 2-36 gives the Frechet distribution for the fastest mile of winds at the ≈10-m (≈33-ft) level for the four locations with the units in meters per second and knots.

The discussion in section 2.2.10.2, devoted to desired lifetime, calculated risk, and design wind relationships with respect to the wind statistics at a particular height (10-m (33-ft) level), is applicable here, except that the reference statistics are with respect to the fastest mile converted to meters per second and knots. (Also see reference 2-22.)

Table 2-36. Frechet distribution of fastest mile wind at the 10-m (33-ft) height of yearly extremes for the indicated locations.

Probability (P)	Design Return Period (T_D) (yr)	Fastest Mile Wind					
		SSC		VAFB		EAFB	
		(m/s)	(kt)	(m/s)	(kt)	(m/s)	(kt)
0.50	2	22.1	42.9	18.0	34.9	11.3	22.0
0.80	5	26.6	51.8	21.6	42.0	15.0	29.1
0.90	10	30.1	58.6	24.4	47.4	18.1	35.2
0.95	20	33.9	65.9	27.4	53.3	21.6	42.0
0.98	50	39.6	76.9	31.8	61.9	27.3	53.0
0.99	100	44.4	86.4	35.7	69.4	32.4	63.1
0.9933	150	47.4	92.2	38.0	73.9	35.1	68.3
0.995	200	49.7	96.7	39.9	77.6	38.6	75.0
0.996	250	51.6	100.4	41.4	80.4	40.8	79.3
0.99667	300	53.2	103.5	42.6	82.9	42.7	83.1
0.9975	400	55.8	108.4	44.6	86.7	45.8	89.1
0.998	500	57.9	112.5	46.2	89.9	48.5	94.2
0.99833	600	59.4	115.5	47.5	92.3	50.5	98.1
0.99875	800	62.6	121.6	50.3	97.7	54.0	105.0
0.999	1,000	64.9	126.1	51.8	100.6	57.6	111.9
γ	Unitless	6.08075		6.19591		4.02093	
$1/\gamma$	Unitless	0.16445		0.16140		0.24870	
$\ln \beta$	Unitless	3.70093		3.49620		2.99989	
β	m/s	20.829		16.968		10.322	
	(kt)	(40.488)		(32.983)		(20.065)	

2.2.10.9.2 Conversion of the Fastest Mile to Peak Winds. The Frechet distributions for the fastest mile were obtained from Thom's analysis for KSC. From these two distributions—the Frechet for the peak winds as well as for the fastest mile—the ratio of the percentiles of the fastest mile to the peak winds were taken. This ratio varied from 1.12 to 1.09 over the range of probabilities from 30 to 99 percent. Thus, we adopted 1.10 as a factor to multiply the statistics of the fastest mile of wind to obtain peak (instantaneous) wind statistics. This procedure is based on the evidence of only one station. A gust factor of 1.10 is often applied to the fastest mile statistics in facility design work to account for gust loads.

2.2.10.9.3 The Peak Wind Profile. The peak wind profile law adopted for the four locations for peak winds at the 10-m (33-ft) level >22.6 m/s (>44 kt) is

$$u = u_{10}\left(\frac{z}{10}\right)^{1/7}, \tag{2.22}$$

where u_{10} is the peak wind at the 10-m (33-ft) height and u is the peak wind at height z in meters.

2.2.10.9.4 The Mean Wind Profile. To obtain the mean wind profile for various averaging times, the gust factors (table 2-32) are applied to the peak wind profile as determined by equation (2.22).

2.2.10.9.5 Design Wind Profiles for Station Locations. The design peak wind profiles for the peak winds in table 2-37 are obtained from the peak wind power law given by equation (2.22), and the mean wind profiles for various averaging times are obtained by dividing by the gust factors for the various averaging times. (The gust factors versus height and averaging times are presented in table 2-32.) The resulting selected design wind profiles for design return periods of 10, 100, and 1,000 yr for the four locations are given in tables 2-38 through 2-46, in which values of τ are given in minutes. The design risk versus desired lifetime for the design return periods of 10, 100, and 1,000 yr is presented in table 2-30.

Table 2-37. Peak winds (fastest mile values times 1.10) for the 10-m (33-ft) reference level for 10-, 100-, and 1,000-yr return periods.

	Peak Winds (u_{10})					
	SSC		VAFB		EAFB	
T_D (yr)	(m/s)	(kt)	(m/s)	(kt)	(m/s)	(kt)
10	33.2	64.5	26.8	52.1	19.9	38.7
100	48.9	95.0	39.3	76.3	35.7	69.4
1,000	71.4	138.7	56.9	110.7	63.4	123.2

Table 2-38. Facilities design wind as a function of averaging time (τ) for a peak wind of 33.2 m/s (64.5 kt) (10-yr return period) for SSC.

Height		Facilities Design Wind as a Function of Averaging Times, τ (min)											
		τ = 0 (peak)		τ = 0.5		τ = 1		τ = 2		τ = 5		τ = 10	
(m)	(ft)	(m/s)	(kt)	(m/s)	(kt)	(m/s)	(kt)	(m/s)	(kt)	(m/s)	(kt)	(m/s)	(kt)
10.0	33	33.2	64.5	25.2	48.9	24.2	47.0	23.1	44.9	21.7	42.2	20.7	40.3
18.3	60	36.2	70.3	28.5	55.4	27.5	53.5	26.5	51.5	25.1	48.7	24.0	46.7
30.5	100	38.9	75.6	31.6	61.4	30.6	59.5	29.5	57.4	28.1	54.6	27.1	52.6
61.0	200	43.0	83.5	36.1	70.1	35.1	68.3	34.1	66.2	32.6	63.4	31.6	61.4
91.4	300	45.5	88.5	38.9	75.6	38.0	73.8	36.9	71.8	35.5	69.0	34.5	67.0
121.9	400	47.4	92.2	41.0	79.7	40.1	77.9	39.0	75.9	37.7	73.2	36.6	71.2
152.4	500	48.5	94.3	42.3	82.2	41.4	80.5	40.4	78.5	39.0	75.8	38.0	73.8

2.2.11 Ground Winds for Runway Orientation Optimization

Runway orientation is influenced by a number of factors; e.g., winds, terrain features, population interference, etc. In some cases, the frequency of occurrence of crosswind components of some significant speed has received insufficient consideration. Aligning the runway with the prevailing wind will not ensure that crosswinds will be minimized. In fact, two common synoptic situations—one producing light easterly winds and the other causing strong northerly winds—might exist in such a relationship that a runway oriented with the prevailing wind might be the least useful to an aircraft constrained by crosswind components. Two methods—one empirical and the other theoretical—based on the bivariate normal distribution for wind vectors, of determining the optimum runway orientation to minimize critical crosswind component speeds are available (ref. 2-23).

Table 2-39. Facilities design wind as a function of averaging time (τ) for a peak wind of 48.9 m/s (95 kt) (100-yr return period) for SSC.

Height		Facilities Design Wind as a Function of Averaging Times, τ (min)											
		τ = 0 (peak)		τ = 0.5		τ = 1		τ = 2		τ = 5		τ = 10	
(m)	(ft)	(m/s)	(kt)	(m/s)	(kt)	(m/s)	(kt)	(m/s)	(kt)	(m/s)	(kt)	(m/s)	(kt)
10.0	33	48.9	95.0	37.1	72.1	35.6	69.2	34.1	66.2	32.0	62.2	30.6	59.4
18.3	60	53.3	103.6	42.0	81.7	40.5	78.8	39.0	75.8	36.9	71.7	35.4	68.8
30.5	100	57.3	111.4	46.5	90.4	45.1	87.6	43.5	84.6	41.4	80.4	40.8	79.3
61.0	200	63.3	123.0	53.1	103.3	51.8	100.6	50.2	97.5	48.1	93.5	46.6	90.5
91.4	300	67.0	130.3	57.3	111.4	55.9	108.7	54.4	105.8	52.3	101.6	50.8	98.7
121.9	400	69.9	135.8	60.4	117.4	59.1	114.8	57.6	111.9	55.5	107.8	54.0	104.9
152.4	500	71.4	138.8	62.2	121.0	60.9	118.4	59.5	115.6	57.4	111.6	55.9	108.7

Table 2-40. Facilities design wind as a function of averaging time (τ) for a peak wind of 71.4 m/s (138.7 kt) (1,000-yr return period) for SSC.

Height		Facilities Design Wind as a Function of Averaging Times, τ (min)											
		τ = 0 (peak)		τ = 0.5		τ = 1		τ = 2		τ = 5		τ = 10	
(m)	(ft)	(m/s)	(kt)	(m/s)	(kt)	(m/s)	(kt)	(m/s)	(kt)	(m/s)	(kt)	(m/s)	(kt)
10.0	33	71.4	138.7	54.1	105.2	52.0	101.1	49.7	96.7	46.7	90.8	44.6	86.7
18.3	60	77.8	151.2	61.3	119.2	59.2	115.1	56.9	110.7	53.8	104.6	51.7	100.5
30.5	100	83.7	162.7	68.0	132.1	65.8	128.0	63.5	123.5	60.4	117.5	58.2	113.2
61.0	200	92.4	179.6	77.6	150.8	75.6	146.9	73.3	142.4	70.2	136.5	68.0	132.2
91.4	300	97.9	190.3	83.6	162.6	81.6	158.7	79.5	154.5	76.3	148.4	74.2	144.2
121.9	400	102.0	198.2	88.1	171.3	86.2	167.5	84.0	163.3	80.9	157.3	78.8	153.1
152.4	500	104.3	202.7	90.9	176.7	89.0	173.0	86.8	168.8	83.8	162.9	81.6	158.7

Table 2-41. Facilities design wind as a function of averaging time (τ) for a peak wind of 26.8 m/s (52.1 kt) (10-yr return period) for VAFB and WSMR.

Height		Facilities Design Wind as a Function of Averaging Times, τ (min)											
		τ = 0 (peak)		τ = 0.5		τ = 1		τ = 2		τ = 5		τ = 10	
(m)	(ft)	(m/s)	(kt)	(m/s)	(kt)	(m/s)	(kt)	(m/s)	(kt)	(m/s)	(kt)	(m/s)	(kt)
10.0	33	26.8	52.1	20.3	39.5	19.5	38.0	18.7	36.3	17.5	34.1	16.8	32.6
18.3	60	29.2	56.8	23.0	44.8	22.2	43.2	21.4	41.6	20.2	39.3	19.4	37.7
30.5	100	31.4	61.1	25.5	49.6	24.7	48.1	23.9	46.4	22.7	44.1	21.9	42.5
61.0	200	34.7	67.5	29.2	56.7	28.4	55.2	27.5	53.5	26.4	51.3	25.6	49.7
91.4	300	36.8	71.5	31.4	61.1	30.7	59.6	29.8	58.0	28.7	55.8	27.9	54.2
121.9	400	38.3	74.5	33.1	64.4	32.4	63.0	31.6	61.4	30.4	59.1	29.6	57.5
152.4	500	39.1	76.1	34.1	66.3	33.4	64.9	32.6	63.3	31.5	61.2	30.7	59.6

Table 2-42. Facilities design wind as a function of averaging time (τ) for a peak wind of 39.3 m/s (76.3 kt) (100-yr return period) for VAFB and WSMR.

Height		Facilities Design Wind as a Function of Averaging Times, τ (min)											
		τ = 0 (peak)		τ = 0.5		τ = 1		τ = 2		τ = 5		τ = 10	
(m)	(ft)	(m/s)	(kt)	(m/s)	(kt)	(m/s)	(kt)	(m/s)	(kt)	(m/s)	(kt)	(m/s)	(kt)
10.0	33	39.3	76.3	29.8	57.9	28.6	55.6	27.4	53.2	25.7	49.9	24.5	47.7
18.3	60	42.8	83.2	33.7	65.6	32.6	63.3	31.3	60.9	29.6	57.6	28.4	55.3
30.5	100	46.0	89.5	37.3	72.6	36.2	70.4	35.0	68.0	33.2	64.6	32.0	62.3
61.0	200	50.8	98.8	42.7	83.0	41.6	80.8	40.3	78.4	38.6	75.1	37.4	72.7
91.4	300	53.9	104.7	46.0	89.5	44.9	87.3	43.7	85.0	42.0	81.7	40.8	79.3
121.9	400	56.1	109.1	48.5	94.3	47.4	92.2	46.2	89.9	44.6	86.6	43.3	84.2
152.4	500	57.4	111.5	50.0	97.2	48.9	95.1	47.7	92.8	46.1	89.6	44.9	87.3

Table 2-43. Facilities design wind as a function of averaging time (τ) for a peak wind of 56.9 m/s (110.7 kt) (1,000-yr return period) for VAFB and WSMR.

Height		Facilities Design Wind as a Function of Averaging Times, τ (min)											
		τ = 0 (peak)		τ = 0.5		τ = 1		τ = 2		τ = 5		τ = 10	
(m)	(ft)	(m/s)	(kt)	(m/s)	(kt)	(m/s)	(kt)	(m/s)	(kt)	(m/s)	(kt)	(m/s)	(kt)
10.0	33	56.9	110.7	43.2	84.0	41.5	80.7	39.7	77.1	37.2	72.4	35.6	69.2
18.3	60	62.1	120.7	49.0	95.2	47.3	91.9	45.5	88.4	43.0	83.5	41.3	80.2
30.5	100	66.8	129.8	54.2	105.4	52.5	102.1	50.7	98.6	48.2	93.7	46.5	90.3
61.0	200	73.7	143.3	61.9	120.3	60.3	117.2	58.4	113.6	56.0	108.9	54.2	105.4
91.4	300	78.1	151.9	66.8	129.8	65.2	126.7	63.4	123.3	61.0	118.5	59.2	115.1
121.9	400	81.4	158.2	70.3	136.7	68.8	133.7	67.0	130.3	64.6	125.6	62.9	122.2
152.4	500	83.2	161.8	72.6	141.1	71.0	138.1	69.3	134.7	66.9	130.1	65.2	126.7

Table 2-44. Facilities design wind as a function of averaging time (τ) for a peak wind of 19.9 m/s (38.7 kt) (10-yr return period) for EAFB.

Height		Facilities Design Wind as a Function of Averaging Times, τ (min)											
		τ = 0 (peak)		τ = 0.5		τ = 1		τ = 2		τ = 5		τ = 10	
(m)	(ft)	(m/s)	(kt)	(m/s)	(kt)	(m/s)	(kt)	(m/s)	(kt)	(m/s)	(kt)	(m/s)	(kt)
10.0	33	19.9	38.7	15.1	29.4	14.5	28.2	13.9	27.0	13.0	25.3	12.4	24.2
18.3	60	21.7	42.1	17.1	33.2	16.5	32.0	15.8	30.8	15.0	29.1	14.4	28.0
30.5	100	23.2	45.1	18.8	36.6	18.3	35.5	17.6	34.2	16.8	32.6	16.2	31.4
61.0	200	25.8	50.1	21.7	42.1	21.1	41.0	20.4	39.7	19.6	38.1	19.0	36.9
91.4	300	27.3	53.1	23.4	45.4	22.8	44.3	22.2	43.1	21.3	41.4	20.7	40.2
121.9	400	28.4	55.3	24.6	47.8	24.0	46.7	23.5	45.6	22.6	43.9	22.0	42.7
152.4	500	29.4	57.1	25.6	49.8	25.1	48.7	24.4	47.5	23.6	45.9	23.0	44.7

Table 2-45. Facilities design wind as a function of averaging time (τ) for a peak wind of 35.7 m/s (69.4 kt) (100-yr return period) for EAFB.

Height		Facilities Design Wind as a Function of Averaging Times, τ (min)											
		τ = 0 (peak)		τ = 0.5		τ = 1		τ = 2		τ = 5		τ = 10	
(m)	(ft)	(m/s)	(kt)	(m/s)	(kt)	(m/s)	(kt)	(m/s)	(kt)	(m/s)	(kt)	(m/s)	(kt)
10.0	33	35.7	69.4	27.1	52.7	26.0	50.6	24.9	48.4	23.4	45.4	22.3	43.4
18.3	60	38.8	75.5	30.6	59.5	29.6	57.5	28.4	55.3	26.9	52.2	25.8	50.2
30.5	100	41.6	80.9	33.8	65.7	32.8	63.7	31.6	61.4	30.0	58.4	29.0	56.3
61.0	200	46.2	89.9	38.8	75.5	37.8	73.5	36.7	71.3	35.1	68.3	34.1	66.2
91.4	300	49.0	95.2	41.9	81.4	40.8	79.4	39.8	77.3	38.2	74.3	37.1	72.1
121.9	400	51.0	99.2	44.1	85.7	43.2	83.9	42.0	81.7	40.5	78.7	39.4	76.6
152.4	500	52.7	102.4	45.9	89.3	45.0	87.4	43.9	85.3	42.3	82.3	41.3	80.2

Table 2-46. Facilities design wind as a function of averaging time (τ) for a peak wind of 63.3 m/s (123 kt) (1,000-yr return period) for EAFB.

Height		Facilities Design Wind as a Function of Averaging Times, τ (min)											
		τ = 0 (peak)		τ = 0.5		τ = 1		τ = 2		τ = 5		τ = 10	
(m)	(ft)	(m/s)	(kt)	(m/s)	(kt)	(m/s)	(kt)	(m/s)	(kt)	(m/s)	(kt)	(m/s)	(kt)
10.0	33	63.3	123.0	48.0	93.3	46.1	89.7	44.1	85.7	41.4	80.5	39.6	76.9
18.3	60	68.8	133.8	54.3	105.5	52.4	101.8	50.4	98.0	47.6	92.6	45.7	88.9
30.5	100	73.7	143.2	59.8	116.2	58.0	112.7	55.9	108.7	53.2	103.4	51.3	99.7
61.0	200	82.0	159.3	68.8	133.8	67.0	130.3	65.0	126.3	62.2	121.0	60.3	117.2
91.4	300	86.8	168.7	74.2	144.2	72.4	140.7	70.4	136.9	67.7	131.6	65.7	127.8
121.9	400	90.4	175.8	78.1	151.9	76.4	148.6	74.5	144.8	71.8	139.5	69.9	135.8
152.4	500	93.4	181.5	81.4	158.2	79.7	154.9	77.7	151.1	75.1	145.9	73.1	142.1

In the empirical method, the runway crosswind components are computed for all azimuth and wind speed categories in the wind rose (ref. 2-23). From these values, the optimum runway orientation can be selected that will minimize the risk of occurrence of any specified crosswind speed.

The theoretical method requires that the wind components are bivariate normally distributed; i.e., a vector wind data sample is resolved into wind components in a rectangular coordinate system, and the bivariate normal elliptical distribution is applied to the data sample of component winds. For example, let x_1 and x_2 be normally distributed variables with parameters (ξ_1, σ_1) and (ξ_2, σ_2). ξ_1 and ξ_2 are the respective means, while σ_1 and σ_2 are the respective standard deviations. Let ρ be the correlation coefficient, which is a measure of the dependence between x_1 and x_2. Now, the bivariate normal density function is

$$p(x_1, x_2) = \left[2\pi\sigma_1\sigma_2\left(1-\rho^2\right)^{1/2}\right]^{-1} \times \exp\left[-\left[2\left(1-\rho^2\right)\right]^{-1}\right] \times \left[\left(\frac{x_1-\xi_1}{\sigma_1}\right)^2 - 2\rho\left(\frac{x_1-\xi_1}{\sigma_1}\right)\left(\frac{x_2-\xi_2}{\sigma_2}\right) + \left(\frac{x_2-\xi_2}{\sigma_2}\right)^2\right]. \quad (2.23)$$

Let α be an arbitrary angle in the rectangular coordinate system. From the statistics in the (x_1,x_2) space, the statistics for any rotation of the axes of the bivariate normal distribution through any arbitrary angle α may be computed (ref. 2-24). Let α denote the desired increments for which runway orientation accuracy is required; e.g., one may wish to minimize the probability of crosswinds with a runway orientation accuracy down to $\alpha = 10^o$. This means we must rotate the bivariate normal axes through every 10°. It is only necessary to rotate the bivariate normal surface through 180° since the distribution is symmetric in the other two quadrants. Let (y_1,y_2) denote the bivariate normal space after rotation.

This rotation process will result in 18 sets of statistics in the (y_1,y_2) space. The quantity y_1 is the head-wind component, while y_2 is the crosswind component. Since we are concerned with minimizing the probability of crosswinds (y_2) only, we now examine the marginal distribution $p(y_2)$ for the 18 orientations. Since $p(y_1,y_2)$ is bivariate normal, the 18 marginal distributions $p(y_2)$ must be univariate normal:

$$p(y_2) = \left[\sigma_2 (2\pi)^{1/2}\right]^{-1} \exp\left[-\frac{1}{2}\left[\frac{(y_2 - \xi_2)}{\sigma_2}\right]^2\right] . \tag{2.24}$$

ξ_2 and σ_2 are replaced by their sample estimates Y_2 and S_{y_2}. Now, let

$$z = \frac{Y_2 - \bar{Y}_2}{S_{y_2}} , \tag{2.25}$$

where y_2 is the critical crosswind of interest and S_{y_2} is the standard deviation of the y_2 with respect to its mean $\bar{y}_2$. The quantity z is a normal variable, and the probability of its exceedence is easily calculated from the tables of the standard normal integral. Since a right or left crosswind (y_2) is a constraint to an aircraft, the critical region (exceedence region) for the normal distribution is two-tailed; i.e., we are interested in twice the probability of exceeding $|y_2|$. Let this probability of exceedence or risk equal R. Now, the orientation for which R is a minimum is the desired optimum runway orientation. The procedure described may be used for any station. Only parameters estimated from the data are required as input. Consequently, many runways and locations may be examined rapidly.

Either the empirical or theoretical method may be used to determine an aircraft runway orientation that minimizes the probability of critical crosswinds. Again, it is emphasized that the wind components must be bivariate normally distributed to use the theoretical method. In practical applications, the following steps are suggested:

(1) Test the component wind samples for bivariate normality if these samples are available.

(2) If the component winds are available and cannot be rejected as bivariate normal using the bivariate normal goodness-of-fit test, use the theoretical method since it is more expedient and easily programmed.

(3) If the component wind data samples are not available and there is doubt concerning the assumption of bivariate normality of the wind components, use the empirical method.

2.3 In-Flight Winds (>150 m)

2.3.1 Introduction

In-flight wind speed profiles (i.e., profiles >150 m or 492 ft) are used in vehicle design studies primarily to establish structural and control system capabilities and to compute performance requirements. The in-flight wind speeds selected for vehicle design may not represent the same percentile value as the design surface wind speed. The selected wind speeds (in-flight and surface) are determined by the desired on-pad stay time and vehicle launch capabilities and can differ in the percentile level. Since the in-flight and surface wind speeds differ in degree of persistence for a given reference time period, they can be treated as being statistically independent for engineering design purposes.

Figure 2-9 provides an illustration of the consideration that must be addressed in the application of upper-level winds in ascent design studies for an aerospace vehicle. The goal is to minimize the loads the vehicle receives, and thus must be designed to accommodate, relative to the upper-level winds and control authority used. To accomplish this analysis, a three-way trade study must be accomplished. The three "rules of thumb" noted in figure 2-9 are of special importance and must be recognized and understood by the atmospheric environment design requirements provider, design engineer, operation engineer, and program management.

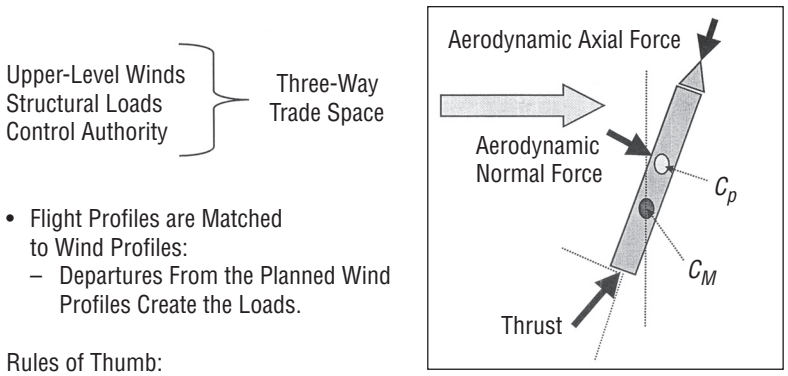

Figure 2-9. Three-way trade space: Upper level winds-structural loads-control authority.

Wind profile information for in-flight design studies is presented in two basic forms: synthetic—scalar and vector—profiles and measured profile samples. There are certain limitations to each of these wind input forms, and their utility in design studies depends on a number of considerations such as (1) accuracy of basic measurements, (2) complexity of input to vehicle design, (3) economy and practicality for design use, (4) ability to represent significant features of the wind profile, (5) statistical assumption versus physical representation of the wind profile, (6) ability of input to ensure control system and structural integrity of the vehicle, and (7) flexibility for use in design tradeoff studies.

An accurate and adequate number of measured wind profiles are necessary for developing a valid statistical description of the synthetic wind profile. Fortunately, current records of data from some locations (KSC in particular) fulfill these requirements, although a continuing program of data acquisition is vital to further enhance the confidence of the statistical information generated. Various methods and sensors for obtaining in-flight profiles include the rawinsonde, radar wind profiler, the FPS-16 radar/Jimsphere, the Automated Meteorological Profiling System (AMPS), and the rocketsonde. The statistical analyses performed on the in-flight wind profiles provide detailed descriptions of the upper winds and an understanding of the profile characteristics, such as temporal and height variations, as well as indications of the frequency and the persistence of transient meteorological systems.

The synthetic—scalar and vector—type of wind profile (see sec. 2.4.5) is the oldest method used to present in-flight design wind data. The synthetic wind profile data are presented in this document because this method of presentation provides a reasonable approach for most design studies when properly used, especially during the early design periods. Also, the concept of synthetic wind profiles is generally understood and employed in most aerospace organizations for design computations. The synthetic wind profile includes the wind speed, wind speed change, maximum wind layer thickness, and gusts that are required to establish vehicle design structural and control system values. Table 2-56 provides standardized normal (univariate) distribution for percentiles and interpercentile ranges.

Currently, launch vehicles for use at various launch sites and in comprehensive space research mission and payload configurations are designed by use of synthetic vector wind and wind shear models without regard to specific wind direction. However, if a vehicle is restricted to a given launch site, flight azimuths, and a specific configuration and mission, wind components (head, tail, left-cross, or right-cross) are often used. Component wind profiles are sometimes used, and, for a given percentile, the magnitudes of component winds are equal to or less than those of the scalar winds. Component or directionally-dependent winds should not be employed in initial design studies unless specifically authorized by the cognizant design organization. Vector wind and vector wind shear models may be more applicable and were used for the Space Shuttle vehicle.

Selection of a set of detailed wind profiles for final design verification and launch delay risk calculations requires the matching of vehicle simulation resolution and technique to frequency or information content of the profile. Detailed wind profile data sets for design verification use are available for KSC and VAFB (see sec. 2.3.11.1). Selected samples of detailed wind profiles are available for other locations. Contact the NASA MSFC Natural Environments Branch.

The synthetic—scalar and vector—wind profile provides a conditionalized wind shear/gust state with respect to the given design wind speed. Therefore, in concept, the synthetic wind profile should produce a vehicle design which has a launch delay risk not greater than a specified design synthetic wind profile value, which is generally the value associated with the design wind speed. This statement, although generally correct, depends on the control system response characteristics, the vehicle structural integrity, etc. A joint condition of wind shear, gust, and speeds is given in selection of detailed wind profiles for design verification. Therefore, the resulting launch delay risk for a given vehicle design is the specified value of risk computed from the vehicle responses associated with the various profiles. For the synthetic profile, a vehicle in-flight wind speed capability and maximum launch delay risk may be stated which is conditional upon the wind/gust design values. However, for the selection of detailed wind profiles, only a vehicle launch risk value may be given since the wind characteristics are treated as a joint event. These two differences in philosophy should be understood to avoid misinterpretation of vehicle response calculation comparisons. In both cases, allowance for dispersions in vehicle characteristics should be made prior to flight simulation through the wind profiles and establishment of vehicle design response or

operational launch delay risk values. The objective is to ensure that an aerospace vehicle will accommodate the desired percentage of wind profiles or conditions in its nonnominal flight mode; i.e., engine-out, etc.

2.3.2 Wind Aloft Climatology

Considerable data summaries (monthly and seasonal) exist on wind aloft statistics for the world. However, it is necessary to interpret these data in terms of the desired vehicle operational capabiltiy engineering design problem and design philosophy. For example, wind requirements for performance calculations relative to aircraft fuel consumption requirements must be derived for the specific routes and design reference period. Such data are available on request. Characteristics of winds aloft are provided in the following sections for the general information of the reader. The Cape Canaveral sea/land breeze conditions encompass both the ground and inflight wind regions below ≈3,000 ft. The characteristics of these winds and associated meteorological characteristics are described in section 2.5, Cape Canaveral (KSC) Sea/Land Breeze Winds.

2.3.3 Wind Component Statistics

Wind component statistics are used in mission planning to provide information on the probability of exceeding a given wind speed in the pitch or yaw planes and to bias the tilt program at a selected launch time. The improved vector wind profile model discussed in section 2.3.10 is directly applicable to the description of these input data. Using this model, the wind component statistics can be computed for various flight azimuths for each month for the pitch plane (range) and yaw plane (cross range) at KSC and VAFB. References 2-25 through 2-27 contain some general background information on the statistical distributions of wind speeds and vector wind components.

2.3.3.1 Upper Wind Correlations. Coefficients of correlations of wind components between altitude levels with means and standard deviations at altitude levels may be used in a statistical model to derive representative wind profiles. A method of preparing synthetic wind profiles by use of correlation coefficients between wind components is described in reference 2-28. In addition, these correlation data are applicable to certain statistical studies of vehicle responses (ref. 2-29).

Data on correlations of wind between altitude levels for various geographical locations are presented in references 2-30 through 2-32. The reports give values of the interlevel and intralevel coefficients of linear correlations between wind components. The linear correlation coefficients between altitudes within the 10- to 15-km altitude region are very high, but decrease with greater altitude separation.

For correlations between wind components, the reader is referred to the work of Buell (refs. 2-33 and 2-34) for a detailed discussion of the subject.

2.3.3.2 Thickness of Strong Wind Layers. Wind speeds in the midlatitudes generally increase with altitude to a maximum of between 8 and 14 km. Above 14 km, the wind speeds decrease with altitude, then increase at higher altitude, depending upon season and location. Frequently, these winds exceed 50 m/s in the jet stream, a core of maximum winds over the midlatitudes in the 8- to 14-km altitudes. The vertical extent of the core of maximum winds, or the sharpness of the extent of peak winds on the wind profile, is important in some vehicle studies. For information concerning the thickness of strong wind layers, the reader is referred to reference 2-35.

Table 2-47 shows values of vertical thickness (based on maximum thickness) of the wind layers for wind speeds for KSC. Similar data for VAFB are given in table 2-48. At both ranges, the thickness of the layer

Table 2-47. Thickness for strong wind layers at KSC.

Quasi-Steady-State Wind Speed	Maximum Thickness		Altitude Range	
(±5 m/s)	(km)	(mi)	(km)	(mi)
50	4	2.5	8.5 to 16.5	5.3 to 10.3
75	2	1.2	10.5 to 15.5	6.5 to 9.6
92	1	0.6	10.0 to 14.0	6.2 to 8.7

Table 2-48. Thickness for strong wind layers at VAFB.

Quasi-Steady-State Wind Speed	Maximum Thickness		Altitude Range	
(±5 m/s)	(km)	(mi)	(km)	(mi)
50	4	2.5	8.0 to 16	5.0 to 9.9
75	2	1.2	9.5 to 14	5.9 to 8.7

decreases with the increase of wind speed; i.e., the sharpness of the wind profile in the vicinity of the jet core becomes more pronounced as wind speed increases.

2.3.3.3 Scalar Wind Speeds (10- to 15-km Altitude Layer). The distributions of scalar wind speed in the 10- to 15-km altitude layer over the United States are shown in figure 2-10 for the 95-percentile values and figure 2-11 for the 99-percentile values. The location of local maximum in the isopleths (maximum wind speeds) is shown by heavy lines with arrows. These winds occur at approximately the level of maximum dynamic pressure for most aerospace vehicles.

2.3.3.4 Temporal Wind Changes. Atmospheric wind fields change with time. Significant wind direction and speed changes can occur over time scales as short as a few minutes or less. There is no upper bound limit on

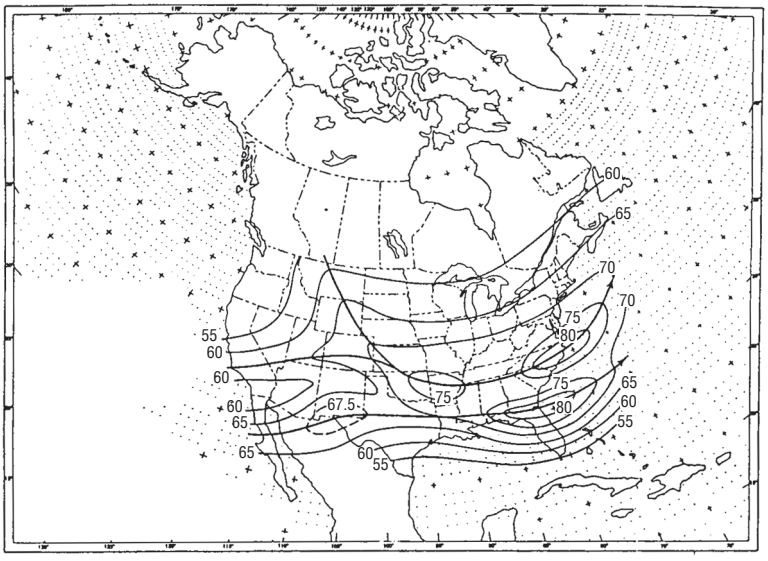

Figure 2-10. Scalar wind speeds (m/s) 95-percentile envelope analysis prepared from windiest month and maximum winds in the 10- to 15-km layer (NASA/NCDC).

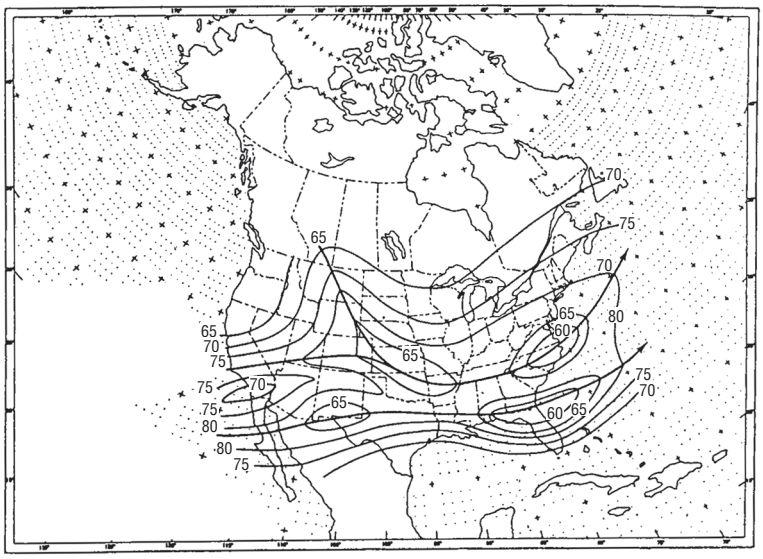

Figure 2-11. Scalar wind speeds (m/s) 99-percentile envelope analysis prepared from windiest month and maximum winds in the 10- to 15-km layer (NASA/NCDC).

the time scale over which the wind field can change. To develop real-time wind biasing programs for aerospace vehicle control and structural load minimization purposes, which involve the use of wind profiles observed a number of hours prior to launch, it is necessary that consideration be given to the changes in wind speed and direction that can occur during the time elapsed from entering the biasing profile into the vehicle control system logic to the time of launch. If the observed wind profile 8 hr prior to launch is to be used as a wind biasing profile, then consideration should be given to the dispersions in wind direction and speed that could occur over this period of time. Wind speed and direction change data are also useful for mission operation purposes. Results of studies conducted to define these dispersions in a statistical context are presented herein. Specialized databases containing pairs of FPS-16 Jimsphere-measured detail wind profiles over time periods of 2 to 12 hr are available upon request to the Natural Environments Branch, Marshall Space Flight Center, AL 35812.

Temporal vector wind change at KSC and VAFB has been studied by Adelfang (refs. 2-36 and 2-37). The joint distribution of the four variables represented by the *U* and *V* components of the wind vector at an initial time and after a specified elapsed time is hypothesized to be quadravariate normal. The 14 statistics of this distribution are presented according to the monthly reference period for altitudes from zero to 27 km. These statistics are used to calculate percentiles of the theoretical distribution of wind component change with respect to time (univariate normal distribution), the joint distribution of wind component change (bivariate normal), the modulus of vector wind change (Rayleigh), and the vector wind at a future time given the vector wind at an initial time (conditional bivariate normal); the large body of statistics contained in these references are not repeated herein. For the purpose of illustrating the application of these statistics, the 95-percentile vector wind change ellipses for time intervals of 12, 24, 36, 48, 60, and 72 hr at 6, 12, and 18 km during April at KSC and during January at VAFB have been calculated. KSC, April and VAFB, January were two of the months representing extreme wind change. Each ellipse illustrated in figure 2-12 was calculated from the bivariate normal statistics of vector wind change given in the referenced reports; each ellipse encompasses 95 percent of the wind change expected for the indicated time interval. The methodology for calculation of wind or wind change ellipses for any percentile is described by Smith (ref. 2-38). The wind change ellipses illustrated in figure 2-12 clearly indicate the strong variation of wind change for time intervals <48 hr, and the relatively large wind change for VAFB.

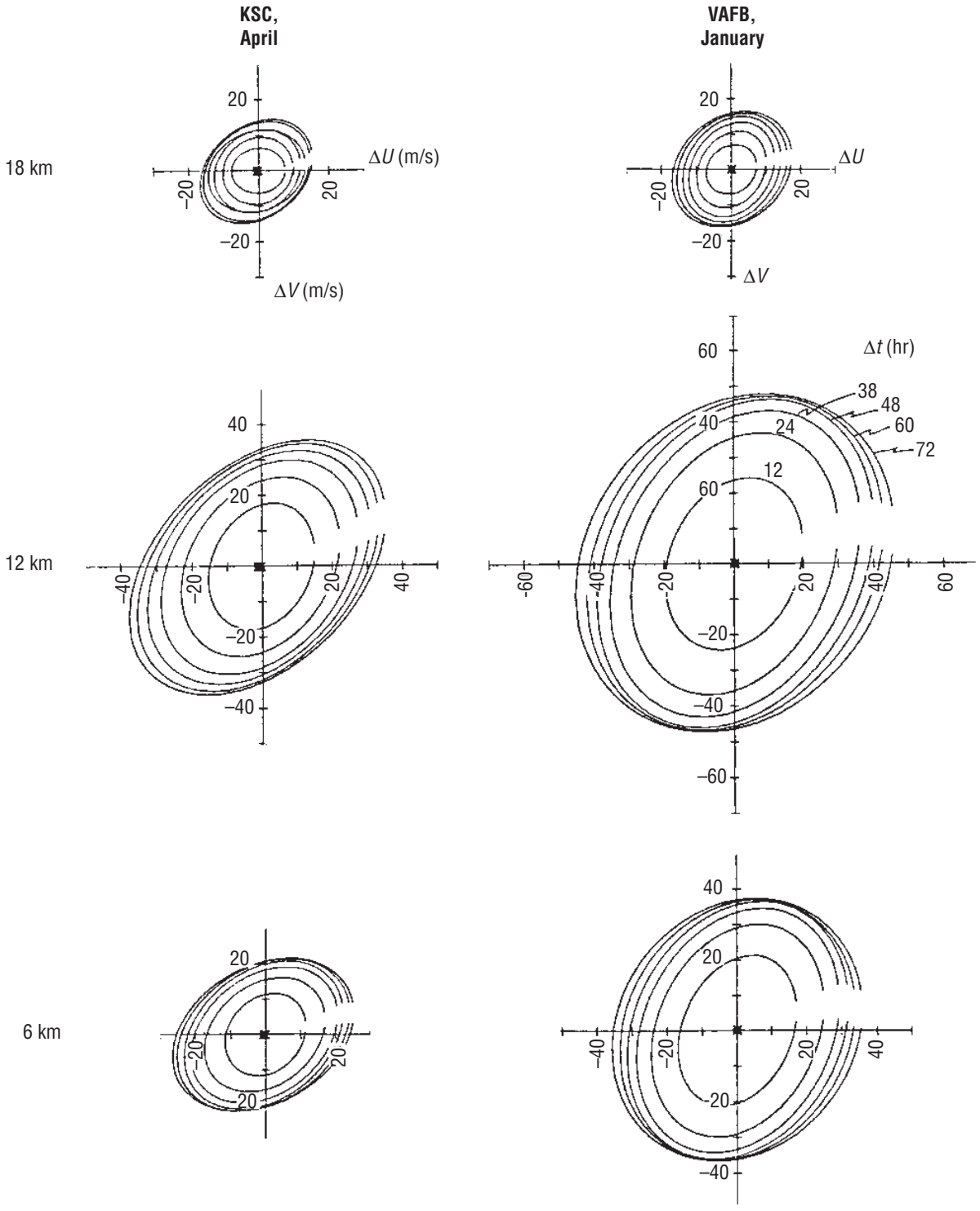

Figure 2-12. KSC, April and VAFB, January 95-percentile vector wind change (ΔU and ΔV) ellipses at 6-, 12-, and 18-km altitude for time intervals of 12, 24, 36, 48, 60, and 72 hr.

The information presented in this section is intended to provide the reader with a general overview on changes that may occur in winds aloft as a function of time for KSC. This information is not intended for use in day-of-launch (DOL) wind biasing. Wind is a vector quantity and a better method to DOL analyses is to use time-conditional wind vector probability ellipses (ref. 2-1). The concepts and statistical methodology applicable for launch systems that use a trajectory and loads assessment based on a DOL wind profile for commit to launch decision are presented in references 2-1, 2-36, and 2-39. They should be consulted for information on this process.

Figure 2-13 (ref. 2-39) is a 12- and 24-hr time-conditional, 50-percent probability ellipses whereby the given wind vectors are four wind vectors that yield the largest relative head-tail and crosswind components. The 85-percent wind probability reference ellipse was selected with respect to a 90° flight azimuth.

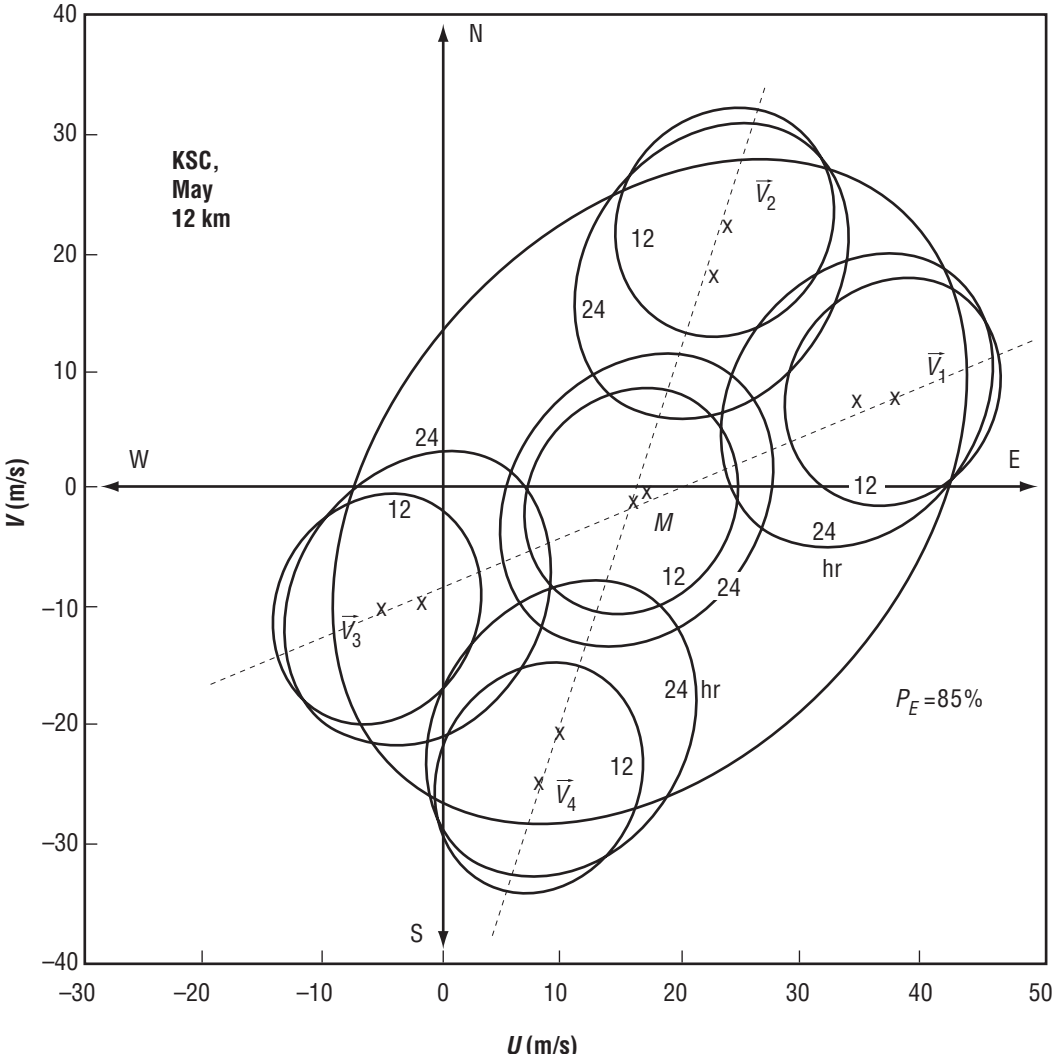

Figure 2-13. Example for 50-percent time-conditional wind probability ellipses for 12 and 24 hr for given vectors (ref. 2-39).

Additional related analyses on temporal wind changes that may provide further insight into this subject have been accomplished at KSC:

(1) A study by Merceret (ref. 2-40) using KSC's 50-MHz Doppler radar wind profiler (DRWP) analyzed the temporal vector wind change over periods ranging from 0.25 to 4 hr. The study was conducted taking advantage of the higher temporal sampling rate of the DRWP compared to the Jimsphere-measured winds used in references 2-36 and 2-37. Six months of winter season (October 1995–March 1996) winds over KSC resulting in over 25,000 profiles comprised the data set for analysis. Extensive quality control was applied to the data as described in reference 2-40. Since climatologically winds aloft during winter are stronger and more variable over KSC, the study provides a worst-case analysis in terms of risk to the launch vehicle.

The study demonstrated that the magnitude of the vector wind changes over a 0.25- to 4-hr period at altitudes between 6 and 17 km (20 to 56 kft) is lognormally distributed, not Gaussian. This was true both for the wind changes at any single level and for the maximum wind change in the entire 6- to 17-km region. The location and shape parameters for the lognormal distributions depended on whether the single level or maximum within the region was selected, and on the time interval. Lognormal distributions produce extreme values more frequently than Gaussian distributions having the same mean and standard deviation. For the observed wind change distributions, the 3σ event is an order of magnitude more likely and the 5σ event is three orders of magnitude more likely than with a Gaussian distribution (ref. 2-41). Therefore, use of Gaussian probabilities for estimating the risk of unacceptable wind changes for launch vehicles may result in a serious and nonconservative error.

(2) The coherence time of wind features is a function of the vertical scales of motion determining the features (refs. 2-42 and 2-43). This has significant implications for the efficient design of wind loads analyses and methodologies (ref. 2-44). Despite major differences in approach, the studies of Merceret (ref. 2-42) and Spiekerman, Sako, and Kabe (ref. 2-43) both obtained relations close to the form

$$(\lambda) = 460*\mathrm{SQRT}\,(t)\ , \tag{2.26}$$

where (λ) is the vertical scale of motion (ft) below which motion is not coherent beyond a time interval, t (min). Merceret used 6 mo of wintertime 50-MHz wind profiler data from KSC with temporal averaging to derive the coherence. Spiekerman, Sako, and Kabe used Jimsphere data from all months of the year at both the Eastern Range (KSC) and the Western Range (VAFB) with overlapping vertical averages to derive the coherence.

2.3.4 Vehicle Ascent Wind Load Alleviation Techniques

In attempting to maintain a desired flight path for an aerospace vehicle through a strong wind region, the vehicle control system could introduce excessive bending moments and orbit anomalies. To reduce this problem, it is sometimes desirable to wind bias the pitch program; i.e., to tilt the vehicle sufficiently to produce the desired flight path and minimize dynamic pressure-level loads with the expected wind profile. Since most in-flight strong winds over KSC are winter westerlies, it is sometimes expedient to use the monthly or seasonal pitch plane median wind speed profile for bias analyses.

Head and tail wind components and right and left crosswind components from altitudes of zero to 70 km can be computed for any flight azimuth used at KSC or VAFB. For applications where both pitch and yaw biasing are used, monthly vector mean winds may be more efficient for wind biasing. Such statistics can be made available upon request, or see section 2.3.9 and reference 2-39 for a new wind biasing technique.

2.3.5 Vector Wind Models

Wind is a vector quantity having a magnitude and direction. A coordinate system and a statistical model are required. The bivariate normal probability distribution is used to model the wind at discrete altitudes. Wind measurements are recorded in terms of wind direction and magnitude. The wind direction is measured in degrees clockwise from true north and is the direction from which the wind is blowing. The wind magnitude (the modulus of the vector) is the scalar quantity and is referred to as wind speed or scalar wind. The standard meteorological coordinate system (fig. 2-14) has been chosen for the wind statistics and tables of statistical parameters.

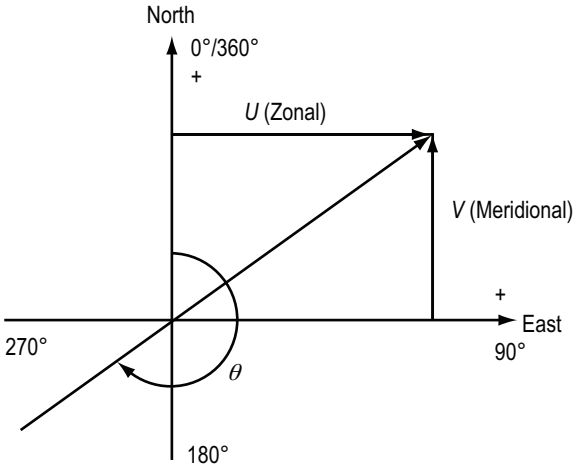

Definitions:

U = zonal wind component, positive west to east in units, m/s ($U = -W \cos\theta$).
V = meridional wind component, positive south to north in units, m/s ($V = -W \sin\theta$).
W = wind speed in units, m/s.
θ = wind direction measured in degrees clockwise from true north and is the direction from which the wind is blowing,

where $0° \le \theta \le 360°$.

Figure 2-14. Meteorological coordinate system.

The bivariate normal probability density function (BNpdf) can be expressed in Cartesian and polar coordinates. Using population notations for the required five statistical parameters, the BNpdf in the usual mathematical Cartesian coordinates is

$$f(\bar{x},\bar{y}) = \frac{1}{2\pi\,\sigma_x\,\sigma_y\sqrt{1-\rho^2}}\,exp\left[\frac{1}{2\left(1-\rho^2\right)}\left[\frac{\left(X-\bar{X}\right)^2}{\sigma_x^2} - \frac{2\rho\left(X-\bar{X}\right)\left(Y-\bar{Y}\right)}{\sigma_x\,\sigma_y} + \frac{\left(Y-\bar{Y}\right)^2}{\sigma_y^2}\right]\right], \qquad (2.27)$$

where $-\infty \le X \le \infty$ and $-\infty \le Y \le \infty$. This function is completely described by the five parameters: the means X and Y, the standard deviations σ_x and σ_y, and the linear correlation coefficient, ρ, between the variables x and y.

The contours of equal probability density form a family of concentric ellipses with respect to the centroid located at the point $\{\bar{x}, \bar{y}\}$. The probability contained within a contour of equal probability density is obtained by integrating the probability density function over the region defined by the contour. This integration is obtained in closed form; the result is called a probability ellipse for the assigned probability area.

Using the properties of the bivariate normal probability distribution to model the wind as a vector quantity at discrete altitudes, many other probability functions can be derived. All that is required are the five bivariate normal statistical parameters with respect to an orthogonal coordinate system. The practical system of equations are given by Smith (ref. 2-38) and repeated in the Range Reference Atmosphere publications (ref. 2-25) with illustrations. In terms of wind statistics, some of these properties are as follows:

(1) The five statistical parameters that have been computed with respect to a meteorological zonal and meridional coordinate system can be rotated to any other orthogonal coordinate system and the properties of the bivariate normal distribution still holds.

(2) The wind components are univariate normally distributed. Percentile values and interpercentile values can be computed.

(3) The conditional distribution of one wind component given the other is univariate normally distributed.

(4) The sum and difference of bivariate normally distributed variates are univariate normally distributed.

(5) The probability ellipse that contains p-percent of the wind vectors can be computed.

(6) The probability density function for wind direction can be derived, and, by numerical integration, the probability for wind direction within any assigned limits can be computed.

(7) The conditional probability density function for wind speed given a wind direction can be obtained.

(8) The conditional probability distribution function for wind speed given a wind direction can be obtained.

(9) The probability density function for wind speed can be derived as a generalized Rayleigh distribution (ref. 2-38). It is expressed as a series of the sum of products of the modified Bessel function.

The equations for the above functions are given in the most general form for all five statistical parameters for the bivariate normal distribution. For assumptions such as independent variates, zero means and equal variances are treated as special cases. With the advent of modern computers, these functions can be readily evaluated and graphic illustrations made. Some of these probability functions are presented in this subsection because of their important role in wind vector modeling.

2.3.5.1 Bivariate Normal Wind Parameters. This section presents a discussion on the properties of the bivariate normal probability distribution as related to modeling wind vectors at discrete altitudes. From the five bivariate normal statistical parameters (i.e., component means of $\overline{U}$ and $\overline{V}$, and standard deviations of S_U

and S_V and the correlation coefficient between U and $\overline{V}$) can be used to derive several other statistics using the equation as presented in reference 2-25. Graphical illustrations for these probability functions are also presented in reference 2-25, the range reference atmospheres (RRAs). The value to the engineer for these statistics is for background on winds aloft climatology at specific sites. There are several publications (refs. 2-25 through 2-27, 2-45) that contain the bivariate normal wind statistical parameters versus altitude. All of these reports give tabulations for the five bivariate normal parameters with respect to the meteorological coordinate system.

The five statistical parameters are:

$\overline{U}$ = monthly mean zonal wind component (m/s)
$\overline{V}$ = monthly mean meridional wind component (m/s)
S_U = standard deviation with respect to the monthly mean for the zonal wind component (m/s)
S_V = standard deviation with respect to the monthly mean for the meridional wind component (m/s)
$R(U,V)$ = correlation coefficient between the two components.

Tables 2-49 through 2-54 are taken from the RRA reference. These statistical parameters are for KSC, February and July; VAFB, December and July; and EAFB, February and July. For the altitude region zero to 27 km, these parameters are from twice daily, serially complete rawinsonde wind measurements. The altitudes from 28 to 86 km are from rocketsonde wind measurements. The period of record is 19 yr for KSC, 10 yr for VAFB, and 12 yr for EAFB. These months for the respective sites are chosen for illustration because they represent winter and summer conditions and reasonably envelop the winds for both sites for all months.

For aerospace vehicle applications, it is often desired to express the wind statistics with respect to the vehicle flight azimuth.

By using coordinate rotation equations, these five statistical parameters can be calculated with respect to any orthogonal coordinates. Let the vehicle flight azimuth, α, be measured in degrees clockwise from true north; the five statistical parameters with respect to the flight axes are then given by the following equations:

(a) The means

$$\overline{X}_a = \overline{U}\sin\alpha + \overline{V}\cos\alpha \tag{2.28}$$

and

$$\overline{Y}_a = \overline{V}\sin\alpha - \overline{U}\cos\alpha \ . \tag{2.29}$$

(b) The variances

$$S^2_{x\alpha} = S^2_U \sin^2\alpha + S^2_V \cos^2\alpha + 2R(U,V)S_U S_V \sin\alpha\cos\alpha \tag{2.30}$$

and

$$S^2_{y\alpha} = S^2_V \sin^2\alpha + S^2_U \cos^2\alpha - 2R(U,V)S_U S_V \sin\alpha\cos\alpha \ . \tag{2.31}$$

Table 2-49. Bivariate normal wind statistics—zonal and meridional, KSC, February.

z (km)	MEAN *U* (m/s)	SD *U* (m/s)	*R*(*U*,*V*)	MEAN *V* (m/s)	SD *V* (m/s)	NOBS
0.003	0.95	2.88	–0.2441	–0.64	3.76	796
1	3.89	7.10	0.0019	1.31	6.92	797
2	8.25	7.61	0.0703	1.58	6.69	797
3	12.24	7.98	0.0992	1.80	7.12	796
4	15.88	8.77	0.1049	2.34	7.68	789
5	19.75	9.85	0.1214	3.00	8.59	788
6	23.62	10.89	0.1674	3.61	9.32	789
7	27.33	12.01	0.2255	4.23	10.15	787
8	31.10	13.27	0.2382	4.56	11.33	780
9	34.85	14.57	0.2235	4.74	12.50	774
10	38.72	15.66	0.2339	4.67	13.52	765
11	41.70	16.01	0.2396	4.25	14.03	741
12	44.48	15.41	0.2197	4.46	14.02	738
13	44.20	14.10	0.2531	4.46	13.03	726
14	40.97	13.01	0.2632	4.00	11.09	710
15	36.52	11.15	0.2558	3.53	9.08	707
16	31.36	9.84	0.2305	3.13	7.95	702
17	25.66	8.80	0.2221	2.41	6.84	690
18	19.71	8.35	0.2387	1.68	5.69	687
19	13.57	7.52	0.2877	1.28	4.46	684
20	9.00	6.84	0.3468	0.68	3.43	682
21	6.17	7.07	0.3594	–0.05	3.29	670
22	4.78	8.04	0.3615	–0.42	3.60	663
23	4.07	7.62	0.3222	–0.46	3.18	659
24	3.72	8.71	0.3311	–0.31	3.39	648
25	3.70	9.51	0.2351	0.06	3.44	638
26	4.20	9.49	0.2374	0.44	3.42	616
27	5.16	9.85	0.2466	0.78	3.48	563
28	6.15	10.22	0.1955	1.30	3.81	533
29	8.25	10.82	0.2804	1.86	4.16	372
30	10.50	11.23	0.3000	2.48	4.31	361
32	15.09	13.11	0.4269	2.73	6.68	111
34	16.58	14.64	0.3381	1.22	5.99	112
36	14.53	15.36	0.2646	–0.75	6.57	116
38	12.09	16.60	0.2709	0.01	7.22	117
40	10.20	18.41	0.0997	1.04	7.87	118
42	9.38	19.01	0.0105	3.46	8.18	120
44	10.98	19.16	0.0868	6.39	9.58	120
46	12.92	21.02	0.1373	7.43	10.87	120
48	15.67	22.74	0.1909	8.18	11.41	120
50	18.89	22.86	0.1345	8.67	12.80	118
52	22.59	23.26	0.1939	8.81	12.55	117
54	27.28	22.08	0.2773	8.57	13.34	115
56	34.85	21.34	0.2476	12.28	14.50	110
58	41.01	20.84	0.3470	14.98	13.60	95
60	46.86	20.79	0.2436	15.12	13.99	82
62	50.67	22.98	0.3723	11.54	14.38	53
64	55.74	18.40	0.1697	6.51	15.74	44
66	57.25	19.22	0.1879	–0.45	17.40	39
68	56.07	17.87	0.2619	–8.14	13.65	30
70	49.27	20.28	0.2182	–10.89	17.35	27
72	52.28	34.81	0.3917	0.86	19.82	19
74	49.06	34.98	0.1233	0.98	23.41	20
76	47.91	35.51	0.1905	0.53	25.58	18
78	42.83	36.38	0.3862	–0.47	26.68	16
80	39.74	37.23	0.4223	–1.47	27.73	16
82	36.47	39.32	0.2424	–0.40	31.12	16
84	33.20	41.30	–0.0659	0.67	34.18	14
86	30.73	45.30	0.8446	0.99	58.79	5
88	29.07	50.84	–	0.56	88.51	–
90	27.41	55.82	–	0.13	110.5	–

Table 2-50. Bivariate normal wind statistics—zonal and meridional, KSC, July.

z (km)	MEAN *U* (m/s)	SD *U* (m/s)	*R*(*U*,*V*)	MEAN *V* (m/s)	SD *V* (m/s)	NOBS
0.003	–0.34	2.30	–0.0423	1.21	1.89	794
1	1.21	4.23	–0.0443	2.48	3.16	792
2	1.28	4.50	0.0794	2.01	3.25	792
3	1.41	4.65	0.0706	1.61	3.30	784
4	1.40	4.58	0.0820	1.29	3.43	779
5	1.30	4.46	0.0145	0.94	3.56	777
6	0.90	4.40	0.0477	0.72	3.67	778
7	0.40	4.56	0.0904	0.23	3.94	777
8	–0.16	5.12	0.1833	–0.30	4.38	777
9	–0.86	5.89	0.2678	–0.87	5.03	774
10	–1.60	6.74	0.3201	–1.52	5.64	767
11	–2.34	7.92	0.3275	–2.22	6.36	764
12	–3.01	8.66	0.3220	–3.19	6.85	758
13	–3.75	9.11	0.2685	–4.17	7.26	754
14	–4.37	8.13	0.2420	–4.65	6.72	750
15	–4.75	6.38	0.2751	–4.02	5.33	750
16	–5.17	4.59	0.3230	–2.84	3.88	746
17	–6.14	3.43	0.2961	–1.91	2.92	738
18	–8.13	3.02	0.1343	–1.67	2.66	739
19	–11.06	2.60	0.1049	–1.23	2.39	732
20	–13.74	2.86	0.2043	–0.22	2.40	721
21	–15.57	3.32	0.1119	0.88	2.44	703
22	–16.21	3.08	–0.0187	1.30	2.12	692
23	–16.84	2.90	–0.1188	1.05	1.98	673
24	–17.53	3.04	–0.1369	0.38	2.22	674
25	–18.20	3.12	–0.0471	–0.25	2.20	663
26	–18.84	3.50	0.0090	–0.66	2.27	628
27	–19.63	4.13	–0.0286	–0.90	3.01	581
28	–20.79	4.00	–0.0951	–0.92	2.59	544
29	–21.89	4.79	–0.0568	–0.93	3.30	433
30	–22.95	4.29	–0.0096	–0.42	2.66	406
32	–26.25	4.77	–0.0798	1.64	3.62	112
34	–27.01	5.07	–0.1080	0.63	3.41	112
36	–29.19	4.54	–0.1421	0.11	3.79	112
38	–32.36	5.49	0.0578	0.16	4.69	113
40	–35.86	5.29	–0.0015	0.02	5.03	114
42	–40.25	6.21	–0.1655	–1.94	5.71	117
44	–46.74	6.07	–0.0448	–0.10	6.91	118
46	–49.20	7.90	0.2535	3.49	7.60	117
48	–50.90	8.74	0.2355	4.55	6.63	117
50	–51.89	8.76	–0.0387	5.17	7.25	116
52	–53.84	9.09	–0.0807	5.74	7.95	115
54	–53.81	10.32	0.0069	5.93	10.82	114
56	–52.11	12.03	0.1768	5.55	11.13	105
58	–49.28	14.87	0.0297	4.01	12.32	93
60	–45.41	16.66	0.1015	4.52	13.28	71
62	–44.14	25.35	0.2682	4.18	17.21	42
64	–38.84	30.84	0.1992	6.93	17.95	28
66	–34.14	29.55	0.2306	6.50	19.14	27
68	–32.89	28.18	–0.0928	11.59	22.23	22
70	–21.50	24.35	–0.2041	–0.97	20.04	20
72	–29.71	25.44	–0.3460	0.24	18.38	16
74	–26.89	28.48	–0.2819	0.28	19.50	12
76	–20.52	31.72	–0.4009	0.05	21.92	10
78	–10.63	35.11	–0.3069	–0.45	25.28	10
80	–0.73	38.21	–0.7128	–0.96	28.23	10
82	5.54	43.52	–0.7536	–0.35	31.30	10
84	11.81	48.25	–0.6736	0.26	34.09	9
86	20.63	63.11	0.0452	0.44	52.13	6
88	31.99	82.83	–0.5731	0.21	75.15	4
90	43.35	98.68	–0.5821	–0.03	92.61	3

Table 2-51. Bivariate normal wind statistics—zonal and meridional, VAFB, December.

z (km)	MEAN *U* (m/s)	SD *U* (m/s)	*R* (*U*,*V*)	MEAN *V* (m/s)	SD *V* (m/s)	NOBS
0.1	0.47	2.70	–0.5086	–1.11	3.00	852
1	0.75	4.32	–0.1554	–2.22	7.20	909
2	3.07	5.64	–0.0641	–3.01	8.20	925
3	5.70	7.22	0.0108	–3.81	9.29	926
4	8.28	9.08	0.0245	–4.42	11.16	929
5	10.45	10.54	0.0855	–4.57	12.42	930
6	12.48	11.97	0.1524	–4.86	14.10	929
7	14.38	13.46	0.2154	–5.32	15.81	925
8	16.18	14.98	0.2640	–5.55	17.13	916
9	17.83	16.06	0.3132	–5.73	18.01	899
10	19.54	16.67	0.3469	–5.98	18.71	883
11	20.87	16.62	0.3358	–5.98	18.00	871
12	21.83	15.39	0.3053	–5.46	16.76	863
13	21.46	13.56	0.3114	–4.52	14.59	859
14	20.02	11.53	0.3466	–3.53	12.71	855
15	17.88	9.76	0.3318	–3.05	10.52	847
16	15.03	8.16	0.3571	–2.71	8.98	837
17	12.3	7.06	0.3808	–2.57	7.55	800
18	9.23	6.12	0.3731	–2.39	6.03	799
19	6.38	5.74	0.3025	–2.61	4.89	792
20	4.08	5.53	0.3206	–2.70	3.94	783
21	2.40	5.73	0.2456	–2.80	3.66	736
22	1.29	6.67	0.2611	–2.66	3.79	725
23	0.57	7.28	0.2533	–2.50	3.65	718
24	0.04	7.84	0.2537	–2.66	3.59	730
25	0.29	8.92	0.3017	–2.53	3.99	720
26	0.88	10.42	0.3533	–2.40	4.54	709
27	2.38	12.18	0.3958	–2.28	4.92	637
28	3.62	13.59	0.4837	–2.42	5.48	595
29	5.83	15.43	0.5419	–2.49	6.14	523
30	8.38	16.91	0.5405	–2.64	7.07	501
32	12.87	21.23	0.6253	–2.34	7.42	142
34	20.66	24.50	0.6840	–1.05	8.81	143
36	28.66	25.74	0.7000	–0.13	9.80	144
38	37.02	26.54	0.6913	0.07	10.53	144
40	43.95	26.37	0.6860	0.35	11.28	144
42	50.11	27.07	0.5720	3.43	13.29	144
44	57.63	27.50	0.4416	6.39	14.22	144
46	64.73	27.95	0.3451	9.57	16.10	144
48	70.51	28.56	0.3387	12.84	16.79	143
50	73.94	29.62	0.2949	14.41	18.13	142
52	75.62	30.96	0.2607	15.44	18.46	141
54	77.17	31.75	0.2244	15.11	18.57	140
56	78.83	31.51	0.1994	12.03	18.45	135
58	78.38	31.65	0.2741	11.21	21.12	121
60	75.95	33.96	0.3312	8.85	24.06	87
62	73.71	31.37	0.3101	3.57	28.78	48
64	72.26	29.19	0.5334	9.03	22.48	39
66	69.46	30.01	0.4224	6.65	23.29	38
68	69.20	31.20	0.2920	4.05	25.52	36
70	68.55	32.93	0.3178	1.09	25.67	34
72	69.22	36.43	0.4664	–1.07	21.88	13
74	64.54	36.34	0.2137	–1.19	25.32	11
76	60.69	36.41	0.3741	–1.50	27.73	10
78	57.67	36.65	0.6515	–2.01	29.36	10
80	54.65	36.88	0.3401	–2.52	30.91	10
82	48.85	38.23	–0.2082	–2.44	34.02	10
84	43.05	39.54	–0.5441	–2.36	36.86	9
86	38.99	43.78	–0.5011	–2.48	61.45	3
88	36.68	50.23	–	–2.79	91.70	–
90	34.37	55.94	–	–3.11	114.19	–

Table 2-52. Bivariate normal wind statistics—zonal and meridional, VAFB, July.

z (km)	MEAN *U* (m/s)	SD *U* (m/s)	*R*(*U*,*V*)	MEAN *V* (m/s)	SD *V* (m/s)	NOBS
0.1	2.05	2.13	–0.5745	–1.78	2.10	725
1	0.25	2.63	–0.2496	–2.06	3.92	753
2	–0.17	2.97	–0.2205	–0.49	3.89	841
3	1.22	3.86	–0.1138	1.35	4.16	842
4	2.01	4.76	0.0281	2.62	4.48	843
5	2.52	5.58	0.0809	3.38	4.83	844
6	3.17	6.47	0.1183	3.91	5.39	844
7	4.22	7.23	0.1317	4.51	6.09	844
8	5.39	8.11	0.1506	5.34	6.83	845
9	6.60	8.98	0.1350	6.55	7.65	844
10	7.84	9.81	0.1361	7.87	8.40	841
11	9.02	10.54	0.1216	9.50	9.25	838
12	9.88	10.56	0.1094	10.60	9.36	834
13	10.01	10.19	0.1522	10.80	9.10	829
14	8.76	8.92	0.2063	9.77	8.04	828
15	6.28	7.35	0.2201	7.62	6.20	824
16	2.87	5.50	0.2045	5.43	4.55	822
17	–0.43	4.09	0.2284	3.54	3.53	789
18	–3.27	3.38	0.2676	2.06	2.73	790
19	–5.64	2.68	0.1751	1.26	2.04	786
20	–7.38	2.39	0.1257	0.82	1.77	775
21	–9.05	2.55	0.0730	0.51	1.78	762
22	–10.44	2.44	0.0627	0.16	1.72	747
23	–11.84	2.44	0.0600	–0.08	1.70	732
24	–13.18	2.55	–0.0250	–0.13	1.81	724
25	–14.18	2.61	–0.0314	–0.09	1.74	724
26	–15.02	2.79	–0.0180	0.05	1.90	708
27	–15.72	3.00	0.0287	–0.03	2.11	675
28	–16.15	2.93	–0.0307	0.06	1.95	588
29	–16.69	3.10	0.0107	0.13	2.22	570
30	–17.42	3.19	0.0323	–0.01	2.11	540
32	–22.68	3.62	–0.1768	1.62	2.74	139
34	–23.71	3.45	0.0008	1.35	3.06	140
36	–26.52	4.35	–0.0731	1.03	3.40	140
38	–29.23	4.81	–0.1289	1.18	4.27	142
40	–33.29	4.27	0.0572	–0.08	4.25	142
42	–38.10	4.87	0.0443	0.05	5.28	142
44	–42.09	5.35	0.0585	2.13	5.87	142
46	–44.74	6.25	0.1210	4.62	5.34	142
48	–47.31	6.55	0.1203	4.97	6.18	142
50	–51.36	7.16	0.1017	5.79	5.95	141
52	–53.83	8.32	0.2111	7.11	7.00	136
54	–54.76	9.04	0.1272	7.42	7.32	129
56	–57.97	10.73	0.1770	5.20	9.87	122
58	–59.85	13.02	0.2448	1.75	12.31	105
60	–60.03	17.21	0.1480	2.25	13.50	76
62	–62.04	20.10	0.0455	5.62	12.38	61
64	–56.71	21.39	0.1401	7.79	11.35	54
66	–45.11	23.71	0.1581	10.43	14.17	51
68	–35.08	21.35	–0.0473	9.30	21.22	49
70	–25.92	22.64	0.0388	5.10	25.12	46
72	–42.34	23.72	–0.2058	–0.28	18.79	19
74	–39.70	26.92	–0.5938	–0.30	20.52	17
76	–35.14	30.10	–0.4357	–0.62	22.89	16
78	–28.65	33.28	–0.2964	–1.24	25.75	15
80	–22.17	36.19	–0.1851	–1.86	28.31	15
82	–14.65	41.22	–0.0680	–2.07	31.00	15
84	–7.13	45.70	0.1098	–2.27	33.48	15
86	1.27	61.18	0.5795	–2.54	52.83	7
88	10.54	81.62	0.3903	–2.88	77.28	4
90	19.80	97.89	0.6983	–3.22	95.68	3

Table 2-53. Bivariate normal wind statistics—zonal and meridional, EAFB, February.

z (km)	MEAN *U* (m/s)	SD *U* (m/s)	*R*(*U*,*V*)	MEAN *V* (m/s)	SD *V* (m/s)	NOBS
0.705	1.36	2.60	0.4729	0.29	1.77	358
1	2.12	5.78	0.4433	–0.87	3.18	363
2	1.16	7.37	0.2754	–2.52	6.01	364
3	4.13	7.56	0.1351	–3.54	7.71	360
4	6.95	8.34	0.1196	–4.81	9.64	359
5	9.26	8.95	0.1264	–5.51	11.40	352
6	11.06	9.89	0.1543	–5.77	12.51	348
7	13.23	11.23	0.1864	–6.58	13.31	342
8	15.49	12.72	0.1709	–6.80	14.70	337
9	18.16	14.73	0.1958	–7.52	16.11	335
10	21.07	16.12	0.1829	–8.11	16.31	331
11	23.47	16.16	0.2012	–8.40	16.01	328
12	24.91	14.92	0.1702	–7.74	14.94	324
13	24.45	13.07	0.1838	–7.10	13.21	323
14	22.88	11.05	0.2646	–6.19	10.65	320
15	20.66	9.90	0.2728	–5.61	8.96	318
16	17.35	8.19	0.2886	–5.08	7.64	293
17	13.61	6.92	0.2768	–4.46	6.28	278
18	10.09	6.48	0.1506	–4.05	5.00	281
19	6.83	5.92	0.0850	–3.58	4.30	274
20	4.07	5.55	–0.0317	–3.11	3.69	268
21	2.04	5.87	–0.1573	–2.85	3.24	259
22	0.54	5.89	–0.1021	–2.41	3.22	247
23	0.08	6.00	0.0402	–2.14	3.01	238
24	0.00	7.07	0.1326	–2.02	3.18	234
25	0.06	8.44	0.1495	–1.79	3.28	228
26	0.77	9.33	0.2308	–1.35	3.42	220
27	2.24	10.85	0.2357	–1.21	3.51	190
28	3.51	12.42	0.3188	–1.12	3.69	180
29	5.55	14.11	0.2416	–0.86	3.97	134
30	7.03	16.01	0.1990	–0.75	4.41	126
32	11.00	18.42	0.4303	–0.72	5.12	166
34	15.60	21.73	0.5111	–0.04	6.45	166
36	20.11	25.01	0.5548	–0.29	7.08	166
38	24.15	28.12	0.5250	–0.09	8.59	169
40	26.99	29.18	0.4533	–0.57	10.75	169
42	29.66	29.52	0.4467	0.22	12.44	169
44	32.20	29.91	0.4457	2.50	15.02	169
46	34.85	30.27	0.3899	4.79	15.87	169
48	36.90	29.29	0.3748	6.94	14.95	168
50	38.93	27.64	0.3590	7.82	16.34	168
52	41.35	26.30	0.3845	7.99	15.73	166
54	45.66	24.75	0.4000	8.16	15.65	158
56	49.56	25.83	0.3846	8.39	15.61	149
58	54.27	25.04	0.4049	9.18	15.42	128
60	60.72	23.64	0.4025	7.84	18.89	91
62	67.99	22.94	0.2683	9.52	17.76	56
64	72.70	26.04	0.0698	8.36	15.26	47
66	73.61	27.15	0.1421	5.79	13.32	44
68	72.47	28.33	0.0140	2.99	12.70	41
70	68.10	22.05	–0.1098	–2.01	17.07	39
72	57.50	34.93	–0.3812	3.45	21.18	21
74	54.51	35.01	–0.6617	3.62	24.57	15
76	50.44	35.28	–0.7052	3.80	26.91	12
78	45.29	35.74	–0.4283	3.96	28.46	10
80	40.14	36.20	–0.0082	4.13	29.93	10
82	35.69	37.75	0.2928	4.24	33.08	9
84	31.24	39.23	0.3783	4.36	35.96	9
86	27.57	43.64	–0.7541	4.50	61.02	4
88	24.67	50.20	–0.9901	4.67	91.58	3
90	21.77	56.00	–	4.84	114.24	–

Table 2-54. Bivariate normal wind statistics—zonal and meridional, EAFB, July.

z (km)	MEAN *U* (m/s)	SD *U* (m/s)	*R* (*U*,*V*)	MEAN *V* (m/s)	SD *V* (m/s)	NOBS
0.705	2.11	1.92	0.5660	1.92	1.68	367
1	5.59	3.98	0.2890	1.30	2.11	373
2	4.33	4.09	0.2619	2.12	3.46	374
3	2.76	4.78	0.1697	3.78	3.74	374
4	1.89	5.36	0.1471	4.17	4.13	371
5	1.96	5.70	0.1885	4.29	4.84	369
6	3.13	6.10	0.1483	4.38	5.13	366
7	4.42	6.31	0.1392	4.92	5.84	355
8	6.00	7.03	0.1503	5.73	6.49	350
9	7.38	7.69	0.0967	6.81	7.25	349
10	8.66	8.40	0.0860	8.31	8.18	341
11	9.62	9.09	0.0858	9.88	9.01	338
12	10.09	9.27	0.0773	10.66	9.62	334
13	9.91	8.76	0.0954	10.99	9.22	333
14	8.78	7.23	0.1832	9.69	7.97	330
15	6.77	5.94	0.2193	7.48	6.52	329
16	3.34	4.62	0.2165	5.05	5.01	322
17	–0.62	3.48	0.2350	3.12	3.75	305
18	–3.96	2.85	0.2846	1.99	3.00	305
19	–6.51	2.54	0.1979	1.49	2.23	302
20	–8.42	2.12	0.1714	1.01	1.94	301
21	–9.90	2.16	0.0712	0.81	2.07	296
22	–11.21	2.19	0.0478	0.51	1.88	293
23	–12.36	2.34	–0.0449	0.36	1.79	286
24	–13.42	2.67	–0.0650	0.31	1.99	281
25	–14.34	2.73	–0.0271	0.26	2.02	266
26	–15.26	2.86	–0.0748	0.38	2.10	259
27	–16.12	3.43	–0.1596	0.44	2.34	238
28	–16.73	3.41	–0.1880	0.02	1.95	189
29	–17.49	3.71	–0.0954	–0.04	2.44	173
30	–18.27	3.38	–0.1203	0.19	2.09	158
32	–22.68	3.62	–0.1768	1.62	2.74	139
34	–23.71	3.45	0.0008	1.35	3.06	140
36	–26.52	4.35	–0.0731	1.03	3.40	140
38	–29.23	4.81	–0.1289	1.18	4.27	142
40	–33.29	4.27	0.0572	–0.08	4.25	142
42	–38.10	4.87	0.0443	0.05	5.28	142
44	–42.09	5.35	0.0585	2.13	5.87	142
46	–44.74	6.25	0.1210	4.62	5.34	142
48	–47.31	6.55	0.1203	4.97	6.18	142
50	–51.36	7.16	0.1017	5.79	5.95	141
52	–53.83	8.32	0.2111	7.11	7.00	136
54	–54.76	9.04	0.1272	7.42	7.32	129
56	–57.97	10.73	0.1770	5.20	9.87	122
58	–59.85	13.02	0.2448	1.75	12.31	105
60	–60.03	17.21	0.1480	2.25	13.50	76
62	–62.04	20.10	0.0455	5.62	12.38	61
64	–56.71	21.39	0.1401	7.79	11.35	54
66	–45.11	23.71	0.1581	10.43	14.17	51
68	–35.08	21.35	–0.0473	9.30	21.22	49
70	–25.92	22.64	0.0388	5.10	25.12	46
72	–42.87	23.68	–0.2058	–0.32	18.80	19
74	–40.21	26.88	–0.5938	–0.34	20.55	17
76	–35.52	30.06	–0.4357	–0.74	22.93	16
78	–28.79	33.24	–0.2964	–1.50	25.76	15
80	–22.05	36.14	–0.1851	–2.25	28.30	15
82	–14.45	41.16	–0.0680	–2.43	30.99	15
84	–6.84	45.64	0.1098	–2.61	33.45	15
86	1.66	61.11	0.5795	–2.90	52.84	7
88	11.05	81.55	0.3903	–3.31	77.32	4
90	20.45	97.81	0.6983	–3.72	95.74	3

(c) The correlation coefficients

$$R(x,y)_{\alpha} = \frac{\mathrm{cov}(x,y)_{\alpha}}{S_{x\alpha} S_{y\alpha}} \ , \tag{2.32}$$

where $\mathrm{cov}(x,y)_{\alpha}$ is the rotated covariance

$$\mathrm{cov}(x,y)_{\alpha} = R(U,V) S_U S_V \left(\sin^2 \alpha - \cos^2 \alpha\right) + \sin\alpha \cos\alpha \left(S_V^2 - S_U^2\right) \ . \tag{2.33}$$

2.3.5.2 Wind Vector Probability Ellipse. Using the meteorological Cartesian notation, the probability ellipse that contains *p*-percent of the wind vectors is expressed in the most general form by the conic equation defined by

$$AX^2 + BXY + CY^2 + DX + EY + F = 0 \ , \tag{2.34}$$

where

$$A = S\frac{2}{V}$$

$$B = -2R(U,V)\, S_U S_V$$

$$C = S\frac{2}{U}$$

$$D = -(B\ \overline{V}\ + 2\ A\ \overline{U}\ )$$

$$E = -(B\ \overline{U}\ + 2\ C\ \overline{V}\ )$$

$$F = A\ (\overline{U}\ )^{\,2} + C\ (\overline{V}\ )^{\,2} + B\overline{U}\ \overline{V}\ - AC\ \{1-[R(U,V)]^{\,2}\}\ \lambda_e{}^2$$

and

$$\lambda_e = \sqrt{-2\ln(1-P)} \ ,$$

where *P* is probability.

For convenient usage, values for the λ parameter to the bivariate normal probability ellipse, λ_e, and for the bivariate circular normal distribution for selected probabilities are given in table 2-55. Circular distributions arise when the component standard deviations are equal and the correlation coefficient is zero.

Equation (2.34) is used to derive other functional relationships that describe the properties of the bivariate normal probability ellipse and for graphical displays. The largest and smallest values for *x* and *y* of a given probability ellipse are given by:

$$X_{(w,s)} = \overline{U} \pm S_U \lambda_e \ , \tag{2.35}$$

$$Y_{(w,s)} = \overline{V} \pm S_V \lambda_e \ . \tag{2.36}$$

Table 2-55. Values of λ for bivariate normal distribution ellipses and circles.

P (%)	λ_e (ellipse)	λ_c (circle)	P (%)	λ_e (ellipse)	λ_c (circle)
0.000	0.0000	0.0000	65.000	1.4490	1.0246
5.000	0.3203	0.2265	68.268	1.5151	1.0713
10.000	0.4590	0.3246	70.000	1.5518	1.0973
15.000	0.5701	0.4031	75.000	1.6651	1.1774
20.000	0.6680	0.4723	80.000	1.7941	1.2686
25.000	0.7585	0.5363	85.000	1.9479	1.3774
30.000	0.8446	0.5972	86.466	2.0000	1.4142
35.000	0.9282	0.6563	90.000	2.1460	1.5175
39.347	1.0000	0.7071	95.000	2.4477	1.7308
40.000	1.0108	0.7147	95.450	2.4860	1.7579
45.000	1.0935	0.7732	98.000	2.7971	1.9778
50.000	1.1774	0.8325	98.168	2.8284	2.0000
54.406	1.2533	0.8862	98.889	3.0000	2.1213
55.000	1.2637	0.8936	99.000	3.0348	2.1460
60.000	1.3537	0.9572	99.730	3.4393	2.4320
63.212	1.4142	1.0000	99.9877	4.2426	3.0000

$$\lambda_e = \sqrt{2}\,\sqrt{-\ln(1-P)}$$

$$\lambda_e = \sqrt{-\ln(1-P)}$$

Using the quadratic equation, solutions for Y in equation (2.34) are made by incrementing X from X_S to X_L and plotting on a scale that has the same range for X and Y, as shown in figure 2-15. Such illustrations are helpful in comparing the wind statistics from month to month and between sites. For example, assume that a vehicle trajectory has been wind biased to the monthly mean wind and the flight azimuth is 180° (south) for VAFB, then at 12-km altitude, the head and tail quartering wind relative to the monthly mean to the 99-percent probability ellipse would be larger than that for an east launch from KSC, wind biased to the monthly mean.

2.3.5.3 Bivariate Normal Distribution in Polar Coordinates. The bivariate normal probability density function expressed in polar coordinates is used to derive the probability distribution for wind speed given the wind direction, and to express the special relationship for wind vectors relative to the monthly mean wind to an assigned probability ellipse. These relationships are used in the selection of wind vectors to the probability ellipse in section 2.3.9 for the synthetic vector wind profile model.

The bivariate normal probability density function in the meteorological polar coordinate system is

$$g(r,\theta) = rd_1 e^{-1/2\left(a^2r^2 - 2br + c^2\right)}\ , \tag{2.37}$$

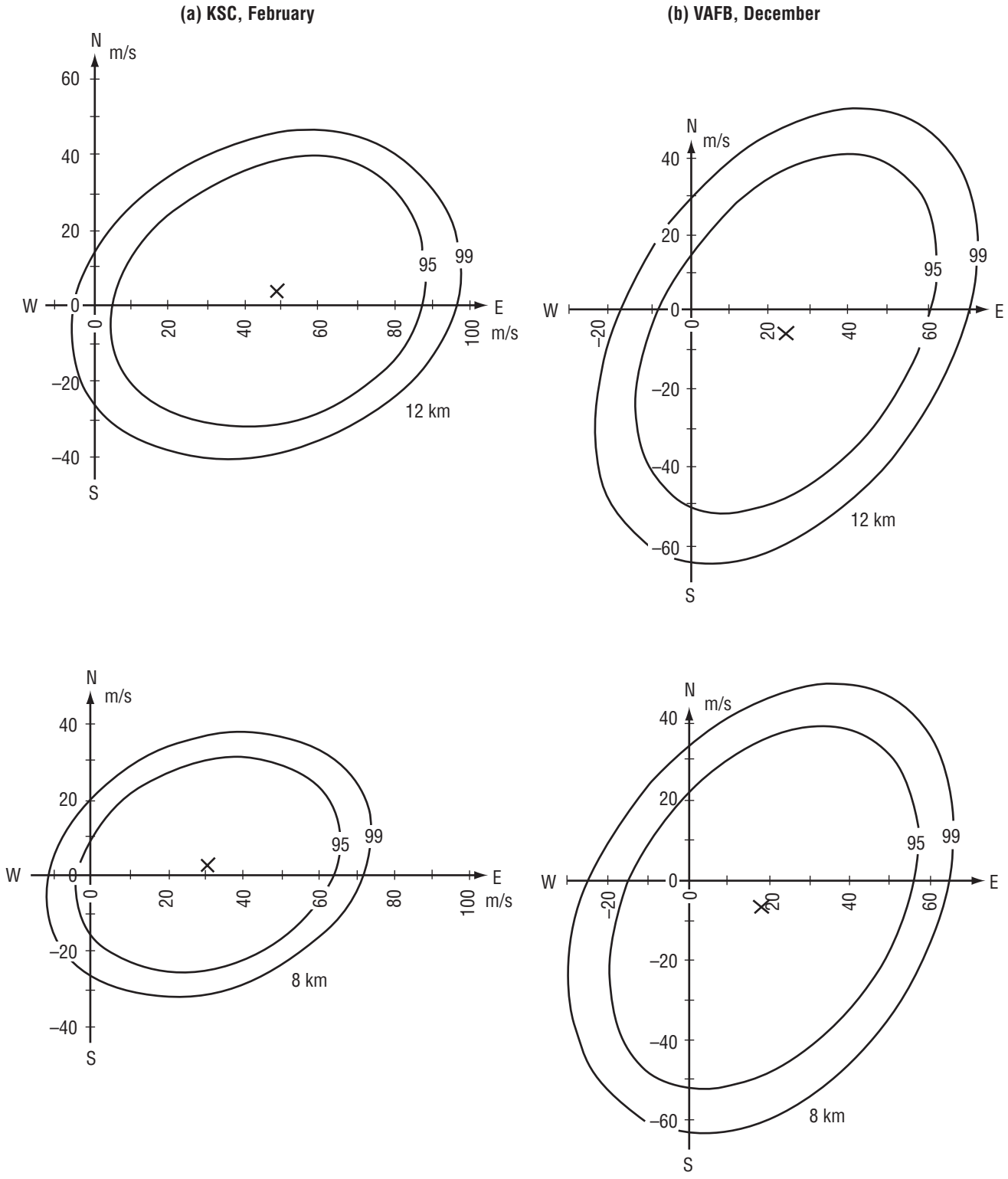

Figure 2-15. Comparison of wind vector probability ellipses (a) KSC, February and (b) VAFB, December.

where

$$a^2 = \frac{1}{(1-\rho^2)}\left[\frac{\sin^2\theta}{\sigma_x^2} - \frac{2\rho\cos\theta\sin\theta}{\sigma_x\sigma_y} + \frac{\cos^2\theta}{\sigma_y^2}\right],$$

$$b = \frac{1}{(1-\rho^2)}\left[\frac{\bar{x}\sin\theta}{\sigma_x^2} - \frac{\rho(\bar{x}\cos\theta + \bar{y}\sin\theta)}{\sigma_x\sigma_y} + \frac{\bar{y}\cos\theta}{\sigma_y^2}\right],$$

$$c^2 = \frac{1}{(1-\rho^2)}\left[\frac{\bar{x}\sin\theta}{\sigma_x^2} - \frac{2\rho xy}{\sigma_x\sigma_y} + \frac{\bar{y}_2}{\sigma_y^2}\right],$$

$$d_1 = \frac{1}{2\pi\sigma_x\sigma_y\sqrt{1-\rho^2}} \ .$$

(Equation (2.37) (ref. 2-38) is given with respect to the mathematical convention for a vector direction, not the meteorological convention.)

$r = \sqrt{x^2 + y^2}$ is the modulus of the vector or speed, and θ is the direction of the vector. After integrating $g(r,\theta)$ over $r = 0$ to ∞, the probability density function of θ is

$$g(\theta) = \frac{d_1}{a^2} e^{1/2c^2}\left[1 + \sqrt{2\pi}\left(\frac{b}{a}\right)e^{1/2\left(\frac{b}{a}\right)^2}\Phi\left(\frac{b}{a}\right)\right], \tag{2.38}$$

where a^2, b, c^2, and d_1 are as previously defined in equation (2.37) and $\Phi(b/a) = \Phi(x) = 1/\sqrt{2\pi}\int_{-\infty}^{x} e^{-1/2t^2}\,dt$ is taken from tables of normal distributions or made available through computer subroutines.

If desired, equation (2.38) can be integrated numerically over a chosen range of θ to obtain the probability that the vector direction will lie within the chosen range; i.e.,

$$F(\theta) = \int_{\theta_2}^{\theta 1} g(\theta)\,d\theta \ . \tag{2.39}$$

One application may be to obtain the probability that the wind flow will be from a given quadrant or sector as, for example, onshore.

2.3.5.4 The Derived Conditional Distribution of Wind Speed Given the Wind Direction (Wind Rose). The conditional probability density function for wind speed, r, given a specified value for the wind direction, θ, can be expressed as

$$f(r \mid \theta) = \frac{a^2 r e^{-\frac{1}{2}\left(a^2r^2 - br\right)}}{1 + \sqrt{2\pi}\left(\frac{b}{a}\right)e^{\frac{1}{2}\left(\frac{b}{a}\right)^2}\Phi\left(\frac{b}{a}\right)}, \tag{2.40}$$

where the coefficients, a and b and the function Φ (b/a) are as previously defined in equations (2.34) and (2.38).

From equation (2.40), the mode (most frequent value) of the conditional wind speed given a specified value of the wind direction is the positive solution of the quadratic equation,

$$a^2b^2 - br - 1 = 0 \ , \tag{2.41}$$

which is

$$(f \mid \theta) = \frac{1}{2a}\left[\left(\frac{b}{a}\right) + \sqrt{4 + \left(\frac{b}{a}\right)^2}\right] . \tag{2.42}$$

The locus of the conditional modal values of wind speed when plotted in polar coordinates versus the given wind directions forms an ellipse.

The noncentral moment for equation (2.40) is expressed as

$$\mu / n = \int_0^\infty r^n f(r \mid \theta)\, dr \ . \tag{2.43}$$

Now the first noncentral moment is identical to the first central moment or the expected value, $E(r \mid \theta)$. The integration of equation (2.43) for the first moment is sufficiently simple to yield practical computations and can be expressed as

$$E(r \mid \theta) = \frac{\left(\frac{b}{a}\right) + \left[1 + \left(\frac{b}{a}\right)^2\right]\sqrt{2\pi}\ e^{\frac{1}{2}\left(\frac{b}{a}\right)^2}\ \Phi\left(\frac{b}{a}\right)}{a\left[1 + \left(\frac{b}{a}\right)\sqrt{2\pi}\ e^{\frac{1}{2}\left(\frac{b}{a}\right)^2}\ \Phi\left(\frac{b}{a}\right)\right]} \ . \tag{2.44}$$

Hence, equation (2.44) gives the conditional mean value of the wind speed given a specified value for the wind direction.

The integration of equation (2.40) for the limits $r = 0$ to $r = r^*$ gives the probability that the conditional wind speed is $\leq r^*$ given a value for the wind direction, θ. This conditional probability distribution function can be written as

$$\Pr\left\{r \leq r^* \mid \theta = \theta_0\right\} = 1 - \left[\frac{e^{-\frac{1}{2}r_s^2} + \sqrt{2\pi}\left(\frac{b}{a}\right)\left\{1 - \Phi\left(r_s\right)\right\}}{e^{-\frac{1}{2}\left(\frac{b}{a}\right)^2 + \sqrt{2\pi}\left(\frac{b}{a}\right)\Phi\left\{\frac{b}{a}\right\}}}\right] \ , \tag{2.45}$$

where

$$r_s = \left[ar^* - \left(\frac{b}{a} \right) \right] .$$

By definition, equation (2.45) is an expression for a "wind rose." Empirical wind rose statistics are often tabulated or graphically illustrated, thus giving the frequency that the wind speed is not exceeded for the wind speed values that lie within assigned class intervals of the wind direction. After evaluation of equation (2.42) for various values of wind speed, r^*, and the given wind directions, θ, interpolations can be performed to obtain various percentile values of the conditional wind speed.

For the special case when b in equation (2.37) equals zero; i.e., for $\bar{x} = \bar{y} = 0,$ the conditional modal values of wind speeds (eq. (2.42)), the conditional mean values of wind speeds (eq. (2.44)), and the fixed conditional percentile values of wind speeds (interpolated from evaluations of eq. (2.45)), when plotted in polar form versus the given wind directions, produce a family of ellipses.

For the special case when $\bar{x} = \bar{y} = 0,$ equation (2.40) reduces to the following simple case:

$$\Pr\{r = r^* \mid \theta = \theta_0\} = 1 - e^{\frac{\left(-a^2 r^{*2}\right)}{2}} . \tag{2.46}$$

There is a special significance of equation (2.46) when related to the bivariate normal probability distribution. If r^* and θ are measured from the centroid of the probability ellipse, then the probability that $r \le r^*$ is the same as the given probability ellipse. Further, solving equation (2.46) for r^* gives

$$r^* = \frac{1}{a} \sqrt{-2 \ln(1 - P)} . \tag{2.47}$$

If a probability ellipse, P, is chosen, equation (2.46) gives the distance of r along any θ from the centroid of the ellipse to the intercept of the probability ellipse. When computing the wind speed probability for a given θ relative to the monthly means, equation (2.47) is applicable.

2.3.5.5 Wind Component Statistics. The univariate normal (Gaussian) probability distribution function is used to obtain wind component statistics. In generalized notations, this probability density function is

$$f(t) = \frac{e\left(-\frac{1}{2} t^2 \right)}{\sqrt{2\pi}} , \tag{2.48}$$

where $t = (X - \xi)/\sigma_x$ is the standard variate, with ξ defining the mean and σ_x the standard deviation.
The cumulative probability distribution function is

$$F(X) = \int_{-\infty}^{X} f(t)\, dt . \tag{2.49}$$

Because this integral cannot be obtained in closed form, it is widely tabulated for zero mean and unit standard deviation. For a convenient reference, selected values of $F(X)$ are given in table 2-56. To emphasize the connotation of probability, $F(X)$ is shown in table 2-56 as $P\{X\}$.

The t values in table 2-56 are used as multiplier factors to the standard deviation to express the probability that a normally distributed variable, X, is less than or equal to a given value as

$$P\{X \leq \text{mean} + t\sigma_x\} = \text{probability, } P \text{ .} \tag{2.50}$$

Table 2-56. Values of t for standardized normal (univariate) distribution for percentiles and interpercentile ranges.

t	$P(X)$	X	$P(X_1 \leq X \leq X_2)(\%)$
–3.0000	0.00135	ξ–3.0000σ	
–2.5758	0.00500	ξ–2.5758σ	
–2.3263	0.01000	ξ–2.3263σ	
–2.2410	0.01250	ξ–2.2410σ	
–2.0000	0.02275	ξ–2.0000σ	
–1.9600	0.02500	ξ–1.9600σ	
–1.6449	0.05000	ξ–1.6449σ	
–1.2816	0.10000	ξ–1.2816σ	
–1.0000	0.15866	ξ–1.0000σ	
–0.8416	0.20000	ξ–0.8416σ	
–0.6745	0.25000	ξ–0.6745σ	
–0.2533	0.40000	ξ–0.2533σ	
0.0000	0.50000	ξ	20 50 60 68.268 80 90 95 95.45 97.5 98 99 99.73
0.2533	0.60000	ξ+0.2533σ	
0.6745	0.75000	ξ+0.6745σ	
0.8416	0.80000	ξ+0.8614σ	
1.0000	0.84134	ξ+1.0000σ	
1.2816	0.90000	ξ+1.2816σ	
1.6449	0.95000	ξ+1.6449σ	
1.9600	0.97500	ξ+1.9600σ	
2.0000	0.97725	ξ+2.0000σ	
2.2410	0.98750	ξ+2.2410σ	
2.3263	0.99000	ξ+2.3263σ	
2.5758	0.99500	ξ+2.5758σ	
3.0000	0.99865	ξ+3.0000σ	
		where $X_1 = \xi - t\sigma$ and $X_2 = \xi + t\sigma$	

For example, when $t = 1.6449$, the probability that X is less than or equal to the mean plus 1.6449 standard deviations is called the 95th percentile value of X. Also given in table 2-56 are the numerical values to express the probability that X falls in the interval X_1 to X_2; i.e.,

$$P\{X_1 \leq X \leq X_2\} = \text{interpercentile range ,} \tag{2.51}$$

where

$$X_1 = \overline{X} - t\sigma_x$$

and

$$X_2 = \overline{X} + t\sigma_x \text{ .}$$

For $t = 1.9602$, the probability that X lies in the interval X_1 to X_2 is 0.95. The values of X_1 and X_2 in this example comprise the 95th interpercentile range.

For a normally distributed variable, the mode (most frequent value) and the median (50th percentile) are the same as the mean value. The means and standard deviations of wind components are used in equations (2.50) and (2.51) to compute the percentile values and interpercentile ranges of the U and V wind components. Equation (2.50) is a straight line on a normal probability graph.

To obtain the wind component statistics with respect to orthogonal coordinate axes other than zonal and meridional, one should use the coordinate rotation equations (2.28) through (2.33).

2.3.5.6 Envelope of Wind Profiles Versus an Envelope of Percentiles. It is a usual practice to plot the points versus altitude for the interpercentile range for wind components; e.g., $U \pm tS_U$, at discrete altitudes and to connect these points. This convenient display can be misinterpreted. Since the winds are not perfectly correlated between all altitude levels, then for the envelope of percentile values; e.g., the 95th interpercentile range ($U \pm 1.96\ S_U$), the percentage of wind profiles would lie on the interpercentile bounds over all altitudes.

The interlevel wind correlations decrease as the altitude interval increases. Suppose that there are five independent wind altitude levels between zero and 12-km altitude; then, the percentage of wind profiles that lie within the bounds of the 95-interpercentile range is only 77.4 percent. This is obtained by $(0.95)^5 = 0.7737$. For five independent wind levels, the required interpercentile range taken at discrete altitudes to envelop 95 percent of the wind profiles is in the 98.98th interpercentile range, $(0.95)^{1/5} = 0.9898$. The percentage of wind profiles that lie within the 95-percent probability ellipses at 1-km intervals from 3- to 16-km altitude based on a 12-yr period of wind records for KSC, approximates this example. The percentage of wind profiles for KSC, April, that lie within the 95-percent wind ellipses taken at 1-km intervals versus altitude is illustrated in figure 2-16. An aerospace vehicle should be designed such that it can fly through a certain percent of the detail wind profiles for the worst monthly reference period, not just an assigned percent of the wind vectors at discrete altitudes. This raises the issue: What size should the wind vector probability ellipses at discrete altitudes be for aerospace vehicle design? This analysis suggests that the monthly 99-percent probability ellipses at discrete altitudes should be used to envelop 95 percent of the wind profiles over the altitudes of primary interest. This subject is further addressed in section 2.3.9 for synthetic vector wind profile models.

2.3.5.7 Extreme Value Wind Shear Model. The wind shear model in this section has several advantages over the classical empirical wind shear model (see sec. 2.4.3). The technique used to derive this new wind shear model is based on an analytically defined probability function: the procedure is objective. The analytical equations permit generalizations to give consistent comparative results. This new model permits computations for any conditional percentile for wind speed shear given any wind speed.

The extreme, largest wind speed shears for various altitude shear intervals that occurred in the 3- to 16-km altitude layer for each of 150 per month Jimsphere wind profiles, described in section 2.3.11.1, were computed. The associated wind speeds for the extreme wind shears were obtained. These data samples were fit by the univariate Gumbel (ref. 2-3) extreme value probability distribution function. A bivariate extreme value distribution function was used to model the extreme value conditional distribution for wind shear given the wind speed. This wind shear model is used to establish a synthetic wind profile model in section 2.3.9. The bivariate extreme value probability distribution has proven to be a powerful modeling tool for wind shear and for aerospace vehicle ascent structural loads (ref. 2-46).

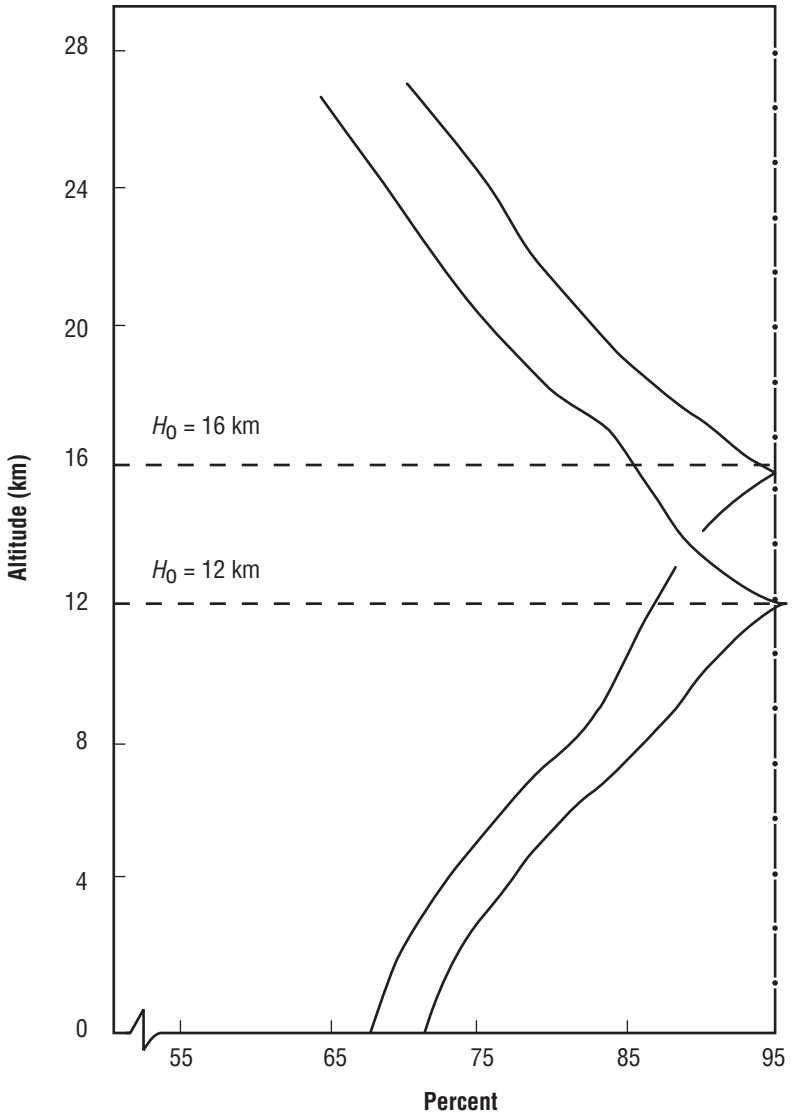

Figure 2-16. Percentage of wind profiles (wind vectors at 1-km intervals) that are within the 95-percent ellipses versus altitude, KSC, April.

There are two forms for the bivariate extreme value probability distribution (ref. 2-47): the *a*-case and the *m*-case. Since the *m*-case is more general than the *a*-case, it is used to model the relationship between the extreme largest wind shear and the wind speed. The probability distribution function for the *m*-case is

$$\Phi(X,Y,m) = \exp\left[-\left(e^{-mX} + e^{-mY}\right)^{\frac{1}{m}}\right], \tag{2.52}$$

where

$$-\infty \le X \le \infty$$
$$-\infty \le Y \le \infty$$

and

$m \geq 1$

is a measure of association (correlation) between the two variables.

X and Y are called the reduced variates, which are defined by

$$X = \frac{(x - \mu_x)}{\alpha_x} \quad , \tag{2.53}$$

and x and y are the extreme largest values for the original variates,

$$Y = \frac{(y - \mu_y)}{\alpha_y} \quad , \tag{2.54}$$

where μ_x,μ_y is the location parameter or modal value and α_x,α_y is the shape parameter. They are estimated from the sample extremes, means $(\bar{x}, \bar{y})$, and standard deviations (s_x,s_y) using Gumbel's (ref. 2-3) modified method of moments:

$$\hat{\alpha}_x = \frac{s_x}{\sigma_n} \text{ and } \hat{\mu}_x = \dot{x} - \hat{\alpha}\bar{y}_n \quad , \tag{2.55}$$

where σ_n and $\bar{y}_n$ are the population parameters. They are a function of sample size, n. For n = 150, σ_n = 1.22534, and $\bar{y}_n$ = 0.56461. For large $n \geq \infty$, $\sigma_n = \pi / \sqrt{6}$ and $\bar{y}_n$ is Euler's constant, 0.57722:

$$\hat{m} = \frac{1}{\sqrt{1 - r(x, y)}} \quad , \tag{2.56}$$

where for the condition that m = 1, equation (2.52) becomes the product of two independent extreme value distributions which are univariate extreme value probability distribution functions. Some further notations are useful (refs. 2-47 and 2-48):

$$\Phi(X, Y; m) = P\{X = X_1, Y \leq Y_2; m\} = \int_{-\infty}^{Y} \int_{-\infty}^{X} \varphi(X, Y; m)\, dX\, dY \quad , \tag{2.57}$$

where $\varphi(X,Y;m)$ is the probability density function defined by

$$\varphi(x, Y; m) = \Phi(X, Y; m) * \left[\left(e^{-mX} + e^{-mY} \right)^{\frac{1}{m}-2} e^{(-mX-mY)} \left\{ \left(e^{-mX} + e^{-mY} \right)^{\frac{1}{m}} + (m-1) \right\} \right] . \tag{2.58}$$

It is important to note that

$$\Phi(X_\infty, Y; m) = \exp\left(e^{-Y}\right) . \tag{2.59}$$

These functions are used in deriving the conditional probability distribution function. The interest is to present tables for the conditional percentile values for wind speed shear given class intervals for wind speed. Let X stand for the reduced variate for wind shear and Y stand for the reduced variate for wind speed. The conditional probability distribution function for assigned values for X for given class intervals for Y is

$$\Pr\{X \le X^* \mid Y_1 \le Y \le Y_2\} = \frac{\Phi(X, Y_2; m) - \Phi(X^*, Y_1; m)}{\Phi(Y_2) - \Phi(Y_1)} \ , \tag{2.60}$$

where the denominator, the univariate extreme value probability distribution function for wind speed,

$$\Phi(Y) = \exp\left(-e^{-Y}\right) \ , \tag{2.61}$$

is evaluated for assigned values for Y_1 and Y_2. The conditional probability distribution function in terms of the reduced variates is then interpolated for assigned conditional percentile values and then converted into the original extreme value variables using equations (2.53) and (2.54). This is the general method used to establish the conditional percentile shears (table 2-57) for the assigned class intervals for wind speed. An alternate conditional probability distribution function is

$$\Pr\{X \le X^* \mid Y = Y_1\} = Z^{\left(\frac{1}{m}-1\right)} e^{\left[-Z^{\frac{1}{m}} - (m-1)Y_1 + e^{-Y_1}\right]} \ , \tag{2.62}$$

where

$$Z = \left(e^{-mX^*} + e^{mY}\right) \ .$$

This conditional probability distribution function is for the given value for Y to exactly equal the assigned value for Y_1 instead of an assigned class interval as presented in equation (2.60). An explicit inverse solution cannot be obtained to find the conditional percentile values for X^* as a function of probability, P. If interactive techniques are used to do this, such as Newton's method, care must be taken for the computational precision for small values of Y_1. The usual practical range for the reduced variates is from –3.5 to 5. The extreme wind speed shear and associated wind speed data computed from the 150 per month Jimsphere samples for KSC revealed that the data for February would encompass the other months. Hence, February is used to typify these wind shear statistics. For computational conveniences, the five required parameters for the bivariate extreme value distribution were fit by empirical equations as a function of altitude shear interval, h, valid for $100 \le h \le 10{,}000$ m. For the extreme largest wind speed shear parameters,

$$\mu_s(h) = 0.4747\, h^{0.47}, \ (100 \le h \le 10{,}000 \text{ m}) \tag{2.63}$$

and

$$a_s(h) = \frac{10\, h}{1{,}300 + h}, (100 \le h \le 10{,}000 \text{ m}) \ . \tag{2.64}$$

Table 2-57. Conditional percentiles of wind speed shear (m/s) given shear height interval (m) and wind speed (m/s) applicable over the 3- to 16-km altitude range, KSC, February.

h = 100 m **Wind Speed Range** (W1 to W2 m/s)

PROB	20-25	25-30	30-35	35-40	40-45	45-50	50-55	55-60	60-65	65-70	70-75	75-80	80-85	85-90
0.36788	3.83	3.91	3.99	4.07	4.16	4.26	4.36	4.47	4.58	4.71	4.84	4.99	5.16	5.35
0.50	4.04	4.12	4.21	4.30	4.41	4.52	4.63	4.77	4.91	5.07	5.24	5.44	5.65	5.88
0.60	4.22	4.30	4.39	4.49	4.60	4.72	4.86	5.00	5.17	5.35	5.56	5.78	6.02	6.27
0.70	4.42	4.51	4.60	4.71	4.82	4.96	5.10	5.27	5.46	5.66	5.89	6.13	6.39	6.67
0.80	4.68	4.77	4.87	4.98	5.11	5.25	5.41	5.60	5.80	6.03	6.27	6.53	6.81	7.09
0.85	4.86	4.95	5.05	5.16	5.29	5.44	5.61	5.80	6.02	6.25	6.51	6.77	7.05	7.34
0.90	5.10	5.19	5.29	5.41	5.54	5.70	5.87	6.07	6.30	6.54	6.80	7.08	7.36	7.65
0.95	5.50	5.59	5.69	5.81	5.95	6.11	6.29	6.50	6.73	6.98	7.25	7.53	7.82	8.11
0.98	6.01	6.11	6.21	6.33	6.47	6.63	6.82	7.03	7.27	7.53	7.80	8.08	8.37	8.66
0.99	6.40	6.49	6.60	6.72	6.86	7.02	7.21	7.43	7.66	7.92	8.19	8.47	8.77	9.06
0.995	6.78	6.87	6.98	7.10	7.24	7.41	7.60	7.81	8.05	8.31	8.58	8.86	9.15	9.45

h = 200 m (W1 to W2 m/s)

PROB	20-25	25-30	30-35	35-40	40-45	45-50	50-55	55-60	60-65	65-70	70-75	75-80	80-85	85-90
0.36788	5.11	5.26	5.42	5.59	5.77	5.95	6.15	6.37	6.60	6.85	7.13	7.43	7.76	8.13
0.50	5.50	5.66	5.83	6.01	6.21	6.43	6.66	6.92	7.20	7.52	7.86	8.24	8.66	9.11
0.60	5.81	5.98	6.16	6.35	6.57	6.81	7.07	7.36	7.68	8.04	8.43	8.86	9.32	9.81
0.70	6.18	6.35	6.54	6.75	6.98	7.23	7.52	7.85	8.20	8.60	9.03	9.50	9.99	10.51
0.80	6.67	6.84	7.03	7.25	7.49	7.77	8.08	8.44	8.83	9.26	9.73	10.22	10.74	11.28
0.85	6.99	7.17	7.36	7.58	7.83	8.12	8.45	8.82	9.22	9.67	10.15	10.66	11.18	11.72
0.90	7.43	7.61	7.81	8.03	8.29	8.59	8.93	9.31	9.73	10.19	10.68	11.20	11.73	12.28
0.95	8.16	8.34	8.54	8.77	9.04	9.34	9.70	10.09	10.53	11.00	11.50	12.03	12.57	13.12
0.98	9.10	9.28	9.49	9.72	9.99	10.30	10.66	11.06	11.51	11.99	12.50	13.03	13.57	14.12
0.99	9.81	9.99	10.19	10.43	10.70	11.01	11.37	11.78	12.23	12.71	13.22	13.75	14.29	14.85
0.995	10.51	10.69	10.89	11.13	11.40	11.72	12.08	12.49	12.93	13.42	13.93	14.46	15.00	15.56

h = 300 m (W1 to W2 m/s)

PROB	20-25	25-30	30-35	35-40	40-45	45-50	50-55	55-60	60-65	65-70	70-75	75-80	80-85	85-90
0.36788	5.98	6.21	6.45	6.69	6.96	7.24	7.53	7.85	8.20	8.57	8.99	9.44	9.94	10.49
0.50	6.52	6.75	7.01	7.28	7.57	7.89	8.24	8.62	9.04	9.50	10.01	10.56	11.17	11.82
0.60	6.96	7.20	7.46	7.75	8.07	8.41	8.80	9.22	9.69	10.21	10.78	11.40	12.07	12.77
0.70	7.47	7.72	7.99	8.29	8.63	9.00	9.42	9.89	10.41	10.98	11.60	12.27	12.98	13.71
0.80	8.13	8.39	8.67	8.99	9.34	9.74	10.20	10.71	11.27	11.89	12.55	13.25	13.99	14.74
0.85	8.58	8.84	9.12	9.45	9.81	10.23	10.70	11.22	11.81	12.44	13.13	13.84	14.59	15.35
0.90	9.19	9.45	9.74	10.07	10.44	10.87	11.36	11.90	12.51	13.16	13.86	14.59	15.34	16.11
0.95	10.19	10.46	10.75	11.09	11.47	11.91	12.41	12.98	13.60	14.27	14.98	15.72	16.48	17.26
0.98	11.49	11.76	12.05	12.39	12.78	13.23	13.74	14.32	14.95	15.63	16.35	17.09	17.86	18.64
0.99	12.46	12.73	13.03	13.37	13.76	14.21	14.73	15.30	15.94	16.62	17.34	18.09	18.86	19.64
0.995	13.43	13.70	14.00	14.34	14.73	15.18	15.70	16.28	16.91	17.60	18.32	19.07	19.84	20.62

h = 400 m (W1 to W2 m/s)

PROB	20-25	25-30	30-35	35-40	40-45	45-50	50-55	55-60	60-65	65-70	70-75	75-80	80-85	85-90
0.36788	6.65	6.94	7.25	7.58	7.93	8.30	8.69	9.11	9.57	10.06	10.61	11.21	11.87	12.59
0.50	7.30	7.61	7.95	8.30	8.68	9.10	9.56	10.05	10.60	11.21	11.87	12.59	13.37	14.21
0.60	7.84	8.16	8.51	8.88	9.29	9.75	10.24	10.80	11.41	12.08	12.81	13.61	14.46	15.35
0.70	8.48	8.80	9.16	9.55	9.99	10.47	11.01	11.62	12.29	13.02	13.81	14.66	15.56	16.48
0.80	9.29	9.63	9.99	10.40	10.86	11.38	11.96	12.62	13.33	14.12	14.96	15.85	16.78	17.73
0.85	9.84	10.18	10.55	10.97	11.44	11.97	12.58	13.25	14.00	14.80	15.66	16.57	17.51	18.47
0.90	10.59	10.93	11.31	11.73	12.22	12.77	13.39	14.08	14.85	15.68	16.56	17.48	18.43	19.40
0.95	11.83	12.17	12.56	12.99	13.48	14.05	14.69	15.40	16.19	17.04	17.93	18.87	19.82	20.80
0.98	13.43	13.77	14.16	14.60	15.10	15.67	16.32	17.05	17.85	18.71	19.61	20.55	21.51	22.49
0.99	14.62	14.97	15.36	15.80	16.30	16.88	17.53	18.26	19.07	19.93	20.83	21.77	22.74	23.72
0.995	15.82	16.16	16.55	16.99	17.49	18.07	18.73	19.46	20.27	21.13	22.04	22.98	23.95	24.93

**h* = height interval (m)

Table 2-57. Conditional percentiles of wind speed shear (m/s) given shear height interval (m) and wind speed (m/s) applicable over the 3- to 16-km altitude range, KSC, February (Continued).

h = 500 m (W1 to W2 m/s)

PROB	20-25	25-30	30-35	35-40	40-45	45-50	50-55	55-60	60-65	65-70	70-75	75-80	80-85	85-90
0.36788	7.18	7.54	7.92	8.33	8.75	9.20	9.69	10.21	10.77	11.39	12.07	12.81	13.62	14.50
0.50	7.94	8.32	8.72	9.16	9.63	10.14	10.70	11.30	11.97	12.71	13.51	14.39	15.34	16.34
0.60	8.56	8.95	9.37	9.83	10.33	10.88	11.49	12.16	12.90	13.72	14.60	15.56	16.58	17.64
0.70	9.29	9.69	10.13	10.61	11.14	11.72	12.38	13.11	13.92	14.80	15.75	16.76	17.82	18.93
0.80	10.24	10.65	11.10	11.59	12.15	12.78	13.48	14.26	15.12	16.06	17.06	18.12	19.22	20.35
0.85	10.88	11.29	11.74	12.25	12.82	13.46	14.19	14.99	15.88	16.84	17.87	18.94	20.06	21.20
0.90	11.74	12.16	12.62	13.13	13.72	14.38	15.12	15.96	16.87	17.85	18.90	19.99	21.11	22.26
0.95	13.18	13.60	14.06	14.59	15.18	15.86	16.63	17.48	18.42	19.42	20.49	21.59	22.72	23.88
0.98	15.03	15.45	15.92	16.45	17.05	17.74	18.52	19.39	20.34	21.35	22.43	23.54	24.67	25.83
0.99	16.42	16.84	17.31	17.84	18.45	19.14	19.92	20.79	21.75	22.77	23.84	24.95	26.09	27.25
0.995	17.80	18.22	18.69	19.22	19.83	20.52	21.31	22.18	23.14	24.16	25.24	26.35	27.49	28.65

h = 600 m (W1 to W2 m/s)

PROB	20-25	25-30	30-35	35-40	40-45	45-50	50-55	55-60	60-65	65-70	70-75	75-80	80-85	85-90
0.36788	7.60	8.03	8.49	8.96	9.47	10.00	10.57	11.19	11.86	12.59	13.39	14.26	15.22	16.25
0.50	8.45	8.90	9.38	9.89	10.44	11.04	11.70	12.41	13.20	14.06	15.00	16.02	17.12	18.28
0.60	9.15	9.61	10.11	10.64	11.23	11.87	12.58	13.37	14.23	15.17	16.20	17.30	18.47	19.69
0.70	9.97	10.44	10.95	11.51	12.13	12.81	13.57	14.42	15.35	16.37	17.46	18.62	19.84	21.10
0.80	11.02	11.50	12.03	12.61	13.26	13.98	14.79	15.70	16.69	17.77	18.91	20.12	21.38	22.66
0.85	11.73	12.22	12.75	13.34	14.00	14.75	15.58	16.51	17.53	18.63	19.81	21.03	22.30	23.60
0.90	12.70	13.19	13.73	14.33	15.00	15.77	16.63	17.58	18.63	19.76	20.95	22.19	23.47	24.78
0.95	14.30	14.80	15.34	15.95	16.64	17.42	18.30	19.28	20.35	21.50	22.71	23.97	25.26	26.57
0.98	16.37	16.87	17.41	18.03	18.73	19.52	20.41	21.41	22.49	23.65	24.87	26.14	27.43	28.75
0.99	17.92	18.41	18.96	19.58	20.28	21.08	21.98	22.97	24.06	25.23	26.45	27.72	29.02	30.33
0.995	19.46	19.96	20.51	21.12	21.83	22.62	23.52	24.52	25.62	26.78	28.01	29.28	30.57	31.89

h = 700 m (W1 to W2 m/s)

PROB	20-25	25-30	30-35	35-40	40-45	45-50	50-55	55-60	60-65	65-70	70-75	75-80	80-85	85-90
0.36788	7.92	8.41	8.93	9.47	10.04	10.66	11.31	12.01	12.77	13.60	14.52	15.51	16.60	17.76
0.50	8.84	9.35	9.90	10.48	11.11	11.79	12.52	13.33	14.22	15.19	16.25	17.39	18.62	19.92
0.60	9.60	10.12	10.69	11.29	11.96	12.68	13.48	14.36	15.33	16.39	17.53	18.77	20.07	21.43
0.70	10.49	11.02	11.60	12.23	12.93	13.70	14.55	15.49	16.54	17.67	18.89	20.18	21.54	22.94
0.80	11.64	12.18	12.77	13.43	14.15	14.96	15.87	16.87	17.98	19.17	20.45	21.79	23.18	24.61
0.85	12.41	12.96	13.56	14.22	14.96	15.79	16.72	17.75	18.89	20.11	21.41	22.77	24.18	25.62
0.90	13.46	14.02	14.62	15.29	16.05	16.90	17.85	18.91	20.08	21.32	22.64	24.02	25.44	26.89
0.95	15.21	15.76	16.38	17.06	17.83	18.70	19.67	20.76	21.94	23.22	24.56	25.95	27.38	28.83
0.98	17.46	18.02	18.63	19.32	20.10	20.98	21.97	23.07	24.27	25.55	26.90	28.30	29.74	31.20
0.99	19.14	19.70	20.32	21.01	21.79	22.67	23.67	24.77	25.98	27.27	28.62	30.02	31.46	32.92
0.995	20.82	21.38	22.00	22.69	23.47	24.36	25.35	26.46	27.67	28.96	30.31	31.72	33.16	34.62

h = 800 m (W1 to W2 m/s)

PROB	20-25	25-30	30-35	35-40	40-45	45-50	50-55	55-60	60-65	65-70	70-75	75-80	80-85	85-90
0.36788	8.27	8.83	9.41	10.02	10.67	11.37	12.10	12.90	13.77	14.71	15.74	16.86	18.08	19.40
0.50	9.26	9.84	10.45	11.11	11.82	12.58	13.41	14.32	15.32	16.41	17.60	18.88	20.24	21.68
0.60	10.07	10.66	11.30	11.98	12.73	13.54	14.44	15.43	16.51	17.70	18.97	20.33	21.77	23.27
0.70	11.02	11.63	12.28	12.99	13.77	14.63	15.59	16.64	17.81	19.06	20.41	21.84	23.33	24.86
0.80	12.25	12.87	13.53	14.27	15.08	15.99	17.00	18.12	19.35	20.67	22.07	23.54	25.07	26.63
0.85	13.08	13.70	14.37	15.12	15.95	16.88	17.92	19.06	20.32	21.67	23.10	24.59	26.13	27.70
0.90	14.21	14.83	15.51	16.27	17.11	18.06	19.13	20.30	21.59	22.96	24.41	25.92	27.47	29.05
0.95	16.07	16.70	17.39	18.15	19.02	19.99	21.07	22.28	23.58	24.98	26.45	27.97	29.53	31.12
0.98	18.48	19.11	19.80	20.57	21.44	22.43	23.53	24.75	26.07	27.48	28.96	30.49	32.06	33.65
0.99	20.28	20.91	21.60	22.38	23.25	24.24	25.35	26.57	27.90	29.31	30.79	32.33	33.90	35.49
0.995	22.07	22.70	23.40	24.18	25.05	26.04	27.15	28.37	29.70	31.12	32.60	34.14	35.71	37.30

**h* = height interval (m)

Table 2-57. Conditional percentiles of wind speed shear (m/s) given shear height interval (m) and wind speed (m/s) applicable over the 3- to 16-km altitude range, KSC, February (Continued).

h = 900 m (W1 to W2 m/s)

PROB	20-25	25-30	30-35	35-40	40-45	45-50	50-55	55-60	60-65	65-70	70-75	75-80	80-85	85-90
0.36788	8.59	9.21	9.85	10.54	11.26	12.03	12.85	13.74	14.71	15.76	16.90	18.16	19.50	20.95
0.50	9.63	10.27	10.96	11.69	12.47	13.32	14.25	15.25	16.36	17.56	18.87	20.27	21.76	23.33
0.60	10.49	11.15	11.85	12.61	13.44	14.34	15.33	16.43	17.62	18.92	20.31	21.80	23.36	24.98
0.70	11.50	12.16	12.89	13.67	14.54	15.49	16.55	17.71	18.98	20.36	21.82	23.37	24.98	26.64
0.80	12.80	13.48	14.21	15.03	15.93	16.93	18.04	19.27	20.61	22.05	23.57	25.16	26.81	28.49
0.85	13.67	14.35	15.10	15.93	16.84	17.87	19.01	20.26	21.63	23.10	24.65	26.26	27.92	29.62
0.90	14.86	15.55	16.30	17.14	18.08	19.12	20.29	21.57	22.97	24.46	26.03	27.66	29.33	31.03
0.95	16.83	17.52	18.28	19.13	20.08	21.15	22.34	23.65	25.07	26.59	28.18	29.82	31.50	33.21
0.98	19.37	20.06	20.83	21.69	22.65	23.73	24.93	26.26	27.70	29.22	30.82	32.47	34.16	35.87
0.99	21.27	21.97	22.74	23.59	24.56	25.64	26.85	28.18	29.62	31.15	32.76	34.41	36.10	37.81
0.995	23.16	23.86	24.63	25.49	26.45	27.54	28.75	30.08	31.53	33.06	34.67	36.32	38.01	39.72

h = 1,000 m (W1 to W2 m/s)

PROB	20-25	25-30	30-35	35-40	40-45	45-50	50-55	55-60	60-65	65-70	70-75	75-80	80-85	85-90
0.36788	8.88	9.55	10.27	11.02	11.81	12.65	13.56	14.54	15.60	16.75	18.01	19.38	20.86	22.42
0.50	9.97	10.67	11.42	12.22	13.08	14.01	15.02	16.13	17.34	18.65	20.07	21.59	23.20	24.88
0.60	10.87	11.59	12.36	13.19	14.10	15.08	16.17	17.36	18.65	20.07	21.57	23.17	24.85	26.58
0.70	11.92	12.65	13.44	14.30	15.25	16.29	17.44	18.70	20.08	21.56	23.14	24.80	26.53	28.30
0.80	13.28	14.02	14.83	15.72	16.70	17.79	19.00	20.33	21.78	23.32	24.96	26.66	28.42	30.22
0.85	14.19	14.94	15.76	16.66	17.66	18.77	20.01	21.37	22.84	24.42	26.08	27.80	29.58	31.38
0.90	15.43	16.19	17.02	17.93	18.95	20.08	21.35	22.73	24.24	25.84	27.52	29.25	31.04	32.85
0.95	17.49	18.25	19.09	20.01	21.05	22.20	23.49	24.91	26.44	28.06	29.76	31.51	33.30	35.12
0.98	20.14	20.91	21.75	22.68	23.73	24.90	26.20	27.63	29.17	30.81	32.52	34.28	36.07	37.90
0.99	22.13	22.89	23.74	24.67	25.72	26.90	28.20	29.64	31.19	32.83	34.54	36.30	38.10	39.92
0.995	24.11	24.87	25.72	26.65	27.70	28.88	30.19	31.63	33.18	34.82	36.53	38.30	40.10	41.92

h = 1,500 m (W1 to W2 m/s)

PROB	20-25	25-30	30-35	35-40	40-45	45-50	50-55	55-60	60-65	65-70	70-75	75-80	80-85	85-90
0.36788	10.03	10.98	11.98	13.04	14.16	15.35	16.64	18.02	19.51	21.14	22.88	24.74	26.72	28.79
0.50	11.29	12.27	13.32	14.44	15.64	16.94	18.34	19.87	21.52	23.30	25.19	27.19	29.28	31.43
0.60	12.31	13.32	14.40	15.55	16.81	18.17	19.66	21.28	23.02	24.88	26.86	28.93	31.07	33.26
0.70	13.51	14.54	15.64	16.83	18.13	19.56	21.12	22.80	24.63	26.57	28.61	30.73	32.90	35.12
0.80	15.06	16.10	17.22	18.45	19.80	21.28	22.90	24.65	26.55	28.54	30.62	32.78	34.98	37.22
0.85	16.10	17.14	18.28	19.52	20.89	22.40	24.04	25.83	27.75	29.77	31.88	34.05	36.26	38.50
0.90	17.51	18.57	19.71	20.97	22.36	23.89	25.57	27.38	29.32	31.36	33.49	35.67	37.89	40.14
0.95	19.85	20.91	22.07	23.34	24.75	26.30	28.00	29.85	31.81	33.87	36.01	38.21	40.44	42.69
0.98	22.86	23.93	25.09	26.37	27.79	29.36	31.08	32.94	34.91	36.99	39.13	41.33	43.57	45.83
0.99	25.12	26.19	27.35	28.63	30.06	31.63	33.35	35.22	37.20	39.28	41.43	43.63	45.86	48.13
0.995	27.37	28.43	29.60	30.88	32.31	33.88	35.61	37.47	39.46	41.54	43.69	45.89	48.13	50.39

h = 2,000 m (W1 to W2 m/s)

PROB	20-25	25-30	30-35	35-40	40-45	45-50	50-55	55-60	60-65	65-70	70-75	75-80	80-85	85-90
0.36788	10.91	12.10	13.35	14.67	16.07	17.56	19.16	20.88	22.73	24.72	26.84	29.09	31.44	33.86
0.50	12.24	13.47	14.77	16.16	17.64	19.25	20.98	22.85	24.84	26.98	29.23	31.58	34.01	36.49
0.60	13.32	14.58	15.91	17.34	18.89	20.57	22.37	24.33	26.42	28.63	30.94	33.35	35.81	38.33
0.70	14.59	15.86	17.22	18.69	20.29	22.03	23.91	25.93	28.09	30.37	32.74	35.18	37.68	40.21
0.80	16.21	17.50	18.89	20.40	22.05	23.84	25.78	27.87	30.09	32.41	34.82	37.29	39.81	42.36
0.85	17.30	18.60	20.01	21.53	23.20	25.02	26.99	29.10	31.35	33.69	36.12	38.60	41.13	43.68
0.90	18.79	20.10	21.51	23.05	24.74	26.59	28.58	30.72	32.99	35.35	37.79	40.29	42.82	45.38
0.95	21.24	22.56	23.98	25.54	27.25	29.12	31.14	33.30	35.59	37.97	40.43	42.93	45.47	48.04
0.98	24.41	25.73	27.16	28.73	30.45	32.33	34.36	36.54	38.84	41.23	43.70	46.21	48.75	51.32
0.99	26.77	28.10	29.53	31.10	32.82	34.71	36.75	38.94	41.24	43.63	46.10	48.61	51.15	53.72
0.995	29.13	30.45	31.89	33.46	35.19	37.07	39.12	41.30	43.61	46.01	48.47	50.98	53.53	56.10

**h* = height interval (m)

Table 2-57. Conditional percentiles of wind speed shear (m/s) given shear height interval (m) and wind speed (m/s) applicable over the 3- to 16-km altitude range, KSC, February (Continued).

h = 2,500 m (W1 to W2 m/s)

PROB	20-25	25-30	30-35	35-40	40-45	45-50	50-55	55-60	60-65	65-70	70-75	75-80	80-85	85-90
0.36788	11.64	13.04	14.51	16.06	17.69	19.43	21.31	23.30	25.45	27.73	30.14	32.66	35.27	37.95
0.50	13.00	14.43	15.96	17.58	19.30	21.17	23.16	25.31	27.58	29.98	32.50	35.11	37.79	40.52
0.60	14.10	15.56	17.12	18.79	20.58	22.51	24.58	26.80	29.16	31.64	34.21	36.87	39.58	42.34
0.70	15.38	16.87	18.45	20.16	22.00	24.00	26.13	28.42	30.84	33.38	36.00	38.68	41.41	44.18
0.80	17.04	18.54	20.16	21.90	23.79	25.83	28.04	30.38	32.85	35.42	38.07	40.78	43.54	46.32
0.85	18.14	19.66	21.28	23.05	24.96	27.03	29.26	31.62	34.12	36.71	39.37	42.09	44.85	47.64
0.90	19.65	21.17	22.81	24.59	26.52	28.62	30.87	33.26	35.78	38.38	41.06	43.79	46.56	49.34
0.95	22.13	23.66	25.32	27.11	29.06	31.18	33.46	35.87	38.40	41.03	43.72	46.45	49.22	52.02
0.98	25.34	26.87	28.53	30.34	32.30	34.43	36.72	39.15	41.69	44.32	47.02	49.76	52.53	55.33
0.99	27.73	29.27	30.93	32.74	34.71	36.84	39.14	41.57	44.11	46.75	49.45	52.19	54.96	57.76
0.995	30.12	31.66	33.32	35.13	37.10	39.24	41.53	43.96	46.51	49.15	51.85	54.59	57.37	60.16

h = 3,000 m (W1 to W2 m/s)

PROB	20-25	25-30	30-35	35-40	40-45	45-50	50-55	55-60	60-65	65-70	70-75	75-80	80-85	85-90
0.36788	12.29	13.86	15.51	17.25	19.10	21.05	23.16	25.38	27.76	30.28	32.93	35.67	38.49	41.37
0.50	13.64	15.26	16.96	18.78	20.72	22.79	25.01	27.38	29.87	32.50	35.23	38.04	40.91	43.83
0.60	14.75	16.39	18.13	20.00	22.00	24.13	26.42	28.87	31.44	34.12	36.90	39.75	42.65	45.58
0.70	16.02	17.69	19.46	21.37	23.42	25.62	27.97	30.47	33.10	35.83	38.65	41.52	44.43	47.38
0.80	17.67	19.35	21.16	23.11	25.20	27.45	29.86	32.40	35.07	37.84	40.68	43.58	46.51	49.47
0.85	18.77	20.47	22.28	24.25	26.36	28.64	31.07	33.64	36.33	39.11	41.97	44.87	47.81	50.77
0.90	20.26	21.97	23.80	25.78	27.92	30.22	32.67	35.26	37.97	40.77	43.63	46.54	49.49	52.45
0.95	22.73	24.45	26.29	28.29	30.44	32.77	35.24	37.86	40.58	43.39	46.26	49.18	52.13	55.10
0.98	25.91	27.64	29.49	31.49	33.66	35.99	38.48	41.11	43.84	46.66	49.54	52.46	55.41	58.38
0.99	28.29	30.02	31.87	33.88	36.05	38.39	40.88	43.51	46.25	49.07	51.95	54.87	57.82	60.79
0.995	30.66	32.39	34.24	36.25	38.43	40.77	43.26	45.89	48.63	51.45	54.33	57.26	60.21	63.18

h = 3,500 m (W1 to W2 m/s)

PROB	20-25	25-30	30-35	35-40	40-45	45-50	50-55	55-60	60-65	65-70	70-75	75-80	80-85	85-90
0.36788	12.87	14.61	16.41	18.32	20.35	22.49	24.78	27.19	29.76	32.47	35.30	38.21	41.19	44.22
0.50	14.21	15.98	17.85	19.84	21.96	24.20	26.61	29.16	31.83	34.63	37.53	40.50	43.53	46.60
0.60	15.30	17.10	19.01	21.04	23.21	25.53	28.00	30.62	33.36	36.21	39.15	42.15	45.20	48.28
0.70	16.56	18.38	20.32	22.40	24.62	26.99	29.52	32.20	34.99	37.88	40.85	43.87	46.93	50.02
0.80	18.18	20.02	22.00	24.10	26.38	28.80	31.37	34.09	36.92	39.85	42.84	45.87	48.95	52.05
0.85	19.26	21.12	23.10	25.23	27.52	29.96	32.57	35.31	38.16	41.09	44.09	47.14	50.22	53.32
0.90	20.73	22.60	24.60	26.74	29.05	31.52	34.14	36.90	39.76	42.71	45.72	48.77	51.86	54.96
0.95	23.16	25.04	27.05	29.21	31.53	34.03	36.67	39.44	42.32	45.29	48.30	51.36	54.45	57.56
0.98	26.29	28.17	30.19	32.36	34.70	37.20	39.85	42.64	45.53	48.49	51.52	54.58	57.67	60.78
0.99	28.63	30.51	32.53	34.71	37.05	39.55	42.21	45.00	47.89	50.86	53.89	56.95	60.04	63.15
0.995	30.96	32.84	34.86	37.04	39.38	41.89	44.55	47.34	50.23	53.20	56.23	59.29	62.38	65.49

h = 4,000 m (W1 to W2 m/s)

PROB	20-25	25-30	30-35	35-40	40-45	45-50	50-55	55-60	60-65	65-70	70-75	75-80	80-85	85-90
0.36788	13.41	15.27	17.23	19.29	21.46	23.76	26.21	28.79	31.52	34.38	37.35	40.40	43.51	46.66
0.50	14.72	16.63	18.65	20.78	23.04	25.45	28.01	30.71	33.53	36.47	39.50	42.61	45.76	48.95
0.60	15.79	17.73	19.78	21.96	24.28	26.75	29.38	32.13	35.01	38.00	41.06	44.19	47.36	50.57
0.70	17.03	18.99	21.07	23.29	25.66	28.18	30.86	33.67	36.60	39.62	42.71	45.86	49.05	52.24
0.80	18.61	20.60	22.71	24.97	27.37	29.95	32.67	35.53	38.49	41.54	44.65	47.81	50.99	54.20
0.85	19.67	21.67	23.79	26.06	28.50	31.09	33.83	36.70	39.68	42.74	45.87	49.04	52.23	55.44
0.90	21.11	23.12	25.25	27.54	29.99	32.61	35.37	38.26	41.25	44.33	47.46	50.63	53.83	57.04
0.95	23.48	25.50	27.65	29.95	32.43	35.06	37.84	40.74	43.75	46.83	49.97	53.15	56.35	59.57
0.98	26.54	28.56	30.72	33.03	35.51	38.16	40.95	43.86	46.08	49.97	53.11	56.29	59.49	62.71
0.99	28.82	30.85	33.01	35.33	37.81	40.46	43.25	46.17	49.19	52.28	55.42	58.60	61.81	65.03
0.995	31.10	33.12	35.28	37.60	40.09	42.74	45.53	48.45	51.47	54.57	57.71	60.89	64.09	67.32

**h* = height interval (m)

Table 2-57. Conditional percentiles of wind speed shear (m/s) given shear height interval (m) and wind speed (m/s) applicable over the 3- to 16-km altitude range, KSC, February (Continued).

h = 5,000 m (W1 to W2 m/s)

PROB	20-25	25-30	30-35	35-40	40-45	45-50	50-55	55-60	60-65	65-70	70-75	75-80	80-85	85-90
0.36788	14.39	16.49	18.66	20.97	23.38	25.96	28.65	31.49	34.46	37.56	40.74	43.99	47.30	50.65
0.50	15.64	17.78	20.02	22.39	24.90	27.57	30.35	33.28	36.34	39.50	42.73	46.03	49.37	52.74
0.60	16.66	18.82	21.11	23.52	26.09	28.79	31.64	34.62	37.73	40.92	44.18	47.49	50.85	54.22
0.70	17.83	20.02	22.33	24.79	27.40	30.15	33.05	36.08	39.21	42.43	45.72	49.04	52.40	55.79
0.80	19.33	21.55	23.89	26.38	29.02	31.82	34.76	37.82	40.99	44.23	47.53	50.87	54.24	57.64
0.85	20.34	22.56	24.91	27.42	30.08	32.90	35.86	38.95	42.12	45.38	48.68	52.02	55.39	58.78
0.90	21.70	23.93	26.30	28.82	31.50	34.34	37.32	40.41	43.61	46.87	50.18	53.53	56.90	60.29
0.95	23.94	26.19	28.57	31.10	33.80	36.65	39.65	42.76	45.96	49.23	52.55	55.91	59.28	62.67
0.98	26.83	29.08	31.47	34.02	36.72	39.59	42.59	45.71	48.92	52.19	55.51	58.87	62.25	65.64
0.99	28.99	31.25	33.64	36.18	38.89	41.76	44.77	47.89	51.10	54.38	57.70	61.06	64.43	67.83
0.995	31.15	33.40	35.79	38.34	41.05	43.92	46.93	50.05	53.26	56.54	59.86	63.22	66.60	69.99

h = 6,000 m (W1 to W2 m/s)

PROB	20-25	25-30	30-35	35-40	40-45	45-50	50-55	55-60	60-65	65-70	70-75	75-80	80-85	85-90
0.36788	15.27	17.53	19.91	22.38	25.02	27.75	30.64	33.68	36.84	40.10	43.44	46.84	50.28	53.76
0.50	16.45	18.77	21.19	23.75	26.45	29.27	32.25	35.36	38.59	41.90	45.28	48.71	52.18	55.68
0.60	17.41	19.76	22.22	24.82	27.55	30.44	33.47	36.63	39.89	43.23	46.63	50.08	53.55	57.05
0.70	18.52	20.89	23.39	26.01	28.79	31.73	34.81	37.99	41.28	44.65	48.07	51.53	55.01	58.51
0.80	19.94	22.33	24.85	27.51	30.33	33.31	36.41	39.63	42.95	46.33	49.77	53.23	56.72	60.23
0.85	20.88	23.29	25.82	28.50	31.34	34.32	37.44	40.67	44.00	47.39	50.83	54.31	57.81	61.32
0.90	22.16	24.58	27.12	29.82	32.67	35.67	38.81	42.06	45.39	48.79	52.23	55.71	59.22	62.74
0.95	24.28	26.70	29.26	31.97	34.84	37.85	41.00	44.26	47.61	51.02	54.47	57.95	61.45	64.97
0.98	27.00	29.43	31.99	34.71	37.58	40.61	43.77	47.04	50.39	53.80	57.25	60.74	64.24	67.76
0.99	29.03	31.46	34.03	36.75	39.63	42.66	45.82	49.09	52.44	55.85	59.31	62.79	66.30	69.81
0.995	31.05	33.48	36.05	38.77	41.65	44.69	47.85	51.12	54.47	57.89	61.34	64.83	68.33	71.85

h = 7,000 m (W1 to W2 m/s)

PROB	20-25	25-30	30-35	35-40	40-45	45-50	50-55	55-60	60-65	65-70	70-75	75-80	80-85	85-90
0.36788	16.06	18.48	20.98	23.63	26.38	29.28	32.34	35.52	38.81	42.20	45.65	49.16	52.70	56.27
0.50	17.18	19.64	22.21	24.90	27.74	30.73	33.85	37.10	40.44	43.87	47.36	50.89	54.45	58.04
0.60	18.08	20.58	23.18	25.91	28.81	31.82	34.98	38.26	41.63	45.09	48.60	52.16	55.75	59.34
0.70	19.13	21.65	24.27	27.06	29.97	33.03	36.22	39.53	42.94	46.41	49.93	53.50	57.09	60.70
0.80	20.47	23.00	25.66	28.46	31.41	34.51	37.74	41.08	44.50	47.99	51.53	55.10	58.69	62.31
0.85	21.35	23.90	26.57	29.39	32.36	35.48	38.72	42.07	45.51	49.01	52.54	56.11	59.70	63.31
0.90	22.56	25.12	27.80	30.64	33.62	36.75	40.00	43.36	46.81	50.31	53.86	57.44	61.03	64.64
0.95	24.55	27.12	29.81	32.66	35.66	38.80	42.07	45.44	48.90	52.41	55.96	59.53	63.13	66.74
0.98	27.10	29.68	32.38	35.23	38.24	41.39	44.67	48.05	51.50	55.02	58.57	62.15	65.75	69.37
0.99	29.01	31.59	34.29	37.15	40.16	43.31	46.59	49.98	53.43	56.95	60.50	64.08	67.68	71.30
0.995	30.91	33.49	36.20	39.05	42.07	45.22	48.50	51.88	55.34	58.86	62.41	66.00	69.60	73.21

h = 8,000 m (W1 to W2 m/s)

PROB	20-25	25-30	30-35	35-40	40-45	45-50	50-55	55-60	60-65	65-70	70-75	75-80	80-85	85-90
0.36788	16.79	19.31	21.96	24.69	27.58	30.62	33.76	37.04	40.42	43.91	47.46	51.07	54.72	58.36
0.50	17.84	20.43	23.10	25.92	28.88	31.96	35.17	38.51	41.95	45.47	49.05	52.68	56.34	60.01
0.60	18.70	21.30	24.03	26.87	29.86	32.99	36.25	39.63	43.10	46.64	50.23	53.86	57.51	61.19
0.70	19.68	22.32	25.06	27.94	30.97	34.15	37.44	40.84	44.34	47.90	51.50	55.13	58.79	62.46
0.80	20.94	23.60	26.36	29.28	32.34	35.54	38.86	42.29	45.80	49.38	53.00	56.64	60.30	63.90
0.85	21.75	24.44	27.23	30.15	33.22	36.44	39.78	43.22	46.73	50.31	53.93	57.58	61.25	64.94
0.90	22.91	25.59	28.38	31.32	34.41	37.64	41.00	44.45	47.97	51.55	55.18	58.83	62.50	66.18
0.95	24.78	27.47	30.28	33.23	36.33	39.57	42.93	46.39	49.93	53.52	57.15	60.80	64.47	68.16
0.98	27.19	29.88	32.69	35.65	38.76	42.01	45.38	46.85	52.39	55.98	59.61	63.27	66.94	70.63
0.99	28.98	31.68	34.50	37.46	40.57	43.82	47.19	50.66	54.20	57.80	61.43	65.09	68.76	72.45
0.995	30.77	33.47	36.29	39.25	42.36	45.61	48.99	52.46	56.00	59.59	63.23	66.88	70.56	74.24

**h* = height interval (m)

Table 2-57. Conditional percentiles of wind speed shear (m/s) given shear height interval (m) and wind speed (m/s) applicable over the 3- to 16-km altitude range, KSC, February (Continued).

h = 9,000 m (W1 to W2 m/s)

PROB	20-25	25-30	30-35	35-40	40-45	45-50	50-55	55-60	60-65	65-70	70-75	75-80	80-85	85-90
0.36788	17.54	20.17	22.86	25.69	28.64	31.72	34.95	38.30	41.76	45.31	48.92	52.58	56.27	60.00
0.50	18.57	21.22	23.98	26.86	29.87	33.03	36.33	39.74	43.24	46.82	50.46	54.13	57.84	61.57
0.60	19.38	22.08	24.86	27.78	30.85	34.04	37.36	40.80	44.33	47.94	51.61	55.30	59.00	62.72
0.70	20.34	23.05	25.86	28.82	31.90	35.13	38.49	41.95	45.51	49.12	52.79	56.49	60.22	63.97
0.80	21.54	24.28	27.13	30.10	33.22	36.48	39.87	43.36	46.93	50.56	54.23	57.94	61.67	65.41
0.85	22.35	25.10	27.95	30.95	34.08	37.36	40.75	44.25	47.83	51.48	55.16	58.87	62.59	66.33
0.90	23.45	26.20	29.07	32.07	35.22	38.51	41.92	45.43	49.02	52.66	56.35	60.06	63.79	67.54
0.95	25.25	28.01	30.89	33.91	37.07	40.37	43.79	47.31	50.91	54.56	58.25	61.96	65.70	69.44
0.98	27.56	30.34	33.22	36.24	39.41	42.72	46.15	49.68	53.28	56.93	60.62	64.34	68.07	71.81
0.99	29.29	32.07	34.95	37.98	41.15	44.47	47.90	51.43	55.03	58.68	62.37	66.09	69.82	73.56
0.995	31.02	33.79	36.68	39.70	42.88	46.19	49.63	53.16	56.76	60.41	64.10	67.82	71.55	75.30

h = 10,000 m (W1 to W2 m/s)

PROB	20-25	25-30	30-35	35-40	40-45	45-50	50-55	55-60	60-65	65-70	70-75	75-80	80-85	85-90
0.36788	18.05	20.77	23.59	26.49	29.54	32.74	36.08	39.52	43.06	46.67	50.34	54.05	57.79	61.56
0.50	18.99	21.78	24.62	27.59	30.72	33.96	37.33	40.81	44.39	48.05	51.76	55.50	59.25	63.02
0.60	19.76	22.56	25.45	28.45	31.59	34.88	38.29	41.80	45.40	49.06	52.77	56.52	60.30	64.09
0.70	20.64	23.47	26.37	29.41	32.60	35.92	39.35	42.89	46.52	50.19	53.91	57.65	61.42	65.21
0.80	21.76	24.60	27.55	30.62	33.82	37.16	40.62	44.18	47.81	51.51	55.24	59.01	62.78	66.56
0.85	22.50	25.37	28.31	31.39	34.62	37.97	41.45	45.02	48.66	52.35	56.08	59.84	63.62	67.41
0.90	23.52	26.39	29.35	32.45	35.68	39.04	42.52	46.10	49.75	53.46	57.20	60.96	64.74	68.53
0.95	25.18	28.06	31.04	34.14	37.39	40.77	44.26	47.85	51.50	55.21	58.96	62.72	66.50	70.29
0.98	27.33	30.21	33.19	36.30	39.56	42.94	46.44	50.04	53.70	57.40	61.15	64.91	68.70	72.49
0.99	28.93	31.81	34.79	37.91	41.17	44.55	48.06	51.65	55.31	59.02	62.77	66.53	70.32	74.11
0.995	30.52	33.40	36.39	39.50	42.76	46.15	49.66	53.25	56.91	60.62	64.37	68.14	71.92	75.71

For the associated wind speed with the extreme largest wind speed shear parameters (meters per second),

$$\mu_w(h) = 34.71 + 0.0071\,h;\ (100 \le h \le 600 \text{ m})\ , \tag{2.65}$$

$$\mu_w(h) = 39.2936 + 0.001127\,h;\ (600 < h \le 10{,}000 \text{ m})\ , \tag{2.66}$$

and

$$\alpha_w(h) = 11.60 \text{ for all } h \ge 100 \text{ m}\ . \tag{2.67}$$

The empirical equation for the *m* parameter is

$$m(h) = 1.27 + 0.00026\,h,\ (100 \le h \le 10{,}000 \text{ m})\ . \tag{2.68}$$

Evaluating this equation for h = 100 m and h = 10,000 m yields the values of 1.296 and 3.870. From equation (2.56), this gives the correlation coefficients between the extreme largest shear and associated wind speed for h = 100 m as 0.4046 and for h = 10,000 m as 0.9332. Hence, as the altitude shear interval increases, this correlation coefficient between the wind shear and wind speed increases.

The above empirical equations for the five bivariate extreme value distribution functions were used in equation (2.60) to establish the conditional percentile values for wind speed shear for the given wind speed class intervals shown in table 2-57. The 99th conditional extreme value wind shear at various shear intervals, h, gives the associated wind speed. As shown, for the given wind speed, the conditional wind shear over large shear intervals exceeds the given wind speed. This indicates that this wind shear model is invalid in this domain.

2.3.5.8 Percentile Values for Extreme Largest Wind Speed Shear. The univariate extreme value distribution for wind speed shear can be computed using the $\mu_s(h)$ and $\alpha_s(h)$ parameters from equations (2.63) and (2.64) in the univariate extreme value probability distribution function. The percentile values for wind speed shear versus shear intervals, $S(h;P)$ (table 2-58) are computed from

$$S(h;P) = \mu_s(h) + \alpha_s(h)\, Y\,, \tag{2.69}$$

where

$Y = -\ln(-\ln P)$
P = probability.

Table 2-58. Percentile values (m/s) versus shear intervals for extreme largest shear (3- to 16-km altitude), KSC, February.

Shear Interval (m)	Percentile										
	36.79	50.00	60.00	70.00	80.00	85.00	90.00	95.00	98.00	99.00	99.50
100	4.13	4.40	4.61	4.87	5.21	5.43	5.74	6.26	6.92	7.42	7.92
200	5.73	6.22	6.62	7.10	7.73	8.15	8.73	9.69	10.93	11.86	12.79
300	6.93	7.62	8.19	8.86	9.74	10.34	11.15	12.50	14.25	15.55	16.86
400	7.93	8.79	9.51	10.36	11.46	12.21	13.23	14.92	17.11	18.76	20.39
500	8.81	9.83	10.68	11.67	12.98	13.86	15.06	17.06	19.65	21.59	23.52
600	9.60	10.75	11.72	12.85	14.33	15.34	16.70	18.98	21.92	24.12	26.32
700	10.32	11.60	12.67	13.93	15.57	16.68	18.19	20.71	23.98	26.42	28.85
800	10.99	12.38	13.55	14.91	16.70	17.91	19.56	22.30	25.85	28.51	31.16
900	11.61	13.11	14.36	15.83	17.75	19.05	20.82	23.76	27.57	30.43	33.28
1,000	12.20	13.80	15.12	16.68	18.72	20.10	21.99	25.12	29.17	32.20	35.23
1,500	14.76	16.73	18.36	20.29	22.80	24.50	26.82	30.68	35.67	39.41	43.13
2,000	16.90	19.12	20.97	23.15	25.99	27.91	30.54	34.90	40.55	44.78	49.00
2,500	18.77	21.18	23.19	25.55	28.64	30.72	33.57	38.31	44.44	49.03	53.61
3,000	20.45	23.01	25.14	27.64	30.91	33.13	36.15	41.17	47.67	52.54	57.40
3,500	21.99	24.66	26.88	29.50	32.92	35.23	38.39	43.64	50.44	55.53	60.60
4,000	23.41	26.18	28.48	31.19	34.73	37.12	40.39	45.83	52.86	58.13	63.38
5,000	26.00	28.91	31.33	34.18	37.90	40.42	43.86	49.57	56.97	62.51	68.03
6,000	28.32	31.34	33.84	36.80	40.65	43.26	46.82	52.74	60.39	66.13	71.85
7,000	30.45	33.54	36.12	39.15	43.10	45.78	49.43	55.50	63.36	69.25	75.12
8,000	32.42	35.58	38.20	41.29	45.33	48.05	51.78	57.97	65.99	72.00	77.98
9,000	34.27	37.47	40.14	43.28	47.38	50.15	53.93	60.22	68.36	74.47	80.54
10,000	36.01	39.25	41.95	45.13	49.28	52.09	55.92	62.29	70.54	76.72	82.88

Using the same procedure, the empirical equations for $\mu_s(h)$ and $\alpha_s(h)$ for the extreme largest wind speed shear in the 3- to 16-km altitude for KSC, July, are

$$\mu_s(h) = 0.5822\, h^{0.36} \tag{2.70}$$

and

$$\alpha_s(h) = 0.0507\, h^{0.57} \quad . \tag{2.71}$$

The KSC, February and July, percentile values for the extreme largest wind speed shear are given in tables 2-58 and 2-59, respectively. Comparing the wind shears (tables 2-58 and 2-59), it is seen that the wind shears are greater during February than July for shear intervals, h, >100 m. This is because the extreme largest wind profile shears are correlated with the wind speed, and as the shear interval increases, the correlation increases.

Table 2-59. Percentile values (m/s) versus shear intervals for extreme largest shear (3- to 16-km altitude), KSC, July.

Shear Interval (m)	Percentile										
	36.79	50.00	60.00	70.00	80.00	85.00	90.00	95.00	98.00	99.00	99.50
100	3.06	3.31	3.53	3.78	4.11	4.33	4.63	5.13	5.79	6.27	6.76
200	3.92	4.30	4.62	4.99	5.48	5.81	6.26	7.01	7.98	8.70	9.42
300	4.54	5.02	5.42	5.89	6.50	6.92	7.48	8.43	9.65	10.56	11.47
400	5.03	5.60	6.07	6.62	7.35	7.84	8.50	9.61	11.05	12.13	13.20
500	5.45	6.10	6.63	7.26	8.08	8.64	9.40	10.66	12.29	13.51	14.73
600	5.82	6.54	7.13	7.83	8.74	9.35	10.20	11.60	13.41	14.76	16.12
700	6.16	6.93	7.58	8.34	9.34	10.01	10.93	12.46	14.44	15.92	17.39
800	6.46	7.30	8.00	8.82	9.89	10.62	11.61	13.26	15.39	16.99	18.58
900	6.74	7.64	8.38	9.26	10.41	11.19	12.25	14.01	16.29	18.00	19.71
1,000	7.00	7.95	8.75	9.68	10.90	11.72	12.85	14.72	17.15	18.96	20.77
1,500	8.10	9.30	10.30	11.48	13.01	14.05	15.47	17.83	20.88	23.17	25.45
2,000	8.98	10.40	11.58	12.96	14.77	16.00	17.67	20.45	24.05	26.74	29.43
2,500	9.74	11.34	12.68	14.25	16.31	17.70	19.60	22.76	26.84	29.90	32.95
3,000	10.40	12.18	13.66	15.41	17.69	19.23	21.34	24.84	29.37	32.77	29.37
3,500	10.99	12.93	14.56	16.46	18.95	20.64	22.94	26.76	31.71	35.42	39.11
4,000	11.53	13.63	15.38	17.44	20.12	21.94	24.43	28.55	33.89	37.89	41.88
5,000	12.49	14.88	16.87	19.20	22.26	24.32	27.14	31.82	37.89	42.43	46.96
6,000	13.34	15.99	18.19	20.79	24.17	26.46	29.59	34.79	41.51	46.56	51.58
7,000	14.10	16.99	19.40	22.23	25.93	28.43	31.84	37.52	44.86	50.37	55.85
8,000	14.80	17.92	20.51	23.57	27.56	30.25	33.94	40.06	47.99	53.93	59.85
9,000	15.44	18.77	21.55	24.82	29.08	31.97	35.91	42.46	50.94	57.29	63.63
10,000	16.04	19.58	22.52	25.99	30.53	33.59	37.78	44.73	53.73	60.48	67.20

2.3.5.9 Percentile Values for Extreme Largest Wind Speed. An estimate for the extreme value probability density function for the extreme largest wind speed in the 3- to 16-km layer can be obtained by evaluating equations (2.50) and (2.51) at the shear interval, h = 10,000 m for the parameters μ_w and α_w. For KSC, February, this gives μ_w = 50.56 m/s and α_w = 11.60 m/s. The percentile values for the extreme largest wind speed is then estimated by

$$W(P) = 50.56 + 11.60\ Y\ , \tag{2.72}$$

where

$Y = -\ln(-\ln P)$
P = probability.

Considering that the wind speed percentile values in table 2-60 are derived from three different methods and three different databases, the agreement is remarkably close.

Table 2-60. Comparison of some wind speed percentile values, KSC.

Probability (%)	Scalar Wind Speed[(a)] (m/s)	Extreme Wind Speed[(b)] (m/s)	Largest *u*-Component[(c)] (m/s)
50	45	54.8	49.8
75	57	65.0	68.1
80	68	68.0	71.0
95	75	85.0	85.8
99	92	103.9	99.1

[(a)] From table 2-73, empirical monthly envelope for percentile values at 12-km altitude.
[(b)] Estimated from equation (2.67), February.
[(c)] The largest zonal wind component to probability ellipses using monthly enveloping bivariate normal parameters at 12-km altitude. From table 3.4 in reference 2-1,
$\bar{u}_A$ = 30.34 m/s and s_{Au} = 22.67 m/s,
$\bar{u}_L = u_A + s_{Au}\ \lambda_e$, where $\lambda_e = \sqrt{\pm 2\ln(1 \pm P)}$.

2.3.6 Gusts—Vertically Flying Vehicles

The steady-state, in-flight wind speed envelopes presented in section 2.3.5 do not contain the gust (high-frequency content) portion of the wind profile. The steady-state wind profile measurements have been defined as those obtained by the rawinsonde system. These measurements as presented in this analysis represent wind speeds averaged over ≈1,000 m in the vertical and, therefore, eliminate features with smaller scales. Smaller scale features are contained in the detailed profiles measured by the FPS-16 radar/Jimsphere system which provides wind measurements averaged over ≈30 m.

A number of attempts have been made to represent the high-frequency content of vertical profiles of wind in a suitable form for use in vehicle design studies. Most of the attempts resulted in gust information that could be used for specific applications, but, to date, no universal gust representation has been formulated. Information

on discrete and continuous gust representations is given below relative to vertically ascending aerospace vehicles. In addition to the extensive work reported herein, other organizations, such as The Aerospace Corporation (ref. 2-49), have studied gust-associated loads analysis.

2.3.7 Discrete Gusts

Idealized discrete gust models have been developed for vehicle design studies and other engineering applications in an attempt to represent, in a physically reasonable manner, characteristics of small-scale wind perturbations associated with vertical profiles of wind velocity. Assessments of elastic body and buffeting response to in-flight wind perturbations or gusts are important in the establishment of vehicle design structural requirements and operational capability. In vehicle response analyses, the discrete gust is applied perpendicular to the launch vehicle longitudinal axis, and it is assumed that the vehicle is instantaneously immersed in the time-dependent gust profile (ref. 2-49). Simulation of the autopilot response to the gust produces the loads that are responses to the gust-induced deviations of the angle of attack and angle of sideslip from the prelaunch-programmed vehicle guidance commands. Launch vehicles can have significant response to gusts with wavelengths below ≈60 m that are not observable with the Jimsphere wind profile measurement system used for DOL rigid body trajectory and loads assessments. Since it is not practical to perform elastic body loads analyses on the DOL because of time constraints and other practical considerations, the commit-to-launch decision is protected for gust uncertainty contributions to elastic body loads uncertainties. This protection is in the form of a load increment (knockdown) that is developed in special engineering studies prior to the DOL.

Two discrete gust models are recommended for use in conjunction with synthetic vector wind profiles for design studies and establishing trajectory and load increments that account for launch vehicle elastic body and buffet response uncertainty on the DOL. The first model is the "classical-NASA" 9-m/s quasi-square wave gust originally developed for Saturn/Apollo and certified for Shuttle program applications (ref. 2-50) (see sec. 2.4.4). The original version of the second model (ref. 2-51) was developed for the Shuttle program in 1997 to improve representation of gusts with half-widths d_m < 100 m that had amplitudes that were overly conservative in the classical model. The 1997 model is an adaptation of the discrete gust model originally developed for military specification (MIL-SPEC) requirements for the flying qualities of piloted aircraft (ref. 2-52 and sec. 2.3.12). The original 1997 model is based on an empirical least-squares fit to the original MIL-SPEC graphical presentation. An updated version of the 1997 model (ref. 2-53), based on a derivation of the MIL-SPEC curve by integration in closed form of the Dryden power spectrum density (PSD) function, is recommended herein. The classical NASA 9-m/s discrete gust model is considered to be the most conservative because of its quasi-square wave form, which was based on the analysis of high-resolution detail wind profiles measured by the FPS-16 radar Jimsphere system (see fig. 2-34 for example). In addition, there is no provision in the classical model for taking into account the expected variation of gust amplitude on gust half-width and altitude. The 1997 model that includes such a variation (refs. 2-51, 2-53, and 2-54), yields smaller gust amplitudes than the classical model for gust half-widths <100 m.

2.3.7.1 Origin of the Classical NASA Discrete (9 m/s) Gust. The original NASA quasi-square wave "flat-top" gust, having an amplitude of 9 m/s with a variable gust width from 50 to 300 m, had an absolute gust gradient of 0.36 s^{-1} for the first and last 25 m (or 9 m/s per 25 m), first appeared in 1963 (ref. 2-55) and was revised (ref. 2-56) with a cosine leading and trailing edge of a 30-m interval (fig. 2-17). The gust amplitude was reduced to 7.65 m/s (0.85 of its value) for the Shuttle ascent design when this discrete gust model was used in conjunction with synthetic wind and wind shear models (see sec. 2.4.4).

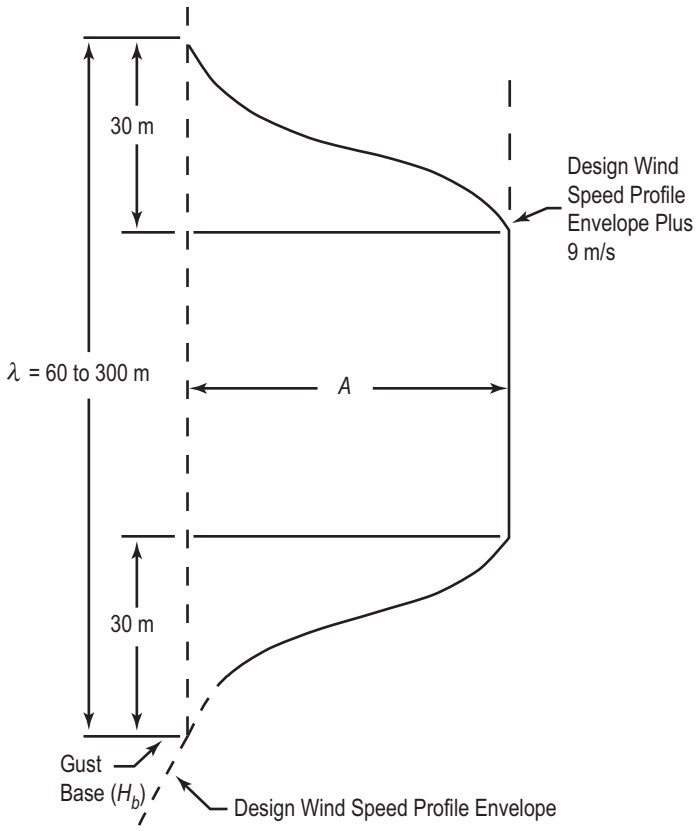

Figure 2-17. Relationship between discrete gust and/or embedded jet characteristics (quasi-square wave shape) and the design wind speed profile envelope.

Early discrete wind gust models for missile design (refs. 2-56 and 2-57) are based on accelerometer measurements of turbulence by aircraft in horizontal flight (refs. 2-58 and 2-59). Common early sources for aircraft accelerometer measurement data in or near thunderstorms are the measurement series during 1941–1942 in the vicinity of Langley Field, VA, and from the Thunderstorm Project near Orlando, FL, in the summers of 1946 and 1947 (refs. 2-59 and 2-60). The 99th percentile value (9.1 m/s) for derived gust magnitude (ref. 2-57) listed in table 2-61 was derived from previously published data (ref. 2-58) from aircraft measurements traversing thunderstorms.

Table 2-61. Percentiles from cumulative probability distribution of gust magnitude for thunderstorm turbulence, 1–14 kft (ref. 2-56).

		Percentile					
		50	**68**	**84.1**	**97.7**	**99.0**	**99.86**
Gust Velocity	m/s	2.40	3.10	4.60	7.80	9.10	12.50
	ft/s	7.87	10.18	15.09	25.59	29.86	41.01

Missing from these early analyses are two important gust characteristics—the gust width and shape. For application of a discrete gust in an elastic body loads analysis, gust widths are chosen to excite vehicle response modes to produce the maximum design response requirement. The gust width for excitation can be as small as 60 m (≈200 ft) for a spacecraft and as large as 450 m (≈1,500 ft) for a heavy-lift launch vehicle (ref. 2-49). The U.S. Air Force Titan and Delta vehicle programs use a 1-cos gust shape with a 9-m/s amplitude and 304-m gust width. The important difference between the Air Force gust model and the classical NASA model is that the rise to 9 m/s takes place over 152 m rather than 30 m for the NASA model. In a study (ref. 2-49) of medium- and heavy-lift vehicle pitch-bending moment responses to the classical NASA classical gust ("flat-top" gust) and the 1-cos gust (1997 model), with both having the same wavelength (≈300 m for medium lift and ≈450 m for heavy lift) and amplitude (≈9 m/s), it was concluded that the NASA classical gust produced larger loads that were as much as 40-percent larger for the heavy-lift vehicle, thus producing a more conservative or "robust" design requirement.

2.3.7.2 Classical NASA Discrete Gust Model. Assuming that a design wind speed profile envelope without a wind shear envelope is to be used in a design study, the classical NASA model defines an associated discrete gust of variable length from 60 to 300 m. The leading and trailing edges conform to a 1-cos buildup and decay within an altitude interval of 30 m, as shown in figure 2-17. The plateau region of the gust can vary in thickness from zero to 240 m. An analytical expression for the value of this gust (u_g) as a function of height, H, above natural grade is given by

$$u_g = \frac{A}{2}\left\{1-\cos\left[\frac{\pi}{30}\left(H-H_b\right)\right]\right\},\ H_b \le H \le H_b + 30 \text{ m}\ ,$$

$$u_g = A,\ H_b + 30 \text{ m} \le H \le H_b + \lambda - 30 \text{ m}\ ,$$

and

$$u_g = \frac{A}{2}\left\{1-\cos\left[\frac{\pi}{30}\left(H-H_b-\lambda\right)\right]\right\},\ H_b + \lambda - 30 \text{ m} \le H \le H_b + \lambda\ , \tag{2.73}$$

where H_b is the height of the base of the gust above natural grade, λ is the gust thickness ($60 \le \lambda \le 300$ m), and A is the gust amplitude in meters per second.

The gust amplitude is a function of H_b, and, for design purposes, the 1-percent risk gust amplitude is given by

$$A = 6 \text{ m/s},\quad H_b < 300 \text{ m}$$

$$A = \frac{3}{700}(H_b - 300) + 6,\ 300 \text{ m} \le H_b \le 1{,}000 \text{ m}$$

and

$$A = 9 \text{ m/s},\ H_b > 1{,}000 \text{ m}\ . \tag{2.74}$$

If a wind speed profile envelope with a buildup and a back-off wind shear envelope (sec. 2.5.3.1) is to be used in a design study, it is recommended that the previously mentioned discrete gust be modified. For wind shear buildup, the modified leading edge 1-cos shape is defined by

$$u_g = 10A\left\{\left(\frac{H-H_b}{30}\right)^{0.9} - 0.9\left(\frac{H-H_b}{30}\right)\right\},\ H_b \le H \le H_b + 30 \text{ m}\ , \tag{2.75}$$

where the height of the gust base, H_b, corresponds to the point where the design wind speed profile envelope intersects the design buildup shear envelope. For a wind speed profile envelope with a back-off wind shear envelope, the 1-cos trailing edge is defined by

$$u_g = 10A\left\{\left(\frac{H_b+\lambda-H}{30}\right)^{0.9} - 0.9\left(\frac{H_b+\lambda-H}{30}\right)\right\},\ H_b+\lambda-30\text{ m} \le h \le H_b+\lambda\ , \tag{2.76}$$

and the leading edge shall conform to a 1-cos shape. In this case, the height, $H_b+\lambda$, of the end of the gust corresponds to the point where the design wind speed profile envelope intersects the design back-off shear envelope. This modification of the 1-cos shape at the leading and trailing edges ensures that the merging of the shear and gust is continuous. This merging reduces the gust amplitude to 0.85 of its original value to account for the nonperfect correlation between wind shear and gust (sec. 2.5.5).

2.3.7.3 NASA 1997 Discrete Gust Model. The basis for the derivation of gust magnitude as a function of gust half-width is given in a MIL-SPEC of requirements for the flying qualities of piloted aircraft (ref. 2-52). This specification is significant because it is based on the same aircraft turbulence data used in studies (refs. 2-52, 2-58, and 2-59) that led to the establishment of the NASA classical 9-m/s gust. The gust model (V) has the 1-cos shape (fig. 2-18) defined by MIL-F-8785B (ref. 2-52):

$$V = 0, \quad d < 0, \quad d > 2\,d_m$$

$$V = \frac{V_m}{2}\left(1-\cos\left(\pi d / d_m\right)\right), \quad 0 \le d \le 2\,d_m\ , \tag{2.77}$$

where V_m is the gust magnitude, d_m is the gust half-width, and d is distance.

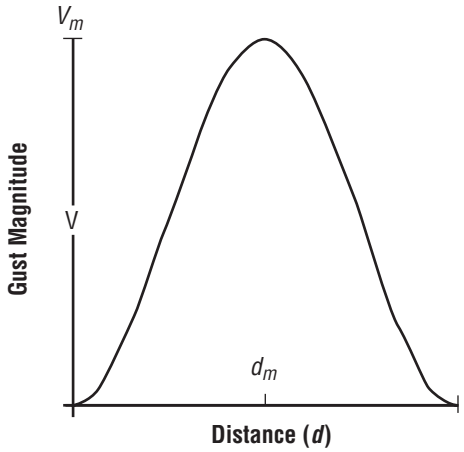

Figure 2-18. Discrete gust model (1 cos).

The MIL-SPEC relationship between nondimensional longitudinal gust magnitude, V_m/σ, and nondimensional gust half-width, d_m/L, heretofore in the form of an empirical least-squares fit (ref. 2-54) to the MIL-SPEC

graphic representation (ref. 2-52), is illustrated for the longitudinal gust component in fig. 2-19, where σ is the standard deviation of atmospheric turbulence and L is the scale length of atmospheric turbulence. The most recent compilation (ref. 2-60) of parameters σ and L as a function of altitude is presented in table 2-62 for severe turbulence.

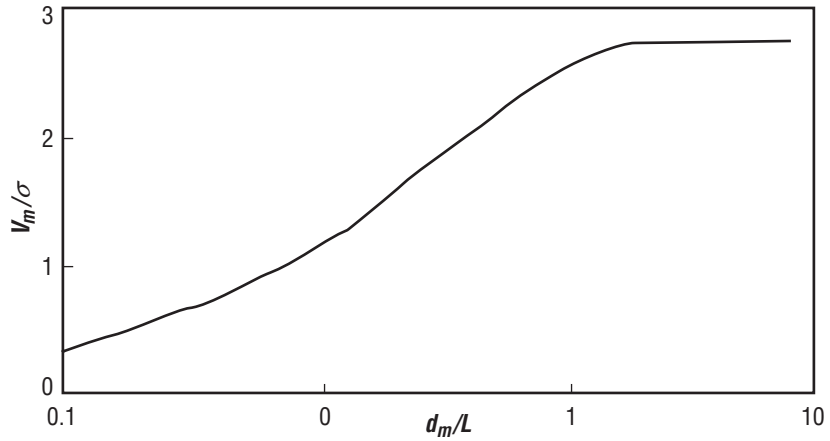

Figure 2-19. Nondimensional discrete gust magnitude V_m/σ as a function of nondimensional gust half-width, d_m/L, longitudinal component (original MIL-SPEC graphical version).

Table 2-62. Mean horizontal turbulence standard deviation, σ_h, length scale, L_h, and probability of severe turbulence as a function of altitude.

Alt. MSL		σ_h	Probability of Severe	L_h
(km)	(kft)	(m/s)	Turbulence	(km)
1	3.3	5.70	0.0250	0.832
2	6.6	5.80	0.0111	0.902
4	13.1	6.24	0.0063	1.040
6	19.7	7.16	0.0056	1.040
8	26.2	7.59	0.0049	1.040
10	32.8	7.72	0.0043	1.230
12	39.4	7.89	0.0034	1.800
14	45.9	6.93	0.0027	2.820
16	52.5	5.00	0.0024	3.400

Preferably, the relationship is derived by integration in closed form of the Dryden PSD model for a variable lower bound for wave number, Ω_i. The equation for the Dryden PSD for the longitudinal component of atmospheric turbulence is

$$\phi(\Omega) = \frac{2\sigma^2 L}{\pi}\left[\frac{1}{1+(L\Omega)^2}\right], \tag{2.78}$$

where $0 \le \Omega \le \infty$, σ^2 is the variance, and L is the turbulence length scale. Integration of equation (2.78) from zero to infinity yields σ^2. Integration from a lower bound other than zero yields a fractional value of σ^2 which is given by

$$\int_{\Omega_i}^{\infty} \phi(\Omega) d\Omega = \sigma^2 \left(1 - \frac{2}{\pi} \tan^{-1}\left(L\Omega_i \right) \right) . \tag{2.79}$$

The square root of the right side of equation (2.79) represents the fractional value of the total standard deviation contributed by the wavelength bands Ω_i to infinity. The derivation of the nondimensional discrete gust magnitude, V_m/σ as a function of nondimensional gust half-width (half-wavelength) that is in good agreement with the MIL-SPEC relationship requires the following assumptions:

(1) The magnitude of the discrete gust is 2.8 times the fractional standard deviation.
(2) The nondimensional gust half-wavelength, d_m/L, is defined by

$$d_m / L = \frac{1}{\pi L \Omega_i} \ ; \tag{2.80}$$

thus,

$$L\Omega_i = \frac{1}{\pi \left(d_m / L \right)} \ . \tag{2.81}$$

Consequently, the nondimensional gust magnitude, V_m/σ, as a function of d_m/L is

$$V_m / \sigma = 2.8 \sqrt{1 - \frac{2}{\pi} \tan^{-1} \left(\frac{1}{\pi \, d_m / L} \right)} \ . \tag{2.82}$$

The derived equation (eq. (2.82)) for the longitudinal gust component is illustrated in figure 2-20. Values for V_m (m/s) at a selected altitude for a specified d_m (m) are calculated using the values of σ (m/s) and L (m) (σ_h and $10^3 L_h$, respectively) given in table 2-62 and the appropriate expression for V_m/σ, which is selected based on the value of d_m/L as described above. The authors caution the reader that the caption at the top of the original table 2-71, which refers to "magnitudes (σ_h and σ_w)," should read "standard deviations (σ_h and σ_w)." This has been verified by the principal author of the original report (ref. 2-60) from which the table was derived.

The derived gust magnitudes for the longitudinal gust component for severe turbulence as a function of altitude and gust half-width, d_m, are listed in table 2-63. The longitudinal component is defined as the horizontal gust in the direction of the mean wind. The longitudinal gust is superimposed with the steady-state wind to excite vehicle structures in an elastic body simulation model.

The probabilities of the occurrence of severe turbulence are listed in table 2-62. At 6 km, the risk for severe turbulence is 0.56 percent; therefore, from tables 2-62 and 2-63, for d_m = 30 m, there is a 0.56-percent risk that a gust magnitude of 4.64 m/s will be exceeded. If the objective is to protect the vehicle for a 1-percent risk for a 30-m half-width gust, it is conservative to protect for the 4.64 m/s gust (0.56-percent risk).

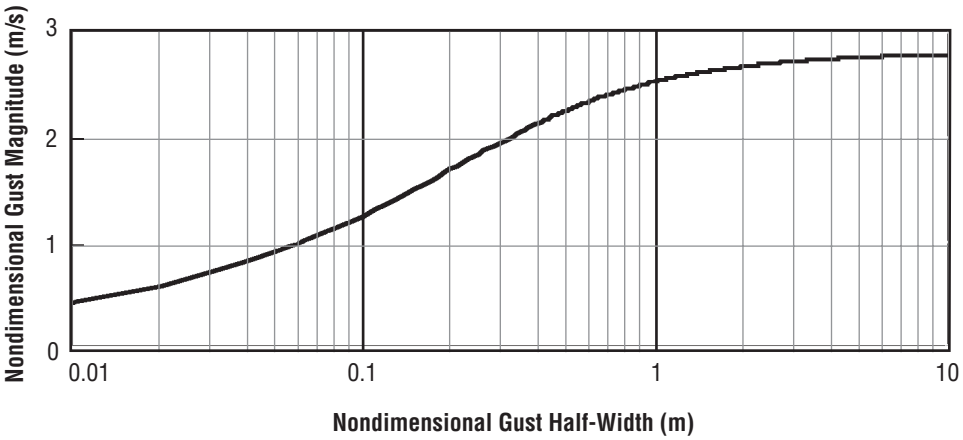

Figure 2-20. Discrete gust model for longitudinal gust magnitude V_m/σ as a function of nondimensional gust half-width, d_m/L, from closed-form integration of Dryden PSD model.

Table 2-63. Discrete longitudinal gust magnitude (m/s) as a function of altitude (km) and gust half-width, d_m (m) for severe turbulence.

Altitude		Gust Half Width (m)									
(km)	(kft)	30	60	90	120	150	180	210	240	270	300
1	3.3	4.12	5.80	7.03	8.01	8.82	9.49	10.05	10.54	10.95	11.30
2	6.6	4.03	5.67	6.89	7.86	8.67	9.35	9.93	10.43	10.85	11.23
4	13.1	4.04	5.69	6.93	7.93	8.77	9.49	10.11	10.65	11.12	11.53
6	19.7	4.64	6.53	7.95	9.10	10.06	10.89	11.60	12.22	12.76	13.24
8	26.2	4.92	6.92	8.42	9.64	10.67	11.54	12.29	12.95	13.52	14.03
10	32.8	4.60	6.49	7.91	9.07	10.06	10.92	11.67	12.33	12.92	13.45
12	39.4	3.89	5.49	6.71	7.72	8.60	9.38	10.07	10.71	11.28	11.80
14	45.9	2.73	3.86	4.72	5.44	6.07	6.64	7.16	7.63	8.07	8.48
16	52.5	1.79	2.53	3.10	3.58	4.00	4.37	4.72	5.03	5.33	5.60

As shown in table 2-63, the smallest gust half-width, d_m, associated with a 9-m/s gust is ≈100 m at 8 km. This half-width is more than 3 times larger than the smallest half-width (30 m) of the NASA classical 9-m/s gust.

This discussion has emphasized the conservatism of the NASA classical model for gust half-widths <100 m. Application of the 1997 model for specifying of gust magnitude requires that adequate protection exists for all vehicle response modes, including those for the gust half-widths >100 m for which gust magnitudes can be larger than 9 m/s.

2.3.7.4 Conclusion. NASA developed a rationale for deriving a discrete gust magnitude that is a function of altitude and gust half-width in 1997. This rationale is based on established methods that are included in MIL-SPEC requirements for the flying qualities of piloted aircraft. This prior specification is significant because it is based on the same aircraft turbulence data used in studies that established the classical NASA 9-m/s discrete gust model. Based on a review of these studies, it has been concluded that application of the classical NASA

model for gust half-widths, d_m, <100 m is conservative. The conservatism of the classical model is attributed to the lack of a relationship between gust magnitude and gust half-width and the associated design philosophy applied to the Saturn-Apollo design. The 1997 model contains such a relationship, which may provide the needed load relief for special unanticipated operational situations that could impact assessments of launch capability. The Shuttle program uses the more conservative classical 9-m/s discrete gust model as the primary tool for DOL protection for the uncertainty of elastic body loads response to a gust during severe turbulence. The conservatism of the classical model may not be restricted to the 9-m/s magnitude for d_m less than ≈100 m. For equivalent magnitudes and $d_m > 30$ m, the classical model could produce higher loads than the 1997 model (ref. 2-49). This may be attributed to the "flat-top" quasi-square wave form of the classical gust and the larger gust gradients that result from constraining the gust buildup and back-off to a 30-m interval. (The two models are illustrated in figure 2-21 for $z = 8$ km and $d_m = 60$ and 150 m.) This may be offset for $d_m > 100$ m because the gust magnitudes of the 1997 model can be >9 m/s. Establishment of the degree of acceptable conservatism of either model for a particular launch vehicle configuration and mission would be the responsibility of systems engineering analysts. Even then, launch vehicle operations managers, are responsible for risk assessments and selection of the model to be used for determining elastic body loads uncertainty. The most conservative gust model may or may not be the best choice for operations capability because launch probability may be needlessly compromised relative to the additional minimization of risk. If the risk is acceptable to launch managers, a less conservative model may be chosen.

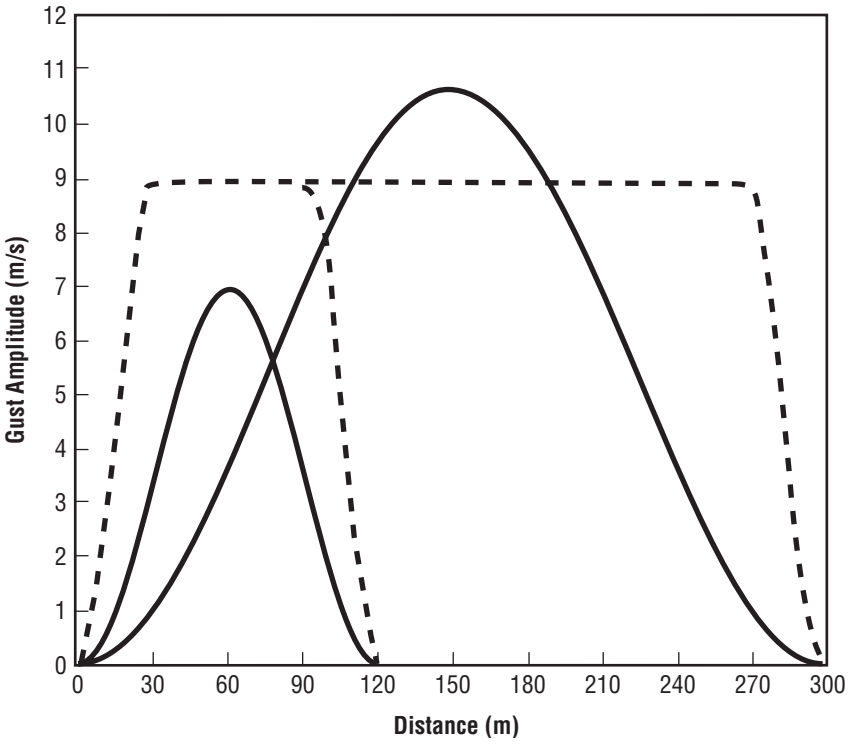

Figure 2-21. NASA classical (dashed) and 1997 (solid) discrete gusts for half-widths of 60 and 150 m.

2.3.8 Gust Spectra

In general, the small-scale motions associated with vertical detailed profiles of wind are characterized by a superposition of discrete gusts and many random components. Spectral methods have been employed to specify the characteristics of this superposition of small-scale motions.

A digital filter was developed to separate small-scale motions from the steady-state wind profile. The steady-state wind profile defined by the separation process approximates those obtained by the rawinsonde system. (This definition was selected to enable use of the much larger rawinsonde data sample in association with a continuous-type gust representation.) Thus, for vehicle design purposes, a spectrum of small-scale motions is representative of the motions included in the FPS-16 radar/Jimsphere measurements, which are not included in the rawinsonde measurements. Therefore, a spectrum of those motions should be considered in addition to the steady-state wind profiles to obtain an equivalent representation of the detailed wind profile. Spectra of the small-scale motions for various probability levels have been determined and are presented in figure 2-22. The spectra were computed from ≈1,200 detailed wind profile measurements by computing the spectra associated with each profile and then determining the probabilities of occurrence of spectral density as a function of vertical wave numbers (cycles/4,000 m). Thus, the spectra represent envelopes of spectral density for the given probability levels.

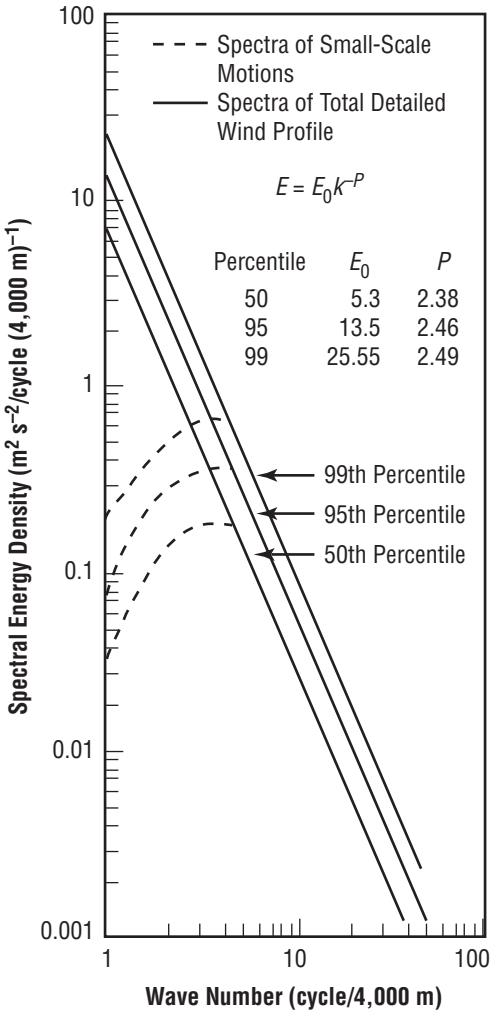

Figure 2-22. Spectra of detailed wind profiles.

Spectra associated with each profile were computed over the altitude range between approximately 4 and 16 km. It has been shown that energy (variance) of the small-scale motions is not vertically homogeneous; i.e., it is not constant with altitude. The energy content over limited altitude intervals and for limited wave number bands may be much larger than that represented by the spectra in figure 2-22. This should be kept in mind when interpreting the significance of vehicle responses when employing the spectra of small-scale motions. Additional details on this subject are available upon request. Envelopes of spectra for detailed profiles without filtering (solid lines) are also shown in figure 2-22.

These spectra are well represented for wave numbers ≥5 cycles per 4,000 m by the equation

$$E(k) = E_0 k^{-p} \ , \tag{2.83}$$

where

E = spectral density at any wave number k (cycles/4,000 m) between 1 and 20, $E_0 = E(1)$
p = a constant for any particular percentile level of occurrence of the power spectrum.

Spectra of the total wind speed profiles may be useful in control systems and other slow response parametric studies for which the spectra of small-scale motions may not be adequate.

The power spectrum recommended for use in elastic body studies is given by the following expression:

$$E(k) = 1.8 \times 10^{-4} k^{-2.43} \ , \tag{2.84}$$

where the spectrum $E(k)$ is defined so that integration over the domain $0 \le k \le \infty$ yields the variance of the turbulence. In this equation, $E(k)$ is now the power spectral density ($m^2\ s^{-2}$/(cycles per meter)) at wave number k (cycles per meter). This function represents the 99-percentile scalar wind spectra for small-scale motions given by the dashed curve and its solid line extension into the high wave number region in figure 2-22. The associated design turbulence loads are obtained by multiplying the load standard deviations by a factor >1 to reflect an acceptable level of risk. For example, a factor of 3 will correspond to a risk of 0.99865, assuming the small-scale motions constitute a Gaussian process. (Spectra for meridional and zonal components are available upon request.)

An alternate power spectrum specification has been developed (ref. 2-61) by combining an analysis of Jimsphere wind measurements and knowledge of the spectrum of clear-air turbulence (CAT) at scales smaller than those reliably measured by Jimsphere. The spectrum covering wavelengths from 1,000 to 200 m was determined by finding the spectrum computed from a random sample of 100 Jimsphere profiles in the 1,000- to 200-m range. The part of the spectrum with the $k^{-2/4}$ shape is the result. Then, to cover wavelengths <200 m, an isotropic-type spectrum corresponding to moderate CAT was added, the $k^{-5/3}$ part. The spectra are specified as

$$E(k_z) = 5.3(10^{-4})\ k_z^{-2/4} + 1(10^{-2})\ k_z^{-5/3}\ , \ \text{for } z \ge 10 \text{ km} \tag{2.85}$$

and

$$E(k_z) = 2.4(10^{-4})\ k_z^{-2/4} + 1(10^{-2}) k_z^{-5/3}\ , \ \text{for } z < 10 \text{ km} \ , \tag{2.86}$$

where

k_z = vertical wave number (cycles/meter)
z = altitude above mean sea level (km).

These spectra are based on KSC measurements but are expected to be applicable at other locations since research suggests that small-scale motions are nearly universal in amplitude. However, the 99-percent spectral envelope level and moderate CAT do not apply near thunderstorms or other locations where turbulence is categorized as severe.

Vehicle responses obtained from application of these turbulence spectra should be added to rigid vehicle responses resulting from use of the synthetic wind speed and wind profile (with the 0.85 factor on shears) but without a discrete gust. One method of application is to inverse Fourier transform from wave number space to height space with random, uniformly distributed phase spectra and add the transformed small-scale winds to synthetic profiles in a Monte Carlo analysis.

2.3.9 Vector Wind Profile Models

2.3.9.1 Background. The most useful engineering design application of a vector wind profile model is to establish preliminary design ranges for angle of attack, α, angle of sideslip, β, aerodynamic pressure, q, and the two aerodynamic load indicators, which are the products: $q\alpha$ and $q\beta$. These and other flight variables are typically derived from ascent flight 6-degrees-of-freedom trajectory simulations using wind model profiles.

Following the preliminary vehicle design using a vector wind profile model, trade studies can be made to establish a requirement to bias steering to reduce wind loads and increase launch probability. When sufficient engineering data have been established, structural loads and performance assessments are made using samples of high-resolution wind profile measurements. Currently, for KSC, this data sample is 150 Jimsphere profiles per month.

2.3.9.2 Models. Wind is a vector quantity having a direction and speed. To model the wind with multivariate normal probability functions, the wind speed and direction are converted to wind components as zonal wind component U (positive west to east) and meridional wind component V (positive south to north).

Assuming that the wind vectors at any altitude are bivariate normally distributed and the wind vectors at two altitudes are quadravariate normally distributed, then the differences in the wind vectors (wind shears) between two altitudes are bivariate normally distributed and the conditional wind shears between two altitudes, given a wind vector at one altitude, are bivariate normally distributed. The conditional wind shears were used in the original vector wind profile model (ref. 2-38) used for Shuttle design and ascent structural loads and performance analysis. A detailed description of the concepts and equations for construction of the original vector wind model profiles is given in reference 2-38.

A wind profile database is required for developing a site-specific vector wind profile model. For KSC, the rawinsonde database for the period 1956–1967 at 1-km intervals from the surface to 27-km altitude was used for the model. The 14 quadravariate normal probability parameters for the wind vectors at two altitudes are the means ($\bar{u}_1, \bar{v}_1, \bar{u}_2, \bar{v}_2$), standard deviations ($s_{u_1}, s_{v_1}, s_{u_2}, s_{v_2}$), and the six correlation coefficients [$r(u_1, v_1)$, $r(u_2, v_2)$, $r(u_1, u_2)$, $r(v_1, v_2)$, $r(u_1, v_2)$, and $r(v_1, u_2)$]. The original vector wind profile model

is based on the quadravariate normal distribution of the components of a given wind vector at a reference altitude (u_1,v_1) and the components of the vector wind shear between the reference altitude and any other altitude (u',v'). The 14 statistical parameters of this distribution are: $\bar{u}_1$, $\bar{v}_1$, $\bar{u}'$, $\bar{v}'$, s_{u_1}, s_{v_1}, $s_{u'}$, $s_{v'}$, $r(u_1,v_1)$, $r(u', v')$, $r(u_1, u')$, $r(v_1, v')$, $r(u_1, v')$, and $r(v_1, u')$.

For the Shuttle vector wind profile model (ref. 2-38), wind vectors are assigned as given values that intercept the 95-percent probability ellipse at a reference altitude. These wind vectors are for clocking angles at 45° increments to the 95-percent ellipse relative to the monthly mean wind. The conditional wind shear statistical parameters are computed for the given wind vectors at the reference altitude. The conditional wind shears are bivariate normally distributed. The expression for the conditional wind shears (u',v'), given the components (u_1^*,v_1^*) of a wind vector at a reference altitude, is

$$f\left(u,\ v|\ u_1^*,\ v_1^*\right) = \frac{f\left(u,\ v,\ u_1^*,\ v_1^*\right)}{f\left(u_1^*,\ v_1^*\right)} \ . \tag{2.87}$$

For simplification, the cross-component correlation coefficients [$r(u_1,v_1)$, $r(u',\ v')$, $r(u_1,\ v')$, $r(v_1,\ u')$] are small and are set equal to zero. In addition, the conditional ellipses for the shears is made circular by setting the conditional standard deviations of the shears equal to a value that is the root mean square (RMS) of the calculated values (ref. 2-38). The intercept 180° from the given wind vector relative to the monthly mean that intercepts the conditional shear circle is then subtracted from the given wind vector. Model wind profiles are constructed by repetition of this process at 1-km intervals for the altitudes above and below the reference altitude.

Figure 2-23 illustrates the dispersion of $q\alpha$, $q\beta$ at Mach 1.05 derived from rigid-body trajectory simulations with the 150 April KSC Jimsphere wind profiles (dots) and the eight vector wind model profiles (dotted circles, refs. 2-62 and 2-63). Each trajectory is wind biased to the April vector mean wind profile. The 95-percent probability ellipse (inner curve) is derived from the bivariate normal statistics (means, standard deviations, and correlation coefficient) of $q\alpha$, $q\beta$ from the 150 Jimsphere cases. This illustrates that this 95th percentile vector wind model produces $q\alpha$, $q\beta$ dispersions that are conservative estimates of the 95th percentile dispersion derived from a sample of Jimsphere wind profiles. When a 7.85-m/s gust (9 m/s times 0.85) is added to the wind profile model profiles at Mach 1.25, the simulated $q\alpha$, $q\beta$ outer curve is at a very high percentile level that was not estimated in the original publications. This example supports the conclusion that it was not necessary in the Shuttle application to add a gust to the modeled profiles to obtain a reasonably conservative estimate of the $q\alpha$, $q\beta$ dispersion at a selected percentile level. Gusts are considered in separate analyses to establish loads attributed to vehicle elastic body gust response (sec. 2.3.7) and to establish vehicle guidance and control system capability.

2.3.9.3 Improved Monthly Vector Wind Profile Model. The procedure for modeling vector wind profiles based on the properties of a quadravariate normal distribution was first published in 1963 by Henry (ref. 2-64). The necessary statistical parameters for this wind-modeling concept have been known since 1960 (ref. 2-65), and touched on in 1969 (ref. 2-66), but it was not until 1994 that this method was fully implemented by Adelfang et al. (ref. 2-67).

Rather than the awkward procedure for computing the conditional wind vector shears as was done for the Shuttle program, a direct method is used to model the conditional bivariate normal probability ellipses for wind vectors at all altitudes above and below the reference altitude of the given wind vectors (refs. 2-67 and 2-68).

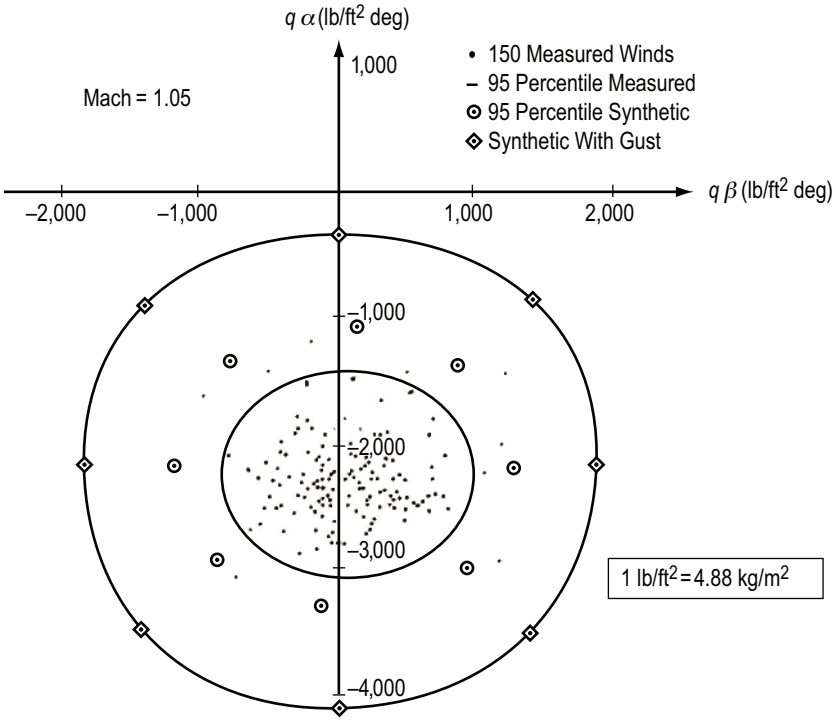

Figure 2-23. STS-1 pitch and yaw aerodynamic load indicators ($q\alpha$, $q\beta$) Mach = 1.05 for 150 April Jimsphere profiles for KSC.

This improved method uses the complete variance-covariance matrix for the wind statistics, expressed as

$$f\left(u_2, v_2 \mid u_1^*, v_1^*\right) = f\frac{\left(u_2, v_2, u_1^*, v_1^*\right)}{f\left(u_1^*, v_1^*\right)} \quad . \tag{2.88}$$

The given wind vectors (u_1^*, v_1^*) are assigned to the 99-percent ellipse at 30° increments relative to the monthly mean wind vector. The conditional wind vector that intercepts the 99-percent conditional wind vector ellipse 180° from the given wind direction approximates the largest wind vector shear. This model uses the 99-percent probability wind ellipses at the discrete reference altitude because ≈95 percent of the wind profiles lie within the 99-percent ellipses over all altitudes. A comparison of the original and improved vector wind profile model is given in table 2-64.

For the KSC wind data sample at 1-km intervals from the surface to 27-km altitude, there are 28 reference altitudes and 12 given wind vectors at each reference altitude from which 12 conditional wind vectors are computed for each altitude above and below each reference altitude. Hence, the complete monthly vector wind profile model has 336 (28×12) wind profiles, expressed in terms of wind speed and direction at the surface to 27-km altitude at 1-km intervals. The monthly mean profile and the 12 wind profiles for KSC, February, for a reference altitude of 12 km are illustrated in figure 2-24 for the zonal wind component (u) and figure 2-25 for the meridional wind component (v).

Table 2-64. Comparison of original (ref. 2-38) and improved vector wind profile models.

Attribute	Original	Improved
Statistical model	Quadravariate normal	Quadravariate normal
Profile construction	Each component of vector wind shear between altitudes H_1 and H_2 is conditional normal, given the corresponding component of the wind at H_1	Components of wind vector at H_2 are conditional bivariate normal, given the wind vector at H_1
Simplifying assumptions	All interlevel and intralevel cross-component correlations are negligible	None
	Conditional ellipse for shears is made circular by taking the "root-summed-square" of the standard deviations	None
Choice of vector on conditional ellipse	Vector shear on conditional ellipse is for clocking angle 180° from the clocking angle of the given wind vector	Wind vector on conditional ellipse is for clocking angle 180° from the clocking angle of the given wind vector

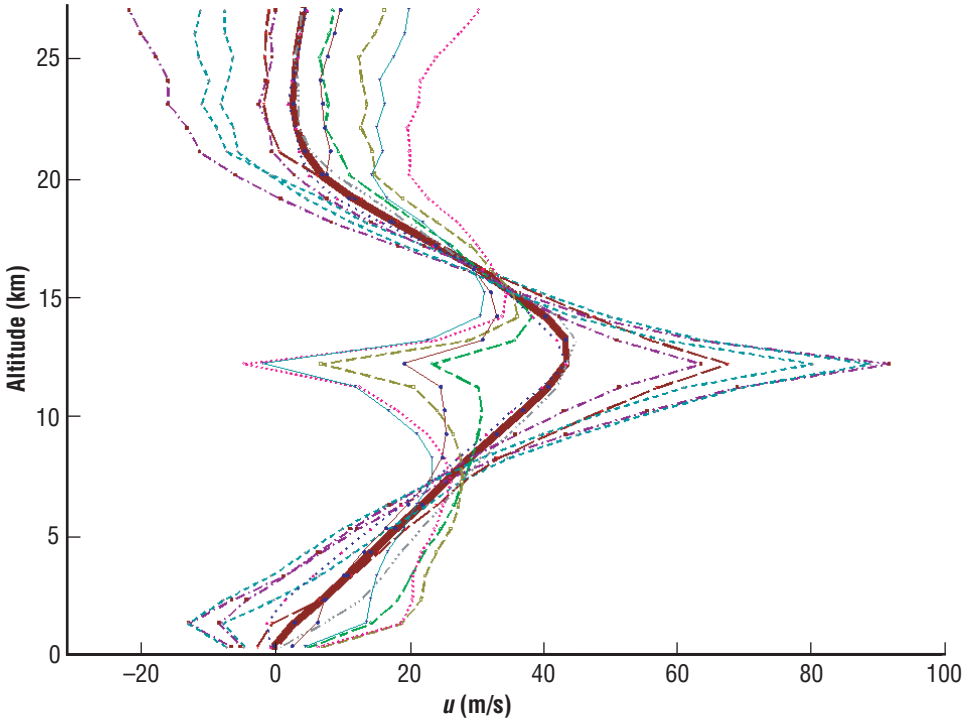

Figure 2-24. Mean profile (thick solid) and vector wind model profiles for H_1 = 12 km, u-component, KSC, February.

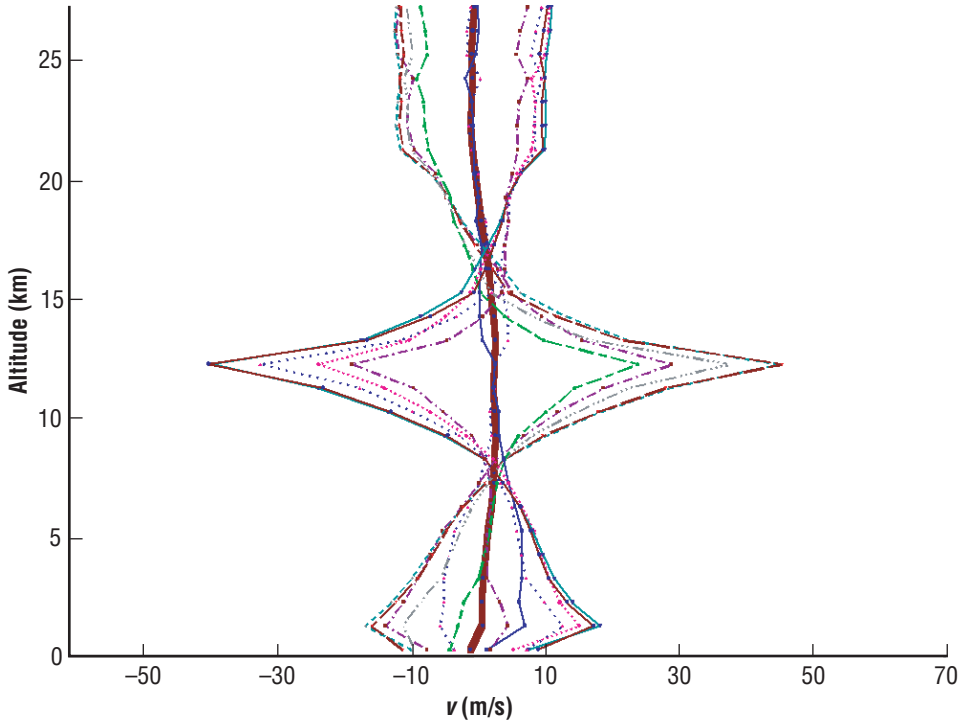

Figure 2-25. Mean profile (thick solid) and vector wind model profiles for H_1 = 12 km, v-component, KSC, February.

A KSC monthly enveloping vector wind model (ref. 2-67) has been used in preliminary design analyses for the U.S. National Launch System (NLS) (ref. 2-69). Aerodynamic load indicators ($q\alpha$, $q\beta$) were calculated with a 6-degree-of-freedom trajectory simulation, for a 90° flight azimuth, using 1,800 (150/mo) KSC Jimsphere wind profiles and 336 wind profiles from the enveloping model. Vehicle steering, established prior to trajectory simulation, was biased with respect to a nominal wind profile defined by the centroids of the KSC 99-percent enveloping wind ellipses (table 2-65). The trajectory simulation includes vehicle control system response to correct for flight wind profile deviation from the nominal wind profile to ensure desired orbit insertion and to satisfy flight propellant reserve requirements. Control system response to off-nominal wind is an important contributor to aerodynamic loads because of the relationship between vehicle control and vehicle attitude, which includes α and β. Trajectory simulation data ($q\alpha$, $q\beta$) at 12 km, near the altitude of maximum Q, are illustrated in figure 2-26.

The 99-percent enveloping ellipse was constructed from the monthly $q\alpha$, $q\beta$ data using the methodology described for wind data in ref. 2-67 (eqs. (2.27) – (2.31)). The five Jimsphere profiles that produced the five extremes of $q\alpha$, $q\beta$ are identified by a monthly profile number. The 12 values of $q\alpha$, $q\beta$ derived from the profiles of the enveloping wind model for a reference altitude of 12 km are identified by clocking angle (zero to 330 at 30° increments). It is indicated that the enveloping wind model produces $q\alpha$, $q\beta$ that are consistently more extreme than even the most extreme values produced from the 1,800 Jimsphere profiles. This result does not necessarily point to a deficiency of the model or the Jimsphere database. If the Jimsphere $q\alpha$, $q\beta$ are used as a standard for the evaluation of the model, then it would not be difficult to make adjustments in the model profile construction process that would produce smaller $q\alpha$, $q\beta$. For example, reduction of the probability level for the ellipse used in the definition of the given wind vector would reduce $q\alpha$, $q\beta$. However, there is a more appropriate standard for evaluation of the model. It is suggested that the standard be the enveloping ellipse of $q\alpha$, $q\beta$

Table 2-65. Nominal wind profile defined by the centroids of the KSC 99-percent monthly enveloping ellipses at each altitude from zero to 27 km at 1-km altitude intervals (derived from monthly bivariate normal statistics for the KSC range reference atmosphere) (refs. 2-67, 2-68, and 2-70).

Altitude (km)	*u* (m/s)	*v* (m/s)
0	–0.54	–0.64
1	2.84	1.31
2	6.27	1.58
3	9.00	1.80
4	12.39	2.34
5	16.10	3.00
6	19.46	3.61
7	22.59	4.23
8	25.79	4.56
9	28.83	4.48
10	31.16	3.65
11	31.56	2.02
12	30.98	0.52
13	27.80	–0.38
14	25.71	–0.62
15	22.63	0.29
16	20.40	0.86
17	17.38	0.90
18	13.84	0.98
19	8.59	0.97
20	3.67	0.71
21	0.99	0.13
22	1.79	–0.42
23	1.03	–0.26
24	2.45	0.06
25	4.14	0.42
26	4.97	0.64
27	5.86	1.26

derived from the database that was used to calculate the statistical parameters of the model, which is the 19-yr serially complete rawinsonde database (see sec. 2.3.11.2). The larger extremes in the 19-yr rawinsonde sample are attributed to the large sample size (≈650 statistically independent profiles per month), which is more than 4 times larger than the Jimsphere monthly total. This comparison of sample size is based on the criteria used in establishment of the Jimsphere database, which required that profiles be separated by a time interval of at least 24 hr.

Jimsphere profile number 89 in January and the model profile for a clocking angle of 300° for a reference height of 12 km produce similar large values of $q\alpha$, $q\beta$ (fig. 2-26). These wind profiles are illustrated in figure 2-27 along with the nominal profile used for wind biasing vehicle steering. The large-scale feature that dominates the Jimsphere and the model profile is the strength of the negative *v* (northerly) component, which is a crosswind relative to the vehicle, for a 90° launch azimuth. This crosswind, which is a deviation of 40 m/s from the nominal wind profile, produces a relatively large β response by the vehicle control system. Since this occurs at an altitude where q is near its maximum value, absolute $q\beta$ is also large (8th largest of the 1,800 trajectory simulations using Jimsphere profiles). The maximum absolute β response produced by the model profiles

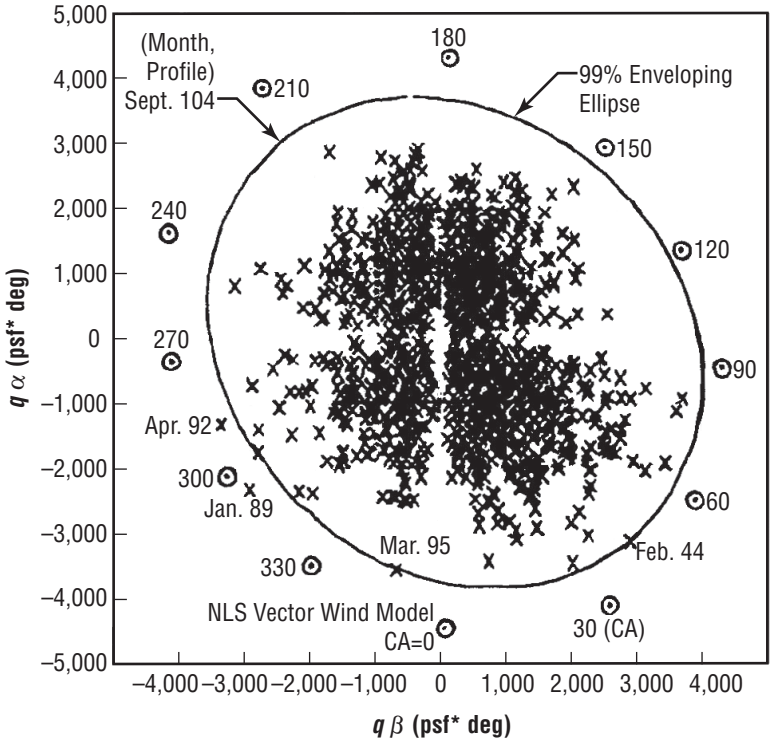

Figure 2-26. Aerodynamic load indicators ($q\alpha$, $q\beta$) at 12 km obtained from trajectory simulations using 1,800 KSC Jimsphere wind profiles (150/mo) and the 12 enveloping vector wind model profiles for a reference altitude = 12 km.

is for clocking angles of 60° and 240°, which have the largest deviation from the nominal crosswind component (47 and 48 m/s, respectively). Absolute $q\beta$ is largest at 90° compared to 60°, because the increase in q at 90° attributed to the in-plane (u) wind component outweighs the slight decrease in β response. The $q\alpha$ extremes are at clocking angles 0° and 180° which have the largest deviations of the in-plane wind component from the nominal wind profile (62.7 and –35 m/s, respectively).

The improved vector wind profile model produces wind profiles that are a reasonable substitute for measured wind profile samples. Model wind profiles produce dispersions in aerodynamic load indicators that cover the dispersion range calculated from an extensive sample of Jimsphere wind profiles. This is accomplished with only 12 model synthetic wind profiles compared to 1,800 Jimsphere profiles for a selected reference altitude. This represents an opportunity for a considerable reduction of computational effort during design phases that require much iteration to establish the merit of various design philosophies.

Table 2-66 and figure 2-28 provide two additional examples of the products that can be produced through the use of the improved vector wind profile model. The 12-vector wind profiles from the KSC vector wind model for a reference height of 9 km are presented for the in-plane (IP) and out-of-plane (OP) wind components relative to a flight azimuth of 90°. Similar products can be produced for any flight azimuth, reference height, and monthly period. This improved vector wind profile model is recommended for baseline preliminary aerospace vehicle ascent design analyses.

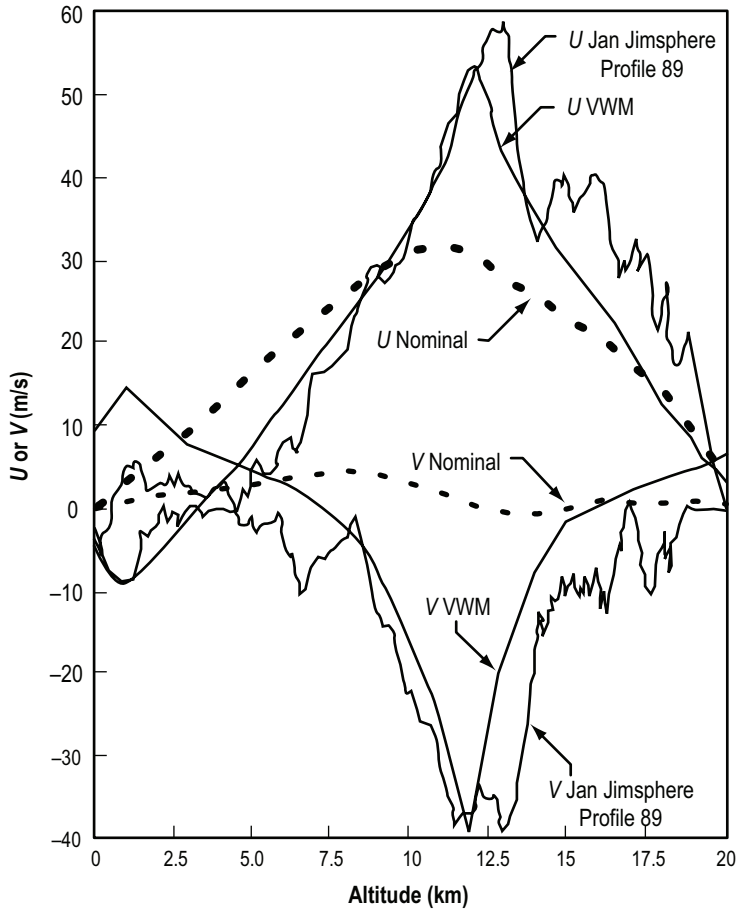

Figure 2-27. Enveloping vector wind model profile for 300° clocking angle and 12-km reference altitude, KSC, January, Jimsphere profile 89 and nominal wind profile used to bias ascent vehicle steering.

2.3.10 Characteristic Wind Profiles to a Height of 18 km (59 kft)

A significant problem in aerospace vehicle design is to provide assurance of an adequate design for flight through wind profiles of various configurations. During the major design phase of an aerospace vehicle, the descriptions of various characteristics of the wind profile are employed in determining the applicable vehicle response requirement. Since much of the vehicle is in a preliminary status of design and the desired detail data on structural dynamic modes and other characteristics are not known at this time, the use of statistical and synthetic representations of the wind profile is desirable. However, after the vehicle design has been finalized and tests have been conducted to establish certain dynamic capabilities and parameters, it is desirable to evaluate the total system by simulated dynamic flight through wind profiles containing adequate frequency resolution (ref. 2-71). The profiles shown in figures 2-29 through 2-34 are profiles of a scalar wind measured by the FPS-16 radar/Jimsphere wind measuring system, and they illustrate the following: (1) Jet stream winds, (2) sinusoidal variation in wind with height, (3) high winds over a broad altitude band, (4) light wind speeds, and (5) discrete gusts.

Table 2-66. Twelve vector wind model profiles plus mean profiles for KSC, February, reference height = 9 km, IP and OP wind components (m/s), for flight azimuth = 90°.

		Profiles											
		1		2		3		4		5		6	
z (km)	(kft)	IP	OP	IP	OP	IP	OP	IP	OP	IP	OP	IP	OP
0	0.0	4.5	–3.6	3.0	–6.6	1.6	–8.2	–1.2	–9.0	–5.1	–7.0	–6.8	–1.8
1	3.3	8.2	–6.2	3.3	–12.2	–2.5	–13.8	–8.8	–12.0	–14.2	–7.0	–17.0	0.8
2	6.6	0.4	–5.5	–5.1	–8.6	–9.6	–8.8	–13.8	–7.3	–17.5	–3.6	–18.9	2.3
3	9.8	–8.5	–4.7	–13.2	–4.8	–15.2	–4.1	–17.5	–3.1	–19.5	–0.1	–19.1	4.5
4	13.1	–16.3	–3.7	–20.1	–1.7	–19.7	–0.2	–19.8	0.1	–20.7	2.1	–19.1	5.8
5	16.4	–24.2	–2.6	–26.9	1.6	–24.2	4.1	–22.4	4.0	–21.8	5.2	–19.2	7.6
6	19.7	–32.8	–0.2	–34.1	6.1	–29.1	9.1	–25.1	8.7	–22.5	8.7	–18.6	8.8
7	23.0	–42.6	1.6	–42.7	10.7	–35.0	14.9	–28.0	14.4	–22.6	13.0	–16.8	10.7
8	26.2	–55.9	2.4	–54.8	16.7	–43.1	24.0	–31.3	24.0	–21.5	20.9	–12.4	15.1
9	29.5	–79.8	3.5	–76.0	27.6	–55.6	40.5	–34.3	40.9	–16.2	34.8	–0.3	23.1
10	32.8	–67.4	4.1	–65.7	20.4	–51.9	28.2	–38.2	27.1	–27.3	22.5	–17.4	15.2
11	36.1	–61.8	5.3	–60.5	16.6	–50.6	20.5	–42.0	18.6	–35.3	15.2	–28.7	10.3
12	39.4	–56.7	5.7	–55.5	12.4	–49.0	13.4	–44.4	11.3	–41.0	9.3	–37.1	6.6
13	42.7	–49.2	7.7	–49.1	9.7	–46.8	8.6	–45.0	6.3	–43.6	4.2	–42.0	2.1
14	45.9	–39.3	7.4	–41.3	7.5	–42.2	6.5	–42.4	4.1	–42.9	1.8	–43.8	0.0
15	49.2	–31.3	6.6	–33.7	5.0	–35.1	3.3	–36.0	0.6	–38.0	–1.6	–40.8	–2.3
16	52.5	–24.4	5.6	–26.6	3.2	–28.3	1.3	–30.0	–1.2	–32.9	–3.0	–36.8	–3.0
17	55.8	–16.0	3.6	–19.3	0.6	–22.5	–0.8	–24.9	–2.3	–28.1	–3.5	–32.3	–3.1
18	59.1	–6.8	3.0	–11.1	–1.9	–16.7	–3.0	–19.7	–3.7	–22.5	–4.3	–26.6	–4.0
19	62.3	–0.5	1.7	–5.1	–3.9	–10.8	–4.7	–13.5	–4.8	–16.0	–5.0	–20.0	–4.2
20	65.6	6.3	1.7	1.8	–5.2	–4.7	–6.3	–7.9	–6.5	–10.9	–6.4	–15.4	–5.4
21	68.9	12.1	0.2	8.4	–8.5	0.2	–10.6	–5.3	–10.3	–10.1	–9.3	–16.0	–6.7
22	72.2	14.9	–0.4	10.5	–9.9	1.8	–11.8	–3.8	–11.3	–8.7	–10.1	–15.1	–7.4
23	75.5	17.3	–0.1	12.6	–10.0	2.7	–11.7	–3.4	–11.2	–8.7	–10.0	–15.4	–7.4
24	78.7	16.5	0.9	11.1	–9.3	2.0	–11.1	–3.0	–11.0	–7.6	–10.3	–14.0	–8.2
25	82.0	18.2	–0.9	12.0	–11.4	1.9	–11.6	–3.1	–10.5	–7.4	–9.1	–13.9	–6.7
26	85.3	19.9	–0.9	12.4	–11.9	1.6	–12.2	–3.8	–11.1	–8.6	–9.7	–15.8	–7.1
27	88.6	22.1	–0.5	11.7	–11.5	1.2	–12.1	–4.3	–11.3	–9.5	–10.2	–17.7	–7.8

These profiles show only a few of the possible wind profiles that can occur. Jet stream winds (fig. 2-29) are quite common over the various test ranges during the winter months and can reach magnitudes in excess of 100 m/s. These winds occur over a limited altitude range, making the wind shears very large.

Figure 2-30 depicts winds having sinusoidal behavior in the 10- to 14-km region. These types of winds can create excessive loads on a vertically rising vehicle, particularly if the reduced forcing frequencies couple with the vehicle control frequencies and result in additive leads. Periodic variations in the vertical wind profile are not uncommon. Some variations are of more concern than others, depending on wavelength and, of course, amplitude.

Figure 2-31 is an interesting example of high wind speeds that occurred over 6 km in depth. Such flow is not uncommon for the winter months. Figure 2-32 shows scalar winds of very low values. These winds were generally associated with easterly flow over the entire altitude interval (surface to 16 km) at KSC. The last examples (figs. 2-33 and 2-34) illustrate two samples of discrete gusts.

Table 2-66. Twelve vector wind model profiles plus mean profiles for KSC, February, reference height = 9 km, IP and OP wind components (m/s), for flight azimuth = 90° (Continued).

		Profiles											
		7		8		9		10		11		12	
z (km)	(kft)	IP	OP	IP	OP	IP	OP	IP	OP	IP	OP	IP	OP
0	0.0	–5.9	3.2	–4.3	6.2	–2.9	7.8	–0.1	8.6	3.8	6.6	5.5	1.4
1	3.3	–15.6	9.5	–10.7	15.4	–4.9	17.1	1.4	15.3	6.8	10.2	9.6	2.4
2	6.6	–16.1	8.5	–10.7	11.6	–6.2	11.8	–1.9	10.3	1.7	6.6	3.1	0.7
3	9.8	–14.9	8.1	–10.2	8.2	–8.2	7.4	–5.9	6.5	–3.9	3.5	–4.3	–1.1
4	13.1	–14.1	7.9	–10.3	5.9	–10.7	4.4	–10.6	4.1	–9.8	2.1	–11.3	–1.6
5	16.4	–13.8	7.6	–11.0	3.3	–13.7	0.9	–15.5	1.0	–16.1	–0.2	–18.7	–2.6
6	19.7	–13.1	6.2	–11.8	–0.1	–16.8	–3.2	–20.8	–2.8	–23.4	–2.7	–27.3	–2.9
7	23.0	–10.6	5.0	–10.5	–4.1	–18.2	–8.3	–25.2	–7.8	–30.5	–6.4	–36.3	–4.1
8	26.2	–4.5	4.4	–5.7	–9.9	–17.4	–17.2	–29.2	–17.2	–38.9	–14.1	–48.1	–8.3
9	29.5	11.3	3.5	7.5	–20.6	–12.9	–33.5	–34.3	–33.9	–52.3	–27.8	–68.3	–16.1
10	32.8	–9.0	2.7	–10.7	–13.6	–24.4	–21.4	–38.2	–20.3	–49.1	–15.8	–59.0	–8.4
11	36.1	–22.5	1.4	–23.8	–9.9	–33.6	–13.9	–42.3	–11.9	–48.9	–8.6	–55.6	–3.6
12	39.4	–33.0	1.2	–34.2	–5.5	–40.7	–6.5	–45.3	–4.3	–48.6	–2.3	–52.6	0.4
13	42.7	–40.3	–0.6	–40.5	–2.7	–42.7	–1.6	–44.5	0.7	–46.0	2.8	–47.5	5.0
14	45.9	–44.0	–0.7	–42.0	–0.8	–41.1	0.2	–41.0	2.5	–40.4	4.9	–39.5	6.6
15	49.2	–42.1	–0.8	–39.7	0.8	–38.4	2.5	–37.5	5.2	–35.5	7.4	–32.6	8.1
16	52.5	–38.8	–0.4	–36.6	2.0	–34.9	3.9	–33.2	6.4	–30.2	8.2	–26.4	8.2
17	55.8	–34.8	0.2	–31.5	3.3	–28.2	4.7	–25.8	6.2	–22.7	7.4	–18.5	7.0
18	59.1	–30.7	–0.2	–26.5	4.7	–20.8	5.8	–17.8	6.5	–15.0	7.2	–11.0	6.8
19	62.3	–25.1	0.3	–20.5	5.9	–14.7	6.6	–12.0	6.8	–9.6	6.9	–5.6	6.2
20	65.6	–22.0	–0.4	–17.5	6.5	–11.0	7.5	–7.8	7.7	–4.8	7.7	–0.3	6.7
21	68.9	–22.5	0.1	–18.8	8.9	–10.6	11.0	–5.1	10.7	–0.3	9.6	5.5	7.1
22	72.2	–23.0	0.1	–18.6	9.6	–9.9	11.5	–4.3	11.1	0.7	9.9	7.0	7.1
23	75.5	–24.2	0.0	–19.5	9.9	–9.7	11.6	–3.5	11.1	1.8	10.0	8.5	7.4
24	78.7	–23.8	–0.7	–18.4	9.5	–9.3	11.3	–4.2	11.2	0.3	10.5	6.7	8.3
25	82.0	–25.9	0.9	–19.8	11.3	–9.6	11.5	–4.7	10.4	–0.3	9.1	6.1	6.7
26	85.3	–28.9	1.2	–21.3	12.1	–10.6	12.4	–5.2	11.3	–0.4	9.9	6.8	7.4
27	88.6	–32.4	1.2	–22.0	12.2	–11.4	12.8	–6.0	12.0	–0.8	10.9	7.4	8.5

2.3.11 Wind Profile Data Availability

2.3.11.1 KSC and VAFB Jimsphere Wind Design Assessment and Verification Database. The Jimsphere wind design assessment and verification data tapes are a very special data set for wind aloft vehicle response and other analytical studies. When properly integrated into a flight simulation program; e.g., Space Shuttle, vehicle operational risks can be more accurately assessed relative to the true representation of wind velocity profile characteristics. The wind velocity profiles contain wind vectors for each 25 m in altitude from near surface to an altitude of ≈18 km. The high-frequency resolution is one cycle per 100 m with an RMS error of ≈0.5 m/s for velocities averaged over a 50-m-height interval. Launch probability statements may be specified from flight simulations and related analyses. Through indepth mathematical and statistical interpretations of these data, specific criteria can be generated on details of vector winds, gusts, shears, and the wind flow field interrelationships.

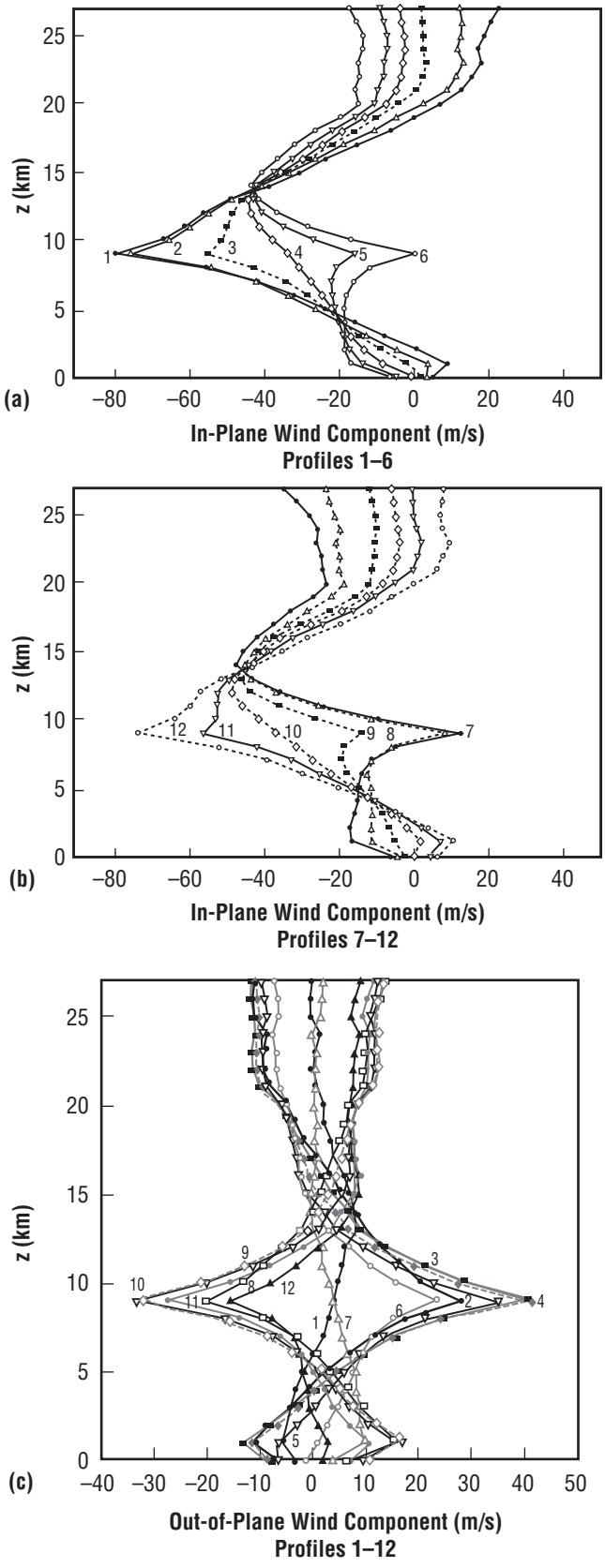

Figure 2-28. Twelve vector wind model profiles, KSC, February, reference height = 9 km, for (a) IP wind component profiles 1–6, (b) IP wind components profiles 7–12, and (c) OP wind component profiles 1–12 for flight azimuth = 90º.

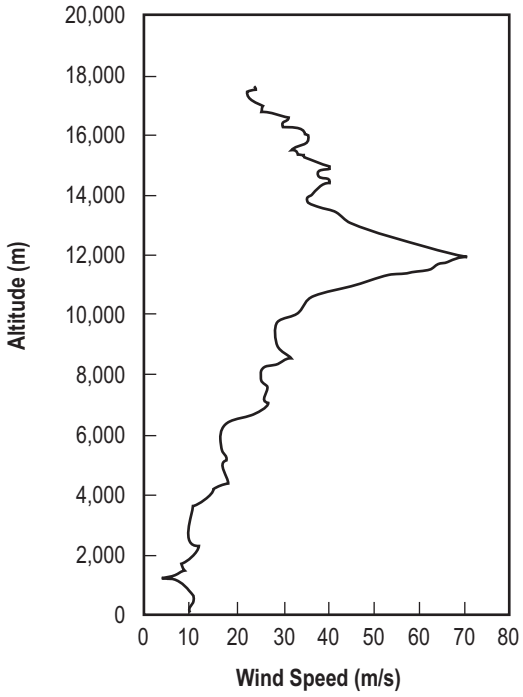

Figure 2-29. Example of jet stream winds.

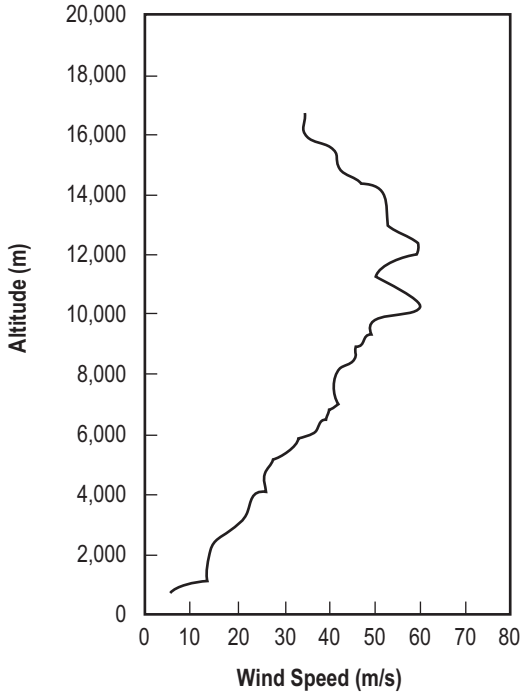

Figure 2-30. Example of sine wave flow in the 10- to 14-km altitude region.

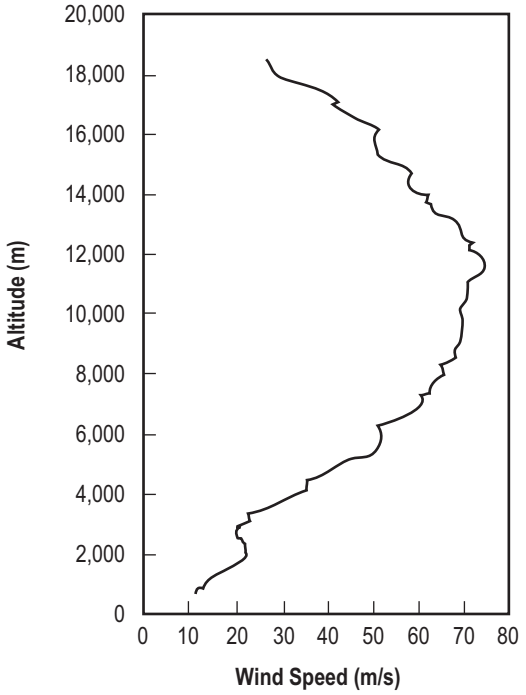

Figure 2-31. Example of high wind speeds over a deep altitude layer.

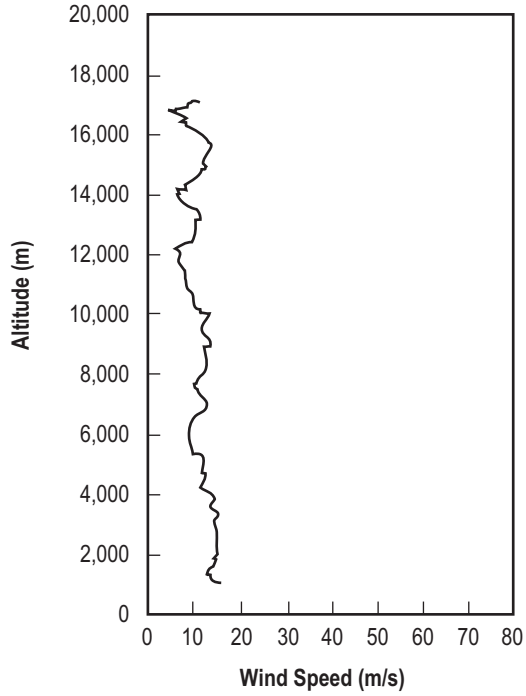

Figure 2-32. Example of low wind speeds.

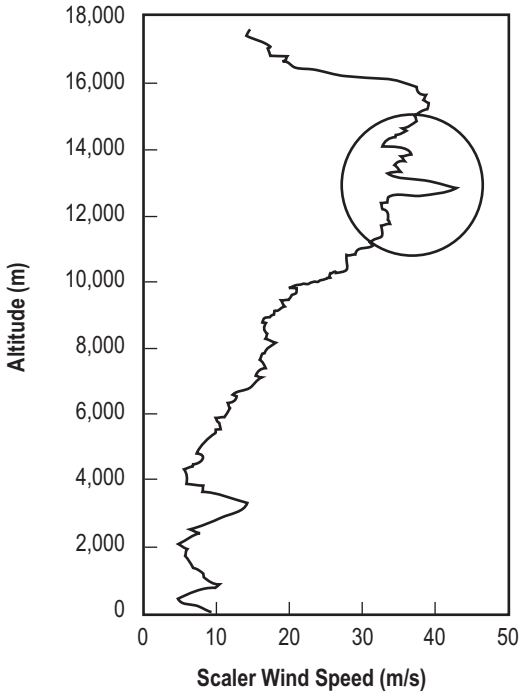

Figure 2-33. Example of a discrete gust observed at 1300Z on January 21, 1968, at KSC.

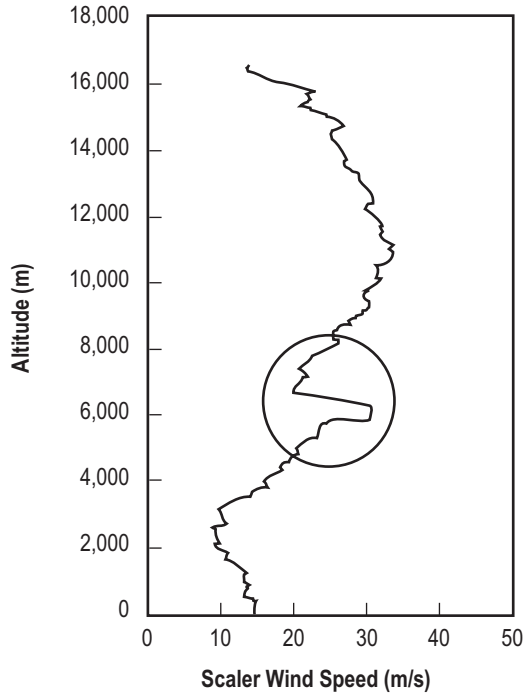

Figure 2-34. Example of a discrete gust observed by a Jimsphere released at 2103Z on November 8, 1967, at KSC.

Two special Jimsphere wind profile data sets of 150 profiles per month are available for KSC and VAFB. In addition, a set of Jimsphere wind profiles separated by given time periods for 2-, 3.5-, 7-, and 10.5-hr pairs grouped according to summer, winter, and transition seasonal months has been prepared for KSC. A similar set of 3.5-hr wind profile pairs has also been assembled for VAFB. These data sets were selected based on an extensive statistical and physical analysis of the vector wind profile characteristics and their representativeness. They have been specified for use in the Space Shuttle program for system design assessment, performance analysis, and pre-launch wind loads calculations.

These data sets are available upon request to the Natural Environments Branch, NASA George C. Marshall Space Flight Center, Marshall Space Flight Center, AL 35812. There are also a large number of Jimsphere wind velocity profile data available for KSC, Point Mugu, WSMR, Green River, Wallops Island, and VAFB.

2.3.11.2 Availability of Rawinsonde Wind Velocity Profiles. Unique serially complete, edited, and corrected rawinsonde wind profile data at 1-km intervals to ≈30 km are available for 19 yr (two observations per day) for KSC, for 9 yr (four observations per day) for Santa Monica, and for 14 yr (two observations per day) for VAFB. A representative serial complete rawinsonde wind profile data set is available for the Wallops Flight Center (12 yr, two observations per day). Qualified requesters may obtain these data upon request to the Environments Group, NASA George C. Marshall Space Flight Center, Marshall Space Flight Center, AL 35812. They are also available as card deck 600 from the National Climatic Data Center, Asheville, NC 28801.

2.3.11.3 Availability of Rocketsonde Wind Velocity Profiles. Rocketsonde wind profile data at 1-km intervals from approximately 20 to 75 km have been collected from various launch sites around the world. These data can be obtained from the World Data Center A, Asheville, NC 28801.

2.3.11.4 Availability of DRWP Wind Velocity Profiles. Quality-controlled wind profiles from the KSC 50 MHz DRWP for the period October 1995 through March 1996 are available. The profiles, covering altitudes from 2 to 18 km in 150-m increments, are available at 5-min intervals. Quality-controlled wind profiles for the Eastern Range network of five 915 MHz DRWP are also available for the period from November 1999 to August 2001. These profiles, covering altitudes from 130 to 2,558 m in 101-m steps, are available at 15-min intervals. The data sets and the associated quality control processes are described in references 2-40 and 2-72, respectively. These data are available from the NASA KSC Weather Office, Mail Code YA-D, Kennedy Space Center, FL 32899.

2.3.11.5 Utility of Data. All wind profile data records should be checked carefully by the user before employing them in any vehicle response calculations. Wherever practical, the user should become familiar with the representativeness of the data and frequency content of the profile used, as well as the measuring system and reduction schemes employed in handling the data. For those organizations that have aerospace meteorology-oriented groups or individuals on their staffs, consultations should be held with them. Otherwise, various government groups concerned with aerospace vehicle design and operation can be of assistance. Such action by the user can prevent expensive misuse and error in interpretation of the data relative to the intended application.

2.3.12 Atmospheric Turbulence Criteria for Horizontally Flying Vehicles

This section presents the continuous random turbulence model for the design of aerospace vehicles capable of flying horizontally, or nearly so, through the atmosphere. In general, both the continuous random model (secs. 2.3.12 and 2.3.13) and the discrete model (sec. 2.3.14) are used to calculate vehicle responses, with the procedure producing the larger response being used for design.

The lateral and vertical components of turbulence are perpendicular to the relative mean wind vector and act in the lateral and vertical directions relative to the vehicle flight path. To a reasonable degree of approximation, in-flight atmospheric turbulence experienced by horizontally flying vehicles can be assumed to be homogeneous, stationary, Gaussian, and isotropic. Under some conditions, these assumptions might appear to be drastic, but for engineering purposes, they seem to be appropriate except for low-level flight in approximately the first 300 m of the atmosphere. It has been found that the spectrum of turbulence first suggested by von Karman appears to be a good analytical representation of atmospheric turbulence. The longitudinal spectrum is given by

$$\Phi_u(\Omega, L) = \sigma^2 \frac{2L}{\pi} \frac{1}{\left[1 + (1.339\, L\Omega)^2\right]^{\frac{5}{6}}} , \tag{2.89}$$

where σ^2 is the variance of the turbulence, L is the scale of turbulence, and Ω is the wave number in units of radians per unit length. The spectrum is defined so that

$$\sigma^2 = \int_0^\infty \Phi_u(\Omega, L)\, d\Omega . \tag{2.90}$$

The theory of isotropic turbulence predicts that the spectra Φ_w of the lateral components of turbulence are related to the longitudinal spectrum through the equation

$$\Phi_w = \frac{1}{2}\left(\Phi_u - \Omega \frac{d\Phi_u}{d\Omega} \right) . \tag{2.91}$$

Substitution of equation (2.89) into equation (2.91) yields

$$\Phi_w = \sigma^2 \frac{L}{\pi} \frac{1 + \frac{8}{3}(1.339\, L\Omega)^2}{\left[1 + (1.339\, L\Omega)^2\right]^{\frac{11}{6}}} . \tag{2.92}$$

The nondimensional spectra $2\pi\, \Phi_u\, \sigma^2\, L$ are depicted in figure 2-35 as functions of ΩL. As $L\Omega > \infty$, Φ_u and Φ_w asymptotically behave like

$$\Phi_u \approx \sigma^2 \frac{2L}{\pi} \frac{(L\Omega)^{-\frac{5}{3}}}{(1.339)^{\frac{5}{3}}} (L\Omega \to \infty) , \tag{2.93}$$

and

$$\Phi_w \approx \sigma^2 \frac{8L}{3\pi} \frac{(L\Omega)^{-\frac{5}{3}}}{(1.339)^{\frac{5}{3}}} (L\Omega \to \infty) , \tag{2.94}$$

consistent with the concept of the Kolmogorov inertial subrange. In addition, $\Phi_w/\Phi_u \to 4/3$ as $\Omega L \to \infty$. Design values of the scale of turbulence L are given in table 2-67. Experience indicates that the scale of turbulence increases as height increases in the first 762 m (2,500 ft) of the atmosphere, and typical values of L range from

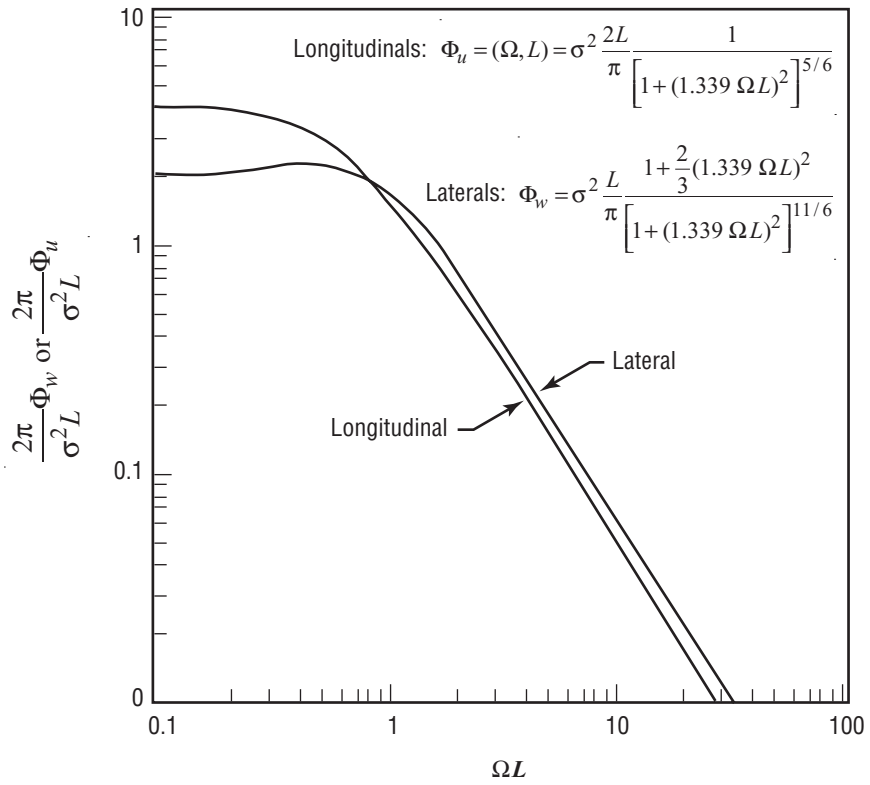

Figure 2-35. The nondimensional longitudinal and lateral, $2\pi\Phi_u/\sigma^2 L$ and $2\pi\Phi_w/\sigma^2 L$, spectra as functions as the dimensionless frequency $L\Omega$.

10 m (≈30 ft) near the surface to 610 m (2,000 ft) at an approximate 762-m (2,500-ft) level; typical values of L are in the order of 762 to 1,829 m (2,500 to 6,000 ft). The scales of turbulence in table 2-67 above the 300-m level are probably low, and they would be expected to give a somewhat conservative or high number of load or stress exceedances per unit length of flight. The scale of turbulence indicated for the first 304.8 m of the atmosphere in table 2-67 is a typical value. The use of this average scale of turbulence may be appropriate for load studies; however, it is inappropriate for control system and flight simulation purposes, in which event the vertical variation of the first 304.8 m of the atmosphere in table 2-67 is a typical value. The use of this average scale of turbulence may be appropriate for load studies; however, it is inappropriate for control system and flight simulation purposes, in which event the vertical variation of the scale of turbulence in the first 300 m of the atmosphere should be taken into account.

The power spectrum analysis approach is applicable only to stationary Gaussian continuous turbulence, but atmospheric turbulence is neither statistically stationary nor Gaussian over long distances. The statistical quantities used to describe turbulence vary with altitude, wind direction, terrain roughness, atmospheric stability, and a host of other variables. Nevertheless, it is valid to a sufficient degree of engineering approximation to recommend that atmospheric turbulence be considered locally Gaussian and stationary and that the total flight history of a horizontally flying vehicle be considered to be composed of an ensemble of exposures to turbulence of various intensities, all using the same power spectrum shape. Furthermore, it is recommended that the following statistical distribution of RMS gust intensities be used:

Table 2-67. Parameters for the turbulence model for horizontally flying vehicles.

Altitude		Mission	Turbulence	P_1	b_1		P_2	b_2		L	
(m)	(ft)	Segment*	Component**	(unitless)	(m/s)	(ft/s)	(unitless)	(m/s)	(ft/s)	(m/s)	(ft/s)
0–304.8	0–1,000	Low-level contour (rough terrain)	V	1.00	0.82	2.7	10^{-5}	3.25	10.65	152.4	500
0–304.8	0–1,000	Low-level contour (rough terrain)	L, L	1.00	0.94	3.1	10^{-5}	4.29	14.06	152.4	500
0–304.8	0–1,000	C, C, D	V, L, L	1.00	0.77	2.51	0.005	1.54	5.04	152.4	500
304.8–672	1,000–2,500	C, C, D	V, L, L	0.42	0.92	3.02	0.0033	1.81	5.94	533.4	1,750
672–1,524	2,500–5,000	C, C, D	V, L, L	0.30	1.04	3.42	0.0020	2.49	8.17	762	2,500
1,524–3,048	5,000–10,000	C, C, D	V, L, L	0.15	1.09	3.59	0.00095	2.81	9.22	762	2,500
3,048–6,096	10,000–20,000	C, C, D	V, L, L	0.062	1.00	3.27	0.00028	3.21	10.52	762	2,500
6,096–9,144	20,000–30,000	C, C, D	V, L, L	0.025	0.96	3.15	0.00011	3.62	11.88	762	2,500
9,144–12,192	30,000–40,000	C, C, D	V, L, L	0.011	0.89	2.93	0.000095	3.00	9.84	762	2,500
12,192–15,240	40,000–50,000	C, C, D	V, L, L	0.0046	1.00	3.28	0.000115	2.69	8.81	762	2,500
15,240–18,288	50,000–60,000	C, C, D	V, L, L	0.0020	1.16	3.82	0.000078	2.15	7.04	762	2,500
18,288–21,336	60,000–70,000	C, C, D	V, L, L	0.00088	0.89	2.93	0.000057	1.32	4.33	762	2,500
21,336–24,384	70,000–80,000	C, C, D	V, L, L	0.00038	0.85	2.80	0.000044	0.55	1.80	762	2,500
Above 24,384	Above 80,000	C, C, D	V, L, L	0.00025	0.76	2.50	0	0	0	762	2,500

*Climb, cruise, and descent (C, C, D)
**Vertical, lateral, and longitudinal (V, L, L)

$$p(\sigma) = \frac{P_1}{b_1}\sqrt{\frac{2}{\pi}}\exp\left(-\frac{\sigma^2}{2b_1^2}\right) + \frac{P_2}{b_2}\sqrt{\frac{2}{\pi}}\exp\left(-\frac{\sigma^2}{2b_2^2}\right), \tag{2.95}$$

where b_1 and b_2 are the standard deviations of σ in nonstorm turbulence. The quantities P_1 and P_2 denote the fractions of flight time or distance flown in nonstorm and storm turbulence. It should be noted that if P_0 is the fraction of flight time or distance in smooth air, then

$$P_0 + P_1 + P_2 = 1. \tag{2.96}$$

The recommended design values of P_1, P_2, b_1, and b_2 are given in table 2-67. Note that over rough terrain, b_2 can be extremely large in the first 304 m (1,000 ft) above the terrain and the b's for the vertical, the lateral, and the longitudinal standard deviations of the turbulence are not equal. Thus, in the first 304 m of the atmosphere above rough terrain, turbulence is significantly anisotropic, and this anisotropy must be taken into account in engineering calculations.

An exceedance model of gust loads and stresses can be developed with the preceding information. Let y denote any load quantity that is a dependent variable in a linear system of response equations; e.g., bending moment at a particular wind station. This system is forced by the longitudinal, lateral, and vertical components of turbulence, and upon producing the Fourier transform of the system, it is possible to obtain the spectrum of y. This spectrum will be proportional to the input turbulence spectra, the function of proportionality being the system transfer function. Upon integrating the spectrum of y over the domain $0 < \Omega < \infty$, we obtain the relationship

$$\sigma_y = A\sigma \ , \tag{2.97}$$

where

A = a positive constant that depends upon the system parameters and the scale of turbulence
σ_y = the standard deviation of y.

If the output y is considered to be Gaussian for a particular value of σ, then the expected number of fluctuations of y that exceed y^* with positive slope per unit distance with reference to a zero mean is

$$N(y^*) = N_0 \exp\left(\frac{|y^{*2}|}{2\sigma_y^2}\right), \tag{2.98}$$

where N_0 is the expected number of zero crossings of y units distance with h positive slope and is given by

$$N_0 = \frac{1}{2\pi\sigma_y}\left[\int_0^\infty \Omega^2 \Phi_y(\Omega) d\Omega\right]^{\frac{1}{2}} . \tag{2.99}$$

In this equation, Φ_y is the spectrum of y and

$$\sigma_y = \left[\int_0^\infty \Phi_y(\Omega) d\Omega\right]^{\frac{1}{2}} . \tag{2.100}$$

The standard deviation of σ_y is related to the standard deviation of turbulence through equation (2.97) and σ is distributed according to equation (2.95). Accordingly, the number of fluctuations of y that exceed y^* for standard deviations of turbulence in the interval σ to $\sigma + d\sigma$ is $N(y^*)p(\sigma)d\sigma$, so that integration over the domain $0 < \sigma < \infty$ yields

$$\frac{M(y^*)}{N_0} = P_1 \exp\left(-\frac{|y^*|}{b_1 A}\right) + P_2 \exp\left(-\frac{|y^*|}{b_2 A}\right), \tag{2.101}$$

where $M(y^*)$ is the overall expected number of fluctuations of y that exceed y^* with positive slope. To apply this equation, the engineer needs only to calculate A and N_0 and specify the risk of failure he wishes to accept. The appropriate values of P_1, P_2, b_1, and b_2 are given in table 2-67. Figures 2-36 and 2-37 give plots of $M(y^*)/N_0$ as a function of $|y^*|/A$ for the various altitudes for the design data given in table 2-67. Table 2-68 provides a summary of the units of the various quantities in this model.

2.3.12.1 Application of Power Spectral Model. To apply equation (2.101), the engineer can either calculate A and N_0 and then calculate the load quantity y^* for a specified value of $M(y^*)$, or calculate A and calculate the load quantity y^* for a specified value of $M(y^*)/N_0$. These design criteria are consistent with the limit load capability of present-day commercial aircraft. The criterion in which $M(y^*)$ is specified is suitable for a mission analysis approach to the design problem. The criterion in which $M(y^*)/N_0$ is specified also is suitable for a design envelope approach to aircraft design.

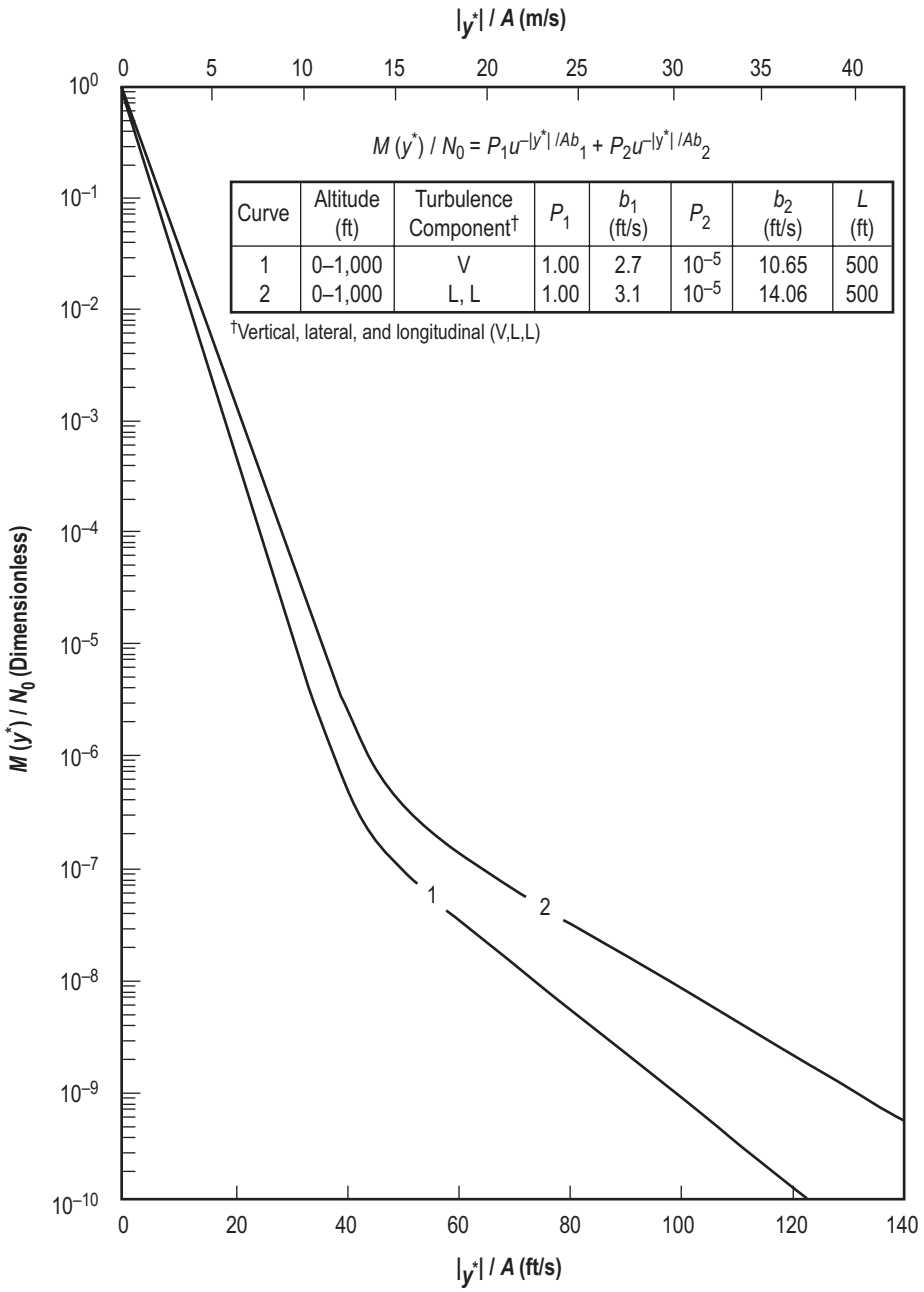

Figure 2-36. Exceedance curves for the vertical, lateral, and longitudinal components of turbulence for the zero to 304-m (zero to 1,000-ft) altitude range.

In the design envelope approach, it is assumed that the airplane operates 100 percent of the time at its critical design envelope point. The philosophy is that if the vehicle can operate 100 percent of the time at any point on the envelope, it can surely operate adequately in any combination of operating points in the envelope. A new vehicle is designed on a limit-load basis for a specified value of M/N_0. Accordingly, $M/N_0 = 6\times10^{-9}$ is suitable for the design of commercial aircraft. To apply this criterion, all critical altitudes, weights, and weight distributions are specified configurations with equation (2.101) for $M/N_0 = 6\times10^{-9}$.

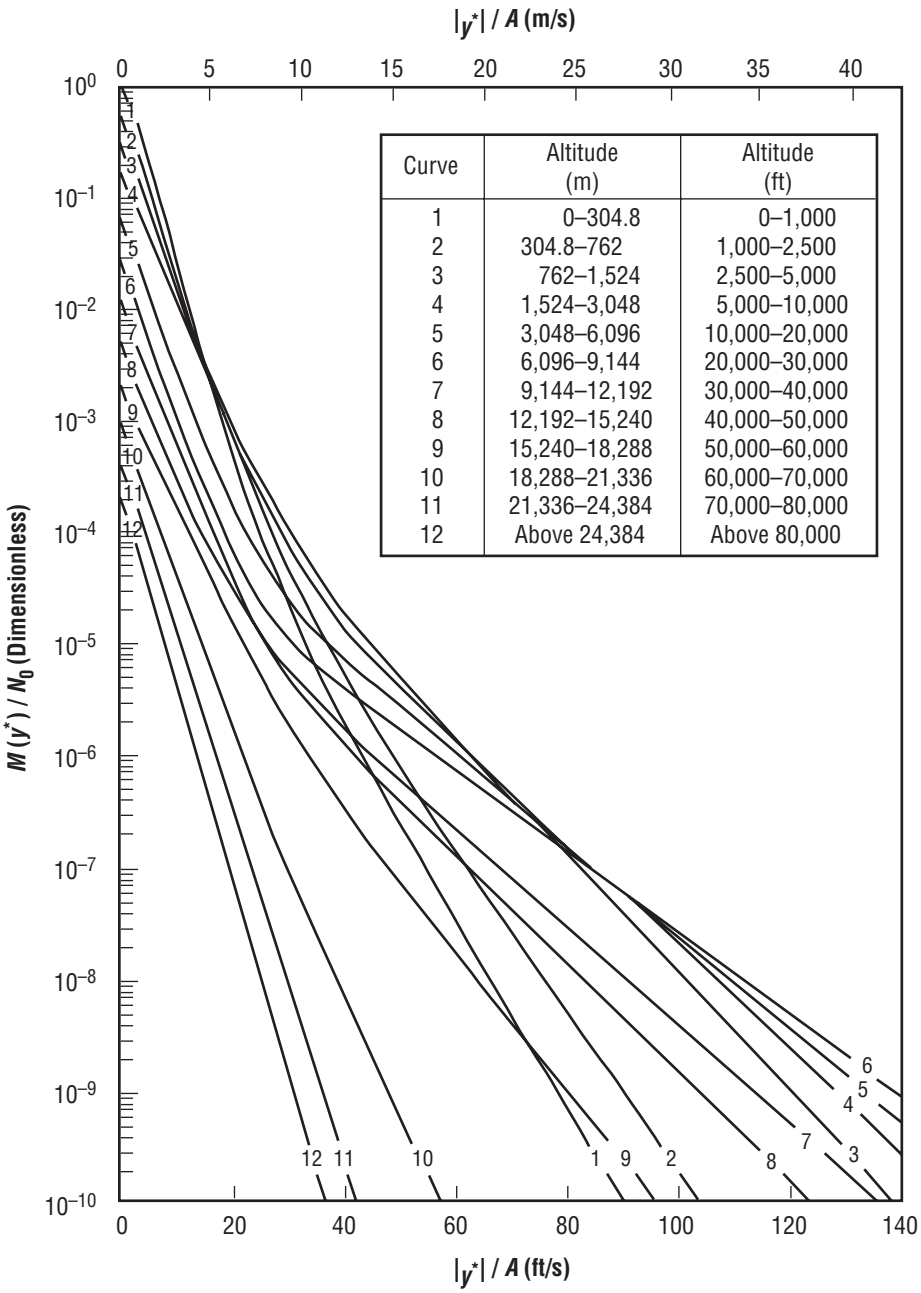

Figure 2-37. Exceedance curves for the vertical, lateral, and longitudinal components of turbulence for various altitude ranges.

In the mission analysis approach, a new aircraft is designed on a limit-load basis for $M = 2\times10^{-5}$ load exceedances per hour. To apply this criterion, the engineer must construct an ensemble of flight profiles which define the expected range of payloads and the variation with time of speed, altitude, gross weight, and center of gravity position. These profiles are divided into mission segments, or blocks, for analysis; average or effective values of the pertinent parameters are defined for each segment. For each mission segment, values of A and N_0 are determined by dynamic analysis. A sufficient number of load and stress quantities are included in the dynamic

Table 2-68. Metric and U.S. customary units of various quantities in the turbulence model for horizontally flying vehicles.

Quantity	Metric Units	U.S. Customary Units
Ω	rad/m	rad/ft
Φ_u, Φ_w	m^2/s^2/rad/m	ft^2/s^2/rad/ft
σ_2	m^2/s^2	ft^2/s^2
L	m	ft
b_1, b_2	m/s	ft/s
P_1, P_2	Dimensionless	Dimensionless
σ_y /A	m/s	ft/s
$\|y^*\|/A$	m/s	ft/s
N_0, N, M	rad/s	rad/s

analysis to ensure that stress distributions throughout the structure are realistically or conservatively defined. Now the contribution of $M(y^*)$ from the ith flight segment is $t_i M_i (y^*/T)$, where t_i is the amount of time spent in the ith flight regime (mission segment), T is the total time flown by the vehicle over all mission segments, and $M_i(y^*)$ is the exceedance rate associated with the ith segment. The total exceedance rate for all mission segments, k, is

$$M(y^*) = \sum_{i=1}^{k} \frac{t_i}{T} N_{0_i} \left(P_1 e^{\frac{|y^*|}{b_1 A}} + P_2 e^{\frac{|y^*|}{b_2 A}} \right) , \tag{2.102}$$

where subscript i denotes the ith mission segment. The limit gust load quantity $|y^*|$ can be calculated with this formula upon setting $M(y^*) = 2\times10^{-5}$ exceedances per hour.

The previously mentioned limit load criteria were derived for commercial aircraft which are normally designed for 50,000-hr lifetimes. Therefore, to apply these criteria to horizontally flying aerospace vehicles which will have relatively short lifetimes would be too conservative. However, it is possible to modify these criteria so that they will reflect a shorter vehicle lifetime. The probability factor, F_p, that a load will be exceeded in a given number of flight hours, T, is

$$F_p = 1 - e^{-TM} \quad . \tag{2.103}$$

If it is assumed that the limit load criterion $M = 2\times10^{-5}$ exceedances per hour is associated with an aircraft with a lifetime T equal to 50,000 hr, this means that $F_p = 0.63$; i.e., there is a 63-percent chance that an aircraft design for a 50,000-hr operating lifetime will exceed its limit load capability at least once during its operating lifetime. This high failure probability, based on limit loads, is not excessive in view of the fact that an aircraft will receive many inspections on a routine basis during its operating lifetime. In addition, after safety factors are applied to the design limit loads, the ultimate load exceedance rate will be on the order of 10^{-8} exceedances per hour. Substitution of this load exceedance rate into equation (2.103) for $T = 50{,}000$ hr yields a failure probability, on an ultimate load basis, of $F_p = 0.0005$. This means that there will be only a 0.05-percent chance that an aircraft will exceed its ultimate load capability during its operating lifetime of 50,000 hr. Thus, a failure probability of $F_p = 0.63$ in the limit load basis is reasonable for design. If we assume that $F_p = 0.63$ is the limit load design failure probability

so that equation (2.103) can be used to calculate design values of M associated with a specified vehicle lifetime. Thus, for example, if we expect a vehicle to fly only 100 hr, then according to equation (2.103), we have $M = 10^{-2}$ exceedances per hour. Similarly, if we expect a vehicle to be exposed to the atmosphere for 1,000 hr of flight, then $M = 10^{-3}$ exceedances per hour.

The corresponding design envelope criterion can be obtained by dividing the preceding calculated values of M by an appropriate value of N_0. In the case of the 50,000-hr criterion, we have $M/N_0 = 6\times10^{-9}$ and $M = 2\times10^{-5}$ exceedances per hour, so that an estimate of N_0 for purposes of obtaining a design criterion is $N_0 = 0.333\times104$ hr^{-1}. Thus, upon solving equation (2.90) for M and dividing by $N_0 = 0.333\times104$ hr^{-1}, the design envelope criterion takes the form

$$\frac{M}{N_0} = \frac{3\times10^{-4}}{T} \ , \tag{2.104}$$

where $F_p = 0.63$. Thus, for a 100-hr aircraft, the design envelope criterion is $M/N_0 = 3\times10^{-6}$ and for a 1,000-hr aircraft, $M/N_0 = 3\times10^{-7}$. The M/N_0 criteria, equation (2.104), was developed from an FAA report that related rationalized power spectra design methods to discrete gust methods to develop a design criteria using power spectral methods. The resulting M/N_0 from the FAA study for 50,000 hr flight lifetime was used to obtain a value of N_0. It was assumed that the ratio M/N_0 is independent of true airspeed. The integral equation (2.99) is divergent. MIL–HDBK–1797, "Flying Qualities of Piloted Aircraft," (ref. 2-73) provided additional information related to this subject.

2.3.13 Turbulence Model for Flight Simulation

The lateral and vertical components of turbulence are perpendicular to the relative mean wind vector and act in the lateral and vertical directions relative to the vehicle flight path. For simulating turbulence in either an analog or digital fashion, the turbulence realizations are to be generated by passing a white-noise process through a passive filter. The model of turbulence as given in section 2.3.12 is not particularly suited for the simulation of turbulence with white noise because the von Karman spectra given by equations (2.89) and (2.92) are irrational. Thus, for engineering purposes, the Dryden spectra may be used for simulating continuous random turbulence. They are given by

$$\text{Longitudinal: } \Phi_u(\Omega) = \sigma^2 \frac{2L}{\pi} \frac{1}{1+(L\Omega)^2} \tag{2.105}$$

and

$$\text{Lateral and vertical: } \Phi_w(\Omega) = \sigma^2 \frac{L}{\pi} \frac{1+3(L\Omega)^2}{\left[1+(L\Omega)^2\right]^2} \ . \tag{2.106}$$

Since these spectra are rational, a passive filter may be generated. It should be noted that the Dryden spectra are somewhat similar to the von Karman spectra. As $\Omega L \to 0$, the Dryden spectra asymptotically approach the von Karman spectra. As $\Omega L \to \infty$ the Dryden spectra behave like $(\Omega L)^{-2}$, while the von Karman spectra behave like $(\Omega L)^{-5/3}$. Thus, the Dryden spectra depart from the von Karman spectra by a factor proportional to $(\Omega L)^{-1/3}$ as $\Omega L \to \infty$, so that at sufficiently large values of ΩL, the Dryden spectra will fall below the von Karman spectra. However, this deficiency in spectral energy of the Dryden spectra with respect to the von Karman spectra is not serious from an engineering point of view. If the capability to use the von Karman spectra is already available, the user should use it in flight simulation rather than the Dryden spectra.

The spectra as given by equations (2.105) and (2.106) can be transformed from the wave number (Ω) domain to the frequency domain (ω rad/s) with a Jacobian transformation by noting that $\Omega = \omega/V$, so that

$$\Phi_u(\omega) = \frac{L}{V}\frac{2\sigma^2}{\pi}\frac{1}{1+\left(\frac{L\omega}{V}\right)^2} \tag{2.107}$$

and

$$\Phi_w(\omega) = \frac{L}{V}\frac{\sigma^2}{\pi}\frac{1+3\left(\frac{L\omega}{V}\right)^2}{\left[1+\left(\frac{L\omega}{V}\right)^2\right]^2} \ . \tag{2.108}$$

The quantity V is the magnitude of the mean wind vector relative to the aerospace vehicle, $u-e$. The quantities u and e denote the velocity vectors of the mean flow of the atmosphere and the aerospace vehicle relative to the Earth. In the region above the 300-m (≈1,000-ft) level, the longitudinal component of turbulence is defined to be the component of turbulence parallel to the mean wind vector relative to the aerospace vehicle ($u-e$).

Details on simulations should be requested from the Natural Environments Branch, NASA Marshall Space Flight Center, Marshall Space Flight Center, AL 35812.

2.3.13.1 Transfer Functions. Atmospheric turbulence can be simulated by passing white noise through filters with the following frequency response functions:

$$\text{Longitudinal: } F_u(j\omega) = \frac{(2k)^{\frac{1}{2}}}{a+j\omega} \tag{2.109}$$

and

$$\text{Lateral and vertical: } F_w(j\omega) = \frac{(3k)^{\frac{1}{2}}\left(\frac{a}{\sqrt{3}}+j\omega\right)}{(a+j\omega)^2} \ , \tag{2.110}$$

where

$$a = \frac{V}{L} \tag{2.111}$$

and

$$k = \frac{a\sigma^2}{\pi} \ . \tag{2.112}$$

To generate the three components of turbulence, three distinct uncorrelated Gaussian white-noise sources should be used.

To define the rate of change of gust velocities about the pitch, yaw, and roll axes for simulation purposes, a procedure consistent with the preceding formulation can be found in section 3.7.5 of reference 2-74, "Application of Turbulence Models and Analyses." This should be checked for applicability.

2.3.13.2 Boundary Layer Turbulence Simulation. The turbulence in the atmospheric boundary layer, defined here for engineering purposes to be approximately the first 300 m (1,000 ft) of the atmosphere, is inherently anisotropic. To simulate this turbulence as realistically as possible, the differences between the various scales and intensities of turbulence should be taken into account. There are various problems associated with developing an engineering model of turbulence for simulation purposes.

The most important problem concerns how one should combine the landing or takeoff steady-state wind and turbulence conditions near the ground; e.g., 18.3-m (60-ft) level, with the steady-state wind and turbulence conditions at approximately the 300-m level. The wind conditions near the ground are controlled by local conditions and are usually derived from consideration of the risks associated with exceeding the design takeoff or landing wind condition during any particular mission. The turbulence environments at and above the 300-m level are controlled by relatively large-scale conditions rather than local landing or takeoff wind conditions, and these turbulence environments are usually derived from a consideration of the risks associated with exceeding the design turbulence environment during the total life or total exposure time of the vehicle to the natural environment. The use of the risk associated with exceeding the design turbulence environment during the total life of the vehicle is justified on the basis that, if the landing conditions are not acceptable, the pilot has the option to land at an alternate airfield, thus, avoiding the adverse landing wind conditions at the primary landing site. Similarly, in the takeoff problem, the pilot can wait until the adverse low-level wind and turbulence conditions have subsided before taking off. The use of the risk associated with exceeding the design turbulence environment during the total life of the vehicle above the atmospheric boundary layer to develop design turbulence environments for vehicle design studies is justified because the pilot does not have the option of avoiding adverse flight turbulence conditions directly ahead of the vehicle. In addition, the art of forecasting in-flight turbulence has not progressed to the point where a flight plan can be established that avoids in-flight turbulence with a reasonably small risk so that design environments can be established on a per flight basis rather than on a total lifetime basis.

How does one then establish a set of values for L and σ for each component of turbulence which merges together these two distinctly different philosophies? It is recommended that design values for each component of turbulence be established at the 18.3- and 304.8-m levels based on the previously stated philosophies. Once these values of σ and L are established, the corresponding values between 18.3- and 304.8-m levels can be obtained with the following interpolation formulas:

$$\sigma(H) = \sigma_{18.3}\left(\frac{H}{18.3}\right)^{p} \tag{2.113}$$

and

$$L(H) = L_{18.3}\left(\frac{H}{18.3}\right)^{q}, \tag{2.114}$$

where $\sigma(H)$ and $L(H)$ are the values of σ and L at height H above natural grade, $\sigma_{18.3}$ and $L_{18.3}$ are the values of σ and L at the 18.3-m level, and p and q are constants selected such that the appropriate values of σ and L occur at the 304.8-m level. Representative values of $L_{18.3}$ for the Dryden spectrum are given by

$$L_{u_{18.3}} = 31.5 \text{ m};\ L_{v_{18.3}} = 18.4 \text{ m};\ L_{w_{18.3}} = 10 \text{ m} \ , \tag{2.115}$$

where subscripts u, v, and w denote the longitudinal, lateral, and vertical components of turbulence, respectively. The corresponding design values of $\sigma_{18.3}$ are given by

$$\sigma_{u_{18.3}} = 2.5_{u_{*0}} \ , \tag{2.116}$$

$$\sigma_{v_{18.3}} = 1.91_{u_{*0}} \ , \tag{2.117}$$

and

$$\sigma_{w_{18.3}} = 1.41_{u_{*0}} \ , \tag{2.118}$$

where u_{*0} is the surface friction velocity which is given by

$$u_{*0} = 0.4 \frac{\bar{u}_{18.3}}{\ln\left(\dfrac{18.3}{z_0}\right)} \ . \tag{2.119}$$

The quantity $\bar{u}_{18.3}$ is the mean wind or steady-state wind at the 18.3-m level, z_0 is the surface roughness length (sec. 2.2.6.2), and SI units are understood. The quantity $\bar{u}_{18.3}$ is related to the 18.3-m-level peak wind speed $u_{18.3}$ (sec. 2.2.4) through the equation

$$\bar{u}_{18.3} = \frac{u_{18.3}}{G_{18.3}} \ , \tag{2.120}$$

where $G_{18.3}$ is the 18.3-m-level gust factor (sec. 2.2.7.1) associated with a 1-hr average wind. This gust factor is a function of the 18.3-m-level peak wind speed so that, upon specifying $u_{18.3}$ and the surface roughness length, the quantity u_{*0} is defined by equation (2.119).

The values of L and σ must satisfy the Dryden isotropy conditions demanded by the equation of mass continuity for incompressible flow. These isotropy conditions are given by

$$\frac{\sigma_u^2}{L_u} = \frac{\sigma_v^2}{L_v} = \frac{\sigma_w^2}{L_w} \tag{2.121}$$

and must be satisfied at all altitudes. The length scales given by equation (2.115) and the standard deviations of turbulence given by equations (2.116)–(2.118) were selected so that they satisfy the isotropy condition given by equation (2.121); i.e.,

$$\frac{\sigma_{u_{18.3}}^2}{L_{u_{18.3}}} = \frac{\sigma_{v_{18.3}}^2}{L_{v_{18.3}}} = \frac{\sigma_{w_{18.3}}^2}{L_{w_{18.3}}} \ . \tag{2.122}$$

At the 304.8-m level, equation (2.121) is automatically satisfied because $\sigma_u = \sigma_v = \sigma_w$ and $L_u = L_v = L_w$.

To calculate the value of $\sigma_{304.8}$ appropriate for performing a simulation, the following procedure is used to calculate the design instantaneous gust from which the design value of $\sigma_{304.8}$ shall be obtained. The procedure consists of specifying the vehicle lifetime T; calculating the limit load design value of M/N_0 with equations (2.89)

to (2.93); and then calculating the limit load instantaneous gust velocity, w^*, say, with equation (2.101) for $A = 1$ with the values of P_1, P_2, b_1, and b_2 associated with the zero to 304.8-m height interval for climb, cruise, and descent in table 2-67. The instantaneous gust velocity w^* should be associated with the 99.98-percent value of gust velocity for a given realization of turbulence. In addition, the turbulence shall be assumed to be Gaussian so that the value of $\sigma_{304.8}$ and the values of σ at the 18.3-m level (eqs. (2.116)–(2.118)) shall be used to determine the values of p for each component of turbulence with equation (2.113); i.e.,

$$p = 0.356 \ln\left(\frac{\sigma_{304.8}}{\sigma_{18.3}}\right) . \tag{2.123}$$

The integral scale of turbulence at the 304.8-m level appropriate for simulating of turbulence with the Dryden turbulence model is $L_{304.8} = 190$ m. This scale of turbulence and the 18.3-m-level scales of turbulence given by equation (2.115) yield the following values of q appropriate for the simulation of turbulence with the Dryden turbulence model in the atmospheric boundary layer:

$$q_u = 0.64 \; ; \; q_v = 0.83 \; ; \; q_w = 1.05 \; . \tag{2.124}$$

The vertical distributions of σ and L given by equations (2.113) and (2.114) satisfy the isotropy condition given by equation (2.108).

Below the 18.3-m level, σ and L shall take on constant values equal to corresponding 18.3-m-level values.

The steady-state wind profile to be used with this model shall be obtained by the procedure given in section 2.3.9.3 for merging ground wind and in-flight wind profile envelopes.

To determine the steady-state wind direction, $\theta(z)$ at any level H between the surface and the 1,000-m level, use the following formula:

$$\theta(H) = \theta_{1,000} + \left[2\left(\frac{H - 1{,}000}{1{,}000}\right) + \left(\frac{H - 1{,}000}{1{,}000}\right)^2\right]\Delta \; , \tag{2.125}$$

where $\theta_{1,000}$ is the selected 1,000-m-level wind direction and H is altitude above the surface of the Earth in meters. The quantity Δ is the angle between the wind vectors at the 10- and 1,000-m levels.

This quantity for engineering purposes is distributed according to a Gaussian distribution with mean value and standard deviation given by

$$\overline{\Delta} = 31^\circ, \; \overline{u}_{1,000} \le 4 \text{ m/s} \; ,$$

$$\overline{\Delta} = 31 - 2.183 \ln\left(\frac{\overline{u}_{1,000}}{4}\right), \; \overline{u}_{1,000} > 4^{-1} \; ,$$

$$\sigma_\Delta = 64 \; , \; \overline{u}_{1,000} \le 4^{-1} \; ,$$

and

$$\sigma_\Delta = 63 e^{-0.0531\left(\overline{u}_{1,000}{}^{-4}\right)}, \overline{u}_{1,000} 4 > \text{m/s} \; , \tag{2.126}$$

where $\bar{u}_{1,000}$ is the 1,000-m level steady-state wind speed. To avoid unrealistic wind direction changes, Δ, between the surface and the 1,000-m level, only those values of Δ that occur in the interval $-180^\circ \leq 0 \leq 180^\circ$ should be used. It is recommended that ±1-percent risk wind direction changes be used for vehicle design studies.

To apply this model, the longitudinal component of turbulence shall be assigned to be that component of turbulence parallel to the horizontal component of the relative wind vector. The lateral component of turbulence is perpendicular to the longitudinal component and lies in the horizontal plane. The vertical component of turbulence is orthogonal to the horizontal plane.

The following procedure shall be used to calculate profiles of σ and L in the first 304.8 m of the atmosphere for simulation of turbulence with the Dryden turbulence model:

(1) Specify the peak wind speed at the 18.3-m level consistent with the accepted risk of exceeding the design 18.3-m-level peak wind speed.

(2) Calculate the steady-state wind speed at the 18.3-m level with equation (2.120).

(3) Calculate the surface friction velocity with equation (2.119).

(4) Calculate the 18.3-m-level standard deviations of turbulence with equations (2.116) through (2.118).

(5) Calculate the 304.8-m-level standard deviation of turbulence consistent with the accepted risks of encountering the design instantaneous gust during the total exposure of the vehicle to the natural environments (remembering $\sigma_u = \sigma_v = \sigma_w$ at the 304.8-m level).

(6) Calculate p_u, p_v, and p_w with equation (2.123).

(7) Calculate the distribution of σ and L with equations (2.123) and (2.124) for the altitudes at and between the 18.3- and 304.8-m levels.

(8) Below the 18.3-m level, σ and L shall take on constant values equal to the 18.3-m-level values of σ and L.

The reader should consult reference 2-73 for a detailed discussion concerning the philosophy and problem associated with the simulation of turbulence for engineering purposes.

2.3.13.3 Turbulence Simulation in the Free Atmosphere (Above 304.8 m). To simulate turbulence in the free atmosphere (above 304.8 m or 1,000 ft), it is recommended that equations (2.101) and (2.104) and the supporting data in table 2-67 be used to specify the appropriate values of σ. The turbulence at these altitudes can be considered isotropic for engineering purposes so that the integral scales and intensities of turbulence are independent of direction. Past studies have shown that when the Dryden turbulence model is being used, the scales of turbulence $L = 533.4$ m in the 304.8- to 672-m-altitude band and $L = 762$ m above the 672-m level in table 2-67 should be replaced with the values $L = 300$ m and $L = 533$ m, respectively (ref. 2-73). This reduction in scales tends to bring the Dryden spectra in line with the von Karman spectra over the band of wave numbers of the turbulence which are of primary importance in the design of aerospace vehicles. Accordingly, it is recommended that these reduced scales be used in the simulation of turbulence above the 304.8-m level when the Dryden model is being used.

To calculate the values of σ above the 304.8-m level appropriate for performing a simulation of turbulence, it is recommended that the procedure used to calculate the 304.8-m level of σ be used. The appropriate values of P_1, P_2, b_1, and b_2 for the various altitude bands above the 304.8-m level are given in table 2-67.

Section 2.3.13.5.1 and table 2-71 give recently updated values of σ, scale length, and probability for light, moderate, and severe turbulence, from 1- to 200-km altitude (ref. 2-75 and 2-76).

2.3.13.4 Design Floor on Gust Environments. If the design lifetime, T, is sufficiently small, it is possible that the turbulence models described herein for horizontally and nearly horizontally flying vehicles will result in a vehicle design gust environment which is characterized by discrete gusts with amplitudes <9 m/s for $d_m/L > 10$ in figure 2-38 above the 1-km level. This is especially true for altitudes above the 18-km level. In view of the widespread acceptance of the 9 m/s gust as a minimum gust amplitude for design studies in the aerospace community and in view of the increased uncertainty in gust data as altitude increases, it is recommended that a floor be established on gust environments for altitudes above the 1-km level so that the least permissible values of σ shall be 3.4 m/s. Applications concerning figure 2-38 are described in subsection 2.3.15.

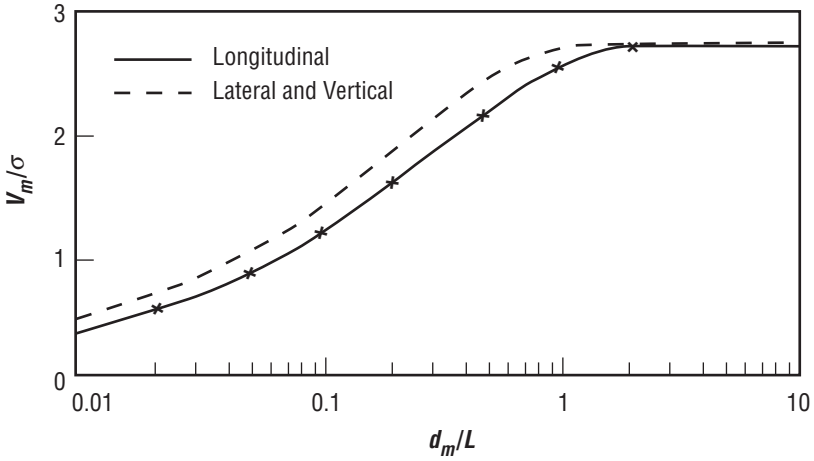

Figure 2-38. Nondimensional discrete gust magnitude, V_m/σ, as a function of nondimensional gust half-width.

2.3.13.5 Multimission Turbulence Simulation. The effects of atmospheric turbulence in both horizontal and near-horizontal flight, during reentry, or atmospheric flight of aerospace vehicles, are important for determining design, control, and "pilot-in-the-loop" effects. A nonrecursive model (based on realistic von Karman spectra) is described. Aerospace vehicles will respond not only to turbulent gusts but also to spatial gradients of instantaneous gusts (roll, pitch, and yaw). The model described (ref. 2-77) simulates the vertical and horizontal instantaneous gusts, and three of the nine instantaneous gust gradients, as shown in table 2-69.

Simulation of turbulence is achieved by passing a white noise process through a filter whose transfer function yields a von Karman power spectrum. The von Karman spectral functions are

$$\Phi_{ii} = \frac{55\sigma^2}{36a\pi^2} \frac{\left[(aLK)^2 - (aLK_i)^2\right]}{\left[1+(aLK)^2\right]^{\frac{17}{6}}} \tag{2.127}$$

Table 2-69. Simulated quantities.

Variable	Spectrum	Comments
U_1	Φ_{11}	Longitudinal gust
U_2	Φ_{22}	Lateral gust
U_3	Φ_{33}	Vertical gust
$\partial U_2/\partial X_1$	$\Phi_{22/33}$	Yaw*
$\partial U_3/\partial X_1$	$\Phi_{33/11}$	Pitch
$\partial U_3/\partial X_2$	$\Phi_{33/22}$	Roll

*X_1, X_2, X_3 are aircraft fixed coordinates with X_1 along the flight path, X_2 the lateral direction, and X_3 vertically upward.

and

$$\Phi_{\frac{ii}{jj}} = \frac{55\sigma^2}{36\pi^2 a^3 L^2} \frac{(aLK_i)^2\left[(aLK)^2 - (aLK_i)^2\right]}{\left[1+(aLK)^2\right]^{\frac{17}{6}}} \quad , \tag{2.128}$$

where

a = von Karman constant (1.339)
σ^2 = variance of turbulence
K = magnitude of wave number vector
K_i = ith component of wave number
L = length scale of turbulence
Φ_{ii} = three-dimensional gust spectrum
$\Phi_{ii/jj}$ = three-dimensional gust gradient spectrum.

Simulating turbulence with a von Karman spectrum is not a simple process, and generating von Karman turbulence fast enough for real-time simulations is difficult. One procedure for real-time simulations involves generating a large number of data sets for each new mission profile. An alternate approach was suggested by Fichtl (ref. 2-78). In this approach, the turbulent spectra are represented in nondimensional form using L, the standard deviation of turbulence, and vehicle true air speed. One set of nondimensional turbulence is generated based on the von Karman spectrum. These databases can be Fourier analyzed to assure that the spectra conform to von Karman's model. To run any mission profile, an efficient real-time routine reads the tapes and transforms them to dimensional format, giving the desired output.

The conversion to dimensional values is accomplished as follows:

$$u_i^* = \sigma_i U_i \quad , \tag{2.129}$$

where

u_i^* = dimensional gust
σ_i = standard deviation of ith gust component;

$$\frac{\partial u_i^*}{\partial x_j^*} = \frac{\sigma_i}{L_j} \frac{\partial u_i}{\partial x_j} \quad , \tag{2.130}$$

where

$\partial u_i^* / \partial x_j^*$ = dimensional gust gradient
L_j = jth length scale of turbulence;

$$\Delta t^* = \frac{aL_1 T}{V} \quad , \tag{2.131}$$

where

Δt^* = dimensional time step
T = dimensionless time step.

Note that Δt^* is not a constant because L_1 and V vary with altitude. To obtain dimensional time, t_N^*, a summation process is involved:

$$t_N^* = \sum_{n=0}^{N} \Delta t_N^* = aT \sum_{n=0}^{N} \frac{L_{in}}{V_n} \quad . \tag{2.132}$$

For digital simulations, turbulence generated with uneven time steps is undesirable. A simple interpolation routine is used to obtain values of turbulence at equal time steps. Specific values of σ_i must be determined for specific applications. Sections 2.3.13.2 through 2.3.13.4 prescribe the techniques for specifying the standard deviation. Values of the turbulent length scales and standard deviations are given in table 2-70 up to 1-km altitudes. Table 2-71 specifies light, moderate, and severe turbulence sigmas, length scales, and probabilities versus altitude from 1 to 200 km. Section 2.3.13.5.1 discusses these newer, updated values.

2.3.13.5.1 New Turbulence Statistics/Model. At altitude levels >1,000 m, new turbulence velocity component magnitudes (σ_u and σ_w), scale lengths (L_x and L_z), and their associated probabilities for light, moderate, and severe turbulence have been assembled and modeled (ref. 2-76). These results are presented in table 2-71. This turbulence modeling update was done to provide the Space Shuttle reentry engineering simulation area with a more realistic/less conservative turbulence model when involved with control system fuel expenditures upon reentry/landing.

2.3.14 Discrete Gust Model—Horizontally Flying Vehicles

Often it is useful for the engineer to use discrete gusts in load and flight control system calculations of horizontally flying vehicles. The discrete gust is defined as follows:

$$V_d = 0, x < 0$$

$$V_d = \frac{V_m}{2}\left(1 - \cos\frac{\pi x}{d_m}\right), 0 \le x \le 2\, d_m$$

$$V_d = 0, x > 2\, d_m \quad , \tag{2.133}$$

Table 2-70. Variation of standard deviation and length scale of turbulence with height within the boundary layer.

Height		Standard Deviation of Turbulence (Severe)			Integral Scales of Turbulence (All)		
(m)	(ft)	Longitudinal σ_1 (m/s)	Lateral σ_2 (m/s)	Vertical σ_3 (m/s)	Longitudinal L_1 (m)	Lateral L_2 (m)	Vertical L_3 (m)
10	32.8	2.31	1.67	1.15	21	11	5
20	65.6	2.58	1.98	1.46	33	19	11
30	98.4	2.75	2.20	1.71	43	28	17
40	131.2	2.88	2.36	1.89	52	35	23
50	164.0	2.98	2.49	2.05	61	42	29
60	196.9	3.07	2.61	2.19	68	49	35
70	229.7	3.15	2.71	2.32	75	56	41
80	262.5	3.22	2.81	2.43	82	63	47
90	295.3	3.28	2.89	2.54	89	69	53
100	328.1	3.33	2.97	2.64	95	75	59
200	656.2	3.72	3.53	3.38	149	134	123
304.8	1,000.0	3.95/4.37*	3.95/4.37*	3.95/4.39*	196/300*	190/300*	192/300*
400	1,312.3	4.39	4.39	4.39	300	300	300
500	1,640.4	4.39	4.39	4.39	300	300	300
600	1,968.5	4.39	4.39	4.39	300	300	300
700	2,296.6	4.39	4.39	4.39	300	300	300
762	2,500.0	4.39/5.70*	4.39/5.70*	4.39/5.70*	300/533*	300/533*	300/533*
800	2,624.7	5.70	5.70	5.70	533	533	533
900	2,952.8	5.70	5.70	5.70	533	533	533
1,000	3,280.8	5.70	5.70	4.67	832	832	624

*Double entries for a tabulated height indicate a step change in standard deviation or integral scale at that height.

where

x = distance

V_m = maximum velocity of the gust which occurs at position $x = d_m$ in the gust.

To apply the model, the engineer specifies several values of the gust half-width, d_m, to cover the range of frequencies of the system to be analyzed. To calculate the gust parameter, V_m, one enters figure 2-38 with d_m/L and reads out V_m/σ. Figure 2-38 is based on the Dryden spectrum of turbulence. Accordingly, the procedures outlined in sections 2.3.13.2 and 2.3.13.3 can be used for specifying the σ's and L's to determine the gust magnitude V_m from figure 2-38. In the boundary layer, three values of V_m will occur at each altitude, one for each component of turbulence. In the free atmosphere, the lateral and vertical values of V_m are equal at each altitude. In general, both the continuous random gust model (secs. 2.3.12 and 2.3.13) and the discrete gust models are often used to calculate vehicle responses, with the procedure producing the larger response being used for design.

2.3.15 Flight Regimes for Use of Horizontal and Vertical Turbulence Models (Spectra and Discrete Gusts)

Sections 2.3.6, 2.3.12, and 2.3.14 contain turbulence (spectra and discrete gusts) models for response calculations of vertically ascending and horizontally flying aerospace vehicles.

Table 2-71. Mean horizontal and vertical turbulence (light, moderate, and severe) magnitudes (σ_h, σ_w), wind scale (L_h and L_w) and probability for encountering turbulence versus altitude (MSL).

Altitude		Light Turbulence			Moderate Turbulence			Severe Turbulence			Turbulence Length Scales	
(km)	(kft)	Horizontal σ_h (m/s)	Vertical σ_w (m/s)	Probability of Light Turbulence	Horizontal σ_h (m/s)	Vertical σ_w (m/s)	Probability of Moderate Turbulence	Horizontal σ_h (m/s)	Vertical σ_w (m/s)	Probability of Severe Turbulence	Horizontal L_h (km)	Vertical L_w (km)
1	3.3	0.17	0.14	0.7760	1.65	1.36	0.1990	5.70	4.67	0.0250	0.832	0.624
2	6.6	0.17	0.14	0.8910	1.65	1.43	0.9790	5.80	4.75	0.0111	0.902	0.831
4	13.1	0.20	0.17	0.9199	2.04	1.68	0.0738	6.24	5.13	0.0063	1.040	0.972
6	19.7	0.21	0.17	0.9294	2.13	1.69	0.0650	7.16	5.69	0.0056	1.040	1.010
8	26.2	0.22	0.17	0.9247	2.15	1.69	0.0704	7.59	5.98	0.0049	1.040	0.980
10	32.8	0.22	0.17	0.9280	2.23	1.73	0.0677	7.72	6.00	0.0043	1.230	1.100
12	39.4	0.25	0.18	0.9464	2.47	1.79	0.0502	7.89	5.71	0.0034	1.800	1.540
14	45.9	0.26	0.19	0.9605	2.62	1.91	0.0368	6.93	5.05	0.0027	2.820	2.120
18	59.1	0.24	0.21	0.9639	2.44	2.10	0.0337	5.00	4.31	0.0024	3.400	2.600
20	65.6	0.22	0.21	0.9703	2.21	2.07	0.0277	4.07	3.81	0.0020	5.000	3.340
25	82.0	0.23	0.20	0.9804	2.26	1.99	0.0180	3.85	3.38	0.0016	8.640	4.410
30	98.4	0.27	0.21	0.9839	2.71	2.09	0.0146	4.34	3.34	0.0015	12.000	6.560
35	114.8	0.37	0.24	0.9797	3.73	2.39	0.0185	5.60	3.59	0.0018	28.600	8.880
40	131.2	0.46	0.26	0.9726	4.59	2.58	0.0249	6.89	3.87	0.0025	35.400	8.330
45	147.6	0.53	0.29	0.9650	5.26	2.87	0.0318	7.89	4.30	0.0032	42.600	6.200
50	164.0	0.62	0.33	0.9575	6.22	3.25	0.0386	9.33	4.88	0.0039	50.100	5.200
55	180.4	0.73	0.42	0.9500	7.27	4.21	0.0455	10.90	6.31	0.0045	57.900	5.300
60	196.9	0.87	0.44	0.9250	8.70	4.40	0.0682	13.06	6.60	0.0068	66.000	6.000
65	213.3	1.01	0.44	0.9000	10.10	4.42	0.0917	15.10	6.63	0.0083	74.400	6.800
70	229.7	1.13	0.41	0.8250	11.30	4.05	0.1620	16.90	6.00	0.0130	83.200	7.500
75	246.1	1.59	0.50	0.7500	15.90	5.04	0.2336	23.80	7.50	0.0164	92.300	8.200
80	262.5	1.92	0.63	0.6750	19.20	6.30	0.3066	28.70	9.50	0.0184	102.000	9.000
85	278.9	2.26	0.83	0.6000	22.60	8.30	0.3810	33.80	12.40	0.0190	111.000	9.700
90	295.3	2.73	1.03	0.4000	27.30	10.30	0.5769	40.90	15.40	0.0231	121.000	10.400
95	311.7	3.32	1.18	0.2000	33.20	11.80	0.7767	49.80	17.70	0.0233	132.000	11.200
100	328.1	3.56	1.14	0.0000	35.60	11.40	0.9804	53.30	17.10	0.0196	153.000	12.700
120	393.7	4.23	1.07	0.0000	42.30	10.70	0.9901	63.40	16.00	0.0099	200.000	15.800
140	459.3	4.43	1.08	0.0000	44.30	10.80	0.9901	66.40	16.10	0.0099	232.000	17.600
160	524.9	4.82	1.17	0.0000	48.20	11.70	0.9901	72.20	17.60	0.0099	270.000	20.000
180	590.6	4.89	1.18	0.0000	48.90	11.80	0.9901	73.30	17.80	0.0099	300.000	22.200
200	656.2	4.95	1.20	0.0000	49.50	12.00	0.9901	74.20	18.10	0.0099	300.000	24.300

The turbulence model for the horizontally flying vehicles was derived from wind profile measurements made with vertically ascending Jimsphere balloons and smoke trails. In many instances, aerospace vehicles neither fly in a pure horizontal flight mode nor ascend or descend in a strictly vertical flight path. At this time, there does not appear to be a consistent way of combining the turbulence models for horizontal and vertical flight paths without being unduly complicated or overly conservative. Also, the unavailability of a sufficiently large data sample of turbulence measurements in three dimensions precludes the development of such a combined model.

Accordingly, in lieu of the availability of a combined turbulence model and for the sake of engineering simplicity, the turbulence model in section 2.3.6 should be applied to ascending and descending aerospace vehicles when the angle between the flight path and the local vertical is ≤30º. Similarly, the turbulence model in sections 2.3.12 and 2.3.14 should be applied to aerospace vehicles when the angle between the flight path and the local horizontal is ≤30º. In the remaining flight path region, between 30º from the local vertical and 30º from the local horizontal, both turbulence models should be independently applied and the most adverse responses used in the design.

2.4 Historical In-Flight Wind Profile Information

The material on the synthetic wind profile environment definitions and requirements for use in aerospace vehicle design and development studies presented in earlier versions of this document are still applicable as information for use in preliminary design analyses. In addition, they provide useful general information on wind characteristics. Therefore, this section has been included in the document to provide a frame of reference on this historical material. Additional historical design wind information may be found in reference 2-1.

Included is information on the following items from the earlier versions of this document: (1) Ascent flight wind change, (2) scalar wind speed envelopes, (3) classical discrete gust, and (4) classical construction of synthetic wind profile.

The 95th percentile in-flight synthetic ascent wind profile design requirement philosophy was to ensure, for the worst wind condition month, that the vehicle would encounter a maximum of 5-percent launch delay risk. In addition, that if the vehicle was launched in the 95th percentile design in-flight synthetic wind profile winds, the associated 99-percent wind shear/gust design requirement was to ensure a maximum of 1-percent risk in compromising the structural loads and control system design (excluding the defined vehicle's design safety factor). For spacecraft descent from orbit, the 99th percentile in-flight synthetic wind profile, and associated 99th percentile shear/gust design requirement philosophy, was used to ensure, for the worst wind condition month, that the vehicle would encounter a maximum of 1-percent risk of exceeding the in-flight winds. This increase to 99 percent for in-flight winds design requirement was to accommodate the inability to monitor weather and thus delay the spacecraft descent subsequent to deorbit decision, the objective being to ensure a launch vehicle that would safely meet the required operational requirements for the intended mission(s) of the program.

2.4.1 Ascent Flight Wind Changes

Figures 2-39 and 2-40 contain idealized 99-percent direction and speed changes as a function of elapsed time and observed or referenced wind speed for altitudes between 150 m and 2 km for KSC. The wind speed may increase or decrease from the reference profile value; thus, envelopes of each category are presented in figure 2-40. Figures 2-41 and 2-42 are the idealized 99-percent wind direction and speed changes as a function of elapsed time and observed or reference wind speed for altitudes between 2 and 16 km.

The data in figures 2-39 through 2-42 are applicable only to the KSC launch area because differences are known to exist in the data for other geographical locations. Conclusions should not be drawn relative to frequency content and phase relationships of the wind profile since the data given herein provide only envelope conditions

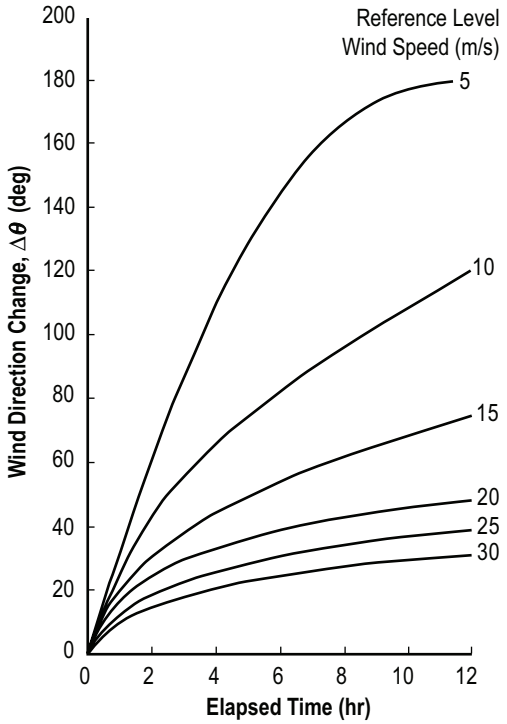

Figure 2-39. Idealized 99-percent wind direction change as a function of time and wind speed in the 150-m to 2-km altitude region of KSC.

for ranges of speed and direction changes. Direction correlations have not been developed between the changes of wind direction and wind speed.

Additional information concerning wind speed and direction changes can be found in reports by Camp and Susko (ref. 2-79) and Camp and Fox (ref. 2-80).

2.4.2 Design Wind Speed Envelopes

The wind data given in section 2.4.2.1 are not expected to be exceeded by the given percentages of time (time as related to the observational interval of the data sample) based upon the strongest winds (windiest) monthly reference period. To obtain the profiles, monthly frequency distributions are combined for each percentile level to give the envelope over all months. The profiles represent horizontal wind flow referenced to the Earth's surface. Vertical wind flow is negligible except for that associated with gusts or turbulence. The scalar wind speed envelopes are normally applied without regard to flight directions. Directional wind criteria for use with the synthetic wind profile techniques should be applied with care and only with specific knowledge of the vehicle mission and flight path since severe launch wind constraints could result for other flight paths and missions.

2.4.2.1 Scalar Wind Speed Envelopes. Scalar wind speed profile envelopes are presented in tables 2-72 through 2-76. These are idealized steady-state scalar wind speed profiles for four active or potential operational aerospace vehicle launch or landing sites; i.e., KSC, VAFB, WSMR, and EAFB. Table 2-76 provides data which envelopes the 95- and 99-percentile steady-state scalar wind speed profile for the same four locations. They are applicable when initial design or operational capability has not been restricted to specific launch and landing sites or may involve several geographical locations. However, if the specific geographical location for application has been determined as being near one of the four referenced sites, then the relevant data should be applied.

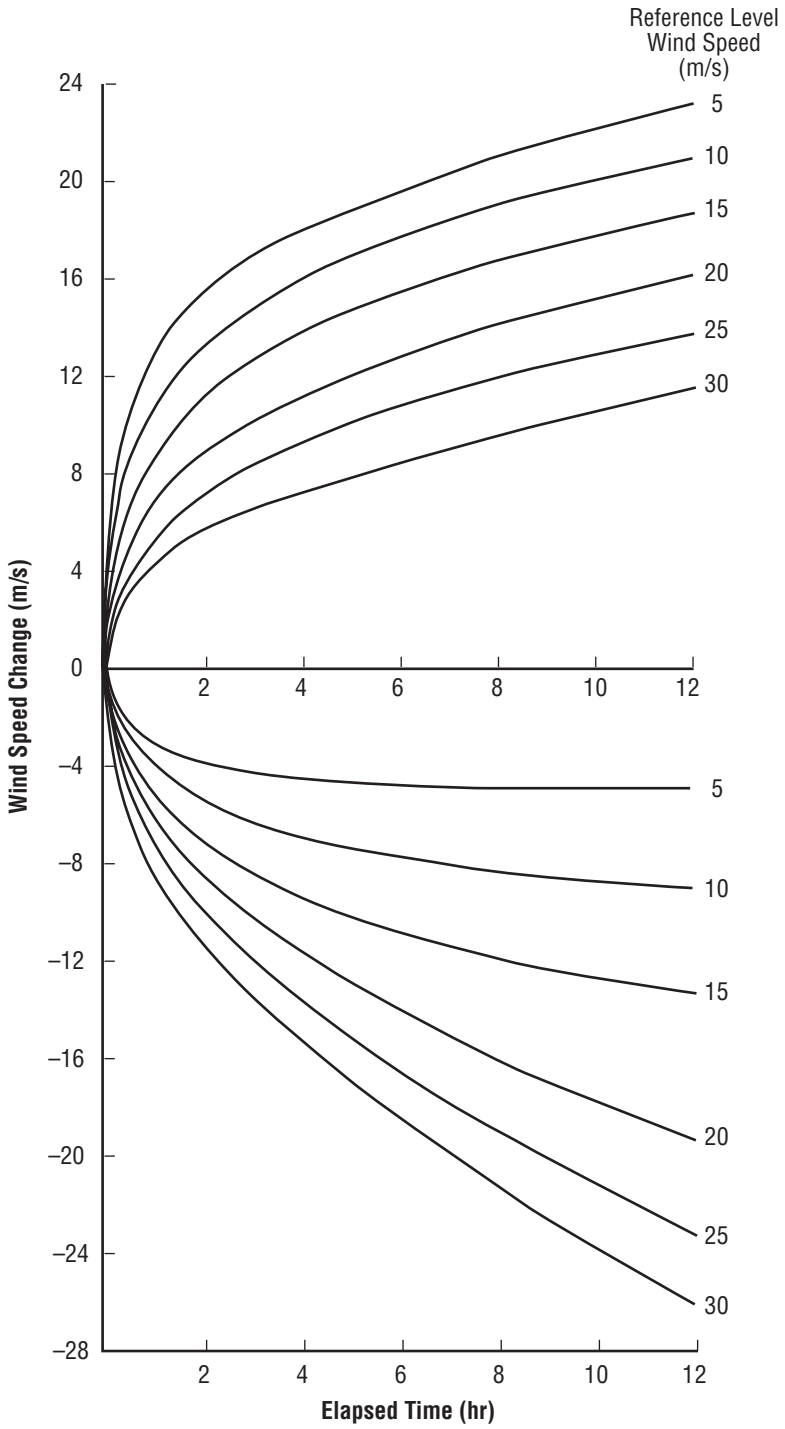

Figure 2-40. Idealized 99-percent wind speed change as a function of time and wind speed in the 150-m to 2-km altitude region of KSC.

These tables provide nondirectional wind data for various percentiles; therefore, the specific percentile wind speed envelope applicable to design should be specified in the appropriate space vehicle specification documentation. For engineering convenience, the design wind speed profile envelopes are given as linear segments between altitude levels; therefore, the tabular values can be linearly interpolated.

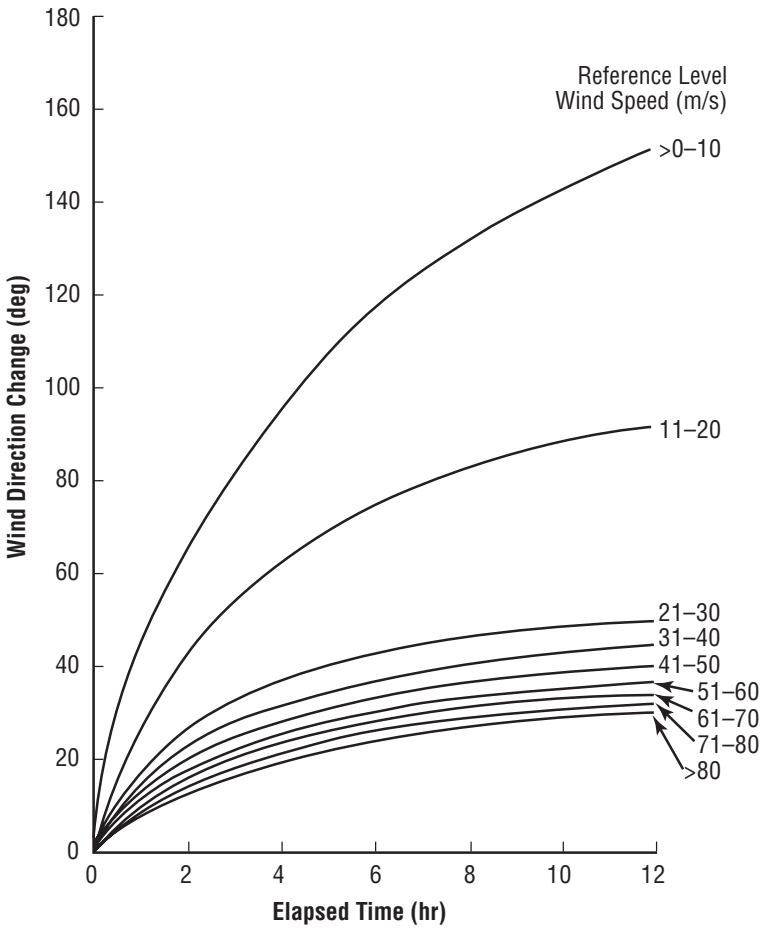

Figure 2-41. Idealized 99-percent wind direction change as a function of time and wind speed in the 2- to 16-km region of KSC.

2.4.3 Classical Empirical Wind Shear Model

This is the classical wind speed shear model that has been used with minor modifications for aerospace vehicle design since the early 1960s. It is based on empirical conditional percentile values for wind speed shear for given values of the wind speed. Here, wind speed shear is by definition the difference in wind speed between two altitudes divided by the altitude interval. If the altitude interval is specified, then the wind speed change between the two altitudes can be called wind shear for the specified shear interval. Refer to section 2.4.3.1.

Historically, two-way empirical frequency distributions for wind speed change for various shear intervals versus wind speed were established by monthly reference periods using rawinsonde databases for the 99th conditional speed change (or wind speed shear for the specified shear intervals) for given wind speed values. These were established and then enveloped over all months to give a worst-case condition. With the availability of Jimsphere wind profile databases, refinements were made for shear intervals <1,000 m. The results are given in tables 2-77 to 2-86 as wind buildup and back-off wind speed change versus scales of distance (shear interval) and further discussed in section 2.4.3.1. When applied to the synthetic scalar wind profile model for aerospace vehicle design, the term wind buildup refers to the change in wind speed up to the reference altitude of the given wind speed and wind back-off refers to the change in wind speed for altitudes above the reference altitude.

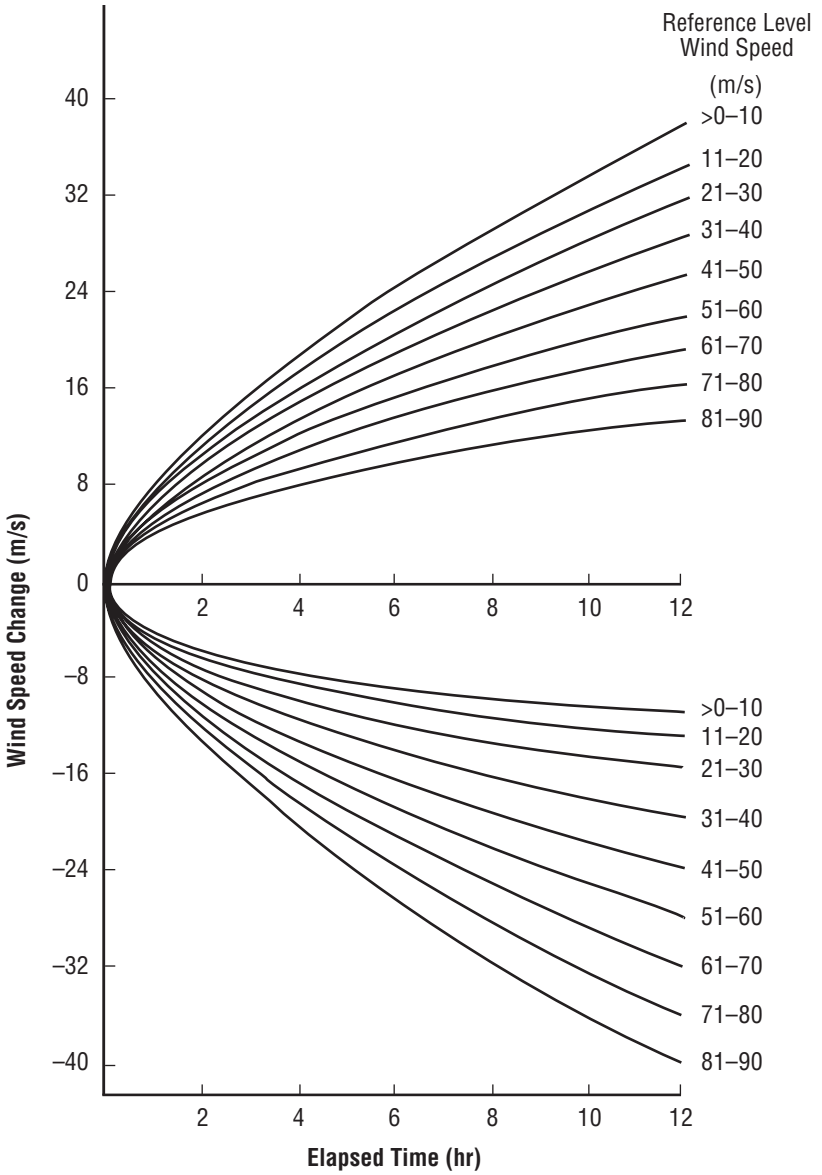

Figure 2-42. Idealized 99-percent wind speed change as a function of time and wind speed in the 2- to 16-km region of KSC.

In statistical terms, tables 2-77 to 2-86 give the 99th conditional wind speed shear for various shear intervals for given wind speed values that envelop all months for each respective site.

2.4.3.1 Buildup/Back-Off Wind Speed Change Envelopes. This section provides representative information on wind speed change (shear) for scales of distance $\Delta H \leq 5{,}000$ m. Wind speed change is defined as the total magnitude (speed) change between the wind vector at the top and bottom of a specified layer, regardless of wind direction. Wind shear is defined as the wind speed change divided by the altitude interval. When applied to aerospace vehicle synthetic profile criteria, it is frequently referred to as a wind buildup or back-off rate, depending upon whether it occurs below (buildup) or above (back-off) the reference height of concern. Thus, a buildup wind value is the change in wind speed that a vehicle may experience while ascending vertically through a specified layer to the known altitude.

Table 2-72. Scale wind speed *W* (m/s) steady-state envelopes as functions of altitude *H* (km) for various probabilities *P* (%) for KSC.

Altitude		Percentile				
(km)	(kft)	50	75	90	95	99
1	3.3	8	13	16	19	24
6	19.7	23	31	39	44	52
11	36.1	43	55	66	73	88
12	39.4	45	57	68	75	92
13	42.7	43	56	67	74	86
20	65.6	7	12	17	20	25
23	75.5	7	12	17	20	25
40	131.2	43	57	70	78	88
50	164.0	75	83	91	95	104
58	190.3	85	96	106	112	123
60	196.9	85	96	106	112	123
75	246.1	15	22	28	30	37
80	262.5	15	22	28	30	37

Table 2-73. Scale wind speed *W* (m/s) steady-state envelopes as functions of altitude *H* (km) for various probabilities *P* (%) for VAFB.

Altitude		Percentile				
(km)	(kft)	50	75	90	95	99
1	3.3	7	10	13	15	19
6	19.7	20	29	36	41	50
11	36.1	31	43	53	60	73
12	39.4	32	44	55	62	79
13	42.7	32	44	55	62	79
20	65.6	6	10	14	17	26
23	75.5	6	10	14	17	26
40	131.2	55	67	82	90	105
50	164.0	79	96	111	120	132
58	190.3	83	107	128	140	164
60	196.9	83	107	128	140	164
75	246.1	50	65	87	98	118
80	262.5	50	65	87	98	118

Table 2-74. Scale wind speed *W* (m/s) steady-state envelopes as functions of altitude *H* (km) for various probabilities *P* (%) for WSMR.

P = 50		*P* = 75		*P* = 90		*P* = 95		*P* = 99	
H	*W*	*H*	*W*	*H*	*W*	*H*	*W*	*H*	*W*
1	4	1	7	1	11	1	13	1	22
2	5	2	8	2	12	2	15	2	22
						7	50	7	68
		9	45	8	49	9	67	9	88
11	42	10	53	11	71	11	76		
13	42	12	55	13	63	12	78	14	88
				15	45	15	52	15	69
20	10	20	14	20	20	20	24	20	41
23	10	23	14	23	20	23	24	23	41
50	85	50	104	50	120	50	130	50	150
60	85	60	104	60	120	60	130	60	150
75	60	75	77	75	93	75	102	75	120
80	60	80	77	80	93	80	102	80	120

Table 2-75. Scale wind speed *W* (m/s) steady-state envelopes as functions of altitude *H* (km) for various probabilities *P* (%) for EAFB.

P = 50		*P* = 75		*P* = 90		*P* = 95		*P* = 99	
H	*W*	*H*	*W*	*H*	*W*	*H*	*W*	*H*	*W*
1	8	1	11	1	16	1	17	1	25
2	8	2	12	2	16	2	18	2	28
				5	30	5	36	5	56
10	29			10	51	10	61	10	77
12	32	11	44	11	56			12	77
15	25	13	39	12	56	12	61	14	65
18	13	17	21	17	28	16	38	16	43
20	9	20	13	20	19	20	23	20	30
23	9	23	13	23	19	23	23	23	30
50	85	50	104	50	120	50	130	50	150
60	85	60	104	60	120	60	130	60	150
75	60	75	77	75	93	75	102	75	120
80	60	80	77	80	93	80	102	80	120

Table 2-76. Scale wind speed *W* (m/s) steady-state envelopes as functions of altitude *H* (km) for various probabilities *P* (%) for all four locations.

P = 95				*P* = 99			
H	***W***	***H***	***W***	***H***	***W***	***H***	***W***
1	22	17	44	1	28	15	70
3	31	20	29	3	38	20	41
		23	29	5	56	23	41
6	54	50	150	6	60	50	170
		60	150	7	68	60	170
10	75	75	120	9	88	75	135
11	76	80	120	11	88	80	135
12	78			12	92		
13	74			13	88		
				14	88		

Table 2-77. Buildup envelopes of 99-percentile wind speed change (m/s), 1- to 80-km reference altitude region, KSC.

Wind Speed at Reference Altitude (m/s)	Altitude Interval (m)									
	5,000	4,000	3,000	2,000	1,000	800	600	400	200	100
≥90	65.6	59.5	52.3	43.5	34.0	29.0	23.8	17.9	11.2	6.8
=80	60.4	55.5	49.7	42.0	32.7	27.7	22.7	17.0	10.6	6.5
=70	56.0	51.7	47.0	40.4	31.2	26.6	21.8	16.4	10.1	6.2
=60	51.3	48.5	44.5	38.6	30.0	25.6	21.1	15.8	9.8	6.0
=50	46.5	45.0	41.2	36.5	28.5	24.4	20.0	15.0	9.2	5.7
=40	38.5	37.7	36.8	34.9	26.5	22.6	18.5	13.8	8.6	5.3
=30	28.0	27.5	26.5	24.5	20.8	17.8	14.5	10.8	6.7	4.1
=20	17.6	17.3	16.6	15.8	14.6	12.5	10.2	7.2	4.7	2.9

Table 2-78. Back-off envelopes of 99-percentile wind speed change (m/s), 1- to 80-km reference altitude region, KSC.

Wind Speed at Reference Altitude (m/s)	Altitude Interval (m)									
	5,000	4,000	3,000	2,000	1,000	800	600	400	200	100
≥90	77.5	74.4	68.0	59.3	42.6	36.4	29.7	22.4	13.8	8.5
=80	71.0	68.0	63.8	56.0	40.5	34.7	28.5	21.4	13.2	8.1
=70	63.5	61.0	57.9	52.0	38.8	33.1	27.0	20.3	12.5	7.7
=60	56.0	54.7	52.3	47.4	36.0	31.0	25.3	18.9	11.7	7.2
=50	47.5	47.0	46.2	43.8	33.0	28.3	23.2	17.5	10.7	6.6
=40	39.0	38.0	37.0	35.3	29.5	25.3	20.6	15.5	9.6	5.9
=30	30.0	30.0	29.4	26.9	22.6	19.4	15.8	11.9	7.3	4.5
=20	18.0	17.5	16.7	15.7	14.2	12.2	9.9	7.5	4.6	2.8

Table 2-79. Buildup envelopes of 99-percentile wind speed change (m/s), 1- to 80-km reference altitude region, VAFB.

Wind Speed at Reference Altitude (m/s)	Altitude Interval (m)									
	5,000	4,000	3,000	2,000	1,000	800	600	400	200	100
≥90	62.1	59.9	57.8	51.5	35.2	30.1	24.6	18.4	11.5	7.0
=80	58.7	57.7	55.6	48.8	33.5	29.0	23.6	17.8	11.0	6.7
=70	55.0	54.5	53.4	48.1	33.0	28.8	23.0	16.8	10.5	6.5
=60	50.4	49.9	49.0	44.0	32.7	27.9	22.8	16.2	9.7	5.3
=50	45.4	44.8	43.7	40.0	29.9	25.4	21.8	15.6	9.2	5.0
=40	38.9	38.7	37.2	34.9	25.1	22.4	19.1	14.9	8.8	4.7
=30	30.0	29.4	28.3	25.4	19.9	17.8	14.8	11.5	7.1	4.2
=20	20.0	19.8	19.5	18.4	15.0	13.1	10.9	8.0	4.7	2.6

Table 2-80. Back-off envelopes of 99-percentile wind speed change (m/s), 1- to 80-km reference altitude region, VAFB.

Wind Speed at Reference Altitude (m/s)	Altitude Interval (m)									
	5,000	4,000	3,000	2,000	1,000	800	600	400	200	100
≥90	66.9	62.5	57.7	49.9	37.5	32.1	26.1	19.7	12.0	7.4
=80	64.1	60.8	56.6	48.3	36.9	31.5	25.6	19.1	11.6	6.8
=70	62.0	59.2	54.8	47.1	36.0	31.0	25.0	18.6	11.2	6.5
=60	57.1	54.5	51.3	45.4	32.6	28.5	23.0	17.1	10.2	5.3
=50	49.6	47.8	45.7	42.1	30.1	25.9	20.8	15.5	9.2	5.0
=40	39.4	38.8	37.9	35.5	25.9	23.5	19.6	14.0	8.2	4.8
=30	29.9	29.3	28.3	26.3	20.5	18.6	15.8	12.2	8.0	4.6
=20	19.8	19.5	19.0	17.7	13.4	12.2	10.7	9.0	6.3	4.3

Table 2-81. Buildup envelopes of 99-percentile wind speed change (m/s), 1- to 80-km reference altitude region, WSMR.

Wind Speed at Reference Altitude (m/s)	Altitude Interval (m)									
	5,000	4,000	3,000	2,000	1,000	800	600	400	200	100
≥90	70.7	67.0	61.2	52.4	42.0	36.0	29.4	22.1	13.6	8.4
=80	66.0	63.0	57.7	50.0	40.2	34.5	28.1	21.2	13.0	8.0
=70	60.2	57.0	53.0	46.5	38.0	32.6	26.6	20.0	12.3	7.6
=60	52.4	50.0	46.5	42.3	35.5	30.5	24.9	18.7	11.5	7.1
=50	44.8	43.0	40.2	36.5	32.0	28.3	23.1	17.4	10.7	6.6
=40	36.4	35.3	33.8	31.0	27.5	23.6	19.3	14.5	8.9	5.5
=30	27.4	26.5	25.6	24.3	20.6	17.7	14.4	10.8	6.7	4.1
=20	18.4	17.7	17.3	16.5	15.0	12.9	10.5	7.9	4.9	3.0

Table 2-82. Back-off envelopes of 99-percentile wind speed change (m/s), 1- to 80-km reference altitude region, WSMR.

Wind Speed at Reference Altitude (m/s)	Altitude Interval (m)									
	5,000	4,000	3,000	2,000	1,000	800	600	400	200	100
≥90	66.2	62.0	57.0	50.0	37.0	31.7	25.9	19.5	12.0	7.4
=80	62.0	58.5	54.0	48.0	35.8	30.7	25.1	18.9	11.6	7.1
=70	57.5	54.5	50.7	44.3	34.2	29.3	23.9	18.0	11.1	6.8
=60	52.6	49.2	45.5	40.5	32.8	28.1	23.0	17.3	10.6	6.5
=50	45.0	42.8	40.1	37.0	31.0	26.6	21.7	16.3	10.0	6.2
=40	36.5	35.5	34.8	33.5	29.3	25.1	20.5	15.4	9.5	5.8
=30	27.4	27.0	26.4	24.8	22.0	19.3	15.8	11.8	7.3	4.5
=20	17.7	17.3	16.7	15.8	14.1	12.1	9.9	7.4	4.6	2.8

Table 2-83. Buildup envelopes of 99-percentile wind speed change (m/s), 1- to 80-km reference altitude region, EAFB.

Wind Speed at Reference Altitude (m/s)	Altitude Interval (m)									
	5,000	4,000	3,000	2,000	1,000	800	600	400	200	100
≥90	69.0	65.0	59.5	52.0	39.5	33.9	27.7	20.8	12.8	7.9
=80	64.9	61.8	56.9	50.0	38.2	32.8	26.7	20.1	12.4	7.6
=70	59.0	57.0	53.0	46.8	37.0	31.7	25.9	19.5	12.0	7.4
=60	51.8	50.4	47.8	43.6	35.5	30.5	24.9	18.7	11.5	7.1
=50	44.8	43.6	41.3	38.2	31.8	27.5	22.4	16.9	10.4	6.4
=40	36.5	35.5	34.3	32.0	26.5	23.0	18.8	14.1	8.7	5.3
=30	28.0	27.3	26.3	24.5	20.8	17.8	14.6	11.0	6.7	4.2
=20	18.0	17.7	17.4	16.7	15.2	13.0	10.6	8.0	4.9	3.0

Table 2-84. Back-off envelopes of 99-percentile wind speed change (m/s), 1- to 80-km reference altitude region, EAFB.

Wind Speed at Reference Altitude (m/s)	Altitude Interval (m)									
	5,000	4,000	3,000	2,000	1,000	800	600	400	200	100
≥90	75.2	72.0	67.3	59.0	42.8	36.7	30.2	22.5	13.9	8.5
=80	68.0	66.3	62.5	55.5	40.8	35.0	28.6	21.5	13.2	8.1
=70	60.4	59.0	56.8	51.4	38.7	33.2	27.0	20.4	12.5	7.7
=60	53.0	51.8	49.3	45.0	36.0	30.9	25.2	19.0	11.7	7.2
=50	44.5	43.3	41.5	38.4	32.0	27.5	22.4	16.9	10.4	6.4
=40	35.7	35.3	34.5	33.0	27.0	23.2	18.9	14.2	8.8	5.4
=30	27.1	27.0	26.9	26.3	21.4	18.4	15.0	11.3	6.9	4.3
=20	18.0	17.0	16.6	15.7	14.2	12.2	9.9	7.5	4.6	2.8

Table 2-85. Buildup envelopes of 99-percentile wind speed change (m/s), 1- to 80-km reference altitude region for all four locations.

Wind Speed at Reference Altitude (m/s)	Altitude Interval (m)									
	5,000	4,000	3,000	2,000	1,000	800	600	400	200	100
≥ 90	71.0	67.0	61.2	52.4	42.0	36.0	29.4	22.1	13.6	8.4
= 80	66.5	63.0	57.7	50.0	40.2	34.5	28.1	21.2	13.0	8.0
= 70	61.2	58.5	53.8	48.1	38.0	32.6	26.6	20.0	12.3	7.6
= 60	54.4	52.5	50.0	44.2	35.5	30.5	24.9	18.7	11.5	7.1
= 50	46.5	45.0	43.7	40.0	33.0	28.3	23.2	17.4	10.7	6.6
= 40	38.9	38.7	37.2	34.9	27.6	23.7	19.3	14.9	8.9	5.5
= 30	30.0	29.4	28.3	25.4	20.8	17.8	14.8	11.5	7.1	4.2
= 20	20.0	19.8	19.5	18.4	15.2	13.1	10.9	8.0	4.9	3.0

Table 2-86. Back-off envelopes of 99-percentile wind speed change (m/s), 1- to 80-km reference altitude region for all four locations.

Wind Speed at Reference Altitude (m/s)	Altitude Interval (m)									
	5,000	4,000	3,000	2,000	1,000	800	600	400	200	100
≥ 90	77.5	74.4	68.0	59.3	42.8	36.7	30.2	22.5	13.9	8.5
= 80	71.0	68.0	63.8	56.0	40.8	35.0	28.6	21.5	13.2	8.1
= 70	63.5	61.0	57.9	52.0	38.8	33.2	27.0	20.4	12.5	7.7
= 60	57.1	54.7	52.3	47.4	36.0	31.0	25.3	19.0	11.7	7.2
= 50	49.6	47.8	46.2	43.8	33.0	28.3	23.2	17.5	10.7	6.6
= 40	39.4	38.8	37.9	35.5	29.5	25.3	20.6	15.5	9.6	5.9
= 30	30.0	30.0	29.4	26.9	22.6	19.4	15.8	12.2	7.3	4.6
= 20	19.8	19.5	19.0	17.7	14.2	12.2	10.7	9.0	6.3	4.3

Back-off magnitudes describe the speed change which may be experienced above the chosen level. Both buildup and back-off wind speed change data are presented in this section as a function of reference-level wind vector magnitude and geographical location. Wind buildup or back-off may be determined for a vehicle with other than a vertical flight path by multiplying the wind speed change by the cosine of the angle between the vertical axis and the vertical trajectory. Wind shears for scales of distance $\Delta H \geq 1{,}000$-m thickness are computed from rawinsonde and rocketsonde observations, while the small-scale shears associated with scales of distance $\Delta H \leq 1{,}000$ m are computed from a relationship developed by Fichtl (ref. 2-81) based on experimental results from FPS-16 radar/Jimsphere balloon wind sensor measurements of the detail wind profile structure. This relationship states that the back-off or buildup wind shear Δu for $\Delta H < 1{,}000$ m for a given risk of exceedance is related to the $\Delta H = 1{,}000$ m shear, $(\Delta u)_{1{,}000}$, at the same risk of exceedance, through the expression

$$\Delta u = (\Delta u)_{1{,}000}\left(\frac{\Delta H}{1{,}000}\right)^{0.7}, \tag{2.134}$$

where ΔH has the units of meters. Equation (2.134) was used to construct tables 2-77 to 2-86 for scales of distance ≤1,000 m.

An envelope of the 99-percentile wind speed buildup is used currently in constructing synthetic wind profiles. For most design studies, the use of this 99-percent scalar buildup wind shear data is warranted. The envelopes for back-off shears have application to certain design studies and should be considered where appropriate. These envelopes are not meant to imply perfect correlation between shears for the various scales of distance; however, certain correlations do exist, depending upon the scale of distance and the wind speed magnitude considered. This method of describing the wind shear for vehicle design has proven to be especially acceptable in preliminary design studies since the dynamic response of the structure or control system of a vehicle is essentially influenced by specific wavelengths as represented by a given wind shear. Construction of synthetic profiles for vehicle design applications is described in section 2.4.5.

Wind speed change (shear) statistics for various locations differ primarily because of prevailing meteorological conditions, orographic features, and data sample size. Significant differences, especially from an engineering standpoint, are known to exist in the shear profiles for different locations. Therefore, consistent vehicle design shear data (99 percentile) representing four active or potentially operational space vehicle launch or landing sites are presented in tables 2-77 through 2-84; i.e., for KSC, VAFB, WSMR, and EAFB. Tables 2-85 and 2-86 envelope the 99-percentile shears from these four locations. They are applicable when initial design or operational capability has not been restricted to a specific launch site or may involve several geographical locations. However, if the specific geographic location for application has been determined as being near one of the four referenced sites, then the relevant data should be applied. Tables 2-77 through 2-86 present wind speed (at any reference altitude between 1 and 80 km) versus any altitude interval (varying between 100 and 5,000 m), resulting in the 99 percentile of wind speed change (in m/s) over that selected altitude interval.

2.4.3.2 Wind Direction Change Envelopes. This section provides representative information on wind direction change, $\Delta\theta$, for scales of distance $\Delta H \leq 4$ km. Wind direction change is defined as the total change in direction of wind vectors at the top and bottom of a specified layer. Wind direction changes can occur above or below a reference point in the atmosphere. As in the case of the wind speed changes in section 2.4.3.1, we will call changes below the reference level buildup wind changes and those above the reference level back-off wind direction changes. These changes can be significantly different. For example, if the reference point is at the 4-km level, the buildup changes between the 1- and 4-km levels will be distinctly different from the back-off changes between the 5- to 7-km levels. This results from the fact that variations of wind direction tend to be larger in the atmospheric boundary layer. In this light, the following model is recommended as an integrated wind direction change criterion for design studies. The model consists of the 8- to 16-km, 99-percent direction changes in figure 2-43 and a set of functions $R(\Delta H, H_r, u_r)$ to transfer these changes to any reference level H_r above the 1-km level, where u_r is the reference level wind speed.

The quantity R is defined such that multiplication of the 8- to 16-km wind direction changes by $R(\Delta H, H_r, u_r)$ will yield the changes in wind direction over a layer of thickness ΔH with top or bottom of the reference level located at height H_r above sea level and reference level wind speed equal to u_r. The functions $R(\Delta H, H_r, u_r)$ for back-off and buildup wind direction changes are defined as follows:

Back-off:

$$R = R^* \qquad 1 \leq H_r < 1.5 \text{ km}$$

$$R = 2(1-R^*)\,(H_r - 1.5) + R^* \qquad 1.5 \leq H_r < 2 \text{ km}$$

$$R = 1 \qquad 2 \text{ km} \leq H_r\,.$$

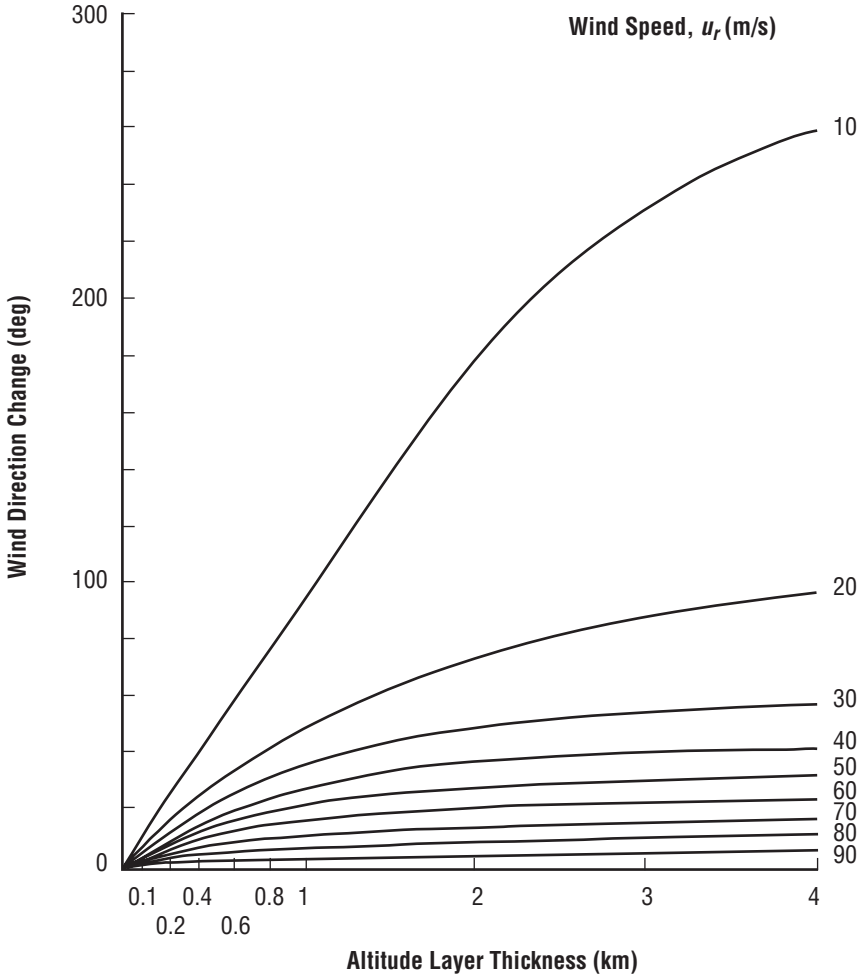

Figure 2-43. Idealized 99-percent wind direction change as a function of wind speed for varying layers in the 8- to 16-km-altitude region of KSC.

Buildup:

$$R = R^* \qquad 0 < H_r \le 2 \text{ km}$$

$$\left.\begin{aligned} R &= \left[\frac{R^*-1}{2}\right]\left[1-\cos\pi\left(\Delta H - H_r + 3\right)\right]+1,\ 1 < \Delta H \le H_r - 2 \\ R &= R^*,\ H_r - 2 < \Delta H \le H_r \end{aligned}\right\} \qquad 2 < H_r \le 3 \text{ km}$$

$$\left.\begin{aligned} R &= 1,\ 0 < \Delta H \le H_r - 3 \text{ km} \\ R &= \left[\frac{R^*-1}{2}\right]\left[1-\cos\pi\left(\Delta H - H_r + 3\right)\right]+1,\ H_r - 3 < \Delta H \le H_r - 2 \\ R &= R^*,\ H_r - 2 < \Delta H \le 4 \text{ km} \end{aligned}\right\} \qquad 3 < H_r \le 6 \text{ km}$$

$$R = 1 \qquad 6 \text{ km} \le H_r \text{ ,}$$

where ΔH and H_r have units of kilometers and R is a nondimensional quantity. The quantity R^* is a function of ΔH and u_r and is given in figure 2-44.

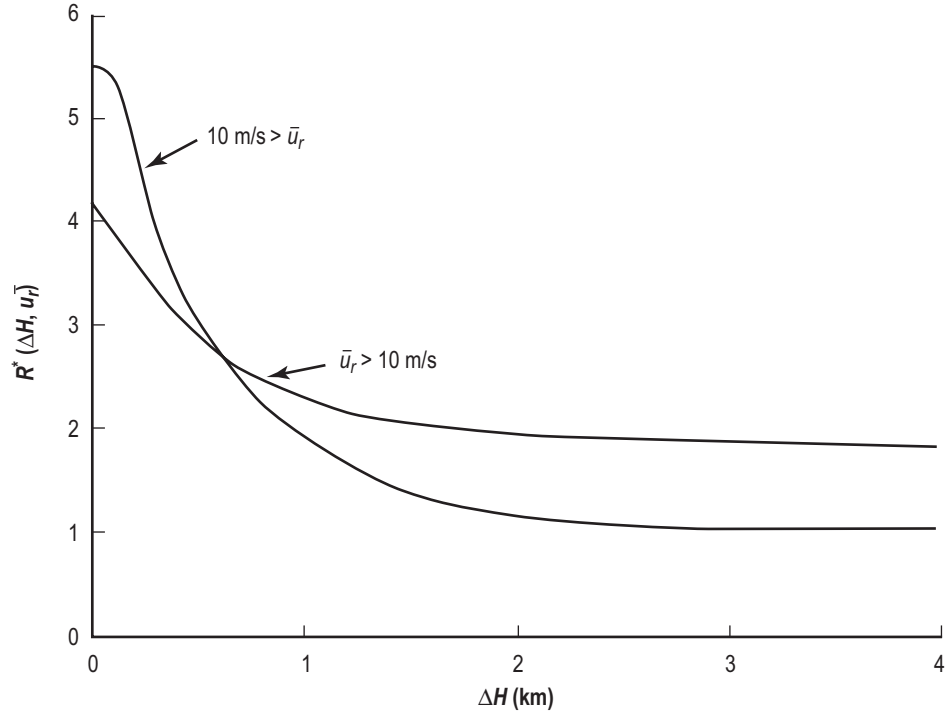

Figure 2-44. The function R^* versus ΔH for various categories of wind speed, $\bar{u}_r$, at the reference level.

To apply these wind direction change data, one first constructs a synthetic wind profile (see sec. 2.4.5), wind profile envelopes, and wind speed envelopes, with or without gusts (see sec. 2.3.6), as the case may be. A reference point is selected at height H_r above sea level on this synthetic wind profile. One then turns the wind direction above or below this point according to the schedule of wind direction changes given by the preceding model. Thus, for example, if the 12-km reference point wind speed and direction are 20 m/s and 90º (east wind; i.e., a wind blowing from the east), then according to the wind direction change model discussed previously, the wind directions at 0.2, 0.6, 1, 2, 3, and 4 km below or above the 12-km reference point, as the case may be, are 107º, 123º, 140º, 165º, 180º, and 190º for clockwise turning of the wind vector starting with the reference point wind vector at 12 km and looking toward the Earth. Counterclockwise turning is also permissible. The direction of rotation of the wind vector should be selected to produce the most adverse wind situation from a vehicle response point of view.

In view of the unavailability of wind direction change statistics above the 16-km level, at this time, it is recommended that the preceding procedure be used for $H_r > 16$ km.

2.4.4 Classical Discrete Gust

Discrete gusts are specified in an attempt to represent, in a physically reasonable manner, characteristics of small-scale motions associated with vertical profiles of wind velocity. Gust structure usually is quite complex

and it is not always understood. For vehicle design studies, discrete gusts are usually idealized because of their complexity and to enhance their utilization.

Well-defined, sharp-edged, and repeated sinusoidal gusts are important types in terms of their influence on space vehicles. Quasi-square wave gusts with amplitudes of ≈9 m/s have been estimated as extreme gusts, and have been used in various NASA aerospace vehicle design studies. These gusts are frequently referred to as embedded jets or singularities in the vertical profile wind (see fig. 2-34). By definition, a gust is a wind speed in excess of the defined steady-state value; therefore, these gusts are employed on top of the steady-state wind profile values.

If a design wind speed profile envelope without a wind shear envelope is to be used in a design study, it is recommended that the associated discrete gust vary in length from 60 to 300 m. The leading and trailing edge should conform to a 1-cos buildup of 30 m and corresponding decay also over 30 m, as shown in figure 2-17. The plateau region of the gust can vary in thickness from zero to 240 m. An analytical expression for the value of this gust (u_g) of height, H, above natural grade is given by

$$u_g = \frac{A}{2}\left(1-\cos\left[\frac{\pi}{30}\left(H-H_b\right)\right]\right), H_b \le H \le H_b + 30 \text{ m} \ ,$$

$$u_g = A, \ H_b + 30 \text{ m} \le H \le H_b + \lambda - 30 \text{ m} \ ,$$

and

$$u_g = \frac{A}{2}\left(1-\cos\left[\frac{\pi}{30}\left(H-H_b-\lambda\right)\right]\right), H_b + \lambda - 30 \text{ m} \le H \le H_b + \lambda \ , \tag{2.135}$$

where H_b is the height of the base of the gust above natural grade, λ is the gust thickness ($60 \le \lambda \le 300$ m), A is the gust amplitude, and meter-kilogram-second units are understood.

The gust amplitude is a function of H_b, and for design purposes, the 1-percent risk gust amplitude is given by

$$A = 6 \text{ m/s} \ , \quad H_b < 300 \text{ m} \ ,$$

$$A = \frac{3}{700}\left(H_b - 300\right) + 6, \ 300 \text{ m} \le H_b \le 1{,}000 \text{ m} \ ,$$

and

$$A = 9 \text{ m/s} \ , \ 1{,}000 \text{ m} < H_b \ . \tag{2.136}$$

If a wind speed profile envelope with a buildup wind shear envelope (sec. 2.3.6) is to be used in a design study, it is recommended that the previously mentioned discrete gust be modified by replacing the leading edge 1-cos shape with the following formula:

$$u_g = 10A\left(\frac{H-H_b}{30}\right)^{0.9} - 0.9\left(\frac{H-H_b}{30}\right), \ H_b \le \text{H} \le H_b + 30 \text{ m} \ . \tag{2.137}$$

The height of the gust base, H_b, corresponds to the point where the design wind speed profile envelope intersects the design buildup shear envelope. If a discrete gust is to be used with a back-off wind shear envelope, then the 1-cos trailing edge shall be given by

$$u_g = 10A\left(\frac{H_b + \lambda - H}{30}\right)^{0.9} - 0.9\left(\frac{H_b + \lambda - H}{30}\right),\ H_b + \lambda - 30\ \text{m} \le h \le H_b + \lambda\,, \tag{2.138}$$

and the leading edge shall conform to a 1-cos shape. In this case, the height, $H_b + \lambda$, of the end of the gust corresponds to the point where the design wind speed profile envelope intersects the design back-off shear envelope. This modification of the 1-cos shape at the leading and trailing edges, as the case may be, results in a continuous merger of the shear envelope and the discrete gust and shear should be reduced to 0.85 of the original value to account for the nonperfect correlation between wind shears and gusts (sec. 2.3.9.2 gives details).

2.4.4.1 Sinusoidal Gust. Another form of discrete gust that has been observed is approximately sinusoidal in nature, where gusts occur in succession. Figure 2-45 illustrates the estimated number of consecutive approximately sinusoidal type gusts that may occur and their respective amplitudes for design purposes. It is extremely important when applying these gusts in vehicle studies to realize that these are pure, mathematical sinusoidal representations that are an oversimplification of what has been observed in nature. These gusts should be superimposed symmetrically upon the steady-state profile. The data presented here on sinusoidal gusts are, at best, initial representations and should be treated as such in design studies.

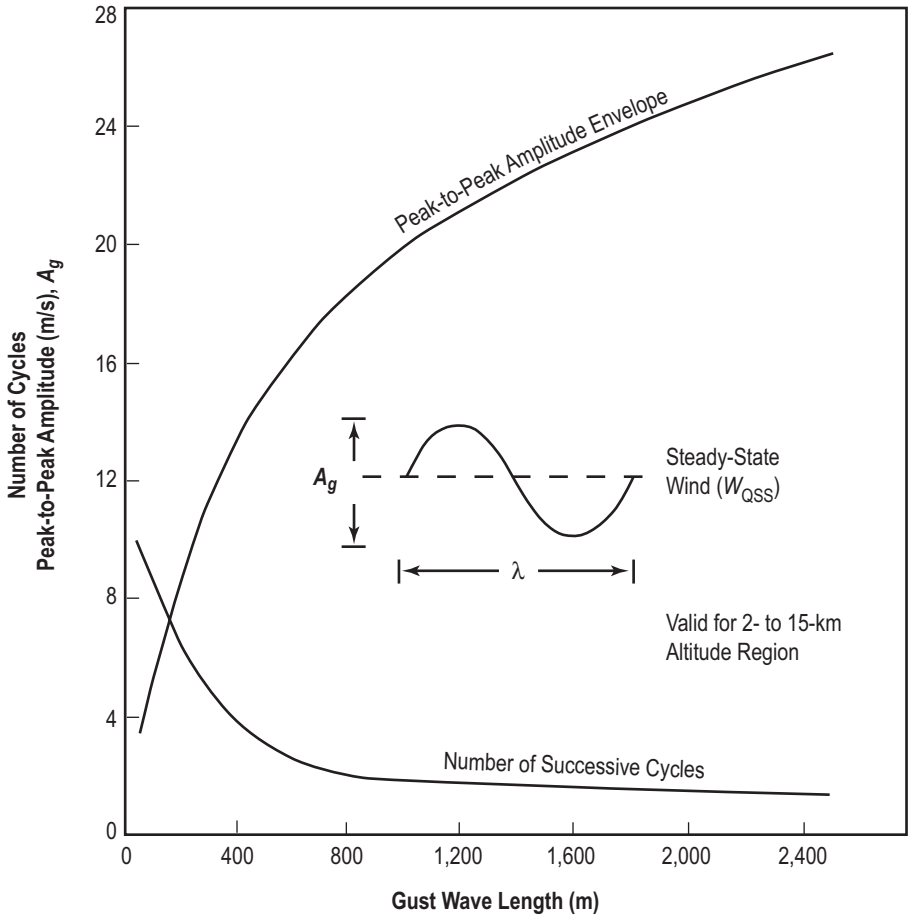

Figure 2-45. Best estimate of expected (≥99 percentile) gust amplitude and number of cycles as a function of gust wavelenth.

2.4.4.2 An Undamped-Damped Sinusoidal Gust Model. The sinusoidal gust profile model presented in this section is an extension of the gust presented in section 2.4.4.1. This model is recommended for idealized analysis to determine to what wind profile perturbations (wavelengths) and amplitudes a vehicle's guidance and control systems and structures respond. The gust model is for wind components (u' and v'). It is completely defined by a simple undamped-damped sine function in terms of gust length, L ($2 \times L$ = wavelength), and phase angle, ϕ, by

$$u' = v' = a_1 e^{[b(H-\theta)H]} \sin\left[\left[\frac{\pi H}{L}\right] + \phi\right], \tag{2.139}$$

where

H = altitude (km)
L = gust length (km)
ϕ = phase angle in radians ($-\pi/2 \le \phi \le \pi/2$)
u' = components (m/s)
v' = components (m/s)
e = 0.0110 km^{-2} for ($0 \le H \le 12$) for all L's
b = –0.0025 km^{-2} for ($12 < H \le 24$) for all L's
a_1 = function of L for the altitude intervals given in table 2-87.

Table 2-87. Gust length (L) versus coefficient a_1 for two altitude regions (H).

L (m)	a_1 (m/s)	
	$0 \le H \le 12$ (km)	$12 < H \le 24$ (km)
400	2.95	5.6375
800	5.00	9.5600
1,600	7.00	13.3834

Three gust lengths are given in this model. The gust amplitude depends on the gust length. For only three phase angles between the components, there are nine possible combinations for each of the three gust lengths. Figures 2-46 to 2-48 illustrate the u-component gust model for the three phases and the three gust lengths. It is recommended that the first engineering analysis be performed using the gust component in-phase and then out-of-phase for each of the three gust lengths added to the profiles of the monthly mean wind components as shown in figures 2-49 and 2-50 for a zero phase angle and a gust length, L, of 800 m.

The gust profile model may also be applied to any other wind component percentile profile or the envelope of the profile of wind vector ellipses. The most significant characteristic of this model is the number of idealized perturbations versus altitude. The amplitudes are in good agreement with the wind shear statistics for corresponding shear intervals and gust lengths. It is no more severe than that given by the previous sinusoidal gust model.

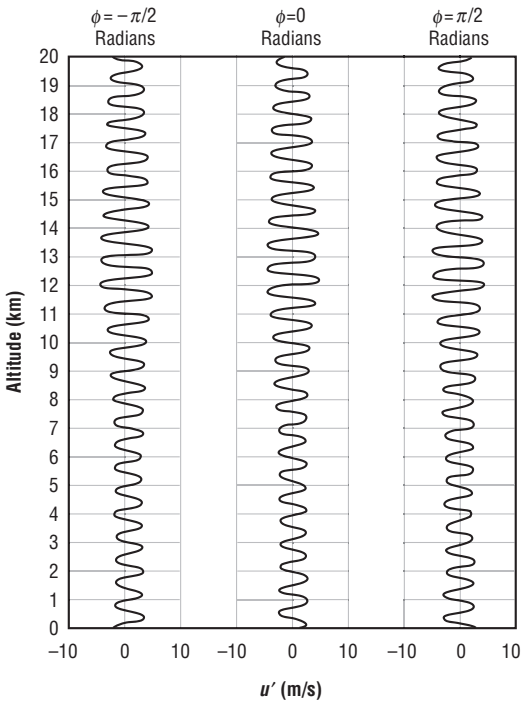

Figure 2-46. Undamped-damped sine gust model: L = 400 m.

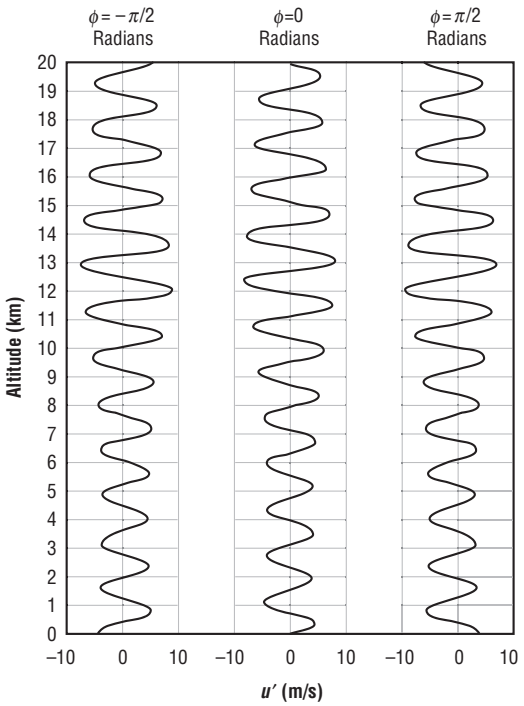

Figure 2-47. Undamped-damped sine gust model: L = 800 m

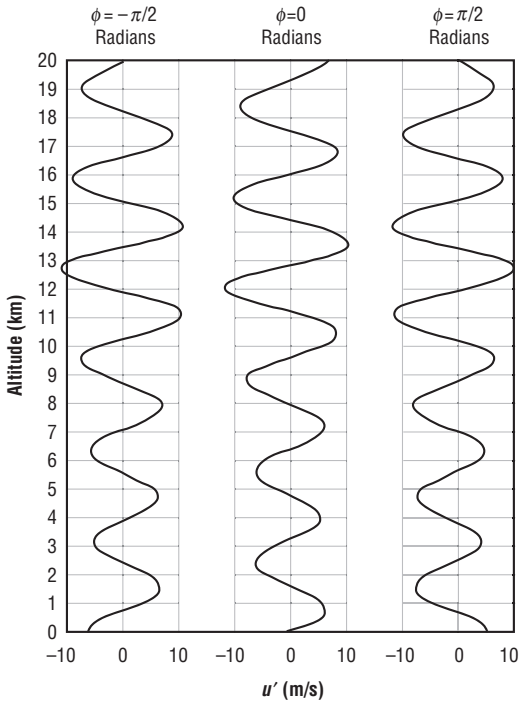

Figure 2-48. Undamped-damped sine gust model: L = 1,600 m.

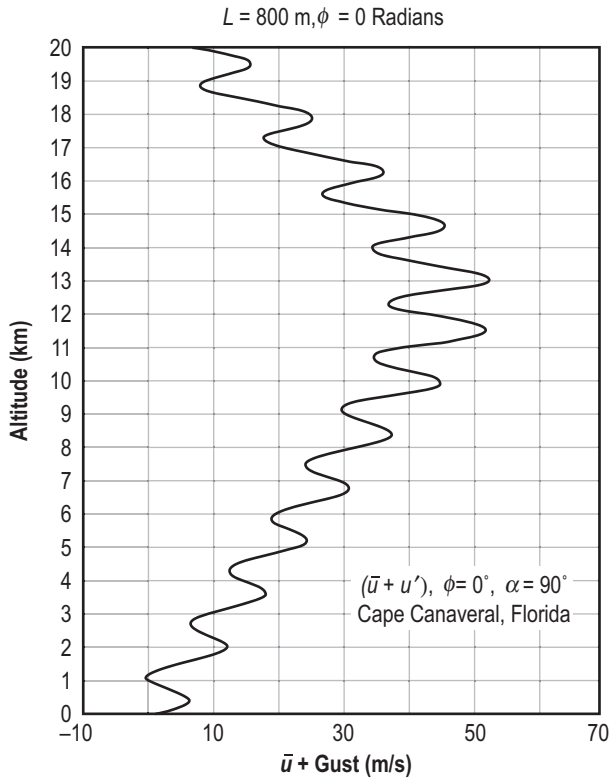

Figure 2-49. Mean zonal wind component combined with gust.

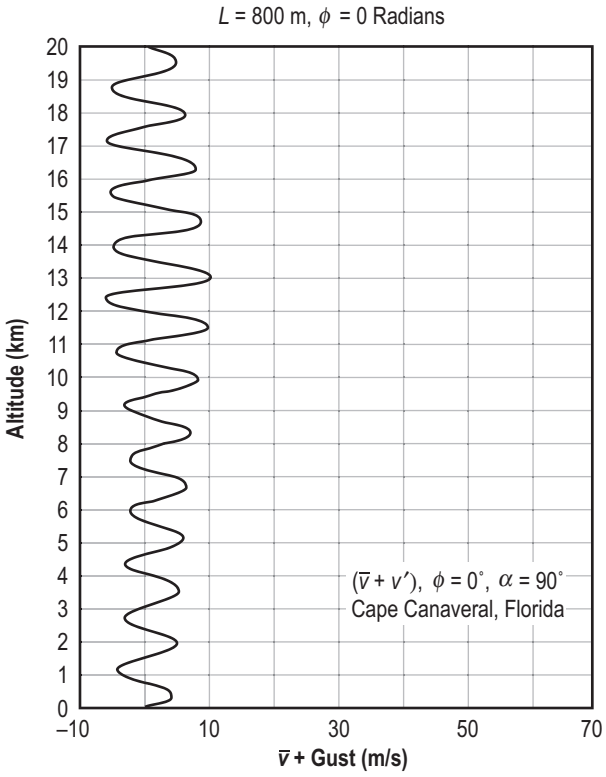

Figure 2-50. Mean meridional wind component combined with gust.

2.4.5 Classical Construction of Synthetic Wind Speed Profiles

Methods of constructing synthetic wind speed profiles are described herein. One method uses wind speed profile envelopes (sec. 2.4.2) and discrete gusts or spectra (sec. 2.3.6) without considering the correlation between the shears and gusts. Another method (sec. 2.4.5.2) takes into account the relationships between the wind shear and gust characteristics.

2.4.5.1 Synthetic Wind Speed Profiles for Vertical Flight Path Considering Only Speeds and Shears. In the method that follows, correlation between the wind speed profile envelope and wind shear envelope is considered. The method is illustrated with the 95-percentile nondirectional (scalar) wind speed profile and the 99-percentile scalar wind speed buildup for KSC (fig. 2-51) and is stated as follows:

(1) Start with a speed on the design wind speed profile envelope at a selected (reference) altitude.

(2) Subtract the amount of the shear (wind speed change) for each required altitude layer from the value of the wind speed profile envelope at the selected altitude. Figure 2-51 presents an example of a 99-percentile shear buildup envelope starting from a reference altitude of 11 km on the KSC 95-percentile wind speed profile envelope (table 2-87). The 10-km wind speed of 41.3 m/s is determined by subtracting 31.7 m/s; i.e., a linearly interpolated shear value for 73 m/s from the 1,000-m column of table 2-77, from 73 m/s.

(3) Plot values obtained for each altitude layer at the corresponding altitudes. (The value of 41.3 m/s, obtained in the example in (2), would be plotted at 10 km.) Continue plotting values until a 5,000-m layer is reached (5,000 m below the selected altitude).

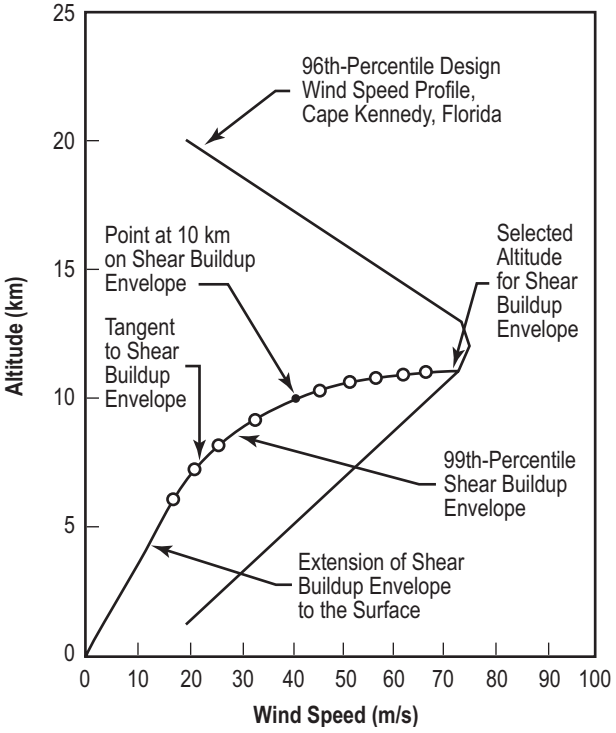

Figure 2-51. Example of synthetic wind speed profile construction without addition of gust.

(4) Draw a smooth curve through the plotted points starting at the selected altitude on the wind speed profile envelope. The lowest point is extended from the origin with a straight-line tangent to the plotted shear buildup curve. This curve then becomes the shear buildup envelope.

2.4.5.2 Synthetic Wind Speed Profiles for Vertical Flight Path Considering Relationships Between Speeds, Shears, and Gusts. In the construction of a synthetic wind speed profile, the lack of perfect correlation between the wind shear and gust can be taken into account by multiplying the shears (wind speed changes) (sec. 2.4.3.1) and the recommended design discrete gusts (sec. 2.3.6) by a factor of 0.85 before constructing the synthetic wind profile. This is equivalent, as an engineering approximation, to taking the combined 99-percentile values for the gusts and shears in a perfectly correlated manner. This approach was used successfully in both the Apollo/Saturn and Space Shuttle vehicle development programs.

Thus, to construct the synthetic wind speed profile (considering relationships between shears, speeds, and gusts, using the wind speed envelopes given in sec. 2.4.2), the following procedure is used:

(1) Construct the shear buildup envelope in the way described in section 2.4.5.1, except multiply the values of wind speed change used for each scale of distance by 0.85. (In the example for the selected altitude of 11 km, the point at 10 km will be found by using the wind speed change of 31.2×0.85, or 25.5 m/s.) This value subtracted from 73 m/s then gives a value of 46.5 m/s for the point plotted at 10 km instead of the value of 41.8 m/s used when shear and gust relationships were not considered.

(2) The discrete gust is superimposed on the buildup wind shear envelope/wind speed profile envelope by adding the gust given by equation (2.135) with leading edge in the region $H_b \le H \le H_b + 30$ m replaced with

equation (2.137). The base of the discrete gust is located at the intersection of the buildup wind shear envelope and the wind speed profile envelope (fig. 2-52). The gust amplitude, A, shall be multiplied by a factor of 0.85 to account for the nonperfect correlation between shears and gusts. Figure 2-53 gives an example of a synthetic profile with shears and gust in combination.

(3) When the gust ends at the design wind envelope, the synthetic wind profile may follow the design wind speed envelope or shear back-off profile. If the synthetic wind profile follows the design wind speed envelope, then the trailing edge of the discrete gust will be a 1-cos shape as given by equation (2.135). If the synthetic wind profile follows the shear back-off profile, then the trailing edge of the discrete gust will be that given by equation (2.138). This modified gust shape will guarantee a continuous transition from the gust to the back-off shear envelope. Vehicle response through both the wind profile envelope with gusts and the synthetic wind profile with shears and gusts in combination should be examined.

(4) If a power spectrum representation (sec. 2.3.8) is used, then disregard all previous references to discrete gusts. Use the 0.85 factor on shears and apply the spectrum as given in section 2.3.8.2.

Figures 2-52 and 2-53 show an example using the 95-percentile design wind speed profile envelope, the 99-percentile wind speed buildup envelope, and the modified 1-cos discrete gust shape.

2.4.5.3 Synthetic Wind Profile Merged to the Ground Wind Profile. Up to this point we have considered only those wind shear envelopes that are linearly extrapolated to a zero wind condition at the ground. This procedure does not allow for the possibility of the vehicle entering a wind shear envelope/gust above the H = 1,000-m altitude in a perturbed state resulting from excitations of the control system by the ground wind profile and the associated ground wind shears and gusts. To allow for these possibilities, it is recommended that the wind shear envelopes which begin above the 3,000-m level be combined with the wind profile envelope and discrete gust as stated in section 2.4.2; however, a linear extrapolation shall be used to merge the wind defined by the shear envelope at the 3,000-m level with the 1,000-m wind on the wind profile envelope.

The steady-state ground wind profile up to the 150-m level is defined by the peak wind profile (sec. 2.2.5.2) reduced to a steady-state wind profile by division with a 10-min average gust factor profile (sec. 2.2.7.1). To merge, this steady-state wind speed in the layer between 150 to 300 m shall take on a constant value equal to the steady-state wind at the 150-m level defined by the peak wind profile and gust factor profile between the surface of the Earth and the 150-m level. The flow between the 300-m level and 1,000-m level shall be obtained by linear interpolation. If the discontinuities in slope of the wind profile at the 150-, 300-, and 1,000-m levels resulting from this merging procedure introduce significant false vehicle responses, it is recommended that this interpolation procedure be replaced with a procedure involving a smooth, continuous function which closely approximates the piece-wise linear segment interpolation function between the 150- and 1,000-m levels with continuous values of wind speed and slope at the 150- and 1,000-m levels.

2.4.5.4 Synthetic Wind Speed Profiles for Nonvertical Flight Path. To apply the synthetic wind profile for other than vertical flight, multiply the wind shear buildup and back-off values by the cosine of the angle between the vertical axis (Earth-fixed coordinate system) and the vehicle's flight path. The gust (or turbulence spectra) is applied directly to the vehicle without respect to the flight path angle. The synthetic wind profile is otherwise developed according to procedures given in section 2.4.5.2.

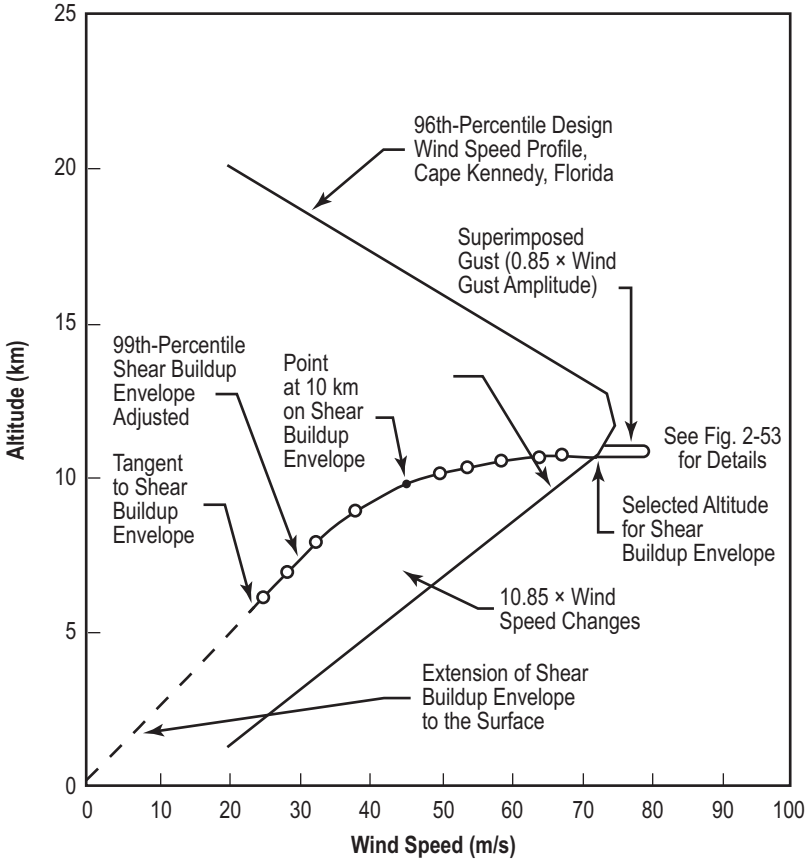

Figure 2-52. Example of synthetic wind profile construction with relationship of wind shears and gusts assumed.

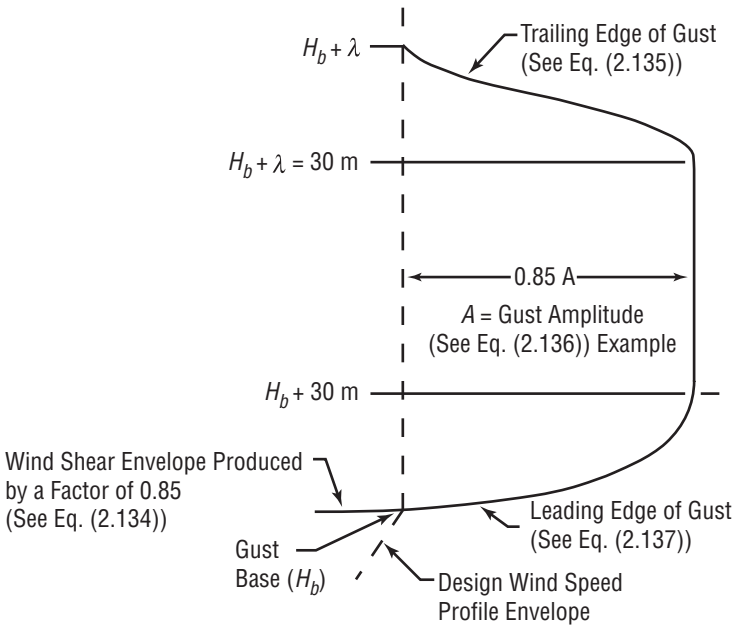

Figure 2-53. Relationship between revised gust shape, wind profile envelope, and speed buildup (shear) envelope.

2.5 Cape Canaveral (KSC) Sea/Land Breeze Winds

The sea breeze (SB) is a thermally driven, mesoscale circulation that develops normally in warm season coastal areas when the daytime land temperature becomes greater than the adjacent water temperature. The relatively cool and moist SB forms after sunrise and moves shoreward when this temperature differential becomes greater than the forcing from the large-scale (L.S.) wind regime that exists. Weaker river breezes can also form. A land breeze (LB) is the opposite of the SB and blows out to sea during the night when the land becomes cooler than the adjacent ocean. Besides the thermal difference between land and water, the strength; i.e., magnitude and extent of the SB or LB, is very dependent on the existing, prevailing, L.S. wind that can either enhance or diminish the generation and movement of the SB. A temperature inversion aloft also tends to cap the vertical growth of the SB circulation cell, limiting its development.

Both the nocturnal LB and the daytime SB at KSC are operationally significant in that their occurrence and timing can impact low-level winds, atmospheric stability, low or high temperatures, fog development, and convective activity. The SB cell itself can create a wind shear in the lowest 3,000 ft of the coastal atmosphere, higher if you consider return flow over the SB insulation. This phenomenon could have an impact on the roll-maneuver of the Shuttle after lift-off.

2.5.1 Sea Breeze

KSC can experience an SB or LB wind effect throughout the year, but they are more noticeable during the more quiescent summer season. The SB front is a region of ascending vertical motion and low-level convergence, which can lead to convection. The curved KSC coastline, along with any interactions between the SB and the local river breeze circulations (with divergent flow), can also produce localized areas of enhanced convergence and convection. Another area of convergence that affects the formation of convection at the Cape is the trailing convergence line (TCL), in which the SB frontal movement produces a quasi-stationary trailing convergence line directly behind the SB front. The Cape's climatological daily expectancy of thunderstorms varies from near 10 percent in May to over 50 percent in August. The sea breeze has been shown to be the dominant factor influencing thunderstorm development in the warm season (ref. 2-82).

Cetola used 2 yr (317 days) of KSC meteorological tower data at the 16.5-m level to document an initial climatology for the Cape Canaveral SB in 1997 (ref. 2-82). This study produced the statistics given in tables 2-88 and 2-89.

Table 2-88. Summertime KSC/Cape Canaveral SB climatology* (ref. 2-82).

	% Days With SB	Avg. Arrival Time of SB (at No. 112)**	% Days With River Breeze	SB Penetrated ≥30 km Inland	% Days When TCL Formed	% Days of SB Thunder-storms	Max. L.S. Wind Threshold for SB
Statistic	194/317=61%	1528Z (1028 EST)	116/317=37%	81% (with 1–4 m/s SB avg. prop. speed)	30/317= 9.5%	53%	12.9 m/s (offshore) 6.7 m/s (onshore)
Remarks	With all L.S. flow (mainly SE & SW, but not NE); SB on 94% of days when calm L.S. winds	From all directions; Earliest avg. 1415Z (NE) and latest avg. 1628Z (SW)	Occurred during weak L.S. wind flow	Penetration reduced when offshore L.S. wind flow >4 m/s		Storms most likely when L.S. wind flow from SW	SB may not be detected if L.S. wind flow values are greater than these

* Based on 194 SB days out of 317 total KSC summer days, observed over 2 yr.
**Range of SB passage times at tower No. 112 is dependent on the L.S. wind flow; SB can vary from 1205Z to 2120Z.

Table 2-89. KSC SB statistics for cloud, temperature change, types, thunderstorms, and SB arrival times (ref. 2-82).

	Percentage of SB Days (when clear or scattered sky in early morning)	Average Land-Sea Temperature Difference	Three Types of SB Passages at KSC (from most common to least common)	Percentage of SB Types Resulting in Thunderstorms (on SB days)
Statistic	88%	5.3 °C (for SB days)	*Type 1 – NE @(57%) *Type 2 – SE @(27%) *Type 3 – NE/SE @(16%) *All types (avg.)	49% 59% 63% 53%
Remark	3% of SB days, when overcast in morning (61% of non-SB days started clear/scattered)	3.7 °C (for non-SB days)	* Direction from which the SB comes into KSC area @ percentage occurring on SB days.	• >80% thunderstorm occurrence, when SB failed to penetrate >10 km inland • 80% of SB days with thunderstorms (occur when L.S. flow from SE or SW)

Nineteen percent of the SB fronts failed to penetrate the entire depth of the Cape meteorological tower network (30 km). Sea breeze passage time at towers was delayed during offshore flow >4 m/s. The average passage time was at 1637Z. For the 11 days in which the SB penetrated <10 km, the average wind speed was 8 m/s and the average passage time was at 1649Z. These weakly penetrating SBs also had a higher probability of thunderstorms. The weaker Banana and Indian River breezes do not significantly reduce the propagation speed of the SB in the Cape area.

Cloud cover and maximum temperatures also play a major role in the formation of the SB, which can then trigger convective thunderstorms. See table 2-89 statistics.

The TCL is infrequent and develops only with the type 3 sea breeze, which occurs with weak L.S. forcing. Convective thunderstorms are 13 percent more likely to occur on SB days with a TCL than without one.

Published in 1979, Reed (ref. 2-83) studied the Cape Canaveral SB using 2½ yr of wind observations taken from five levels on the KSC 150-m meteorological tower No. 313. He determined that the sea/land breeze wind components (u,v) at KSC showed an elliptical clockwise diurnal oscillation whose amplitude increased with height. Initially the sea breeze blows perpendicular to the coastline (westward), but throughout the day, friction and the Coriolis effect act to veer the winds toward the north, more parallel to the coastline. The monthly wind component averages for the 150-m level were the largest in May (4.3 m/s) and the smallest in January (1.3 m/s). The daily passage of the SB and its associated wind shift from seaward to landward flow (at low levels) arrived as early as 1430Z (0930 EST) in November and as late as 1800Z (1300 EST) in January. Summer shifts generally came between 1500Z and 1600Z (1000 and 1100 EST).

The Florida SB frontal height is seldom greater than ≈300 m (≈1,000 ft) (ref. 2-84), but it can be ≈500 m (≈1,500 ft) or higher in vertical thickness. Its influence can even exceed 1 km (≈3,000 ft) above the surface for low-level flow (refs. 2-83 and 2-84). See table 2-90 for values of maximum sea and land breeze frontal thickness, penetration, and return flow estimates. The typical oceanic return flow (seaward) aloft (associated with a low-level SB) normally is weaker, and at KSC, can exist up to and beyond 2 km above ground level. However, worldwide, the return flow can exist up to the 700-mb level (≈3 km, or ≈10,000 ft), and can even have a vertical range of influence extending from 1 to 4 km above ground/sea level.

Table 2-90. KSC SB/LB front/return flow thickness, penetration, and wind speed (refs. 2-85 through 2-87).

	Maximum Vertical Depth Above Surface*	Typical Maximum Wind Speed*
SB front	Depth=1 km	6.5 m/s
SB return flow	Depth=2.6 km	Less than SB above
SB penetration	90 km inland and 110 km seaward	–
LB front	Depth >0.3 km	4 m/s
LB return flow	Depth=2 km	Less than LB above

*Worldwide extremes can exceed these values.

A temperature inversion aloft will tend to limit the vertical growth of the SB frontal depth, and thereby its return flow as well.

The KSC SB can propagate inward a considerable distance, whereas the river breeze tends to remain almost stationary. The western propagation speed of the SB front generally averages between 2.7 and 2.9 m/s for the two modes of flow over KSC. When this western-moving SB penetrates around 60 or 70 km inland, it sometimes collides with the opposite, west coast, eastern propagating sea breeze which then creates an area of greater convection/storm cells. These storm cells normally then propagate eastward toward the Atlantic coast with an average return speed of 9 to 14.3 m/s for the two modes of flow (ref. 2-88).

2.5.2 Sea Breeze Extreme Wind Shear

The onset of a coastal sea breeze circulation cell can alter the wind field from the surface to over 3 km altitude by producing a vertical wind shear that previously may not have existed. The Shuttle roll maneuver can occur from 120 m (0.12 km) to over 1,120 m (1.12 km), depending upon the Shuttle's mission/flight plan, launch inclination, etc. Therefore, we need to estimate the magnitude of wind shear associated with the development of a sea breeze and ascertain if it might present a problem to the launch roll maneuver.

During descent, it has been determined that hazardous vertical wind shear, which can affect aircraft landing, normally occurs in the lowest 100 m (boundary layer) above the ground. These shear values range from 0.084 s^{-1}; i.e., 2.5 m/s over 30 m vertical thickness, up to 0.160 s^{-1}; i.e., 5 m/s over 30 m (ref. 2-89). Low-level extreme wind shears have been measured at the KSC 150-m tower No. 313 and at other coastal and noncoastal sites around the world via various methods. The most extreme wind shear measured at tower No. 313—for a high wind case—was a value of 0.160 s^{-1} between the 120- to 150-m level. Lower tower levels gave higher 30-m-interval wind shears; i.e., 0.173 s^{-1} between 90 and 120 m, with higher maximum shear values measured below these altitude levels (ref. 2-89). These extreme values resulted from high wind conditions and not necessarily because of the onset of an intense sea or land breeze. Above 3-km altitude, NASA has computed wind shear percentiles for July that apply to the KSC 3- to 16-km altitude levels. These 99-percent wind shears, for height intervals ranging from 100- to 1,000-m, range from 0.063 s^{-1} to 0.019 s^{-1}, respectfully (ref. 2-90).

Other investigators have also documented extreme values of low-level wind shear near KSC or at other similar coastal sites. Stewart (ref. 2-91) presented wind shear aloft data along the 80th meridian by month. The 99-percentile worst month value for a 1-km shear interval between zero and 1 km, interpolated for the KSC latitude, was ≈0.020 s^{-1}. Essenwanger (ref. 2-92) presented extreme wind shear results measured by radiosonde at the coastal site of Miami, FL. He presented shear at both 50- and 100-m intervals from zero to 1.5 km (in 0.5-km steps). The 50-m interval wind shears were greater in magnitude than the 100-m shears, and gave

maximum values of 0.202 s^{-1}, 0.184 s^{-1}, and 0.172 s^{-1} at 0–0.5 km, 0.5–1 km, and 1–1.5 km, respectively. Again, these extreme wind shears probably resulted from storminess rather than sea breeze effects.

Aviation experience tells us that a shear of 0.084 to 0.160 s^{-1} (over 30 m) could present a low-level problem in aircraft landing. Since wind shear values have been measured at coastal Miami that exceed these aviation redline values, the question exists regarding what low-level wind shear magnitudes could develop only from a coastal sea or land breeze onset.

With regard to estimating a typical extreme sea breeze-generated, low-level wind shear, not much is given in the literature. However, some sea breeze front and return flow information is available and can be used to infer a maximum possible vertical sea breeze-developed wind shear value.

At KSC, the sea breeze frontal height can range from 20 m up to >1 km above ground level (AGL). The return flow circulation can range from 0.5 km up to >2-km altitude AGL, with a maximum of 2.6 km (ref. 2-93). The altitude within the sea breeze front—in which the maximum horizontal easterly wind speed normally occurs—can vary from 100 to 700 m, but normally is near 400 m. The altitude of the return flow westerly wind maximum normally occurs between 1.3- to 2.5-km altitude, but normally is near 1.6 km (refs. 2-94 and 2-95).

The maximum KSC area sea breeze wind speed can range up to ≈6.5 m/s (westward). The maximum wind speed aloft of the return flow is normally weaker than the near-surface sea breeze winds. However, if the prevailing winds aloft are westerly, the return flow winds can be enhanced up to perhaps ≈6.5 m/s (eastward) or more. Taking the altitude of 700 m (for sea breeze maximum wind) and 1.3 km (for return flow maximum wind), we arrive at a 13 m/s horizontal wind speed difference that occurs over a 600-m altitude interval. This results in an estimated vertical wind shear of ≈0.022 s^{-1} over this 600-m interval. This shear value would correspond to a 3- to 16-km KSC July (600 m) 98-percentile vertical wind shear. KSC winter months experience stronger vertical wind shears than in July.

The vertical wind speed, above the surface sea breeze frontal area, occurring between 0.7- and 1-km altitude, can vary in magnitude between 2.6 and 3 m/s, maximum (refs. 2-94 and 2-95).

This estimated sea breeze wind shear value (and wind vertical velocity above the sea breeze front) can be used in roll maneuver or other engineering calculations for an approximate maximum sea breeze vertical wind shear that could be encountered.

2.5.3 Land Breeze

Accurate predictions of the KSC land breeze are critical for toxic material dispersion forecasts associated with space launch missions, as wind direction and low-level stability can change with the onset of an LB (ref. 2-96). Over a 7-yr KSC period of record, Case produced the following LB results, as shown in tables 2-91 and 2-92 for the 393 LB events that occurred.

Land breezes can occur during any month of the year, but were most common for KSC in April (7.1 avg./mo), May, July, and August. While the least common months for LB occurrence were during December (2.1 avg./mo) and January. The land breeze circulation at KSC is generally much weaker than the sea breeze in both velocity and height of development.

Table 2-91. KSC LB occurrences (ref. 2-96).

	Nonconvective Months	Convective Months	Annual
Months	Oct–May	June–Sept	Jan–Dec
Percent LBs	63.1%	36.9%	100%
Avg. No. LB/season	35.4/cool season	20.7/warm season	56.1/yr
Avg. No. LB/month	4.4/cool month	5.2/warm month	4.7/mo

Table 2-92. KSC LB characteristics (ref. 2-96).

	Result
LB Depth:	
Deep (>150 m)	>80% of deep events had SB on prior afternoon
Shallow (<150 m)	<40% of shallow events had SB on prior afternoon
LB Onset Time:	
Latest: Oct–Jan	6.5 to 8 hr after sunset
Earliest: May–July	4 to 5 hr after sunset
Direction of LB:	
Oct–Nov	From the NW
Apr–Aug	From the W or SW
Winter	From any direction
LB front passage: Stability effect; i.e., temperature change	• Decrease in near-surface stability; i.e., temperature decrease at 54 ft (16.5 m) and an increase at 6 ft (1.8 m) • Negligible effect in near-surface stability in summer months • Fog was more common at night with an LB in place

2.6 Other Wind Subsection Locations

Wind information is also presented within other sections of this document. The wind correction factor for surfaces with respect to radiation balances is given in section 4.5.5.2. Extreme surface winds dealing with tornadoes, hurricanes, and foehn are in section 5.2.2.5. The wind speed effect on falling raindrops is in section 7.2.4.3. The wind effect on falling hail is in section 7.2.7.3.2. Winds affecting sand and dust storms are presented in section 10.3.3. The wind effects on buildings involving tornadic and hurricane forces are in section 12.2. Winds relating to other phenomena including gustnado, landspout, waterspout, firewhirl, and downburst/microburst are presented in section 12.5. The hurricane wind fatigue model is given in section 12.6.1, while wind/rain damage to the Thermal Protection System is mentioned in section 12.6.2. Estimating hurricane wind gusts over land and the decay after landfall are presented in sections 12.6.6.2.4 and 12.6.6.2.5, respectively. Hurricane wind probabilities are described in section 12.6.7.2, while KSC hurricane peak winds are presented in section 12.6.9.2. Nor'easter information is given in section 12.6.10. Severe wind weather site maps are given in section 12.7, while section 12.8 presents a unique set of measured landfall wind speeds from Hurricane Ivan. Wind statistical procedures used in mission planning are in section 15.1.1. In-flight wind exceedance probabilities are expressed in section 15.1.3. Finally, the prelaunch Shuttle wind monitoring plan is presented in section 15.2.

REFERENCES

2-1. Smith, O.E.; and Adelfang, S.I.: "A Compendium of Wind Statistics and Models for the NASA Space Shuttle and Other Aerospace Vehicle Programs," *NASA CR–1998–208859*, NASA Marshall Space Flight Center, AL, October 1998.

2-2. Carter, E.A.; and Schuknecht, L.A.: "Peak Wind Statistics Associated With Thunderstorms at Cape Kennedy, Florida," *NASA CR–61304*, NASA Marshall Space Flight Center, AL, August 1969.

2-3. Gumbel, E.J.: *Statistics of Extremes*, Columbia University Press, New York, NY, 1958.

2-4. Smith, O.E.; Falls, L.W.; and Brown, S.C.: "Research Achievements Review," Vol. II, Report No. 10, "Terrestrial and Space Environment Research at MSFC," *NASA TM X–53706*, NASA Marshall Space Flight Center, AL, 1967.

2-5. Lee, R.F.; Goodge G.W.; and Crutcher, H.L.: "Surface Climatological Information for Twelve Selected Stations for Reentry Vehicles," *NASA CR–61319*, NASA Marshall Space Flight Center, AL, 1970.

2-6. Goodge, G.W.; Bilton, T.H.; and Quinlin, F.T.: "Surface Climatological Information for Twelve Selected Stations for Reentry Vehicles," *NASA CR–61342*, NASA Marshall Space Flight Center, AL, 1971.

2-7. Fichtl, G.H.; and McVehil, G.E.: "Longitudinal and Lateral Spectra of Turbulence in the Atmospheric Boundary Layer at the Kennedy Space Center," *J. Appl. Meteor.*, Vol. 9, No. 1, pp. 51–63, February 1970.

2-8. Blackadar, A.K.; Dutton, J.A.; Panofsky, H.A.; et al.: "Investigation of the Turbulent Wind Field Below 150-m Altitude at the Eastern Test Range," *NASA CR–1410*, NASA Marshall Space Flight Center, AL, August 1969.

2-9. McVehil, G.E.; and Camnitz, H.G.: "Ground Wind Characteristics at Kennedy Space Center," *NASA CR–1418*, NASA Marshall Space Flight Center, AL, September 1969.

2-10. Fichtl, G.H.; Kaufman, J.W.; and Vaughan, W.W.: "Characteristics of Atmospheric Turbulence as Related to Wind Loads on Tall Structures," *J. Spacecraft & Rockets*, Vol. 6, No. 12, pp. 1396–1403, December 1969.

2-11. Fichtl, G.H.: "Problems in the Simulation of Atmospheric Boundary Layer Flows," AGARD–DP–140 (1973) 2-1, Presented at AGARD Flight Mechanics Panel Symposium on Flight in Turbulence, England, May 1973.

2-12. Fichtl, G.H.: "Wind Shear Near the Ground and Aircraft Operations," *J. Spacecraft & Rockets*, Vol. 9, No. 11, pp. 765–770, November 1972.

2-13. Fichtl, G.H.: "Probability Distribution of Vertical Longitudinal Shear Fluctuations," *J. Appl. Meteor.*, Vol. 11, No. 6, pp. 918–925 September 1972.

2-14. Fichtl, G.H.: "Standard Deviation of Vertical Two-Point Longitudinal Velocity Differences in the Boundary Layer," *Boundary-Layer Meteorology*, Vol. 2, pp. 137–151, 1971.

2-15. Luers, J.K.; and Reese, J.B.: "Effects of Shear on Aircraft Landing," *NASA CR–2287*, Marshall Space Flight Center, AL, July 1973.

2-16. Luers, J.K.: "A Model of Wind Shear and Turbulence in the Surface Boundary Layer," *NASA CR–2288*, Marshall Space Flight Center, AL, July 1973.

2-17. Sowa, D.: "Low-Level Wind Shear," D.C. Flight Approach, No. 20, Douglas Aircraft Co., Long Beach, CA, 1974.

2-18. Barr, N.M.; Gangaas, D.; and Schaeffer, D.R.: "Wind Models for Flight Simulator Certification of Landing and Approach Guidance and Control Systems," Report No. FAA–RD–74–206, U.S. Department of Transportation, Federal Aviation Administration, Washington, DC 20590, December 1974.

2-19. Lewell, W.S.; and Williamson, G.G.: "Wind Shear and Turbulence Around Airports, *NASA CR–2752*, NASA Marshall Space Flight Center, AL, October 1976.

2-20. Camp, D.W.; and Kaufman, J.W.: "Comparison of Tower Influence on Wind Velocity for NASA's 150-Meter Meteorological Tower and a Wind Tunnel Model of the Tower," *J. Geophys. Res.*, Vol. 75, No. 6, February 20, 1970.

2-21. Thom, H.C.S.: "New Distributions of Extreme Winds in the United States," J. Structural Division, in *Proc. Am. Soc. Civ. Engr.*, ST–7, pp. 1787–1801, July 1968.

2-22. Thom, H.C.S.: "Distribution of Extreme Winds Over Oceans," *J. Waterways, Harbors, and Coastal Engr. Div.*, *Proc. Am. Soc. Civ. Engr.*, Vol. 99, No. WW1, pp. 1–17, February 1973.

2-23. Falls, L.W.; and Brown, S.C.: "Optimum Runway Orientation Relative to Crosswinds," *NASA TN D–6930*, NASA Marshall Space Flight Center, AL, September 1972.

2-24. Falls, L.W.; and Crutcher, H.L.: "Determination of Statistics for Any Rotation of Axes of a Bivariate Normal Elliptical Distribution," *NASA TM X–64595*, NASA Marshall Space Flight Center, AL, May 1971.

2-25. IRIG Document No. 104-63, Range Reference Atmosphere Documents published by Secretariat, Range Commander's Council, White Sands Missile Range, NM, 1963.

2-26. Falls, L.W.: "Normal Probabilities for Cape Kennedy Wind Components—Monthly Reference Periods for All Flight Azimuths, Altitudes 0 to 70 km," *NASA TM X–64771*, NASA Marshall Space Flight Center, AL, April 16, 1973.

2-27. Falls, L.W.: "Normal Probabilities for Vandenberg AFB Wind Components—Monthly Reference Periods for All Flight Azimuths, 0- to 70-km Altitudes," *NASA TM X–64897*, NASA Marshall Space Flight Center, AL, January 1975.

2-28. Henry. R.M.: “A Statistical Model for Synthetic Wind Profiles for Aerospace Vehicle Design and Launching Criteria,” *NASA TN D–1813*, NASA Langley Research Center, AL, 1963.

2-29. Bieber, R.E.: “Missile Structural Loads by Nonstationary Statistical Methods,” Technical Report No. LMSD 49703, Lockheed Missile and Space Division, Huntsville, AL, April 1959; Also available as DDC AD220595 or NTIS PB157733.

2-30. Vaughan, W.W.: “Interlevel and Intralevel Correlations of Wind Components for Six Geographical Locations,” *NASA TN D–561*, NASA Marshall Space Flight Center, AL, December 1960.

2-31. Daniels, G.E.; and Smith, O.E.: “Scalar and Component Wind Correlations Between Altitude Levels for Cape Kennedy, Florida, and Santa Monica, California,” *NASA TN D–3815*, NASA Marshall Space Flight Center, AL, April 1968.

2-32. Cochrane, J.A.; Henry, R.M.; and Weaver, W.L.: “Revised Upper Air Wind Data for Wallops Island Based on Serially Complete Data for the Years 1956 to 1964,” *NASA TN D–4570*, NASA Langley Research Center, Hampton, VA, May 1968.

2-33. Buell, C.E.: “Correlation Functions for Wind and Geographical on Isobaric Surfaces,” *J. Appl. Meteor.*, Vol. II, No. 1, pp. 51–59, February 1972.

2-34. Buell, C.E.: “Variability of Wind With Distance and Time on an Isobaric Surface,” *J. Appl. Meteor.*, Vol. II, No. 7, pp. 1085–1091, October 1972.

2-35. Truppi, L.E.: “Probabilities of Zero Wind Shear Phenomena Based on Rawinsonde Data Records,” *NASA TM X–53452*, NASA Marshall Space Flight Center, AL, April 1966.

2-36. Adelfang, S.I.: “Analysis of Vector Wind Change With Respect to Time for Cape Kennedy, Florida,” *NASA CR–15077*, NASA Marshall Space Flight Center, AL, August 1978.

2-37. Adelfang, S.I.: “Analysis of Vector Wind Change With Respect to Time for Vandenberg Air Force Base, California,” *NASA CR–150776*, NASA Marshall Space Flight Center, AL, August 1978.

2-38. Smith. O.E.: “Vector Wind and Vector Wind Shear Models 0- to 27-km Altitude for Cape Kennedy, Florida, and Vandenberg AFB, California,” *NASA TMX–73319*, NASA Marshall Space Flight Center, AL, July 1976.

2-39. Smith, O.E.; Adelfang, S.I.; Batts, G.W.; and Hill, C.K.: “Wind Models for the NSTS Ascent Trajectory Biasing for Wind Load Alleviation,” *NASA TM–100375*, NASA Marshall Space Flight Center, AL, August 1989.

2-40. Merceret, F.J.: “Rapid Temporal Changes of Midtropospheric Winds,” *J. Appl. Meteor.*, Vol. 36, No. 11, pp. 1567–1574, 1997.

2-41. Merceret, F.J.: “Risk Assessment Consequences of the Lognormal Distribution of Mid-Tropospheric Winds,” *J. Spacecraft & Rockets*, Vol. 35, No. 1, pp. 111–112, 1998.

2-42. Merceret, F.J.: “The Coherence Time of Mid-Tropospheric Wind Features as a Function of Vertical Scale From 300 m to 2 km,” *J. Appl. Meteor.*, Vol. 39, pp. 2409–2420, 2000.

2-43. Spiekerman, C.E.; Sako, B.H.; and Kabe, A.M.: “Identifying Slowly Varying and Turbulent Wind Features for Flight Loads Analysis,” *J. Spacecraft and Rockets*, Vol. 37, pp. 426–433, 2000.

2-44. Kabe, A.M.; Spiekerman, C.E.; Kim, M.C.; and Lee, S.S.: “Refined Day-of-Launch Atmospheric Flight Loads Approach,” *J. Spacecraft and Rockets*, Vol. 27, pp. 453–458, 2000.

2-45. Johnson, D.L.; and Brown, S.C.: “Surface to 90-km Winds for Kennedy Space Center, Florida, and Vandenberg AFB, California,” *NASA TM–78233*, NASA Marshall Space Flight Center, AL, July 1979.

2-46. Smith, O.E.; Adelfang, S.I.; and Brown, R.P.: “Ascent Structural Wind Loads for the National Space Transportation System (NSTS),” in *Proceedings of AIAA 26th Aerospace Sciences Meeting*, Paper No. AIAA–88–0293, Reno, NV, January 11–14, 1988.

2-47. Gumbel, E.J.; and Mustafi, C.K.: “Some Analytical Properties of the Bivariate Extremal Distributions,” *J. Amer. Statist. Assoc.*, Vol. 62, pp. 569–588, June 1967.

2-48. Gumbel, E.J.; Mustafi, C.K.; and Smith, O.E.: “Tables of the Probability and Density Functions for the Bivariate Extremal Distributions,” Department of Industrial Engineering, Columbia University, New York, NY, April 1968.

2-49. Kim, M.C.; Kabe, A.M.; and Lee, S.S.: “Statistical Analysis of Atmospheric Flight Gust Loads Analysis,” *J. Spacecraft and Rockets*, Vol. 37, No. 4, pp. 443–445, July–August 2000.

2-50. *Space Shuttle Flight and Ground System Specification*, Volume X, Appendix 10.10, Natural Environment Design Requirements, NASA NSTS 07700, Volume X, Book 2, Revision M, p. 10.10-26, June 9, 1999.

2-51. Johnson, D.: “Wind Gust Procedure for Shuttle Ascent,” NASA MSFC Memorandum EL23 (13–97), March 25, 1997.

2-52. “Military Specification Flying Qualities of Piloted Airplanes,” *MIL–F–8785B (ASG)*, August 7, 1969.

2-53. Adelfang, S.I.; and Smith, O.E.: “Gust Models for Launch Vehicle Ascent,” in *Proceedings of 36th Aerospace Sciences Meeting*, Paper No. AIAA 98–0747, Reno, NV, January 1998.

2-54. Adelfang, S.I.; and Smith, O.E.: “Wind Gust for Shuttle Ascent, Part II,” White Paper prepared for Electromagnetics and Aerospace Environments Branch, NASA Marshall Space Flight Center, in support of Shuttle Systems Integration Office, March 25, 1997.

2-55. Johnson, D.L. (ed.): “Terrestrial Environment (Climatic) Criteria Guidelines for Use in Aerospace Vehicle Development,” *NASA TM 4511*, NASA Marshall Space Flight Center, AL, August 1993.

2-56. Vaughan, W.W.: “Analysis of Discrete Atmospheric Gust Velocity Data for Use in Missile Design and Performance Studies,” *ABMA Report No. DA–TR–68–59*, November 20, 1959.

2-57. NACA Technical Note 4332, "An Approach to the Problem of Estimating Severe and Repeated Gust Loads for Missile Operations," by Press, H. and Steiner, R., Langley Aeronautical Laboratory, Langley Field, VA, September 1958.

2-58. Tolefson, H.B.: "Summary of Derived Gust Velocities Obtained from Measurements Within Thunderstorms," NACA Report 1285 (supersedes NACA Technical Note 3538), Langley Aeronautical Laboratory, Langley Field, VA, July 27, 1955.

2-59. Tolefson, H.B: "Preliminary Analysis of NACA Measurements of Atmospheric Turbulence Within a Thunderstorm—U.S. Weather Bureau Thunderstorm Project," NACA Technical Note 1233, Langley Aeronautical Laboratory, Langley Field, VA, January 29, 1947.

2-60. Justus, C.G.; Campbell, W.C.; Doubleday, M.K.; and Johnson, D.L.: "New Atmosphere Turbulence Model for Shuttle Applications," *NASA TM 4168*, NASA Marshall Space Flight Center, AL, January 1990.

2-61. Smith, S.A.: "Revised Gust Model," Memo ES44–(147–89), NASA Marshall Space Flight Center, Earth Science and Applications Division, Environmental Analysis Branch, October 24, 1989.

2-62. Smith, O.E.; and Austin L.D., Jr.: "Sensitivity Analysis of the Space Shuttle to Ascent Wind Profiles," *NASA TP 1988*, NASA Marshall Space Flight Center, AL, March 1982.

2-63. Smith, O.E.; and Austin L.D., Jr.: "Space Shuttle Response to Ascent Wind Profiles," *J. Guidance Control and Dynamics*, AIAA, Vol. 6, No. 5, pp. 355–360, September–October 1983.

2-64. Henry, R.M.: "A Statistical Model for Synthetic Wind Profiles for Aerospace Vehicle Design and Launching Criteria," *NASA TN D–1813*, NASA Langley Research Center, AL, 1963.

2-65. Vaughan, W.W.: "Interlevel and Intralevel Correlations of Wind Components for Six Geographical Locations," *NASA TN P–561*, NASA Marshall Space Flight Center, AL, December 1960.

2-66. Daniels, G.E.; and Smith, O.E.: "Scalar and Component Wind Correlations Between Altitude Levels for Cape Kennedy, Florida and Santa Monica, California," *NASA TN D–3815*, NASA Marshall Space Flight Center, AL, April 1968.

2-67. Adelfang, S.I.; Smith, O.E.; and Batts, G.W.: "Ascent Wind Model for Launch Vehicle Design," *J. Spacecraft and Rockets*, Vol. 9, No. 3, pp. 502–508, May–June 1994.

2-68. Adelfang, S.I.: "User's Guide for Monthly Vector Wind Profile Model," *NASA/CR—1999–209759*, NASA Marshall Space Flight Center, AL, May 1999.

2-69. Gray, J.: "Ups and Downs of the NEW Space Launcher," *Aerospace America*, Vol. 30, pp. 26–31, June 1992.

2-70. Document 361-83, Cape Canaveral, Florida, Range Reference Atmosphere, 0- to 70-km Altitude, Secretariat, Range Commander's Council, White Sands Missile Range, NM, February 1983.

2-71. Fichtl, G.H.; Camp, D.W.; and Vaughan, W.W.: *Detailed Wind and Temperature Profiles, Clear Air Turbulence and It's Detection*, Yih-Hc Pao and Arnold Goldburg (eds.), Plenum Press, New York, pp. 308–333, 1969.

2-72. Lambert, W.C.; Merceret, F.J.; Taylor, G.E.; and Ward, J.G.: "Performance of Five 915-MHz Wind Profilers and an Associated Automated Quality Control Algorithm in an Operational Environment," *J. Atmos. and Ocean. Tech.*, Vol. 20, pp. 1488–1495, 2003.

2-73. "Flying Qualities of Piloted Aircraft," *MIL-HDBK-1797*, Department of Defense, 1997.

2-74. Chalk, C.R.; Neal, P.; Harris, T.; et al.: "Background Information and User Guide for MIL–F–8758B (ASG), 'Military Specification—Flying Qualities for Piloted Airplanes," AFFDL–TR–69–72, Air Force Flight Dynamics Laboratory, Air Force Systems Command, 1969.

2-75. Dutton, J.A.: "Broadening Horizons in Prediction of the Effects of Atmospheric Turbulence on Aeronautical Systems," AIAA Selected Reprints Series, Vol. XIII, The Earth's Atmosphere, W.W. Vaughan and L.L. DeVries (eds.), Published by the American Institute of Aeronautics and Astronautics, New York, 1972.

2-76. Justus, C.G.; Campbell, C.W.; Doubleday, M.K.; and Johnson, D.L.: "New Atmospheric Turbulence Model for Shuttle Applications," *NASA TM–4168*, NASA Marshall Space Flight Center, AL, January 1990.

2-77. Tatom, F.B.; and Smith, S.R.: "Advanced Shuttle Simulation Turbulence Tapes (SSTT) User's Guide," Engineering Analysis, Incorporated, Contract NAS8–33818, NASA Marshall Space Flight Center, September 29, 1981.

2-78. Fichtl, G.H.: "A Technique for Simulating Turbulence for Aerospace Vehicle Flight Simulation Studies," *NASA TM–78141*, NASA Marshall Space Flight Center, AL, November 1977.

2-79. Camp, D.W.; and Susko, M.: "Percentage Levels of Wind Speed Differences Computed by Using Rawinsonde Wind Profile Data From Cape Kennedy, Florida," *NASA TM X–53461*, NASA Marshall Space Flight Center, AL, May 1966.

2-80. Camp, D.W.; and Fox, P.A.: "Percentage Levels of Wind Speed Differences Computed by Using Rawinsonde Wind Profile Data From Santa Monica, California," *NASA TM X–53428*, NASA Marshall Space Flight Center, AL, October 1966.

2-81. Fichtl, G.H.: "Small-Scale Wind Shear Definition for Aerospace Vehicle Design," *J. Spacecraft & Rockets*, Vol. 9, No. 2, pp. 79–83, February 1972.

2-82. Cetola, J.D.: "A Climatology of the Sea Breeze at Cape Canaveral, Florida," MS Thesis, College of Arts and Sciences, Florida State University, Tallahassee, FL, 56 pp., 1997.

2-83. Reed, J.W.: "Cape Canaveral Sea Breezes," *J. Appl. Meteor.*, Vol. 18, pp. 231–235, February 1979.

2-84. Winsberg, M.D.; O'Brien, J.O.; Zierden, D.; and Griffin, M.: *Florida Weather*, 2nd Ed., University Press of Florida, 218 pp., 2003.

2-85. Laird, N.F.; Kristovich, D.A.R.; Rauber, R.M.; et al., "The Cape Canaveral Sea and River Breezes: Kinematic Structure and Convective Initiation," *Mon. Wea. Rev.*, Vol. 123, pp. 2942–2956, October 1995.

2-86. Zhong, S.; and Takle, E.S.: "An Observational Study of Sea- and Land-Breeze Circulation in an Area of Complex Coastal Heating," *J. Appl. Meteor.*, Vol. 31, pp. 1426–1438, December 1992.

2-87. Tunney, D.A.: "Numerical Studies of the Georgia Coast Sea Breeze," Master's Thesis, Department of Meteorology, Florida State University, Tallahassee, FL, 166 pp., 1996.

2-88. Rubes, M.T.; Cooper; H.J.; and Smith, E.A.: "A Study of the Merritt Island, Florida Sea Breeze Flow Regimes and Their Effect on Surface Heat and Moisture Fluxes," *NASA—CR–4537*, Marshall Space Flight Center, AL, July 1993.

2-89. Alexander, M.B.; and Camp, D.W.: "Analysis of Low-Altitude Wind Speed and Direction Shears," *J. Aircraft*, Vol. 22, No. 8, pp. 705–712, August 1985.

2-90. Johnson, D.L.: "Terrestrial Environment (Climatic) Criteria Handbook for Use in Aerospace Vehicle Development," *NASA–HDBK–1001*, August 11, 2000.

2-91. Stewart, D.A.: "Wind Shear and Baroclinicity in Cross Sections Along 80º W," U.S. Army Missile Command, RR–TR–67–4, February 1967.

2-92. Essenwanger, O.M.: "Use of Radiosonde Data to Derive Atmospheric Wind Shears for Small Shear Increments," Within AGARD Report No. 626, on "Effects of Surface Winds and Gusts on Aircraft Design and Operation," November 1974.

2-93. Cangialosi, J.: "An Analysis of the South Florida Sea Breeze Circulation: An Idealized Study," University of Miami/RSMAS Report, 2003.

2-94. Atkins, N.T.; and Wakimoto, R.M.: "Observations of the Sea-Breeze During CaPE, Part II: Dual-Doppler and Aircraft Analysis," *Mon. Wea. Rev.*, Vol. 123, pp. 944–969, April 1995.

2-95. Atkins, N.T.; and Wakimoto, R.M.: "Influence of the Synoptic-Scale Flow on Sea Breezes Observed During CaPE," *Mon. Wea. Rev.*, Vol. 125, pp. 2112–2130, 1997.

2-96. Case, J.L.; Wheeler, M.M.; Manobianco,, J.; Weems, J.W.; and Roeder, W.P.: A 7-yr Climatological Study of Land Breezes Over the Florida Spaceport, *J. Appl. Meteor.*, Vol. 44, pp. 340–356, 2005.

Terrestrial Environment (Climatic) Criteria Guidelines for Use in Aerospace Vehicle Development, 2008 Revision

NASA/TM—2008–215633
December 2008

D.L. Johnson, Editor

Section 3: Atmospheric Thermodynamic Properties and Models

TABLE OF CONTENTS

LIST OF FIGURES

LIST OF TABLES

LIST OF TABLES (Continued)

LIST OF ACRONYMS AND SYMBOLS

CIRA	COSPAR International Reference Atmosphere
EAFB	Edwards Air Force Base
GGUAS	Global Girded Upper Air Statistics
GRAM	Global Reference Atmospheric Model
GUACA	Global Upper Air Climatic Atlas
KSC	Kennedy Space Center
MAP	Middle Atmospheric Program
MET	Marshall Engineering Thermosphere
MG	Meteorology Group
MSFC	Marshall Space Flight Center
MSL	mean sea level
NASP	National Aero-Space Plane
NIAM	NASP Integrated Atmospheric Model
PRA	Patrick Reference Atmosphere
RCC	Range Commanders Council
RRA	Range Reference Atmosphere
VAFB	Vandenberg Air Force Base
WSMR	White Sands Missile Range

NOMENCLATURE

CV	coefficients of variation
M	molecular weight; multiplication factor
P	pressure
R	universal gas constant
r	correlation coefficients
T	temperature
T_V	virtual temperature
V	volume
w	mixing ratio of water vapor to dry air
ρ	mass density

3. ATMOSPHERIC THERMODYNAMIC PROPERTIES AND MODELS

3.1 Introduction

Section 3 presents the surface and inflight thermodynamic parameters—temperature, pressure, and density—of the atmosphere in a statistical and a modeling mode. The applicable model should be selected for design use based on the operational requirements for the aerospace vehicle. Mean and extreme values of these thermodynamic parameters can be used in application to many aerospace vehicle design and operational problems, such as (1) research planning and engineering design of remote Earth sensing systems, (2) vehicle design and development, and (3) vehicle trajectory analysis, dealing with vehicle thrust, dynamic pressure, aerodynamic drag, aerodynamic heating, vibration, structural and guidance limitations, and reentry analysis (ref. 3-1). The first part of this section gives median and extreme values of these thermodynamic variables at sea level and surface level. The thermodynamic variables are then presented as a function of altitude in terms of median and extreme values. An approach is also presented for relating temperature, pressure, and density as independent variables, with a method to obtain simultaneous values of these variables at discrete altitude levels. A subsection on reentry is presented, giving atmospheric models for use in reentry heating, trajectory, etc., analyses. Specific sites presented in this section include Kennedy Space Center (KSC), FL, Vandenberg Air Force Base (VAFB), CA, Edwards Air Force Base (EAFB), CA, and White Sands Missile Range (WSMR), NM. The NASA Marshall Space Flight Center (MSFC) Global Reference Atmospheric Model, 2007 (GRAM-07) provides inflight atmospheric thermodynamic variables for all geographical sites (see sec. 3.8). If other U.S. or world site surface extreme thermodynamic parameter values are needed, consult section 5. See Section 10 for information on atmospheric constituents. Many of the atmospheric models described in this section are available as a computer program or subroutine from the Natural Environments Branch, Engineering Directorate, NASA Marshall Space Flight Center, Marshall Space Flight Center, AL 35812.

3.2 Standard Atmosphere

A standard atmosphere is a vertical description of atmospheric temperature, pressure, and density that is usually established by international agreement and taken to be representative of the Earth's atmosphere. The first standard atmospheres established by international agreement were developed in the 1920s, primarily for the purposes of pressure altimeter calibrations and aircraft performance calculations. Later, some countries, notably the United States, also developed and published standard atmospheres. The term reference atmosphere is used to identify vertical descriptions of the atmosphere for specific geographical locations or globally, such as GRAM-07. These were developed by organizations for specific applications, especially as the aerospace industry began to mature after WWII. The term standard atmosphere has in recent years also been used by national and international organizations to describe vertical descriptions of atmospheric trace constituents, the ionosphere, aerosols, ozone, atomic oxygen, winds, water vapor, planetary atmospheres, etc. The history of standard and reference atmospheres are presented and summarized in references 3-1 through 3-4. Key atmospheric engineering models are given in references 3-5 through 3-10.

3.2.1 U.S. Standard Atmosphere—Sea Level Values (Ref. 3-5)

A standard value of sea level atmosphere pressure is defined as that pressure exerted by a 760-mm column of mercury at standard gravity (9.80665 m/s^2) at 45.5425° N. latitude and at a temperature of 273.15 K (0 °C). The recommended unit for meteorological use is 1,013.25 hPa or mb. Standard temperature is used in physics to indicate a temperature of 0 °C—the ice point—and a pressure of 1 standard atmosphere (1,013.25 hPa or mb). In meteorology, the term standard temperature has no generally accepted meaning, except that it may refer

to the temperature at zero pressure-altitude in the standard atmosphere. The annual standard sea level values of temperature, pressure, and density that have been used for years are temperature of 288.15 K (15 °C), pressure of 1013.25 mb (760 mm of Hg), and density of 1,225.00 g m^{-3}. These values are summarized in table 3-1.

Table 3-1. Annual standard sea level values of temperature, pressure, and density.

Atmospheric	International Standard Units	U.S. Customary Units
Temperature	15 °C (288.15 K)	59 °F (518.67 °R)
Pressure	1.013250×10^5 N/m^2 (Newton/m^2 is equivalent to a Pascal (Pa) in SI units; a Pascal is equivalent to 100 millibars (mb))	2,116.22 lb/ft^2 (14.696 lb/in^2)
Density	1.2250 kg/m^3	0.076474 lb/ft^3

3.2.2 U.S. Standard Atmosphere—Altitudes Above Sea Level Values (Ref. 3-5)

The portion of the U.S. Standard Atmosphere up to 32 km is identical with the ICAO Standard Atmosphere, 1964, and below 50 km with the ISO Standard Atmosphere, 1973. For this reason, in addition to providing an excellent description of the atmosphere model development and extending beyond conventional aircraft operations, the U.S. Standard Atmosphere, 1976, has been used for figures 3-1 and 3-2 to illustrate the vertical distribution of atmospheric temperature. Figure 3-1 provides an illustration of the temperature-height profiles to >90 km of the U.S. Standard Atmosphere, 1976, and the lowest and highest mean monthly temperatures obtained for any location between the Equator and pole.

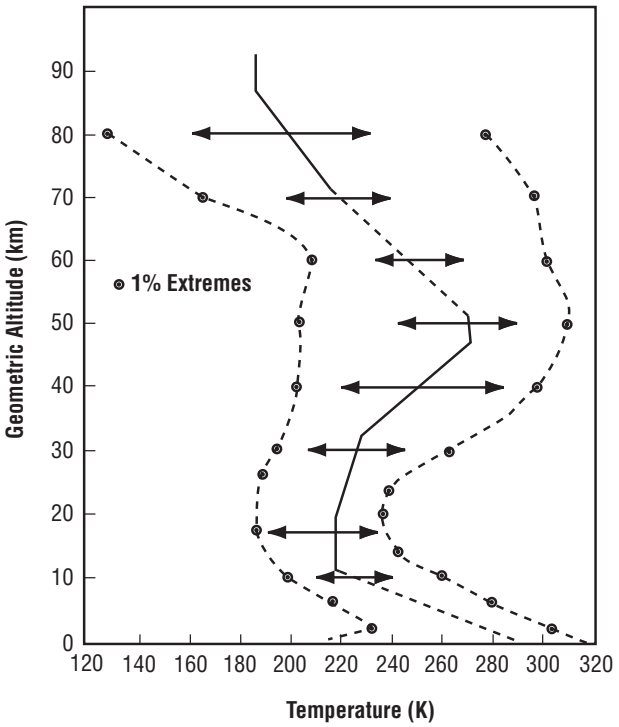

Figure 3-1. Range of systematic variability of temperature around the U.S. Standard Atmosphere, 1976 (ref. 3-5).

For altitudes above ≈100 km, significant variations in the temperature, and thus density, occur due to solar and geomagnetic activity over the period of a solar cycle. Variations in the temperature-height profiles for various degrees of solar and geomagnetic activity are presented in figure 3-2. Profile (A) gives an appreciation of the lowest temperature departures expected at solar cycle minimum, profile (B) represents average conditions at solar cycle minimum, profile (C) represents average conditions at a typical solar cycle maximum, and profile (D) gives the highest temperatures to be expected during a period of exceptionally high solar and geomagnetic activity.

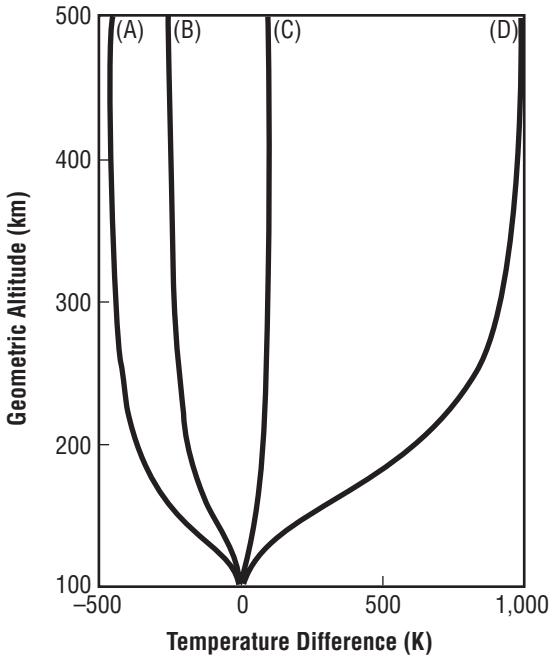

Figure 3-2. Departures of the temperature-altitude profiles from that of the U.S. Standard Atmosphere, 1976, for various degrees of solar activity (ref. 3-5).

Currently, some of the most commonly used standard and reference atmospheres include:

- COSPAR International Reference Atmosphere (CIRA), 1986
- ISO Standard Atmosphere, 1975
- NASA Global Reference Atmosphere Model (GRAM), 2007
- NRL MSIS Reference Atmosphere, 2000.
- RCC/MG Range Reference Atmospheres (RRAs)
- U.S. Standard Atmosphere, 1976
- U.S. Standard Atmosphere Supplements, 1966

In 1996, the American Institute of Aeronautics and Astronautics first published a *Guide to Reference and Standard Atmosphere Models* (ref. 3-3). This document has been updated and provides information on the principal features for over 70 global, regional, middle atmosphere, thermosphere, test ranges, and planetary reference and standard atmospheric models.

3.3 Surface Atmospheric Thermodynamic Parameters

3.3.1 Atmospheric Temperature

3.3.1.1 Temperature Definition. The normal thermodynamic definition of temperature, the derivative of energy with respect to entropy, applies to the atmospheric environment.

There is also a virtual temperature, T_V, of a sample of moist air defined as the temperature at which dry air of the same total pressure would have the same density as the sample of moist air:

$$T_V \cong T\,(1+0.61\,w)\ , \tag{3.1}$$

where w = mixing ratio of water vapor to dry air (g/g).

By substituting T_V into the ideal gas law in place of T, the variations of temperature and humidity are accounted for (to within the limits of ideal gas approximation):

$$PV = (R/M)\,T_V\ , \tag{3.2}$$

where

P = pressure
V = volume
M = molecular weight, where $M_{\text{dry air}} = 28.966$ and $M_{\text{water vapor}} = 18.016$
R = universal gas constant = 8.31436×10^7 erg$\times$K$^{-1}\times$g mol^{-1}.

3.3.1.2 Surface Temperature. Median and extreme values of surface atmospheric temperature for various NASA sites of interest are presented in section 3.4.1. Temperature-aloft statistics are also presented in section 3.4.1. Other U.S. and world surface temperature extremes are given in sections 5.1.3.1 and 5.2.2.1, respectively. Extreme and 95th-percentile values of surface temperature for selected areas are given in section 4.5.2 (table 4-10). Other radiation balance temperature effects, including hourly KSC diurnal temperature extremes and compartment temperatures, are presented in section 4.6.

3.3.2 Atmospheric Pressure

3.3.2.1 Pressure Definition. Atmospheric pressure (also called barometric pressure) (P) is the force exerted, as a consequence of gravitational attraction, by the mass of the column of air of unit cross section lying directly above the area in question. It is expressed as force per unit area (Newtons per square meter or Newtons per square centimeter or millibars).

3.3.2.2 Surface Pressure. The total variation of pressure from day to day is relatively small (<7 mb). Diurnal, semidiurnal, and terdiurnal tidal variations can all affect the normal surface atmospheric pressure pattern. Rapid and greater variations of pressure occur as the result of the passage of frontal systems, while the passage of a hurricane can cause larger (Hurricane Wilma with ≅97 mb drop in 24 hr), but still not significant, changes for pressure environment design of space vehicles. The pressure drop in a tornado is significant and can exceed 20 percent of ambient during the few seconds of its passage. Surface pressure extremes for various locations and their extreme ranges are given in table 3-2. The data at these locations were mostly taken from their respective surface weather observation summaries (see ref. 3-11 for example). Extreme surface pressures across the United States and around the world are given in sections 5.1.3.4 and 5.2.2.4, respectively.

Table 3-2. Surface station pressure extremes (values apply to station elevation above mean sea level (MSL)).

Location	Units	Pressure			Station Elevation	
		Maximum	Mean	Minimum†	(m)	(ft)
MSFC, AL	N/m^2	102,100.0	99,540.0	97,210.0		
	mb	1,021.0	995.4	972.1	196	644
	lb/in^2	14.8	14.4	14.1		
		1,020.8				
KSC, FL	N/m^2	103,600.0	101,670.0*	99,970.0	5	16
	mb	1,036.0	1,016.7*	999.7		
	lb/in^2	15.0	14.7*	14.5	2.7‡	9‡
VAFB, CA	N/m^2	102,000.0	100,250*	99,010.0	113	371
	mb	1,020.0	1,002.5*	990.1		
	lb/in^2	14.8	14.5*	14.4	112.2‡	368‡
EAFB, CA	N/m^2	95,560.0	93,410.0*	92,030.0	706	2,316
	mb	955.6	934.1*	920.3		
	lb/in^2	13.9	13.5*	13.3	701.7‡	2,302‡
MAF, LA	N/m^2	104,160.0	101,780.0	99,900.0		
	mb	1,041.6	1,017.8	999.0	2	6
	lb/in^2	15.1	14.8	14.5		
SSC, MS	N/m^2	104,410.0	101,640.0	99,150.0		
	mb	1,044.1	1,016.4	991.5	9	31
	lb/in^2	15.1	14.7	14.4		
JSC, TX	N/m^2	103,960.0	101,530.0	99,530.0		
	mb	1,039.6	1,015.3	995.3	15	50
	lb/in^2	15.1	14.7	14.4		
WSMR, NM	N/m^2	89,010.0	87,130.0*	85,200.0		
	mb	890.1	871.3*	852.0	1,292	4,239
	lb/in^2	12.9	12.6*	12.4		

* The mean values given here will differ from the median surface values as given in tables 3-11 through 3-13 and reference 3-8.

† Hurricane-influenced low pressures are not given here.

‡ Runway elevations above MSL.

3.3.2.3 Surface Pressure Change:

(1) A gradual rise or fall in pressure of 3 mb (0.04 lb in^{-2}) and then a return to original pressure can be expected within a 24-hr period for locations noted in table 3-2.

(2) A maximum pressure change (frontal passage change) of 6 mb (0.09 lb in^{-2}) (rise or fall) can be expected within a 1-hr period for all localities noted in table 3-2.

3.3.2.4 Pressure Decrease With Altitude:

(1) Pressure decrease is approximately logarithmic with height. Materials transported in mountainous terrain or in cargo compartments of aircraft must be packaged to stand the pressure differential without damage.

Near sea level; i.e., <3 km, the pressure will vary ≈1 mb for each 10-m change in altitude. Figure 3-3 shows the 1976 U.S. Standard Atmosphere's pressure decrease up to 5-km altitude (ref. 3-5). The U.S. 76 standard atmospheric pressure decreases to ≈75 percent of its surface value by 2,500 m (8,200 ft) altitude; ≈50 percent by 5,500 m (18,000 ft); and ≈25 percent by 10,500 m (34,400 ft).

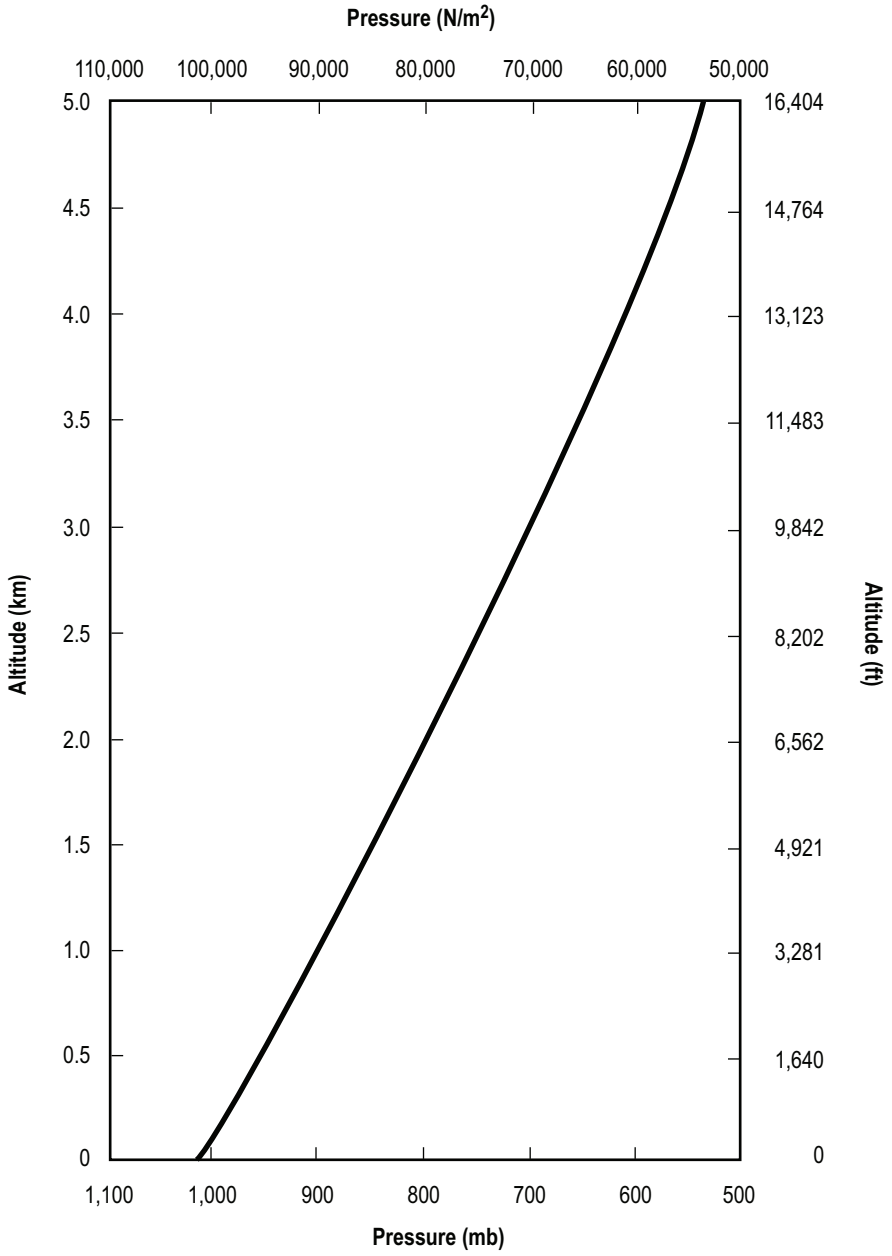

Figure 3-3. Pressure change with altitude for packaging materials (ref. 3-5).

(2) Ambient atmospheric pressure also needs to be considered in payload design. During launch and rapid ascent in the atmosphere, the payload can experience a quick ambient atmospheric pressure drop to almost zero from a surface value of 1,013 mb. Since some payloads may not tolerate low atmospheric pressures, one may need to vent internal air and/or use a barometric switch for switching functions in payload electrical subsystems. More detailed data on pressure distribution with altitude are given in section 3.4.2.

3.3.3 Atmospheric Density

3.3.3.1 Density Definition. Mass density (ρ) is the ratio of the mass of a substance to its volume. (It also is defined as the reciprocal of specific volume.) Density is usually expressed in grams per cubic centimeter or kilograms per cubic meter.

3.3.3.2 Surface Density. Generally, the horizontal distance variation of atmospheric density at the Earth's surface between the measured station value and the area of interest; i.e., launch pad, runway, at a given location is small and should have no significant effect on preflight planning and operations for a launch vehicle. Table 3-3 gives annual median density values at the surface for the four main test ranges.

Table 3-3. Annual median surface densities.

Area	Surface Altitude		Source of Data (Reference No.)	Atmospheric Density	
	(m*)	(ft)		kg/m^3	lb/ft^3
KSC, FL	5	16	3-6	1.1830	7.385×10^{-2}
VAFB, CA	113	371	3-7	1.2190	7.610×10^{-2}
WSMR, NM	1,292	4,239	3-8, item (5)	1.0580	6.661×10^{-2}
EAFB, CA	706	2,316	3-16	1.1210	6.998×10^{-2}

*Station elevation above MSL.

Atmospheric density, especially low density, is important to aircraft takeoff and landing operations and should therefore be considered when designing runway lengths or planning operations such as the Space Shuttle orbiter ferry flights. Table 3-4 gives low-density values that are equaled or exceeded ≈5 percent of the time during the hottest part of the day in summer. Typical associated temperatures needed for engine power calculations are also listed. Since low density occurs at high elevation and for high temperatures, only the highest enroute airfield and the ferry flight terminals were considered. Since KSC and VAFB density extremes are given in section 3.4.3, only EAFB and Biggs AFB are listed here.

Table 3-4. Low surface density (5 percentile worst day of the year reference) and accompanying temperatures for orbiter ferry operations.

Location	Low Density			Temperature	
	kg/m^3	lb/ft^3	Percent Departure From U.S. 76*	°C	°F
EAFB, CA	1.0246	6.396×10^{-2}	–10.5	39.4	103
Biggs AFB, TX	0.97555	6.09×10^{-2}	–10.5	37.8	100

*Departure from U.S. Standard Atmosphere, 1976 (ref. 3-5).

3.3.3.3 Surface Density Variability and Altitude Variations. Data on the variation of surface density and density aloft about its median annual values can be found in section 3.4. The MSFC Global Reference Atmosphere, 2007 (ref. 3-9) will also provide monthly mean density values versus altitude together with variability for any latitude/longitude location on the globe.

3.4 Inflight Atmospheric Thermodynamic Parameters

Median and extreme values of atmospheric temperature, pressure, and density versus altitude are presented in this section for various sites of primary interest to NASA. References 3-12 and 3-13 give worldwide extremes of the thermodynamic parameters aloft.

3.4.1 Inflight Atmospheric Temperature

3.4.1.1 Air Temperature at Altitude. Median and extreme air temperatures for the following list of test ranges were compiled from frequency distributions of radiosonde-measured temperature data from zero through 30-km altitude. Above 30-km altitude, mean and extreme temperatures for the different test ranges were obtained from meteorological rocketsonde observations:

(1) KSC air temperature values with altitude are given in table 3-5 (ref. 3-6).
(2) VAFB air temperature values with altitude are given in table 3-6 (ref. 3-7).
(3) EAFB air temperature values with altitude are given in table 3-7 (ref. 3-8, item (6)).
(4) WSMR air temperature values with altitude are given in table 3-8 (ref. 3-8, item (5)).

Table 3-5. KSC air temperatures at various altitudes.

Geometric Altitude		Minimum		Median*†		Maximum	
(km)	(ft)	(°C)	(°F)	(°C)	(°F)	(°C)	(°F)
Surface (0.005 MSL)	16	–7.2	19	23.5	74	37.2	99
1	3,281	–8.9	16	17.4	63	27.8	82
2	6,562	–10.0	14	12.2	54	21.1	70
3	9,843	–11.1	12	7.1	45	16.1	61
4	13,123	–13.9	7	1.8	35	11.1	52
5	16,404	–20.0	–4	–4.1	25	5.0	41
6	19,685	–26.1	–15	–10.5	13	–1.1	30
7	22,966	–33.9	–29	–17.4	1	–7.2	19
8	26,247	–41.1	–42	–24.8	–13	–13.9	7
9	29,528	–50.0	–58	–32.4	–26	–21.1	–6
10	32,808	–56.1	–69	–40.0	–40	–30.0	–22
16.2	53,150	–80.0	–112	–70.3	–95	–57.8	–72
20	65,617	–76.1	–105	–62.8	–81	–47.8	–54
25	82,021	–67.5	–90	–51.4	–61	–38.9	–38
30	98,425	–58.9	–74	–42.4	–44	–30.0	–22
35	114,829	–47.4	–53	–30.6	–23	–14.6	6
40	131,234	–36.7	–34	–17.8	0	1.9	35
45	147,638	–23.0	–9	–6.3	21	12.8	55
50	164,042	–18.2	–1	–2.5	27	22.0	72
55	180,446	–34.4	–30	–12.4	10	18.9	66
60	196,850	–28.5	–19	–26.1	–15	17.0	63

*For higher altitudes, see reference 3-6 and table 3-11.
†Median values aloft are annual values taken from reference 3-6.

Table 3-6. VAFB air temperatures at various altitudes.

Geometric Altitude		Minimum		Median*†		Maximum	
(km)	(ft)	(°C)	(°F)	(°C)	(°F)	(°C)	(°F)
Surface (0.1 MSL)	371	–3.9	25	12.7	55	37.8	100
1	3,281	–3.6	26	13.3	56	33.4	92
2	6,562	–7.0	19	10.1	50	28.0	82
3	9,843	–15.2	5	5.1	41	17.6	64
4	13,123	–22.6	–9	–1.0	30	12.1	54
5	16,404	–29.7	–22	–7.5	18	3.3	38
6	19,685	–35.6	–32	–14.4	6	–2.7	27
7	22,966	–43.3	–46	–21.8	–7	–9.9	14
8	26,247	–47.4	–53	–29.5	–21	–15.9	3
9	29,528	–51.3	–60	–37.3	–35	–26.8	–16
10	32,808	–57.0	–71	–44.6	–48	–31.2	–24
16.3	53,478	–76.0	–105	–64.0	–83	–51.0	–60
20	65,617	–74.9	–103	–59.8	–76	–49.0	–56
25	82,021	–69.3	–93	–51.2	–60	–39.2	–39
30	98,425	–63.7	–83	–42.7	–45	–29.4	–21
35	114,829	–53.0	–63	–32.1	–26	–5.8	22
40	131,234	–42.2	–44	–19.3	–3	17.8	64
45	147,638	–30.5	–23	–5.8	21	27.6	82
50	164,042	–18.2	–1	–2.0	28	28.0	82
55	180,446	–21.8	–7	–6.8	20	31.6	89
60	196,850	–25.1	–13	–20.5	–5	35.7	96

*For higher altitudes, see reference 3-7 and table 3-12.

†Median values aloft are annual values taken from reference 3-7.

Reference 3-14 presents a classic description of the vertical temperature profile characteristics (and the variability of the tropopause level) by altitude, month, and latitude. Reference 3-15 presents a climatological summary involving the analysis of 25 yr of Cape Canaveral, FL, rawindsonde data consisting of various monthly-mean vertical profiles of temperature, wind, and moisture for KSC.

3.4.1.2 Extreme Cold Temperature. Extreme cold temperatures for nonheated compartments during aircraft flight for KSC, VAFB, EAFB, and WSMR are given in table 3-9. Hot compartment temperatures are given in section 4, paragraph 4.6.5.

3.4.2 Inflight Atmospheric Pressure

3.4.2.1 Atmospheric Pressure at Altitude. Envelopes of atmospheric pressure extremes for all four locations (KSC, VAFB, EAFB, and WSMR) are given in table 3-10. These values were taken from pressure frequency distributions of radiosonde observations from the four test ranges. Pressure means and extremes were computed above 25-km altitude using meteorological rocketsonde measurements.

Mean and extreme values of station pressure for many locations of interest are given in table 3-2, whereas median pressure values up to 90-km altitude for the four key sites are given in tables 3-11 through 3-13, and in reference 3-8. The U.S. Standard Atmosphere's pressure decrease with altitude is illustrated in figure 3-1.

Table 3-7. EAFB air temperatures at various altitudes.

Geometric Altitude		Minimum		Median*†		Maximum	
(km)	(ft)	(°C)	(°F)	(°C)	(°F)	(°C)	(°F)
Surface (0.7 MSL)	2,316	–15.6	4	16.1	61	45.0	113
1	3,281	–6.0	21	16.2	61	35.3	96
2	6,562	–12.9	9	11.2	53	26.2	79
3	9,843	–16.9	2	5.1	42	19.0	66
4	13,123	–23.4	–10	–1.0	30	10.7	51
5	16,404	–29.7	–21	–7.5	17	5.2	41
6	19,685	–35.2	–31	–14.4	4	–2.9	27
7	22,966	–42.0	–44	–21.8	–9	–12.1	10
8	26,247	–48.9	–56	–29.5	–23	–17.4	1
9	29,528	–55.0	–67	–37.3	–37	–24.2	–12
10	32,808	–58.8	–74	–44.7	–50	–30.8	–23
17.8	58,399	–78.0	–108	–64.3	–82	–53.0	–63
20	65,617	–73.5	–100	–59.8	–76	–49.6	–57
25	82,021	–73.2	–100	–51.2	–62	–40.4	–41
30	98,425	–66.1	–87	–42.7	–49	–29.1	–20
35	114,829	–54.2	–66	–32.1	–26	–5.7	22
40	131,234	–42.2	–44	–19.3	–3	17.8	64
45	147,638	–30.5	–23	–5.8	21	27.6	82
50	164,042	–18.2	–1	–2.0	28	28.0	82
55	180,446	–21.8	–7	–6.8	20	31.6	89
60	196,850	–25.1	–13	–20.5	–5	35.7	96

*For higher altitudes, see reference 3-16 and table 3-13.
†Median values aloft are annual values taken from reference 3-8, item (6).

3.4.3 Inflight Atmospheric Density

3.4.3.1 Atmospheric Density at Altitude. The density of the atmosphere decreases rapidly with height, decreasing to one-half of the surface value at ≈7-km altitude. Density is also variable at a fixed altitude, with the greatest relative variability occurring at ≈70-km altitude in the high northern latitudes (60° N.). Other altitudes of maximum density variability occur around the surface and 16 km. Altitudes of minimum variability occur around 8-, 24-, and 90-km altitude. See figures 3-4 through 3-6 in section 3.6.

Density varies with latitude in each hemisphere, with the mean annual density near the surface increasing toward the poles. In the region around 8-km altitude in the Northern Hemisphere; e.g., the density variation with latitude and season is small. Above 8 km to ≈28 km, the mean annual density decreases toward the north. Mean monthly densities between 30 km and 90 km increase toward the north in July and toward the equator in January (refs. 3-9 and 3-17).

Drag on a reentering spacecraft, which is a direct function of atmospheric density at a given altitude for a specific vehicle, like the Space Shuttle, has varied up to 19 percent over a few seconds, resulting from “patchy” density variations (density “pot holes”). The designer must recognize that atmospheric density variations do occur, and they will highly influence engine performance, specific fuel consumption, drag, and flight control (ref. 3-18). GRAM-07 (ref. 3-9) has been designed to reproduce typical density variations that can be encountered along a given flight path and should be considered in vehicle design, both ascent and reentry.

Table 3-8. WSMR air temperatures at various altitudes.

Geometric Altitude		Minimum		Median*		Maximum	
(km)	(ft)	(°C)	(°F)	(°C)	(°F)	(°C)	(°F)
Surface (1.3 MSL)	4,239	–25.6	–14	14.6	58	44.4	112
2	6,562	–11.7	11	12.7	55	31.1	88
3	9,843	–18.9	–2	6.0	43	22.2	72
4	13,123	–23.9	–11	–0.8	31	12.8	55
5	16,404	–31.1	–24	–7.5	19	6.1	43
6	19,685	–36.1	–33	–14.2	6	0	32
7	22,966	–42.2	–44	–21.1	–6	–7.2	19
8	26,247	–48.9	–56	–28.3	–19	–13.9	7
9	29,578	–55.0	–67	–35.6	–32	–21.1	–6
10	32,808	–60.0	–76	–42.7	–45	–27.2	–17
16.5	54,134	–80.0	–112	–66.3	–87	–47.8	–54
20	65,617	–77.8	–108	–61.0	–78	–52.2	–62
25	82,021	–68.4	–91	–52.2	–62	–39.2	–39
30	98,425	–58.9	–74	–44.3	–48	–26.1	–15
35	114,829	–52.2	–62	–33.2	–28	–7.8	18
40	131,234	–41.8	–43	–19.7	–3	5.0	41
45	147,638	–30.5	–23	–7.9	18	19.6	67
50	164,042	–29.1	–20	–5.8	22	25.9	79
55	180,446	–28.7	–20	–11.7	11	30.2	86
60	196,850	–35.8	–32	–19.9	–4	28.0	82
65	213,255	–36.5	–34	–30.2	–22	31.3	88

*Median values aloft are annual values taken from reference 3-8, item (5).

Table 3-9. Lower atmospheric temperature extremes applicable for all locations (KSC, VAFB, EAFB, and WSMR).

Maximum Flight Altitude (Geometric) of Aircraft Used for Transport		Compartment Cold Temperature Extreme	
(m)	(ft)	(°C)	(°F)
3,048	10,000	–25	–13
4,572	15,000	–35	–31
6,096	20,000	–45	–49
7,620	25,000	–50	–58
9,144	30,000	–57	–71
10,668	35,000	–65	–85
12,192	40,000	–70	–94
13,716	45,000	–75	–103

Considerable data are now available on the mean density and its variability below 30 km at the various test ranges from the data collected for preparation of the RCC RRAs (ref. 3-8). Additional information on the seasonal variability of density below 30 km is presented in reference 3-17. Above 30 km, the data are less plentiful and the accuracy of the temperature measurements—used to compute some densities—decreases with altitude.

Table 3-10. Atmospheric pressure extremes versus altitude, applicable for all locations (KSC, VAFB, EAFB, and WSMR).

Geometric Altitude (above MSL)		Atmospheric Pressure			
		Maximum		Minimum	
(km)	(ft)	(mb)	(lb/in^2)	(mb)	(lb/in^2)
0	0	(Use values in table 3-2 for surface pressure for each station)			
3	9,800	730	10.60	680	9.86
6	19,700	510	7.40	457	6.63
10	32,800	295	4.28	251	3.64
15	49,200	135	1.96	116	1.68
20	65,600	60	8.7×10^{-1}	51	7.4×10^{-1}
25	82,000	30	4.4×10^{-1}	22	3.2×10^{-1}
30	98,400	14.5	2.1×10^{-1}	10.4	1.5×10^{-1}
35	114,800	7.4	1.1×10^{-1}	4.9	7.1×10^{-2}
40	131,200	3.8	5.5×10^{-2}	2.4	3.5×10^{-2}
45	147,600	2.0	2.9×10^{-2}	1.2	1.7×10^{-2}
50	164,000	1.2	1.7×10^{-2}	6.1×10^{-1}	8.8×10^{-3}
55	180,400	6.0×10^{-1}	8.7×10^{-3}	3.1×10^{-1}	4.5×10^{-3}
60	196,800	3.2×10^{-1}	4.6×10^{-3}	1.6×10^{-1}	2.3×10^{-3}
65	213,300	1.7×10^{-1}	2.5×10^{-3}	8.3×10^{-2}	1.2×10^{-3}
70	229,700	8.5×10^{-2}	1.2×10^{-3}	4.1×10^{-2}	5.9×10^{-4}
75	246,100	3.1×10^{-2}	4.5×10^{-4}	2.1×10^{-2}	3.0×10^{-4}
80	262,500	1.4×10^{-2}	2.0×10^{-4}	8.9×10^{-3}	1.3×10^{-4}
85	278,900	5.9×10^{-3}	8.6×10^{-5}	3.7×10^{-3}	5.4×10^{-5}
90	295,300	2.6×10^{-3}	3.8×10^{-5}	1.4×10^{-3}	2.0×10^{-5}

(Use values in table 3-2 for surface pressure for each station)

Extreme minimum and maximum values of density for the KSC and VAFB are given in table 3-14. These extreme density values approximate the $\pm3\sigma$ (corresponding to the normal distribution) density values. The relative deviations of density for KSC and VAFB given in table 3-14, are, respectively, defined as percentage departures from the Patrick Reference Atmosphere (ref. 3-6) and the Vandenberg Reference Atmosphere (ref. 3-7).

Median values of surface density for different locations of interest are given in table 3-3, and mean values with altitude are given in tables 3-11 through 3-13 and in reference 3-8.

3.5 Simultaneous Values of KSC Temperature, Pressure, and Density at Discrete Altitude Levels

3.5.1 Introduction

This section presents simultaneous values of temperature, pressure, and density as guidelines for aerospace vehicle design considerations. The necessary assumptions and the lack of sufficient statistical data samples restrict the precision with which these data can currently be presented. The analysis is limited to KSC.

Table 3-11. KSC (Patrick) Reference Atmosphere (PRA-63) (ref. 3-6).

Geometric Altitude (MSL) Z (km)	Kinetic Temperature T (K)	Virtual Temperature T_V (K)	Atmospheric Pressure P (N/cm^2)	Atmospheric Density ρ (kg/m^3)
0	296.68	299.37	1.01701+1	1.18355+0
2	285.33	286.53	8.05212+0	9.79028–1
4	274.92	275.31	6.31517+0	7.99157–1
6	262.68	262.74	4.90089+0	6.49834–1
8	248.34	248.33	3.75320+0	5.26518–1
10	233.14	233.15	2.82776+0	4.22555–1
12	218.82	218.82	2.09093+0	3.33021–1
14	208.16	208.16	1.51990+0	2.54326–1
16	203.04	203.04	1.09118+0	1.87177–1
18	205.30	205.30	7.80974–1	1.32392–1
20	210.35	210.35	5.63157–1	9.31938–2
22	215.37	215.37	4.08992–1	6.61933–2
24	219.81	219.81	2.99188–1	4.74789–2
26	223.45	223.45	2.20382–1	3.43825–2
28	226.44	226.44	1.63274–1	2.51190–2
30	230.79	230.79	1.21463–1	1.83341–2
32	235.32	235.32	9.09051–2	1.34578–2
34	240.07	240.07	6.84299–2	9.93010–3
36	245.04	245.04	5.18072–2	7.36542–3
38	250.16	250.16	3.94480–2	5.49342–3
40	255.31	255.31	3.02092–2	4.12202–3
42	260.28	260.28	2.32624–2	3.11347–3
44	264.82	264.82	1.80045–2	2.36846–3
46	268.59	268.59	1.39948–2	1.81515–3
48	271.19	271.19	1.09106–2	1.40158–3
50	270.61	270.61	8.51802–3	1.09655–3
52	267.31	267.31	6.63932–3	8.65267–4
54	263.13	263.13	5.15531–3	6.82532–4
56	258.26	258.26	3.58521–3	5.37567–4
58	252.87	252.87	3.06511–3	4.22275–4
60	247.10	247.10	2.34420–3	3.30489–4
62	241.11	241.11	1.78185–3	2.57452–4
64	235.00	235.00	1.34542–3	1.99444–4
66	228.89	228.89	1.00864–3	1.53525–4
68	222.84	222.84	7.50591–4	1.17342–4
70	216.91	216.91	5.54143–4	8.89980–5
72	211.14	211.14	4.05760–4	6.69493–5
74	205.51	205.51	2.94587–4	4.99355–5
76	200.02	200.02	2.12002–4	3.69234–5
78	194.60	194.60	1.51198–4	2.70674–5
80	189.15	189.15	1.06843–4	1.96775–5
82	183.56	183.56	7.47938–5	1.41944–5
84	180.65	180.65	5.18782–5	1.00043–5
86	180.65	180.65	3.59147–5	6.92584–6
88	180.65	180.65	2.48690–5	4.79578–6
90	180.65	180.65	1.72244–5	3.32158–6

NOTE: Within table, the number format for 10^{-x} is shown as $-x$.

Table 3-12. VAFB Reference Atmosphere (VRA-71) (ref. 3-7).

Geometric Altitude (MSL) Z (km)	Kinetic Temperature T (K)	Virtual Temperature T_V (K)	Atmospheric Pressure P (N/cm^2)	Atmospheric Density ρ (kg/m^3)
0	285.88	287.15	1.01899+1	1.23618+0
2	283.30	283.59	8.02435+0	9.85756–1
4	272.17	272.35	6.27618+0	8.02762–1
6	258.71	258.79	4.85388+0	6.53426–1
8	243.68	243.70	3.69780+0	5.28600–1
10	228.50	228.50	2.77068+0	4.22426–1
12	217.79	217.79	2.03786+0	3.25934–1
14	212.89	212.89	1.48392+0	2.42845–1
16	209.46	209.46	1.07403+0	1.78628–1
18	210.39	210.39	7.76046–1	1.28512–1
20	213.39	213.39	5.63983–1	9.20191–2
22	217.34	217.34	4.10463–1	6.58104–2
24	220.68	220.68	3.00775–1	4.74989–2
26	223.11	223.11	2.22059–1	3.46574–2
28	226.09	226.09	1.64058–1	2.52891–2
30	230.43	230.43	1.22067–1	1.84539–2
32	234.66	234.66	9.12335–2	1.35440–2
34	238.84	238.84	6.85327–2	9.99594–3
36	243.35	243.35	5.17707–2	7.41121–3
38	248.38	248.38	3.93437–2	5.51828–3
40	253.89	253.89	3.00832–2	4.12777–3
42	259.62	259.62	2.31396–2	3.10498–3
44	265.00	265.00	1.78959–2	2.35255–3
46	269.19	269.19	1.39041–2	1.79938–3
48	270.97	270.97	1.08385–2	1.39342–3
50	271.16	271.16	8.45501–3	1.08625–3
52	270.79	270.79	6.60657–3	8.49939–4
54	268.26	268.26	5.14789–3	6.68511–4
56	264.09	264.09	3.99676–3	5.27219–4
58	258.74	258.74	3.08929–3	4.15944–4
60	252.61	252.61	2.37542–3	3.27585–4
62	246.07	246.07	1.81566–3	2.57051–4
64	239.38	239.38	1.37858–3	2.00620–4
66	232.78	232.78	1.03911–3	1.55505–4
68	226.40	226.40	7.77072–4	1.19570–4
70	220.28	220.28	5.76248–4	9.11308–5
72	214.39	214.39	4.23554–4	6.88241–5
74	208.58	208.58	3.08459–4	5.15182–5
76	202.61	202.61	2.22508–4	3.82588–5
78	196.11	196.11	1.58952–4	2.82366–5
80	188.60	188.60	1.12437–4	2.07684–5
82	180.65	180.65	7.86738–5	1.51716–5
84	180.65	180.65	5.44290–5	1.04962–5
86	180.65	180.65	3.76643–5	7.26323–6
88	180.65	180.65	2.60693–5	5.02723–6
90	180.65	180.65	1.80492–5	3.48063–6

NOTE: Within table, the number format for 10^{-x} is shown as $-x$.

Table 3-13. EAFB Reference Atmosphere (ERA-75) (ref. 3-16).

Geometric Altitude (MSL) Z (km)	Kinetic Temperature T (K)	Virtual Temperature T_V (K)	Atmospheric Pressure P (N/cm^2)	Atmospheric Density ρ (kg/m^3)
0.706	289.27	290.27	9.34079+0	1.12105+0
2	284.35	284.70	8.00722+0	9.79796–1
4	272.17	272.35	6.27618+0	8.02762–1
6	258.71	258.79	4.85388+0	6.53426–1
8	243.68	243.70	3.69780+0	5.28600–1
10	228.50	228.50	2.77068+0	4.22426–1
12	217.79	217.79	2.03786+0	3.25934–1
14	212.89	212.89	1.48392+0	2.42845–1
16	209.46	209.46	1.07403+0	1.78628–1
18	210.39	210.39	7.76046–1	1.28512–1
20	213.39	213.39	5.63983–1	9.20191–2
22	217.34	217.34	4.10463–1	6.58104–2
24	220.68	220.68	3.00775–1	4.74989–2
26	223.11	223.11	2.22059–1	3.46574–2
28	226.09	226.09	1.64058–1	2.52891–2
30	230.43	230.43	1.22067–1	1.84539–2
32	234.66	234.66	9.12335–2	1.35440–2
34	238.84	238.84	6.85327–2	9.99594–3
36	243.35	243.35	5.17785–2	7.41121–3
38	248.38	248.38	3.93437–2	5.51828–3
40	253.89	253.89	3.00832–2	4.12777–3
42	259.62	259.62	2.31396–2	3.10498–3
44	265.00	265.00	1.78959–2	2.35255–3
46	269.19	269.19	1.39041–2	1.79938–3
48	270.97	270.97	1.08385–2	1.39342–3
50	271.16	271.16	8.45501–3	1.08625–3
52	270.79	270.79	6.60657–3	8.49939–4
54	268.26	268.26	5.14789–3	6.68511–4
56	264.09	264.09	3.99676–3	5.27219–4
58	258.74	258.74	3.08929–3	4.15944–4
60	252.61	252.61	2.37542–3	3.27585–4
62	246.07	246.07	1.81565–3	2.57051–4
64	239.38	239.38	1.37858–3	2.00620–4
66	232.78	232.78	1.03911–3	1.55505–4
68	226.40	226.40	7.77072–4	1.19570–4
70	220.28	220.28	5.76248–4	9.11308–5
72	214.39	214.39	4.23554–4	6.88241–5
74	208.58	208.58	3.08459–4	5.15182–5
76	202.61	202.61	2.22508–4	3.82588–5
78	196.11	196.11	1.58952–4	2.82366–5
80	188.60	188.60	1.12437–4	2.07684–5
82	180.65	180.65	7.86738–5	1.51716–5
84	180.65	180.65	5.44290–5	1.04962–5
86	180.65	180.65	3.76643–5	7.26323–6
88	180.65	180.65	2.60693–5	5.02723–6
90	180.65	180.65	1.80492–5	3.48063–6

NOTE: Within table, the number format for 10^{-x} is shown as $-x$.

Table 3-14. Atmospheric density maximum (±3σ) and minimum (≈3σ) versus altitude for KSC and VAFB.

Altitude*		KSC Density				VAFB Density			
		Maximum		Minimum		Maximum		Minimum	
(km)	(ft)	(kg/m^3)	Percent Deviation From PRA-63	(kg/m^3)	Percent Deviation From PRA-63	(kg/m^3)	Percent Deviation From VRA-71	(kg/m^3)	Percent Deviation From VRA-71
0	0	1.326	12.0	1.141	–3.6	1.302	5.3	1.140	–7.8
2	6,600	1.047	6.1	9.947×10^{-1}	–3.0	1.046	6.1	9.518×10^{-1}	–3.5
4	13,100	8.287×10^{-1}	3.7	7.824×10^{-1}	–2.1	8.484×10^{-1}	5.7	7.766×10^{-1}	–3.3
6	19,700	6.706×10^{-1}	3.2	6.355×10^{-1}	–2.2	6.906×10^{-1}	5.7	6.299×10^{-1}	–3.6
8	26,200	5.428×10^{-1}	3.1	5.055×10^{-1}	–4.0	5.601×10^{-1}	6.0	4.971×10^{-1}	–6.0
10	32,800	4.352×10^{-1}	3.0	3.938×10^{-1}	–6.8	4.624×10^{-1}	9.5	3.835×10^{-1}	–9.2
15	49,200	2.345×10^{-1}	7.0	1.979×10^{-1}	–9.7	2.337×10^{-1}	12.0	1.851×10^{-1}	–11.3
20	65,600	1.002×10^{-1}	4.5	8.751×10^{-2}	–6.1	1.001×10^{-1}	8.8	8.420×10^{-2}	–8.5
25	82,000	4.274×10^{-2}	5.9	3.790×10^{-2}	–6.1	4.460×10^{-2}	10.0	3.634×10^{-2}	–10.4
30	98,400	1.976×10^{-2}	7.8	1.700×10^{-2}	–7.3	2.085×10^{-2}	13.0	1.634×10^{-2}	–11.5
35	114,800	9.427×10^{-3}	10.3	7.640×10^{-3}	–10.6	9.786×10^{-3}	13.8	7.505×10^{-3}	–12.8
40	131,200	4.637×10^{-3}	12.5	3.512×10^{-3}	–14.8	4.747×10^{-3}	15.0	3.424×10^{-3}	–17.0
50	164,000	1.275×10^{-3}	16.3	8.630×10^{-4}	–21.3	1.325×10^{-3}	2.02	8.473×10^{-4}	–22.0
60	196,800	3.946×10^{-4}	19.4	2.465×10^{-4}	–25.4	4.422×10^{-4}	35.0	2.359×10^{-4}	–28.0
70	229,700	1.100×10^{-4}	23.6	6.666×10^{-5}	–25.1	1.203×10^{-4}	32.0	6.197×10^{-5}	–32.0
80	262,500	2.342×10^{-5}	19.0	1.596×10^{-5}	–18.9	2.617×10^{-5}	26.0	1.433×10^{-5}	–31.0
90	295,300	3.684×10^{-6}	10.9	2.930×10^{-6}	–11.8	4.177×10^{-6}	20.0	2.785×10^{-6}	–20.0

* Geometric altitude above MSL.

3.5.2 Method of Determining Simultaneous Values

An aerospace vehicle design problem that often arises in considering natural environmental data is stated by the following question: "How should the extremes (maxima or minima) of temperature, pressure, and density be combined (1) at discrete altitude levels and (2) versus altitude?" As an example, suppose one wants to know what temperature and pressure should be used simultaneously with a maximum density at a discrete altitude. From statistical principles set forth by Dr. C.E. Buell (ref. 3-19), the solution results by allowing mean density plus three standard deviations to represent maximum density and using the coefficients of variations, correlations, and mean values as expressed in equation (3.3):

$$\text{Maximum } \rho = \left(\bar{\rho} + 3\sigma_\rho\right) = \bar{\rho}\left(1 + 3\frac{\sigma_\rho}{\bar{\rho}}\right) = \bar{\rho}\left\{1 + 3\left[\underbrace{\left(\frac{\sigma_P}{\bar{P}}\right)r\left(P\rho\right)}_{A} - \underbrace{\left(\frac{\sigma_T}{\bar{T}}\right)r\left(\rho T\right)}_{B}\right]\right\} . \tag{3.3}$$

The associated values for pressure and temperature are the last two terms of equation (3.3), (A) and (B). Appropriate values of correlation coefficients (r) and coefficients of variation (CV) are obtained from table 3-15.

In general, the three extreme equations of interest for ρ, P, and T are:

$$\text{Extreme } \rho = \left(\rho \pm M\sigma_\rho\right) = \bar{\rho}\left[1 \pm M\left(\frac{\sigma_\rho}{\bar{\rho}}\right)\right] = \bar{\rho}\left\{1 \pm M\left[\left(\frac{\sigma_P}{\bar{P}}\right) r(P\rho) - \left(\frac{\sigma_T}{\bar{T}}\right) r(\rho T)\right]\right\} \tag{3.4}$$

$$\text{Extreme } P = \left(\bar{P} \pm M\sigma_P\right) = \bar{P}\left[1 \pm M\left(\frac{\sigma_P}{\bar{P}}\right)\right] = \bar{P}\left\{1 \pm M\left[\left(\frac{\sigma_\rho}{\bar{\rho}}\right) r(P\rho) + \left(\frac{\sigma_T}{\bar{T}}\right) r(PT)\right]\right\} \tag{3.5}$$

and

$$\text{Extreme } T = \left(\bar{T} \pm M\sigma_T\right) = \bar{T}\left[1 \pm M\left(\frac{\sigma_T}{\bar{T}}\right)\right] = \bar{T}\left\{1 \pm M\left[\left(\frac{\sigma_P}{\bar{P}}\right) r(PT) - \left(\frac{\sigma_\rho}{\bar{\rho}}\right) r(\rho T)\right]\right\}, \tag{3.6}$$

where M denotes the multiplication factor to give the desired deviation. The values of M for the normal distribution and the associated percentile levels are shown in table 3-16.

The two associated atmospheric parameters that deal with a third extreme parameter are listed in more detail in table 3-17.

It must be emphasized that this procedure is to be used at discrete altitudes only. Whenever extreme profiles of pressure, temperature, and density are required for engineering application, the use of these correlated variables at discrete altitudes is not satisfactory. Section 3.6 deals directly with this problem, since profiles of only extreme values of pressure, temperature, or density from zero to 90-km altitude is unrealistic in the real atmosphere.

3.6 Extreme Hot and Cold Atmospheric Profiles for KSC, VAFB, and EAFB

Section 3.6 gives the two extreme density profiles that correspond to the summer (hot) and winter (cold) extreme atmospheres for KSC (tables 3-18a and 3-18b), VAFB (tables 3-19a and 3-19b), and EAFB (tables 3-20a and 3-20b). See references 3-20 and 3-16 for VAFB and EAFB, respectively, for detailed information pertaining to extreme atmospheres. Associated values of extreme temperature and pressure versus altitude are also tabulated. These extreme atmospheric profiles should be used in ascent design analyses at all altitudes. For reentry studies, they are to apply only from 30 km to the surface for vehicles to be used at KSC, VAFB, or EAFB. For those aerospace vehicles with ferrying capability, design calculations should use these extreme profiles in conjunction with the hot or cold day design ambient air temperatures over runways from paragraph 5.1.3.1 of section 5. The extreme atmosphere producing the maximum vehicle design requirement should be utilized to determine the design.

The envelopes of density deviations given in table 3-14 imply that a typical individual extreme density profile may be represented by a similarly shaped profile; e.g., deviations of density are either all negative or all positive from sea level to 90-km altitude. However, examination of many individual density profiles shows that when large positive deviations of density occur at the surface, correspondingly large negative deviations will occur near 15-km altitude and above. Such a situation occurs during the winter season (cold atmosphere). The reverse is also true—density profiles with large negative deviations at lower levels will have correspondingly large positive deviations at higher levels. This situation occurs in the summer season (hot atmosphere) (figs. 3-4 through 3-6).

Table 3-15. Coefficients of variation and discrete altitude level correlation coefficients between pressure-density $r(P\rho)$, pressure-temperature $r(PT)$, and density-temperature $r(\rho T)$, KSC, annual.

Altitude (km)	Coefficients of Variation (*CV*)			Correlation Coefficients (r)		
	$\sigma(\rho)/\rho$ (%)	$\sigma(P)/P$ (%)	$\sigma(T)/T$ (%)	$r(P\rho)$ (unitless)	$r(PT)$ (unitless)	$r(\rho T)$ (unitless)
0	1.8000	0.6000	1.5000	0.6250	0.3500	–0.9500
1	1.7000	0.5500	1.6000	0.3382	–0.0156	–0.9462
2	1.5000	0.8000	1.5900	0.1508	0.3609	–0.8675
3	1.1800	0.9800	1.5700	–0.0485	0.6606	–0.7818
4	0.9700	0.8500	1.4000	–0.1799	0.7318	–0.8021
5	0.8000	0.8700	1.3400	–0.2864	0.8203	–0.7830
6	0.7400	0.8400	1.2600	–0.2690	0.8246	–0.7666
7	0.8800	0.9800	1.4200	–0.1633	0.7913	–0.7324
8	0.9000	1.1300	1.4700	–0.0364	0.7910	–0.6402
9	1.1800	1.4700	1.6200	0.2678	0.7124	–0.4854
10	1.6300	1.7500	1.7200	0.4840	0.5588	–0.4553
11	1.8800	1.8000	1.7800	0.5328	0.4485	–0.5174
12	2.1500	1.8700	1.8500	0.5841	0.3320	–0.5717
13	2.3800	1.9000	1.8500	0.6470	0.1946	–0.6220
14	2.6200	1.9200	1.7700	0.7373	–0.0066	–0.6804
15	2.7800	1.8800	1.6700	0.8107	–0.2238	–0.7520
16	2.8800	1.8400	1.7100	0.8262	–0.3154	–0.7953
17	2.8800	1.8000	1.7000	0.8338	–0.3537	–0.8113
18	2.7500	1.7500	1.7000	0.8036	–0.2706	–0.7904
19	2.5000	1.7800	1.6700	0.7449	–0.0492	–0.7031
20	2.2700	1.8500	1.6500	0.6969	0.1625	–0.5944
21	2.0800	1.9500	1.6200	0.6786	0.3325	–0.4672
22	1.9800	2.1200	1.5700	0.7087	0.4565	–0.3041
23	1.9200	2.3200	1.4800	0.7721	0.5659	–0.0870
24	1.9500	2.4000	1.4300	0.8032	0.5831	–0.0157
25	2.0000	2.4300	1.4200	0.8116	0.5682	–0.0196
26	2.0800	2.5000	1.5000	0.8006	0.5565	–0.0523
27	2.1500	2.6000	1.5800	0.7948	0.5640	–0.0528
28	2.2300	2.6700	1.7500	0.7591	0.5584	–0.1161
29	2.3700	2.6300	1.8700	0.7249	0.4877	–0.2479
30	2.5200	2.6300	1.9200	0.7228	0.4211	–0.3224
31	2.7000	2.7000	2.0000	0.7257	0.3704	–0.3704
32	2.8800	2.7500	2.0800	0.7279	0.3142	–0.4222
33	3.0700	2.7300	2.1700	0.7260	0.2310	–0.5014
34	3.2700	2.6800	2.2300	0.7361	0.1223	–0.5817
35	3.4800	2.6000	2.3200	0.7454	0.0027	–0.6647
36	3.7000	2.5000	2.4300	0.7587	–0.1263	–0.7421
37	3.9200	2.3700	2.5500	0.7793	–0.2686	–0.8129
38	4.1200	2.4600	2.6300	0.7947	–0.3096	–0.8232
39	4.3300	2.6400	2.6900	0.8084	–0.3199	–0.8163
40	4.5500	2.7900	2.7680	0.8220	–0.3442	–0.8176
41	4.7500	2.8600	3.0200	0.7958	–0.3046	–0.8192
42	4.9300	2.9200	3.2600	0.7712	–0.2706	–0.8215
43	5.1300	3.0000	3.3400	0.7850	–0.3075	–0.8309
44	5.3200	3.1800	3.3500	0.8037	–0.3270	–0.8252
45	5.5000	3.2400	3.6000	0.7797	–0.2912	–0.8261

Table 3-15. Coefficients of variation and discrete altitude level correlation coefficients between pressure-density $r(P\rho)$, pressure-temperature $r(PT)$, and density-temperature $r(\rho T)$, KSC, annual (Continued).

Altitude (km)	Coefficients of Variation (*CV*)			Correlation Coefficients (r)		
	$\sigma(\rho)/\rho$ (%)	$\sigma(P)/P$ (%)	$\sigma(T)/T$ (%)	$r(P\rho)$ (unitless)	$r(PT)$ (unitless)	$r(\rho T)$ (unitless)
46	5.6700	3.3200	3.8300	0.7571	–0.2539	–0.8242
47	5.8300	3.4100	3.9800	0.7489	–0.2402	–0.8232
48	5.9800	3.4800	4.1900	0.7284	–0.2090	–0.8223
49	6.1300	3.5900	4.1400	0.7572	–0.2540	–0.8241
50	6.2700	3.6900	4.1900	0.7644	–0.2633	–0.8232
51	6.4200	3.8200	4.0800	0.7984	–0.3201	–0.8260
52	6.5500	3.9100	4.1800	0.7950	–0.3103	–0.8234
53	6.7000	4.0100	4.2700	0.7953	–0.3089	–0.8222
54	6.8000	4.0700	4.3100	0.7990	–0.3164	–0.8232
55	6.9200	4.1400	4.3700	0.8016	–0.3220	–0.8241
56	7.0300	4.2100	4.4200	0.8043	–0.3267	–0.8244
57	7.1500	4.2800	4.4700	0.8081	–0.3351	–0.8258
58	7.2700	4.3600	4.5100	0.8127	–0.3434	–0.8263
59	7.3700	4.4200	4.5400	0.8172	–0.3530	–0.8277
60	7.4700	4.4800	4.5900	0.8188	–0.3565	–0.8283
61	7.5700	4.5400	4.6300	0.8217	–0.3629	–0.8293
62	7.6500	4.7000	4.8600	0.7926	–0.2805	–0.8076
63	7.7500	4.9000	5.0000	0.7778	–0.2256	–0.7878
64	7.8300	5.1500	5.1500	0.7602	–0.1558	–0.7602
65	7.9000	5.3800	5.3800	0.7342	–0.0781	–0.7342
66	7.9800	5.5700	5.4400	0.7324	–0.0505	–0.7170
67	8.0300	5.6600	5.4700	0.7326	–0.0408	–0.7099
68	8.0700	5.7700	5.4000	0.7437	–0.0429	–0.6998
69	8.1000	5.8200	5.5100	0.7331	–0.0215	–0.6957
70	8.1200	5.8700	5.4900	0.7369	–0.0208	–0.6911
71	8.1200	5.8900	5.4700	0.7392	–0.0205	–0.6885
72	8.0700	5.7900	5.3800	0.7459	–0.0426	–0.6973
73	8.1200	5.6500	5.2900	0.7615	–0.1008	–0.7216
74	8.0700	5.5000	5.1700	0.7733	–0.1432	–0.7383
75	7.9000	5.2900	5.4100	0.7313	–0.0901	–0.7452
76	7.6800	4.9900	5.6500	0.6779	–0.0383	–0.7606
77	7.3800	5.0100	6.1600	0.5628	0.1390	–0.7403
78	7.0500	5.0400	6.5200	0.4587	0.2771	–0.7267
79	6.6800	5.1100	6.8400	0.3508	0.4045	–0.7145
80	6.3200	5.2700	6.7800	0.3265	0.4730	–0.6784
81	5.9500	5.3600	6.7200	0.2975	0.5342	–0.6482
82	5.5800	5.5200	6.6600	0.2800	0.5942	–0.6057
83	5.2500	5.1300	6.6100	0.1891	0.6259	–0.6475
84	4.9200	4.7800	6.5600	0.0855	0.6645	–0.6877
85	4.6300	4.4700	6.5100	–0.0232	0.7032	–0.7272
86	4.4000	4.1900	6.4500	–0.1271	0.7363	–0.7647
87	4.2000	3.9600	6.4000	–0.2296	0.7694	–0.7983
88	4.0200	4.0500	6.3400	–0.2344	0.7874	–0.7838
89	3.8800	4.1400	6.2800	–0.2255	0.7986	–0.7665
90	3.7800	4.0400	5.9600	–0.1608	0.7798	–0.7432

Table 3-16. *M* values for normal distribution and associated percentile levels.

M	Percentile
Mean –3 standard deviations	0.135
Mean –2 standard deviations	2.275
Mean –1 standard deviations	15.866
Mean ±0 standard deviations = median	50.000
Mean +1 standard deviations	84.134
Mean +2 standard deviations	97.725
Mean +3 standard deviations	99.865

Table 3-17. Parameters for extreme density, temperature, and pressure.

	Extreme Density	Extreme Temperature	Extreme Pressure
$P_{\text{assoc.}}=$	$\overline{P}\left[1\pm\left\{M\left(\frac{\sigma_P}{\overline{P}}\right)r(P\rho)\right\}\right]$	$\overline{P}\left[1\pm\left\{M\left(\frac{\sigma_P}{\overline{P}}\right)r(PT)\right\}\right]$	–
$T_{\text{assoc.}}=$	$\overline{T}\left[1\pm\left\{M\left(\frac{\sigma_T}{\overline{T}}\right)r(\rho T)\right\}\right]$	–	$\overline{T}\left[1\pm\left\{M\left(\frac{\sigma_T}{\overline{T}}\right)r(PT)\right\}\right]$
$\rho_{\text{assoc.}}=$	–	$\overline{\rho}\left[1\pm\left\{M\left(\frac{\sigma_\rho}{\rho}\right)r(\rho T)\right\}\right]$	$\overline{\rho}\left[1\pm\left\{M\left(\frac{\sigma_\rho}{\overline{\rho}}\right)r(P\rho)\right\}\right]$

Use + sign when extreme parameter is maximum and – sign when extreme parameter is minimum.

The two extreme KSC density profiles of figure 3-4 are shown as percent deviations from the Patrick Reference Atmosphere, 1963 density profile (ref. 3-6). The two profiles obey the hydrostatic equation and the ideal gas law. The extreme density profiles shown up to 30-km altitude were observed in the atmosphere. The results shown above 30-km altitude are somewhat speculative because of the limited data from this region of the atmosphere. Quasi-isopycnic levels (levels of minimum density variation) are noted at approximately 8 and 86 km. Another level of minimum density variability is seen at 24 km, and levels of maximum variability occur at zero, 15-, and 68-km altitude. The associated extreme virtual temperature profiles for KSC are given in figure 3-7.

The two VAFB extreme density profiles are shown in figure 3-5 as percent deviations from the Vandenberg Reference Atmosphere, 1971. Levels of minimum density variation are located at approximately 8-, 30-, and 90-km altitude. Levels of maximum variability occur at 0, 15, and 73 km. The hot and cold VAFB virtual temperature profiles are shown in figure 3-8.

The two EAFB extreme density profiles are shown in figure 3-6 as percent deviations from the Edwards Reference Atmosphere, 1975. The hot and cold EAFB virtual temperature profiles are shown in figure 3-9. These extreme density and temperature profiles again have structures similar to the KSC and VAFB models. Temperatures below ≈10-km altitude are virtual temperatures. Virtual temperature includes moisture to avoid computation of the specific gas constant for moist air (sec. 3.3.1.1).

Table 3-18a. KSC summer (hot) atmosphere (KHA-71).

Geometric Altitude (MSL) (km)	Kinetic Temperature T (K)	Virtual Temperature T_V (K)	Atmospheric Pressure P (N/cm^2)	Atmospheric Density ρ (kg/m^3)	Relative Deviation (T_V) Percent From PRA-63 RD (T^*) %	Relative Deviation (P) Percent From PRA-63 RD (P) %	Relative Deviation (ρ) Percent From PRA-63 RD (ρ) %
0	307.40	309.90	1.01000+1	1.13537+0	3.5	–0.7	–4.1
2	294.70	296.37	8.06143+0	9.47571–1	3.4	0.1	–3.2
4	282.00	282.85	6.36690+0	7.84181–1	2.7	0.8	–1.9
6	269.32	269.32	4.97073+0	6.42972–1	2.5	1.4	–1.1
8	255.79	255.79	3.83152+0	5.21824–1	3.0	2.1	–0.9
10	242.26	242.26	2.91191+0	4.18724–1	3.9	3.0	–0.9
12	228.20	228.20	2.17801+0	3.32493–1	4.3	4.2	–0.2
14	213.60	213.60	1.59836+0	2.60682–1	2.6	5.2	2.5
16	199.00	199.00	1.14755+0	2.00889–1	–2.0	5.2	7.3
18	200.00	200.00	8.13695–1	1.41732–1	–2.6	4.2	7.1
20	208.33	208.33	5.82229–1	9.73585–2	–1.0	3.4	4.5
22	215.67	215.67	4.22016–1	6.81728–2	0.1	3.2	3.0
24	222.00	222.00	3.08751–1	4.84476–2	1.0	3.2	2.1
26	228.33	228.33	2.27940–1	3.47755–2	2.2	3.4	1.2
28	234.67	234.67	1.69726–1	2.51992–2	3.8	3.9	0.3
30	241.00	241.00	1.27321–1	1.84051–2	4.4	4.8	0.4
32	247.33	247.33	9.61987–2	1.35465–2	5.1	5.9	0.7
34	253.67	253.67	7.32790–2	1.00657–2	5.7	7.1	1.3
36	260.00	260.00	5.61455–2	7.52274–3	6.1	8.4	2.1
38	265.77	265.77	4.32945–2	5.67493–3	6.2	9.8	3.3
40	271.54	271.54	3.35705–2	4.30688–3	6.4	11.1	4.5
42	277.31	277.31	2.61721–2	3.28794–3	6.5	12.5	5.8
44	283.08	283.08	2.05077–2	2.52378–3	6.9	13.9	6.6
46	288.85	288.85	1.61481–2	1.94746–3	7.5	15.4	7.3
48	294.62	294.62	1.27777–2	1.51091–3	8.6	17.1	7.8
50	297.50	297.50	1.01482–2	1.18840–3	9.9	19.2	8.4
52	289.00	289.00	8.03999–3	9.69103–4	8.1	21.1	12.0
54	280.50	280.50	6.32437–3	7.85430–4	6.6	22.9	15.1
56	272.00	272.00	4.93788–3	6.32455–4	5.3	23.9	17.7
58	263.50	263.50	3.82537–3	5.05788–4	4.2	24.8	19.8
60	255.00	255.00	2.93909–3	4.01549–4	3.2	25.4	21.5
62	246.50	246.50	2.23836–3	3.16317–4	2.2	25.8	22.9
64	238.00	238.00	1.68846–3	2.47098–4	1.3	25.5	23.9
66	229.50	229.50	1.26059–3	1.91294–4	0.3	24.9	24.6
68	221.00	221.00	9.30524–4	1.46662–4	–0.8	24.0	25.0
70	212.50	212.50	6.78561–4	1.11268–4	–2.0	22.5	25.0
72	204.00	204.00	4.88448–4	8.34696–5	–3.4	20.5	24.7
74	195.50	195.50	3.47004–4	6.18641–5	–4.9	17.9	23.9
76	187.00	187.00	2.43192–4	4.52595–5	–6.5	14.6	22.6
78	178.50	178.50	1.67780–4	3.26383–5	–8.3	10.5	20.5
80	170.00	170.00	1.12901–4	2.31514–5	–10.1	5.7	17.6
82	170.00	170.00	7.55119–5	1.55048–5	–7.4	1.0	9.1
84	170.00	170.00	5.06592–5	1.03855–5	–5.9	–2.6	3.5
86	170.00	170.00	3.39222–5	6.97136–6	–5.9	–5.9	0.0
88	170.00	170.00	2.27356–5	4.67110–6	–5.9	–9.1	–3.4
90	170.00	170.00	1.51348–5	3.10707–6	–5.9	–12.2	–6.6

NOTE: Within table, the number format for 10^{-x} is shown as $-x$.

Table 3-18b. KSC winter (cold) atmosphere (KCA-71).

Geometric Altitude (MSL) (km)	Kinetic Temperature T (K)	Virtual Temperature T_V (K)	Atmospheric Pressure P (N/cm^2)	Atmospheric Density ρ (kg/m^3)	Relative Deviation (T_V) Percent From PRA-63 RD (T^*) %	Relative Deviation (P) Percent From PRA-63 RD (P) %	Relative Deviation (ρ) Percent From PRA-63 RD (ρ) %
0	274.50	275.00	1.02700+1	1.30099+0	–8.1	1.0	9.9
2	264.70	265.00	7.97353+0	1.04820+0	–7.5	–1.0	7.1
4	254.90	255.00	6.13058+0	8.37528–1	–7.4	–2.8	4.8
6	245.24	245.24	4.66465+0	6.62784–1	–6.7	–4.8	2.0
8	235.87	235.87	3.51072+0	5.18423–1	–5.0	–6.5	–1.6
10	227.67	227.67	2.61414+0	4.00022–1	–2.4	–7.6	–5.3
12	220.59	220.59	1.92692+0	3.04362–1	0.8	–7.9	–8.6
14	214.29	214.29	1.40710+0	2.28093–1	3.0	–7.4	–10.1
16	209.49	209.49	1.01913+0	1.69535–1	3.1	–6.6	–9.5
18	208.28	208.28	7.34536–1	1.22832–1	1.4	–6.0	–7.2
20	209.00	209.00	5.29299–1	8.82292–2	–0.6	–6.0	–5.3
22	210.91	210.91	3.82184–1	6.31426–2	–2.1	–6.5	–4.6
24	213.63	213.63	2.77005–1	4.51690–2	–2.8	–7.4	–4.9
26	216.78	216.78	2.01682–1	3.23964–2	–3.0	–8.5	–5.8
28	220.08	220.08	1.47487–1	2.33454–2	–2.3	–9.7	–7.0
30	223.31	223.31	1.08321–1	1.69107–2	–3.2	–10.8	–7.9
32	226.44	226.44	7.99577–2	1.23019–2	–3.8	–12.0	–8.6
34	229.60	229.60	5.93149–2	8.98540–3	–4.3	–13.4	–9.5
36	233.84	233.84	4.41165–2	6.57245–3	–4.6	–14.9	–10.8
38	239.02	239.02	3.30396–2	4.81532–3	–4.5	–16.2	–12.3
40	244.20	244.20	2.49012–2	3.55236–3	–4.4	–17.6	–13.8
42	249.38	249.38	1.88809–2	2.63764–3	–4.2	–18.8	–15.3
44	254.55	254.55	1.43942–2	1.96985–3	–3.9	–20.1	–16.8
46	259.73	259.73	1.10347–2	1.47978–3	–3.3	–21.2	–18.5
48	264.91	264.91	8.50858–3	1.11871–3	–2.3	–22.1	–20.2
50	267.50	267.50	6.58344–3	8.57370–4	–1.2	–22.7	–21.8
52	267.50	267.50	5.09811–3	6.63959–4	0.1	–23.2	–23.3
54	264.64	264.64	3.94567–3	5.19359–4	0.6	–23.5	–23.9
56	261.79	261.79	3.04283–3	4.04911–4	1.4	–23.7	–24.7
58	258.93	258.93	2.33950–3	3.14785–4	2.4	–23.7	–25.4
60	256.07	256.07	1.79403–3	2.44083–4	3.6	–23.4	–26.1
62	253.21	253.21	1.37225–3	1.88792–4	5.0	–23.0	–26.7
64	250.36	250.36	1.04675–3	1.45631–4	6.5	–22.2	–27.0
66	247.50	247.50	7.95920–4	1.11993–4	8.1	–21.2	–27.1
68	244.64	244.64	6.02732–4	8.58059–5	9.8	–19.8	–26.9
70	241.79	241.79	4.54550–4	6.54950–5	11.5	–17.9	–26.4
72	238.93	238.93	3.41463–4	4.98157–5	13.2	–15.7	–25.5
74	236.07	236.07	2.56128–4	3.78041–5	14.9	–12.9	–24.2
76	233.21	233.21	1.92122–4	2.86884–5	16.6	–9.5	–22.4
78	230.36	230.36	1.43852–4	2.17018–5	18.4	–5.5	–20.2
80	227.50	227.50	1.05991–4	1.62312–5	20.3	–0.8	–17.5
82	221.00	221.00	7.81453–5	1.23199–5	20.4	4.5	–13.2
84	214.50	214.50	5.71060–5	9.27639–6	18.7	10.1	–7.3
86	208.00	208.00	4.13394–5	6.92224–6	15.1	15.1	–0.1
88	201.50	201.50	2.96044–5	5.11897–6	11.5	19.0	6.7
90	195.00	195.00	2.09474–5	3.74532–6	7.9	21.7	12.8

NOTE: Within table, the number format for 10^{-x} is shown as $-x$.

Table 3-19a. VAFB summer (hot) atmosphere (VHA-73) (ref. 3-20).

Geometric Altitude (MSL) (km)	Kinetic Temperature T (K)	Virtual Temperature T_V (K)	Atmospheric Pressure P (N/cm^2)	Atmospheric Density ρ (kg/m^3)	Relative Deviation (T_V) Percent From VRA-71 RD (T^*) %	Relative Deviation (P) Percent From VRA-71 RD (P) %	Relative Deviation (ρ) Percent From VRA-71 RD (ρ) %
0	310.40	312.70	1.01000+1	1.12520+0	8.9	–0.9	–9.0
2	296.80	298.59	8.07642+0	9.42286–1	5.3	0.7	–4.4
4	283.20	284.48	6.38872+0	7.82355–1	4.5	1.8	–2.5
6	269.60	270.37	4.99378+0	6.43448–1	4.5	2.9	–1.5
8	256.00	256.26	3.85219+0	5.23688–1	5.2	4.2	–0.9
10	240.53	240.53	2.92684+0	4.23899–1	5.3	5.6	0.4
12	223.20	223.20	2.17953+0	3.40178–1	2.5	7.0	4.4
14	205.87	205.87	1.58478+0	2.68177–1	–3.3	6.8	10.4
16	195.70	195.70	1.12412+0	2.00106–1	–6.6	4.7	12.0
18	200.74	200.74	7.95730–1	1.38101–1	–4.6	2.5	7.4
20	207.82	207.82	5.69371–1	9.54397–2	–2.6	1.0	3.7
22	214.89	214.89	4.12139–1	6.68144–2	–1.1	0.4	1.5
24	221.97	221.97	3.01463–1	4.73175–2	0.6	0.2	–0.4
26	229.05	229.05	2.22578–1	3.38482–2	2.7	0.3	–2.3
28	236.12	236.12	1.65959–1	2.44859–2	4.4	1.2	–3.2
30	243.20	243.20	1.24774–1	1.78725–2	5.5	2.2	–3.1
32	249.44	249.44	9.45606–2	1.32071–2	6.3	3.6	–2.5
34	255.67	255.67	7.21309–2	9.82767–3	7.1	5.3	–1.7
36	261.91	261.91	5.53982–2	7.36860–3	7.6	7.0	–0.6
38	268.14	268.14	4.28172–2	5.56344–3	8.0	8.8	0.8
40	274.38	274.38	3.32792–2	4.22565–3	8.1	10.6	2.4
42	280.61	280.61	2.60056–2	3.22793–3	8.1	12.4	4.0
44	286.85	286.85	2.04445–2	2.48289–3	8.2	14.3	5.6
46	293.08	293.08	1.61641–2	1.92235–3	8.9	16.2	6.7
48	296.20	296.20	1.28182–2	1.50758–3	9.3	18.3	8.2
50	296.20	296.20	1.01776–2	1.19701–3	9.2	20.4	10.2
52	296.20	296.20	8.08051–3	9.50404–4	9.4	22.3	11.8
54	287.91	287.91	6.39556–3	7.73812–4	7.3	24.2	15.8
56	279.63	279.63	5.02673–3	6.26232–4	5.9	25.8	18.8
58	271.34	271.34	3.92216–3	5.03576–4	4.9	27.0	21.1
60	263.06	263.06	3.03703–3	4.02224–4	4.1	27.9	22.8
62	254.77	254.77	2.33271–3	3.18976–4	3.5	28.5	24.1
64	246.49	246.49	1.77625–3	2.51029–4	3.0	28.8	25.1
66	238.20	238.20	1.34000–3	1.95943–4	2.3	28.9	26.0
68	229.91	229.91	1.00067–3	1.51604–4	1.6	28.8	26.8
70	221.63	221.63	7.39117–4	1.16191–4	0.6	28.3	27.5
72	213.34	213.34	5.39672–4	8.81491–5	–0.5	27.5	28.1
74	205.06	205.06	3.89199–4	6.61538–5	–1.7	26.3	28.4
76	196.77	196.77	2.77271–4	4.90758–5	–2.9	24.6	28.3
78	188.49	188.49	1.94712–4	3.59435–5	–3.9	22.3	27.2
80	180.20	180.20	1.34206–4	2.59447–5	–4.5	19.3	24.9
82	180.20	180.20	9.18913–5	1.77441–5	–0.3	16.7	17.0
84	180.20	180.20	6.29807–5	1.21765–5	–0.3	15.5	15.8
86	180.20	180.20	4.31919–5	8.33893–6	–0.3	14.2	14.5
88	180.20	180.20	2.96783–5	5.71060–6	–0.3	12.9	13.2
90	180.20	180.20	2.01511–5	3.90816–6	–0.3	11.7	11.9

NOTE: Within table, the number format for 10^{-x} is shown as $-x$.

Table 3-19b. VAFB winter (cold) atmosphere (VCA-73) (ref. 3-20).

Geometric Altitude (MSL) (km)	Kinetic Temperature T (K)	Virtual Temperature T_V (K)	Atmospheric Pressure P (N/cm^2)	Atmospheric Density ρ (kg/m^3)	Relative Deviation (T_V) Percent From VRA-71 RD (T^*) %	Relative Deviation (P) Percent From VRA-71 RD (P) %	Relative Deviation (ρ) Percent From VRA-71 RD (ρ) %
0	272.10	272.70	1.01800+1	1.30047+0	–5.0	–0.1	5.2
2	260.86	261.22	7.88092+0	1.05101+0	–7.9	–1.8	6.6
4	249.62	249.74	6.03127+0	8.41315–1	–8.3	–3.9	4.8
6	238.30	238.30	4.55804+0	6.66334–1	–7.9	–6.1	2.0
8	226.90	226.90	3.39765+0	5.21654–1	–6.9	–8.1	–1.3
10	220.87	220.87	2.49937+0	3.94219–1	–3.3	–9.8	–6.7
12	220.20	220.20	1.83347+0	2.90065–1	1.1	–10.0	–11.0
14	219.53	219.53	1.34374+0	2.13232–1	3.1	–9.5	–12.2
16	218.87	218.87	9.83871–1	1.56602–1	4.5	–8.4	–12.3
18	218.20	218.20	7.19692–1	1.14902–1	3.7	–7.3	–10.6
20	219.20	219.20	5.26594–1	8.36900–2	2.7	–6.6	–9.1
22	220.20	220.20	3.85822–1	6.10388–2	1.3	–6.0	–7.3
24	221.20	221.20	2.83123–1	4.45893–2	0.2	–5.9	–6.1
26	222.20	222.20	2.08033–1	3.26157–2	–0.4	–6.3	–5.9
28	223.20	223.20	1.53042–1	2.38865–2	–1.3	–6.7	–5.5
30	224.20	224.20	1.12781–1	1.75244–2	–2.7	–7.6	–5.0
32	225.20	225.20	8.32025–2	1.28706–2	–4.0	–8.8	–5.0
34	229.60	229.60	6.16129–2	9.34844–3	–3.9	–10.1	–6.5
36	234.00	234.00	4.58777–2	6.82981–3	–3.8	–11.4	–7.8
38	238.40	238.40	3.43580–2	5.02066–3	–4.0	–12.7	–9.0
40	242.80	242.80	2.58661–2	3.71133–3	–4.4	–14.0	–10.1
42	247.20	247.20	1.95663–2	2.75710–3	–4.8	–15.4	–11.2
44	251.60	251.60	1.48762–2	2.05959–3	–5.1	–16.9	–12.4
46	256.00	256.00	1.13715–2	1.54768–3	–4.9	–18.3	–14.0
48	258.20	258.20	8.71913–3	1.17640–3	–4.7	–19.6	–15.6
50	258.20	258.20	6.69192–3	9.02894–4	–4.8	–20.9	–16.9
52	258.20	258.20	5.13323–3	6.92657–4	–4.7	–22.3	–18.5
54	255.43	255.43	3.93843–3	5.37093–4	–4.8	–23.5	–19.7
56	252.65	252.65	3.00886–3	4.14851–4	–4.3	–24.7	–21.3
58	249.88	249.88	2.29069–3	3.19393–4	–3.4	–25.8	–23.2
60	247.10	247.10	1.73914–3	2.45237–4	–2.2	–26.7	–25.1
62	244.33	244.33	1.31731–3	1.87851–4	–0.7	–27.4	–26.9
64	241.55	241.55	9.95395–4	1.43540–4	0.9	–27.8	–28.5
66	238.78	238.78	7.50022–4	1.09377–4	2.6	–28.0	–29.8
68	236.01	236.01	5.62873–4	8.30355–5	4.2	–27.8	–30.7
70	233.23	233.23	4.20198–4	6.27451–5	5.9	–27.2	–31.2
72	230.46	230.46	3.11980–4	4.71759–5	7.5	–26.2	–31.4
74	227.68	227.68	2.30470–4	3.53189–5	9.2	–24.8	–31.1
76	224.91	224.91	1.70264–4	2.64292–5	11.0	–22.9	–30.6
78	222.14	222.14	1.26467–4	1.98240–5	13.3	–20.5	–29.9
80	219.36	219.36	9.43661–5	1.49002–5	16.3	–17.6	–29.1
82	216.59	216.59	6.84452–5	1.09730–5	19.9	–13.9	–28.2
84	215.20	215.20	4.93374–5	7.98684–6	19.1	–9.4	–23.9
86	215.20	215.20	3.59130–5	5.81396–6	19.1	–4.6	–20.0
88	215.20	215.20	2.61438–5	4.23253–6	19.1	0.3	–15.8
90	215.20	215.20	1.90330–5	3.08138–6	19.1	5.5	–11.9

NOTE: Within table, the number format for 10^{-x} is shown as $-x$.

Table 3-20a. EAFB summer (hot) atmosphere (EHA-75) (ref. 3-16).

Geometric Altitude (MSL) (km)	Kinetic Temperature T (K)	Virtual Temperature T_V (K)	Atmospheric Pressure P (N/cm^2)	Atmospheric Density ρ (kg/m^3)	Relative Deviation (T_V) Percent From ERA-75 RD (T^*) %	Relative Deviation (P) Percent From ERA-75 RD (P) %	Relative Deviation (ρ) Percent From ERA-75 RD (ρ) %
0.7	316.45	318.05	9.29000+0	1.01756+0	9.6	–0.5	–9.2
2	300.67	301.46	8.04214+0	9.29341–1	5.9	0.4	–5.2
4	284.48	285.00	6.37015+0	7.78659–1	4.7	1.5	–3.0
6	268.92	269.16	4.97668+0	6.44131–1	4.0	2.5	–1.4
8	254.92	254.92	3.83393+0	5.23930–1	4.6	3.7	–0.9
10	241.23	241.23	2.91079+0	4.20355–1	5.6	5.1	–0.5
12	227.04	227.04	2.17387+0	3.33561–1	4.3	6.7	2.3
14	212.84	212.84	1.59320+0	2.60764–1	–0.0	7.4	7.4
16	198.65	198.65	1.14285+0	2.00419–1	–5.2	6.4	12.2
18	207.65	207.65	8.16392–1	1.36963–1	–1.3	5.2	6.6
20	214.23	214.23	5.91070–1	9.61192–2	0.4	4.8	4.5
22	218.38	218.38	4.30924–1	6.87411–2	0.5	5.0	4.5
24	222.53	222.53	3.16101–1	4.94846–2	0.8	5.1	4.2
26	226.69	226.69	2.33206–1	3.58394–2	1.6	5.0	3.4
28	230.84	230.84	1.72959–1	2.61005–2	2.1	5.4	3.2
30	235.00	235.00	1.29000–1	1.91239–2	2.0	5.7	3.6
32	239.15	239.15	9.66936–2	1.40849–2	1.9	6.0	4.0
34	246.76	246.76	7.29929–2	1.03052–2	3.3	6.5	3.1
36	254.36	254.36	5.55635–2	7.60930–3	4.5	7.3	2.7
38	261.97	261.97	4.26481–2	5.67157–3	5.5	8.4	2.8
40	269.58	269.58	3.29812–2	4.26250–3	6.2	9.6	3.2
42	277.18	277.18	2.56820–2	3.22755–3	6.8	11.0	4.0
44	284.79	284.79	2.01373–2	2.46297–3	7.5	12.5	4.7
46	292.40	292.40	1.58997–2	1.89494–3	8.6	14.3	5.2
48	296.20	296.20	1.26103–2	1.48314–3	9.3	16.4	6.4
50	296.20	296.20	1.00125–2	1.17761–3	9.2	18.4	8.4
52	296.20	296.20	7.94989–3	9.35009–4	9.4	20.3	10.0
54	287.91	287.91	6.29186–3	7.61269–4	7.3	22.2	13.9
56	279.63	279.63	4.94523–3	6.16080–4	5.9	23.7	16.9
58	271.34	271.34	3.85861–3	4.95412–4	4.9	24.9	19.1
60	263.06	263.06	2.98778–3	3.95703–4	4.1	25.8	20.8
62	254.77	254.77	2.29489–3	3.13804–4	3.5	26.4	22.1
64	246.49	246.49	1.74742–3	2.46960–4	3.0	26.8	23.1
66	238.20	238.20	1.31829–3	1.92767–4	2.3	26.8	24.0
68	229.91	229.91	9.84449–4	1.49145–4	1.6	26.7	24.7
70	221.63	221.63	7.27181–4	1.14307–4	0.6	26.2	25.4
72	213.34	213.34	5.30913–4	8.67226–5	–0.5	25.4	26.0
74	205.06	205.06	3.82895–4	6.50828–5	–1.7	24.2	26.3
76	196.77	196.77	2.72746–4	4.82824–5	–2.9	22.5	26.2
78	188.49	188.49	1.91569–4	3.53618–5	–3.9	20.3	25.2
80	180.20	180.20	1.32041–4	2.55060–5	–4.5	17.4	22.9
82	180.20	180.20	9.02891–5	1.74789–5	–0.3	14.8	15.1
84	180.20	180.20	6.19698–5	1.19743–5	–0.3	13.6	13.9
86	180.20	180.20	4.23431–5	8.20160–6	–0.3	12.4	12.6
88	180.20	180.20	2.90775–5	5.62477–6	–0.3	11.1	11.4
90	180.20	180.20	1.98078–5	3.84521–6	–0.3	9.8	10.1

NOTE: Within table, the number format for 10^{-x} is shown as $-x$.

Table 3-20b. EAFB winter (cold) atmosphere (ECA-75) (ref. 3-16).

Geometric Altitude (MSL) (km)	Kinetic Temperature T (K)	Virtual Temperature T_V (K)	Atmospheric Pressure P (N/cm^2)	Atmospheric Density ρ (kg/m^3)	Relative Deviation (T_V) Percent From ERA-75 RD (T_V) %	Relative Deviation (P) Percent From ERA-75 RD (P) %	Relative Deviation (ρ) Percent From ERA-75 RD (ρ) %
0.7	273.15	273.65	9.39000+0	1.19539+0	–5.7	0.5	6.6
2	264.71	265.06	7.96264+0	1.04652+0	–6.9	–0.6	6.8
4	251.67	251.79	6.11233+0	8.45689–1	–7.6	–2.6	5.4
6	239.65	239.65	4.62679+0	6.72573–1	–7.4	–4.7	2.9
8	228.65	228.65	3.45563+0	5.26494–1	–6.2	–6.6	–0.4
10	222.48	222.48	2.54834+0	3.99023–1	–2.6	–8.0	–5.5
12	221.15	221.15	1.87275+0	2.95006–1	1.5	–8.1	–9.5
14	219.82	219.82	1.37372+0	2.17708–1	3.3	–7.4	–10.4
16	218.48	218.48	1.00575+0	1.60365–1	4.3	–6.4	–10.2
18	217.15	217.15	7.34954–1	1.17907–1	3.2	–5.3	–8.3
20	217.48	217.48	5.36679–1	8.59659–2	1.9	–4.8	–6.6
22	217.82	217.82	3.92083–1	6.27082–2	0.2	–4.5	–4.7
24	218.15	218.15	2.86583–1	4.57648–2	–1.2	–4.7	–3.7
26	219.91	219.91	2.09783–1	3.32322–2	–1.4	–5.5	–4.1
28	221.68	221.68	1.53949–1	2.41935–2	–2.0	–6.2	–4.3
30	223.44	223.44	1.13252–1	1.76572–2	–3.0	–7.2	–4.3
32	225.20	225.20	8.35144–2	1.29190–2	–4.0	–8.5	–4.6
34	229.60	229.60	6.18410–2	9.38307–3	–3.9	–9.8	–6.1
36	234.00	234.00	4.60475–2	6.85513–3	–3.8	–11.1	–7.5
38	238.40	238.40	3.44851–2	5.03925–3	–4.0	–12.4	–8.7
40	242.80	242.80	2.59613–2	3.72509–3	–4.4	–13.7	–9.8
42	247.20	247.20	1.96382–2	2.76744–3	–4.8	–15.1	–10.9
44	251.60	251.60	1.49321–2	2.06726–3	–5.1	–16.6	–12.1
46	256.00	256.00	1.14139–2	1.55352–3	–4.9	–17.9	–13.7
48	258.20	258.20	8.75152–3	1.18076–3	–4.7	–19.3	–15.3
50	258.20	258.20	6.71674–3	9.06220–4	–4.8	–20.6	–16.6
52	258.20	258.20	5.15508–3	6.95519–4	–4.7	–22.0	–18.2
54	255.43	255.43	3.95301–3	5.39081–4	–4.8	–23.3	–19.4
56	252.65	252.65	3.01997–3	4.16381–4	–4.3	–24.5	–21.0
58	249.88	249.88	2.29916–3	3.20568–4	–3.4	–25.5	–22.9
60	247.10	247.10	1.74555–3	2.46135–4	–2.2	–26.4	–24.8
62	244.33	244.33	1.32215–3	1.88541–4	–0.7	–27.1	–26.6
64	241.55	241.55	9.99067–4	1.44072–4	0.9	–27.6	–28.2
66	238.78	238.78	7.52785–4	1.09777–4	2.6	–27.7	–29.5
68	236.01	236.01	5.64923–4	8.33397–5	4.2	–27.5	–30.4
70	233.23	233.23	4.21743–4	6.29730–5	5.9	–26.9	–31.0
72	230.46	230.46	3.13067–4	4.73404–5	7.5	–26.0	–31.1
74	227.68	227.68	2.31276–4	3.54486–5	9.2	–24.6	–30.9
76	224.91	224.91	1.70860–4	2.65102–5	11.0	–22.7	–30.3
78	222.14	222.14	1.26944–4	1.98898–5	13.3	–20.3	–29.6
80	219.36	219.36	9.46903–5	1.49574–5	16.3	–17.3	–28.9
82	216.59	216.59	6.87218–5	1.10025–5	19.9	–13.6	–27.9
84	215.20	215.20	4.95183–5	8.01647–6	19.1	–9.0	–23.6
86	215.20	215.20	3.60456–5	5.83524–6	19.1	–4.3	–19.7
88	215.20	215.20	2.62412–5	4.24784–6	19.1	0.7	–15.5
90	215.20	215.20	1.91021–5	3.09271–6	19.1	5.8	–11.2

NOTE: Within table, the number format for 10^{-x} is shown as $-x$.

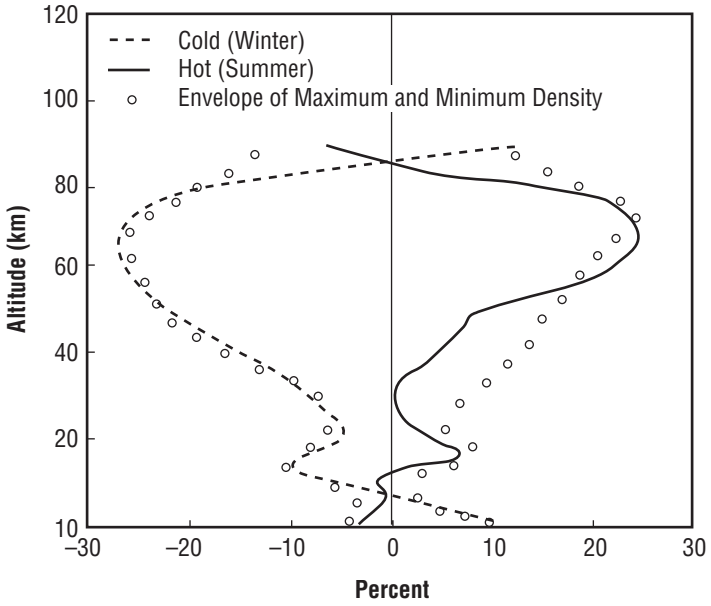

Figure 3-4. Relative deviations (%) of extreme KSC density profiles with respect to PRA-63.

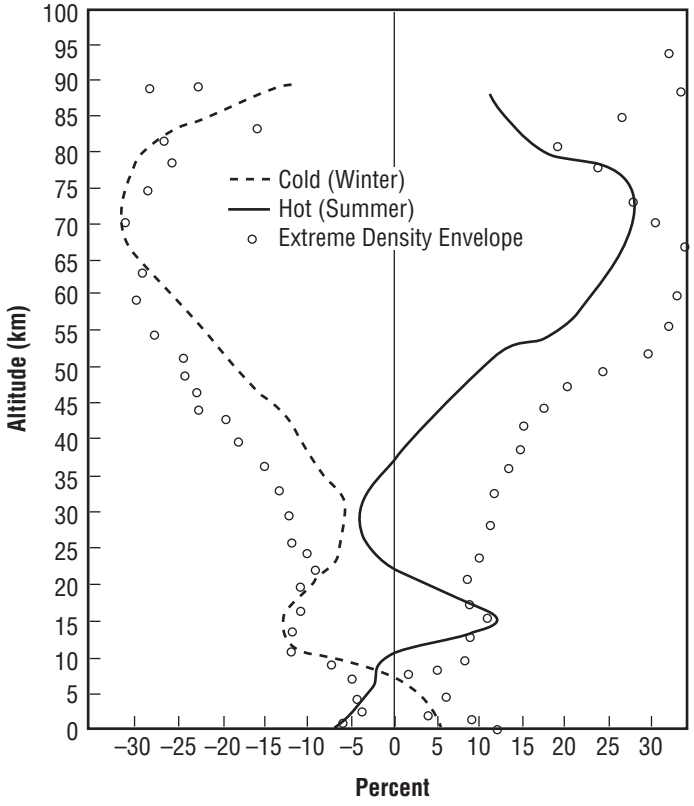

Figure 3-5. Relative deviations (%) of VAFB density profiles with respect to VRA-71.

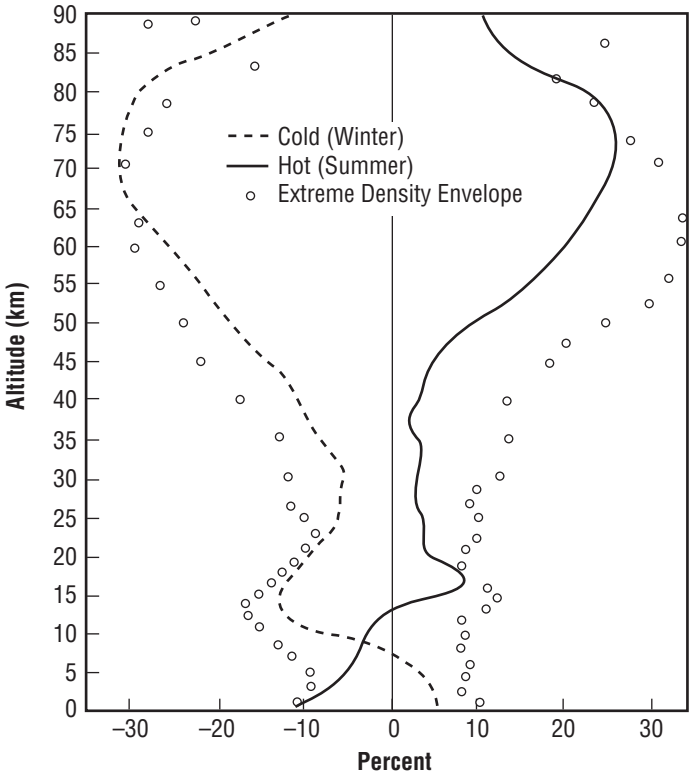

Figure 3-6. Relative deviations (%) of extreme EAFB density profiles with respect to ERA-75.

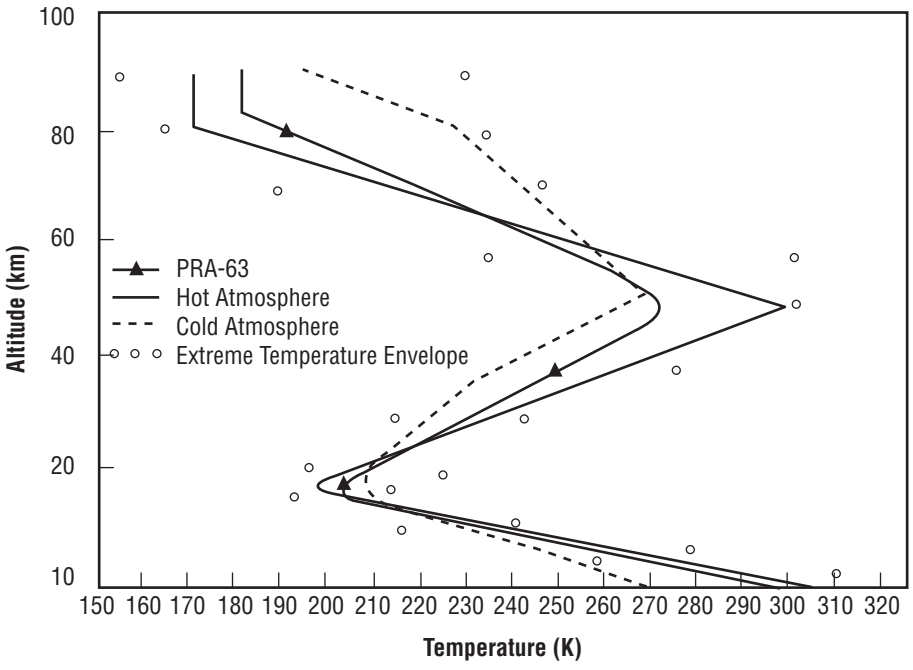

Figure 3-7. Virtual temperature profiles of the KSC hot, cold, and PRA-63.

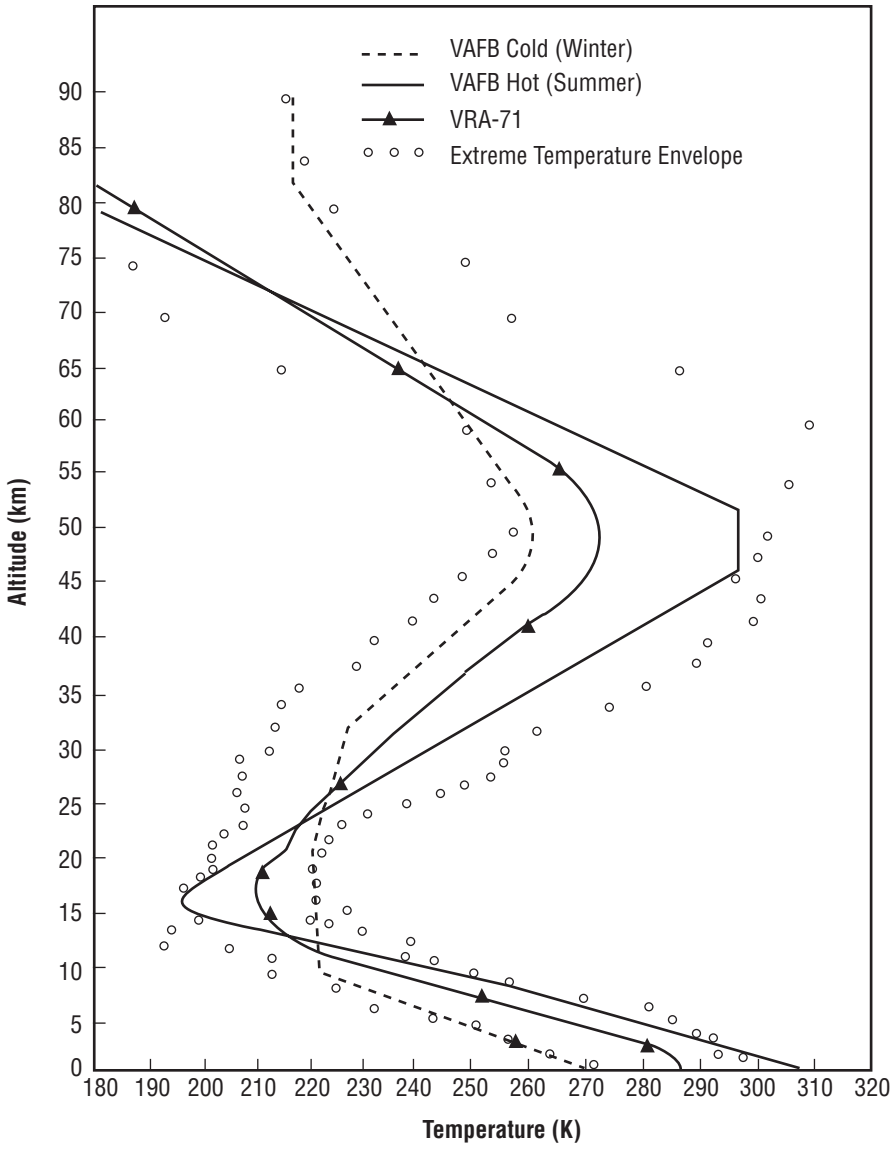

Figure 3-8. Virtual temperature profiles of the VAFB hot, cold, and VRA-71.

3.7 Range Reference Atmospheres

In design and preflight analysis of aerospace vehicles, average atmospheric models are used to represent the mean or median thermodynamic conditions with respect to altitude. For general worldwide design, the U.S. Standard Atmosphere, 1976 (ref. 3-5) is used but site-specific atmosphere models are needed at each launch location. A group of 17 RRAs from the RCC/MG as documented in reference 3-8 have been prepared to represent the thermodynamic medians within the first 70-km altitude at various ranges and launch locations. (Twelve of these RRAs along with five additional RRA sites; i.e., for Argentia, New Foundland; China Lake NAWC, CA; EPG Fort Huachuca, AZ; Roosevelt Roads, PR; and Yuma PG, AZ, are available from the EAFB Web site. However, these 17 electronic RRAs are currently being rechecked for accuracy.) To date, a total of 29 different site RRAs have been issued. References 3-10 and 3-21 (supplemental atmospheres) together with reference 3-9, which describes the GRAM, are also useful in this regard. The GRAM-07 was constructed such that it provides a close approximation to the respective RRAs.

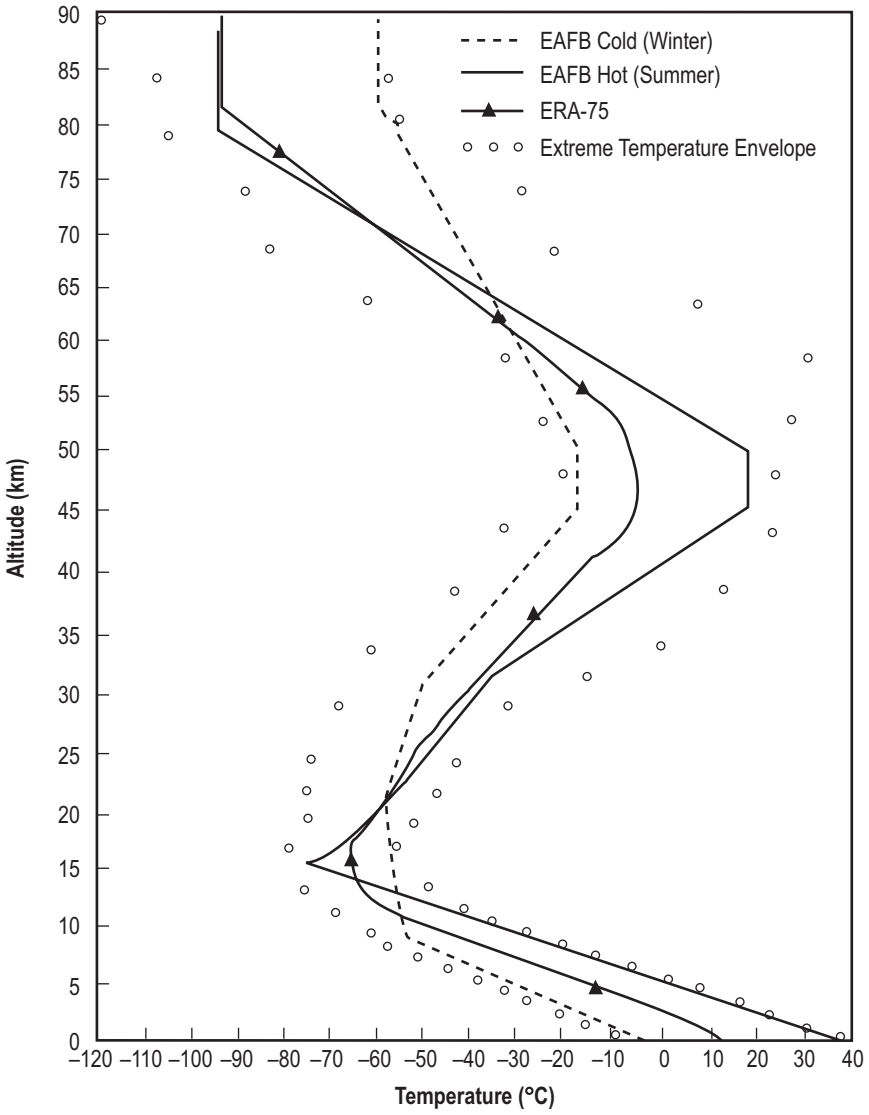

Figure 3-9. Virtual temperature profiles of the EAFB hot, cold, and ERA-75.

A major new feature of the GRAM-07 is the (optional) ability to use data (in the form of vertical profiles) from a set of RRAs as an alternate to the usual GRAM climatology. With this feature, it is possible, for example, to simulate a flight profile that takes off from the location of one RRA site; e.g. EAFB, using the range reference atmospheric data to smoothly transition into an atmosphere characterized by the GRAM climatology, then smoothly transition into an atmosphere characterized by a different RRA site; e.g., WSMR, NM, to be used as the landing site in the simulation. Data for 12 RRA sites are provided. The user can also prepare data for any other site desired for use in this mode.

The Patrick Reference Atmosphere (PRA-63) is a more extensive reference atmosphere presenting data to 700-km altitude for KSC. Because of the utility of this atmosphere, a simplified version is given as table 3-11 from reference 3-6. Criteria for orbital studies are given in reference 3-22.

Reference atmospheres are also available for VAFB (ref. 3-7 and table 3-12) and EAFB (ref. 3-16 and table 3-13). These provide an annual reference atmosphere model to 700 km and have been designated as computer subroutines VRA-71 and ERA-75, respectively.

In tables 3-11 through 3-13, the reference atmosphere values are given for these three sites in standard computer printout, where the two-digit numbers that are at the end of the tabular value (number preceded by E) indicate the power of 10 by which the respective principal value must be multiplied. For example, a tabular value indicated as 2.9937265E 02 is 299.37265.

A detailed listing and description of many worldwide reference and standard atmospheric models is given in reference 3-3.

3.8 MSFC Global Reference Atmospheric Model (Ref. 3-9)

The NASA MSFC GRAM-07 was developed in response to the need for a design reference atmosphere that provides complete global geographical variability, and complete altitude coverage—surface to orbital altitudes. Like the previous versions of Earth GRAM, the 2007 model provides estimates of means and standard deviations for atmospheric parameters such as density, temperature, and winds, for any month, at any altitude and location within the Earth's atmosphere. Earth GRAM can also provide profiles of statistically-realistic variations; i.e., with Dryden energy spectral density, for any of these parameters along computed or specified trajectory. This perturbation feature makes Earth GRAM especially useful for Monte Carlo dispersion analyses of guidance and control systems, thermal protection systems, and similar applications. Some of these applications have included operational support for Shuttle entry, flight simulation software for X-33 and other vehicles, entry trajectory and landing dispersion analyses for the Stardust and Genesis missions, planning for aerocapture and aerobraking for Earth-return from lunar and Mars missions, 6 degree-of-freedom entry dispersion analysis for the Multiple Experiment Transporter to Earth Orbit and Return (METEOR) system, and more recently, the Crew Exploration Vehicle (CEV).

The GUACA (or GGUAS) data cover the altitude region from zero to 27 km (in the form of data at the surface and at constant pressure levels from 1,000 mb to 10 mb). The middle atmospheric region (20 to 120 km) data set is compiled from Middle Atmosphere Program (MAP) data and other sources referenced in the GRAM-90 and GRAM-95 reports. The highest altitude region (above 90 km) is simulated by the Marshall Engineering Thermosphere (MET) model, specifically the 2007 version (MET-2007). Smooth transition between the altitude regions is provided by fairing techniques. Unlike interpolation (used to "fill in" values across a gap in data), fairing is a process that provides a smooth transition from one set of data to another in regions over which they overlap; e.g., 20 to 27 km for GUACA/GGUAS and MAP data and 90 to 120 km for MAP data and the MET model). Figure 3-10 provides a graphical summary of the data sources and height regions. Earth GRAM-07 retains the capability of the previous version but also contains several new features listed in section 3.8.1.

3.8.1 New GRAM-07 Model Features

- Uses 2006 revised Range Reference Atmospheres.
- 'Auxiliary profile' feature added. Allows user to input any thermodynamic or wind profile.
- New thermospheric model, MSFC MET-2007 added.
- Thermospheric model, NRL MSIS E-00, and associated Harmonic Wind Model (HWM-93) added.
- Thermospheric model, Jacchia-Bowman 2006 added.
- Earth Reference Ellipsoid updated to WGS 84.
- Various Perturbation Model revisions made.

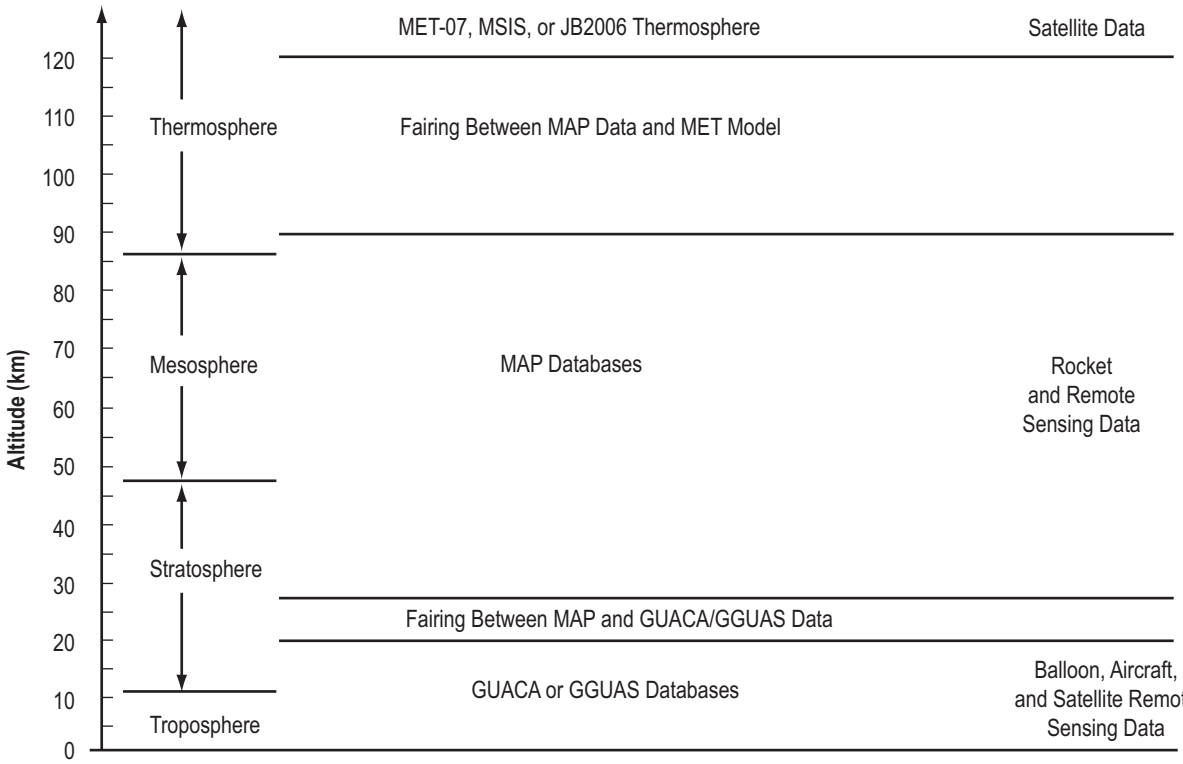

Figure 3-10. Schematic summary of the atmospheric regions in the GRAM-07 program and sources for the models and data on which the mean monthly GRAM-07 values are based (ref. 3-9).

3.8.2 Reentry Atmospheric Model

The atmospheric model recommended for all reentry analyses, except lower altitudes specified in section 3.6, is GRAM-07 (ref. 3-9). This model generates monthly profiles of atmospheric variables—wind, pressure, temperature, and density—along any vehicle trajectory from orbital altitudes to sea level on a worldwide basis. GRAM-07 can also generate many different realistic, simulated atmospheric profiles. A Monte Carlo procedure utilizing correlative techniques with the daily variability of the atmospheric parameters has been used to construct the individual atmospheric profiles.

The GRAM-07 model has been computerized and is available to give these variables and their structure as a function of the three spatial coordinates—latitude, longitude, and altitude—and of the time domain—monthly. The GRAM-07 model is a composite of other atmospheric models melded together with new techniques to join models and simulate perturbations. The GRAM-07 computer program is available from the Natural Environments Branch, Engineering Directorate, NASA Marshall Space Flight Center, Huntsville, AL 35812.

3.8.3 Atmospheric Model for Simulation

A National Aero-Space Plane (NASP) Integrated Atmospheric Model (NIAM) (ref. 3-23) was developed at NASA Ames Research Center/Dryden Flight Research Center under guidance from MSFC, for NASP engineering design and flight simulation studies. The NIAM is based on an earlier version of GRAM, but has been expanded to incorporate other specific, realistic atmospheric thermodynamic and wind (turbulence) perturbations.

NIAM is specific to NASP and was developed for real-time simulations, but is also appropriate for use in NASP offline control, structure, and propulsion subsystem design activities, and in batch simulations. It was developed to simulate ascent, cruise, and descent of the X-30.

3.9 Atmospheric Orbital Altitude Model

General environmental criteria for NASA orbital studies are given in reference 3-22. The atmospheric model baselined to be used in all space station design studies is the MET (refs. 3-24 through 3-26). A good description of the upper atmospheric variations that have been programmed into the MSFC orbital altitude atmospheric model can be obtained from references 3-22 and 3-28. The above-mentioned GRAM-07 model (ref. 3-9) also has the NASA MET-2007 model within its upper structure above 120-km altitude. This 2007 version of the NASA Marshall Engineering Thermospheric Model (MET-2007) is described in reference 3-29.

Like previous versions of MET, the 2007 model consists of a computer program and subroutines which provide information on atmospheric properties for the altitude range 90 to 2,500 km as a function of latitude, longitude, time, and solar flux and geomagnetic indices. For a given latitude, longitude, and time, the MET-2007 model yields values for the following parameters: exospheric temperature (K); local temperature (K); N_2 number density (m^{-3}); O_2 number density (m^{-3}); O number density (m^{-3}); Ar number density (m^{-3}); He number density (m^{-3}); H number density (m^{-3}); average molecular weight (kg/kmol); total mass density (kg/m^3); total pressure (Pa); ratio of specific heats; pressure scale height (m); specific heat at constant pressure (J/kg K); and specific heat at constant volume (J/kg K). MET-2007 retains the capability of the previous version (MET-2.0) but also contains several improvements which include the following:

- Corrections for inconsistency between constituent number density and mass density.
- Representation of gravity above an oblate spheroid Earth shape, rather than using a spherical Earth approximation.
- Treatment of day of year as a continuous variable in the semiannual term, rather than as an integer day.
- Treatment of year as either 365 or 366 days in length (as appropriate), rather than all years having length 365.2422 days.
- Allows continuous variation of time input, rather than limiting time increments to integer minutes.

REFERENCES

3-1. Johnson, D.L.; Roberts; B.C.; Vaughan, W.W.; and Justus, C.G.: "Atmospheric Models for Engineering Applications," *AIAA–2003–0894*, AIAA 41st Aerospace Sciences Meeting, Reno, NV, January 6–9, 2003.

3-2. Johnson, D.L.; Vaughan, W.W.; and Roberts, B.C.: "Reference and Standard Atmosphere Models," in *Proceedings of the 10th Aviation, Range, and Aerospace Meteorology Conference*, American Meteorological Society, Boston, MA, May 13–16, 2002.

3-3. *Guide to Reference and Standard Atmospheric Models*, ANSI/AIAA G-003C-2008, American Institute of Aeronautics and Astronautics, Reston, VA, 2008.

3-4. Champion, K.S.W.: "Early Years of Air Force Geophysics Research Contributions to Internationally Recognized Standard and Reference Atmospheres," *Technical Report PL–TR–95–2164*, Air Force Phillips Laboratory (now Air Force Research Laboratory), Hanscom AFB, MA, 1995.

3-5. *U.S. Standard Atmosphere, 1976*, U.S. Government Printing Office, Washington, DC, October 1976.

3-6. Smith, O.E.; and Weidner, D.K.: "A Reference Atmosphere for Patrick AFB, Florida, Annual (1963 Revision)," *NASA TM X–53139*, NASA Marshall Space Flight Center, AL, September 23, 1964.

3-7. Carter, E.A.; and Brown, S.C.: "A Reference Atmosphere for Vandenberg AFB, California, Annual (1971 Version)," *NASA TM X–64590*, NASA Marshall Space Flight Center, AL, May 10, 1971.

3-8. Range Reference Atmosphere Documents published by Secretariat, Range Commanders Council (RCC), Meteorology Group (MG), White Sands Missile Range, NM. The following Reference Atmospheres have been published under this title, except (18):

(1) Kwajalein Missile Range—Range Reference Atmosphere zero to 70-km altitude, RCC Document 360-82, 1982.

(2) Cape Canaveral, FL—Range Reference Atmosphere zero to 70-km altitude, RCC Document 361-83, February 1983.

(3) Vandenberg Air Force Base, CA—Range Reference Atmosphere zero to 70-km altitude, RCC Document 362-83, April 1983.

(4) Dugway, UT—Range Reference Atmosphere zero to 30-km altitude, RCC Document 363-83, June 1983.

(5) Wallops Island, VA—Range Reference Atmosphere zero to 70-km altitude, RCC Document 364-83, July 1983.

(6) White Sands Missile Range, NM—Range Reference Atmosphere zero to 70-km altitude, RCC Document 365-83, August 1983.

(7) Edwards AFB, CA—Range Reference Atmosphere zero to 70-km altitude, RCC Document 366-83, August 1983.

(8) Eglin AFB, FL—Range Reference Atmosphere zero to 30-km altitude, RCC Document 367-83, August 1983.

(9) Taquac, Guam Island—Range Reference Atmosphere zero to 30-km altitude, RCC Document 368-83, September 1983.

(10) Point Mugu, CA—Range Reference Atmosphere zero to 70-km altitude, RCC Document 369-83, September 1983.

(11) Barking Sands, HI—Range Reference Atmosphere zero to 70-km altitude, RCC Document 370-83, December 1983.

(12) Ascension Island, South Atlantic—Range Reference Atmosphere zero to 66-km altitude, RCC Document 371-84, January 1984.

(13) Wake Island, North Pacific—Range Reference Atmosphere zero to 70-km altitude, RCC Document 376-91, August 1991.

(14) Nellis Range Complex, NV—Range Reference Atmosphere zero to 30-km altitude, RCC Document 377-91, August 1991.

(15) Shemya, AK—Range Reference Atmosphere zero to 70-km altitude, RCC Document 380-91, August 1991.

(16) Thule, Greenland—Range Reference Atmosphere zero to 70-km altitude, RCC Document 379-91, August 1991.

(17) Fairbanks, AK—Range Reference Atmosphere zero to 30-km altitude, RCC Document 378-91, August 1991.

(18) Kodiak Island, AK—Rawlins, M.A.; Johnson, D.L.; and Batts, G.W.: "A Characterization of the Terrestrial Environment of Kodiak Island, AK, for the Design, Development, and Operation of Launch Vehicles," Paper No. 6.6, Presented at the 9th AMS Conference on Aviation, Range, and Aerospace Meteorology, Orlando, FL, September 11–15, 2000.

3-9. Leslie, F.W.; and Justus, C.G.: "The NASA MSFC Earth Global Reference Atmospheric Model–2007 Version," NASA/TM—2008–215581, Marshall Space Flight Center, AL, November 2008.

3-10. *U.S. Standard Atmosphere Supplements, 1966*, U.S. Government Printing Office, Washington, DC, 1966.

3-11. "Revised Uniform Summary of Surface Weather Observations—Edwards AFB, CA," Part F, USAF-ETAC, Data Processing Division, Air Weather Service (MAC), Federal Building, Asheville, NC, March 20, 1974.

3-12. Tattelman, P.; Kantor, A.J.; and Willand, J.H.: "Model Profiles of Temperature and Density up to 80 km Based on Extremes at Selected Altitudes," *AIAA Journal*, Vol. 26, No. 10, pp. 1246–1253, October 1988.

3-13. "Global Climatic Data For Developing Military Products," DOD Document MIL-HDBK-310 (superseding MIL-STD-210C), June 23, 1997.

3-14. Smith, J.W.: "The Vertical Temperature Distribution and the Layer of Minimum Temperature," *J. Appl. Meteor.*, Vol. 2, No. 5, pp. 655–667, October 1963.

3-15. Hagemeyer, B.C.; Schmocker, G.K.; and Hileman, K.E.: "Mean Atmosphere Over Cape Canaveral, Florida," NOAA Technical Attachment SR/SSD 91–11, March 1, 1991.

3-16. Johnson, D.L.: "Hot, Cold, and Annual Reference Atmospheres for Edwards Air Force Base, California (1975 Version)," *NASA TM X–64970*, NASA Marshall Space Flight Center, AL, November 1975.

3-17. Smith, J.W.: "Density Variations and Isopycnic Layer," *J. Appl. Meteorol.*, Vol. 3, No. 3, pp. 290–298, June 1964.

3-18. Hale, N.W.; Lamotte, N.O.; and Garner, T.W.: "Operational Experience With Hypersonic Flight of the Space Shuttle," *AIAA–2002–5259*, 11th AIAA/AAAF International Conference—Space Planes and Hypersonic Systems, Orleans, France, September 2002.

3-19. Buell, C.E.: "Some Relations Among Atmospheric Statistics," *J. Meteorol.*, Vol. 11, pp. 238–244, June 1954.

3-20. Johnson, D.L.: "Hot and Cold Atmospheres for Vandenberg AFB, California (1973 Version)," *NASA TM–64756*, NASA Marshall Space Flight Center, AL, June 26, 1973.

3-21. Cole, A.E.; and Kantor, A.J.: "Air Force Reference Atmospheres," *AFGL–TR–78–0051*, Air Force Surveys in Geophysics, No. 382, February 28, 1978.

3-22. Anderson, B.J.; and Smith, R.E.: "Natural Orbital Environment Guidelines for Use in Aerospace Vehicle Development," *NASA TM–4527*, NASA Marshall Space Flight Center, AL, June 1994.

3-23. Schilling, L.J.: "Definition of the NASP Integrated Atmospheric Model," Document Version 2.2, NASP Government Work Package 24A, "Atmospheric Modeling," NASA Ames-Dryden Flight Research Facility Report, October 22, 1991.

3-24. Hickey, M.P.: "The NASA Marshall Engineering Thermosphere Model," *NASA CR–179359*, NASA Marshall Space Flight Center, AL, July 1988.

3-25. Hickey, M.P.: “An Improvement in the Numerical Integration Procedure Used in the NASA Marshall Engineering Thermosphere Model,” *NASA CR–179389*, NASA Marshall Space Flight Center, AL, August 1988.

3-26. Hickey, M.P., “A Simulation of Small-Scale Thermospheric Density Variations for Engineering Applications,” *NASA CR–4605*, NASA Marshall Space Flight Center, AL, May 1994.

3-27. Johnson, D.L.; and Smith, R.E.: “The MSFC/J70 Orbital Atmospheric Model and the Data Bases for the MSFC Solar Activity Prediction Technique,” *NASA TM–86522*, NASA Marshall Space Flight Center, AL, November 1985.

3-28. Owens, J.K.; Niehuss, K.O.; Vaughan, W.W.; and Shea, M.A.: “NASA Marshall Engineering Thermosphere Model—1999 Version (MET-99) and Implications for Satellite Lifetime Predictions,” COSPAR, *Advances in Space Research*, Vol. 26(1), pp. 157–162, 2000.

3-29. Justus, C.G.; Duvall, A.; and Keller, V.W.: “Trace Constituent Updates in the Marshall Engineering Thermosphere and Global Reference Atmospheric Model,” *Advances in Space Research*, Vol. 38, pp. 2429–2432, 2006.

Terrestrial Environment (Climatic) Criteria Guidelines for Use in Aerospace Vehicle Development, 2008 Revision

NASA/TM—2008–215633
December 2008

D.L. Johnson, Editor

Section 4: Solar and Thermal Radiation

TABLE OF CONTENTS

TABLE OF CONTENTS (Continued)

LIST OF FIGURES

LIST OF TABLES

LIST OF ACRONYMS AND SYMBOLS

ASTM	American Society for Testing and Materials
CMDL	Climate Monitoring and Diagnostics Laboratory
CO_2	carbon dioxide
EAFB	Edwards Air Force Base
GSFC	Goddard Space Flight Center
HBCU	Historically Black Colleges and Universities
IR	infrared
JSC	Johnson Space Center
KSC	Kennedy Space Center
LST	local standard time
MSFC	Marshall Space Flight Center
NOAA	National Oceanic and Atmospheric Administration
NREL	National Renewable Energy Laboratory
PW	precipitable water
TMY2	typical meteorological year, version 2
UV	ultraviolet
VAFB	Vandenberg Air Force Base
WMO	World Meteorological Organization
WRC	World Radiation Center
WRR	World Radiometric Reference
WSMR	White Sands Missile Range

NOMENCLATURE

E	emittance of surface; irradiance
E_i	emittance of object
f_w	correction for wind speed
I_{DH}	direct horizontal solar radiation
I_{dH}	diffuse scattered radiation
I_{DN}	direct normal incident solar radiation
I_i	blackbody with several radiation sources
I_{TH}	horizontal solar radiation
I_{TN}	total normal solar radiation
I_{TS}	total radiation received at surface
m	air mass
S	solar constant
$\mathcal{T}'$	transmittance
T	temperature
T_A	air temperature
T_R	blackbody temperature
T_S	surface temperature
W	wind speed
w	mixing ratio of water vapor to dry air; Wien's displacement constant; wind speed; vertical component of turbulence (subscript)
α	azimuth
β	tilt angle
δ	optical depth
δ_c	cloud optical depth
θ	zenith angle; wind direction
λ	wavelength; gust thickness parameter
$\lambda_{\max}$	wavelength of maximum radiation intensity for the blackbody
ρ	linear correlation coefficient; mass density
ρ_S	atmospheric density at sea level

4. SOLAR AND THERMAL RADIATION

4.1 Introduction

Environments, such as solar (shortwave, or ultraviolet (UV) plus visible) radiation and thermal (long-wave, or infrared (IR)) radiation and ambient air temperature, can produce undesirable effects on aerospace vehicles while they are being fabricated, transported, tested, on the pad, or in flight. The ground support system may also be affected. Effects on the vehicles and ground support system include:

(1) Unequal heating resulting in stresses of various types.

(2) Temperature extremes (high or low) occurring inside or on the vehicle surface which may cause equipment malfunctions or uncomfortable/undesirable conditions for manned missions.

(3) Difficulties aligning vehicle parts at interfaces, and calibration of research and development (R&D) instruments on the vehicle because of variations in size, thermal effects, and/or shape with temperature.

4.1.1 Solar and Thermal Environments Zero to 90 km

Because of these and other effects, information on the radiation and thermal environment at the Earth's surface and up to 90-km (295,000-ft) altitude is presented in the following order:

(1) Thermal definitions.

(2) Extraterrestrial solar radiation over small wavelength intervals that irradiate the atmosphere from approximately 20- to 90-km altitude.

(3) Solar radiation transmitted, absorbed, and scattered through various atmospheres in small wavelength interval irradiances.

(4) Extreme values of total horizontal, diffuse, total normal incident, and total 45° surface solar radiation at various times of day at the Earth's surface for various geographic locations.

(5) Application of solar radiation in design.

(6) Methods of using surface emittance and the effect of wind speed to determine temperatures on surfaces exposed to solar and thermal radiation.

(7) Extreme and mean values of monthly air temperature at the Earth's surface at various times of day.

(8) Extreme temperature changes, surface skin temperatures, and compartment temperature values.

4.1.2 Solar and Thermal Environments in Low-Earth Orbit

Specifications of solar and thermal radiation in low-Earth orbit, including Earth-reflected solar radiation, and Earth-emitted thermal radiation, are provided elsewhere (refs. 4-1 and 4-2).

4.2 Definitions

The solar and thermal radiation terms used in this section are defined as follows:

Absorption bands are a portion of the electromagnetic spectrum where radiation is absorbed and emitted by atmospheric gases such as water vapor, carbon dioxide, and ozone.

Absorptivity (or absorptance) for any object is the fraction of the radiant energy falling on the object that is absorbed or transferred into heat. It is the ratio of radiation absorbed by any substance to that absorbed under the same conditions by a blackbody.

Air mass is the relative amount of atmosphere that solar radiation passes through, considering the vertical path at sea level as unity; i.e., when the Sun is at the zenith, directly overhead. Air mass will always be >1 when the path deviates from vertical. For transmission of direct sunlight, air mass is a function of solar zenith angle. At small solar zenith angles θ, air mass is $\approx 1/\cos(\theta)$.

Air temperature (at "surface") is the ambient air temperature measured under standard conditions of height, ventilation, and radiation shielding (ref. 4-3). Unless an exception is stated, surface air temperatures given in this document are temperatures measured under these standard conditions.

Atmosphere centimeters (atm-cm) is a measure of total overhead column amount of a gaseous constituent, such as ozone. It is the depth (in centimeters) a layer of the constituent would have if the entire constituent column were brought to the surface and adjusted to standard temperature and pressure.

Atmospheric transmittance is the ratio between the intensity of the extraterrestrial solar radiation and the intensity of the solar radiation after passing through the atmosphere.

Astronomical unit (au) is the mean distance of Earth from the Sun (1.496×10^8 km).

Blackbody is an ideal emitter that radiates energy at the maximum possible rate per unit area at each wavelength for any given temperature and which absorbs all incident radiation at all wavelengths. Its absorptivity is always 1; i.e., it is also an ideal absorber.

Blackbody temperature is computed from irradiance (E) (W/m^2) by the Stefan-Boltzmann relation, applicable for blackbodies:

$$E = \sigma T^4 \quad , \tag{4.1}$$

where σ is the Stefan-Boltzmann constant (5.670×10^{-8} W/m^2 K^{-4}). Thus, blackbody temperature is given from irradiance (E) by

$$T = (E/\sigma)^{1/4} \quad . \tag{4.2}$$

Diffuse (sky) radiation (I_{dH}) is the solar radiation reaching the Earth's surface after having been scattered from the direct solar beam by molecules and particles in the atmosphere. It is measured at the Earth's surface by subtracting the direct solar radiation from the total horizontal radiation.

Direct normal incident (I_{DN}) radiation: see normal incident.

Direct solar radiation is the solar radiation received by an object on a line directly from the Sun. It does not include diffuse radiation.

Emittance (or emissivity) is the ratio of the energy emitted by a body at a specific temperature to the energy that would be emitted by a blackbody at the same temperature. All bodies emit energy in different amounts compared to a blackbody at various wavelengths; i.e., low-temperature bodies emit more strongly in the IR rather than the visible spectrum. The absorptivity of an object is numerically equal to the emittance of the object at the same wavelengths: emittance is always <1.

Extraterrestrial solar radiation is that solar radiation received outside the Earth's atmosphere at 1 au from the Sun. The term "solar spectral irradiance" is used when the extraterrestrial solar radiation is considered by wavelength intervals.

Fraunhofer lines are the dark absorption lines or bands in the solar spectrum caused by gases in the outer portion of the Sun and Earth's atmosphere. These lines are due to absorption by atoms (sharp lines) or molecules (broad lines) in the gaseous state.

Horizontal solar radiation is the solar radiation measured on a horizontal surface. This is frequently referred to as "global radiation," "total horizontal radiation," or "total hemispherical radiation." Both direct solar and diffuse sky radiation are included.

Irradiance is the amount of radiation energy per unit time (power) emitted by or received by an object in unit surface area; e.g., in W/m^2. In some sources, emitted irradiance is called "exitance" to distinguish it from received irradiance. If the distribution of radiation power per unit surface area is given as a function of wavelength, it is referred to as "spectral irradiance"; e.g., in $W/m^2\ \mu m^{-1}$.

Normal incident (I_{DN}) solar radiation is the radiation received on a surface, normal to the direction of the Sun, direct from the Sun. A very small amount of diffuse sky radiation is typically also measured with I_{DN} measuring instruments.

Optical depth is a coefficient for determining transmittance ($\mathcal{T}$) through a given atmospheric path. The transmittance decreases with path length due to absorption and scattering by a given atmospheric constituent. Direct beam transmittance through the entire atmosphere (containing a given constituent) is

$$\mathcal{T} = e^{-\delta m} \quad , \tag{4.3}$$

where δ is optical depth (for the constituent) and m is air mass (as a function of solar zenith angle). Unless otherwise stated in this section, optical depth is evaluated at a wavelength of 0.5 μm.

Precipitable water is the depth (in centimeters) of the overhead column of water vapor, if brought to the surface and precipitated out as liquid water.

Sky temperature is the average effective blackbody temperature of the sky. It is computed by equation (4.2) from downwelling IR irradiance at the surface (IR irradiance received at the surface from all levels of the atmosphere). While this radiation is sometimes termed nocturnal radiation, it also takes place during daylight hours. Sky temperature is typically lower (and under clear skies, much lower) than measured air temperature.

Solar constant is the normally incident solar irradiance received outside the Earth's atmosphere at the Earth's mean distance (1 au) from the Sun. Based on older measurements, and the 1956 International Pyrheliometric Scale, the solar constant was long taken to be 1,353 W/m^2. More recently, the World Meteorological Organization (WMO) has adopted a new radiometer scale called the World Radiometric Reference (WRR), based on a data set of over 25,000 ground-based absolute radiometric measurements maintained at the World Radiation Center (WRC) in Davos, Switzerland. Based on the WRR scale, the WRC summarized eight ground-based solar constant measurements (ref. 4-4) made from 1969 to 1980 and recommended a solar constant of 1,367 W/m^2. This value has a standard deviation of 1.6 W/m^2 and a largest difference (among values averaged) of ±7 W/m^2. Recently, the American Society for Testing and Materials (ASTM) (ref. 4-5) recommended a solar constant of 1,366.1 W/m^2. This value is the mean from six different satellites from 1978 to 1998. The ASTM value has a standard deviation of 0.6 W/m^2 and a largest difference of ±3 W/m^2. For solar constant 1,367 W/m^2, the effective blackbody temperature of the Sun is 5,777 K.

Solar radiation is the total electromagnetic radiation emitted by the Sun, with 99 percent of the total found in the wavelength band between 0.2 and 4.0 μm.

Thermal radiation is the electromagnetic radiation emitted by any substance as the result of the thermal excitation of the molecules. Thermal radiation usually refers to the region of middle infrared and far infrared regions of spectrum ranging in wavelength from about 3 to 25 μm.

Total solar radiation means irradiance from all wavelengths covering the entire solar spectrum from the extreme UV to the far IR. Depending upon context, "total" may also mean combined direct-plus-diffuse solar irradiance. Combined direct-plus-diffuse irradiance is also sometimes referred to as global radiation.

Transmittance is the ratio of the power (energy per unit time) transmitted through a layer relative to the radiation power incident on the layer. Unless stated otherwise in this section, the layer under consideration is the entire atmosphere.

4.3 Solar Radiation

4.3.1 Introduction

The Sun emits energy in the electromagnetic spectrum from $<10^{-7}$ to $>10^5$ μm. This radiation ranges from solar cosmic rays through very long wave radio emissions. The total amount of radiation from the Sun is nearly constant in intensity with time (see further discussion in sec. 1.2.1 of ref. 4-2).

Of the total electromagnetic spectrum of the Sun, radiant energy from the portion of the spectrum between 0.22 and 20 μm contributes 99.98 percent of the total electromagnetic energy from the Sun (table 4-1). Almost all

Table 4-1. Spectral ranges for solar radiation.

Spectral Region (μm)	Distribution (%)	Solar Irradiance (W/m^2)
Ultraviolet, below 0.38	6.36	86.9
Visible, 0.38 to 0.78	47.82	653.7
Infrared, above 0.78	45.82	626.4

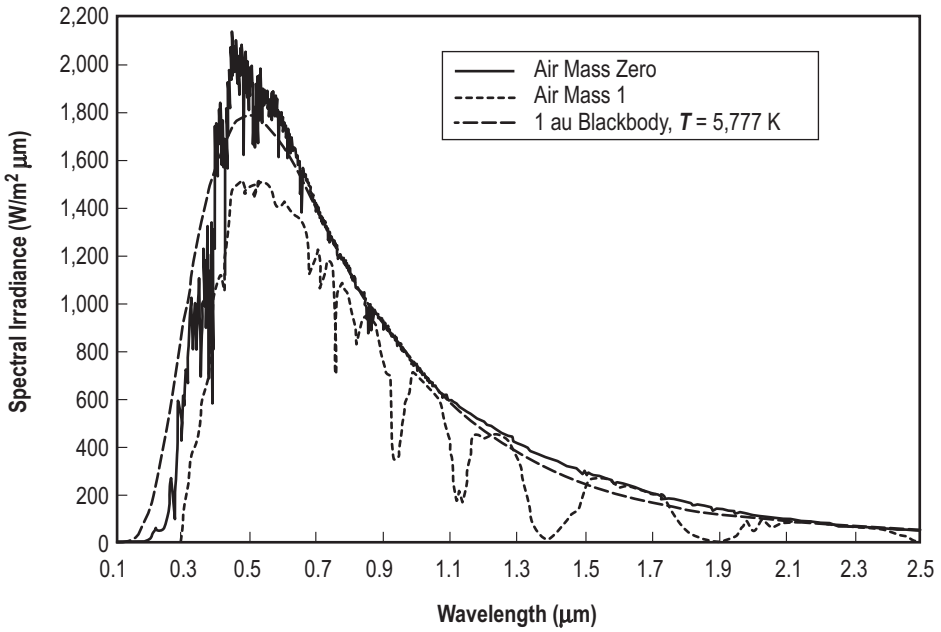

Figure 4-1. Normal incident direct solar spectral irradiance at air mass zero outside the Earth's atmosphere at 1 au (ref. 4-5). (Copyright ASTM—reprinted with permission) at air mass 1 (sea level), and blackbody spectral irradiance at $T = 5{,}777$ K (normalized to 1 au). Air mass 1 spectrum (from table 2 in ref. 4-6) includes effects of Rayleigh scattering, 1.42 cm precipitable water, 0.34 atm-cm ozone, and aerosol optical depth of 0.1 at 0.5-μm wavelength. Spectral absorption features are due primarily to ozone, water vapor, and CO_2.

of the remaining 0.02 percent of the solar spectrum occurs at wavelengths longer than 20 μm. The spectral distribution of this region closely resembles the emission of a blackbody radiating at 5,777 K (fig. 4-1).

Solar radiation, observed at an altitude high enough that the Earth's atmosphere does not absorb the radiation, is distributed in a continuous spectrum with many narrow absorption bands caused by the elements and molecules in the colder parts of the solar atmosphere. These absorption bands are the Fraunhofer lines, whose widths are usually very small ($<10^{-4}$ μm in most cases).

The Earth's atmosphere also partially absorbs solar radiation. The major portion of the solar radiation reaching the Earth's surface is between about 0.3 and 4 μm. The distribution of the solar energy outside the Earth's atmosphere (extraterrestrial, at 1 au, on a surface normal to the Sun) is given in table 4-1. Solar irradiance values in this table are based on a solar constant value of 1,367 W/m^2.

Solar radiation and its transmittance characteristics through the atmosphere are presented in the following sections.

4.3.2 Spectral Distribution of Radiation

All objects radiate energy in some portion of the electromagnetic spectrum. The amount and frequency of the radiation distribution is a function of temperature. The higher the temperature the greater the amount of total energy emitted and the higher the frequency (shorter the wavelength) of the peak energy emission. According to Wien's displacement law for blackbodies,

$$\lambda_{\max} = \frac{w}{T_R} \ , \tag{4.4}$$

where

w = Wien's displacement constant (2,898 μm K)
$\lambda_{\max}$ = wavelength of maximum radiation intensity for the blackbody
T_R = blackbody temperature.

With a characteristic blackbody temperature of 5,777 K, the solar spectrum peaks at $\lambda_{\max} \approx 0.5$ μm, and includes significant contributions from wavelengths up to ≈3 μm. Temperatures characteristic of Earth's surface and atmosphere are about 250–300 K, so the spectrum from terrestrial radiation sources peaks at about 10–11 μm, and has no significant contribution from wavelengths below ≈3 μm. The wavelength region near 3 μm thus serves as a convenient dividing point between the "solar spectrum"; i.e., below ≈3 μm, and the "terrestrial spectrum"; i.e., above ≈3 μm. Spectral irradiance from the solar spectrum is also more intense than from the terrestrial spectrum. Peak intensity of the extraterrestrial solar spectral irradiance distribution (at ≈0.5 μm) is ≈80 times greater than peak intensity of the typical terrestrial spectral irradiance distribution (at ≈10 μm).

4.3.3 Atmospheric Transmittance of Solar Radiation

Earth's atmosphere is composed of a mixture of gases, aerosols, and dust that absorb, scatter, and emit radiation in different amounts at various wavelengths. Effects on the transmittance of direct beam solar radiation through the atmosphere are therefore contributed by a number of processes. A number of atmospheric constituents actively absorb solar radiation, especially at selective wavelengths or throughout relatively broad wavelength bands. Atmospheric molecules, whose radii are smaller than about one-tenth the wavelength of the light, scatter radiation out of the beam (Rayleigh scattering). Aerosols, water droplets in hazy air, and hydrospheres (cloud water droplets, ice particles, and rain drops) also scatter solar radiation, without regard to the diameter of the particles (Mie scattering).

4.3.3.1 Absorbed Radiation. Primary absorbers of solar radiation include ozone, carbon dioxide (CO_2), water vapor, and atomic and molecular oxygen. Below ≈0.3 μm wavelength, nitrogen, atomic and molecular oxygen, and ozone effectively absorb all extraterrestrial solar radiation before it reaches Earth's surface. Throughout most of the rest of the solar spectrum, primary absorbers are ozone, water vapor, and CO_2. Once a photon is absorbed from the beam of solar radiation, it is effectively lost from the spectrum of solar radiation. It may be "reradiated," but only with the spectral distribution of terrestrial radiation (peaking at ≈10 μm).

4.3.3.2 Diffuse (Scattered) Radiation. When solar radiation, which is a nearly parallel beam of light, enters the Earth's atmosphere, air molecules, and aerosols, such as dust particles and water droplets, scatter (diffuse) part of the radiation. The diffuse or scattered radiation then reaches Earth's surface as nonparallel light from all directions. Scattering does not appreciably alter the spectral distribution, so diffuse radiation still has the spectral distribution of sunlight (peaking at ≈0.5 μm).

4.3.4 Solar Spectral Irradiance Distribution

Table 4-2 presents abbreviated data from the ASTM wavelength distribution of solar radiation at air mass zero; i.e., outside the Earth's atmosphere (ref. 4-5). A complete table of higher resolution air mass zero solar spectral irradiance is given in reference 4-5. Figure 4-1 shows a graph of the air mass zero ASTM solar spectral irradiance curve plus solar spectral irradiance at Earth's surface (normal incidence; air mass 1) on a clear day (ref. 4-6), as well as the spectral irradiance distribution from a blackbody at 5,777 K. Air mass 1 direct spectral irradiance in figure 4-1 was computed by a simple model described in reference 4-6. Spectral irradiance, both within and at the bottom of the atmosphere, can also be computed with the LOWTRAN 7 model and computer code (ref. 4-7) or the higher resolution model MODTRAN (ref. 4-8). Equations for computing direct and diffuse solar spectral irradiance at Earth's surface under cloud-free conditions, by the model described in reference 4-6, are also given in reference 4-9.

Solar spectral irradiance values in table 4-2 and figure 4-1 are for average Earth-Sun distance (1 au), a condition that occurs on approximately April 4 and October 5. At other times of the year, total solar irradiance and solar spectral irradiance vary inversely with square of the seasonally varying Earth-Sun distance. Air mass zero solar irradiance varies from a minimum of ≈1,321 W/m^2 at Earth's aphelion (approximately July 4) to a maximum of ≈1,413 W/m^2 at Earth's perihelion (approximately January 3). Thus, during the course of a year, total solar irradiance and air mass zero and air mass 1 solar spectral irradiance vary by about ±3.4 percent from their values in table 4-2 and figure 4-1. Cyclic changes in total solar irradiance and solar spectral irradiance due to solar activity variations with the solar cycle are generally <1 W/m^2 (0.07 percent). For further discussion of solar variability, see sections 1.2.1 and 1.2.2 of reference 4-1.

Air mass 1 direct solar spectral irradiance in figure 4-1 was computed (with a model described in ref. 4-6) for 1.42 cm precipitable water, 0.34 Atm-cm ozone, and aerosol optical depth of 0.1 at 0.5 μm. (Section 4.3.3.1 discusses atmospheric absorption.) Spectral irradiance curves for several other combinations of ozone, water vapor, and aerosols are given in both tabular and graphical forms in reference 4-6. Either LOWTRAN (ref. 4-7), the higher resolution MODTRAN (ref. 4-8), or the spectral model described in references 4-9 and 4-10 can also be used to compute solar spectral irradiance or IR radiances under a variety of cloud-free or cloudy conditions.

Clouds have an obvious and significant effect on solar spectral irradiance, both in terms of their effect on scattered radiation and their impact on the spectral distribution (color) of solar radiation. Figure 4-2 shows global (direct-plus-diffuse) horizontal spectral irradiance under cloud-free conditions (cloud optical depth equals zero) and for uniform cloud layers of cloud optical depths (δ_c) from 3 to 100. For $\delta_c = 3$ or larger, there is no appreciable direct beam radiation; the cloud effectively transmits only diffuse or scattered radiation (beam transmittance for air mass 1, $\delta_c = 3$ is ≈0.05). As cloud optical depth increases, color of cloud-transmitted (diffuse) solar radiation changes from blue to gray. This is illustrated in figure 4-2, which shows spectral irradiance for $\delta_c = 0$ having much larger intensity in blue wavelengths (approximately 0.45–0.5 μm) than in red (approximately 0.65–0.75 μm). As δ_c increases, the spectral irradiance curves become much flatter with wavelength (more gray) throughout the visible part of the spectrum. Spectral irradiances in figure 4-2 were computed with the model described in reference 4-10.

Table 4-2. Abbreviated ASTM standard solar spectral irradiance (normal incidence), outside atmosphere at 1 au (ref. 4-5). Copyright ASTM—reprinted with permission.

λ	E_λ	$D_{o-\lambda}$	λ	E_λ	$D_{o-\lambda}$
0.14	9.833×10^{-2}	0	0.57	1,797	31.39
0.16	0.3195	3.1×10^{-4}	0.58	1,801	32.71
0.18	2.042	2.0×10^{-3}	0.59	1,758	34.01
0.20	10.83	1.1×10^{-2}	0.60	1,745	35.29
0.22	44.93	5.2×10^{-2}	0.62	1,663	37.78
0.23	49.64	8.7×10^{-2}	0.64	1,610	40.18
0.24	51.83	0.12	0.66	1,527	42.48
0.25	59.81	0.16	0.68	1,485	44.68
0.26	129.1	0.23	0.70	1,438	46.82
0.27	222.1	0.36	0.72	1,360	48.87
0.28	212.9	0.52	0.75	1,272	51.76
0.29	441.0	0.76	0.8	1,132	56.16
0.30	526.0	1.12	0.9	882.6	63.53
0.31	634.5	1.54	1.0	719.7	69.40
0.32	746.5	2.05	1.2	487.1	78.23
0.33	948.7	2.67	1.4	342.5	84.30
0.34	947.3	3.36	1.6	243.5	88.59
0.35	969.5	4.06	1.8	167.1	91.60
0.36	985.2	4.78	2.0	115.0	93.66
0.37	1,129	5.55	2.2	81.73	95.10
0.38	1,091	6.36	2.4	58.78	96.13
0.39	1,093	7.16	2.6	43.86	96.88
0.40	1,518	8.12	2.8	33.43	97.45
0.41	1,712	9.30	3.0	25.93	97.88
0.42	1,740	10.56	3.2	20.45	98.22
0.43	1,625	11.79	3.4	16.36	98.49
0.44	1,826	13.06	3.6	13.26	98.71
0.45	2,030	14.47	3.8	10.87	98.89
0.46	2,077	15.97	4.0	8.977	99.03
0.47	2,049	17.48	4.5	5.674	99.30
0.48	2,057	18.98	5	3.691	99.47
0.49	1,955	20.45	6	1.879	99.68
0.50	1,948	21.88	7	1.022	99.78
0.51	1,911	23.29	8	0.6041	99.84
0.52	1,806	24.65	10	0.2663	99.90
0.53	1,861	26.00	15	6.106×10^{-2}	99.96
0.54	1,861	27.36	20	1.755×10^{-2}	99.98
0.55	1,867	28.72	50	1.769×10^{-3}	100.00
0.56	1,808	30.07	–	–	–

*Note: Lines indicate change in wavelength interval of integration.
λ = wavelength (μm); E_λ = solar spectral irradiance averaged over small bandwidth centered at λ ($1/W^2m$); and $D_{o-\lambda}$ = percentage of the solar constant (ASTM value = 1,366.1 W/m^2) associated with wavelengths shorter than λ.

4.3.5 Dependence of Direct and Global Solar Radiation on Air Mass and Optical Depth

Solar spectral irradiances, such as in figures 4-1 and 4-2, computed by models in references 4-9 and 4-10, can be integrated to yield total (all wavelengths) direct or global (direct-plus-diffuse) irradiance. Table 4-3 gives

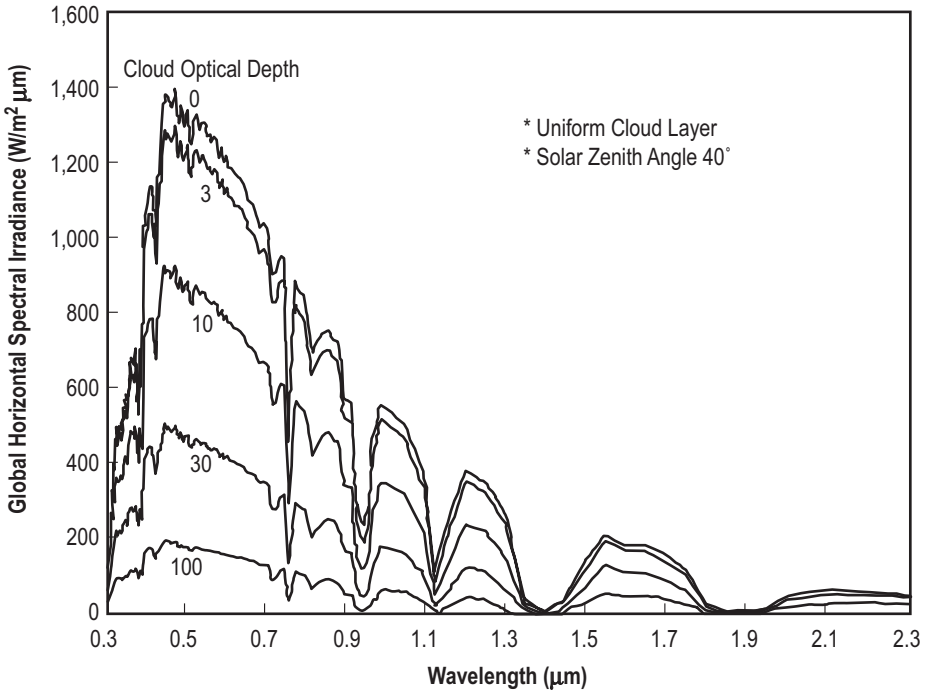

Figure 4-2. Global horizontal solar spectral irradiance at solar zenith angle 40° for cloud-free conditions and cloud optical depths from 3 to 100.

Table 4-3. Direct normal irradiance (W/m^2) under cloud-free conditions for several aerosol optical depths (δ) and PW values (in centimeters) as a function of solar zenith angle (θ) (in degrees) or air mass. Ozone column amount is 0.34 atm-cm.

θ	Air Mass	δ = 0 PW = 1	δ = 0.1 PW = 1	δ = 0.1 PW = 2	δ = 0.2 PW = 1	δ = 0.2 PW = 2
0	1.000	1,075	1,006	980	942	918
20	1.063	1,066	994	968	927	902
40	1.304	1,035	950	924	874	849
60	1.993	959	845	818	747	722
75	3.808	816	650	625	524	502
80	5.580	719	525	502	392	373
85	10.323	558	333	313	210	196

results for direct normal irradiance under cloud-free conditions for several values of aerosol optical depth (δ) and precipitable water (PW) (in centimeters) values as a function of solar zenith angle or air mass. Table 4-4 provides similar data for direct irradiance on a horizontal surface.

Table 4-5 gives spectrally-integrated global (direct-plus-diffuse) irradiance on a horizontal surface, computed from the model discussed in reference 4-10, for various cloud optical depths (δ_c) as a function of solar zenith angle (θ) (in degrees), or air mass. Column labeled $\delta_c = 0$ in table 4-5 is for cloud-free conditions.

Table 4-4. Direct irradiance on a horizontal surface (W/m^2) under cloud-free conditions for several aerosol optical depths (δ) and PW values (in centimeters) as a function of solar zenith angle (θ) (in degrees) or air mass. Ozone column amount is 0.34 atm-cm.

θ	Air Mass	δ = 0 PW = 1	δ = 0.1 PW = 1	δ = 0.1 PW = 2	δ = 0.2 PW = 1	δ = 0.2 PW = 2
0	1.000	1,075	1,006	980	942	918
20	1.063	1,002	934	910	871	848
40	1.304	793	728	708	669	650
60	1.993	480	422	409	373	361
75	3.808	211	168	162	136	130
80	5.580	125	91	87	68	65
85	10.323	49	29	27	18	17

Table 4-5. Global (direct-plus-diffuse) irradiance on a horizontal surface (W/m^2) for various cloud optical depths (δ_c) as a function of solar zenith angle (θ) (in degrees) or air mass. Aerosol optical depth is 0.15, precipitable water is 1.5 cm, and ozone column amount is 0.3 atm-cm.

θ	Air Mass	δ_c = 0	δ_c = 3	δ_c = 10	δ_c = 30	δ_c = 100
0	1.000	1,090	1,055	760	386	131
20	1.063	1,017	972	691	350	119
40	1.304	807	739	505	254	87
60	1.993	491	409	268	135	46
75	3.808	219	164	109	55	19
80	5.580	132	97	65	33	11
85	10.323	54	42	29	15	5

4.4 Use of Solar Radiation in Design

4.4.1 Introduction

Section 4.4 presents a description of total solar radiation, its definitions, and applications for use in design. Standard solar radiation sensors measure the intensity of direct solar radiation from the Sun falling on a horizontal plane at the Earth's surface, plus the diffuse (scattered) radiation from the total sky hemisphere. Diffuse radiation is smallest in dry, clean air; it increases with increasing humidity or dust in the air. On partially cloudy days, increasing cloud amount also causes increased diffuse radiation by providing more opportunity for radiation to reach the surface only after scattering has occurred. With extremely dense clouds or fog, solar radiation will be nearly all diffuse, with the total measured amount being much less than the solar radiation on a clear day (table 4-5). Highest (≥95 percentile) values of global horizontal solar radiation occur under very clear skies or under conditions of scattered fair weather cumulus clouds which reflect additional solar radiation onto the measuring sensor.

4.4.2 Direct Sunlight and Differential Heating

When radiation data are used in design studies, direct solar radiation should be applied from one direction as parallel rays. At the same time, diffuse radiation must be applied as rays from all directions of a hemisphere.

Because direct sunlight provides heat (from radiation) from a specific direction, differential heating of an object occurs; i.e., one part is heated more than another. This may result in stress and deformation; e.g., the side of a launch vehicle facing the Sun is heated, while the sky may cool the opposite side. This differential heating causes the vehicle to bend away from the Sun sufficiently for this effect to be a required consideration in the design of platforms surrounding the vehicle. These platforms are used to ready the vehicle on the launch pad and must be designed to prevent damage to the vehicle skin from the platform, as the vehicle bends.

4.4.3 Total Solar Radiation Computations and Extreme Conditions

Ten years of total horizontal solar and diffuse radiation data were selected from measuring stations at Apalachicola, FL, and Santa Maria, CA. Analysis was conducted on these data to determine the frequency distribution of solar radiation for use in design for geographic locations noted in tables 4-6 and 4-7. The data analysis was made by the National Oceanic and Atmospheric Administration (NOAA), National Climatic Data Center, under contract to NASA Marshall Space Flight Center (MSFC).

Table 4-6. Extreme values of solar radiation for VAFB, West Coast Transportation, Santa Susana, WSMR, Brigham City, and EAFB.

Time of Day (LST)	Total Horizontal Solar Radiation (W/m^2)		Diffuse Radiation* (W/m^2)		Total Normal Incident Solar Radiation (W/m^2)		Total 45° Surface Solar Radiation (W/m^2)	
	June							
	Extreme	95 Percentile	Extreme	95 Percentile	Extreme	95 Percentile	Extreme	95 Percentile
0500	0	0	0	0	0	0	0	0
0600	112	77	14	28	795	544	28	0
0700	321	279	35	56	934	753	132	112
0800	572	530	42	63	1,074	962	237	216
0900	809	774	28	56	1,213	1,129	586	537
1000	1,011	990	0	21	1,248	1,192	830	781
1100	1,143	1,088	0	70	1,248	1,178	969	913
1200	1,178	1,136	0	56	1,213	1,171	1,039	962
1300	1,178	1,143	0	49	1,213	1,171	1,039	976
1400	1,108	1,074	42	84	1,213	1,171	934	899
1500	1,011	969	0	42	1,248	1,185	795	760
1600	844	830	0	14	1,248	1,192	620	544
1700	607	579	21	35	1,178	1,115	237	125
1800	321	293	35	56	969	858	132	91
1900	98	84	14	28	830	648	28	0
2000	0	0	0	0	0	0	0	0
	December							
	Extreme	95 Percentile	Extreme	95 Percentile	Extreme	95 Percentile	Extreme	95 Percentile
0800	0	0	0	0	0	0	0	0
0900	244	223	28	35	1,108	969	690	593
1000	453	418	21	35	1,143	1,067	899	844
1100	600	558	0	28	1,283	1,143	1,143	1,039
1200	669	620	14	42	1,248	1,178	1,213	1,136
1300	690	620	0	42	1,283	1,185	1,248	1,143
1400	593	558	7	28	1,248	1,143	1,108	1,039
1500	460	418	14	35	1,178	1,074	934	844
1600	265	216	14	35	1,143	962	725	607
1700	0	0	0	0	0	0	0	0

*Diffuse radiation, associated with total horizontal solar radiation extremes.

Table 4-7. Extreme values of solar radiation for KSC, SSC, JSC, New Orleans, Gulf Transportation, and MSFC.

Time of Day (LST)	Total Horizontal Solar Radiation (W/m^2)		Diffuse Radiation* (W/m^2)		Total Normal Incident Solar Radiation (W/m^2)		Total 45° Surface Solar Radiation (W/m^2)	
	June							
	Extreme	95 Percentile	Extreme	95 Percentile	Extreme	95 Percentile	Extreme	95 Percentile
0500	0	0	0	0	0	0	0	0
0600	84	49	0	0	760	697	0	0
0700	293	251	35	49	899	725	132	112
0800	572	495	28	70	1,108	906	237	188
0900	858	711	0	70	1,108	1,032	342	286
1000	941	906	14	42	1,108	1,074	690	662
1100	1,060	1,011	21	63	1,108	1,074	830	795
1200	1,102	1,067	70	112	1,143	1,081	899	864
1300	1,102	1,046	70	139	1,143	1,067	899	864
1400	1,046	1,004	35	84	1,108	1,060	830	760
1500	941	906	14	42	1,108	1,060	725	662
1600	767	704	35	84	1,074	1,004	376	307
1700	537	502	35	63	1,039	927	237	209
1800	335	279	21	42	1,004	795	132	125
1900	77	56	0	0	795	697	98	21
2000	0	0	0	0	0	0	0	0
	December							
	Extreme	95 Percentile	Extreme	95 Percentile	Extreme	95 Percentile	Extreme	95 Percentile
0700	0	0	0	0	0	0	0	0
0800	112	70	0	0	934	781	446	349
0900	321	293	28	42	1,004	948	655	620
1000	551	495	7	49	1,178	1,115	969	899
1100	662	641	14	28	1,248	1,171	1,143	1,088
1200	760	711	0	21	1,248	1,185	1,213	1,157
1300	732	711	0	21	1,248	1,241	1,213	1,157
1400	655	620	14	35	1,213	1,164	1,108	1,136
1500	551	488	0	21	1,213	1,095	969	885
1600	321	286	28	42	1,074	976	690	634
1700	112	70	0	0	934	781	446	349
1800	0	0	0	0	0	0	0	0

*Diffuse radiation, associated with total horizontal solar radiation extremes.

4.4.3.1 Computing Total Normal Incident Solar Radiation. The basic data used in computing the total (direct-plus-diffuse, or global) normally-incident radiation (I_{TN}) were measured hourly averages (in W/m^2) of global (direct-plus-diffuse) horizontal solar radiation (I_{TH}) and estimated diffuse (scattered) radiation (I_{dH}) for each hour of the day for a 10-yr period at two locations: Apalachicola, FL (to represent Kennedy Space Center (KSC)) and Santa Maria, CA (to represent Vandenberg Air Force Base (VAFB)). These values were used to compute frequency distributions. Diffuse sky radiation intensities (I_{dH}) were empirically estimated for each intensity based on the measured amount of total (global) horizontal solar radiation (I_{TH}), and solar zenith angle (θ), similar to methods used in reference 4-11. After the diffuse radiation (I_{dH}) is subtracted from the global horizontal solar radiation, the resultant direct horizontal radiation (I_{DH}) can be used to compute the direct normal incident radiation (I_{DN}) by using equation (4.5) (refs. 4-12 through 4-14):

$$I_{DN} = I_{DH}/\cos\theta \ , \tag{4.5}$$

where

I_{DN} = direct normal incident solar radiation
I_{DH} = direct horizontal solar radiation = $I_{TH} - I_{dH}$
θ = solar elevation angle.

Values of total normal solar radiation (I_{TN}) were found by adding the direct normal incident solar radiation (I_{DN}) and the diffuse sky radiation (I_{dH}) as previously estimated from the above-referenced contract with NOAA and presented in tables 4-6 and 4-7; i.e.,

$$I_{TN} = I_{DN} + I_{dH} \ . \tag{4.6}$$

This method of finding the total normal solar radiation may produce a slight overestimate for low solar elevation because the sky hemisphere may be intercepted by the ground surface above the normal horizon. This error is insignificant, however, when extreme values are used and would be small for values equal to or greater than the mean plus one standard deviation.

To determine the amount of solar radiation on a south-facing surface, with tilt angle β, the following equations can be used:

$$I_{D\beta} = I_{DH} (\cos \beta + \tan \theta \cos \alpha \sin \beta) \ , \tag{4.7}$$

where

$I_{D\beta}$ = intensity of direct solar radiation on an approximately south-facing surface with tilt angle β
I_{DH} = direct horizontal solar radiation = $I_{TH} - I_{dH}$
α = Sun's azimuth measured from the south direction (toward west positive)
θ = solar zenith angle = angle between local zenith and direction to Sun
β = tilt angle of surface = angle between local zenith and normal to plane of surface.

If diffuse radiation were to be included, the following equation to obtain total (direct-plus-diffuse) irradiance can be used:

$$I_{T\beta} = I_{D\beta} + I_{dH} \ . \tag{4.8}$$

Adding the full amount of diffuse irradiance from the total sky dome (I_{dH}) is appropriate as a design estimate, although this assumption ignores several effects that may increase or decrease the actual amount of diffuse irradiance received on the tilted surface at a given time. Some of these effects are:

- A wedge of sky (with vertex angle β) is not viewed by the tilted surface.
- An equal wedge of the surface's field of view has radiance contributed by ground-reflected radiation.
- Anisotropic sky radiance may be greater (or less) than average in the direction of surface tilt.
- Topography or structures may shade the tilted surface from part of the sky (also an effect on $I_{D\beta}$).

Some of these factors are discussed in more detail in chapter 11 of reference 4-15.

4.4.3.2 Solar Radiation Extremals. To present the solar radiation data in a simplified form, the month of June was selected to represent Northern Hemisphere summer (longest period of daylight), and December was selected for Northern Hemisphere winter (shortest period of daylight). The June Santa Maria, CA, data for normal incident solar radiation (I_{DN}) were measured at the Earth's surface. These data were scaled (increased) using July values for the period from 1100 to 1900 hr to reflect the higher values that occur early in July (first week) during the afternoon. This was done because of the frequent fog that starts during early morning in June and lasts most of the day.

Tables 4-6 and 4-7 give both extreme values (highest measured value of record) and the 95th-percentile values for the different types of solar radiation as a function of hours of the day. The values given for diffuse radiation occurred in association with the extremes and the 95th percentiles of the other solar radiations given. Direct sunlight with surrounding cumulus clouds may give significantly higher values of radiation. Since the diffuse sky radiation decreases with increasing total horizontal solar radiation, the values given in tables 4-6 and 4-7 are smaller than the greatest values of diffuse radiation that occurred during the period of record. They should be used with the other extreme values. Tables 4-6 and 4-7 present the total solar radiation intensities received on a south-facing surface, with the normal to the surface at 45° from local zenith, as dictated by equation (4.7). The solar radiation data recommended for use in design are given in table 4-8 and figure 4-3 versus time of day.

Table 4-8. Recommended design high and design low solar radiation (ref. 4-16).

Time of Day (LST)	Design High Solar Radiation		Time of Day (LST)	Design Low Solar Radiation	
	Btu/ft^2/hr	W/m^2		Btu/ft^2/hr	W/m^2
0500	0	0	0655	0	0
1100	363	1,145	1100	70	221
1400	363	1,145	1300	80	252
2000	0	0	1710	0	0

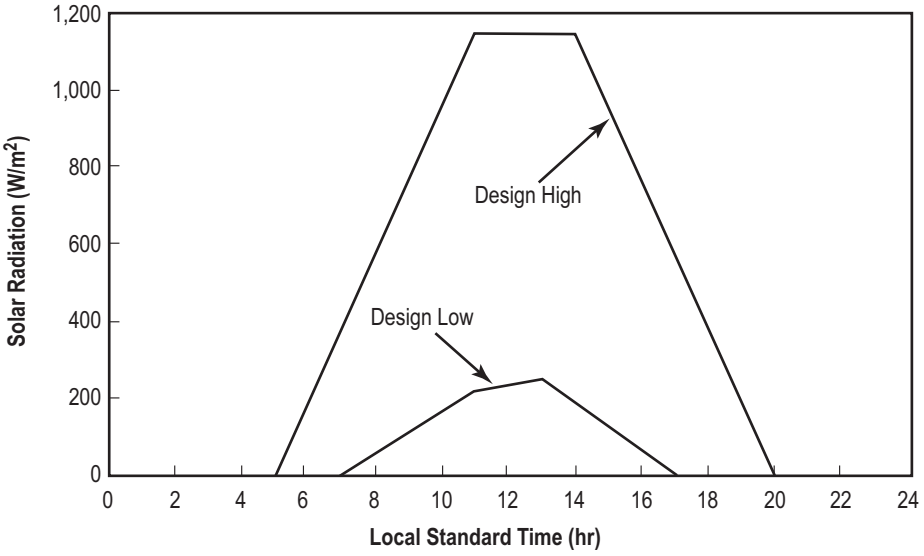

Figure 4-3. Recommended design solar radiation at ground level (ref. 4-16).

The design high curve for solar radiation in figure 4-3 presents recommended design values for clear day direct incident solar radiation to a horizontal surface. Actual radiation absorbed by a surface would be a function of surface optical properties and surface geometry relative to the Sun vector. The design low curve for solar radiation presents cloudy day diffuse solar radiation that would apply to all surfaces. Actual radiation absorbed by these surfaces would also be a function of surface optical properties. These data should be used in conjunction with sky temperature defined in section 4.3.5.1. Note: Design curve represents direct incident solar radiation to a horizontal surface, and represents diffuse incident radiation to any surface.

4.4.3.3 Variation With Altitude. The direct solar radiation intensity on a surface will increase with altitude above the Earth's surface, with clear skies, according to the following approximate equation:

$$I_{DN}(Z) = I_{DN}(0) + [S - I_{DN}(0)][1 - \rho_Z/\rho_S] \ , \tag{4.9}$$

where

$I_{DN}(Z)$ = intensity of solar radiation normal to surface at required height Z
$I_{DN}(0)$ = intensity of solar radiation normal to surface at the Earth's surface assuming clear skies
ρ_Z = atmospheric density at required height (from 1976 U.S. Standard Atmosphere, 1966 U.S. Standard Atmosphere Supplements, or this document) (kg/m^3)
ρ_S = atmospheric density at sea level (from U.S. Standard Atmospheres, U.S. Standard Atmosphere Supplements, or this document) (kg/m^3)
S = solar constant; e.g., 1,367 W/m^2.

The diffuse solar radiation I_{dH} also decreases with altitude above the Earth's surface. For clear skies, a good estimate of the value can be obtained from the following equation:

$$I_{dH}(Z) = 523 - 0.4076\, I_{DN}(Z) \ , \tag{4.10}$$

where

$I_{dH}(Z)$ = intensity of diffuse radiation (W/m^2) at height Z
$I_{DN}(Z)$ = intensity of solar radiation (W/m^2) normal to surface at height Z.

Equation (4.10) is valid for values of $I_{DN}(Z)$ from equation (4.9) up to 1,283 W/m^2. For values >1,283 W/m^2, $I_{dH} = 0$.

4.4.3.4 Solar Radiation During Extreme Wind Conditions. When ground winds exceed the 95-, 99-, or 99.9-percentile design winds given in section 2, clouds, rain, or dust usually are present. Therefore, the intensity of the incoming solar radiation will be less than the maximum values given in tables 4-6 and 4-7. Maximum values of solar radiation intensity to use with corresponding wind speeds are given in table 4-9.

4.5 Thermal Radiation

4.5.1 Introduction

Objects receiving solar radiation absorb some of the energy and reradiate energy in the IR band. The exchange of energy will heat or cool an object and also influence surrounding objects. The temperature

Table 4-9. Solar radiation maximum values associated with extreme wind values.

Steady-State Ground Wind Speed at 18-m Height	Huntsville, New Orleans, Stennis, Johnson, Gulf Transportation, Eastern Range, Western Range, West Coast Transportation, and Wallops Flight Facility			White Sands Missile Range		
(m/s)	(kJ/m^2s)	(W/m^2)	(Btu/ft^2hr)	(kJ/m^2s)	(W/m^2)	(Btu/ft^2hr)
10	0.837	837	265	1.046	1,046	332
15	0.558	558	177	0.697	697	221
≥20	0.349	349	111	0.558	558	177

of an object is a function of air temperature and the absorptance (and emittance) of the object, which can vary with wavelength. Thermal radiation usually refers to the region of the middle and far infrared regions of the spectrum, ranging in wavelength from ≈3 to 25 μm.

4.5.2 Extreme Temperatures and Sky Radiation

Table 4-10 presents values of expected extreme surface temperatures and sky radiation for selected locations of interest to NASA, based on at least a 10-yr period of record for each location. Surface temperatures are primarily the result of incoming and outgoing radiative energy along with convection effects. As a blackbody radiator, the clear sky is considered equivalent to a cold surface. The radiation temperature of the clear sky is the same during day and night. It is the clear sky acting as a cold sink, without the incoming solar radiation heating from the surface, that causes air temperatures to be colder at night than during the day. At night, clouds act as a barrier to outgoing longwave radiation. Clouds absorb outgoing IR radiation and emit radiation at a lower temperature, making the effective atmospheric temperature warmer than the clear sky. Thus, air near the ground does not cool as much as on a cloud-free night. Although not a significant factor, atmospheric dust, which is related to wind speed, and pollution aerosols behave in a similar fashion. Therefore, the greatest cooling of the Earth's surface occurs during calm conditions (no mixing with warmer air) and clear skies.

Radiation interchange with the sky should be based on the design high and design low effective sky temperatures of 50 and –30 °F (10 and –34 °C), respectively (ref. 4-16). These are representative of any global launch site or reentry region.

4.5.3 Average Solar Absorptance of Objects

In thermal engineering studies, the visible color of a surface is not important for low-temperature radiation, which is influenced by the longwave (IR; approximately 3- to 100-μm wavelength) absorptance and emittance of the surface. For high-temperature radiation, such as exposure to solar radiation, the color does affect the visible portion of the spectrum, but this is only a smaller but significant segment of the full shortwave solar spectrum (approximately 0.2- to 3-μm wavelength). Spectrally selective surfaces may differ in shortwave and longwave absorptivity and emissivity, as was shown in tests with thermistors having different spectral responses when used on radiosondes at MSFC (ref. 4-17) and also at GSFC (ref. 4-18). A list of values of longwave hemispheric emissivity and shortwave solar absorptivity for various surfaces and different colors of paint is presented in reference 4-11. An object's change of temperature (above or below the air temperature), which is a measure of heating or cooling, is proportional to the emittance and absorptivity. Therefore, one factor in the accuracy of determining the temperature of a surface exposed to radiation is related to the accuracy of the values of emittance and absorptivity available. Spectral distribution curves of emittance/absorptance are available for many surfaces.

Table 4-10. Surface air and sky radiation temperature extremes.

Area	Surface Air Temperature Extremes[a]					Sky Radiation	
		Maximum		Minimum			
	Temperature	Extreme	95%[b]	Extreme	95%[b]	Extreme Minimum Equivalent Temperature	Equivalent Radiation (W/m^2)
Huntsville, AL	°C	40.0	36.7	–23.9	–12.8	–30.0	198
	°F	104	98	–11	9	–22	
KSC, FL[c]	°C	37.2	35.0	–7.2	0.6	–15.0	252
	°F	99	95	19	33	5	
VAFB, CA[c]	°C	37.8	29.4	–3.9	1.1	–15.0	252
	°F	100	85	25	34	5	
EAFB, CA	°C	45.0	41.7	–15.6	–7.8	–30.0	198
	°F	113	107	4	18	–22	
Hickam Field, Honolulu, Oahu	°C	33.9	32.8	11.1	15.6	–15.0	252
	°F	93	91	52	60	5	
Andersen Air Force Base, Guam	°C	34.4	31.1	18.9	22.2	–15.0	252
	°F	94	88	66	72	5	
Santa Susana, CA[d]	°C	46.7	36.1	–7.8	1.7	–15.0	252
	°F	116	97	18	35	5	
Thiokol Wasatch Division, UT[e]	°C	41.7	35.6	–33.9	–16.1	–30.0	198
	°F	107	96	–29	3	–22	
New Orleans, LA[f]	°C	38.9	35.0	–10.0	–3.3	–17.8	241
	°F	102	95	14	26	0	
Stennis Space Center, MS[g]	°C	39.4	35.6	–14.4	–2.2	–17.8	241
	°F	103	96	6	28	0	
Continent transportation (rail, truck, river barge)	°C	47.2	–	–34.4	–	–30.0	198
	°F	117	–	–30	–	–22	
Ship transportation (West Coast, Panama Canal, Gulf of Mexico)	°C	37.8	–	–12.2	–	–15.0	252
	°F	100	–	10	–	5	
JSC, TX[h]	°C	42.2	36.7	–13.3	–2.2	–17.8	241
	°F	108	98	8	28	0	
GSFC—Wallops Flight Facility, VA	°C	38.3	33.3	–20.0	–5.6	–17.8	241
	°F	101	92	–4	22	0	
WSMR, NM[i]	°C	44.4	38.9	–25.6	–10.0	–30.0	198
	°F	112	102	–14	14	–22	

[a] The extreme maximum and minimum temperatures will be encountered during periods of wind speeds less than ≈1 m/s.
[b] Based on daily extreme (maximum or minimum) observations for worst month.
[c] Sky temperature limits for shuttle launch at KSC and VAFB as given in NSTS 07700, appendix 10.10, are 50 °F for a design high and –30 °F for a design low.
[d] Includes extreme temperature observations at Canoga Park Pierce College, CA.
[e] Includes extreme temperature observations at Thiokol Plant 78/Thiokol Propulsion FS, UT.
[f] Applies for the Michoud Assembly Facility (New Orleans, LA) and the Slidell Computer Complex (Slidell, LA). Note, the extreme minimum temperature for Slidell is –13.3 °C (8 °F).
[g] Includes extreme temperature observations at Picayune, MS.
[h] Includes extreme temperature observations at Houston Hobby Airport, TX.
[i] Also applies for Northrup Strip. Includes extreme temperature observations at Alamogordo and Holloman AFB, NM. Note, the nearby White Sands National Monument has an extreme minimum temperature of –31.7 °C (–25 °F).

Knowing the emittance/absorptance curve, the average emittance/absorptance of any surface can be computed. For example, solar absorptance can be computed by the following method:

(1) Divide the spectral absorptance curve; i.e., that is given in figure 4-4, into small bandwidth intervals that have small or no change within the interval.

(2) Using the same intervals from the solar spectral irradiation; i.e., from table 4-2, multiply each value of absorptance over the selected interval by the percentage of radiant power over the interval.

(3) Sum the resultant products to give the average solar absorptance of the surface.

Table 4-11 and figure 4-4 give an example of absorptance computations for a white surface using data from figure 4-4 and table 4-2. Similar computations can be made for other sources of radiation such as the night sky or cloudy skies as long as the wavelength band for the absorptance spectral data corresponds with the long-wave irradiance data.

Table 4-11. Computation of solar absorptance of white paint ($BaSO_4$ and MgO) exposed to direct solar radiation above the Earth's atmosphere.

Bandwidth Center Wavelength λ (μ)	Absorptance at Bandwidth Center (ratio)	Average Absorptance Over Bandwidth (ratio)	Solar Radiation at Air Mass Zero for Wavelength $<\lambda$ (%)	Solar Radiation Over Interval (%)	Product of Average Absorptance and Percent Solar Radiation Over Interval Divided by 100
0.300	0.73	–	1.12	–	–
0.330	0.45	0.590	2.67	1.55	0.0091
0.350	0.37	0.410	4.06	1.39	0.0057
0.500	0.36	0.365	21.88	17.82	0.0650
0.580	0.29	0.325	32.71	10.83	0.0352
0.700	0.23	0.260	46.82	14.11	0.0367
0.800	0.22	0.225	56.16	9.34	0.0210
0.900	0.30	0.260	63.53	7.37	0.0192
1.000	0.44	0.370	69.40	5.87	0.0217
1.200	0.60	0.520	78.23	8.83	0.0459
1.400	0.70	0.650	84.30	6.07	0.0395
1.600	0.79	0.745	88.59	4.29	0.0320
1.900	0.83	0.810	92.63	4.04	0.0327
50.000	0.83	0.830	100.00	7.37	0.0612
Sum = Average Emittance = 0.425					

4.5.4 Computation of Surface Temperature From One Radiation Source

Absolute temperature must be used in the following computations, except in equation (4.13). Units of solar radiation must be in the same unit system as the Stefan-Boltzmann constant.

The extreme value of temperature that a surface can reach when exposed to daytime (solar) or nighttime (night sky) radiation with no wind (calm), assuming it has no mass transfer or heat transfer within the object, is

$$T_S = T_A + E\,\Delta T_{BS} \ , \tag{4.11}$$

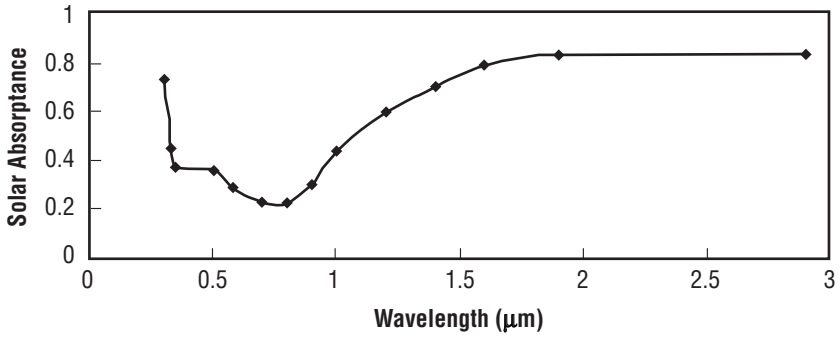

Figure 4-4. Plot of measured solar absorptance of $BaSO_4$ and MgO (white paint) versus wavelength when exposed to the solar spectrum.

where

T_S = surface temperature (K)
T_A = air temperature (K)
E = emittance of surface
ΔT_{BS} = surface temperature differential producing an increase in blackbody temperature (K) from daytime solar radiation (plus); or a decrease in blackbody temperature (K) from day or nighttime sky radiation (minus), calculated from

$$\Delta T_{BS} = \left(\frac{I_{TS}}{\sigma} \right)^{1/4} - T_A \ . \tag{4.12}$$

Equation (4.12) gives the surface radiative balance; i.e., absorbed radiation equals emitted radiation.

Extreme values of ΔT_{BS} can be obtained from figure 4-5 or table 4-12, where

I_{TS} = total radiation (solar by day) (sky for night) received at surface. These values can be extremes from tables 4-6 through 4-10.
σ = Stefan-Boltzmann constant
= 5.670×10^{-8} W/m^2 K^4
= 1.714×10^{-9} Btu/hr ft^2 K^4
= 8.312×10^{-11} g-cal/cm^2 K^4.

The term $(I_{TS}/\sigma)^{1/4}$ equals the extreme blackbody surface temperature.

Figure 4-5 shows the surface temperature differential (ΔT_{BS}) with respect to air temperature for a surface with an emittance between zero and 1 during calm winds. The temperature difference, after correction for wind speed, is added or subtracted to the air temperature to give the surface (skin) temperature. Wind speed has a great effect on temperature, not because it changes the radiation portion of the heat transfer, but because it makes the convective heat transfer significant (fig. 4-5).

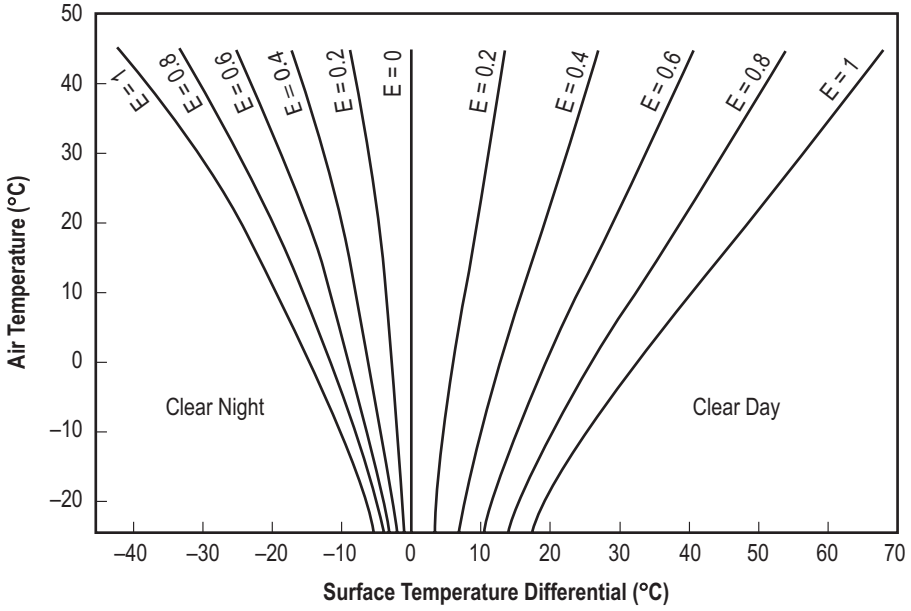

Figure 4-5. Extreme surface (skin) temperature differential (ΔT_{BS}) with respect to air temperature (T_A) of an object near the Earth's surface (zero to 300 m) for clear sky and emittance (E).

Table 4-12. Extreme surface (skin) temperature (T_S) warmer or colder than the air temperature (T_A) of an object near the Earth's surface.

Air Temperature (°C)	Surface Temperature Differential (°C)									
	Clear Night					Clear Day				
	Wind Speed (m/s)					Wind Speed (m/s)				
	0	2	4	10	20	0	2	4	10	20
	Correction Factor					Correction Factor				
	1.00	0.25	0.17	0.11	0.08	1.00	0.25	0.17	0.11	0.08
–25	–5.0	–1.2	–0.8	–0.6	–0.4	16.9	4.2	2.9	1.9	1.4
–20	–6.5	–1.6	–1.1	–0.7	–0.5	19.2	4.8	3.3	2.1	1.5
–15	–8.2	–2.0	–1.4	–0.9	–0.6	22.0	5.5	3.7	2.4	1.8
–10	–10.2	–2.6	–1.7	–1.1	–0.8	25.1	6.3	4.3	2.8	2.0
–5	–12.2	–3.0	–2.1	–1.3	–1.0	28.5	7.1	4.8	3.1	2.3
0	–14.5	–3.6	–2.5	–1.6	–1.2	32.0	8.0	5.4	3.5	2.6
5	–16.9	–4.2	–2.9	–1.9	–1.4	36.0	9.0	6.1	4.0	2.9
10	–19.4	–4.8	–3.3	–2.1	–1.6	40.0	10.0	6.8	4.4	3.2
15	–21.9	–5.5	–3.7	–2.4	–1.8	44.0	11.0	7.5	4.8	3.5
20	–24.6	–6.2	–4.2	–2.7	–2.0	48.0	12.0	8.2	5.3	3.8
25	–27.4	–6.8	–4.6	–3.0	–2.2	52.0	13.0	8.8	5.7	4.2
30	–30.5	–7.6	–5.2	–3.4	–2.4	56.0	14.0	9.5	6.2	4.5
35	–34.0	–8.5	–5.8	–3.7	–2.7	60.0	15.0	10.2	6.6	4.8
40	–37.7	–9.4	–6.4	–4.1	–3.0	64.0	16.0	10.9	7.0	5.1
45	–41.7	–10.4	–7.1	–4.6	–3.3	68.0	17.0	11.6	7.5	5.4

Note: Values are given for solar absorptivity and an emittance value of 1;, i.e., blackbody. Temperature differences for other emittance can be determined by multiplying tabular value by the appropriate emittance.

If a correction for wind speed is desired, equation (4.11) can be written as

$$T_S = T_A + E\left(\Delta T_{BS}\right)\frac{f_w}{100} \ , \tag{4.13}$$

where f_w is the correction (in percent) for wind speed from figure 4-6. Equations (4.11)–(4.13) are only for computing the effect of one source of radiation on a surface. When more than one radiation source is received by an object, a more complex method must be used, as given in section 4.5.5. The value of f_w is for sea level (pressure = 1,013.25 mb). For higher altitudes use

$$f_{w_{\text{alt}}} = f_w\left(\rho_{\text{alt}} / \rho_{\text{sea level}}\right) \ . \tag{4.14}$$

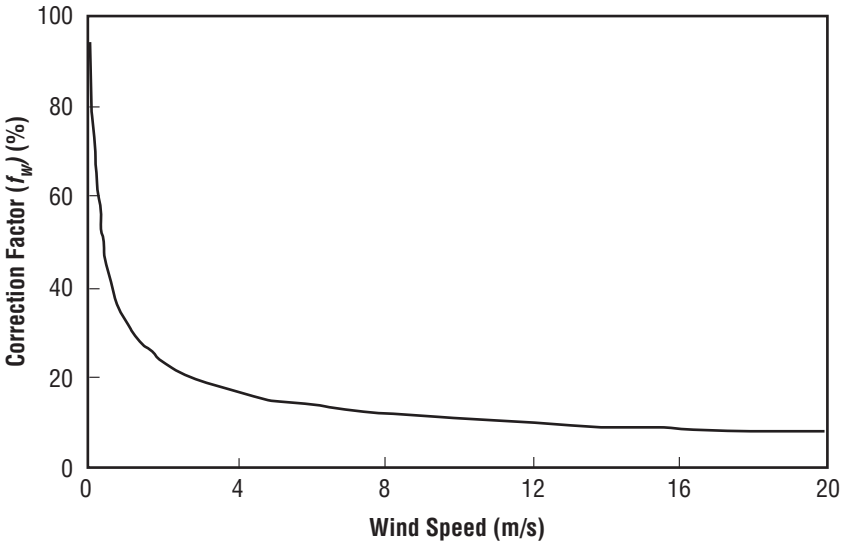

Figure 4-6. Wind speed (W) correction factor (f_w, percent of total) for the surface temperature differential (ΔT_{BS}) (obtained from fig. 4-5) of an object near the Earth's surface (zero to 300 m) for clear sky. Valid only for a pressure of 1 atm (1,013.25 mb).

4.5.5 Computation of Surface Temperature From Several Simultaneous Radiation Sources

If a blackbody has several radiation sources (I_i) and no forced or natural convection (calm wind), then the total radiation balance can be computed from the Stefan-Boltzmann law:

$$\sigma T^4 = \sum_i^n I_i \quad i = 1, 2, 3, \ldots n \ . \tag{4.15}$$

4.5.5.1 Surface Temperature Differential. The temperature differential (ΔT_{BS}) between the surface and the air for an emitting surface is between zero and 1 during calm wind. The temperature difference, after correction for wind speed, is added or subtracted to the air temperature to give the surface (skin) temperature.

Then

$$T - T_A = \Delta T_{BS} = \left(\frac{\sum_i^n I_i}{\sigma} \right) - T_A \ , \tag{4.16}$$

where T_A is the air temperature.

4.5.5.2 Wind Speed Correction Factor. The wind speed correction factor (f_w) (percent of total) for surface temperature differential (ΔT_{BS}) is obtained from figure 4-6. This is valid only for a pressure of 1 atm.

For any object within the Earth's atmosphere exposed to thermal radiation, the following function can be used:

$$\Delta T_{BS} = f_w \left(\frac{\sum_i^n E_i I_i}{\sigma} \right)^{1/4} - T_A \ , \tag{4.17}$$

where

E_i = emittance of object for corresponding radiation source I_i:

$$\Delta T_{BS} = T - T_A \ , \tag{4.18}$$

$$f_w = \frac{0.325}{\sqrt{w}} \ , \tag{4.19}$$

where

f_w = wind effect (convection) correction factor
w = wind speed (m/s).

4.6 Temperature

4.6.1 Introduction

Several types of temperatures in the Earth's boundary layer must be considered in design:

(1) Air temperatures at surface level (normally measured at a height of 1.22 m (4 ft) above a grass surface in special shelter) (see sec. 4.6.2). Temperatures at various altitudes above the surface are given in the Reference Atmosphere tables of section 3.

(2) Changes of air temperature due to changes in solar radiation intensity (usually the rapid changes that occur in <24 hr) are given in section 4.6.3.

(3) Measurement of surface or skin temperature of a surface exposed to radiation is presented in section 4.6.4.

(4) Temperatures within a closed compartment (see sec. 4.6.5).

4.6.2 Extreme Air Temperature Near the Surface

Surface air temperature extremes (maximum, minimum, and 95-percentile values) and the extreme minimum sky radiation are given in table 4-10 for various geographical areas. Maximum and minimum temperatures should be expected to last only a few hours during a daily period. Generally, the maximum temperature is reached between 12 a.m. and 5 p.m., while the minimum temperature is reached just before sunrise. Table 4-13 shows the maximum and minimum design air temperatures for each hour at KSC. These curves represent a cold and hot extreme day. The method of sampling the day (frequency of occurrence of observations) will result in the same extreme values if the same period of time for the data is used. A given percentile value of temperature will be different for hourly, daily, and monthly data reference periods. Selection of the reference period depends on the engineering application. Table 4-14 gives monthly mean ambient surface temperatures, standard deviations, and 2.5 and 97.5 percentiles of temperature values for KSC and VAFB. United States and worldwide temperature extremes are given in section 5.

4.6.3 Extreme Air Temperature Change Over Time

For all sites, recommended design values of extreme air temperature changes (thermal shock) are:

(1) An increase of air temperature of 10 °C (18 °F) with a simultaneous increase of solar radiation (measured on a normal surface) from 347 W/m^2 (110 Btu/ft^2 hr) to 1,293 W/m^2 (410 Btu/ft^2 hr) can occur in a 1-hr period. Likewise, the reverse change of the same magnitude can occur for decreasing air temperature and solar radiation.

(2) A 24-hr change can occur with an increase of 27.7 °C (50 °F) in air temperature in a 5-hr period, followed by 4 hr of constant air temperature, then a decrease of 27.7 °C (50 °F) in a 5-hr period, followed by 10 hr of constant air temperature.

For KSC, the 99.9-percentile air temperature changes are:

(1) An increase of air temperature of 5.6 °C (11 °F) with a simultaneous increase of solar radiation (measured on a normal surface) from 347 W/m^2 (110 Btu/ft^2 hr) to 1,117 W/m^2 (354 Btu/ft^2 hr), or a decrease of air temperature of 9.4 °C (17 °F) with a simultaneous decrease of solar radiation from 1,117 W/m^2 (354 Btu/ft^2 hr) to 347 W/m^2 (110 Btu/ft^2 hr) can occur in a 1-hr period.

(2) A 24-hr temperature change can occur as follows: An increase of 16.1 °C (29 °F) in air temperature (wind speed under 5 m/s) in an 8-hr period, followed by 2 hr of constant air temperature (wind speed under 5 m/s), then a decrease of 21.7 °C (39 °F) in air temperature (wind speed between 7 and 10 m/s) in a 14-hr period.

Table 4-13. Maximum and minimum design surface air temperatures at each hour for KSC, based on Patrick AFB and KSC records.

Time of Day (LST)	Annual Maximum Temperature		Annual Minimum Temperature [a],[b]	
	°C	°F	°C	°F
0100	28.9	84	–3.3	26
0200	28.9	84	–3.9	25
0300	29.4	85	–4.4	24
0400	28.3	83	–4.4	24
0500	28.9	84	–5.0	23
0600	29.4	85	–5.6	22
0700	30.6	87	–6.1	21
0800	31.1	88	–5.6	22
0900	33.3	92	–3.9	25
1000	34.4	94	–2.2	28
1100	35.0	95	–1.7	29
1200	36.1	97	–0.6	31
1300	37.2	99	0	32
1400	36.1	97	2.8 (3.3)	37 (38)
1500	36.7	98	2.8 (3.9)	37 (39)
1600	36.1	97	2.2 (4.4)	36 (40)
1700	36.1	97	1.1 (4.4)	34 (40)
1800	35.0	95	0 (1.7)	32 (35)
1900	33.3	92	–0.6	31
2000	31.7	89	–1.1	30
2100	31.1	88	–1.7 (–1.1)	29 (30)
2200	30.0	86	–2.2 (–1.7)	28 (29)
2300	30.0	86	–2.2	28
2400	30.0	86	–2.2	28

[a] Many KSC minimum temperatures are representative of the January 21–22, 1985, cold spell. This cold spell altered most minimum temperature values. These values given represent annual extreme conditions, but can also be used in a continuous 24-hr cycle of extreme KSC cold temperature conditions starting at 9 a.m. January 21 (25 °F) through 8 a.m. January 22 (22 °F). The minimum values given for 1400 through 1800, 2100, and 2200 are not representative of the January 1985 cold spell. Cold spell values for these hours in January 21, 1985, are presented in brackets to the right. Note that the envelope of maximum and minimum values cannot be used in a continuous time cycle. They are an envelope of maximum and minimum values for the period of record used in the analysis.

[b] Note that the minimum temperature of record for this location, as given in table 4–10, is –7.2 °C (19 °F).

4.6.4 Surface (Skin) Temperature

The surface temperature of an object exposed to radiation (solar, day sky, or night sky) is usually different from the air temperature (refs. 4-19 and 4-20). The extreme difference in temperature between a black-body and the surrounding air temperature is given in table 4-12 and figure 4-5 for exposure to a clear night (or day) sky or to the Sun on a clear day with calm winds. A change in air flow across an object will change the heat transfer, resulting from radiation and convection-conduction. The difference in temperature between air and the object will decrease with increasing wind speed. Figure 4-6 provides information for making the correction for wind speed. Values of surface (skin) temperature differentials are also given in table 4-12 for different wind speeds.

4.6.5 Compartment Temperatures

4.6.5.1 Introduction. A cover that encloses an air space will conduct heat to (or remove heat from) the inside air when the cover is heated by solar radiation, or cooled by the night sky. This often causes the

Table 4-14. Monthly mean, standard deviations (STD), and 2.5- and 97.5-percentile values of surface air temperature for KSC and VAFB.

Month	KSC				VAFB			
	Monthly Mean or 50 Percentile (°F)	Standard Deviation 30-Day Average	Percentiles		Monthly Mean or 50 Percentile (°F)	Standard Deviation 30-Day Average	Percentiles	
			30-Day 2.5%* (°F)	Average 97.5%* (°F)			30-Day 2.5%* (°F)	Average 97.5%* (°F)
January	59.9	3.5	53.1	66.7	50.9	1.7	47.6	54.2
February	59.8	4.8	50.4	69.2	51.1	2.0	47.1	55.1
March	64.4	3.1	58.3	70.5	51.6	1.8	48.1	55.1
April	70.1	1.3	67.6	72.6	52.4	1.6	49.3	55.5
May	74.5	0.9	72.8	76.2	53.2	1.1	51.2	55.7
June	77.8	1.3	75.3	80.3	55.6	1.7	52.2	59.0
July	79.2	1.2	76.8	81.6	56.9	1.7	53.0	59.5
August	78.9	0.7	77.6	80.2	58.3	1.7	55.0	61.6
September	78.5	1.1	76.3	80.6	59.2	2.0	55.3	63.1
October	73.9	1.7	70.3	77.1	58.6	1.8	55.0	62.2
November	67.0	2.8	61.3	72.4	54.7	2.1	50.5	58.9
December	60.6	3.0	54.8	66.4	51.0	2.7	45.7	56.3

*Recommended for use in solid rocket motor propellant bulk temperature predictions for design analyses. See (ref. 4-16) Natural Environment Design Requirements—appendix 10.10 of NSTS 07700, volume X.

compartment's air space to be considerably hotter or cooler than the surrounding air. The temperature reached in a compartment depends on the location of the air space with respect to the heated surface, the type, thickness, and optical properties of the surface material, the type of construction, and the insulating value of the material. Adding more layers of material with high insulating value on the inside surface of the compartment will greatly reduce the heating or cooling of the air inside (refs. 4-21 and 4-22).

4.6.5.2 Compartment High-Temperature Extreme. A compartment's probable average high temperature of 87.8 °C (190 °F) for a period of 1 hr and an average high temperature of 65.6 °C (150 °F) for a period of 6 hr must be considered at all geographic locations when aircraft or other transportation equipment is stationary on the ground without air conditioning. These extremes will be found at the top and center of the compartment (refs. 4-21 and 4-22).

4.7 Data on Air Temperature Distribution With Altitude

Data on the vertical distribution of air temperature (external to compartment) are given in section 3.4.1.

4.8 Other Sources of Solar and Thermal Radiation Data

4.8.1 Introduction

There are several Web-based sources of solar and thermal radiation data. Much of these data consist of daily total radiation, and/or time series of hourly (or shorter time average) radiation values. These data do not contain information on extremes or 95-percentile hourly values, as in tables 4-6 through 4-10. However, time series data are available from a wide range of locations from which extreme and percentile values could be computed. The following four databases are summarized below: (1) NASA's Surface meteorology and Solar Energy (SSE)

data, (2) the Department of Energy National Renewable Energy Laboratory (NREL) Solar Radiation Resource Information data, (3) NOAA's Climate Data Inventories, and (4) the NOAA Climate Monitoring and Diagnostics Laboratory (CMDL) Solar and Thermal Atmospheric Radiation (STAR) data.

4.8.2 NASA Surface Meteorology and Solar Energy (SSE) Data

SSE data contain global, satellite-derived information for over 100 solar energy and meteorology parameters (ref. 4-23), as well as daily total global (direct-plus-diffuse) radiation by year and month for 1,195 ground sites worldwide. Satellite-derived parameters include daily total solar radiation, midday solar radiation (1.5-hr average), daily total clear-sky solar radiation, number of clear-sky days, hourly solar radiation at selected hours of the day, frequency of cloud amounts, daily average temperature and temperature range, Earth surface (skin) temperature, and other radiation and meteorological parameters.

4.8.3 National Renewable Energy Laboratory (NREL) Data

NREL data include a wide variety of solar radiation and other solar energy-related data (ref. 4-24), in the form of time series from a number of solar radiation monitoring networks, and in map and atlas format:

- The Historically Black Colleges and Universities (HBCU) Solar Radiation Monitoring Network provides 5-min-averaged measurements of global and diffuse horizontal solar irradiance over a 10-yr period. Three HBCU stations also measured 5-min-averaged direct normal solar irradiance.

- National Solar Radiation Database Daily Statistics Files contain average and standard deviations of daily total solar energy (direct normal, diffuse horizontal, and global horizontal) for each station-year-month and each station-year for 30 yr from 239 U.S. stations. Meteorological elements are also available for monthly averages, annual averages, and 30-yr averages.

- Hourly Data Files, derived from the National Solar Radiation Database, contain time series of hourly global horizontal solar irradiance, direct normal solar irradiance, and diffuse horizontal solar irradiance for 239 U.S. sites.

- The Atlas for *The Solar Radiation Data Manual For Buildings* gives maps of daily total solar radiation incident on the outside of building surfaces at a variety of orientations. These data are also available in spreadsheet format.

- The Atlas for *The Solar Radiation Manual for Flat-Plate and Concentrating Collectors* provides maps of average, minimum, and maximum daily total solar radiation for a 30-yr period. Maps of minimum and maximum values are composites of specific months and years for which each site achieved its minimum or maximum amounts of solar radiation. These data are also available in spreadsheet format.

- Typical Meteorological Year, Version 2 (TMY2) data sets were derived from 30 yr of National Solar Radiation Database information at 239 U.S. sites. The TMY2s are monthly data sets of hourly values of solar radiation and meteorological elements, composited into a 1-yr period. Each 1-yr TMY2 data set consists of 12 monthly data sets, with each month selected as being "typical" or average for the 30-yr period of record. Because TMY2 data represent typical rather than extreme conditions, they are not suited for designing systems to meet worst-case conditions occurring at a location.

- NOAA Network Radiation Data includes time series of hourly direct normal and global horizontal radiation from 39 U.S. stations.

- Solar Energy Meteorological Research and Training Sites Network data are time series from five U.S. university sites over one or more years of a 5-yr period. Some data are hourly time series; some are 1-min time series. Typical data sets include direct normal, diffuse, global horizontal, global on tilted surface(s), UV, Net IR, temperature, dewpoint, wind speed, wind direction, station pressure, and other parameters.

- NREL's Spectral Solar Radiation Database contains spectral solar radiation data representing a range of sites with a variety of atmospheric conditions (or climates) over about a 2-yr period. One spectroradiometer measured almost daily at Cape Canaveral, and contributed nearly 2,800 spectra to the database.

4.8.4 NOAA Climate Data Inventories Data

NOAA Climate Data Inventories Data include time series of hourly Airways Solar Radiation data, Surface Airways Hourly meteorological data, and National Solar Radiation Database data (ref. 4-25). These contain hourly values of direct normal, global horizontal, and diffuse horizontal radiation, as well as visibility and other meteorological parameters. The Climate Data Inventories also include time series of direct, global, diffuse, UV, and IR radiation, as well as meteorological data from the United States Incident Solar Radiation Observations (15-min and hourly data), and from the U.S. Solar Radiation Balance Observations (hourly data).

4.8.5 NOAA Climate Monitoring and Diagnostics Laboratory Data

NOAA's Climate Monitoring and Diagnostics Laboratory data from the Solar and Thermal Atmospheric Radiation Observation Network (ref. 4-26) of ≈15 worldwide sites includes data from seven ongoing, long-term observational programs, with four current sites having operated continuously for more than 20 yr. Parameters include direct, diffuse, and global solar irradiance, broadband thermal irradiance, column precipitable water amount, aerosol optical depth, and a variety of other types of radiation and meteorological data.

REFERENCES

4-1. Anderson, B.J.; Justus, C.G.; and Batts, G.W.: "Guidelines for the Selection of Near-Earth Thermal Environment Parameters for Spacecraft Design," *NASA/TM—2001–211221*, NASA Marshall Space Flight Center, AL, October 2001.

4-2. Justus, C.G.; Batts, W.; Anderson, B.J.; and James, B.F.: "Simple Thermal Environment Model (STEM) User's Guide," *NASA/TM—2001–211222*, NASA Marshall Space Flight Center, AL, October 2001.

4-3. Middleton, W.E.K.; and Spilhaus, A.F.: *Meteorological Instruments*, University of Toronto Press, Third Edition, revised 1960.

4-4. Fröhlich, C.; and Wehrli: "Spectral Distribution of Solar Irradiance from 25000 nm to 250 nm," World Radiation Center, Davos, Switzerland, 1981.

4-5. American Society for Testing and Materials, "Solar Constant and Zero Air Mass Solar Spectral Irradiance Tables," ASTM Standard E490-00a, ASTM Committee E-21 on Space Simulation and Applications of Space Technology, December 2000.

4-6. International Commission on Illumination (Commission Internationale de L'Eclairage): "Solar Spectral Irradiance," CIE Publication 85 (ISBN 3–900–734–22–4), CIE Technical Committee TC2-17, C.J. Kok, F. Kasten, and C.G. Justus (eds.), 1989.

4-7. Kneizys, F.S.; Shettle, E.P.; Abreu, L.W.; et al.: "Users Guide to LOWTRAN 7," AFGL–TR–88–0177, Project 7670, Air Force Geophysics Laboratory, Hanscom AFB, MA, August 1988.

4-8. Wang, J.; and Anderson, G.P.: "Validation of FASCOD3 and MODTRAN3: Comparison of Model Calculations with Interferometer Observations from SPECTRE and ITRA," in Passive Infrared Remote Sensing of Clouds and the Atmosphere II, D.K. Lynch (ed.), in *Proc. SPIE*, Vol. 2309, pp. 170–183, 1994; *Applied Optics*, Vol. 35, pp. 6028–6040, 1996.

4-9. Justus, C.G.; and Paris, M.V.: "A Model for Solar Spectral Irradiance and Radiance at the Bottom and Top of a Cloudless Atmosphere," *Journal of Climate and Applied Meteorology*, Vol. 24, pp. 193–201, 1985.

4-10. Paris, M.V.; and Justus, C.G.: "A Cloudy-Sky Radiative Transfer Model Suitable for Calibration of Satellite Sensors," *Remote Sensing of Environment*, Vol. 24, pp. 269–285, 1988.

4-11. Parmalee, G.V.: "Irradiation of Vertical and Horizontal Surfaces by Diffuse Solar Radiation From Cloudless Skies," *Heating, Piping, and Air Conditioning*, Vol. 26, pp. 129–136, August 1954.

4-12. *ASHRAE Handbook of Fundamentals*, American Society of Heating, Refrigerating, and Air Conditioning Engineers, New York, 1967.

4-13. Becker, C.F.; and Boyd, J.S.: "Solar Radiation Availability on Surfaces in the United States as Affected by Season, Orientation, Latitude, Altitude, and Cloudiness," *Journal of Solar Engineering, Science and Engineering*, Vol. 1, pp. 13–21, January 1957.

4-14. Ornstein, M.P.: "Solar Radiation," *Journal of Environmental Sciences*, Vol. 5, pp. 24–27, April 1962.

4-15. Iqbal, M.: *An Introduction to Solar Radiation*, Academic Press, New York, 1983.

4-16. "Space Shuttle—Flight and Ground System Specification," Level II Program Definition and Requirements, NASA–JSC, NSTS 07700, Vol. X, Rev. J.; "Natural Environment Design Requirements," Appendix 10.10, June 14, 1990.

4-17. Daniels, G.E.: "Errors of Radiosonde and Rocketsonde Temperature Sensors," *Bulletin American Meteorological Society*, Vol. 49, No. 1, pp. 16–18, January 1968.

4-18. Schmidlin, F.J.; Luers, J.K.; and Huffman, P.D.: "Preliminary Estimates of Rocketsonde Thermistor Errors," *NASA TP–2637*, National Aeronautics and Space Administration, Washington, DC, September 1986.

4-19. Fishenden, M.; and Saunders, O.A.: "The Calculation of Heat Transmission," His Majesty's Stationary Office, London, 1932.

4-20. Daniels, G.E.: "Measurement of Gas Temperature and the Radiation Compensating Thermocouple," *Journal of Applied Meteorology*, Vol. 7, pp. 1026–1035, 1968.

4-21. Porter, W.L.: "Occurrence of High Temperatures in Standing Boxcars," Technical Report EP–27, Headquarters Quartermaster Research and Development Center, United States Army, Natick, MA, February 1956.

4-22. Cavell, W.W.; and Box, R.H.: "Temperature Data on Standard and Experimental Cartridges in Pilot Ejection Devices in a B47E Aircraft Stationed at Yuma, Arizona," Memo Report No. M60–16–1, Frankford Arsenal, Pitman-Dunn Laboratories Group, Philadelphia, PA, 1960.

4-23. NASA Earth Science Enterprise Program: *Surface Meteorology and Solar Energy Data Set*, <http://eosweb.larc.nasa.gov/cgi-bin/sse/sse.cgi?+s1>, 2004.

4-24. U.S. Department of Energy National Renewable Energy Laboratory: *Solar Radiation Resource Information*, <http://rredc.nrel.gov/solar/>, 2004.

4-25. National Oceanic and Atmospheric Administration National Climatic Data Center: *Climate Data Inventories*, <http://lwf.ncdc.noaa.gov/oa/climate/climateinventories.html>, 2004.

4-26. National Oceanic and Atmospheric Administration Climate Monitoring and Diagnostics Laboratory: *Solar and Thermal Atmospheric Radiation*, <http://www.cmdl.noaa.gov/star/>, 2004.

Terrestrial Environment (Climatic) Criteria Guidelines for Use in Aerospace Vehicle Development, 2008 Revision

NASA/TM—2008–215633
December 2008

D.L. Johnson, Editor

Section 5: United States and World Surface Extremes

TABLE OF CONTENTS

LIST OF FIGURES

LIST OF TABLES

NOMENCLATURE

dP	pressure difference
dZ	altitude difference
g	gravity
p	probability
S_T	standard deviation
$\hat{T}$	temperature
$\overline{T}$	mean temperature
y_s	number of standard deviations
ρ	density

5. UNITED STATES AND WORLD SURFACE EXTREMES

5.1 United States Surface Extremes

Most NASA programs involving the launch and reentry of aerospace vehicles are conducted in or near the United States. Section 5 provides extremes of those atmospheric variables not included elsewhere in this document that may be critical to such programs. Statistical data discussed in this section include air temperature, snowfall, hail, and atmospheric pressure. Section 5.2—World Surface Extremes—provides a more general discussion of atmospheric extremes on a global scale for temperature, dewpoint, precipitation, pressure, and wind speed.

5.1.1 Environments Included

The parameters included are as follows:

(1) Air temperature—extreme maximum and minimum.
(2) Snowfall/snow loads—24-hr maximum and storm maximum.
(3) Hail—maximum size.
(4) Atmospheric pressure—extreme maximum and minimum.

Information for other mean and extreme atmospheric parameters relative to the principal locations covered by this document is available from the appropriate sections in this document. Air temperature statistics are presented in sections 3.3.1, 3.4.1, 4.5.2, and 4.6. Snowfall is presented in section 7.2.6, hail in 7.2.7, and air pressure in 3.3.2 and 3.4.2.

5.1.2 Source of Data

The extremes presented here have been prepared using data from National Weather Service stations and published articles, such as reference 5-1. They represent the highest or lowest extreme value measured at each station. The length of record varies from station to station, but most values represent more than 15 yr of record. Where unusual geographical features in a local area affect an extreme value, such as the minimum temperature on a high mountain peak, it generally will not be shown on the maps unless a National Weather Service station is located there.

The extremes represent measurements during the period of record for essentially all meteorological parameters. Because this period covers only a few decades for most locations, it is obvious that there is a risk that the extremes will be exceeded in future years. However, the values are considered appropriate as guidelines for use in critical engineering design studies relative to probable occurrence of atmospheric extremes during expected operational lifetime.

The World Meteorological Organization (WMO) has issued a WMO world weather/climate extremes archive available at <http://wmo.asu.edu/>. Their Web site includes high and low temperature, rainfall extremes, pressure records, aridity, wind speeds, tropical cyclones, and tornadoes. Data are arranged by both hemisphere and continent.

5.1.3 Extreme Design Environments

The values of extreme maxima and minima in this section are for recommended design guidelines and may or may not reflect extrapolation (theoretical or otherwise) of actual measured values over the available period of record.

5.1.3.1 Air Temperature. The distribution of extreme maximum air temperatures in the United States is shown in figure 5-1, while figure 5-2 shows the extreme minimum temperature distribution. Extreme U.S. temperatures (°F) with their locations and dates of occurrence are given in table 5-1 (ref. 5-2). To convert to °C, use this formula: °C = 5/9 (°F−32). Figures 5-3 and 5-4 (maps from reference 5-3) show the mean temperature and standard deviations of temperatures for January and July.

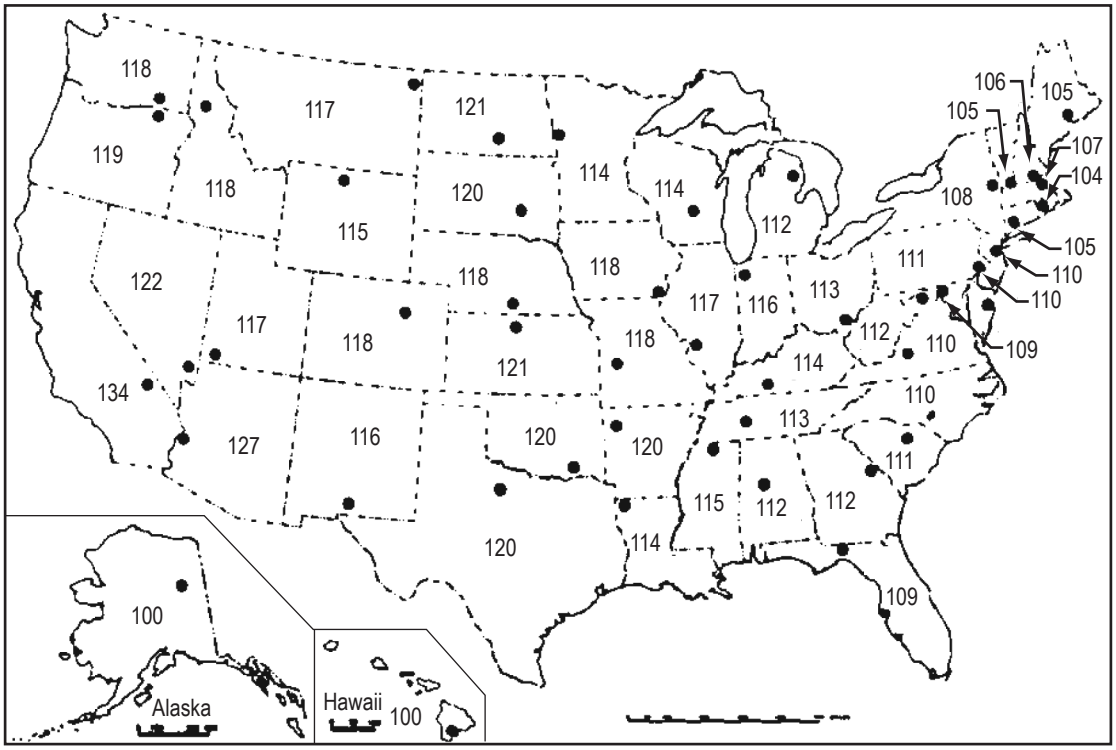

Figure 5-1. Maximum temperatures (°F) on record and locations by state. For conversions from °F to °C, use the following equation:

$$T\ ^{\circ}\mathrm{C} = \frac{5}{9}\left(T\ ^{\circ}\mathrm{F} - 32\right) .$$

To estimate the temperature, $\hat{T}$, that is less than or equal to a probability, p, (corresponding to the normal distribution) from figures 5-3 and 5-4, find from the appropriate figure, by interpolation as needed, the mean temperature, $\overline{T}$ and the standard deviation, S_T. Then, substitute these in equation (5.1):

$$\hat{T} = \overline{T} + S_T y_s \left(^{\circ}\mathrm{F}\right) . \tag{5.1}$$

Values of y_s for various normal probability levels are shown in table 5-2.

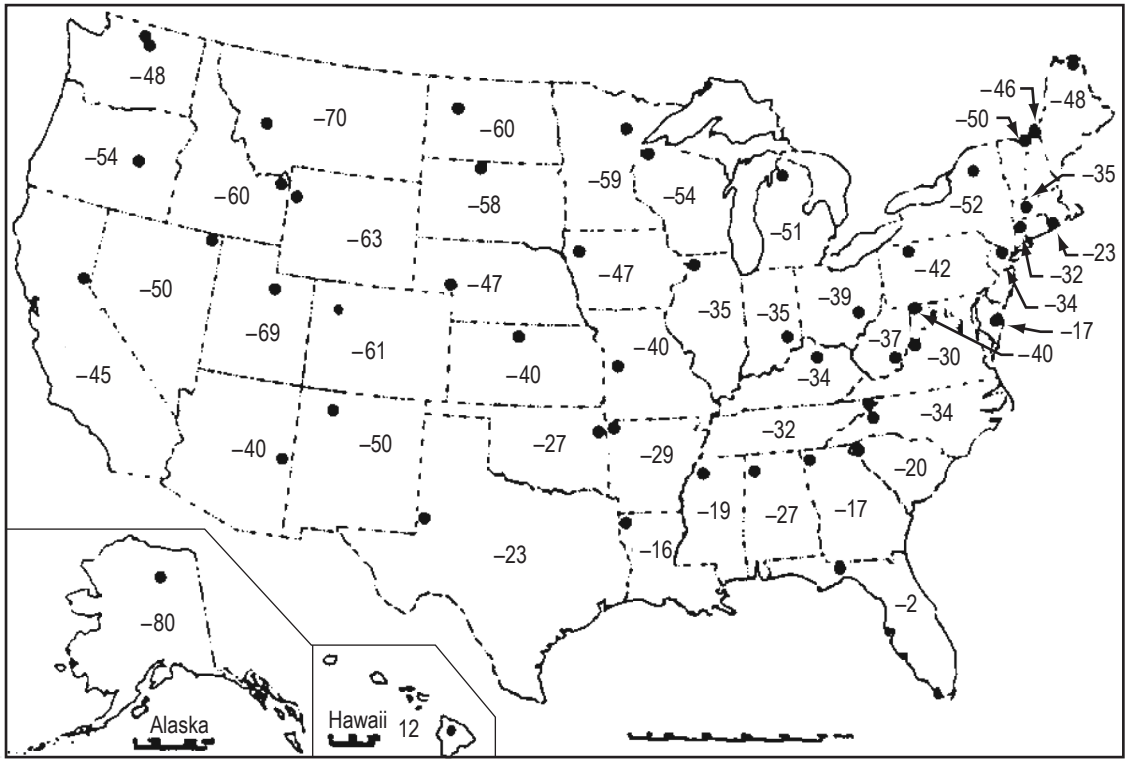

Figure 5-2. Minimum temperatures (°F) on record and locations by state. For conversions from °F to °C, use the following equation:

$$T\ ^{\circ}\mathrm{C} = \frac{5}{9}\left(T\ ^{\circ}\mathrm{F} - 32\right) .$$

Table 5-1. Extremes of temperature and sea level pressure for the United States (ref. 5-1).

Temperature					Sea Level Pressure				
	°C	°F	Location	Date	N/m^2	mb	in Hg	Location	Date
High									
Contiguous United States	57	134	Greenland Ranch, CA	July 10, 1913	106,400	1,064	31.42	Miles City, MT	December 24, 1983
Hawaii	38	100	Pahala	April 27, 1931	102,670	1,026.7	30.32	Honolulu	February 10, 1919
Alaska	38	100	Fort Yukon	June 27, 1915	107,860	1,078.6	31.85	Northway	January 31, 1989
Low									
Contiguous United States	–57	–70	Rogers Pass, MT	January 20, 1954	95,490	954.9	28.2	Canton, NY Block Island, RI	January 3, 1913 March 7, 1932
United States (Hurricane)	–	–	–	–	89,230	892.3	26.35	Matecumbe Key, FL	September 2, 1935
Hawaii	–11	12	Mauna Kea Observatory	May 17, 1979	97,200	972	28.7	Barking Sands	November 23,1982
Alaska	–62	–80	Prospect Creek	January 23, 1971	92,500	925	27.31	Dutch Harbor	October 25,1977

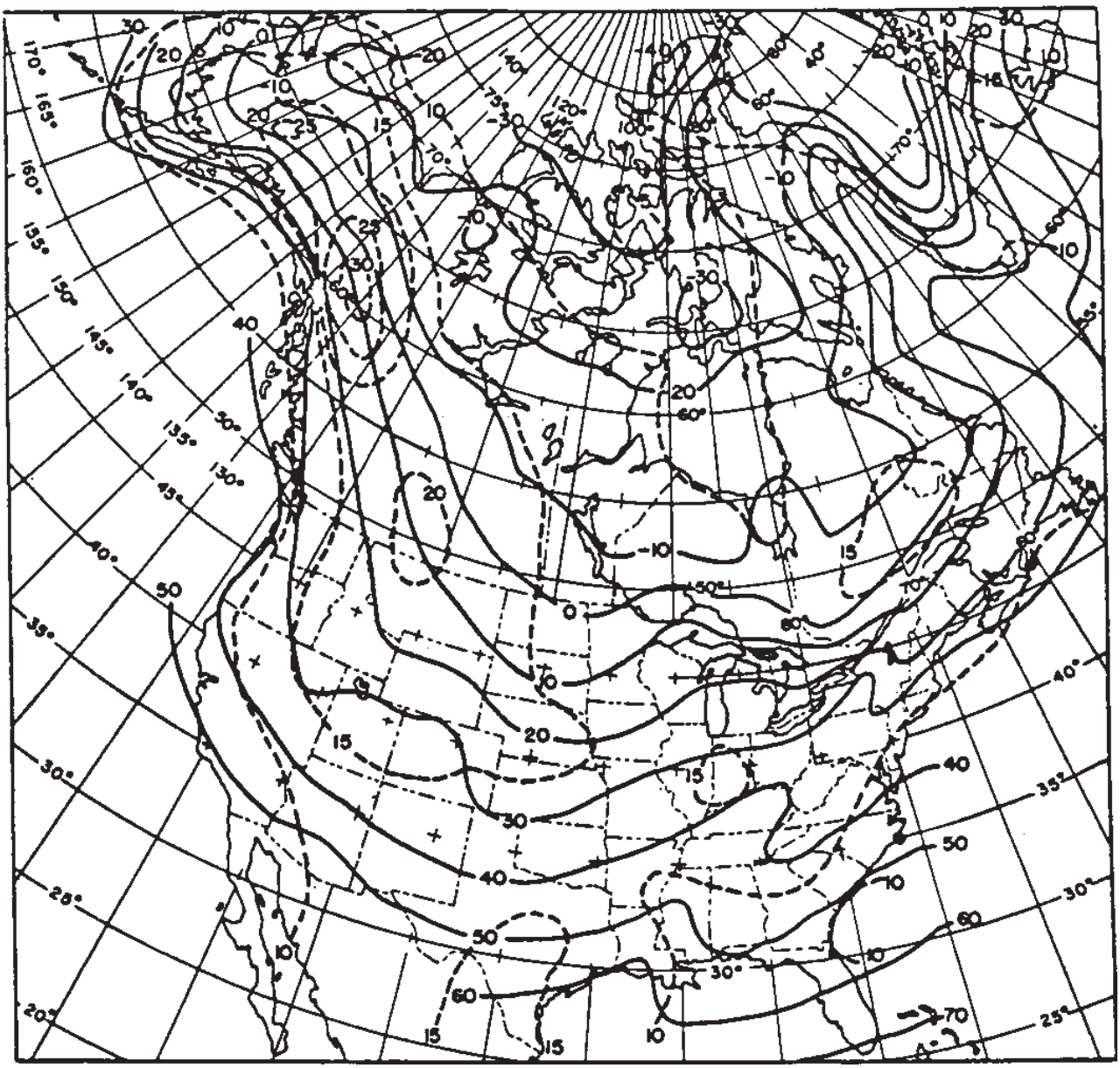

Figure 5-3. Isotherms of January hourly surface temperatures. (Approximate mean values (°F) are shown by solid lines, standard deviations (°F) by broken lines.) The approximations were made to give the best estimates of lower 1- to 20-percentile values of temperature based on a normal distribution (ref. 5-3). For conversions from °F to °C, use the following equation:

$$T\ ^{\circ}\mathrm{C} = \frac{5}{9}\left(T\ ^{\circ}\mathrm{F} - 32\right) .$$

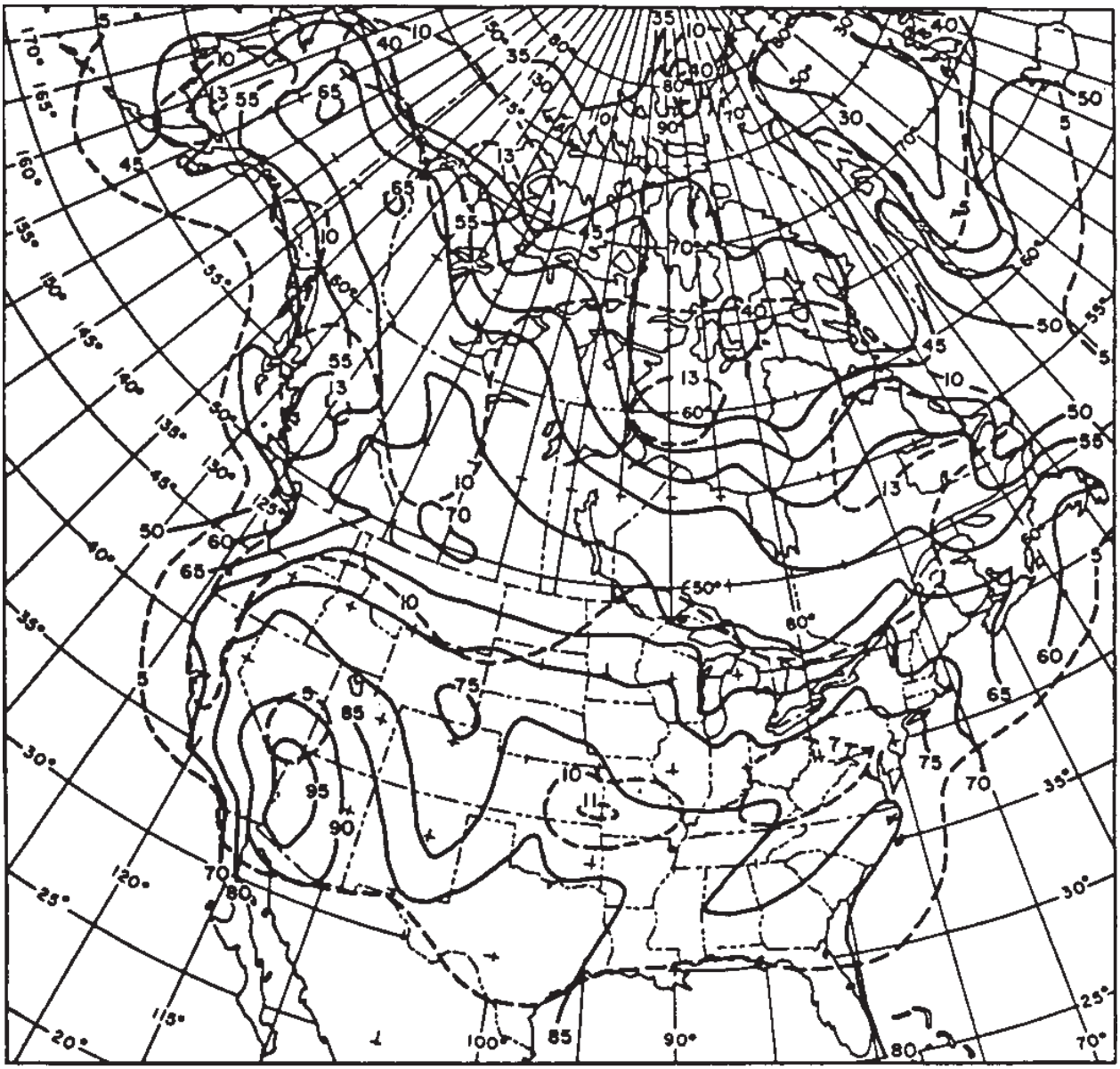

Figure 5-4. Isotherms of July hourly surface temperatures. (Approximate mean values (°F) are shown by solid lines, standard deviations (°F) by broken lines.) The approximations were made to yield the best estimates of upper 80- to 99-percentile values based on a normal distribution (ref. 5-3). For conversions from °F to °C, use the following equation:

$$T\ ^{\circ}\mathrm{C} = \frac{5}{9}\left(T\ ^{\circ}\mathrm{F} - 32\right) .$$

Table 5-2. Various normal probability level values of y_s.

Cold Temperatures (Fig. 5-3)		Hot Temperatures (Fig. 5-4)	
p	y_s	p	y_s
0.20	–0.84	0.80	0.84
0.10	–1.28	0.90	1.28
0.05	–1.65*	0.95	1.65*
0.025	–1.96	0.975	1.96
0.01	–2.33	0.99	2.33

*The 95th percentile value is recommended for hot-day design ambient temperatures over runways for landing-takeoff performance calculation using figure 5-4; the 5th percentile is recommended for cold-day design.

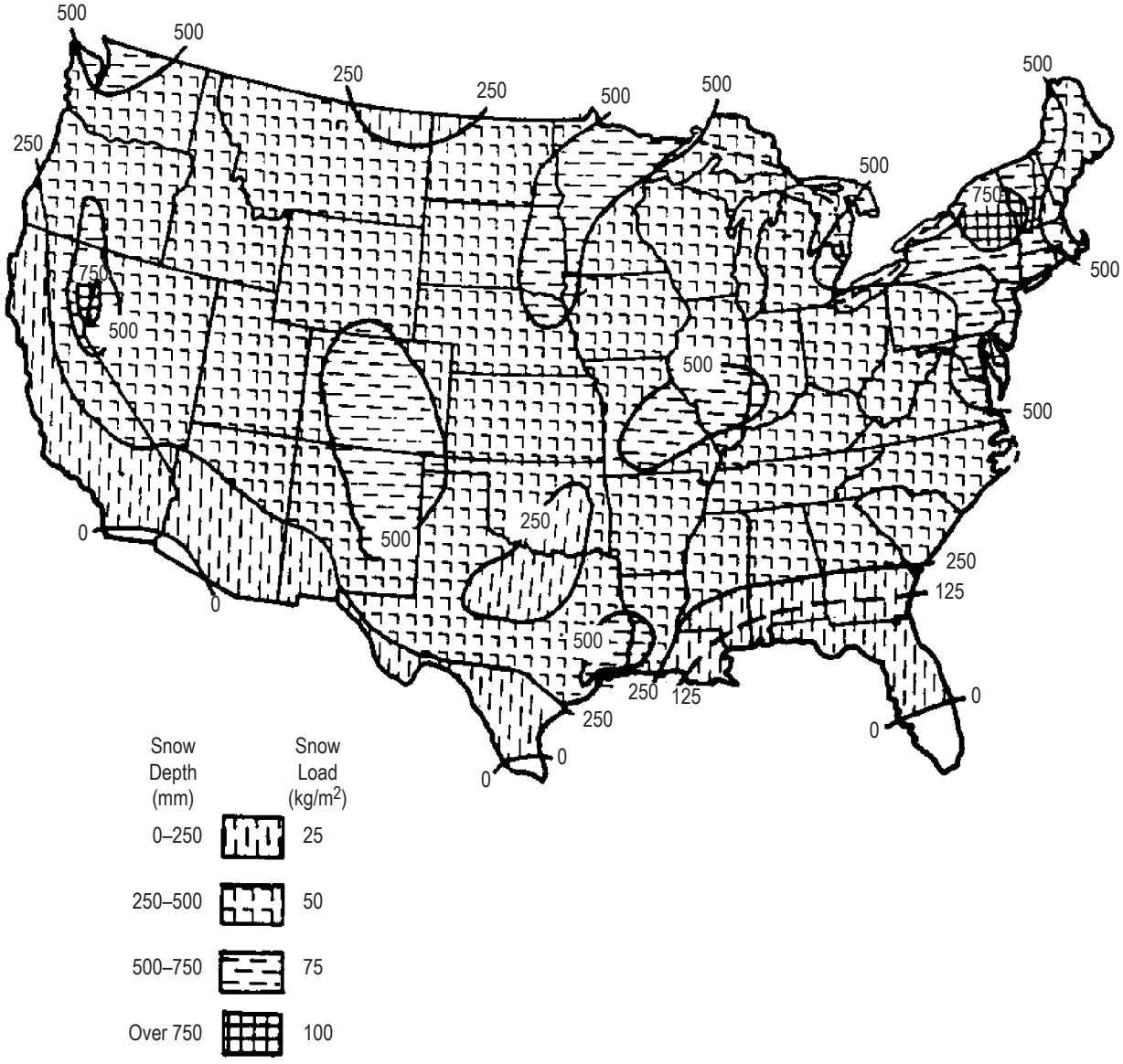

Figure 5-5. Extreme 24-hr maximum snowfall (mm) and maximum snow load (kg/m^2).

5.1.3.2 Snowfall/Snow Load. Figures 5-5 and 5-6 show the maximum depth of snow and the corresponding snow loads for the contiguous United States. Figure 5-5 shows the maximum depth for a 24-hr period; figure 5-6 shows the maximum depth and the corresponding snow loads for a snow period. The extreme value map (fig. 5-6) shows the same snow depth as in the 24-hr map in the southern low elevation areas of the United States since snow storms seldom exceed 24 hr in these areas. The greatest 24-hr snowfall was 1,930 mm (76 in) at Silver Lake, CO, April 14–15, 1921. One storm gave 4,800 mm (189 in) at Mt. Shasta Ski Bowl, CA, on February 13–19, 1959 (ref. 5-4). The greatest snowfall in one calendar month is 9,906 mm (390 in) which occurred at Tamarack, CA, during January 1911.

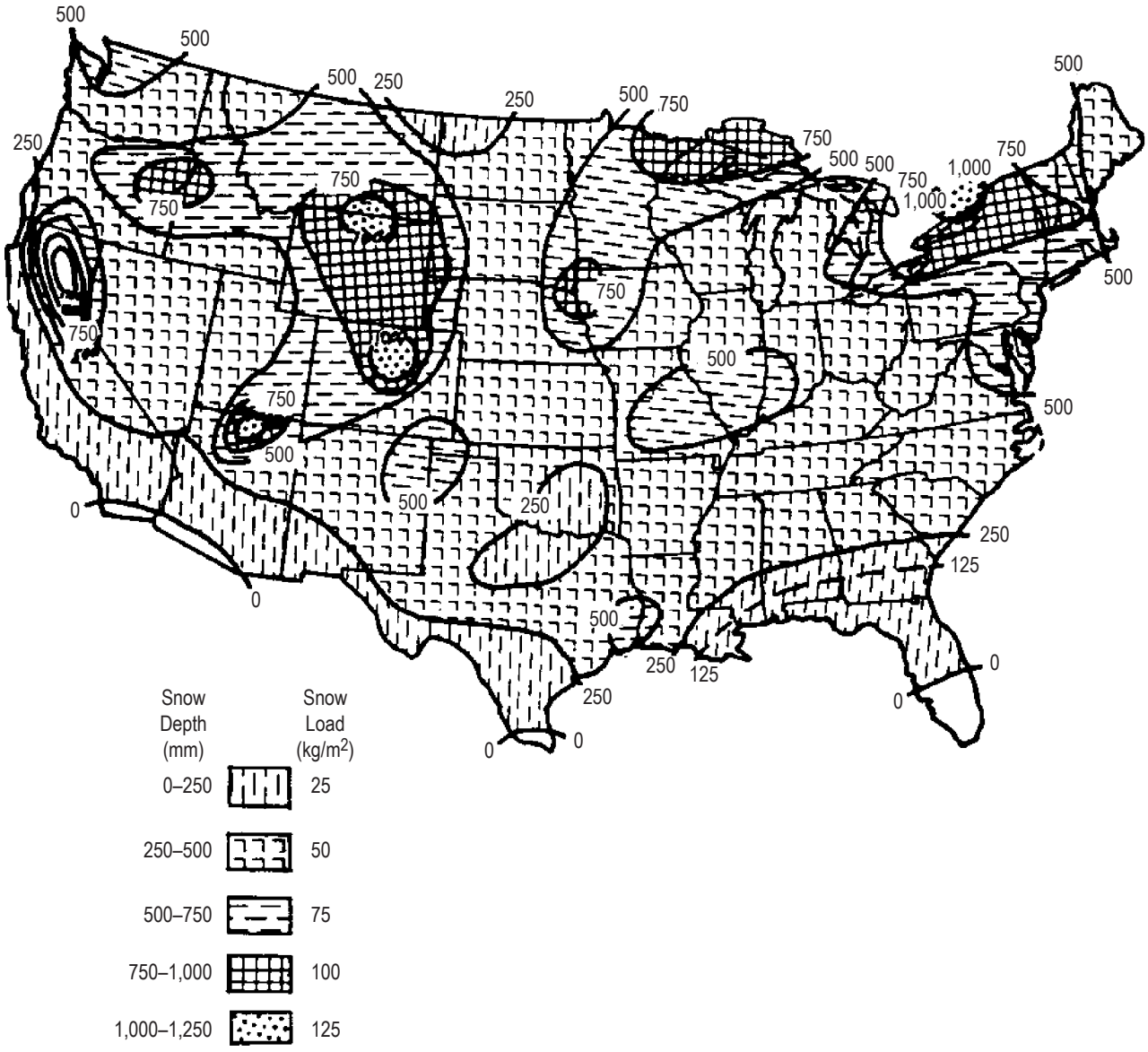

Figure 5-6. Extreme storm maximum snowfall (mm) and maximum snow load (kg/m^2).

Terrain, combined with the general movement of weather systems, has a great effect on the amount of fall, accumulation, and melting of snow. Also, the length of a single storm varies over different areas. In some mountain regions, much greater amounts of snowfall have been recorded than are shown on the maps. Also, the snow in these areas may remain for the entire winter. For example, in a small valley near Soda Springs, CA, a seasonal snow accumulation of 7.9 m (26 ft) with a density of ≈0.35 g/cm^3 was recorded. This gives a snow load of 2,772 kg/m^2 (567.7 lb/ft^2). The snow pack at Soda Springs is the greatest on record in the United States and is nearly double that of the previous record in the same area. A study of the maximum snow loads in the Wasatch Mountains of Utah showed that for a 100-yr return period at 2,740 m (9,000 ft) altitude, a snow load of 1,220 kg/m^2 (250 lb/ft^2) could be expected (ref. 5-5). Snowfall and snow load statistics for NASA sites are presented in section 7.2.6.

Snow characteristics and loading for particular sites are given in section 7.4.

5.1.3.3 Hail. The distribution of maximum-sized hailstones in the United States is shown in figure 5-7. The sizes are for single hailstones and not conglomerates of several hailstones frozen together. The heaviest officially recorded hailstone in the United States weighed 757 g (1.67 lb) and fell September 3, 1970, at Coffeyville, KS. The largest size, offically measured, hailstone was 7 in (17.78 cm) in diameter with a circumference of 18.75 in (47.63 cm), and fell June 22, 2003, near Aurora, NE (ref. 5-6). Section 7.2.7 presents further information concerning hail characteristics and climatology.

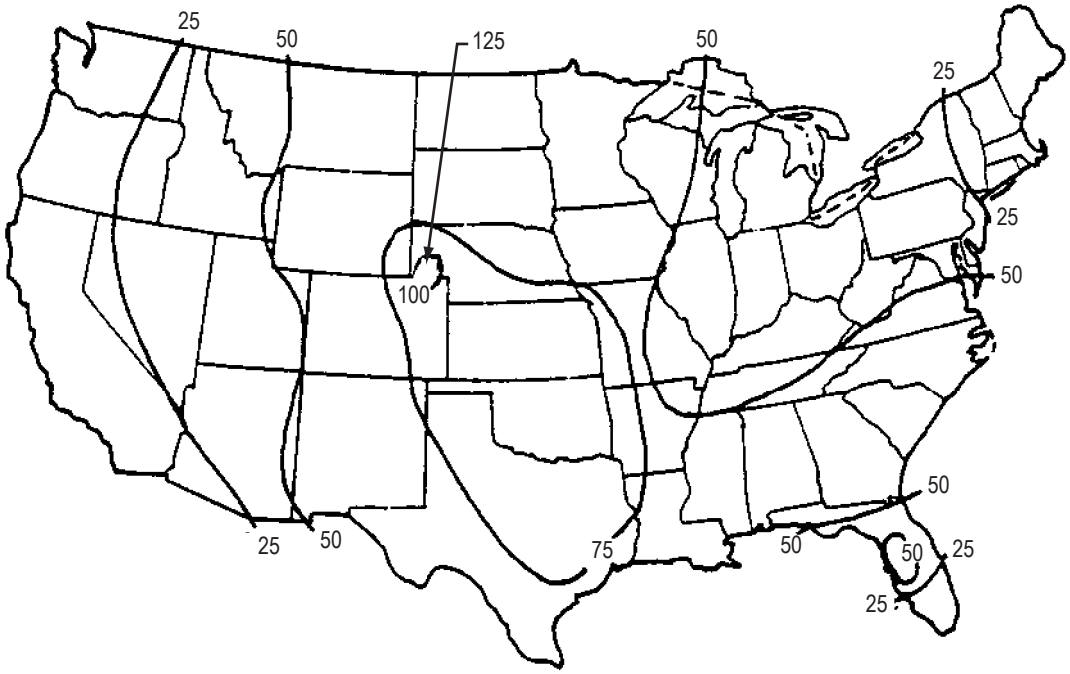

Figure 5-7. Extreme maximum hailstone diameters (mm).

5.1.3.4 Atmospheric Pressure. The extreme in atmospheric pressure normally given in the literature refers to the pressure that would have occurred if the station were at sea level. The surface weather map published by the U.S. National Weather Service uses sea level pressures to assist in map analysis and forecasting. These sea level pressure values are obtained from station pressures by using the hydrostatic equation,

$$-dP = \rho g dZ \ , \tag{5.2}$$

where

dP = pressure difference
ρ = density
g = gravity
dZ = altitude difference.

The sea level data are valid for design purposes only at locations with elevations near sea level. As an example, for the former highest officially reported sea level pressure observed in the United States of 106,330 N/m^2 (1,063.3 mb) at Helena, MT, (ref. 5-7), the station pressure was approximately 92,100 N/m^2 (921 mb) because the station is 1,187 m (3,893 ft) above mean sea level.

Figures 5-8 and 5-9 show the distribution of extreme maximum and minimum station pressures in the United States. Because of the direct relationship between pressure and station elevation, figures 5-10 through 5-13 can be used with a knowledge of the station elevation to obtain the extreme maximum and minimum U.S. station pressure values. Similar maps and graphs in U.S. Customary Units are given in reference 5-8.

Extreme temperatures and sea level pressures for the United States are given in table 5-1 (refs. 5-2, 5-7, 5-9, and 5-10). Reference 5-10 also contains surface atmosphere extreme criteria for vehicle launch and transportation areas. Surface and aloft atmospheric pressure statistics for NASA sites are presented in sections 3.3.2 and 3.4.2, respectively.

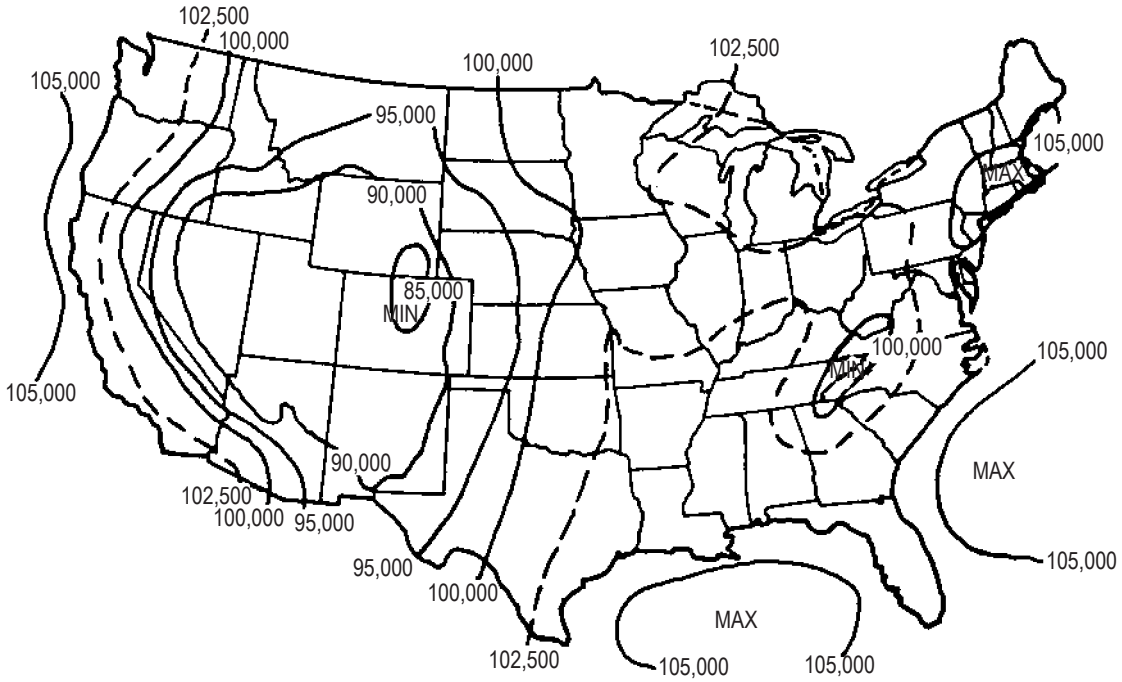

Figure 5-8. Maximum absolute station pressure (N/m^2).

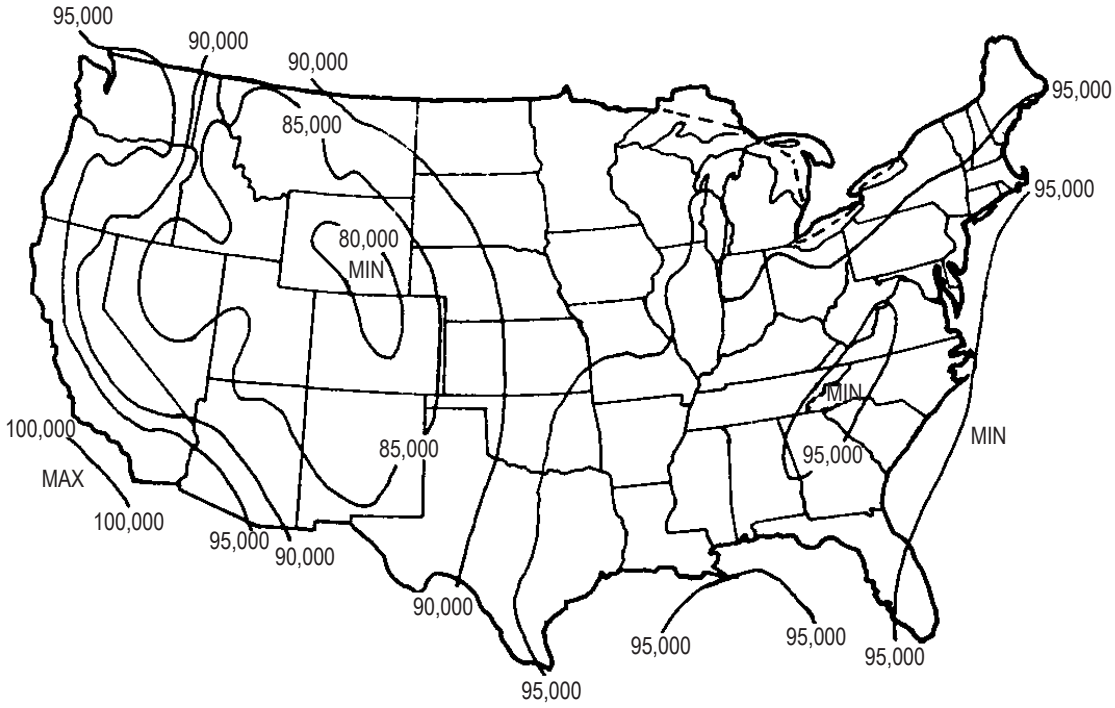

Figure 5-9. Minimum absolute station pressure (N/m^2).

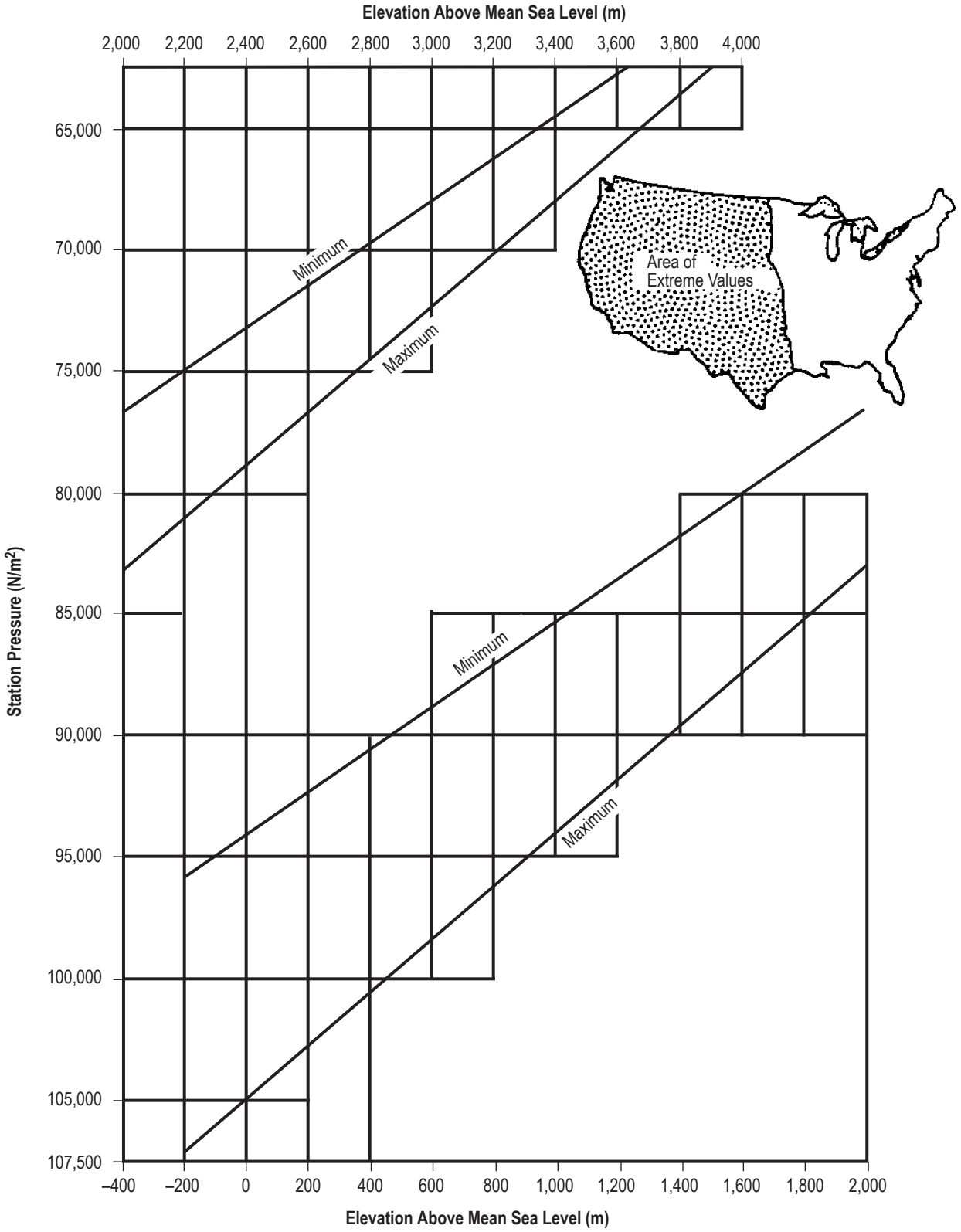

Figure 5-10. Extreme pressure values versus elevation for Western United States.

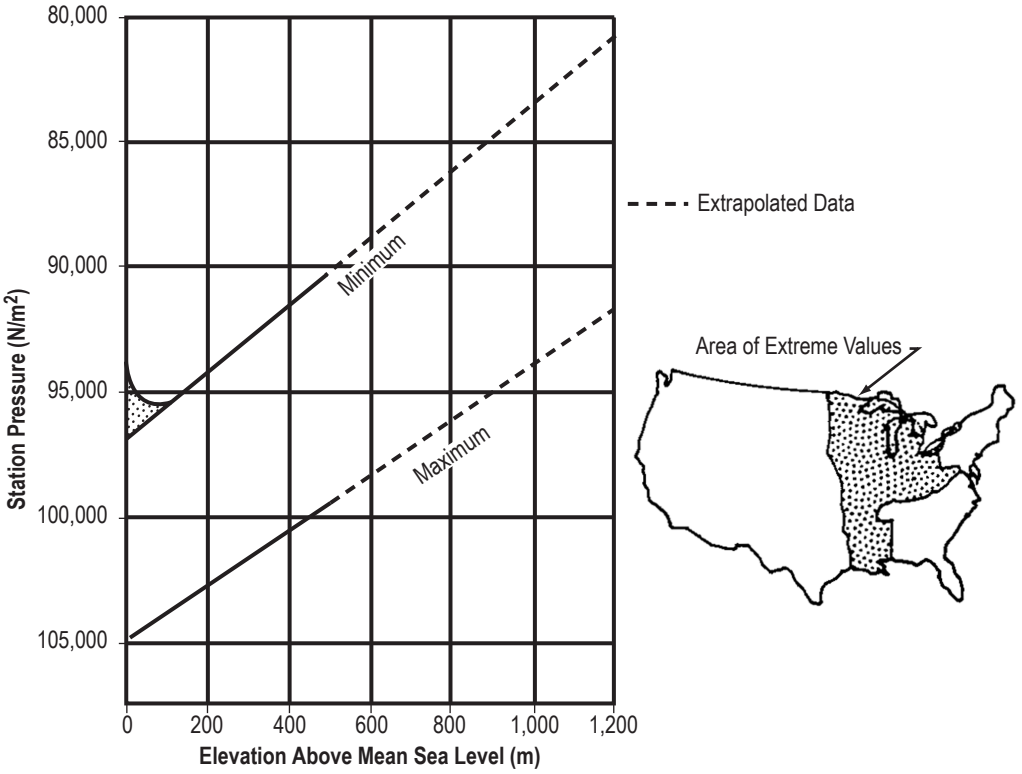

Figure 5-11. Extreme pressure values versus elevation for Central United States.

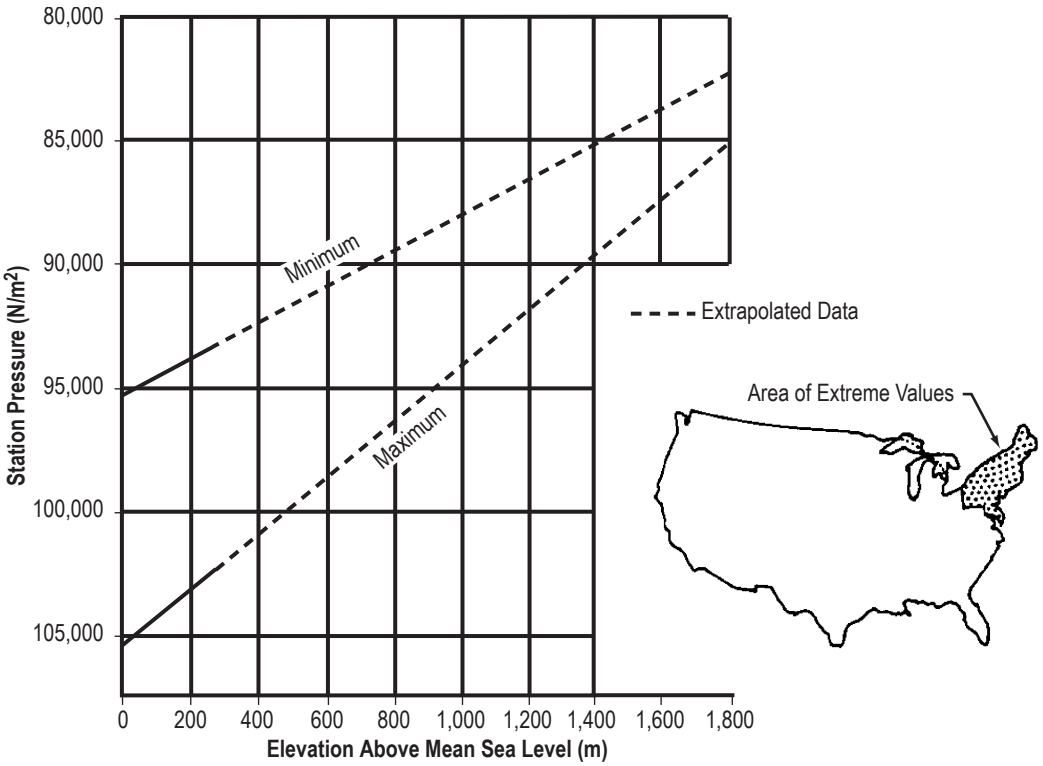

Figure 5-12. Extreme pressure values versus elevation for Northeastern United States.

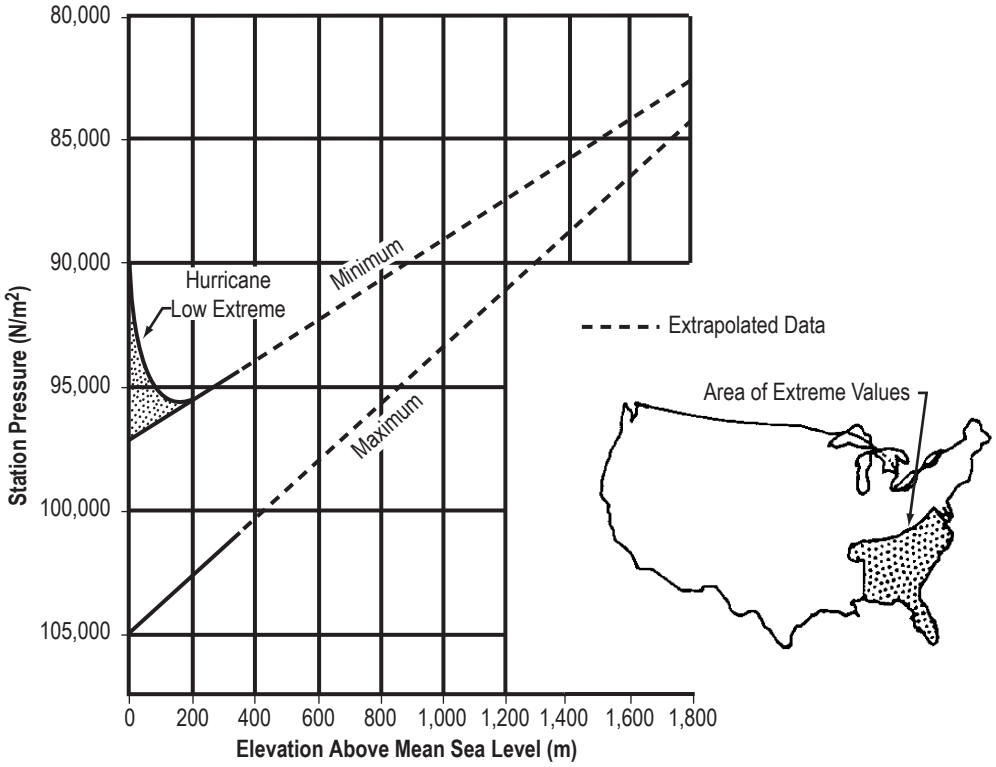

Figure 5-13. Extreme pressure values versus elevation for Southeastern United States.

5.2 World Surface Extremes

Section 5.2 provides world extreme values for atmospheric temperature, dewpoint, precipitation, pressure, and wind speed.

5.2.1 Sources of Data

A great amount of atmospheric data have been collected throughout the world that may be used for statistical studies. "World Weather Records" (ref. 5-11), compiled by the National Oceanic and Atmospheric Administration, provides a summary of mean values of meteorological data. The publication "Weather Extremes" (ref. 5-1) is extremely valuable for its listing of extreme values of surface meteorological parameters.

The Earth Sciences Laboratory of the U.S. Army Topographic Laboratories at Fort Belvoir, VA, has collected worldwide data on meteorological extremes that are published in AR 70-38 (ref. 5-12). For AR 70-38, the Earth Sciences Laboratory prepared world maps that show worldwide absolute maximum and minimum temperatures. These maps are reproduced in this section in figures 5-14 and 5-15.

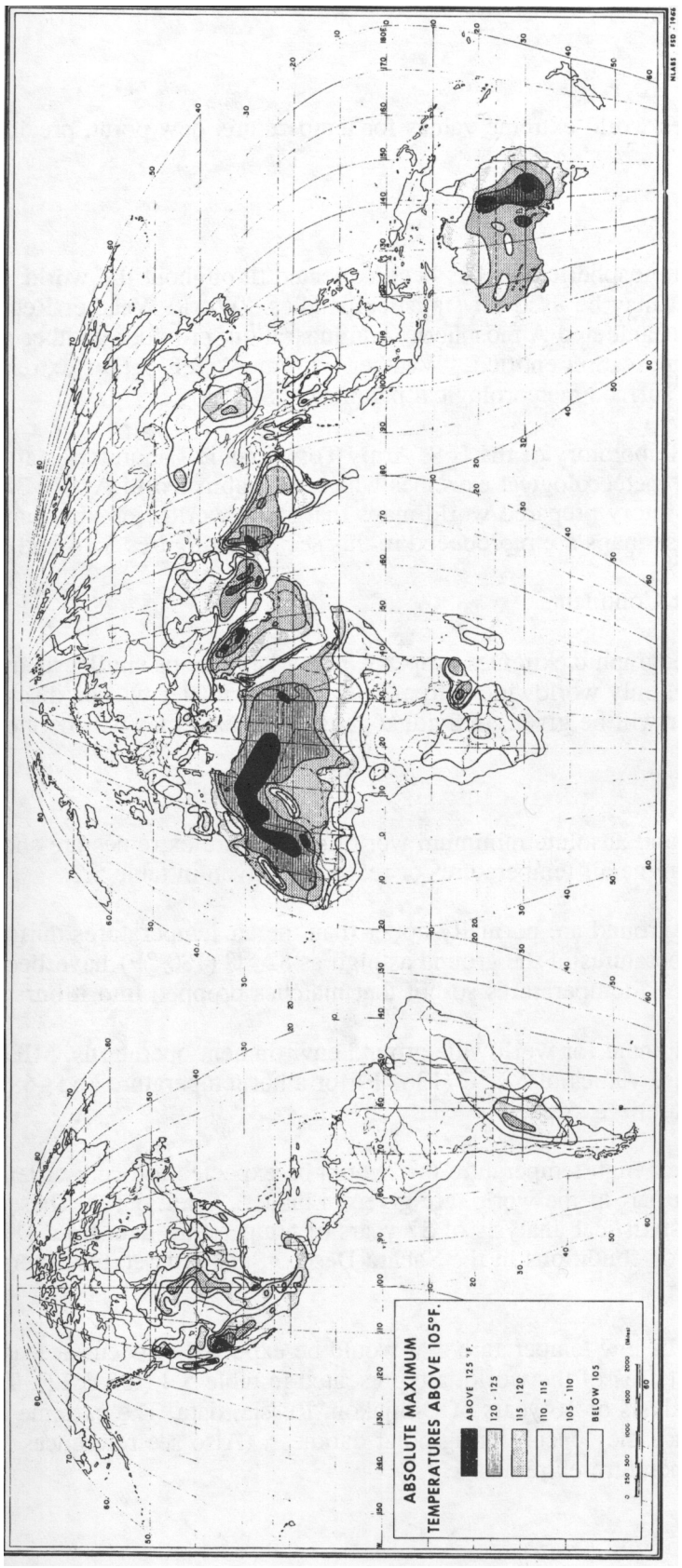

Figure 5-14. Worldwide absolute maximum temperature above 41 °C (105 °F) (ref. 5-12).

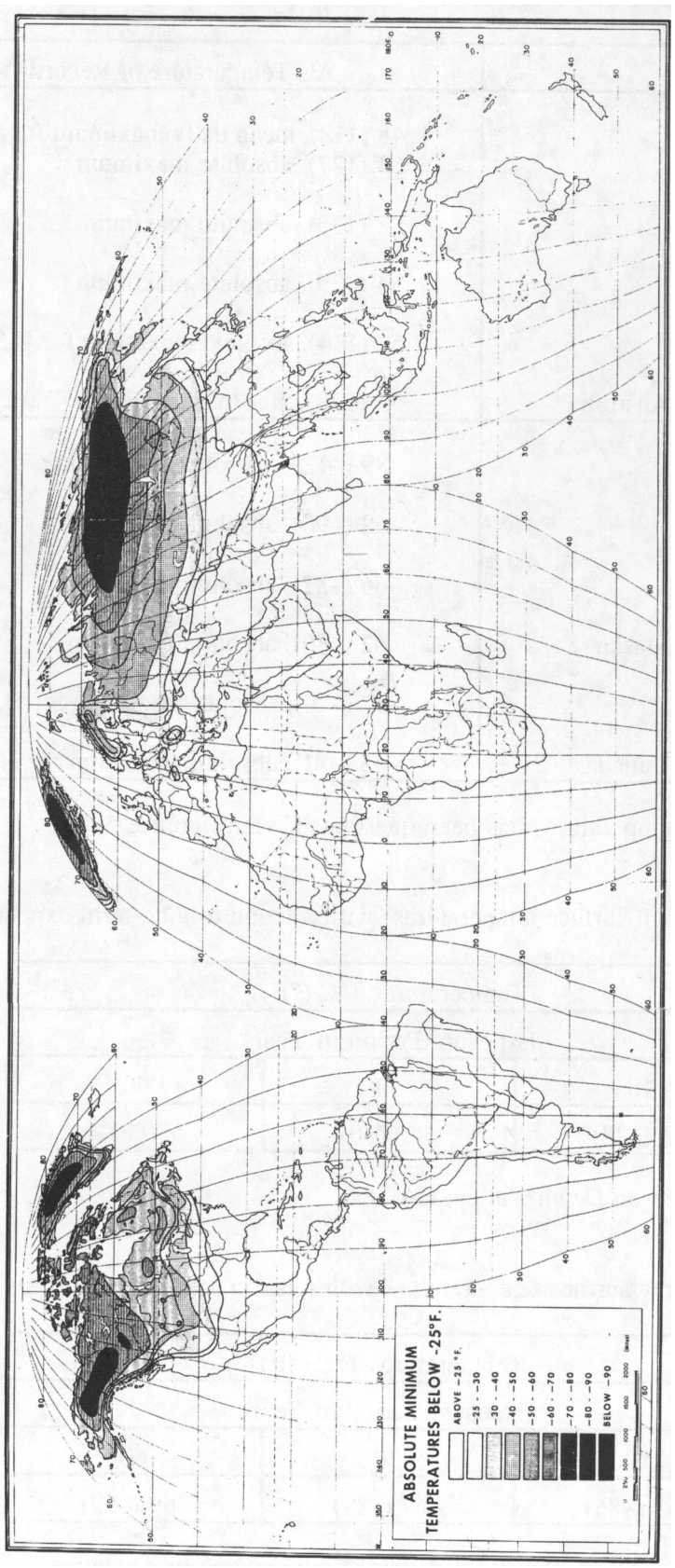

Figure 5-15. Worldwide absolute minimum temperature below –32 °C (–25 °F) (ref. 5-12).

5.2.2 World Extremes Over Continents

To present all the geographic extremes properly, many maps similar to figures 5-14 and 5-15 would be required. Therefore, only worldwide extremes of each parameter will be discussed, and available references on each parameter will be given. Individual geographic extremes will be mentioned when pertinent.

5.2.2.1 Temperature. Worldwide maximum and minimum temperatures are shown in figures 5-14 and 5-15. Some geographical extreme air temperatures of record are given in table 5-3.

Table 5-3. Extreme surface air temperature records.

Location	Air Temperature Records		
	Maximum/Minimum	°C	°F
Salah, Africa	Mean daily maximum for 45 days	48	118
	Absolute maximum	53	127
El Azizia, Libya*	Absolute maximum	58	136
Tirat Tsvi, Israel	Absolute maximum	54	129
Death Valley, CA*	Absolute maximum for United States	57	134
Cloncurry Queensland, Australia	Absolute maximum	53	128
Vostok, Antarctica	Absolute minimum	–89	–129
Ojmjakon, Siberia	Absolute minimum	–68	–90
Northice, Greenland	Absolute minimum	–66	–87
Prospect Creek Camp, AK	Absolute minimum	–62	–80
Rogers Pass, MT	Absolute minimum for United States	–57	–70
Snag, Yukon Territory, Canada	Absolute minimum for North America	–63	–81

*The validity of these temperatures has been questioned; see reference 5-4.

During the daytime, temperatures at the ground are normally hotter than the air temperatures. In Loango, Congo, Africa, ground temperatures as high as 82 °C (180 °F) have been measured. At Stuart, Australia, the sand has reached temperatures so hot that matches dropped into it burst into flame.

In designing equipment for worldwide ground operations, MIL-STD-210C (ref. 5-13) now uses extreme temperature values of 58 °C (136 °F) and –68 °C (–90 °F), excluding Antarctic extremes.

The long-term extremes of maximum temperature that would be expected at least once during a 10- to 60-yr period, in the hottest part of the world, are given in table 5-4 (ref. 5-13). These extreme temperatures were derived from a statistical analysis of 57 yr of temperature data from Death Valley, CA, which is considered representative of conditions in the Sahara Desert. Such temperatures persist for 1 to 3 hr during the day.

The long-term extremes of minimum temperature that would be expected at least once during a 10- to 60-yr period, in the coldest area of the world, are presented in table 5-5 (ref. 5-13). These values were derived from a statistical analysis of 16 yr of Ojmjakon, Russia, data. Temperatures in Antarctica were not considered in the study. The extreme minimum temperatures persist for longer periods since they occur during polar darkness. Also see references 5-14 and 5-15 regarding probabilities of surface temperature extremes. Surface and aloft atmospheric temperature information for NASA sites is given in sections 3.3.1, 3.4.1, 4.5.2, and 4.6.

Table 5-4. Extreme high surface temperatures with relation to long-term exposure (ref. 5-13).

Exposure Return Period (yr)	Temperature	
	°C	°F
10	53	128
30	54	130
60	55	131

Table 5-5. Extreme low surface temperatures with relation to long-term exposure (ref. 5-13).

Exposure Return Period (yr)	Temperature	
	°C	°F
10	–65	–86
30	–67	–89
60	–69	–92

5.2.2.2 Dewpoint. High dewpoints associated with high temperatures can be detrimental to equipment and make living conditions very uncomfortable. Some examples of high global dewpoints are:

(1) The northern portion of the Arabian Sea in April and May: 29 °C (85 °F) dewpoint.

(2) The Red Sea in July: 32 °C (89 °F) dewpoint.

(3) The Caribbean Sea (includes the western end of Cuba and the Yucatan Peninsula, Mexico) in July: 27 °C (81 °F) dewpoint.

(4) The northern portion of the Gulf of California: 30 °C (86 °F) dewpoint.

(5) The Persian Gulf (Sharjah, Arabia) in July: 34 °C (93 °F) dewpoint.

A discussion of atmospheric humidity is presented in section 6.

5.2.2.3 Precipitation. The worldwide distribution of precipitation is highly variable; some areas do not receive rain for years, while others receive torrential rain many months of the year. Precipitation is also seasonal; for example, Cherrapunji, India, with its world record total of 2,647 cm (1,042 in) of precipitation in a year, has a mean monthly precipitation of less than 2.54 cm (1 in) in December and January. Arica, Chile, had no rain between October 1903 and December 1917. The longest dry period for a U.S. location was 767 days, Bagdad, CA, October 3, 1912, to November 8, 1914.

The heaviest precipitation for >12 hr usually occurs during monsoons. Conversely, high rainfall rates for short periods (<12 hr) usually occur during thunderstorms and over much smaller areas. Some world records for various periods of rainfall are given in table 5-6 (ref. 5-4).

Table 5-6. World rainfall records.

Station	Time Period	Amount	
		cm	in
Unionville, MD	1 min	3.1	1.23
Plum Point, Jamaica	15 min	20	8
Holt, MO	60 min	31	12
D'Hanis, TX	3 hr	51	20
Foc-Foc, LaReunion Island	12 hr	114	45
Foc-Foc, LaReunion Island	1 day	183	72
Cherrapunji, India	30 day	930	366.14
Cherrapunji, India	1 year	2,647	1,041.73
Highest average annual precipitation: World: 1,168 cm (460 in), Mt. Waialeale, Kauai, HI Contiguous United States.: 366 cm (144 in), Wynoochee, WA Lowest average annual precipitation: World: 0.08 cm (0.03 in), Arica, Chile Contiguous United States: 4.4 cm (1.63 in), Death Valley, CA			

Indepth information on precipitation is given in section 7.2 with world record rainfall also being discussed in section 7.2.2.

5.2.2.4 Pressure. Extremes of surface atmospheric pressure for use in design must be derived from the measured station pressures, not from the calculated sea level pressures that are usually published.

Station pressures exhibit great variability between locations because of altitude differences. The lowest station pressures occur at the highest altitudes. The highest station pressures occur at either the lowest elevation stations (below sea level) or in the arctic regions in cold air masses at or near sea level.

Court (ref. 5-16) published an interesting discussion on world pressure extremes. Typical extreme high and low pressure values are given in table 5-7 (refs. 5-1 and 5-4).

Surface and aloft pressure values are given in sections 3.3.2 and 3.4.2, respectively.

Table 5-7. Extreme pressure values for selected areas.

Station	Elevation Above Sea Level		Sea Level Pressure (mb)	
	m	ft	Lowest	Highest
Lahasa, Tibet	3,685	12,090	645*	652*
Sedom, Israel	–389	–1,275	–	1,081.8
Portland, ME	19	61	–	1,056
Northway, AK	NA	NA	–	1,078.6
Qutdligssat, Greenland	3	10	–	1,063.4
In the Typhoon Tip, 16°44' N., 137°46' E., October 12, 1979	–	–	870**	–
Agata, Siberia	261	855	–	1,083.8

*Monthly means.
**Lowest sea level pressure on record.

5.2.2.5 Surface Wind. Extreme surface winds occur during several types of meteorological conditions: tornadoes, hurricanes or typhoons, mistral winds, and Santa Ana winds. In design, each type of wind needs special consideration. For example, the probability of tornadic winds is very small compared with the probability of mistral winds, which may persist for days. The world's highest recorded peak wind gust of 103 m/s (231 mph) occurred atop Mt. Washington, NH, (height 1,916 m (6,288 ft)) on April 12, 1934. The highest 5-min average wind speed of 84 m/s (188 mph) also occurred at Mt. Washington (ref. 5-1). Section 2 presents a complete discussion of winds.

5.2.2.5.1 Tornadoes and Whirlwinds. Tornadoes are rapidly revolving circulations (vortices) normally associated with a severe thunderstorm. Although a tornado is extremely destructive, the average tornado path is only about 400 m (1/4 mi) wide and seldom more than 26 km (16 mi) long. However, there have been instances when tornadoes have caused major destruction along paths more than 1.6 km (1 mi) wide and 483 km (300 mi) long. The probability of any one point being in a tornado path is very small; therefore, designing structures to withstand tornadoes is usually not considered except for special situations. Wind speeds in tornadoes have been estimated to exceed 134 m/s (260 kt or 300 mph). See sections 12.3 and 12.4 for further information regarding tornadoes.

A whirlwind is a small-scale, rotating column of air. Dust devils and waterspouts are the smaller and far less intense whirlwinds. The largest Florida Keys water spouts can produce tangential wind speeds up to 90 m/s (200 mph), while large, mature dust devils have yielded wind velocities up to 40 m/s (90 mph).

5.2.2.5.2 Hurricanes (typhoons). Hurricanes (also called typhoons, willy-willies, tropical cyclones, and many other local names) are large storms of considerable intensity that normally originate in tropical regions between the equator and 25° latitude. Hurricanes often are accompanied by heavy rain. Since the hurricanes of the West Indies are as intense as others throughout the world, design winds based upon these hurricanes would be representative for any geographical area.

Section 2 gives hurricane design winds for Kennedy Space Center (KSC), FL. Although the strongest winds recorded in a hurricane near KSC are weaker than winds from thunderstorms in the same area, the probability still exists that much stronger winds could result from hurricanes near KSC. Extreme hurricane winds applicable to ground equipment located anywhere in the world are given in table 5-8 (ref. 5-13). The maximum gust velocity observed in the United States is 89.4 m/s (174 kt or 200 mph), recorded during hurricane Camille. Elsewhere, typhoon winds have been recorded at speeds up to 100 m/s (195 kt or 224 mph) (ref. 5-4).

Section 12.6 gives further information regarding hurricanes.

Table 5-8. Extreme winds (m/s) in hurricane (typhoon) areas with relation to risk and desired lifetime (3.1-m reference height).

Extreme Wind Speeds (m/s)*†				
	Planned Lifetime (yr)			
Risk (%)	2	5	10	25
10	69*	79*	86*	97*
10	61†	72†	80†	91†

*Extreme wind based on 2-s gusts (annual extreme).
†Extreme wind based on 1-min steady wind associated with the 2-s gust.

5.2.2.5.3 Mistral Winds. The mistral wind is a strong polar current between a large anticyclone and a low pressure center. These winds frequently have a temperature below freezing. The mistral of the Gulf of Lions and the Rhone Valley, France, is the best known example. Although winds of 37 m/s (83 mph) have been recorded in the area of Marseilles, France, much stronger winds have occurred to the west of Marseilles in the more open terrain, where even railway trains have been blown over. Mistrals blow in the Rhone Valley ≈100 days a year.

5.2.2.5.4 Foehn-Type Winds. In contrast to mistrals, Santa Ana winds, which occur in southern California west of the coast range of mountains, are hot and dry and have speeds up to at least 21 m/s (41 mph). Chinook winds are the name of the foehn-type winds of the Rocky Mountains which can cause temperature rises of 20 to 40 °F in 15 min, mainly due to adiabatic warming of the subsiding air. Similar winds, called Foehn winds, occur in the Swiss Alps and the Andes, but, because of the local topography, they have slower speeds. The destructiveness of these winds is not from their speeds, but from their high temperatures and dryness, which can do considerable damage to blooming trees, crops, exposed equipment, and instruments that may be sensitive to prolonged heat and dryness. They “fan” wildfires.

REFERENCES

5-1. Schmidli, R.J.: "Weather Extremes," NOAA Technical Memorandum NWS WR-28, revised October 1991.

5-2. "Temperature Extremes in the United States," Environmental Information Summaries, C-5, NOAA Environmental Data Service, Asheville, NC, December 1987.

5-3. Valley, S.L.: *Handbook of Geophysics and Space Environments*, McGraw-Hill Book Company, Inc., New York, 1965.

5-4. Riordan, P.; and Bourget, P.G.: "World Weather Extremes," Report ETL-0416, U.S. Army Engineer Topographic Laboratories, Ft. Belvoir, VA, December 1985.

5-5. Brown, M.J.; and Williams, P., Jr.: "Maximum Snow Loads Along the Western Slopes of the Wasatch Mountains of Utah," *Journal of Applied Meteorology*, Vol. 15, No. 3, pp. 123–126, 1962.

5-6. Guyer, J.L.; and Ewald, R.: "Record Hail Event—Examination of the Aurora, Nebraska Supercell of 22 June 2003," 22nd AMS Conference on Severe Local Storms, Hyannis, MA, October 2004.

5-7. Ludlum, D.M.: "Extremes of Atmospheric Pressure in the United States," *Weatherwise*, Vol. 15, No. 3, pp. 106–115, 1962.

5-8. Daniels, G.E.: "Values of Extreme Surface Pressure for Design Criteria," Proceedings, Institute of Environmental Sciences, 11th Annual Technical Meeting, Mt. Prospect, IL, pp. 283–288, 1965.

5-9. Ludlum, D.M.: "Extremes of Atmospheric Pressure," *Weatherwise*, Vol. 24, No. 3, pp. 130–131, 1971.

5-10. Surface Atmospheric Extremes (Launch and Transportation Areas) NASA Space Vehicle Design Criteria (Environment), *NASA SP-8084*, Marshall Space Flight Center, AL, May 1972.

5-11. "World Weather Records, 1951-60," U.S. Department of Commerce, Weather Bureau, Superintendent of Documents, U.S. Government Printing Office, Washington, DC, 1968.

5-12. "Research, Development, Test, and Evaluation of Materiel for Extreme Climatic Conditions," AR-70-38, Headquarters, Dept. of the Army, Washington, DC, September 15, 1979.

5-13. Military Standard 310: "Department of Defense Handbook—Global Climatic Data for Developing Military Products," Department of Defense, MIL-HDBK-310, June 23, 1997.

5-14. Tattleman, P.; and Kantor, A.J.: "Atlas of Probabilities of Surface Temperature Extremes: Part I—Northern Hemisphere," AFGL-TR-76-0084, 1976.

5-15. Tattleman, P.; and Kantor, A.J.: "Atlas of Probabilities of Surface Temperature Extremes: Part II—Southern Hemisphere," AFGL-TR-77-0001, December 27, 1976.

5-16. Court, A.: "Improbable Pressure Extreme: 1,070 mb," *Bulletin of the American Meteorological Society*, Vol. 50, No. 4, pp. 248–250, April 1969.

Terrestrial Environment (Climatic) Criteria Guidelines for Use in Aerospace Vehicle Development, 2008 Revision

NASA/TM—2008–215633
December 2008

D.L. Johnson, Editor

Section 6: Humidity

TABLE OF CONTENTS

LIST OF FIGURES

LIST OF TABLES

LIST OF ACRONYMS

KSC	Kennedy Space Center
VAFB	Vandenberg Air Force Base
WSMR	White Sands Missile Range

NOMENCLATURE

e	vapor pressure (mb)
L_v	latent vaporization
p	atmospheric pressure (mb)
r	mixing ratio (g/kg)
T	air temperature (K)
T_D	dewpoint temperature (K)
T_F	frost point temperature (K)
ρ_v	absolute humidity (g/m^3)

6. HUMIDITY

6.1 Introduction

Measurements of the amount of water vapor in the atmosphere are difficult to make reliably and accurately. The commonly used methods are susceptible to both long- and short-term contamination. One of the most widely used methods involves measuring the temperature depression produced by evaporating water into the atmosphere. This method is subject to errors induced by contamination of the evaporating moisture and is complicated at times when either the wet-bulb or ambient temperature is below freezing. The process becomes especially complex when ambient temperature is above freezing and wet-bulb temperature is below freezing. Over the years, humidity-sensing technologies and instrumentation have evolved and include: (1) Gravimetric train, (2) aspirated (or sling) psychrometer, (3) condensation type (chilled mirror), (4) capacitance-type electret, (5) hair-type mechanical hygrometer, (6) Lyman Alpha hygrometer, (7) surface acousic wave type hygrometer, and (8) LiCl saturated salt gyrometer, with the gravimetric train absorption method probably being the most accurate, and the chilled mirror being next in absolute measurement accuracy (ref. 6-1). Reference 6-2 is dated but summarizes the various instrumentation and methods used in measuring the amount of moisure in the air.

The water vapor or moisture content of the atmosphere plays a significant role in the fabrication, test, operations, and flight of aerospace vehicles because it can cause both physical and chemical deterioration of materials as well as affect vehicle functions. Some effects atmospheric moisture can have on aerospace vehicles are:

(1) Minute particulates can be corrosive when they settle from the air. The rate of corrosion increases with humidity.

(2) Humidity can affect the performance of electronic equipment; i.e., changes the dialectic constants of capacitors, decreases the breakdown voltage between potentials, and causes deterioration of electronic components through metallic corrosion or electrode chemical reactions.

(3) Organic growth, bacteria, and fungi thrive in warm, moist air, consequently degrading performance of aerospace systems and sensors.

(4) The low temperatures of cryogenic fuels cool the moist air, often producing condensation and icing or frost, which can be detrimental to vehicle operation.

For propulsion systems, including air breathing systems that are sensitive to water vapor (humidity), it is recommended that the water vapor concentrations at altitude in section 6.4 be used to assess efficiency of engine performance and establish design requirements.

Section 6 defines the terminology associated with water vapor and discuss some of the effects of the vapor. Various tests are required to measure the effects of water vapor as early as possible in a program development cycle. Most of these tests are outlined in references 6-3 and 6-4; however, some test criteria for specific sites are described herein. Section 7 provides water vapor and moisture information associated with precipitation, fog, and icing.

6.2 Definitions

The following are definitions associated with humidity (ref. 6-5):

Absolute Humidity (or vapor density): In a system of moist air, the ratio of the mass of water vapor present to the volume occupied by the mixture; i.e., the density of the water vapor component. Usually expressed in grams of water vapor in a cubic meter of air.

Condensation: The physical process by which a vapor becomes a liquid that would be deposition; the opposite of evaporation. Condensation in the atmosphere occurs only in the presence of a condensation nucleus.

Critical Point: The thermodynamic state in which the liquid and gas phases of a substance co-exist in equilibrium at the highest possible temperature. (At higher temperatures, the liquid phase will not exist.)

Deposition: The process by which water changes phase directly from a vapor into a solid (ice) without first becoming a liquid.

Dewpoint Temperature: The temperature to which a given parcel of air must be cooled at constant pressure and constant water vapor content in order for saturation to occur.

Dry-Bulb Temperature: The temperature of the air. The temperature registered by the dry-bulb thermometer of a psychrometer—sometimes referred to as ambient temperature.

Evaporation: The phase transition in which the liquid that would be sublimation is transformed into the gaseous state; the opposite of condensation. In meteorology, evaporation is usually restricted to a liquid becoming a gas, while sublimation refers to phase changes between solids and gases.

Frost Point: The temperature to which air must be cooled at constant pressure and constant humidity to achieve saturation with respect to ice at or below 0 °C (32 °F). Below 0 °C (32 °F), the frost point becomes greater than the dewpoint since the saturation vapor pressure over ice is less than the saturation vapor pressure over water.

Humidity: A general measure of the water vapor content in air. See absolute humidity, relative humidity, specific humidity, mixing ratio, and dewpoint.

Hydrology: The branch of physical geography that deals with the waters of the Earth exclusive of the oceans. The moisture—vapor, liquid, and solid—in the atmosphere is one phase of the "hydrologic cycle."

Hygrometer: An instrument that measures the water vapor content of the atmosphere.

Hygrometry: The study that deals with the measurements of the humidity and other gases of the atmosphere.

Latent Heat of Condensation: The heat released per unit mass as water vapor condenses to form water droplets.

Latent Heat of Vaporization: The heat absorbed per unit mass as water is vaporized into the gaseous state. The inverse of the latent heat of condensation can be estimated within 0.8 percent for temperature (T) within the range of meteorological interest by equation (6.1) (ref. 6-6):

$$L_v = (2{,}500 - 2.274T\ ^\circ\text{C})\ \text{Joules/gram} \quad . \tag{6.1}$$

More precise values are available from a table in reference 6-7.

Mixing Ratio: The ratio of the mass of water vapor to the mass of dry air, containing the vapor. May be approximated by the specific humidity, usually expressed in units of grams per kilogram.

Moisture: A term usually referring to the water vapor content of the atmosphere, or to the total water substance—gaseous, liquid, and solid—present in a given volume of air.

Moisture Inversion: An increase with altitude of the moisture content of the air; specifically, the layer through which this increase occurs, or the altitude at which the increase begins.

Relative Humidity: The dimensionless ratio of the actual vapor pressure of the air to the saturation vapor pressure with respect to water, for the ambient air temperature. Relative humidity above 100 percent occurs—particularly with respect to ice—which gives rise to dew and frost. This may be relevant to surfaces that are locally colder—by radiation or otherwise.

Saturation: The condition in which the partial pressure of any fluid constituent is equal to its maximum possible partial pressure under the existing environmental conditions, such that any increase in the amount of that constituent without a change in the surrounding conditions will create a thermodynamically unstable environment where, if a nucleation site exists, condensation will occur. When air is saturated, the relative humidity is 100 percent.

Specific Humidity: In a system of moist air, the dimensionless ratio of the mass of water vapor to the total mass of the system. It may be expressed in grams of water vapor per kilogram of moist air, and is very nearly numerically equivalent to the mixing ratio.

Sublimation: The transition of a substance from the solid phase directly to the vapor phase, without passing through an intermediate liquid phase.

Supersaturation: The condition existing in a given portion of the atmosphere—or other space—when the relative humidity is >100 percent; i.e., when it contains more water vapor than is needed to produce saturation with respect to a plane surface of pure water or pure ice.

Vapor: A substance existing in a gaseous state at a temperature lower than that of its critical point. Above its critical temperature it becomes a gas and no amount of pressure will produce any condensation; but as a vapor, increasing pressure can eventually cause liquification. It is formed by evaporation or sublimation and can become liquefied with compression.

Vapor Concentration: (Previously called absolute humidity (ref. 6-8).) The ratio of the mass of water vapor present to the volume occupied by the mixture; i.e., the density of the water content. This is usually expressed in grams of water vapor per cubic meter of air.

Vapor Pressure: The pressure exerted by the molecules of a given vapor. For a pure, confined vapor, vapor pressure is the pressure on the walls of its containing vessel. For a vapor mixed with other vapors or gases, it is that vapor's contribution to the total pressure; i.e., its partial pressure. The pressure of saturated water vapor over water or ice at 0 °C is 6.11 mb, and over water at 100 °C is 1,013.3 mb.

Vapor Temperature: The temperature that dry air would have if its pressure and density were equal to those of a given sample of moist air.

Wet-Bulb Temperature: The temperature read from a well-ventilated wet-bulb thermometer. More formally, "The temperature an air parcel would have if cooled adiabatically to saturation at constant pressure by evaporation of water into it, all latent heat being supplied by the parcel." The thermometer reading can be used on a psychometric chart to determine the corresponding values of relative humidity, dewpoint, etc.

6.3 Vapor Concentration

6.3.1 Background Information

A significant amount of moisture exists in the atmosphere, the majority is by evapotranspiration from the Earth's surface. The Earth's equatorial region is the main source of moisture supplied to the atmosphere. Broad-scale evaporation takes place in this area due to the vast oceanic area and moist land regions in addition to the warm climatic conditions.

Since the molecular weight of water vapor is less than the molecular weight of dry air, moist air is less dense than dry (drier) air. This contributes in a small way to the lower atmospheric pressure that is common to warm, moist air masses. To a larger extent, the dynamic variations of global circulation are due to the pressure difference between moist (warm) and dry (cold) air driven mainly by temperature differences.

The various measures of water vapor are related to each other, as shown by table 6-1 (ref. 6-9), and in the following approximate equations:

- Vapor pressure in terms of frost point:

$$\log_{10} e = -2{,}485/T_F + 3.5665 \log_{10} T_F - 0.0032098 T_F + 2.0702 \tag{6.2}$$

- Vapor pressure in terms of dewpoint:

$$\log_{10} e = -2{,}949.1/T_D - 5.028 \log_{10} T_D + 23.832 \tag{6.3}$$

- Absolute humidity (g/m^3) (vapor concentration) in terms of vapor pressure and air temperature:

$$\rho_v = 216.68\ e/T \tag{6.4}$$

- Mixing ratio (g/kg) in terms of vapor pressure and atmospheric pressure:

$$r = 621.97\ e/(p-e)\ , \tag{6.5}$$

where

e = vapor pressure (mb)
p = atmospheric pressure (mb)
r = mixing ratio (g/kg)
T = air temperature (K)
T_D = dewpoint temperature (K)
T_F = frost point temperature (K)
ρ_v = absolute humidity (g/m^3).

Table 6-1. Correspondence between the several measures of water vapor content (ref. 6-9; derived from ref. 6-7).

Dew-Point (K)	Frost Point (K)	Vapor Pressure (mb)	Absolute* Humidity (g/m^3)	Mixing Ratio (g/kg)								
				1,000 mb	850 mb	700 mb	500 mb	400 mb	100 mb	50 mb	10 mb	1 mb
313		7.378+1	5.119+1	4.980+1	5.941+1	7.361+1	1.080+2	1.411+2	**	**	**	**
308		5.624+1	3.963+1	3.725+1	4.427+1	5.456+1	7.910+1	1.020+2	8.008+2	**	**	**
303		4.243+1	3.038+1	2.769+1	3.282+1	4.029+1	5.786+1	7.399+1	4.590+2	**	**	**
298		3.167+1	2.305+1	2.044+1	2.417+1	2.959+1	4.219+1	5.363+1	2.886+2	**	**	**
293		2.337+1	1.730+1	1.495+1	1.766+1	2.156+1	3.059+1	3.870+1	1.899+2	5.462+2	**	**
288		1.704+1	1.283+1	1.083+1	1.278+1	1.557+1	2.201+1	2.775+1	1.279+2	3.217+2	**	**
283		1.227+1	9.399	7.762	9.146	1.113+1	1.569+1	1.973+1	8.707+1	2.024+2	**	**
278		8.719	6.797	5.495	6.471	7.870	1.107+1	1.389+1	5.946+1	1.314+2	**	**
273	273	6.108	4.847	3.839	4.519	5.492	7.710	9.664	4.049+1	8.659+1	9.764+2	**
268	268.6	4.215	3.407	2.644	3.112	3.780	5.300	6.637	2.739+1	5.728+1	4.533+2	**
263	264.1	2.863	2.358	1.794	2.110	2.562	3.590	4.492	1.834+1	3.779+1	2.495+2	**
258	259.6	1.912	1.605	1.197	1.408	1.709	2.393	2.993	1.213+1	2.474+1	1.470+2	**
253	255.1	1.254	1.074	7.847–1	9.227–1	1.120	1.568	1.960	7.903	1.601+1	8.919+1	**
248	250.5	8.070–1	7.047–1	5.048–1	5.936–1	7.204–1	1.008	1.260	5.603	1.021+1	5.461+1	**
243	245.8	5.088–1	4.534–1	3.182–1	3.742–1	4.540–1	6.352–1	7.938–1	3.183	6.397	3.335+1	6.443+2
238	241.2	3.139–1	2.856–1	1.963–1	2.308–1	2.801–1	3.918–1	4.896–1	1.960	3.931	2.016+1	2.846+2
233	236.5	1.891–1	1.757–1	1.183–1	1.390–1	1.687–1	2.360–1	2.948–1	1.179	2.362	1.199+1	1.450+2
273	273	6.107	4.847	3.839	4.518	5.492	7.709	9.668	4.048+1	8.658+1	9.759+2	**
267.3	268	4.015	3.246	2.518	2.963	3.599	5.047	6.322	2.604+1	5.433+1	4.722+2	**
261.8	263	2.597	2.139	1.627	1.913	2.324	3.255	4.075	1.660+1	3.409+1	2.182+2	**
256.2	258	1.652	1.387	1.034	1.216	1.476	2.067	2.592	1.045+1	2.126+1	1.231+2	**
250.8	253	1.032	8.835–1	6.456–1	7.592–1	9.214–1	1.289	1.613	6.490	1.311+1	7.158+1	**
245.3	248	6.323–1	5.521–1	3.955–1	4.650–1	5.643–1	7.895–1	9.872–1	3.961	7.969	4.199+1	**
239.9	243	3.798–1	3.385–1	2.375–1	2.792–1	3.388–1	4.740–1	5.926–1	2.373	4.763	2.456+1	3.809+2
234.6	238	2.233–1	2.032–1	1.396–1	1.642–1	1.993–1	2.787–1	3.483–1	1.393	2.791	1.420+1	1.788+2
229.3	233	1.283–1	1.192–1	8.026–2	9.434–2	1.144–1	1.600–1	2.001–1	7.996–1	1.601	8.084	9.154+1
224.1	228	7.198–2	6.836–2	4.503–2	5.293–2	6.422–2	8.981–2	1.122–1	4.483–1	8.970–1	4.510	4.824+1
	223	3.935–2	3.821–2	2.463–2	2.895–2	3.512–2	4.910–2	6.135–2	2.450–1	4.901–1	2.457	2.548+1
	218	2.092–2	2.078–2	1.309–2	1.539–2	1.867–2	2.611–2	3.261–2	1.302–1	2.604–1	1.304	1.329+1
	213	1.080–2	1.098–2	6.761–3	7.947–3	9.640–3	1.347–2	1.684–2	6.723–2	1.344–1	6.725–1	6.791
	208	5.006–3	5.627–3	3.386–3	3.979–3	4.826–3	6.749–3	8.427–3	3.365–2	6.728–2	3.362–1	3.381
	203	2.615–3	2.784–3	1.639–3	1.926–3	2.336–3	3.265–3	4.076–3	1.628–2	3.254–2	1.627–1	1.631
	198	1.220–3	1.334–3	7.646–4	8.986–4	1.090–3	1.524–3	1.902–3	7.593–3	1.518–2	7.590–2	7.597–1
	193	5.472–4	6.138–4	3.423–4	4.023–4	4.882–4	6.828–4	8.530–4	3.406–3	6.810–3	3.404–2	3.405–1
	188	2.353–4	2.710–4	1.472–4	1.730–4	2.099–4	2.936–4	3.668–4	1.465–3	2.928–3	1.464–2	1.464–1
	183	9.672–5	1.144–4	6.051–5	7.111–5	8.629–5	1.207–4	1.508–4	6.020–4	1.204–3	6.016–3	6.016–2

*At saturation only.

**Atmospheric saturation is not possible at this ambient temperature and pressure.

Table 6-1 shows the correspondence between dewpoint and frost point, vapor pressure, and mixing ratio. The table also gives the absolute humidity (vapor density) corresponding to the other measures when the air is saturated. When air is saturated, its vapor pressue is a direct function of air temperature. The absolute humidity is actually the water vapor density within the air, and an isobaric increase of the temperature will decrease the absolute humidity while the other measures in table 6-1 remain the same. To relate mixing ratio to the other measures of water vapor content, the atmospheric pressure must be given. When the mixing ratio remains constant, as it does in adiabatic lifting of unsaturated air, the dewpoint will decrease with increasing altitude (ref. 6-9). Extreme dewpoints are discussed in section 5.2.2.2.

6.3.2 Testing

Testing is a necessary precaution to minimize failure due to atmospheric moisture. The effects of moisture are measured by humidity cycling, a procedure in which test items are placed in a closed chamber where temperature and relative humidity are closely regulated to simulate environmental conditions (ref. 6-4). Chamber test procedures and criteria for various systems and their associated electrical-mechanical components are usually identified in the various system requirements documents. This document recommends testing criteria based on actual environmental records, including extreme values, to promote realism about the actual environment.

NASA's External Tank Verification Plan (ref. 6-10) lists the following general statements under Test Controls and Test Methods:

(1) The item is sealed or potted and subjected to a seal test.

(2) The item is located in a controlled humidity or air-conditioned environment during operation and is protected from humidity when not operating.

(3) The item is subjected to propellant compatibility testing which is considered to be a more severe environment.

(4) The item is fabricated from materials which preclude corrosion by humidity. This requires additional and different quality control standards than those discussed previously.

The Space Shuttle Program, Shuttle Master Verification Plan Document, states that humidity and other environmental parameter tests will use the procedures outlined in Military Standard 810 (latest version—MIL-STD 810F (ref. 6-4)).

A temperature of 71 °C (160 °F) and 95-percent relative humidity represent a dewpoint temperature of 69 °C (156 °F), which is much higher than any natural extreme in the world. Dewpoints above 32 °C (90 °F) are extremely unlikely in nature (ref. 6-11), since the dewpoint temperature is limited by the source of the water vapor; i.e., the surface temperature of the water body from which the water evaporates (ref. 6-12). The following paragraphs contain site-specific humidity criteria to be used in aerospace vehicle testing.

6.3.2.1 Test Criteria for Large Vapor Concentrations at Surface.

• Huntsville, New Orleans, and Kennedy Space Center (KSC)

(1) An extreme humidity cycle of 24 hr with a wind of <5 m/s (9.7 kt): Three hours of 37.2 °C (99 °F) air temperature at 50-percent relative humidity and a vapor concentration of 22.2 g/m^3 (9.7 gr/ft^3), 6 hr of decreasing air temperature to 24.4 °C (76 °F) with relative humidity increasing to 100 percent (saturation), 8 hr of decreasing air temperature to 21.1 °C (70 °F) with condensation of 3.8 g of water as liquid per cubic meter of

air (1.7 gr of water per cubic foot of air) with relative humidity remaining at 100 percent,* and 7 hr of increasing air temperature to 37.2 °C (99 °F) and a decrease to 50-percent relative humidity (fig. 6-1).

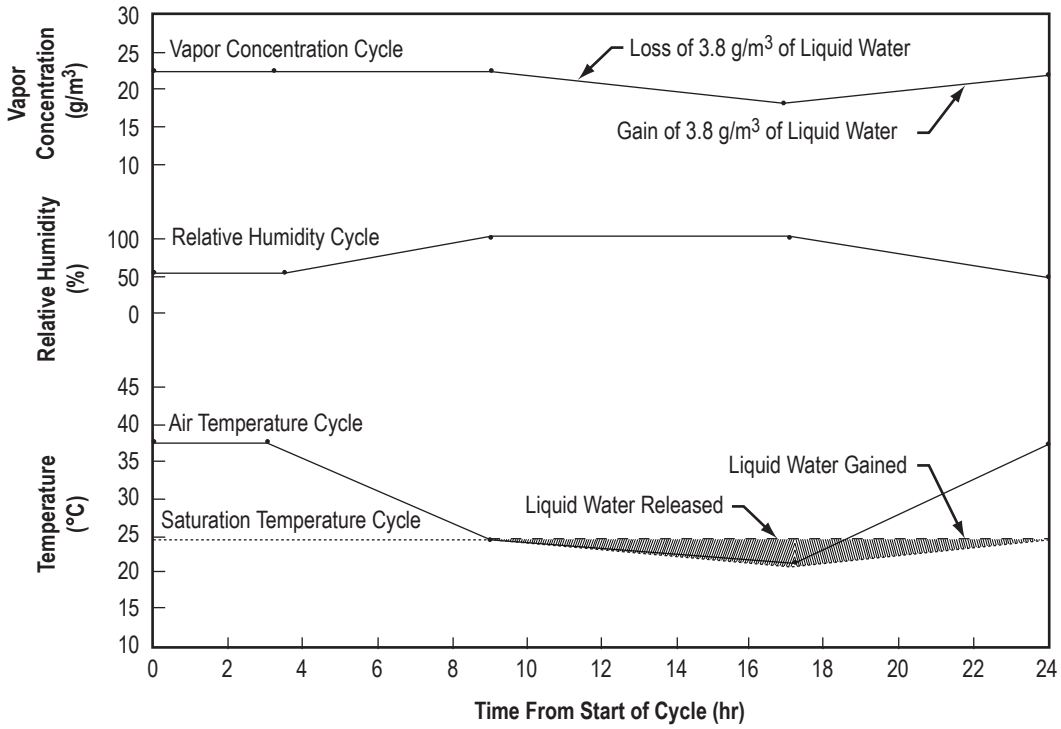

Figure 6-1. Extreme high vapor concentration cycle for Huntsville, AL, New Orleans, LA, and KSC, FL.

(2) An extreme relative humidity between 75 and 100 percent and air temperature between 22.8 °C (73 °F) and 27.8 °C (82 °F), which would result in corrosion and bacterial and fungal growths, can be expected for a period of 15 days. A humidity of 100 percent occurs one-fourth of the time at the lower temperature in cycles not exceeding 24 hr. Any loss of water vapor from the air by condensation is replaced from outside sources to maintain at least 75-percent relative humidity at the higher temperature.

• Vandenberg Air Force Base (VAFB)

(1) An extreme humidity cycle of 24 hr with a wind of <5 m/s (9.7 kt): Three hours of 23.9 °C (75 °F) air temperature at 75-percent relative humidity and a vapor concentration of 16.2 g/m^3 (7.1 gr/ft^3), 6 hr of decreasing air temperature to 18.9 °C (66 °F) with relative humidity increasing to 100 percent, 8 hr of decreasing air temperature to 12.8 °C (55 °F) with condensation of 5 g of water as liquid per cubic meter of air (2.2 gr of water per cubic foot of air) with relative humidity remaining at 100 percent, and 7 hr of increasing air temperature to 23.9 °C (75 °F) and a decrease to 75-percent relative humidity (fig. 6-2).

*The release of water as a liquid on the test object may be delayed for several hours after the start of this part of the test because of thermal lag in a large test object. If the lag is too large, the test should be extended in time for each cycle to allow condensation.

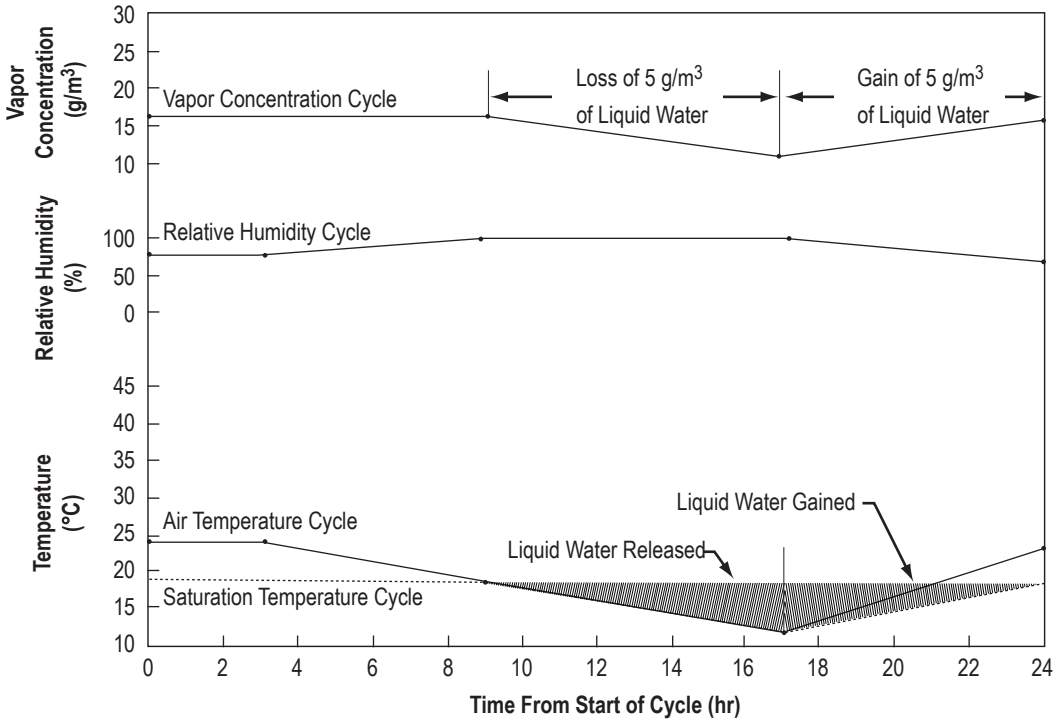

Figure 6-2. Extreme high vapor concentrations for VAFB.

(2) Bacterial and fungal growth should present no problem because of the cooler temperatures in this area. For corrosion, an extreme relative humidity of between 75 and 100 percent and air temperature between 18.3 °C (65 °F) and 23.3 °C (74 °F) can be expected for a period of 15 days. The humidity should be 100 percent during one-fourth of the time at the lower temperature in cycles not exceeding 24 hr. Any loss of water vapor from the air condensation is replaced from outside sources to maintain at least 75-percent relative humidity at the higher temperature.

• White Sands Missile Range (WSMR)

(1) This area is located at ≈1,216 m (≈4,000 ft) above sea level and is on the eastern side of higher mountains. The mean annual rainfall of ≈250 mm (≈10 in) is rapidly absorbed in the sandy soil. Fog rarely occurs; therefore, at this location, a high vapor concentration over periods longer than a few hours (6–9 hr) need not be considered.

6.3.2.2 Low Vapor Concentration at Surface.

6.3.2.2.1 Introduction. Low water vapor concentration can occur at very low temperatures or at high temperatures when the air is very dry. In both cases, the dewpoints are very low. However, in the case of low dewpoints and high temperatures, the relative humidity also is low. When any storage area or compartment of a vehicle is heated to temperatures well above the ambient air temperature, such as the high temperature of the storage area in an aircraft standing on the ground in the Sun, the relative humidity will be even lower than the relative humidity of the ambient air. These two types of low water vapor concentrations have entirely different environmental effects. In the case of low air temperatures, ice or condensation may form on equipment, while in the high-temperature, low-humidity condition, organic materials may dry and split or otherwise deteriorate. When a storage

area or aircraft is considerably warmer than the ambient air—even when the air is cold—the drying increases even more. Low relative humidities may also produce another problem—static electricity. Static electrical charges on equipment may ignite fuel, result in shocks to personnel when discharged, or interfere with performance of the microelectronic components of the system. Because of these dangers, the two types of low water vapor concentrations (dry extreme) are given for testing criteria in section 6.3.2.2.2.

6.3.2.2.2 Surface Extremes for Low Vapor Concentration.

• Huntsville and WSMR

(1) An air temperature of –11.7 °C (11 °F) and a vapor concentration of 2.1 g/m^3 (0.9 gr/ft^3), with a relative humidity between 98 and 100 percent for a duration of 24 hr.

(2) An air temperature of 28.9 °C (84 °F), a vapor concentration of 4.5 g/m^3 (2 gr/ft^3)—corresponding to a dewpoint of 1.1 °C (30 °F), and a relative humidity of 15 percent occurring for 6 hr; a maximum relative humidity of 34 percent at an air temperature of 15.6 °C (60 °F) for the remaining 18 hr of the day for a 10-day period.

• New Orleans and KSC

(1) An air temperature of –2.2 °C (28 °F) and a vapor concentration of 4.2 g/m^3 (1.8 gr/ft^3), with a relative humidity between 98 and 100 percent for a duration of 24 hr.

(2) An air temperature of 22.2 °C (72 °F), a vapor concentration of 5.6 g/m^3 (2.4 gr/ft^3)—corresponding to a dewpoint of 2.2 °C (36 °F), and a relative humidity of 29 percent occurring for 8 hr; a maximum relative humidity of 42 percent at an air temperature of 15.6 °C (60 °F) for the remaining 16 hr of the day for a 10-day period.

• VAFB

(1) An air temperature of –2.2 °C (28 °F) and a vapor concentration of 4.2 g/m^3 (1.8 gr/ft^3), with a relative humidity between 98 and 100 percent for a duration of 24 hr.

(2) An air temperature of 37.8 °C (100 °F), a vapor concentration of 4.8 g/m^3 (2.1 gr/ft^3)—corresponding to a dewpoint of 0 °C (32 °F), and a relative humidity of 11 percent occurring for 4 hr; a maximum relative humidity of 26 percent at an air temperature of 21.1 °C (70 °F) for the remaining 20 hr of the day for a 10-day period.

6.3.3 Compartment Vapor Concentration at Surface

For testing to simulate conditions in the interior of an aircraft or space vehicle compartment, the following criteria should be used for all locations:

• A low water vapor concentration extreme of 10.1 g/m^3 (4.4 gr/ft^3), corresponding to a dewpoint of 11.1 °C (52 °F) at a temperature of 87.8 °C (190 °F).

• Relative humidity of 2 percent occurring for 1 hr.

- A linear change over a 4-hr period to an air temperature of 37.8 °C (100 °F).

- A relative humidity of 22 percent occurring for 15 hr, then a linear change over a 4-hr period to the initial conditions.

6.4 Vapor Concentration at Altitude

Vapor concentration generally decreases with altitude in the troposphere, because temperature decreases with altitude. Stratospheric and mesospheric levels of atmospheric moisture are small. Figure 6-3 presents an interim reference model for the mean and variability of middle atmospheric water vapor (ref. 6-13). It represents mean, Northern Hemisphere, mid-latitude, springtime, mixing ratios (ppmv) along with its variability (bars) and accuracies (parentheses). The data presented in sections 6.4.1 and 6.4.2 are appropriate for design purposes.

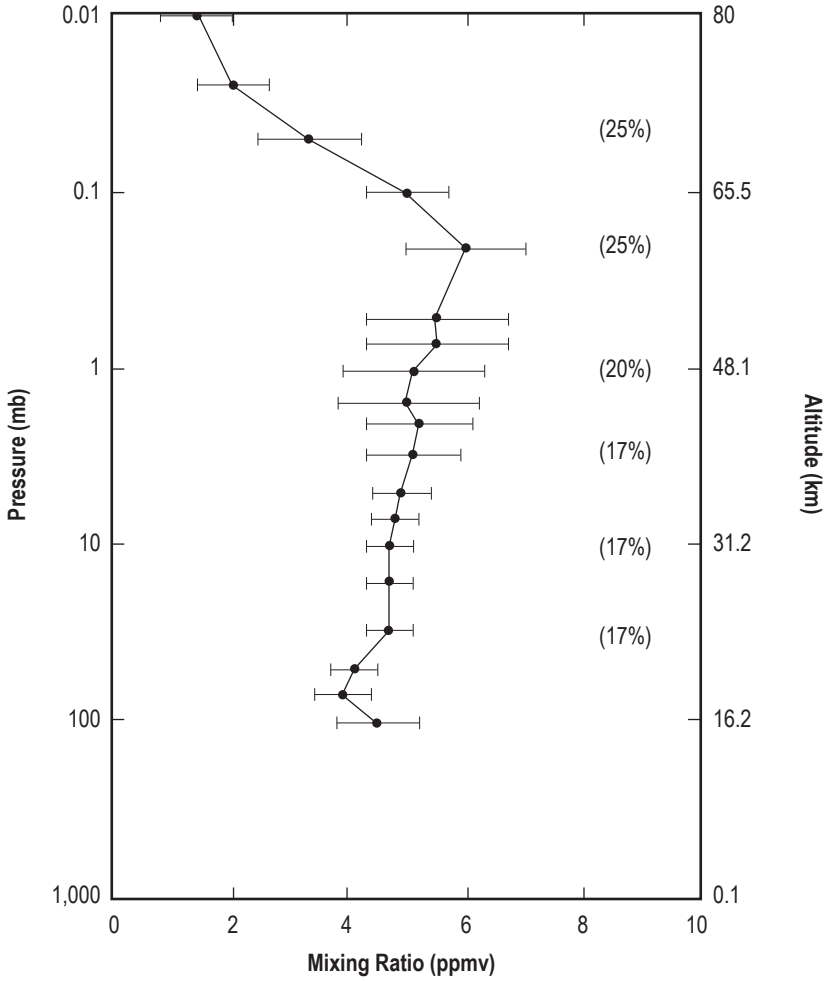

Figure 6-3. Reference profile of middle atmosphere mixing ratio mean, variability, and accuracy; representative of North Hemisphere, mid-latitude, springtime conditions (ref. 6-13).

6.4.1 High Vapor Concentration at Altitude

The following tables present the relationship between maximum vapor concentration and the associated temperature normally expected as a function of altitude:

- Maximum vapor concentrations for KSC (table 6-2).
- Maximum vapor concentrations for WSMR (table 6-3).
- Maximum vapor concentrations for VAFB (table 6-4).

Table 6-2. Maximum vapor concentrations for KSC.

Geometric Altitude		Maximum Vapor Concentration		Temperature Associated With Maximum Vapor Concentration	
(km)	(ft)	(g/m^3)	(gr/ft^3)	(°C)	(°F)
SFC (0.005 m.s.l.)	(16)	27	11.8	30.5	87
1	3,300	19	8.8	24.5	76
2	6,600	13.3	5.8	18	64
3	9,800	9.3	4.1	12	54
4	13,100	6.3	2.8	5.5	42
5	16,400	4.5	2	–0.5	31
6	19,700	2.9	1.3	–6.8	20
7	23,000	2	0.9	–13	9
8	26,200	1.2	0.5	–20	–4
9	29,500	0.6	0.3	–27	–17
10	32,800	0.3	0.1	–34.5	–30
16.2	53,100	0.025	0.01	–57.8	–72
20	65,600	0.08	0.03	–47.8	–54

Table 6-3. Maximum vapor concentrations for WSMR.

Geometric Altitude		Maximum Vapor Concentration		Temperature Associated With Maximum Vapor Concentration	
(km)	(ft)	(g/m^3)	(gr/ft^3)	(°C)	(°F)
SFC (1.2 m.s.l.)	(3,989)	16	7	21.5	71
2	6,600	13.2	5.8	18.9	66
3	9,800	9	3.9	12.8	55
4	13,100	6.8	3	7.8	46
5	16,400	4.9	2.1	2.2	36
6	19,700	3.4	1.5	–2.2	28
7	23,000	2.2	1	–10	14
8	26,200	1.3	0.6	–16.1	3
9	29,500	0.6	0.3	–22.8	–9
10	32,800	0.2	0.1	–30	–22
16.5	54,100	0.08	0.03	–47.8	–54
20	65,600	0.05	0.02	–52.2	–62

Table 6-4. Maximum vapor concentrations for VAFB.

Geometric Altitude		Maximum Vapor Concentration		Temperature Associated With Maximum Vapor Concentration	
(km)	(ft)	(g/m^3)	(gr/ft^3)	(°C)	(°F)
SFC (0.113 m.s.l.)	371	17.5	7.6	30.5	87
1	3,300	14.8	6.5	24.2	76
2	6,600	10.0	4.4	20.6	69
3	9,800	7.5	3.3	11.0	52
4	13,100	5.0	2.2	4.7	41
5	16,400	3.7	1.6	–1.4	30
6	19,700	2.3	1.0	–8.1	17
7	23,000	1.6	0.7	–12.5	10
8	26,200	0.8	0.3	–20.2	–4
9	29,500	0.4	0.2	–28.2	–19
10	32,800	0.2	0.1	–34.3	–30

6.4.2 Low Vapor Concentration at Altitude

The values presented as low extreme vapor concentrations in the following tables are based on data measured by standard radiosonde equipment:

- Minimum vapor concentrations for KSC (table 6-5).
- Minimum vapor concentrations for WSMR (table 6-6).
- Minimum vapor concentrations for VAFB (table 6-7).

Table 6-5. Minimum vapor concentrations for KSC.

Geometric Altitude		Minimum Vapor Concentration		Temperature Associated With Minimum Vapor Concentration	
(km)	(ft)	(g/m^3)	(gr/ft^3)	(°C)	(°F)
SFC (0.005 m.s.l.)	(16)	1.5	0.7	7	45
1	3,300	0.5	0.2	6	42.8
2	6,600	0.2	0.1	0	32
3	9,800	0.1	0.04	–11	12.2
4	13,100	0.1	0.04	–14	6.8

Table 6-6. Minimum vapor concentrations for WSMR.

Geometric Altitude		Minimum Vapor Concentration		Temperature Associated With Minimum Vapor Concentration	
(km)	(ft)	(g/m^3)	(gr/ft^3)	(°C)	(°F)
SFC (1.2 m.s.l.)	(3,989)	1.2	0.5	–1	30
2	6,600	0.9	0.4	–5	23
3	9,800	0.6	0.3	–12	10
4	13,100	0.4	0.2	–20	–4
5	16,400	0.2	0.1	–26	–15
6	19,700	0.1	0.04	–36	–33
7	23,000	0.09	0.03	–42	–44
8	26,200	0.07	0.03	–49	–56
9	29,500	0.03	0.01	–55	–67
10	32,800	0.02	0.01	–60	–76

Table 6-7. Minimum vapor concentrations for VAFB.

Geometric Altitude		Minimum Vapor Concentration		Temperature Associated With Minimum Vapor Concentration	
(km)	(ft)	(g/m^3)	(gr/ft^3)	(°C)	(°F)
SFC (0.113 m.s.l.)	371	1.6	0.7	4.5	40
1	3,300	0.7	0.3	–1.4	30
2	6,600	0.4	0.2	–7.5	19
3	9,800	0.3	0.1	–12.6	9
4	13,100	0.1	0.04	–19.4	–3
5	16,400	0.07	0.03	–27.3	–17
6	19,700	0.03	0.01	–35.1	–31
7	23,000	0.02	0.009	–39.5	–39

REFERENCES

6-1. Yankee Environmental Systems, Inc., "Meterological Hygrometers—Accuracy and Sampling Systems," YES Bulletin CMACC1, <http://www.yesinc.com/products/methyg.html>, 2003.

6-2. Johnson, D.L.: "Instruments for Measuring the Amount of Moisture in the Air," *NASA TM–78190*, Marshall Space Flight Center, AL, August 1978.

6-3. "Global Climatic Data For Developing Military Products," MIL-HDBK-310, June 23, 1997.

6-4. "Military Standard, Environmental Test Methods," MIL-STD-810F, January 1, 2000.

6-5. "Glossary of Meteorology," American Meteorological Society, Boston, MA, 1996.

6-6. Fleagle, R.G.; and Businger, J.A.: *An Introduction to Atmospheric Physics*, Academic Press, New York, NY, p. 96, 1965.

6-7. *Smithsonian Meteorological Tables*, Sixth Edition, Prepared by R. List, Smithsonian Institution Press, Washington, DC, 1984.

6-8. Sheppard, P.A.: "The Physical Properties of Air With Reference to Meteorological Practice and the Air-Conditioning Engineer," *ASME*, Vol. 71, pp. 915–919, 1949.

6-9. "Handbook of Geophysics and Space Environment," Air Force Geophysics Laboratory, Air Force Systems Command, U.S. Air Force, 1985.

6-10. "External Tank Verification Plan," MMC-ET-TM01-B, Contract No. NAS8-30300, WBS No. 1.6.6.2, DR. NO. TM01, Martin Marietta, Michoud Assembly Facility, New Orleans, LA, September 9, 1974.

6-11. Sissenwine, N.; and Court, A.: "Climate Extremes for Military Equipment," Report No. 146, Environmental Protection Branch, Research and Development Division, Office of the Quartermaster General, Washington, DC, 1951.

6-12. Sverdrup, H.V.: *Oceanography for Meteorologists*, Prentice-Hall, Inc., New York, NY, 1942.

6-13. Remsberg, E.E.; Russell III, J.M.; and Wu, C.-Y.: "An Interim Reference Model for the Variability of the Middle Atmosphere Water Vapor Distribution," *Adv. Space Res.*, Vol. 10, No. 6, pp. (6)51–(6)64, 1990.

Terrestrial Environment (Climatic) Criteria Guidelines for Use in Aerospace Vehicle Development, 2008 Revision

NASA/TM—2008–215633
December 2008

D.L. Johnson, Editor

Section 7: Precipitation, Fog, and Icing

TABLE OF CONTENTS

TABLE OF CONTENTS (Continued)

LIST OF FIGURES

LIST OF FIGURES (Continued)

LIST OF TABLES

LIST OF TABLES (Continued)

LIST OF ACRONYMS

AGL	above ground level
CAMS	Climate Anomaly Monitoring System
CDD	cloud droplet distribution
DWC	drizzle water content
EAFB	Edwards Air Force Base
ET	external tank
FZDZ (or ZL)	freezing drizzle
FZRA (or ZR)	freezing rain
GSE	ground support equipment
KSC	Kennedy Space Center
LST	local standard time
LWC	liquid water content
MED	mean effective diameter
MSFC	Marshall Space Flight Center
MVD	median volumetric diameter
NASA	National Aeronautics and Space Administration
NCAR	National Center for Atmospheric Research
NCDC	National Climatic Data Center
NOAA	National Oceanic and Atmospheric Administration
NSSL	National Severe Storm Laboratory
NWS	National Weather Service
OPI	OLR Precipitation Index
RH	relative humidity
RWC	rain water content

LIST OF ACRONYMS (Continued)

SAE	Society of Automotive Engineers
SLF	Shuttle launch facility
SLW	supercooled liquid water
SRB	solid rocket booster
STS	Space Transportation System
TIPM	total ice particle mass (g/m^3)
TPS	Thermal Protection System
VAB	Vehicle Assembly Building
VAFB	Vandenberg Air Force Base
WSMR	White Sands Missile Range

NOMENCLATURE

A	angular deviation
C	constants for location; rate of climb
D	duration; hailstone diameter
D_h	duration of rainfall in hours
D_m	time in minutes
E	collection efficiency
F	freezing fraction
H	horizontal extent
K	11.5
k	constant used in hail terminal velocity calculation (s^{-1})
M	hail and rain intensity; liquid water content
R or r	rain rate
R_p	rain rate (mm/hr or in/hr)
t	time
V	velocity
VT	terminal velocity
W	water content; terminal velocity
λ	mean number of independent hailstorm days per year

7. PRECIPITATION, FOG, AND ICING

7.1 Introduction

Precipitation, fog, and icing are atmospheric phenomena of interest to the design, fabrication, and flight of aerospace vehicles. In some arid areas of the world, however, precipitation does not occur for several years. Likewise, in areas of moderate to heavy rainfall, there are periods of time without rain. Because precipitation does occur in discrete events, statistical representation may be misleading; therefore, caution must be taken to ensure that data relative to the desired location are used. See section 6 for information on humidity (water vapor or moisture).

7.2 Precipitation

Precipitation is usually defined as any or all forms of hydrometeors (water particles), liquid or solid, that fall from clouds and reach the ground. Formally, water particles are defined as a major class of hydrometeor but are distinguished from cloud, fog, dew, rime, frost, etc. in that they must "fall," and are distinguished from cloud and virga in that they must reach the ground. In this publication, the definition is extended to those hydrometeors which do not reach the ground but impinge on a flying surface, such as space vehicles. Accumulation is reported in depth over a horizontal surface; i.e., millimeters or inches for liquid phase, and in depth or depth-of-water equivalent for the frozen phase. The seven general forms of precipitation include rain, drizzle, freezing rain, freezing drizzle, hail, ice pellets (sleet), and snow. The definitions of terms can be further addressed by consulting reference 7-1. Rain and drizzle are further described as follows:

- Rain—A type of liquid precipitation in the form of liquid water drops with diameters >0.5 mm (>0.02 in), or, if widely scattered, the drops may be smaller. There is no universal agreement on the precise dividing line between rain and drizzle. However, many texts suggest drizzle drop diameters are near 0.5 mm (>0.02 in) and smaller. Rain-associated events such as rain erosion are presented in section 7.2.5, while floods are given in section 13.2.2.4.

- Drizzle—A type of liquid precipitation composed of very small, numerous, and uniformly dispersed water drops that may appear to float while following air currents; consists of water drops with a diameter of 0.2–0.5 mm (0.01–0.02 in) falling through the atmosphere. Drizzle falls to the ground, usually from low stratus clouds.

Rain-associated events, such as rain erosion, are presented in section 7.2.5, while floods are given in section 13.2.2.4. A unique method for estimating extreme 24-hr rainfall, for any site, is presented in section 7.5.

7.2.1 Rain and Rain-Producing Conditions

There are six major rainfall-producing atmospheric processes:

(1) Monsoon—The monsoon, which produces the greatest precipitation amount, is a seasonal reversal of wind that blows for long periods of time (weeks to months) from one direction. (Most world records of rainfall rates for periods >12 hr are a result of monsoons.) When these winds blow from the water to land with a rising land elevation, the orographic lifting of the moisture-laden air releases precipitation in heavy amounts. In Cherrapunji, India, 9,144 mm (360 in) of rain has fallen in a 1-mo period from monsoon rains. The amount of rain from monsoons at low elevations is considerably less than at higher elevations.

(2) Thunderstorm—The thunderstorm (local storm), which can generate high rates of precipitation for relatively short periods, is associated with cumulonimbus clouds and results from the lifting of unstable moist air, heating of the land mass, lifting by frontal systems, or a combination of these conditions. The thunderstorm is a consequence of "triggering" atmospheric instability, defined loosely as an overturning of air to achieve a stable condition. Strong wind gusts, heavy rain, severe electrical discharges, and sometimes hail occur within the thunderstorm. Thunderstorms most frequently occur in the late afternoon and, as their name implies, are always accompanied by lightning and thunder.

(3) Rain shower—Precipitation from a convective cloud often produces a type of precipitation called a rain shower. Showers are characterized by the suddenness with which they start and stop and by rapid changes of intensity.

(4) Cold and warm front precipitation—Cold and warm frontal systems are frequently accompanied by bands of steady, light precipitation. Frontal-produced precipitation can persist for several days, depending on the movement of synoptic scale weather systems. When two masses of air meet at a frontal boundary—one more dense than the other—the lighter air mass (warm) slides up over the more dense cold air mass. If sufficient moisture is in the air mass being lifted, the moisture condenses and falls as precipitation, either rain or snow, depending on the temperature of the air masses.

(5) Hurricane—Hurricanes produce heavy rain associated with strong winds. A hurricane is a severe "tropical storm" with a maximum 1-min sustained wind speed >33 m/s (>64 kt). They form over the various oceans and seas, nearly always in tropical latitudes. Winds exceeding 90 m/s (175 kt) have been measured, and rainfall can be torrential. The counterpart in the Western Pacific is the typhoon.

(6) Orographic effects—Orographic effects should not be overlooked in a discussion of rainfall. Hilly or mountainous islands located in persistently moist air flow regions receive extreme rainfall as a result of the moist air being lifted to the condensation level (frequently 2,000- to 5,000-ft altitude). This phenomenon accounts for wide variations in precipitation amounts between different locations on mountainous islands.

7.2.2 World Record Rainfall

In design analysis, the maximum amounts of rainfall over various periods need to be considered. These extreme values vary considerably in different areas of the world, but in areas of similar climatic conditions, the extreme values are similar. To best study the maximum amounts of rainfall that have occurred worldwide for different periods, log-log graph paper is used. Figure 7-1 shows these worldwide values, with the upper bounds shown as a straight line with the equation

$$R = 363\sqrt{D_h}\,(\text{mm}) \text{ or } R = 14.3\sqrt{D_h}\,(\text{in}) \ , \tag{7.1}$$

where R is the depth of rainfall in millimeters or inches for period D (duration), and D_h is the duration of rainfall in hours. Due to the lack of sufficient objective data at less than ≈20-min duration, much greater scatter in individual measurements is observed, which reduces the reliability in this region of the graph. World precipitation extremes are also discussed in section 5.2.2.3.

7.2.2.1 Global Rain Climate Regions. Crane and Blood (ref. 7-4) provided an analysis and associated model to estimate rain rate distributions for worldwide rain rate climate regions. The rain rate climatic regions to use with Crane's model are provided in figure 7-2. The associated estimated rain rate distributions for figure 7-2 are provided in table 7-1. Additional information on the application of Crane's model, with emphasis on rain attenuation issues may be found in reference 7-5. Crane's model is based on the use of geophysical data to determine the surface point rain rate and variations of rain rate.

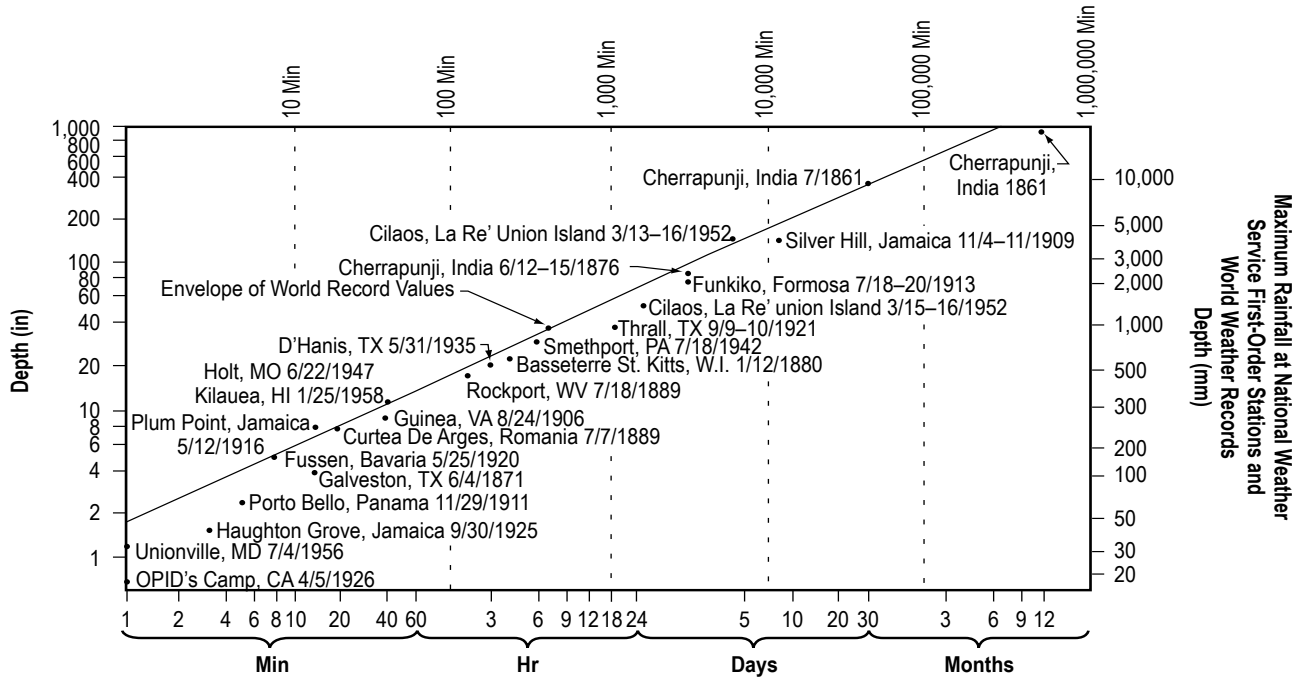

Figure 7-1. World record rainfalls and an envelope of world record values (after refs. 7-2 and 7-3).

To determine a rain rate (R_p in mm/hr), pick a global climate zone A to H from the Crane rain climate regions map (fig. 7-2), then look up the rain rate from the table. The range given in the Crane model is from 0.001 to 5 percent. Example: For a relatively rare rainstorm (0.001 percent of the year, or ≈315 s, which is ≈5 min), very heavy rainfall rates would be predicted, with the value depending on the climate region determined by the coordinates. However, a more common storm that might be experienced a total of 2 percent of the year (≈7.3 days) would have a much smaller rainfall rate.

7.2.2.2 Global Monthly Precipitation Averages. Global maps of average monthly precipitation amounts (in mm/mo) are available online at <http://oceanography.geol.ucsb.edu/~gs4/s2004/resources/Precip_Lamont.htm> (ref. 7-6), produced by The University of California – Santa Barbara, which ties electronically into the Columbia University Earth Institute precipitation database. This monthly precipitation database is derived from NOAA's Climate Prediction Centers CAMS_OPI monthly precipitation climatology database (ref. 7-6). The CAMS_OPI (Climate Anomaly Monitoring System & OLR Precipitation Index) is a precipitation estimation technique which produces real-time monthly analyses of global precipitation. Observations from surface rain gauges (CAMS) are merged with precipitation estimates from a satellite algorithm (OPI), and the data extend from 1979 through 1995. As an example, figure 7-3 illustrates the average global precipitation for January.

7.2.2.3 U.S. 24-hr Precipitation Extremes. The state record for the most extreme 24-hr U.S. precipitation is given in figure 7-4, along with the location for such event (ref. 7-7).

7.2.3 Statistics of Rainfall Occurrences

One set of statistical data on precipitation will not be satisfactory for all design needs. Therefore, several sets of statistics are presented in the sections that follow for Kennedy Space Center (KSC), Edwards Air Force Base (EAFB), Vandenberg Air Force Base (VAFB), and New Orleans. For any return period, a unique method for estimating extreme 24-hr rainfall, for any site, is presented in section 7.5.

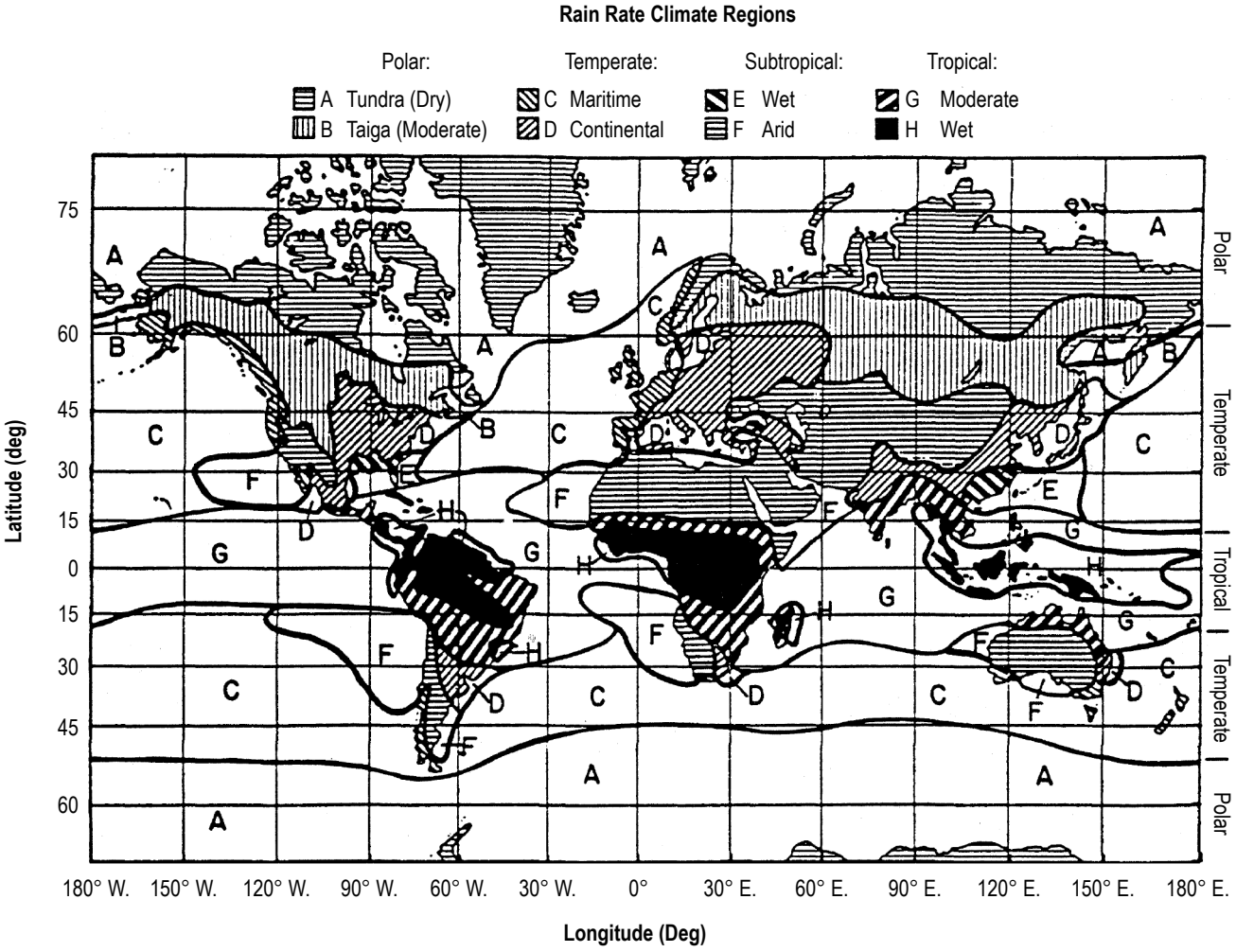

Figure 7-2. Global rain rate climate regions including the ocean areas (ref. 7-4).

7.2.3.1 Design Rainfall Rates. For design and testing, the rate of rainfall per unit time is more useful than the total depth of rainfall. Figure 7-5 shows the 99th percentile envelope design curves for several locations, return periods, and world record values plotted as the rate per hour (in/hr and mm/hr) versus duration.

The KSC and VAFB design rainfall rate curves are shown in figure 7-5 with the 5-yr and 100-yr return periods for a few select stations. The 5-yr and 100-yr return period data were taken from rainfall intensity-duration-frequency curves published by the U.S. Department of Commerce, Weather Bureau (ref. 7-8). These data were analyzed by using the extreme value method of Gumble (ref. 7-9). Although based on an earlier data set, the results are still considered representative for the locations cited.

The term “return period” is a measure of the average time interval between occurrences of a specific event. For example, the 99th percentile rainfall rate for Tampa, FL, is ≈10 in/hr for a duration of 6 min (from fig. 7-5 and table 7-2). On average, this rainfall rate can be expected to return in 100 yr at Tampa. Return periods can be expressed as probabilities, as shown in table 7-2.

Table 7-1. Rain rate distributions (R_p, in mm/hr) for the rain climate regions of the Crane global model (ref. 7-3).

Rain Rate Exceeded. Global % of Year (P%)	Corresponding Time/Year Rain Rate Occurs	Rain Climate Region											
		A	B	B1	B2	C	D1	D2	D3	E	F	G	H
0.001	5 min	28.1	52.1	42.6	63.8	71.6	86.6	114.1	133.2	176.0	70.7	197.0	542.6
0.002	11 min	20.9	41.7	32.7	50.9	58.9	69.0	88.3	106.6	145.4	50.4	159.6	413.9
0.003	16 min	17.5	36.1	27.8	43.8	50.6	60.4	75.6	93.5	130.0	41.4	140.8	350.3
0.005	26 min	13.8	29.2	22.3	35.7	41.4	49.2	62.1	78.7	112.0	31.9	118.0	283.4
0.01	1 hr	9.9	21.1	16.1	25.8	29.5	36.2	46.8	61.6	91.5	22.2	90.2	209.3
0.02	1.8 hr	6.9	14.6	11.3	17.6	19.9	25.4	34.7	47.0	72.2	15.0	66.8	152.4
0.03	2.6 hr	5.5	11.6	9.0	13.9	15.6	20.3	28.6	39.9	62.4	11.8	55.8	125.9
0.05	4 hr	4.0	8.6	6.8	10.3	11.5	15.3	22.2	31.6	50.4	8.5	43.8	97.2
0.1	9 hr	2.5	5.7	4.5	6.8	7.7	10.3	15.1	22.4	36.2	5.3	31.3	66.5
0.2	18 hr	1.5	3.8	2.9	4.4	5.2	6.8	9.9	15.2	24.1	3.1	22.0	43.5
0.3	26 hr	1.1	2.9	2.2	3.4	4.1	5.3	7.6	11.8	18.4	2.2	17.7	33.1
0.5	44 hr	0.5	2.0	1.5	2.4	2.9	3.8	5.3	8.2	12.6	1.4	13.2	22.6
1	88 hr	0.2	1.2	0.8	1.4	1.8	2.2	3.0	4.6	7.0	0.6	8.4	12.4
2	7.3 day	0.1	0.5	0.4	0.7	1.1	1.2	1.5	2.0	3.3	0.2	5.0	5.8
3	11 day	0.0	0.3	0.2	0.4	0.6	0.6	0.9	0.8	1.8	0.1	3.4	3.3
5	18.3 day	0.0	0.2	0.1	0.2	0.3	0.2	0.3	0.0	0.2	0.1	1.8	1.1

Region Category:
- Region A = Polar tundra (dry)
- Region B = Polar taiga (moderate)
- Region C = Temperate meritime
- Region D1 = Temperate continental (dry)
- Region D2 = Temperate continental (mid)
- Region D3 = Temperate continental (wet)
- Region E = Subtropic (wet)
- Region F = Subtropic (arid)
- Region G = Tropical (moderate)
- Region H = Tropical (wet)

Assuming the Following Precipitation Type & Rate:
- Drizzle = 0.25 mm/hr
- Light rain = 1 mm/hr
- Moderate rain = 4 mm/hr
- Heavy rain = 16 mm/hr
- Thunderstorm = 35 mm/hr
- Intense thunderstorm = 100 mm/hr

(See figure 7-5 for actual design rainfall rates. Figure 7-6 also gives similar definitions of rain intensity categories as above, but versus drop diameter.)

Values of design rainfall for various locations of interest for aerospace vehicle operations, and worldwide extremes of rainfall, are given in tables 7-3 through 7-6 with values of the corresponding drop size. The worldwide extremes would not normally be used for design of space vehicles but may be needed for facility design, tracking stations, etc. The values of rainfall rates are represented with the following equation:

$$r = \frac{C\sqrt{D_m}}{D_m} = \frac{C}{\sqrt{D_m}} \quad , \tag{7.2}$$

where

r = rate in millimeters per hour or inches per hour
D_m = time in minutes
C = constants for location (given in table 7-7).

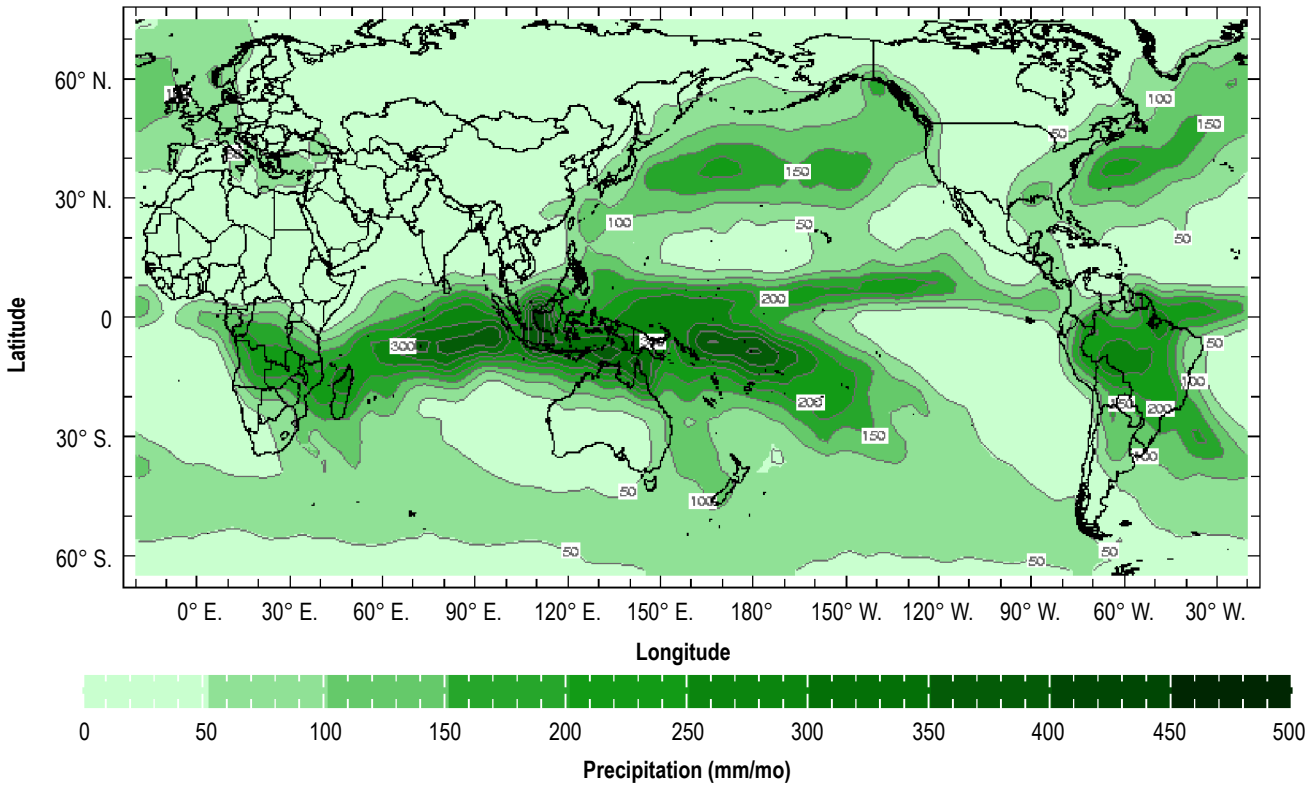

Figure 7-3. NOAA January global precipitation average based on NOAA's data analysis (ref. 7-6).

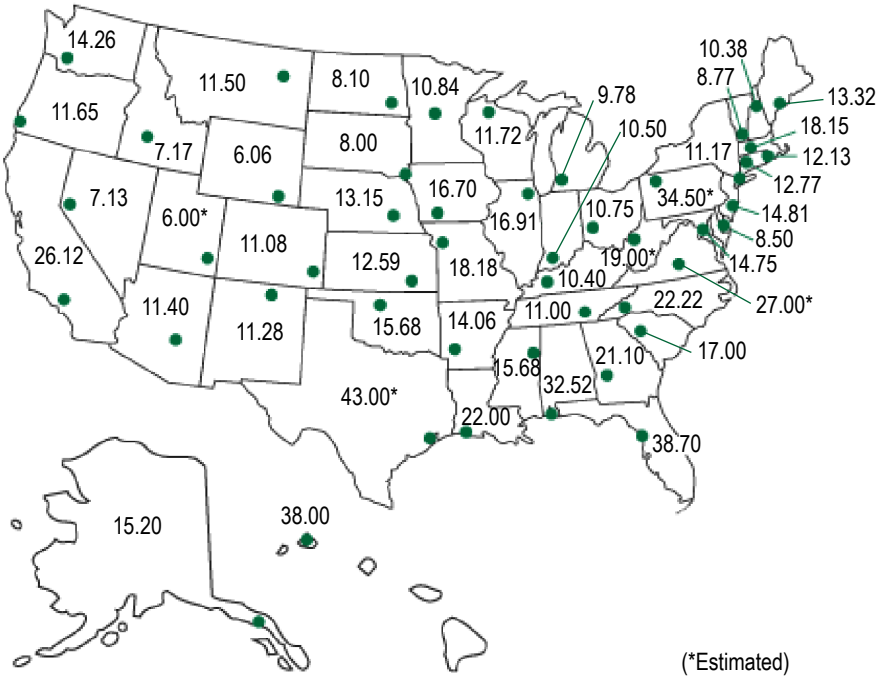

Figure 7-4. Record maximum 24-hr precipitation (1 in = 2.54 cm) by state with location, through 1998 (ref. 7-7).

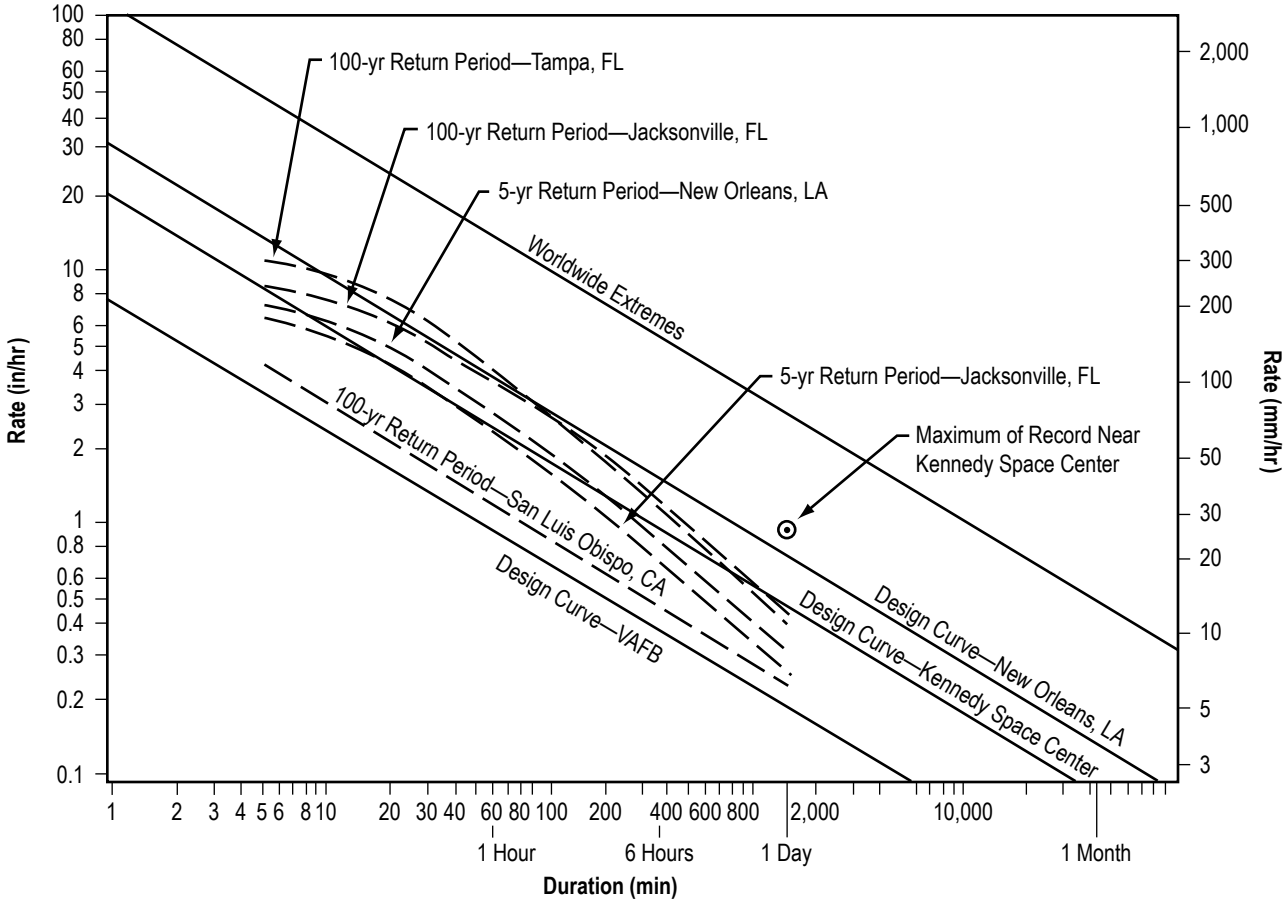

Figure 7-5. Design rainfall rates (99th percentile).

Table 7-2. Relationship of return periods to probabilities.

Return Period (yr)	Percentile (%)	Return Period (yr)	Percentile (%)
2	50	50	98
5	80	100	99
10	90	1,000	99.9

The design rainfall rates in figure 7-5 and tables 7-3 through 7-6 are based on precipitation occurrences; i.e., if precipitation is occurring, what is the probability of exceeding a given rate? These data are based on occurrences over a year and would be used in the design of items continuously exposed, such as launch facilities. These design values are based on a minimum 10-yr period of record for the locations cited.

7.2.3.2 Precipitation Exceedance Probability. Values for each month with the probability that precipitation will not exceed a specified amount in any one day are given for several selected sites of aerospace vehicle design interest—KSC, EAFB, VAFB, and New Orleans, LA—in tables 7-8 through 7-11, respectively. The values should not be interpreted to mean that the amount of precipitation occurs uniformly over the 24-hr period,

Table 7-3. Design rainfall, KSC and Huntsville, AL, based on yearly largest rate for stated time periods.*

Time Period	Rainfall Rate (*r*)		Rainfall Total Accumulation		Raindrop Size			
					Average		Largest	
	(mm/hr)	(in/hr)	(mm)	(in)	(mm)	(in)	(mm)	(in)
1 min	492	19.4	8	0.3	2.0	0.08	6.0	0.24
5 min	220	8.7	18	0.7	2.0	0.08	5.8	0.23
15 min	127	5.0	32	1.25	2.0	0.08	5.7	0.22
1 hr	64	2.5	64	2.5	2.0	0.08	5.0	0.20
6 hr	26	1.0	156	6.1	1.8	0.07	5.0	0.20
12 hr	18	0.7	220	8.7	1.6	0.06	4.5	0.18
24 hr	13	0.5	311	12.2	1.5	0.06	4.5	0.18

*Use average rate of fall for raindrops of 6.5 m/s for all time periods.

Table 7-4. Design rainfall, New Orleans, LA, based on yearly largest rate for stated time periods.

Time Period	Rainfall Rate (*r*)		Rainfall Total Accumulation		Raindrop Size			
					Average		Largest	
	(mm/hr)	(in/hr)	(mm)	(in)	(mm)	(in)	(mm)	(in)
1 min	787	31.0	13	0.5	2.1	0.08	6.0	0.24
5 min	352	13.9	29	1.2	2.0	0.08	6.0	0.24
15 min	203	8.0	51	2.0	2.0	0.08	5.7	0.22
1 hr	102	4.0	102	4.0	2.0	0.08	5.5	0.22
6 hr	41	1.6	249	9.8	1.9	0.07	5.0	0.20
12 hr	29	1.2	352	13.9	1.8	0.07	5.0	0.20
24 hr	21	0.8	498	19.6	1.6	0.06	5.0	0.20

*Use average rate of fall for raindrops of 6.5 m/s for all time periods.

since it is more likely that most or all of the amounts occurred in a short period of the day. The 100-percent values in the tables imply a chance of exceeding certain amounts of precipitation during most of the months; however, it should be realized that the length of available data records is not long and that there is always a chance of any meteorological extreme being exceeded.

7.2.3.3 Kennedy Space Center Rainfall Rates Versus Duration Probability. Rainfall rates of various durations for the 50th, 95th, and 99th percentiles, given a day with rain in the greatest rain month, are given in table 7-12 for KSC. The precipitation amounts should not be interpreted to mean that the rain fell uniformly for a brief period for the referenced time periods with no rain during the remainder of the time period. As an example, the 99th percentile total of 49 mm (1.93 in); i.e., left column, 99th percentile, 1-hr duration as shown in table 7-12, could have occurred as follows: 25 mm (0.98 in) could have fallen during a 5-min period within a particular hour, with an additional 24 mm (0.95 in) of rainfall for another 5-min period, making a total of 49 mm (1.93 in) for a total of ≈10 min. Subsequently, no rain would have fallen for 50 min during the hypothetical 1-hr period. The 99th percentile rainfall data are referenced since such extremes are important to consider in vehicle and facility design studies. Table 7-3 has rainfall rates listed as well as total accumulation, raindrop size, etc., for various periods at KSC and Huntsville, which are also valuable data to use as vehicle criteria.

Table 7-5. Design rainfall, VAFB, EAFB, and WSMR based on yearly largest rate for stated time periods.*

Time Period	Rainfall Rate (*r*)		Rainfall Total Accumulation		Raindrop Size			
					Average		Largest	
	(mm/hr)	(in/hr)	(mm)	(in)	(mm)	(in)	(mm)	(in)
1 min	197	7.7	3	0.1	2.0	0.08	5.6	0.22
5 min	88	3.5	7	0.3	2.0	0.08	5.3	0.21
15 min	51	2.0	13	0.5	2.0	0.08	5.0	0.20
1 hr	25	1.0	25	1.0	1.8	0.07	5.0	0.20
6 hr	10	0.4	62	2.4	1.5	0.06	4.6	0.18
12 hr	7	0.3	88	3.5	1.3	0.05	4.3	0.17
24 hr	5	0.2	124	4.9	1.3	0.05	4.0	0.16

*Use average rate of fall for raindrops of 6.5 m/s for all time periods; except use 6, 5.8, and 5.5 m/s for 6, 12, and 24 hr, respectively.

Table 7-6. Design rainfall, worldwide extremes, based on envelope of record values (fig. 7-1) for stated time periods.*

Time Period	Rainfall Rate (*r*)		Rainfall Total Accumulation		Raindrop Size			
					Average		Largest	
	(mm/hr)	(in/hr)	(mm)	(in)	(mm)	(in)	(mm)	(in)
1 min	2,813	110.8	47	1.8	2.5	0.10	8.0	0.31
5 min	1,258	49.5	105	4.1	2.2	0.09	8.0	0.31
15 min	726	28.6	182	7.1	2.1	0.08	8.0	0.31
1 hr	363	14.3	363	14.3	2.0	0.08	8.0	0.31
6 hr	148	5.8	890	35.3	2.0	0.08	5.8	0.23
12 hr	105	4.1	1,258	49.5	2.0	0.08	5.5	0.22
24 hr	74	2.9	1,779	70.1	2.0	0.08	5.2	0.20

*Use average rate of fall for raindrops of 6.5 m/s for all time periods.

Table 7-7. Constants (C) to use with equation (7.2) for rainfall rates at various sites.

	KSC, Huntsville	New Orleans	VAFB, EAFB, and WSMR	World Extremes
C (for mm/hr)	491.87	786.99	196.75	2,813.48
C (for in/hr)	19.365	30.984	7.746	110.767
Use values of *r* as given in:	Table 7-3	Table 7-4	Table 7-5	Table 7-6

Table 7-8. Probability that precipitation will not exceed a specific amount in any one day, KSC.

Amount							
(mm)	(in)	Jan. %	Feb. %	March %	Apr. %	May %	June %
0.00	0.00	68.1	60.8	62.2	70.6	64.2	54.7
Trace	Trace	77.1	71.4	71.3	80.0	76.2	65.7
0.25	0.01	79.0	74.3	72.5	82.7	79.4	68.4
1.27	0.05	84.8	79.4	77.5	86.6	84.7	74.1
2.54	0.10	87.1	82.3	81.6	89.3	89.4	75.8
6.35	0.25	90.0	85.8	87.8	93.5	92.9	82.8
12.70	0.50	93.9	91.6	91.6	95.9	96.4	90.8
25.40	1.00	97.1	96.1	96.3	98.0	99.3	97.1
63.50	2.50	99.4	100.0	99.5	99.5	100.0	99.8
127.00	5.00	100.0	100.0	99.8	99.8	100.0	100.0
Amount							
(mm)	(in)	July %	Aug. %	Sept. %	Oct. %	Nov. %	Dec. %
0.00	0.00	56.8	52.6	40.0	47.4	62.1	64.2
Trace	Trace	65.8	63.9	53.9	61.6	74.2	78.1
0.25	0.01	68.4	66.2	57.5	63.9	77.2	81.0
1.27	0.05	73.2	69.4	62.7	72.0	83.9	86.8
2.54	0.10	75.8	74.9	67.9	76.8	86.9	89.4
6.35	0.25	83.5	80.7	75.8	85.5	90.8	93.3
12.70	0.50	88.3	88.4	83.7	91.3	92.6	96.5
25.40	1.00	93.8	93.6	92.2	95.5	96.2	99.1
63.50	2.50	99.6	99.7	97.4	99.4	99.2	100.0
127.00	5.00	99.6	100.0	99.8	99.7	99.5	100.0

7.2.3.4 Rainfall Rate Distribution With Altitude. Rainfall rates at various altitudes in percent of the surface rates are given in table 7-13 for all areas (ref. 7-10). Values in table 7-13 are representative of summer rain rates (from 2.8 through 10.3 mm/hr) in temperate latitudes for updrafts from 0.1 to 0.4 m/s. Thunderstorm updrafts can be larger.

Tattleman (ref. 7-11) modeled the mil-standard, worldwide, extreme rainfall rates with height based on estimates of surface rates occurring 0.5, 0.1, and 0.01 percent of the time for the greatest month in the severest rain areas of the world, also for the 42- and 1-min world record rainfalls. These five extreme cases are representative of surface rainfall rates of 36 to 1,872 mm/hr (1.4 to 73.7 in/hr).

Precipitation above the ground is generally colder than at the ground and frequently occurs as supercooled drops which may cause icing on objects moving through the drops. Such icing can be expected to occur when the air temperature is about –2.2 °C (28 °F). The major factors that influence the rate of ice formation are (1) the amount of liquid water, (2) the droplet size, (3) air speed, and (4) the size and shape of the airfoil. For further icing aloft information, see subsection 7.4.2.2. Terminal fall velocities for various raindrops with diameters from 0.05 to 0.70 cm are given in table 7-14.

Table 7-9. Probability that precipitation will not exceed a specified amount in any one day, EAFB.

Amount							
(mm)	(in)	Jan. %	Feb. %	March %	Apr. %	May %	June %
0.00	0.00	81.7	81.8	82.6	86.7	95.1	98.8
Trace	Trace	88.0	88.9	89.6	93.8	98.6	99.5
0.25	0.01	88.9	89.5	91.3	94.8	99.0	99.5
1.27	0.05	91.7	92.1	93.8	96.4	99.1	99.5
2.54	0.10	93.5	93.5	95.5	97.6	99.4	99.5
6.35	0.25	96.9	95.6	98.0	99.0	100.0	99.9
12.70	0.50	98.8	98.3	99.1	99.6	100.0	100.0
25.40	1.00	99.8	99.6	99.8	100.0	100.0	100.0
63.50	2.50	100.0	100.0	99.9	100.0	100.0	100.0
127.00	5.00	100.0	100.0	100.0	100.0	100.0	100.0

Amount							
(mm)	(in)	July %	Aug. %	Sept. %	Oct. %	Nov. %	Dec. %
0.00	0.00	94.7	95.2	94.6	93.0	89.8	85.2
Trace	Trace	99.0	98.1	97.8	95.8	94.2	90.8
0.25	0.01	99.3	98.1	98.2	96.1	94.4	91.4
1.27	0.05	99.7	98.9	98.9	97.2	96.4	93.7
2.54	0.10	99.7	99.3	98.9	98.2	97.0	94.9
6.35	0.25	100.0	99.6	99.2	99.2	98.4	96.7
12.70	0.50	100.0	99.9	99.8	99.6	99.3	99.0
25.40	1.00	100.0	100.0	99.9	99.7	100.0	99.9
63.50	2.50	100.0	100.0	100.0	100.0	100.0	100.0
127.00	5.00	100.0	100.0	100.0	100.0	100.0	100.0

7.2.3.5 Hydrometeor Characteristics With Altitude. Raindrops falling on the Earth's surface may originate at a higher altitude as some other form of hydrometeor, such as ice or snow. The liquid water content of these hydrometeors per unit volume will have a distribution similar to that given in table 7-15 for rainfall. A summary of the hydrometeor characteristics from reference 7-13 is given in table 7-15.

7.2.3.6 Kennedy Space Center Precipitation and Freezing Temperatures. Since the thermal protection system (TPS) tiles on the Space Shuttle are sensitive to precipitation that can infiltrate and freeze, causing possible TPS internal structural degradation, a study was done in 1998 to determine the frequency of such rain events at KSC, Florida (F). The entire hourly surface weather observational record at KSC, from 1957 through 1991, was analyzed for all months. Table 7-16 presents these KSC hourly results applicable for the colder months of November through March.

The KSC month of January experienced the most hourly occurrences (214) of precipitation when the surface ambient air temperature was ≤0 °C (32 °F). This resulted in only a 0.82-percent occurrence when considering all the hours over the 35-yr period of record. The frequency occurrence of precipitation when the temperatures are ≤–2.2 °C (≤28 °F) are also given.

Table 7-10. Probability that precipitation will not exceed a specified amount in any one day, VAFB.

Amount							
(mm)	(in)	Jan. %	Feb. %	March %	Apr. %	May %	June %
0.00	0.00	69.4	70.4	61.7	70.4	71.8	70.0
Trace	Trace	79.1	75.9	72.2	80.4	94.0	94.8
0.25	0.01	81.1	76.9	74.6	82.5	96.8	97.7
1.27	0.05	83.5	81.4	83.9	87.9	98.0	100.0
2.54	0.10	88.3	84.4	85.9	90.8	98.8	100.0
6.35	0.25	91.5	90.4	91.5	95.4	99.6	100.0
12.70	0.50	95.1	94.4	96.3	97.5	100.0	100.0
25.40	1.00	98.3	96.9	98.7	99.2	100.0	100.0
63.50	2.50	99.9	99.9	99.5	100.0	100.0	100.0
127.00	5.00	100.0	100.0	99.9	100.0	100.0	100.0

Amount							
(mm)	(in)	July %	Aug. %	Sept. %	Oct. %	Nov. %	Dec. %
0.00	0.00	62.4	63.4	77.9	79.4	73.3	73.8
Trace	Trace	98.2	94.9	95.4	95.1	82.6	80.6
0.25	0.01	98.9	98.1	95.8	95.5	83.3	83.1
1.27	0.05	100.0	98.8	97.5	95.9	85.9	87.4
2.54	0.10	100.0	99.5	97.9	96.7	87.4	89.2
6.35	0.25	100.0	99.9	98.7	97.5	90.0	93.5
12.70	0.50	100.0	100.0	99.9	98.7	94.4	97.1
25.40	1.00	100.0	100.0	100.0	99.5	98.8	99.6
63.50	2.50	100.0	100.0	100.0	99.9	99.9	100.0
127.00	5.00	100.0	100.0	100.0	100.0	100.0	100.0

Given that there is precipitation, how many times does the air temperature become ≤0 °C (≤32 °F), and ≤–2.2 °C (≤28 °F), within the next 6 hr at KSC? Table 7-17 answers this question for December, the only month with this occurrence. The 6-hr increment can be changed to whatever time increment is needed.

Since the relative humidity (RH) of the air at KSC, many times, is close to or near saturation (≈100 percent), whenever the temperature approaches freezing, one can use 100 percent as a worst case to represent the RH between the time of last precipitation and the time of the first freezing temperature. This is because freezing at KSC normally occurs in the late night/early morning hours when the diurnal RH cycle tends to be saturated.

7.2.4 Rain Laboratory Test Simulation

In the laboratory, simulated rain droplets are usually produced by using a single orifice, mounted above the equipment being tested. Such a test will not necessarily duplicate the natural occurrence of precipitation and may or may not reflect the true effect of natural precipitation on the equipment since a single orifice produces drops of nearly the same size.

Each test should be evaluated to determine if the following factors which occur in natural precipitation are important in the test.

Table 7-11. Probability that precipitation will not exceed a specified amount in any one day, New Orleans, LA.

Amount							
(mm)	(in)	Jan. %	Feb. %	March %	Apr. %	May %	June %
0.00	0.00	77.1	70.2	73.6	79.7	75.9	72.2
0.25	0.01	77.7	71.1	74.1	79.9	76.4	72.6
1.27	0.05	80.9	74.5	78.1	81.9	78.0	77.7
2.54	0.10	85.7	76.4	81.0	83.6	82.9	82.3
5.08	0.20	89.1	80.4	82.8	87.0	86.5	85.3
12.70	0.50	94.0	88.8	88.6	91.2	92.2	90.3
25.40	1.00	97.4	93.8	92.9	95.3	95.6	93.8
50.80	2.00	98.9	97.8	97.9	97.8	99.0	98.8
127.00	5.00	99.7	99.7	99.7	100.0	100.0	100.0
254.00	10.00	100.0	100.0	100.0	100.0	100.0	100.0
Amount							
(mm)	(in)	July %	Aug. %	Sept. %	Oct. %	Nov. %	Dec. %
0.00	0.00	54.5	70.1	69.2	84.4	83.4	77.6
0.25	0.01	55.8	71.3	71.1	85.6	84.7	78.2
1.27	0.05	61.4	74.4	76.3	88.2	85.7	80.7
2.54	0.10	67.4	79.3	79.2	90.5	87.4	83.2
5.08	0.20	73.3	83.5	84.4	93.4	89.4	85.2
12.70	0.50	81.5	92.4	90.3	96.0	94.0	91.9
25.40	1.00	91.5	95.7	94.5	98.0	97.3	95.2
50.80	2.00	96.7	98.2	98.0	99.7	98.3	99.4
127.00	5.00	100.0	100.0	99.0	100.0	99.7	99.7
254.00	10.00	100.0	100.0	100.0	100.0	100.0	100.0

Table 7-12. Highest rainfall rate versus duration for various probabilities, given a day with rain for the highest rain month, KSC.

	Percentile											
	50				95				99			
Duration	(mm)	(in)	(mm/hr)	(in/hr)	(mm)	(in)	(mm/hr)	(in/hr)	(mm)	(in)	(mm/hr)	(in/hr)
5 min	5.6	0.22	66.0	2.6	18.0	0.72	221.0	8.7	25.0	1.00	305.0	12.0
15 min	5.8	0.23	24.0	0.93	22.0	0.88	89.0	3.5	33.0	1.30	132.0	5.2
1 hr	6.4	0.25	6.4	0.25	30.0	1.17	30.0	1.17	49.0	1.93	49.0	1.93
6 hr	7.1	0.28	1.3	0.05	39.0	1.55	6.6	0.26	81.0	3.18	13.0	0.53
24 hr	10.9	0.43	0.5	0.02	67.0	2.62	2.8	0.11	127.0	5.00	5.3	0.21

7.2.4.1 Rain Droplets Rate of Fall. Natural rain droplets usually fall a sufficient distance to reach their terminal velocity (maximum rate of fall). Simulation of such fall rates in the laboratory requires the droplets

Table 7-13. Distribution of rainfall rates with height.

For All Four Locations*			For World Extremes†		
Height (Geometric) Above Surface		Surface Rate	Height Above Surface		Surface Rate
(km)	(mi)	(%)	(km)	(mi)	(%)
SFC	SFC	100	SFC	SFC	100
1	0.6	90	2	1.2	100
2	1.2	75	4	2.5	100
3	1.9	57	6	3.7	100
4	2.5	34	8	5.0	74
5	3.1	15	10	6.2	51
6	3.7	7	12	7.5	35
7	4.3	2	14	8.7	22
8	5.0	1	16	9.9	11
9	5.6	0.1	18	11.2	3
10 and over	6 and over	<0.1	20	12.4	0

*Summer type rainfall in temperate latitudes representing 2.8 through 10.3 mm/hr rain rates (ref. 7-10).
†Mil-Std: For worst month, in severest rain area, representing 36 through 1,872 mm/hr rain rates (ref. 7-11).

Table 7-14. Values of terminal velocities of raindrops (ref. 7-12).

Drop Diameter		Terminal Velocity	
(mm)	(in)	(m/s)	(mph)
1	0.04	4.0	8.9
2	0.08	6.5	14.5
3	0.12	8.1	18.1
4	0.16	8.8	19.7
5	0.20	9.1	20.4
6	0.24	9.1	20.4
7	0.28	9.1	20.4

to fall a suitable distance. Large droplets (4-mm (0.16-in) diameter and greater) will require approximately 12 m (39 ft) to reach terminal velocity unless they are released under pressure.

Values of terminal velocities of water droplets were measured by Gunn and Kinzer (ref. 7-15). Their results provided the values in table 7-14. Reference 7-12 should be consulted for more detailed information. Gunn and Kinzer found that water droplets >5.8 mm (>0.23 in) in diameter would usually break up before the terminal velocity was reached.

7.2.4.2 Raindrop Size and Rate Distribution. A knowledge of raindrop sizes is required (1) to simulate rainfall tests in the laboratory, (2) to know the fall rate of the raindrops and impact energy, and (3) for use in erosion tests of materials.

Table 7-15. Summary of hydrometeor characteristics (ref. 7-13).

Type of Hydrometeor	Altitude (km)	Drop Diameter (μm)		Concentration per Unit Volume (cm^3)		Liquid Water Content per Unit Volume ($g\ m^{-3}$)		Ambient Temperature (°C)
	Range	Range	Rep.	Range	Rep.	Range	Rep.	Range=
Layer clouds	sfc-1.5	<1–40	11	<10–10,000	500	<0.1–1	0.2	30 to –15
Layer clouds	2.5–7.5	<1–50	12	<20–1,000	100	<0.1–1	0.2	20 to –25
Layer clouds (ice crystals)	7.5–15	<10–10,000	100	<0.1–10	0.2	<0.01–0.1	0.02	–10 to –55
Convective clouds								
Fair weather cumulus	0.5–8	<1–75	12	<10–10,000	300	<0.1–1	0.5	20 to –30
Cumulus congestus	0.5–13	<1–200	25	<10–10,000	150	<1–10	4	20 to –55
Continuous type rain	sfc-6	<500–3,000	1,000	<50–3,000*	500*	<0.05–0.7	0.1	30 to –15
Shower type rain	sfc-13	<500–7,000	2,000	<10–3,000*	500*	<0.1–30	1	30 to –55
Coalescence (warm) rain	sfc-5	<100–1,000	500	<500–50,000*	3,000*	<0.05–0.1	0.1	30 to 0
Hail	sfc-13	<0.01–13 cm	0.8 cm	<0.5–1,000*	50*	<0.1–0.9**	0.8**	30 to –55
Ice and snow crystals	sfc-13	<100–20,000	5,000	<1–1,000*	100*	<0.001–0.7***	0.07***	5 to –55

Rep.: Representative value or value most frequently encountered.
* Per m^3
** Density of particles (g/cm^3)
*** Mass of crystals (mg)

Table 7-16. Occurrences and percentage of hourly KSC precipitation when ambient temperature is ≤0 °C (≤32 °F) and ≤–2.2 °C (≤28 °F) by winter month (ref. 7-14).

Month	No. $T \leq 32$ °F	(%)	No. $T \leq 28$ °F	(%)
November	1	0	0	0
December	127	0.49	48	0.18
January	214	0.82	52	0.20
February	72	0.30	10	0.04
March	18	0.07	0	0

Table 7-17. Number of occurrences and percentage of hourly KSC precipitation when followed within 6 hr by freezing temperatures ≤0 °C (≤32 °F) and ≤–2.2 °C (≤28 °F) (ref. 7-14).

Month	No. $T \leq 32$ °F	(%)	No. $T \leq 28$ °F	(%)
December	5	0.56	1	0.11

At the Earth's surface, the size of the raindrops varies with the rate of rainfall per unit time; the heavier the rainfall, the larger the drops. Any one rainstorm will contain a variety of raindrop sizes ranging from <0.5 mm (the lower limit of size measurement) to >4 mm. The more intense the storm (the higher the rate of rainfall), the larger some of the drops will be. The raindrop size distribution depends critically on the origin of the rain. Reference 7-11 shows the probability of occurrence of various raindrop sizes with relation to types

of rain-producing storms: (1) Thunderstorms, (2) rain showers, and (3) continuous rain. Thunderstorms have the greatest occurrence of the larger drops (over 2 mm). Rain showers have the next greatest occurrence, while continuous rain produces the lowest occurrence of the larger drops. Rain drop sizes below 2 mm in diameter occur with near equal probability from all types of storms. In comparing drop sizes with various rainfall rates, the larger drops occurred with the highest probability for the greatest rainfall rates. Raindrops over 8 mm in diameter are not expected to occur frequently because the fall rate breaks these large drops into smaller ones once they exceed ≈5.8 mm in diameter (ref. 7-16).

Naturally occuring rainfall has a variety of drop sizes (diameter) with a typical distribution shown in figure 7-6 (ref. 7-12). Rainfall rates (in mm/hr) are also given in this figure with respect to the various rainfall intensity categories. The moderate to extremely heavy rain distribution could be simulated by a number of orifices that produce droplets of approximately 1-, 2-, 3-, 4-, and 5-mm diameter released at the appropriate water pressure to provide the desired terminal velocity. For the drizzle distribution, the use of a single orifice to produce 1-mm droplets would be suitable.

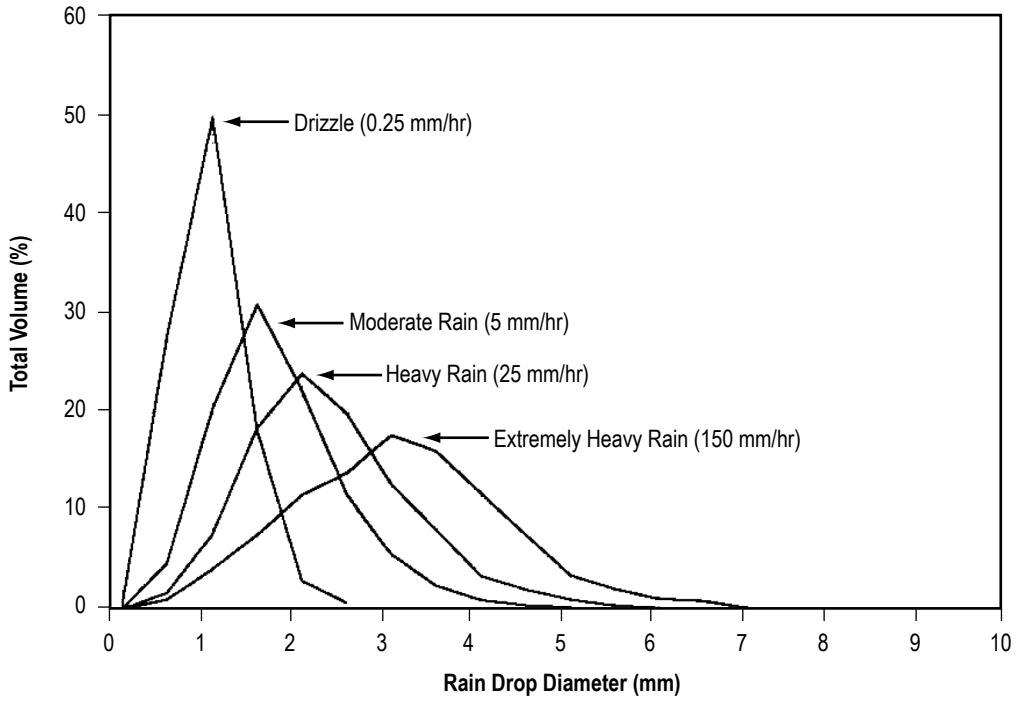

Figure 7-6. Distribution of drop sizes of rain (ref. 7-12).

7.2.4.3 Wind Speed Effect. In most cases of natural rain there is wind blowing in a near horizontal direction. This wind modifies the droplet path from vertical to a path at some angle to the vertical, thus causing the rain droplets to strike at an angle. In addition, unless the equipment is streamlined in the direction of the wind, small vortices may develop at the surface of the equipment. These vortices may cause much of the precipitation to flow in a variety of directions, including upward against the bottom of the equipment.

Studies of thunderstorms with rainfall rates from 12.7 to 76.2 mm/hr (0.5 to 3 in/hr) have shown an average mean wind speed of 5 m/s (11 mph). Peak winds were as high as 16 m/s (36 mph). In nearly all thunderstorms, peak winds are at least 5 m/s (11 mph) greater than the mean wind speed for the rain region of the storm.

7.2.4.4 Temperature Effect. The air temperature near the surface (1.22 m reference height) usually decreases several degrees after the start of rainfall. The amount of the temperature decrease is greatest in the summer, when relative humidity is smallest, about 8 ºC (14 ºF), when the air temperature is high (>32 ºC (>90 ºF). During winter, the air temperature decrease is usually about 2.8 ºC (5 ºF). At the end of a summer rainfall, after an hour or so, the air temperature will usually increase again to nearly the same values as before the storm, but during winter there is no general pattern of warming.

7.2.4.5 Rainfall Laboratory Test Recommendations. The following items need to be considered for rainfall tests in the laboratory:

- Raindrop size distribution:
  – Rates ≤25 mm/hr, drop size of 1 mm.
  – Rates >25 mm/hr, drop size from 1 to 5 mm.

- Fall rate of drops—Drops should fall at least 12 m (39 ft) to obtain terminal velocity or be released under pressure to provide the desired terminal velocity.

- Wind speed—A mean wind of 5 m/s (11 mph) with gusts of 15 m/s (34 mph) of 30-s duration at least once in each 15-min period.

- Temperature—The temperature in the chamber should decrease from 32 ºC (90 ºF) to 24 ºC (75 ºF) after the start of rainfall for representative summer tests and should be maintained at 10 ºC (50 ºF) for winter tests. The decrease in air temperature may be obtained by using water at, or slightly below, 24 ºC (75 ºF) for the summer tests.

7.2.4.6 Kennedy Space Center Idealized Rain Cycle. For some studies and laboratory tests, it may be desirable to use an extreme rain cycle with associated drop sizes, wind speeds, and temperatures. The values from table 7-12 can be used in any combination of rainfall rate and duration such that the total accumulation does not exceed the table 7-12 value for the selected time period and percentile level. The percentile level should be compatible with the risk the operator is willing to accept. The 95-percentile values have a 5-percent risk of being exceeded; the 99-percentile values have only a 1-percent risk.

If wind speed, temperature, and raindrop size (diameter) are included in the test, the following values may be used with both 95- and 99-percentile rain rates:

- Wind speed:
  – 5.1 m/s, gusts to 15.4 m/s (10 kt, gusts to 30 kt)
  – Gust lasting 2 min applied every 15 min.

- Temperature:
  – Summer: Before: 32 ºC (90 ºF) During: 24 ºC (75 ºF)
  – Winter: Before: 13 ºC (55 ºF) During: 10 ºC (50 ºF)

- Drop diameter:
  – Average = 2 mm
  – Largest 1 percent = 5.9 mm

Table 7-18 shows some rain cycle examples using 95-percentile values from table 7-12.

Table 7-18. Rain cycle examples using 95-percentile values from table 7-12.

Period of Rainfall		Rate (mm/hr)	Rate (in/hr)	Total Accumulation (mm)	Total Accumulation (in)
1 hr		29.7	1.17	2.97	1.17
3 hr		11.9	0.47	35.8	1.41
For 1-hr cycle, use	10 min	12.7	at: 0.5	29.7	1.17
	3 min	221.0	8.7		
	5 min	88.9	3.5		
	42 min	13.0	0.51		
For 3-hr cycle, use	15 min	5.1	at: 0.2	35.8	1.41
	30 min	12.7	0.5		
	5 min	88.9	3.5		
	25 min	12.7	0.5		
	105 min	8.9	0.35		

The table 7-18 1-hr cycle example consists of four time segments that total 1 hr, with their four respective rain rates given for each part of that 1 hr. However, total cycle rainfall accumulation is not to exceed 1.17 in (30 mm) (value from table 7-12).

7.2.5 Rain Erosion

Rain erosion is caused by the stress resulting from liquid droplets impinging a solid surface. This stress may dent or crack the surface or result in a mass loss (ref. 7-12). Multiple impacts can cause three times the damage of a single impact (ref. 7-17). With the advent of high-speed aircraft, careful consideration must be given in selecting materials to prevent the erosion of paint coatings, structural plastics, and metallic parts.

7.2.5.1 Rain Erosion Criteria. The magnitude of rain erosion can be influenced by many factors, such as impact velocity, drop size, density, viscosity, and surface tension. Different techniques have been applied to determine the effects of impact velocities on erosion. Tables listing erosion rates for various materials at specific velocities are found in references 7-18 and 7-19.

Tests by A.A. Fyall at the Royal Aircraft Establishment (ref. 7-20) on single rain droplets have shown that the rain erosion rate may increase considerably with lower air pressure (higher altitude) because of the decreased cushioning effect of the air on the droplets at impact.

7.2.6 Snow

For design purposes, all forms of frozen precipitation except large hail will be referred to as snow. It encompasses snow pellets, snow grains, ice crystals, ice pellets, and small, soft hail. The accumulation of snow on a surface produces stress. For a flat, horizontal surface, the stress is proportional to the weight of the snow directly above the surface. For long, narrow objects, such as pipes or wires lying horizontally above a flat surface (which can accumulate the snow), the stress can be figured as approximately equal to the weight of the wedge of snow with the sharp edge along the object and extending above the object in both directions at ≈45° to the vertical. (In such cases, the snow load would be computed for the weight of the snow wedge above the object and not the total snow depth on the ground.) The weight of new-fallen snow on a surface varies between 0.5 kg/m^2 per cm (0.25 lb/ft^2 in) of depth and 2 kg/m^2 per cm (1.04 lb/ft^2 in) of depth, depending on the atmospheric conditions at the time of the snowfall. Snow near 0 °C (32 °F) (wet snow) can build up on power lines to >10 times line diameter and lead to failure. Wind can cause galloping (wind-induced oscillations) which enhance failure. U.S. snowfall and snowfall statistics are also given in section 5.1.3.2.

7.2.6.1 Snow Loads at Surface. Maximum snow loads at the following locations are:

- Huntsville, White Sands Missile Range (WSMR), and EAFB—for horizontal surfaces, a snow load of 25 kg/m^2 (5.1 lb/ft^2) per 24-hr period (equivalent to a 25.4 cm (10-in) snowfall) to a maximum of 50 kg/m^2 (10.2 lb/ft^2) in a 72-hr period, provided none of the snow is removed from the surface during that time, should be considered for design purposes.

- VAFB—For horizontal surfaces, a maximum snow load of 10 kg/m^2 (2 lb/ft^2) per one 24-hr period (equivalent to a 4-in snowfall) should be considered for design purposes.

- KSC and New Orleans area snow loads need not be considered.

7.2.6.2 Falling Snow Particle Size. Snow particles may penetrate openings (often openings of minute size) in equipment and cause a malfunction of mechanical or electrical components, either before or after melting. Particle size, associated wind speed, and air temperature to be considered are as follows:

- Huntsville and EAFB—Snow particles 0.1-mm (0.0039-in) to 5-mm (0.20-in) diameter; wind speed 10 m/s (19 kt); air temperature –17.8 °C (0 °F).

- VAFB and WSMR—Snow particles 0.5-mm (0.020-in) to 5-mm (0.20-in) diameter; wind speed 10 m/s (19 kt); air temperature –5 °C (24 °F).

Falling snow has a median mass concentration of 0.15 g/m^3, with a maximum concentration of ≈2 g/m^3 (ref. 7-21). Snowfall intensity with its liquid equivalent rate is given in table 7-19 as a function of visibility (ref. 7-22).

Table 7-19. Snowfall intensity and rate (liquid equivalent) as a function of visibility (ref. 7-22).

NWS Snow Intensity	Visibility		SAE/NCAR Snowfall Rate (liquid equivalent)	
	km	mi	mm/hr	in/hr
Light	1 or more	5/8 or more	<1	<0.04
Moderate	<1 to 0.5	<5/8 to 5/16	1 to 2.5	0.04 to 0.1
Heavy	<0.5	<5/16	>2.5	>0.10

7.2.7 Hail

Hail is frozen precipitation in the form of balls or irregular lumps of ice that is always produced by convective clouds, nearly always cumulonimbus (thunderstorm clouds), as a result of convective lift. A small ice pellet is lifted into the upper levels of a cumulonimbus cloud where it collides with supercooled water. As this water freezes, layer by layer, it causes the ice pellet to grow in size until it becomes too heavy and falls out of the cloud. If it does not melt by the time it hits the ground it is known as hail. A good current reference on thunderstorms and hail is found in reference 7-23. Section 7.2.7 contains many figures and information obtained from reference 7-24. Hailstone diameter extremes for the United States are given in section 5.1.3.3.

By definition, hail has a diameter of 5 mm (0.20 in) or more and a specific gravity between 0.60 and 0.92. Hailfalls are small-scale areal phenomena, with a relatively infrequent occurrence rate at any given geographical location. The resulting time and space variability of hail is its prime characteristic. Small hail, sleet, and freezing rain are distinguished from hail as follows:

- Small hail—Precipitation in the form of semitransparent round or conical grains of frozen water under 5 mm (0.25 in) in diameter. Each grain consists of a nucleus of soft hail (ball of snow) surrounded by a very thin ice layer. The grains are not crisp and do not usually rebound when striking a hard surface.

- Soft hail (graupel)—Snow pellets, generally 2–5 mm (0.08–0.20 in) in diameter, formed in a convective cloud when supercooled water droplets collide and freeze on impact. Their density averages 0.6 gm/cm^3 (37.5 lb/ft^3).

- Hailstones—A single unit of hail, ranging in size from that of a pea to that of a grapefruit; i.e., from <0.5 cm (<0.2 in) to >13 cm (<5.1 in) in diameter. Hailstones have a mean density of ≈0.8 gm/cm^3 (50 lb/ft^3) .

- Hailstreaks—An elongated area hit by a single volume of hail produced by a convective storm. The dimensions and orientation of the hailstreak are due to movement of the thunderstorm cell.

- Sleet (ice pellets)—A mixture of rain and snow, a mix of rain and hail, or melting snow.

- Freezing rain—Rain that falls in liquid form, but freezes upon impact with cold surfaces to form a coating of glaze upon the ground or on exposed objects.

There are two areas of confusion regarding hail—its definition and the assessment of damage. First is the question of whether snow or ice pellets (often called "small hail") are hailstones. Sleet has also been confused with small hail, but convective cloud origin and size of stone are two factors that separate hail from any other form of frozen hydrometeors. The second area of confusion associated with hail concerns delineating crop loss due to hail. This type of loss often includes damage by wind, either that with the hail or that before or after the hail. The wind-induced damage may be mistaken as damage due to hail.

Standard hail sizes are given in table 7-20.

Table 7-20. Hailstone size scale.

	Diameter	
	(cm)	(in)
B.B., pea, marble*	<1.91	<3/4
Dime*	<1.91	<3/4
Nickel	1.91	3/4
Penny	1.91	3/4
Quarter	2.54	1
Half dollar	3.18	1 1/4
Walnut	3.81	1 1/2
Golf ball	4.45	1 3/4
Hen egg	5.08	2
Tennis ball	6.35	2 1/2
Baseball	6.99	2 3/4
Grapefruit	10.16	4
Softball	11.43	4 1/2

*Not considered severe
Source: NOAA—National Weather Service Forecast Office, Melbourne, FL

7.2.7.1 North American Hail Characteristics. While North American hail data and information are generally sparse, there is much more information available here than for any other location. Hail phenomena studies have generally centered on hailstones, point hailfalls, hailstreaks, hailstorms, hailswaths, and hail days over areas of various sizes.

The principal hail area on the North American continent is located on the lee side of the Rocky Mountains where frequent and intense hail occurs; hailstones tend to be smaller but cause great damage over the Great Plains region. Another high-frequency hail area, related to spring storms, that tends to be larger stones extends from Michigan to Texas. However, less crop damage is observed there because hail activity largely precedes the crop season.

The worldwide hail occurrence pattern is characterized by a greater hail frequency in the continental interiors of the mid-latitudes, with decreasing frequencies seaward, poleward, and equatorward. Most thunderstorm-produced hail is either orographically or frontally induced, although the Great Lakes affect the frequency of hail in that region. There are very few local-type hailstorms away from the mountains. The United States average hail days pattern is shown in figure 7-7, ranging from <1 day up to 9 days (peaking in Wyoming).

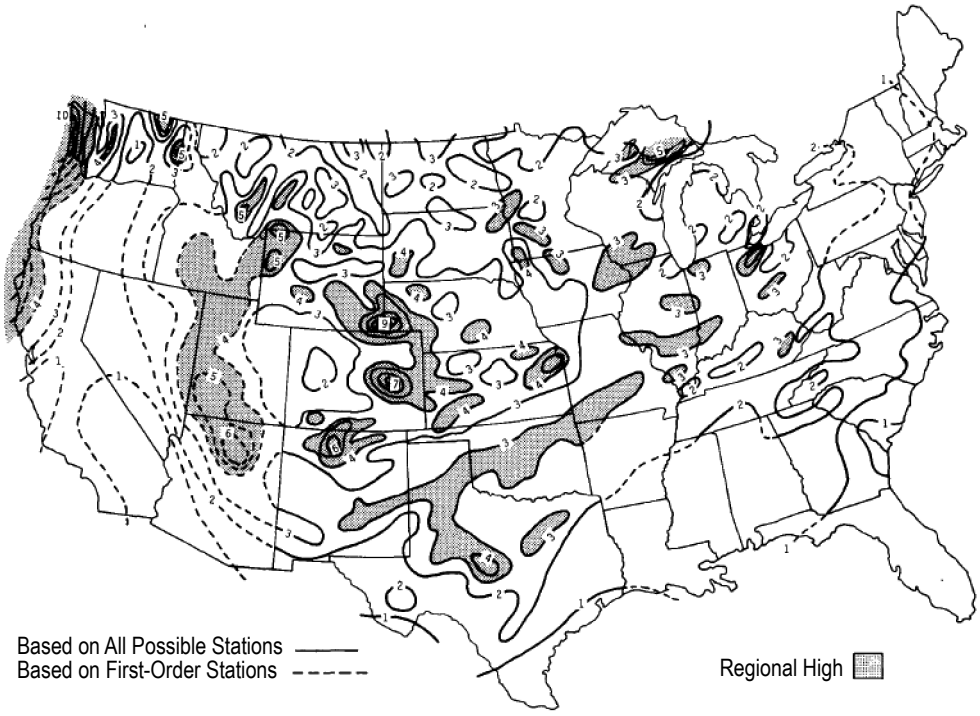

Figure 7-7. Average number of hail days based on point frequencies (ref. 7-24).

Four key hail characteristics—average frequency, primary cause of hail, peak hail season, and hail intensity—were analyzed in order to delineate hail regions within the United States. Figure 7-8 indicates that 14 hail regions exist across the United States, with a marine-effect influence on the West Coast and in the lee of the Great Lakes.

Although most hail is produced by thunderstorms, the special climatologies of hail and thunderstorm differ in some respects. The main difference is that thunderstorms generally exhibit a latitudinal distribution across North America, whereas hail has an intercontinental maxima with frequency decreasing outward in all directions.

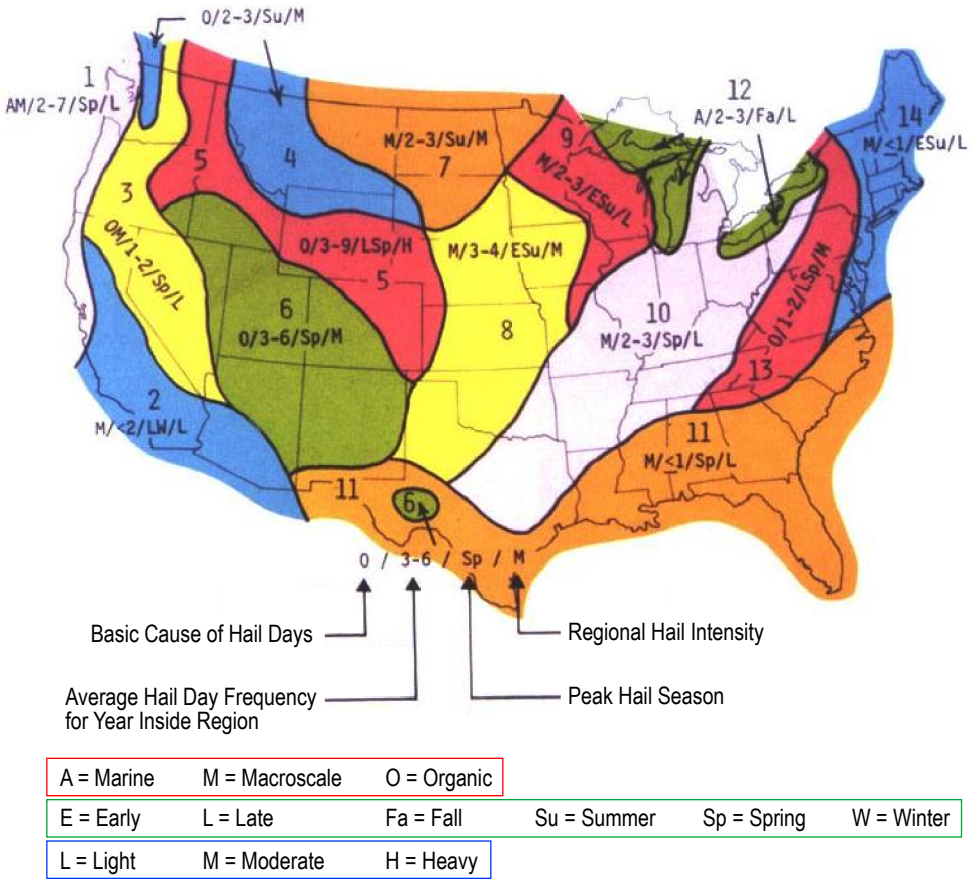

Figure 7-8. Fourteen hail regions of the United States (ref. 7-24).

The "intensity" of hail produces the damage. Intensity is a direct function of the number of stones, their size, and the wind speed. A hail intensity pattern has been developed specifically for potential property loss. The development of this pattern incorporated insurance data, stone size data, and extreme wind frequency data. The hail intensity pattern shown in figure 7-9 indicates a north-south oriented maximum located in the Great Plains region. This is the region of the continental United States in which large hailstones—the major factor in property/crop loss—are most frequent and high winds occur most often.

An important difference between soft hail and hailstones (in the conventional sense) is their density; hailstone density (0.8 g/cm^3 or 50 lb/ft^3) is close to ice (0.92 g/cm^3 or 57.4 lb/ft^3). The damage can be computed from the stone's kinetic energy. The density of soft hail is close to 0.60 g/cm^3 (37.5 lb/ft^3).

Since hailstone sizes as well as the number of stones are important to intensity, size distributions help account for regional differences. Hailstone sizes have not been systematically measured throughout the United States, but small-area studies have provided some information. Figure 7-10 indicates that the greatest frequency of large stones is found in the lee of mountain localities like Colorado. Small hailstones dominate in Illinois, New England, and mountain-top areas of Arizona. An Illinois hailfall averages 24 stones per hailpad (930 cm^2 or 1 ft^2), and only ≈2 percent of these are more than 1.3 cm (0.5 in) in diameter. In northeast Colorado, a hailfall averages 202 stones per hailpad, and more than half (51 percent) of these are larger than 1.3 cm.

The season of greatest hail activity varies across the country. East of the Great Plains, maximum hail activity occurs in the spring months, starting in March in the far south and in May in the northern states. In the

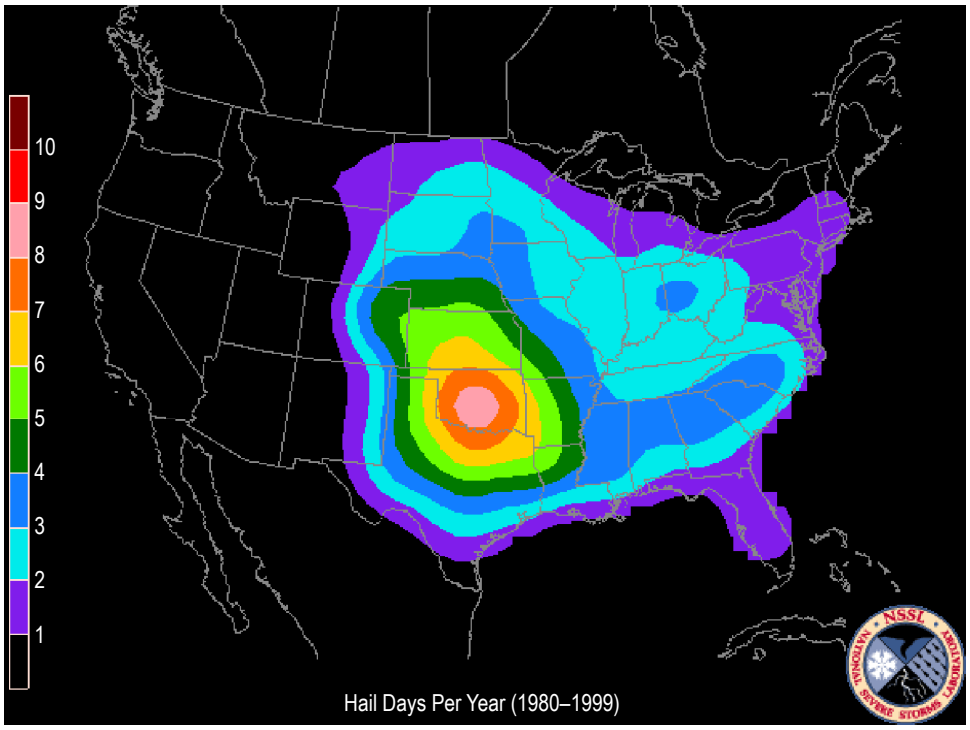

Figure 7-9. Twenty-year (1980–1999) U.S. average number of hail days per year (with hail ≥1.9 cm (≥¾-in) diameter) within an 80-km- (50-mi-) grid square (source: NOAA/NSSL).

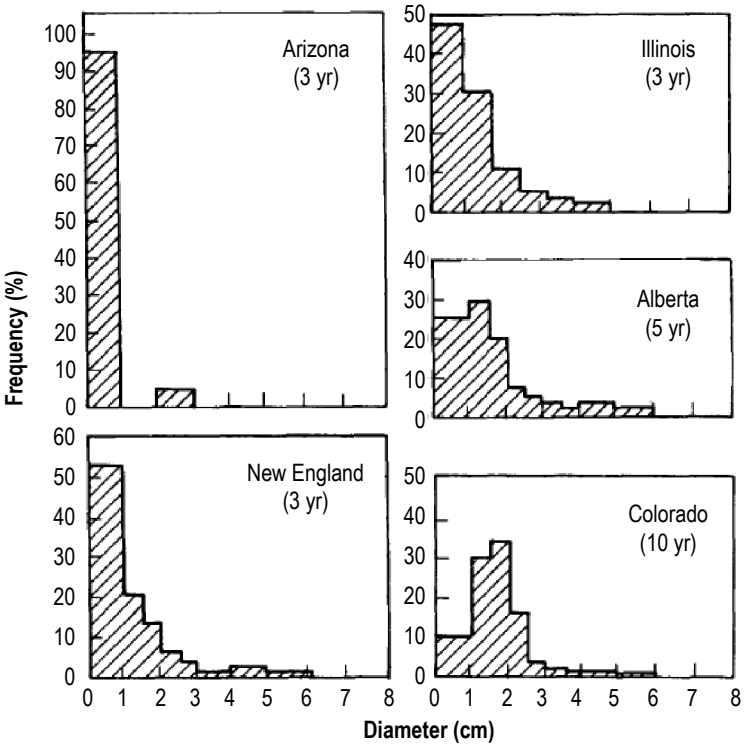

Figure 7-10. Frequency distributions of maximum hailstone sizes reported from many hailfalls at different locales (ref. 7-24).

lee-of-the-mountain states, maximum hail activity occurs in the summer months. The Great Lakes area is the only place in North America where maximum hail occurs in fall months. Along the West Coast, certain areas have maximum hail in late winter or spring.

In large areas such as Iowa, Illinois, or Colorado, hail occurs on ≈70 percent of all days with thunderstorms. In the Midwest, 50 percent of all thunderstorms connected with warm fronts and low pressure centers produce hail, but 75 percent of the thunderstorm days associated with cold fronts or stationary fronts are hail days.

Hail may also be accompanied by moderate to heavy rainfall, tornadoes, or damaging wind. Crop-damaging hailstorms in Nebraska, Colorado, and Kansas are generally associated with moderate rains of 0.2 to 1 in (0.5 to 2.5 cm), and 25 percent of the rain through the entire crop season falls with damaging hail. Hail days in Illinois typically have rainfall so heavy it averages nearly half (48 percent) of the monthly average. There have been cases where hailstones, falling at the same time or immediately before heavy rains, have blocked drains and downspouts, preventing much of the rain runoff from flat roofs and thereby causing roof collapse from the weight of the rainfall and hail (ref. 7-25).

A study of tornadoes in Illinois shows that major large tornadoes—those having tracks longer than 40 km (>25 mi)—always have hailfalls somewhere near their track. During 1951 to 1960, nearly 96 percent of the 103 tornado days in Illinois were also hail days, and 12 percent of all hail days in Illinois were tornado days as well.

Damaging wind with hail is another critical factor in crop loss, and the Illinois studies show that wind-blown hailstones occurred in 60 percent of all hailfalls. Whenever this happens, an average of 66 percent of the hailstones at any one point are windblown.

7.2.7.1.1 Hailfall Duration. The duration of hailstorms is also variable. The average duration of hail near the mountains is 10 to 15 min, while in the Midwest it is 3 to 6 min. Hailstreaks, which have a median size of 20.7 km^2 (8 mi^2), last an average of 10 min. A hailstreak is an area hit by a single volume of hail produced in a storm. A single storm may produce one or many hailstreaks. Reference 7-26 presents mean hail durations in the United States of between 5 and 10 min, while maximum hail durations worldwide have ranged from 20 min to 90 min.

7.2.7.2 Global Hail Characteristics. Dai (ref. 7-27) analyzed three hourly synoptic weather reports from ≈15,000 stations and ships from 1975 to 1997. Figure 7-11 presents the Dai results of the average annual number of hail days globally. It shows that hail, including small hail associated with thunderstorms, is more common at middle and high latitudes than at low latitudes. Hail days are most frequent over the North Atlantic up to 40 days/yr) and North Pacific (15–20 days/yr), whereas, hail rarely occurs over low-latitude warm oceans (≤1 day/yr). Hail is also frequent over the Qinghai-Tibet Plateau and the Indian subcontinent, western Canada, and western tropical Africa (5–10 days/yr). Winter and summer seasonal hail days maps are also available globally, as are global thunderstorm days maps (ref. 7-27).

7.2.7.3 Kennedy Space Center Hail Storm Damage. Severe thunderstorms can produce hail which can hit and possibly damage a launch vehicle, a launch component, or ground support equipment (GSE) if that item is not protected. Hail impact to the external tank's (ET's) outer foam insulation poses no threat to the ET's structural integrity, but there is the likelihood that ice could form inside the hail-produced divots once the tank is loaded with super-cold propellants and possibly impact the orbiter during ascent. NASA's Shuttles have been struck five times while at the launch pad, or outside the VAB, while undergoing preparation for launch. Four of these Shuttle examples follow. It appears from these occurrences that about once in every 8 to 9 yr the Shuttle has been damaged by hail on the pad.

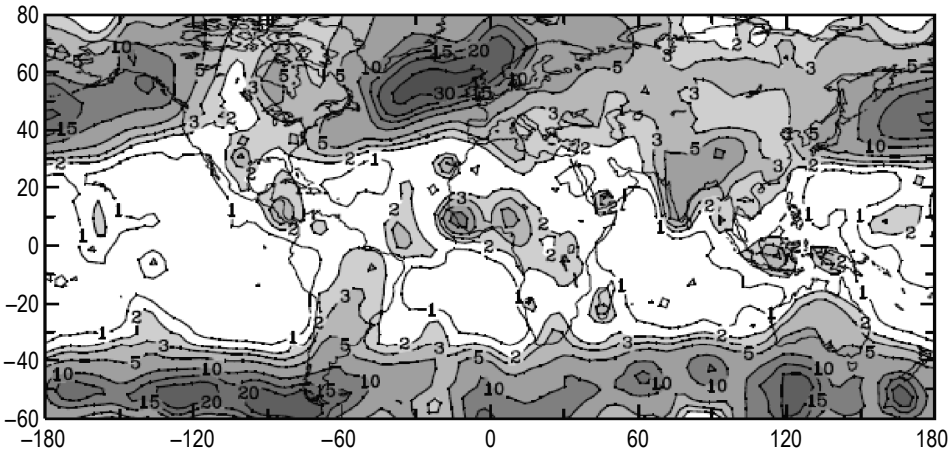

Figure 7-11. Average annual number of hail days globally (ref. 7-27).

The Space Shuttle *NSTS 07700,* Volume X, hail requirement 3.1 (ref. 7-28) is stated as follows: "It shall not be necessary to consider the environmental effects of hail as specified in *NASA TMX-64757* in the structural design of the ET, Orbiter, or SRB, except that the Orbiter shall have capability to withstand hail impact (crew safety) on the windshield during the landing phase. Specified hail criteria shall, however, be retained for scheduling considerations, design of GSE, and Shuttle flight element protective covering" (ref. 7-29).

7.2.7.3.1 Kennedy Space Center Shuttle Hail Damage Examples. Over a 25-yr time period (1982–2007), the Space Shuttle vehicles have experienced hail damage at least four times while exposed to the environment:

(1) STS-117 (February 26, 2007)—The STS-117 *Atlantis* Shuttle was hit by wind-driven, golf ball-sized hail from a thunderstorm while on the launch pad. Damage included 1,000–2,000 divots in the ET's foam insulation and minor damage to ≈26 heat shield tiles on the Shuttle's left wing. Figure 7-12 shows the damage that occurred. STS-117 had to been rolled back to the VAB for repair, causing an extended launch delay.

Figure 7-12. STS-117 ET hail damage, February 2007.

(2) STS-96 (May 8, 1999)—The upper portion of the *Discovery* STS-96 ET was also hit by hail while on the pad. The orbiter and solid rocket boosters (SRBs) were not damaged. *Discovery* was then rolled back to the VAB, and inspections indicated ≈728 hail impacts on the ET TPS needed repair. This caused a 1-wk delay on scheduled launch.

(3) STS-38 (August 1990)—During the rollback of STS-38 *Atlantis* for a hydrogen fuel leak fix, the *Atlantis* vehicle, while parked outside the VAB about a day, suffered minor hail damage to tiles during a thunderstorm.

(4) STS-4 (June 1982)—The STS-4 *Columbia* orbiter was damaged by hail while on the pad the night before launch, but not the ET or SRB. Hail extensively damaged the orbiter's surface TPS tiles. Some of the damage on the right wing was repaired on the pad with a densification slurry prior to launch. Water absorption to the tiles from the rain storms also occurred.

7.2.7.3.2 Further Shuttle Hail Questions and Answers. The following three questions/answers about Shuttle ET hail damage arose after the 1999 Shuttle hail incident:

(1) Hail density—How much does it vary? (The *NASA Handbook 1001* (ref. 7-30) only gives one value, but no range.)

Answer: The value of 0.9 g/cm^3 given in the *NASA Handbook 1001* originated from the following paragraph taken from the Air Force *Handbook of Geophysics and the Space Environment* of 1985 (ref. 7-31, sec. 16.2.2): "The density (weight per unit volume) of hailstones is a variable with little documentation. For some large, natural hailstones in several storms in the mid-western United States, estimates ranged from 0.828 to 0.867 g/cm^3. Hence, a rounded value of 0.9 g/cm^3 is deemed acceptable in calculations of impact energy."

(2) Hail impact angle—Does it depend on the vertical wind profile? If so, how much?

Answer: The question is, how much horizontal velocity is imparted by the wind to the hail. The answer can only be stated qualitatively: The hailstone essentially integrates the force of the wind which is a highly variable quantity along the path of the hailstone. We must also assume that the hailstone is fully mature and well below the turbulent cloud that produced it.

Hail impact angle can be estimated from the velocity vectors formed by the terminal velocity (vertical component) and the horizontal wind-induced hail velocity attributed to the horizontal wind (integrated over the local vertical) (ref. 7-32). The terminal velocity (*VT*) can be estimated from equation (7.3):

$$VT = k\sqrt{D} / 100 \ , \tag{7.3}$$

where *VT* is in m/s, *D* is in cm, and the best estimate of *k* is 1,630 (ref. 7-31); thus, for $D = 2.54$ cm (1 in), $VT = 25.98$ m/s.

Assuming that the horizontal component of the hail velocity is equivalent to the vertically integrated local horizontal velocity of the wind (say within tens of meters above the ground or above the point of impact), then the angular deviation (*A*) of the hailstone velocity from the vertical is

$$A = \arctan (\mathrm{WS}/VT) \ . \tag{7.4}$$

Thus, for a 2.54-cm (1-in) hail diameter and a wind speed of 25.98 m/s (50.5 kt), $A = 45$ deg; similarly, for a wind speed of 12.99 m/s (25.25 kt), $A = 26.56$ deg.

From this rather primitive analysis, we conclude that wind speed can affect hail impact angle. However, the affect is more "local," say within tens of meters from the impact point.

Figure 7-13 illustrates angular deviation from the vertical as a function of hailstone diameter and various wind speeds. There are other factors, such as local turbulence, that could contribute to uncertainty of these estimates.

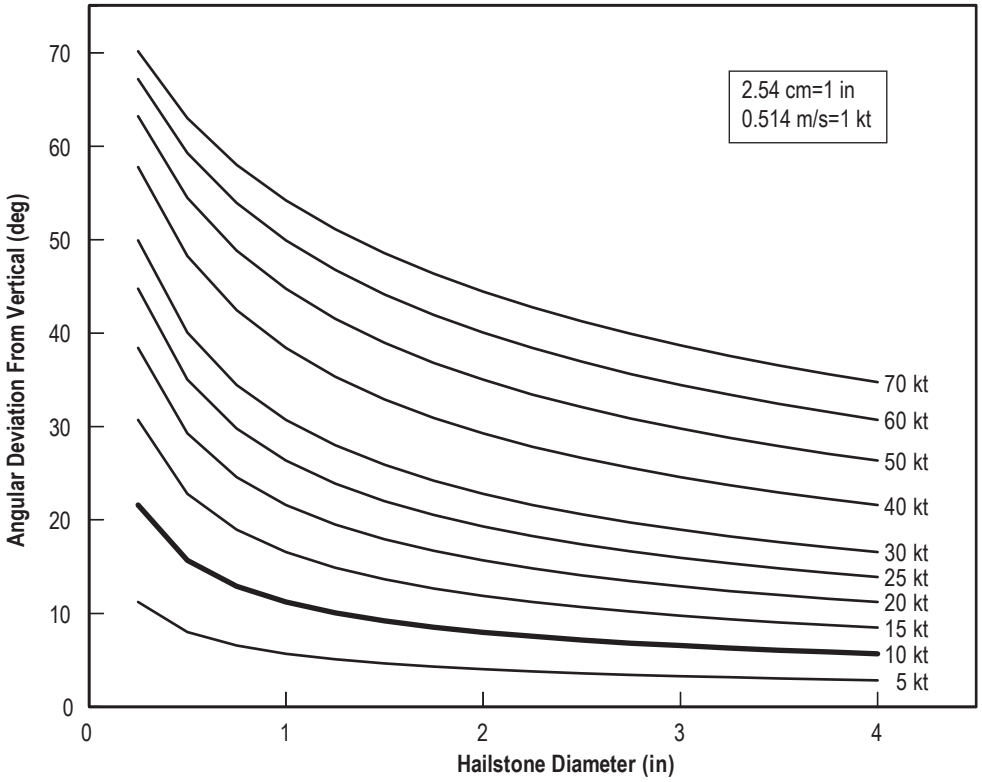

Figure 7-13. Angular deflection of hail from the vertical given hailstone diameter and wind speed (ref. 7-32).

(3) Hail size—How much does hail size vary with horizontal distance? The ET is 73 m (240 ft) in diameter. If you have a point measurement at the top of the ET, how much might hail size vary on the sides of the ET?

Answer: It is reasonable to assume that there is no significant variation within the dimensions of the vehicle with regard to the natural hail input. However, there could be local vehicle and pad structure-induced aerodynamic affects that either concentrate or dilute hail impacts on critical vehicle structures.

7.2.7.4 Surface Hail Statistics at NASA Facilities. An estimate of hail characteristics has been made at selected space vehicle development and test locations. Figures 7-14 through 7-16 and table 7-21 give estimated hail characteristics for KSC, VAFB, EAFB, WSMR, Northrup Strip, Marshall Space Flight Center (MSFC), and

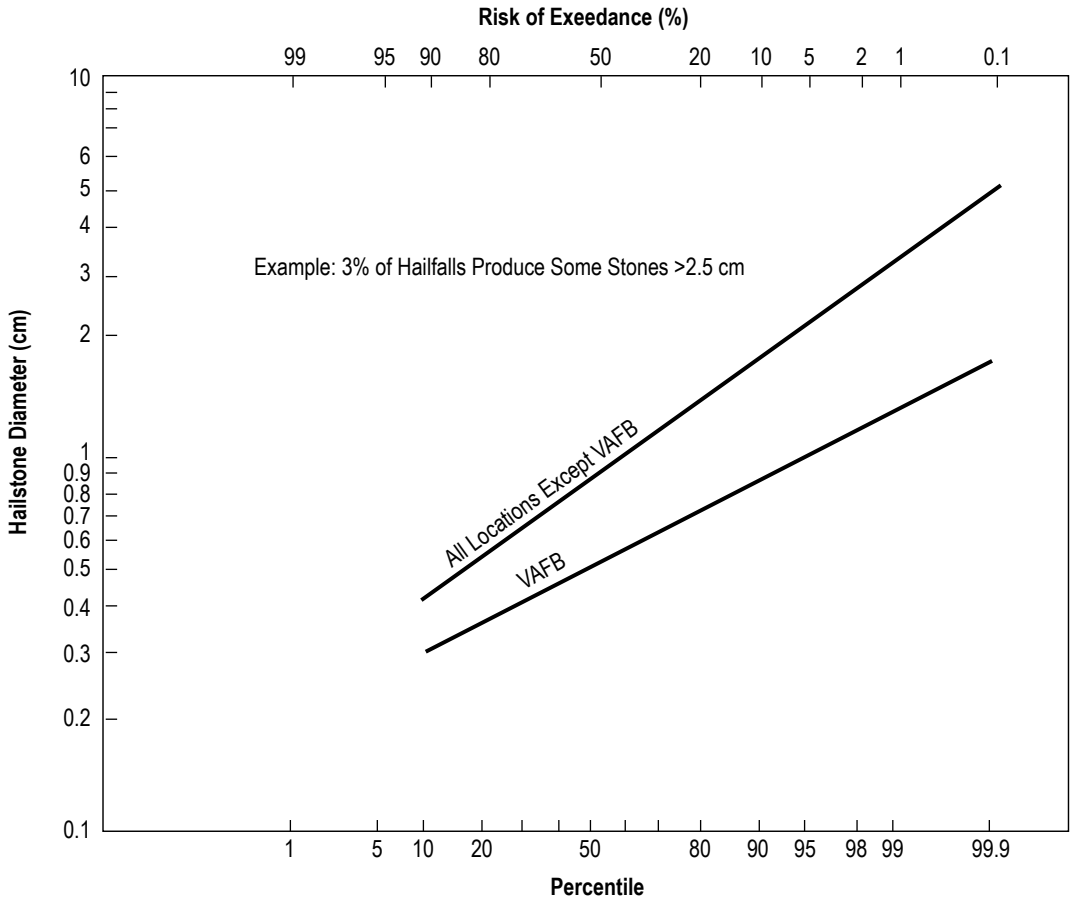

Figure 7-14. Probability curve for maximum hailstone size per hailfall.

Stennis Space Center. Since no direct measurements, except for the number of hail days, exist for these locations, for design purposes, all other items were estimated from Illinois hailpad measurements reported by Changnon (ref. 7-24). Hail characteristics estimated for use in evaluating hail protection needs and requirements are:

- Hailstone size—Figure 7-14 gives the risk in percent of a point hailfall producing stones larger than indicated sizes. For example, only 3 percent of the hailfalls at KSC will produce stones larger than 2.5 cm (1 in), while 50 percent will produce some stones larger than 0.9 cm (0.35 in).

- Hailstone terminal velocity—The general expression for the terminal velocity of a sphere is given in reference 7-4. However, for quick calculations, the best estimate of hailstone terminal velocity, as reported by several investigators, is given by the expression:

$$W = K\sqrt{D} \ , \tag{7.5}$$

where

W = terminal velocity (m/s)
D = hailstone diameter (cm)
K = 11.5.

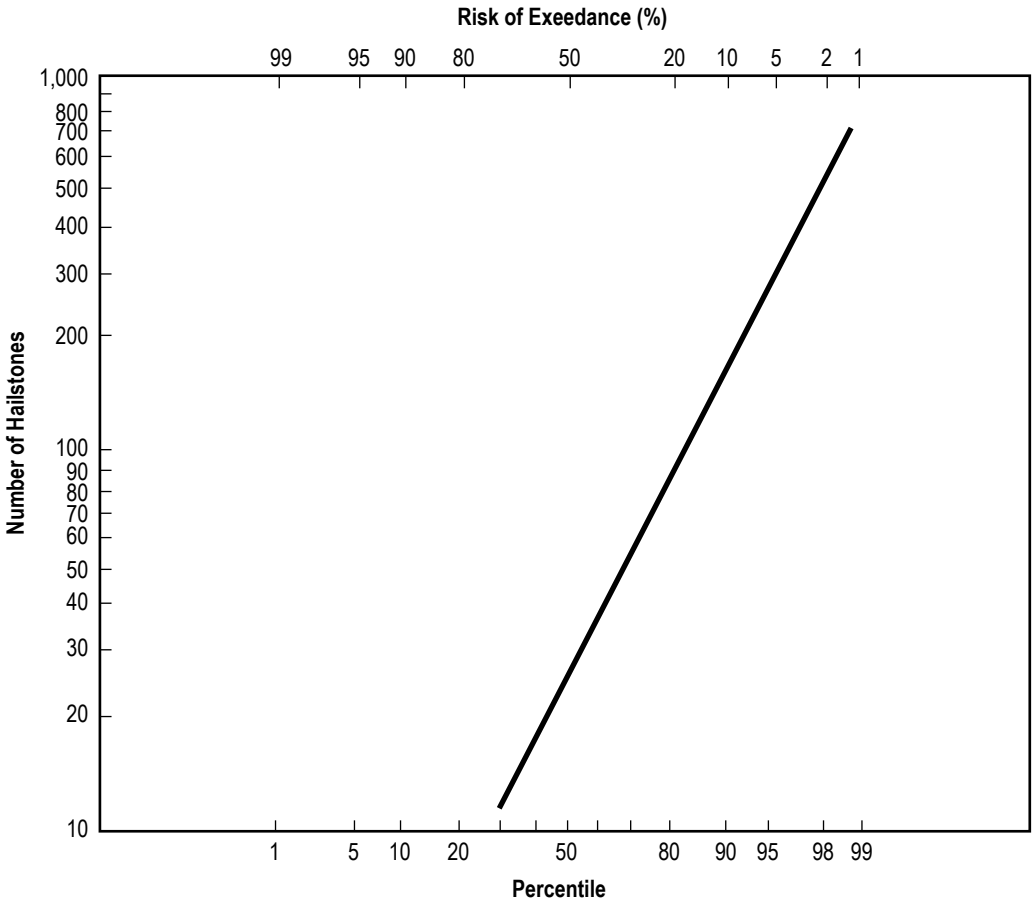

Figure 7-15. Probability curve for the number of stones impacting a 0.09-m^2 (1-ft^2) hailpad per hailfall.

Figure 7-17 gives an estimate of the hailstone terminal velocity and impact kinetic energy impact as a function of hailstone size (ref. 7-33).

- Number of hailstones per hailfall—Values used for space vehicle locations were taken from Illinois measurements which showed that hailfalls average 24 stones/hailpad 0.09 m^2 (1 ft^2) and that only 5 percent of the storms produced more than 300 stones per hailpad 0.09 m^2 (1 ft^2). These numbers were used to prepare figure 7-15.

- Horizontal velocity of hailstones—These values (fig. 7-16) were derived from peak wind speed distributions for each space vehicle location. These wind speeds may be different from other Shuttle design values because only hail season winds were used rather than the windiest period concept.

- Density of hailstones—A generally-accepted average value for the density of hail at all locations is 0.80 g/cm^3 (50 lb/ft^3) (ref. 7-1).

- Recommended procedures for evaluating protection requirements:

  – Use 50-percent values for stone size and number of stones.
  – Use 5-percent risk horizontal wind speeds.
  – Calculate risk of experiencing a hailfall during a specified continuous exposure period from:

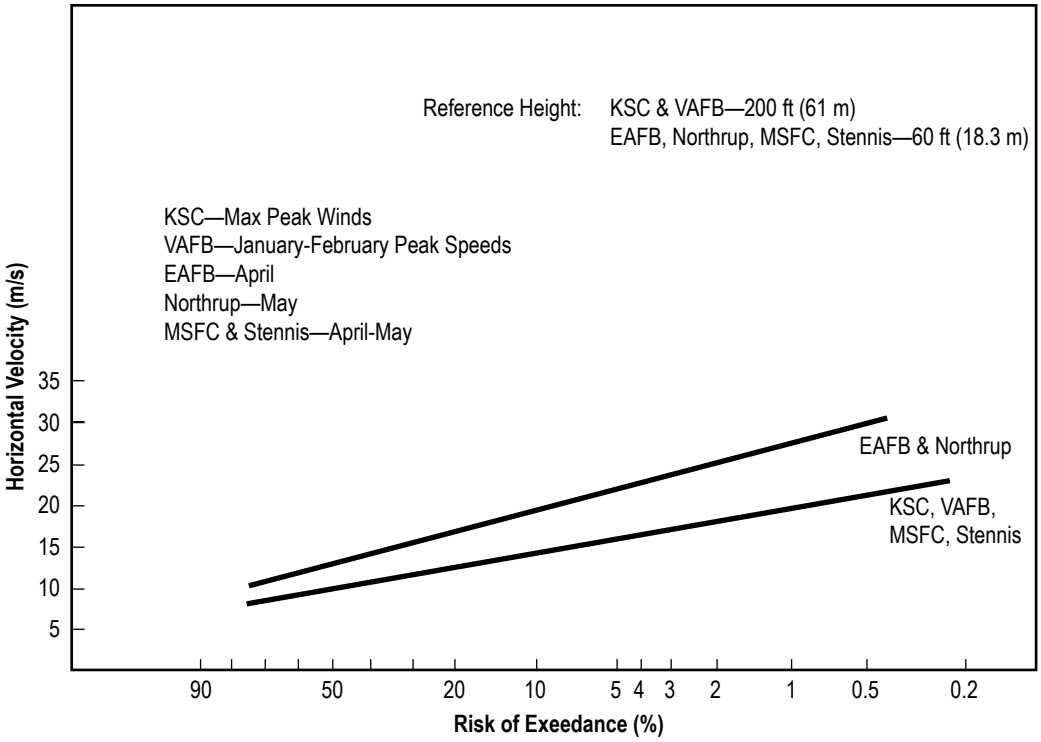

Figure 7-16. Probability exceedance curve for horizontal hailstone velocity.

Table 7-21. Estimated hail characteristics at selected space vehicle locations.

Estimated Hail Characteristics	KSC	VAFB	EAFB	Northrup	MSFC	Stennis
Exposure time risk						
Worst month reference period (%)	1	8	5	12	17	3
Worst 6 months reference period (%)	7	41	25	53	67	18
Mean number of hailstorm days per year	0.1	1.1	0.6	1.5	2.2	0.4
Average point of duration of hailfall (min)	5	5	5	5	5	5
Average number of hailstones per hailpad (1 ft^2)	24	24	24	24	24	24
Average density of hailstones (g/cm^3)	0.8	0.8	0.8	0.8	0.8	0.8
Size-diameter and terminal velocity						
Representative size (50-percent risk) (cm)	0.9	0.5	0.9	0.9	0.9	0.9
Terminal velocity (m/s)	11	8	11	11	11	11
Large size (5-percent risk) (cm)	2.2	1.0	2.2	2.2	2.2	2.2
Terminal velocity (m/s)	17	11.5	17	17	17	17
Horizontal velocity—all directions*						
Mean speed (m/s)	9	9	13	13	9	9
5-percent risk speed (m/s)	15	15	22	22	15	15
Months of max frequency	May	Jan–Feb	Feb–Apr	May–July	April	Apr–May
Period of record (yrs)	22	20	28	30	9	28

*KSC and VAFB reference height = 61 m (200 ft). All others = 18 m (60 ft).

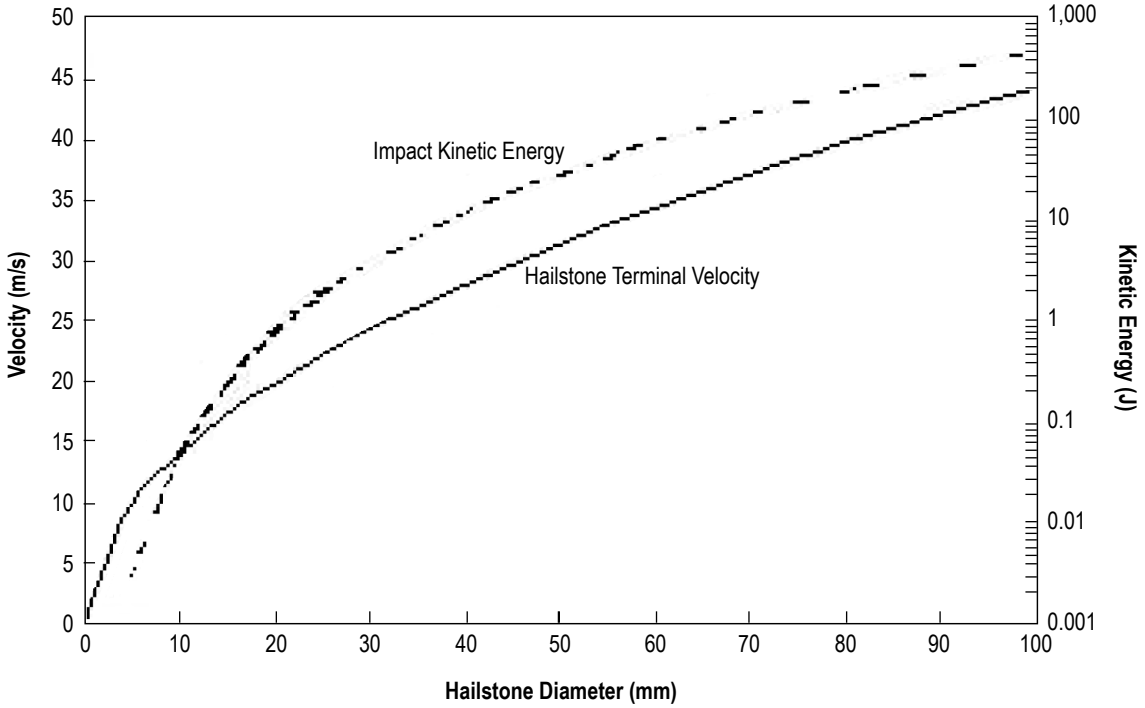

Figure 7-17. Terminal velocity and kinetic energy impact of hailstones (ref. 7-33).

$$\text{Risk} = 1 - e^{-\lambda t} \quad , \tag{7.6}$$

where

λ = mean number of independent hailstorm days per year
t = exposure time in years.

Various estimated hail characteristics at selected NASA-associated space vehicle operation locations are given in table 7-21. Maps of hail occurrences near various NASA sites are presented in section 12.7.

7.2.7.4.1 Kennedy Space Center Hail Statistics. After the STS-96 Shuttle hail damage incident in 1999, various KSC-related hail statistics were assembled by MSFC and KSC using data available at that time (ref. 12-34). These local KSC hail statistics are summarized and presented in table 7-22. Table 7-22 merely indicates that, based on annual hail statistics, as the area of interest gets smaller, the probability of hail events in that area also gets smaller. However, if worst-month statistics are considered, then the probabilities do go up, as indicated in table 7-22.

Figure 7-18 was generated by S. Adelfang (internal MSFC study) for the 1999 ET hail analysis, using Brevard County, FL, hail statistics—only for hail ≥1.9 cm (≥0.75 in). There were 34 large hail events occurring over the 26-yr period (1970–1995) in which hail ≥1.9 cm (≥0.75 in) fell in Brevard County. This is reflectant of the 1.3 hailfalls/yr value given in table 7-22. A hail event is defined as occurrence of hail size (≥1.9 cm) (≥0.75 in) at one or more locations within 1 hr.

Table 7-22. Local KSC hail statistics (ref. 7-34).

Area	Location	Source	POR	No. Years	No. Hailfalls/yr.	One Hailfall Event (in years)
County	Brevard Co.	MSFC	70–95	26	1.3*	0.77
Area	CCAS/KSC	KSC	94–99	6	1.0	1.00
Point	SLF (worst mo**)	NCDC	78–88	11	2.19 (0.6% of days)	0.46
Point	SLF (annual)	NCDC	78–88	11	0.37(0.1% of days)***	2.74
Pad-Pt.	LC39	KSC	82–99†	17	0.11	9.00

*Brevard Co., FL, hail statistics from 1970–1995 (26 yr) reflect only when hail was ≥1.9 cm (≥0.75 in); therefore, "all" hail would give higher statistics.
**Worst month from NCDC/SOCS is April and May.
***Matches KSC's SLF value for annual.
†Time from STS-4 to STS-96.

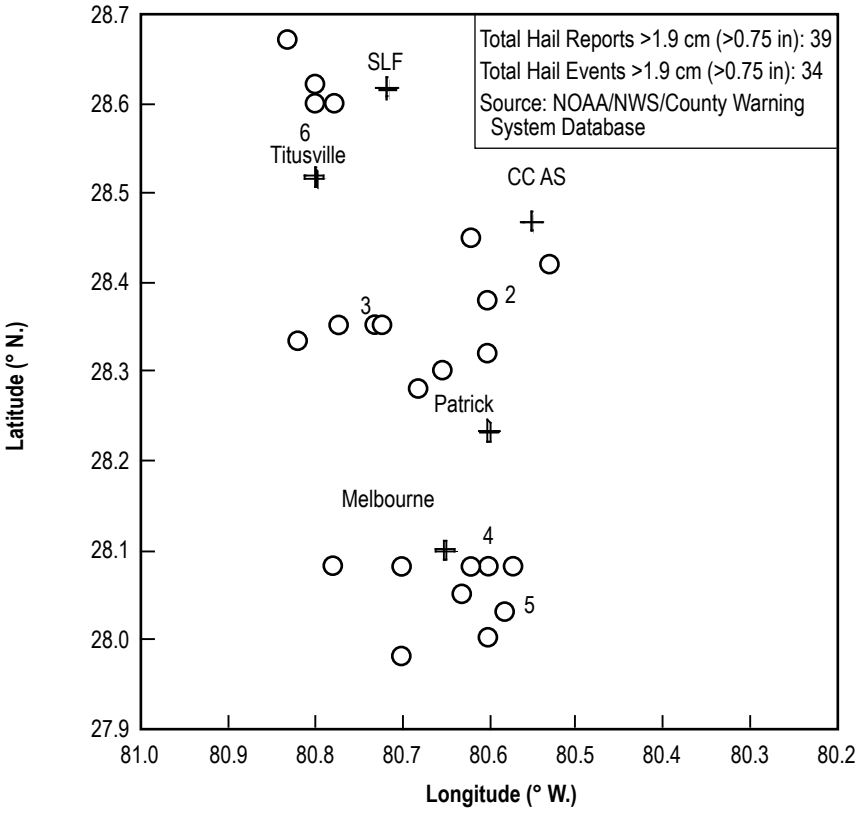

Figure 7-18. Location of reported hail ≥1.9 cm (≥0.75 in) in Brevard County, FL, from 1970–1995 (ref. 7-32).

A breakdown of these large hail events by hour and month were calculated. Ninety-one percent of all large hail events occurred within the 5-mo period from March through July. Likewise, for all months, the hours 1 p.m.–4 p.m. EST garners 59 percent of all events, while from 1 p.m.–8 p.m. EST encompasses 88 percent of all large hail events within the County. If one looks at only the 5-mo hail season period, only for the hours from 1 p.m.–8 p.m., this encompasses 79 percent of the yearly large hail events in Brevard County.

The actual locations of these 39 Brevard County hail reports (of hail ≥1.90 cm (≥0.75 in)) associated with the 34 large hail events are displayed in figure 7-18. The size of hail is generally smaller along the KSC coastal area and larger inland.

7.2.7.4.2 Kennedy Space Center Hail Probability. Figure 7-19 presents the daily average of the probability of hail at KSC.

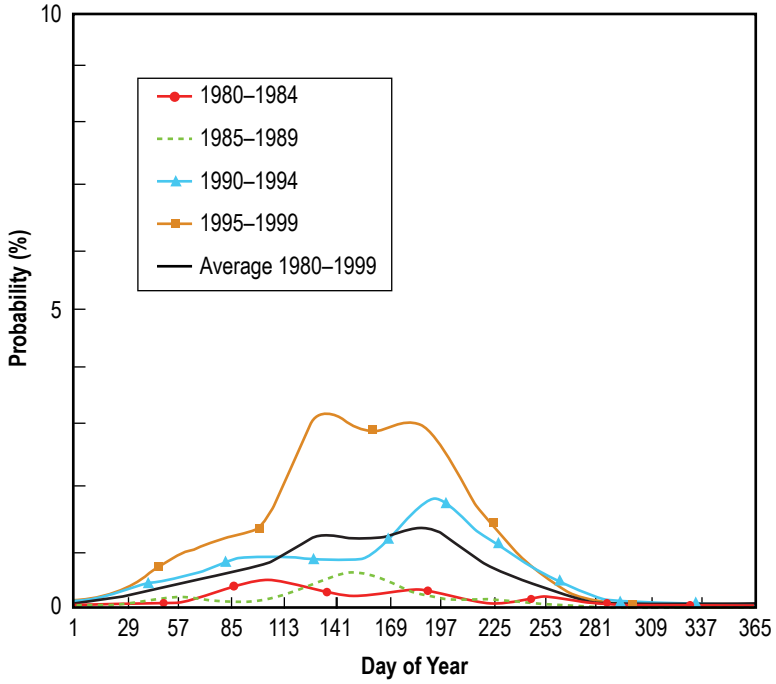

Figure 7-19. KSC 20-yr and various 5-yr averages of the probability of hail on any given day at KSC (source: NOAA/NSSL).

7.2.7.4.3 Kennedy Space Center Pad Hail Probability. The occurrence probability of damaging hail size for KSC is given below for various diameter sizes of hail. If hail size is:

≥0.64 cm (≥0.25 in) = 80 percent (damaging)
≥0.89 cm (≥0.35 in) = 50 percent
≥1.90 cm (≥0.75 in) = 10 percent
≥2.54 cm (≥1.00 in) = 2 percent.

To calculate an example of the KSC pad annual damaging hail probability, the following can be assumed:

(1) Shuttle is on pad for 8 mo (2/3 yr).
(2) Damaging hail probability is 80 percent (of hail occurrences).
(3) Pad probability of hail is 0.37.

Therefore, the annual probability of damaging hail (≥0.64 cm (≥0.25 in)) when the Shuttle is on the pad is:

$$P = P\,(\text{hail}) \times P\,(\text{damaging hail if hail occurs}) \times P\,(\text{Shuttle on pad}) = 0.37 \times 0.80 \times 0.67 = 19.8 \text{ percent.} \quad (7.7)$$

7.2.7.5 Hail Distribution With Altitude. Although it should not be the practice to design space vehicles for flight in thunderstorms, data on hail distribution with altitude are presented as an item of importance. In general, the probability of hail increases with altitude from the surface to ≈6 km (≈19,700 ft) and then decreases rapidly with increasing height. Data on hailstone size versus altitude, with a 0.1-percent encounter probability while enroute aloft for 322 km (200 mi), in the worst month, worst area, are given in table 7-23 (ref. 7-35). When including thunderstorm data from several areas, investigators have estimated probabilities of encountering hail versus altitude, as presented in table 7-24 (ref. 7-36). This supports the general shape of the vertical distribution. Further, it appears expedient to assume that any level between 3 and 6 km (≈9,800 and 19,700 ft) can become one of maximum hail concentration at any one time.

Table 7-23. Estimate of hailstone size equaled or exceeded, with a 0.1-percent probability of encounter by an aircraft while enroute aloft for 322 km (200 mi), in most severe month and area (ref. 7-35).

Altitude		Estimate of Hailstone Size	
(km)	(ft)	(cm)	(in)
1.5	4,921	1.2	3.1
3.0	9,843	2.4	6.1
4.6	15,092	2.4	6.1
6.1	20,013	2.4	6.1
7.6	24,934	1.9	4.8
9.1	29,856	1.7	4.3
10.7	35,105	1.5	3.8
12.2	40,026	1.1	2.8
13.7	44,948	0	0

Table 7-24. Estimates of the probability of encountering hail of any size at a single-point location by altitude (ref. 7-36).

Altitude		
(km)	(ft)	Probability
Ground level	Ground level	0.000448
1.5	4,921	0.000448
3.0	9,843	0.00314
4.6	15,092	0.00314
6.1	20,013	0.00314
7.6	24,934	0.00134
9.1	29,856	0.00100
10.7	35,105	0.00067
12.2	40,026	0.00034
13.7	44,948	0.000

7.2.7.6 Hail Liquid Concentration With Altitude. Extreme rain and hail conditions have caused engine rundowns during commercial airplane flights. This subsection quantifies the rain and hail threat in terms of the probability of encountering a storm of a given intensity (concentration). Included are recommended hail and rain liquid water concentration levels that can be used for design and certification of turbine engines. The probability and the magnitude of the worst-case hail (and rain) aloft situation, in terms of the liquid water content, is presented in figures 7-20 and 7-21, respectively (ref. 7-33).

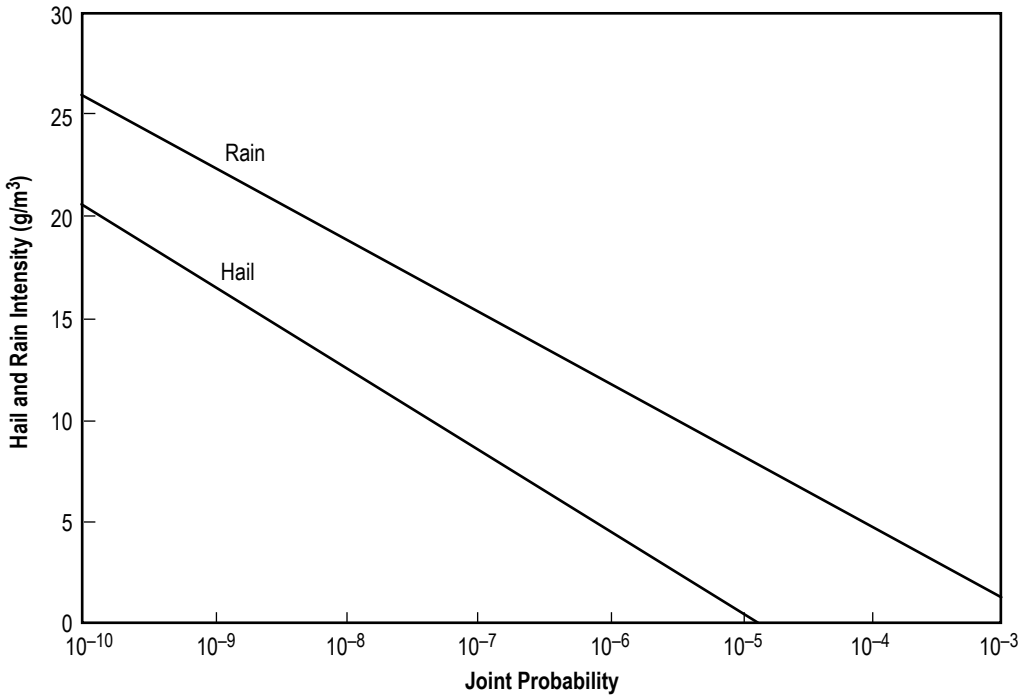

Figure 7-20. Probability of hail and rain intensity (in terms of water content (g/m^3)) (ref. 7-33).

Hail and rain intensity (M) levels are defined here in terms of hail water content and liquid water content, as a function of the probability. This represents the probability of a hail or rain storm occurring at a location at a given intensity level. The intensity levels apply at a single point in the worst known location for rain and hail conditions; i.e., the curves describe the likelihood of rain or hail of a given intensity occurring at the location in the world most likely to have that intensity (ref. 7-33).

Equation (7.8) can be used to convert rain rate (R) (mm/hr) into liquid water content (M) (g/m^3) (ref. 7-26):

$$M = 0.62R^{0.913} \quad . \tag{7.8}$$

7.3 Fog

7.3.1 Fog Introduction

Fog is a visible aggregate of minute water droplets suspended in the atmosphere near the Earth's surface, or a cloud in contact with the Earth's surface. Fog is responsible for reducing visibility to <1 km (0.62 mi) and down to zero. Fog is classified as either warm or supercooled, depending on whether the ambient temperature

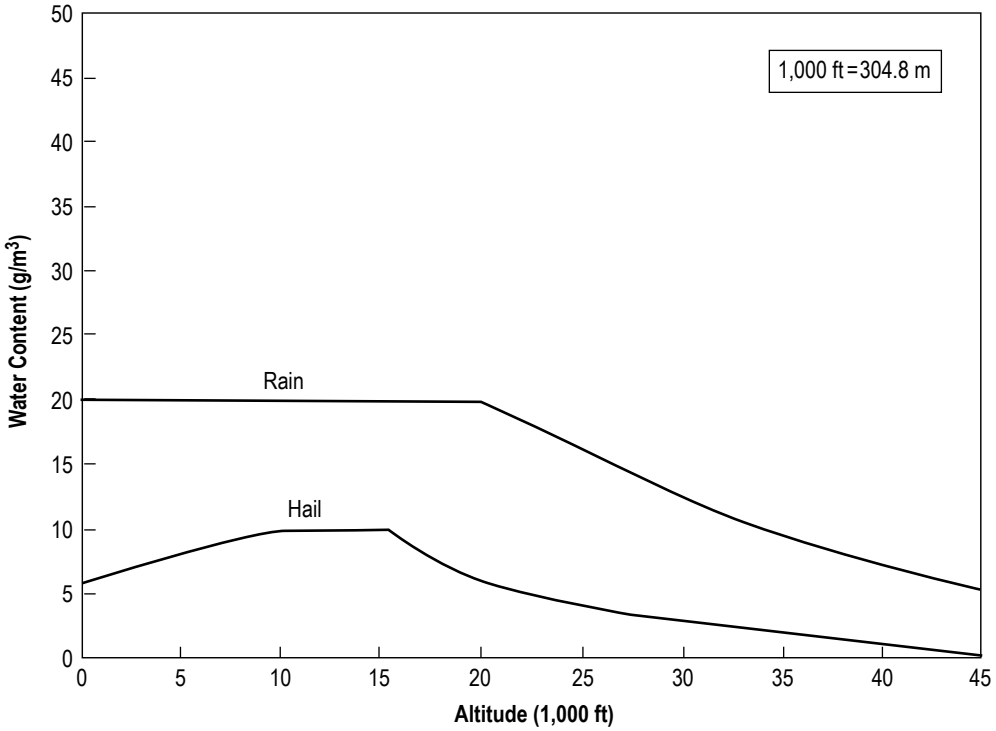

Figure 7-21. Recommended hail and rain values for turbine engine certification. The curves represent hail (or rain) water content (g/m^3) occurring at a single point at a worst known location for hail (or rain) conditions (adapted from ref. 7-33).

is above or below 0 ºC. Figure 7-22 shows the Space Shuttle vehicle *Challenger* during the December 8, 1982, STS-6 rollout to launch pad 39A in a fog environment. Fog definitions are based on reference 7-1.

Figure 7-22. Shuttle *Challenger* rollout to pad in fog (NASA).

Fogs are formed either by cooling the air until the water vapor condenses or by adding additional water vapor into the air which then condenses. The conditions most favorable for the formation of fog are high relative humidity, light surface winds, ground temperature colder than that of the air, and no clouds. Condensation nuclei are very abundant everywhere. Fog occurs more frequently in coastal areas than in inland areas because of an abundance of water vapor.

7.3.2 Fog Types

Fog types include (1) radiation fog, (2) advection fog, (3) up-slope fog, (4) frontal fog, (5) steam fog, (6) ice (crystal) fog, and (7) salt fog. A brief description of each fog type follows:

(1) Radiation fog forms over land on clear nights when the Earth loses heat very rapidly to the atmosphere (radiational cooling), and the air temperature falls to or below its dewpoint so that condensation occurs. If the wind is calm, the fog will be very shallow or will be reduced to a dew or frost deposit. If winds are present ≈2.6 m/s (≈5 kt), then the fog will thicken and deepen. These fogs do not occur at sea since the sea surface does not cool as the land does. Ground fog is usually a radiation fog with a depth of <6 m (<20 ft), whereas a shallow ground fog has a depth of <2 m (<6 ft).

(2) Advection fog is caused by the movement (advection) of mild, humid air over a colder surface, and the consequent cooling of that air to below its initial dewpoint. These fogs occur in coastal areas because the moist, warm air moves inland over the colder land in the winter. In summer, the warm, moist air may be carried out to sea, where it forms a fog over the cool water (sea fog), usually due to a cold ocean current, and then the sea breeze advects the fog inland. These summer fogs are common along the coast of California.

(3) Up-slope fog forms when stable, moist air moves up sloping terrain and is adiabatically cooled by expansion to or below its original dewpoint. This cooling produces condensation, and fog forms. An up-slope wind is necessary for the formation and maintenance of this type of fog.

(4) Frontal fog is associated with frontal zones and frontal passages. Three types of frontal fog are as follows: (1) Warm-front prefrontal fog, (2) cold-front, postfrontal fog (where rain falls into cold, stable air and raises the dewpoint temperature), and (3) frontal-passage fog (mixing of warm and cold air masses in the frontal zone, or by sudden cooling of air over moist ground).

(5) Steam fog forms by the movement of cold air over a warmer water surface. The water evaporating from the surface condenses in the colder air, forming fog. Steam fog rises from the surface of lakes, rivers, and oceans, and has the appearance of rising streamers. It seldom becomes dense.

(6) Ice (crystal) fog is not common. This fog normally occurs at high latitudes under calm conditions when the air temperature is less than approximately –30 ºC, and as water vapor from the exhaust of aircraft engines, automobiles, etc., is produced. The vapor changes directly to ice particles (crystals) instead of condensing directly to liquid drops. The suspension of the ice crystals (10–100 μm in diameter) in the atmosphere produces the ice fog. Ice fog is produced at or near the surface and contrails at altitude. These fogs can persist from a few minutes to several days and are quite a problem in arctic or polar regions. A similar “freezing fog” is composed of supercooled water droplets that freeze on contact with solid objects; e.g., parked aircraft.

(7) Sea salt particles and sea fog (salt fog), which develops along a coastal area, is presented in subsection 10.3.2.

7.3.3 Fog Characteristics

Some typical microphysical characteristics of both radiation and advection types of fogs are given in table 7-25. General U.S. fog statistics are presented in figure 7-23.

Table 7-25. Characteristics of radiation and advection fog (ref. 7-30).

Fog Microphysical Characteristics	Radiation Fog (Inland)	Advection Fog (Coastal)
Diameter of drops (avg.)	10 μm	20 μm
Typical drop size	5 to 35 μm	7 to 65 μm
Liquid water content	110 mg/m^3	170 mg/m^3
Droplet concentration	200 cm^{-3}	40 cm^{-3}
Vertical depth:		
Typical	100 m	200 m
Severe	300 m	600 m
Horizontal visibility	100 m	300 m

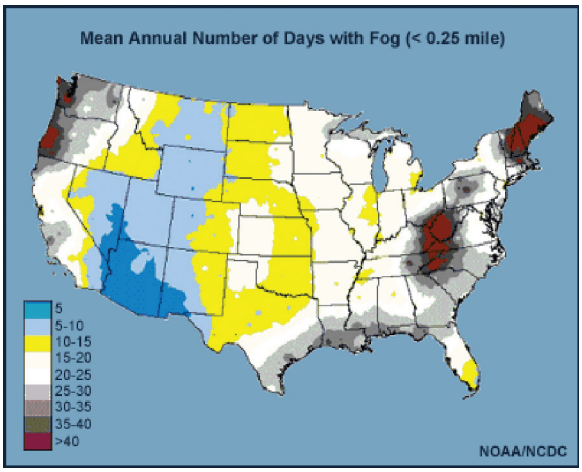

Figure 7-23. Mean annual number of U.S. days with fog (visibility ≤0.4 km (≤0.25 mi)) (NOAA/NCDC).

7.3.4 Fog at Vandenberg Air Force Base and Kennedy Space Center

7.3.4.1 Probability of Fog or Precipitation. Annually, VAFB has more than twice the number of fog days than does KSC. However, the winter months of December, January, and February have about equal number of fog days at both sites. Figures 7-24 and 7-25, showing the percentage frequency of precipitation or fog with visibility ≤0.8 km (0.5 mi) at VAFB and KSC, were developed from hourly observations. Certain VAFB and KSC climatic characteristics that are significant to aerospace mission planning and operations are immediately apparent. That is, potentially unfavorable climatic conditions for launch activities occur mainly during summer night and early morning hours at VAFB but during summer afternoons at KSC. This, of course, is due to the high frequency of fog at VAFB and summer afternoon showers in central Florida.

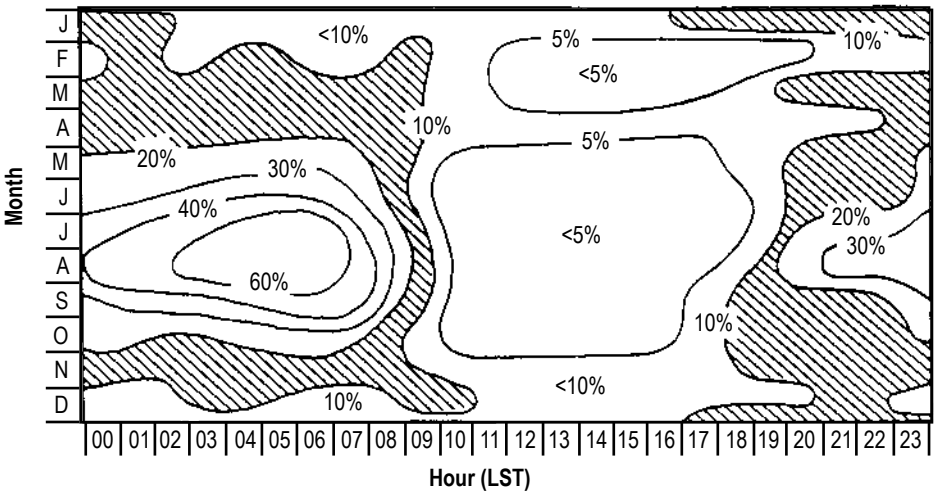

Figure 7-24. Probability of precipitation or fog with visibility ≤0.8 km (≤0.5 mi) at VAFB.

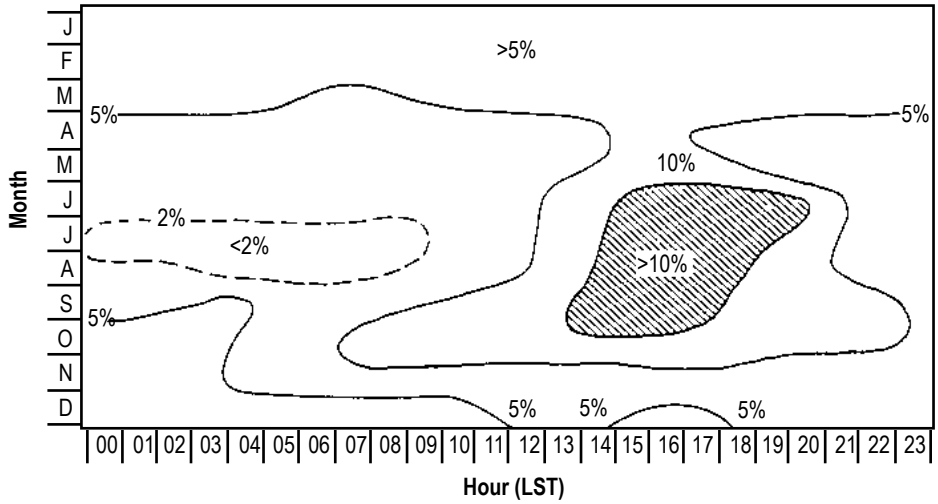

Figure 7-25. Probability of precipitation or fog with visibility ≤0.8 km (≤0.5 mi) at KSC.

For climatological studies useful for inputs into operational design data for spacecraft and aircraft operations, the Federal Aviation Administration has produced a tabulation of ceilings, visibilities, wind, and weather data by various periods of the day and by various temperature and wind categories for 41 airports (ref. 7-35).

7.3.4.2 Kennedy Space Center Fog Climatology. A 5-yr (1986–1990) study was conducted at KSC (ref. 7-36) to improve the 90-min fog forecasts made in support of Space Shuttle landing at KSC. This concerns rapid fog development that would affect the <11.3 km (<7 statute mile) visibility flight rule (4-64) in effect for end-of-mission Shuttle landings at KSC. Space Shuttle program flight rule 4-64 also states that <8 km (<5 statute miles) can be used as the go/no-go decision visibility constraint, under certain other measurement conditions. Therefore, fog statistics for both <11.3 km (<7 mi) and <8 km (<5 mi) were developed for these two visibility criteria. Over the 5-yr study period, 335 fog events occurred at KSC for the <11.3-km (<7-mi) criteria, and 267 fog events for <8-km (<5-mi) criteria.

The KSC fog season is normally defined as October 1 through April 30, although fog occurs during other months of the year (table 7-26). The fog climatology for the KSC area is complicated by the Cape Canaveral topography with numerous water bodies (rivers, ocean), its land mass, and with land/sea breeze effects. Of all the fog cases, only 36 fog events were completely analyzed, resulting in KSC fog events falling into three categories:

- Advection fog (21/36 = 58 percent)
- Prefrontal fog (13/36 = 36 percent)
- Radiation fog (2/36 = 6 percent).

Table 7-26. Normally expected fog days at KSC (ref. 7-37).

Jan.	Feb.	Mar.	Apr.	May	June	July	Aug.	Sept.	Oct.	Nov.	Dec.	Annual
13	10	9	7	7	6	4	6	4	7	8	12	93 Days

However, using all the fog event cases, the time of fog onset and dissipation are given in table 7-27.

Table 7-27. KSC fog onset and dissipation time: Range and peak hours (ref. 7-36).

Number of KSC Fog Cases:	335	267
Visibility Criteria	<11.3 km (<7 Statute Miles)	<8 km (<5 Statute Miles)
Fog onset time: range of hours	0500 – 1459 UTC	0500 – 1459 UTC
Fog onset time: peak hour	0900 – 0959 UTC	1000 – 1059 UTC
(peak hour percent frequency)	95/335 = 28.4%	46/267 = 17.2%
Fog dissipation time: range of hours	1000 – >2000 UTC	1000 – >2000 UTC
Fog dissipation time: peak hour	1300 – 1359 UTC	1200 – 1259 UTC
(peak hour percent frequency)	75/335 = 22.4%	62/267 = 23.2%

7.4 Icing

7.4.1 Tank Ice Formation

The deposit or coating of ice on an object, caused by the impingement and freezing of liquid hydrometeors, is called icing. The type of ice which will form on the outside exposed surfaces of cryogenic tanks is related to the temperature of the tank surface, the precipitation rate, drop size, and wind (air velocity relative to the tank). In general, the larger the drop size and the higher the temperature, precipitation rate, and wind speed, the denser the ice will form until a condition is reached at where surface temperatures are too high for additional ice formation. If the precipitation is sufficiently warm and a high precipitation rate, it may warm the tank sufficiently to melt ice that formed previously. The types of icing are defined as follows:

- Glaze or clear—A coating of ice, generally clear and smooth but usually containing some air pockets, formed on exposed objects by the freezing of a film of supercooled water deposited by rain, drizzle, fog, or possibly condensed from supercooled water deposited most often by freezing rain or freezing drizzle.

- Rime—A white or milky and opaque granular deposit of ice formed by the rapid freezing of supercooled water or fog drops as they impinge upon a cold exposed object.

Table 7-28 summarizes ice types for various tank wall temperatures with moderate precipitation (over 10 mm/hr (0.4 in/hr)).

Table 7-28. Ice types as a function of tank wall temperatures.

Temperature of Tank Wall			Density Range		
(°C)	(°F)	Type of Ice	(g/cm^3)	(lb/ft^3)	Remarks
–5 to 0	23 to 32	Clear ice	0.69	60	Hard, dense ice
–9 to –5	15 to 23	Milky ice or clear ice with air bubbles	0.69 to 0.85	43 to 53	
Below –9	Below 15	Rime ice	0.29 to 0.40	18 to 25	Crumbly

7.4.2 Natural Icing Formation

Ice formation/freezing rain has the potential to cause impact damage to an aerospace vehicle's thermal protection system (TPS), jam aerodynamic controls, obscure the windows, and jam exposed mechanisms, including latches, hinges, air data probe, and antennas. Subsequent effects include degraded TPS; damage to control effectors; additional vehicle weight; reduced aerodynamic efficiency; inability to close, open, or latch external doors; and loss of communications. Icing could occur during a launch in any visible moisture (clouds, fog) that is below freezing temperature. The accumulation of ice on a vehicle may reduce performance, compromising mission objectives. During ascent, the exposure would be brief, but a bigger problem could occur during the vehicle's approach in the landing phase.

Precipitation in the form of freezing rain or freezing drizzle can cause icing for items exposed on the ground, impacting facilities, and powerlines with much added weight, causing potential loss.

7.4.2.1 Freezing Rain/Drizzle Near Surface Level. Freezing rain and freezing drizzle are the ultimate enemies that can drastically roughen large surface areas or distort airfoil shapes and make flight extremely dangerous (ref. 7-38):

- Freezing rain (ZR or FZRA)—The most common type of freezing rain occurs in the lowest few thousand feet in winter. Freezing rain has a warm (T>0 ºC) (>32 ºF) layer above it and usually a deep snow cloud above that. Ground temperatures may be only –1 or –2 ºC (30 or 28 ºF), but in the middle of the freezing rain layer above (layer may be up to 2,134 m (7,000 ft) deep maximum), temperatures can reach –9 ºC (16 ºF) or below. Elevated freezing rain can occur in summer-like convective clouds that are vigorously growing above the freezing level.

- Freezing drizzle (ZL or FZDZ)—Freezing drizzle can form with no warm layer above it, and it can form within some stratiform-type clouds. Low-lying drizzle clouds can extend from near ground level up to 13,000 ft AGL. Elevated freezing drizzle may occur in separate supercooled liquid droplet clouds (<0 ºC (<32 ºF)) between 1,524 and 6,096 m (5,000 and 20,000 ft), with cloud layers usually < 2,438 m (<8,000 ft) deep (ref. 7-39).

A good summary of surface-level freezing rain, freezing drizzle, and ice pellets across the United States and Canada is presented by Cortinas et al. (ref. 7-40). These types of precipitation occur most frequently across the central and eastern portions of the United States (east of the Rockies) from November to March. An area of relatively high occurrence (>6 days annually) extends from northwest Texas northeastward to New England. This glaze-belt will experience presentation with surface ice accumulations between 0.64 and 1.27 cm (0.25 and 0.50 in) once every 3 yr. Freezing precipitation and ice pellets occur most frequently during wintertime in the Northeast but are usually short lived. The greatest frequency of freezing drizzle occurs through the western portion of the Central Plains. The frequency of both freezing rain and freezing drizzle combined will produce a broad swath that extends from the western high plains through the Great Lakes region, to the eastern slope of the Appalachians, and into New England. A median of 10 annual hours of this precipitation combination encompasses this region, with higher values within (ref. 7-40).

The horizontal graphical distribution of freezing rain contains five freezing rain maxima (fig. 7-26). Spatial variability is high, with large gradients surrounding the maxima. Temporally, the freezing rain maximum first appears in the month of December and persists through February. During the 9-yr period (1982–1990) over 60 observations of freezing rain were made at Greensboro, NC, for the month of February; only eight were made in March (ref. 7-42). The State of Florida encounters 0 to 5 hr per year of freezing precipitation.

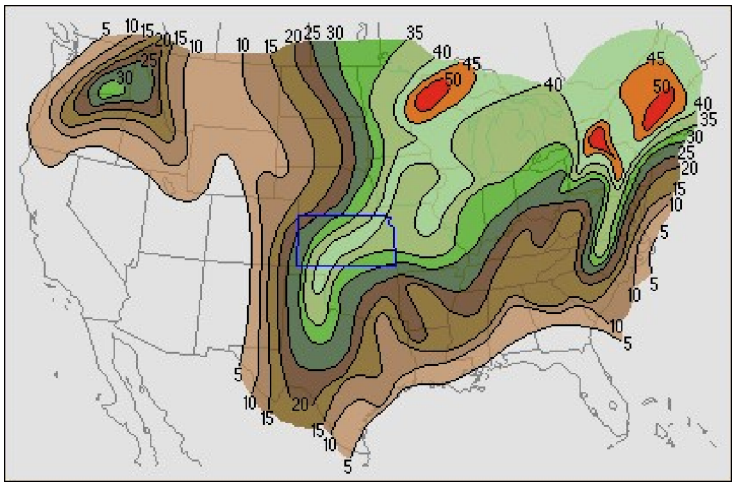

Figure 7-26. Frequency of freezing precipitation (FZRA & FZDZ) in hours per year. Climatology was taken at 207 stations, from 30 yr of data (ref. 7-41).

Relative to all types of winter (freezing and frozen) precipitation, the percentages of freezing rain appear to be highest in the Southeast from North Carolina to Louisiana. In this region, 20 to 40 percent of all winter precipitation is in the form of freezing rain (fig. 7-27). It is important to note that in the Northeast, where the number of freezing rain observations is very high, freezing rain constitutes <10 percent of the total winter precipitation. For the remainder of the country, <10 percent of all winter precipitation is in the form of freezing rain. Nationally, freezing rain accounts for a very small portion of the total winter precipitation spectrum (ref. 7-42).

7.4.2.2 Icing Aloft.

7.4.2.2.1 Aircraft Icing. Aircraft icing is an atmospheric condition that leads to the formation of ice on an aircraft. Visible moisture and static air temperatures, at or below freezing (0 ºC), are the two atmospheric elements

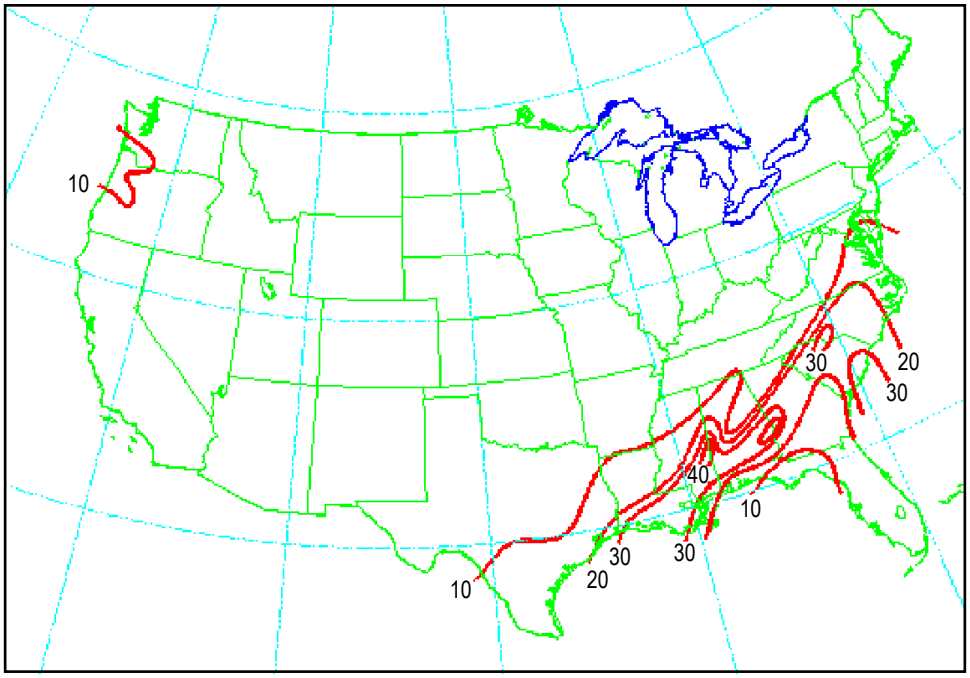

Figure 7-27. Percentage of freezing rain to total winter precipitation, September through April, 1982–1990 (ref. 7-42).

necessary for aircraft icing. Aircraft icing forms by the freezing of supercooled cloud drops and is always determined by aerodynamical considerations. Much of the material presented here was taken from references 7-43 and 7-44.

Atmospheric icing on a vertically rising launch vehicle may not be significant, since the vehicle may only traverse the potential cloud icing altitudes only a few seconds. Launch rules may also prohibit the vehicle's path through any type of potential icing clouds. (See subsection 7.4.2.2.5 on vertical ascent icing.) This subsection applies much more directly to horizontally flying NASA aircraft.

The space or aircraft icing hazard comes from the fact that undisturbed cloud droplets generally remain liquid even at temperatures several tens of degrees below freezing. A water droplet in this below freezing liquid state is referred to as a supercooled liquid water (SLW) droplet. SLW droplets exist at temperatures down to –40 ºC (–40 ºF) and generally do not turn into ice until disturbed. When SLW droplets collide with a passing vehicle or aircraft, the droplets freeze nearly instantaneously to form ice on exposed vehicle surfaces. The amount of ice depends primarily on the liquid water content (LWC) of the cloud, the size of the droplets, the temperature of the vehicle surfaces, and on the horizontal or vertical extent of the supercooled clouds along the flight path. The rate of ice accretion on vehicle components is directly proportional to the liquid water content of the supercooled cloud in which the flight takes place.

Three categories of ice normally form on aircraft—rime, glaze (or clear), and mixed. Table 7-29 contrasts the typical differences between rime and glaze ice. Rime ice normally forms a spearhead-like shape that conforms to the leading-edge geometry, and contains air pockets, causing it to be less dense and therefore brittle. It does reduce the aerodynamic efficiency of aircraft lifting surfaces. Glaze or clear ice creates buildup shapes that can significantly disrupt the airflow over the airfoil and thus lead to greater drag, smaller lift, and smaller maximum angles of attack. Glaze ice can also cover a surface in a sheet of ice, and is considered to be more serious

Table 7-29. Generalized differences between rime and glaze ice.

Condition	Rime Ice	Glaze Ice
Temperature	Cold: <–10 °C (<14 °F)	Warm: 0 to –10 °C (32 to 14 °F)
LWC	Low	High
Density	Low	High
Airspeed	Low	High
Color	Milky/opaque	Glossy/clear
Texture	Rough	Smooth
Runback	No	Yes
Fragility	Brittle	Hard
Water droplet size	Small	Large
Airfoil ice shape	Streamlined/spearheaded	Single or double horn

than rime ice, due primarily to the greater amount of LWC available and the resulting high rate of accretion. Glaze ice horns are denser and less streamlined as well. In reality, mixed or intermediate ice is most often formed possessing characteristics of both rime and glaze ice. Also, snow or ice may be mixed with the accumulation, further reducing lift and increasing drag.

7.4.2.2.2 Key Icing Aloft Terminology/Specifics. The following are key icing aloft terminology:

MED – mean effective diameter (μm)
MVD – median volumetric diameter (μm)
LWC – liquid water content (g/m^3)
CDD – cloud droplet distributions
μm – micron ($1\ \mu m = 1 \times 10^{-6}$ m).

MED and MVD describe the average size of a droplet in an SLW droplet distribution. Federal Aviation Regulations give droplet sizes in terms of MED, which is the droplet diameter that divides the total water volume present in the given droplet distribution in half; i.e., half the water volume is contained in the larger drops and the other half in the smaller drops. MVD is essentially that same definition except that the diameter is obtained by actual drop size measurements. MVD is generally assumed to be equivalent to MED.

LWC is the amount (grams) of liquid that is contained in a parcel (m^3) of air, and does not include water in vapor form. The additional energy within cumuliform clouds over stratiform clouds allows them to hold more SLW. Therefore, the greatest icing threat occurs at temperatures less than –15 ºC (5 ºF) for stratiform clouds and less than –20 ºC (–4 ºF) for cumuliform clouds.

The greatest icing hazards occur in warm weather cumulonimbus clouds, or developing thunderstorms, where LWCs up to 5 g/m^3 (3.1×10^{-4} lb/ft^3) have been reported. However, the freezing level in these clouds is usually above 3,048 m (10,000 ft) and icing hazards are therefore of little concern to aircraft at lower levels. Frontal systems, lake effects, and orographic situations are the principal candidates for contributing the most significant LWCs in wintertime cloud systems at altitudes below 3,048 m (10,000 ft). The horizontal extent of icing encounters versus altitude is more critical with wintertime layer clouds than with smaller area convective summer clouds.

The maximum observed LWC normally occurs between 2,134 and 2,743 m (7,000 and 9,000 ft) (with a value of 1.5 to 1.7 g/m^3 (9.4×10^{-5} to 1.1×10^{-4} lb/ft^3)), then decreasing with altitude up to 3,048 m (10,000 ft). A secondary maximum (≈1.4 to 1.6 g/m^3 (8.7×10^{-5} to 1×10^{-4} lb/ft^3)) typically occurs between 1,219 to 1,829 m (4,000 to 6,000 ft) (typical wintertime layer clouds) and a minor peak (≈0.7 g/m^3) (4.4×10^{-5} lb/ft^3) at ≈610 m (≈2,000 ft). For all cloud types, 99 percent of LWC observed values are <1.1 g/m^3, and 95 percent are <0.6 g/m^3. Supercooled LWCs >1.7 g/m^3 may be possible below 3,048 m (10,000 ft) in deep convective clouds with bases that are relatively warm and below 1,219 m (4,000 ft).

Clouds contain a range of droplet sizes (see table 7-15) called a cloud droplet distribution (CDD). The LWC of a distribution can be calculated by determining the number of droplets and their associated diameters contained in a cloud sample. Normally, the entire distribution can be represented adequately by the MVD. However, when the MVD is small and the distribution of particle sizes varies widely from the median within the cloud, it may be more accurate to model the entire range of droplet sizes.

Cloud droplet sizes normally range from 2 to 50 μm in diameter. MVDs in supercooled clouds below 3,048 m (10,000 ft) generally are <35 μm, since any droplets larger than ≈100 μm tend to fall as precipitation. MVDs <15 μm are so small that they are normally convected around aircraft surfaces.

Outside air temperature for SLW droplets is from freezing to a minimum of –40 ºC (–40 ºF). At –40 ºC (–40 ºF), all water is converted to ice crystals homogeneous nucleation; therefore, the risk of structural icing is very low.

Cloud types producing icing are mainly stratiform, “spread out,” and cumuliform, “heaped up.” Cirroform clouds are based at or above 20,000 ft and are composed entirely of ice crystals, and air at these altitudes is usually too cold to present an icing hazard. Stratiform clouds are associated with stable air masses and have smaller droplet sizes and lower LWC than cumuliform clouds, but have much greater horizontal extents. Table 7-30 compares the features of stratiform and cumuliform clouds with regard to maximum potential icing values. Figures 7-28 and 7-29 (ref. 7-45) present these maximum type cloud icing results in graphical form, with liquid water content versus mean effective drop diameter at the various air temperatures.

Table 7-30. Comparison of continuous (stratiform), and intermittent (cumuliform), maximum icing conditions (ref. 7-44).

Condition	Stratiform Clouds (Continuous Maximum)	Cumuliform Clouds (Intermittent Maximum)
Temperature range	0 to –30 °C	0 to –30 °C and possibly to –40 °C
	(32 to –22 °F)	(32 to –22 °F and possibly to –40 °F)
Droplet range	15 to 40 μm	15 to 50 μm
LWC range	0.04 to 0.8 g/m^3	0.1 to 2.9 g/m^3 (possibly 0.05 to 2.9 g/m^3)
Pressure altitude range	Zero to 22,000 ft (6,706 m)	4,000 to 22,000 ft (1,219 to 6,706 m) and possibly up to 30,000 ft (9,144 m)
Reference horizontal extent	17.4 nmi (32.2 km)	2.6 nmi (4.8 km)
Horizontal extent range	5 to 310 nmi (9.3 to 574 km)	0.26 to 5.21 nmi (0.5 to 9.6 km)

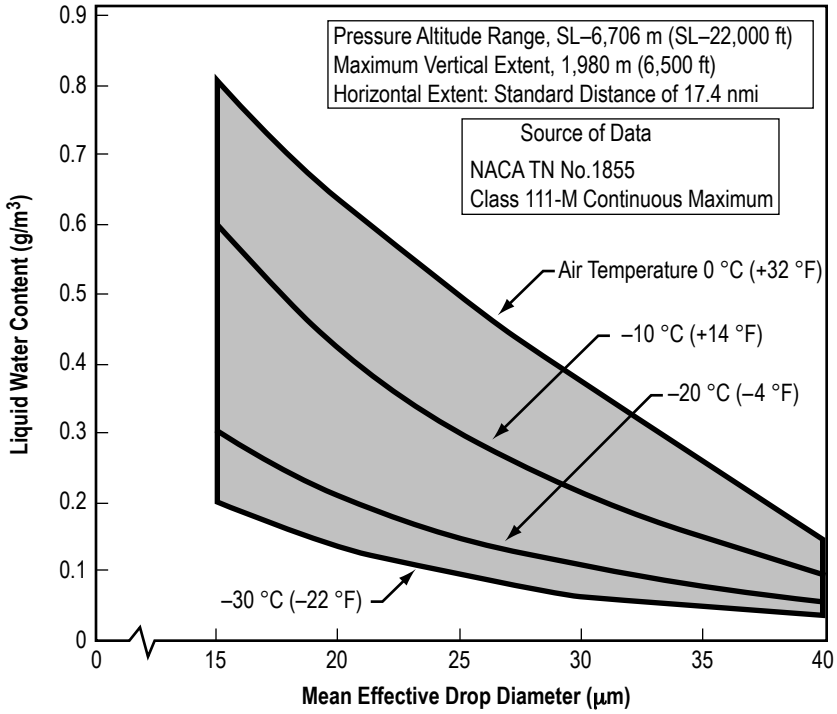

Figure 7-28. Continuous maximum stratiform cloud atmospheric icing conditions (ref. 7-45).

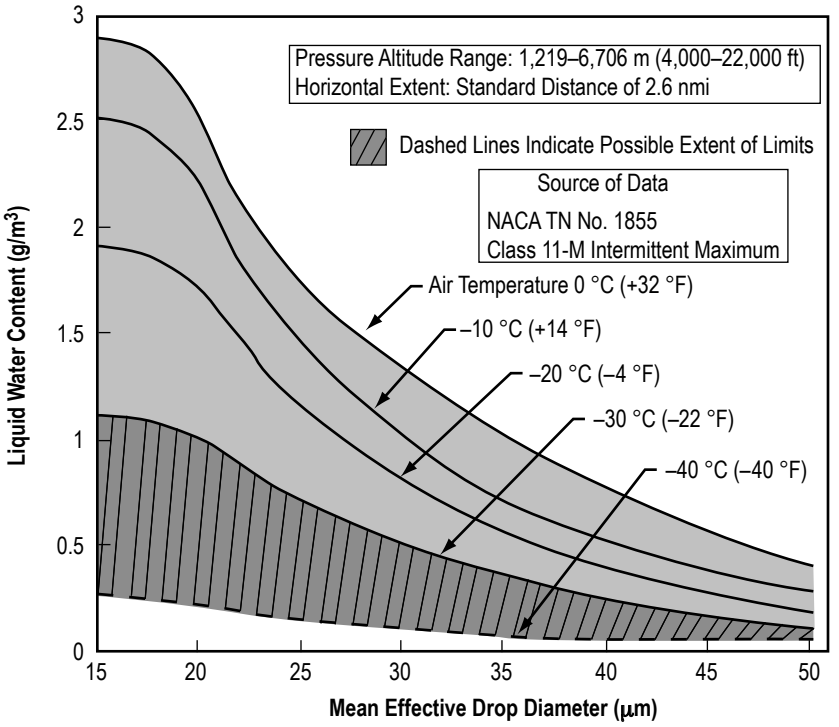

Figure 7-29. Intermittent maximum cumuliform cloud atmospheric icing conditions (ref. 7-45).

The potential for winter time (November–March) icing aloft in North America is presented in figure 7-30, which gives a percent of expected icing conditions over that entire timeframe. Ice can form on aircraft surfaces at 0 ºC (32 ºF) or colder when liquid water is present. Also, all clouds are not alike, as there are dry (very low) clouds (clouds with little moisture) as well as wet clouds. Table 7-31 gives the general risk magnitude of inflight icing flying through clouds or precipitation as a function of cloud temperature (ref. 7-38).

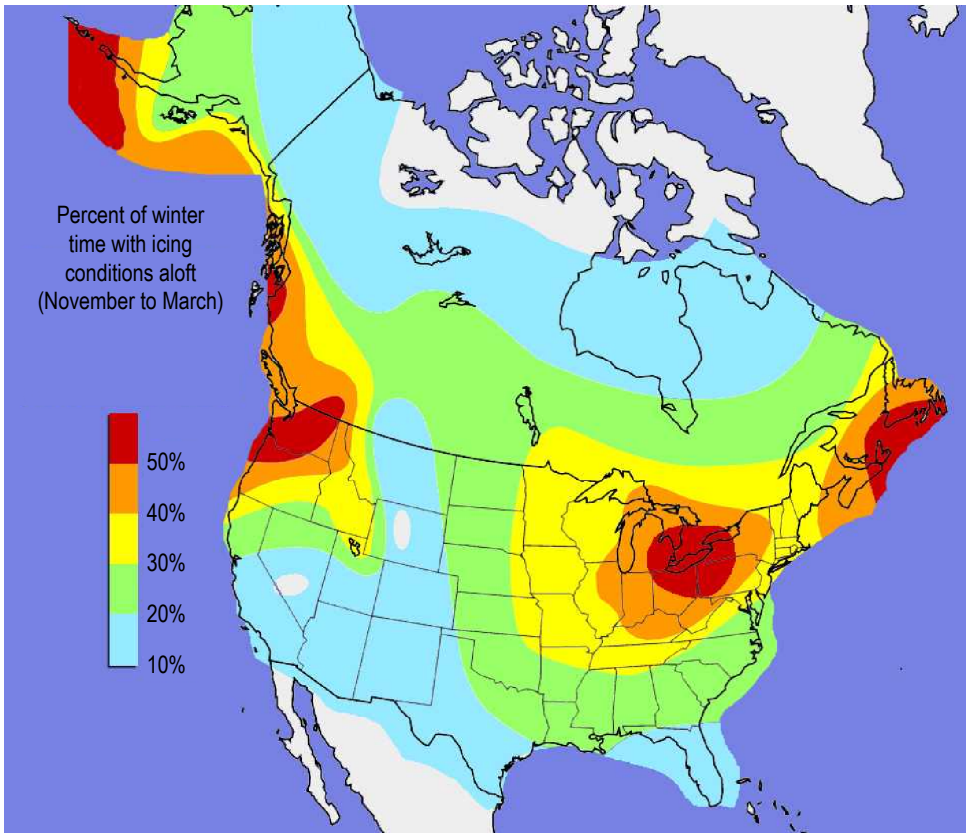

Figure 7-30. Potential North America winter time icing aloft (ref. 7-38).

Table 7-31. Icing risk aloft as a function of cloud (or precipitation) temperature (ref. 7-38).

Icing Risk Aloft—Cloud Type	Cloud/Precipitation Temperature (°C (°F))		
	High Risk	Medium Risk	Low Risk
Cumulus clouds	0 to –20 °C (32 to –4 °F)	–20 to –40 °C (–4 to –40 °F)	Less than –40 °C (Less than –40 °F)
Stratiform clouds	0 to –15 °C (32 to 5 °F)	–15 to –30 °C (5 to –22 °F)	Less than –30 °C (Less than –22 °F)
Rain and drizzle	0 °C and below (32 °F and below)		

7.4.2.2.3 Design Standard Values – Freezing Rain/Drizzle. Proposed representative design standard values for both freezing rain (ZR) and freezing drizzle (ZL) are presented in table 7-32 (ref. 7-39).

Table 7-32. Representative values of variables in freezing rain (ZR) and drizzle (ZL) (ref. 7-39).

Parameter	Freezing Rain (ZR)		Freezing Drizzle (ZL)	
	Representative Value	Range	Representative Value	Range
RWC or DWC (g/m^3)	RWC= 0.15	RWC= 0 to 0.3	DWC= 0.08	DWC= 0 to <0.3
Drop size (diameter)	(a)	0.25 to 4 mm	(b)	50 to 500 μm
Temperature (°C)	–2 (at ground) –7 (at 1 km)	0 to –12	–2 (at ground) –2 to –10 (at 3–5 km)	0 to –15
Altitude (AGL) (ft) = (km) =	 0 to 3,300 0 to 1	 0 to 6,900 0 to 2	 0 to 15,000 0 to 4	 0 to 17,000 0 to 5

	(a)				(b)				
Dropsize Interval (mm or μm)	0.5–1 mm	1–1.5 mm	1.5–2 mm	2–3 mm	50–100 μm	100–200 μm	200–300 μm	300–400 μm	400–500 μm
RWC or DWC (g/m^3)	0.07	0.04	0.03	0.01	0.021	0.035	0.010	0.012	0.003
Droplets/liter	0.4	0.03	0.01	0.002	120	20	1.2	0.6	0.08

7.4.2.2.4 Altitude Dependence. A good indicator of icing severity is the altitude dependence of the average ice accretion per icing encounter; i.e., the mass of ice accreted per unit area on an object moving at velocity (V) for a time (t) through a cloud with SLW content (W), as given by

$$M = EWVtF = WH \quad , \tag{7.6}$$

where

E = collection efficiency of the object (depends on its shape, and is approximately a log function of the airspeed and the droplet diameter); assumed as unity or at least a constant.
Vt = horizontal extent, or H.
F = freezing fraction (which can be assumed to be equal to unity).

When all supercooled cloud types are considered together, icing conditions between altitudes of 610 and 3,048 m (2,000 and 10,000 ft) are similar in regard to the maximum amount of ice accretion to be expected per icing encounter.

Horizontal extents for icing are altitude dependent and preferred altitudes appear at 1,219 to 1,829 m (4,000 to 6,000 ft) AGL, and again at ≈2,438 (≈8,000 ft) (ref. 7-43).

7.4.2.2.5 Icing Through Clouds During Near-Vertical Ascent. Icing frequencies of occurrence and the severity of icing cloud layers were measured by fighter aircraft over an approximate 1 yr span at Duluth, MN, August 1955 through June 1956, and at Seattle, WA, November 1955 through September 1956. The aircraft conducted near vertical climb and descent trajectories though clouds at these northern U.S. latitudes. The results of this study are presented in table 7-33 (ref. 7-46).

Table 7-33. Summary of near vertical aircraft icing trajectories (ref. 7-46).

Icing percent frequency occurrences	0–3% (summer); 9% (fall/winter/spring); 5% average*
Ice thickness measured	<0.08 cm (<1/32 in) (average); <1.27 cm (<1/2 in) (maximum)
Altitude of icing	70% to 75% of encounters occurred <15,000 ft

*59 icing encounters in 1,174 flights

To calculate the probability of average liquid-water content when icing is encountered during climb or descent, first calculate the concentration of liquid water between the base and top of a cloud layer. The liquid-water content increases with the height above the cloud base, and with the temperature at the cloud base. To determine the ice accretion in a vertical traverse through a cloud layer, only the average water content between the base and top needs to be calculated. The resulting probability distribution of average liquid-water content is shown in figure 7-31. The distribution indicates that 0.2 g/m^3, for example, will be exceeded in 46 percent of the encounters, whereas 0.9 g/m^3 can be expected in only one icing cloud in 100.

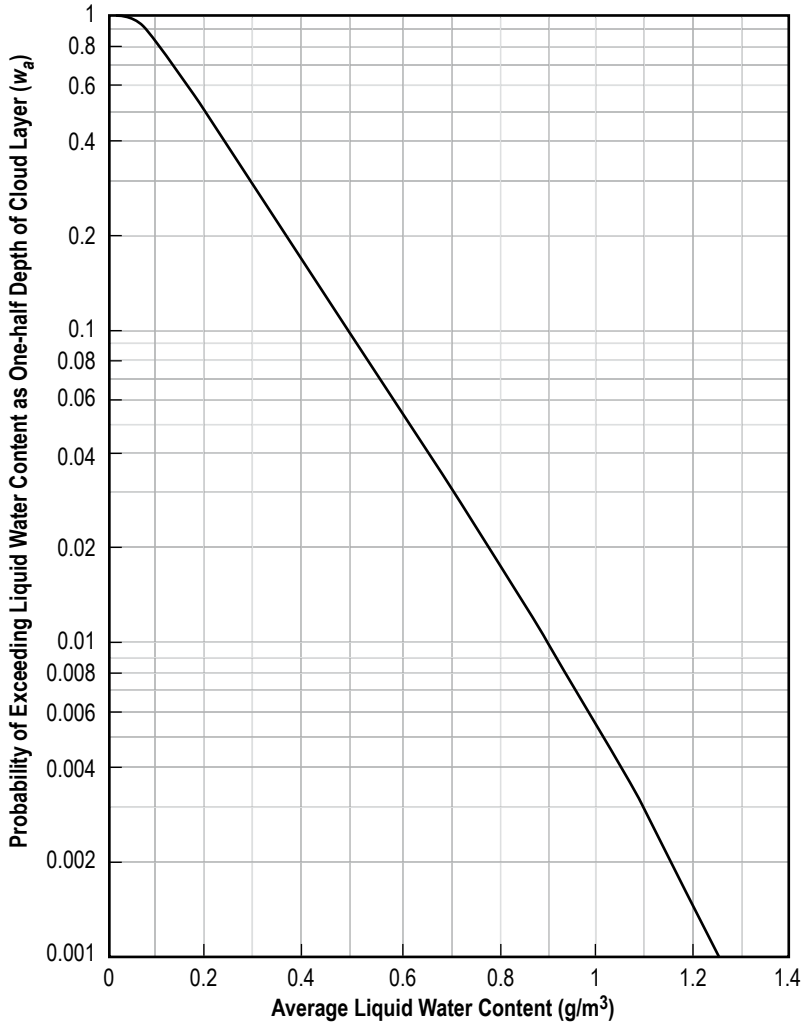

Figure 7-31. Probability distribution of average liquid-water content based on adiabatic lifting in icing clouds encountered during climb or descent (ref. 7-46).

The amount of ice collected is a function of the product of the average water content in the cloud layer and the distance traveled in passing through the cloud layer. This distance can be expressed in terms of the ratio of the airspeed (V) (kt) to the rate of climb (C) (ft/min). Decreasing values of this ratio, V/C, represent steeper flight path angles and therefore shorter distances through a cloud of a given depth. Considering the overall icing frequency experienced by the fighter aircraft, a ¼-in ice accretion could be expected to occur once in ≈12,000 flights at a V/C ratio of 0.03, or 14 times per year at a V/C ratio of 0.32. In large-scale airline operations, the maximum accretion would not be expected to exceed about 1½ in at a moderate climb angle, equivalent to a V/C ratio of 0.12 (240 kt at 2,000 ft/min).

7.4.2.3 Maximum Ice Cloud Particle Data. The maximum estimated ice cloud and cirrus cloud statistics versus altitude are given in table 7-34. This includes particle sizes, extent, TIPM, and temperatures.

Table 7-34. Proposed ice/snow specifications for in-flight conditions aloft through clouds, including range and representative values (ref. 7-47).

	Anvil Clouds >7,620 m (>25,000 ft)		Cirrus Clouds Deep Winter Storms >6,096 m (>20,000 ft)		Other Snow/Ice Clouds <6,096 m (<20,000 ft)			
Parameter	Range	Rep. Values	Range	Rep. Values	Range	Rep. Values	Range	Rep. Values
Altitude	7.6–15.2 km (25K–50 kft)	7.6–10.7 km (25K–35 kft)	6.1–15.2 km (20K–50 kft)	6.1–10.7 km (20K–35 kft)	NA	NA	NA	NA
Temperature	–25 to –60 °C	–25 to –35 °C	–20 to –50 °C	–20 to –50 °C	0 to –20 °C	0 to –20 °C	–20 to –30 °C	–20 to –30 °C
Ice mass	≤ 2.5 g/m^3	1 g/m^3	0 to 0.2 g/m^3	0.05 g/m^3	0–3 g/m^3	0.6 g/m^3*	0–1 g/m^3	0.2 g/m^3
Ice mass					0–1 g/m^3	0.4 g/m^3**		
Max diameter	1–10 mm	1–10 mm	0–3 mm	1 mm	1–10 mm	1–8 mm	1–5 mm	1–4 mm
Horizontal extent	Unknown	9.3–37 km (5–20 nmi)	9.3–185 km (5–100 nmi)	37 km† (20 nmi)†				
Horizontal extent		185–926 km (100–500 nmi)	185–926 km (100–500 nmi)	185 km‡ (100 nmi)‡				

Note: The representative values in this table do not include hail or heavy rain, nor graupel or other large particles that can be found in the updraft cores of thunderstorms. Values for this table are based on analyses of 7,600 nmi of select ice particle measurements in a variety of cloud types over the United States at altitudes up to 30,000 ft above sea level.

*Horizontal extent <56 km (<30 nmi).

**Horizontal extent >56 km (>30 nmi).

†Cirrus clouds.

‡Deep winter storms.

7.5 Daily Extreme Rainfall Return Period Amount for Any Site

Rainfall generally follows a Gamma distribution rather than a Gaussian distribution. Whereas one cannot estimate its extreme value by simply looking at the ends of a bell curve, a Gamma distribution can be applied to measured 24-hr extreme rainfall data samples for any site. The waiting time between extreme rainfall events becomes relevant here. By looking at the top 30 (or more) 24-hr rainfall events for a station, one can estimate the values for an extreme rainfall event for any given period of time at that site. For instance, to determine the extreme rainfall values for a 25-, 50-, 100- or 200-yr period for a given site, the extreme value x for a period of n years is then determined by:

$$x = \psi - B \ln[-\ln(\mathrm{F})] \ ,$$

where

$\psi = A - \gamma\beta$
A = average
γ = Euler's constant (0.557)
$\beta = 0.78\ \sigma$
σ = standard deviation
$F = (n-1)/n$.

An example for the top 30 Johnstown, PA, 24-hr rainfall events gives the following:

Input: $A = 2.90$ in
$\sigma = 1.23$ in
$\beta = 0.96$ in
$\psi = 2.37$ in
for n = 25, 50, 100, and 200 yr.

Output:
25-yr event = 5.43 in
50-yr event = 6.10 in
100-yr event = 6.77 in
200-yr event = 7.43 in.

Source:
<http://climate.met.psu.edu/features/other/rainextreme.php>
Pennsylvania State University—College of Earth and Mineral Sciences.

REFERENCES

7-1. Geer, I.W.: "Glossary of Weather and Climate," American Meteorological Society, Boston, MA, 1996.

7-2. Fletcher, R.D.; and Sartos, S.: Air Weather Service Technical Report No. 105-81, 1951.

7-3. Riordan, P.; and Bourget, P.G.: "Worldwide Weather Extremes," ETL-0416, Engineer Topographic Laboratories, U.S. Corps of Engineers, Fort Belvoir, VA, December 1985.

7-4. Crane R.K.; and Blood, D.W.: "Handbook for the Estimation of Microwave Propagation Effects—Link Calculations for Earth-Space Paths: (Path Loss and Noise Estimation)," Technical Report. No. 1, Document No. P-7376-TRI, for NASA Goddard Space Flight Center, *NASA–CR–165002*, June 1979.

7-5. Crane, R.K.: *Electromagnetic Wave Propagation Through Rain*, John Wiley & Sons, Inc., 1996.

7-6. University of California—Santa Barbara, "Precipitation Climatology: Averages, of the Same Month, Over a Number of Years, of Precipitation," <http://oceanography.geol.ucsb.edu/~gs4/s2004/resources/Precip_Lamont.htm>, 2006.

7-7. NOAA NCDC, Asheville, NC, <http://1wf.ncdc.noaa.gov/img/climate/severeweather/s24hrpre.gif>.

7-8. "Rainfall Intensity-Duration-Frequency Curves for Selected Stations in the United States, Alaska, Hawaiian Islands, and Puerto Rico," Technical Paper No. 25, U.S. Department of Commerce, Washington, DC, December 1955.

7-9. Gumble, E.J.: *Statistics of Extremes*, Columbia University Press, 1958.

7-10. Valley, S.L.: *Handbook of Geophysics and Space Environments*, McGraw-Hill Book Company, Inc., New York, April 1965.

7-11. Tattleman, P.; and Willis, P.T.: "Model Vertical Profiles of Extreme Rainfall Rate, Liquid Water Content, and Drop-Size Distribution," AFGL-TR-85-0200, ERP No. 928, September 6, 1985.

7-12. Houghton, D.D.: *Handbook of Applied Meteorology*, John Wiley and Sons, Inc., New York, 1985.

7-13. Vaughan, W.W.: "Distribution of Hydrometeors With Altitude for Missile Design and Performance Studies," ABMA DA-TM-138-59, U.S. Army Ballistic Missile Agency, Huntsville, AL, 1959.

7-14. Johnson, D.: "KSC Precipitation & Freezing Temperature Analysis (preliminary)," NASA Marshall Space Flight Center Internal Branch Note from Dale Johnson-EL23 to Lee Foster-ED31, dated 18 September 1998.

7-15. Gunn, R.; and Kinzer, G.: The Terminal Velocity of Fall for Water Droplets in Stagnant Air, *Journal of Meteorology*, Vol. 6, pp. 243–248, 1949.

7-16. Beard, K.V.; Johnson, D.B.; and Baumgardner, D.: "Aircraft Observations of Large Raindrops in Warm, Shallow, Convective Clouds," *Geophysical Research Letters*, Vol. 13, pp. 991–994, October 1986.

7-17. Springer, G.S.: *Erosion by Liquid Impact*, Scripta Publishing Company, 1976.

7-18. Reinecke, W.G.: "High Speed Erosion in Rain and Ice," *Proceedings of Fifth International Conference on Erosion by Liquid and Solid Impact*, Cambridge University, U.K., Vol. 5, Section 8, September 3–6, 1979.

7-19. Heymann, F.J.: "Conclusions From the ASTM Interlaboratory Test Program With Liquid Impact Erosion Facilities," Proceedings of Fifth International Conference on Erosion by Liquid and Solid Impact, Cambridge University, U.K., Vol. 5, Section 20, September 3–6, 1979.

7-20. Moteff, J.: "Pneumatic Erosion Effects on Microstructure of Metals and Alloys," TLSP: Progress Report for January to April 1982.

7-21. Jeck, R.K.: "Snow and Ice Particle Sizes and Mass Concentrations at Altitudes Up to 9 km (30,000 ft)," FAA Office of Aviation Research, Final Report—DOT/FAA/AR-97/66, August 1998.

7-22. Rasmussen R.; and Cole, J.A.: "How Snow Can Fool Pilots," National Center for Atmospheric Research, Research Applications Program, July 22, 2002.

7-23. Changnon, S.A.: "Thunderstorms Across the Nation: An Atlas of Storms, Hail and Their Damages in the 20th Century," Changnon Climatologist, 801 Buckhorn, Mahomet, IL 61853, 2001.

7-24. Changnon, S.A., Jr.: "The Scale of Hail," *Journal of Applied Meteorology*, Vol. 16, No. 6, pp. 626–648, July 1977.

7-25. Kelly, D.L.; Schaefer, J.T.; and Doswell, C.A.: "Climatology of Non-Tornadic Severe Thunderstorm Events in the United States," *Monthly Weather Review*, Vol. 113, No. 11, pp. 1997–2014, November 1985.

7-26. Patnoe, M.W.; and Moravec, B.A.: "Rain and Hail Threat to Aviation: A Probability Analysis of Extreme Rain/Hail Concentrations Aloft," *AIAA–1997–5654*, 1997 World Aviation Congress, Anaheim, CA, October 13–16, 1997.

7-27. Dai, A.: "A Global Climatology of Thunderstorm, Hail and Tornado Days," in *Proceedings of AMS Symposium on Precipitation Extremes: Prediction, Impacts, & Responses*, Albuquerque, NM, pp. 137–138, January 14–19, 2001.

7-28. NASA JSC, NSTS 07700, Volume X – Book 2, Space Shuttle Flight and Ground System Specification, Natural Environment Design Requirements, Appendix 10.10., June 9, 1999.

7-29. Daniels, G.E., Ed.: Terrestrial Environment (Climatic) Criteria Guidelines For Use in Aerospace Vehicle Development, 1973 Revision, Table 14.8, p. 14.9, *NASA TMX–64757*, Marshall Space Flight Center, AL, July 5, 1973.

7-30. Johnson, D.L., Ed.: "Terrestrial Environment (Climatic) Criteria Handbook for Use in Aerospace Vehicle Development," *NASA-HDBK-1001*, August 11, 2000.

7-31. Jursa, A.S.: “Handbook of Geophysics and the Space Environment,” Air Force Geophysics Laboratory, Air Force Systems Command, U.S. Air Force, 1985.

7-32. Adelfang, S.I.: Internal MSFC/ED44 Study Done in Support of the NASA KSC External Tank Hail Protection—Feasibility Assessment Meeting of July 16, 1999.

7-33. Moravec, B.A.; and Patnoe, M.W.: “Recommended Values of Rain and Hail Concentrations to be Considered in the Design of Turbine Engines,” *AIAA–1997–5655*, AIAA and SAE 1997 World Aviation Congress, Anaheim, CA, October 13–16, 1997.

7-34. Johnson, D.: “KSC Hail and Lightning Criteria and Climatology for use in the Space Shuttle Composite Nose Cone (CNC) Project,” White Paper Preliminary Version 1.0, NASA MSFC Environments Group ED44, October 29, 1999. Assembled in support of the NASA KSC External Tank Hail Protection—Feasibility Assessment Meeting of July 16, 1999.

7-35. “Climatological Summaries—Visibilities Below 1/2 Mile and Ceilings Below 200 Feet,” FAA-RD-69-22, FA-67-WAI-12, National Weather Record Center, Asheville, NC, June 1969.

7-36. Wheeler, M.M.; Atchison, M.K.; Schumann, R.; et al., ”Analysis of Rapidly Developing Fog at the Kennedy Space Center, 1986–1990, Final Report,” Applied Meteorology Unit/ENSCO, Inc., Under Contract NASA 10-11844, October 29, 1993.

7-37. KSC Online; Weather Status Reports, Fog: Fog Days Normally Expected, <http://www-pao.ksc.nasa.gov/kscpao/status/weatstat/2005/months.htm>, 2004.

7-38. AOPA-Air Safety Foundation, “Aircraft Icing,” Safety Advisor – Weather No. 1, #SA11-11/02, FAA Flight Safety Branch, 2002.

7-39. Jeck, R.K.: “Representative Values of Icing-Related Variables Aloft in Freezing Rain and Freezing Drizzle,” DOT/FAA/AR-TN95/119, March 1996.

7-40. Cortinas, J.V.; Bernstein, B.C.; Robbins, C.C.; and Strapp, J.W.: “An Analysis of Freezing Rain, Freezing Drizzle, and Ice Pellets Across United States and Canada: 1976–90,” *Weather and Forecasting*, Vol. 19, No. 2, pp. 377–390, April 2004.

7-41. Bernstein, B.C.; and Brown, B.G.: A Climatology of Supercooled Large Drop Conditions Based Upon Surface Observations and Pilot Reports of Icing. *Preprints*, Seventh Conference on Aviation, Range, and Aerospace Meteorology, AMS, Long Beach, CA, pp. 82–87, 1997.

7-42. Robbins, C.C.: “A Climatology of Freezing Rain in the Contiguous United States: Preliminary Results,” 15th AMS Conference on Weather Analysis and Forecasting, Norfolk, VA, August 19–23, 1996.

7-43. Jeck, R.K.: “A New Data Base of Supercooled Cloud Variables for Altitudes up to 10,000 Feet AGL and the Implications for Low Altitude Aircraft Icing,” Final Report, DOT/FAA/CT-83/21 (NRL Report 8738), August 1983.

7-44. Vukits, T.J.: “Overview and Risk Assessment of Icing for Transport Category Aircraft and Components,” AIAA No. 2002–0811, AIAA 40th Aerospace Sciences Meeting & Exhibit, Reno, NV, January 14-17, 2002.

7-45. Aircraft Ice Protection, Draft, U.S. Department of Transportation, Federal Aviation Administration, Advisory Circular – AC No: 20-73A, 20 February 2003.

7-46. Perkins, P.J.: "Icing Frequencies Experienced During Climb and Descent by Fighter-Interceptor Aircraft," NACA Technical Note 4314, July 1958.

7-47. Jeck, R.K.: "Snow and Ice Particle Sizes and Mass Concentrations at Altitudes up to 9 km (30,000 ft)," Final Report DOT/FAA/AR-97/66, Federal Aviation Administration, U.S. Department of Transportation, August 1998.

Terrestrial Environment (Climatic) Criteria Guidelines for Use in Aerospace Vehicle Development, 2008 Revision

NASA/TM—2008–215633
December 2008

D.L. Johnson, Editor

Section 8: Cloud Phenomena and Cloud Cover Models

TABLE OF CONTENTS

LIST OF FIGURES

LIST OF TABLES

LIST OF ACRONYMS AND SYMBOLS

CH_4	methane
GRAM–07	Global Reference Atmospheric Model–07
HIRS	high resolution infrared sounder
LIDAR	light, detection, and ranging
MSFC	Marshall Space Flight Center
NAC	nacreous cloud
NLC	noctilucent cloud
NOAA	National Oceanic and Atmospheric Administration
NRL	Navel Research Laboratory
OH	hydroxyl
PMC	polar mesospheric cloud
PMSE	polar mesospheric summer echos
PSC	polar stratospheric cloud
SAGE	Stratospheric Aerosol and Gas Experiment
SME	solar mesosphere explorer
UV	ultraviolet

8. CLOUD PHENOMENA AND CLOUD COVER MODELS

8.1 Introduction

Section 8 presents information on cloud phenomena that can be applied in various NASA flight project design and mission planning studies. Included is discussion and criteria regarding the high altitude/high latitudinal cloud phenomena existing at stratospheric and mesospheric altitudes. This information is provided to alert designers and planners to the fact that cloud systems/particles exist above the troposphere that need to be considered during vehicle ascent, reentry, launch, or horizontal flight above 12 km (39,340 ft) altitude. Cloud phenomena-related information is also presented in other sections of this Handbook and includes such topics as humidity in section 6, precipitation/icing/hail/fog in section 7, and atmospheric electricity in section 9.

An update for section 8 was included in the 2000 Handbook about a global cloud cover model (ref. 8-1) along with a global four-dimensional atmospheric thermodynamic/moisture model (ref. 8-2), which had been developed at NASA Marshall Space Flight Center (MSFC) mainly for NASA Earth resources/Earth viewing purposes from spaceborne platforms. These models are not included in this revision, as the four-dimensional atmospheric model (ref. 8-2) has been superceded by the NASA MSFC Earth Global Reference Atmospheric Model–2007 (GRAM–07) (ref. 8-3). However, the GRAM–07 does not output moisture parameters. Recent cloud cover information and models are currently available in a variety of published documents for those having an interest in this subject. Some of the applicable cloud models include the U.S. Air Force-developed PCloudS–2.2 statistical model, as well as their Real-Time Nephanalysis and Cloud-Free Line of Sight models. The University of Wisconsin's High-Resolution Infrared Radiometer Sounder model, as well as the Goddard Institute for Space Studies/NASA-developed International Satellite Cloud Climatology project are other current cloud models which could be considered for possible use.

8.2 Interaction Model of Microwave Energy and Atmospheric Variables

MSFC sponsored the development of an "Interaction Model of Microwave Energy and Atmospheric Variables," a complete description about the effects of atmospheric moisture on microwaves (ref. 8-4). While clouds are opaque in the visible and infrared wavelengths, the microwave part of the electromagnetic spectrum is unique in that cloud and rain particles vary from very weak absorbers and scatterers to significant contributors to the electromagnetic environment. This is illustrated in figures 8-1 through 8-3, which are extracted from the final report on the interaction model (ref. 8-4).

8.2.1 Scattering and Extinction Properties of Water Clouds Over the Range of 10 cm to 10 μm

Figures 8-1 and 8-2 show the unit-volume scattering and extinction properties of two modeled cloud drop distributions computed using Mie theory. Figure 8-1 gives the extinction coefficient, in units of Neper (Np), as a function of wavelength. Figure 8-2 presents the single scattering albedo for two cloud models representing low stratus and rainy conditions. The curves show the wavelength regimes appropriate to the two cloud types in which scattering effects are relatively unimportant, and in which the extinction coefficient follows the simple Rayleigh ($1/\lambda^2$) dependence.

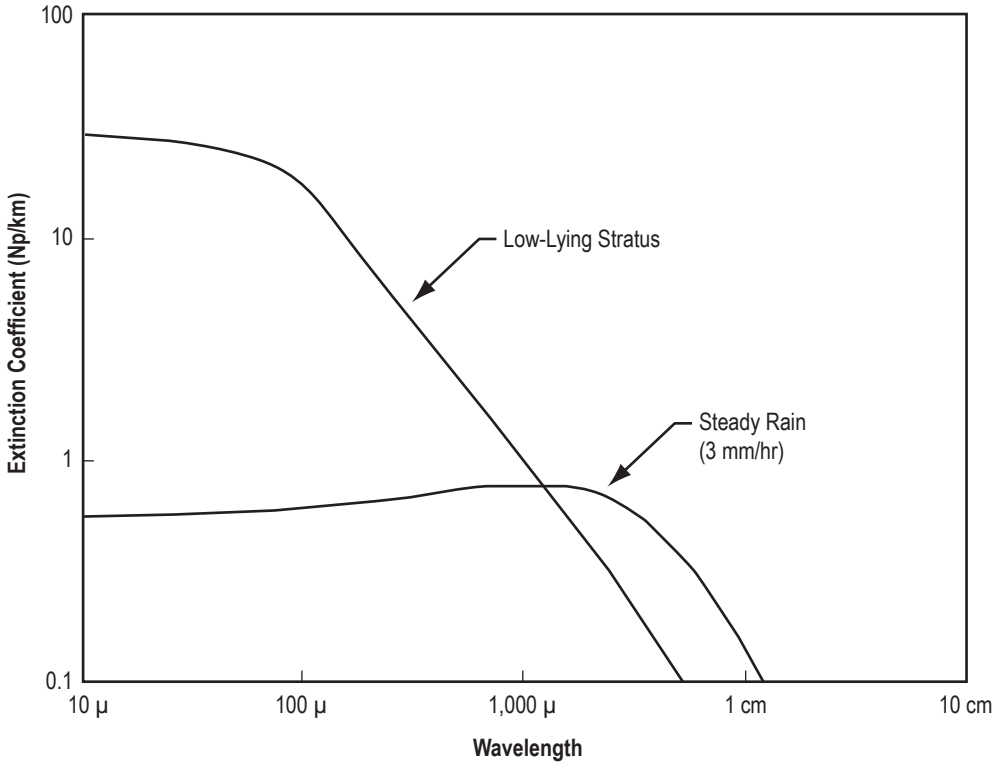

Figure 8-1. Extinction coefficient as a function of wavelength.

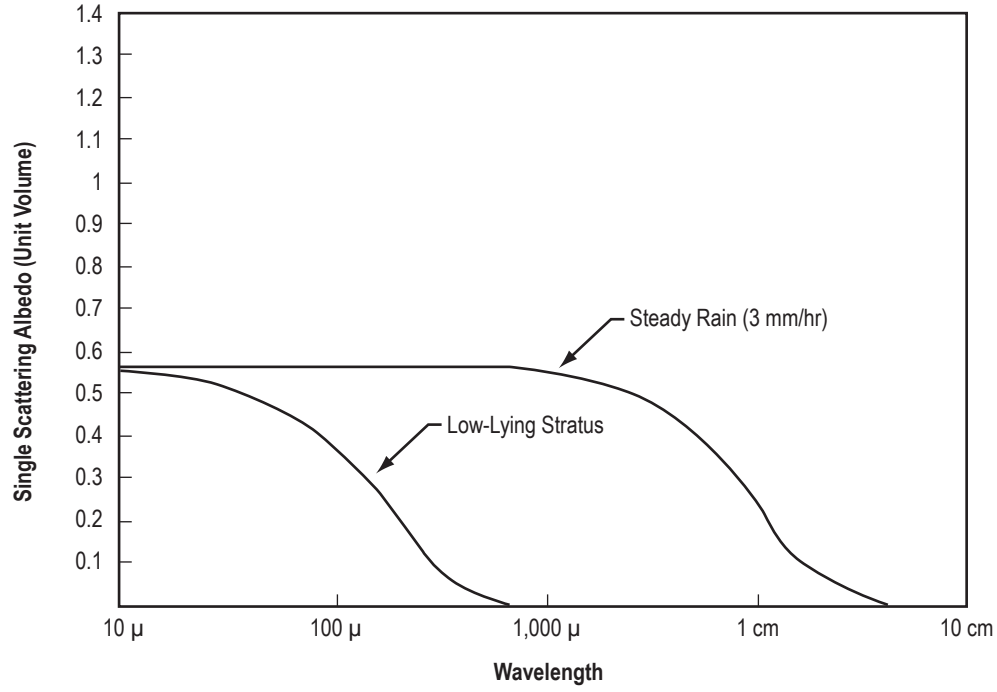

Figure 8-2. Single scattering albedo for two cloud models.

8.2.2 Zenith Opacity Due to Atmospheric Water Vapor as a Function of Latitude

In the preparation of figure 8-3, 5 yr of climatological data from the Massachusetts Institute of Technology Planetary Circulations project were used to obtain mean water vapor distributions applicable to the latitudes 0° N., 30° N., and 90° N., corresponding to tropical, midlatitude, and arctic conditions. The total water vapor content for the three cases is 4.5, 2.5, and 0.5 g/cm^3, respectively. The curves demonstrate the effect of climatological extremes in simulating and predicting the influence of atmospheric water vapor on surface observations from a space observer over the range of 10 to 350 GHz. A detailed report on the interaction model (ref. 8-4) is available upon request.

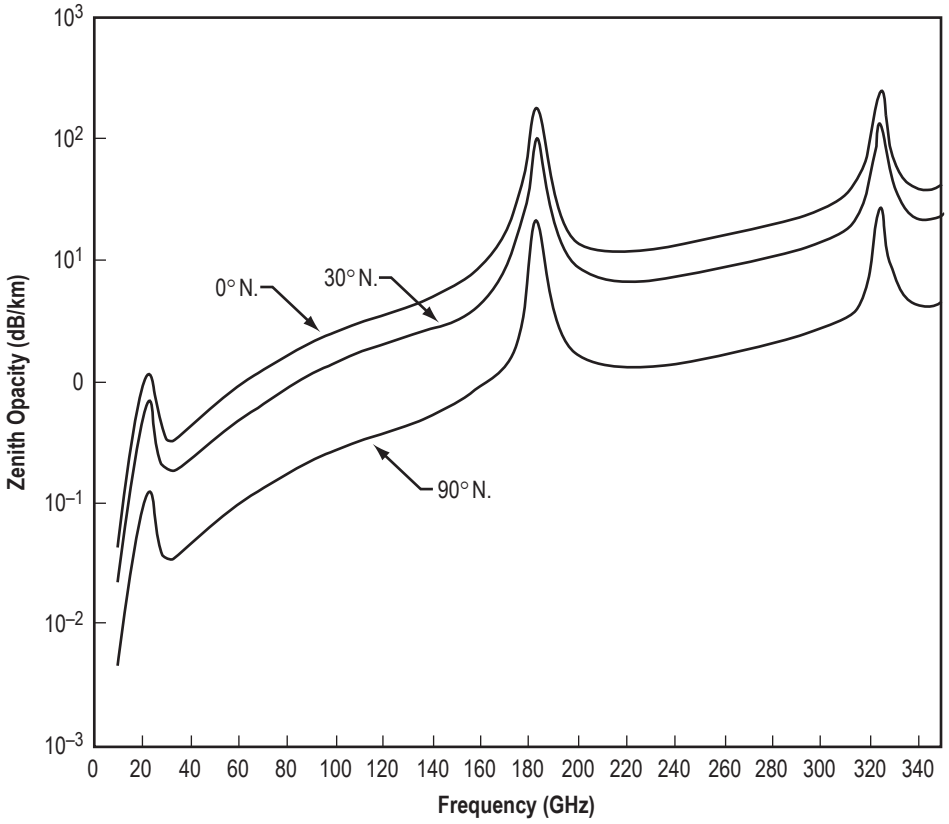

Figure 8-3. Zenith opacity.

8.3 Stratospheric and Mesospheric Clouds

Four types of high-altitude clouds are presented in this section to alert designers and planners that cloud systems/particles exist above the troposphere which need to be considered when observations or vehicle reentry, launch, or horizontal flight above 12-km altitude is desired. Two related types of stratospheric cloud phenomena are presented that occur at stratospheric altitudes (15 to 30 km) and are called polar stratospheric clouds (PSCs) and nacreous clouds (NACs). Two similar types of upper mesospheric clouds (80 to 85 km altitude), called polar mesospheric clouds (PMCs) and noctilucent clouds (NLCs), will also be discussed briefly. The PSCs can be frozen aerosol particles, whereas the PMCs consist mainly of water ice. See section 10 for more information on atmospheric constituents, aerosols, and chemistry.

8.3.1 Stratospheric Clouds

8.3.1.1 Polar Stratospheric Clouds. Polar stratospheric clouds were discovered in the late 1970s when they were observed as extinction amounts in the stratospheric aerosol measurement II and limb infrared monitor of stratosphere satellite data (ref. 8-5). They are probably not the visually observed NACs, but nacreous is a special subset of PSCs (ref. 8-6). They appear not to be related to orographic features and appear larger and more persistent than NACs. PSCs may not even be visible to the ground observer. Therefore, these high extinction stratospheric layers (aerosol related) were named polar stratospheric clouds (refs. 8-5 and 8-7).

PSCs are frozen aerosol particles observed during local winter over both polar regions whenever the ambient temperature falls below ≈195 K. On one occasion they were observed extending continuously from 80° N. to the pole. The clouds are layered with the maximum amount near 20 km, close to the region of minimum stratospheric temperature. The layers are thin, <1 to 2 or more kilometers thick (thicker in the Antarctic) in the altitude range of 10 to 30 km. Multiple layers of PSCs can exist. PSCs descend in altitude during the course of the winter until they reach an altitude of ≈15 km at the end of winter. Antarctic PSCs generally occur at lower altitudes (<17 km) than Arctic PSCs (17 to 25 km). PSCs are also linked to the ozone depletion/hole over the poles (ref. 8-8). This is in agreement with the predicted mean flow in the polar vortex, resulting in a strong gradient across the polar night jet stream which lasts until the springtime breakup. This feature is in good agreement with the observed aerosol properties. A good source for general properties of PSCs and their role in stratospheric ozone depletion can be found in reference 8-9. The reader also is referred to section 10, Stratospheric Aerosol, since polar stratospheric clouds are closely associated with stratospheric aerosols; although, in some respects, they do resemble aerosols, especially type Ib PSCs.

PSC characteristics change rapidly, most likely due to fluctuations in local temperature, water vapor, or wind shear. The clouds are apparently formed from frozen nuclei consisting primarily of either a mixture of nitric acid, sulpheric acid and water (type I), or water ice particles (type II). See table 8-1. Small amounts of other compounds, such as sulfuric and hydrochloric acid in solid solution also can exist with these two mixtures in the formation of PSCs (ref. 8-12). Type I PSCs are subdivided into types Ia, Ib, and Ic. Type Ia is represented by tri- or di-hydrated nitric acid (NAT or NAD), and Ib by a ternary solution of nitric acid, sulfuric acid, and water. Type Ib PSCs exist as supercooled liquid droplets, whereas type Ia, like type II particles, exist as ice crystals. Type Ic consists of small, solid particles of hydrated nitric acid. The clouds are much more prevalent in the Antarctic due to its colder (by 3.5 K) stratospheric temperatures than in the Arctic. If they were illuminated, these polar stratospheric clouds would have the appearance of a thin cirrus or cirrostratus veil. The clouds are not formed at the level of maximum aerosol concentration but near the level of minimum temperature. References 8-5 through 8-7, 8-10, and 8-12 through 8-15 describe PSCs and their characteristics. Although different kinds of PSCs exist that may have different compositions, they exist as highly supercooled/supersaturated liquid drops.

8.3.1.2 Nacreous Clouds. NACs, also called mother-of-pearl clouds, luminous clouds, or stratospheric veil clouds are infrequently observed, thin stratospheric clouds appearing lenticular, brilliantly colored, and stationary in wintertime over the high latitudes of both hemispheres; i.e., Scandinavia, Alaska, and Antarctica, when the Sun is below the horizon. Over a 103-yr winter period (1870–1972), over 156 days (average 1.51 obs/yr) have been recorded in which NACs (no aircraft contrails included) have been observed at various high-latitude Northern Hemispheric sites, with 84 percent of these occurring from December through February. In the Antarctic winter (June to September), over 140 NAC sightings in 100 yr have occurred in these sparse reporting areas (ref. 8-16). NACs have been observed between 17- and 31-km altitude (average 23 km), and occur preferentially downwind of mountain ranges. This indicates an orographic origin due to lee waves producing up to 40-km

Table 8-1. PSC design criteria (refs. 8-9 through 8-11).

	Type I	Type II
Composition/phase	Type Ia: HNO_3^*-$3H_2O$ (ice) Type Ib: $HNO_3/H_2SO_4/H_2O$ liquid Type Ic: HNO_3/H_2O solid Also: mixture of Ia and Ib	H_2O (ice)
Concentration	2 cm^{-3}	0.03 cm^{-3}
General range	1 to 10 cm^{-3} (at 20 km)	0.005 to 0.1 cm^{-3} (at 15 km)
Mass density	20 ppbm	400 ppbm
Radius	0.5 μm	≥6 μm
Range	0.1 to ≥10 μm	0.1 to ≥10 μm
Temperature	<195 K Antarctic	<188 K Arctic
Altitude	15 km	20 km
Range	11–22 km	17–25 km
Time of occurrence	June to October	December to March
Associated stratospheric	7 ppmv	7 ppmv
Water vapor content: avg.		
Upper limit	15.5 ppmv	21.5 ppmv
Horizontal extent	10 to 10^3 km	10 to 10^3 km
Geographic extent	From 70° to Pole	From 70° to Pole
Duration	Hours to months	Hours to months

*Nitric acid mixture, >40-percent concentration

wavelengths in the NAC bands. NACs are a special subset of PSCs, but it is not yet clear that the two-cloud phenomena are the same (ref. 8-6). NACs are composed of micrometer-sized water ice particles (crystals) with sizes on the order of 1 to 2 μm in radius, and life times are >10 min at 20-km, 1 ppm of water is equivalent to 5 particles cm^{-3} of size 1.5 μm. An approximate maximum radius of ≈4 μm at 20-km altitude can be determined, assuming 3 ppm of water condensing to form 1 particle cm^{-3}. It is generally believed that NACs form by deposition of water on preexisting stratospheric aerosol particles (sulfate) when stratospheric temperatures are typically at or below –85 °C. Therefore, the number concentration of NAC particles should be equal to that of stratospheric aerosols (approximately 5 to 20 cm^{-3} at 20 km).

8.3.2 Mesospheric Clouds

Section 8.3.2 discusses the mesospheric cloud phenomena called (1) noctilucent clouds (NLCs), (2) polar mesospheric clouds (PMCs), and (3) polar mesospheric summer echos (PMSEs). All occur at cold, upper mesospheric altitudes (80- to 85-km altitude), at high latitudes and during each hemisphere's summer. These cloud regions can be a concern for reentering spacecraft; i.e., Space Shuttle, since it may pass through these clouds at high speeds and the cloud particles may affect the craft or its performance. At hypersonic speeds, these clouds may present a corrosion/abrasion hazard (erosion) to forward Thermal Protection System surfaces, increase drag, and may result in abnormal operation of turbojet or scramjet engines (ingestion of particles). The concentration of ice particles could upset guidance, with roll and angle of attack transients, increased Reaction Control System propellant usage and ranging errors. The magnitude of these effects would depend on cloud particle size, number density, and composition. Simulations have shown the vehicle actually skipping off the cloud. The Space Shuttle program has elected to avoid them entirely, so the Shuttle does not currently reenter through the high-latitude zone of NLC occurrence. The threat of NLCs has greatly impacted the operation of the Space Shuttle (ref. 8-17). Therefore, the properties—cloud particle size, including volume density and extent (seasonal/latitudinal/altitudinal/layer

thickness—of these mesospheric clouds are presented in this section. Their frequency and risk/probability of occurrence are also considered here.

8.3.2.1 Mesospheric Cloud Background and Observational Facts.

8.3.2.1.1 Noctilucent Clouds—The highest clouds of Earth (average 83 km (51.6 mi) height) are mesospheric, occurring in the cold, high-latitude regions surrounding both geographical poles. The clouds occur seasonally during their respective summer seasons (June–August in the Northern Hemisphere, and December–February in the Southern Hemisphere). From the ground they are seen typically low on the horizon, within the twilight arch near the Sun's position below the horizon. These clouds are given different names, depending upon their mode of observation. NLCs are their ground-based manifestation, visible as bright cloud features seen against the comparatively dark sky during twilight, when the Sun's rays still strike the clouds while the lower atmosphere is in darkness. At latitudes greater than ≈70°, the summer sky never becomes sufficiently dark to view NLCs at any time of the year. At the lower latitude boundary, ≈55°, the air is normally too warm at any season to support water ice particles. These observing constraints restrict visibility to solar depression angles between 6° and 16°. At night they are invisible due to the absence of sunlight. However, active light, detection, and ranging (LIDAR) techniques reveal their presence at all times, regardless of local time or solar illumination. The 55°–70° latitude region is called the NLC "zone of visibility," or simply the NLC "zone." Occasionally, NLCs are seen outside the "classical" NLC zone. In June 1999, they were photographed and measured by a LIDAR as far south as 41° N. (ref. 8-18).

NLCs are most frequent at the center of the NLC zone, around 60° latitude. From a series of LIDAR measurements, NLC brightness and height have been found to vary with local time at the Arctic LIDAR Observatory for Middle Atmosphere Research in Norway, with both a 12-hr and (weaker) 24-hr periodicity (ref. 8-19). This behavior appears to depend on the longitude of the observing site, since such behavior was not found at a second LIDAR observatory in Greenland (ref. 8-20). Northern NLC occurrence has been monitored by amateur observers for many decades, and a seasonal pattern has emerged from these data. The behavior is approximately defined as Gaussian, centered on ≈15 days following the solstice. See figure 8-4. Southern NLC occurrence appears to be quite similar, relative to the summer solstice, although there are too few observations to perform a statistical analysis. Satellite observations provide a much better north/south comparison.

8.3.2.1.2 Polar Mesospheric Clouds—PMCs are almost certainly the same clouds as NLCs but viewed from space. Because it is possible to distinguish clouds from the atmospheric background even during the daytime hours while the atmosphere is fully sunlit, space-based instrumentation allows PMCs to be viewed in their entirety, all the way to the pole. The detectability of these very thin clouds depends on the geometry of observation. Optimum contrast is achieved when observing at the atmospheric limb, because of the low background radiance scattered from the upper mesosphere. Detecting PMCs in the nadir is impossible at visible wavelengths because of the overwhelmingly bright Earth (Earth albedo). However, in the ultraviolet part of the spectrum, they are distinguishable against the relatively dark Earth albedo (ref. 8-22). PMCs are occasionally seen from space in the 40°–45° band around the summer solstice (ref. 8-23).

It is now established that these are north-south hemispheric differences in PMC properties. In particular, the north has more clouds (by ≈40 percent), and are brighter than their southern counterparts. Additionally, LIDAR observations at the South Pole show that PMCs are several kilometers higher than in the north (ref. 8-24). These differences are explained by different Earth-Sun distances during the respective summers, and also by the different dynamical states of the lower atmosphere in the Arctic and Antarctic. Because of different

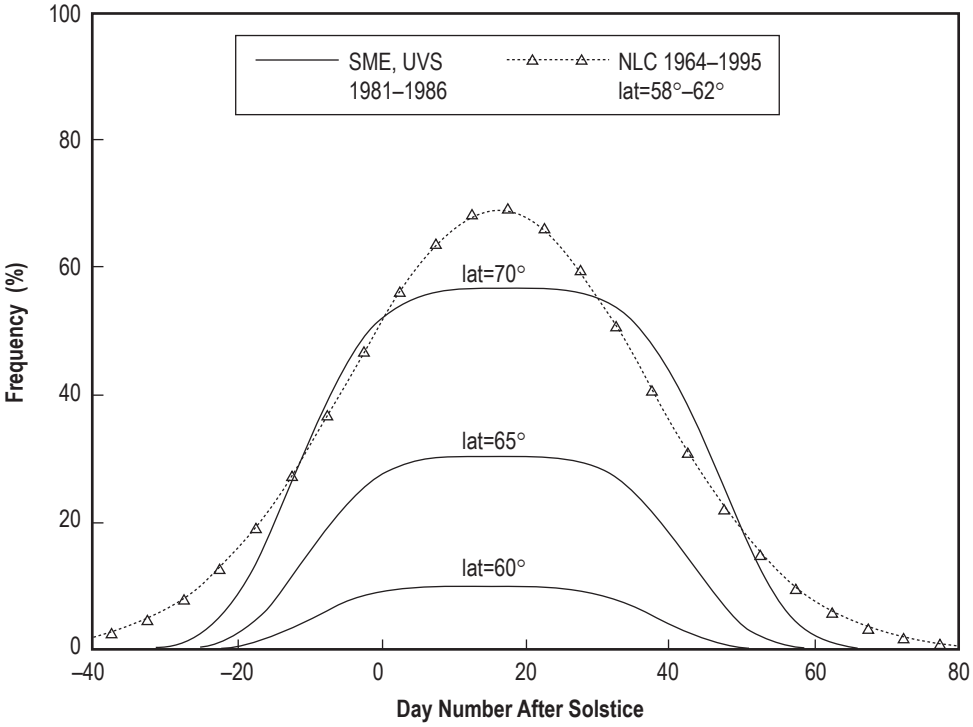

Figure 8-4. Northern and Southern Hemisphere 5-yr average PMC occurrence rate as a function of day number after summer solstice (ref. 8-21).

topographies in the two hemispheres, the tropospheric and stratospheric winds are distinctly different in the two hemispheres. Since these lower atmospheric regions are the sites of wave generation, and are also the medium through which the waves must propagate, mesospheric dynamics has a different morphology between summer hemispheres (ref. 8-25).

As far as is known, there are no inherent differences in PMCs and NLCs, although there are insufficient simultaneous space- and ground-based observations to definitely rule out physical differences. Because PMCs are generally observed poleward of the NLC zone, they are located closer to the cold source regions where the temperature approaches 100 K (–279.7 °F). Summertime temperatures at mesopause heights are colder than in winter, which accounts for the distinct seasonality of mesospheric clouds. Although seemingly paradoxical, the summertime cooling phenomenon is now well understood as an indirect dynamical effect of atmospheric wave forcing. Summertime upwelling of air causes both expansional cooling and advective transport of water vapor from the lower mesosphere and stratosphere, thus explaining the existence of water ice supersaturation during the 3-mo cloud period. Maximum numbers of PMCs/NLCs occur 2–3 wk following the summer solstice. Cloud composition is water ice which has been empirically verified for very bright clouds (ref. 8-26). The particles are expected to be pure ice, with moderately nonspherical shapes. Very small dust cores of silicate matter may exist at the inner core since these particles seem to be necessary to begin the nucleation process.

A good historical review of NLC observations is found in reference 8-27. References 8-28 through 8-30 have more up-to-date information that includes knowledge gained from the space era. More recent scientific journals contain numerous papers describing modern developments as in references 8-22 and 8-31.

8.3.2.1.3 Polar Mesospheric Summer Echos—PMSEs are strong radar echoes that appear during the NLC season. They are closely related to charged ice particles that reduce the diffusivity of electrons such that very small spatial scale structures in the electron gas can exist. The radar echoes are caused by highly structured plasma density fluctuations, concentrated in thin layers, perhaps controlled by the breakup of upward propagating gravity waves and tides. Some of the morphology of PMSEs is similar to that of NLCs. At polar latitudes, they occur with 100 percent probability during midsummer. More information is given in reference 8-32.

8.3.2.2 Mesospheric Cloud Formation. Mesospheric clouds are believed to form (nucleate) on pre-existing aerosol particles, most likely produced by meteoric ablation and recondensation ("meteor smoke"). The formation rate of new ice particles is largest near the temperature minimum (≈88-km altitude). They grow slowly at this altitude, and despite their number density being quite high (perhaps 1,000 cm^{-3}), they are not optically visible due to their small areas. In order for the particles to scatter light efficiently, they need to grow many hours to reach optically efficient sizes (>20 nm radius).

As the newly formed subvisible particles acquire water by sublimation in the supersaturated region of the mesopause, their increasing mass accelerates their downward sedimentation. They eventually fall out of the region of saturation and vanish (near 83 km). Where the air becomes unsaturated, the particles are largest, and because of the strong dependence of scattering cross section on particle size, this is where they are visible to optical measurement techniques—either passive scattering of sunlight or active scattering by LIDARs. This size dependence of the scattering also accounts for the thinness of the optically visible layers, which are often <1 km thick. In fact, the particles apparently occupy the thicker region between about 82 and 90 km, but their altitude-dependent sizes greatly affect what is observed optically. The relative thinness of the layers also makes it possible to view wave structure. Atmospheric waves; e.g., gravity waves or tidal waves, perturb the heights of the layers by several kilometers. There are many aspects of cloud microphysics that are not well understood. The difficulties of measurement in this inaccessible region explain our relative ignorance of many of the cloud processes.

8.3.2.3 Physical Properties of Mesospheric Clouds. Although the chemical composition of mesospheric cloud particles has been established to be water ice, their size distribution is not well known. However, numerous experiments over the past several decades have determined that the effective spherical radii range between 20 and 100 nm, with a typical size range between 30 and 50 nm. The smaller ice nanoparticles are believed to be ubiquitous in the supersaturated regions of the summertime polar region (ref. 8-33). Although invisible by optical means, their presence is inferred from the existence of PMSE, mentioned earlier. The smallness of particle size relative to the wavelength of light causes NLCs to have a bluish color (ref. 8-34). However, this color is determined mostly by the extinction of light through the ozone layer, which removes yellow light. The particles are too small to produce haloes, sundogs, and the various optical phenomena associated with lower atmosphere ice and water particles. The clouds are too thin to have any perceptible effects on starlight. However, as noted earlier, the small extinction—a few percent at most—of sunlight by PMCs can be detected by sensitive instruments in space when the light is attenuated at the Earth's limb.

Estimates of the physical properties of mesospheric clouds and their environment are summarized in table 8-2. All quantities refer to the NLC zone and the summertime polar mesosphere. The column mass of the clouds is more reliable than the particle radius, since they are constrained by the available water content. Typical characteristics of NLCs are presented in table 8-3.

The seasonal climatology for NLCs/PMCs is given in table 8-4, showing a comparison of PMC seasonal properties for 1981–1985 with NLC properties (1885–1972).

Table 8-2. Estimates of physical properties and characteristics of mesospheric clouds (NLCs/PMCs) and their environments* (refs. 8-27 and 8-37).

Properties:
Cloud heights: 81–86 km, average = 83 km
Cloud column mass: $2x10^{-9}$ to $6x10^{-8}$ gm/cm^2 range
Ice particle size: 20–100 nm, with most in the 35- to 70-nm range
Ice particle concentration: 100–200 cm^{-3} (5- to 500-cm^{-3} range)
Ice particle column number: 10^6- to 10^8-cm^{-2} range
Water mixing ratio: 1 to 4 ppmv (up to 10–15 ppmv in the presence of cloud processing)
Temperature at cloud heights: <150 K (< –122 °C)
Temperature at mesopause height (88 km): 100 to 140 K (–172 to –132 °C)
Cloud thickness: 0.5–2.5 km
Cloud extent: 100 s to 1,000 s of kilometers, with small-scale structure down to meters

*Note: Some of the values have been updated to reflect modern information.

Table 8-3. Typical NLC/PMC characteristics (refs. 8-27 and 8-37).

Color	Bluish-white
Height	82.7 km average, 95 km maximum, 79 km minimum
Latitude of observations	50° to 80°; optimum ≈60°
Season of observation—Northern Hemisphere	Mid-May through mid-August
—Southern Hemisphere	Mid-November through mid-February
Time of visibility	While the solar depression angle varies from 6° to 16°
Spatial extent	10^4 to more than $4x10^7$ km^2; can cover considerable parts of latitudinal belts north of 45°
Duration	Several minutes to more than 5 hr
Average velocity	40 m/s towards the southwest*
Thickness in the vertical	0.5 to 2 km
Vertical wave amplitude	1.5 to 3 km
Ambient temperature when NLCs present	150 K (–190 °F)
Polarization	Strongly linearly polarized in same sense as, but more than, twilight sky

*Individual bands often move in different directions and at speeds differing from the NLC display as a whole. Apparent motions of NLCs across the sky are not necessarily indicative of wind speeds, because wave patterns move with their own specific phase speeds, even at times, moving against the mean wind vector.

Table 8-4. Mesospheric cloud seasonal climatology* (ref. 8-37).

	South PMC	North PMC	North NLC
Beginning date**	–32	–23	–38
Ending date	61	64	50
Time of maximum	7–16	16–22	16–20
Duration of season (days)	93	87	88
Lower latitude boundary	60°	55°	50°†
Months observed	Dec–Feb	May–Aug	May-Aug
Interannual variability	±20%	±20%	Factors up to 4
Altitude (km)‡	83.5–85	83–84	81.5–85.5

*Times are given in days after summer solstice.
**Begins at high latitude 10 to 20 days before lower latitude observation. South season begins somewhat earlier and ends earlier than north season (see fig. 8-5).
†This indictes the latitude of the observer, not the clouds, which occurs 3°–5° poleward.
‡Height data were taken from figure 8-4 by Chu (ref. 8-24).

8.3.2.3.1 Vertical Structure of Noctilucent Clouds: In situ NLC measurements have been made during the NLC–93 rocket campaign at Esrange, Sweden (ref. 8-35). The results indicate little vertical variation (vertically homogeneous) of the population throughout most of the 1.6-km NLC layer (from 82.6 to 84.2 km, with the brightness peak around 83 km). The lower part of the cloud exhibited an increase in particle size and a decrease in particle density towards the cloud base, since these larger cloud particles are being sedimented out of the cloud at the end of their life cycle. This has also been observed independently using optical means by von Savigny et al. (ref. 8-37). For a chosen mean water content of 4 ppm mixing ratio (the normal range of variability is 0.5 to 5 ppm around 80-km altitude), particle radii of 55–65 nm are inferred at the brightness peak near 83 km, with particle number densities between 35 and 70 cm^{-3} at the peak. NLC particle radii normally range from 50 nm to perhaps 220 nm in extreme circumstances. Since water vapor is not measured, it needed to be assumed to deduce the particle properties. For an assumed range of mean water content of 2 and 10 ppm, peak radii of 74 and 44 nm and number densities of 14 and 360 cm^{-3} are deduced, respectively (ref. 8-35).

8.3.2.4 Mesospheric Cloud Frequency, Climatology, and Probabilities. PMC occurrence rate, defined as the number of clouds viewed in a time interval divided by the total number of observations, may be thought of as the probability of viewing a cloud from space. The daily occurrence rate is rarely 100 percent, meaning that the cloud distribution is "patchy," undoubtedly due to wave perturbations on a variety of spatial and temporal scales. The experience of the Ultraviolet Spectrometer Experiment on board the solar mesosphere explorer (SME) spacecraft is summarized in figure 8-5 (ref. 8-21), where the 5-yr (1981–1986) average PMC occurrence rate is plotted against day number measured from summer solstice (ref. 8-21). Each solid curve refers to a 5°-wide bin of north latitude. The dashed curves refer to the southern PMC seasons (6 mo separated in actual time). The curves are analytic functions that are fitted to the actual 5-yr average frequencies, accumulated into 5-day time bins. The actual behavior is much more complicated, and during any given year, can vary by as much as 20 percent from the smoothed function shown in figure 8-5. A comparison of the PMC seasonal behavior in the vicinity of the NLC

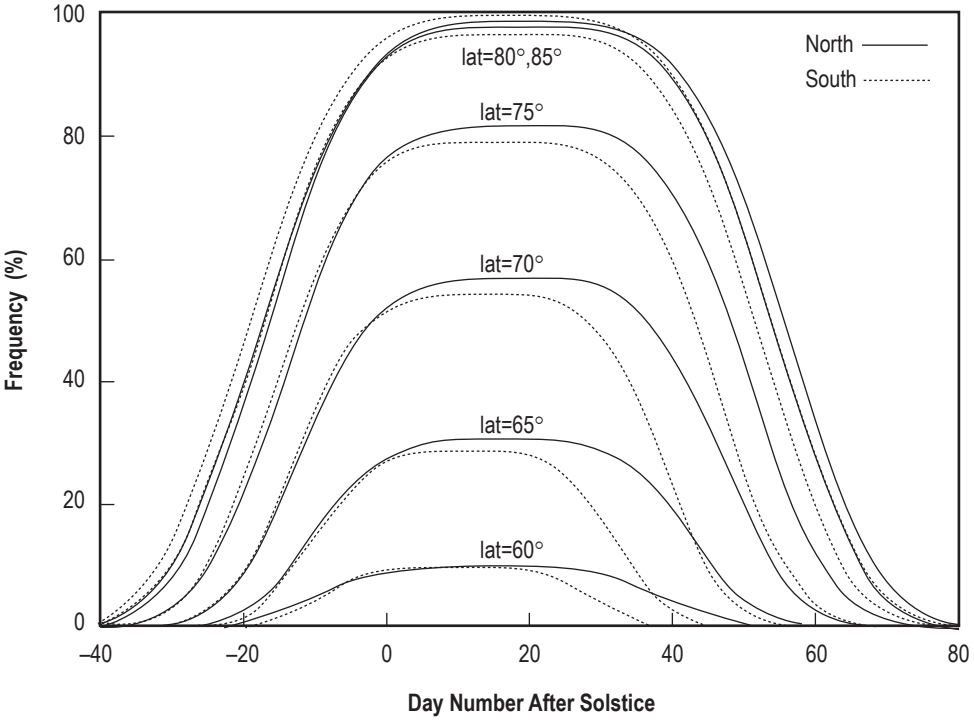

Figure 8-5. Northern Hemispheric 32-yr NLC seasonal frequency plotted with respect to PMC occurrence frequency (ref. 8-21).

zone is made with the corresponding NLC frequency in figure 8-4. Here, the NLC frequency is not defined in the same way as the satellite quantity. Rather, it is defined as the number of clouds seen on that day over a large number of years, divided by the total number of years in the data set. It is interpretated as the probability that on a given summer evening/morning (up to 4–5 hr total duration, depending upon latitude), NLCs will be viewed at some location in the sky. Thus, the numerical values should not be directly compared. Nonetheless, this comparison is useful because it shows that the seasonal cycle of activity of both PMCs and NLCs are similar, even peaking at nearly the same day relative to the solstice. It should be mentioned that NLC sightings can be relatively rare during some seasons, particularly around the times of solar maximum activity. For example, during the previous solar maximum (in 1992), the number of NLC nights reported by the Canadian-Alaskan network of observers was 12. In contrast, some seasons produce many more cloud sightings. The same North American (Canada/American) NLC network reported the greatest number of NLC nights (53) in their 15-yr history during the summer of 2003 (ref. 8-38), despite the fact that the preceding year coincided with the last solar maximum.

Recently, the PMC database has verified an inverse relationship between PMC occurrence frequency and solar activity; i.e., they are less often seen at solar maximum throughout the 11-yr solar cycle. Stronger anticorrelation values are observed in the Northern Hemisphere; i.e., $R_{solar} = -0.87$) (ref. 8-39). Even though the solar cycle seems to be an important factor in determining overall cloud activity, there are other important sources of interannual variability that are not understood.

The occurrence of NLCs seems to be increasing. For the past 25 yr, the UV brightness of the seasonally-averaged PMC observed by satellites has increased significantly in both hemispheres, amounting to ≈1 percent/year (refs. 8-22 and 8-30). This change is not observable from the ground because of the overall smallness of the effect, and because of observational difficulties present in ground-based data that mask such subtle effects. The reasons for the increase are not known; although, it has been long suspected that increases in water vapor, associated with enhanced methane (CH_4) levels are at least partly responsible. If CH_4 is indeed the cause, and this is not yet proven, this would verify the speculation that NLCs are anthropogenic in origin (ref. 8-37). Their "discovery" in 1885 may have been their first appearance due to the enhanced CH_4 caused by the industrial revolution, and specifically, the increase in population with the associated growth of agriculture, mining, etc. The first observations also may have been influenced by the earlier Krakatoa eruption, occurring in 1883 (refs. 8-40 and 8-41). This subject is still a point of debate, and has caused many lively discussions at professional meetings. The point of contention is that the natural interannual variability of NLCs masks any underlying trends, and that longer data sets (50 yr or more) are needed to distinguish natural variability from a systematic long-term effect (ref. 8-42). On the other hand, it is claimed that if the trend is large enough, and most of the natural variability is understood; e.g. solar effects, then the effects may be separated in a statistically significant way. Furthermore, a causal explanation is readily available in terms of CH_4 buildup (ref. 8-43).

8.3.2.5 Noctilucent Cloud Types. Fogle and Haurwitz (ref. 8-27) have classified NLCs as follows:

- Type I. Veils—These are the simplest. They are very tenuous with no well-defined structure, and are often present as a background for other categories or forms. They are somewhat like cirrus clouds of uncertain shape; however, occasionally they exhibit a faintly visible fibrous structure.

- Type II. Bands—These are long streaks with diffuse edges (type IIa) or sharply defined edges (type IIb). They are sometimes hundreds of kilometers long and often occur in groups arranged approximately parallel to each other or interwoven at small angles—perhaps visible evidence of gravity waves propagating through the region. Occasionally, an isolated band is observed. Bands change very little with time, and blurred bands with little movement are often the predominant structure in the NLC field. When they do move, it is often in a direction

and speed that is different from that of the display as a whole. Very closely spaced thin streaks, called serrations, are occasionally seen in the veil background. They look like a continuous cloud mass since the serrations are separated by only a few kilometers.

- Type III. Billows—These are groups of closely spaced short bands that sometime consist of straight and narrow, sharply outlined parallel short bands (type IIIa). Sometimes they exhibit a wave-like structure (type IIIb). The distance separating pairs of billows is ≈10 km. Billows sometimes lie across the direction of the long bands and their alignment usually differs noticeably in portions of the sky. Unlike the long bands, billows may change their form and arrangement, or even appear and disappear within a few minutes.

- Type IV. Whirls—Whirls with varying degrees of curvature are also observed in veils, bands, and billows; infrequently, complete rings with dark centers are formed. Whirls of small curvature (<1°) are classified as type IVa, while whirls having a single simple band or several bands with a radius of 3° to 5° are classified as type IVb. Larger scale whirls are classified as type IVc.

- Type V. Amorphous—These are similar to veils in that they have no well-defined structure, but they are brighter and more readily visible than the veil type NLCs.

8.3.2.6 Polar Mesospheric Clouds From Shuttle Exhaust? Scientists at the Naval Research Laboratory (NRL) (ref. 8-44) have determined that the exhaust plume from NASA's Space Shuttle (which is ≈97 percent water vapor) can travel northward to the Arctic thermosphere where it descends to form ice and creates PMCs. The NRL's middle atmospheric, high-resolution spectrograph satellite instrument launched on STS–85 in August 1997 followed in its orbit the Shuttle plume's rapid poleward transport and then observed a discrete region of ice clouds as they appeared in the Arctic mesosphere near the end of the mission. Water contained in these clouds was consistent with the amount injected into the thermosphere during the Shuttle's east coast ascent. About half of the Shuttle's water vapor exhaust was injected into the thermosphere between 108- to 114-km altitude, and was determined to be transported to the Arctic in a little over a day. The plume was ≈1,100 km long with a diameter of ≈3 km. Ground-based measurements of mesospheric water vapor also supported this hypothesis. As the water vapor moved to the Arctic, UV destroyed some of the plume. The remaining plume fell from the warmer thermosphere down to the colder (–40 °C) mesospheric regions where the water vapor condensed into ice particles and the clouds (polar mesospheric) formed.

Stevens (ref. 8-44) indicated that 3 yr earlier, the middle atmosphere high-resolution spectrograph investigation also observed a large hydroxyl (OH) cloud at ≈110 km altitude northeast of the United States 20 hr after STS–66 was launched in November 1994 from Kennedy Space Center. This OH cloud was at the same altitude as an extended trail of water vapor exhaust released from the Shuttle's main engines <10 min after launch. Because the upper mesosphere is relatively dry, the contribution of the launch vehicle's exhaust to the local water vapor budget may be significant.

Even more remarkable, the NRL group found that the plume from the ill-fated *Columbia* launch in January 2003 was carried to the Southern Hemisphere summertime polar region within 3 to 4 days. The plume —at ≈110 km altitude containing ≈400 tons (≈363,000 kg) of water vapor, was ≈1,000 km long and ≈3 km in diameter—maintained its integrity, producing a burst of PMCs during southern summer. In addition, LIDAR measurements at Rothra, Antarctica, revealed that metallic iron (produced by the main Shuttle engines) was contained in the transported plume, a marker that makes the identification undeniable (ref. 8-45). Note that the Shuttle, at the proper orbit inclination and during a PMC season, could help generate its own PMC field that the Shuttle could possibly fly through during its return to Earth.

8.4 Cirrus Clouds and Contrails

8.4.1 Cirrus Clouds

Cirrus clouds are globally widespread and are important modulators of incoming solar and outgoing terrestrial radiation of the Earth-atmosphere energy budget (ref. 8-46). Cirrus clouds are upper tropospheric clouds above 6 to 8 km (20,000 to 25,000 ft) altitude, usually consisting of small ice crystals (generally >25 μm in diameter), where the ambient temperature is generally below –30 ºC. Cirrus clouds have a silken appearance. The stratosphere is normally so dry that cirrus and PSCs form only during polar winter. Most frequently, cirrus clouds occur in layers with thicknesses averaging ≈1.5 km, with horizontal dimensions of hundreds or even thousands of kilometers. Cirrus clouds typically cover from 20 to 40 percent of the Earth's surface (at times even up to ≈70 percent over the tropics). Ground-based observations indicate ≈13 percent mean cirrus cover over ocean areas, and ≈23 percent over land, whereas, satellite observations indicate a greater coverage of ≈40 percent (ref. 8-47).

Once formed, cirrus crystals can grow rapidly until they reach ≈50 μm, when their growth slows. Measured cirrus particle sizes range from 10 to 2,000 μm. Cirrus ice crystal concentrations normally range from 0.01 to 0.1 cm^{-3} (mean of 0.03 cm^{-3}), but can range from less than 0.0001 to 10 cm^{-3} (ref. 8-47). A 10-yr database (1986–1996) of cirrus cloud LIDAR measurements for a U.S. midlatitude site (Salt Lake City, Utah) (ref. 8-48) produces the climatological properties of cirrus heights, thicknesses, and temperatures that are given in table 8-5. Dowling and Radke (ref. 8-49) reviewed the existing literature to determine typical global values (and measured ranges) for the physical properties of cirrus clouds. Their results are presented in table 8-6, and these values should be used in any engineering design studies. The average global frequency of cirrus cloud occurrence, along with other atmospheric clouds, is summarized in table 8-7.

Table 8-5. Midlatitude (Utah) 10 yr-average cirrus cloud height-thickness and temperature properties (refs. 8-47 and 8-48).

	Annual Average (Height or Thickness)		Seasonal Range of Average (Height or Thickness)		Cloud Temperature		Sesonal Range of Average Cloud Temperature	
Cirrus Cloud Parameter	(km)	(ft)	(km)	(ft)	(°C)	(°F)	(°C)	(°F)
Cloud height:								
Cloud base height	8.79	28,839	8.4–9.1	27,559–29,856	–37.4	–35.3	–32.6 to –39	–26.7 to –38.2
Cloud top height	11.02	36,155	10.71–11.15	35,138–36,581	–53.9	–65.0	–47.6 to –55.9	–53.7 to –68.6
Cloud thickness:								
Layer envelope	2.23	7,316	2.02–2.31	6,627–7,579				
Multiple layer	1.24	4,068	1.13–1.38	3,707–4,528				
All layers	1.81	5,938	1.6–1.93	5,249–6,332				

8.4.2 Contrails

Contrails (condensation trails) are manmade, line-shaped clouds that only form at very high altitudes (usually above 8 km) by jet aircraft engine exhaust when the ambient air is extremely cold (less than –40 ºC (–40 ºF)) and moist.

Table 8-6. Typical global values and measured ranges of the physical properties of cirrus clouds (ref. 8-49).

Cirrus Cloud Properties	Typical Value	Measured Range
Cloud thickness	1.5 km	0.1 to 8 km
Cloud-center altitude*,**	9 km	4 to 20 km
Crystal number density (concentration)	0.03 cm^{-3} (30 L^{-1})	10^{-7} to 10^{1} cm^{-3} (10^{-4} to 10^{4} L^{-1})
Ice water content (condensed)	0.025 g/m^3	10^{-4} to 1.2 g m^{-3}
Crystal size (length)	250 μm	1 to 8,000 μm

*One year of SAGE global satellite measurements indicated a cirrus mean altitude of 7 km at the poles and increasing to near 13.5 km altitude at both 5° S. and N. latitudes (ref. 8-49).

**The typical cirrus cloud-center height roughly occupies the altitude range from 70% to 80% of the local tropopause height anywhere on Earth (ref. 8-49), as cirrus generally form within the upper troposphere, and beneath the local tropopause. Although thin cirrus clouds have been detected within the lower stratosphere above the local tropopause (ref. 8-50).

Table 8-7. Types and average properties of global* clouds** (refs. 8-51 through 8-53).

	Tropical Height of Base		Midlatitude Height of Base		Polar Height of Base		Global % Frequency of Occurrence (Oceans)	Global % Areal Coverage (Oceans)	Global % Frequency of Occurrence (Land)	Global % Areal Coverage (Land)
Cloud Type	(km)	(ft)	(km)	(ft)	(km)	(ft)				
Develop Vertically	0–3	0–9,840	0–3	0–9,840	0–3	0–9,840				
Cumulus							33	12	14	5
Cumulonimbus							10	6	7	4
Low Level										
Stratocumulus	0–2	0–6,560	0–2	0–6,560	0–2	0–6,560	45	34	27	18
Stratus	0–2	0–6,560		0–6,560		0–6,560	45	34	27	18
Nimbostratus	0–4	0–13,125		0–13,125		0–13,125	6	6	6	5
Mid Level	2–8	6,560–26,250	2–7	6,560–22,970	2–4	6,560–22,970	46	22	35	21
Altocumulus										
Altostratus										
High Level	7–18	22,970–59,055	5–13	16,400–42,650	3–8	9,840–26,250	37	13	47	23
Cirrus										
Cirrostratus										
Cirrocumulus										

*Overlapping clouds often coexist over the same area.

**A good summarized cloud cover map database (based on 1982–2001 ISCCP data), giving monthly (with annual) mean percent global cloud cover, is given at the University of Manitoba Web site: <http://home.cc.umanitoba.ca/~jander/clouds/globalclouds.html> (ref. 8-54).

If the air is very dry, contrails will not form behind the plane, but if the air is moist, a contrail will form. Contrails will usually grow wider and fuzzier as time passes. Sometimes they can take on the characteristics of a natural cirrus cloud and no longer look like contrails after only a half hour or more. Contrails can last for a few minutes or longer than a day (ref. 8-55). Jet engine exhaust provides only a very small portion of the water vapor that forms the ice in persistent contrails, since contrails are mostly composed of water naturally present along the aircraft flight path. After initial ice cloud formation, if the ambient humidity is low (or below the conditions for ice condensation to occur), the contrail will dissipate quickly. However, if the humidity is high, the contrail will persist, and the newly formed ice particles will continue to grow by deposition of water from the surrounding atmosphere. Once formed, a contrail develops or dissipates in the same manner as a naturally generated cirrus cloud. Contrails spread due to the aircraft-generated air turbulence, differences in wind speed along the flight track, and possibly through solar heating. Enough particles are normally present in the surrounding

atmosphere, however, that particles from the engine are not required for contrail formation. The ice particles evaporate when local atmospheric conditions become dry (low relative humidity). The ice particles fall slowly, and thermal/humidity conditions in the lower atmosphere cause the ice particles to sublimate (ref. 8-56).

Contrails are normally composed of ice crystals with trace amounts of exhaust products such as sulfates, soot, and other small particles. The relative humidity with respect to liquid water temporarily reaches the saturation point (100 percent) in the plume mixture of ambient air and hot exhaust gases in order for contrail formation to occur. Tiny droplets develop on background aerosols or on aerosols formed by exhaust products. Because of the cold ambient air temperature, the small water droplets instantly freeze and grow via vapor-to-ice deposition as long as the relative humidity with respect to ice remains above the saturation point. Contrails dissipate via sublimation if the air is below the saturation point, or if by precipitation, into unsaturated layers below the flight level (ref. 8-57). Contrails often form ahead of advancing fronts in the poleward flow of an upper level trough where conditions are not quite optimum enough for natural cirrus development. They can occur at multiple atmospheric levels as the formation conditions often cover a large depth of the atmosphere, as air traffic uses a wide range of altitudes.

Contrails can also form within cirrus clouds, where they are manifest as reduced particle sizes or local thickening of the cloud. Aircraft exhaust can also affect supercooled liquid water clouds. The aircraft introduces ice nuclei that cause freezing of the cloud droplets, resulting in a rapid depletion of the available water vapor onto the frozen droplets. These newly formed ice crystals quickly grow large enough to fall out of the cloud, resulting in a fall-streak below the cloud and a gap (distrail) within the cloud. Smaller and less frequent contrails (of liquid water droplets) also can form briefly at the warmer temperatures behind the leading edges of aircraft wings flying at high speed in a humid atmosphere.

8.4.2.1 Contrail Statistics. The National Oceanic and Atmospheric Administration/high-resolution infrared sounder (HIRS) satellite 22-yr global data record (1979–2001) indicates that clouds of all types are found in ≈75 percent of all HIRS observations. High-level clouds (cirrus) are found in ≈33 percent of the HIRS observations, with an over-land maximum in summer for both hemispheres. Low- and middle-level clouds are found with a frequency of ≈49 and ≈26 percent, respectively, within this HIRS data sample field of view (ref. 8-58). Persistent line-shaped contrails are estimated to cover, on average, ≈0.1 percent of the Earth's surface (see fig. 8-6), with the highest percentages of cover over Europe and the U.S. associated with the greatest volume of air traffic (ref. 8-56).

Persistent contrails can last for hours while growing to several kilometers in width and 200 to 400 m in depth during the first 1-hr time frame (ref. 8-56). When contrails persist, the particles typically grow to 30 μm, with a range of 5 to 100 μm (ref. 8-59). Particle sizes >1,000 μm have been observed, and these sizes are usually associated with natural cirrus clouds. The number density of persistent contrail ice crystals ranges from 10 to 200^{+} cm^{-3}, and is much larger than in natural cirrus clouds. Normally, there are larger particles (up to 300 μm in diameter) on the contrail edges that are similar in size to natural cirrus, while within the contrail core, much smaller particles exist (ref. 8-47). Tables 8-7 and 8-8 present statistics on contrail particle size and number density. The contrail microphysics indicates a mean optical depth (τ) between 0.1 and 0.4, while its range can vary between 0.01 and 2 (ref. 8-59).

A single aircraft flying for <1 hr in a moist atmosphere was observed to cause a cirrus cloud that eventually covered up to 4,000 km^2 (1,540 mi^2) and lasted for over 6 hr. Other contrails and contrail clusters were observed to cover areas of 12,000 to 35,000 km^2 (4,630 to 13,510 mi^2). Figure 8-7 illustrates the extent (over the

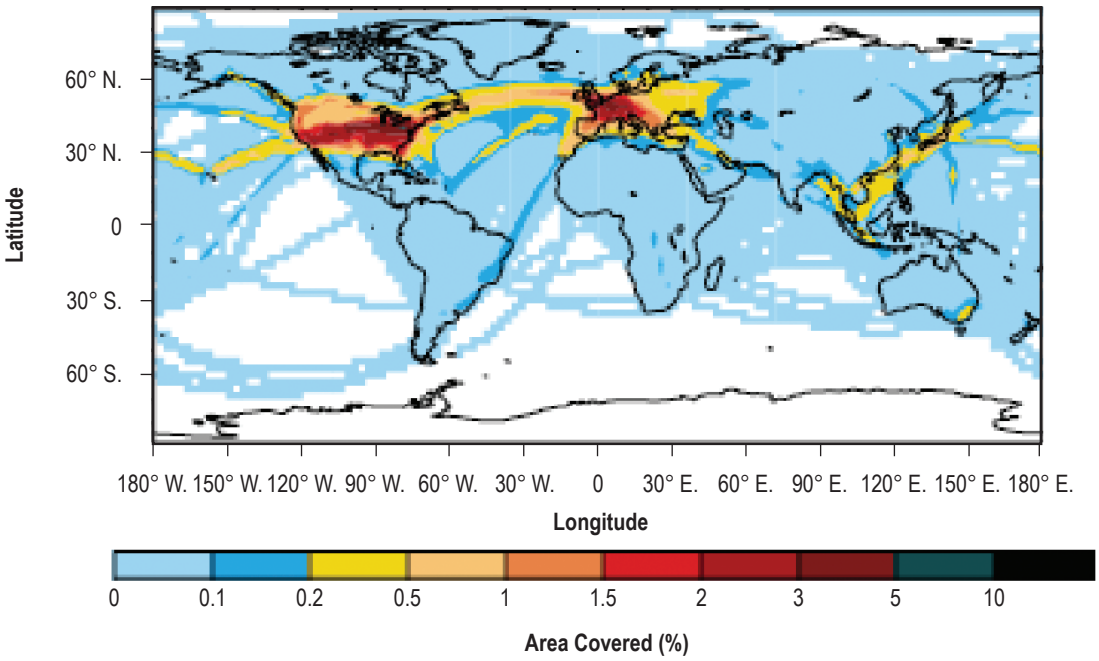

Figure 8-6. Estimated global persistent contrail coverage (in percent area cover) for the 1992 Worldwide Aviation Fleet. The global mean cover is 0.1 percent (ref. 8-56).

Table 8-8. Contrail particle size versus time (ref. 8-47).

Contrail: Plume Age (time)	Particle Size: Mean Radius (μm)	Particle Size: Radius Range (μm)	Particle Size: Max Radius (μm)
30 to 70 s	2	0.02 to 10	22
2 min	2 to 5	–	–
10 min to 1 hr	–	32 to 100	75 to 2,000

southern United States) that contrails can contribute to the local cloud cover (ref. 8-60). United States data (from 19 U.S. locations) indicate that contrail frequency peaks around February/March with a minimum during July. Annual mean persistent contrail frequency (not the cover) for the 19 sites was 13 percent (ref. 8-61).

8.4.2.2 Contrail Example. Contrail formation for a given aircraft flight can be accurately predicted if the ambient atmospheric temperature and humidity conditions are known (ref. 8-56). Figure 8-8 presents two air parcels, A and B (or D and E). Parcel B (or E) represents the engine exhaust. As the exhaust mixes with the environment (parcel A or D), its resultant temperature and corresponding vapor pressure will follow the dotted line. Where this dashed mixing line intersects the liquid saturation line (at point F) is where the parcel becomes saturated and a contrail may form (but not at point C). Two other examples (mixing lines III and IV) are also given in this figure that would produce contrails (ref. 8-62). Ackerman and Knox (ref. 8-63) offer an interactive graph on the internet (at <http://profhorn.aos.wisc.edu/wxwise/AckermanKnox/chap15/contrail_applet.html>) which shows

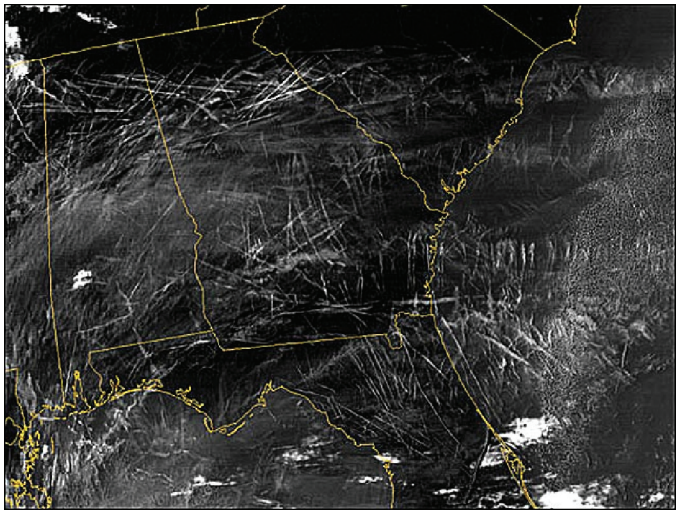

Figure 8-7. NASA's Terra satellite (MODIS) image of widespread aircraft contrails over the Southeastern United States during the morning of January 29, 2004 (ref. 8-60).

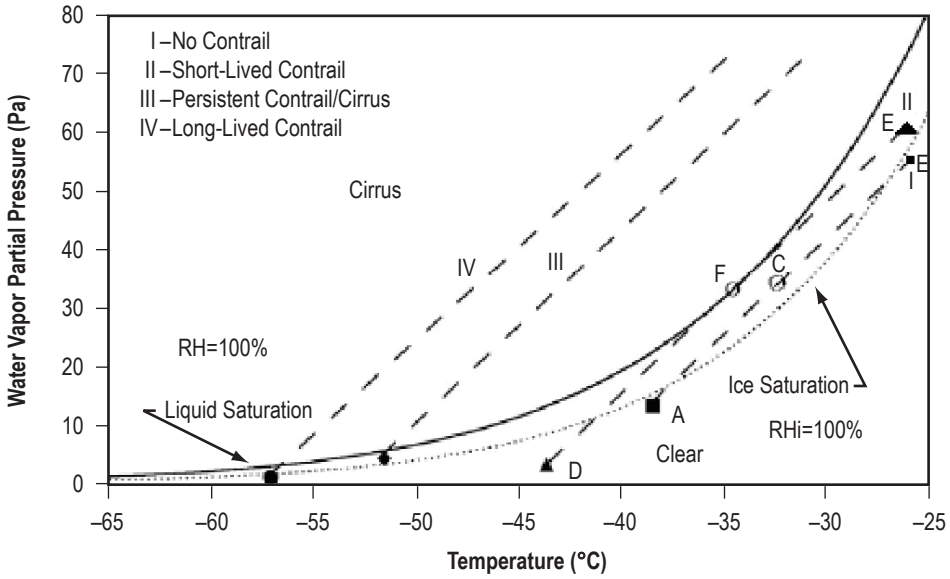

Figure 8-8. Contrail formation: Mixing of ambient air and exhaust (ref. 8-62).

air temperature versus water partial pressure. One then can choose an ambient temperature and relative humidity to simulate a flight and predict whether contrails develop. The degree of supersaturation impacts the density of the contrail, while the ambient relative humidity impacts the rate of contrail dissipation. The wind speed impacts the rate of spreading of the contrail (ref. 8-63).

Table 8-9. Contrail and cirrus ice particle number mean radius, number density, and surface area density (ref. 8-47).

Ice Crystals	Radius (μm)	Number Density (cm^{-3})	Surface Area Density ($\mu m^2\ cm^{-3}$)
Young contrail (0.1 to 0.5 s)	0.3–1	10^4–10^5	10^4–10^5
Persistent contrail (10 min to 1 hr)	1–15	10–500	10^3–10^4
Young cirrus	5–10	1	10^2–10^4

REFERENCES

8-1. Brown, S.C.; and Jeffries, W.R., III: "A New NASA/MSFC Mission Analysis Global Cloud Cover Data Base," *NASA TR–2448*, Marshall Space Flight Center, AL, March 1985.

8-2. Spiegler, D.B.; and Fowler, M.G.: "Four-Dimensional Worldwide Atmospheric Models (Surface to 25-km Altitudes)," Allied Research Associates, Inc., *NASA CR–2082*, Marshall Space Flight Center, AL, July 1972.

8-3. Leslie, F.W.; and Justus, C.G.: "The NASA MSFC Earth Global Reference Atmospheric Model–2007 Version," NASA/TM—2008–215581, Marshall Space Flight Center, AL, November 2008.

8-4. Gaut, N.E.; and Reifenstein, E.C., III: "Interaction Model of Microwave Energy and Atmospheric Variables," Environmental Research and Technology, Inc., Final Report of Contract NAS8–26275, TR No. 13, 1971.

8-5. Farrukh, U.O.: "Polar Stratospheric Cloud Sightings by SAM II: 1978–1982," *NASA CR–177995*, Marshall Space Flight Center, AL, March 1986.

8-6. McCormick, M.P.; and Hamill, P.: "Characteristics of Polar Stratospheric Clouds as Observed by SAM II, SAGE, and LIDAR," *J. Meteor. Soc. Japan*, Vol. 63, No. 2, pp. 267–276, April 1985.

8-7. Hamill, P.; and McMaster, L.R.: "Polar Stratospheric Clouds—Their Role in Atmospheric Processes," *NASA CP–2318*, 1984.

8-8. Hofmann, D.J.; Deshler, T.L.; Aimedieu, P.; et al.: "Stratospheric Clouds and Ozone Depletion in the Arctic During January 1989," *Nature*, Vol. 340, pp. 117–121, July 13, 1989.

8-9. Seinfeld, J.H.; and Pandis, S.N.: *Atmospheric Chemistry and Physics*, Wiley Interscience, New York, 1998.

8-10. Kinne S.; Toon, O.B.; Toon, G.C.; et al.: "Measurements of Size and Composition of Particles in Polar Stratospheric Clouds From Infrared Solar Absorption Spectra," *J. Geophys. Res.*, Vol. 94, No. D14, pp. 16,481–16,491, November 30, 1989.

8-11. Toon, O.B.; Tabazadeh, A.; Browell, E.V.; and Jordan, J.: "Analysis of LIDAR Observations of Arctic Polar Stratospheric Clouds During January 1989, *J. Geophys. Res.*, Vol. 105, No. D16, pp. 20,589–20,615, August 27, 2000.

8-12. Hamill, P.; Turco, R.P.; and Toon, O.B.: "On the Growth of Nitric and Sulfuric Acid Aerosol Particles Under Stratospheric Conditions," *J. Atmos. Chem.*, Vol. 7, pp. 287–315, 1988.

8-13. McCormick, M.P.; and Trepte, C.R.: "Polar Stratospheric Optical Depth Observed Between 1978 and 1985," *J. Geophys. Res.*, Vol. 92, No. D4, pp. 4297–4306, April 20, 1987.

8-14. Kent, G.S.; Poole, L.R.; and McCormick, M.P.: "Characteristics of Arctic Polar Stratospheric Clouds as Measured by Airborne LIDAR," *J. Atmos. Chem.*, Vol. 43, No. 20, pp. 2149–2161, October 15, 1986.

8-15. Steele, H.M.; Hamill, P.; McCormick, M.P.; and Swissler, T.J.: "The Formation of Polar Stratospheric Clouds," *J. Atmos. Sci.*, Vol. 40, pp. 2055–2067, August 1983.

8-16. Stanford, J.L.; and Davis, J.S.: "A Century of Stratospheric Cloud Reports: 1870–1972," *Bull. AMS*, Vol. 55, No. 3, pp. 213–219, March 1974.

8-17. Hale, N.W.; Lamotte, N.O.; and Garner, T.W.: "Operational Experience With Hypersonic Flight of the Space Shuttle," AIAA–2002–5259, 11th AIAA/AAF International Conference on Space Planes and Hypersonic Systems and Technologies, Orleans, France, September 2002.

8-18. Wickwar, V.B.; Taylor, M.J.; Herron, J.P.; and Martineau, B.A.: "Visual and LIDAR Observations of Noctilucent Clouds Above Logan, Utah, at 41.7 °N," *J. Geophys. Res.*, Vol. 107, No. D7, p. 4054, doi:10.1029/2001JD001180, 2002.

8-19. Fiedler, J.; Baumgarten, G.; and von Cossart, G.: "Mean Diurnal Variations of Noctilucent Clouds During 7 Years of LIDAR Observations at ALOMAR," *Annales Geophys.*, Vol. 23, pp. 1175–1181, June 3, 2005.

8-20. Thayer, J.P.; Rapp, M.; Gerrard, A.J.; et al.: "Gravity-Wave Influences on Arctic Mesospheric Clouds as Determined by a Rayleigh LIDAR at Sondestrom, Greenland," *J. Geophys. Res.*, Vol. 108, No. D8, p. 8449, doi:10.10129/2002JD002363, 2003.

8-21. Shettle, E.P.; Burton, S.P.; Olivero, J.J.; et al.: "SAGE II Measurements of Polar Mesospheric Clouds," in the Memoirs Brit. Astron. Assoc., *Mesospheric Clouds,* Vol. 45, M. Gadsden and N.D. James, eds., 2002.

8-22. DeLand, M.T.; Shettle, E.P.; Thomas, G.E.; and Olivero, J.J.: "A Quarter-Century of Satellite PMC Observations," *J. Atmos. & Solar Terres. Physics*, Vol. 68, pp. 9–29, 2006.

8-23. Merkel, A.W.: "Dynamical Influences on Polar Mesospheric Clouds Observed From the Student Nitric Oxide Explorer," Ph.D. Dissertation, University of Colorado, 2002.

8-24. Chu, X.; Nott, G.J.; Espy, P.J.; et al.: "LIDAR Observations of Polar Mesospheric Clouds at Rothera, Antarctica (67.5°S., 68°W.)," *Geophys. Res. Lett.*, Vol. 31, No. L02114, doi:10.1029/2003GL018638, 2004.

8-25. Siskind, D.E.; Stevens, M.H.; and Englert, C.R.: "A Model Study of Global Variability in Mesospheric Cloudiness," *J. Atmos. Sol. Terr. Phys.*, Vol. 67, No. 5, pp. 429–519, 2005.

8-26. Hervig, M.; Thompson, R.E.; McHugh, M.; et al.: "First Confirmation That Water Ice is the Primary Component of Polar Mesospheric Clouds," *Geophys. Res. Lett.*, Vol. 38, pp. 971–974, 2001.

8-27. Fogle, B.; and Haurwitz, B.: "Noctilucent Clouds," *Space Sci. Rev.*, Vol. 6, No. 3, pp. 279–340, 1966.

8-28. Gadsden, M.; and Schroder, W.: *Noctilucent Clouds*, 165 pp., Springer-Verlag, New York, 1989.

8-29. Thomas, G.E.: "Mesospheric Clouds and the Physics of the Mesospause Region," *Rev. Geophys.*, Vol. 29, pp. 553–576, 1991.

8-30. Thomas, G.E.: "Global Change in the Mesosphere-Lower Thermosphere Region: Has it Already Arrived?" *J. Atmos. Sol. Terr. Phys.*, Vol. 58, pp. 1629–1656, 1996.

8-31. Thayer, J.P.; Thomas, G.E.; and Lubken, F.-J.: "Foreword: Layered Phenomena in the Mesopause Region," *J. Geophys. Res.*, Vol. 108, No. D8, p. 8434, doi:10.1029/2002JD003295, 2003.

8-32. Lübken, F.-J.; Zecha, M.; and Höffner, J.: "Temperatures, Polar Mesospheric Summer Echoes and Noctilucent Clouds Over Spitzbergen (78°N), *J. Geophys. Res.*, Vol. 109, No. D11203, doi:10.1029/2003JD004247, 2004.

8-33. von Zahn, U.; and Berger, U.: "Persistent Ice Cloud in the mid-Summer Upper Mesosphere at High Latitudes: Three-Dimensional Modeling and its Interactions With the Ambient Water Vapor," *J. Geophys. Res.*, Vol. 108, No. D8, p. 8451, doi: 10.1029/2002JD002409, 2003.

8-34. Ostdiek, V.J.; and Thomas, G.E.: "Visible Spectra and Chromaticity of Noctilucent Clouds," *J. Geophys. Res.*, Vol. 98, pp. 20,347–20,356, 1993.

8-35. Gumbel, J.; and Witt, G.: "In situ Measurements of the Vertical Structure of a Noctilucent Cloud," *Geophys. Res. Lett.*, Vol. 25, No. 4, pp. 493–496, February 15, 1998.

8-36. von Savigny, C.; Petelina, S.V.; Karlsson, B.; et al.: "Vertical Variation of NLC Particle Sizes Retrieved From Odin/OSIRIS Limb Scattering Observations," *Geophys. Res. Lett.*, Vol. 32, L07806, doi 10.1029/2004GL021982, April 7, 2005.

8-37. Thomas, G.E.; and Olivero, J.J.: "Climatology of Polar Mesospheric Clouds 2, Further Analysis of Solar Mesospheric Explorer Data," *J. Geophys. Res.*, Vol. 94, No. D12, pp. 14,673–14,681, October 20, 1989.

8-38. Zalick, M.: NLC CAN-AM Report, Summer, 2004, available from Mark Zalcik, E-mail: bluegrama@shaw.ca, 2004.

8-39. DeLand, M.T.; Shettle, E.P.; Thomas, G.E., and Olivero, J.J.: "Solar Backscattered Ultraviolet (SBUV) Observations of Polar Mesospheric Clouds Over Two Solar Cycles," *J. Geophys. Res.*, Vol. 108, No. D8, p. 8445, doi:10.1029/2002JD002398, 2003.

8-40. Thomas, G.E.; and Olivero, J.J.: "Noctilucent Clouds as Possible Indicators of Global Change in the Mesosphere," *Adv. Space Res.*, Vol. 28, pp. 937–946, 2001.

8-41. Thomas, G.E.: "Are Noctilucent Clouds Harbingers of Global Change in the Middle Atmosphere?" *Adv. Space Res.*, Vol. 32, No. 9, pp. 1737–1746, 2003.

8-42. von Zahn, U.: "Are Noctilucent Clouds Truly a 'Miner's Canary' for Global Change?" *Eos Trans*. AGU, Vol. 84, pp. 261, 264, 2003.

8-43. Thomas, G.E., Olivero, J.J.; DeLand, M.; and Shettle, E.P.: Comment on "Are Noctilucent Clouds Truly a 'Miner's Canary' for Global Change?" *Trans*. AGU, Vol. 84, No. 36, pp. 352–353, 2003.

8-44. Stevens, M.H.; Gumbel, J.; Englert, C.R.; et al.: "Polar Mesospheric Clouds Formed From Space Shuttle Exhaust," *Geophys. Res. Lett.*, Vol. 30, No. 10, p. 1546, doi:10.1029/2003GL017249, 2003.

8-45. Stevens, M.H.; Meier, R.R.; Chu, X.; et al.: "Antarctic Mesospheric Clouds Formed From Space Shuttle Exhaust," *Geophys. Res. Lett.*, Vol. 32, No. 13, L13810, doi:10.1029/2005GL023054, 2005.

8-46. Sassen, K.; Liou, K-N; Takano, Y.; and Khvorostyanov, V.I.: "Diurnal Effects in the Composition of Cirrus Clouds," *Geophys. Res. Lett.*, Vol. 30, No. 10, p. 1539, doi:10.1029/2003GL017034, 2003.

8-47. *Aviation and the Global Atmosphere*, Chapter 3: Aviation-Produced Aerosols and Cloudiness, United Nations Environment Programme/Global Resource Information Database (UNEP/GRID) Cambridge University Press, 1999.

8-48. Sassen, K.; and Campbell, J.R.: "A Midlatitude Cirrus Cloud Climatology From the Facility for Atmospheric Remote Sensing, Part I: Macrophysical and Synoptic Properties," *JAS*, Vol. 58, pp. 481–496, March 1, 2001.

8-49. Dowling, D.R.; and Radke, L.F.: "A Summary of the Physical Properties of Cirrus Clouds," *J. Appl. Meteor*, Vol. 29, pp. 970–978, September 1990.

8-50. Keckhut, P.; Hauchecorne, A.; Bekki, S.; et al.: "Indications of Thin Cirrus Clouds in the Stratosphere at Mid-Latitudes," European Geosciences Union, *Atmospheric Chemistry and Physics*, Vol. 5, pp. 3407–3414, 2005.

8-51. Warren, S.G.; Hahn, C.J.; London, J.; et al.: "Global Distribution of Total Cloud Cover and Cloud Type Amounts Over Land," NCAR Technical Note TN-273+STR, NCAR, Boulder, CO, 1986.

8-52. Warren, S.G.; Hahn, C.J.; London, J.; et al.: "Global Distribution of Total Cloud Cover and Cloud Type Amounts Over Land," NCAR Technical Note TN-317+STR, NCAR , Boulder, CO, 1988.

8-53. Veerabuthiran, S.: "High-Altitude Cirrus Clouds and Climate," *Resonance*, Vol. 9, No. 3, pp. 23–32, March 2004.

8-54. "Global Cloud Cover Maps," World Climate Research Program, <http://home.cc.umanitoba.ca/~jander/clouds/globalclouds.html>, 2006.

8-55. Minnis, P.: "Contrails–Aviation's Clouds," in *S'Cool Breeze*, Vol. 1, Issue 3, December 1998.

8-56. "Aircraft Contrails Factsheet," EPA430-F-00-005, U.S. Environmental Protection Agency, September 2000.

8-57. Minnis, P.: "Contrails," in *Encyclopedia of Atmospheric Sciences*, J. Holton, J. Pyle, and J. Curry, eds., Academic Press, London, Elsevier Science Ltd., 2003.

8-58. Menzel, W.P.; Wylie, D.P.; Jackson, D.L.; and J.J. Bates: "Using 22 Years of HIRS Observations to Infer Global Cloud Trends," International ATOVS Working Group, ITSC XIV Proceedings, Beijing, China, May 25–31, 2005.

8-59. Minnis, P.: "Contrails and Climate Studies," Presented at the 2003 UEET Conference, Cleveland, OH, October 30, 2003.

8-60. "Aircraft Contrails," *NASA Earth Observatory*, News, New Images, 2004.

8-61. Minnis, P.; Ayers, J.K.; Nordeen, M.L.; and Weaver, S.P.: "Contrail Frequency Over the United States From Surface Observations," *Journal of Climate*, Vol. 16, pp. 3447–3462, November 1, 2003.

8-62. Minnis, P.: "Contrails and Cirrus Clouds," The Roaring 20th Aviation Noise and Air Quality Symposium, AMS 81st Annual Meeting, Palm Springs, CA, February 27–March 2, 2005.

8-63. Ackerman, S.; and Knox, J.: "Meteorology: Understanding the Atmosphere—Contrails," <http://profhorn.aos.wisc.edu/wxwise/AckermanKnox/chap15/contrail>, Accessed 2005.

Terrestrial Environment (Climatic) Criteria Guidelines for Use in Aerospace Vehicle Development, 2008 Revision

NASA/TM—2008–215633
December 2008

D.L. Johnson, Editor

Section 9: Atmospheric Electricity and Thunderstorms

TABLE OF CONTENTS

TABLE OF CONTENTS (Continued)

LIST OF FIGURES

LIST OF FIGURES (Continued)

LIST OF TABLES

LIST OF ACRONYMS

ARP	aerospace-recommended practices
CC	continuing current
CCAFS	Cape Canaveral Air Force Station
CG	cloud to ground
CGLSS	Cloud-to-Ground Lightning Surveillance System
DC	direct current
DoD	Department of Defense
EAFB	Edwards Air Force Base
ELF	extremely low frequency
elves	emission of light and very low frequency from EMP sources
EMP	electromagnetic pulse
ER	Eastern Range
ESD	electrostatic discharge
ET	external tank
FAA	Federal Aviation Administration
GHCC	Global Hydrology and Climate Center
IC	intracloud
KSC	Kennedy Space Center
LAP	Lightning Advisory Panel
LCC	launch commit criteria
LDAR	Lightning Detection and Ranging (system)
LIS	lightning imaging sensor
LLTV	low-light television
LMS	lightning mapper sensor
LPC	large peak current
LPLWS	Launch Pad Lightning Warning System
LPS	Lightning Protection System
LWT	Launch Weather Team

LIST OF ACRONYMS (Continued)

MCS	mesoscale convective system
MDF	magnetic direction finder
MEIDEX	Mediterranean Israeli Dust Experiment
MKS	meter-kilogram-second (system)
MSFC	Marshall Space Flight Center
NLDN	National Lightning Detection Network
NTr	nontriggered (lightning)
OTD	optical transient detector
P-static	precipitation static
RP	return period
SAE	Society of Automotive Engineers
SRB	solid rocket booster
tiger	transient ionospheric glow emission in red
TL	transmission line
TLE	transient luminous events
TOA	time of arrival
Tr	triggered or triggering (lightning)
TRMM	Tropical Rainfall Measuring Mission
trolls	transient red optical luminous lineament superficially
TS	thunderstorms
URL	user selectable layer composite reflectivity
U.S.	United States
USAF	United States Air Force
VAFB	Vandenberg Air Force Base
VAHIRR	volume-averaged, height-integrated radar reflectivity
VARR	volume-averaged radar reflectivity
VHF	very high frequency
VLF	very low frequency

NOMENCLATURE

a	an empirically derived constant; units are per second
b	an empirically derived constant; units are per second
c	$(\mu_o \varepsilon_o)^{-1/2}$, the speed of light
D	distance
d	increment of altitude
di/dt	peak current derivative
E	electric field intensity
E_c	function of altitude
E_I	electric field intensity: induction term
E_R	electric field intensity: radiation term
E_S	electric field intensity: electrostatic term
F	number of lightning flashes
H	altitude
I	current
I_o	initial current
i	current
$L(t)$	height of return stroke wavefront at time
N_g	area density of strikes
P	probability
Q	charge transfer
R	resistive impedence
r	distance
t	time
v	constant return-stroke wavefront velocity
z	altitude
ε_o	permittivity of free space
θ	angle between current upper channel and the observers view of the channel increment
μ_o	permeability of free space
τ	time increment
$\int_i^2 dt$	action integral

9. ATMOSPHERIC ELECTRICITY AND THUNDERSTORMS

9.1 Introduction

Atmospheric electricity must be considered in the design, transportation, and operation of aerospace vehicles. Aerospace vehicles that are not adequately bonded and otherwise protected can be electronically upset, damaged, or destroyed by a direct lightning stroke to the vehicle or the launch support equipment while on the ground or after launch (refs. 9-1 through 9-3). Damage can also result from the current induced in the vehicle from changing electric fields produced by a nearby lightning stroke. The effect of the atmosphere as an insulator and conductor of high-voltage electricity at various atmospheric pressures must also be considered. High-voltage systems aboard the vehicle that are not properly designed can arc or break down at low atmospheric pressure.

Section 9 begins with an introductory discussion of electrostatic charge and discharge (sec. 9.2). Then a description of the global electrical circuit (sec. 9.3) is given. Section 9.4 discusses the charging mechanisms and electrical structure of thunderclouds and gives the reader a basic understanding of the frequency of occurrence of thunderstorms across the United States (U.S.). The characteristics of lightning discharges and various lightning detection systems are described in section 9.5. Lightning damage and protection are discussed in section 9.6.

Section 9.7 is devoted to lightning current test standards that have been adopted for improving the protection of aerospace vehicles (refs. 9-4 and 9-5). In this section, five current test waveforms are given which can be used in the design, development, and test of aerospace vehicles. These test waveforms represent components of a severe lightning strike event. Section 9.8 provides a description and listing of the current natural and triggered lightning launch commit criteria (LCC) for manned and unmanned space launches.

Thunderstorm electrical characteristics are presented in section 9.4, with the frequency of thunderstorm occurrence given in section 9.4.2. Further thunderstorm-related information is given in section 12.5.5, dealing with severe thunderstorm downburst/microburst type winds. Section 12.7 presents severe wind, hail, and tornadic weather associated with thunderstorms. Thunderstorm-related hail statistical characteristics are presented in section 7.2.7, and hail extremes are given in section 5.1.3.3.

9.2 Electrostatic Charge and Discharge

NASA bonding criteria for aerospace launch vehicles, spacecraft, payloads, and flight equipment is given in NASA-STD-4003 (ref. 9-6). The Department of Defense (DoD) standard for electromagnetic environmental effects is given in DoD MIL-STD-464 (ref. 9-7).

9.2.1 Electrostatic Definitions

Static electricity is defined as an electrical charge caused by an imbalance of electrons on the surface of a material. This imbalance produces an electric field that can be measured and that can influence other objects at a distance.

Electrostatic discharge (ESD) is defined as a single event, rapid transfer of charge between bodies having different electrical potentials.

Triboelectric charging is defined as creating electrostatic charge by contact and separation of materials. It involves the transfer of electrons between materials (ref. 9-8).

Precipitation static (P-static) is caused by an inflight aircraft coming in contact with uncharged solid or liquid particles. When this happens, the positive element of the particle is reflected away from the aircraft, while the negative particle adheres to the skin of the aircraft. When a sufficient negative voltage level is reached, the aircraft may go into "corona" and will discharge the static electricity from the extremities of the aircraft, causing a static burst (ref. 9-9).

9.2.2 Electrostatic Charge

Electrostatic charges can be caused by tribocharging, precipitation static effects, fluid flow, air flow, space and launch vehicle charging, separation of elements, and other charge generation mechanisms. Electrostatic charges must be controlled and dissipated in order to avoid fuel ignition and ordnance hazards, to protect personnel from shock hazards, and to prevent performance degradation or damage to electronics (ref. 9-6).

9.2.3 Electrostatic Discharge

Static discharges generally occur in clouds not considered to be thunderstorms; the charge centers are smaller. During Instrument Flight Rules conditions, electrical charges are generated on the aircraft's skin as it collides with small ice and water particles in the atmosphere. This is called triboelectric charging. Triboelectric charging increases with aircraft speed—it affects all modern jet aircraft. The charge increases until the electric field around sharp curvature points on the aircraft becomes large enough to create an ionized path for a sparking discharge. High-resistance materials, such as windshields, may also accumulate patches of electrical charge. If these flash over adjacent aircraft skin areas, a streaming discharge occurs.

The electrical capacitance of an in-flight aircraft is relatively small, so only a limited amount of electric charge can be accumulated. This charge continues to build on various areas of the aircraft's outer skin until the local electric field increases to a value sufficient to produce a discharge to the air. Normally, this electrification is slowly leaked or discharged back to the atmosphere. However, it can create an instantaneous discharge a number of feet in length, and be accompanied by a percussive noise; i.e., a loud bang. These discharges generally are less violent than lightning, but sometimes are intense enough to destroy or damage components such as transistors or integrated circuits. Computers can really be disabled—they may be physically damaged or a resident program can be altered, resulting in internal information alterations and erroneous output.

Triboelectric charging also may cause St. Elmo's Fire, or the aircraft charge can bleed off invisibly into the air. Sometimes, electromagnetic radiation—spurious radio signals—due to small sparks created by turboelectric charging can be coupled into the aircraft's antenna and cause static. This is often called P-static, because it frequently occurs when the aircraft has become charged by flying through precipitation. Many meteorological conditions seem to favor the chances of static discharges. Heavy precipitation plays a major role in most cases. Nonprecipitating clouds—stratus or small cumulus—lead to very slight chances. Precipitating clouds increase the chances: the heavier the precipitation, the greater the probability of static discharge (ref. 9-10).

9.2.4 Precipitation Static

Precipitation static (P-static) is caused by an aircraft or spacecraft flying through cloud particles—rain, sleet, hail, fog, ice, or snow—or dry precipitation—dust, haze, and volcanic ash—which causes a charging of the aircraft, and subsequent ionization of the air at sharp extremities. This ionization causes broadband electromagnetic radiation, which radios detect as static, and also causes visible glow (St. Elmo's Fire).

P-static decreases instantaneously with a lightning flash because the flash neutralizes the main charge centers, collapsing the electric field, thereby reducing the intensity of P-static discharges. P-static and lightning are two independent phenomena which frequently, but not always, occur in the same conditions. P-static has been reported with ≈50 percent of all reported strikes to commercial and military aircraft, and it often is used by air crews to warn of an impending strike (ref. 9-11).

Air crew personnel can be affected during flight, and ground personnel can be affected after landing. P-static deserves special emphasis because of the increased sensitivity of electronic equipment, wider frequency spectrum for new communications systems, and increased use of composite materials (ref. 9-12).

P-static depends on the type and density of the particulate, the speed of the aircraft, the material of the aircraft, and perhaps the shape of the aircraft. Modern aircraft have static dissipaters on the trailing edge of wings to bleed the charge and mitigate the effect of P-static. If the aircraft is not equipped with static dischargers, or has an ineffective static discharger system when a sufficient negative voltage level is reached, the aircraft may go into "corona." That is, it will discharge the static electricity from the extremities of the aircraft, such as the wing tips, horizontal stabilizer, vertical stabilizer, antenna, propeller tips, etc. The following is a list of problems caused by P-static based on a summary of many pilot reports for many different aircraft:

- Complete loss of very high frequency (VHF) communications.
- Erroneous magnetic compass readings (30 percent in error).
- High-pitched squeal on audio.
- Motor boat sound on audio.
- Loss of all avionics in clouds.
- Very low frequency (VLF) navigation system inoperative most of the time.
- Erratic instrument readouts.
- Weak transmissions and poor receptivity of radios.
- St. Elmo's Fire on windshield.

Each of these symptoms is caused by one general problem of the airframe. It indicates the inability of the accumulated charge to flow easily to the wing tips and tail of the airframe, and properly discharge to the airstream (ref. 9-9).

9.3 Global Electrical Circuit

During fair weather, there is a downward-directed electric field in the atmosphere below the ionosphere. Above this layer is a region of high electrical conductivity known as the electrosphere that extends upward to the top of the ionosphere. The magnitude of the fair weather electric field near the Earth's surface, averaged over the entire globe, is ≈120 V/m, decreasing with height to ≈3 percent of its surface value at 10 km. The potential difference between the electrosphere and the Earth is between 200 and 500 kV. A downward-directed fair weather electric field implies that the electrosphere carries a net positive charge and the Earth's surface a net negative charge. The system can be considered a giant spherical capacitor, with the Earth being the inner conductor, the electrosphere the outer conductor, and the air between the dielectric. The electric field remains nearly constant even though the current flowing in the air ($\approx 2 \times 10^{-12}$ A/m^2) is large enough to discharge the capacitor in a matter of minutes. Thunderstorms throughout the world act as electrical generators to keep the Earth-electrosphere "capacitor" charged. Positive charge in the upper portions of thunderstorms is leaked into the base of the electrosphere through the relatively highly conducting air at these levels. Although the electrical conductivity of air below thunderstorms is low, the presence of very large electric fields results in the flow of positive charges upward from the Earth through trees and other pointed objects. Negative charge is primarily deposited on the Earth's surface by lightning and precipitation. Figure 9-1 shows a schematic of the pivotal role thunderstorms play in the global electrical circuit (ref. 9-13).

9.4 Thunderstorm Electrical Characteristics

9.4.1 Cloud Electrification

Under the proper meteorological conditions, a layer of the atmosphere can be lifted by a variety of external forces; e.g., surface heating, terrain effects, fronts, etc. In very unstable humid atmospheres, this lifting can result in the development of a cumulonimbus cloud (or thundercloud) whose top extends to altitudes where the

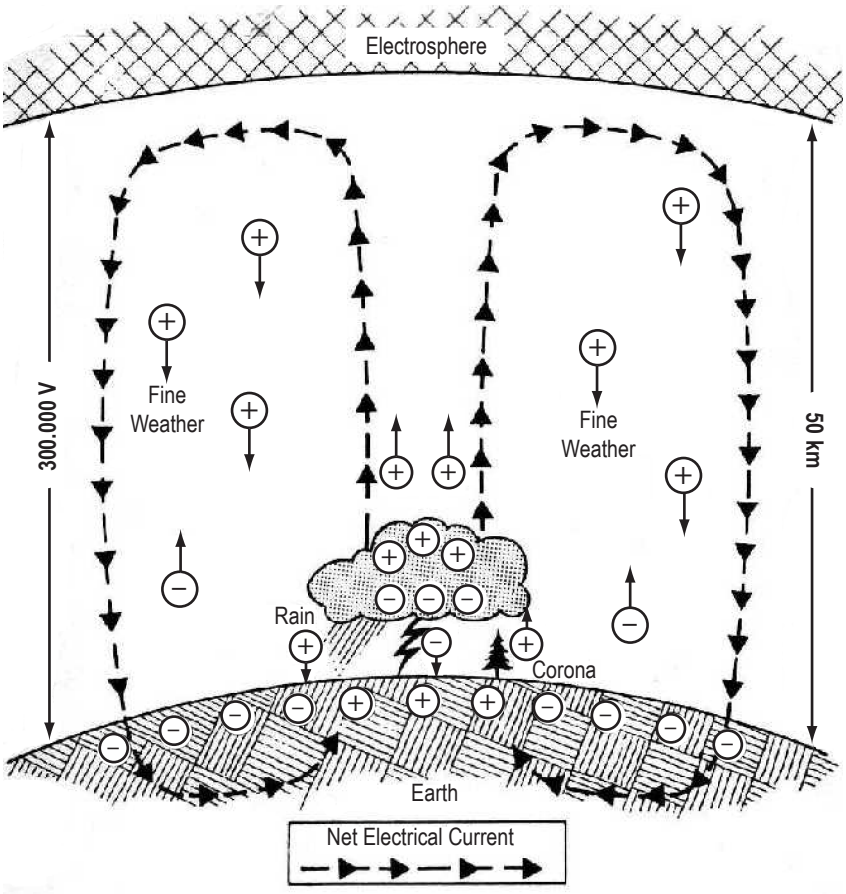

Figure 9-1. Schematic of the global electrical circuit between the Earth's surface and the electrosphere (ref. 9-13).

ambient air temperature is well below freezing. The electrified nature of a thundercloud is fundamentally related to processes occurring at both the microphysical and cloud-size scales.

9.4.1.1 Charge Separation Mechanisms. All clouds are electrified to some degree. Updrafts in some convective clouds can lead to sufficient electrical charge separation to produce thunderclouds. The processes involved in this charge separation are not yet fully understood. Several electrification mechanisms have been theorized, including charge transfer from colliding polarized cloud particles, thermoelectric effects where positive ions migrate toward colder cloud particles, and the gathering of charge from riming graupel and ice crystals (ref. 9-14).

Table 9-1 summarizes a variety of charge separation processes that occur at the microphysical and cloud-size scales (ref. 9-15). These processes vary in importance depending on the developmental stage of the convective cloud. However, it has been suggested that both induction and interface charging are the primary electrification mechanisms in convective clouds (ref. 9-16). Inductive charging involves bouncing collisions between particles in the external field. The amount of charge transferred between the polarized drops at the moment of collision depends on the time of contact, the contact angle (no charge transferred at grazing collisions), the charge relaxation time, and the net charge on the particles. Interface charging involves the transfer of charge due to contact or freezing potentials during the collisions between riming precipitation particles and ice crystals. The sign and magnitude of the charge transfer depended on the temperature, liquid water content, ice crystal size, and impact velocity.

Table 9-1. Charging mechanisms in clouds and thunderstorms (ref. 9-15).

Mechanism	Microscale	Cloud Scale	Major Roles
Diffusion charging	Ion capture by diffusion	–	Removes ions within cloud
Drift charging	Ion capture in drift currents	Drift currents Convection (Sedimentation)	Charges particles Enhances field
Selective ion charging	Ion capture by polarized drops	Sedimentation (Convection)	Charges particles Enhances field
Breakup charging	Collisional breakup of polarized drops	Sedimentation (Convection)	Charges drops
Induction charging	Charge transfer between polarized particles	Sedimentation (Convection)	Charges particles Enhances field
Convection charging	Space-charge production ion capture in drift currents	Convection	Enhances field (Charges particles)
Thermoelectric charging	Charge transfer between particles of differing temperatures	Sedimentation (Convection)	(Charges particles)
Interface charging	Charge transfer between particles involving contact potentials (freezing potentials)	Sedimentation (Convection)	Charges particles Enhances field

9.4.1.2 Thundercloud Electrical Structure. Figure 9-2 illustrates a simplified schematic showing the charge analysis from nearly 50 soundings through convective thunderclouds (ref. 9-17). Normally, in the convective updraft region, there are four charge regions, alternating in polarity, with the lowest being a positive charge region. The left side of figure 9-2 shows the charged regions associated with convection outside the updraft. This structure is typically seen in mesoscale convective systems (MCSs) (ref. 9-17). The thundercloud charge distribution has been inferred using a variety of balloon and aircraft, and remote measurements. For example, ground-based measurements of lightning field changes obtained from a field mill network at Kennedy Space Center (KSC) have been analyzed to determine the charges deposited by lightning in Florida thunderstorms (ref. 9-18). Figure 9-3 summarizes some of these results. The circles represent negative charge centers associated with cloud-to-ground lightning, while the vectors indicate moment charges due to cloud discharges. These results are consistent with the charge distribution given in figure 9-2.

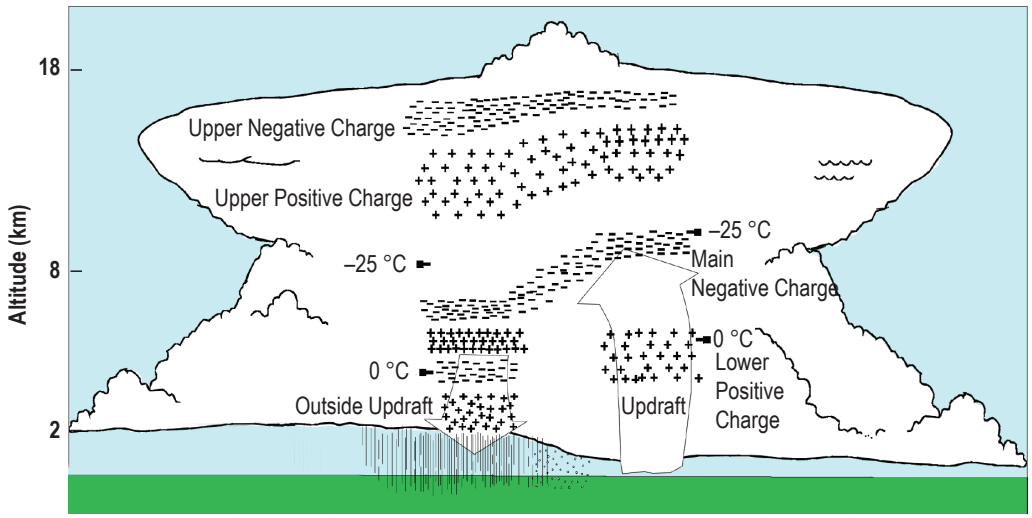

Figure 9-2. Vertical charge structure in the convection region of a thundercloud (ref. 9-17).

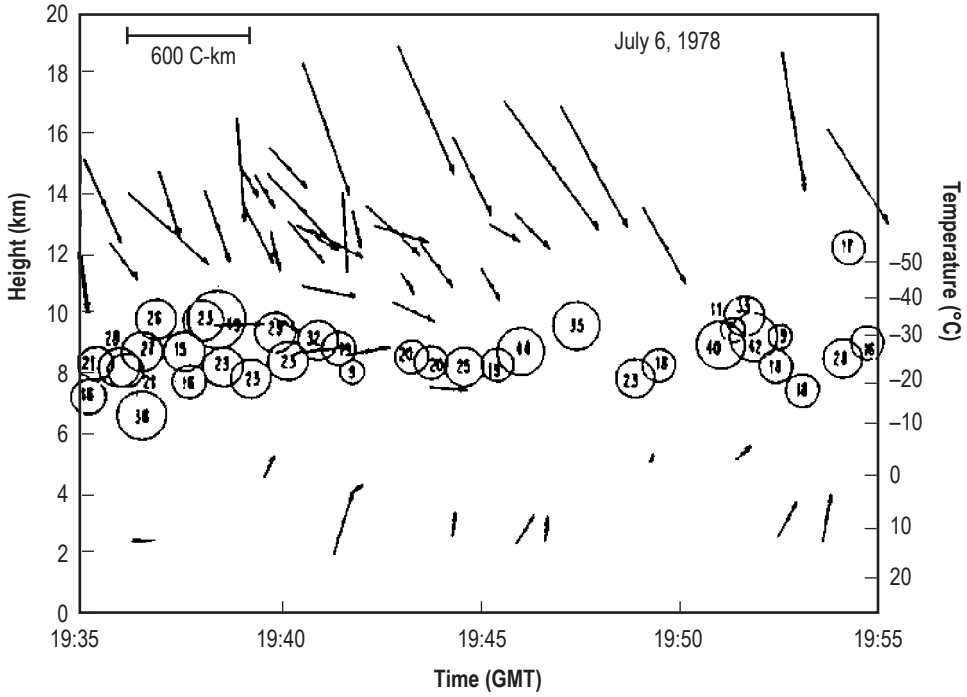

Figure 9-3. Charges deposited by lightning in a Florida thunderstorm (ref. 9-18).

9.4.2 Frequency of Occurrence of Thunderstorms

Audible thunder is an indication of nearby thunderstorm activity, and its occurrence is recorded routinely at meteorological stations around the world. If thunder is heard one or more times in a day, that day is counted as one "thunder day." These data provide the most readily available and longest term measurement of worldwide thunderstorm occurrence. Figures 9-4 and 9-5 show the average isoceraunic distribution, or number of thunder days per year, for the United States and world, respectively. Maxima in thunder days for the United States occur in the Florida Peninsula and along the eastern side of the Rocky Mountains in Colorado. On a global scale, Central Africa, Central America, and the northern part of South America receive the majority of thunderstorms (>100 per year) due to the proximity of these areas to the Intertropical Convergence Zone. Thunder day data from 227 global stations have been examined for secular variations during the period 1901–1980 (ref. 9-21). The frequency of thunderstorm durations across the United States can be obtained from reference 9-22, while the diurnal variation of U.S. thunderstorms is available from reference 9-23. A specific climatological study of Florida summer thunderstorms is documented in reference 9-24. A severe thunderstorm climatology presenting extreme hailfall and associated strong winds is given in reference 9-25. The extreme hail characteristics given in reference 9-25 are also presented in section 9.5. Thunder day statistics as a function of month for KSC, Edwards Air Force Base (EAFB), and Vandenberg Air Force Base (VAFB) are given in tables 9-2 through 9-4.

Thunder day statistics are inadequate for many applications because (1) the duration of lightning activity is unknown, (2) the data do not provide a measure of lightning flashing rates, (3) there is no distinction between intracloud and cloud-to-ground discharges, and (4) the range of audibility of thunder can be quite variable and typically limited to 25 km (16 mi) and depends on station location and atmospheric conditions.

Thunderstorm-generated downbursts (microbursts), in general and for KSC, are discussed in section 12.5.5. Severe thunderstorms, and their effects (lightning, hail, strong winds), are discussed in section 12.7.1.

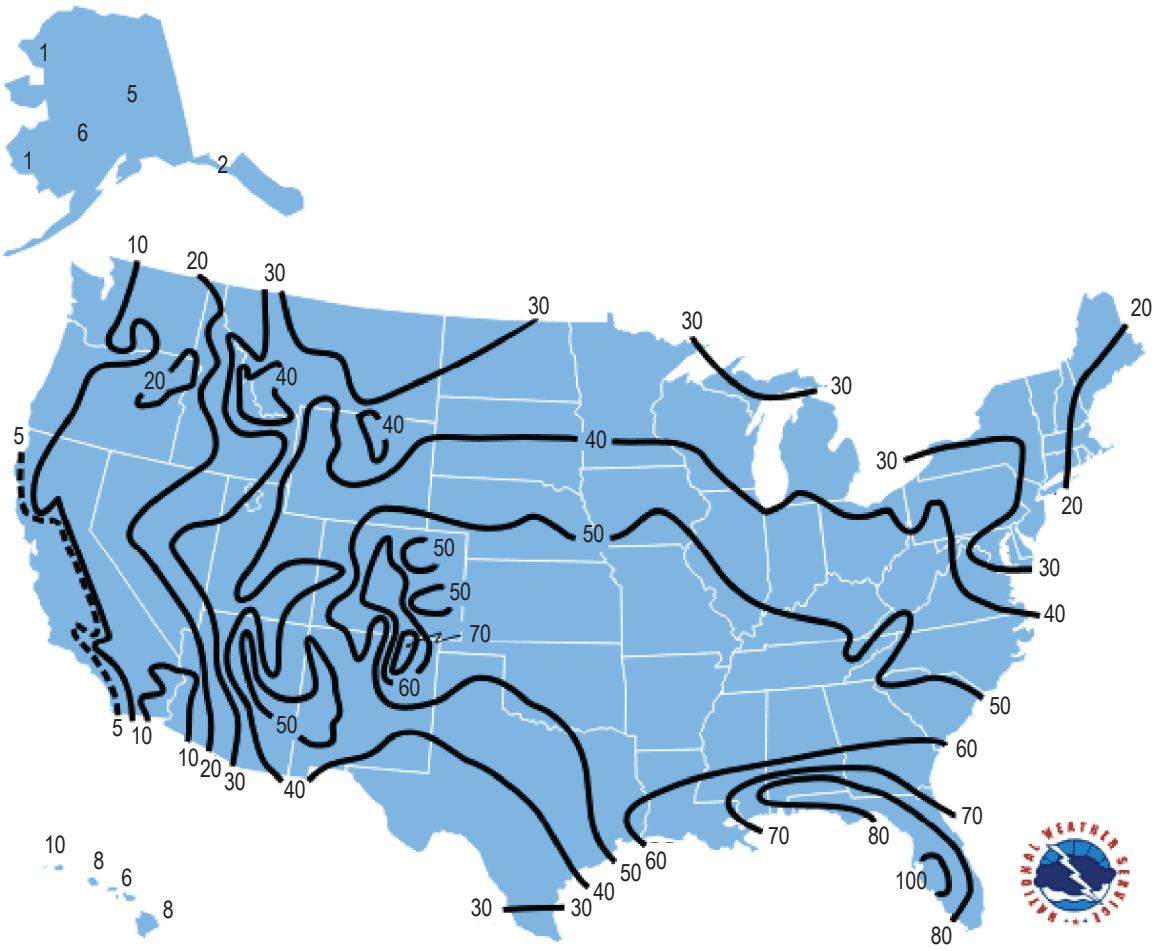

Figure 9-4. Average number of thunderstorm days per year for the United States (ref. 9-19).

9.5 Lightning Characteristics

There are ≈1,800 thunderstorms at any time over the Earth. The United States experiences more than 25 million lightning flashes each year. Most strikes occur either at the beginning or end of a thunderstorm. Each lightning can be >5 mi in length and can travel at speeds of 60,000 m/s. Lightning can reach more than 50,000 ºF and contain 1 to 100 million volts (ref. 9-26).

As discussed in section 9.4.1.1, updrafts can lead to electrical charge separation in thunderclouds. When sufficient charge buildup and separation occurs, the potential gradient between the cloud and the ground, or between various regions of the cloud, increases and eventually exceeds the critical breakdown potential for air. (Note: Use of the term "potential" in this section is understood to refer to the electric potential.) The resulting dielectric breakdown becomes a lightning flash. Although lightning is most commonly associated with the cumulonimbus thundercloud, it can also occur in sandstorms, snowstorms, and ash clouds from erupting volcanoes. The following sections describe several types of lightning and their associated characteristics.

Ice within a cloud may be a key element in which lightning can develop. Ice collisions within a cloud due to rising and sinking cloud motions can cause a separation of electrical charges there (ref. 9-26).

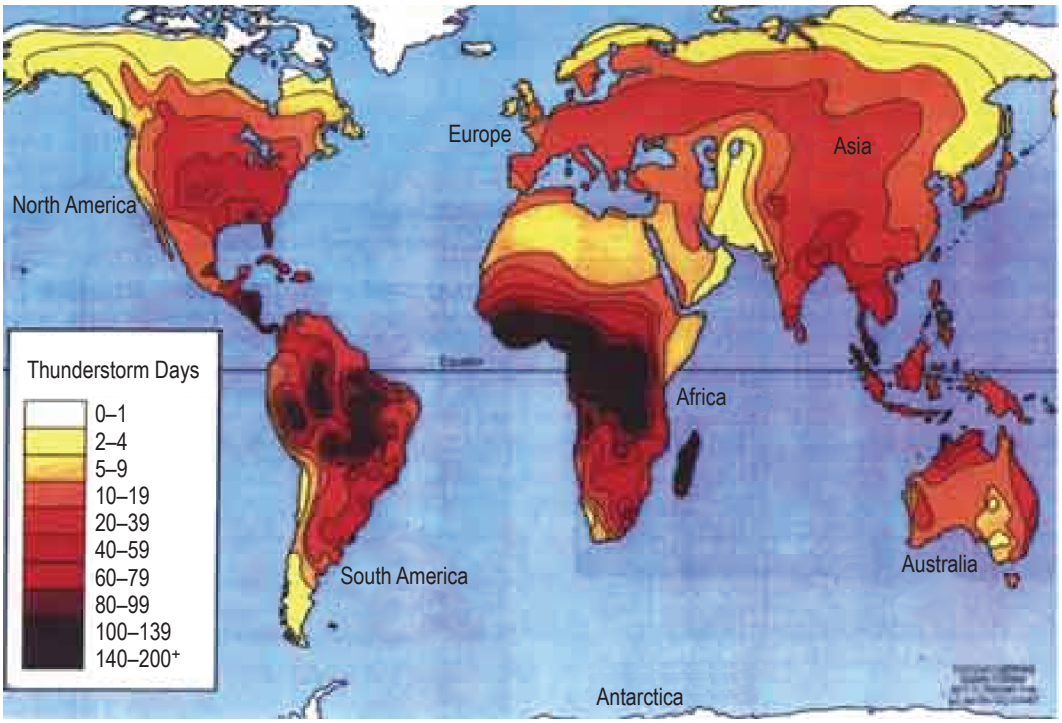

Figure 9-5. Average number of thunderstorm days per year for the world (ref. 9-20).

Table 9-2. Monthly thunder day statistics for KSC (1957–2001).

	Months												
	1	2	3	4	5	6	7	8	9	10	11	12	Annual
Mean number of TS days	0.9	1.5	2.8	2.9	7.1	12.9	15.5	14.5	9.8	3.5	1.3	1	73.7
Maximum number of TS days	4	5	7	7	17	22	24	23	18	13	5	6	107
Number of observations (days)	1,368	1,242	1,333	1,307	1,377	1,322	1,383	1,383	1,323	1,336	1,293	1,336	16,003
Total number of TS days	39	69	128	130	319	581	698	652	439	158	58	46	3,317
Percent of days with TSs	2.8	5.6	9.6	9.9	23.2	43.9	50.5	47.1	33.2	11.8	4.5	3.4	20.7

Table 9-3. Monthly thunderstorm day statistics for EAFB (1971–2001).

	Months												
	1	2	3	4	5	6	7	8	9	10	11	12	Annual
Mean number of TS days	0	0.1	0.2	0.3	0.8	0.6	1.1	1.6	1	0.4	0.1	0.1	6.4
Maximum number of TS days	1	2	2	2	5	6	6	5	5	3	2	1	21
Number of observations (days)	885	836	908	874	904	868	856	878	825	867	824	835	10,360
Total number of TS days	1	4	6	8	24	18	35	51	32	14	4	2	199
Percent of days with TSs	0.1	0.5	0.7	0.9	2.6	2.1	4.1	5.8	3.9	1.6	0.5	0.2	1.9

Table 9-4. Monthly thunderstorm day statistics for VAFB (1959–2001).

	Months												
	1	2	3	4	5	6	7	8	9	10	11	12	Annual
Mean number of TS days	0	0.2	0.1	0	0	0.1	0	0.1	0.3	0	0.1	0	1
Maximum number of TS days	1	2	2	1	0	1	1	1	4	1	1	1	6
Number of observations (days)	942	888	969	948	964	954	970	995	934	940	898	913	11,315
Total number of TS days	2	9	5	2	0	3	2	3	11	1	6	1	45
Percent of days with TSs	0.2	1	0.5	0.2	0	0.3	0.2	0.3	1.2	0.1	0.7	0.1	0.4

9.5.1 Cloud-to-Ground Lightning

The most common types of lightning are those that occur between the cloud and the ground, called cloud-to-ground (CG) lightning, and between charge centers within a cloud, called intracloud (IC) lightning. A study by Boccippio et al. (ref. 9-27) has shown that the mean IC to CG lightning ratio (IC:CG) over the continental United States is in the range of 2.64:1 to 2.94:1 sustantial variability exists as shown later in figure 9-12. Although IC lightning is important to consider in the operation of aerospace vehicles, there is much less information on the characteristics of IC lightning than on those of CG lightning. Therefore, this section will concentrate on CG lightning, due to extensive data and research.

As shown in figure 9-6, CG lightning begins in the cloud with a preliminary breakdown process that is not well understood. There seems to be good agreement, however, that this process takes place at roughly the zero to –20 °C level in the cloud, in the region from which negative charge is eventually lowered to ground. This initial breakdown is followed by the stepped leader process that lowers negative charge to ground in a series of steps that typically last 1 ms and are each ≈50 m in length. As the stepped leader approaches the Earth, the fields near exposed objects on the ground may become large enough that one or more upward discharges are initiated. This begins the attachment process. One or more of the upward connecting discharges will move up to intersect the stepped leader channel, usually a few tens of meters above the ground. The distance between the tip of the stepped leader and the object about to be struck, at the time when the connecting discharge is initiated, is referred to as the striking distance and is an important parameter in lightning protection design.

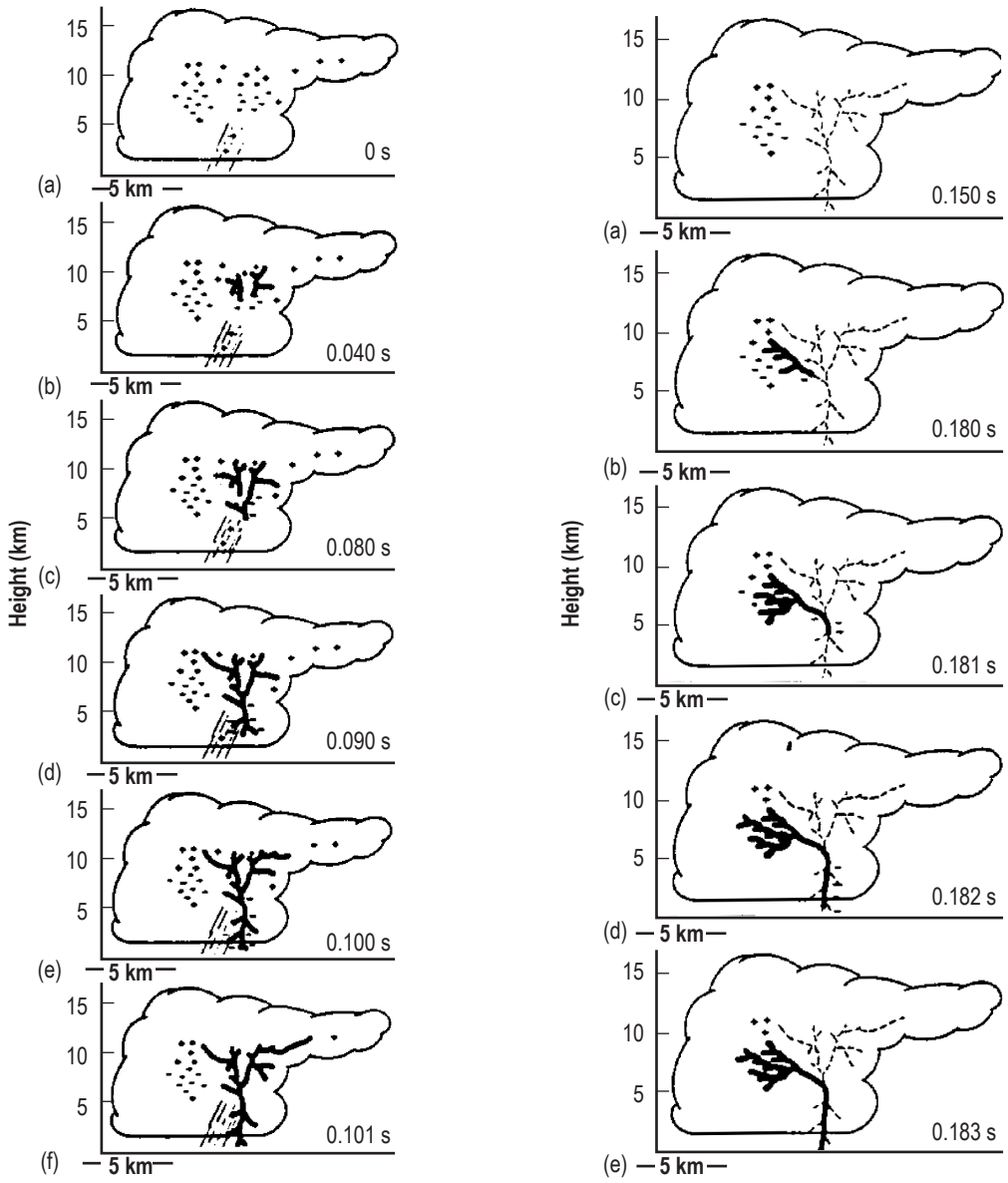

Figure 9-6. First column is a sketch of the luminous processes that form the stepped leader and the first return stroke in a CG lightning flash. Second column shows the development of a lightning dart-leader and a return stroke subsequent to the first in a CG lightning (ref. 9-28).

When contact between the stepped leader and the connecting discharge occurs, the first return stroke is initiated. This high-current breakdown wave effectively carries ground potential upward at roughly one-third the speed of light. If additional charge is made available in the cloud, a dart leader may propagate down the residual first return stroke channel. Once electrical connection is made between the dart leader and the ground, a second return stroke is possible. (Second, third, etc., return strokes are collectively referred to as subsequent strokes.) Currents that follow return strokes and that persist for up to several hundreds of milliseconds are sometimes observed and are called continuing currents. Cloud-to-ground lightning does not always follow the exact same path on return strokes. Krider (Personal Communication, 2008) in 1997 measured close to 400 CG flashes and ≈35 percent struck the ground in two or more places, separated by tens of meters. Or, on the average, each flash struck the ground in 1.45 places. This means that the chance of being struck by lightning is ≈45 percent higher than the number of actual flashes. Table 9-5 summarizes the important physical characteristics of (negative) CG discharges; i.e., those that bring negative charge to Earth as described above.

Approximately 40 percent of all lightning is CG, of which only 5 to 10 percent of CG flashes are positive. Positive lightning tends to occur during the cold season (>25 percent of the time in U.S. winters and 3–5 percent in summers), and during the dissipating stages of thunderstorms. The positive lightning peak current magnitude is thereby also greater in winter than in summer. Positive lightning flashes can occur from long horizontal channels and also from relatively shallow clouds. Whereas, negative flashes tend to decrease with decreasing cloud thickness. This has been measured within the shallower inner band regions of hurricanes. Positive flashes might be initiated from the upper main positive charge region of the thunderstorm, or at times, even if the main positive charge resides below the main negative charge region. Positive flashes usually are composed of only a single stroke, while ≈80 percent of negative flashes contain multiple strokes. Since positive flashes originate in the upper part of a storm, its electrical field normally is much stronger than a negative strike. It exhibits a longer flash duration and its peak discharge can be up to 10 times greater than a negative strike, as much as >300 KA and 1 billion volts.

Bipolar CG lighting has also been measured in which lightning current waveforms exhibiting polarity reversals within the same flash do occur. Measurements have indicated that from 5 to over 14 percent of flashes can be bipolar. Most all bipolar flashes result from being initiated by an upward-propagating leader from the strike object (ref. 9-30).

9.5.2 Triggered Lightning

Triggered lightning can be a threat to aerospace vehicles after launch (also known as artificially initiated lightning). This type of lightning is caused by the rocket and its electrically conductive exhaust plume passing through a sufficiently strong preexisting electric field. Triggered lightning is caused by the compression of the ambient electric field until the critical breakdown potential of air is reached or exceeded. See figure 9-7. Due to this compression, the electric fields required for triggered lightning are two orders of magnitude less than those required for natural lightning (ref. 9-32).

The danger of rocket-triggered lightning was first realized moments after the launch of Apollo 12 in 1969 at KSC (refs. 9-1 and 9-2). The rocket triggered two lightning strikes during a nonnatural lightning-producing weather situation. The lightning strikes produced major system upsets, but only minor permanent damage. The vehicle and crew survived and were able to complete their mission. This event led to the implementation of a set of lightning LCC, which are rules designed to avoid lightning threats to launch vehicles.

Table 9-5. Typical negative CG lightning characteristics (adapted from ref. 9-29).

CG flash	
Number of return strokes*	3 to 4
Time between return strokes	50 ms
Duration of flash	0.5 s
Charge transferred	25 C
Stepped leader	
Duration	10 to 30 ms
Step length	50 m
Step interval time	50 μs
Average velocity	1 to 2×10^5 m/s
Step velocity	$>5\times10^7$ m/s
Charge lowered	10 C
Average current	100 to 1,000 A
Peak step current	≥1 kA
Upward discharge	
Length	10 to 20 m (above flat terrain) 20 to 100 m (above tall structures)
First return stroke	
Peak current**	10 to 30 kA
Peak current rate of rise	100 kA/μs
Velocity	1×10^8 m/s
Dart leader	
Duration	2 ms
Average velocity	0.5 to 1×10^7 m/s
Charge lowered	1 C
Average current	1 kA
Dart-stepped leader	
Step length	10 m
Step interval time	10 μs
Average velocity	1×10^6 m/s
Subsequent return strokes	
Peak current	10 kA
Current rate of rise	100 kA/μs
Velocity	1×10^8 m/s
Continuing current	
Duration	0.1 s
Current	100 to 300 A
Charge transfer	10 C

*Positive CG number of return strokes (usually only one).
**Peak current may exceed 30 kA (see sec. 9.5.6).

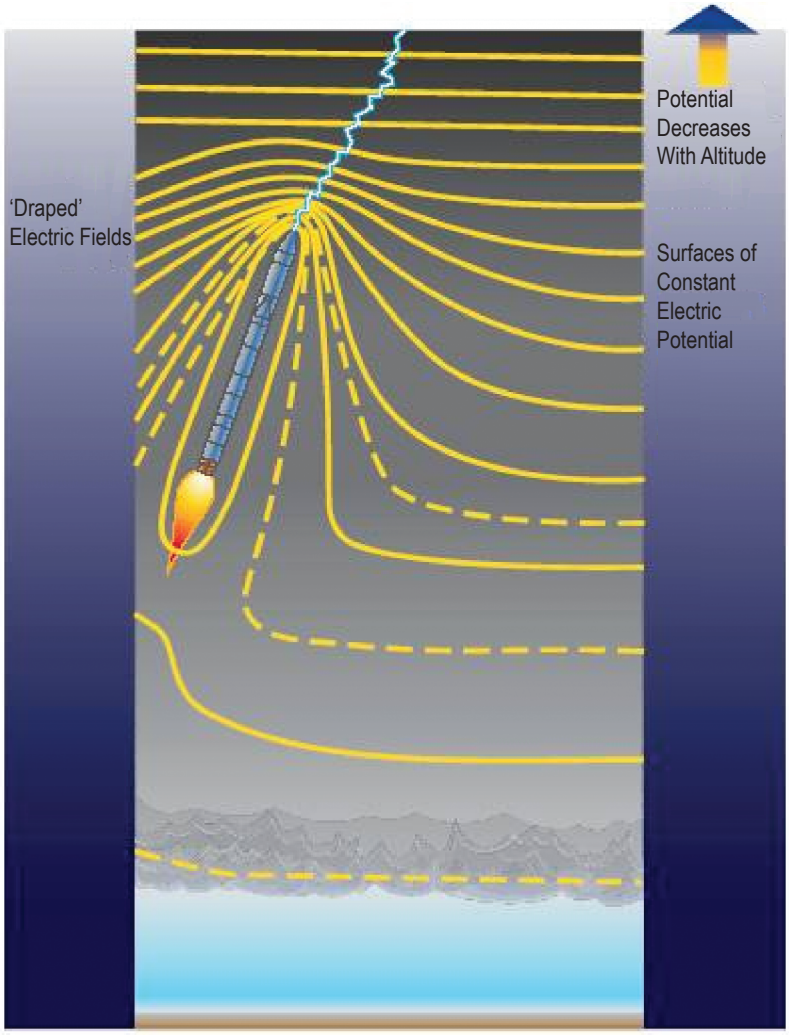

Figure 9-7. Compression of the ambient electric potential field caused by an ascending rocket-triggered lightning can occur due to the increased potential (gradient), relative to the ambient potential, at the rocket's tip (from ref. 9-31).

The next major event was the 1987 Atlas/Centaur-67 accident at KSC (ref. 9-3). The rocket caused a triggered lightning strike in nonnatural lightning weather similar to the Apollo 12 incident that disrupted the vehicle guidance electronics. As a result, the rocket yawed unexpectedly and Range Safety was forced to destroy the vehicle. In the proceeding years, several studies and working groups produced many lightning LCC revisions and recommendations (ref. 9-32). The most recent lightning LCC revision occurred in 1999 (ref. 9-33) by the Lightning Advisory Panel (LAP), which advises the United States Air Force (USAF) and NASA on LCC issues. These criteria are a set of 11 rules that are used to protect against the natural and triggered lightning threat to in-flight vehicles. The lightning LCC include rules for cloud thickness, attached and detached electrified anvil clouds, and surface electric fields. Electrified anvil clouds can be particularly troublesome during the warm season, especially due to the abundance of sea- and land breeze-induced thunderstorms (ref. 9-34). A total of 4.7 percent of the launches from October 1, 1988, to September 1, 1997, were scrubbed and 35 percent were delayed due to the lightning LCC (ref. 9-32). Section 9.8 lists the lightning LCC rules.

An interesting conclusion from the 1983 to 1986 Florida triggered lightning studies was that all triggered flashes were of the classical type that lowered negative charge (ref. 9-35). The Florida triggered study in 1990 and in Alabama in 1991 also found lowered negative charge, and reported a 38-kA peak current measurement (ref. 9-36). That positive flashes are less common at KSC latitudes is evidenced by Mach's analysis of 130 KSC strokes in 1986 (ref. 9-37). Of these, 86 were negative CG natural, 41 negative triggered, 1 positive triggered, and 2 positive CG natural strokes (97.7 percent negative and 2.3 percent positive). The 86 negative CG strokes had a peak current of 84 kA while the two positive CG strokes had peak current values of 125 and 150 kA (ref. 9-37). Hence, peak positive currents should still be considered. Rocket-triggered flash currents peaked at 60 kA (mean 15 kA) from 1985 to 1987 (ref. 9-38). The entire 1984 to 1991 summer rocket-triggered lightning program at KSC produced only one peak return stroke current of magnitude 99 kA (ref. 9-39). Artificially triggered lightning strokes are very similar to the subsequent strokes of natural lightning (refs. 9-36 and 9-40). Triggered lightning current strikes to instrumented aircraft have generally been of lower than natural CG lightning measured at ground level (refs. 9-35 and 9-41).

9.5.2.1 Lightning Strikes Versus Altitude. Figure 9-8 summarizes the results of five studies of the altitude at which lightning-related aircraft incidents occur, for both piston (cruise 3–4.5 km alt.) and jet aircraft (cruise 9 km). For jets, which cruise at much higher altitudes, most strikes occur either while climbing to a cruising altitude, or during landing, and when the aircraft is within a cloud; i.e., when the aircraft passes through the region of the cloud where the ambient temperature is near 0 ºC. The majority of strikes are associated with turbulence and precipitation (ref. 9-42).

9.5.3 Transient Luminous Events

9.5.3.1 Historical Background. Although eyewitnesses reported luminous events above thunderstorms for over 100 yr (ref. 9-43), but with no detailed documentation, these events were given little credence by the atmospheric electricity community. Strong evidence was presented in July 1989 when scientists in Minnesota were testing a low-light television (LLTV) camera for an upcoming sounding rocket launch. By accident, videotape from the camera captured illuminated columns extending into the stratosphere above distant thunderstorms about 250 km (155 mi) away (ref. 9-44). Observations from the Space Shuttle's LLTV camera archive from 1989 to 1991 provided 17 additional examples of luminous phenomenon above thunderstorms across the globe (ref. 9-45). It was determined that these events were associated with tropospheric lightning that were often among the brightest, and longest lasting, in the region. This suggested that the luminous events above thunderstorms were caused, directly or indirectly, by energetic lightning discharges (ref. 9-45). On the first observing night from the Yucca Ridge Field Station near Fort Collins, CO, in 1993, scientists reported 248 luminous events from a large mesoscale convective system (MCS) in Kansas within a 4-hr period (ref. 9-46). Initially, these events were referred to as "cloud-to-space" and/or "cloud-to-ionosphere" lightning. Later, they were renamed based on individual characteristics and are known as sprites (or red sprites), blue jets, blue starters, elves, sprite halos, pixies, tigers, and trolls (transient red optical luminous lineament superficially). As a group, they have been termed transient luminous events (TLEs). TLEs are similar to lightning in that just as the Earth conducts electricity and attracts lightning, so does the ionosphere. A large lightning stroke appears to launch a rising electromagnetic pulse (EMP) that excites the thin air above it until it emits light (ref. 9-47). Figure 9-9 illustrates the typical locations and characteristics of the various TLEs. Sentman (ref. 9-49) has summarized the characteristics and dimensions of the various TLEs, and these are presented in table 9-6.

9.5.3.2 Elves, Blue Jets/Starters, Tigers, Pixies, Gnomes, Halos, and Trolls. Elves (emission of light and very low frequency from EMP sources) are extremely brief (<1 ms) flat disks of dim light that occur between 75- and 105-km altitudes in the lower ionosphere. Sometimes they appear with sprites, but usually not. Elves expand rapidly to a horizontal disk of approximately 100 to 500 km. Elves occur above both positive and negative

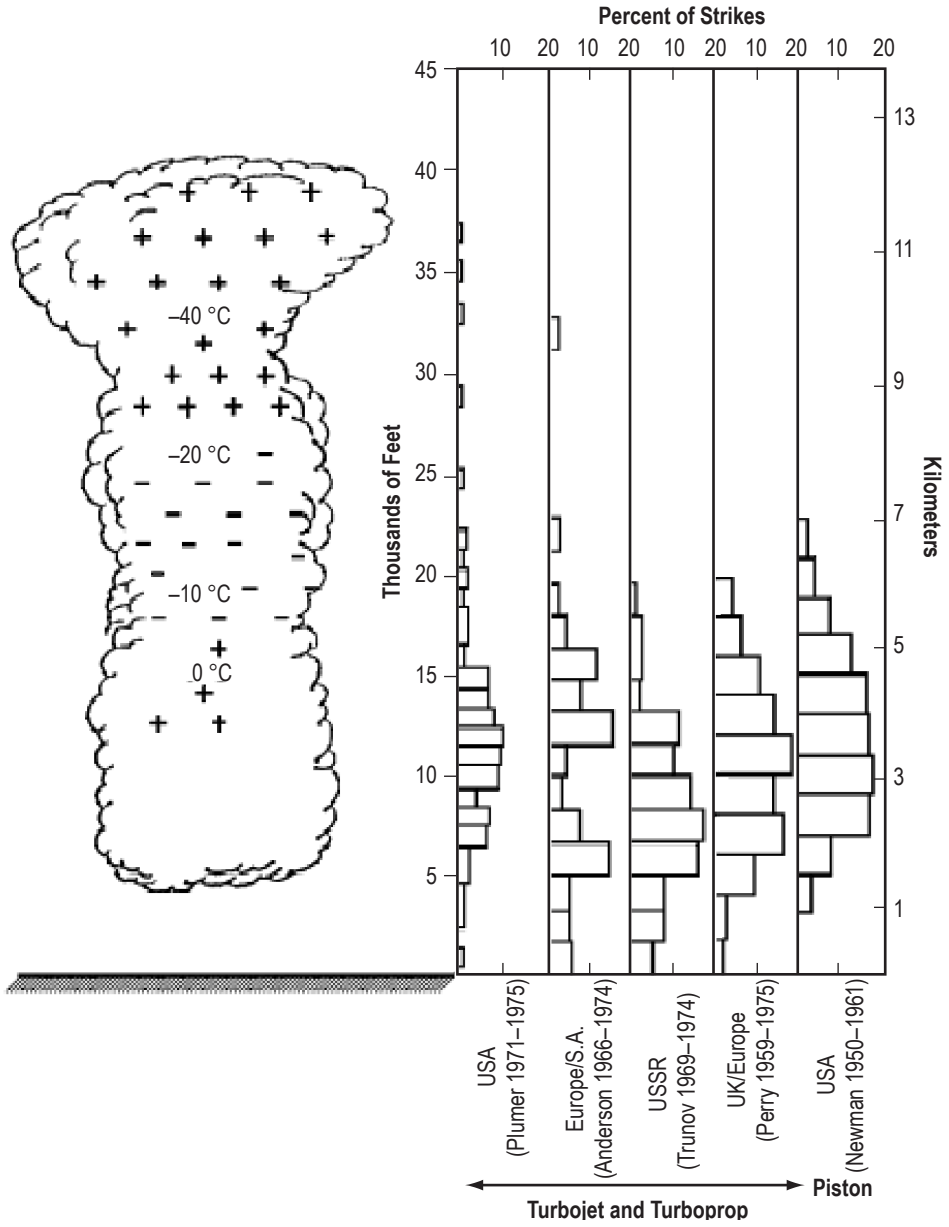

Figure 9-8. Aircraft lightning incidents versus altitude (ref. 9-42).

polarity clouds. Elves most likely result when an EMP propagates through the ionosphere. It is believed that elves are caused by the heating of the lower ionosphere by electromagnetic pulses generated by lightning discharges. Though they can be accompanied by sprites, there origin is different (EMP). Elves appear to be similar to halos, but occur at higher altitudes (above 95 km), at the bottom of the ionosphere (refs. 9-50 and 9-51).

Sprite halos are disks of light, like elves, but are smaller and lower, beginning at ≈85 km and moving down to 70 km, with lateral extents of 40–70 km. They last about a millisecond and are followed by sprites, which seem to grow from their disks. Sprite halos are thought to be an initial stage of sprites (ref. 9-47).

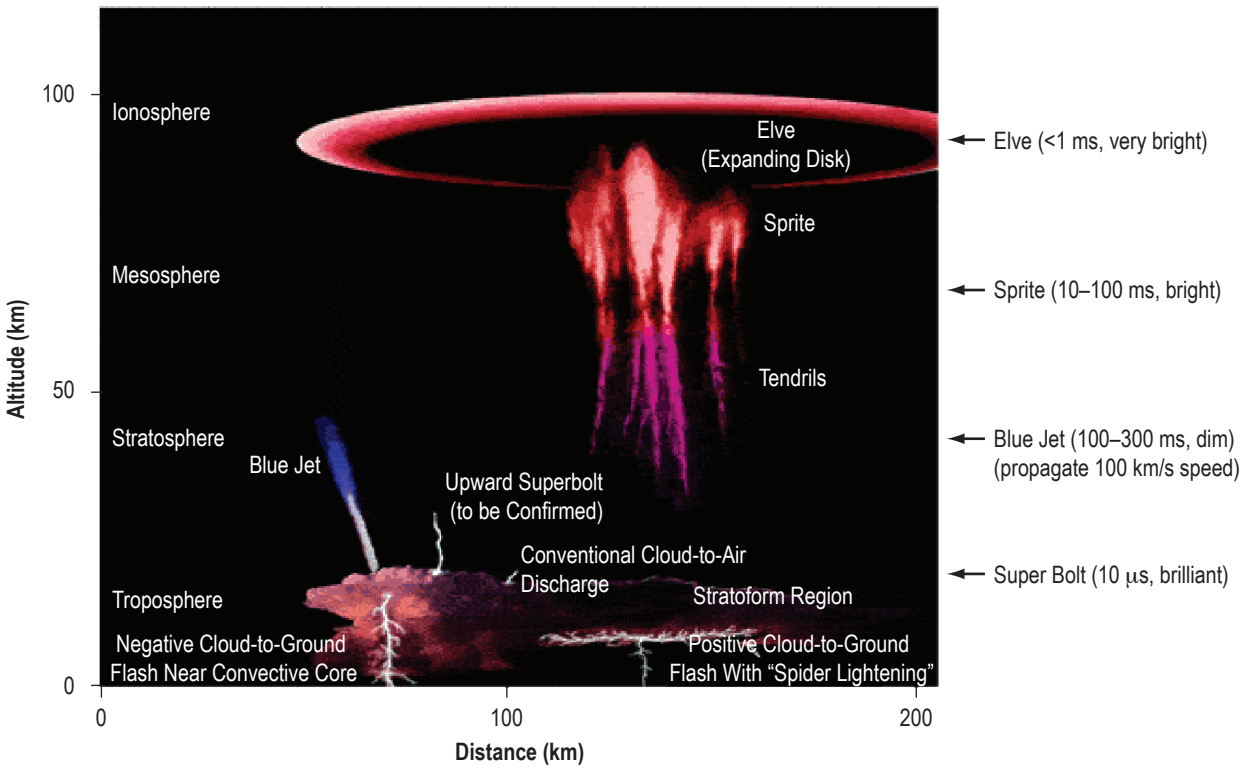

Figure 9-9. Schematic of typical characteristics and locations of TLEs (ref. 9-48).

Table 9-6. Principal types of transient luminous events in the upper atmosphere associated with thunderstorms/lightning (ref. 9-49).

Type of TLE	Altitude Regime (Approximate km)	Transverse Dimension	Spatial Characteristics	Apparent Motion	Duration	Inventory of No. of Observations (est.)
Sprites	50–90	≈1–20 km	Top (>80 km) diffuse; Bottom (<70 km) structured	Top-upward Bottom-downward	Few ms	>10,000
Elves	100	>100 km	Diffuse	Lateral expansion	Few ms	100's
Blue jets	18–45	Few km	Structured	Upward	100s ms	<100
Giant blue jets	18–75	Few km	Structured	Upward	100s ms	<10
Halos	75	≈50 km	Diffuse	Downward	≈ms	1,000's
Trolls	60–70	≈km	Structured	Upward (within decaying sprite tendrils)	100s ms	100's
Pixies	15–18	≈100's m	Compact	Stationary (storm-cloud tops)	100s ms	10's (?)

Blue jets and blue starters are both a rare class of high-altitude optical phenomenon, distinct from sprites, that were first observed in 1994. Blue jets appear as cone-shaped narrow beams (15º) of blue light (possibly positive) that propagate upward from the tops of thunderstorms (>15-km altitude) at speeds of about 100–120 km/s

and reaching altitudes of 40–50 km. They are not directly related to CG lightning, and are not aligned with the local magnetic field. They may be associated with heavy hailstorms in the clouds beneath them. Blue starters are low-level flashes and dots that do not grow into blue jets. They are brighter and shorter than blue jets, reaching an altitude of only ≈20 km) (refs. 9-51 and 9-52).

Gigantic blue jets were first described as "a hybrid of blue jet and sprite." The upper part resembles a sprite while the lower half is jet-like, and this event visually spans from the lower atmosphere to the E-layer ionosphere just under 100-km altitude. The duration ranges from 200 to 400 ms—longer than typical sprites (ref. 9-47).

Trolls superficially resemble blue jets, yet they are clearly dominated by red emissions. Moreover, they occur after an especially vigorous sprite in which tendrils have extended downward to near cloud tops. The trolls exhibit a luminous head leading a faint trail and move upwards (much like blue jets) initially around 150 km/s, gradually decelerating and disappearing by ≈60-km altitude. It is still not known whether the preceding sprite tendrils actually extend to the physical cloud tops or if the trolls emerge from the storm cloud per se (ref. 9-53).

During the 2003 Space Shuttle MEIDEX sprite campaign, Yair documented that an unusual transient atmospheric emission had been observed and recorded. This emission was called TIGER (transient ionospheric glow emission in red). The emission was delayed 0.23 s from a preceding visual lightning flash that was horizontally displaced over 1,000 km from the thunderstorm event. Yair indicated that many sprites were observed during MEIDEX, as well as two different types of elves—the classic, donut-shaped elves and the thin, arch-shaped elves with no hole (ref. 9-54).

Gnomes are small, very brief white spikes of light that point upward from the cloud top of a large thundercloud's anvil top, specifically the "overshoot dome," caused as strong updrafts push rising moist air slightly above the anvil. They appear ≈150 m wide and ≈1 km high, and last a few microseconds (33- to 136-ms duration) (ref. 9-55).

Pixies are so small that they appear as points that are <100 m across. In the video that first documented them, they appear scattered across the overshoot dome (15- to 18-km altitude), flashing seemingly at random. Pixies and gnomes appear to be a pure white color, like ordinary lightning, and they do not accompany lightning strokes (ref. 9-55).

9.5.3.3 Nonluminous Emissions. First observed by both the ALEXIS and FORTE satellites in the 1990s, transionospheric pulse pairs are very intense VHF pulses originating from thunderstorms at frequencies between 20 and 200 MHz. They are 10,000 times stronger than sferics produced by normal lightning and last 5 μs. The second impulse is due to the reflection on Earth of the first impulse, and it usually is separated by 10 to 110 μs from the first impulse.

First detected by the Compton Gamma Ray Observatory, gamma-ray bursts (1 ms) occur over thunderstorm regions. Their source is believed to lie at altitudes >30 km (19 mi). Sprites could be produced by an avalanche of relativistic electrons (energies >1 MeV). This electron beam could interact with the air molecules and produce both x-ray radiation and secondary gamma radiation. The sprites have an energy of ≈20 eV. However, the gamma-ray bursts have an energy of 1 million eV (ref. 9-51).

9.5.3.4 Sprites. Like lightning, sprites are electrical discharges. They are driven by a strong electrical field above a thunderstorm, and so are associated with regular lightning (ref. 9-56). Sprites are best described as transient, vertically elongated areas of luminosity suspended above cloud tops, typically in clusters, but sometimes alone. They have brief durations, with a red main body that typically spans an altitude range of 40 to 95 km

(ref. 9-57) (with the brightest regions in the 66- to 74-km range) and lateral dimensions of 5–30 km (ref. 9-57). Faint bluish tendrils often extend downward from the main body of sprites to ≈40 km. Studies have shown a link between sprites and positive CG lightning having large currents. Observations of two summertime MCSs indicated that more than 80 percent of sprites were coincident with positive CG lightning in the stratiform region of the MCSs (ref. 9-58). The peak currents in these positive CG strokes were in the upper 3–15 percent of the current distribution estimated by lightning mapping networks. Positive sprites in the Midwestern United States are normally most common in the stratiform precipitation regions of mature MCSs larger than 10 to 20×10^4 km^2 (ref. 9-55). The stratiform region is typically the area where positive CG lightning produces large charge moment changes—the product of the charge lowered to ground and the altitude from which it was removed. Signatures from extremely low frequency (ELF) sferics indicate that the charge moment from sprite-producing positive CG lightning is on the order of 1,000 C-km (refs. 9-55, 9-59, and 9-60).

The mechanisms involved in the production of sprites are not well understood. It has been suggested that sprites are caused by (1) the rapid removal of positive charge from a large charge layer, which then stresses the mesosphere to dielectric breakdown (ref. 9-58), or (2) runaway electrons in the strong electric field above storms (ref. 9-61). The relationship between sprites, Q-bursts, and positive CG strokes was confirmed and preference established for them to occur in decaying portions of thunderstorms (refs. 9-57, 9-62 through 9-64).

Sprites can occur worldwide above strong storms (ref. 9-65). All lightning does not produce sprites. Of the positive strokes, only ≈10 percent create sprites, etc. (ref. 9-66). Oceanic sprites tend to be brighter than the land sprites (ref. 9-67).

Lyons says that sprite flashes may be hazardous to spacecraft and aircraft (ref. 9-68). Using the CG National Lightning Detection Network (NLDN) climatology, an estimate was made of the chances of the Space Shuttle encountering a sprite (or elve) during descent to KSC. The probability is approximately one in a hundred, higher than the chances of a direct strike by conventional lightning during conditions conducive to thunderstorm activity (ref. 9-69). Sprites, however, appear to be weak in comparison to CG strikes, despite being directly related.

Lyons concluded the following in a recent analysis (ref. 9-48): The average positive (+) CG peak current for the entire United States is 35.5 kA (+), with a peak occurrence of +580 kA; the average negative (–) CG peak current is 30.4 kA (–) (with a peak occurrence of –957 kA). For the entire United States, ≈95 percent of all CG flashes are negative in polarity with ≈87 percent being large peak current (LPC) CGs; i.e., CGs ≥ 75 kA. This indicates that the vast majority of LPC strokes nationally are negative in polarity. However, for the Central United States, ≈70 percent of all LPC CGs are negative (≈30 percent positive). These positive CGs in the Central United States constitute ≈67 percent of all national NLDN LPC +CGs. This makes the region one of high positive CG counts where sprites occur most frequently. In the Central United States, the occurrence of positive and negative LPC CGs, as a percent of all LPC CGs, is approximately 9 and 22 percent, respectively.

In contrast, LPC –CGs preferentially occur over the coastal waters of the Gulf of Mexico and throughout the southern United Sates. A total of ≈1.46 million LPC CGs occurred over the southern United States, including the Atlantic and the Gulf, the vast majority are negative (≈86 percent), with ≈14 percent positive. This national peak region for maximum negative LPC CG activity includes the KSC area.

The large peak current statistics of Lyons still offer a small probability of occurrence. On a national basis, the LPC−CGs (≥75 kA) constitute 2.23 percent of all negative CGs. However, the LPC +CGs (≥75 kA) represent 7.37 percent of all positive CGs. For LPC CGs ≥200 kA and ≥400 kA, the percentages fall, but +LPC CGs still represent a greater percentage than –LPC CGs. Positive CGs ≥200 kA represent ≈8 percent of all LPC +CGs, while negative CGs ≥200 kA represent ≈0.02 percent of all LPC−CGs. For LPC CGs ≥400 kA, the probabilities fall to 0.00044 and 0.00009 percent, respectively, for positive and negative. The overall U.S. probability

of occurrence of CGs (+ or –) ≥75 kA, ≥200 kA, and ≥400 kA is approximately 2.46, 0.018, and 0.0001 percent, respectively.

In 2005, Duke University researchers (ref. 9-56) captured the best images ever produced of sprites. Based on the observations, sprites normally begin ≈80 km (≈50 mi) high as downward-moving "streamers" that appear spontaneously or at the bottom of a halo—diffuse flashes of light often associated with sprites. The streamers then branch out as they move down. At the same time, a brighter column of light expands both up and down from the starting point, followed by bright streamers that shoot higher into the sky. Also, new details of "isolated dots"; i.e., bright spots of light, that often glow longer than any other portion of the sprite, are possibly a result of when individual streamers presumably collide as a result of electrostatic attraction between them.

9.5.3.5 Sprites Observed Over Kennedy Space Center. Sprites have been observed over the KSC, FL, area. During the 1997 summer field season at KSC, Dr. Mark Stanley (Personal Communication, February 1998), New Mexico Institute of Technology, captured at least 4 days of sprite data. Dr. Stanley remarked about his measurements: "I was surprised by how many positive CG's I detected during my KSC field program last summer (mid-May to mid-July). However, the ratio of negative CG's to positive CG's was probably still quite high due to the very large numbers of the former." Even Michael Maier (Personal Communication, February 1998), Computer Sciences, Raytheon, PAFB, indicated: "In the KSC area our data shows the largest peak currents are from negative flashes, not positive. However, the frequency distributions for positive flashes show a higher percentage of positives having big currents relative to negatives." According to Maier, positive flashes account for only 2 to 4 percent of CG strokes at KSC. A conclusion from this is that if the sprite occurrence and positive CG correlation does exist, sprite occurrence should be less in Florida than in the Midwest.

Dr. Stanley also stated: "Most of the sprites that I detected while at KSC were associated with positive CG's, though there may have been at least one which was caused by an inter-cloud (IC) flash. In two years of research I have not detected a sprite which could clearly be associated with a negative CG. The static electric field change data that I obtained at KSC indicates that positive CG's associated with sprites on June 22nd had range-normalized step field changes significantly larger than those of average negative CG's from the same storm. However, the differences were not spectacular, which seems to indicate that these positives were probably all less than 100 kA. However, I can say something about the continuing currents (CC's) which often follow positive CG's, but sometimes negative CG's. My electrostatic field change measurements of CG's clearly indicate that positive CG's are considerably more violent (by at least an order of magnitude) on average, than negatives in regards to CC current magnitude. This is, in my opinion, the reason why positive CG's cause sprites and negatives don't. The peak current does not seem to be relevant to whether a particular positive CG will initiate a sprite."

D. Boccippio, Hydrology Research Office, NASA Marshall Space Flight Center, used all May through October 1995 NLDN CG data within 1,000 km (620 mi) of KSC, FL, to compute diurnal cycles for "positive" CG currents >50 kA, >100 kA, and >200 kA (Personal Communication, January 1998). Data counts were tallied each hour. For positive flashes >50 kA and >100 kA, the peak count (>2,000 and >400, respectively) occurs at 0000 UTC (2000 EDT). The minimum count (about 940 and 165, respectively) occurs at 0600 UTC (0200 EDT). This indicates that diurnal amplitude modulation is about a factor of 2 for positive strokes near KSC. The diurnal cycle for peak positive CG currents >200 kA was less discernible due to the small sample size (count between 7 and 32 over 24 hr).

Boccippio's diurnal positive CG KSC results differ with the diurnal results of Santis (ref. 9-70). However, Santis used the total NLDN database (positives and negatives) for the entire United States between June 12 and October 9, 1996. Santis' uniform diurnal cycle of CG strikes peaked at 1700 EDT (≈13 percent) with a minimum at 1000 EDT (<2 percent).

9.5.4 Lightning Detection and Location Systems

The monitoring of lightning is important during aerospace vehicle operations. This is especially true for the Florida peninsula due to its abundance of thunderstorm activity. Several systems are used by the Air Force's 45th Weather Squadron to monitor lightning activity at the ER. The Launch Pad Lightning Warning System (LPLWS) is a network of ≈30 ground-based electric field mills that measure the electric field at the surface and detect electric discharges in the vicinity of the ER (ref. 9-71). Data from the LPLWS is used for evaluating the lightning LCC electric field rules. (See sec. 9.8.) The effective range of the LPLWS is ≈20 km (12 mi). The Cloud-to-Ground Lightning Surveillance System (CGLSS) is a network of six IMPACT ESP ground-based magnetic direction finder (MDF) sensors operated by the USAF (ref. 9-72). The MDF sensors use the magnetic field from a CG lightning flash to determine the azimuth to the ground strike point (ref. 9-73). The CGLSS uses the intersection of azimuths from two or more sensors to determine the location of the ground flash. The effective range of the CGLSS is ≈100 km. The Lightning Detection and Ranging (LDAR) system is a network of seven sensors that detect CC, IC, and CG lightning pulses (ref. 9-71). The LDAR uses a time-of-arrival (TOA) technique to determine the location of lightning pulses. With this method, locations are established by taking the difference between the arrival times of the same lightning pulse signal to different LDAR sensors. The effective range of the LDAR system is ≈100 km (ref. 9-71).

On a larger scale, the National Lightning Detection Network (NLDN) operated by Vaisala, Inc. employs 113 IMPACT ESP sensors and covers nearly 20 million km^2 (7.7 million mi^2) of the continental United States, Alaska, Canada, and portions of Mexico (ref. 9-74). With this network, thunderstorms can conveniently be monitored and tracked from the CG lightning that they produce. The U.S. National Lightning Detection Network (NLDN) is part of NALDN. An important phenomenological parameter that aids in the design of lightning protection systems (LPSs) is the average lightning flash density; i.e., the number of lightning ground strikes per square kilometer per year. This parameter is critical in almost all lightning protection designs, such as the lightning overvoltage protection of a utility power line, since the number of power outages or related failures is directly proportional to the number of CG discharges per unit area per year (ref. 9-29). Climatic statistics on ground strike flash densities derived from lightning location systems are now available. Figure 9-10 shows the average ground flash density over the continental United States for the years 1989 through 1998.

Satellites are ideal platforms for observing lightning over large regions of the Earth. Instruments carried on satellites in low-Earth orbit have provided additional data on the geographical and seasonal distribution of thunderstorms and lightning. New information has been gathered, in particular, for regions over the oceans that could not be monitored adequately using ground-based lightning location systems. Using results of recent thunderstorm investigations that include observations with high-altitude NASA U-2 aircraft, space sensors capable of mapping both IC and CG lightning discharges during the day and night with a spatial resolution of 10 km (6.2 mi); i.e., storm scale resolution, and high detection efficiency; i.e., 90 percent, have been developed. One such instrument, called the lightning imaging sensor (LIS) was selected for the Tropical Rainfall Measuring Mission (TRMM). In addition, there is great interest in placing a similar imager up into geostationary orbit. This sensor, called the lightning mapper sensor (LMS), would have improved capabilities that include continuous monitoring of thunderstorm evolution. The predecessor (engineering model) of LIS, called the optical transient detector (OTD), and the LIS itself each detect the diffuse, multiple-scattered lightning optical emissions from cloud top. Hence, unlike the NLDN described above, these nadir-staring imagers detect the total (ground and cloud) lightning flash rate. Figures 9-11 and 9-12 provide the OTD-derived total flash rate and ratio of IC-to-CG lightning for the contiguous United States (ref. 9-27). The high-resolution annual flash rate for the global distribution of lightning from a combined 9 yr of observations of the NASA OTD (April 1995–March 2000) and LIS (January 1998–December 2003) instruments is provided in figure 9-13.

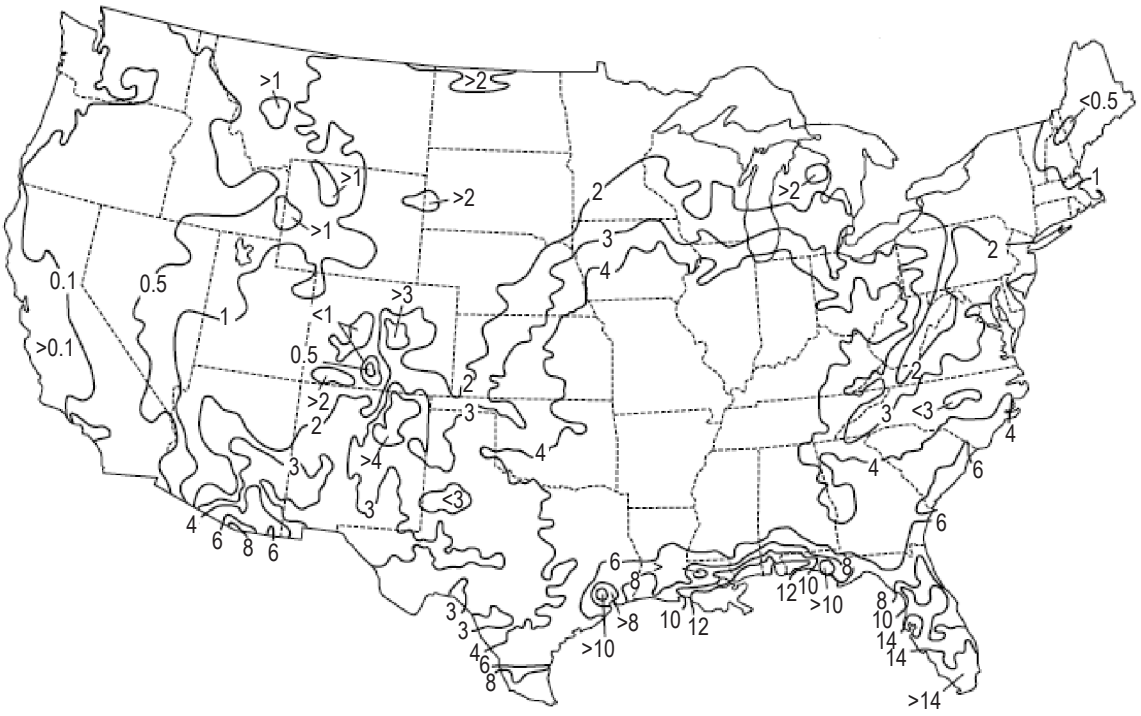

Figure 9-10. Average U.S. lightning flash density (in flashes/km^2/yr) for the years 1989–1998 (ref. 9-75).

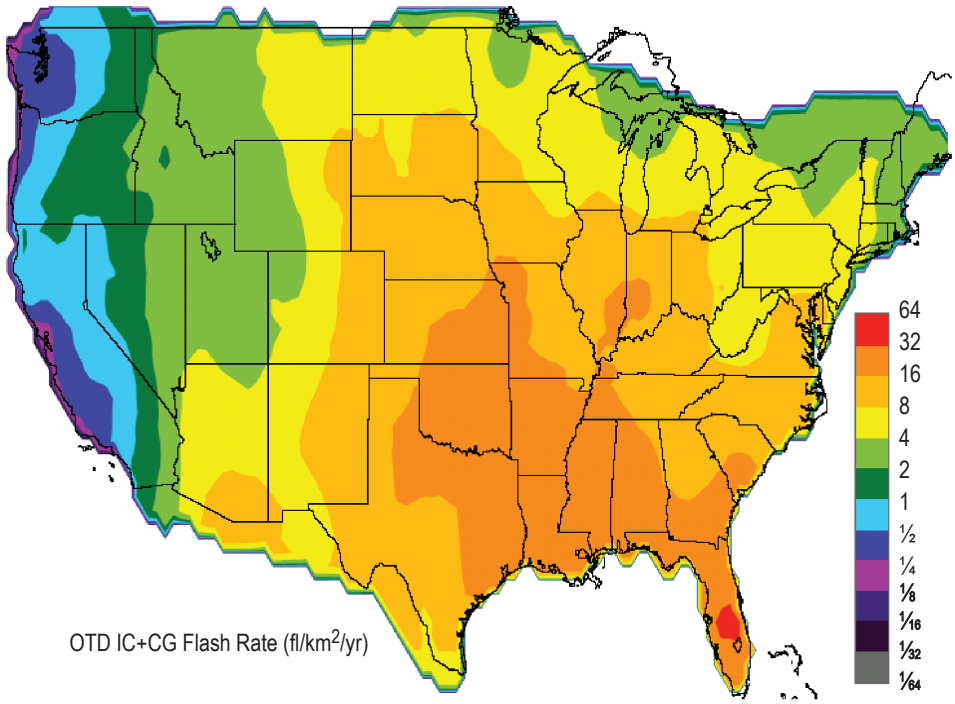

Figure 9-11. Average OTD-derived total (IC+CG) flash rate for the United States (in flashes/km^2/yr) (from ref. 9-27).

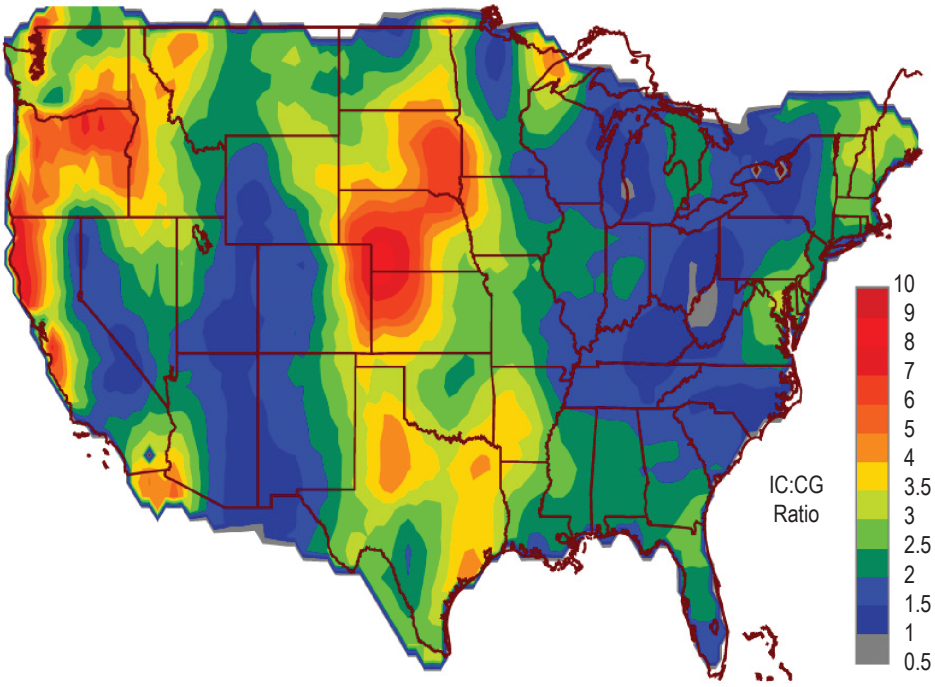

Figure 9-12. Average OTD-derived total IC–CG lightning flash rate ratio for the United States (from ref. 9-27).

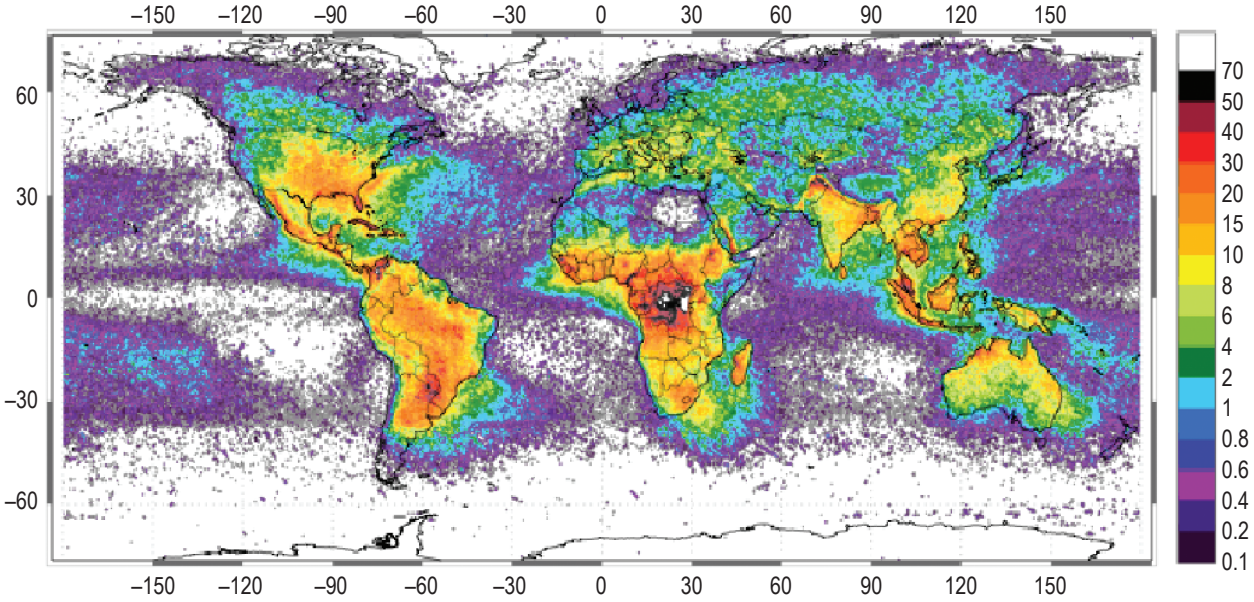

Figure 9-13. OTD- and LIS-derived global lightning annual flash rate distribution (courtesy of the MSFC/GHCC Lightning Team) (ref. 9-76).

9.5.5 Lightning Climatology for Eastern Range (KSC Area), Edwards Air Force Base, and Vandenberg Air Force Base

9.5.5.1 Eastern Range. The formation of cumulonimbus clouds in the ER is strongly dependent on the time of day and season. During the summer months, convergence zones develop within the boundary layer between the sea breeze winds and the large-scale flow. These zones are focal points for thunderstorm formation. Also, the presence of wind shear aloft allows the thunderstorms to grow vertically, which intensifies the charge gradient within the cloud. Studies have shown that these warm season convergence zones develop more frequently in the ER area when there is a southwest flow in the low-level wind pattern (ref. 9-77). For the other months, frontal passages are the primary cause of thunderstorm formation and do not depend on time of day. Figure 9-14 and table 9-7 provide insight into the diurnal variation of CG lightning flashes occurring at the ER. Figure 9-15 shows the mean annual CG lightning flash density for the ER. Data were obtained from the NLDN for the years 1988–2001.

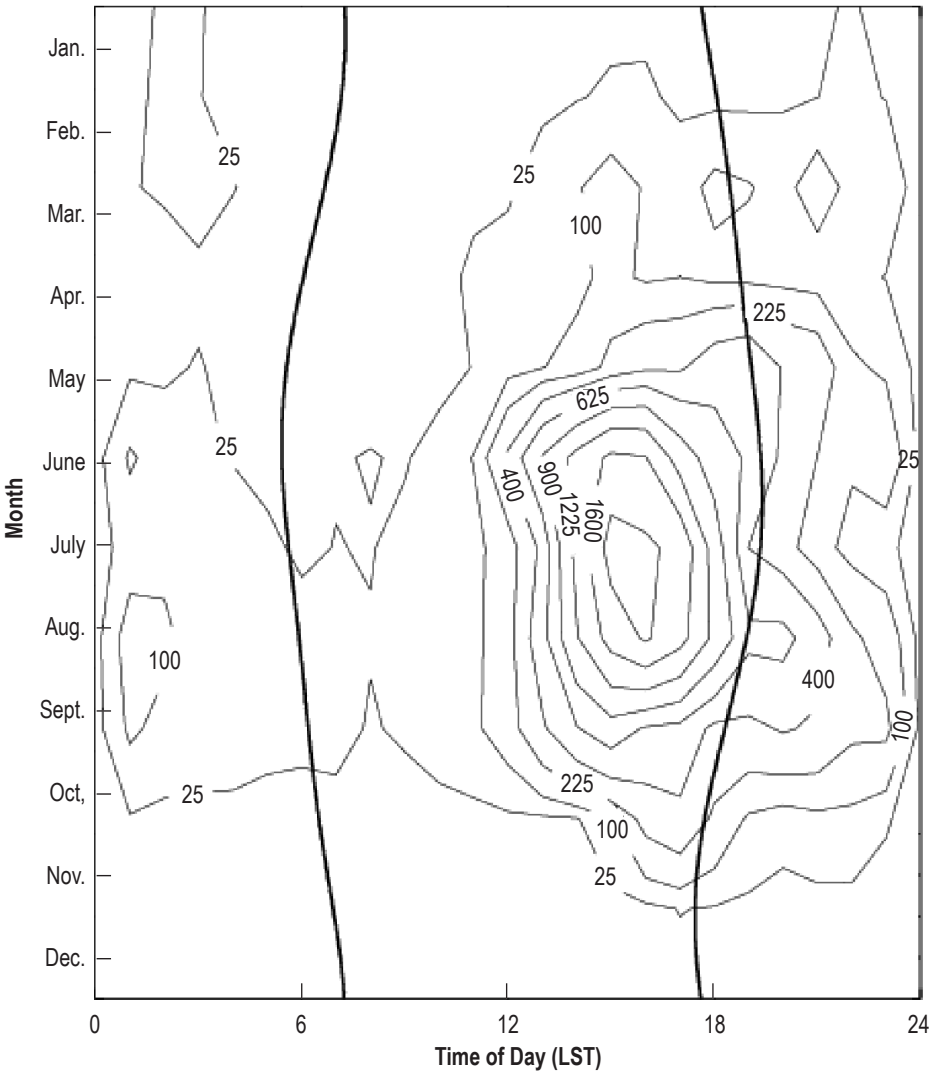

Figure 9-14. Diurnal variation of average CG lightning flashes per year within a 50-km (31-mi) radius of the Eastern Range from 1988–2001. Solid lines represent sunrise and sunset (NASA/MSFC/Natural Environments Branch).

Table 9-7. Diurnal variation of CG lightning flashes for the Eastern Range. Only CG flashes within a 50-km (31-mi) radius of the Eastern Range for the years 1988–2001 were used. Numbers represent the 14-yr average number of CG flashes (NASA/MSFC/Natural Environments Branch).

Hour (LST)	Jan.	Feb.	Mar.	Apr.	May	June	July	Aug.	Sept.	Oct.	Nov.	Dec.	Annual
0	3	16	22	4	12	111	51	147	116	20	11	0	513
1	35	33	31	3	15	59	70	122	72	11	11	0	462
2	29	26	56	10	29	41	51	52	65	8	14	0	381
3	7	17	27	7	8	20	82	29	62	8	9	0	276
4	6	9	12	2	3	13	34	31	45	5	3	1	164
5	3	3	4	2	4	8	17	41	40	6	2	2	132
6	8	5	8	1	6	21	26	30	38	13	3	1	160
7	4	2	5	2	1	28	22	28	22	19	3	2	138
8	7	0	3	2	1	20	40	37	31	7	2	1	151
9	12	0	7	6	2	52	41	52	50	9	2	7	240
10	3	0	11	37	28	103	78	76	82	8	2	5	433
11	9	2	13	59	56	435	145	163	158	13	4	9	1,066
12	9	5	67	37	97	925	448	537	371	13	12	3	2,524
13	8	22	93	78	132	1,336	1,346	1,203	612	20	9	2	4,861
14	10	33	139	127	270	1,679	2,221	1,749	776	92	4	8	7,108
15	8	36	93	86	365	1,617	2,108	2,081	597	277	8	4	7,280
16	7	11	63	101	375	1,058	1,904	1,733	549	351	27	2	6,181
17	8	7	123	73	522	757	1,060	1,137	350	199	20	4	4,260
18	6	9	106	68	582	589	398	682	354	84	12	0	2,890
19	8	16	71	64	386	361	282	697	418	45	9	1	2,358
20	18	25	152	49	336	223	145	495	371	74	5	2	1,895
21	30	35	70	42	114	118	61	251	257	71	6	2	1,057
22	9	23	60	23	85	179	38	162	257	30	7	5	878
23	1	43	35	6	26	156	42	168	234	23	9	0	743
Totals	248	378	1,271	889	3,455	9,909	10,710	11,703	5,927	1,406	194	61	46,151

Table 9-8 shows the monthly and annual 50th and 99th percentile and maximum values for the first return stroke peak current obtained from the NLDN for the years 1988–2001. Also given is the risk (percent) of exceeding a 200-kA lightning flash. The lightning test waveform typically used for vehicle design has a first return stroke peak current of 200 kA. The lightning test waveform for design is described in section 9.7.

9.5.5.2 Edwards Air Force Base. Figure 9-16 and table 9-9 describe insight into the diurnal variation of CG lightning flashes occurring in the vicinity of EAFB. Figure 9-17 shows the mean annual CG lightning flash density for EAFB. Data were obtained from the NLDN for the years 1988–2001.

Table 9-10 shows the monthly and annual 50th and 99th percentile and maximum values for first return stroke peak current obtained from the NLDN for the years 1988–2001. Also given is the risk (percent) of exceeding a 200-kA lightning flash. The lightning test waveform typically used for vehicle design has a first return stroke peak current of 200 kA. The lightning test waveform for design is described in section 9.7.

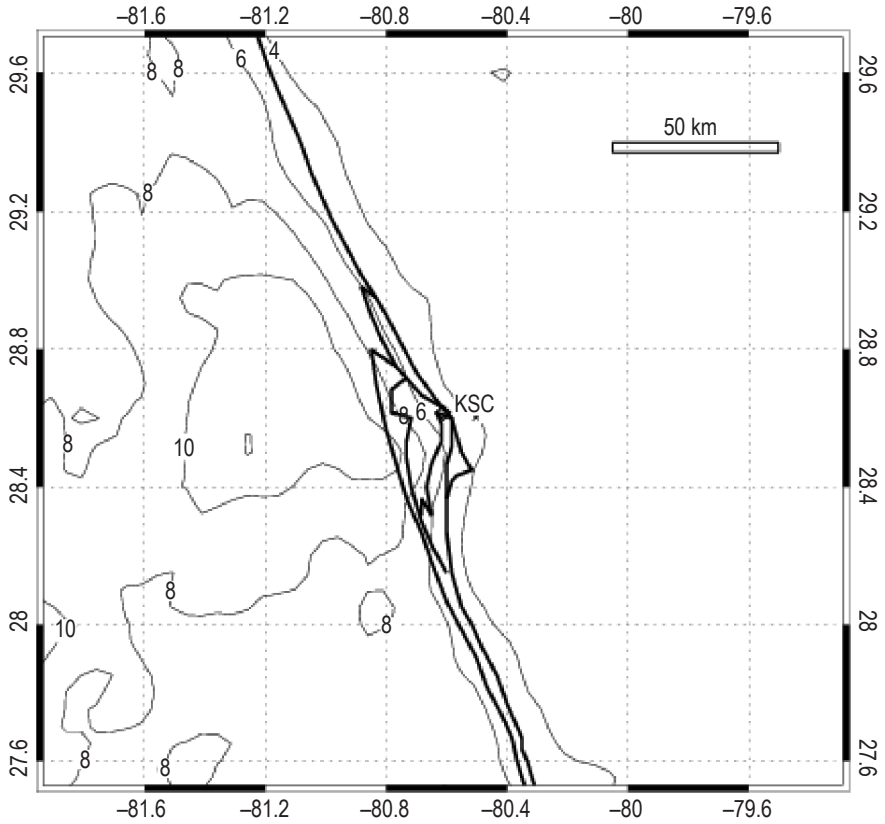

Figure 9-15. Mean annual CG lightning flash density (flashes/km^2/yr) for the Eastern Range. Map shows a local maximum in flash density (≈12 flashes/km^2/yr) just west of Cape Canaveral due to the sea breeze convergence zone (NASA/MSFC/Natural Environments Branch).

Table 9-8. Cloud-to-ground lightning peak current statistics for the Eastern Range for 1988–2001. Only + and – flashes within 50 km (31 mi) of the Eastern Range are considered. Peak current values (in kA) are the absolute value of the first return stroke only (NASA/MSFC/ Natural Environments Branch).

	Jan.	Feb.	Mar.	Apr.	May	June	July	Aug.	Sept.	Oct.	Nov.	Dec.	Annual
50th Percentile	23.2	19.5	19.9	23.8	22.2	24.9	25.3	26.6	26.4	26.9	27.1	26.9	25.3
99th Percentile	113.9	87.7	90.3	91.2	74.8	84.7	81.5	89.2	110.0	97.2	128.8	144.2	89.9
Maximum	187.8	200.1	226.0	170.9	191.3	236.8	738.3	260.1	250.3	385.7	178.8	208.7	738.3
Risk (%) >200 kA	0	0.018	0.023	0	0	0.006	0.032	0.013	0.019	0.02	0	0.118	0.016

9.5.5.3 Vandenberg Air Force Base. Compared to the ER, lightning events at VAFB are 3–5 orders of magnitude less; however, the maximum peak lightning current is of comparable magnitude. Figure 9-18 and table 9-11 describe the diurnal variation of CG lightning flashes occurring in the vicinity of VAFB. Figure 9-19 shows the mean annual CG lightning flash density for VAFB. Data were obtained from the NALDN for the years 1988–2001.

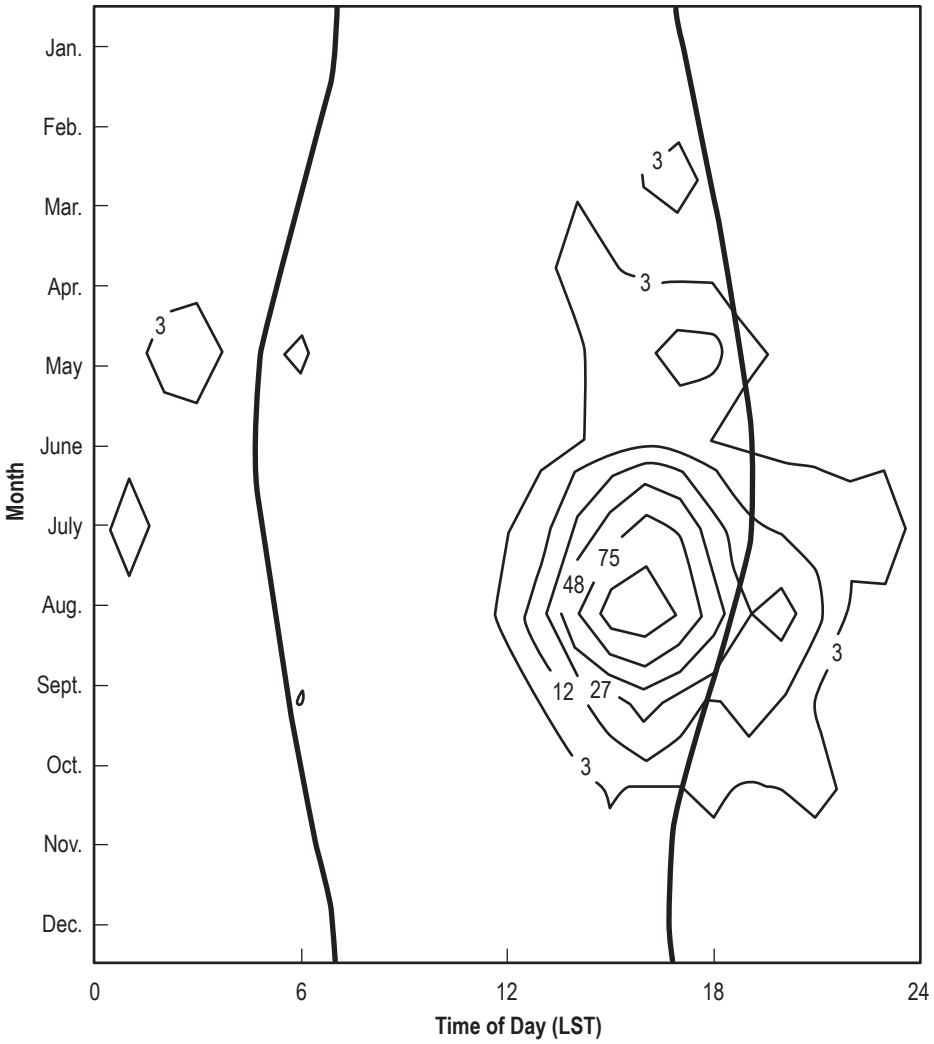

Figure 9-16. Diurnal variation of average CG lightning flashes per year within a 50-km (31-mi) radius of EAFB from 1988–2001. Solid lines represent sunrise and sunset (NASA/MSFC/Natural Environments Branch).

Table 9-12 shows the monthly and annual 50th and 99th percentile and maximum values for the first return stroke peak current obtained from the NLDN for the years 1988–2001. Also given is the risk (percent) of exceeding a 200-kA lightning flash. The lightning test waveform typically used for vehicle design has a first return stroke peak current of 200 kA. The lightning test waveform for design is described in section 9.7.

9.5.6 Kennedy Space Center Lightning and Lightning Peak Current Probabilities

Lyons et al. produced a large peak lightning current climatology for the contiguous United States, consisting of ≈60 million CG flashes over 14 summer months from 1991–1995 (ref. 9-48). This climatology was compiled with data taken from the NLDN. The greatest –CG peak current recorded was –957 kA, while the greatest +CG value was +580 kA. This indicates that, although relatively rare, large peak current CG lightning flashes can occur from thunderstorms. Sensitive avionics boxes and other spacecraft payloads and electronics can be seriously affected if not properly shielded from such extreme lightning strikes and their effects. This subsection

Table 9-9. Diurnal variation of CG lightning flashes for EAFB. Only CG flashes within a 50-km (31-mi) radius of EAFB for the years 1988–2001 were used. Numbers represent the 14-yr average number of CG flashes (NASA/MSFC/Natural Environments Branch).

Hour (LST)	Jan.	Feb.	Mar.	Apr.	May	June	July	Aug.	Sept.	Oct.	Nov.	Dec.	Annual
0	0	0	0	0	0	0	7	0	2	0	0	0	9
1	0	0	0	0	6	0	0	1	0	0	0	0	7
2	0	0	0	0	7	0	1	1	0	0	0	0	9
3	0	0	0	0	1	0	2	0	1	0	0	0	4
4	0	0	0	0	2	0	0	2	2	1	0	0	7
5	0	0	0	0	4	0	0	2	3	0	0	0	9
6	0	0	0	0	0	0	1	1	1	1	0	0	4
7	0	0	0	0	0	0	1	0	2	0	0	0	3
8	0	0	0	0	0	0	0	0	0	0	0	0	0
9	0	0	0	0	0	0	0	0	0	0	0	0	0
10	0	0	0	0	0	0	1	0	0	0	0	0	1
11	0	0	0	0	3	0	3	5	0	0	0	0	11
12	0	0	1	2	1	2	6	21	3	0	0	0	36
13	0	1	3	5	2	3	30	72	10	0	0	0	126
14	0	1	1	3	6	4	58	126	17	4	0	0	220
15	0	1	3	1	11	8	88	133	35	2	0	0	282
16	0	1	5	1	17	5	72	106	18	3	0	0	228
17	0	3	2	0	15	3	33	60	10	5	0	0	131
18	0	2	1	0	4	1	14	26	20	2	0	0	70
19	0	0	0	0	2	1	9	35	11	3	0	0	61
20	0	0	0	0	1	0	9	14	3	5	0	0	32
21	0	0	0	0	1	0	6	1	1	2	0	0	11
22	0	0	0	0	0	0	8	0	2	1	1	0	12
23	0	0	0	0	0	0	12	0	2	0	0	0	14
Total	0	9	16	12	83	27	361	606	143	29	1	0	1,287

presents estimated probabilities of both conventional and extreme peak current lightning strikes that could occur in the KSC area, affecting space vehicles and/or their components.

9.5.6.1 KSC Lightning Strike Probabilities. Mach presented a paper entitled, "Shuttle Lightning Threat Analysis," (ref. 9-78) that gives KSC lightning probability estimates for the various Shuttle operation phases. Mach's estimates do not consider all possible pathways for lightning to damage the Shuttle systems. The three operational phases in his paper that would be of main interest here are during rollout, at-pad, and launch.

For rollout, high current damage (of 200 kA) to the solid rocket booster (SRB) and continuing current to the external tank (ET) are the two greatest possibilities for major Shuttle damage. The probability for lightning damage to an SRB is 1 in 3,200,000 yr (or 3.1×10^{-7}). For ET damage, it is 1 in 55,000 yr (or 1.9×10^{-5}).

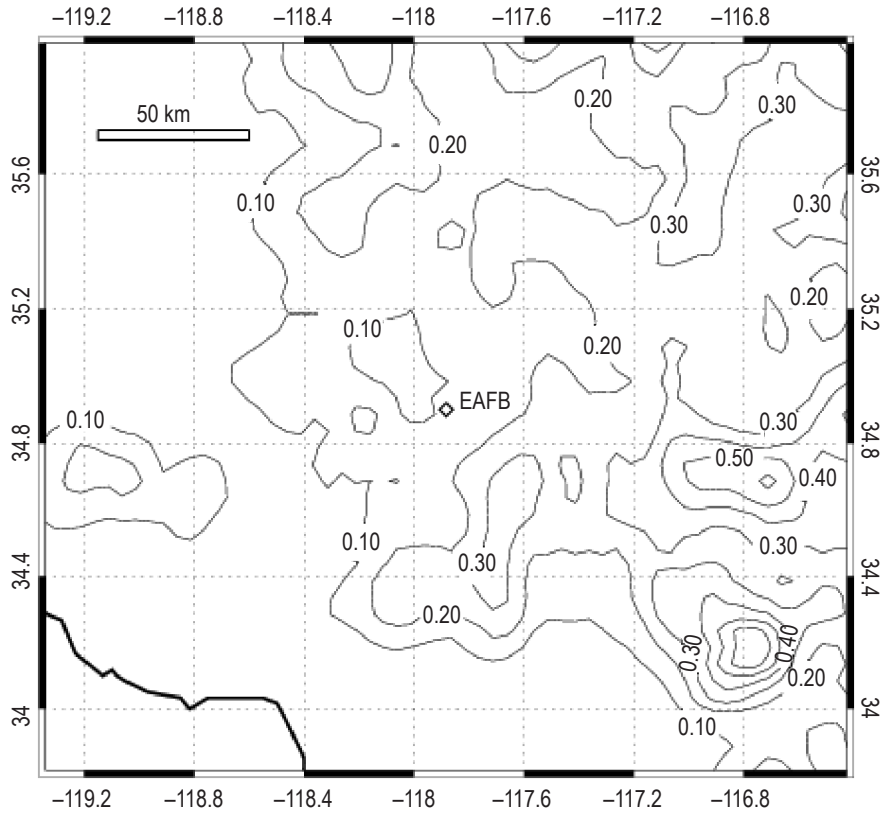

Figure 9-17. Mean annual CG lightning flash density (flashes/km^2/yr) for EAFB (NASA/MSFC/Natural Environments Branch).

Table 9-10. Cloud-to-ground lightning peak current statistics for EAFB for 1988–2001. Only + and – flashes within 50 km (31 mi) of EAFB are considered. Peak current values (in kA) are the absolute value of the first return stroke only (NASA/MSFC/Natural Environments Branch).

	Jan.	Feb.	Mar.	Apr.	May	June	July	Aug.	Sept.	Oct.	Nov.	Dec.	Annual
50th Percentile	65.9	32.2	24.8	22.4	20.3	20.3	18.0	18.5	17.9	24.6	29.0	33.1	18.6
99th Percentile	119.2	241.3	197.8	223.3	96.7	79.8	52.8	49.1	55.0	91.5	68.3	73.3	60.4
Maximum	119.2	241.3	212.2	223.3	297.4	171.2	94.8	177.3	115.6	156.0	68.3	73.3	297.4
Risk (%) >200 kA	0	2.632	0.495	0.599	0.084	0	0	0	0	0	0	0	0.033

On the pad, it is estimated that the KSC LPS's catenary wire will shield the Shuttle from ≈97.2 percent of all pad area strikes (≈2.8 percent not diverted). Mach calculated that if there are ≈1.8 pad strikes/yr, and each Shuttle will spend ≈2 wk on the pad, then the yearly probability of SRB damage from lightning is 9.5×10^{-5} (RP=11,000 yr). The yearly probability for ET damage is 5.6×10^{-3} (RP=178 yr). Approximately one out of every 400 strikes to the pad will damage the ET. Therefore, as indicated earlier, the maximum probability of a lightning strike of "any" current magnitude hitting the Shuttle directly while protected on the pad is 0.028 (2.8 percent).

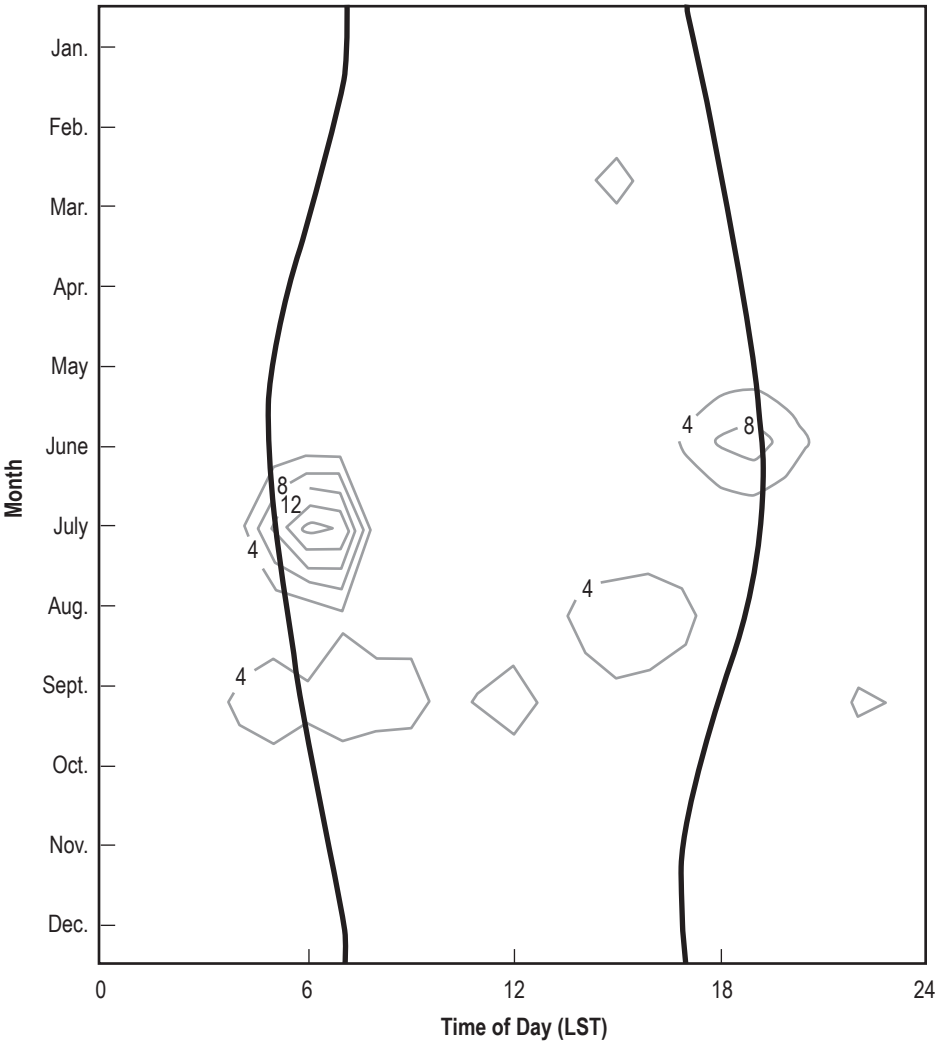

Figure 9-18. Diurnal variation of average CG lightning flashes per year within a 50-km (31-mi) radius of VAFB from 1988–2001. Solid lines represent sunrise and sunset (NASA/MSFC/Natural Environments Branch).

During the boost phase of launch, the probability of the Shuttle vehicle and exhaust intercepting a "natural" (not triggered) lightning flash from a nearby storm was calculated, assuming the following conditions: A low flash rate (1/min) to a high flash rate (60/min); distance from the storm edge being 2-, 5-, and 10-nmi standoffs; ascent time of ≈50 s; and eight launches per year. Mach's resulting probability estimates are presented in table 9-13.

If Shuttle LCC regarding natural lightning are followed during countdown/launch, the estimated probability of the Shuttle being struck by any magnitude lightning is 1 in 23,000 (or 0.0043 percent). The only LCC rule applied here is the 5- and 10-nmi standoff to thunderstorms (ref. 9-79). Not included are triggered lightning from anvils, cloud thickness and ceiling, and any other LCC rules. Mach presents various other Shuttle element lightning strike and lightning ignition probabilities in his paper.

Table 9-11. Diurnal variation of CG lightning flashes for VAFB. Only CG flashes within a 50-km (31-mi) radius of VAFB for the years 1988–2001 were used. Numbers represent the 14-yr average number of CG flashes (NASA/MSFC/Natural Environments Branch).

Hour (LST)	Jan.	Feb.	Mar.	Apr.	May	June	July	Aug.	Sept.	Oct.	Nov.	Dec.	Annual
0	1	1	0	0	0	0	0	0	1	0	0	0	3
1	0	0	0	0	0	0	0	0	2	0	0	0	2
2	2	0	0	0	0	0	1	0	1	0	0	0	4
3	2	0	1	0	0	2	2	0	5	0	0	0	12
4	0	0	2	0	0	1	13	0	8	0	0	0	24
5	0	1	0	0	0	0	22	0	5	0	0	0	28
6	0	1	0	0	0	0	20	3	7	0	0	1	32
7	0	1	0	0	0	0	0	3	6	1	0	0	11
8	0	1	0	0	0	0	0	2	6	0	0	0	9
9	0	1	0	0	0	0	0	1	3	0	0	0	5
1	0	0	0	0	0	0	0	1	4	0	0	0	5
11	0	0	1	0	0	0	0	1	6	0	0	0	8
12	0	0	2	0	0	0	0	1	3	0	0	0	6
13	0	0	3	0	1	0	0	6	1	0	0	1	12
14	1	0	5	0	0	0	0	7	3	0	0	0	16
15	0	1	3	0	0	0	0	8	2	0	0	0	14
16	0	3	1	0	0	5	0	6	1	0	0	1	17
17	0	1	0	0	0	9	0	0	1	0	0	0	11
18	0	2	0	0	0	10	0	0	2	0	0	1	15
19	0	0	0	0	0	6	0	1	2	0	0	0	9
20	0	0	0	0	0	3	0	0	1	0	0	0	4
21	0	0	0	0	0	1	0	0	5	1	0	0	7
22	0	0	0	0	0	0	0	0	4	0	0	0	4
23	1	1	0	0	0	0	0	1	2	0	0	0	5
Total	7	14	18	0	1	37	58	41	81	2	0	4	263

9.5.6.2 KSC Estimated Peak Lightning Current Probabilities. A study was done to calculate what the various peak lightning current; i.e., 200, 100, and 50 kA, probabilities are at KSC if the Space Shuttle were hit by CG lightning while being rolled out to pad 39, while being exposed on pad 39, and for triggered (Tr) lightning on ascent. Second, peak lightning current probability statistics were needed if all the lightning LCC rules were followed, but the Shuttle were hit by nontriggered (NTr) lightning while in the boost/launch phase. The complete calculations, results, and references used in the study are documented in reference 9-80. Some of the pertinent worst-case, estimated, peak lightning current, point probability information was extracted and is presented in table 9-14. Consult reference 9-80 for more detailed information and other probabilities.

Keep in mind that the lightning probabilities given in this subsection are only estimates. As Gabrielson states, “It is difficult, if not impossible to establish a probability for lightning strikes with a high level of confidence” (ref. 9-81). Also Mach states, “All probabilities are estimates and can be in error by more than an order of magnitude” (ref. 9-75). One should note that the empirical KSC CG lightning peak current probability risk values given in section 9.5.5.1 (table 9-8) are greater than the stated probabilities given here for a peak

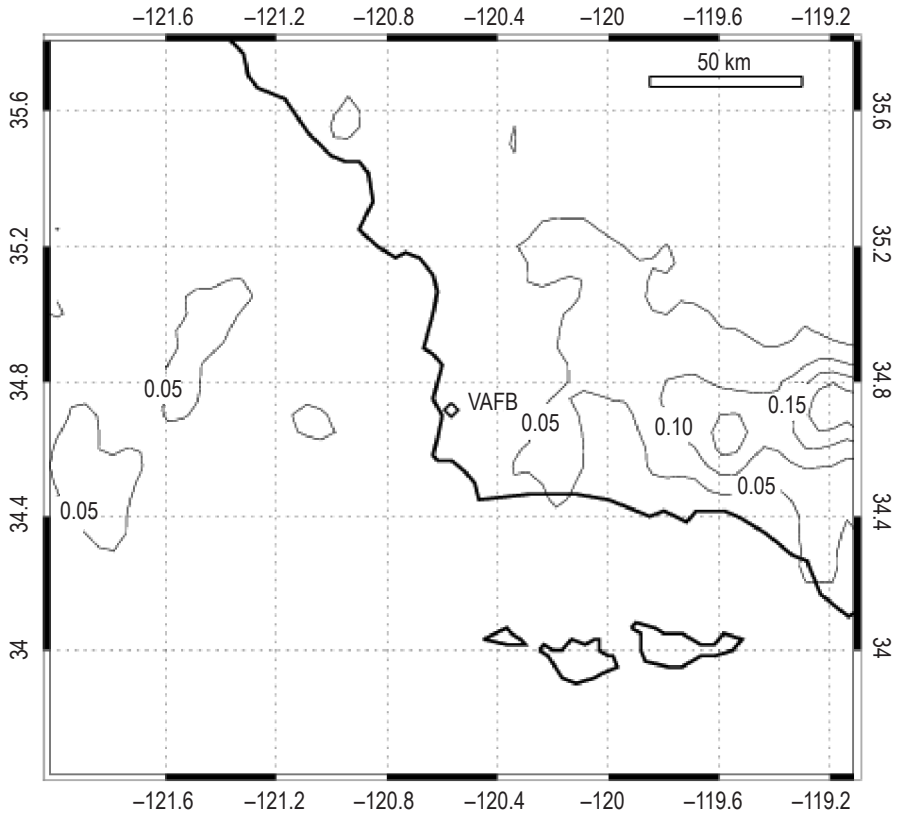

Figure 9-19. Mean annual CG lightning flash density (flashes/km^2/yr) for VAFB (NASA/MSFC/Natural Environments Branch).

Table 9-12. Cloud-to-ground lightning peak current statistics for VAFB for 1988–2001. Only flashes within 50 km (31 mi) of VAFB are considered. Peak current values (in kA) are the + and – values of the first return stroke only (NASA/MSFC/Natural Environments Branch).

	Jan.	Feb.	Mar.	Apr.	May	June	July	Aug.	Sept.	Oct.	Nov.	Dec.	Annual
50th Percentile	41.8	41.2	34.0	57.2	25.8	23.8	36.7	34.6	34.4	30.2	42.1	39.8	32.9
99th Percentile	165.5	186.4	215.6	190.5	114.8	63.5	109.6	126.3	139.8	84.8	152.6	175.2	141.3
Maximum	165.5	187.5	250.4	190.5	114.8	85.6	125.8	157.7	258.3	84.8	152.6	175.2	258.3
Risk (%) >200 kA	0	0	1.825	0	0	0	0	0	0.182	0	0	0	0.186

Table 9-13. Probability estimates for natural CG lightning to strike STS on launch* (ref. 9-78).

Exposure Time (s)	Standoff From Storm Edge (nmi)	Standoff From Storm Edge (km)	Storm Severity Flash Rate (min^{-1})	Probability Per Year (%)	Probability Return Period (yr)
50	2	3.7	High = 60	0.625	160
50	5 (LCC)	9.3	Avg. = 6	0.00434	23,000
50	10 (LCC)	18.5	Low = 1	0.00007	1,300,000
50	10 (LCC)	18.5	High = 60	0.00434	23,000

*Assuming eight Shuttle launches per year

Table 9-14. KSC worst-case* lightning peak current probability (P) estimates for various Shuttle mission phases (ref. 9-80).

Space Shuttle Operational Mission Phase	Lightning Peak Current Probability (%)/Return Period (RP) (yr)					
	≈P>200 kA (%)	RP (yr)	≈P>100 kA (%)	RP (yr)	≈P>50 kA (%)	RP (yr)
Roll-out to pad[1]	0.00218	(45,963)	0.00590	(16,934)	0.01150	(8,696)
Roll-out to pad[2]	0.0399	(2,508)	0.108	(924)	0.21	(475)
On-pad[3]	0.00226	(44,220)	0.06138	(1,629)	0.11953	(837)
Launch[4] (NTr)	0.00030	(329K)	0.00083	(121K)	0.00161	(62,274)
Launch[5] (Tr)	TBD	TBD	TBD	TBD	TBD	TBD

*The KSC's SLC40 more conservative peak lightning current probability statistics are not shown here, but are given in reference 9-80.

[1]Assume roll-out in evening hours in worst (peak) lightning month, with no forecasting assumed.

[2]Special roll-out case: During worst (peak) lightning month and peak afternoon hours, with no weather forecasting.

[3]Assume on-pad Shuttle protected by pad lightning system.

[4]Launch (nontriggered lightning), where Shuttle protected by LCC "storm distance rule" only.

[5]Launch (triggered lightning): Triggered lightning comments:

- Gabrielson calculated that the probability for any magnitude lightning strike will increase (by a factor of ≈140,000) for a 10-m-tall vehicle triggering lightning (within 10 km) on ascent, under moderate storm/lightning conditions, as compared to the vehicle being hit by any magnitude lightning strike while stationary on level ground (ref. 9-81).
- Man-launched rocket-triggered lightning discharges are generally less in current magnitude than natural CG discharges. During 9 yr (1984–1991) of the rocket-triggered lightning current measurement program at KSC, the highest rocket-triggered lightning current measured was 99 kA (ref. 9-39).

current of >200 kA. This is due to the larger areal extent used for the empirical table 9-8 statistics, while much smaller area and point theoretical statistics were considered for the calculations here.

9.5.6.3 Probability of Kennedy Space Center Thunderstorms. There is always a lightning threat to personnel, the launch vehicle, and equipment whenever thunderstorms occur in the area. Figure 9-20 gives the probability of Cape Canaveral Air Force Station (CCAFS) thunderstorms by month and local time of day. Figure numbers denote the probability of the occurrence of thunderstorms, expressed in percent. Thunderstorms can be expected ≈25 percent of the time at 3 to 5 p.m. any day in July. Relative to thunderstorm activity, the best time of day to launch in July is 1 to 10 a.m., when the thunderstorm probability is lowest. The best months to launch at KSC, for any hour, are during October through February (ref. 9-31). Figure 9-14 and table 9-7 in section 9.5.5.1 present similar month versus hour results but of CG lightning flashes for the KSC/Eastern Range (ER) area.

9.5.6.4 Probability of Closest Lightning Strike. Using the U.S. NLDN lightning network data, a method by Krider and Kehoe (ref. 9-82) has been developed which allows for the estimation of the chance that the nearest lightning strike will occur within a specified distance R of any origin location (chosen at random) within a circular area. This calculation is based given only the average area density of strikes statistic (N_g) in units of number of flashes/km^2/time, where time can be expressed in terms of month, year, etc. Note that the spatial scale where the attachment (or the strike probability) is not to be affected by the strike object itself; i.e., a tall tower will have a larger "striking distance" and area of exposure than a person standing in the open. A tall structure could actually initiate an upward type I discharge.

Assuming each strike as a random event and that the spatial pattern of the strike points has a homogeneous Poisson distribution; i.e., N_g has complete spatial randomness, the probability for the nearest strike being within a distance r and $r + dr$ of the origin can then be determined. The most probable nearest-neighbor distance was calculated as:

$$r_{mp} = 1/[\sqrt{2\pi N_g}] \tag{9.1}$$

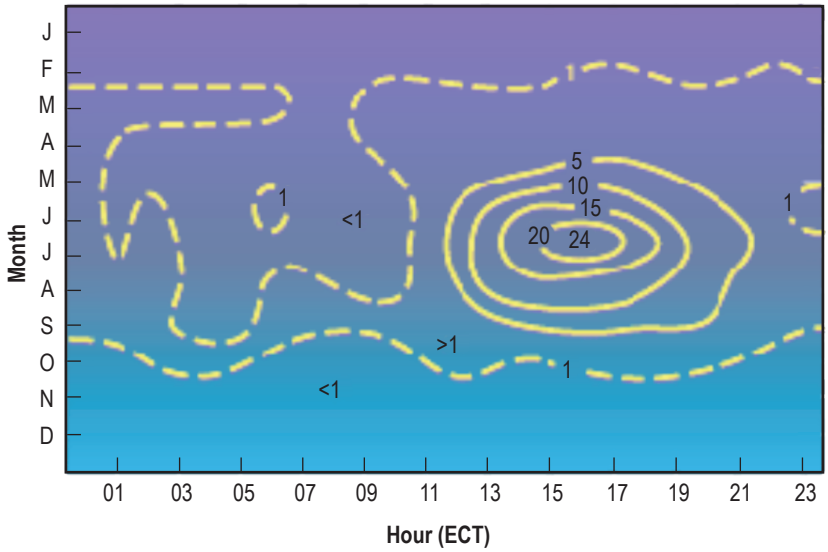

Figure 9-20. Probability of CCAFS/KSC thunderstorms by month and hour (ref. 9-31).

along with derived mean and variance equations.

Thereby, the probability (P) that the closest strike is within a distance R is:

$$P(\leq R) = 1 - \exp\left(-N_g \pi R^2\right); \tag{9.2}$$

or solving for R:

$$R = \left[-\ln(1-P)/(\pi N_g)\right]^{1/2} \quad . \tag{9.3}$$

Now the most probable distance to the 2nd, 3rd, ...nth nearest neighbor is then calculated as:

$$r_{mp,n} = \sqrt{[(2n-1)/(2\pi N_g)]} \tag{9.4}$$

along with derived mean and variance equations.

Figure 9-21 shows plots of probability P versus radial distance R computed using equation (9.2) for eight different values of N_g.

9.6 Cloud-to-Ground Lightning Damage and Protection

Damaging effects due to lightning include human injury or death, forest fires, communication and power system failures, and hazards to civil, commercial, and military aircraft and aerospace vehicles. Section 9.5 discussed the basic characteristics of a lightning discharge, which is important to understand to determine valid protection standards. Knowledge of lightning currents and radiation fields is fundamental in this understanding, and data on these quantities are discussed below. This section will concentrate primarily on ground discharges.

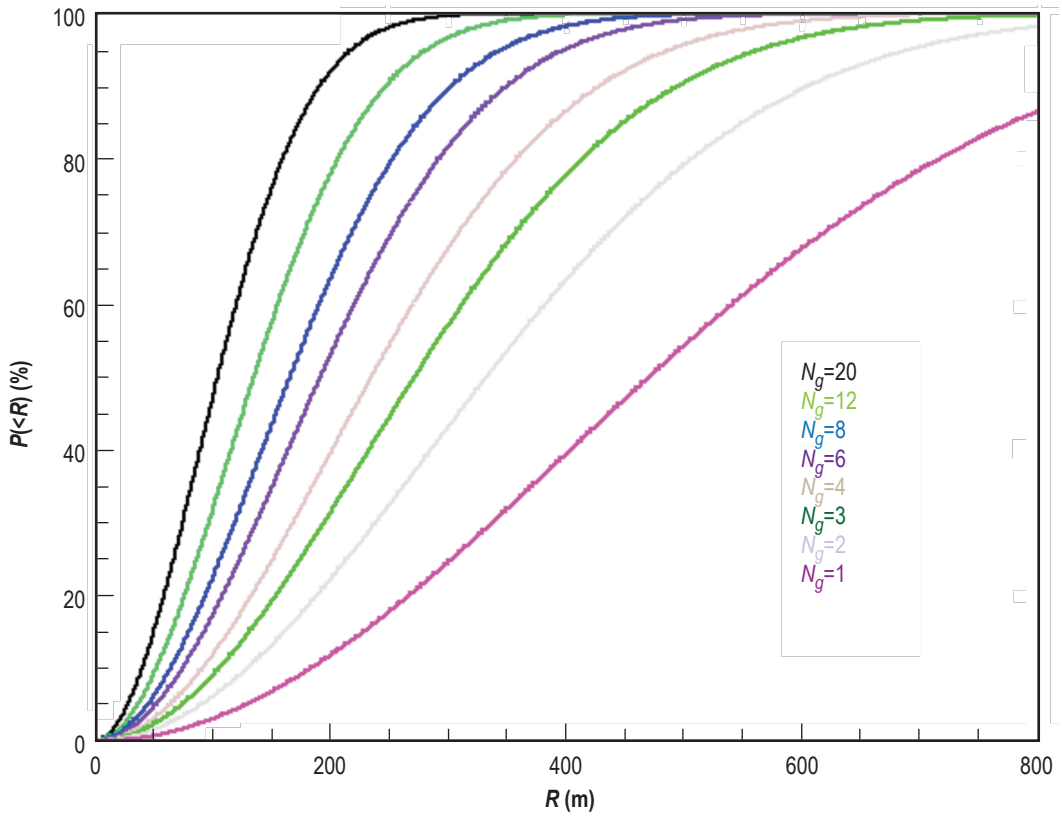

Figure 9-21. Probability that the nearest flash will be within a distance, R, for various values of N_g in F/km^2 (ref. 9-82).

9.6.1 Lightning Current Damage Parameters

Several lightning current parameters are important in assessing the potential for lightning damage: the peak current (i), the peak current derivative (di/dt), the charge transfer—the integral of current over time (Q) and the action integral—the integral of the square of the current over time) ($\int i^2 dt$).

For objects that have primarily a resistive impedance, the peak voltage that develops across the object will depend on the peak current. A large voltage that develops at one end or across an object may lead to discharges through the air and around the object, or from the object to ground, creating a short circuit.

For objects and systems that consist primarily of an inductive impedance, such as cabling in electronics systems or electrical connections on printed circuit boards, the peak voltage will be proportional to the time derivative of the current. For example, if a current with a peak di/dt of 1 kA/µs (one hundredth of a typical lightning peak di/dt value) is injected into a straight length of wire with an inductance of 1 µH/m, a voltage of 1,000 V will develop across 1 m of the wire. It is easy to imagine the damage this could produce in solid-state electronic systems that are sensitive to transient voltages in the tens-of-volts range.

The heating or burnthrough of metal sheets such as airplane wings or metal roofs is, to a crude approximation, proportional to the charge transferred during the lightning strike. Generally, large charge transfers occur during the long-duration, low-current amplitude portions of lightning discharges such as the continuing current phase, rather than during the short-duration, high-current amplitude return stroke processes.

The heating of electrically conducting materials and the explosion of nonconducting objects is, to a first approximation, determined by the value of the action integral since the quantity $\int i^2 R dt$ is Joule heating. (R is the resistive impedance.) Generally, electrical heating vaporizes internal material, and the resulting increase in pressure causes a fracture or explosion to occur.

9.6.2 Tower Measurements of Current

Table 9-15 summarizes values of typical lightning current parameters obtained from tower measurements atop Mt. San Salvatore in Switzerland (ref. 9-28). The data in parentheses are from tower measurements in Italy (ref. 9-83).

Table 9-15. Negative cloud-to-ground lightning current parameters measured in strikes to instrumented towers—percentage of cases exceeding tabulated value (refs. 9-28 and 9-83).

Parameter (units)	Number of Events	95%	50%	5%
Peak current (kA)				
First strokes	101 (42)	14	30 (33)	80
Subsequent strokes	135 (33)	4.6	12 (18)	30
Peak *di/dt* (kA/μs)				
First strokes	92 (42)	5.5	12 (14)	32
Subsequent strokes	122 (33)	12	40 (33)	120
Charge (C)				
First strokes	93	1.1	5.2	24
Subsequent strokes	122	0.2	1.4	11
Flash (all strokes)	94	1.3	7.5	40
Action integral (A^2 s)				
First strokes	91	6×10^3	5.5×10^4	5.5×10^5
Subsequent strokes	88	5.5×10^2	6×10^3	5.2×10^4
Front duration (μs)*				
First strokes	89 (42)	1.8	5.5 (9)	18
Subsequent strokes	118 (33)	0.22	1.1 (1.1)	4.5
Stroke duration (μs)**				
First strokes	90 (42)	30	75 (56)	200
Subsequent strokes	115 (33)	6.5	32 (28)	140
Time between strokes (ms)	133	7	33	150
Flash duration				
Including single-stroke flashes	94	0.15	13	1,100
Excluding single-stroke flashes	39	31	180	900

*2 kA to peak

**2 kA to half-peak amplitude value

9.6.3 Triggered Lightning Current Measurements

It is often argued that triggered lightning realistically simulates natural lightning and may be used in studies of lightning physics and lightning protection technology. The first successful attempts to trigger lightning over land were performed at St. Privat d'Allier in south-central France. In this and similar experiments that followed, a small antihail rocket, ≈85 cm tall and weighing 2.7 kg, was fired upward into a thundercloud and carried a wire that unspooled from the ground. The rocket developed a maximum speed of ≈200 m/s and could reach an altitude

of ≈700 m in 5 s. Cotton-covered steel wire (0.18-mm diameter) was used. An upward leader was initiated from the top of the rocket when the rocket reached a typical altitude of 200 to 300 m. A triggering attempt was generally successful if the static field at the ground was ≥10 kV/m, though success also depended on the particular storm and the amount of natural lightning activity. Rocket heights at the time of initiation were between 50 and 530 m with a mean of 210 m. Fields at the time of successful launches ranged from –6 to –17 kV/m with a mean of 10 kV/m.

Since the initial experiments at St. Privat d'Allier, additional experiments have been performed in Japan, New Mexico, and Florida. The results of these experiments are summarized in table 9-16. Note that the four basic lightning current "damage parameters" discussed above are included in the table.

9.6.4 Inferring Damage Parameters From Lightning Fields

In addition to measuring lightning current parameters directly from tower strikes as cited above, one can infer values of the current and current derivative from measurements of the radiated fields. The variety of discharge processes which occur during a lightning flash generate electromagnetic radiation over a broad range of frequencies ranging from near direct current to the microwave band. A variety of lightning processes, including leaders, certain IC discharges, and return strokes, produce large-amplitude radiation field changes in a fraction of a microsecond. Abruptly changing fields have important implications in the design of lightning protection equipment and are of interest because they imply large and rapid current variations.

Only in about the last 20 yr have accurate measurements of the fastest lightning field variations been made. This is due partly to the increased availability of suitable recording equipment. It is due also to the realization that, since high-frequency content of lightning fields is degraded by propagation over land, fast-field changes can be adequately observed only if the propagation path from the lightning to the recording station is entirely over salt water.

Figure 9-22 is a schematic representation of simultaneous photographic and electric field measurements for a multiple-stroke, CG lightning flash. This illustrates typical lightning field variations in different frequency intervals and on different timescales.

Electric field variations less than a few tens of megahertz are commonly measured using broadband antenna systems. The sensing element is often a flat conductor that is placed horizontally on the Earth's surface (ref. 9-91). A current flows to and from the antenna in response to a changing external electric field. The antenna current is then integrated to give an output voltage proportional to E. In "slow antenna" systems, an amplifier decay time constant of several seconds is used. This is several times longer than the duration of the flash, and an accurate record of the entire field change is obtained. "Fast antenna" systems have a shorter decay time constant, typically hundreds of microseconds, so that the amplifier output voltage will recover to near zero between separate events. In this way, the structure of each impulsive component within a discharge can be studied with the full dynamic range of the amplifier.

Note that the schematic slow E-field record (fig. 9-22) is dominated by large transitions produced by the separate return strokes. More slowly varying fields, representing charge transport occurring during leader processes and continuing currents, are also detected with slow antenna systems.

Table 9-16. Mean lightning current parameters for rocket-triggered lightning events (refs. 9-84 through 9-90).

Parameter (units)	Number of Events	Percentage of Cases Exceeding Tabulated Value 90%	50%	10%	Maximum Value
Peak current (kA)					
France*	94	2	12	29	42
New Mexico*	35	4	18	30	40
Florida (1985–1988)	231	5.5	12	26	60
France (1986)	9		13		48
Peak *di*/*dt* (kA/μs)					
Florida (1985)	31	61	102	171	250
Florida (1987, 1988)	74	42	125	215	411
France (1986)	9		78		139
Charge (C) per stroke			0.35**		
New Mexico	35		0.95‡		
Charge (C) per flash					
France	94	4	50	100	140
New Mexico	35	6	35	175	
Action integral (A^2 s)					
France	94	3×10^2	6×10^3	5×10^4	3×10^5
Flash duration (ms)					
France	94	70	350	850	1,300
New Mexico	35	250	470	940	
Percentage of flashes with only a continuous current phase					
France	40%				
New Mexico	20%				
Number of pulses per flash					
France**	94	4	350	11	53
New Mexico**	35		470	10**	

*Distribution of only the largest peak current in each flash.
**Only pulses with peak currents ≥3 kA were included.
‡Only pulses with peak currents ≥10 kA were included.

The fine structure of large amplitude fast *E*-field impulses is shown on expanded timescales below the fast *E*-field record in figure 9-22. These highly time-resolved *E*-field signatures are complicated by a variety of discharge processes. In figure 9-22(b) is a schematic depiction of the VHF lightning radiation that would be detected using a tuned, narrowband receiver. Radiation at these frequencies is currently being used in time-of-arrival and interferometric systems to locate and follow lightning channel growth and propagation in thunderstorm clouds.

To infer the lightning current and current derivative from the radiated fields, one begins by considering the fields emitted by a straight, vertical current element of length *H* above a perfectly conducting ground (ref. 9-92). The geometry for this calculation is given in figure 9-23.

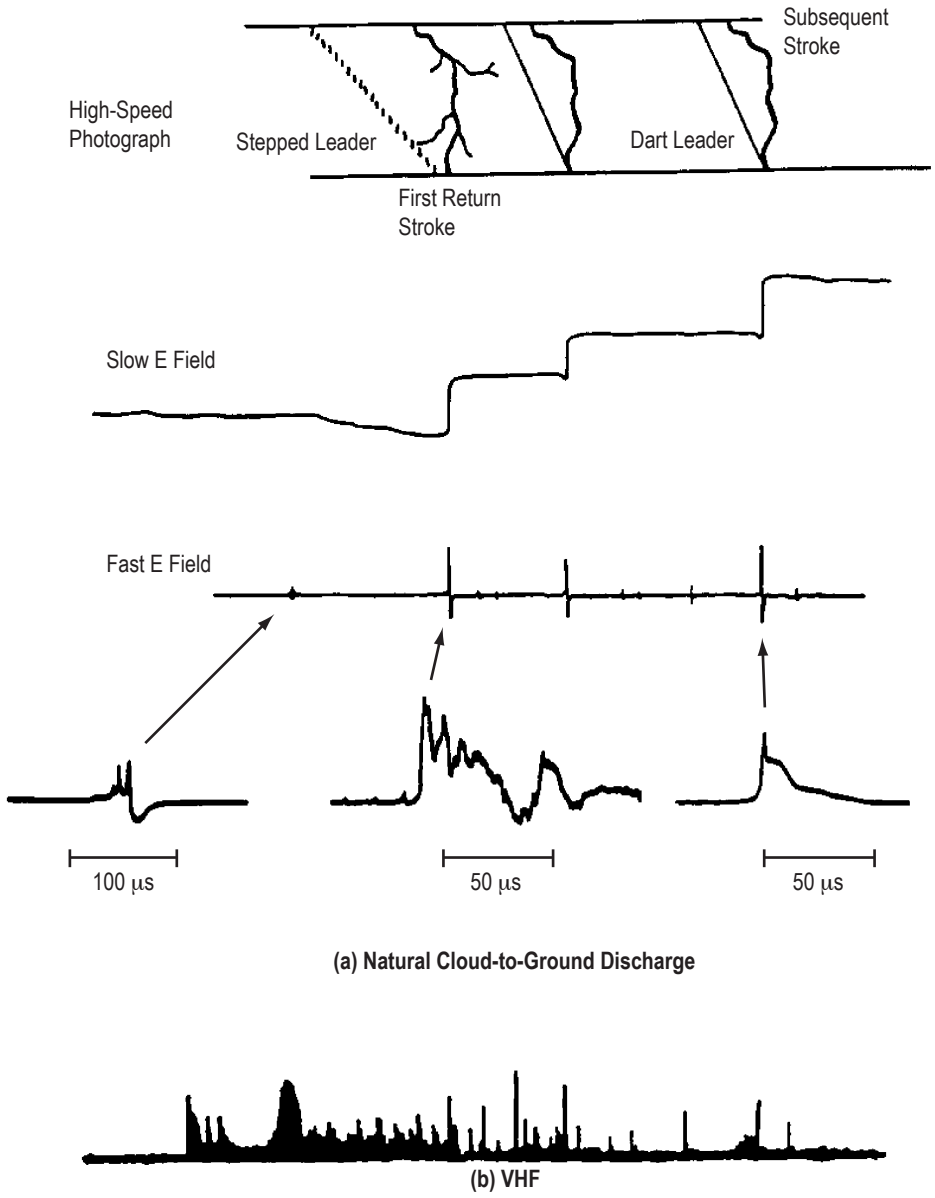

Figure 9-22. Simultaneous photographic and electric field measurements for (a) a multiple stroke, cloud-to-ground lightning flash and (b) a VHF lightning radiation signature (adapted from ref. 9-29).

The total electric field for an observer at P is then found by adding the electric field due to current flow at all heights. The electrical field intensity E is perpendicular to the ground plane. D is the distance from the bottom of a straight vertical channel of height H, due to the return stroke current $i(z,t)$, which is calculated in the z direction within a short section of channel dz above the ground plane. A given waveshape propagates up the lightning channel at velocity v behind the wavefront; i.e., $i(z, t) = i\,(t–z/v)$. The current and the electric field have the same waveshape until the return stroke wavefront reaches the top of the channel, a time typically between 20 and 200 μs.

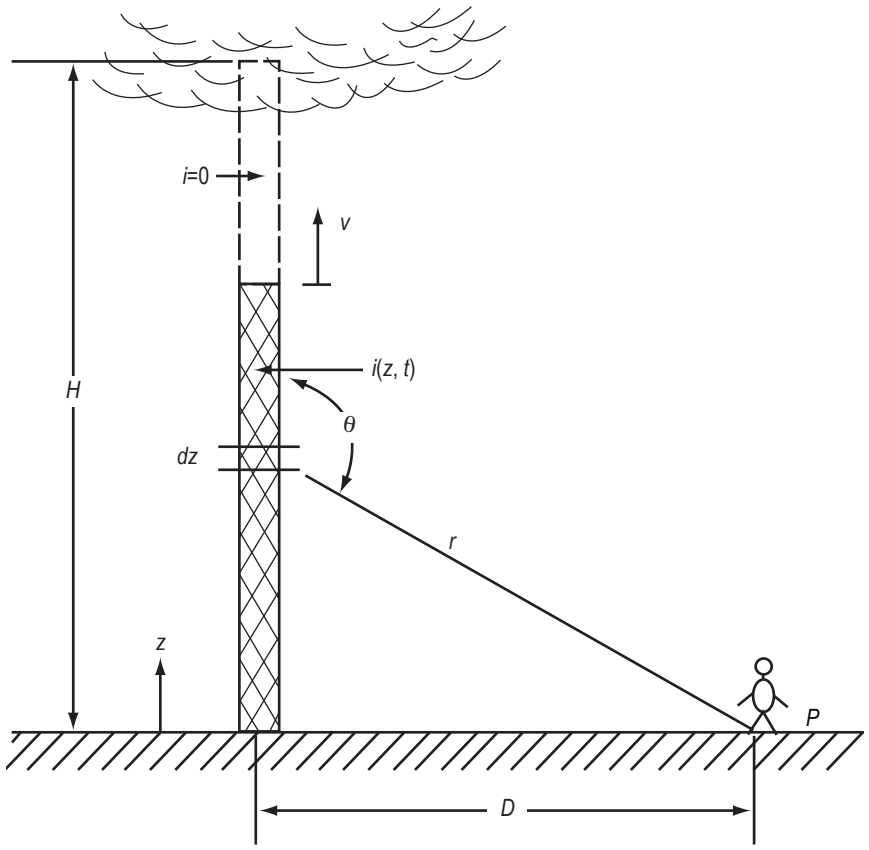

Figure 9-23. Geometry used in computing the electric field intensity of the lightning return stroke (ref. 9-92).

The electric field intensity (E) at the ground at a distance (D) from the ground-strike point, in MKS units, can be expressed in terms of current as:

$$\vec{E}_{\text{total}} = \frac{1}{2\pi\varepsilon_0}\int_0^H \left(E_R + E_I + E_S\right) dz\hat{z} \ , \tag{9.5}$$

where

$$E_R = -\frac{\sin^2\theta}{c^2 r}\frac{\partial i}{\partial t}\left(z, t - r/c\right) = \text{radiation term} \ ,$$

$$E_I = \frac{\left(2 - 3\sin^2\theta\right)}{cr^2} i\left(z, t - r/c\right) = \text{induction term} \ ,$$

and

$$E_S = \frac{\left(2 - 3\sin^2\theta\right)}{r^3}\int_0^t i\left(z, \tau - r/c\right) d\tau = \text{electrostatic term} \ ,$$

where

ε_o = permittivity of free space
μ_o = permeability of free space
c = $(\mu_o \varepsilon_o)^{-1/2}$, the speed of light
$i(z,t)$ = vertical channel current (a function of z and t)
v = constant return-stroke wavefront velocity
t = time
τ = time increments
z = altitude
H = cloud altitude
dz = increment of altitude z
i = current
r = distance from observer at P to channel location of dz increment
θ = angle between the current upper channel and the observers view of the channel increment dz.

The radiation or "far-field" component decays more slowly with distance than the other components and thus becomes dominant at large distances.

It is not possible to solve equation (9.5) for the current in terms of measured electric fields. Rather, it is necessary to assume a functional form for the channel current—a function of time and channel height. If it is possible to adjust current model parameters until good agreement with measured fields and the observed wavefront speed is obtained, then the model current is assumed to be a realistic approximation to the true current. A realistic current model would be of practical importance because (1) return stroke currents and statistical distributions of current parameters could be determined from remote measurements of lightning fields, and (2) realistic fields could be calculated for use in "coupling" calculations, as might be used to determine voltages induced on power lines from a nearby lightning strike.

The model most widely used to derive lightning currents from measured fields is the transmission line (TL) model (ref. 9-93). The TL model assumes that current measured at the ground propagates up the channel at a constant velocity, without distortion, much as it would along a lossless transmission line. The TL model current has the following functional dependence:

$$i(z,t) = i(0, t - z/v) \qquad z \le L(t)$$

$$i(z,t) = 0 \qquad z > L(t) \quad . \tag{9.6}$$

Here, $L(t)$ is the height of the return stroke wavefront at time (t). A particularly simple relationship between the currents and the radiation belts, at a distance (r), is obtained for the TL model current:

$$i(t) = \frac{2\pi\varepsilon_0 c^2 r}{v} E_R(r, t + r/c)$$

$$\frac{di}{dt}(t) = \frac{2\pi\varepsilon_0 c^2 r}{v} \frac{dE_R}{dt}\left(r, t + r/c\right) \quad . \tag{9.7}$$

These equations are the basis for field-inferred current parameters. In the TL model, since the same current wave shape passes all points on the channel, charge is only transferred from the bottom of the channel to the top, and

the leader channel is not discharged. There is poor agreement, therefore, between model and measured fields at longer times. In practice, these relations are applied at or before the time of peak return stroke current. A typical value of a peak field derivative for CG return strokes is ≈40 V/m/μs.

9.7 Lightning Test Standards

In section 9.7, lightning current standards that have been adopted for the design and verification of lightning protection for aerospace vehicles are reviewed. The aerospace industry has generally kept better pace with advancements in our understanding of lightning processes and changes in vehicle design. Reviews of lightning test standards used in the aerospace industry have been given by reference 9-94. A discussion of lightning protection techniques is beyond the scope of this document. A comprehensive treatment of lightning protection of aircraft may be found in reference 9-95.

9.7.1 Historical Perspective

The first airplane lightning protection test standards were published in the mid-1950s by the Federal Aviation Administration (FAA) (ref. 9-96) and the U.S. DoD (ref. 9-97). MIL-B-5087 dealt exclusively with the electrical bonding of aircraft components. Bonding refers to a low-resistance electrical connection between components that is sufficient to withstand lightning currents. At the time, it was generally believed that the damaging effects of lightning were limited to the exterior of the aircraft or structures directly exposed to a lightning strike. (See ref. 9-98 for a review of the direct effects of lightning.) It was felt that sufficient protection would be provided if these components were adequately bonded to the main airframe. The FAA circular dealt exclusively with the protection of aircraft fuel systems.

Two spectacular incidents in the 1960s indicated clearly that other lightning-related effects could lead to catastrophic accidents. On December 8, 1963, a lightning strike ignited fuel in the reserve tank of a Boeing 707 commercial airliner. The left wing of the aircraft was destroyed and 81 people on board were killed. In 1969, Apollo 12 was launched into clouds that had not been producing lightning. The Saturn V rocket artificially triggered two discharges. The lightning strikes produced major system upsets, but only minor permanent damage, and the vehicle and crew survived and were able to complete their mission (ref. 9-1). These and other accidents motivated the FAA and the DoD to request that the Society of Automotive Engineers (SAE) committee on electromagnetic compatibility (SAE-AE4) formulate improved lightning protection design and test standards. The report issued by that group (ref. 9-99) quickly became the standard for the U.S. civil aviation industry. A revision of that report followed in 1978 (ref. 9-100). The 1978 report, given a blue cover, became known as the “blue book” and was adopted for both civil and military aircraft and by foreign certification agencies. The 1978 report was superseded by the SAE Aerospace Recommended Practices (ARP) 5412 report in 1999 (ref. 9-5). The SAE-defined lightning environment was formally incorporated into military protection specifications in MIL-STD-1757 (ref. 9-101), and a revised MIL-STD-1757A (ref. 9-102), and by the FAA in Advisory Circular 20-53A (ref. 9-103). MIL-STD-1757A was cancelled in 1996 and MIL-STD-464 (ref. 9-7) now addresses electromagnetic environmental effects.

A panel was convened in the early 1970s to formulate lightning protection standards for the NASA Space Shuttle program. The result of that activity was the publication of the “Shuttle Lightning Protection Criteria Document,” NSTS-07636 (ref. 9-4). The lightning environment defined in that document predated and differed somewhat from that in the SAE 1978 report, but the key aspects of the current test waveforms were nearly the same.

Several more recent trends in the design of aerospace vehicles have resulted in an increased vulnerability to the indirect effects of lightning. These developments include the use of nonmetallic, lightweight, composite materials in the skin and structure of the vehicle that do not shield the interior of the aircraft as efficiently as

a metal body, and an increased reliance on digital flight control electronics as opposed to analog and mechanical systems. In these cases, the lightning damage occurs not as a direct result of the lightning currents, but from spurious signals that are induced or coupled into the interior of the vehicle where they may damage or upset electronic processing equipment (ref. 9-104). A recent example of the hazards associated with indirect lightning effects is provided by the Atlas/Centaur accident that occurred in March 1987 (ref. 9-3). Investigation of that incident determined that the vehicle was struck by a triggered CG flash. The lightning current caused a transient signal to be coupled into the Centaur's digital computer unit where data in a single memory location were changed. The computer subsequently issued an erroneous yaw command that resulted in large dynamic stresses being placed on the vehicle, causing the vehicle to break up.

Indirect lightning hazards have required additional changes in the philosophy of protection design. Also, in an effort to better evaluate the lightning hazards, new research programs were undertaken in the 1980s by NASA, the USAF, the FAA, and the French Government. Experimental results from these studies have been incorporated into the most recent aerospace vehicle lightning standards (refs. 9-4 and 9-5).

9.7.2 Severe Direct Lightning Strike Current Test Waveforms

Five current component waveforms that would represent a severe lightning strike event are specified in the SAE 1999 report (ref. 9-5), which is the industry standard for transport aircraft. The SAE 1987 test specifications, which are identical to the SAE 1999 test specifications, have been incorporated into the most recent (1994) revision of the "Shuttle Lightning Protection Criteria Document" (ref. 9-4). The SAE 1987 current waveforms are illustrated in figure 9-24 (current component H not shown) and consist of the following:

- Component A

This waveform represents the first return stroke with a peak current of 200 kA, and is defined mathematically by:

$$I(t) = I_o \left(e^{-at} - e^{-bt} \right)^{*} \quad , \tag{9.8}$$

where I_O is 218,810 A, $a = 11{,}354\ s^{-1}$, $b = 647{,}265\ s^{-1}$, and t is time in seconds. This waveform component has a very large peak current, peak current derivative, and action integral.

- Component B

This component represents an intermediate current following the first return stroke. Component B has an average amplitude of 2 kA and transfers 10 C of charge. This component is described by a double exponential of the form shown in equation (9.8) with $I_O = 11{,}300$ A, $a = 700\ s^{-1}$, and $b = 2{,}000\ s^{-1}$.

- Component C

This waveform represents a continuing current. Component C is a square waveform with a current amplitude between 200 and 800 A and a duration of between 1 and 0.25 s chosen to give a total charge transfer of 200 C. The primary purpose of this waveform is charge transfer.

---

*Note: Current pulses cannot truly be described by a double exponential (e) form, as it actually represents a quasi-exponential form ($\in$). However, e can be used.

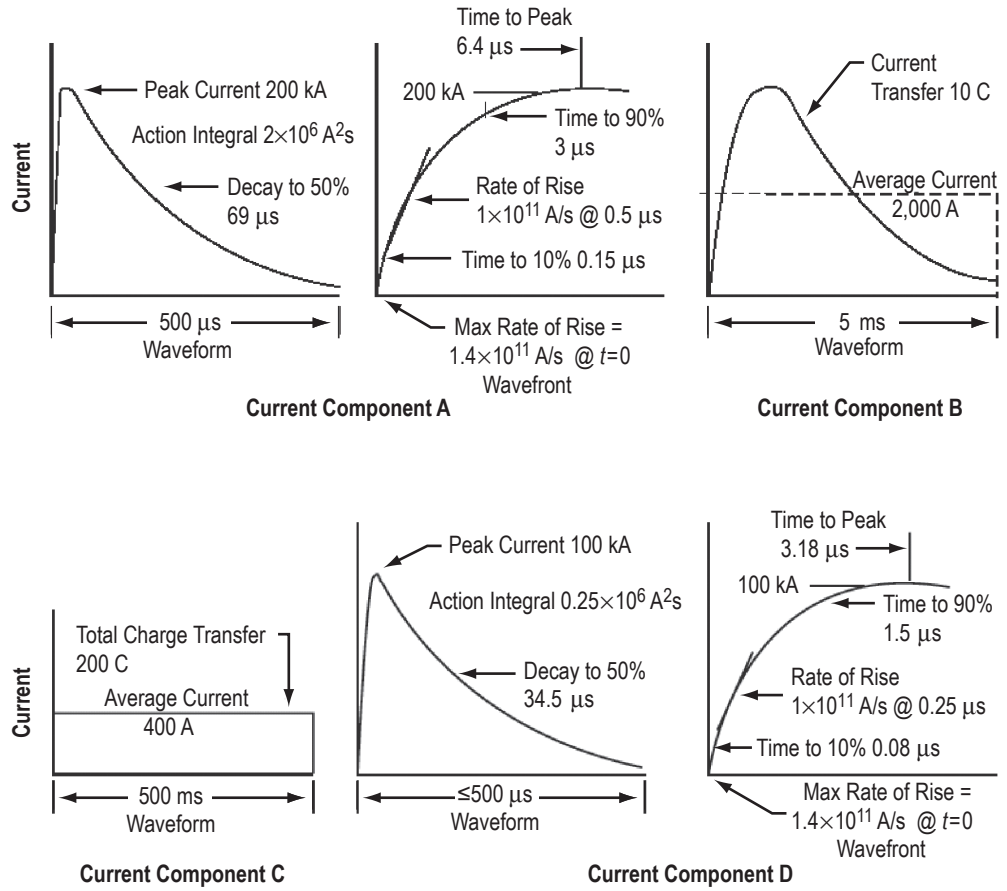

Figure 9-24. SAE 1987 current test waveforms for severe direct lightning strikes to aircraft (ref. 9-100).

• Component D

Component D represents a subsequent stroke with a peak current of 100 kA. This component is described by a double exponential of the form shown in equation (9.8) with $I_O = 109{,}405$ A, $a = 22{,}708$ s^{-1}, and $b = 1{,}294{,}530$ s^{-1}.

• Component H

Component H is a short-duration, high rate of rise current pulse with a peak current amplitude of 10 kA. This test waveform incorporates important characteristics of lightning discharges recorded during triggered strikes to instrumented aircraft in flight. This waveform is also defined by a double exponential with $I_O = 10{,}572$ A, $a = 187{,}191$ s^{-1}, and $b = 19{,}105{,}100$ s^{-1}. Component H has a peak current derivative of 2×10^{11} A/s.

Figure 9-25 depicts and lists the key aspects of a lightning environment composed of external idealized current components A, B, C, and D. The test values, a peak current of 200 kA, a charge transfer of 200 C, and an action integral of 2×10^6 A^2 s, occur at the 1-percent level or less in negative ground discharges. However, ≈10 percent of positive ground discharges, while generally more infrequent, would be expected to exceed these test values. The peak current derivative test value, 1.4×10^{11} kA/μs, probably does not represent a severe-level test. Referring back to table 9-16, note that 10 percent of the return strokes triggered in Florida during 1987 and 1988 had current derivatives that exceeded 215 kA/μs. A maximum peak *di*/*dt* value of 411 kA/μs has been

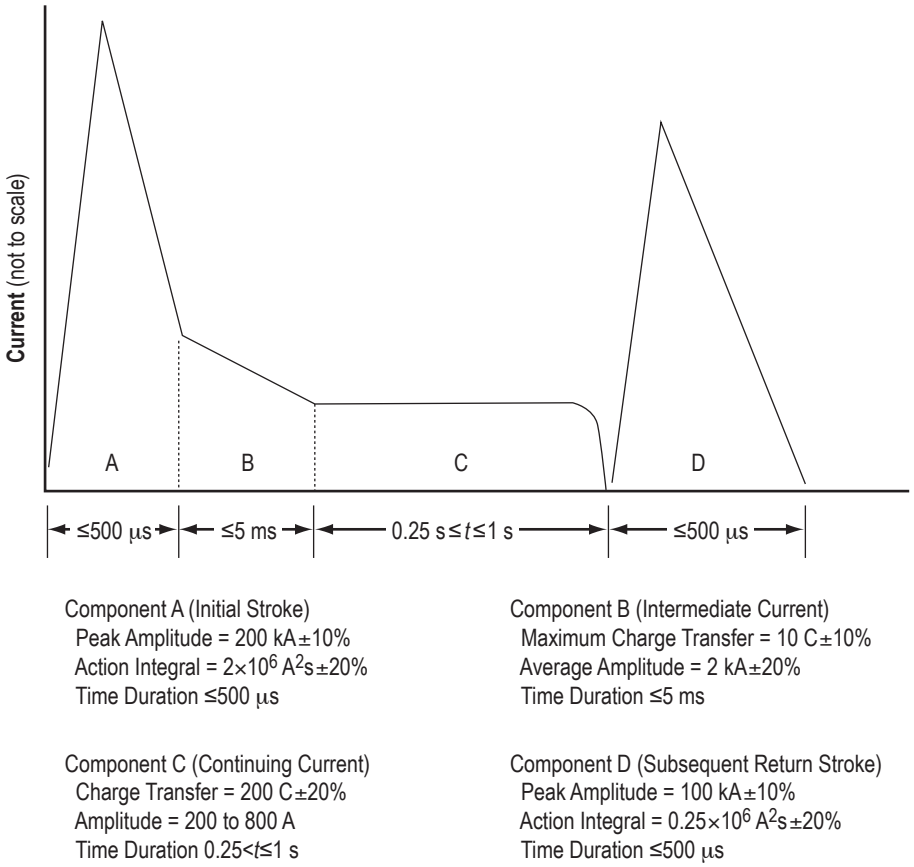

Figure 9-25. Lightning current waveform composed of components A, B, C, and D (ref. 9-100).

measured in Florida, for a stroke with a peak current of ≈60 kA. A *di*/*dt* value of 380 kA/μs was recorded during measurements conducted with the NASA F-106 aircraft.

A typical negative ground flash consists of a first return stroke followed by several subsequent strokes. For protection against direct effects, it is adequate to consider only one return stroke (component A or D). For a proper evaluation of indirect effects, such as coupling into the interior of aerospace vehicles, it is necessary to consider the multiple stroke nature of an actual flash. For this purpose, a multiple stroke consisting of a component D current pulse followed by 13 randomly spaced subsequent strokes of 50-kA peak amplitude (component D divided by 2), all occurring within 1.5 s, has been defined. The multistroke test waveform is illustrated in figure 9-26.

Rapid sequences of pulses with low-peak current amplitude, but large current derivative values, were observed during the lightning strike measurements made with instrumented aircraft. While a single-current pulse, like component H, is not likely to cause physical damage, a burst of randomly distributed pulses may cause interference or upset some systems. A test standard consisting of component H current pulses occurring repetitively, in a 2-s period in 20 randomly spaced groups of 20 pulses each has been defined. This multiple burst (MB) and multiple stroke (MS) waveform is illustrated in figure 9-27.

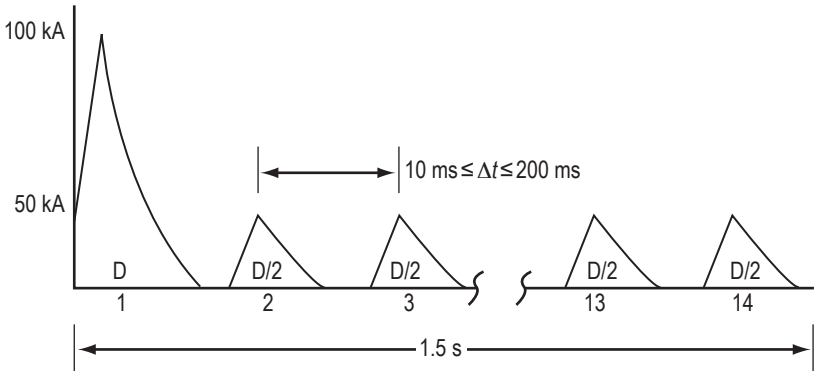

Figure 9-26. Multiple stroke lightning current test waveform consisting of one current component D followed by 13 current components D/2's distributed over a period of up to 1.5 s (ref. 9-100).

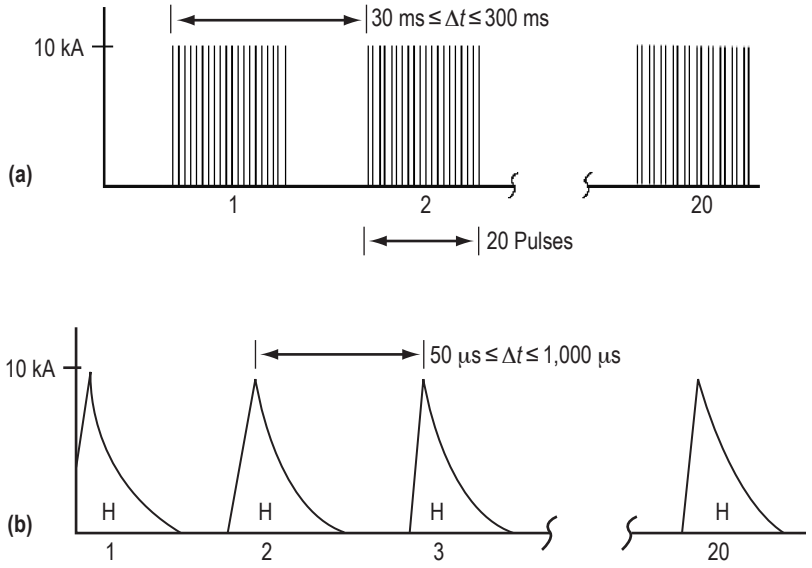

Figure 9-27. Multiple burst (a) and multiple stroke (b) waveform set with one burst being composed of 20 pulses (ref. 9-100).

The idealized waveforms described above are appropriate for design analyses. The cost of constructing a simulator capable of delivering these test waveforms to actual vehicles may be prohibitive. In that case, actual testing may involve the use of different waveforms. It must be possible, however, to extrapolate or scale the test results made with the alternate waveforms to the severe hazard level described above.

9.8 Natural and Triggered Lightning Launch Commit Criteria

Presented below are the rules for the natural and triggered lightning LCC discussed in section 9.5.2 (taken from ref. 9-33).

9.8.1 Launch Commit Criteria Introduction

A committee known as the NASA/USAF Lightning Advisory Panel (LAP) was formed to recommend changes to the USAF and NASA lightning LLC for manned and unmanned space launches. The LAP also provides an independent scientific assessment of and advice on lightning-related issues to the KSC Weather Office, the 45th Weather Squadron, and the 30th Weather Squadron.

The objective of the lightning LLC is to minimize the hazards to integrated launch vehicles after launch from vehicle-triggered lightning, natural lightning, and electrification resulting from interactions with the environment during the ascent phase of the mission. The primary protection method is to hold (delay) the launch while a hazardous condition exists. The best way to ensure safety from atmospheric electrical hazards, and also to improve launch availability, is to use the electric field environment and its time development along and near the flight path.

The lightning LLC constraints given in this section (taken from ref. 9-105) supercedes the lightning LCC recommendations made by the LAP in May 1998 and published as "Natural and Triggered Lightning Launch Commit Criteria (LCC)," The Aerospace Corporation, Aerospace Report No. TR-99 (1413)-1, January 15, 1999 (ref. 9-33). References 9-106 and 9-107 provide more background information relative to the new lightning LCC.

The user of this information should check with the KSC Weather Office, Air Force 45th Weather Squadron, or Air Force 30th Weather Squadron to ensure the most current LLC are being utilized.

9.8.2 Natural and Triggered Lightning Launch Commit Criteria

The Launch Weather Team (LWT) must have clear and convincing evidence that the following hazard avoidance criteria are not violated. Even when these criteria are not violated, if any other hazardous condition exists, the LWT will report the threat to the launch director. The launch director may HOLD at any time based on the instability of the weather.

Notice: Any changes to this section will require coordination with the 45th Space Wing Range Safety Office (RSO).

9.8.2.1 Lightning. Do not launch under the following conditions:

(1) Do not launch for 30 min after any type of lightning occurs in a thunderstorm if the flight path will carry the vehicle within 10 nmi of that thunderstorm.

(2) Do not launch for 30 min after any type of lightning occurs within 10 nmi of the flight path,

unless,

(a) The cloud that produced the lightning is not within 10 nmi of the flight path,

(b) There is at least one working field mill within 5 nmi of each such lightning flash,

and

(c) The absolute values of all electric field measurements at the surface within 5 nmi of the flight path and at the mill(s) specified in (b) above have been <1,000 V/m for 15 min.

Notes:

- Anvils are covered in section 9.8.2.3.
- If a cumulus cloud remains 30 min after the last lightning occurs in a thunderstorm, then criteria in section 9.8.2.2 apply.

Definitions: Anvil, electric field measurement at the surface, flight path, thunderstorm, within

9.8.2.2 Cumulus Clouds. Do not launch under the following conditions:

(1) Do not launch if the flight path will carry the vehicle within 10 nmi of any cumulus cloud with its cloud top higher than the –20 ºC level,

(2) Do not launch if the flight path will carry the vehicle within 5 nmi of any cumulus cloud with its cloud top higher than the –10 ºC level,

(3) Do not launch if the flight path will carry the vehicle through any cumulus cloud with its cloud top higher than the –5 ºC level,

(4) Do not launch if the flight path will carry the vehicle through any cumulus cloud with its cloud top between the 5 ºC and –5 ºC levels,

unless,

(a) The cloud is not producing precipitation,

(b) The horizontal distance from the center of the cloud top to at least one working field mill is <2 nmi,

and

(c) All electric field measurements at the surface within 5 nmi of the flight path and at the mill(s) specified in (b) above have been between –100 and 500 V/m for 15 min.

Note: Cumulus clouds in criterion 9.8.2.2 do not include altocumulus, cirrocumulus, or stratocumulus.

Definitions: Cloud top, electric field measurement at the surface, flight path, precipitation, within

9.8.2.3 Anvil Clouds

9.8.2.3.1 Attached Anvils. Do not launch under the following conditions:

(1) Do not launch if the flight path will carry the vehicle through or within 10 nmi of a nontransparent part of any attached anvil cloud for the first 30 min after the last lightning discharge in or from the parent cloud or anvil cloud.

(2) Do not launch if the flight path will carry the vehicle through or within 5 nmi of a nontransparent part of any attached anvil cloud between 30 min and 3 hr after the last lightning discharge in or from the parent cloud or anvil cloud unless both of the following conditions are satisfied:

(a) The portion of the attached anvil cloud within 5 nmi of the flight path is located entirely at altitudes where the temperature is colder than 0 ºC

and

(b) The volume-averaged, height-integrated radar reflectivity (VAHIRR) is less than +33 range corrected reflectivity (dBZ) – thousand feet (kft) (+10 dBZ km) everywhere along the portion of the flight path where any part of the attached anvil cloud is within the specified volume.

(3) Do not launch if the flight path will carry the vehicle through a nontransparent part of any attached anvil cloud more than 3 hr after the last lightning discharge in or from the parent cloud or anvil cloud unless both of the following conditions are satisfied:

(a) The portion of the attached anvil cloud within 5 nmi of the flight path is located entirely at altitudes where the temperature is colder than 0 ºC

and

(b) The VAHIRR is less than +33 dBZ-kft (+10 dBZ-kkm) everywhere along the portion of the flight path where any part of the attached anvil cloud is within the specified volume.

9.8.2.3.2 Detached Anvil Clouds. For the purposes of this section, detached anvil clouds are never considered debris clouds. Do not launch under the following conditions:

(1) Do not launch if the flight path will carry the vehicle through or within 10 nmi of a nontransparent part of a detached anvil cloud for the first 30 min after the last lightning discharge in or from the parent cloud or anvil cloud before detachment or after the last lightning discharge in or from the detached anvil cloud after detachment.

(2) Do not launch if the flight path will carry the vehicle between 0 (zero) and 5 nmi from a nontransparent part of a detached anvil cloud between 30 min and 3 hr after the time of the last lightning discharge in or from the parent cloud or anvil cloud before detachment or after the last lightning discharge in or from the detached anvil cloud after detachment unless subparagraph 1.4.C.2.b.1 or subparagraph 1.4.C.2.b.2 is satisfied:

(a) This section is satisfied if all three of the following conditions are met:

(1) There is at least one working field mill within 5 nmi of the detached anvil cloud,

(2) The absolute values of all electric field measurements at the surface within 5 nmi of the flight path and at the mill(s) specified in subparagraph 1.4.C.2.b.1) have been <1,000 V/m for 15 min,

and

(3) The maximum radar return from any part of the detached anvil cloud within 5 nmi of the flight path has been <10 dBZ for 15 min.

(b) This section is satisfied if both of the following conditions are met:

(1) The portion of the detached anvil cloud within 5 nmi of the flight path is located entirely at altitudes where the temperature is colder than 0 ºC.

(2) The VAHIRR is less than +33 dBZ-kft (+10 dBZ-km) everywhere along the portion of the flight path where any part of the detached anvil cloud is within the specified volume,

and

(3) Do not launch if the flight path will carry the vehicle through a nontransparent part of a detached anvil cloud unless subparagraph 1.4.C.2.c.1) or subparagraph a.4.C.2.c.2) is satisfied.

(a) This section is satisfied if both of the following conditions are met:

(1) At least 4 hr have passed since the last lightning discharge in or from the detached anvil cloud

and

(2) At least 3 hr have passed since the time that the anvil cloud is observed to be detached from the parent cloud.

(b) This section is satisfied if both of the following conditions are met:

(1) The portion of the detached anvil cloud within 5 nmi of the flight path is located entirely at altitudes where the temperature is colder than 0 ºC

and

(b) The VAHIRR is less than +33 dBZ-kft (+10 dBZ-km) everywhere along the portion of the flight path where any part of the detached anvil cloud is within the specified volume.

Note: Detached anvil clouds are never considered debris clouds, nor are they covered by criteria in section 9.8.2.4

Definitions: Anvil; cloud base; cloud edge; cloud top; debris cloud; electric field measurements at the surface; field mill; flight path; volume-averaged, height-integrated radar reflectivity (VAHIRR); nontransparent; specified volume; transparent; within

9.8.2.4 Debris Clouds. Do not launch under the following conditions:

(1) Do not launch if the flight path will carry the vehicle through any nontransparent parts of a debris cloud during the 3-hr period defined below,

(2) Do not launch if the flight path will carry the vehicle within 5 nmi of any nontransparent parts of a debris cloud during the 3-hr period defined below,

unless,

(a) There is at least one working field mill within 5 nmi of the debris cloud,

(b) The absolute values of all electric field measurements at the surface within 5 nmi of the flight path and at the mill(s) specified in 9.8.2.4(2)(a) have been <1,000 V/m for 15 min,

and

(c) The maximum radar return from any part of the debris cloud within 5 nmi of the flight path has been <10 dBZ for 15 min.

The 3-hr period in 9.8.2.4 (1) and (2) above begins at the time when the debris cloud is observed to have detached from the parent cloud or when the debris cloud is observed to have formed from the decay of the parent cloud top below the altitude of the –10 ºC level. The 3-hr period begins anew at the time of any lightning discharge that occurs in the debris cloud.

Definitions: Cloud top, debris cloud, electric field measurement at the surface, flight path, nontransparent, within

9.8.2.5 Disturbed Weather. Do not launch under the following conditions:

(1) Do not launch if the flight path will carry the vehicle through any nontransparent clouds that are associated with a weather disturbance having clouds that extend to altitudes at or above the 0 ºC level and contain moderate or greater precipitation or a radar bright band or other evidence of melting precipitation within 5 nmi of the flight path.

Definitions: Associated, flight path, moderate precipitation, nontransparent, weather disturbance, within

9.8.2.6 Thick Cloud Layers. Do not launch under the following conditions:

Do not launch if the flight path will carry the vehicle through nontransparent parts of a cloud layer that is:

(1) Greater than 4,500 ft thick and any part of the cloud layer along the flight path is located between the 0 ºC and the –20 ºC levels

or

(2) Connected to a cloud layer that, within 5 nmi of the flight path, is >4,500 ft thick and has any part located between the 0 ºC and the –20 ºC levels,

unless

(a) The cloud layer is a cirriform cloud that has never been associated with convective clouds, is located entirely at temperatures of –15 ºC or colder, and shows no evidence of containing liquid water; e.g., aircraft icing.

Definitions: Associated, cloud layer, flight path, nontransparent

9.8.2.7 Smoke Plumes. Do not launch under the following conditions:

(1) Do not launch if the flight path will carry the vehicle through any cumulus cloud that has developed from a smoke plume while the cloud is attached to the smoke plume, or for the first 60 min after the cumulus cloud is observed to have detached from the smoke plume.

Note: Cumulus clouds that have formed above a fire but have been detached from the smoke plume for more than 60 min are considered cumulus clouds and are covered in criterion 9.8.2.2.

Definitions: Flight path

9.8.2.8 Surface Electric Fields. Do not launch under the following conditions:

(1) Do not launch for 15 min after the absolute value of any electric field measurement at the surface within 5 nmi of the flight path has been >1,500 V/m,

(2) Do not launch for 15 min after the absolute value of any electric field measurement at the surface within 5 nmi of the flight path has been >1,000 V/m,

unless,

(a) All clouds within 10 nmi of the flight path are transparent

or

(b) All nontransparent clouds within 10 nmi of the flight path have cloud tops below the 5 ºC level and have not been part of convective clouds with cloud tops above the –10 ºC level within the last 3 hr.

Notes: Electric field measurements at the surface are used to increase safety by detecting electric fields due to unforeseen or unrecognized hazards. For confirmed failure of one or more field mill sensors, the countdown and launch may continue.

Definitions: Cloud top, electric field measurement at the surface, flight path, nontransparent, transparent, within

9.8.2.8.1 Electric Fields Aloft. Criteria in 9.8.2.3 through 9.8.2.7, and 9.8.2.8(2) need not be applied if, during the 15 min prior to launch time, the instantaneous electric field aloft, throughout the volume of air expected to be along the flight path, does not exceed E_c, where E_c is shown as a function of altitude in figure 9-28.

Note: The thresholds on electric field measurements at the surface in criterion 9.8.2.8 and elsewhere in these LCC are lower than 5 kV/m to allow for the effect of the surface screening layer.

Definitions: Flight path, electric field measurement aloft

9.8.2.8.2 Triboelectrification (the production of electrostatic charges by friction). Do not launch under the following conditions:

Do not launch if a vehicle has not been treated for surface electrification and the flight path will go through any clouds above the –10 ºC level up to the altitude at which the vehicle's velocity exceeds 3,000 ft/s.

Note: A vehicle is considered "treated" for surface electrification if:

(a) All surfaces of the vehicle susceptible to ice particle impact have been treated to assure:

(1) That the surface resistivity is $<10^9$ ohms/square

and

(2) That all conductors on surfaces, including dielectric surfaces that have been treated with conductive coatings, are bonded to the vehicle by a resistance that is $<10^5$ Ω,

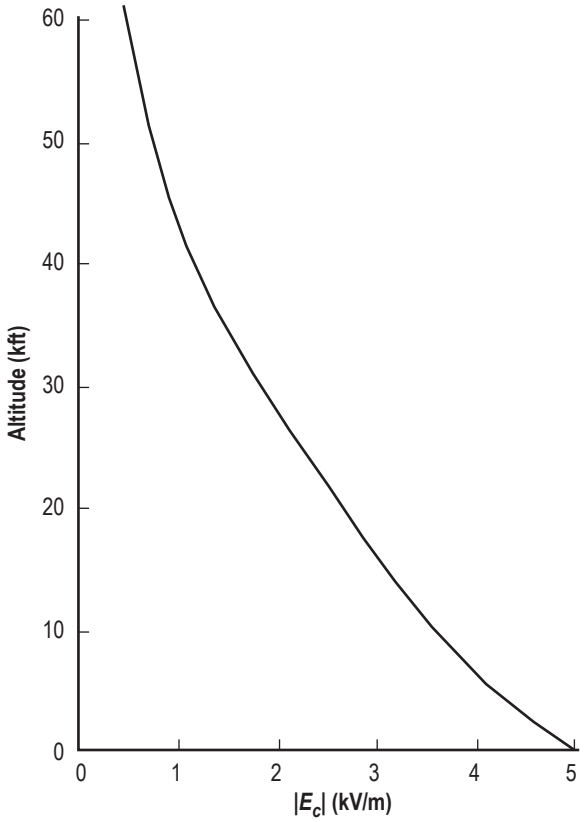

Figure 9-28. Instantaneous critical field (E_c) versus altitude.

or

(b) It has been shown by test or analysis that electrostatic discharges (ESD) on the surface of the vehicle caused by triboelectrification by ice particle impact will not be hazardous to the launch vehicle or the mission.

Definitions: Flight path

See section 9.8.2.9 for definitions.

9.8.2.9 Definitions

Anvil: Stratiform or fibrous cloud produced by the upper level outflow or blow-off from thunderstorms or convective clouds.

Associated: Used to denote that two or more clouds are causally related to the same weather disturbance or are physically connected. *Associated* is not synonymous with occurring at the same time. An example of clouds that are *not* associated is air mass clouds formed by surface heating in the absence of organized lifting. Also, a cumulus cloud formed locally and a physically separated cirrus layer generated by a distant source are not associated, even if they occur over or near the launch site at the same time.

Subsidiary definition: Weather disturbance

Bright band: An enhancement of radar reflectivity caused by frozen hydrometeors falling through the 0 ºC level and beginning to melt.

Cloud base: The visible cloud base is preferred. If this is not possible, then the (0) zero dBZ radar-reflectivity cloud base is acceptable.

Cloud edge: The visible cloud edge is preferred. If this is not possible, then the (0) zero dBZ radar reflectivity cloud edge is acceptable.

Cloud layer: A vertically continuous array of clouds, not necessarily of the same type, whose bases are approximately at the same level.

Cloud top: The visible cloud top is preferred. If this is not possible, then the (0) zero dBZ radar reflectivity cloud top is acceptable.

Cumulonimbus cloud: Any convective cloud with any part above the –20 ºC temperature level.

Debris cloud: Any cloud, except an anvil cloud, that has become detached from a parent cumulonimbus cloud or thunderstorm, or that results from the decay of a parent cumulonimbus cloud or thunderstorm.

Subsidiary definition: Cumulonimbus cloud

Electric field measurement at the surface: The 1-min arithmetic average of the vertical electric field (Ez) at the ground measured by a ground-based field mill. The polarity of the electric field is the same as that of the potential gradient; i.e., the polarity of the field at the ground is the same as the dominant charge overhead.

Note: Electric field contours shall not be used for the electric field measurement at the surface.

Field mill: A specific class of electric field sensors that uses a moving, grounded conductor to induce a time-varying electric charge on one or more sensing elements in proportion to the ambient electrostatic field.

Flight path: The planned flight path including its uncertainties (“error bounds”).

Moderate precipitation: A precipitation rate of 0.1 in/hr or a radar reflectivity factor of 30 dBZ.

Nontransparent: Sky cover through which forms are blurred, indistinct, or obscured is nontransparent.

Note: Nontransparency must be assessed for launch time. Sky cover through which forms are seen distinctly only through breaks in the cloud cover is considered nontransparent. Clouds with a radar reflectivity of 0 (zero) dBZ or greater are also considered nontransparent. Translucent or opaque.

Subsidiary definition: Transparent weather disturbance—A weather system where dynamical processes destabilize the air on a scale larger than the individual clouds or cells. Examples of disturbances are fronts, troughs, and squall lines.

Optically thin: Having a vertical optical thickness of unity or less at visible wavelengths.

Precipitation: Detectable rain, snow, sleet, etc., at the ground, or virga, or a radar reflectivity >18 dBZ.

Specific volume: Volume bounded in the horizontal by vertical, plane, perpendicular sides located 5.5 km (3 nmi) north, east, south, and west of the point on the flight track, on the bottom by the 0 ºC level, and on the top by the upper extent of all clouds.

Transparent: Synonymous with optically thin. Sky cover is transparent if higher clouds, blue sky, stars, the disk of the Sun, etc., can be distinctly seen from below, or if the Sun casts distinct shadows of objects on the ground, or if terrain, buildings, lights on the ground, etc., can be distinctly seen from above.

Note: Visible transparency is required. Transparency must be assessed for launch time. Sky cover through which forms are seen distinctly *only* through breaks in the cloud cover is considered nontransparent.

Subsidiary definitions: Nontransparent

Thunderstorm: Any convective cloud that produces lightning.

Volume-Averaged, Height-Integrated Radar Reflectivity (VAHIRR): Product of the volume-averaged radar reflectivity (VARR) and the average cloud thickness within a specified volume relative to a point along the flight track (units of dBZ-km)

where

the VARR is the arithmetic average (in dBZ) of the cloud radar reflectivity within the specified volume. Normally, a radar processor will report reflectivity values interpolated onto a regular, three-dimensional array of grid points. Any such grid point within the specified volume is included in the average if and only if it has a radar reflectivity ≥0 dBZ

and where

the average cloud thickness is the altitude difference (in kilometers) between the average top and the average base of all clouds within the specified volume. The cloud base to be averaged is the higher of (1) the 0 ºC level and (2) the lowest extent (in altitude) of tall cloud radar reflectivities 0 dBZ or greater. Similarly, the cloud top to be averaged is the highest extent (in altitude) of all cloud radar reflectivities 0 dBZ or greater. Given the grid-point representation of a typical radar processor, allowance must be made for the vertical separation of grid points in computing cloud thickness: The cloud base at any horizontal position shall be taken as the altitude of the corresponding base grid point minus half of the grid-point vertical separation. Similarly, the cloud top at that horizontal position shall be taken as the altitude of the corresponding top grid point plus half of this vertical separation. Thus, a cloud represented by only a single grid point having a radar reflectivity equal to or greater than 0 dBZ within the specified volume would have an average cloud thickness equal to the vertical grid-point separation in its vicinity.

Note: The VAHIRR measurement must be made in the absence of significant attenuation by intervening storms or by water or ice on the radome itself. The VAHIRR measurement is invalid at any point on the flight track that is within 20 km of any radar reflectivity of 35 dBZ or greater at altitudes of 4 km above mean sea level or greater, and at any point that is within 20 km of any type of lightning that has occurred in the previous 5 min. The specified volume must not contain any portion of the cone of silence above the radar, nor any portion of any sectors that may have been blocked out for payload-safety reasons. The individual grid point reflectivities used to determine either the VARR or the average cloud thickness must be meteorological reflectivities.

Subsidiary definition: Specified volume

Note: See section 9.2.8.3, "Interim Instructions for Implementation of VAHIRR."

Weather disturbance: A weather system where dynamical processes destabilize the air on a scale larger than the individual clouds or cells. Examples of disturbances are fronts, troughs, and squall lines.

Within: Used as a function word to specify a margin in all directions—horizontal, vertical, and slant separation—between the cloud edge or top and the flight path. For example, "*within* 10 nmi of a thunderstorm cloud" means that there must be a 10-nmi margin between every part of a thunderstorm cloud and the flight path.

Subsidiary definitions: Cloud edge, cloud top, flight path

9.8.2.10 Interim Instructions for Implementation of VAHIRR. The VAHIRR quantity referred to in section 1.4.C. and the definitions require computation of both a volume average reflectivity and an average cloud thickness. These quantities are then multiplied to produce the VAHIRR. Neither of these quantities is available yet as a product on the WSR-88D and WSR-74C radar systems used to support launch operations. This instruction provides a methodology for evaluating VAHIRR criteria with currently available radar products. The methodology provides a result that is more conservative than a direct VAHIRR computation, but it should still permit the launch users to achieve much of the benefit of the VAHIRR feature.

9.8.2.10.1 Part I, Determination of Average Cloud Thickness. The definition of VAHIRR requires determination of the average cloud top and the average cloud base above the height of the 0 ºC isotherm within a square having sides 5.5 km (3 nmi) north, east, south, and west of the ground projection of each point in the flight track. Average cloud thickness is defined as the difference of these two numbers. If the average cloud thickness cannot be determined at each point on the flight track, the maximum thickness within 5.5 km (3 nmi) of the flight track may be used.

To determine the average cloud top height, the launch weather team may use any existing radar product that gives the height of the 0 dBZ cloud top, including "maximum height of reflectivity" and cross section products. If the average height cannot be determined, the maximum height of the 0 dBZ reflectivity may be used. If the maximum height cannot be determined, use 18 km (60 kft) for the average cloud top.

The average height of the cloud base should be derived from radar data. It is the average of the higher of (a) the bottom of the portion of the cloud producing a radar reflectivity of 0 dBZ or greater or (b) the height of the 0 ºC isotherm where the 0 dBZ reflectivity extends below that level. If the average height of the cloud base cannot be determined, use the higher of (a) the height of the 0 ºC isotherm or (b) the lowest portion of the cloud producing a radar reflectivity of 0 dBZ or greater anywhere within each 5.5 km (3 nmi) square defined above.

9.8.2.10.2 Part II, Volume Averaged Radar Reflectivity. There is no operationally feasible way to use existing radar products to compute a volume average reflectivity. A conservative substitute is the maximum reflectivity since the volume average will always be smaller than the maximum. The WSR-88D has a "User Selectable Layer Composite Reflectivity (URL)" product and the WSR-74C has a "Max" product with user selectable base and top. The LWT should configure these products with the bottom of the layer at the height of the 0 ºC isotherm and the top above the height of the highest radar beam within 7.8 km (4.2 nmi) of the ground-protected flight track in the scan strategy being used. The WSR-88D product will have to be configured at the radar product generator (RPG) and included in the product scheduler for the principal user processor (PUP) used by the LWT.

9.8.2.10.3 Part III, Evaluating the Constraint. The VAHIRR constraint is satisfied for a point on the flight track if the "URL" or "Max" radar product (see part II above) everywhere within the corresponding square (defined above) is <10 dBZ-km divided by the average cloud thickness in km within the same square (see part I above). (In English units, this threshold would become 33 dBZ-kft divided by the average cloud thickness in kft.) This constraint must be satisfied for every point on the flight track.

REFERENCES

9-1. "Analysis of Apollo 12 Lightning Incident," Document No. MSC-01540, prepared jointly by Marshall Space Flight Center, Kennedy Space Center, and Manned Spacecraft Center (now Johnson Space Center), National Aeronautics and Space Administration, <http://ntrs.nasa.gov/archive/nasa/casi.ntrs.nasa.gov/19720066106_1972066106.pdf>, February 1970.

9-2. Brook, M.; Holmes, C.R.; and Moore, C.B.: "Lightning and Rockets—Some Implications of the Apollo 12 Lightning Event," *Naval Research Reviews*, Vol. 23, No. 4, pp. 1–17, April 1970.

9-3. Christian, H.J.; Mazur, V.; Fisher, B.D.; et al.: "The Atlas/Centaur Lightning Strike Incident," *J. Geophys. Res.*, Vol. 94, pp. 13,169–13,177, 1989.

9-4. National Aeronautics and Space Administration, "Lightning Protection Criteria Document," *NSTS-07636*, Rev. G., Johnson Space Center, Houston, TX, April 15, 1994.

9-5. Society of Automotive Engineers, Aerospace Recommended Practice 5412, "Aircraft Lightning Environment and Related Test Waveforms," November 1, 1999.

9-6. NASA Technical Standard, "Electrical Bonding for NASA Launch Vehicles, Spacecraft, Payloads, and Flight Equipment," *NASA-STD-4003*, September 8, 2003.

9-7. Department of Defense Interface Standard, "Electromagnetic Environmental Effects Requirements for Systems," *MIL-STD-464*, March 18, 1997.

9-8. The ESD Association, "Basics of Electrostatic Discharge Part One—An Introduction to ESD," ESD Association, <http://www.esda.org/esdbasics1.htm>, March 27, 2000.

9-9. Procockpit, Section 7-5-10, Precipitation static, <http://www.procockpit.com/aim751.htm>, 2006.

9-10. Carr, A.L.: "Probability of Lightning Conditions," 2WW/FM-88/003, 2d WW Forecaster Memo, May 1988.

9-11. Fisher B.D.; Taeuber, R.J.; and Crouch, K.E.: "Implications of a Recent Lightning Strike to a NASA Jet Trainer," *AIAA-88-0394*, AIAA 26th Aerospace Sciences Meeting, Reno, NV, January 11–14, 1988.

9-12. MIL-HDBK-237C, Department of Defense Handbook, Electromagnetic Environmental Effects and Spectrum Certification Guidance for the Acquisition Process, July 17, 2001.

9-13. Pennsylvania State University, "Global Electric Circuit," College of Earth and Mineral Sciences, Atmospheric Physics II: Physics and Chemistry of the Clouds, Meteo 437, Fall 2004.

9-14. MacGorman, D.R.; and Rust, W.D.: *The Electrical Nature of Storms*, Oxford University Press, New York, NY, 1998.

9-15. Beard, K.V.K.; and Ochs, H.T.: "Charging Mechanisms in Clouds and Thunderstorms," in *The Earth's Electrical Environment*, E.P. Krider and R.G. Roble (eds.), National Academy Press, Washington, DC, pp. 114–130, 1986.

9-16. Lhermitte, R.; and Williams, E.: "Cloud Electrification," *Rev. Geophys. Space Phys.*, Vol. 21, pp. 984–992, 1983.

9-17. Stolzenburg, M.; Rust, W.D.; and Marshall, T.C.: "Electrical Structure in Thunderstorm Convective Regions, 3, Synthesis," *J. Geophys. Res.*, Vol. 103, pp. 14,097–14,108, 1998.

9-18. Koshak, W.J.; and Krider, E.P.: "Analysis of Lightning Field Changes During Active Florida Thunderstorms," *J. Geophys. Res.*, Vol. 94, pp. 1165–1186, 1989.

9-19. NOAA/NWS, Jetstream—An Online School for Weather, <http://www.srh.noaa.gov/jetstream/mesoscale/tstrm_intro.htm>, March 9, 2004.

9-20. National Lightning Safety Institute, "World Lightning Map," Section 6.2.1, <http://www.lightningsafety.com>, 2006.

9-21. Changnon, S.A., Jr.: "Secular Variations in Thunder-Day Frequencies in the Twentieth Century," *J. Geophys. Res.*, Vol. 90, pp. 6181–6194, 1985.

9-22. Robinson, P.J.; and Easterling, D.R.: "The Frequency Distribution of Thunderstorm Durations," *J. Appl. Meteor.*, Vol. 27, pp. 77–82, January 1988.

9-23. Easterling, D.R.; and Robinson, P.J.: "The Diurnal Variation of Thunderstorm Activity in the United States," *J. Climate Appl. Meteor.*, Vol. 24, pp. 1048–1058, October 1985.

9-24. Michaels, P.J.; Pielke, R.A.; Mcqueen, J.T.; and Sappington, D.E.: "Composite Climatology of Florida Summer Thunderstorms," *Mon. Wea. Rev.*, Vol. 115, No. 11, pp. 2781–2791, November 1987.

9-25. Kelly, D.L.; Schaefer, J.T.; and Doswell III, C.A.: "Climatology of Nontornadic Severe Thunderstorm Events in the United States," *Mon. Wea. Rev.*, Vol. 113, No. 11, pp. 1997–2014, November 1985.

9-26. NOAA, National Weather Service, "Lightning Safety: Lighting Science," <http://www.lightningsafety.noaa.gov/science.htm>, 2008.

9-27. Boccippio, D.J.; Cummins, K.L.; Christian, H.J.; and Goodman, S.J.: "Combined Satellite- and Surface-Based Estimation of the Intracloud-Cloud-to-Ground Lightning Ratio Over the Continental United States," *Mon. Wea. Rev.*, Vol. 129, pp. 108–122, 2001.

9-28. Berger, K.; Anderson, R.B.; and Kroninger, H.: "Parameters of Lightning Flashes," *Electra*, Vol. 80, No. 41, pp. 23–37, 1975.

9-29. Uman, M.A.: *The Lightning Discharge*, Vol. 39 in International Geophysics Series, Academic Press, Orlando, FL, 377 pp., 1987.

9-30. Rakov, V.A.: "A Review of Positive and Bipolar Lightning Discharges," *AMS BAMS*, pp. 767–776, June 2003.

9-31. The Aerospace Corporation: "Protecting Space Systems from Lightning," *Crosslink*, pp. 38–39, Summer 2001.

9-32. Roeder, W.P.; Sardonia, J.E.; Jacobs, S.C.; et al.: "Lightning Launch Commit Criteria at the Eastern Range/ Kennedy Space Center," *Paper 99-0890*, AIAA 37th Aerospace Sciences Meeting and Exhibit, Reno, NV, January 11–14, 1999.

9-33. The Aerospace Corporation: "Natural and Triggered Lightning Launch Commit Criteria (LCC)," Aerospace Report No. TR-99 (1413)-1, January 15, 1999.

9-34. Garner, T.; Lafosse, R.; Bellue, D.; and Priselac, E.: "Problems Associated With Identifying, Observing, and Forecasting Detached Thunderstorm Anvil for Space Shuttle Operations," AMS 7th Conference on Aviation, Range, and Aerospace Meteorology, Long Beach, CA, pp. 302–306, February 2–7, 1997.

9-35. Uman, M.: *The Lightning Discharge*, International Geophysics Series, Vol. 39, Academic Press, Inc., 1987.

9-36. Fisher, R.J.; Schnetzer, G.H.; Thottappillil, R.; et al.: "Parameters of Triggered-Lightning Flashes in Florida and Alabama," *J. Geophys. Res.*, Vol. 98, No. D12, pp. 22,887–22,902, December 20, 1993.

9-37. Mach, D.; and Rust, D.: "Photoelectric Return-Stroke Velocity and Peak Current Estimates in Natural and Triggered Lightning," *J. Geophys. Res.*, Vol. 94, No. D11, pp. 13,237–13,247, September 20, 1989.

9-38. Bankson, N.: "Lightning Current Rate of Rise in the New Lightning Flash Model for the Space Shuttle Program," 1991 International Aerospace & Ground Conference on Lightning and Static Electricity, Vol. 1, pp. 5-1 through 5-14, Cocoa Beach, FL, April 16–19, 1991.

9-39. Jafferis, W.: "Rocket Triggered Lightning—Kennedy Space Center and Beyond," 1995 International Aerospace and Ground Conference on Lightning and Static Electricity, pp. 57-1, September 26–28, 1995.

9-40. Depasse, P.: "Statistics on Artificially Triggered Lightning," *J. Geophys. Res.*, Vol. 99, No. D9, pp. 18,515–18,522, September 20, 1994.

9-41. Fisher, F.; Perala, R.A.; and Plumer, J.A.: "Lightning Protection of Aircraft," Chapter 2, Lightning Technologies, Inc., Pittsfield, MA, 1990.

9-42. Uman, M.; and Rakov, V.: "The Interaction of Lightning With Airborne Vehicles," *Progress in Aerospace Sciences*, Vol. 39, pp. 61–81, 2003.

9-43. Lyons, W.A.; Armstrong, R.A.; Williams, E.R.; and Bering, E.A.: "The Hundred Year Hunt for the Sprite," *Eos, Trans. Amer. Geophys. Union*, Vol. 81, pp. 373–377, 2000.

9-44. Franz, R.C.; Nemzek, R.J.; and Winckler, R.J.: "Television Image of a Large Upward Electrical Discharge Above a Thunderstorm System," *Science*, Vol. 249, pp. 48–51, 1990.

9-45. Boeck, W.L.; Vaughan, Jr., O.H.; Blakeslee, R.J.; et al.: "The Role of the Space Shuttle Videotapes in the Discovery of Sprites, Jets and Elves," *J. Atmos. Solar-Terr. Phys.*, Vol. 60, pp. 669–677, 1998.

9-46. Lyons, W.A.: "Low-Light Video Observations of Frequent Luminous Structures in the Stratosphere Above Thunderstorms," *Mon. Wea. Rev.*, Vol. 122, pp. 1940–1946, 1994.

9-47. Geology: "Sprites and Their Siblings," in About: Geology, <http://geology.about.com/od/sprites/a/sprites.htm>, 2007.

9-48. Lyons, W.A.; Uliasz, M.; and Nelson, T. E.: “Large Peak Current Cloud-to-Ground Lightning Flashes During the Summer Months in the Contiguous United States,” *Mon. Wea. Rev.*, Vol. 126, pp. 2217–2233, 1998.

9-49. Sentman, D.D.: “Overview of Transient Luminous Events,” Space Science Laboratory Seminar Series, University of California Berkeley, February 15, 2005.

9-50. Fukunishi, H.; Takahashi, Y.; Kubota, M.; and Sakanoi, K.: “Elves: Lightning-Induced Transient Luminous Events in the Lower Ionospher,” *Geophys. Res. Lett.*, Vol. 23, pp. 2157–2160, 1996.

9-51. “Sprites and Jets,” <http://www.spritesandjets.com/>, August 24, 2006.

9-52. Wescott, E.M.; Sentman, D.; Osborne, D.; et al.: “Preliminary Results From the Sprites94 Aircraft Campaign: 2. Blue Jets,” *Geophys. Res. Lett.*, Vol. 22, pp. 1209–1212, 1995.

9-53. Lyons, W.; Nelson, T.; and Fossum, J.: “Results From the Sprites ‘99 and Steps 2000 Field Programs,” Paper 5B.3, AMS 20th Conference on Severe Local Storms, Orlando, FL, September 11–16, 2000.

9-54. Yair, Y.; Price, C.; Ziv, B.; et al.: “Space Shuttle Observation of an Unusual Transient Atmospheric Emission,” *Geophys. Res. Lett.*, Vol. 32, L02801, doi:10.1029/2004GL021551, 2005.

9-55. Lyons, W.; Nelson, T.; Armstrong, R.; et al.: “Upward Electrical Discharges From Thunderstorm Tops,” *Bull. AMS*, Vol. 84, pp. 445–454, April 2003.

9-56. NASA News, “Clearest Video of Lightning-generated “Sprites” High Above Thunderstorms Captured,” Earth Observatory, Media Alerts Archive, February 15, 2006.

9-57. Sentman, D.D.; Wescott, E.M.; Osborne, D.L.; et al.: “Preliminary Results From the Sprites94 Aircraft Campaign: 1. Red Sprites,” *Geophys. Res. Lett.*, Vol. 22, pp. 1205–1208, 1995.

9-58. Boccippio, D.J.; Williams, E.R.; Heckman, S.J.; Lyons, et al.: “Sprites, ELF Transients, and Positive Ground Strokes,” *Science*, Vol. 269, pp. 1088–1091, 1995.

9-59. Williams, E.R.: “The Positive Charge Reservoir for Sprite-producing Lightning,” *J. Atmos. Sol. Terr. Phys.*, Vol. 60, pp. 689–692, 1998.

9-60. Huang, E.; Williams, E.; Boldi, R.; et al.: “Criteria for Sprites and Elves Based on Schumann Resonance Observations,” *J. Geophys. Res.*, Vol. 104, pp. 16,943–16,964, 1999.

9-61. Roussel-Dupré, R.; and Gurevich, A.V.: “On Runaway Breakdown and Upward Propagating Discharges,” *J. Geophys. Res.*, Vol. 101, pp. 2297–2311, 1996.

9-62. Fullekrug, M.; Reising, S.C.; and Lyons, W.A.: “On the Accuracy of Arrival Azimuth Determination of Sprite-associated Lightning Flashes by Earth-Ionosphere Cavity Resonances,” *Geophys. Res. Lett.*, Vol. 23, No. 25, pp. 3691–3694, December 15, 1996.

9-63. Inan, U.S.; Bell, T.F.: and Pasko, V.P.: “VLF Signatures of Ionospheric Disturbances Associated With Sprites,” *Geophys. Res. Lett.*, Vol. 22, No. 24, pp. 3461–3464, December 15, 1995.

9-64. Staff: Geography Institute, University of Alaska, "Red Sprites and Blue Jets," <http://elf.gi.alaska.edu/>, 1997.

9-65. Lyons, W.: "Sprites, Elves, and Blue Jets," *Weatherwise*, Vol. 50, pp. 19–23, August-September, 1997.

9-66. Marshall, L.: "Capturing Sprites and Elves From Afar," Penn. State and AGU Release, December 16, 1996.

9-67. Hsu, R.; Chen, A.; Lee, L.; et al., "Transient Luminous Events in the Vicinity of Taiwan," *J. Atmos. Solar-Terr. Phys.*, Vol. 65, pp. 561–566, 2003.

9-68. Wakefield, J.: "High Altitude Flashes Mystify Scientists," *EOS/AGU*, Vol. 75, No. 51, pp. 601–602, December 20, 1994.

9-69. Lyons, W.: "Final Report—Sensor System to Monitor Cloud-to-Stratosphere Electrical Discharges," Submitted to NASA/KSC under NASA SBIR Phase II, Contract NAS10-12113, April 25, 1996.

9-70. Santis, L.: "The Calculated Risk of Experiencing a Lightning Caused Unplanned Detonation," in *ISEE Proc. 14th Annual Symposium on Explosives and Blasting Research*, New Orleans, LA, pp. 107–119, February 8–11, 1998.

9-71. Harms, D.E.; Boyd, B.F.; and Lucci, R.M.: "Weather Systems Supporting Launch Operations at the Eastern Range," *Paper AIAA 98-0744*, 36th Aerospace Sciences Meeting and Exhibit, Reno, NV, January 12–15, 1998.

9-72. Ward, J.G.; Cummins, K.L.; and Krider, E.P.: "Comparison of the KSC-ER Cloud-to-Ground Lightning Surveillance System (CGLSS) and the U.S. National Lightning Detection Network™ (NLDN)," Poster Paper P.2.6, 13th AMS Conference on Aviation, Range, and Aerospace Meteorology, New Orleans, LA, January 2008.

9-73. Krider, E.P.; Noggle, R.C.; and Uman, M.A.: "A Gated Wideband Magnetic Direction Finder for Lightning Return Strokes," *J. Appl. Meteorol.*, Vol. 15, pp. 301–306, 1976.

9-74. Cummins, K.L.; Pyle, R.B.; and Fournier, G.: "An Integrated North American Lightning Detection Network," Proceedings 11th Conference on Atmospheric Electricity, pp. 218–221, Guntersville, AL, June 7–11, 1999.

9-75. Global Atmospherics, Inc., NLDN data provided by the NASA Lightning Imaging Sensor (LIS) Instrument Team and the LIS Data Center via the Global Hydrology Resource Center (GHRC) located at the Global Hydrology and Climate Center (GHCC), Huntsville, AL, through a license agreement with Global Atmospherics, Inc. (GAI). The data available from the GHRC are restricted to LIS science team collaborators and to NASA EOS and TRMM investigators.

9-76. Christian, H.: "Global Lightning Observation," Presented at the Space Science Seminar, University of California—Berkeley, February 15, 2005.

9-77. Reap, R.M.: "Analysis and Prediction of Lightning Strike Distributions Associated With Synoptic Map Types Over Florida," *Mon. Wea. Rev.*, Vol. 122, pp. 1698–1715, 1994.

9-78. Mach, D.: “Shuttle Lightning Threat Analysis,” in *Proc. AMS 3rd International Conference on the Aviation Weather Systems*, Anaheim, CA, pp. 92–95, January 30–February 3, 1989.

9-79. NASA Johnson Space Center, “Shuttle Launch Commit Criteria and Background,” NSTS-16007, Rev. H, Change No. 077, dated May 30, 2007.

9-80. Johnson, D.L.; and Vaughan, W.W.: “Analysis and Assessment of Peak Lightning Current Probabilities at the NASA Kennedy Space Center,” *NASA/TM—2000–210131*, Marshall Space Flight Center, AL, May 1999.

9-81. Gabrielson, B.: “The Aerospace Engineer’s Handbook of Lightning Protection,” Interference Control Technologies, Inc., 1988.

9-82. Krider E.P.; and Kehoe, K.E.: “On Quantifying the Exposure to Cloud-to-Ground Lightning,” Chapter 7 in *Recent Progress in Lightning Physics*, C. Pontikis, G. Berger, and E. Hicks (eds.), pp. 95–107, 2005.

9-83. Garbagnati, E.; and Lo Pipero, G.B.: “Parameter von Blitzstromen,” Elektrotech. Z., ETA-A, Vol. 103, pp. 61–65, 1982.

9-84. Saint Privat d’Allier Research Group: “Eight Years of Lightning Experiments at Saint Privat d’Allier,” *Revue Generale de l’Electricite*, No. 9, pp. 561–582, 1982.

9-85. Hubert, P.; Laroche, P.; Eybert-Berard, A.; and Barret, L.: “Triggered Lightning in New Mexico,” *J. Geophys. Res.,* Vol. 89, pp. 2511–2521, 1984.

9-86. Leteinturier, C.; Weidman, C.; and Hamelin, J.: “Current and Electric Field Derivatives in Triggered Lightning Return Strokes,” *J. Geophys. Res.*, Vol. 95, pp. 811–828, 1990.

9-87. Eybert-Berard, L.; Barret, L.; and Berlandis, J.P.: “Campagne Foudre aux Etats Unis, Kennedy Space Center (Florida), Proramme RTLP 85,” Report SST/ASP 86-01, Centre d’Etudes Nucleaires de Grenoble, Box 85 X, 38041 Grenoble Cedex, France, 1986 (in French).

9-88. Barret, L.; Boulay, G.; and Eybert-Berard, A.: “Campagne Foudre RTLP 86, Kennedy Space Center (Florida) USA, Recueil des Resultats Bruts au 01.12.86,” Report STT/ASP 86-12/LB-mA, Centre d-Etudes Nucleaires de Grenoble, Box 85 X, 38041 Grenoble Cedex, France, 1986 (in French).

9-89. Eybert-Berard, A.; Barret, L.; and Berlandis, J.P.: “Campagne d’Experimentations Foudre RTLP 1987 (NASA Kennedy Space Center, Florida, USA),” Report STT/Lasp 88-21-AEB/LB/JPB-pD, Centre d’Etudes Nucleaires de Grenoble, Box 85 X, 38041 Grenoble Cedex, France, 1988 (in French).

9-90. Eybert-Berard, A.; Barret, L.; Berlandis, J.P.; and Terrier, G.: “Characterisations des Decharges Electomagnetiques Provoquees, Campagne RTLP 1988, NASA Kennedy Space Center, Florida (USA),” Report STT/LASP 89-21/AEB/LB/JPB/GT-pD, Centre d’Etudes Nucleaires de Grenoble, Box 85 X, 38041 Grenoble Cedex, France, 1989 (in French).

9-91. Krider, E.P.; Weidman, C.D.; and Noggle, R.C.: “The Electric Fields Produced by Lightning Stepped Leaders,” *J. Geophys. Res.*, Vol. 82, pp. 951–960, 1977.

9-92. Uman, M.A.; Brantley, R.D.; Lin, Y.T.; et al.: "Correlated Electric and Magnetic Fields From Lightning Return Strokes," *J. Geophys. Res.*, Vol. 80, No. 3, pp. 373–376, 1975.

9-93. Uman, M.A.; and McLain, D.K.: "Lightning Return-Stroke Current From Magnetic and Radiation Field Measurements," *J. Geophys. Res.*, Vol. 75, pp. 5143–5147, 1970.

9-94. Clifford, D.W.; Crouch, K.W.; and Schulte, E.H.: "Lightning Simulation and Testing," *IEEE Trans. Electromag. Comp.*, EMC-24, pp. 209–224, 1982.

9-95. Fisher, F.A.; Plumer, J.A.; and Perala, R.A.: "Lightning Protection of Aircraft," Lightning Technologies Inc., Pittsfield, MA, 1990.

9-96. Federal Aviation Administration: "Protection of Aircraft Fuels Systems Against Lightning," *U.S. FAA Advisory Circular 25-3*, Washington, DC, November 10, 1965.

9-97. U.S. Department of Defense: "Bonding, Electrical, and Lightning Protection for Aerospace Systems," *U.S. Military Specification MIL-B-5087B*, October 15, 1964.

9-98. Plumer, J.A.; and Robb, J.D.: "The Direct Effects of Lightning on Aircraft," *IEEE Trans. on Electromag. Comp.*, EMC-24, pp. 158–172, 1982.

9-99. Society of Automotive Engineers: "Lightning Test Waveforms and Techniques for Aerospace Vehicles and Hardware," Report of SAE Committee AE-4, Special Task F, May 5, 1976.

9-100. Society of Automotive Engineers: "Lightning Test Waveforms and Techniques for Aerospace Vehicles and Hardware," Report of SAE Committee AE-4L, June 20, 1978.

9-101. U.S. Department of Defense: "Lightning Qualification Test Techniques for Aerospace Vehicles and Hardware," *U.S. Military Standard MIL-STD-1757*, June 17, 1980.

9-102. U.S. Department of Defense: "Lightning Qualification Test Techniques for Aerospace Vehicles and Hardware," *U.S. Military Standard MIL-STD-1757A*, June 20, 1983.

9-103. Federal Aviation Administration: "Protection of Airplane Fuel Systems Against Fuel Vapor Ignition Due to Lightning," *U.S. FAA Advisory Circular 20-53A*, Washington, DC, April 12, 1985.

9-104. Perala, R.A.; Rudolph, T.; and Eriksen, F.: "Electromagnetic Interaction of Lightning With Aircraft," *IEEE Trans. on Electromag. Comp.*, EMC-24, pp. 173–203, 1982.

9-105. Koons, H.C.; and Walterscheid, R.L.: "Lightning Launch Commit Criteria," *Aerospace Report No. TR-95(5566)-1*, The Aerospace Corporation, El Segundo, CA, February 1, 1996.

9-106. Roeder, W.P.; and McNamara, T.M.: "A Survey of the Lightning Launch Commit Criteria," AMS 2nd Conference on Meteorological Applications of Lightning Data, Atlanta, GA, January 28–30, 2006.

9-107. Krider, E.P.; Christian, H.J.; Dye, J.E.; et al.: "Natural and Triggered Lightning Launch Commit Criteria, 12th Conference on Aviation, Range and Aerospace Meteorology, Atlanta, GA, January 29–February 2, 2006.

Terrestrial Environment (Climatic) Criteria Guidelines for Use in Aerospace Vehicle Development, 2008 Revision

NASA/TM—2008–215633
December 2008

D.L. Johnson, Editor

Section 10: Atmospheric Constituents

TABLE OF CONTENTS

TABLE OF CONTENTS (Continued)

LIST OF FIGURES

LIST OF TABLES

LIST OF ACRONYMS AND SYMBOLS

Al_2O_3	aluminum oxide
AO_4	sulfate
Br	bromine
C	carbon
Ca	calcium
$CaSO_4$	calcium sulfate
CCN	cloud condensation nuclei
Cl	chlorine
Cr	chromium
Cu	copper
EDT	eastern daylight time
Fe	iron
GOES	Geostationary Satellite Server
GPC	gas-to-particle conversion
H^+	hydrogen ion
HCC	hexavalent chromium compound
H_2O	water
H_2SO_4	sulphuric acid
$H_4Al_2Si_2O_9$	kaolinite
HCl	hydrogen chloride
HNO_3	nitric acid
IMPROVE	interagency monitoring of protected visual environment
K	potassium
$KAlSi_3O_8$	orthoclase
KSC	Kennedy Space Center
Mg	magnesium
MAF	Michoud Assembly Facillity
MBL	marine boundary layer
Mn	monel

LIST OF ACRONYMS AND SYMBOLS (Continued)

N	nitrogen
Na	sodium
NaCl	sodium chloride, salt
NH_3	ammonia
NH_4	ammonium
NHO_3	nitric acid
Ni	nickel
NO_x	nitrogen oxide
NO_3	nitrate
NOAA	National Oceanic and Atmospheric Administration
NPS	National Park Service
O_2	oxygen
O_3	ozone
P	phosphorus
PM	particulate matter
PMEL	permissible exposure limit
PSC	polar stratospheric cloud
RH	relative humidity
S	sulphur
SAL	Saharan air layer
SAM II	Stratospheric Aerosol Measurement (satellite)
SiO_2	quartz
SO_2	sulfur dioxide
SO_4^{2-}	sulfate ion
SRB	solid rocket booster
SRM	solid rocket motor
STS	Space Transportation System
VAB	Vehicle Assembly Building

NOMENCLATURE

B	$(0.38 - \log r)/0.65$
b_{abs}	attenuation coefficient by absorption
b_{ext}	attenuation coefficient by extinction
b_{sca}	attenuation coefficient by scattering
b_x	attenuation coefficient
$b_{x,i}$	associated attenuation coefficient
C	pixel contrast
$C1$	coefficient
$C2$	coefficient
$C3$	coefficient
$C4$	coefficient
C_{ss}	sea salt concentration
$C(x)$	contrast of pixel
D	diameter
D_p	particle diameter
D_{pg}	mass median diameter
d	radius interval
dN	number of particles in radius interval
F	flux density
$F(x)$	flux density of light
$F_b(x)$	equilibrium flux density associated with a background
f_i	fraction of the ith constituent
H	height
H_p	typical marine scale height
i	number of aerosol species
M	mass
$M(0)$	surface mass concentration
$M(z)$	desired aerosol mass concentration
N	number limit
$n(r)$	size distribution function
r	radius of particle

NOMENCLATURE (Continued)

r_d	dry particle radius
r_w	wet particle radius
S	average sea salt concentration
u^*	friction velocity
V	volume concentration
W	wind speed
x	length
x_c	visual range
Z	height/altitude
σ_g	geometric standard deviation
σ_x	optical cross section

10. ATMOSPHERIC CONSTITUENTS

10.1 Introduction

Gases and particles in the atmosphere must be considered during aerospace vehicle development in order to avoid detrimental effects to the vehicle on the ground or in flight. Some of these effects include corrosion, abrasion, and optical hindrances. These effects are explained later in this section. The intensity of damage depends on the source (type), location, and concentration of the particles. The particles (solid or liquid droplets) suspended in the air are termed aerosols. Several comprehensive references are available that provide discussions of atmospheric composition, chemistry, aerosols, and radiation (refs. 10-1 through 10-5). Useful discussions of methods for measuring aerosol properties are provided in reference 10-6.

10.1.1 Sources of Particles

Airborne particles develop from both primary (direct) and secondary (indirect) sources (ref. 10-7).

10.1.1.1 Primary Sources. The following are the primary sources of airborne particles:

- Meteorites—extraterrestrial or interplanetary dust.
- World oceans—sea salt particles.
- Arid and semiarid regions—soil dust, road dust, etc.
- Terrestrial materials—volcanic debris.
- Terrestrial biota—biological material.
- Fossil fuel combustion, biomass burning.

10.1.1.2 Secondary Sources. The secondary source of atmospheric particles is gas-to-particle conversions (GPCs) where chemical reactions convert natural and man-made atmospheric trace gases into liquid and solid particles. Important secondary aerosols include the following:

- Sulfates, from processing sulfur dioxide (SO_2) in the presence of water (H_2O) to form sulfuric acid and subsequent neutralization in the presence of, for example, ammonia from fertilizers and livestock into ammonium sulfates.

- Nitrates (NO_3), from processing of nitrogen (N) compounds in ammonia-rich environments into ammonium nitrate.

- Organics, which arise from reaction of ozone (O_3), hydroxyl, and nitrate radicals with volatile organic compounds, such as isoprene from vegetation, to form condensible hydrocarbons and organonitrates.

10.1.2 Distribution of Particles

The distribution of aerosols is regionally dependent. Particles may have a “local” distribution as well as a “regional” distribution. The local aerosol is generated in areas surrounding factories, volcanoes, and other direct sources of aerosol. Since this aerosol can greatly affect an aerospace facility, the site should be surveyed for possible problems. Factors such as wind speed, distance from source, altitude, and particle size play an important part

in determining the makeup and concentration of a local aerosol. These same factors also affect regional aerosol concentrations. On a regional scale, number concentrations of particles in the atmosphere increase rapidly with decreasing particle size, to sizes smaller than 0.1-μm radius. Work cited in references 10-7 through 10-9 show that the concentrations and size distributions are highly variable with altitude. Some examples of these variations are given in section 10.3.

Natural aerosol size distributions are trimodal and their evolution is dependent on number, surface area, and composition. Aerosol particles ranging from 0.1 to 1 μm are in the "accumulation mode" because they tend to grow from smaller particles by coagulation or condensation. The "fine mode" consists of particles around 0.01 μm, usually resulting from combustion or GPC. Dust, fly-ash, sea spray, and other particles that are larger than 1 μm make up the "coarse particle mode." This mode is usually derived from mechanical processes (ref. 10-10).

10.1.3 Upper Atmospheric Aerosols

Atmospheric aerosols can exist at stratospheric levels (15- to 30-km altitude) as well as in the troposphere. The stratospheric aerosols, consisting mainly of liquid sulfuric acid droplets, are divided into three catogories: (1) Background aerosols, (2) volcanic aerosols, and (3) polar stratospheric cloud (PSC) particles (ref. 10-11). Section 8.5.1.1 gives more information regarding PSCs. Table 10-1 presents the basic characteristics of stratospheric aerosols.

Table 10-1. Characteristics of stratospheric aerosols (ref. 10-12).

Particle Type	Sulfate Aerosol	Type I PSC	Type II PSC	Meteoric Dust	Rocket Exhaust
Physical state	Liquid or slurry with crystals	Solid nitric acid trihydrate, solid solutions	Solid crystal, hexagonal or cubic basis	Solid granular irregular or spherical	Solid spheres or irregular surface ablated debris
Particle radius (μm, 10^{-6} m)	0.01–0.5, ambient 0.01–10, volcanic	0.3–3	1–100	1–100, micrometeorites 0.01–0.1, smoke	0.1–10
Number (cm^{-3})	≈1–10	≈0.1–10	«1	10^{-6}, 100 μm 10^{-3}, 1 μm	10^{-4}, 10 μm 10^{-2}, 1 μm
Principal composition	H_2SO_4/H_2O ≈70%/30%	HNO_3/H_2O ≈50%/50%	H_2O	SiO_2, Fe, Ni, Mg; C	Al_2O_3
Trace composition	NH_4^+, NO_3	HCl SO_4^{2-}	HNO_3, HCl	SO_4^{2-} (surface)	Cl^-, SO_4^{2-} (surface)
Physical characteristics	Dust inclusions, in solution	Equidimensional crystalline or droplets	Elongated crystals with polycrystalline structure	Irregular mineral grains, grain defects	Homogeneous composition; smooth spheres
Distribution	Global, ambient region, volcanic, 12-to 35-km altitude	Polar winter 14- to 24-km altitude	Polar winter 14- to 24-km altitude	≈Global >12-km altitude	Global >12-km altitude
Residence time	≈1–2 yr ambient ≈1–3 yr volcanic	≈1 day to weeks	≈hours	<1 mo (micrometeorites) 1–10 yr (meteoritic smoke)	<1 yr

Background aerosols are those aerosols observed under normal stratospheric temperatures higher than 195 K (not volcanic) and are primarily supercooled sulfuric acid (H_2SO_4) (75 percent by weight) in H_2O solution. They are formed by heterogeneous nucleation on preexisting particles. Small amounts of ammonium ions or meteoritic material may also be present.

Large volcanic eruptions can inject both sulfurous gases and ash (radii <3 μm) into the stratosphere. These gases are responsible for the rapid generation (within a few weeks or months) of sulfuric acid aerosols which remain at stratospheric altitude levels for several months or even years. The exponential 1/e decay time for the integrated aerosol backscattering was found to range between 12 and 18 mo. Low levels of other species, such as chlorine (Cl) and nitrogen oxide (NO_x), can also be observed. Abundant halide particles (radii of 2 to 3 μm), probably derived from chlorine-rich alkali magma, are also present (ref. 10-11).

The size distributions of volcanic aerosols (shown in fig. 10-1 for an El Chichon simulation) exhibit a trimodal structure that evolves with time. The principal size modes are (1) a nucleation mode, which is most prominent at early times and at sizes near 0.01 μm, (2) a sulfate accumulation mode, which evolves initially from the nucleation mode (by coagulation and condensation) and increases in size to ≈0.3 μm after 1 yr, and (3) a large-particle "ash" mode (of solid mineral and salt particles) that settles out of the layer in 1 or 2 mo. A primary feature of the volcanic aerosol size distribution after several months is a greatly enhanced sulfate accumulation mode. The increased aerosol size is caused by accelerated growth in the presence of enhanced sulfuric acid vapor concentrations that are maintained by continuing SO_2 chemical conversion (ref. 10-12).

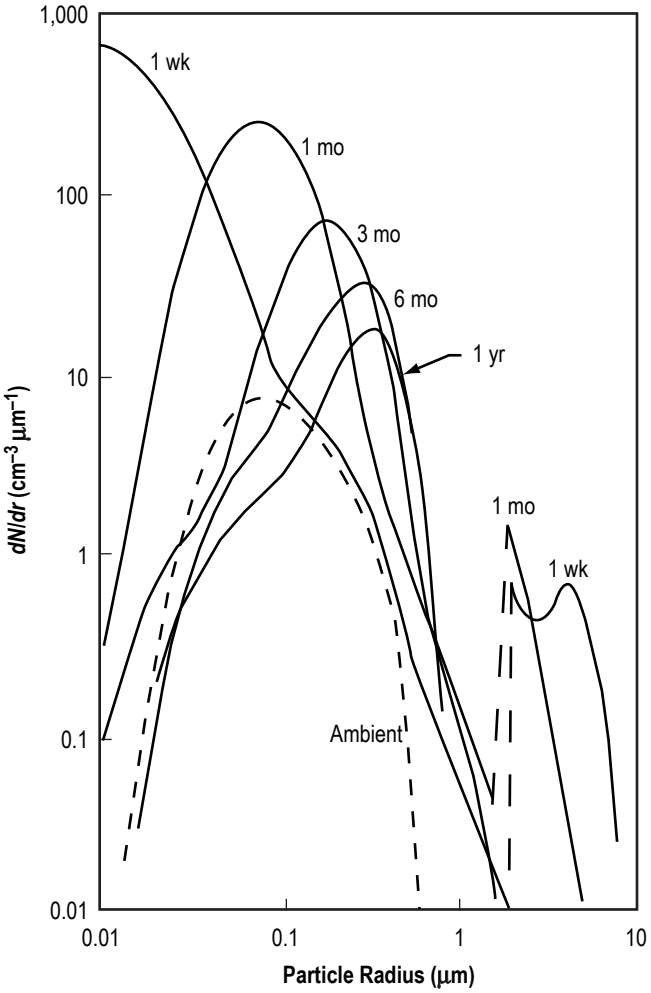

Figure 10-1. Evolution of the volcanic aerosol size distribution at 20 km in the simulated El Chichon eruption cloud. Size distributions are shown at various times, and are compared to the ambient size distribution (ref. 10-12).

PSCs form when aerosol particles encounter cold temperatures (<195 K) in wintertime polar regions and are formed by excess condensation of water vapor on background stratospheric sulfate particles. Nitric acid (NHO_3) and hydrochloric acid (HCl) may also impinge onto the PSC particles. Section 8 provides a more indepth study of PSCs.

Aerosol particles with a radius >0.1 μm typically obey a size distribution of the form (refs. 10-1 and 10-10):

$$n(r) = dN/d(\log r) \quad , \tag{10.1}$$

where

r = radius of particle
dN = number of particles in the radius interval $d(\log r)$.

10.2 Threats Caused by Atmospheric Particles

Abrasion, optical hindrances, and corrosion are the main problems caused by gases and airborne particles that must be considered during aerospace vehicle development. For an example of specific launch-related threats, refer to section 10.3.5.

10.2.1 Abrasion

Aerosol particles usually follow the airflow around an object. However, if the momentum of the particles is sufficiently great, they will deviate from the flow path to impact the surface. Whether or not impaction occurs depends on the particle size, shape, and density and on air density; the relative speed of the aerosol and object; and the size and shape of the object. Impaction theory is reviewed in reference 10-13. The greater the size and density of the particles and the greater the relative aerosol velocity, the greater is the likelihood of impact.

The effect of the impact depends on the physical characteristics of the particle and the impact surface, the velocity of the particle, and the angle of impact. Direct impact of dry particles on a surface may cause abrasion, and when voids are filled with dry particles, they may interfere with or cause wear on moving parts. Particles can also clog various mechanisms or produce electrical shorts.

The degree of hardness, i.e., the resistance offered by a mineral to abrasion or scratching, is often compared using the Mohs scale of hardness. This scale of mineral hardness was devised in 1822 by a German mineralogist, Fredrich Mohs, and has been used because of its simplicity and usefulness. The scale is made up of a number of minerals of increasing hardness, as given in table 10-2, with a comparison of other materials given in table 10-3 (ref. 10-14). A complete listing, as well as mineral breaking or cleaving shapes, can be found in reference 10-15. Mohs scale of hardness is used as a guide to determine which materials will abrade or scratch other materials. A material can be scratched by another material of an equal or greater hardness number.

Two minerals included in table 10-3 are halite (NaCl) and kaolinite ($H_4Al_2Si_2O_9$). Halite, a naturally-occurring salt, indicates the general hardness of sea salt particles. Although NaCl is usually cube shaped, it may be an irregular shape if broken. Kaolinite, an aluminum silicate, is a common clay mineral, usually a crystal plate, that makes up many of the fine particles in the air from sandy soils.

The larger and harder sand particles, primarily quartz (SiO_2), are usually rounded but may be jagged. Volcanic ash particles, consisting of SiO_2, orthoclase ($KAlSi_3O_8$), and various other minerals, are usually jagged.

Table 10-2. Mohs scale of hardness for minerals.

Mohs Relative Hardness	Mineral
1	Talc
2	Gypsum
3	Calcite
4	Fluorite
5	Apatite
6	Orthoclase
7	Quartz
8	Topaz
9	Carborundum
10	Diamond

Table 10-3. Mohs hardness values for some other materials.

Material	Hardness
Lead	1.5
Aluminum	2–2.5
Halite (sea salt)	2–2.5
Kaolinite	2–2.5
Zinc	2.5
Copper	2.5–3
Gold	2.5–3
Brass	3–4
Iron	4–5
Platinum	4.3
Glass	4.5–6.5
Steel	5–8.5
Volcanic ash	6–7

Gypsum particles ($CaSO_4 \bullet 2H_2O$) are at times raised by winds over arid areas, especially in the White Sands, NM, area, which is almost entirely gypsum. Most smog particles are droplets of soft organic particles or salts, although some harder particles, such as fly-ash from power plants, may be present.

A discussion of rain erosion is covered in section 7.

10.2.2 Optical Hindrances

Atmospheric aerosols affect optical properties in a variety of ways. The optical effects of an aerosol depend on the sizes, complex refractive indices (optical constants), and shapes of the particles (refs. 10-16 through 10-18). One of the most evident manifestations of air pollution is the production of haze, which causes a reduction in visibility or visual range. Particles may also coat optical and transparent surfaces to affect visibility.

The optical properties of the atmospheric aerosol are governed by the morphology and complex index of refraction (chemical composition) of the particulate matter, and are articulated by their extinction coefficient and angular distribution of scattered light. With optical cross sections denoted σ_x, $x = \text{sca}$ and ext for scattering and extinction, respectively, the corresponding attenuation coefficients for a volume of air populated by a single species of particle is given by

$$b_x = \int_0^\infty n(r)\left\langle \sigma_x(r) \right\rangle d(\log r) \Big/ \int_0^\infty n(r)\, d(\log r) \,, \tag{10.2}$$

where r represents the characteristic size of the particle. In this expression, the brackets denote an averaging over particle orientation, and can be omitted for the case of spherical particles. Attenuation by absorption may also be obtained simply as $b_{\text{abs}} = b_{\text{ext}} - b_{\text{sca}}$.

Any air mass in the atmosphere will contain more than one type of aerosol. For a mixture of N species in a given aerosol, the attenuation coefficient is given by

$$b_x = \sum_{i=1}^{N} f_i b_{x,i} \,, \tag{10.3}$$

where f_i and $b_{x,i}$ are the fraction of the ith constituent and its associated attenuation coefficient, respectively.

The ability to distinguish an element of a scene depends on the contrast of that element with other features. Contrast is defined for the human eye as a number ranging from –1 to 1, with –1 representing a totally white, undiminished pixel viewed against a black background. A contrast of 1 is obtained for a black object viewed against a white background.

Let $F(x)$ denote the flux density (in W/cm^2) of light arriving along a sight path of length (x) from a scene pixel, and $F_b(x)$ denote an equilibrium flux density associated with a background; e.g., the sky. The pixel's contrast can be quantified as

$$C(x) = \frac{F_b(x) - F(x)}{F_b(x)} \,. \tag{10.4}$$

Contrast varies with $F(x)$, which depends on the composition of the intervening atmosphere. $F(x)$ increases when light that was not originally directed along the line of sight is scattered toward the observer by particles lying in the sight path. If only single-scattering processes are taken into account, then it can be shown that

$$C(x) = C(0)\exp(-b_{\text{ext}}x) \,. \tag{10.5}$$

The average viewer is sensitive to contrasts on the order of 0.02. This is the basis for the Koschmeider equation for visual range x_c for a pixel with $C(0) = 1$:

$$x_c = \frac{3.912}{b_{\text{ext}}} \,. \tag{10.6}$$

In a particle-free atmosphere, Rayleigh scattering limits visual range at sea level to ≈300 km, beyond which distance the object being sought would be obscured by the intervening blue sky.

This discussion applies to a single wavelength of light or to an integration of the radiant flux entering the eye over the range of its spectral response. For other spectral ranges, and for polarimetric radiance transfer, similar definitions of contrast apply, so that the utility of this quantity is readily extended to electro-optic sensing of the environment for a wide variety of applications. When the assumption of single scattering is violated, the flux densities for the desired polarimetric quantites must be calculated with more rigorous treatments of radiative transfer. This subject is discussed in references 10-19 through 10-21. The effect of aerosols on optical and infrared transmission may be assessed using the LOWTRAN 7 computer code.

The National Park Service (NPS) maintains a monitoring network at national parks and at a number of wilderness areas that provides valuable data on aerosol extinction at those sites. Originally consisting of 36 monitoring stations, the network is currently expanding to a total of 143 stations. The aerosol samplers operated by the NPS provide data on total aerosol mass and extinction. In addition, the aerosol composition is determined in terms of mass fractions for sulfates, nitrates, organics, soot, and mineral dust. The program goes by the acronym IMPROVE (Interagency Monitoring of PROtected Visual Environments). Further information, including archived aerosol data, can be found in reference 10-22.

10.2.3 Corrosion

Certain atmospheric gases may cause aerospace vehicle metals to react chemically and cause corrosion. Atmospheric corrosion is the degradation of a material exposed to the air and its pollutants and is the cause of more failures in terms of cost and tonnage than any other single environment. The basic types of atmospheric corrosion are often classified and defined as follows (ref. 10-12):

- Dry corrosion—corrosion that occurs in the absence of moisture. Usually, this corrosion occurs very slowly unless elevated temperatures exist.

- Damp corrosion—corrosion occurring when there is moisture in the air. When the relative humidity (RH) reaches a specific critical value (around 70 percent), a thin layer of moisture on the metal surface provides an electrolyte for current transfer, and consequently increases the rate of corrosion.

- Wet corrosion—visible water layers caused by sea spray, dew, or rain cause wet corrosion. Wet corrosion usually occurs most rapidly due to the high conductivity.

10.2.3.1 Introduction. Corrosion is the decaying or destruction of a material caused by the environment. Fontana defines corrosion as, “the deterioration of a material due to its reaction with its environment,” while Uhlig defines it as “the destructive attack of a metal by chemical or electrochemical reaction with its environment.” Metals corrode because they are used in environments where they are chemically unstable. In fact, only copper and the precious metals gold, silver, platinum, etc. are found in nature in their metallic state. All other metals including iron, the metal most commonly used in structural applications, are processed from minerals or ores into metals, most of which are inherently unstable in their environments. While corrosion is a natural process that cannot be prevented, corrective measures can control it. The cost of corrosion to the United States is ≈$300 billion/year, even though a significant percent of this cost could be prevented at the design level (refs. 10-23 and 10-24).

Because corrosion is a natural electrochemical action that affects all metals to one extent or another, the conditions needed to initiate corrosion are moisture (the electrolyte), a conductor (the metal), and a difference

in potential between the areas of the metal. Moisture is the most important element in corrosion as it increases the electrical conductivity of the environment in contact with the metal.

One of the most common and recognized forms of corrosion occurs when processed steel seeks to revert to its more stable form of ferrous oxide or rust (a product of corrosion). While some oxides, such as that present on stainless steel, can provide protection from corrosion, others can actually accelerate the corrosion rate. What is important then is not that metals will corrode, but at what rate and in what form. If the expected corrosion rate is high, or the form of attack is such that it will lead to a structural failure, protective measures need to be applied (ref. 10-25).

One example where protective measures had to be taken was at the NASA Kennedy Space Center (KSC) Vehicle Assembly Building (VAB) that was stricken with concrete corrosion problems, which ultimately led to the failure of the concrete roof. This failure occurred as a result of years of salt spray exposure to the reinforcing steel rods within the concrete roof, creating a powerful corrosion cell within the concrete. This corrosion cell caused the iron within the steel to be converted to iron oxide (rust). Because this rust took up more volume than the iron it was replacing, the rust exerted great internal pressure on the surrounding concrete, which caused it to crack and lead to some concrete chunks falling and putting the Shuttle and personnel at risk. The solution was to apply cathodic protection to prevent corrosion of the reinforcing steel bars inside the concrete mass. Because chlorides were determined to be the main cause of the attack and are negatively charged ions, a small, negative direct current applied to the reinforcing steel repelled the cholorides, preventing the corrosion to be established (ref. 10-26). Coating the surface is another way to protect concrete exposed to the atmosphere (refs. 10-23 and 10-24).

As was the case in the aforementioned example from KSC, chlorides found in marine environments are the main reason for the aggressive corrosive attack on steel and metals in seawater. The main types of marine corrosion of interest to the design engineer are uniform, pitting, and crevice corrosion. Aqueous corrosion for steel sheet pilings in the marine environment is important to consider in design or prevention. For example, the Shuttle solid rocket booster (SRB) casings are exposed directly to the Atlantic Ocean (salt water) environment prior to being picked up after a launch. Therefore, it was imperative to think about corrosion in the design phase of this project. Vehicle corrosive consideration is needed, which should also be applied to (1) transportation to KSC, (2) type of storage while at KSC, (3) transportation to the launch pad, and (4) length of stay on the launch pad prior to launch.

10.2.3.2 Types of Corrosion. Corrosion can be categorized into various specific types; e.g., atmospheric corrosion, aqueous corrosion, and other types, such as soil corrosion, concrete corrosion, etc. Atmospheric corrosion severity tends to vary in different locations, so it has been customary to classify the different corrosion environments as rural, urban, industrial, marine, or a combination of these.

10.2.3.3 Forms of Corrosion. There are various forms of corrosion identified at KSC: (1) Uniform (or general corrosion), (2) galvanic corrosion, (3) concentration cell corrosion, (4) pitting corrosion, (5) crevice corrosion, (6) filiform corrosion, (7) intergranular corrosion, (8) stress corrosion cracking, (9) corrosion fatigue, (10) fretting corrosion, (11) erosion corrosion, (12) dealloying, (13) hydrogen damage, (14) corrosion in concrete, and (15) microbial corrosion (refs. 10-23 and 10-24).

Some investigators have defined general corrosion depth as (ref. 10-27):

- Mild: Depth <0.001 in (<25 μm),
- Moderate: 0.001<depth<0.01 in (25<depth<250 μm)
- Severe: Depth >0.01 in (>250 μm).

10.2.3.4 Kennedy Space Center Corrosivity. The launch environment at KSC is extremely corrosive mainly due to five parameters: (1) Ocean salt spray, (2) heat, (3) humidity, (4) rainfall, and (5) UV sunlight, along with acidic exhaust from Shuttle SRBs. Currently, KSC maintains ≈$2 billion worth of unique equipment and facilities, including two launch complexes, three mobile launch platforms, two crawler transporters, and various testing equipment, that all need protection (refs. 10-23 and 10-24).

In order to get a better understanding of atmospheric exposure at KSC, the KSC Corrosion Technology Laboratory (Atmospheric Exposure Test Facility site) was established and has been cited as the most extensive atmospheric corrosion test site in the United States. It is located at latitude 28.7° N., longitude 80.6° W., and sits ≈100 ft from the Atlantic high tide line. Over the years, thousands of coated test panels, stress corrosion cracking specimens, and commercially produced components have been evaluated in this extreme Florida seacoast environment. The two Shuttle launch pads, 39A and 39B, are located <1.6 km (≈1 mi) from the Atlantic Ocean and are exposed daily to salt spray and high humidity. The hydrochloric acid (HCl) and intense heat generated during a launch increase the natural corrosive conditions and have a detrimental effect on any protective coatings, structures, and machinery at the pads. The two SRBs emit more than 91 metric tons (100 tons) of exhaust during the first 10 s of launch, including 28,000 kg (61,729 lb) of aluminum oxide (Al_2O_3) and 17,000 kg (37,478 lb) of HCl. A cloud of HCl and powdery Al_2O_3 dust falls over the 2.6 km^2 (1 mi^2) area about the pad. Serious structural damage requiring partial pad replacement could occur within 5 yr if a pad is left unprotected. While being transported to the launch pad, the orbiter is subjected to an almost constant salt spray from the nearby ocean, with high humidity, allowing for the formation of condensation on all surfaces open to the atmosphere. The landing natural environment, along with the launch effects, must also be considered in selecting materials and corrosion protection finishes for the orbiter. Extended pad stays are also of concern due to the coastal exposure and the daily condensation of dew deposited onto the orbiter structure (refs. 10-23 and 10-24).

Because the KSC environment has been shown to cause the highest corrosion rate of any test site in the continental United States (see table 10-4), samples exposed at this site should weather or degrade at rates far in excess of the rates experienced at other sites. Figure 10-2 shows the KSC variation of the corrosion rate (measured as weight loss), and the salt (NaCl) content of the atmosphere, as a function of distance (decreases exponentially) from the Atlantic Ocean (refs. 10-23 and 10-24).

At KSC, salt is present in the local atmosphere under all weather conditions, with the highest average aerosol salt concentration under east winds. The average atmospheric salt concentration does not vary significantly from the ground up to 120 m height (ref. 10-28). Keep in mind that average corrosion rates are just that. Corrosion can vary considerably depending on the test conditions, locations, and weather patterns.

For design, Shuttle metals were required to meet MSFC-SPEC-250A, "Protective Finishes for Space Vehicle Structures and Associated Flight Equipment; General Specifications for Class II Requirements." The orbiter was designed to have no structural failure due to corrosion within a 10-yr or 100-mission life. The four potential major types of orbiter corrosion mechanisms are galvanic, concentration cell, uniform and mechanical. These mechanisms can result in pitting, intergranular corrosion, cracking, filiform, erosion, fretting, and tarnishing (refs. 10-23 and 10-24).

10.2.3.4.1 Barge Transportation. Another corrosion consideration is if space launch vehicle components are transported by barge (with open barn type covering) to KSC from Michoud Assembly Facility (MAF). The seawater salt spray may need to be considered, as the transportation barge can take up to 5 days to travel from MAF to KSC. Titanium alloys are, in general, considered highly resistant to stress corrosion cracking from NaCl salt. The National Oceanic and Atmospheric Administration (NOAA)/PMEL studies indicate that the Earth's sea water has between 3.1 and 3.8 percent salinity, with ≈3.5 percent (or 35 parts per thousand) in the Gulf and Atlantic between MAF and KSC. Therefore, every 1 kg of sea water has ≈35 g of dissolved salts (mostly the ions of

Table 10-4. Corrosion rates of carbon steel calibrating specimens at various test locations* (refs. 10-23 and 10-24).

Location	Type of Environment	µm/yr	Corrosion Rate** (mils/yr)
Vancouver Island, BC, Canada	Rural marine	13	0.5
Pittsburgh, PA	Industrial	30	1.2
Cleveland, OH	Industrial	38	1.5
Limon Bay, Panama Canal Zone	Tropical marine	61	2.4
East Chicago, IL	Industrial	84	3.3
Brazos River, TX	Industrial marine	94	3.7
Daytona Beach, FL	Marine	295	11.6
Pont Reyes, CA	Marine	500	19.7
Kure Beach, NC (24 m from ocean)	Marine	533	21.0
Galeta Point Beach, Panama Canal Zone	Marine	686	27.0
Kennedy Space Center, FL (beach)	Marine	1,070	42.0

*Data extracted from reference 10-29.
**2-yr average.

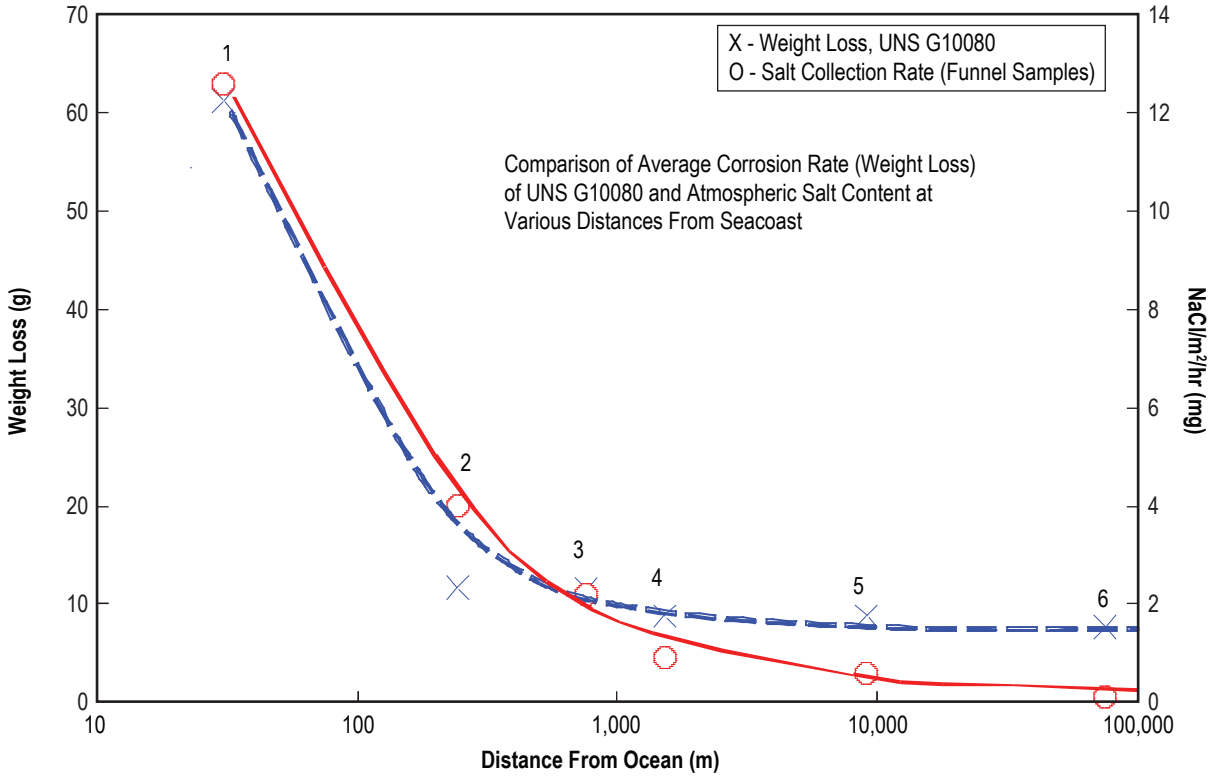

Figure 10-2. KSC corrosion rate (measured as weight loss) of AISI 1008 steel, and salt content of the atmosphere as a function of distance from the Atlantic Ocean.

sodium chloride: Na^+, Cl^-. The actual salt spray contaminate that might be encountered by the launch component is highly dependent upon the wave height and period, the atmospheric wind speed and direction, the design and speed of the barge, the barge direction relative to the waves, the time of exposure to the spray, and the nature of the protective covering (ref. 10-30).

The KSC atmospheric exposure site is at point 1 (30 m/100 ft), Launch complex 41 is at point 2 (244 m/800 ft), and complex 39A (Space Shuttle launch site) is at point 3 (762 m/2,500 ft). Points 4 and 5 represent other locations at KSC (1,585 m/5,200 ft and 9.7 km/6 mi). Point 6 corresponds to an urban area of Orlando, FL (50 mi) (refs. 10-23, 10-24, and 10-31).

10.2.3.5 Rate of Atmospheric Corrosion. The rate of atmospheric corrosion depends on many different atmospheric variables, as mentioned in section 10.2.3.4, as well as surface shape and properties. Table 10-5 provides average corrosion rates over 10- and 20-yr intervals for certain surface metals (ref. 10-32).

Table 10-5. Average atmospheric corrosion rates of various metals (mils/yr) for 10- and 20-yr exposure times (ref. 10-32).

	Atmosphere					
	New York, NY (Urban-Industrial)		La Jolla, CA (Marine)		State College, PA (Rural)	
Metal	10 yr	20 yr	10 yr	20 yr	10 yr	20 yr
Aluminum	0.032	0.029	0.028	0.025	0.001	0.003
Copper	0.047	0.054	0.052	0.050	0.023	0.017
Lead	0.017	0.015	0.016	0.021	0.019	0.013
Tin	0.047	0.052	0.091	0.112	0.018	–
Nickel	0.128	0.144	0.004	0.006	0.006	0.009
65% Ni, 32% Cu, 2% Fe, 1% Mn (Monel)	0.053	0.062	0.007	0.006	0.005	0.007
Zinc (99.9%)	0.202	0.226	0.063	0.069	0.034	0.044
Zinc (99%)	0.193	0.218	0.069	0.068	0.042	0.043
0.2% C Steel (0.02% P, 0.05% S, 0.05% Cu, 0.02% Ni, 0.02% Cr)	0.48	–	–	–	–	–
Low-alloy steel (0.1% C, 0.2% P, 0.04% S, 0.03% Ni, 1.1% Cr, 0.4% Cu)	0.09	–	–	–	–	–

Note: Corrosion rates are given in mils/yr (1 mil/yr = 0.025 mm/yr). Values cited are one-half reduction of specimen thickness.

10.2.3.6 Protection From Atmospheric Corrosion. Prevention of atmospheric corrosion can be temporary or close to permanent. During transport or storage, lowering the atmospheric humidity by artificial methods may temporarily prevent corrosion. Additionally, changing the surface material or applying a protective coating can provide a longer-term solution. In determining the material requirements for any application, the type of environment must be considered. Tables 10-6 and table 10-7 list the corrosivities of various environments (ref. 10-33). The "relative corrosivity" at the various sites (tables 10-6 and 10-7) is simply a unitless multiple of the corrosion rate at either the least corrosive site or at a minor site (listed as 1.0).

Table 10-6. Relative corrosivity of atmospheres at different locations (ref. 10-33).

Location	Type of Atmosphere	Average Weight Loss of Iron Specimens in 1 Yr (mg/cm^2)	Relative Corrosivity
Khartoum, Sudan	Dry island (arid)	0.08	1.0
Singapore	Tropical/marine	0.69	9.0
State College, PA	Rural	1.90	25.0
Panama Canal Zone	Tropical/marine	2.28	31.0
Kure Beach, NC (250 m, or 800 ft, lot)	Marine	2.93	38.0
Kearny, NJ	Industrial	3.92	52.0
Pittsburgh, PA	Industrial	4.88	65.0
Frodingham, UK	Industrial	7.50	100.0
Daytona Beach, FL	Marine	10.34	138.0
Kure Beach, NC (25 m, or 80 ft, lot)	Marine	35.68	475.0

Table 10-7. Measured atmospheric corrosion rates for steel and zinc (ref. 10-33).

Site	Location	Type of Atmosphere	Relative Corrosivity*	
			Steel	Zinc
1	Normal Wells, Northwest Territory	Rural	0.02	0.2
2	Saskatoon, Saskatchewan	Rural	0.2	0.2
9	State College, PA*	Rural	1.0	1.0
17	Pittsburgh, PA (roof)	Industrial	1.8	1.5
18	London (Battersea), UK	Industrial	2.0	1.2
27	Bayonne, NJ	Industrial	3.4	3.1
28	Kure Beach, NC (250 m, or 800 ft, site)	Marine	3.6	1.9
31	London (Stratford), UK	Industrial	6.5	4.8
33	Point Reyes, CA	Marine	9.5	2.0
37	Kure Beach, NC (25 m, or 80 ft, site)	Marine	33.0	6.4

*The average weight losses on two 100- by 150-mm (4- by 6-in) specimens after 1 yr of exposure at the indicated site were used to calculate the relative corrosivity of the site. The losses in the rural atmosphere at State College, PA, were taken as unity and the relative corrosiveness at each of the other sites is given in this table as a fraction or a multiple of unity.

There are a number of ways of controlling corrosion (refs. 10-23 and 10-24). The choice depends on economics, safety requirements, and a number of technical considerations. The KSC Corrosion Technology Laboratory can provide guidance on corrosion control. Some of these controlling ways are as follows:

(1) Engineering design—a process that includes design for purpose, manufacturability, inspection, and maintenance. One consideration often overlooked in designing manufactured products is drainage, which allows any water to drain instead of collect and cause corrosion.

(2) Materials selection:

- Carbon steel—used in most large metal structures. A rust film can form without drainage. Hydrogen embrittlement and environmental cracking may occur. Protective coatings, cathodic protection, and corrosion inhibitors are all extensively used to prolonging the life of carbon steel structures at KSC.

- Stainless steel—a common alternative to carbon steel. The most common is austenitic stainless steel (18 percent chromium and 8 percent nickel), as it is frequently immune to general corrosion but may experience pitting, crevice corrosion, and/or stress corrosion cracking in certain situations.

- Aluminum or its alloys—widely used in aerospace applications where their favorable strength-to-weight ratios make them the structural metal of choice. However, if the protective aluminum oxide film breaks down, it can allow extensive intergranular corrosion and pitting. This frequently occurs in aluminum alloys where cathodic precipitates can cause local galvanic couples where corrosion can easily occur.

- Copper alloys, such as brasses and bronzes—commonly used in piping, valves, and fittings. They are subject to stress corrosion cracking (around ammonia compounds), dealloying, galvanic corrosion (when coupled with steel and other metals), and erosion corrosion due to their relative softness.

- Titanium—a metal very common in nature and extensively used in the aerospace industry. There are two general types of titanium alloys—aerospace alloys and corrosion resistant alloys, although both are more corrosion resistant than most other metals. Titanium alloys suffer from crevice corrosion when in the presence of high temperatures, a tight crevice, and a saltwater application. The mechanism of this attack is similar to that seen on crevice corrosion of stainless steel.

(3) Protective coatings—very commonly used in corrosion control and can be metallic, organic, or waterborne organic. They can be applied as a liquid paint but filiform corrosion can occur underneath organic coatings.

(4) Corrosion inhibitors—chemicals that can be added to controlled environments to reduce the corrosivity of these environments; e.g., chemicals added to antifreeze. There has been corrosion inhibitor research at KSC involving inhibitors added to protective coatings.

(5) Corrosion allowances—Engineering designers determine how much metal is necessary to withstand an anticipated load. They usually overdesign using a mechanical load safety factor ranging from 20 percent to over 300 percent. Additionally, they may also need to consider adding a corrosion allowance necessary for keeping the structure safe from corrosion.

(6) Cathodic protection—an electrical means of corrosion control by applying galvanic currents to slow down corrosion. KSC research uses these systems for minimizing corrosion of embedded steel in concrete structures.

The design of any new launch vehicle, like the new Constellation vehicles, and its redesigned launch sites, structures, facilities, and ground support equipment will also need to be protected from corrosion and deterioration. Unfortunately, some corrosion protection coatings that have been used in the past may not be available for use on the new launch vehicle systems. For example, the permissible exposure limit (PEL) for the hexavalent chromium compounds (HCCs), used for aluminum alloy corrosion protection, was significantly reduced by the Occupational Safety and Health Administration from 100 $\mu g/m^3$ to only 5 $\mu g/m^3$. Also, HCCs may also be banned entirely worldwide due to their hazard potential and costs. While possible replacements have been identified, there is currently no replacement product available that has been certified for manned space flight at this time (refs. 10-23 and 10-24).

10.3 Characteristics of Specific Particles

This section describes characteristics of some particles that should be considered in aerospace vehicle design. Table 10-8 gives estimates of the sizes of various particles (refs. 10-7 and 10-34), but the actual sizes can vary greatly, depending on the specific atmospheric conditions. Typical sizes for suspended water droplets (fog) can be found in section 7.

Table 10-8. Estimated size ranges of natural occurring atmospheric particles (ref. 10-7).

Particle Type	Radii Size (μm)
Extraterrestrial	0.1–1,000
Sea salt	0.02–60
Crustal aerosol	0.02–100
Volcanic ash*	0.1–10
Combustion and secondary particles (average)	<1
Indirect sources	Under 0.1

*Directly after the eruption, particles as large as 5 mm (0.2 in) can be found (ref. 10-34).

10.3.1 Extraterrestrial Dust

Extraterrestrial dust is usually formed by the breakup of meteoroids and orbital debris. It reaches the troposphere through processes such as gradual sedimentation, stratospheric subsidence, followed by a rapid pursing from the stratosphere into the troposphere in the "tropospheric folds." Within the troposphere, the extraterrestrial dust is concentrated around the polar regions. The larger dust particles are "fluffy and compacted aggregates" while the smaller particles (submicrometer) are more dense (ref. 10-7). The residence time of these particles in the stratosphere and troposphere ranges from months to years.

10.3.2 Sea Salt Particles

Salt (NaCl) particles, whether from the ocean or areas where salt occurs naturally on the continents, can be detrimental to space vehicles and associated systems because of their corrosive actions and their ability to coat transparent areas until they become opaque. Salt attacks many metals, and the corrosion is especially rapid at high humidities and high temperatures. Salt solutions also provide a conductive path that can alter or short electrical circuits.

10.3.2.1 Marine Aerosols. Small aerosol particle droplets are ejected into the atmosphere when bubbles burst at the sea surface in white caps. This source of aerosol particles from the ocean is very important since sea salt particles are very good cloud condensation nuclei (CCN), and hence, can control cloud albedo and lifetime. Sea salt aerosol has a large influence on the atmospheric sulfur cycle and influences the climate effects of the natural or anthropogenic sulfate aerosol. This aerosol source also plays a role in corrosion and plant stress coastal regions and for the sea-air water flux.

Sea salt also is an important tracer of the climate record of Arctic and Antarctic snow and ice cores. Besides sea salt, the primary marine aerosol also has an organic component, which results both from natural

(biogenic) and man-made sources, dissolved in the surface water or as a thin film on the water surface. The primary marine aerosol source plays a role for the transfer of pollutants from the ocean to the atmosphere.

Sea salt is also responsible for a large fraction of the nonsea salt sulfate formation since it is an important sink for SO_2 in the marine atmospheric boundary layer. Furthermore, the alkalinity of sea salt as CCN affects aqueous chemistry. Submicrometer sea salt competes with sulfate to influence the number of CCN (ref. 10-35). Over wide oceanic areas, sea salt is the most efficient aerosol component to scatter solar radiation. Sea salt aerosol constitutes an important component of the global background aerosol loading. Sea salt particles also influence the aerosol composition in coastal environments as they contribute surfaces for heterogenous chemical reactions with condensable and volatile species (H_2SO_4, HNO_3, and NH_3) (ref. 10-36).

Sea water contains ≈3.5 percent sea salt by weight, of which ≈86 percent is composed of Na and Cl. SO_4^{2-}, Mg, Ca, K, and Br add to the NaCl to give ≈99.5 percent of the total sea salt composition (ref. 10-1). The marine atmospheric boundary layer consists of (1) a microlayer (viscous sublayer) ≈1 cm thick, (2) the surface layer (within first 10 m above sea surface), also called the constant flux layer (≈10 to ≈100 m thick), and (3) the transition layer (≈50 to ≈1,000 m thick) (ref. 10-37).

Since the oceans cover over 70 percent of the world's surface, sea salt particles are the most common aerosol component (ref. 10-38). Estimates of the yearly production of sea salt aerosol can range up to 10^{10} metric tons per year (10^4 Tg/yr or 10^{16} g/yr) (ref. 10-38), with a settling velocity of ≈0.307 cm/s for a 10-μm-diameter sea salt particle (ref. 10-39). The estimated least sea salt flux is ≈1,000 Tg yr^{-1} and the best estimate is ≈1,300 Tg yr^{-1} (ref. 10-1). It is estimated that 10^{15}–10^{16} g yr^{-1} of sea salt particles with radii <20 μm are emitted, or approximately 30–75 percent of the total global production of particulates from natural sources. Probably ≈10 percent of these emitted salts are subsequently deposited to land, with the remainder deposited to oceans. The ocean is a major natural source of atmospheric particulates, as well as a sink for material deposited from the atmosphere (ref. 10-40).

The global marine total aerosol maximum value is ≈15,000 ng/m^3 (or ≈1.5×10^{-5} g/m^3). This maximum lies between ±45° to ±75° N. and S. latitudes (ref. 10-41). The average global yearly burden of sea salt is ≈12 mg/m^2, with estimates ranging between 11 and 22 mg/m^2. The global mean radiative impact (forcing) of sea salt is approximately –1.1 W/m^2 (for cloudy skies) and approximately –2.2 W/m^2 (for clear skies) (ref. 10-42). Sea salt composes ≈64 percent of marine aerosols (ref. 10-39).

The marine aerosols are transported back to the sea via wet (rain) and dry removal processes (ref. 10-43). A model predicts that dry deposition accounts for 60–70 percent of the total sea salt removed from the atmosphere, while in-cloud and below-cloud precipitation scavenging accounts for about 1 percent and 28–39 percent of the remainder, respectively (ref. 10-44).

10.3.2.2 Marine Aerosol Size and Concentration. The typical marine aerosol spectrum spans more than five orders of magnitude in both particle size and concentration (ref. 10-45). Marine atmospheric particle size distributions are usually characterized by three modes, based on mass or volume distributions, as shown in table 10-9. They represent the typical background aerosol size distributions (mass median diameter (D_{pg}), geometric standard deviations (σ_g), and typical volume concentration (V)) (ref. 10-1). The claim that the marine aerosol minus the background aerosol equals the sea salt aerosol is incorrect; i.e., marine – background ≠ sea salt) (ref. 10-46).

From figure 10-3 that gives typical aerosol concentration data curves, it is observed that urban environments are characterized by greater concentrations of aerosol particles (as much as 10^5 particles/cm^3), while the maritime environment is characterized by the smallest particle concentrations; i.e., a maximum of

Table 10-9. Typical background marine aerosol particle size modes and distribution (ref. 10-1).

Particle	Fine Particles		Coarse Particles*
Mode	Nuclei mode	Accumulation mode	Coarse mode
Particle diameter range	$D_p < 0.1$ μm	$0.1 < D_p < 0.6$ μm	$D_p > 0.6$ μm
Typical mass median diameter	$D_{pg} = 0.019$ μm	$D_{pg} = 0.3$ μm	$D_{pg} = 12$ μm
Typical geometric std. dev.	$\sigma_g = 1.6$	$\sigma_g = 2$	$\sigma_g = 2.7$
Typical volume concentration	$V = 0.0005$	$V = 0.1$	$V = 12$

*The coarse particles (composed primarily of sea salt, but continental dust can contribute) contain ≈95% of the total mass of all maritime aerosols, but only 5% to 10% of the total particle number.

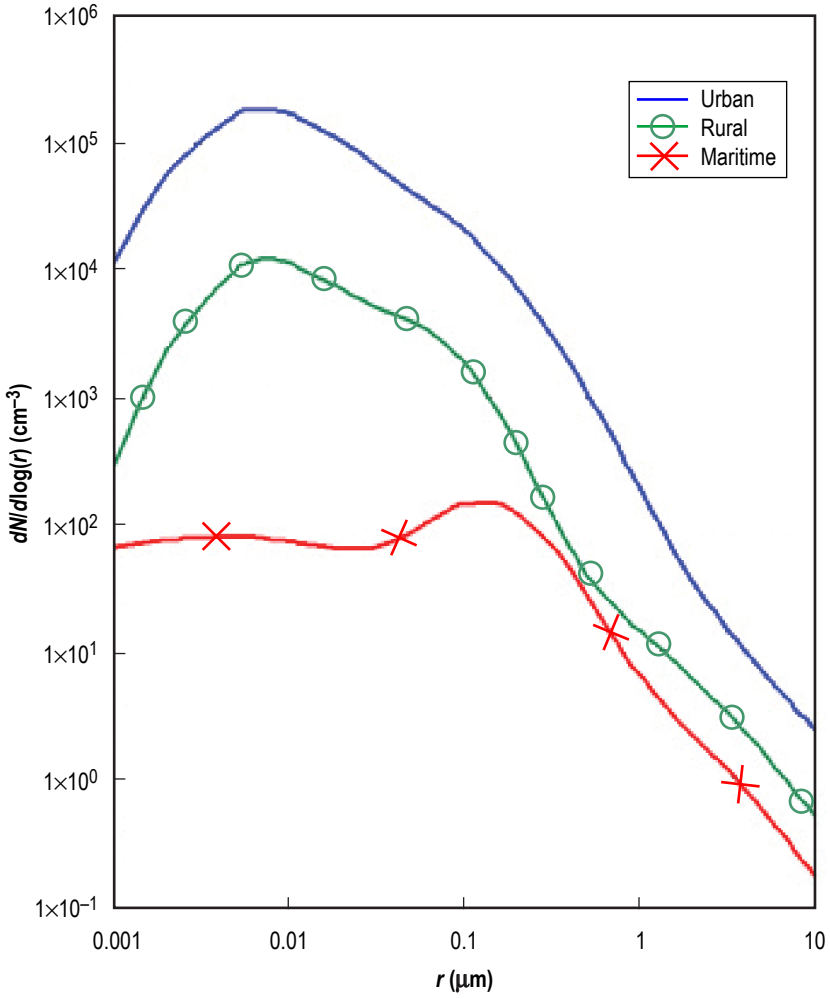

Figure 10-3. Model size distributions describing the typical aerosol concentrations for urban, rural, and maritime environments (data from ref. 10-47; ref. 10-48).

≈100 particles/cm^3. This maximum concentration is mainly within the accumulation mode at ≈0.1 μ, while the coarse mode particles are mainly composed of sea salt, resulting from the evaporation of sea spray. Coarse particles represent ≈95 percent of the total mass of maritime aerosols (ref. 10-47).

The distribution of the marine aerosol mass concentration in the vertical typically shows an exponential decrease with altitude up to a height (H_p), with a constant mass concentration above this level. For maritime air, the marine aerosol values versus height (Z) are presented in table 10-10. The equation that determines them at any altitude between zero and 2,500 m is given as:

$$M(z) = M(0) \exp(-Z/H_p) \quad , \tag{10.7}$$

where

$M(0)$ = surface mass concentration, i.e., 15 μg/m^3
H_p = typical marine scale height (of 900 m)
$M(z)$ = desired aerosol mass concentration at a desired altitude (Z).

Table 10-10. Mean and range of marine aerosol and marine sea salt particle concentrations in maritime air masses versus altitude (ref. 10-1).

Altitude (m)	Marine Aerosol		Marine Aerosol	Sea Salt Aerosol
	Range of Aerosol Number Concentration (cm^{-3})	Typical No. Concentration Value* (cm^{-3})	Typical Aerosol Mass Concentration Value** M (μg/m^3)	Typical Sea Salt Number Concentration Value* (cm^{-3})
Sea Level	10–3,000	100–400	15	5–30
1,000	125–700		6	
2,000	250–350		2	
2,500	275–325		1	
≥3,000	300		1	

* In marine boundary layer.

**Typical sea salt mass concentrations within the lowest 20 m of the marine atmosphere normally range between 10 and 20 μg/m^3, but they increase rapidly with wind speed (ref. 10-49). The average mass volume concentration of marine particulate matter near sea level ranges from 1 to 4 μg/m^3 for PM1, and 10 μg/m^3 for PM10, where PM1 and PM10 represent particulate matter measured with aerodynamic diameters smaller than 1 and 10 μm, respectively.

Above 2,500-m altitude, the marine aerosol mass concentration stays about constant with increasing altitude at ≈1 μg/m^3 (ref. 10-1).

10.3.2.3 Sea Salt Formation. Most airborne sea salt droplets are formed by the breaking of myriads of air bubbles at the surface of the sea. The bubbles are produced by whitecaps or breaking waves, and, to a lesser extent, by rain or snow falling on the water. During the warming of water in the spring, it has been hypothesized that bubbles might form if air supersaturation occurs based on the inverse relation between the solubility of air in water and temperature. Whitecaps begin to appear when the wind speed is >3 m/s, and at ≈8 m/s, about 1 percent of the sea is covered with whitecaps. On average, the world's oceans have a whitecap coverage of ≈3.5 percent. The whitecap source area increases approximately with the square of the wind speed (ref. 10-38).

The bubble spectrum in a whitecap extends from <0.1 mm to at least 10-mm diameter. The bubble flux to the ocean surface is typically estimated to be about 2×10^6 m^{-2}s^{-1}, with most bubbles being <1 mm. Upon bursting at the water surface, some of the surface free energy of a bubble is converted into the kinetic energy

of a jet of water that rises rapidly from the bottom of the collapsing bubble cavity. The jet becomes unstable and, depending upon bubble size, breaks into a set of 1 to 10 jet drops. Generally, the smaller the bubble the more jet drops are produced. The first (top) jet drop is ≈1/10 the bubble diameter, with the maximum jet drop ejection height increasing with bubble size, reaching nearly 20 cm (for 2-mm bubbles) (ref. 10-38). Initial jet drop vertical velocities can range from 5 to 20 m/s (ref. 10-37). For bubbles greater than 7 or 8 mm, no jet drops are produced. Also, film drops are produced by the bursting of the thin film of water that separates the air in the bubble from the atmosphere. Most film drops are <4 μm diameter; however, some can be >100 μm. It has been suggested that for bubbles <7 mm, the maximum film-drop production (≈75) is for bubbles in the narrow size range of 2 to 2.5 mm.

Most of the mass of the salt aerosol in the marine atmosphere probably originates from jet drops, while the most aerosol number concentrations probably come from the smaller film drops (ref. 10-38). The larger spume drops are produced by direct tearing from the wave tips under high wind speeds in excess of 9 m/s (ref. 10-50). The largest drops (≈1 cm diameter) are produced by splashing, not by bubbles, and play little role since they return to the sea almost immediately. The concentration of all bubbles is $\approx 10^8/m^3$. The film drop rate of production has been estimated at $\approx 2 \times 10^4/m^2 s$, whereas the jet drop rate of production in whitecap regions is $\approx 1.5 \times 10^6/m^2 s$ (ref. 10-38). Both the jet and film drops ejected into the atmosphere are mixed upward by convection and turbulence.

The equivalent RH over a sea water surface is ≈98 percent (ref. 10-38). If the ambient RH is less than approximately 70 to 74 percent, the drops evaporate and become supersaturated with sea salt—a phase change occurs to produce sea salt particles. If humidities exceeding 75 percent are then encountered, the sea salt particles again become droplets (ref. 10-49). Sea salt particle size is directly related to the ambient RH (ref. 10-42). The hardness of sea salt is given in table 10-3.

Sea salt particles, unlike dust, are "hygroscopic." Their size will change with the ambient RH. The growth of sea salt particles with RH is approximated by the following equation:

$$r_w = \left\{ \left(\left[C1 r_d^{C2} \right] / \left[C3 r_d^{C4} - \log \mathrm{RH} \right] \right) + r_d^3 \right\}^{1/3} , \tag{10.8}$$

where

r_w = wet particle radius (cm)
r_d = dry radius
RH = relative humidity (%)
$C1 = 0.7674$
$C2 = 3.079$
$C3 = 2.573 \times 10^{-11}$
$C4 = -1.424$ (ref. 10-51).

The diameter of a salt particle is approximately one-fourth that of the parent sea water drop. Depending on RH, drops produced by the sea exist in the atmosphere as either sea water drops, brine drops, or sea salt particles, but they are all called sea salt particles. The mass concentration of salt (in $\mu g/m^3$) just above the ocean surface can be estimated from equation (10.9):

$$C = 4.26 \exp(0.16\, W) , \tag{10.9}$$

for wind speed (W) varying from 1 to 21 m/s (ref. 10-47).

Salt concentration increases exponentially with wind speed. Wind ranging from 1 to 35 m/s (at 600- to 800-m level aloft) encompasses a range of particle weight from 1 to 10^5 μg, representing drop sizes of ≈2 to >80 μm radius, which produce dry sea salt particles from 0.5 to >20 μm radius (ref. 10-38).

A relationship of the sea salt production rate has also been developed using only whitecap coverage and wind speed. This production rate is given by:

$$dF/dr = 1.373 W^{3.41} r^{-3} (1 + 0.057 r^{1.05}) 10^{1.19} e^{-B^2} \quad , \tag{10.10}$$

where

W = 10-m wind speed (m/s)
r = particle radius (μm)
B = (0.38 –log$r$)/0.65 (ref. 10-52).

10.3.2.4 Marine and Sea Salt Aerosols Versus Altitude. Atmospheric temperature inversions over the oceans, such as the tropical inversion, tend to keep sea salt particles below a few kilometers in altitude. Above such inversions, the particles are largely of continental origin, except near clouds or near the residues from dissipated clouds. Table 10-10 lists a few average concentrations of marine and sea salt aerosols with respect to altitude (refs. 10-49 and 10-50).

Since sea salt particle concentrations and size distributions also depend on the wind speed, figure 10-4 presents the mass concentrations at two altitudes (15 m and 600–800 m) as shown as a function of wind speed. The salt concentrations at altitudes of 600 to 800 m increase exponentially from a few micrograms per cubic meter at a wind speed of 5 m/s, to ≈600 μg/m^3 at winds of 35 m/s. Typical sea salt mass concentrations in the lowest 20 m of the atmosphere are around 10 to 20 μg/m^3, but they increase rapidly with wind speed. Number concentrations range from 10^5 to 10^6/m^3 for particles >4 μm as sea water drops, but at least 10 times more for smaller drops. (See table 10-10.) On-shore winds passing over a heavy surf zone can carry salt particles rising from the surf into shore areas with a salt concentration ≈100 times more than found in the air over the open sea, and equal or exceeding that found in hurricanes (refs. 10-49 and 10-50).

The sea salt mass concentration (C_{ss}) versus altitude (from 1 to ≈300 m height) and wind speed can be expressed on average as a power law relationship (for winds between 3.5 and 14 m/s) as:

$$C_{ss} = 5(6.3 \times 10^{-6} Z)^{(0.21 - 0.39 \log W)} \quad , \tag{10.11}$$

where C_{ss} is in μg/m^3, height (Z) is in meters, and wind speed (W) at 10-m height is in meters per second. Above 300 m, the sea salt concentration profile typically decreases exponentially with a 500-m scale height (ref. 10-38). No significant sea salt is found above 750 mb (≈2,560 m) (ref. 10-42).

10.3.2.5 Sea Salt Inversion. Since the marine air generally has a shallow temperature inversion aloft which strongly inhibits mixing to heights above 1,000 m, sea salt concentration decreases over the altitude range from 0.2 to >2,500 m as shown in figure 10-5. Figure 10-5 shows sea salt concentration versus altitude and wind speed, giving typical concentration values of >30 μg/m^3 at surface levels (under 14 m/s high wind conditions), and decreasing to <1 μg/m^3 at 2,500 m altitude. At lower wind speeds (≤8 m/s), a salt concentration inversion appears between approximately 300- and 600-m altitude (ref. 10-38). The average sea salt concentration (S) versus height (H) can be expressed as a power law relationship for wind speeds (W) ranging between 3.5 and 14 m/s as:

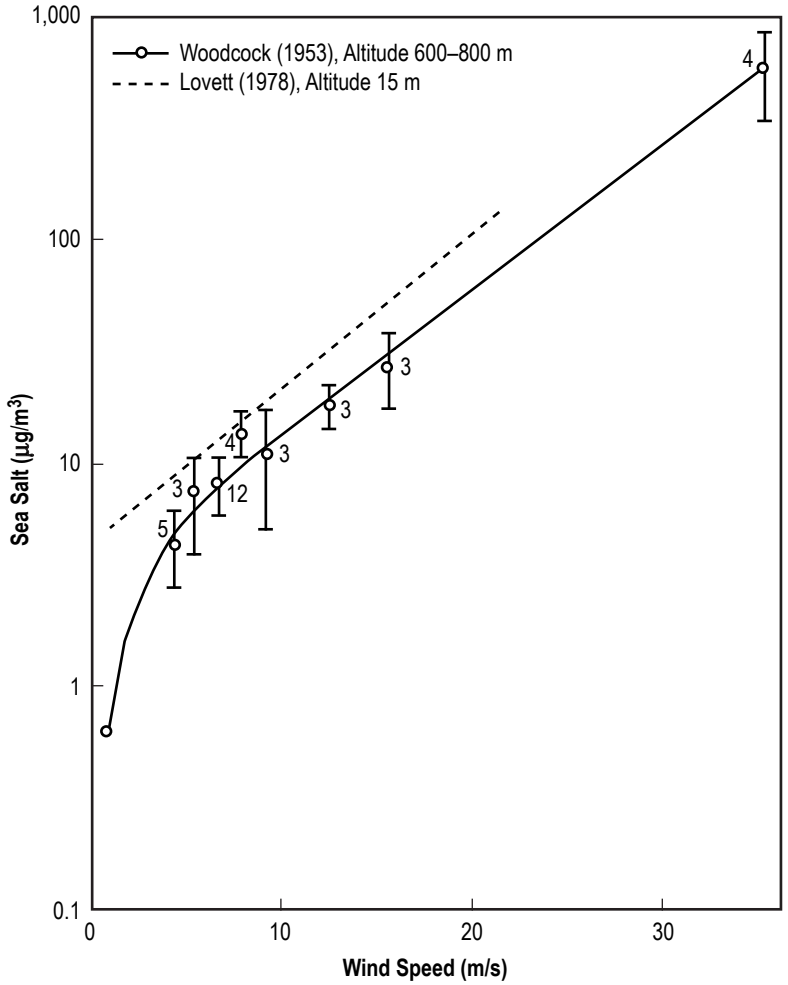

Figure 10-4. Sea salt concentration at two altitudes as a function of wind speed near the surface of the sea. The number of observations averaged for each data point is given, as well as standard deviation (ref. 10-34).

$$S = 5(6.3\times10^{-6}\,H)^{\,(0.21-0.39\log W)}\ , \tag{10.12}$$

where H is height in meters and W is wind speed in meters per second.

10.3.2.6 Salt Fog. Fog developing over a coastal area can be influenced by the marine environment and can contain sea salt (NaCl) which can degredate equipment and materials. Salt fog, humidity, and atmospheric corrosive agents, such as sulphur, act against printed wiring boards and metalwork in causing failures and damage. Humidity can cause corrosion through oxidation and galvanic corrosion, and can result in short circuits with the presence of electrolytes. Salt fog can cause typical failure modes in equipment by either accelerating the corrosion process and/or short circuit—through the formation of a salt bridge—electrical connections. Coatings and finishes are the mitigation techniques for salt fog (ref. 10-53).

Most types of fog form when the RH reaches 100 percent at ground level. Fog can form quickly and can dissipate just as rapidly. An important exception to the general rule is sea fog. This is due to the peculiar effect of salt. Clouds of all types require minute particles upon which water vapor can condense. Over the ocean

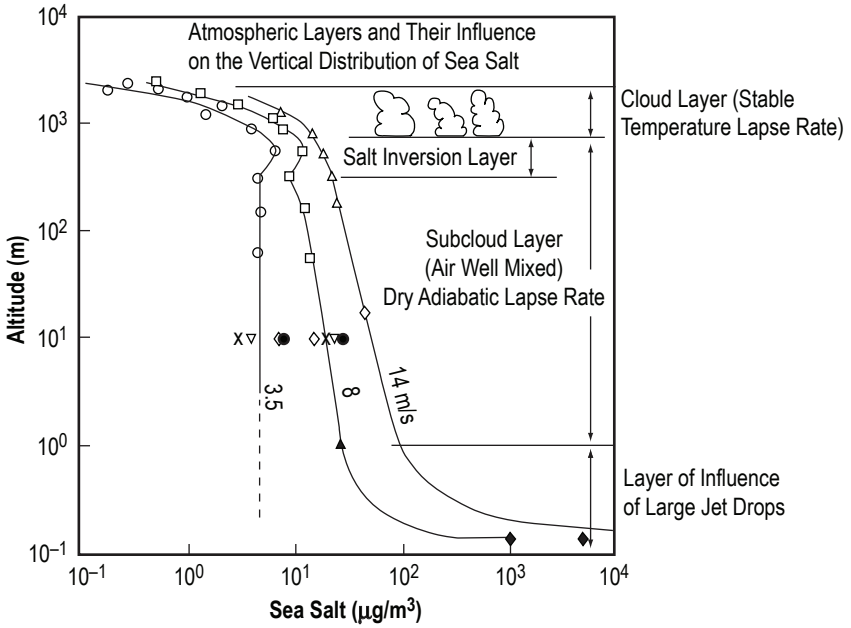

Figure 10-5. Sea salt concentration as a function of altitude and wind speed (altitude ranges from <0.2 to >2,000 m) (ref. 10-38).

surface, the most common particles are salt from salt spray produced by breaking waves. Except in areas of storminess, the most common areas of breaking waves are located near coastlines, hence the greatest densities of airborne salt particles are there. Condensation on salt particles has been observed to occur at humidities as low as 70 percent, thus fog can occur even in relatively dry air in suitable locations such as the California coast. Typically, such lower humidity fog is preceded by a transparent mistiness along the coastline as condensation competes with evaporation, a phenomenon that is typically noticeable in the afternoon (ref. 10-54).

The salt fog test (method 509.3) as outlined in MIL-STD-810E (ref. 10-55) should be followed to determine the resistance of equipment to the effects of an aqueous salt atmosphere. This type of atmosphere could impose three degradation effects on materials and equipment; i.e., corrosion, electrical, and physical effects.

The characteristics of marine fog droplets and salt nuclei are presented in references 10-56 and 10-57 Sections 7.8 and 7.9 present a general and a location-specific discussion of fog.

10.3.3 Sand and Dust

10.3.3.1 Impact/Effects of Sand and Dust. Sand storms contain large amounts of dust and sand particles (crustal-derived aerosols, mainly silicates) that can be dispersed over regional or global scales. Dust/sandstorms mainly present health and transportation hazards. They reduce visibility, layer on skin and clothes, infiltrate buildings, and find their way into food and drinking water. Pounding sand and dust storms also wear away textile materials, and wreak havoc on machinery, electronics, and buildings. Blowing sand and dust scour surfaces and wear away protective coverings; i.e., glass becomes frosted, wire wrap wears away, and electric circuits ground out. Dust compacts easily, solidifies with little added moisture, and combines with lubricants, often resulting in clogged and/or jammed equipment and machinery. Dust and sand storms also set up electrostatic discharges that, while not typically fatal, can have negative consequences in fueling operations and computer or electrical systems (ref. 10-58). The world's deserts graph can be found in reference 10-59. In urban areas, the resuspension of dust by traffic or other methods must also be considered (ref. 10-16).

10.3.3.2 Definitions. There is a slight difference between the definition of a sandstorm and a dust storm. A sandstorm is basically a wind storm that carries sand through the air, forming a relatively low sand cloud near the ground. Typical sandstorms only reach heights of up to 15 m (49 ft), and contain sand particles with average sizes between 0.15 and 0.3 mm, with wind speeds exceeding 4.5 m/s (10 mph). They generally last as long as wind speeds persist. Dust storms are a similar phenomena but have distinctly different characteristics. They form in semiarid/arid regions where small dust (and sand) particles are literally blown into the air. Dust particles are small enough to be lifted aloft by currents of turbulent air and are carried into suspension. Thunderstorm vertical downdrafts of chilled air may locally strike the ground with velocities of 11.2 to 22.4 m/s (25 to 50 mph), thereby causing fine particles to be swept upwards hundreds or thousands of feet into the air (ref. 10-58).

10.3.3.3 Introduction. Dust and sand are transported through the air by wind blowing across a disturbed soil area. Strong winds are required to uplift the submicron sand and dust particles, because strong adhesive forces exist between the particles and the ground (refs. 10-58 and 10-60). Dense vegetation (shelterbelts) and ground cover also provide considerable protection from strong winds (refs. 10-61 and 10-62). The concentration of these particles is highly dependent on wind speed—the higher the speed, the greater the volume of sand and dust, the nature of the soil, and the amount of moisture in the soil and in the air (ref. 10-63). Threshold air velocities for the input of soil particles into the air increase with different types of soil surfaces in the following order: disturbed soils, except disturbed heavy clay soils; sand dunes; alluvial and aeolian sand deposits; disturbed playa (dry lake) soils; skirts of playa centers; and desert pavements (alluvial deposits) (ref. 10-64).

Some of the finest beach sand is ≈90 μm in diameter, which places it into the particle pollution size of "coarse" particles (2.5 to >40 μm). Particulate matter concentrations can increase dramatically due to natural episodic (or human caused) events which includes rare dust/sand storms. Arid desert conditions in the southwestern United States make this region more vulnerable to wind-blown dust than other regions of the nation. California experiences dust in two general regions. One region extends into southwestern Arizona and covers all southeastern California with maxima north of the Salton Sea and the western Mojave Desert. The second region is situated in central California. Figures 10-6 through 10-8 give maps on the characteristics—probability and durations—of dust storms in the southwestern United States that reduce the visibility to <1 km (<0.625 mi). Figure 10-9 presents an actual photo of a north Texas dust storm swirling in a counterclockwise direction and moving toward the northeast as it sweeps into Oklahoma. The image was taken on January 1, 2006, from the Aqua satellite and measured ≈500 km (300 mi) across. It has been determined from satellite imagery that the source regions for most of the United States observed winter and spring sand/dust storms originates from an area of northeastern Mexico, which includes some areas in southern New Mexico and western Texas (ref. 10-66). Most dust events are caused by passage of weather fronts and troughs and down mixing of upper-level winds. Cyclone development and thunderstorms result in the most dramatic dust clouds with the lowest visibilities (ref. 10-67). Dust sources from the southwestern United States and northwestern Mexico are only recently becoming well characterized by satellite imagery, especially during the windy seasons of winter and spring. The mechanical analyses of dune sands at White Sands dune field, New Mexico, has grain sizes ranging from clay through very coarse, with the dominant grain size being medium (being up to 89 percent medium sand in some of the samples taken) (ref. 10-68).

10.3.3.4 Haboob. Like many semiarid climates in the southwestern United States, Whites Sands, NM, is subject to extreme events, which includes dust and sand storms. A common sand storm found in the Sahara Desert and in the southwestern United States is called a haboob (Arabic for "phenomena" and "wind"), which is associated with a convective thunderstorm with gusty downdrafts (downbursts with average winds of 35–50 kt (18–26 m/s)) but no rain, since it evaporates before reaching the ground. This type of storm can be 96–145 km (60–90 mi) wide. Their average height extends from 1.52 to 2.44 km (5,000 to 8,000 ft) at the peak of the event, but has been recorded as high as 4.6 km (15,000 ft). The average hoboob duration is ≈3 hr, and visibility improves

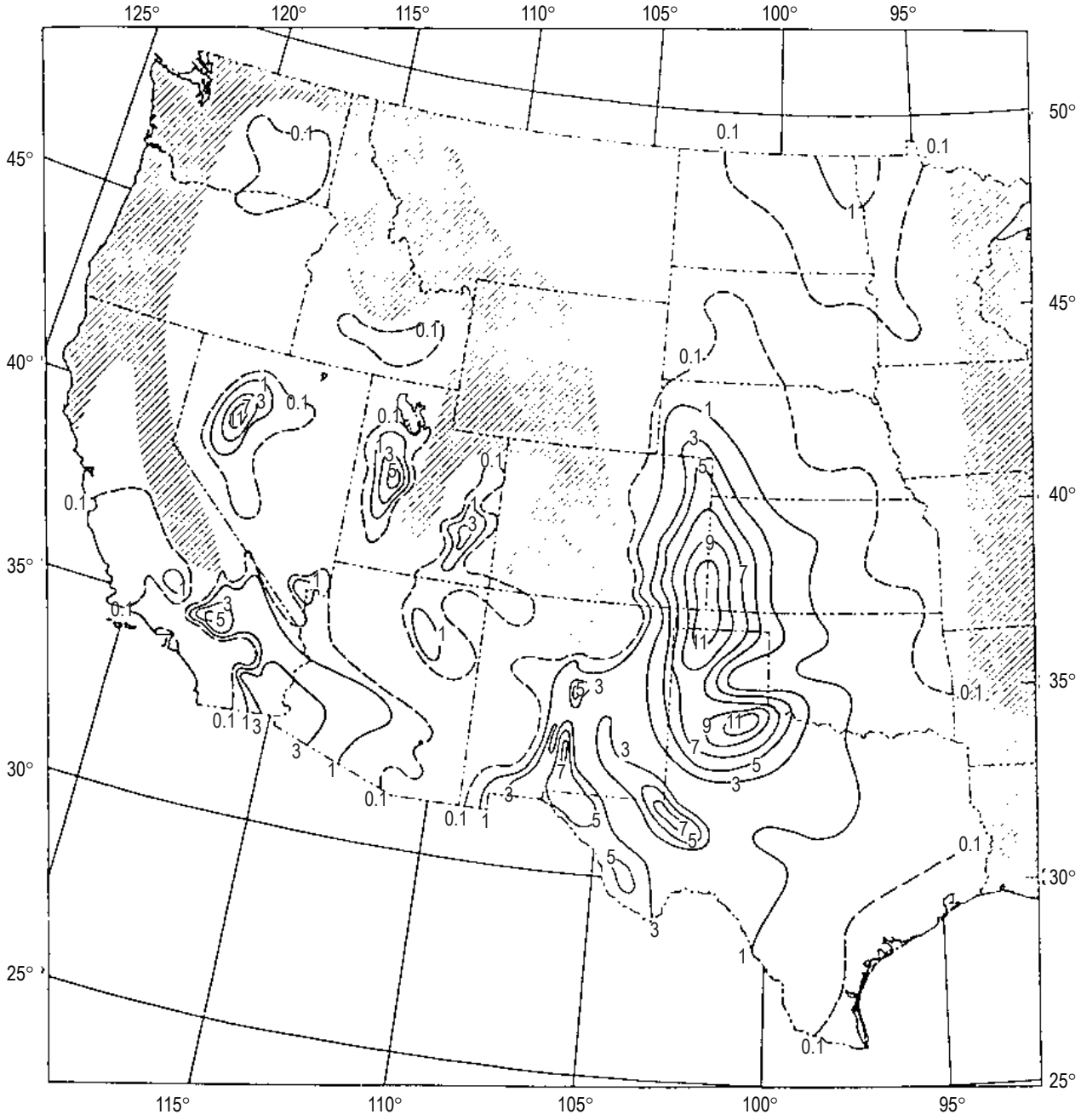

Figure 10-6. Annual average number of hours of dust episode visibility <1 km (<5/8 mi) in the western United States (ref. 10-62).

soon after passage of the gust front. Most dust particles within these storms range from 10 to 50 μm, but larger millimeter-sized particles can also be blown about. The finer particles settle at ≈0.08 m/s (≈1,000 ft/hr) when the haboob finally dissipates (ref. 10-59).

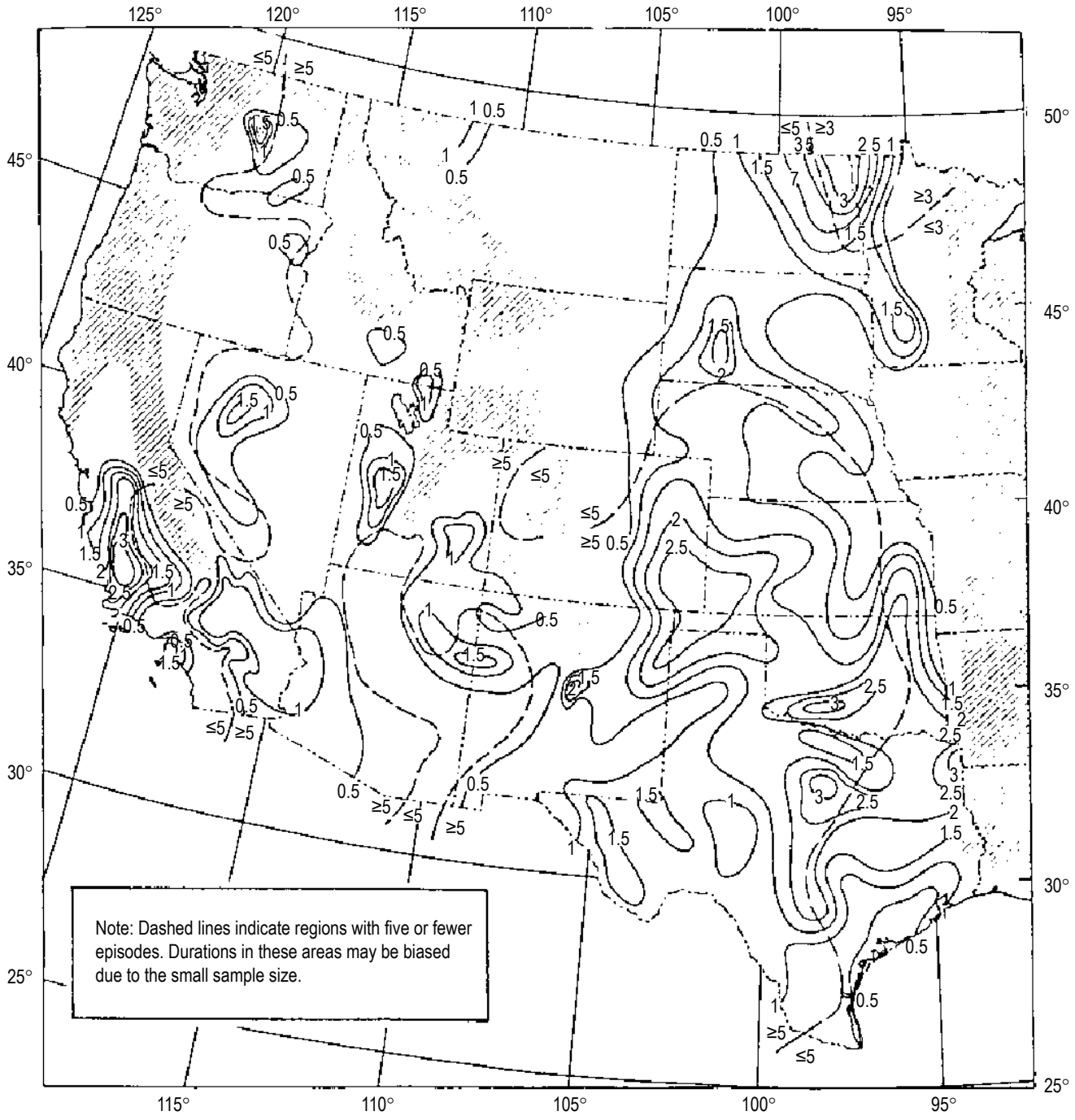

Figure 10-7. Average duration (hr) of dust episodes with visibility <1 km (<5/8 mi) in the western United States (ref. 10-62).

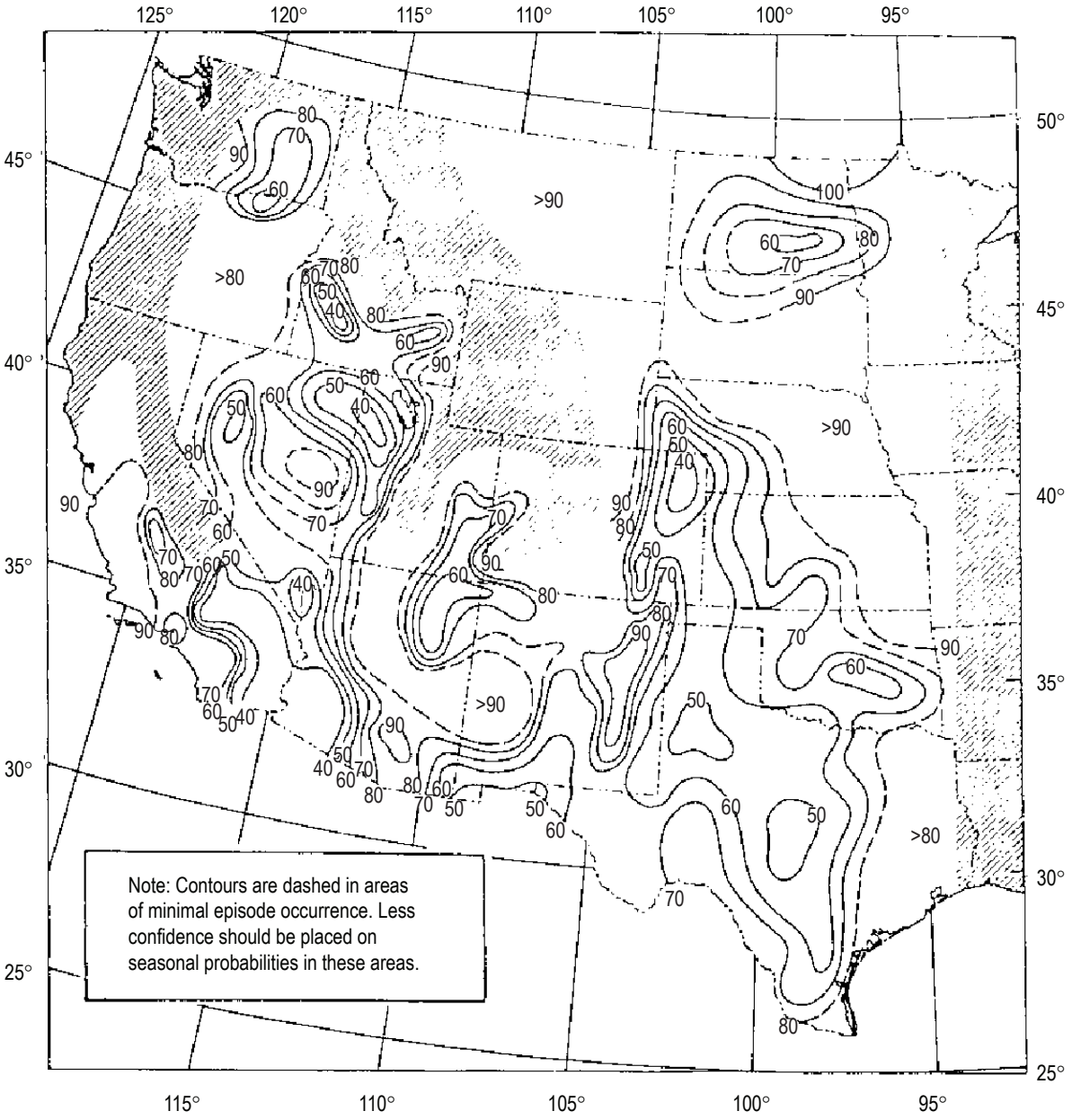

Figure 10-8. Probability (percent) of dust episodes with visibility <1 km (<5/8 mi) occurring during primary season in western United States (ref. 10-62).

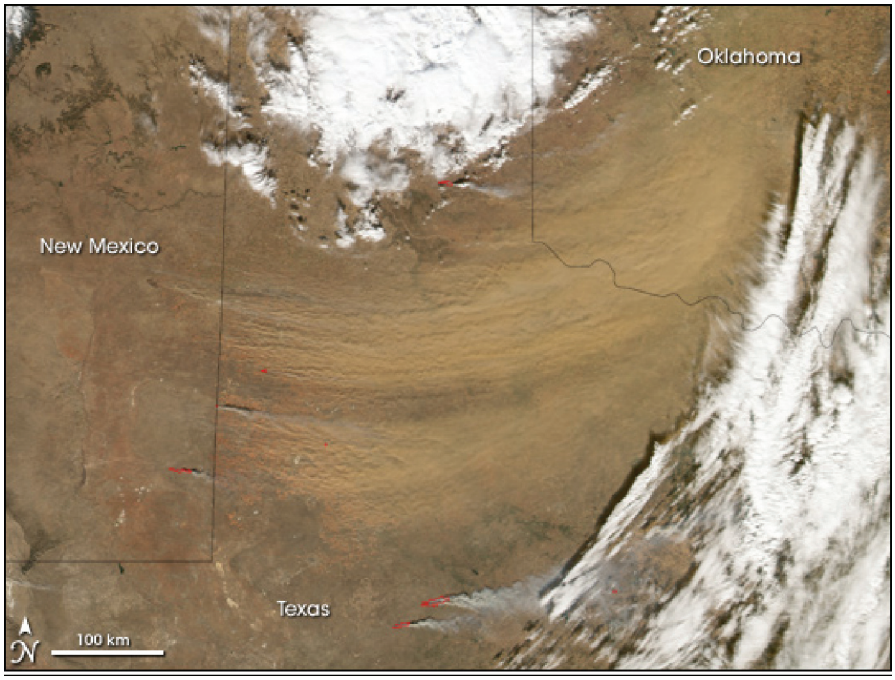

Figure 10-9. January 1, 2006, Texas dust storm as viewed by the Aqua satellite (ref. 10-65).

10.3.3.5 Dust Devils. Dust devils are a very common wind phenomenon that occur throughout much of the world. These dust-filled vortices, created by strong surface heating, with clear skies and light winds, are generally smaller and less intense than a tornado. They have typical diameters from 10 to 300 ft, with an average height of approximately 150–300 m (500–1,000 ft), and last only a few minutes before dissipating, although some have persisted an hour or more. Wind speeds in larger dust devils can reach 27 m/s (60 mph) or greater (ref. 10-67). Many detailed characteristics of dust devils can be found in reference 10-69.

10.3.3.6 Global Dust Storms. The effects of dust storms are mostly in the lower 2 km of the atmosphere, although fine dust can reach great heights and travel great distances. Giant sand storms from the Sahara Desert can blow across the Atlantic to South America, the Caribbean, and the southeastern United States (normally in summer), transporting several hundred million tons of dust each year. Sandstorms originating in China's Gobi Desert occasionally cross the Pacific (normally in spring) to the United States (ref. 10-67). For Asian dust transported to the west coast of North America, about 30–50 percent of the dust mass has a diameter of 2.5 μm, which can represent a significant public health hazard to people with chronic respiratory problems (ref. 10-70). The April 6–7, 2001, sandstorm over north China was observed over an area of 1.34 million km^2, with a mean dust particle radius of 1.44 μm, and a mean optical depth (at 11 μm) of 0.79. The mean burden of dust was ≈4.8 tons/km^2 and the main portion of the storm contained 6.5 million tons of dust. This sandstorm reached the United States 2 wk later, blanketing areas from Canada to Arizona with a layer of fine particles (ref. 10-70).

10.3.3.6.1 Global Storm Properties. Globally speaking, the average height of a dust storm is 0.9 to 1.8 km (3,000 to 6,000 ft), and stronger storms have dust reaching 2.44–3.1 km (8,000–10,000 ft). Dust haze associated with extreme storms have been documented as high as 10–12 km (35,000–40,000 ft) (ref. 10-58). A major dust storm event can be classified as one with >1,000 $\mu g/m^3$, while a smaller dust event is 200–1,000 $\mu g/m^3$ (ref. 10-71). The larger the particles, the stronger the wind required to lift them into the air. However, for any long-range transport, there also needs to be considerable vertical motion. Summer dust storms are associated with a greater vertical motion due to higher temperatures and resulting convective currents, but are more

limited in areal coverage than in spring. Dust storms generally subside by midnight. On the edges of blowing dust and within 278 km (150 nmi) downstream, visibility is 0.8–4.8 km (½–3 mi). Beyond that, and as the dust settles, visibility quickly returns to 3.2–8 km (2–5 mi). See reference 10-59.

Visibility will often remain at 6–10 km (4–6 mi) in dust haze for days after a dust storm, and will settle when winds drop below the speed necessary to carry the particles. See reference 10-59. In summer, dust haze persists nearly constantly. Intense dust storms reduce visibility to near zero in and near source regions. Dust will settle when the winds die down to below the speed necessary to carry the particles. In general, the worst visibility occurs within 6 m (20 ft) of the surface and above that, particles begin to settle out into layers (by particle size) of progressively better visibility conditions. Slant range visibility is typically worse than straight-line visibility (ref. 10-64). Sandstorms occur in and mainly affect arid and semiarid areas in the middle latitudes and in inland desert areas. Dust storms are typically 200 km (124 mi) wide and can carry 20 to 30 m tons of dust (some up to 100 m tons). In areas under the protection of shelterbelts (hedge of trees designed to lessen the wind force), sparse forests can protect an area 24–38 times that of the height of the trees, which can reduce the wind speed by 34 to 41 percent on average (ref. 10-61). See reference 10-59 for wind speeds required to lift particles of varying sizes. The size limits of sand grains are given in table 10-11 (ref. 10-72).

Table 10-11. Size limits of sand grains (ref. 10-72).

Sand Type	Size	
	(mm)	(in)
Pebble, cobble, boulder	>4	>1/16
Granule	2–4	1/12–1/6
Very coarse sand	1–2	1/25–1/12
Coarse sand	1/2–4	1/50–1/25
Medium sand	1/4–1/2	1/100–1/25
Fine sand	1/8–1/4	1/200–1/100
Very fine sand	1/16–1/8	1/400–1/200
Silt	1/256–1/16	1/6,250–1/400
Clay	<1/256	<1/6,250

Wind speeds from 5.1 to 12.9 m/s (10 to 25 kt) will move dust and sand particles from 80 to 1,000 µm. Normally, wind shear creates the turbulence and horizontal roll vortices that loft the dust up and away from the surface. As a rule of thumb, if the wind at the surface is blowing 7.7 m/s (15 kt), then the wind at 305 m (1,000 ft) above the ground needs to be ≈15 m/s (≈30 kt). An unstable boundary layer (from extreme daytime heating) favors dust storm formation by producing vertical motions that are required to loft dust particles. A stable boundary layer, or a low-level temperature inversion, suppresses vertical motions and limits the vertical extent of dust lofting. A derived, modeling parameter that combines both "turbulent" and "unstable" properties is called "friction velocity." A friction velocity (u^*) of 60 cm/s is typically required to raise dust (ref. 10-59).

The size and density of sand-dust particles determine the movement pattern. Refer to table 10-12 for the movement and suspension of particles under a wind speed force of 15 m/s, in which the threshold wind velocity (15 cm above ground surface) can lift up and transport dust grains of 0.05–0.1 mm (diameter) is 3.5 to 4 m/s. There are three modes of transport, depending upon the particle's size, shape, and density. The suspension mode involving dust particles of <0.1 mm in diameter and clay particles of 0.002 in diameter are small in size and light in density, allowing them to be transported at altitudes up to 6 km and move over distances up to 6,000 km.

Table 10-12. Movement of soil particles under a wind force of 15 m/s (ref. 10-62).

Particle Size		Period of Suspension (time (s))	Comment/Description
(mm)	(in)		
0.1	3.9×10^{-3}	0.3–3	Fine sand
0.01	3.9×10^{-4}	0.83–8.3	Dust, can go up to 700 m high
0.001	3.9×10^{-5}	0.9–9.5	Fine clay can go up to 77 km high

Saltating particles (those between 0.01 and 0.5 mm diameter) leave the surface but are too large to be suspended. The remaining particles above 0.5 mm are transported in the creep mode; i.e., roll along the ground with the wind. About 50 to 80 percent of all soil being transported is carried in this creep mode (ref. 10-63). Reference 10-63 presents much more detailed information on dust and sand storms than is presented here. Table 10-13 summarizes the typical characteristics observed of the various dust-related storm phenomena.

Table 10-13. Typical/average characteristics of dust-related storm phenomena (refs. 10-57, 10-58, 10-63, 10-67, 10-68, and 10-70).

Local Phenomena	Height	Typical Particle Size	Wind Speed	Storm Width	Duration	Other Information
Dust storm	0–2 km (3K–6 kft)	80–1,000 μm	5–13 m/s (12–29 mph)	200 km (125 mi)	Day(s) to weeks	Small storm: 1,000 $\mu g/m^3$ Large storm: 200–1,000 $\mu g/m^3$
Sandstorm	15 m (50 ft)	150–300 μm	>4.5 m/s (>10 mph)	–	As long as winds persist	–
Haboob	1.5–2.4 km (5K–8 kft)	10–50 μm	Downdrafts of 18–26 m/s (40–58 mph)	97–145 km (60–90 mi)	Up to 3 hr	Dust settles at 85 mm/s (3.3 in/s)
Dust devil	150–300 m (500–1,000 ft)	–	Up to and >27 m/s (up to and >60 mph)	3–91 m diameter (10–300 ft diameter)	A few minutes	–

10.3.3.7 Global Dust Transport to the United States. Up to three billion tons of dust are blown (aeolian dust) around the world annually, and dust storms originating in Saharan Africa have increased tenfold over the past 50 yr, threatening human health and coral reefs thousands of miles away, and contributing to climatic change (ref. 10-73). Mauritania in North Africa, which had an average of two dust storms a year in the early 1960s, now has 80 per year.

Each year several hundred-million tons of African dust are transported westward at 3 to 4.6 km (10,000 to 15,000 ft) by easterly trade winds over the Atlantic to Florida, the Caribbean, Central America, and South America, creating many biological problems. The heavier particles quickly drop away, but the particles that survive the 5- to 7-day journey across the ocean are a hundred times smaller than the diameter of the finest human hair. Dr. Joe Prospero, University of Miami, has been measuring dust on the island of Barbados since 1965. His graph showed a dramatic increase in dust flux beginning with the onset of the North Africa drought that started around 1970, with peak years occurring in 1973, 1983, and 1987. Variations in dust concentration measured in the Caribbean and Western Atlantic correlate with rainfall deficits in North Africa, especially in the Sahel region. Satellite imagery shows that African dust is transported mainly toward the Caribbean and equatorial regions of South America during North American winter and spring, and then shifts north towards Florida and the southeast United States during the summer months of June through September (ref. 10-74). Figure 10-10 gives modeled summer seasonal mean surface dust concentration, based on a 22-yr simulation (1979–2000) of dust transport with the

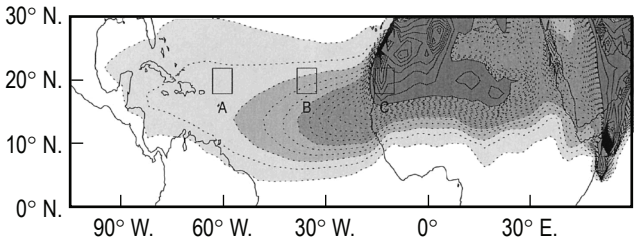

Contour Values:

Shading	Concentration µg/kg
Light	10 to 30
Light to Medium	30 to 60
Medium	60 to 200
Heavy	>200

Figure 10-10. Modeled seasonal mean of surface dust concentrations for the summer season (June, July, August, and September) from Africa to the United States (ref. 10-75).

transport model described in reference 10-75. High surface concentration values >200 µg/kg were initially simulated in North Africa.

The state of Florida receives more than 50 percent of the African dust that hits the United States. In July 2000 alone, nearly 8 million tons of dust from Africa's Sahara Desert reached as far west as Puerto Rico, which equaled approximately one-fifth of the total year's dust deposit. Winds blow ≈20 percent of dust from a Saharan storm out over the Atlantic Ocean, and ≈20 percent of that, or ≈4 percent of a single storm's dust, reaches all the

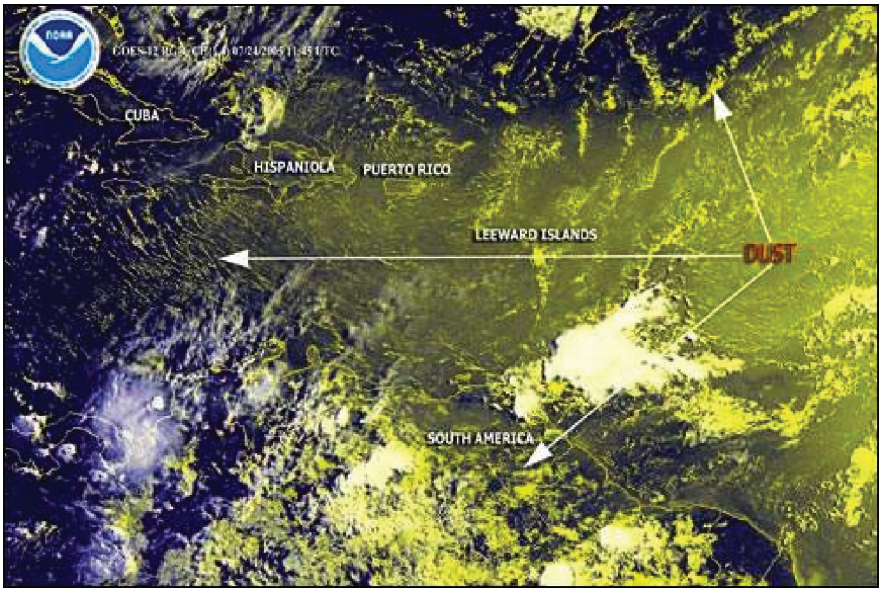

Figure 10-11. July 24, 2005, NOAA-GOES image of African dust storm arriving in the western Atlantic.

way to the west side of the Atlantic. Once the African dust cloud is over the ocean, the cloud can be 1.6–3.2 km (1 to 2 mi) thick and can extend from 3 to several km (2 to several miles) above the sea surface (ref. 10-76). Figure 10-11 gives the July 24, 2005, NOAA-GOES image of an African dust storm arriving in the western Atlantic, where it was expected to pass mostly over the Caribbean and South Florida. North Central Florida would be on the periphery of the cloud. NASA's STS-114 Shuttle launch took place on July 26, 2005, at 10:39 a.m. EDT.

Springtime dust from Asia (China's Takla and Gobi Deserts) also affects clouds over the western United States and has extended inland and beyond (ref. 10-77). It takes about 5 to 7 days for the dust to reach the United States west coast (ref. 10-78). In April 2001, a dust storm from Asia blew across the United States and finally disappeared from satellite images after traversing two-thirds of the Atlantic toward England.

10.3.3.8 Saharan Dust and Thunderstorm Behavior in Florida. Scientists have discovered that tiny particles of dust from the Saharan Desert can affect thunderstorms in Florida in various ways. Dust can affect (1) the size of a thunderstorm's "anvil" or top, (2) the strength and number of warm updrafts (rising air), and (3) the amount of rain that builds up and falls from the "heat generated" or convective thunderstorms (refs. 10-79 and 10-80).

When Saharan dust is in the air, the thunderstorm anvils created by Florida's convective thunderstorms tend to be a little smaller in area, but they tend to be better organized and thicker. The researchers also noticed that the updrafts of warm, moist air that build into thunderstorms were stronger, and that there were more of these updrafts produced in the presence of the dust. The scientists concluded that the overall effect of the Saharan dust on the surface rainfall was to reduce it (ref. 10-80).

10.3.3.9 Dust Storms and Hurricanes. The Saharan air layer (SAL) (or Saharan outbreak) is a deep, well-mixed, warm, dry, and dusty layer that forms over the Sahara Desert and Sahel regions of North Africa during late spring, summer, and early fall, and usually moves out over the tropical Atlantic Ocean. As this air mass advances westward from the African coast via a midlevel easterly jet, it is undercut by cool, moist, low-level air. This forms a temperature inversion at the base of the SAL over the ocean surface. The SAL usually extends between 1,500 and 6,000 m (5,000 and 20,000 ft) vertically, with ≈50 percent less moisture than a typical tropical sounding and strong winds of ≈10–25 m/s (≈25–55 mph). SAL often covers a large area of the tropical Atlantic coincident with the Atlantic hurricane season. Satellite imagery reveals that when the SAL engulfs tropical waves, tropical disturbances, or preexisting tropical cyclones, its dry air, temperature inversion, and strong vertical wind shear can inhibit their ability to strengthen. The SAL's dry air can act to weaken a tropical storm by inhibiting updrafts in the storm, and may have a negative impact on intensification (ref. 10-81).

10.3.4 Volcanic Particles, Ash, and Gaseous Constituents

Volcanic eruptions are normally followed by an emission of dust or ash and release of significant quantities of reactive gases. The emission rate, occurrence, and size distribution of the ash cannot be predicted by common meteorological methods because of the unpredictable timing and the different intensities of volcanoes.

The plume from a volcanic eruption is composed of large particles, ash, and gases. The plume may reach an altitude of 55 km (35 mi). Its dispersion characteristics vary greatly by eruption type and local weather. The largest particles have local/small area debris footprints (≈1° lat, long). Ash fallout has a regional/subcontinental footprint. This was demonstrated by the Mount St. Helen's eruption in 1980. The plume height reached 27 km (17 mi) with an ejecta volume >10 km^3. Gaseous constituents and subsequent aerosol production from volcanoes can have global coverage (ref. 10-82).

During the few days following an eruption, the distribution of the ash and gases is concentrated around the volcanic site, but over the following few months, a 2- to 4-km layer is formed above the troposphere over much of the world (ref. 10-83). Although most volcanic aerosol is found in the stratosphere, some of the aerosol is transported to high tropospheric layers and into polar regions (ref. 10-7). More detailed volcanic particle and ash information is given in section 13.2.5.

Figure 10-12 gives a timeline of some of the volcanic stratospheric aerosol optical depths (at $\lambda = 0.55$ μm) over the last 150 yr. Also shown are the calculated PSC optical depths based on SAM II aerosol extinction profiles (at 1 μm) in the Arctic (ref. 10-84).

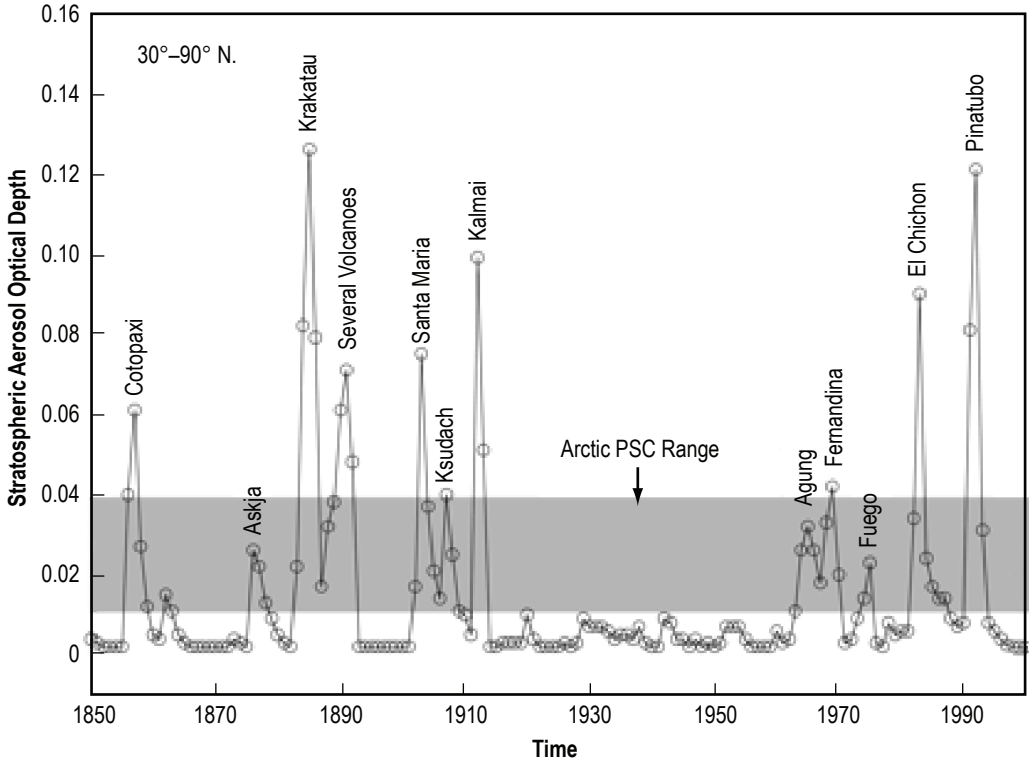

Figure 10-12. Stratospheric aerosol optical depth from major volcanic eruptions (ref. 10-84).

Table 10-14 presents some estimates of the annual tropospheric aerosol and gas emission rates from volcanoes, and from other sources, into the atmosphere. Table 10-15 presents estimates of the annual volcanic SO_2 release rates into the atmosphere (ref. 10-85).

10.3.5 Combustion and Other Man-Induced Aerosol

Secondary and combustion aerosols are formed by three major processes: gas-to-particle conversion resulting from physical or chemical changes, condensation of a supersaturated gas, and direct emissions of solids or liquids from the combustion sources (ref. 10-16). The particles resulting from primary combustion are carbonaceous (soots) or noncarbonaceous (fly-ash). The inorganic ionic aerosols, which include sulfate and nitrate aerosol particles, are produced by secondary processes through condensation. These aerosols are usually submicron size unless further aggregation of the particles occurs. The number and mass concentrations are highly dependent on location and time (ref. 10-91).

Table 10-14. Estimates of some tropospheric aerosol and gas emission rates from volcanoes and other sources (ref. 10-85).

Material	Mean Annual Emission Rate (Tg/yr)*	Range (Tg/yr)
Primary particle emissions:		
Sea salt	3,340	1,000–6,000
Soil dust	2,150	1,000–5,000
Carbonaceous aerosols	150	66–220
Fine ash**	20	NA
Volcanic sulfate return flux***	0.5–2	0–25
Gas-particle conversion emissions:	(Tg S/yr)	(Tg S/yr)
Biogenic sulfides	25	12–42
Anthropogenic SO_2	79	60–110
Volcanoes (SO_2), troposphere only	5–10	3–25

*Tg/yr = terragrams per year: 1 Tg = 10^{12} g = 10^6 metric tons. S = sulfur.
**Fine ash production from small volcanic eruptions.
***Time-averaged volcanic sulfate return flux to the upper troposphere from the stratosphere.

Table 10-15. Estimates of volcanic SO_2 release to the atmosphere* with range values** (ref. 10-85).

All Volcanic Emissions			Sporadic Volcanic Emissions***,† (Tg S/yr)	Total Volcanic Emissions‡ (Tg S/yr)
Continuously Erupting (Tg S/yr)	Nonerupting (Tg S/yr)	Total (Tg S/yr)		
1.2	3.4	4.6	4.8	9.4
Range: NA	Range: NA	Range: 3–4.7	Range: 2–6.3	Range: 6.7–10.5

*Estimates are from Stoiber et al. (ref. 10-86).
**Range values include estimates from Andres and Kasgnoc (ref. 10-87) and Halmer et al. (ref. 10-88).
***Includes both small eruptions that release SO_2 only to the troposphere, and large eruptions that release SO_2 to the stratosphere.
†The time-averaged sulfur flux to the stratosphere from large eruptions is ≈0.5–2 Tg S/yr, from Halmer et al. (ref. 10-88) and Pyle et al. (ref. 10-89).
‡Malmer (ref. 10-90) presents all estimates of volcanic gas SO_2 emissions into the atmosphere over the last 30 yr, which range from 1.5–50 Tg S/yr.

The AMS "Glossary of Meteorology" defines pyrocumulus (or pyroconvection) as a cumulus cloud formed by a rising thermal from a fire, or enhanced by buoyant plume emissions from an industrial combustion process. This process can inject substantial amounts of smoke into the upper troposphere and lower stratosphere.

Industrial and anthropogenic activities in eastern North America provide a major source of secondary and combustion aerosol. Atmospheric pollutants tend to be trapped beneath atmospheric temperature inversions. Incidents of severe smog usually are associated with such inversions. In the Los Angeles Basin, the pollutants are frequently trapped and cannot disperse because the Basin is surrounded on the north, east, and south by mountain ranges higher than the inversions, with frequent prevailing easterly winds.

The firing of solid rocket motors (SRMs) during a rocket launch or static test is an example of an emission source which is of particular importance for aerospace activities. The byproducts of the SRMs include a significant amount of gaseous hydrogen chloride (HCl) and particulate Al_2O_3. The mass fractions of HCl and Al_2O_3 in SRM exhaust are 0.21 and 0.3, respectively. In test and launch configurations that utilize substantial amounts of cooling or sound suppression water, or when rain, fog, or other natural sources of water are present,

the HCl gas and Al_2O_3 particulates will combine with the water, yielding an acidic deposition which will be dispersed by the exhaust plume over the facility and may be carried downwind as well. The amounts and location of deposition are strongly influenced by the configuration of the water spray, as well as by wind and other meteorological factors. Concentrations of a few deposition spots per square centimeter are typical within a few kilometers of a Shuttle launch. In one extremely windy case (STS-2), trace amounts of deposition were found up to 22 km (14 mi) downwind from the launch site. See section 11 for additional discussion.

For the aerospace design engineer, the most serious issue is usually the heavy deposition that occurs within 1 km (0.6 mi) of the firing location (for systems like the Shuttle which use large quantities of sound suppression water). For the Shuttle, the initial deposition is usually about one-third Al_2O_3 solids by volume in a moderately acidic (≈2 N) solution. Once dispersed over the facility, the solution generally evaporates quite rapidly. However, the water vaporizes more rapidly than the acid, resulting in a highly concentrated acidic solution for a short time—typically a few minutes on an open surface. The rate of evaporation depends on wind speed, ambient humidity, air temperature, and surface temperature. For the Shuttle launch system, there are sufficient quantities of deposition to impact both vegetation and animal life within 1 km of the launch facility, as well as to be corrosive to man-made structures. When the evaporation potential of the HCl is high (warm temperatures, low humidity, and moderate to high wind speeds), the immediate corrosion damage is typically not evident except on the most sensitive surfaces. However, even in this situation, the acid greatly increases the bonding between the Al_2O_3 particulates and the exposed surface. The surface may be coated with particulates that will not come off without direct scrubbing. This material is hygroscopic and will enhance corrosion over long periods of time. The addition of chemical additives to the water source is an option for reducing the bonding potential.

Gaseous HCl, which is either released during a firing or is the result of evaporation of this deposition, can also be a corrosion hazard at or near the facility, especially for sensitive electronic systems. Concentrations in the 5- to 10-ppm range have been measured at the Shuttle launch site in the hours following a launch. As one would expect, the most severe cases tend to correlate with times when the ground was wet from rain prior to the launch. Special precautions should be taken whenever extensive electronic equipment is to be located close to the launch pad or test site. Computer or other electronic equipment is usually very sensitive to HCl gas; an 8- to 10-hr exposure may render a system inoperable. Electronics are often sensitive to gas concentrations of 10 to 100 ppb, and concentrations above this level may be encountered intermittently for at least 2 days following an SRM firing. The threshold limit value for HCl exposure for workers is 5 ppm, and the exposure limit for the public is 1 ppm (ref. 10-92). See section 11 for a discussion of far field effects.

10.3.5.1 Acid Rain. Acid rain is rain with a pH in the range of 4 to 5 and is common in the northeastern United States, southeastern Canada, and in Europe. This rain is a result of the HNO_3 vapor, H_2SO_4 vapor, and HCl vapor being dissolved in rain drops. A pH of 5.6 has been selected to be the neutral point below which precipitation is said to be acidified (ref. 10-93). Acid rain can occur anywhere in the United States. The maximum concentrations occur in the northeastern United States over the Ohio River Valley, southern Ontario, Canada, and western New York State. The lowest (highest acidity) observed values of annual pH are between 4 and 4.2 and are centered in this area. Table 10-16 gives mean annual values of ion concentrations, deposition, and pH for this area in 1982 (ref. 10-93).

Acidic deposition can also occur in dry (in gaseous or particulate form) as well as in the wet form with precipitation. Acid rain measurements are generally expressed in terms of constituent concentration (mg/L) and deposition (g/m^2) of sulfate (SO_4^{2-}), or nitrate (NO_3^-), and hydrogen ions (H^+) in precipitation or in terms of pH.

The availability of the hydrogen ion allows acid rain to react with materials, including minerals and plants, that it comes in contact with. The other sulfate, nitrate, chloride, ammonium, and calcium ions are also more abundant in acid rain and contribute to its detrimental effects (ref. 10-93).

Table 10-16. Mean annual concentration and deposition in 1982 of hydrogen, sulfate, and nitrate ion in wet deposition for sites in the precipitation chemistry database, when pH <4.2 (ref. 10-93).

	Concentration (mg/L)	Deposition (g/m^2)
H^+	0.073	0.065
SO_4^{2-}	3.497	3.079
NO_3^-	2.240	1.984

Increases in the acidity of precipitation are caused by the many industrial, energy producing, and transportation-related activities that release acidic wastes into the atmosphere. At the present time, between 75 and 100 million metric tons of anthropogenic, or man-made, sulfur emissions are released into the atmosphere yearly (ref. 10-94). At the Eastern Range, annual average pH values of 4.58 are observed (ref. 10-95).

10.4 Gaseous Constituents

Gaseous as well as particulate matter can cause detrimental effects on aerospace vehicles and ground equipment due to various chemical reactions/processes. Nitrogen (N_2) and oxygen (O_2) make up ≈99 percent by volume (98.6 percent by weight) of the lower atmosphere. These two atmospheric constituents along with CO_2, H_2O, and ozone (O_3) are the gases of primary concern. H_2O is discussed in section 6 of this document. Stratospheric ozone depletion is discussed in section 8.5.1.1.

10.4.1 Average Atmospheric Constituents

The variability (range) of many atmospheric trace gases is quite large. However, given in table 10-17 are the average or typical gas concentration values expected at both ground level and with altitude. Seasonal, diurnal, locational, and other changes can all add to the variability of various atmospheric constituents. The mean values presented in table 10-17 are based on model information taken from references 10-94 and 10-96. An average constituent value at altitude can be obtained from table 10-16 by linear interpolation between the listed altitude/concentration values. See references 10-94 and 10-96 for more exact curves. Table 10-17 gases have a very large latitudinal and longitudinal gradient, due to short lifetimes, causing a large range of local concentrations with altitude to possibly exist.

Table 10-17. Average concentrations (standard atmosphere values) of various gaseous constituents from the Earth's surface up to 900-km altitude (refs. 10-94 and 10-96).

Constituent	Typical Concentration		Constituent	Typical Concentration	
	Altitude (km)	ppbv*		Altitude (km)	ppbv*
N_2	0 and above	7.81×10^8	COS	0	<0.05
O_2	0 and above	2.09×10^8	NH_3	0	0.5
				12 and above	<0.01
Rare Gases	0	Very small	H_2	0 to 90	560
O_3	0	27	CH_4	0	1,700
	7	50		10	1,700
	22	3,650		40	564
	40	7,300		50	210
	75	250		90	140
	90	700			
N_2O	0	320	SO_2	0	0.3
	9	320		30	0.01
	32	117		70	0.04
	49	5		90	0.002
	90	0.5			
NO	0	0.3	CO	0	150
	12	0.3		10	100
	18	0.2		21	12
	40	11		50	46
	70	11		90	5,840
	90	213			
NO_2	0	0.02	CO_2	0	330,000
	10	0.02		75	330,000
	18	0.8		90	310,000
	35	7.3			
	50	0.4			
	90	0.2			
H_2S	0	0.1	HNO_3 (vapor)	0	0.05
	2	0.03		15	0.45
	10	0.01		22	5.5
	26 and above	10^{-15}		50	0.06
				90	0.03
CS_2	0	0.07	H_2SO_4 (vapor)	0 to 90	Small except in localized areas
	14	0.03			
	32 and above	10^{-15}			

*ppbv=parts per billion volume.

1 km=0.621 mi.

REFERENCES

10-1. Seinfeld, J.H.; and Pandis, S.N.: *Atmospheric Chemistry and Physics: From Air Pollution to Climate Change*, John Wiley and Sons, New York, 1998.

10-2. Finlayason-Pitts, B.J.; and Pitts, J.N., Jr.: *Chemistry of the Upper and Lower Atmosphere*, Academic Press, San Diego, 2000.

10-3. Jacobson, M.Z.: *Fundamentals of Atmospheric Modeling*, Cambridge University Press, Cambridge, 2000.

10-4. Brasseur, G.P.; Orlando, J.J.; and Tyndall, G.S.: *Atmospheric Chemistry and Global Change*, Oxford University Press, New York, 2000.

10-5. American Institute of Aeronautics and Astronautics, "Guide to Global Aerosol Models (GAM)," *AIAA G-065-1999e*, 1999.

10-6. Baron, P.A.; and Willeke, K.: *Aerosol Measurement: Principles, Techniques, and Applications,* 2nd Edition, Wiley, New York, 2001.

10-7. d'Almeida, G.A.; Koepke, P.; and Shettle, E.P.: "Atmospheric Aerosols Global Climatology and Radiative Characteristics," pp. 11–24, A. Deepak, Publishing, Hampton, VA, 1991.

10-8. "U.S. Standard Atmosphere," United States Government Printing Office No. 003-017-00323-0, Washington, DC, October 1976.

10-9. Blifford, I.H.; and Ringer, L.D.: "The Size and Number Distribution of Aerosols in the Continental Atmosphere," *J. Atmos. Sci.*, Vol. 26, pp. 716–726, 1969.

10-10. Jennings, S.G.: "Physical Characteristics of the Natural Atmospheric Aerosol," TSLP: Final Technical Report, p. 2, March 1975–September 1976.

10-11. Kent, G.S.; and Yue, G.K.: "The Modeling of CO_2 Lidar Backscatter From Stratospheric Aerosols," *J. Geophys. Res.*, Vol. 96, No. D3, pp. 5279–5292, March 20, 1991.

10-12. Turco, R.: "Upper-Atmosphere Aerosols: Properties and Natural Cycles," Chapter 3B of "The Atmospheric Effects of Stratospheric Aircraft: A First Program Report," *NASA RP-1272*, pp. 63–91, January 1992.

10-13. Cadle, R.D.: *The Measurement of Airborne Particles*, Wiley-Interscience, New York, p. 342, 1975.

10-14. Lide, D.R.: *CRC Handbook of Chemistry and Physics*, 73rd Edition, CRC Press, Inc., Boca Raton, FL, 1992.

10-15. Ford, W.E.: *Dana's Manual of Mineralogy*, 13th Edition, John Wiley & Sons, Inc., New York and Chapman & Hall, London, 1912.

10-16. Patterson, E.M.: *Size Distributions, Concentrations, and Composition of Continental and Marine Aerosols*, in Atmospheric Aerosols: Their Formation, Optical Properties, and Effects, A. Deepak (ed.), Spectrum Press, Hampton, VA, 1982.

10-17. Bohren, C.F.; and Huffman, D.R.: *Absorption and Scattering of Light by Small Particles*, Wiley Interscience, New York, 1998.

10-18. Mishchenko, M.I.; Hovenier, J.W.; and Travis, L.D. (eds.), *Light Scattering by Nonspherical Particles*, Academic Press, New York, 2000.

10-19. Liou, K.N.: *Radiation and Cloud Processes in the Atmosphere*, Oxford University Press, New York, 1992.

10-20. Kattawar, G.W. (ed.): *Selected Papers on Multiple Scattering in Plane-Parallel Atmospheres and Oceans*: *Methods*, SPIE Milestone Series, Vol. MS42, SPIE Press, Washington, 1991.

10-21. Kattawar, G.W.; and Adams, C.N.: "Stokes Vector Calculations of the Submarine Light Field in an Atmosphere-Ocean With Scattering According to a Rayleigh Phase Matrix: Effect of Interface Refractive Index on Radiance and Polarization," *Limnol. Oceanogr.*, Vol. 34, pp. 1453–1472, 1989.

10-22. "Interagency Monitoring of Protected Visual Environments," <http://vista.cira.colostate.edu/improve>, Accessed 2007.

10-23. Calle, L.M.: NASA KSC Corrosion Technology Laboratory Web site: <http://corrosion.ksc.nasa.gov/>, 2008.

10-24. Calle, L.M.: *Corrosion Control in Space Launch Vehicles, in Corrosion Control in the Aerospace Industry*, S. Benavides (ed.), Woodhead Publishing Limited Abington Hall, Abington, Cambridge, CB21 6AH, UK, 2008.

10-25. Pile Buck International, Inc., "Corrosion and Protection of Sheet Piling," <http://pz27.pilebuckinternational.com/maintenance/corrosion.php>, accessed 2007.

10-26. MATCOR, "Protecting NASA Signature Building From Corrosion," MATCOR Corrosion News, pp.1 and 3, <http://www.matcor.com>, Fall 2006.

10-27. Grandt, A.F.: "Fundamentals of Structural Integrity—Damage Tolerant Design and Nondestructive Evaluation," Wiley-Interscience, 2003.

10-28. Dickinson, M.J.: "Local Atmosphere Salt Profile," Shuttle Study Task No. 0031, Addendum II, KSC SST-0031 Addendum 2, October 1976.

10-29. Coburn, S.: *Atmospheric Corrosion,* in *Metals Handbook*, Ninth Ed., Vol. 1, Properties and Selection, Carbon Steels, American Society for Metals, Metals Park, OH, p. 720, 1978.

10-30. Keller, V.W.: MSFC EV44 Internal White Paper, 2007.

10-31. Morrison, J.D.: "Report on the Relative Corrosivity of Atmospheres at Various Distances From the Seacoast," NASA Kennedy Space Center, Report MTB 099-74, January 1980.

10-32. Pohlman, S.L.: *General Corrosion*, Metals Handbook, Ninth Edition, Vol. 13–Corrosion, ASM International, United States, pp. 80–83, 1987.

10-33. Money, K.L.: *Corrosion Testing in the Atmosphere*, Metals Handbook, Ninth Edition, Vol. 13–Corrosion, ASM International, United States, pp. 204–206, 1987.

10-34. Prata, A.J.: "Observations of Volcanic Ash Clouds in the 10–12 μm Window Using AVHRR/2 Data," *International J. Remote Sensing*, Vol. 10, Nos. 4 and 5, pp. 751–761, 1989.

10-35. Guelle, W.; Schulz, M.; and Balkanski, Y.: "Influence of the Source Formulation on Modeling the Atmospheric Global Distribution of Sea Salt Aerosol," *J. Geophys. Res.*, Vol. 106, No. D21, pp. 27,509–27,524, November 16, 2001.

10-36. Shankar, U.; Bhave, P.V.; Vukovich, J.M., and Roselle, S.J.: "Implementation and Initial Applications of Sea Salt Aerosol Emissions and Chemistry Algorithms in the CMAQ v4.5-AERO4 Module," University of North Carolina, <www.cep.unc.edu/empd>, Accessed 2007.

10-37. Lykossov, V.: "Atmospheric and Oceanic Boundary Layer Physics – Chapter 3," in *Wind Stress Over the Ocean*, I. Jones and Y. Toba (eds.), Cambridge University Press, pp. 54–81, 2001.

10-38. Banchard, D.C.; and Woodcock, A.H.: "The Production, Concentration and Vertical Distribution of the Sea-Salt Aerosol," *Annals New York Academy of Sciences*, Vol. 338, No. 1, pp. 330–347, 1980.

10-39. Prospero, J.M.: "The Chemical and Physical Properties of Marine Aerosols: An Introduction—Chapter 2, in *Chemistry of Marine Water and Sediments*, A. Gianguzza et al. (eds.), Springer-Verlag Berlin, Heidelberg, pp. 35–82, 2002.

10-40. Cawse, P.A.: "Inorganic Particulate Matter in the Atmosphere—Chapter 1," in *Environmental Chemistry—Vol. 2*, H. Bowen (ed.), The Royal Society of Chemistry, 1982.

10-41. Heintzenberg, J.; Covert, D.C.; and Van Dingenen, R.: "Size Distribution and Chemical Composition of Marine Aerosols: A Compilation and Review," *Tellus*, Vol. 52B, pp. 1104–1122, 2000.

10-42. Grini, A.; Myhre, G.; Sundet, J.K.; and Isaksen, I.S.A.: "Modeling the Annual Cycle of Sea Salt in the Global 3D Model Oslo CTM2: Concentrations, Fluxes, and Radiative Impact," *J. Climate*, Vol. 15, pp. 1717–1730, July 1, 2002.

10-43. Duce, R.A.: "SCOPE21—The Major Biogeochemical Cycles and Their Interactions," Chapter 16, Biogeochemical Cycles and the Air-Sea Exchange of Aerosols, <www.icsu-scope.org/downloadpubs/scope21/chapter16.html>, Accessed 2007.

10-44. Gong, S.L.; Barrie, L.A.; Prospero, J.M.; et al.: "Modeling Sea-Salt Aerosols in the Atmosphere 2 – Atmospheric Concentrations and Fluxes," *J. Geophys. Res.*, Vol. 2, No. D3, pp. 3819–3830, 1997.

10-45. O'Dowd, C.D.; Smith, M.H.; Consterdine, I.E.; and Lowe, J.A.: "Marine Aerosol, Sea-Salt, and the Marne Sulphur Cycle: A Short Review," *Atmos. Environ.*, Vol. 31, No. 1, pp. 73–80, 1997.

10-46. Jaenicke, R.: "Problems of the Distribution of the Global Aerosol," *Russian Chemical Reviews*, Vol. 59, No. 10, pp. 959–972, 1990.

10-47. Jaenicke, R.: “Tropospheric Aerosols – Chapter 1,” in *Aerosol-Cloud-Climate Interactions*, P.V. Hobbs (ed.), Academic Press, Inc., NY, pp. 1–31, 1993.

10-48. Tardif, R.: “Interactions Between Aerosols and Fog,” RAP/UCAR ATOC 5600 Internet Class, Entitled: Physics and Chemistry of Clouds & Aerosols, Under Program in Atmospheric and Oceanic Sciences, University of Colorado at Boulder, 2007.

10-49. McGillis, W. (ed.): “The Surface Ocean-Lower Atmosphere Study,” Project 2.2 – Surface Spray In Situ Modeling Studies, <www.us-solas.org:8080/>, pp. 35–38, Accessed 2007.

10-50. Blanchard, D.C.: “The Ejection of Drops From the Sea and Their Enrichment With Bacteria and Other Materials: A Review,” *Estuaries*, Vol. 12, No. 3, pp. 127–137, September 1989.

10-51. Chuang, C.C.; and Grant, K.E.: “Simulations of Optical Properties of Dust and Sea Salt for Use in Global Climate Models,” in *Proceedings of 10th ARM Science Team Meeting*, pp. 1–5, San Antonio, TX, March 13–17, 2000.

10-52. Fitzgerald, J.W.: “Marine Aerosols: A Review,” *Atmospheric Environment*, Vol. 25A, No. 3/4, pp. 533–545, 1991.

10-53. Straznicky, I.: “Understanding the Elements of Ruggedization,” <www.milcotsdigest.com>, July–August 2006.

10-54. “Fog,” *Wikipedia*, <http://en.wikipedia.org/wiki/Fog>, 2007.

10-55. Military Standard: Environmental Test Methods and Engineering Guidelines, MIL-STD-810E, AMSC F4766, July 14, 1989.

10-56. Woodcock, A.H.: “Marine Fog Droplets and Salt Nuclei—Part I,” *J. Atmos. Sci.*, Vol. 35, pp. 657–664, April 1978.

10-57. Woodcock, A.H.: “Marine Fog Droplets and Salt Nuclei—Part II,” *J. Atmos. Sci.*, Vol. 38, pp. 129–140, January 1981.

10-58. NOAA Magazine, “*Dust Storms, Sand Storms and Related NOAA Activities in the Middle East*,” NOAA Commerce Dept., Story 86, April 7, 2003.

10-59. Boyer, J.: “Forecasting Dust Storms,” University Corporation for Atmospheric Research, 2003, <http://www.meted.ucar.edu/mesoprim/dust/print.htm>, Accessed 2007.

10-60. Twomey, S.: *Atmospheric Aerosols*, Elsevier Scientific Publishing Company, New York, p. 27, 1977.

10-61. Longjun, C.: “Large-Scale Sandstorm Disasters—Their Causes and Prevention Measures,” <www.Chinagate.com.cn>, 2005.

10-62. Changery, M.J.: “A Dust Climatology of the Western United States,” NUREG/CR-3211, National Oceanic and Atmospheric Administration, Prepared for U.S. Nuclear Regulatory Commission, National Climatic Data Center, Asheville, NC, April 1983.

10-63. Youlin, Y.; Squires, V.; and Qi, L.: "Global Alarm: Dust and Sandstorms from the World's Drylands," United Nations Publication, p. 14, August 2001.

10-64. Higdon, M.: "Rules of Thumb for Dust Storms," *AFCCC Strategic Weather Now*, Vol. 1, No. 3, 3 pp., March 2004.

10-65. "Dust Storm in Texas," NASA Earth Observatory, <http://earthobservatory.nasa.gov/Newsroom/NewImages/images.php3?img_id=17148>, January 5, 2006.

10-66. Rivera-Rivera, N.I.; Bleiweiss, M.P.; Hand, J.L.; and Gill, T.E.: "Characterization of Dust Storms Sources in Southwestern U.S. and Northwestern Mexico Using Remote Sensing Imagery," Paper P3.9 presented at 14th AMS Conference on Satellite Meteorology and Oceanography, Atlanta, GA, January 29–February 2, 2006.

10-67. EPA, "The Particle Pollution Report (Current Understanding of Air Quality and Emissions Through 2003)," EPA 454-R-04-002, December 2004.

10-68. McKee, E.D.: "Structures of Dunes at White Sands National Monument, New Mexico (and a comparison with structures of dunes from other selected areas), *Sedimentology*, Vol. 7, No. 1, pp. 1–69, 1966.

10-69. Balme, M.; and Greeley, R.: "Dust Devils on Earth and Mars," A U.S. Geological Survey Workshop, Flagstaff, AZ, September 19–20, 2005.

10-70. Gu, Y.; Rose, W.I.; and Smith, G.J.S.: "Retrieval of Mass and Sizes of Particles in Sandstorms Using Two MODIS IR Bands: A Case Study of April 7, 2001 Sandstorm in China," *Geophys. Res. Lett.*, Vol. 30, No. 15, p. 1805, 2003.

10-71. Draxler, R.R.; Gillette, D.A.; Kirkpatrick, J.S.; and Heller, J.: "Estimating PM10 Air Concentrations From Dust Storms in Iraq, Kuwait, and Saudi Arabia," *Atmospheric Environment*, Vol. 35, pp. 4315–4330, January 30, 2001.

10-72. National Park Service—Dept. of the Interior, White Sands Geology, Chapter 9, "Climate of White Sands: Figures 9-7 & 9-8," <http://www.nps.gov/archive/whsa/Geology%20of%20White%20Sands/Chap09/Chap09%20Main.html>, 2005.

10-73. Gaia, V.: "Dust Storms on the Rise Globally," <NewScientist.com> news service, August 20, 2004.

10-74. Schmidt, L.: "When the Dust Settles," NASA Earth Observatory, NASA GSFC DAAC, EROS Data Center, May 18, 2001.

10-75. Jones, C.; Mahowald, N.; and Luo, C.: "The Role of Easterly Waves on African Desert Dust Transport," *J. Climate*, Vol. 16, pp. 3617–3628, November 15, 2003.

10-76. NASA Goddard Space Flight Center, 2004 Earth Feature Story, "Africa to Atlantic, Dust to Dust," February 10, 2004.

10-77. Toon, O.B.: "African Dust in Florida Clouds," *Nature*, Vol. 424, pp. 623–624, August 7, 2003.

10-78. Taylor, D.A.: "Dust in the Wind," *Focus: Environmental Health Perspectives*, Vol. 110, No. 2, 8 pp., February 2002.

10-79. NASA Feature, “Saharan Dust Affects Thunderstorm Behavior in Florida,” January 10, 2005.

10-80. Van den Heever, S.; Carrio, G.G.; Cotton, W.R.; and Straka, W.C.: “The Impacts of Saharan Dust on Florida Storm Characteristics,” Paper Presented at 16th AMS Conference on Planned and Inadvertent Weather Modification, San Diego, CA, January 11, 2005.

10-81. Dunion, J.P.; and Velden, C.S.: “The Impact of the Saharan Air Layer on Atlantic Tropical Cyclone Activity,” *Bull. Am. Meteor. Soc.*, Vol. 85, No. 3, pp. 353–365, 2004.

10-82. Kessinger, C.; Tsui, T.; Herzegh, P.; et al.: “Oceanic Weather Product Development Team,” Presentation at 2005 NASA ASAP Science Review Meeting, Boulder, CO, April 13–14, 2005.

10-83. Blanchard, D.C.: “The Production, Distribution, and Bacterial Enrichment of Sea-Salt Aerosol,” *Air-Sea Exchange of Gases and Particles*, D. Reidel Publishing Company, pp. 407–454, 1983.

10-84. Tabazadeh, A.; Drdla, A.K.; Schoeberl, M.R.; et al.: “Arctic ’Ozone Hole’ in a Cold Volcanic Stratosphere,” *Proc. Natl. Acad. Sci.*, Vol. 99, No. 5, pp. 2609–2612, 2002.

10-85. Mather, T.A.; and Pyle, D.M.: “Tropospheric Volcanic Aerosol,” in *Volcanism and the Earth’s Atmosphere, Geophys. Mono. 139*, 10.1029/139GM12, pp. 189–212, 2003.

10-86. Stoiber, R.E.; Williams, S.N.; and Huebert, B.: “Annual Contribution of Sulfur Dioxide to the Atmosphere by Volcanoes,” *J. Volcanol. Geotherm. Res.*, Vol. 33, pp. 1–8, 1987.

10-87. Andres, R.J.; and Kasgnoc, A.D.: “A Time-Averaged Inventory of Subaerial Volcanic Sulfur Emissions,” *J. Geophys. Res.*, Vol. 103, pp. 25,251–25,261, 1998.

10-88. Halmer, M.M.; Schmincke, H-U.; and Graf, H.F.: “The Annual Volcanic Gas Input into the Atmosphere, in Particular into the Stratosphere: A Global Data Set for the Past 100 Years,” *J. Volcanol. Geotherm. Res.*, Vol. 115, pp. 511–528, 2002.

10-89. Pyle, D.M.; Beattie, P.D.; and Bluth, G.J.S.: “Sulphur Emissions to the Stratosphere from Explosive Volcanic Eruptions,” *Bull. Volcanol.*, Vol. 57, pp. 663–671, 1996.

10-90. Malmer, M.M.: “An Overview: 30 Years of Estimating Volcanic Gas Emissions into the Atmosphere,” *Geophys. Res. Abs.*, Vol. 8, 03270, 2006, University of Colorado at Boulder, 2007.

10-91. Cadle, R.D.; Kiang, C.S.; and Louis, J.F.: “The Global Scale Dispersion of the Eruption Clouds From Major Volcanic Eruptions,” *J. Geophys. Res.*, Vol. 81, pp. 3125–3132, 1976.

10-92. Anderson, B.J.; and Keller, V.W.: “A Field Study of Solid Rocket Exhaust Impacts on Near-Field Environment,” *NASA TM-4172*, NASA Marshall Space Flight Center, AL, January 1990.

10-93. Barchet, W.R.: “Acid Rain: A Primer on What, Where, and How Much,” Pacific Northwest Laboratory Report PNL-SA-13199, April 1985.

10-94. Anderson, G.P.; Chetwynd, J.H., Clough, S.A.; et al.: “AFGL Atmospheric Constituent Profiles (0–120 km),” AFGL-TR-86-0110, Environmental Research Papers, No. 954, Air Force Geophysics Laboratory, Hanscom AFB, MA, May 15, 1986.

10-95. Madsen, B.C.; Dreschel, T.W.; and Hinkle, C.R.: "Characterization and Evaluation of Acid Rain in Central Florida From 1978 to 1987—Ten Year Summary Report," *NASA TM-102149*, NASA Kennedy Space Center, FL, January 1989.

10-96. Smith, M.A.H.: "Compilation of Atmospheric Gas Concentration Profiles From 0 to 50 km," *NASA TM–83289*, Langley Research Center, VA, March 1982.

Terrestrial Environment (Climatic) Criteria Guidelines for Use in Aerospace Vehicle Development, 2008 Revision

NASA/TM—2008–215633
December 2008

D.L. Johnson, Editor

Section 11: Aerospace Vehicle Exhaust, Toxic Chemical Release, and Accoustic Propagation

TABLE OF CONTENTS

LIST OF FIGURES

LIST OF TABLES

LIST OF ACRONYMS AND SYMBOLS

AEGL	acute emergency guidance level
AIHA	American Industrial Hygiene Association
Al_2O_3	aluminum oxide
Ar	argon
ARC	Ames Research Center
BlastDFO	blast distance focusing overpressure
CALPUFF	air quality dispersion model
CAS	chemical abstract service
CCAFS	Cape Canaveral Air Force Station
CDC	Center for Disease Control
Cl	chlorine
CO	carbon monoxide
CO_2	carbon dioxide
COBRA	Common Object Request Broker Architecture
CRTF	common real-time debris footprint
CSU	Colorado State University
DG	dry gulch
DOT	Department of Transportation
EPA	Environmental Protection Agency
ER	Eastern Range
ERDAS	Eastern Range dispersion assessment system
ERF	exposure response function
ERPG	Emergency Response Planning Guidelines
FDH	formaldehyde dimethylhydrazone
Fe	iron
$FeCl_2$	iron chloride
FEMA	Federal Emergency Management Agency
H	hydrogen
H_2	hydrogen gas
H_2O	water

LIST OF ACRONYMS AND SYMBOLS (Continued)

HCl	hydrogen chloride
HES	human-health risk assessment expert system
HNO_3	nitric acid
HYPACT	hybrid particle and concentration transport
ILRO	intelligent launch and range operations
KSC	Kennedy Space Center
LANL	Lan Alamos National Laboratory
LATRA	launch area toxic risk assessment (model)
LATRA3D	launch area toxic risk assessment three-dimensional (model)
LCC	launch commit criteria
LH_2	liquid hydrogen
LOC	level of concern
lox	liquid oxygen
MARSS	meteorological and range safety support
MDS	display component
MSHA	Mine Safety and Health Administration
N_2	nitrogen gas
N_2H_2HCl	hydrazine hydrochloride
N_2H_4	hydrazine
N_2O_4	nitrogen tetroxide
NO_2	nitrogen dioxide
NIOSH	National Institute of Occupational Safety and Health
OB	ocean breeze
OSHA	Occupational Safety and Health Administration
PCAD	product of combustion atmospheric dispersion
PEL	permissible exposure limit
PPRO	data acquisition component
QRAS	quantitative risk assessment system
RAMS	regional atmospheric modeling system
RD3D	range dispersion three-dimensional
REEDM	rocket exhaust effluent diffusion model
RS	range safety

LIST OF ACRONYMS AND SYMBOLS (Continued)

SRB	solid rocket booster
SRM	solid rocket motor
SSME	Space Shuttle main engine
STEL	short-term exposure limit
SV	sonic velocity
TES	toxic-gas exposure expert system
THC	toxic hazard corridor
TWA	time-weighted average
UDMH	unsymmetrical dimethylhydrazine
USAF	United States Air Force
VAFB	Vandenberg Air Force Base
VR	virtual range
VTB	virtual test bed
WES	weather expert system
WR	Western Range

NOMENCLATURE

a	coefficient; speed of sound
b	coefficient
C_p	peak (centerline) concentration
c	coefficient
E_c	expectation of casualty
e	base of the natural logarithm. a constant equaling 2.71828
h	vehicle height
Q	release rate
R	gas constant
T	absolute temperature
T_k	time for vehicle to reach altitude
t	time
t_b	burn time
X	downwind distance
z	altitude
γ	ratio of specific heats
ΔT	temperature difference
σ_θ	standard deviation of the wind direction (degree)

11. AEROSPACE VEHICLE EXHAUST, TOXIC CHEMICAL RELEASE, AND ACCOUSTIC PROPAGATION

11.1 Introduction

This section of the handbook is intended to provide aerospace engineers and scientists with background information in the areas of tropospheric air quality and environmental assessment to assist them in the planning, design, testing, and operation of space vehicle systems. It deals primarily with the release of hazardous materials from the launch of space vehicle systems, spills of toxic fuels, potential accidents, plus accoustic (blast) propagation.

The three main toxic diffusion/dispersion models currently in use at the Eastern Range (ER) and at NASA Kennedy Space Center (KSC) are the launch area toxic risk assessment (LATRA) model, rocket exhaust effluent diffusion model (REEDM) 7.13, and the launch area toxic risk assessment three-dimensional (LATRA3D) model.

A listing of models and systems is presented in section 11.9. Many of the model definitions have been expanded to include more detailed information/descriptions about the model or system in question, and how that item is used or fits in with respect to other models, etc. A detailed description is given defining the various diffusion problems encountered, followed by some specific information given concerning some of the commonly used range models.

This document lists the various acceptable exposure standards by providing a Web site location as to where to find these levels (see table 11-6). It does not necessarily state the allowable exposure protection levels. A higher level NASA document, signed by the NASA Administrator, tells the various NASA Centers what they should be using NASA-wide regarding these acceptable exposure levels. Currently, that exists in NPR 8715.5, as it calls for adherence to Emergency Response Planning Guidelines (ERPGs). In an upcoming rewrite of this NPR document, it will be revised to indicate adherence to Acute Exposure Guideline Levels (AEGLs).

11.2 Definitions

Atmospheric diffusion—The spreading of gaseous and/or particulate matter by turbulent motions in the atmosphere (often used interchangeably with dispersion).

Ceiling—The maximum short-term average concentration above which exposure should never occur or the lowest height above ground level at which the clouds at and below that level obscure more than five-tenths of the total sky.

Cloud stabilization—The point at which a cloud with initial vertical momentum and/or buoyancy ceases to rise because it has reached approximate equilibrium with ambient conditions.

Concentration—The amount (mass) of a substance in a given volume of air (as in milligrams per cubic meters) or the relative amount of a substance given as a ratio (as in parts per million).

Confidence level—The probability that a specified concentration or dosage will not be exceeded.

Conflagration—A raging fire that results when solid fuels or propellants are ignited.

Continuous release—A release of air pollutants over an extended period of time, as in the case of evaporation from a liquid spill or stack emissions.

Deflagration—An explosion and raging fire that occur when hypergolic liquid propellants are mixed together.

Deposition—Material deposited on the ground surface in mass per unit area (see gravitational deposition and washout).

Dispersion—The spreading of gaseous and/or particulate matter by turbulent motions in the atmosphere (often used interchangeably with diffusion).

Doppler acoustic sounder—A remote sensing device that uses the doppler shift of acoustic waves to measure vertical wind profiles up to a maximum of 600 to 1,000 m above the surface.

Dosage—Time-integrated concentration (typical units are milligram minutes per cubic meter).

Emission rate—Mass or quantity of an air pollutant released to the atmosphere per unit time (typical units are grams per second).

Entrain—To draw or pull outside air into a plume volume by turbulent motions. The result of entrainment is growth and dilution of the plume volume.

Evaporation rate—Amount of vapor released to the atmosphere per unit time from the surface of a liquid (typical units are milligrams per minute).

Gravitational deposition—Surface deposition (fallout) due to gravitational settling of particles or drops.

Hazard distance—The maximum distance to a concentration, dosage, or deposition greater than or equal to a specified critical value.

Hypergolic reaction—An explosive chemical reaction that takes place when hypergolic propellants (liquid fuel and oxidizer) are mixed together.

Instantaneous release—A short-term release of air pollutants by an explosion, flash fire, etc.

Inversion—A thermally stable atmospheric layer within which the temperature increases with increasing height.

Isopleth—A constant value line or contour level. Isopleths are used to visualize the area at or above a given concentration.

Lapse rate—The rate of atmospheric temperature decrease with height.

Mixing layer—Atmospheric layer above the surface within which vertical turbulent mixing takes place (also referred to as the mixed layer or surface mixing layer).

Mixing layer height—Height (depth) of surface mixing layer. Mixed layer height is important when the plume grows vertically high enough to be restricted by this limit height of mixing. In general, the larger the mixing height the lower the pollutant concentration would be at long distances.

Pasquill stability category—A letter indicator for the following six atmospheric stability categories: very unstable (A), unstable (B), slightly unstable (C), neutral (D), stable (E), and very stable (F). An extremely stable (G) category is sometimes used. Pasquill Classes are an attempt to classify weather conditions important to the rate of diffusion in the atmosphere.

Permissable exposure limit (PEL)—An allowable average concentration of a pollutant, usually for an 8-hr work day.

Precipitation scavenging—See washout.

Rawinsonde—A balloon-borne meteorological instrument package used to obtain upper-air measurements of winds, barometric pressure, temperature, and humidity.

Spill rate—Amount (mass or volume) of a chemical that escapes or spills from a casing or container per unit time.

Surface roughness length—A micrometeorological measure of how rough the surrounding terrain is, depending on obstacles to wind flow such as buildings, hills, trees, and vegetation. Surface roughness directly affects turbulence levels especially in the stable and neutral cases and thus to dispersion rates.

Time-mean concentration—The mean concentration over a specified averaging time.

Time-weighted average—See permissible exposure limit.

Troposphere—The first 10 to 17 km of the atmosphere within which, on average, temperature decreases with height.

Upper-air sounding—Vertical profiles of temperature, relative humidity, winds, and pressure versus altitude, usually obtained from rawinsonde measurements.

Vapor pressure—The pressure of vapor in equilibrium with a liquid at a given temperature.

Washout—Surface deposition of a substance removed from the atmosphere by precipitation.

11.3 Background

During the launch of the Space Shuttle vehicle, the burning of liquid hydrogen (LH_2) fuel with liquid oxygen (lox) at extreme high temperatures inside the three Space Shuttle main engines (SSMEs), and the burning of the solid propellant mixture of ammonium perchlorate oxidizer, aluminum powder fuel, iron oxide catalyst, polymer binder, and epoxy curing agent in the two solid rocket boosters (SRBs) result in the formation of a large cloud of hot, buoyant, toxic (hydrogen chloride (HCl)) exhaust gases near ground level. The exhaust cloud subsequently rises and entrains into ambient air until the temperature and density of the cloud reaches an approximate equilibrium with ambient conditions (ref. 11-1). During a normal Shuttle launch, the total exhaust of HCl is ≈163 tons during the first 15 km of flight. About 73 more tons are exhausted at higher altitudes in the first 2 min after launch. If a "loss of vehicle" event occurs close enough to lift-off, under certain meteorological conditions, the ground concentration could exceed 7 ppm, which is the short-term exposure limit (STEL) of HCl for normal people (ref. 11-2).

NASA, along with the U.S. Air Force (USAF), has pursued the development of computerized atmospheric dispersion models for predicting the behavior of rocket exhaust clouds in the troposphere since the mid-1960's. These models are used to assess the environmental impact of exhaust products from rocket engines with respect to air quality standards, toxicity thresholds, and potential bio-ecological effects and to evaluate requirements, if any, for launch constraints. In 1973, a joint program for rocket exhaust prediction and launch monitoring was initiated by NASA for all Titan launches from KSC. Now, for all launches, the gas dispersion model provides a ground concentration prediction and a resulting expectation of casualty which is assessed against launch commit critiera (LCC) contained in AFSPCMAN 91-710 (ref. 11-3) and NPR 8715.5 (ref. 11-4) for go/no-go decisions.

Meteorological conditions at the time of launch are a critical factor in the behavior of rocket exhaust buoyant cloud rise and subsequent downwind transport and diffusion. The rocket engines also leave an exhaust trail from normal launches, which extend throughout the depth of the troposphere and above. One important factor

is the vertical temperature profile of the lower atmosphere, followed in importance by the wind speed and direction vertical profiles. As with the classical air pollution meteorology, the presence of stable air layers determines whether or not emissions will get trapped near the ground surface or will mix through a deeper, well-ventilated air volume. The presence of a temperature inversion and its proximity to the thermally stabilized rocket exhaust cloud are significant parameters affecting ground-level concentrations of rocket exhaust gases, especially the temperature at which the exhaust cloud is generated at, along with the distribution of the propellant mass that provides the source of the emission (ref. 11-1).

The rates of atmospheric diffusion over water are different than over land. Diffusion over land is on average three times greater than diffusion over water when the water temperature is colder than air temperature over land. For onshore flow, the abrupt change from water to land conditions produces an internal boundary layer that begins at the shoreline and grows in depth with distance inland. Because the land surface is generally warmer than the water, the internal boundary layer is convective and is referred to as a thermal internal boundary layer. The transport distance required to complete the transition from over-water to over-land diffusion rates is a function of changes in aerodynamic surface roughness, height above ground, wind speed, and the vertical temperature profile (ref. 11-5).

11.3.1 Shuttle Fuel Expenditure

Bardina and Thirumalainambi (ref. 11-1) calculated the fuel expenditure rates for normal Shuttle launches by averaging the fuel expenditure rates for the engines over the approximate period from lift-off until the vehicle is ≈3,000 m (≈10,000 ft) above the Earth's surface. The fuel expenditure rates for the single-engine burn are an average of the normal firing period of the engine. For the slow burn, the rates are an average over the estimated total burn time of the scattered propellants. Table 11-1 provides the effective fuel heat contents, which are used in calculating buoyant cloud rise for normal launches and plume rise for launch failures, including the effects of heat produced by afterburning as well as heat losses due to radiation.

Table 11-1. Space Shuttle fuel expenditure and heat content (ref. 11-1).

Property	Space Shuttle
For normal launch:	
Fuel expenditure rates (W (gs^{-1}))	1.5219×10^{7}
Effective fuel heat content (H ($calg^{-1}$))	1,479.1
For single-engine burn:	
Fuel expenditure rates (W (gs^{-1}))	3.8451×10^{6}
Effective fuel heat content (H ($calg^{-1}$))	1,062.4
Burn time (s)	132
For slow burn:	
Fuel expenditure rates (W (gs^{-1}))	9.8873×10^{5}
Effective fuel heat content (H ($calg^{-1}$))	1,000
Burn time (s)	1,027

*There are two types of Shuttle launches—normal and abnormal (launch failures). For a normal launch, the assumption is made that all engines operate normally. In the case of a launch failure (single-engine burn on pad), one solid engine of the Space Shuttle vehicle is assumed to fail to ignite, causing the vehicle to remain on hold-down configuration while the other solid engine is assumed to ignite and burn with the pad deluge system operating normally. In the other failure mode (slow burn on pad), an on-pad explosion is assumed to rupture the casings of the solid engines, scattering solid propellant over the area in the vicinity of the launch pad (ref. 11-1).

Table 11-2 gives the Space Shuttle exhaust cloud constituents (for both the solid rocket motor (SRM) and the SSME), expressed as a fraction of the total mass of the exhaust products, along with a partial SRM weight fraction listing. The four main SRM exhaust component weight fractions listed have been adjusted to yield the weight of HCl, aluminum oxide ($Al_2 0_3$), carbon dioxide (CO_2), and carbon monoxide (CO) in the exhaust cloud multiplied by the appropriate fuel expenditure rates in table 11-1 (ref. 11-1).

Table 11-2. Space Shuttle exhaust cloud constituents (fraction by mass/weight) for SSME and SRM (refs. 11-1 and 11-6).

Exhaust Component	SSME (mass)	SRM (mass)	SRM (weight)
$Al_2 0_3$ (l and s)*	–	0.30210	0.1828
CO	–	0.23293	0.00042
HCl	–	0.20918	0.1146
H_2O	0.95939	0.10151	**
N_2	0.000307***	0.08586	**
$C0_2$	–	0.03949	0.2503
H_2	0.03547	0.01884	**
$FeCl_2$ (g, l, and s)	–	0.00598	**
Cl	–	0.00303	**
H	0.000085	0.00020	**
Fe (g and c)	–	0.00015	**
Ar	0.00471***	–	**
Traces	0.000038	0.00073	**

Note: l=liquid, s=solid, and g=gas.
*Unless otherwise noted, or as noted by g, where other phases are present, the species are in the gaseous phase.
**Component weight not taken into account here.
***Ar and N_2 occur as dissolved impurities in the lox that is employed as the oxidizer in an SSME.

The cloud rise and dispersion calculations for normal Shuttle launches require specification of the time/height profile of the launch vehicle. The vehicle flight profile data for the first 3,000 m above the surface are used to obtain a least-squares curve fit to the expression

$$T_k = az^b + c \ , \tag{11.1}$$

where T_k is time for the vehicle to reach the altitude z. The values of the Shuttle coefficients are tabulated in table 11-3. As an example, for $z = 3{,}000$ m, $T_k \sim 28$ s.

Table 11-3. Space Shuttle launch time/height profile coefficients (ref. 11-1).

Coefficients	Coefficient Value
a	0.652213
b	0.468085
c	0.375

*Coefficients used in equation (11.1).

The NASA Ames Research Center (ARC) cloud and plume rise model can then be applied from this point on within their Web-based toxic gas dispersion model virtual test bed Shuttle launch operation simulation studies (ref. 11-1). Note that this ARC model is not the NASA model used by the Space Transportation System program.

11.3.2 NASA Expert System for Simulated Launch Operations

ARC has developed a set of contingency rules for LCC. A distributed expert system for launch operations can operate concurrently to derive ultimate "go/no-go" decisions within the scenario of a launch or landing of a space vehicle. Implemented on this Web server are three different expert systems that derive decisions based on launch contingency rules: (1) The weather expert system (WES), (2) toxic-gas exposure expert system (TES), and (3) the human-health risk assessment expert system (HES). These expert systems are supported by real-time and model data to make an optimized decision, with the uncertainty involved in the decision-making process being the reflectance of the physical models rather than the expert system by itself. This distributed expert system acts as an advisory system and can be transformed into an autonomous decision support system by implementing suitable intelligent agents among the distributed expert system.

The WES is crucial for launch decision making, as the Shuttle launch site weather rules characterize certain aspects of the environment related to the launching or landing site, the time, the pad or runway conditions, the mission durations, etc. WES acquires weather data for the continental United States or the world. The TES model calculates peak concentration and deposition downwind from normal launches. Vertical profiles up to 3,000 ft of the meteorological parameters (of WS, WD, T, P, Td) are used as inputs for a gas dispersion model. The output of the toxic gas dispersion model forms as an input to the TES. The rules for the TES are based on downrange, peak chemical concentration, and type of launch. The HES uses a probabilistic model that is based on Monte Carlo simulations with a limited amount of data for toxic response functions to humans.

The toxic gas dispersion model computes chemical concentration with respect to downrange. These results form as inputs to human health risk assessment models (ref. 11-7). Before deriving launch decisions, the near real-time weather data have to be collected near the launch pad and the planned trajectory of the vehicle so that weather forecasting models can predict weather during the launch window. The gas dispersion model predicts the toxic gas dispersion in the region of interest. Once the prediction models compute the predicted weather and toxic gas concentration, it can be directed to the corresponding expert system to derive the launch status based on weather, toxic gas dispersion, and human health risk (ref. 11-7). Note that this NASA expert system is not in place at KSC, as it is only an internal ARC product.

11.4 Potential Environmental Threats

11.4.1 Threat Overview

The handling, test firing, and launching of aerospace vehicle systems involve hazardous materials that present many potential environmental threats. Personnel, flora, fauna, equipment, and facilities are all threatened to some degree, depending on their sensitivity and the hazardous materials involved. Contact with a hazardous material may be direct (at the source) or indirect (arising from the atmospheric transport and diffusion (dispersion) of the material). In addition to hazardous materials, the launch and reentry of aerospace vehicles produce sonic booms that occasionally have adverse impacts.

The primary atmospheric environmental hazards associated with the handling, test firing, and launch of aerospace vehicle systems are produced by the fuels and propellants used by these systems. Modern space vehicle systems use both liquid and solid propellants. Although storage and handling normally do not present hazards for SRMs, they do for liquid fuels. LH_2 and lox are highly explosive, but are not otherwise a threat

to the environment. Hypergolic liquid fuels, on the other hand, are extremely hazardous if released to the atmosphere by a leak or spill. The pollutants of concern in the exhaust from a liquid-fueled rocket consist of both combustion products and unburned fuel and oxidizer. The unused hypergolic fuel and oxidizer in a space vehicle that returns to Earth present a hazard that should not be overlooked.

The pollutants of principal concern in current rocket exhaust clouds are Al_2O_3, HCl, CO, hydrazine (N_2H_4), unsymmetrical dimethylhydrazine (UDMH), formaldehyde dimethylhydrazone (FDH), nitrogen tetroxide (N_2O_4), and hydrazine hydrochloride (N_2H_2HCl). The toxic effects of Al_2O_3 are those of a nuisance dust such as irritation to the eyes and mucous membranes of the respiratory tract. HCl is highly corrosive to human tissue, and its inhalation can damage the teeth and irritate or damage the mucous membranes of the upper respiratory tract, depending on the concentration. Carbon monoxide (CO) has an affinity for hemoglobin 210 times that of oxygen and, by combining with hemoglobin, renders blood incapable of carrying oxygen to the tissues. Thus, carbon monoxide can cause hypoxia (oxygen deficiency), followed by unconsciousness or death at higher concentrations. Exposure to hydrazine can cause irritation of the nose and throat, followed by itching, burning, and swelling of the eyes (temporary blindness may occur) and damage the kidney, liver, and blood systems. Hydrazine also possesses carcinogenic properties. When heated, hydrazine hydrochloride decomposes into hydrazine and hydrogen chloride and may therefore have the toxic potential of both chemicals. UDMH exposure at high concentrations can lead to tremors and then seizures, and it has both mutagenic and carcinogenic properties. Because FDH breaks down into reaction products similar to those of UDMH, it is assumed to have similar toxicological properties. Nitrogen tetroxide decomposes into various nitrogen oxides of which nitrogen dioxide is of greatest concern. Toxic effects produced by nitrogen dioxide range from irritation of the eyes and nose, to lung damage, to death, depending on the exposure time and concentration.

11.4.2 Static Firings and Launches

The potential environmental threat presented by normal firings of liquid-fueled engines is small because the major pollutants in the exhaust are carbon dioxide and small amounts of nitrogen oxides and carbon monoxide. The pollutants of primary concern in the exhaust from a solid-fueled rocket motor are aluminum oxide and hydrogen chloride. Aluminum oxide, an abrasive used in many types of sanding and grinding materials, can damage optical and precision equipment. As a dust, it is subject to Environmental Protection Agency (EPA) and state ambient air quality standards for particulates with aerodynamic equivalent diameters <10 μm. However, because these standards are for long-term exposures (the standards are 24-hr average and annual geometric mean concentrations of 150 and 50 $\mu g/m^3$, respectively), the short-term impacts caused by rocket launches and test firings generally do not threaten them. Hydrogen chloride, which can exist as a vapor or in water as an acid, is both corrosive and toxic. There is some evidence that hydrogen chloride in low concentrations can adversely affect electronic equipment (ref. 11-8). In systems where deluge and/or sound suppression water is directed into the exhaust of SRMs, airborne droplets containing hydrogen chloride and other exhaust products are likely. For SRB processing and even under certain launch conditions, perchlorate (a toxic chemical contaminate) has been produced and is a potential water pollutant.

The degree of damage to flora by contact with a hazardous material depends on the species, the hazardous material, the magnitude of the exposure, and the ambient humidity. The presence of water on a leaf generally enhances damage. Potential threats range from partial but recoverable foliage damage to total destruction. The Air Pollution Control Association publication, “Recognition of Air Pollution Injury to Vegetation: A Pictorial Atlas” (ref. 11-9), illustrates and discusses the effect on flora of many air pollutants. Experience at KSC (ref. 11-10) reveals that a single launch of the Space Shuttle can cause severe plant damage within 1 km of the launch facility, and minor loss of photosynthetic tissue due to deposition of water droplets containing aluminum oxide. Hydrogen chloride has been observed more than 10 km from the launch pad. The degree of damage is spotty and varies widely with distance and from launch to launch. Over a 30-mo period, covering the first nine

Space Shuttle launches, the number of plant species in the vicinity of launch complex 39A declined from an average of 7.8 per study area to 5.1. The KSC soil is very basic and has great buffering capacity, thereby the more susceptible species return.

11.4.3 Accidental Releases

Many hazardous materials must be stored near rocket test or launch facilities because they are used as fuels, oxidizers, solvents, and cleaners. As indicated by the toxicity tables in section 11.7, the accidental release of any of these materials poses a serious threat to the environment. Indeed, accidental releases of hazardous materials are a far greater threat to personnel safety, flora, and fauna than are normal rocket firings. Section 11.6 provides additional information about accidental releases.

11.4.4 Acoustic Threats

The atmosphere acts as a lens that can refract acoustic (sound) waves upward or downward, depending on the vertical profile of the speed of sound. At any height in the atmosphere, the speed of sound is equal to the sum of the temperature-dependent acoustic wave propagation speed and the wind speed component in the direction of propagation. If the speed of sound decreases with height, the acoustic wave will be refracted upward. Conversely, if the speed of sound increases with height, the acoustic wave will be refracted downward. Because the acoustic wave propagation speed increases with height in a temperature inversion (an atmospheric layer within which temperature increases with height), an inversion layer above an acoustic source (explosion, rocket firing, etc.) will cause a portion of the wavefront to be refracted back to the surface with a resulting sound enhancement, especially downwind of the source. The noise produced by the firing of a space vehicle system generally does not present an environmental threat other than startling animals or triggering the fall of loose plaster on buildings in the vicinity. The launch and reentry of space vehicles usually produces sonic booms. Depending on the meteorological conditions, these booms may be focused to yield large overpressures capable of causing damage such as broken windows. The magnitude of a sonic boom, which depends on the flying vehicle's speed and size, is measured in decibels, pascals, kilograms per square meter, or pounds per square foot of overpressure. The sonic booms from conventional aircraft typically cause overpressures of 2.44 to 9.76 kg/m^2 (0.5 to 2 lb/ft^2), while those from the Space Shuttle have been as high as 29.3 kg/m^2 (6 lb/ft^2).

11.5 Atmospheric Effects on Transport and Diffusion

Some of the most serious environmental threats associated with the handling, test firing, and launching of space vehicle systems occur when hazardous materials are transported by the atmosphere to large distances, downwind. Atmospheric conditions govern the speed and direction of downwind travel of the airborne material, the rate of dilution, and the rate of evaporation. A brief discussion of the phenomena that control atmospheric transport and diffusion processes is given below. A more detailed discussion can be found in references such as the *Handbook of Applied Meteorology* (ref. 11-11) and *Atmospheric Science and Power Production* (ref. 11-12).

Wind direction determines the direction of travel for material released into the atmosphere, and wind speed determines the time required for material to travel from the point of release to a downwind point of concern area. A receptor is what is actually exposed; i.e., a person, group of people, etc. Wind directions are reported as directions from which the wind is blowing. For example, a north wind will transport material to the south. Calm or light and variable winds present very difficult cases because the travel path of released material is unpredictable. Consequently, precautions must be taken in all directions.

The atmospheric diffusion of a cloud or plume of gases or aerosols (small drops or particles) released near the surface is determined by atmospheric turbulence (wind fluctuations caused by atmospheric eddies) and the depth of the surface mixing layer. Wind fluctuations caused by eddies smaller than the cloud or plume mix it with ambient air, while larger wind fluctuations move the cloud or plume in its entirety. Turbulence consists of mechanical and convective components. The mechanical component is produced by forced airflow over surface roughness elements, which include vegetation, terrain, and man-made structures. Mechanical turbulence increases as the wind speed or roughness of the surface increases. Convective turbulence is caused by eddies that occur as a result of thermal instability. The atmosphere is thermally unstable if the adiabatic (no exchange of heat with the surroundings) cooling of a small "parcel" of air displaced upward results in a parcel that is warmer (less dense) than the surrounding air. As the parcel will continue to rise, thermal instability acts to increase vertical motions. On the other hand, if the atmospheric temperature decreases with height less rapidly than the adiabatic rate, an air parcel adiabatically displaced upward will be colder (denser) than the surrounding air. In this case of thermal stability, buoyancy forces will act to suppress the vertical motion and return the parcel to its original level. The neutral case occurs when the atmospheric temperature decreases with height at the adiabatic rate of 0.01 °C/m. In general, the convective component is the dominant component of atmospheric turbulence on days when winds are light and solar heating of the surface results in thermal instability, while the mechanical component is dominant at night or whenever there is an adiabatic thermal stratification. Because lower atmospheric turbulence is produced by surface effects (flow over surface roughness and surface heating), atmospheric turbulence extends through only a finite depth of the lower atmosphere. This layer in which turbulent mixing occurs is called the surface mixing or boundary layer.

Diffusion models use turbulence (wind fluctuation) measurements or stability parameters to characterize diffusion rates. The standard deviations of the wind direction and elevation angles are the most common turbulence measurements. Some stability parameters vary continuously and others divide diffusion rates into discrete categories. One of the simplest and most widely used stability classification techniques is a modified version of the scheme proposed by Pasquill (ref. 11-13). The six or seven Pasquill stability categories range from A for very unstable conditions to F or G for very or extremely stable conditions. The popularity of the Pasquill stability categories is, in part, explained by the fact that they can be determined from standard airport surface weather observations of wind speed, cloud cover, and ceiling height. Wind speed is used as an indicator of the mechanical component of atmospheric turbulence, while the cloud cover and ceiling height are used to modify the solar radiation incident at the top of the atmosphere. This modified solar radiation is used as an indicator of the convective component of turbulence.

Precipitation falling through an atmosphere containing a hazardous gas or aerosol tends to scavenge it and deposit it at the surface. The amount of material scavenged depends on the type and rate of precipitation and the material being scavenged. Some pollutants such as hydrogen chloride are readily absorbed by water, while others such as particulate matter depend on impaction as the removal process. Small particles may also act as nuclei for the formation of clouds and precipitation. Although precipitation scavenging can significantly reduce atmospheric concentrations of the scavenged material, the amount of material deposited at the surface can also be dramatic because material is removed from the entire vertical column through which the precipitation is falling.

Evaporative spills of hazardous liquids used as rocket propellants, or for other purposes such as cleaning solvents, are among the most serious potential environmental threats. The evaporation rate is controlled by the liquid's physical characteristics such as molecular weight and vapor pressure, and meteorological factors such as the temperature and wind speed. In general, evaporation increases as the wind speed and/or temperature increase. Also, evaporative losses to the atmosphere increase as the evaporating surface area increases.

11.6 Specific Sources of Air Pollutants

11.6.1 Storage

The major threat to the environment from a stored toxic liquid such as a hypergolic fuel or oxidizer is that a leak, spill, or handling accident may release the material into the atmosphere. In addition, the toxicity of other chemicals such as cleaning solvents and payload materials must be considered. Hypergolic materials (nitrogen tetroxide, in particular) evaporate at ambient temperatures, producing vapors that are transported downwind and dispersed by normal atmospheric processes. Hypergolic materials are toxic to most life, and are highly flammable and some are corrosive. The probability of an accidental release of toxic materials from a storage facility is highest when material transfers take place. Potential release scenarios include broken transfer lines, connection failures, accidents by vehicles transporting hazardous materials, and damage to the storage facility resulting from a vehicle accident.

11.6.2 Static Firings and Launches

The exhaust products of rocket motor firings may contain hazardous materials, depending upon the chemical mix of the fuel. In general, the exhaust from rocket engines that exclusively burn liquid oxygen and liquid hydrogen or RP-1 contain water and carbon dioxide, which are not considered hazardous. All other fuels produce materials that have effects on the environment ranging from a nuisance to an extreme hazard. The current SRMs produce exhaust clouds containing aluminum oxide, hydrogen chloride, carbon dioxide, water, nitrogen, and various other trace materials after the rapid chemical reactions have been completed. Of these materials, hydrogen chloride and aluminum oxide are hazardous. Some SRMs contain other metals such as beryllium, which is very toxic and requires special precautions if released into the atmosphere.

Water is often injected into the exhaust of SRMs to protect the launch pad or test facility or to suppress sound. Much of this water is atomized by the mechanical shears and turbulence generated by the exhaust flows. If large quantities are used, water may be expelled onto the area near the launch pad or mixed with the exhaust gas. Droplets carried aloft with the exhaust plume may rain out of the exhaust cloud as it travels downwind, as is the case of the Space Shuttle (ref. 11-14). Significant quantities of hydrogen chloride and aluminum oxide can be scavenged from the exhaust cloud by this process. Water droplets which come in contact with the exhaust gases, whether from rain or dewfall prior to the launch or from the launch pad ground system, mix with the exhaust gases and leave small pools and drops of dilute hydrochloric acid on the ground in the vicinity of the launch pad. This acid is initially 2 normal, but as the water evaporates, it typically increases to ≈11 normal where it remains until the drop is completely evaporated. At this point, the hydrogen chloride evaporates along with the water. As the deposited acid solution evaporates, the ambient concentration of gaseous hydrogen chloride rises to a peak and then decreases as the drops are depleted, and only the acid in the surface soil and the more slowly evaporating pools are available to fuel the ambient concentration. The peak ambient hydrogen chloride concentrations measured at KSC after the launches of Space Shuttle missions 41D and 51A were 3 and 9 ppm, respectively. These typically peak concentrations occurred normally 1.5 to 2 hr after the launches, although the ambient hydrogen chloride concentration after both missions gradually decreased to ≈1 ppm within several more hours. Small rises in ambient concentration were reported after sunrise for 2 days after mission 51A.

In addition to a normal firing, exhaust products can be released into the atmosphere by the accidental breakup of an SRM and the subsequent burning of its pieces on the ground, which is called a conflagration. Although the exhaust products are nearly identical to those of a normal firing, changes in the heat produced and the time elapsed while burning can cause both the magnitude of the hazard and the downwind hazard distance to greatly increase.

As noted above, liquid-fueled rocket engines other than those fueled with liquid oxygen and hydrogen or RP-1 produce exhaust clouds that contain hazardous materials. The current hypergolic-fueled rocket engines primarily burn hydrazine-based fuels with nitrogen tetroxide as the oxidizer. The exhaust products from a normal firing of these engines include nitrogen oxides that can be toxic. A greater threat than a conflagration for these vehicles is a deflagration in which the fuel and oxidizer come in contact with each other, resulting in a hypergolic explosion. The hypergolic explosion is a fairly common event that usually takes place when a space vehicle is aborted in flight. However, there also have been cases that occurred on or near the Earth's surface. For example, a Titan II missile was involved in a hypergolic explosion near Demascus, Arkansas, in 1980. Hypergolic explosions produce clouds that contain nitrogen tetroxide, hydrazine, and other hazardous products. Fragments of burning solid propellant that fall to the ground can produce ground fires with toxic plumes, and the hypergolic fuels of upper stages combine to produce a toxic cloud in the lower atmosphere. Long downwind hazard distances can result from deflagrations of hypergolic-fueled space vehicle systems because of the quantities and toxicities of the materials that are released.

11.6.3 Fires

Fires that involve toxic propellants or other hazardous materials are another potential threat to the environment. In general, air pollutants released by these fires include both uncombusted toxic materials and toxic products of combustion. Because the heat generated by a fire usually is small compared to that produced by a rocket launch, the buoyant rise of the plume from a fire is generally less than that of an exhaust cloud. Consequently, fires can produce toxic clouds relatively close to the Earth's surface, resulting in little chance for horizontal dispersion to take place before the toxic clouds mix to the surface. The hazards produced by fires are very difficult to evaluate because it is difficult to quantify the amount of material involved, the efficiency of combustion, the chemical reactions that take place, and the effects of fire fighting on the combustion chemistry. Most of what is known about these fires comes from test burns of toxic materials under controlled conditions.

11.6.4 Transportation

The transportation of toxic materials presents threats to the environment resulting from numerous scenarios that are beyond the scope of the current discussion. These scenarios range from small leaks to the rupture of rail cars containing toxic materials. The U.S. Department of Transportation and most State and local governments have established rules, guidelines, and procedures for the transportation of toxic materials, established by material classification and, in some cases, by individual materials.

11.6.5 Payloads

The upper stages and the payloads of some space vehicle systems contain hazardous materials. The contents of these stages must therefore be investigated as part of the hazards analysis for the system. In addition to fuels and oxidizers, electrical and other power sources may contain hazardous materials. Also, nuclear power sources are common for some types of payloads. Although the threat of radioactive hazards goes beyond the scope of this document, it is mentioned here for completeness.

11.7 Toxicity Criteria

The Agency's Chief Medical Officer, who serves as the Designated Agency Safety and Health Official, establishes the exposure criteria for which employees at NASA facilities shall follow. NASA follows the American Conference of Governmental Industrial Hygienist—Threshold Limit Values except where the Occupational Safety and Health Administration (OSHA) standards are more stringent. Individual NASA Centers may elect to enforce more stringent exposure standards, but that is generally the exception. Exposure standards for visitors

or the public are very different. In these instances EPA, the American Industrial Hygiene Association (AIHA), or other state, community, or consensus standards may be followed.

For toxic propellant or combustion byproducts, a range should prevent exposure to concentrations above the level of concern (LOC) or equivalent established by the EPA, Federal Emergency Management Agency (FEMA), OSHA, National Institute of Occupational Safety and Health (NIOSH) of the Centers for Disease Control (CDC), the American Conference of Government Industrial Hygienists, or Department of Transportation unless an EPA AEGL exists for a toxicant that is more conservative than the LOC; i.e., lower after reduction for duration of exposure.

The chemical formulas, molecular weights, and chemical abstract service (CAS) numbers for air pollutants that are contained in rocket exhaust clouds or that may be released by spills of liquid rocket fuels are listed in tables 11-4 and 11-5, respectively. Table 11-5 also includes other hazardous liquids such as cleaning solvents that are commonly found at test and launch facilities. See table 11-6 for a listing of Web sites that contain exposure criteria established by various organizations for the commodities listed in tables 11-4 and 11-5.

Table 11-4. Chemical formulas, molecular weights, and CAS numbers for rocket exhaust products.

Chemical	Chemical Formula	Molecular Weight	CAS No.
Aluminum oxide	Al_2O_3	101.96	1344–28–1
Hydrogen chloride	HCl	36.46	7647–01–0
Carbon monoxide	CO	28.01	630–08–0
Hydrazine	N_2H_4	32.06	302–01–2
Unsymmetrical (1,1-) dimethylhydrazine (UDMH)	$(CH_3)_2N_2H_2$	60.12	57–14–7
Formaldehyde dimethylhydrazone (FDH)	$(CH_3)_2N\text{-}N\text{-}CH_2$	72.11	2035–89–4
Nitrogen tetroxide	N_2O_4	92.02	10544–72–6
Hydrazine hydrochloride	$N_2H_4 \cdot HCl$	68.52	2644–70–4

At the ER, both AEGL and ERPG regulations are adhered to. AEGLs have been established for all propellants used in the space program. The ER Range Safety office uses all three levels of AEGLs as a tiered approach for protecting personnel when using deterministic toxic dispersion modeling; i.e., modeling that produces output products without accounting for probability of occurrence. Units are in ppm or ml/m^2. AEGLs are the preferred exposure standard, provided an AEGL exists for the commondity of concern, which they do for all propellants used in the space program at Cape Canaveral Air Force Station (CCAFS)/KSC and at the Vandenberg Air Force Base (VAFB). If AEGLs exist for the commodity of concern, use them. If not, use other recognized national consensus standards. NASA Range Safety (RS) Program document NPR 8715.5 (ref. 11-4) is currently being revised to replace ERPG guidance with AEGLs for NASA as the exposure standard to use when protecting NASA personnel. KSC currently uses ERPG level 2 for SRB hydrogen chloride Shuttle launch analysis.

ERPGs were developed through the AIHA as planning guidelines to anticipate human adverse health effects caused by exposure to toxic chemicals. The ERPG are clearly defined and are based on extensive, current data. The rationale for selecting each value is explained, and other pertinent information is also provided. Each guideline identifies the substance, its chemical and structural properties, animal toxicology data, human experience, existing exposure guidelines, the rationale behind the selected value, and a list of references. The three tiers of each ERPG in 2007 are defined as follows:

Table 11-5. Chemical formulas, molecular weights, and CAS numbers for liquid rocket fuels, solvents, and cleaners.

Chemical	Chemical Formula	Molecular Weight	CAS No.
Aerozine–50	$(CH_3)_2N_2H_2 \cdot N_2H_4$	41.81	8065–75–6
Hydrazine	N_2H_4	32.06	302–01–2
Hydrazine (54%)	$N_2H_4 \cdot H_2O$	50.07	7803–57–8
Unsymmetrical (1,1-) dimethylhydrazine (UDMH)	$(CH_3)_2N_2H_2$	60.12	57–14–7
Monomethylhydrazine (MMH)	$CH_3N_2H_3$	46.09	60–34–4
Fuming nitric acid (IRFNA)	HNO_3	57.20	7697–37–2
Nitrogen tetroxide	N_2O_4	92.02	10544–72–6
n-Butyl alcohol	$CH_3(CH_2)_3OH$	74.12	71–36–3
t-Butyl alcohol	$(CH_3)_3COH$	74.12	75–65–0
Benzene	C_6H_6	78.12	71–43–2
Freon 12	Cl_2CF_2	120.91	75–71–8
Isopropyl ether	$(CH_3)_2CHOCH(CH_3)_2$	102.18	108–20–3
Acetone	CH_3COCH_3	58.08	67–64–1
Xylene	C_8H_{10}	106.17	1330–20–7

- ERPG-1—The maximum airborne concentration below which it is believed that nearly all individuals could be exposed for up to 1 hr without experiencing other than mild transient health effects or perceiving a clearly defined, objectionable odor.

- ERPG-2—The maximum airborne concentration below which it is believed that nearly all individuals could be exposed for up to 1 hr without experiencing or developing irreversible or other serious health effects or symptoms which could impair an individual's ability to take protective action.

- ERPG-3—The maximum airborne concentration below which it is believed that nearly all individuals could be exposed for up to 1 hr without experiencing or developing life-threatening health effects.

AEGLs are intended to describe the risk to humans resulting from once-in-a-lifetime or rare exposure to airborne chemicals. Acute exposures are single, nonrepetitive exposures for not more than 8 hr. The National Advisory Committee for AEGLs is developing these guidelines to help both national and local authorities, as well as private companies, deal with emergencies involving spills or other catastrophic exposures. AEGLs represent threshold exposure limits for the general public and are applicable to emergency exposure periods ranging from 10 min to 8 hr. AEGL-3, AEGL-2, and AEGL-1 values, as appropriate, will be developed for each of five exposure periods (10 min, 30 min, 1 hr, 4 hr, and 8 hr) and will be distinguished by varying degrees of severity of toxic effects. It is believed that the recommended exposure levels are applicable to the general population, including infants and children, and other individuals who may be susceptible. The three AEGLs have been defined as follows:

- AEGL-1—Airborne concentration (expressed as parts per million or milligrams per cubic meter (ppm or mg/m^3)) of a substance above which it is predicted that the general population, including susceptible individuals, could experience notable discomfort, irritation, or certain asymptomatic nonsensory effects. However, the effects are not disabling and are transient and reversible upon cessation of exposure.

Table 11-6. Listing of various toxic reference guidelines, regulations, and standards (ref. 11-15).

Reference Code	Reference Summary	Source/Link(s)
CAS No.	Chemical Abstract Service (CAS) of the American Chemical Society—Gives unique identifiers for chemical substances.	www.cas.org
DOT UN No.	Department of Transportation (DOT)—Transportation standards are given.	setonresourcecenter.com/cfr/dot.htm 49 CFR 172.101 Hazardous Materials Table
RTECS No.	NIOSH Registry of Toxic Effects of Chemical Substances (RTECS)—Compendium of toxicity chemical data by name and degree.	www.cdc.gov/niosh/rtecs
NFPA 704: H-F-R-Special Hazard	National Fire Protection Association (NFPA)—Standard System for the Identification of the Hazards of Materials for Emergency Response, 1996 Edition. Hazard standards for short-term acute exposure to a material under conditions of fire, spill, or similar emergencies.	www.nfpa.org (for standard) www.ehs.ufl.edu/HAZCOM/nfpa704.pdf (for Hazardous Material Code Identification. NFPA 704, 1996 Edition)
NIOSH	National Institute for Occupational Safety and Health (NIOSH)—NIOSH Pocket Guide to Chemical Hazards (Publication No. 2005-149).	www.cdc.gov/niosh/npg/default.html or www.cdc.gov/niosh/npg/pdfs/2005-149.pdf
AIHA – ERPGs*	American Industrial Hygiene Association (AIHA)—AIHA 2007 Emergency Response Planning Guidelines (ERPGs) to anticipate human adverse health effects caused by exposure to toxic chemicals. Consisting of three tiers of guidelines (ERPG-1, ERPG-2, and ERPG-3).	www.aiha.org/1documents/Committees/ERP-erpglevels.pdf (for 2007 AIHA ERPG's)
ACGIH	American Conference of Governmental Industrial Hygienists (HCGIH)—Threshold limit values (TLVs) and biological exposure endices (BEIs) based on the documentation of the TLVs for chemical substances/physical agents and BLIs, 2007.	www.acgih.org
OSHA	Occupational Safety and Health Administration (OSHA)—OSHA sets enforceable permissible exposure limits (PELs) to protect workers against the health effects of exposure to hazardous substances. PELs are regulatory limits on the amount or concentration of a substance in the air.	www.osha.gov/SLTC/pel
AEGLs*	EPA's Acute Exposure Guideline Levels (AEGLs)—Intended to describe the risk to humans resulting from once-in-a-lifetime, or rare, exposure to airborne chemicals dealing with emergencies involving spills or other catastrophic exposures. Acute exposures are single, nonrepetitive exposures for ≤8 hr.	www.epa.gov/oppt/aegl
EPCRA EHS	EPA's Emergency Planning & Community Right to know Act (EPCRA)—42 U.S.C. 11001 et seq. (1986). Law was designated to help local communities protect public health, safety, and the environment from chemical hazards.	yosemite.epa.gov/oswer/ceppoweb.nsf/content/epcraOverview.htm
CERCLA	The Comprehensive Environmental Response, Compensation and Liability Act (CERCLA)—Hazardous Substances – Emergency Release Notification. Releases of CERCLA hazardous substances in quantities ≥ to their reportable quantity are subject to reporting under CERCLA.	yosemite.epa.gov/oswer/ceppoweb.nsf/content/epcraOverview.htm
EPCRA Section 313	Emergency Planning and Community Right To Know Act of 1986 (EPCRA)—Toxic Chemicals – Toxic Release Inventory (TRI) Reporting. Emissions, transfer, and waste management data for chemicals listed under section 313 to be reported annually as part of the community right-to-know provisions of EPCRA.	yosemite.epa.gov/oswer/ceppoweb.nsf/content/epcraOverview.htm
RMP	Risk Management Plan (RMP)—Clean Air Act (CAA) Section112(r) List of Substances for Accidental Release Prevention – RMP. EPA developed a list of 77 toxic substances and 63 flammable substances.	yosemite.epa.gov/oswer/ceppoweb.nsf/content/RMPS.htm?OpenDocument
PSM	Process Safety Management (PSM)—The Clean Air Act Amendment (CAAA) promulgates a chemical process safety standard to prevent accidental release of chemicals that could pose a threat to employees.	www.osha.gov
GENIUM	Genium's Handbook of Safety, Health and Environmental Data for Common Hazardous Substances, 1999.	www.genium.com/hazmat
CI	Chlorine Institute, Inc.—The Chlorine Manual, Fifth Ed., 1986.	www.chlorineinstitute.org
USEPA	U.S. EPA—Chemical Summary for Chlorine Prepared by Office of Pollution Prevention and Toxics, EPA 749-F-94-010a, August 1994.	www.epa.gov/chemfact/s_chlori.txt
NLM	U.S. National Library of Medicine (NLM)—National Institute of Health.	hazmap.nlm.nih.gov
CHEM	Chemical Engineers' Handbook, Fifth Ed., McGraw-Hill Book Company.	www.mcgraw-hill.com
GPSA	Gas Processors Suppliers Association (GPSA)—Engineering Data Book, 12th Ed., 2004.	gpsa.gasprocessors.com
PSYS	University of Oxford, Physical and Theoretical Chemistry Laboratory, Safety Data for Methane.	physchem.ox.ac.uk

*ERPG and AEGL regulations are followed at ER/KSC.

- AEGL-2—Airborne concentration (expressed as ppm or mg/m^3) of a substance above which it is predicted that the general population, including susceptible individuals, could experience irreversible or other serious, longlasting adverse health effects or an impaired ability to escape.

- AEGL-3—Airborne concentration (expressed as ppm or mg/m^3) of a substance above which it is predicted that the general population, including susceptible individuals, could experience life-threatening health effects or death.

For Space Shuttle firings, the Committee on Toxicology (ref. 11-16) recommends 1-hr and 24-hr short-term public exposure emergency guidance levels of 1 ppm of HCl.

11.8 Standard Hazard Assessment and Mitigation Procedures

11.8.1 General

It is a requirement by law that the number one mechanism that NASA employs to mitigate exposure hazards are engineering controls. Standard assessment and mitigation procedures for the potential atmospheric hazards associated with the handling, test firing, and launching of space vehicle systems typically consist of identification and quantification of the threats, preparation of operations and contingency plans, training, and implementation. At most installations, a team under the direction of the safety office or similar organization is in place to perform these tasks. Each activity or process that could release a hazardous material to the atmosphere should be identified in advance. (See sec. 11.5 for a discussion of the most common threats and sec. 11.7 for additional details.) Mathematical simulation models such as those described in section 11.10, can then be used to quantify the magnitude of each potential hazard. Based on the results of this quantitative hazard assessment (worst-case credible spill), operations and contingency plans should be developed to minimize each potential hazard. For example, transfer operations for toxic liquids can be restricted to periods when meteorological conditions are such that an accidental release would be unlikely to produce hazardous concentrations in downwind areas where access cannot be restricted. Operations and contingency plans with clearly defined responsibilities must be developed, and employees must be trained in their required actions under both routine and emergency conditions. All employees should know and be trained to perform their responsibilities in the event of a planned or accidental release long before the release occurs.

Preplanning for possible events that may threaten the environment is a management responsibility, but management must be provided with sufficient information to make informed decisions when developing routine operational procedures, contingency plans, and emergency response procedures such as evacuation and decontamination procedures. The availability of the necessary resources under adverse conditions must be addressed as part of the planning process. For example, if computer facilities are required, arrangements must be made for backups in the event of a power failure. Similarly, provisions must be made for communications in the event of a power outage that would render most telecommunication systems unusable. Also, if predictive models are used in hazard assessment during routine or emergency operations, the data required to execute these models must be routinely acquired and available for use.

11.8.2 Storage

A procedure should be established to maintain proper controls and accurate inventories for all hazardous materials located at each installation where space vehicle activities take place. This inventory should include the materials, amounts, locations, possible hazards, toxicity levels, and any special emergency procedures to be followed. Liquid hydrogen, liquid oxygen, and hypergolic materials require special storage facilities. Housekeeping and inspection programs must be ongoing because neglect and corrosion are likely causes of leaking containers.

Evaporative losses to the atmosphere increase as the evaporating surface area increases. Consequently, containment is generally required to retain any spilled material within a specific area and prevent the development of a large evaporating surface. Many storage facilities include a means of covering the containment area to prevent evaporation into the atmosphere. The possibility of vandalism must be considered at every storage site. Preventive measures such as security, restricted access, and shielding may be required. Employees at storage sites must be trained in all aspects of hazardous material storage and handling. Plans for a material transfer and the necessary precautions must be completed well in advance of the actual transfer. All potential release scenarios should be considered, and responses to these scenarios such as decontamination and/or cleanup should be part of employee training. Employees must be kept in a ready state and must be thoroughly familiar with their responsibilities in order to prevent breakdowns and confusion in the event of an accident.

11.8.3 Static Firings and Launches

The static firing of a rocket engine or motor, or the launch of an aerospace vehicle system, produces a large, thermally buoyant cloud of exhaust products that usually includes toxic materials. This cloud grows rapidly through the entrainment of ambient air and rises until it reaches approximate equilibrium with the surrounding atmosphere. Because this exhaust cloud cannot be prevented, a static firing or launch must be planned and conducted so as to minimize its downwind impact. This mitigation is typically accomplished by restricting static firings and launches to periods when atmospheric conditions are not conducive to pollutant concentration, dosage, or deposition values that may have an unacceptable impact in uncontrolled downwind areas. Atmospheric transport and diffusion (dispersion) models normally are used to define the atmospheric constraints on a static firing or launch and may be used in near real time to assist in operational go/no-go decisions. In addition to considering normal firings and launches, model calculations should be performed for all credible accident scenarios; i.e., conflagrations and deflagrations. Sound propagation models can be used in a similar manner to minimize adverse noise impacts.

11.8.4 Mathematical Modeling

Mathematical models such as those described in section 11.10 often play a key role in hazard assessment and mitigation procedures. If so, procedures for the routine execution of the selected models must be established and followed. Also, the individuals responsible for performing the model calculations must have a working knowledge of the concepts upon which they are based as well as be entirely familiar with their operational details. If not, erroneous predictions, breakdowns, and confusion can be expected, especially under the pressure of an emergency.

It is important that the output of mathematical models used for hazard assessment meet the requirements of the end user, typically the safety office, program manager, or other decision makers. Thus, several different output formats such as overlays and tabular listings may be required. Provisions should always be made for model output conversion between metric and English units.

As an example of a typical procedure for using a hazard assessment model, assume that a dispersion model is routinely used at the launch complex for a hypergolic-fueled space vehicle. The meteorological parameters required as input to the model are routinely measured and also forecasted. At the start of each day, the planned operations are reviewed and the model is executed for all possible release scenarios for the toxic propellants under existing or forecast meteorological conditions. The model's predictions are then presented in an appropriate format to the safety office or other users, and the predictions are also filed for future reference. The model predictions are updated as required throughout the day's operations to reflect changes in meteorological or other conditions. In the event that a release to the atmosphere occurs, a postevent analysis is performed to determine the model's performance through a comparison of model predictions with all available measurements.

11.8.5 Briefings

The manner in which a mathematical model's predictions are presented to management and others is as important as the accuracy of the predictions themselves. During the planning stages, management and other users should be provided with a detailed explanation of the selected models, and they should participate in the development of formats for briefing materials that best meet their needs. If a selected model is designed to be safe-sided; i.e., biased toward overestimation of potential hazards, as is the case with most hazard assessment models, decision makers should be made aware of this. Graphical presentations such as the depiction of the predicted hazard area on an installation map can be a very effective means of providing readily understandable results. However, too much graphical detail; e.g., concentration isopleths well below the hazard criterion that cover large areas, can be misleading and should be avoided. If there is no predicted hazard, a simple statement to that effect is usually all that is needed.

11.8.6 Public Awareness

Contingency plans for planned or accidental releases of toxic materials to the atmosphere must recognize the possibility that these materials could be transported to uncontrolled areas in hazardous concentrations. The elected and appointed public officials responsible for these uncontrolled areas should be briefed on the potential hazards and the actions that have and will be taken to prevent or minimize adverse impacts. Written agreements between the test or launch facility and external agencies such as fire and police departments should be negotiated to define areas of responsibility and actions to be taken in the event of a planned or accidental release. To the extent possible, external agencies should be encouraged to participate in the routine training exercises in order to test the contingency plans. If it is anticipated that planned test or launch activities will require temporary restricted access to or evacuation of some normally uncontrolled areas, the general public as well as their officials should be made aware of these requirements and the reasons why they are necessary. Press releases to the local news media and public meetings are some techniques used to inform the public of plans to protect their safety. NASA follows all applicable community right-to-know regulations, and these regulations dictate certain public interaction requirements.

11.9 Models and Systems

This section lists the main diffusion/dispersion type of models and systems currently used in toxic cloud, vehicle breakup, and acoustic hazard analysis at the ER and the Western Range (WR). An abbreviated listed version of these models is also presented in table 11-7. Section 11.10 further expands on some of the following models:

AFTOX—A Gaussian puff/plume dispersion model that was developed and is used by the USAF to calculate toxic corridors/concentrations downwind from accidental hazardous chemical liquid or gas releases to the atmosphere. It is limited to nondense gases, and can directly calculate the evaporation rate from liquid spills from a point or area source. AFTOX treats instantaneous or continuous releases from any elevation, and can calculate the rise of buoyant plumes. The code calculates evaporative emissions from liquid spills, but dense gases are not accounted for. Output consists of concentration contour plots of concentration at a location, and the maximum concentration at a given elevation and time. AFTOX was intended to be a replacement for the older empirical ocean breeze (OB)/dry gulch (DG) model.

BLAST—Blast overpressure assessment model, originally developed and modernized by ACTA, Inc. and put in operational use at the ER as "BLAST" (ref. 11-17). The original BLAST, BLASTO, BLASTI, BLASTM, BLASTX, BLASTC, and BOOM are all outdated and obselete; they are no longer in use at either the ER or WR.

Table 11-7. Summary of computer models and systems available for NASA/ER hazard assessment evaluation.

Model/System	Type of Model	Description/Applicability
AFTOX	Gaussian puff/plume diffusion model	Instantaneous and continuous chemical liquid and gas releases from any elevation. Includes buoyant rise for stack plumes and evaporation for liquid spills. Replaces older OB/DG model.
BlastDFO	Physics-based model with both probabilistic and deterministic modules	A physics-based computer model used to assess far field blast overpressure. Currently used to determine the risk from flying glass resulting from the overpressure hazard of a catastrophic launch abort.
CALPUFF	Multilayer, multispecies, nonsteady-state puff air quality dispersion model	Predicts/simulates the time and space toxic concentrations for each pollutant regarding its transport, transformation, and removal. Uses CALMET (meteorological model) and CALPOST (postprocessing package).
CRTF	Probabilistic debris dispersion model	Calculates impact location of each piece of debris after a launch vehicle explosion.
ERDAS	Dispersion assessment system	Produces meteorological forecasts and enhanced dispersion estimates and runs all Range Safety toxic and blast physics models.
FATEPEN2	Debris fragment dispersion model	Used within the ILRO-VTB system.
HYPACT	Lagrangian particle and Eulerian concentration transport model	Used for vehicle processing-related spills within ERDAS. Uses plume info from REEDM and disperses plume using RAMS. To replace OB/DG.
ILRO-VTB	Real-time Web-based virtual test bed software system	Commands and controls communication and intelligent simulation environment of ground vehicle, launch, and range operation activities. REEDM and CALPUFF are used within ILRO-VTB.
JAVA3D	Debris dispersion graphics simulation model	Can simulate a Shuttle explosion during launch.
LATRA	Probabilistic toxic risk assessment model	Incorporates toxic launch commit criteria by performing Monte Carlo runs considering launch normal and failure modes, and computing population casualty statistics from wind-blown toxic emissions. REEDM simulates the dispersion for LATRA.
LATRA3D	Launch area toxic risk assessment three-dimensional model	A computer program designed to estimate serious injury casualties given potential exposure of the general public and mission support personnel to toxic rocket propellant chemicals. This model is a statistical risk model built around a Gaussian puff atmospheric transport and dispersion model.
OB/DG	Empirical diffusion model equation	Nonlaunch day continuous toxic model used for analysis, display, and prediction of the dispersion of toxic releases during vehicle processing on nonlaunch day within the ERDAS.
RAMS	Three-dimensional, multiple-nested grid mesoscale numerical weather prediction model	Contained within ERDAS to provide emergency response guidance in the event of an accidental material release or aborted vehicle launch.
REEDM 7.13	Deterministic, Gaussian-type toxic gas diffusion model coupled to a wind field model	Supports launch day toxic dispersion modeling, static firings, normal launches, conflagrations, and deflagrations.
VR	Virtual range is a range safety Monte Carlo simulation environment	Determines expectation of casualties (E_c) resulting from toxic gas dispersion (CALPUFF), caused by failed space launch and subsequent explosion of spacecraft after lift-off. Also, capable of determining E_c from falling debris (CRTF).
VTB	Virtual test bed software	Simulates the mission, control, ground vehicle, launch, and range operations.
WES	Weather expert system module within VTB	To support "go/no-go" decisions for NASA Shuttle operations within the ILRO-VTB program. Also used in mission planning activities.

BLASTFX—Blast modeling software developed by Northrop Grumman Mission Systems to determine the effects of explosives against facilities and people in those facilities. Damage caused by blast overpressure waves, which often are the most destructive (ref. 11-18).

BlastDFO (blast distant focusing overpressure)—A physics-based computer model, available on the meteorological and range safety support (MARSS) system, used at both the ER and WR to assess the risk posed

by glass breakage associated with far-field blast overpressure due to a catastrophic launch abort. It does not do any toxic modeling. MARSS was replaced by the Eastern Range dispersion assessment system (ERDAS) in 1996 (refs. 11-19 and 11-20). BlastDFO, developed by ACTA, Inc. for USAF use at the ER and WR, evolved from the BLAST, BLASTX, and BLASTC models. It includes modules and databases to calculate and assess potential explosive yields, acoustic ray traces, receptor overpressures, glass breakage, base and community population and window information, human vulnerability, and individual and collective expectation of casualty (E_c). Wind speed gradients and atmospheric temperature gradients are paramount in determining acoustic wave propagation, with relative humidity and atmospheric pressure also being involved to a lesser extent. BlastDFO also provides maps showing focusing areas and average overpressure isopleths.

CALPUFF—An air quality dispersion model, developed by Earth Tech, and adopted by EPA. It predicts the toxic concentrations for each toxicant at hourly intervals (ref. 11-21). CALPUFF is a multilayer, multispecies, nonsteady-state puff dispersion model that can simulate the effects of time and space-varying meteorological conditions on pollutant transport, transformation, and removal (ref. 11-22). CALPUFF has been accepted by EPA as a guideline model used in their regulatory applications involving the long-range (>50 km) transport of pollutants (ref. 11-21). The EPA approved a CALPUFF update to version 5.8 on June 23, 2007 (ref. 11-23).

CALMET—A diagnostic three-dimensional meteorological model that develops hourly wind and temperature fields input for CALPUFF (ref. 11-21).

CALPOST—A postprocessing package for CALPUFF output files, and it summarizes the results of the simulation (ref. 11-21).

CRTF (common real-time debris footprint)—State-of-the-art debris dispersion model used by NASA that generates a probabilistic dispersion for the impact location of each piece of debris after a vehicle explosion (ref. 11-18).

ERDAS (Eastern Range dispersion assessment system)—A USAF computing platform configured to produce routine mesoscale meteorological forecasts and enhanced dispersion estimates for the KSC/CCAFS region, and run the entire suite of RS physics models used to assess toxic and blast hazards in order to protect personnel and property engage in vehicle processing, material handling, launch preparation, and launch support activities. ERDAS is a system of interconnected computer workstations designed to acquire, process, and disseminate nearly real-time meteorological data and the outputs from the atmospheric toxic diffusion math models. ERDAS includes a regional atmospheric modeling system (RAMS) and hybrid particle and concentration transport (HYPACT) (ref. 11-20). In 1994, ERDAS was delivered to provide emergency response guidance for the 45th Space Wing/ Eastern Range Safety operations at KSC and CCAFS in the event of a hazardous material release or an aborted vehicle launch. Mesoscale forecasting is currently performed by the RAMS where model output can be used for meteorological support and for three-dimensional toxic hazard predictions. This prognostic gridded data from RAMS are available to ERDAS for display and for input to the HYPACT model. The HYPACT model provides three-dimensional dispersion predictions using the RAMS forecast grids to represent the environmental conditions (ref. 11-24). ERDAS supports both daily operations as well as prelaunch and postlaunch activities. Launch support utilizes ERDAS to produce hazard predictions for exhaust effluent and blast effects in order to determine whether a safe launch can be conducted. The ERDAS “windflow” map display also provides calculation and display of toxic dispersion predictions produced by OB/DG and the display of REEDM output. Other useful tools within ERDAS include BlastDFO and HYPACT. ERDAS consists of a data acquisition component (PPRO) and a display component (MDS). The PPRO retrieves measurements from the sensors, reformats them, performs a statistical quality control analysis, and then disseminates all results to the MDS display component. The MDS workstation provides the user with all the tools necessary to display the real-time and forecast data and to use them for real-time warnings as well as hazard predictions. Local user-controllable models include: (1) Two- and

three-dimensional vehicle processing diffusion, (2) two- and three-dimensional catastrophic launch abort modeling, (3) blast effects prediction with estimated public risk factors, and (4) real-time weather alert monitor with user-defined criteria.

FATEPEN2—A debris fragment dispersion model (ref. 11-22) used within the intelligent launch and range operations (ILRO)-virtual test bed (VTB) system.

HYPACT (hybrid particle and concentration transport) model—Used for a release during vehicle processing. HYPACT within ERDAS obtains plume information from REEDM, and then diffuses the plume using the RAMS-predicted wind and potential temperature fields to advect and disperse the particles. HYPACT has been used as a replacement model for OB/DG (ref. 11-20). HYPACT is a combination of a Lagrangian particle model and an Eulerian concentration transport model developed at Colorado State University (CSU) and ASTeR, Inc. (ref. 11-25).

ILRO-VTB (intelligent launch and range operations-virtual test bed) software—A real-time Web-based command and control, communication, and intelligent simulation environment of ground-vehicle, launch, and range operation activities (ref. 11-22). ILRO-VTB is not used at KSC for Shuttle launches. VTB simulates the operations of a suborbital vehicle of mission, control, ground-vehicle engineering, launch, and range operations. The test bed supports a wide variety of Shuttle missions in real time with ancillary modeling capabilities such as weather forecasting, lightning tracker, toxic gas dispersion model, debris dispersion model, telemetry, trajectory modeling, ground operations, payload models, etc. All models are linked using Common Object Request Broker Architecture (CORBA). REEDM is the toxic gas dispersion model within ILRO-VTB used to characterize the chemical emissions associated with a launch vehicle catastrophic failure. CALPUFF can simulate the effects of space and time-varying meteorological conditions on pollutant transport, etc. (ref. 11-22).

The ILRO-VTB is the tool and the process to integrate information technology for analyzing end-to-end Shuttle and space launch simulations with special features of virtual reality, scientific visualization, and command and control. Four areas are focused within the test bed: (1) Weather modeling, (2) orbital dynamics and telemetry, (3) range safety (gas and debris dispersion model), and (4) decision modeling (ref. 11-26).

JAVA3D—A debris dispersion graphics simulation model used by NASA to simulate a Shuttle explosion during launch (ref. 11-27).

LATRA (launch area toxic risk assessment)—The LATRA probabilistic model was developed for the USAF RS incorporating toxic LCC in terms of an expectation of casualty, to perform numerous Monte Carlo runs within a single LATRA run which considers the consequences of numerous launch failure modes of various probabilities and uncertainties in weather inputs and demographic factors. It can compute population casualty statistics, both collectively and individually, for the various population catagories. LATRA provides commanders at CCAFS with an evaluation of the possibility of wind-blown toxic emissions reaching civilian and military personnel near the area (ref. 11-26). The LATRA model assists commanders in determining the risks to military personnel and civilians, both on base and off base, from exposure to emissions from normal and failed launches. REEDM simulates the dispersion of a rocket's emission for LATRA under prevailing weather conditions (ref. 11-28).

LATRA3D (launch area toxic risk assessment three-dimensional)—Both a probabilistic and deterministic toxic dispersion model. A computer program designed to estimate serious injury casualties given potential exposure of the general public and mission support personnel to toxic rocket propellant chemicals. This model is a statistical risk model built around a Gaussian puff atmospheric transport and dispersion model. Toxic emission sources are modeled using from one to thousands of independent puffs that are released into a three-dimensional

windfield and tracked downwind over small time steps. The rise and growth of buoyant puffs are modeled with empirical air entrainment coefficients using a Briggs cloud rise formulation. The statistical aspect of LATRA3D is linked to random sampling of vehicle failure times and random sampling of selected model parameters such as input weather data uncertainty. Each Monte Carlo sample generates one possible realization of a toxic emission along with its resulting casualty expectation. The internal puff dispersion model, when coupled with the input population data, yields predictions of chemical exposure expressed in parts per million and time duration at each population center. Indoor chemical concentrations are predicted for various types of shelters using air exchange rates and predicted outdoor concentration. Once the time duration and concentration level of chemicals has been predicted for each population location, the probability of causing casualties at each population center is computed using exposure response functions (ERFs). The output products produced by LATRA3D include (1) concentration contours at ground or user-selected altitudes, (2) estimation of maximum concentration and location for a given scenario, (3) risk to the public at mild, moderate, and severe injury levels expressed in terms of both cumulative and individual casualty expectations, (4) identification of population centers at risk, and (5) optional risk profile that gives a sense of potential for catastrophic risk. It is the current toxic hazard assessment model being used by USAF/ER RS.

OB/DG (ocean breeze/dry gulch) model—Used for analysis, display, and prediction of the dispersion of toxic releases during vehicle processing on nonlaunch day within the ERDAS system.

RAMS (regional atmospheric modeling system)—A three-dimensional, multiple-nested grid mesoscale numerical weather prediction model (ref. 11-20). RAMS is contained within the ERDAS to provide emergency response guidance for CCAFS and KSC operations in the event of an accidental hazardous material release or aborted vehicle launch (ref. 11-29).

REEDM (rocket exhaust effluent diffusion model)—A deterministic, Gaussian-type model developed by H.E. Cramer Co, Inc. in 1982. REEDM Version 7.13 is a well-understood tool currently used to predict toxic hazard corridors (THCs) (acid deposition, HCl, nitric acid (HNO_3), and nitrogen dioxide (NO_2)) in support of launch day toxic modeling operations (ref. 11-20). REEDM can predict rocket engine exhaust and conflagration dispersions (ref. 11-30). REEDM is used at both CCAFS (ER) and VAFB (WR).

VR (virtual range)—An RS Monte Carlo simulation environment in determining the expectation of casualties (E_c) resulting from the toxic effects of gas dispersion caused by a failed space launch and subsequent explosion of a spacecraft shortly after lift-off. Also, it is capable of determining the E_c resulting from falling debris and from blast overpressure wave propagation (ref. 11-18). Safety is needed for the public, the astronauts, the workforce/surrounding infrastructure, and for aircraft/ships in the vicinity of the spaceport from gas, debris, and blast. CALPUFF (a toxicity gas dispersion model), BLASTFX (blast modeling software), and CRTF (a debris dispersion model) are the three current models used in VR, and linked to a Monte Carlo simulation. The capabilities of VR are being enhanced in order to predict the E_c from all three hazard sources, along with input flight trajectories, weather information, and Geographic Information System information will ultimately benefit the RS office. Virtual range is designed to be modular, allowing for interchangeability between various software (ref. 11-18).

VTB (virtual test bed)—Software used to simulate the mission, control, ground vehicle, launch, and range operations (ref. 11-31).

WES (weather expert system)—A critical module of the VTB development to support "go/no-go" decisions for Space Shuttle operations in the ILRO-VTB NASA program. As weather plays a critical role in launch and range operations, WES is to make expertise available to decision makers who need answers quickly for situation assessment. WES can also be used in launch planning (ref. 11-30).

11.10 Computer Models

11.10.1 Model Background

Table 11-7 summarizes the computerized models or systems most frequently used in quantitative hazard assessments for rocket motor or engine test firings, space vehicle launches, and related activities that could release hazardous materials to the atmosphere. With the exception of the BLAST sound propagation models, all of the models in table 11-7 are atmospheric transport and diffusion (dispersion) type models. (In addition to the dispersion models in table 11-7, a product of combustion atmospheric dispersion (PCAD) model is currently being privately developed.) Although all of the dispersion models in table 11-7 except the empirical OB/DG model are based on widely used Gaussian diffusion model concepts, there are significant differences in model complexity and the applications for which they are designed. An overview of each model is given below with greatest emphasis placed on the REEDM because it is the only model applicable to static firings, normal launches, conflagrations, and deflagrations. REEDM was originally developed for NASA (ref. 11-32) to provide near real-time predictions of rocket exhaust concentrations in support of Space Shuttle missions. The Marshall Space Flight Center multilayer diffusion model (ref. 11-33) was used to test and develop the procedures and algorithms used within REEDM (refs. 11-34 through 11-36) before the model was used to support the first launches of the Space Shuttle from KSC.

In 2004, MSFC documented a model comparison study on toxic gas exposure risks associated with a potential Shuttle catastrophic failure (ref. 11-37). These results indicated that the CALPUFF diffusion model proved somewhat superior to the REEDM 7.08 model. However, since then, REEDM has been significantly improved. The range dispersional three-dimensional (RD3D) deterministic model was upgraded into the currently used LATRA3D probabilistic model (which has CALPUFF and SKYPUFF within it) for protecting all people on Range property, including KSC (Paul Rosati, Personal Communications 2008).

11.10.2 Rocket Exhaust Effluent Diffusion Model Version 7.13

REEDM version 7.13 is a deterministic, Gaussian-type model originally developed by H.E. Cramer Co., Inc. in 1982. REEDM version 7.13 is currently used to predict THCs (acid deposition, HCl, HNO_3, and NO_2) in support of launch day toxic modeling operations, supporting the environmental impact statement for the Shuttle (ref. 11-20). REEDM can predict rocket engine exhaust and conflagration dispersions (ref. 11-30). REEDM is used at both CCAFS (ER) and VAFB (WR).

The REEDM version 7.13 computer program is used to assess the air quality impacts of the exhaust products produced by large rocket motors or the burning of rocket fuels. The model is designed to calculate peak and time-mean concentration, dosage, and surface deposition, resulting from both gravitational settling and precipitation scavenging of exhaust cloud constituents downwind of normal launches, launch failures, and static firings. There are several modes when this model can be used—normal launch mode when everything operates normally, conflagration mode where an on-pad explosion ruptures the SRB's casings, and the deflagration mode which simulates a catastrophic fireball caused by a hypergolic liquid reaction.

REEDM also incorporates three modes of operation—operational, research, and diagnostic. The operational mode is designed for launch support operations and automatically calculates many necessary program input variables. The research mode permits the user to examine and change program parameters; e.g., fuel loads, diffusion parameters, etc. In the diagnostic mode, a very detailed output of the model calculations may be obtained.

The main input requirements of the REEDM program are meteorological data in the form of rawinsonde measurements and the rocket vehicle parameters. Rawinsonde profiles of wind speed and direction, temperature

and dewpoint, barometric pressure, relative humidity, and air density are required up to ≈3,000 m (≈10,000 ft). Meteorological tower and doppler acoustic sounder measurements of wind direction and elevation angle standard deviations may optionally be used to specify atmospheric turbulence. Other meteorological parameters required by the model include the cloud cover, cloud ceiling height, and mixing depth. Rocket vehicle parameters (source inputs) required by REEDM depend on the vehicle and launch scenario. Default rocket vehicle parameters are provided in a database file for the Space Shuttle, Titan II, Titan 34D, Titan IV, Delta 2914, Delta 3914, and Minuteman II. In general, the required vehicle parameters for SRBs are the solid fuel load, the solid fuel burn rate, the heat released per unit mass of the solid fuel, and the pollutant (hydrogen chloride, aluminum oxide, etc.) emissions per unit mass of the solid fuel. Similarly, the required vehicle parameters for hypergolic rocket engines are the total liquid fuel and oxidizer loads, the fuel and oxidizer flow rates, and the ignition time of the liquid engine after the SRB ignites. Rocket vehicle parameters required for both solid motors and liquid hypergolic engines include the coefficients a, b, and c of equation (11.2):

$$t = ah^b + c \quad , \tag{11.2}$$

where t is time and h is vehicle height above ground level. The REEDM program also has an option to use a mesoscale wind field model to account for the effects of complex terrain on the low-level circulation. The use of this feature required terrain elevations for a grid system surrounding the launch site.

The REEDM program output options include tables of peak concentrations, total dosages, cloud arrival and departure times, and time-mean concentrations at user-specified downwind distances; tables of maximum ground-level deposition at user-specified downwind distances; and tables of precipitation deposition expressed as either maximum deposition or minimum surface water pH at user-specified downwind distances. The program produces a summary or very detailed print output, depending on the mode of operation. The more detailed print output includes intermediate calculations such as plume rise, cloud position, and turbulence parameters. Graphics output options consist of plots of vertical profiles of the meteorological data; plots of centerline peak or time-average concentration, dosage, or deposition versus downwind distance; and isopleth (contour) plots of peak or time-mean concentration, dosage, and deposition. Examples of REEDM plots of centerline peak concentration, concentration/distance table, and peak concentration isopleths are shown in figures 11-1, table 11-8, and figure 11-2, respectively. See table 11-9 for an example of a LATRA expectation of casualty for assessing both collective and individual risk from exposure to a toxicant resulting from a catastrophic launch abort at CCAFS of a Delta II vehicle.

11.10.3 Launch Area Toxic Risk Assessment Three-Dimensional Model

The LATRA3D model is a computer program designed to estimate serious injury casualties given potential exposure of the general public and mission support personnel to toxic rocket propellant chemicals. The model provides user options to simulate sources of emission that are either hot buoyant exhaust gases from burning propellant (liquid or solid) or neutrally buoyant propellant vapors from liquid spills or gaseous venting. The model requires several data input files: (1) A control file that specifies the scenario and desired type of analysis, (2) a launch vehicle database specifying the types, amounts of ignition time, and burn rates for propellants used in various stages of the launch vehicle, (3) a launch vehicle flight trajectory file giving the position and velocity of the vehicle as a function of time, (4) a solid propellant fragmentation file that is required for simulation of the explosion and breakup of the vehicle that uses one or more SRMs, (5) weather input data files for the time and region of concern, (6) a chemical thermodynamic properties database used to support an internal equilibrium combustion model, (7) an ERF toxicological data input file for the chemicals of concern, (8) a population library file defining location, number, and sheltering of people in the area of concern, (9) a launch vehicle failure rate file defining failure modes and failure probabilities for the vehicle, and (10) weather covariance statistics.

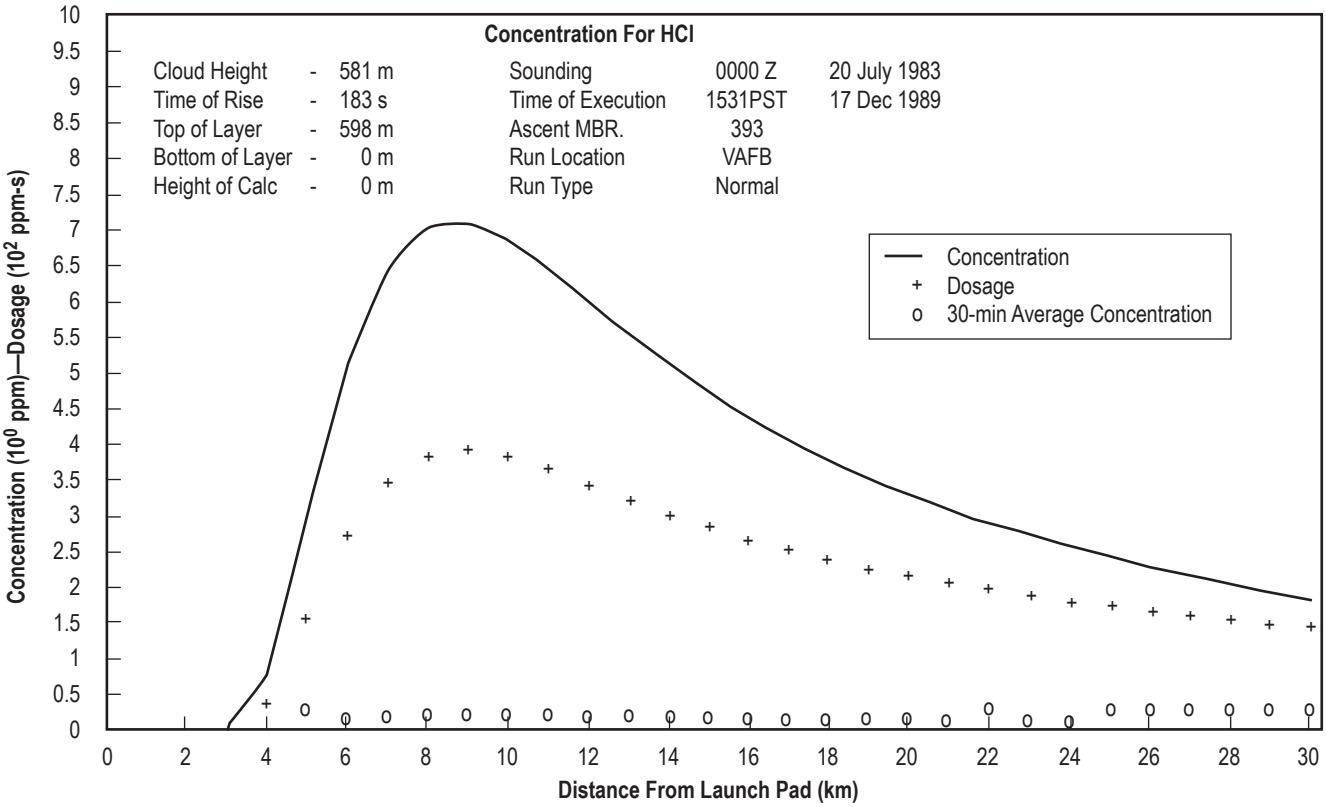

Figure 11-1. Example REEDM plot of centerline peak HCl concentration versus downwind distance for a Space Shuttle launch.

LATRA3D is a statistical risk model built around a Gaussian puff atmospheric transport and dispersion model. Toxic emission sources are modeled using from one to thousands of independent puffs that are released into a three-dimensional windfield and tracked downwind over small time steps. The rise and growth of buoyant puffs are modeled with empirical air entrainment coefficients using a Briggs cloud rise formulation. The rise of buoyant puffs is terminated when neutral buoyancy with the surrounding atmosphere is achieved. Interaction of puff material diffusion with atmospheric boundary layers is considered. Neutrally buoyant puffs continue downwind transport and growth based on interpolation of the wind speed and atmospheric turbulence intensity at the time-varying puff locations. Puffs are tracked until they become diluted below a user-prescribed threshold or leave the windfield domain defined by the user. Puffs with time-varying mass are permitted and typically used in rocket emission analyses. Multiple puff types, based on chemical composition, may be tracked simultaneously. The model includes a fourth-order Runga-Kutta drag corrected impact predictor used to estimate the trajectories and impact locations of solid propellant fragments ejected from vehicle explosion samples at random altitudes. Toxic emissions produced along the burning fragment trajectories are modeled. LATRA3D is intended for use at space launch facilities and is applicable to large rocket exhaust plumes with transport distances of interest in the 1- to 50-km range.

The statistical aspect of LATRA3D is linked to random sampling of vehicle failure times and random sampling of selected model parameters such as input weather data uncertainty. Each Monte Carlo sample generates one possible realization of a toxic emission along with its resulting casualty expectation. The internal puff dispersion model, when coupled with the input population data, yields predictions of chemical exposure expressed in parts per million and time duration at each population center. Indoor chemical concentrations are predicted for various types of shelters using air exchange rates and predicted outdoor concentration. Once the time duration

Table 11-8. Example REEDM concentration/distance for a Delta II launch from CCAFS—maximum centerline calculations. Concentration of HCl at a height of 0.0 downwind from a Delta 7925 conflagration launch (calculations apply to the layer between 0.0 and 1,915.4 m).

Range From Pad (m)	Bearing From Pad (deg)	Peak Concentration (ppm)	Cloud Arrival Time (min)	Cloud Departure Time (min)
1,000.5293	217.6349	144.8415	1.2933	8.8407
2,000.2646	218.5666	69.7382	6.7131	14.2898
3,000.1765	218.8772	39.2904	12.1219	19.7500
4,000.1323	219.0326	25.1247	17.5200	25.2209
5,000.1060	219.1258	17.3814	22.9077	30.7021
6,000.0884	219.1880	12.6767	28.2856	36.1932
7,000.0757	219.2323	9.6025	33.6541	41.6936
8,000.0664	219.2656	7.4841	39.0140	47.2027
9,000.0586	219.2915	5.9644	44.3656	52.7199
10,000.0527	219.3123	4.8394	49.7098	58.2446
11,000.0479	219.3292	3.9851	55.0471	63.7762
12,000.0439	219.3433	3.3229	60.3780	69.3142
13,000.0410	219.3553	2.8007	65.7031	74.8580
14,000.0381	219.3655	2.3827	71.0230	80.4070
15,000.0352	219.3744	2.0441	76.3380	85.9609
16,000.0332	219.3822	1.7669	81.6486	91.5191
17,000.0312	219.3890	1.5382	86.9553	97.0814
18,000.0293	219.3951	1.3483	92.2583	102.6473
19,000.0273	219.4006	1.1899	97.5580	108.2164
20,000.0273	219.4055	1.0572	102.8548	113.7886
Range	Bearing	144.842 (Max Peak Concentration)		
1,000.5	217.6			

and concentration level of chemicals has been predicted for each population location, the probability of causing casualties at each population center is computed using ERFs. ERFs are based on toxicological data for the propellant chemicals of concern (currently limited to HCl, NO_2, and HNO_3) and are defined as dose probit functions representing the cumulative probability of adverse health effects given increasing concentration exposure. The lower bounds of ERF curves represent the level of exposure below which no person in the exposed population is expected to become a casualty. The upper bounds of ERF curves represent the level of exposure above which 100 percent of the exposed population is expected to become casualties. Currently, LATRA3D has defined ERF data for HCl, NO_2, and HNO_3 chemicals for exposures of 10, 30, 60, and 120 min. ERFs are also defined for healthy adults and sensitive individuals.

The output products produced by LATRA3D include (1) concentration contours at ground or user-selected altitudes, (2) estimation of maximum concentration and location for a given scenario, (3) risk to the public at mild, moderate, and severe injury levels expressed in terms of both cumulative and individual casualty expectations, (4) identification of population centers at risk, and (5) optional risk profile that gives a sense of potential for catastrophic risk. Model results are evaluated in light of acceptable risk standards applied at the Federal launch ranges and the Federal Aviation Administration.

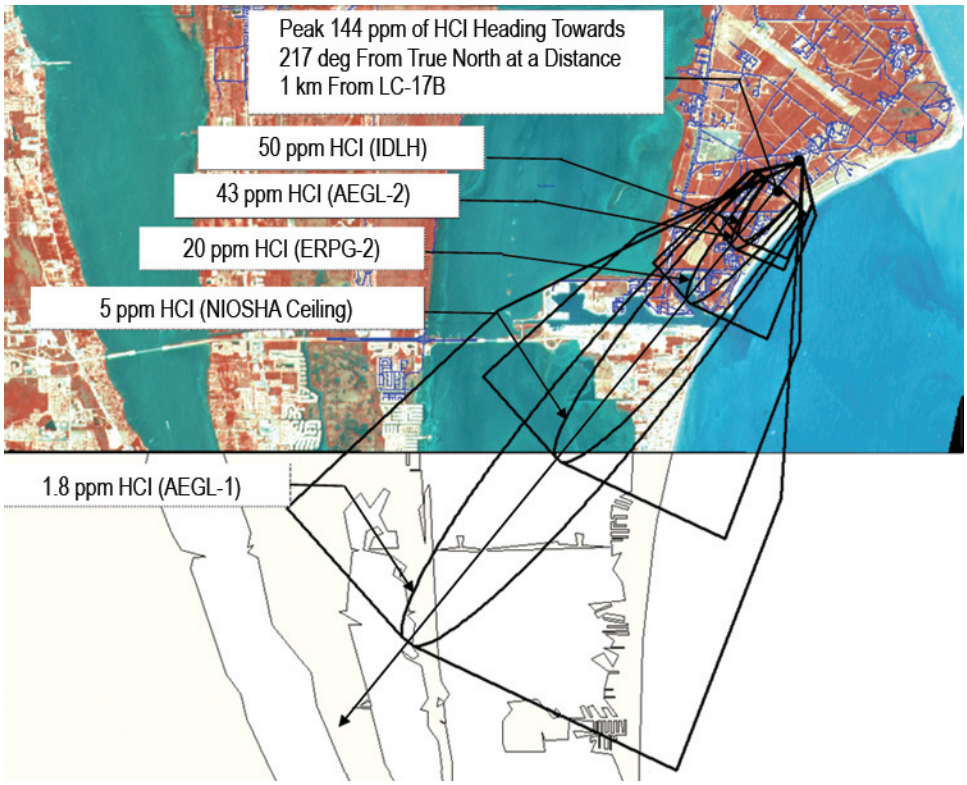

Figure 11-2. Example REEDM plot of HCl concentrations in part per million for a Delta II launch from CCAFS.

LATRA3D is written in Fortran and designed for use on Windows- or Linux-based personal computers and workstations. The program and supporting data files require several megabytes of hard disk storage and a minimum of 256K RAM. Typical execution time for a rocket launch and failure analysis is on the order of 10 to 30 min on a 2.6 GHz CPU computer. Execution time increases in proportion to the number of Monte Carlo simulations performed and the number of puffs generated in the source models.

11.10.4 Nonlaunch Day Vehicle Processing Toxic Modeling

Toxic spills not heated by fire or explosion occur during launch vehicle processing. Tools for this hazard assessment at the ER are provided by the ERDAS. The OB/DG model is one of two models used within the ERDAS to assess vehicle processing toxic diffusion at the ER. OB/DG information is embedded into a two-dimensional wind field grid to produce toxic hazard corridors for assessment of potential hazards. The HYPACT model, a pollutant trajectory and concentration model, is the other model where HYPACT obtains the plume information from REEDM, and diffuses the plume using the RAMS-predicted wind and potential temperature fields to advect and disperse the particles vertically and horizontally. HYPACT has been used as a replacement model for OB/DG (ref. 11-20). AFTOX can also replace the older OB/DG model.

11.10.4.1 Hybrid Particle and Concentration Transport Model. The HYPACT model is used for spills during vehicle processing. HYPACT within ERDAS obtains plume information from REEDM, and then diffuses the plume using the RAMS-predicted wind and potential temperature fields to advect and disperse the particles. HYPACT has been used as a replacement model for OB/DG (ref. 11-20). HYPACT is a combination of a Lagrangian particle model and an Eulerian concentration transport model developed at CSU and ASTeR, Inc. (ref. 11-25).

Table 11-9. Example LATRA expectation of casualty, both collective and individual, for a Delta II launch from CCAFS.

Forecast time:	–0.40 hour	Date: 10/25/2006	Time: 20:14
CONFLAGRATION	E_c and P_c		
Vehicle:	DELTA 7925		
Launch Date/Time:	25/10/2006 2037L		
Launch Pad:	17		
Receptor File:	g3399.nit		
Weather Profile:	rea2303.298		
Number of Monte Carlo Runs:	1,000		

	Total E_c (xE–6)			Max. Individual Risk (xE–6)		
	Mild	Moderate	Severe	Mild	Moderate	Severe
General Public:	152,829.69	3,384.17	34.27	948.27	96.72	1.20
CCAF Area:	6,327.11	215.97	0.70	902.39	66.37	0.32
KSC Area:	0.00	0.00	0.00	0.00	0.00	0.00
Spectators (on base):	0.00	0.00	0.00	0.00	0.00	0.00
Combined:	159,156.78	3,600.14	34.97			

E_c Values by Receptor for All Scenarios			Rel From Pad			Total E_c (xE–6)			Max. Ind. Risk (xE–6)		
Receptor ID/ Description		Location	Range	Bearing	Total Population	Mild	Moderate	Severe	Mild	Moderate	Severe
69	OFF-69	Cape Canaveral	5,700.2	217.0	16,699	95,638.81	663.16	4.53	665.47	21.42	0.17
8	OFF-8	Port Canaveral	4,236.7	220.3	100	18,473.74	1,840.12	22.82	948.27	96.72	1.20
1	OFF-1	Port Canaveral	5,481.1	219.3	1,553	12,541.63	276.10	1.88	657.41	26.89	0.19
7	OFF-7	Port Canaveral	5,462.3	225.9	100	7,653.04	427.65	4.98	396.02	22.49	0.26
429	OFF-429	Port Canaveral	6,360.9	228.7	353	2,204.80	20.76	0.00	196.55	10.28	0.00
437	OFF-437	Port Canaveral	6,527.2	230.6	449	2,043.67	16.51	0.00	140.70	8.22	0.00
426	OFF-426	Port Canaveral	6,502.3	229.9	353	1,816.39	17.86	0.00	156.45	8.88	0.00
81	OFF-81	Cape Can/Coco	8,041.7	208.0	4,276	1,742.00	0.53	0.00	158.04	0.08	0.00
433	OFF-433	Port Canaveral	5,955.8	219.8	93	1,691.17	16.76	0.06	540.82	16.19	0.06
3	OFF-3	Port Canaveral	7,289.9	240.0	5,852	1,505.31	30.95	0.00	23.62	0.84	0.00
431	OFF-431	Port Canaveral	6,493.2	229.3	235	1,230.63	9.20	0.00	170.59	9.10	0.00
2	OFF-2	Port Canaveral	7,052.9	241.5	5,340	1,205.26	32.62	0.00	18.83	0.96	0.00
430	OFF-430	Port Canaveral	6,638.2	230.9	258	1,050.73	7.37	0.00	129.86	7.34	0.00
4	OFF-4	Port Canaveral	7,374.8	237.6	2,829	1,041.10	16.42	0.00	37.44	0.91	0.00
435	OFF-435	Port Canaveral	5,681.3	220.4	40	699.97	0.54	0.00	174.99	0.14	0.00
67	OFF-67	Port Canaveral	6,981.1	231.7	688	573.24	5.01	0.00	103.12	5.01	0.00
5	OFF-5	Cocoa Beach	11,736.5	211.4	342	397.23	0.27	0.00	28.10	0.02	0.00
434	OFF-434	Port Canaveral	6,493.2	229.3	57	240.92	0.02	0.00	48.18	0.00	0.00
432	OFF-432	Port Canaveral	6,136.3	239.4	161	231.86	2.28	0.00	42.22	2.28	0.00
436	OFF-436	Port Canaveral	6,493.2	229.3	40	192.73	0.02	0.00	48.18	0.00	0.00
413	CCF-413	NOTUBERM 9	3,382.1	213.6	4	3,609.57	40.24	0.00	902.39	10.06	0.00
258	CCF-258	1115	2,282.5	230.4	2	1,367.71	92.70	0.38	683.86	46.35	0.19
415	CCF-415	RB–14 9	2,112.5	229.8	1	842.59	66.37	0.32	842.59	66.37	0.32

11.10.4.2 AFTOX. The USAF toxic chemical dispersion model (ref. 11-38) is an interactive computer program designed to predict toxic chemical concentrations and dosages downwind of an accidental release. The program can also predict the dispersion of a buoyant stack plume. AFTOX is based on SPILLS, a model developed by the Shell Oil Company (ref. 11-39).

The AFTOX model requires chemical, source, and meteorological inputs. The AFTOX program contains a data file of the properties of 76 toxic chemicals. If the chemical to be modeled is not in this file, the model will request the chemical's molecular weight and vapor pressure. The molecular weight is used to convert concentrations to units of parts per million, while the vapor pressure is used in the evaporation calculations. If the molecular weight is not known, concentrations must be output in units of milligrams per cubic meter. If the vapor pressure is not known, AFTOX makes the worst-case assumption that the evaporation rate equals the spill rate. The program allows the user to update or modify its chemical data file. The AFTOX model's source inputs consist of the type of release (continuous or instantaneous, liquid and/or gas) and parameters that are dependent on the type of release. For a stack, these inputs include the emission rate, volumetric flow rate, and exit temperature. For a chemical spill, these inputs include the spill rate, total time of release, height of release, area of spill, and pool temperature. The AFTOX model's meteorological inputs consist of the air temperature, wind speed and direction, standard deviation of wind direction (optional), sky cover and cloud category (low, middle, or high), ground condition, and mixing layer height.

Three output options are available with the AFTOX program: (1) A plot of concentration isopleths for up to three user-specified contour values, (2) the concentration at a user-specified location and time, and (3) the maximum concentration at a user-specified height and time after the spill. If the plot option is selected, the isopleth plot includes a hazard sector that represents the area expected to contain the minimum contour value ≈90 percent of the time. This feature accounts for the fact that the concentration predicted by a diffusion model at a given downwind distance is the mean value that would be expected at that distance if the same release were made a number of times under similar meteorological conditions. Thus, hazard distances longer than indicated by the concentration isopleth can be expected ≈50 percent of the time. All AFTOX output is directed to the user's terminal.

11.10.4.3 Ocean Breeze/Dry Gulch. The OB/DG diffusion model (ref. 11-40) is an empirical equation that predicts centerline concentration as a function of downwind distance for a ground-level release. The OB/DG equation was developed by the USAF to consider the downwind hazards of accidental spills of propellants from the Titan II missile at Cape Canaveral, Florida, and VAFB, California. The model is based on three field experiments conducted by the Air Force Cambridge Research Laboratories. The first, Project Prairie Grass (refs. 11-41 through 11-43), was conducted near O'Neill, Nebraska. The other two diffusion experiments took place at Cape Canaveral and VAFB and were named Ocean Breeze (ref. 11-44) and Dry Gulch (ref. 11-45), respectively. The composite data set from the Prairie Grass, Ocean Breeze, and Dry Gulch experiments was divided into two, with the first half of the data used to derive the OB/DG model equation and the second half used to test it. The regression fit to the first half of the data yielded

$$C_p/Q = (0.00211)\, X^{-1.96}\, \sigma_\theta^{-0.506}\, (\Delta T + 10)^{4.33} \quad , \tag{11.3}$$

where

C_p = peak (centerline) concentration (g/m^3) at downwind distance X (m)

Q = release rate (g/s)

σ_θ = standard deviation of wind direction (degrees)

ΔT = temperature difference (°F) between 56 and 6 ft.

The OB/DG model is limited by its empirical basis. For example, it generally predicts shorter hazard distances than other diffusion models at night with stable meteorological conditions because it is principally based on day-time trials. Also, it is not applicable to instantaneous releases or to large buoyant clouds or plumes. Because the OB/DG model considers peak concentrations only, it cannot provide information on ground-level concentration patterns.

The advantage of the OB/DG model is that it requires minimal meteorological inputs and computer resources. Consequently, it has served for decades as a simple way of estimating hazard distances downwind of spills of toxic propellants. Over the years, the OB/DG equation has been implemented in forms ranging from nomograms to computer programs. Many variations and modifications such as changes in units of input parameters have been made for specific applications. If an existing OB/DG computer program is used, the exact model formulation should therefore be determined.

11.10.5 BLAST Acoustic Propagation

Based on the original work by Plotkin (ref. 11-46), BLAST was developed for use by the USAF at the ER and WR. The model uses rawinsonde profiles of pressure, temperature, and winds as meteorological inputs and the flight profile as source inputs. Some versions of BLAST go beyond the prediction of sonic boom focus overpressures and combine population densities with predicted overpressures to estimate window damage.

To eliminate an overly conservative approach where limitations were placed on the launch vehicle based on wind direction, the BLAST Overpressure Assessment Mode was developed and put into operational use at the ER in 1981. In the mid-1990's, BLASTX and BLASTC were certified for use on the ER and WR, respectively. The main differences between the two codes were related to ray tracing due to terrain differences between the two ranges. In 2003, these codes were combined to create BlastDFO, and since then, a steady stream of modification and enhancements have been made to the BlastDFO code; however, the core models have not changed significantly. BlastDFO evaluates inadvertent detonation hazards as a function of meteorological conditions. Blast waves initially travel supersonically through the air, but with further distance traveled, their propagation is nearly identical to that of acoustic waves. Therefore, Snell's Law, which describes the propagation of acoustic waves, is used in BlastDFO to predict effects of blast waves at intermediate ranges. Acoustic waves propagate through the atmosphere as wavefronts along ray paths determined by the local sonic velocity (SV). Estimates of the relative attenuation or enhancement of blast overpressure (or acoustic energy) are based on the divergence or convergence of these ray paths at a given site. The predicted overpressure is correlated with the expected damage to windows, etc. to provide an expectation of casualty (E_c) output.

The four atmospheric parameters of wind, temperature, relative humidity, and pressure, and how they change in the vertical, play a major role in acoustic wave propagation. They determine the local speed of sound and sonic velocity for the existing or modeled atmosphere. The speed of sound is the rate at which acoustic waves travel in still air, whereas the SV includes the directional effect of the wind. The relationship of the SV profile and the focusing of acoustic waves is based on Snell's Law. When the SV decreases with altitude, the wavefronts are refracted upward and the ray paths bend away from the ground, and when the sonic velocity increases with altitude, wavefronts are refracted downward and the ray paths bend toward the ground. See figure 11-3 illustrating the five basic types of SV conditions. If a temperature inversion exists, in which the temperature increases with altitude, the sonic velocity also increases with altitude above ground. Within the inversion layer, the acoustic ray paths are refracted downward, back toward the ground. In the event of a large inadvertent detonation, strong blast overpressures may be expected at significantly greater distances from the launch pad. Ray focusing can occur from a combination of temperature and wind effects aloft; i.e., from a high-altitude inversion layer, causing the ray paths to initially bend upward, but to turn back toward the ground and focus there (ref. 11-47).

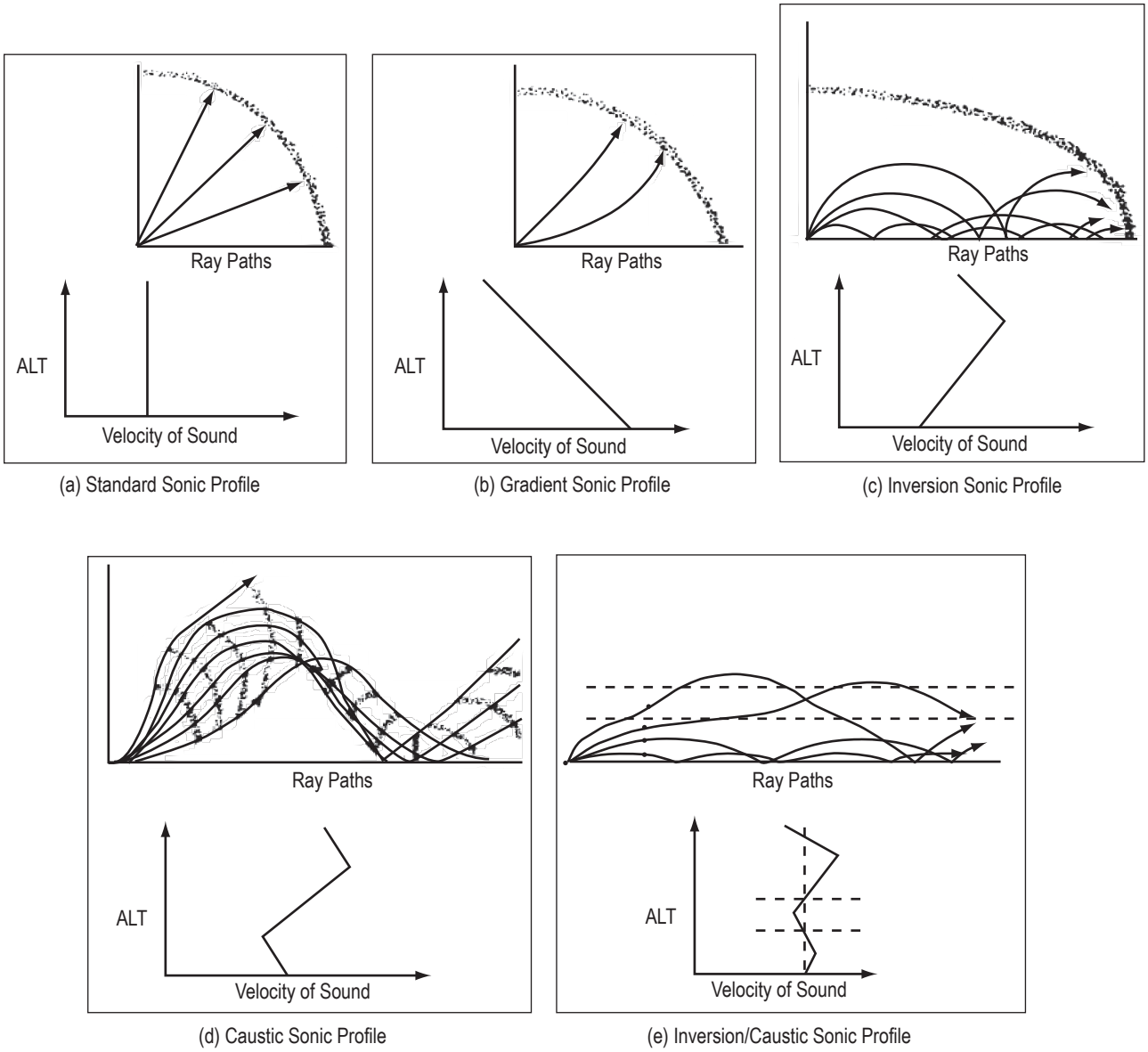

Figure 11-3. Types of sonic propagation conditions: (a) Standard sonic profile, (b) gradient sonic profile, (c) inversion sonic profile, (d) caustic sonic profile, and (e) inversion/caustic sonic profile (ref. 11-17).

11.10.5.1 Speed of Sound. The speed of sound, the atmosphere's structure, and acoustics are related. The speed of sound (a) depends on the type of medium and the temperature of the medium:

(a) For calorically perfect air:

$$a = \text{sqrt}\,(\gamma_{\text{perf}}\, R\, T)\ , \tag{11.4}$$

where

γ_{perf} = ratio of specific heats = constant = 1.4 for air at standard temperature pressure.

R = gas constant (286 $m^2/s^2/K$ for air).

T = absolute temperature K (or 273.15 + °C).

(b) For calorically imperfect air, γ = ratio of specific heats = $\gamma(T)$:

$$a = \text{sqrt}\,(R\,T\,[\gamma(T)]\,) = \text{sqrt}\,(R\,T\,\{1 + [(\gamma_{perf} - 1)] / [1 + (\gamma_{perf} - 1)]\;\;[(\theta/T)^2\;\;[(e^{\theta/T}) / (e^{\theta/T} - 1)^2]]\}. \qquad (11.5)$$

where

θ = 3,056 K (ref. 11-48).

REFERENCES

11-1. Bardina, J.; and R. Thirumalainambi: "Web-based Toxic Gas Dispersion Model for Shuttle Launch Operations," in Modeling, Simulation and Calibration of Space-based Systems, *SPIE*, Vol. 5420, pp. 136–144, September 2004.

11-2. Rabelo, L.; Sepulveda, J.; Compton, J.; et al.: "Disaster and Prevention Management for the NASA Shuttle During Lift-Off," *Disaster Prevention and Management*, Vol. 15, No. 2, pp. 262–274, 2006.

11-3. Air Force Specifications Manual AFSPCMAN 91-710, <http://www.afspc.af.mil/library/launchsafety/index.asp>.

11-4. NASA Procedural Requirements Document 8715.5 (effective date of requirement July 8, 2005), <http://www.hq.nasa.gov/office/codeq/doctree/87155.htm> and <http://nodis-dms.gsfc.nasa.gov/restricted_directives/displayDir.cfm?Internal_ID=N_PR_8715_0005_&page_name=main>.

11-5. Nappo, C.J.; and Essa, K.S.M.: "Modeling Dispersion From Near-Surface Tracer Releases at Cape Canaveral, Florida," *Atmospheric Environment*, Vol. 35, pp. 3999–4010, February 18, 2001.

11-6. Bowyer, J.M.: "Rocket Motor Exhaust Products Generated by the Space Shuttle Vehicle During Its Launch Phase (1976 Design Data)," *JPL Pub 77-9/NASA-CR-154107*, March 1, 1977.

11-7. Bardina, J.E.; and Thirumalainambi, R.: "Distributed Web-Based Expert System for Launch Operations," *Proceedings of the 2005 Winter Simulation Conference*, pp. 1291–1297, 2005.

11-8. Anderson, J.; and Keller, V.W.: "A Field Study of Solid Rocket Exhaust Impact on the Near-Field Environment," *NASA TM–4172*, January 1990.

11-9. Jacobson, J.S.; and Hill, A.C.: "Recognition of Air Pollution Injury to Vegetation—A Pictorial Atlas," Air Pollution Control Association, Pittsburgh, PA, 1970.

11-10. Schmalzer, P.A.; Hinkle, C.R.; and Breininger, D.: "Effects of Space Shuttle Launches STS-1 Through STS-9 on Terrestrial Vegetation of the John F. Kennedy Space Center," *NASA Technical Memorandum 83103*, Kennedy Space Center, FL, September 1985.

11-11. Houghton, D.D. (ed.): *Handbook of Applied Meteorology*, John Wiley & Sons, New York, 1985.

11-12. Randerson, D. (ed.): *Atmospheric Science and Power Production*, DOE/TIC-27601 (NTIS Accession No. DE84005177), Technical Information Center, U.S. Department of Energy, 1984.

11-13. Pasquill, F.: "The Estimation of the Dispersion of Windborne Materialm," *Meteorology Magazine*, Vol. 90, pp. 33–49, 1961.

11-14. Anderson, B.J.; and Keller, V.W.: "Acidic Deposition Production Mechanism—Space Shuttle Environmental Effects—The First Five Flights," *NASA TM–107825*, Kennedy Space Center, FL, pp. 155–156, 1983.

11-15. Nevada Division of Environmental Protection, Chemical Accident Prevention Program, <http://ndep.nv.gov/BAQP/cap/docs/chem/Source_References_071102.pdf>, November 2, 2007.

11-16. Emergency and Continuous Exposure Guidance Levels for Selected Airborne Contaminants, Volume 7, Ammonia, Hydrogen Chloride, Lithium Bromide, and Toluene, Board on Environmental Studies and Toxicology, Commission on Life Sciences, National Research Council, National Academy Press, Washington, DC, 1987.

11-17. Boyd, B.F.; Harms, D.E.; Rosati, P.N.; et al.: "Weather Support to Range Safety for Forecasting Atmospheric Sonic Propagation," Presented at the 9th AMS Conference on Aviation, Range and Aerospace Meteorology, Orlando, FL, September 11–15, 2000.

11-18. Sala-Diakanda, S.N.; Rabelo, L.; Rosales, S.A., et al.: "Integration Study of Prospective Hazards Models for the Enhancement of a Virtual Range Simulation Model," *Proceedings of the 2005 Winter Simulation Conference*, pp. 2427–2436, 2005.

11-19. NASA Range Safety Annual Report, Special Interest Items: Distant Focusing Overpressure (DFO), 2006.

11-20. Boyd, B.F.; Fitzpatrick, M.E.; Parks, C.R.; et al.: "Ensuring Environmental Safety for Space Launch," 2006 AMS 12th ARAM, Atlanta, GA, 2006.

11-21. Rabelo, L.C.; Sepulveda, J.; Compton, J.; and Turner, R.: "Simulation of Range Safety for the NASA Space Shuttle," *Aircraft Engineering & Aerospace Technology: An International Journal*, Vol. 78, No. 2, pp. 98–106, 2006.

11-22. Bardina, J; and Thirumalainambi, R.: "Intelligent Launch and Range Operations Virtual Test Bed (ILRO-VTB)," *Proceedings of SPIE Enabling Technologies for Simulation Science VII*, pp. 141–148, March 31, 2003.

11-23. TRC, The Atmospheric Studies Group, "The CALPUFF Modeling System: Official CALPUFF Web Site," <http://www.src.com/calpuff/calpuff1.htm>, 2008.

11-24. Case, J.L.; Manobianco, J.; Dianic, A.V.; and Wheeler, M.M.: "Verificatin of High-Resolution RAMS Forecasts Over East-Central Florida During the 1999 and 2000 Summer Months," *Weather and Forecasting*, Vol. 17, pp. 1133–1151, December 2002.

11-25. Dianic, A.; and Magnuson, E.: "An Operational System for Launch Area Hazard Prediction and Mitigation," in 41st Space Congress, April 2004.

11-26. Bardina, J.; and Thirumalainambi, R.: "Modeling and Simulation of Shuttle Launch and Range Operations," ESM-10, 18th European Simulation Multi-Conference, Magdelourg Germany, June 13–16, 2004.

11-27. Thirumalainambi, R.; and Bardina, J.: "Debris Dispersion Model Using JAVA3D," *Proceedings of 18th European Simulation Multi-conference*, 6 pp., 2004.

11-28. Thirumalainambi, R.; and Bardina, J.: "Human Health Risk Assessment Simulations in a Distributed Environment for Shuttle Launch," SPIE Defense and Security Symposium, Vol. 5420, pp. 126–135, 2004.

11-29. Case, J.: "Final Report on the Evaluation of the Regional Atmospheric Modeling System in the Eastern Range Dispersion Assessment System," *NASA CR—2001–210259*, Kennedy Space Center, FL, 2001.

11-30. Arnold, S.L.; Dianic, A.V.; and Magnuson, E.G.: "The Meteorological and Range Safety Support (MARSS) System: A GIS-Based Tool for Launch Area Hazard Prediction and Visualization," 21st International Conference on Interactive Information Processing Systems (IIPS) for Meteorology, Oceanography and Hydrology, P2.2 paper, 8 pp., January 9–13, 2005.

11-31. Thirumalainambi, R.; and Bardina, J.E.: "Web-based Weather Expert System (WES) for Space Shuttle Launch," IEEE International Conference on Systems, Man and Cybernetics, Vol. 5040, Issue 5, October 5–8, 2003.

11-32. Bjorklund, J.R., et al.: "User's Manual for the REEDM (Rocket Exhaust Effluent Diffusion Model) Computer Program," *NASA Contractor Report 3646*, Marshall Space Flight Center, AL, December 1982.

11-33. Bjorklund, J.R.; and Dumbauld, R.K.: "User's Instructions for the NASA/MSFC Cloud-Rise Preprocessor Program—Version 6, and the NASA/MSFC Multilayer Diffusion Program—Version 6," *NASA Contractor Report 2945*, Marshall Space Flight Center, AL, January 1971.

11-34. Stevens, J.B.; Susko, M.; Kaufman, J.W.; and Hill, C.K.: "An Analytical Analysis of the Dispersion Predictions for Effluent From Saturn V and Scout-Algol III Rocket Exhausts," *NASA Technical Memorandum X-2935*, Marshall Space Flight Center, AL, October 1973.

11-35. Kaufman, J.W.; Susko, M.; and Hill, C.K.: "Prediction of Engine Exhaust Concentrations Downwind from the Delta-Thor Telsat-A Launch of November 9, 1972," *NASA Technical Memorandum X-2939*, Marshall Space Flight Center, AL, November 1973.

11-36. Susko, M.; Hill, C.K.; and Kaufman, J.W.: "Downwind Hazard Calculations for Space Shuttle Launches at Kennedy Space Center and Vandenberg Air Force Base," *NASA Technical Memorandum X-3162*, Marshall Space Flight Center, AL, December 1974.

11-37. Anderson, B.J.; and McCaleb, R.C.: "Toxic Gas Exposure Risks Associated With Potential Shuttle Catastrophic Failures," *NASA/TP—2004–213284*, Marshall Space Flight Center, AL, June 2004.

11-38. Kunkel, B.A.: "User's Guide for the Air Force Toxic Chemical Dispersion Model (AFTOX)," Report No. AFGL-TR-811-0009, ERP No. 992, Air Force Geophysics Laboratory, Hanscom Air Force Base, MA, 1981.

11-39. Fleischer, M.T.: "SPILLS—An Evaporation/Air Dispersion Model for Chemical Spills on Land," Shell Development Company, NTIS Accession No. PB 83109470, 1980.

11-40. Kunkel, B.A.: "An Evaluation of the Ocean Breeze/Dry Gulch Dispersion Model (OB/DG)," AFGL-TR-84-0313 ERP. No. 900, Air Force Geophysics Laboratory, Hanscom Air Force Base, MA, 1984.

11-41. Barad, M.L. (ed.): "Project Prairie Grass, A Field Program in Diffusion, Volume I," AFCRC-TR-511-235(I), AD-152573, 1951.

11-42. Barad, M.L. (ed): "Project Prairie Grass, A Field Program in Diffusion, Volume II," AFCRC-TR-511-235(II), AD-152573, 1951.

11-43. Haugen, D.A. (ed.): “Project Prairie Grass, A Field Program in Diffusion, Volume III,” AFCRC-TR-511-235(III), AD-217076, 1959.

11-44. Haugen, D.A.; and Fuguay, J.J. (eds.): “The Ocean Breeze and Dry Gulch Diffusion Programs, Volume 1,” AFCRL-63-791(I), AD-428436, 1963.

11-45. Haugen, D.A.; and Taylor, J.H. (eds.): “The Ocean Breeze and Dry Gulch Diffusion Programs, Volume 2,” (AFCRL-63-791(II), AD-427687, 1963.

11-46. Plotkin, J.K.; and Cantrill, J.M.: “Prediction of Sonic Boom at a Focus. Wyle Laboratories,” WR75-7, October 1975.

11-47. Boyd, B.F.; Harms, D.E.; Rosati, P.N.; et al.: “Weather Support to Range Safety for Forecasting Atmospheric Sonic Propagation,” *Proceedings of 9th AMS Conference on Aviation, Range and Aerospace Meteorology*, pp. 432–437, 2000.

11-48. “Speed of Sound,” NASA GRC, <http://www.grc.nasa.gov/WWW/BGH/sound.html> and <http://www.grc.nasa.gov/WWW/K-12/airplane/sound.html>, 2008.

Terrestrial Environment (Climatic) Criteria Guidelines for Use in Aerospace Vehicle Development, 2008 Revision

NASA/TM—2008–215633
December 2008

D.L. Johnson, Editor

Section 12: Occurrences of Tornadoes, Hurricanes, and Related Severe Weather

TABLE OF CONTENTS

TABLE OF CONTENTS (Continued)

LIST OF FIGURES

LIST OF FIGURES (Continued)

LIST OF FIGURES (Continued)

LIST OF TABLES

LIST OF TABLES (Continued)

LIST OF ACRONYMS

ACE	Accumulated Cyclone Energy (index)
ACF	annual coverage fraction
AFB	Air Force Base
AGL	above ground level
AOML	Atlantic Oceanographic and Meteorological Laboratory
APC	atmospheric pressure change
ARC	Ames Research Center
B-scale	Beaufort scale
CCAFS	Cape Canaveral Air Force Station
CPA	closest point of approach
CST	Central Standard Time
DFRC	Dryden Flight Research Center
DI	damage indicator
DOD	degrees of damage
EAFB	Edwards Air Force Base
EDT	Eastern Daylight Time
EF-scale	Enhanced F-scale (tornado intensity)
ET	external tank
FR	family residence
F-scale	Fujita scale (tornado intensity)
GPS	global positioning system
GRC	Glenn Research Center
GSFC	Goddard Space Flight Center
HDP	Hurricane Destruction Potential (index)
HDQT	Headquarters (NASA)
HRD	Hurricane Research Division
HRSI	high-temperature reusable surface insulation (tiles)
Hur	hurricane

LIST OF ACRONYMS (Continued)

JLI	Johnson lag index
JPL	Jet Propulsion Laboratory
JSC	Johnson Space Center
KSC	Kennedy Space Center
LaRC	Langley Research Center
LC	launch complex
LCC	Launch Control Center
LDAR	lightning detection and ranging
LH	landfalling hurricane
LRSI	low-temperature reusable surface insulation (tiles)
LST	Local Standard Time
MAF	Michoud Assembly Facility
MEOW	maximum envelope of winds
MSFC	Marshall Space Flight Center
NOAA	National Oceanic and Atmospheric Administration
NTC	Net Tropical Cyclone (index)
NWS	National Weather Service
PAFB	Patrick Air Force Base
POR	period of record
SATT	Site Assessment of Tornado Threat (tornado program)
SLF	Shuttle Landing Facility
S-S	Salfir-Simpson
SSC	Stennis Space Center
SWH	significant wave height
TC	tropical cyclone
TD	tropical depression
TPS	thermal protection system
TS	tropical storm
T-scale	TORRO scale
UAH	The University of Alabama in Huntsville

UK	United Kingdom
U.S.	United States
USAF	United States Air Force
VAFB	Vandenberg Air Force Base
VAB	Vehicle Assembly Building
VIF	Vehicle Integration Facility
WFF	Wallops Flight Facility
WS	wind speed
WSMR	White Sands Missile Range
WSTF	White Sands Test Facility

NOMENCLATURE

A	area
B	B-scale
D	distance storm has advanced inland
E	(a type of) force
i	probability of landfall
M_T	maximum tangential velocity
m	years
N	number of years
n	probability of landfalls in a subsequent year
P	pressure
P_0	minimal sea level pressure
$P(E_0)$	probability of no event
$P(E_1)$	probability of one or more events
R	ratio of surface to wind
r	radius
T	T-scale
t	time since landfall
U	wind speed
U_{10}	wind speed at 10 m
U_z	wind speed at height z, other than 10 m (32.8 ft)
V	initial landfall wind speed
V_f	storm forward speed
V_t	wind speed after landfall
v	velocity
x	mean number of tornadoes
z	height

12. OCCURRENCES OF TORNADOES, HURRICANES, AND RELATED SEVERE WEATHER

12.1 Introduction

Severe weather may adversely affect the design, transportation, test, and operation of aerospace vehicles. This section contains information of such atmospheric phenomena, especially directed toward providing those involved in mission planning and operations with an indepth understanding and insight into the characteristics and what to expect from severe weather conditions that may affect the operation of an aerospace vehicle. Tornado and hurricane characteristics are presented in this section, along with landspouts, waterspouts, gustnadoes, severe weather downbursts, Nor'easters, and thunderstorm effects. The reader is referred to section 9 for a discussion of lightning and thunderstorm activity, and to section 7.2.7 for information regarding precipitation and hail criteria. Severe worldwide weather conditions, including tornado, waterspout, dust devil, and hurricane extreme winds are further described in section 5.2.2.5.

12.2 Severe Wind Effects on Buildings/Facilities (ref. 12-1)

Building failures occur when winds produce forces on buildings that were not designed or constructed to withstand severe winds. Failures also occur when the breaching of a window or door creates a large opening in the building envelope. These openings allow wind to enter buildings, where it again produces forces that the buildings were not designed to withstand. Other failures may be attributed to poor or improper construction techniques, poor selection of building materials, and inadequate design wind criteria. The most severe winds come from tornadoes and tropical cyclones (TCs), as well as severe thunderstorms.

12.2.1 Tornado Winds and Damage

In a simplified tornado model, there are three regions of tornadic winds:

(1) Near the surface, close to the core or vortex of the tornado, the winds are complicated and include the peak at-ground wind speeds and are dominated by the tornado's strong rotation. In this region, strong, upward motions can carry debris upward, as well as around the tornado.

(2) Near the surface, away from the tornado's vortex, the flow is a combination of the tornado's rotation, inflow into the tornado, and the background wind. The importance of the rotational winds as compared to the inflow winds decreases with distance from the tornado's vortex. The flow in this region is extremely complicated. The strongest winds are typically concentrated into relatively narrow swaths of strong, spiraling inflow rather than a uniform flow into the tornado's vortex circulation.

(3) Above the surface, typically above the tops of most buildings, the flow tends to become nearly circular. In a tornado, the diameter of the core or vortex circulation can change with time, so it is impossible to say precisely where one region of the tornado's flow ends and another begins. Also, the visible condensation/debris funnel cloud associated with and typically labeled the vortex of a tornado is not always the edge of the strong extreme winds. Rather, the visible condensation/debris funnel cloud boundary is determined by the temperature and moisture content of the tornado's inflowing air. The highest wind speeds in a tornado occur at a radius measured from the tornado vortex center that can be larger than the edge of the visible funnel cloud's radius.

Tornado damage to buildings can occur as a result of three types of forces: (1) Wind-induced forces, (2) forces induced by changes in atmospheric pressure, and (3) forces induced by debris impact.

The atmospheric pressure in the center of the tornado vortex is lower than the ambient atmospheric pressure. When a tornado vortex passes over a building, the outside pressure is lower than the ambient pressure inside the building. This atmospheric pressure change (APC) in a tornado may cause outward-acting pressures on all surfaces of the building. If there are sufficient openings in the building, air flowing through the openings will equalize the inside and outside atmospheric pressures, and the APC-induced forces will not be a problem. However, openings in the building envelope also allow wind to enter the building and cause internal pressures in addition to the wind-induced aerodynamic external pressures. Maximum APC occurs in the center of a tornado vortex where winds are assumed to be zero. A simple tornado vortex model suggests that, at the radius of the maximum winds, APC is one-half of the maximum value. Thus, for tornado loadings, two situations for the state of the building should be considered: (1) Sealed building or (2) vented building (with openings). For a sealed building, the maximum design pressure occurs when wind-induced aerodynamic pressure is combined with one-half APC-induced pressure. For a vented building, the maximum design pressure occurs when wind-induced aerodynamic pressure is combined with wind-induced internal pressure. Due to differential pressures created by tornadoes, buildings have been known to literally explode.

Tornadic winds tend to lift and accelerate debris such as roof gravel, sheet metal, tree branches, broken building components, and other heavier items. This debris can impact building surfaces and perforate them. Large debris, such as automobiles, tends to tumble along the ground. The impact of this debris can cause significant damage to wall and roof components. However, each debris impact affects the structure for an extremely short duration, probably <1 s. For this reason, the highest wind load and the highest impact load are not considered likely to occur at precisely the same time.

12.2.2 Hurricane Winds and Damage

Hurricanes are one of the most destructive forces of nature on Earth. A hurricane is a type of tropical cyclone (rotating counterclockwise in the Northern Hemisphere) originating over tropical waters. Tropical cyclones are classified as follows:

- Tropical depression (TD) (named storm)—An organized system of clouds and thunderstorms with a defined circulation and maximum sustained winds of 17 m/s (38 mph) or less.

- Tropical storm (TS)—An organized system of strong thunderstorms with a defined circulation and maximum sustained winds of 17.4–32.6 m/s (39–73 mph).

- Hurricane (Hur)—An intense tropical weather system with a well-defined circulation and sustained winds of 33.1 m/s (74 mph) or higher. In the western Pacific, hurricanes are called typhoons, and similar storms in the Indian Ocean are called cyclones.

Recently, there has been increased recognition of the fact that wind speed, storm surge, and inland rainfall are not necessarily coupled. For example, some hurricanes have strong winds but little rainfall and vice versa. There is growing interest in classifying hurricanes by separate scales according to the risks associated with each of these threats (ref. 12-1).

12.3 Tornadoes

The tornado poses a significant threat to life and property somewhere in the United States (U.S.) at nearly any time of the year. A tornado is a violently rotating column of air extending from a thunderstorm to the ground that may appear transparent until dust and debris are picked up or a cloud forms within the funnel (ref. 12-2). The tornado is a small-scale byproduct of its parent thunderstorm. Less than 1 percent of thunderstorms produce tornadoes. Tornadoes occur over a wide spectrum of strengths, sizes, and lifetimes. Of the 800–1,400 tornadoes

reported in the United States each year, ≈86 percent can be characterized as weak, 13 percent as strong, and 1 percent as violent. In general, weak tornadoes have lifetimes <10 min, widths around 100 m (109 yd), and paths <1.6 km (1 mi) in length. Typical tornadic wind speeds are on the order of ≈50 m/s (≈110 mph), while strong tornado speeds may be in excess of 112 m/s (250 mph) (ref. 12-2.). While weak tornadoes account for <5 percent of all tornado fatalities, they are still potentially dangerous and are often more difficult to identify because of their short lifetimes and sometimes innocuous precursor signals. Strong and violent tornadoes may last for as little as 10 min to over 2 hr in extreme cases and may be produced in cyclic fashion from the same thunderstorm. In such cyclic events, each individual tornado may last for tens of minutes, with the damage sometimes affecting a nearly continuous path from tens of kilometers to more than 160 km (100 mi) long and about 1 km (1,094 yd) or more wide. Often, such storms also produce large hail and damaging, nontornadic (straight-line) winds. Severe thunderstorm downdraft winds are also discussed here. Remotely sensed measurements of wind speeds in tornadoes made in recent years indicate that winds may range upward to about 135 m/s (300 mph) (ref. 12-3).

Tornadoes are sometimes observed in association with hurricanes in Florida and along the coastal states. See subsection 12.3.5.3. Fortunately, the aerial extent of tornadoes is small compared with hurricanes. Tornado paths are predominately from the southwest direction (59 percent), with 72 percent of all F5-scale tornadoes being from the southwest (ref. 12-4). Figure 12-1 shows the U.S. average annual tornado incidence per 25,900 km^2 (10,000 mi^2) for all tornadoes between 1953 and 2004. On this map, the months of peak tornado activity and average number of annual occurrences are also given for each state (ref. 12-2). The three main centers of greatest tornado incidence occur around Florida, Oklahoma, and Indiana. Alaska and Puerto Rico offer zero average tornadoes, while Hawaii averages one annual tornado and 1.6 tornadoes per 25,900 km^2 (10,000 mi^2). Figure 12-2 presents the U.S. tornado activity per 9,583 km^2 (3,700 mi^2) for the strongest (F3–F5) tornadoes over the time period of 1950–1998, whereas, weaker tornadoes are not included in figure 12-2 analyses. A funnel cloud is defined when the air column does not reach the ground. Discussion of the Fujita tornado intensity scale (F-scale) is presented in subsection 12.3.3.

12.3.1 World Tornadoes

Tornadoes occur in many countries around the world, although three out of every four tornadoes touch down in the United States. Globally, the middle latitudes (between about 30° and 50° latitude) provide the most favorable conditions for tornadoes to form. This is the region where cold, polar air comes up against warmer, subtropical air, and often where winds at different levels of the lower atmosphere produce verticle wind shear that can impart rotation to a storm cell. See figure 12-3. In terms of absolute tornado counts, the United States leads the world with an average of over 1,000 tornadoes recorded each year. A distant second is Canada, with around 100 per year. Australia may also be close in terms of tornado potential, but its sparse population helps make its tornado climatology difficult to determine. Other Southern Hemispheric countries experiencing a significant number of tornadoes include New Zealand, South Africa, and Argentina. In the Northern Hemisphere, much of middle Europe from Italy north into England and Russia are tornado susceptible. At least 50 tornadoes were reported in England in an 82-yr period ending in 1949, with October being the peak tornado month. In fact, the United Kingdom (UK) has more tornadoes, relative to its land area, than any other country. Fortunately, most UK tornadoes are relatively weak. Tornadoes are rare in the tropics. Japan, eastern China, northern India, Pakistan, and Bangladesh have tornadoes, as well as Bermuda and the Fiji Islands. On June 24, 1904, a killer tornado swept through portions of Moscow, Russia, taking at least 24 lives. On March 19, 1978, a tornado struck New Delhi, India; 17 persons perished and 700 were injured. In 1995, hundreds were reported killed by a tornado in Pakistan (refs. 12-6 and 12-7).

12.3.2 General U.S. Tornado Statistics

Table 12-1 gives a number of general tornado statistics for the United States, in terms of average, maximum, and range of tornadoes.

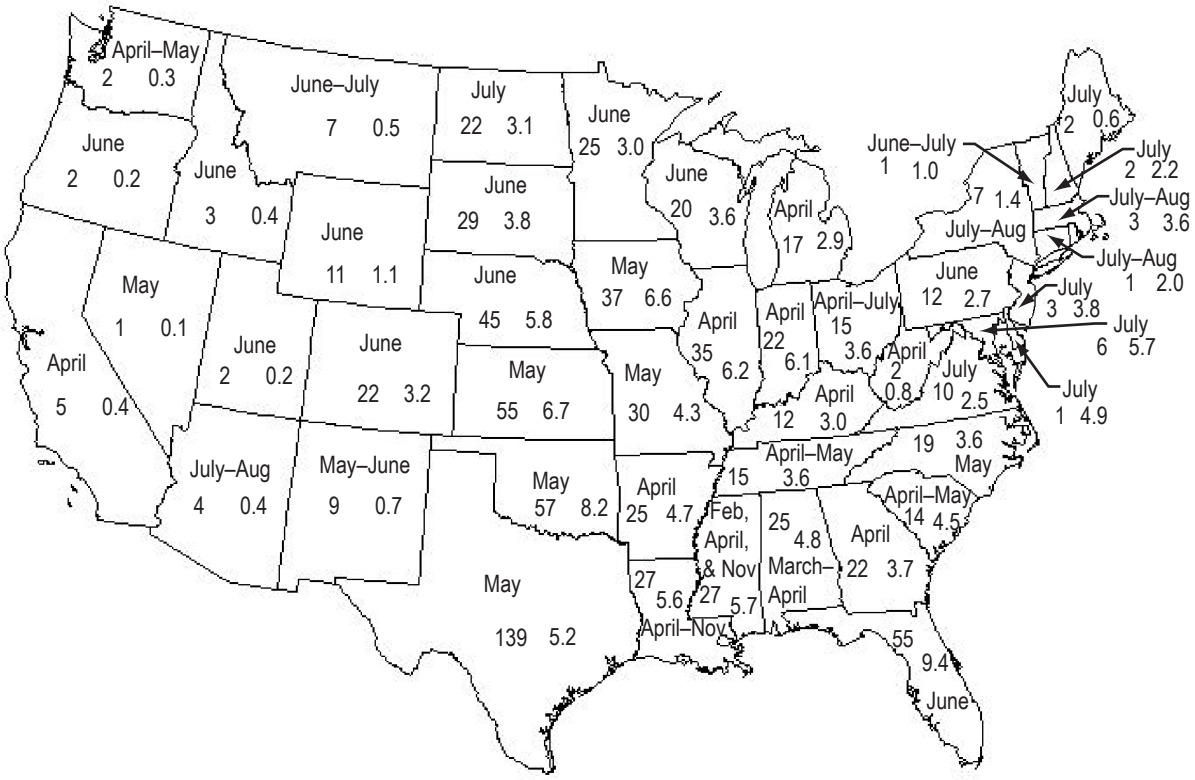

Figure 12-1. Average annual number of tornadoes (left) and tornadoes per 25,900 km^2 (10,000 mi^2) (right) by state (1953–2004), and month(s) of peak tornado activity (ref. 12-2).

Figure 12-4 presents a modeled "hit probability" across the path of a tornado with an embedded suction vortex. The AMS "Glossary of Meteorology" defines suction vortices as smaller-scale secondary vortices within a tornado core that orbit around a central axis. The wind speeds associated with the "parent" vortex in which the subvortices are embedded might be relatively weak compared to those in the transient subvortices. But the existence of multiple vortices is also not a reliable indicator of the possibility of strong intensity. The occurrence of multiple vortices depends on the so-called "swirl ratio," which is the ratio of the tangential velocity to the vertical velocity. Generally speaking, as the swirl ratio increases, the likelihood of multiple vortices increases; i.e., the existence of multiple vortices is airflow that is increasingly dominated by the tangential winds compared to the vertical winds. Note that even dust devils can have multiple vortices, so a multivortex tornado need not be particularly intense (ref. 12-9).

Figure 12-5 presents an idealized vertical distribution of maximum wind speed associated with an F4 tornado, with and without multiple vortices, which can be used for estimating tornadic wind speed with altitude (ref. 12-10).

Given a tornado path width and/or path length, figure 12-6 presents the empirically derived probability of the various Fujita damage/wind F-scales (F-scale is discussed in subsection 12.3.3). The weaker tornadoes (F0–F2) tend to have shorter widths and lengths, while the stronger tornadoes (F3–F5) tend to have longer widths and lengths. For example, given a width of ≈1,600 m (≈5,249 ft), around 45 percent of the tornadoes are violent (F4–F5), whereas for widths of ≈500 m (≈1,640 ft), only 10 percent of the tornadoes are violent.

It is true that the size of the damage swath and tornado intensity are related, at least statistically. As width and, to a lesser extent, the length of the path increase, the more probable the F-scale increases as well. Therefore,

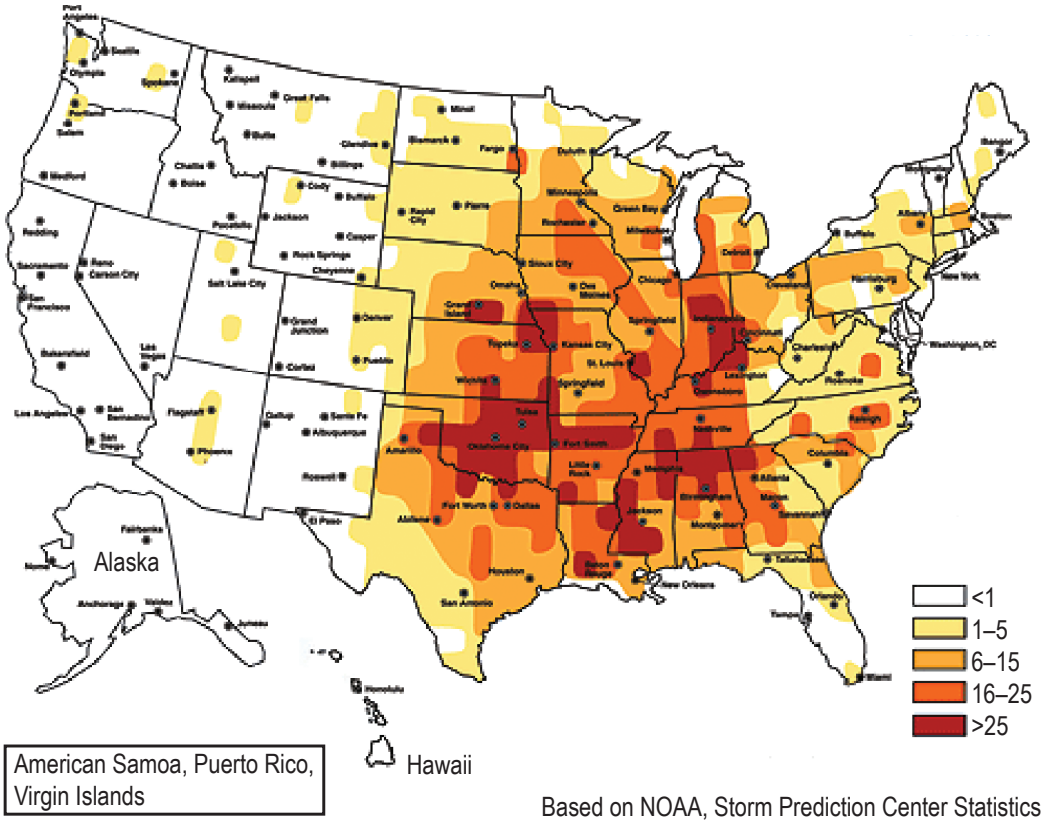

Figure 12-2. Number of strong (F3–F5) U.S. tornadoes per 9,580 km^2 (3,700 mi^2) (1950–1998) (ref. 12-5).

Figure 12-3. Regions of the world with increased likelihood of experiencing tornadoes (ref. 12-6).

Table 12-1. Various general U.S. tornado statistics (ref. 12-8).

U.S. Tornado Statistics	Average (*A*)/ Maximum (*M*)/ Range (*R*)	Comments or Background
Tornado direction	*A*=From SW to NE	Or W to E, or from any direction
Tornado duration	*A*=<10 min	*R*=several seconds to >1 hr
Yearly tornado frequency	*R*=1,000–1,200	With 60–70 fatalities, and ≈1,500 injuries
Time of tornado occurrence	*A*=3 to 9 p.m. LST	Or any time
Worst tornado month	*A*=May, then June	May 2003 with maximum of 543 recorded
Tornado forward speed	*A*=13.4 m/s (30 mph)	*R*=approximately stationary to 31.3 m/s (70 mph)
Maximum rotating wind speed	*M*=>112 m/s (>250 mph)	Unknown upper limit
Highest measured tornadic wind	*M*=142 m/s (318 mph)**	Doppler radar, F5, Bridge Creek, OK, May 3, 1999
Widest observed path	*M*=4 km (2½ mi) wide	Hallam, NE, F4 tornado, May 22, 2004
Longest observed path	*M*=352 km (219 mi) long	Tri-state tornado, March 18, 1925
Highest elevation tornado	*M*=3048 m (10,000 ft) ASL	Sequoia National Park, CA, July 7, 2004
Measured tornado pressure drop	*M*=2.95-inHg (100-mb) drop	Via "turtle," Manchester, SD, tornado June 24, 2003
Hurricane-spawned tornadoes	Do occur	In supercells within the outer bands, in hurricane NE quadrant, (NNW through ESE of center). Hurricane Beulah in 1967 spawned 115 tornadoes
Probability of a tornado hit	About once/1,000 yr	Probability tornado can hit any square mile of land
Deadliest U.S. tornado	*M*=695 killed	Tri-state tornado, March 18, 1925
Deadliest U.S. tornado day	*M*=April 3, 1974	308 people killed
Biggest tornado outbreak	*M*=147 tornadoes	April 3–4, 1974, in 13 U.S. states; 310 killed and 5,454 injured; 48 were killer tornadoes, 7 were rated F5 and 23 rated F4
City with most tornado hits	*M*=Oklahoma City, OK	Oklahoma leads with known total now of 112, through 2003, followed by Huntsville, AL* (site of NASA Marshall Space Flight Center)

*Based on Tatom SATT (ref. 12-8) statistics through 2003; using tornado-affected land area within a 32.2-km (20-mi) radius of center of cities with population >100,000.
**Unofficial: measured via doppler radar above the Earth's surface and not at ground level.

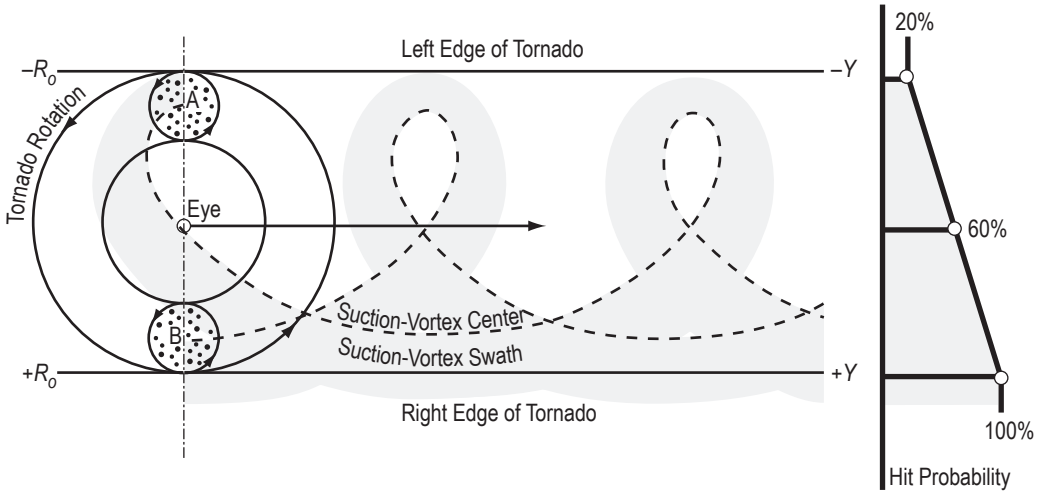

Figure 12-4. The hit probability across the path of a tornado width (R_o) with two embedded suction vortices (ref. 12-10).

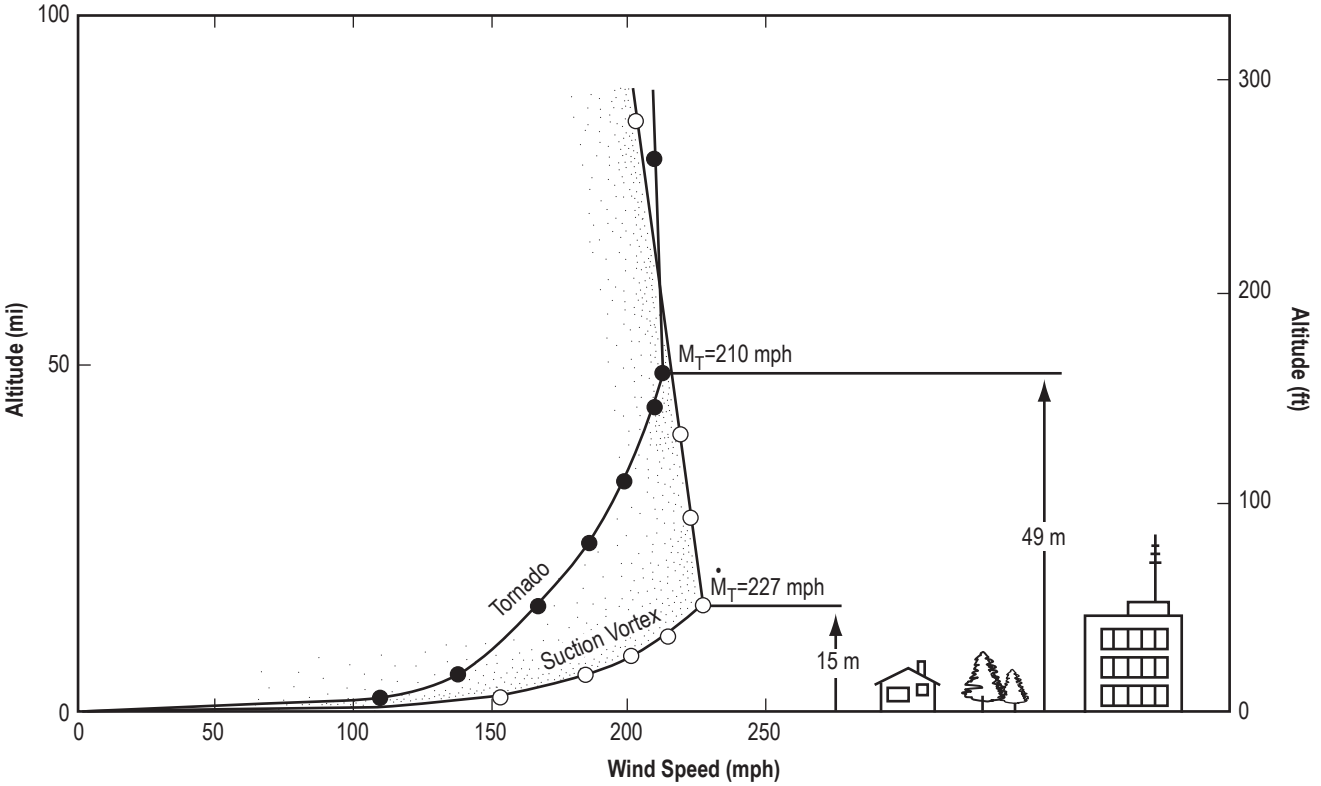

Figure 12-5. Vertical distribution of F4 tornado maximum wind speeds with embedded suction vortex (ref. 12-10).

it would be logical to assume that tornado size is a way to gauge its intensity. This statistical relationship does not hold, unfortunately, for "specific tornadoes," as a statistical tendency does not equate to a general rule. For any given tornado, the windfield is a complicated function of space and time. The tornado results ultimately from a process of conservation of angular momentum (sometimes referred to as vortex stretching).

12.3.3 Fujita Tornado Intensity/Damage Scale

The F-scale was introduced by Fujita (ref. 12-4) in 1971 to rank tornadoes as to how much damage they cause. Fujita initially established the scale categories by connecting the Beaufort wind scale with the Mach 1 speed of sound. For each category, Fujita then estimated how strong the wind (the fastest 0.4 km (0.25 mi) wind) must have been to cause observed damage at the height of the damaged structure. The resulting classification became known as the Fujita scale (or Fujita-Pearson scale). The original 13-point constructed intensity scale was later reduced down to the final 6-point scale (F0–F5), after it was realized that F7–F12 levels did not occur.

The primary limitations of the original Fujita scale are a lack of damage indicators (DIs), no account of construction quality, variability, and no definitive correlation between damage and wind speed. These limitations have led to an inconsistent rating of tornadoes and, in some cases, an overestimate of tornado wind speeds. Therefore, the enhanced F-scale (EF-scale) was implemented by the National Oceanic and Atmospheric Administration (NOAA) on February 1, 2007, for better estimating the strength of tornadoes in the United States by estimating the strongest 3-s wind gust based on 28 DIs consisting of 28 classes of buildings, structures, and trees.

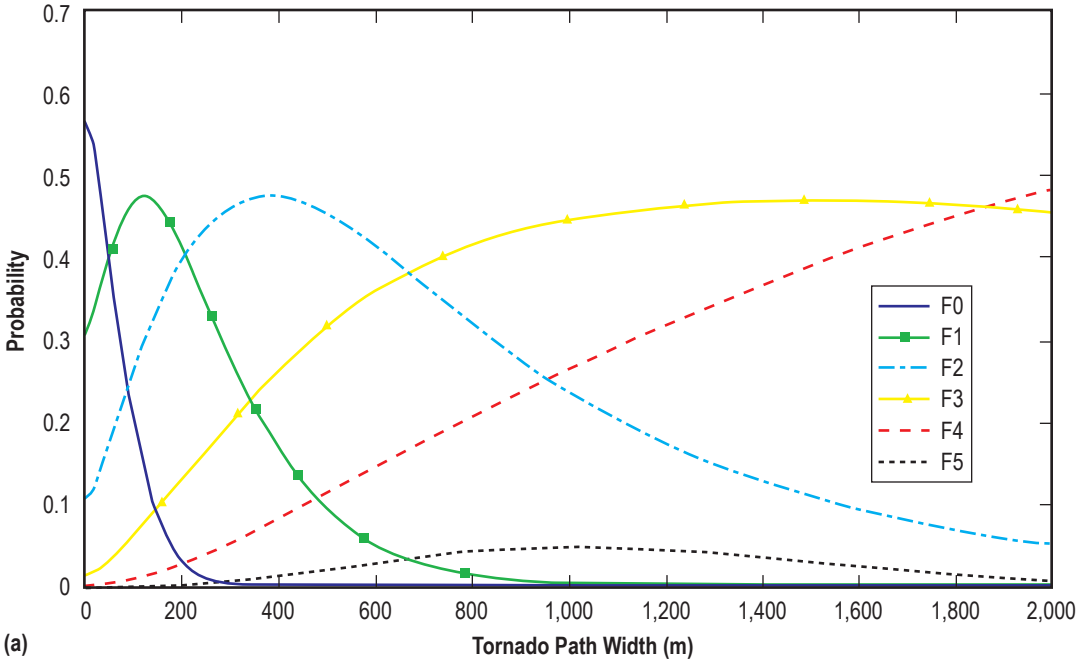

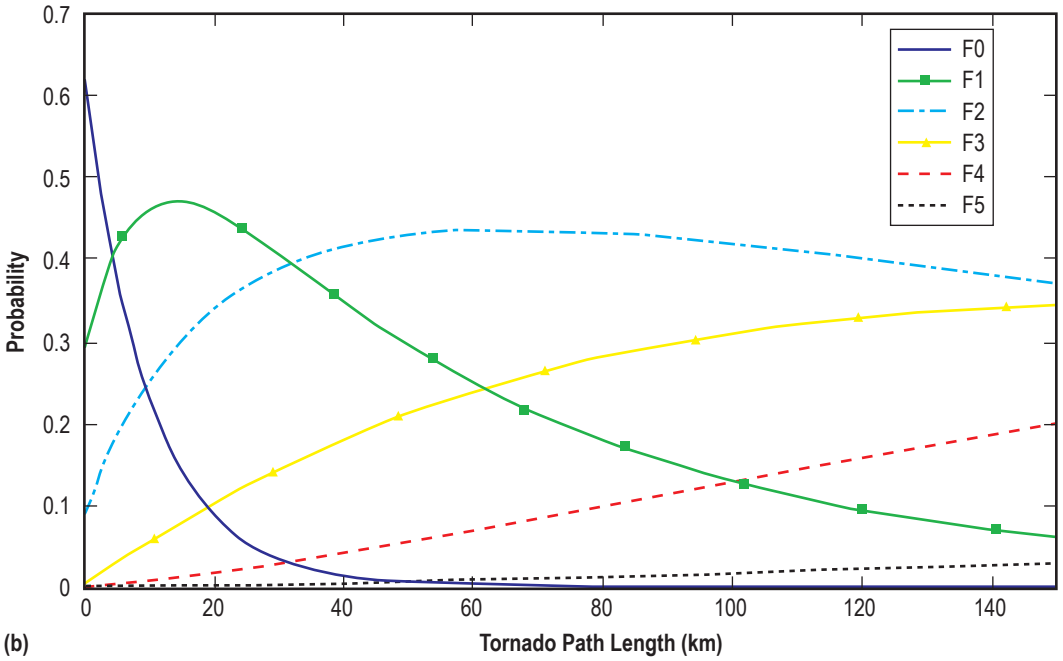

Figure 12-6. Probability of the F-scale rating given (a) path width and (b) path length (figures were constructed from data provided by H. Brooks) (ref. 12-9).

For each DI, several degrees of damage (DODs) are identified. The EF-scale is still a set of wind estimates (not measurements) based on damage. It uses 3-s gusts estimated at the point of damage based on a judgment of eight levels of damage using the 28 indicators.

When using the EF-scale to determine the tornado's rating, one begins with the 28 DIs. Each one of the indicators has a description of the typical construction for that category of indicator. The next step is to find the DOD. Each DOD within each category is given and the expected estimate of wind speed; i.e., a lower bound of wind speed and an upper bound of wind speed, will then result. See reference 12-11 for the DI and DOD values. As an example, a tornado moves through a neighborhood and walls in an area of homes are knocked down. Here, the DI would be No. 2—one or two family residences (FR12); the typical construction being a brick veneer siding home. The DOD would be a 9: most walls collapsed in the bottom floor. Thus, the estimated range of winds would be 57–80 m/s (127–178 mph), with the expected wind speed of 68 m/s (152 mph). Now, taking this number to the EF-scale, the damage would be rated EF-3 with winds between 61 and 74 m/s (136 and 165 mph). One would need to go to references 12-11 and 12-12 to actually utilize the EF-scale method described here.

Since the historic F-scale tornado database should be preserved, the following correlation relating the F-scale with the EF-scale, based on wind speed, was derived. The F-scale wind speeds were first converted to a 3-s gust frame of reference. The original F-scale categories were then used (F0, F1, etc.) with the DODs of the new EF-scale. A regression analysis was then done to obtain the proper relationship, with equation, as shown in figure 12-7.

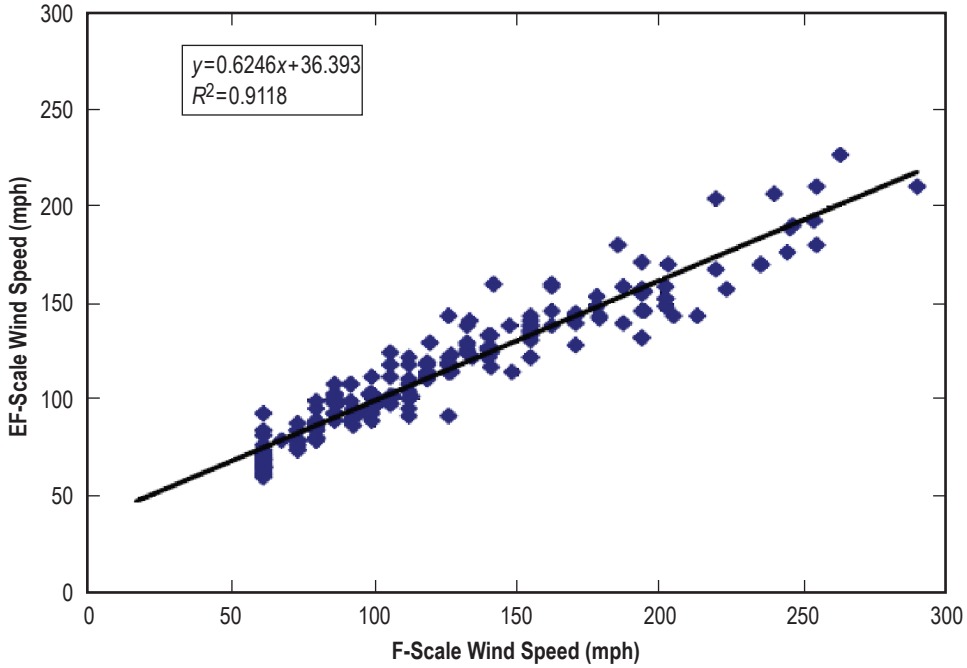

Figure 12-7. Correlation of F-scale and EF-scale wind speeds (ref. 12-11).

Table 12-2 describes some statistical characteristics of both the old 6-point F-scale and the new EF-scale. Table 12-3 gives total tornado occurrence and tornado path length statistics, including a percentage of both, for a 70-yr U.S. period of record (1916–1985). It is broken down for each F-scale parameter (ref. 12-4).

In the early 1970s, another tornado wind speed scale was proposed; i.e., an international worldwide tornado T-scale (TORRO) based on the Beaufort scale (B-scale), since the Fujita damage scale (F-scale) was developed for North America but less convenient if used elsewhere. Forces on the T-scale span the digital range zero to 10. The T-scale is a wind speed intensity scale rather than a damage scale, as is the B-scale, modified for the

Table 12-2. The F-scale, EF-scale, T-scale, and B-scale (refs. 12-4, 12-10, and 12-13).

Fujita Scale	Tornado Damage	Winds* (m/s, mph, kt)	Tornado Frequency** (%)	Path Length*** Range		Mean Width*** Range		Enhanced Fujita Scale	Operational EF-Scale 3-s Gust (m/s, mph, kt)	Torro Scale (0–10)	Beaufort Scale (8–28)
				(km)	(mi)	(m) or (km)	(mi)				
F0	Light (gale)	17.9–32.2 m/s 40–72 mph 35–62 kt	39	<1.6	<1	5–15 m	6–17 yd (<0.01 mi)	EF0	29–38 m/s 65–85 mph 56–74 kt	–0.15	7.7
F1	Moderate (weak)	32.6–50.1 m/s 73–112 mph 63–97 kt	36	1.6–5	1–3.1	16–50 m	18–55 yd (0.01–0.03 mi)	EF1	38.4–49.2 m/s 86–110 mph 75–96 kt	1.8	11.5
F2	Considerable (strong)	50.5–70.2 m/s 113–157 mph 98–136 kt	19	5.1–15.9	3.2–9.9	51–160 m	56–175 yd (0.04–0.09 mi)	EF2	49.6–60.4 m/s 111–135 mph 97–117 kt	3.7	15.4
F3	Severe	70.6–92.1 m/s 158–206 mph 137–179 kt	5	16–50	10–31	161–518 m 0.16–0.5 km	176–566 yd (0.1–0.31 mi)	EF3	60.8–73.8 m/s 136–165 mph 118–143 kt	5.6	19.2
F4	Devastating	92.5–116.2 m/s 207–260 mph 180–226 kt	1	51–159	32–99	0.51–1.59 km	0.32–0.99 mi	EF4	74.2–89.4 m/s 166–200 mph 144–174 kt	7.5	23.1
F5	Incredible	116.7–142.2 m/s 261–318 mph 227–276 kt	<1	160–507	100–315	1.60–5 km	1.0–3.1 mi	EF5	>89.4 m/s >200 mph >174 kt	9.5	26.9
F6–F12	Inconceivable	142.6 m/s 319 mph to speed of sound	<<<1	Unknown	Unknown	Unknown	Unknown	>EF5	EF no rating	–	–

* Based on the fastest 0.4-km (0.25-mi) wind. The respective 3-s gust values are slightly larger than the 0.4-km (0.25-mi) wind speeds.

** Taken from reference 12-14.

*** The above guidelines are based on conceptual wind speeds, path widths, and path lengths. Most tornadoes do not follow these guidelines, however. Some of the most intense tornadoes have traveled <161 km (<100 mi). On the other hand, an F2 tornado has produced a path width up to 229 m (250 yd) and a path length of 30.6 km (19 mi), which does not follow the above guidelines.

Note: Important note about F-scale winds: Do not use F-scale winds literally. These precise wind speed numbers are actually guesses and have never been scientifically verified. Different wind speeds may cause similar-looking damage from place to place—even from building to building. Without a thorough engineering analysis of tornado damage, in any event, the actual wind speeds needed to cause that damage are unknown.

Table 12-3. F-scale U.S. tornado occurrences and path length characteristics over a 70-yr period (1916–1985) (ref. 12-4).

F-Scale	F0	F1	F2	F3	F4	F5	All F
Total No. of tornadoes	7,911	11,574	7,963	2,878	640	88	31,054
Percentage of total tornadoes	25.5	37.3	25.6	9.3	2	0.3	100
Total tornado path lengths in km (mi)	15,421 (9,582)	48,650 (30,230)	68,941 (42,838)	46,360 (28,807)	28,041 (17,424)	5,028 (3,124)	212,442 (132,005)
Percentage of total path lengths	7.3	22.9	32.5	21.8	13.2	2.4	100
Mean path length in km (mi)	1.9 (1.2)	4.2 (2.6)	8.7 (5.4)	16.1 (10)	43.8 (27.2)	57.1 (35.5)	6.9 (4.3)

higher wind speeds of tornadoes, based on 3-s gusts. The exact relationship between the T-scale (T) and B-scale (B) can be expressed as:

$$T = (B/2 - 4), \text{ or } B = 2\,(T + 4) \ . \tag{12.1}$$

The relationship between the velocity of the wind (v) and B-scale number (B) is

$$v(\text{mi/hr}) = 1.87\ B^{(3/2)}, \text{ or } v\,(\text{m/s}) = 0.837 B^{(3/2)} \ . \tag{12.2}$$

Therefore, the relationship between the T-scale (T) and wind intensity (v) is

$$v\,(\text{mi/hr}) = 5.289\,(T+4)^{3/2}, \text{ or } v\,(\text{m/s}) = 2.367(T+4)^{3/2} \ . \tag{12.3}$$

Now Fujita's F-scale relationship with wind velocity (v) is

$$v\,(\text{m/s}) = 14.09(F+2)^{3/2}, \text{ or } v\,(\text{m/s}) = 6.30(F+2)^{3/2} \ . \tag{12.4}$$

Table 12-2 presents all four of these tornado scales, as related to the F-scale's damage and wind speed criteria.

Fujita calculated what the maximum tornadic wind speeds would be with a 10^{-7} or 1/10,000,000 per year probability of occurrence. These wind speed categories are presented in figure 12-8 for the continental United States. The highest wind speed of 138 m/s (308 mph) with a 10^{-7} per year probability was found to be located in both central Oklahoma and northern Alabama. Wind speeds of 143 m/s (320 mph) appear to be a reasonable maximum speed for tornadoes east of 105º longitude (eastern and central U.S.); while 80 m/s (180 mph) maximum is reasonable west of 105º longitude (ref. 12-15).

12.3.4 Site Assessment of Tornado Threat Database and NASA Facilities

The Site Assessment of Tornado Threat (SATT) 3.0 tornado program is a program that gives tornado results expressed in an annual coverage fraction (ACF) probability for any circular, radial area about a location. The ACF is an annual tornado probability that is based on the total area covered by tornadoes within the region of interest, divided by the area of the region of interest and the number of years of data considered. All historic tornado path widths and path lengths within a selected circular area are used in producing ACF statistics. It is an "area" type of tornado probability statistic (refs. 12-8 and 12-16).

The most tornado-prone spot (point location) within each U.S. state that has a NASA facility within it is given in table 12-4 for a 53-yr data period. These calculations are from the SATT 3.0 tornado program (refs. 12-8 and 12-16). The total number of tornadoes within a 32.2-km (20-mi) radius of the point is presented, along with the number of weak to strong tornadoes. The ACF is calculated for each circular area about each point, along with the direction and the number of miles the tornado-prone location is from a NASA facility. Note that the hotspot in Alabama ranks high nationally in ACF value, and is located within 10 mi of NASA Marshall Space Flight Center (MSFC). Also, this Alabama location ties Oklahoma and exceeds Nebraska in the total number of strong F4 and F5 tornado occurrences with 11. The number of tornadoes along with their ACF values, for California, Florida, New Mexico, and Utah indicates that these states generally have weak and/or short-lived tornadoes.

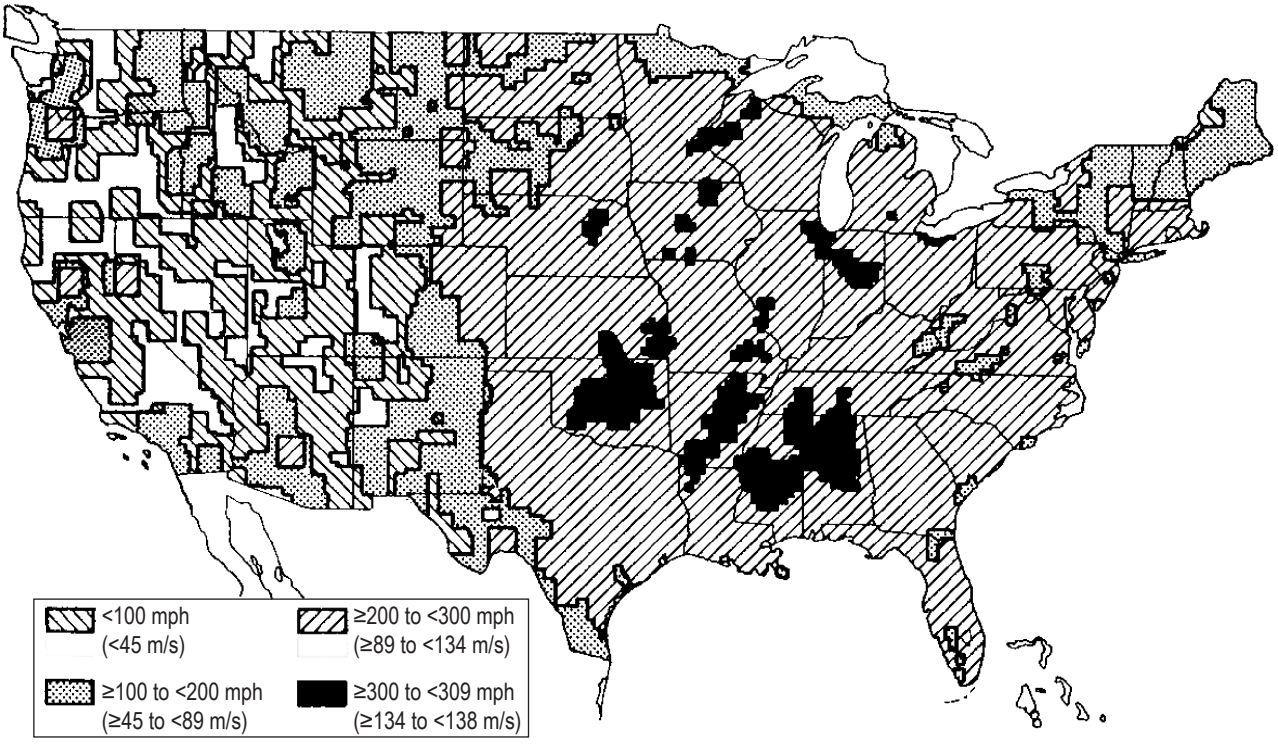

Figure 12-8. Distribution of the maximum wind speeds of tornadoes expected to occur with a 10^{-7} or 1/10,000,000 per year probability which is required for protecting nuclear power plants in the United States (ref. 12-4).

For various sites of interest to NASA, based on SATT 3.0 with National Weather Service (NWS) data from 1950 through 2001, the number of tornadic events and the average area of tornadoes are presented in table 12-5 for each tornadic intensity level, as well as an overall value for all intensities (refs. 12-8 and 12-16). Further tornado path length and width statistics are given in tables 12-2 and 12-3.

In Thom's analysis (ref. 12-17), based on data from 1953 through 1962 for Iowa and Kansas tornadoes, the mean tornado path length and width were computed. For mean path length, a value of 6.34 km (3.94 mi) was given, while for path width, a value of 140.8 m (154 yd) was given. Based on the computed value of mean path length and width, Thom computed a mean path area of 7.31 km^2 (2.8209 mi^2). Although Thom suggested that the path length and width for tornadoes should be analyzed from place to place to determine whether or not they were invariant, he also developed an equation for tornado probability based on the assumption that the value for mean path area was a constant (7.31 km^2 (2.8209 mi^2)).

By means of SATT 3.0, based on an analysis of all Iowa and Kansas tornadoes from 1953 through 1962, the ACF is 6.3547×10^{-4}. This involves 813 tornadoes and corresponds to an average path area of 2.79 km^2 (1.0771 mi^2). Such a value, which is ≈38 percent of Thom's value, appears to be more accurate because of the more rigorous computational technique employed by SATT 3.0.

Contrary to Thom's assumption that the mean path area can be treated as a constant, the value of the mean path area actually varies from place to place. Clearly, the local values not only vary greatly from place to place, but all are smaller than Thom's value.

Table 12-4. Most tornado-prone spot for NASA facility states over the 53-yr POR (1950–2002)* (refs. 12-8 and 12-16).

State	Spot Location Latitude (N)/ Longitude (W)	No. Tornadoes Within 32 km (20 mi) of Spot**	ACF (%)***	Approximate Distance From NASA Facility
Alabama	34°48m/86°41m	56 (8-15-16-6-6-5)	0.1349	16 km (10 mi) N of MSFC
California	33°53m/118°4m	40 (26-9-5-0-0-0)	0.0151	254 km (158 mi) ESE of VAFB 114 km (71 mi) S of EAFB/DFRC 373 km (232 mi) SE of ARC 35 km (22 mi) SE of JPL
Florida	28°26m/81°18m	72 (27-25-14-5-1-0)	0.0316	66 km (41 mi) WSW of KSC
Louisiana	32°30m/93°32m	86 (5-40-16-19-6-0)	0.0975	430 km (267 mi) NW of MAF
Maryland	38°45m/76°55m	43 (8-23-7-4-1-0)	0.0260	27 km (17 mi) S of GSFC
Mississippi	31°58m/89°28m	74 (9-22-20-16-7-0)	0.1397	179 km (111 mi) N of SSC
New Mexico	33°55m/103°00m	37 (26-7-4-0-0-0)	0.0259	367 km (228 mi) ENE of WSTF
Ohio	41°42m/84°39m	46 (8-13-16-5-4-0)	0.0794	235 km (146 mi) W of GRC
Tennessee	35°14m/87°28m	38 (7-11-10-6-2-2)	0.1382	98 km (61 mi) NW of MSFC
Texas	35°21m/100°10m	57 (26-11-5-10-6-0)	0.0980	801 km (498 mi) NW of JSC
Utah	40°19m/110°11m	3 (2-0-0-1-0-0)	0.0148	246 km (153 mi) SE of Thiokol
Virginia	37°14m/77°11m	39 (4-14-9-6-6-0)	0.0374	76 km (47 mi) WNW of LaRC 171 km (106 mi) W of WFF
Washington, DC†	38°48m/77°02m	45 (9-24-7-4-1-0)	0.0226	10 km (6 mi) S of HDQT
USA (Nebraska)‡	40°46m/98°07m	116 (48-40-14-6-5-3)	0.2036	(Does not apply)
Oklahoma	35°34m/96°31m	86 (18-19-22-16-8-3)	0.1800	(Does not apply)

*There is the possibility that the tornado-prone location in an adjacent state may be closer to the NASA facility than the tornado-prone location in the home state.

**Total number of tornadoes, followed by a breakdown of that number by the Fujita tornado intensity levels (F0–F1–F2–F3–F4–F5).

***ACF is the annual, average, area fraction of the land disturbed by tornadoes within the 32-km (20-mi) circle land area (in percent). Calculated from SATT 3.0 model.

†Since Washington, DC, has such small land area, the calculation of the most tornado-prone spot for Washington, DC, included data from Virginia and Maryland which are within 32 km (20 mi) of the point in question.

‡The most tornado-prone spot in the United States is at this location in Nebraska.

These preceding results imply that the last two columns in table 12-4 in *NASA-HDBK-1001* of 2000 (ref. 12-18) are not accurate. With this point in mind, by means of SATT 3.0, based on NWS data from 1950 through 2001, a revised version for table 12-4 has been generated, and is presented in table 12-6. In this table, in place of 1º squares with surface areas A_2 corresponding to column 4, circular regions have been used with radii corresponding to column 5, such that the surface areas match the values of A_2 given in column 4.

The probability of one or more tornadoes in N years in an area (A_1) is given by

$$P\left(A_1; N\right) = 1 - \exp\left(\left(-\bar{x} \times A_1 \times N\right) / A_2\right) , \tag{12.5}$$

where $\bar{x}$ is the mean number of tornadoes in a circular region equivalent to a 1º square. (Personal Communication—credit is due Dr. J. Goldman, International Center for the Solution of Environmental Problems, Houston, TX, for this form of the probability expression.) Two area sizes for A_1 were chosen, corresponding to 7.3 km^2

Table 12-5. Tornado event characteristics (refs. 12-8 and 12-17).

Tornado Intensity	F0	F1	F2	F3	F4	F5	ALL F
Tornado No.	N_{T0}	N_{T1}	N_{T2}	N_{T3}	N_{T4}	N_{T5}	N_T
Area (km^2) Area (mi^2)	A_{T0} (km^2) A_{T0} (mi^2)	A_{T1} (km^2) A_{T1} (mi^2)	A_{T2} (km^2) A_{T2} (mi^2)	A_{T3} (km^2) A_{T3} (mi^2)	A_{T4} (km^2) A_{T4} (mi^2)	A_{T5} (km^2) A_{T5} (mi^2)	A_T (km^2) A_T (mi^2)
State:							
Alabama	275 1.295×10^{-1} 5.00×10^{-2}	436 5.903×10^{-1} 2.28×10^{-1}	355 1.755×10^{0} 6.78×10^{-1}	143 3.992×10^{0} 1.542×10^{0}	39 $1.389\times10^{+1}$ 5.364×10^{0}	16 $1.250\times10^{+1}$ 4.828×10^{0}	1,264 1.763×10^{0} 6.81×10^{-1}
California	190 9.673×10^{-3} 3.736×10^{-3}	63 8.627×10^{-2} 3.332×10^{-2}	24 1.125×10^{0} 4.347×10^{-1}	2 2.350×10^{-3} 9.077×10^{-4}	0 0 0	0 0 0	279 1.229×10^{-1} 4.748×10^{-2}
Florida	1,464 2.698×10^{-2} 1.042×10^{-2}	738 1.627×10^{-1} 6.286×10^{-2}	311 6.131×10^{-1} 2.368×10^{-1}	36 2.084×10^{0} 8.048×10^{-1}	4 $1.374\times10^{+1}$ 5.306×10^{0}	1 2.101×10^{-2} 8.117×10^{-3}	2,554 1.880×10^{-1} 7.262×10^{-2}
Louisiana	310 3.663×10^{-2} 1.415×10^{-2}	643 4.370×10^{-1} 1.688×10^{-1}	283 1.314×10^{0} 5.075×10^{-1}	125 3.065×10^{0} 1.184×10^{0}	18 3.824×10^{0} 1.477×10^{0}	2 $1.067\times10^{+1}$ 4.120×10^{0}	1,381 8.233×10^{-1} 3.180×10^{-1}
Mississippi	285 1.414×10^{0} 5.463×10^{-1}	505 8.158×10^{-1} 3.151×10^{-1}	376 2.258×10^{0} 8.721×10^{-1}	153 6.750×10^{0} 2.607×10^{0}	48 $1.001\times10^{+1}$ 3.866×10^{0}	11 7.014×10^{0} 2.709×10^{0}	1,378 2.367×10^{0} 9.141×10^{-1}
New Mexico	303 3.726×10^{-2} 1.439×10^{-2}	102 2.633×10^{-1} 1.017×10^{-1}	30 6.289×10^{-1} 2.429×10^{-1}	5 5.685×10^{-1} 2.196×10^{-1}	0 0 0	0 0 0	440 1.360×10^{-1} 5.254×10^{-2}
Texas	3,173 9.817×10^{-2} 3.792×10^{-2}	1,983 4.324×10^{-1} 1.670×10^{-1}	1,125 1.217×10^{0} 4.702×10^{-1}	336 3.630×10^{0} 1.402×10^{0}	73 $1.428\times10^{+1}$ 5.514×10^{0}	6 8.194×10^{0} 3.165×10^{0}	6,696 7.244×10^{-1} 2.798×10^{-1}
Utah	68 7.705×10^{-2} 2.976×10^{-2}	21 2.089×10^{-1} 8.067×10^{-2}	7 2.064×10^{-1} 7.971×10^{-2}	1 $2.526\times10^{+1}$ 9.755×10^{0}	0 0 0	0 0 0	97 3.746×10^{-1} 1.447×10^{-1}
Eastern U.S. longitude <95° W.	7,493 2.091×10^{-1} 8.076×10^{-2}	9,036 5.515×10^{-1} 2.130×10^{-1}	5,331 1.885×10^{0} 7.281×10^{-1}	1,784 5.711×10^{0} 2.206×10^{0}	673 9.103×10^{0} 3.516×10^{0}	94 9.981×10^{0} 3.855×10^{0}	24,411 1.387×10^{0} 5.356×10^{-1}
Western U.S. longitude >95° W.	10,400 1.453×10^{-1} 5.614×10^{-2}	5,777 5.820×10^{-1} 2.248×10^{-1}	3,073 1.824×10^{0} 7.046×10^{-1}	973 6.113×10^{0} 2.361×10^{0}	274 $1.143\times10^{+1}$ 4.413×10^{0}	42 $1.657\times10^{+1}$ 6.400×10^{0}	20,539 9.862×10^{-1} 3.809×10^{-1}

(2.8 mi^2) and 2.59 km^2 (1 mi^2). The first size for A_1 was chosen because vital industrial complexes for most locations are of this general size. The second size was selected because it corresponds to 2.59 km^2 (1 mi^2), which is a commonly used unit measure of area. Thus, with these two values of A_1, an evaluation of equation (12.5) for values of $\bar{x}$ and A_2, for the stations given in table 12-6, yields the results presented in table 12-7. This table presents the probability of one or more tornadoes in 7.3 km^2 (2.8209 mi^2) and 2.59 km^2 (1 mi^2) areas in 1, 10, and 100 yr for the eight locations previously noted.

It is noted that for $A_1 << A_2$ and $N < 100$, equation (12.5) can be approximated by

$$P\left(A_1; N\right) = \left(\bar{x} \times A_1 \times N\right) / A_2 \quad . \tag{12.6}$$

Table 12-6. Tornado statistics for NASA stations specified (1950–2001) (refs. 12-8 and 12-16).

Station	Number of Tornadoes in Circular Region	Mean Number Tornadoes Per Year in Circular Region	Area* (A_2) of Circular Region		Radius of Circular Region		Annual Coverage Fraction (yr^{-1})	Recurrence Interval 1/ACF (yr)
			(km^2)	(mi^2)	(km)	(mi)		
Marshall Space Flight Center, Alabama	134	2.58	10,179	3,930	56.89	35.36	8.069×10^{-4}	1,239
Kennedy Space Center, Florida	124	2.38	10,839	4,185	58.73	36.50	7.498×10^{-5}	13,337
Vandenberg AFB, California	3	0.0577	10,179	3,930	56.89	35.36	4.827×10^{-10}	2.071×10^{9}
Edwards AFB, California	8	0.154	10,179	3,930	56.89	35.36	1.851×10^{-8}	5.402×10^{7}
Michoud, Louisiana	101	1.94	10,645	4,110	58.20	36.17	3.627×10^{-5}	27,571
Stennis SC, Mississippi	196	3.77	10,645	4,110	58.20	36.17	7.150×10^{-4}	1,399
Johnson Space Center, Texas	310	5.96	10,736	4,145	58.44	36.32	3.121×10^{-4}	3,204
White Sands, New Mexico	7	0.135	10,412	4,020	57.55	35.77	1.017×10^{-6}	9.833×10^{5}

*Area of circular region equal to area of 1° square.

Table 12-7. Probability of one or more tornadoes in a 7.3-km^2 (2.82-mi^2) area and a 2.59-km^2 (1-mi^2) area in 1, 10, and 100 yr for NASA sites (refs. 12-8 and 12-16).

Station	Mean Number of Tornadoes Per Year in Circular Region*	$P(A_2{:}N)$ A_2=7.3 km^2 (2.8 mi^2)			$P(A_2{:}N)$ A_2=2.59 km^2 (1 mi^2)		
		N=1 yr	N=10 yr	N=100 yr	N=1 yr	N=10 yr	N=100 yr
Marshall Space Flight Center, Alabama	2.58	1.850×10^{-3}	1.835×10^{-2}	1.69×10^{-1}	6.563×10^{-4}	6.543×10^{-3}	6.354×10^{-2}
Kennedy Space Center, Florida	2.38	1.603×10^{-3}	1.591×10^{-2}	1.48×10^{-1}	5.685×10^{-4}	5.671×10^{-3}	5.528×10^{-2}
Vandenberg AFB, California	0.0577	4.142×10^{-5}	4.14×10^{-4}	4.133×10^{-3}	1.468×10^{-5}	1.468×10^{-4}	1.467×10^{-3}
Edwards AFB, California	0.154	1.105×10^{-4}	1.105×10^{-3}	1.099×10^{-2}	3.919×10^{-5}	3.918×10^{-4}	3.911×10^{-3}
Michoud, Louisiana	1.94	1.331×10^{-3}	1.323×10^{-2}	1.247×10^{-1}	4.719×10^{-4}	4.709×10^{-3}	4.611×10^{-2}
Stennis SC, Mississippi	3.77	2.564×10^{-3}	2.554×10^{-2}	2.280×10^{-1}	9.169×10^{-4}	9.131×10^{-3}	8.765×10^{-2}
Johnson Space Center, Texas	5.96	4.048×10^{-3}	3.975×10^{-2}	3.334×10^{-1}	1.437×10^{-3}	1.428×10^{-2}	1.339×10^{-1}
White Sands, New Mexico	0.135	9.473×10^{-5}	9.469×10^{-4}	9.428×10^{-3}	3.358×10^{-5}	3.358×10^{-4}	3.353×10^{-3}

*With area equal to corresponding 1° square.

An interpretation of the statistics in table 12-7 is given using Kennedy Space Center (KSC) as an example. There is a 14.8-percent chance that at least one tornado will hit within a 7.3 km^2 (2.82 mi^2) area at KSC in 100 yr. For a 2.59 km^2 (1 mi^2) area at KSC, the chance of at least one tornado hit in 100 yr is 5.51 percent. If several structures within a 7.3-km^2 (2.82-mi^2) area at KSC are vital to a space mission and these structures are not designed to withstand the wind and internal pressure forces of a tornado, then there is a 14.8-percent chance that one or more of these vital structures will be damaged or destroyed by a tornado in 100 yr. If the desired lifetime of these structures (or 7.3-km^2 (2.82-mi^2) industrial complex) is 100 yr and the risk of destruction by tornadoes is accepted in the design, then the design risk or calculated risk of failure of at least one structure due to tornado occurrences is 14.8 percent. This example indicates that the probability of occurrence of an event that is rare in 1 yr becomes rather large when taken over many years, and that estimates for the desired lifetime versus design risk for structures discussed in subsection 2.2.10 of section 2 should be made with prudence.

Using SATT statistics, the number of tornadoes per 2,590 km^2 (1,000 mi^2) (POR 1950–2001) for the top 15 major U.S. cities, using a radius of 64.4 and 32.2 km (40 and 20 mi) from its center, ranks Houston, TX, as No. 2 behind Oklahoma City, OK, in both categories. Huntsville, AL, ranks No. 11 and 13 for the 64.4- and 32.2-km (40- and a 20-mi) radius, respectively (refs. 12-8 and 12-16).

Further tornado information and statistics relating to various NASA sites of interest are given in reference 12-19.

12.3.5 Tornado Occurrences at NASA Sites

Tornado occurrences at or near NASA sites are presented in this section. Further occurrence maps of tornadoes (and hail/wind) for various NASA sites are given in section 12.7.

12.3.5.1 Southeastern U.S. Tornadoes. The Southeastern United States can be divided up into five subregional areas indicated in table 12-8. Southern regional tornado statistics for a 39-yr POR (1950–1988), consisting of the number of tornadoes per year per area, along with the percentage of very strong tornadoes (≥F3), are presented therein (ref. 12-20). Florida Peninsula tornadoes are the most numerous although only about 1 percent are strong tornadoes, whereas the Interior Southeast area ranks third in the Southeast, but ranks first in strong tornadoes with 11.6 percent.

Table 12-8. Southeastern U.S. tornado areas and statistics for a 39-yr POR (1950–1988) (ref. 12-20).

Southeast United States Tornado Region*	States Included	No. Tornadoes/ Year/Area**	Tornadoes ≥F3 (%)
Central Atlantic Coast (Wallops)	Virginia/North Carolina/northeast Tennessee	3.64	4.5
South Atlantic Coast	South Carolina/east Georgia/north Florida	2.42	5.7
Florida Peninsula (Kennedy)	Florida Peninsula	12.1	1.1
Interior Southeast (Marshall)	East Arizona/north Mississippi/north Alabama/Tennessee	4.5	11.6
Gulf Coast (Stennis/Michoud)	Southeast Louisiana/south Mississippi/south Alabama, and southwest Georgia/Florida Panhandle	6.3	7.9

*NASA facility indicated here.
**Tornado data normalized to an standard unit area of 25,900 km^2 (10^4 mi^2).

12.3.5.2 Marshall Space Flight Center/Huntsville/Madison County, AL, Tornadoes. Although Huntsville (Madison County), AL, has had numerous tornadoes since 1950, two in particular have ventured close to MSFC facilities on Redstone Arsenal. The April 3–4, 1974, Super Tornado Outbreak in the South and Midwest produced an F3 tornado on the evening of April 3 that touched down near west gate 7 of Redstone Arsenal 1.6 km (1 mi) south-southwest of Madkin Mountain) at ≈10:40 p.m. LST. Then the tornado hit a glancing blow and caused damage to the MSFC Headquarters Building 4200 (large cracks in stairwell wall and some windows out) before proceeding over the gap in Madkin Mountain (northeast of Building 4200). There it dropped into the troop area at ≈10:53 p.m., skipping across the Arsenal area where it either damaged or destroyed 96 buildings. There were no deaths, but 26 people were injured on the Arsenal (ref. 12-21).

The Huntsville 1989 F4 Tornado of November 15, 1989, struck the southern portion of the city around 4:30 p.m. LST. Twenty-one people died with 463 injured. This tornado touched down initially on Redstone Arsenal. At 4:15 p.m., the Huntsville NWS observed a wall cloud and rainfree base with the thunderstorm. At ≈4:25 p.m., NASA meteorologists in Building 4610 observed rotation in the wall cloud. The initial point of Arsenal damage occurred 1.6 km (1 mi) south-southwest of Madkin Mountain near the intersection of Fowler and Mills Roads. The tornado continued on a northeast track passing northeast of Arsenal Building 5250, doing

damage before exiting the Arsenal and going through the old Huntsville airport area. Then it destroyed businesses and cars on Huntsville's Airport Road. However, no deaths occurred on the Arsenal itself (ref. 12-22).

Two other weaker tornadoes have also come close to the NASA facilities on Redstone Arsenal. On August 16, 1985, at 3:30 p.m. LST, an F1 tornado spawned by remnants of Hurricane Danny apparently first touched down ≈0.4 km (≈0.25 mi) west of the airfield at Redstone Arsenal and moved north to the Jeff area, very near the track of a tornado that had occurred less than an hour earlier. A three-story test building was damaged at Redstone Arsenal. Second, an F2 tornado occurred on June 26, 1994, at 9:50 p.m. LST that began on the north side of Madison, continuing south across the east side of Madison, and extending into the northern portion of the Redstone Arsenal. Homes and businesses were damaged or destroyed as well as numerous trees downed. Extensive damage around Madison's Bob Jones High School occurred (ref. 12-23).

12.3.5.3 Florida Tornadoes. Florida leads the nation in tornadoes per square mile, although Florida tornadoes generally are not as intense as those in the Midwest or Great Plains. They are generally F0 and F1. Hagemeyer did a study of 1,505 tornadoes at or south of 30° latitude in Florida from 1950 through 1994, and found 35 tornado outbreak cases in which four or more tornadoes occurred in 4 hr or less. Tornado outbreak cases accounted for 3.4 percent of all tornado days but caused 62 percent of all tornado deaths (and/or injuries). Seventy-seven percent of the outbreaks were associated with extratropical cyclones, March and April being the peak months, while July and August had no outbreaks. The total Florida Peninsula tornadoes peak from May through August (ref. 12-24).

12.3.5.3.1 Kennedy Space Center/Brevard County, FL, Tornadoes. One-hundred eight tornadoes have been reported in Brevard County between January 1, 1950, and March 31, 2007. This area includes the KSC facility (ref. 12-25). Some of these tornado cases close to KSC are described below.

12.3.5.3.2 February 22–23, 1998, Central Florida Tornado Outbreak. Three thunderstorm supercells during the late night and early morning hours of February 22–23, 1998, spawned the most devastating tornado outbreak ever to occur in the state of Florida in terms of loss of life and property damage. Forty-two people died and over 260 others were injured when seven confirmed tornadoes touched down. Four of the tornadoes were long lived and produced damage tracks of 12.9 to 61.2 km (8 to 38 mi). The estimated wind speed for three of these tornadoes reached 89 m/s (200 mph) (the high end of the F3 intensity Fujita scale). Two (Nos. 6 and 7) of the F1 tornadoes touched down in Brevard County in the early morning hours. Tornado No. 6 struck the southwest portion of Titusville just after 1:38 a.m. Tornado No. 7 occurred at ≈2:30 a.m. near Port Canaveral. The tornado formed over the Banana River and moved east-northeast for ≈6.4 km (≈4 mi), crossing Port Canaveral and dissipating before reaching the Atlantic Ocean. No casualties were reported, but over 130 structures were either damaged or destroyed by tornadoes Nos. 6 and 7. All seven of the tornadoes were relatively narrow with a path width of 46 to 91 m (50 to 100 yd) in most places. See figure 12-9 (ref. 12-26).

12.3.5.3.3 Florida Tornado-Lightning Correlation. During the tornado outbreak of February 23, 1998, intense intracloud lightning activity was produced by one of the nocturnal tornadic storms that hit central Florida. Total lightning flash density during the interval 04:50–05:00 UTC was observed by the KSC lightning detection and ranging (LDAR) system. A lightning "jump" associated with the intensifying updraft occurred ≈20 min prior to the tornado. The total flash rate exceeded 400 flashes per minute and began to diminish 10–15 min prior to the tornado. See figure 12-10 (refs. 12-27 and 12-28).

Tornado-producing supercells are normally characterized by extreme lightning flash rates, but just before a tornado forms, a rapid decrease in the lightning counts is seen. This apparently is caused by downdrafts that spawn the tornadoes. To actually predict tornado formation based on this precursor would require considerable additional research. A significant finding about these severe storms is that most of the lightning is in-cloud, not cloud-to-ground (ref. 12-28).

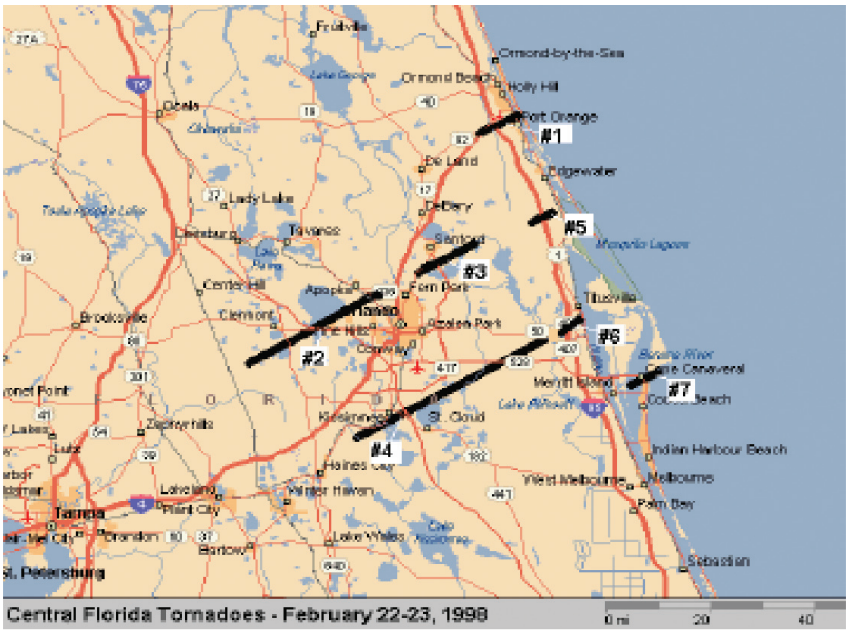

Figure 12-9. Tornado ground tracks for the February 22–23, 1998, Florida outbreak (ref. 12-26).

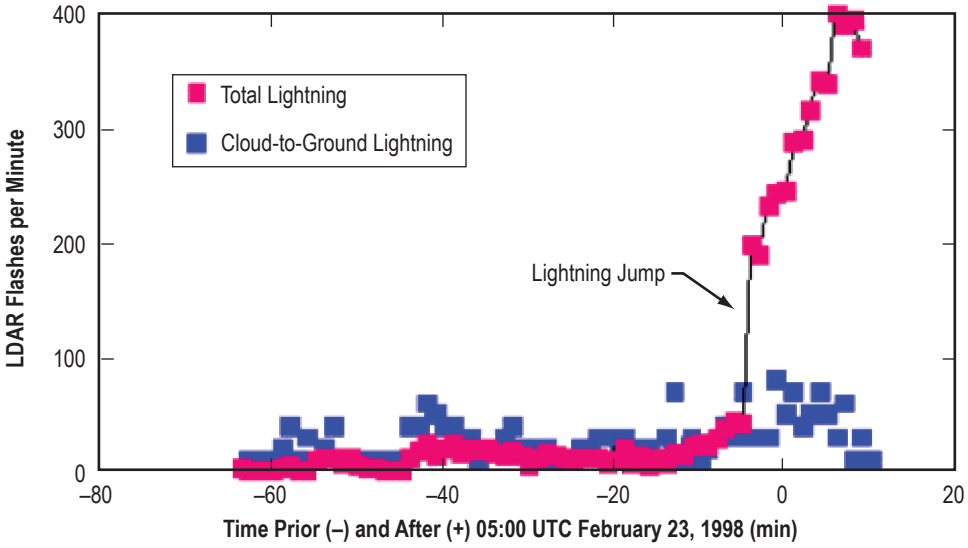

Figure 12-10. Total lightning flash density by KSC LDAR system prior to a February 23, 1998, Florida tornado formation (refs. 12-27 and 12-28).

12.3.5.3.4 Some Near-Kennedy Space Center Tornado Occurrences. The following are some tornado occurrences near KSC:

March 31, l972—Morning to afternoon: Squall line tornadoes were reported in Allenhurst (Brevard Co.) and at KSC.

June 18–19, 1972—Statewide: The outer rain bands of Hurricane Agnes produced almost 2 dz tornadoes and wind storms from the Keys to Cape Canaveral. Tornado injuries include 12 in Cape Canaveral, Brevard County.

March 24, 1983—Morning: A strong squall line moved across peninsular Florida, producing tornadoes in Cocoa Beach, Merritt Island, and Melbourne in Brevard County.

September 16, 1990—F0 tornadic waterspout near Cape Canaveral.

March 30, 1996—Afternoon to evening: Tornadoes occurred in Brevard County. A waterspout/tornado touched down in Merritt Island and Cape Canaveral, tearing out windows and damaging roofs. Golf ball-sized hail 4.45 cm (1.75 in) fell in Brevard County.

June 15, 2001—At least one tornado touched down at KSC just before 4 p.m., ≈1.6 km (≈1 mi) north of the Shuttle launch facility, according to KSC radar. No damage was reported (ref. 12-29).

June 24, 2001—A highly electrified thunderstorm anvil was just east of Cape Canaveral. This anvil was associated with a thunderstorm complex that produced severe weather throughout Brevard County, including a tornado at KSC. A tornado was sighted and photographed on the ground (in swamp) at 18:30Z inbetween pads 39A and 39B, but also in between LCC and the pads. See figure 12-11 (Internal NASA e-mail correspondence between KSC and MSFC, June 29–July 10, 2001, and Merceret report (ref. 12-30)).

Figure 12-11. June 24, 2001, tornado at KSC between pads 39A and 39B about 1830Z.

September 14, 2001—Four tornadoes struck Brevard County (associated with Tropical Storm Gabrielle) after tracking from Sarasota to Cape Canaveral. Three were F0 and one was F1 as it moved through the town of Cocoa, FL (as confirmed by weather observers at Patrick Air Force Base (PAFB)).

October 23, 2005—One tornado was reported near KSC at Cape Canaveral, generated from Hurricane Wilma, which caused some structural damage, but no injuries.

July 20, 2006—A video of a tornado over water was taken at KSC (ref. 12-31).

12.3.5.4 California Tornadoes. California normally is thought to be a fairly nonprone tornado state, with few and relatively weak tornadoes. However, during the first 4 mo of 2005, there were 26 confirmed tornadoes in California, compared to their normal average of 4. Although the central valley is a known region of tornado activity in California, they can occur most anywhere, including the south coast, southeast desert, and central and north coast regions. For the period of 1950–1992, in the Los Angeles basin, there were 3.19 tornadoes/km^2 yr as compared to the state of Oklahoma where there were 2.86 tornadoes/km^2 yr for the same period. Overall, Oklahoma averages 53.1 tornadoes/yr (1950–2006), wile California averages 5.5 tornadoes/yr (1950–2004). Most tornadoes in California, with the exception of the southeast desert region, occur in the cool (winter) season (≈80 percent occur during November to April). In the plains, they occur during the warm (spring-summer) season. California tornado path length and width are short, with an average length of 2.4 km (1.5 mi) and average width of 90 m (98 yd) (ref. 12-32). California tornadoes have an average intensity much less than the national average. For the 303 California tornadoes from 1950 through 2004, 80 percent were F0 and F1, with 55 percent being F0, 7 percent being F2, and 1 percent being F3 (ref. 12-33).

12.3.5.4.1 NASA DFRC/EAFB and VAFB Tornado Occurrence: DFRC/EAFB covers over 300,000 acres and is located in the Mojave Desert mainly in southeastern Kern County, CA. Ten tornadoes (9 F0 and 1 F1) have occurred within Kern County between 1950 and 2004. Tornado occurrence is rare at EAFB. Only one F0 tornado has occurred near EAFB, on June 26, 1995. It occurred 8 km (5 mi) northwest of EAFB with a 3.2-km (2-mi) path length and a 15-m (17-yd) width (ref. 12-33).

Vandenberg Air Force Base (VAFB) is located on the Pacific coast in Santa Barbara County, CA, where four tornadoes have occurred in that county between 1950 and 2004 (2 F0 and 2 F1). Tornado occurrence is relatively rare. Only one F0 tornado has occurred near VAFB on November 29, 2001, touching down at Santa Maria, CA (ref. 12-33).

12.3.5.5 Johnson Space Center/Houston/Harris County, TX, Tornadoes. Over the years, many tornadoes have occurred near Johnson Space Center (JSC). The tornado outbreak of March 30, 2002, produced 23 tornadoes throughout mid, east, and the southeastern sections of Texas. Four tornadoes occurred just west of Harris County, while an F3 tornado with path length of 1.6 km (1 mi) and a width of 55 m (60 yd) produced $350,000 of damage in Harris County 4.8 km (3 mi) south of LaPorte (≈8 km (≈5 mi) northeast of JSC) (ref. 12-34).

The November 17, 2003, tornado outbreak produced 24 tornadoes in Texas with 6 occurring in Harris County and 5 in Galveston County. Three tornadoes were just 8 to 10 km (5 to 6 mi) west of JSC, while 3 were north and northeast of JSC, with the closest of them being 11 to 13 km (7 to 8 mi) north of JSC. Also, 2 tornadoes touched down ≈16 km (≈10 mi) south of JSC (ref. 12-35). One of these tornadoes produced F0 damage 18 m (20 yd) wide and 1.6 km (1 mi) long as it traveled from Galveston County (Friendswood area) across Clear Creek and 0.4 km (1/4 mi) into Harris County, 8 km (5 mi) west of JSC. The November 21, 1992, tornado outbreak produced one F1 tornado within 10 km (6 mi) west of JSC (ref. 12-36). Also see table 12-9 for a more detailed statistical study of JSC tornadoes.

12.3.5.6 Site Assessment of Tornado Threat Statistics for Johnson Space Center, TX. In 1999, an earlier version of the SATT 2.0 tornado program was run by MSFC specifically for the JSC (Ellington AFB, TX) coordinates (29° 36′ latitude and 95°10′ longitude) for a 175.1-km (108.8-statute mi) radius circular area (equivalent to a 3° latitude/longitude square in total area) centered at JSC. The square area considered was 96,392 km^2 (37,217 mi^2). All months, all hours (CST), all tornado intensities (from F0 to F5), for all 46 yr (1950–1995) of tornado data were used in this SATT analysis. All historic tornado path widths and path lengths around JSC were used in producing the ACF statistic as given here. SATT calculates an "area" type of tornado probability statistic, as the ACF is an annual tornado probability that is based on the total area covered by tornadoes within the region of interest, divided by the area of the region of interest and the number of years of data considered.

Table 12-9. SATT tornado statistics for JSC, TX (ref. 12-19).

Tornado Parameter	1º Square Surrounding JSC	3º Square Surrounding JSC
Equivalent area	10,710 km^2 (4,135 mi^2)	96,392 km^2 (37,217 mi^2)
Circular area radius	*r*=58.4 km (36.3 mi)	*r*=175.1 km (108.8 mi)
ACF tornado probability	3.53×10^{-4}	1.2×10^{-4}
Return period	2,825 yr	8,333 yr
Total No. tornadoes	282 (yearly avg.=6.1	813 (yearly avg.=17.7)
No. tornadoes with tracks	49 (yearly avg.=1.1)	159 (yearly avg.=3.5)
Percent tornadoes with tracks	17.4%	19.6%
Prevailing tornado direction	Feb.–July: W through SW=66% Aug.–Jan.: W through SW=70% Feb.–July: SW through S=34% Aug.–Jan.: SW through S=80%	Feb.–July: W through SW=70% Aug.–Jan.: W through SW=62% Feb.–July: SW through S=30% Aug.–Jan.: SW through S=57%
Percent tornadoes by hour	12 to 18 hr (LST)=49% 7 to 18 hr (LST)=76%	12 to 18 hr (LST)=48% 7 to 18 hr (LST)=73%
Tornadoes by month	Maximum is May=21% (58 tornadoes) March–July=46% (129 tornadoes) Aug.–Nov.=37% (104 tornadoes)	Maximum is May=20% (164 tornadoes) March–July=45% (367 tornadoes) Aug.–Nov.=33% (268 tornadoes)
Tornadoes by year	Minimum=0 (for 6 yr) Maximum=42 (for 1983)	Minimum=0 (for 1951) Maximum=89 (for 1983)
Tornadoes by intensity	F0=47.5% F0 and F1=80.9% F0 to F3=99.3% F2 to F4=19.1% F5=0%	F0=46% F0 and F1=77.2% F0 to F3=99.6% F2 to F4=22.8% F5=0%

Results indicated that a total of 813 tornadoes touched down within this circular area around JSC, of which 159 tornadoes had tracks (paths). This results in an ACF probability of 1.20×10^{-4} for the ≈3º square surrounding the JSC area. This also means that the mean recurrence interval (in years) for a tornado striking a point in this 3º square is 8,333 yr.

For comparison purposes, SATT was also run for an ≈1º latitude/longitude box about JSC and results for both runs are given in table 12-9. Some of these tornado statistics show a coastal (1º square) versus inland (3º square) influence. For additional information, refer to reference 12-19. More up-to-date tornado statistics combining only Harris and Galveston Counties, which was taken over a longer 58-yr period of record from January 1950 through March 2007, also give the same tornado intensity percentile values within 1 percent of the values given in table 12-9.

12.3.6 Tornadic and Severe Storm Stability Indices

The use of diagnostic variables in severe storm forecasting has been utilized over the years as a helpful tool in the forecasting of severe weather (severe thunderstorms/tornadoes). Normally, these measured atmospheric parameters have been developed in the form of a stability type of index, which gives a measure of the instability of the atmosphere conducive to severe weather occurrence. Instability, along with moisture, lift, and wind shear, are four basic ingredients necessary for severe convective weather formation. The stability index itself is not a "magic bullet," but only one item the forecaster can consider when preparing the forecast. Doswell (ref. 12-37) lists 14 indices that have been developed in which he gives many of the pitfalls encountered when using them. The NOAA NWS Forecast Office in Louisville, KY, (ref. 12-38) lists 16 direct indices, along with a total of 29 indices and/or methods that have been used in the past.

Johnson (ref. 12-39) analyzed severe tornadic weather measurements taken during two NASA campaigns (AVE-IV and AVE-SESAME-I), in which many soundings were taken over the Great Plains for these two different timeframes—April 1975 and April 1979, respectively. Using both AVE-IV prestorm and storm balloon soundings, Johnson developed a lag index called the JLI (Johnson lag index) which expresses the instability relationship of the atmosphere between the benign and the severe atmospheric regimes. Therefore, a time difference, between nonsevere and severe weather soundings was factored into the JLI, which then can be used to express a type of prestorm forecast capability. Johnson then independently tested the derived JLI on the AVE-SESAME-I data set and obtained favorable results. The JLI outperformed the other 14 indices in forecasting severe/tornadic weather for Abilene, TX, up to 6 hr prior to actual severe weather occurrence. Although the JLI does show promise as a potential forecast index for Great Plains tornadoes during this one test case, more testing of the index is needed.

12.4 Tornadoes Generated From Hurricanes

The danger of a hurricane landfall on a U.S. coastal area is always present during the Atlantic hurricane season from June 1 through November 30. Besides the hurricane's damaging high winds, the threat of storm surge flooding, rainfall flooding, lightning, and hurricane-generated tornadoes are possible.

Gentry (ref. 12-40) determined that nearly all full-intensity hurricanes whose centers cross the U.S. coastline (south of Long Island, NY, and east of Brownsville, TX) have tornadoes associated with them. Also, ≈60 percent of tropical storms crossing onto land produce tornadoes.

Most hurricane-spawned tornadoes form either near the hurricane core (≈20 percent) or in the outer rainbands within 100 km (62 mi) (≈80 percent) of the hurricane center, and frequently spawn northeast and east of the center (between 20° and 120° azimuth) where the tipping and convergence terms of the vorticity equation are the largest; i.e., where the lowest atmospheric layers are slowed by ground friction, with the upper 850-mb- (25.1-inHg-) level winds still moving at high hurricane speeds, thus creating strong vertical shear in the horizontal wind component. In most cases, the tornadoes form closer to the water (coastline) than to the hurricane center (with the center being farther inland). Finally, as a hurricane moves farther inland and loses its tropical characteristics, some tornadoes do form, but these do not have the genesis characteristics of the classical hurricane-spawned tornado. Hurricane-generated tornadoes can occur at any local time, but ≈50 percent were found to occur between 1200 and 1800 LST. Figure 12-12 presents the locations of all hurricane-associated tornadoes, occurring between 1972 and 1980 (ref. 12-40), as a function of distance from the coastline. Hurricane David's ground track is plotted in figure 12-12, as a reference for the David tornado occurrences.

There have been 159 documented tropical cyclones (hurricanes or tropical storms) that have spawned tornadoes in the United States from 1811 through 2005 (ref. 12-41). A total of 1,927 tornadoes and waterspouts have been recorded for these 159 events. There have been at least 25 tropical cyclones that each produced 20 or more tornadoes. Hurricane Ivan in 2004 produced the most tornadoes with 127 (in addition to 4 waterspouts). Hurricane Georges in 1998 spawned 48 tornadoes, but had a maximum in producing 9 waterspouts. For all recorded tropical cyclones with tornadoes, the average number of tornadoes per tropical cyclone event is 11.7.

From 1980 through 2005, only a total of 112 tornadoes with intensity F2–F5 have been documented for the 87 tornado-producing tropical cyclone events occurring over this 26-yr period. Hurricane Ivan in 2004 produced the most moderate to strong F2–F5 tornadoes with 18. However, the average is only 1.3 F2–F5 tornadoes per event, since 57 of the 87 tropical cyclones (or 66 percent) produced only F1 tornadoes, indicating that most hurricane-generated tornadoes are weaker than their Great Plains and Midwest tornado counterparts (ref. 12-41). There have been no F5-rated tropical cyclone tornadoes, and only two F4s, since reliable records commenced in 1950. Tropical cyclones may spawn tornadoes from a day or two prior to landfall to up to 3 days after landfall, with most occurring on the day of landfall or the next day. Some hurricane tornadoes have been

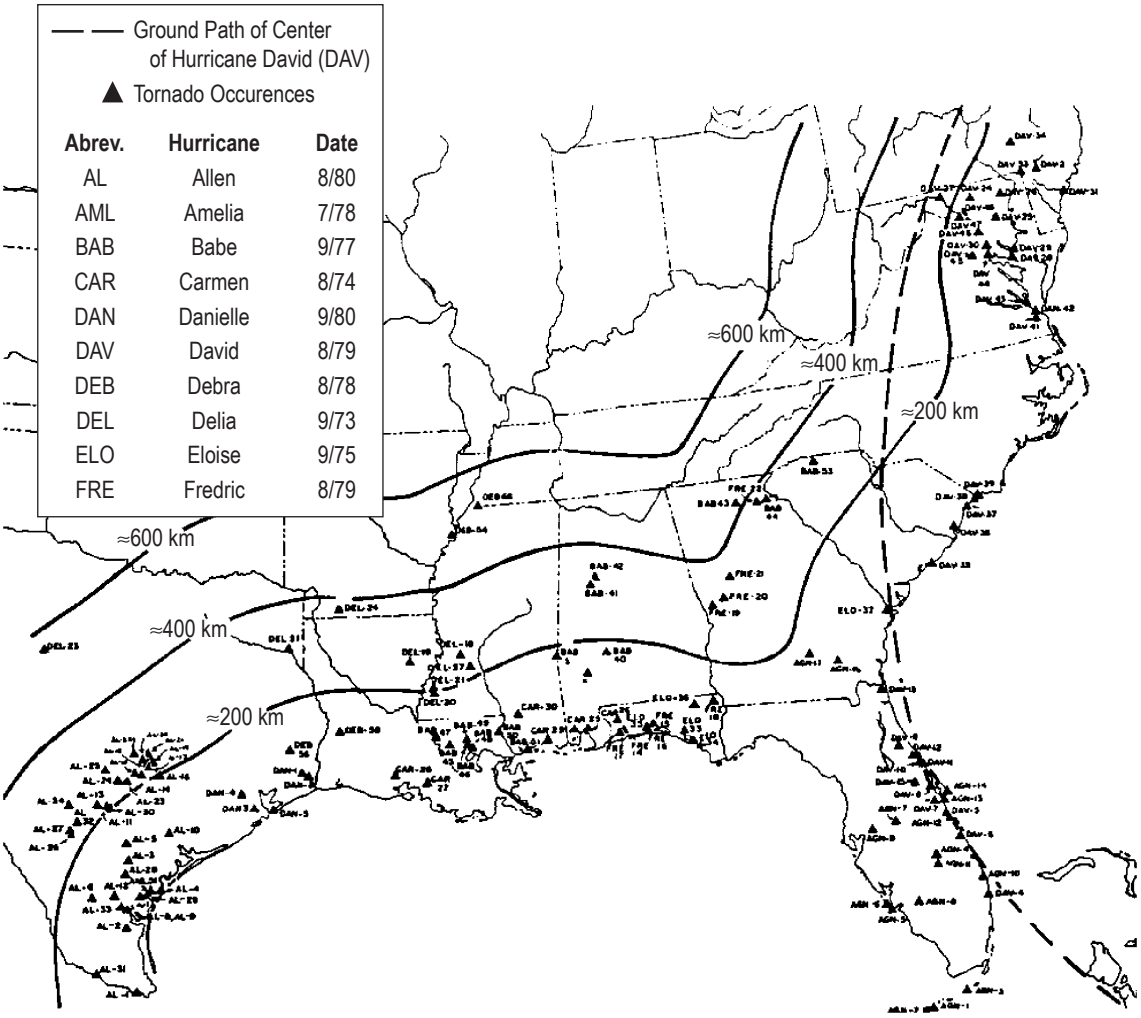

Figure 12-12. Location of tornadoes associated with hurricanes for the period 1972–1980 with indications of the distance from the coast (ref. 12-40).

documented as forming in the inner core, or even in the eyewell (ref. 12-42). Most tornadoes occur within 240 km (150 mi) of the coast (ref. 12-43).

The year 2004 had seven U.S. landfalling tropical cyclones spawning a total of 339 tornadoes, the most for any year (as well as 10 waterspouts). Eight TCs during 2005 produced a total of 226 tornadoes, while during 1967, a total of 115 tornadoes were spawned—all by Hurricane Beulah. Hurricane Frances (Saffir-Simpson (S-S) category 4) spawned 106 tornadoes (5 of F2–F5) from September 4–8, 2004, only to be followed shortly by Hurricane Ivan (S-S category 5) with another 127 tornadoes (18 of F2–F5) during September 15–17, 2004. Ivan produced four killer tornadoes. Also, all the tropical cyclone-generated tornadoes in 2004 were east of a line extending from near Pensacola, FL, up through the Appalachian Mountains (refs. 12-41 and 12-44). This is rare because, normally, tropical cyclone landfalls along the Gulf coast produce more tornadoes than those along the Atlantic coast. From 1948 to 1986, there were 60 U.S. landfalling hurricanes in the Atlantic basin, producing 96 tornadoes (1.6 tornadoes/landfall and 4 tornadoes/tornadic landfall), whereas there were 93 landfalling hurricanes in the Gulf basin, producing 521 tornadoes (5.6 tornadoes/landfall and 7.9 tornadoes/tornadic landfall) (refs. 12-45 and 12-46).

Nearly all hurricane-generated tornadoes develop to the right of the hurricane track in the right-front or northeast quadrants of the hurricane, with radial peaks near the core at ≈100 km (≈62 mi) from the storm center, and in the outer rainbands at ≈300 km (≈186 mi) distance from the storm center, with short tracks or brief touchdowns. Tornadoes that occur closest to the center (at ranges of 0–200 km (0–124 mi)) occur mostly on the day of landfall, with proportionately fewer tornadoes occurring in the outer rainbands. However, on days following landfall, tornado occurrences show an increasing preference for the outer rainbands (at ranges of 200–400 km (124–248 mi)). See figure 12-13. Outer rainband tornadoes generally occur in the early afternoon, with a maximum between noon and 3 p.m. due to some impact from solar heating. Whereas, near-core tornadoes seem to occur more during the early morning hours along the Gulf coast, and early evening along the Atlantic coast. Tornadic hurricanes move at ≈6 m/s (≈13 mph), whereas nontornadic hurricanes move at speeds either ≈4 m/s (≈9 mph) or slower, or in some cases at speeds >15 m/s (>34 mph). Although tornado occurrence is also a strong function of hurricane size and intensity, large tornado-producing hurricanes (producing 8 or more tornadoes) had an average peak sustained surface wind of 47.1 m/s (105 mph), whereas tropical cyclones producing no tornadoes or a single tornado had peak sustained surface winds averaging <29 m/s (<65 mph) (ref. 12-45).

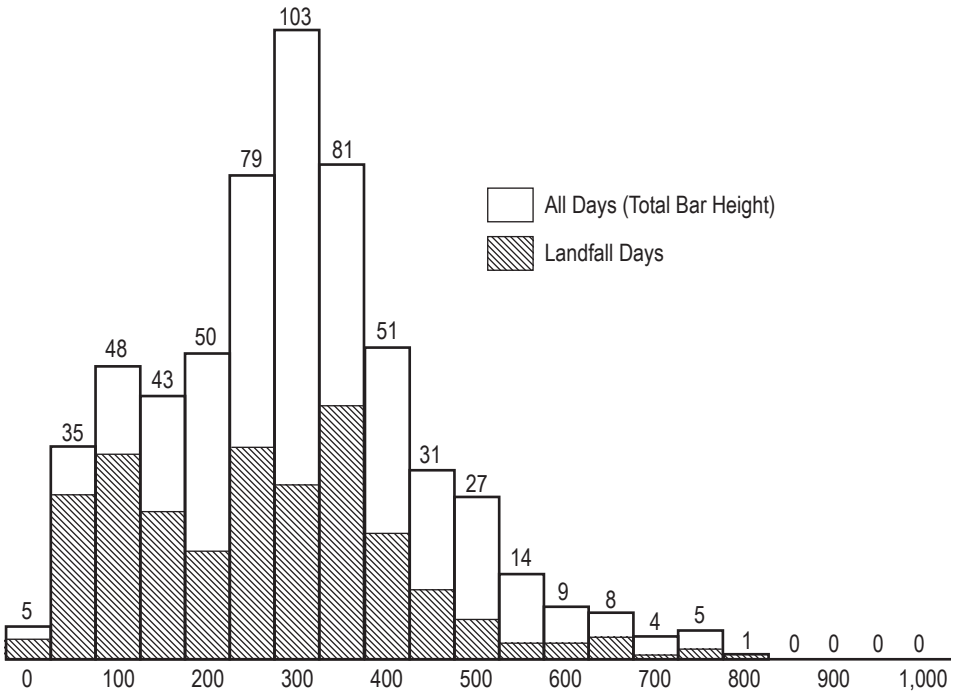

Figure 12-13. Distribution (ordinate) of reported hurricane tornadoes over a 39-yr period (1948–1986) on landfall day and for all days relative to landfall, at given kilometer ranges from the center of hurricane absissa (ref. 12-46).

For a 39-yr U.S. hurricane data sample from 1948–1986, ≈59 percent of all the tropical cyclones produced at least one tornado. Some of the hurricane tornadoes were spawned as long as 5 or more days after landfall, although the rate of production was quite small after the third day (ref. 12-46).

Figure 12-13 gives the distribution of the ranges (in kilometers) of all 626 hurricane-tornadoes reported between 1948 and 1986, from their respective hurricane center. This is for all days relative to the hurricane landfall (total bar height), and also relative to landfall day itself (hatched area). There is a distinct peak in the 200- to

400-km (124- to 249-mi) interval, with a "shoulder" just inside the 160-km (99-mi) range. When only tornadoes occurring on the "day of landfall"; i.e., within 12 hr of the time of hurricane landfall, are plotted, the "shoulder" becomes a distinct separate peak (ref. 12-46).

A factor that probably reduces the tornado threat from landfalling Atlantic basin hurricanes is the fact that the Atlantic coast tends to parallel the mean hurricane track heading, so that most landfalls do not penetrate far inland. This hurricane "grazing" feature also means that the tornado-prone, right-front quadrant of a hurricane has relatively little exposure to actually land on the Atlantic coastal areas (ref. 12-46).

12.4.1 Hurricane-Generated Tornado Outbreak Statistics

Verbout et al. studied tornado outbreaks associated with 83 landfalling hurricanes in the North Atlantic basin over 51 yr (1954–2004) (ref. 12-47). They classified the tornado outbreaks into three categories:

(1) Outbreaks—hurricanes associated with the number of tornadoes exceeding a certain annual threshold value, and at least 8 or more F1 tornadoes at time of landfall. Eighteen of the 83 hurricanes (22 percent) fell into this category.

(2) Nonoutbreaks included 37 hurricanes (44 percent) that fell into the category of having less than a certain annual threshold value.

(3) Mid-class hurricane landfalls included 28 hurricanes (34 percent) that were neither outbreak nor nonoutbreak hurricanes.

They determined that 78 percent (14 of 18) of outbreak hurricanes were S-S category 2 or greater intensity at landfall, while only 32 percent (12 of 37) of nonoutbreak hurricanes were category 2 or greater at landfall. Their results, therefore, suggest that outbreak hurricanes are more likely to occur if the hurricane is an S-S category 2 or higher at landfall. Of the 83 hurricane landfalls, only 14 (or 17 percent) had no reported tornadoes. Thirty-four of the 83 landfalls were category 1, and only 2 were category 5 at landfall. Forty were category 2 or greater, and 43 were categories 0 or 1. Thirty-five percent (14 of 40) of category 2 or greater were associated with outbreaks, and 30 percent (12 of 40) with nonoutbreaks.

The 83 hurricanes, 27 percent of the hurricane landfalls on the southern coast were outbreaks, whereas 13 percent on the eastern coast were outbreaks. Nearly all landfalling outbreak hurricanes recurved northeastward after landfall, while nonoutbreak hurricanes tended to fall into two categories. Those making landfall on the east coast tended to recurve northward, while many making landfall over the southern coast did not recurve. Forty-eight percent of hurricanes that made landfall on southern coasts and did recurve were outbreaks, while 19 percent that made landfall and did not recurve were outbreaks. Therefore, hurricanes that made landfall along the southern coast of the United States and recurved northeastward were more likely to produce tornadoes than those that made landfall along the east coast or those that made landfall along the southern coast but did not recurve. Most east coast landfalls do not penetrate far inland, but quickly recurve back over the ocean and are less likely to produce a large number of tornadoes. Since ≈87 percent of tornado-producing hurricanes make landfall in Florida on its west coast, this places the right-front quadrant of the hurricane directly over the state (ref. 12-47).

12.4.2 Hurricane-Generated Tornado Examples

Hurricane Agnes produced 32 tornadoes of which 28 hit Florida from Key West to just south of Daytona Beach. These included 2 F3, 9 F2, 11 F1, and 6 F0 tornadoes along with seven reports of severe thunderstorms in Florida from 2:15 a.m. EDT, June 18, 1972, until 4:50 a.m. EDT, June 19, 1972. The plot of the tornadoes and

severe thunderstorms relative to the track of Agnes is shown in figure 12-14. Agnes produced the most tornadoes, the most F2 and greater tornadoes, most death/injury-producing tornadoes of any outbreak in Florida history. It was the fourth deadliest tornado outbreak in Florida history, and its deadliest tropical cyclone outbreak. Agnes ranks as the third deadliest in U.S. history, since 1900, behind Hurricane Hilda in October 1964 (22 dead) and Hurricane Carla in September 1961. Agnes produced the deadliest prelandfall tropical cyclone tornado outbreak in U.S. recorded history (ref. 12-48).

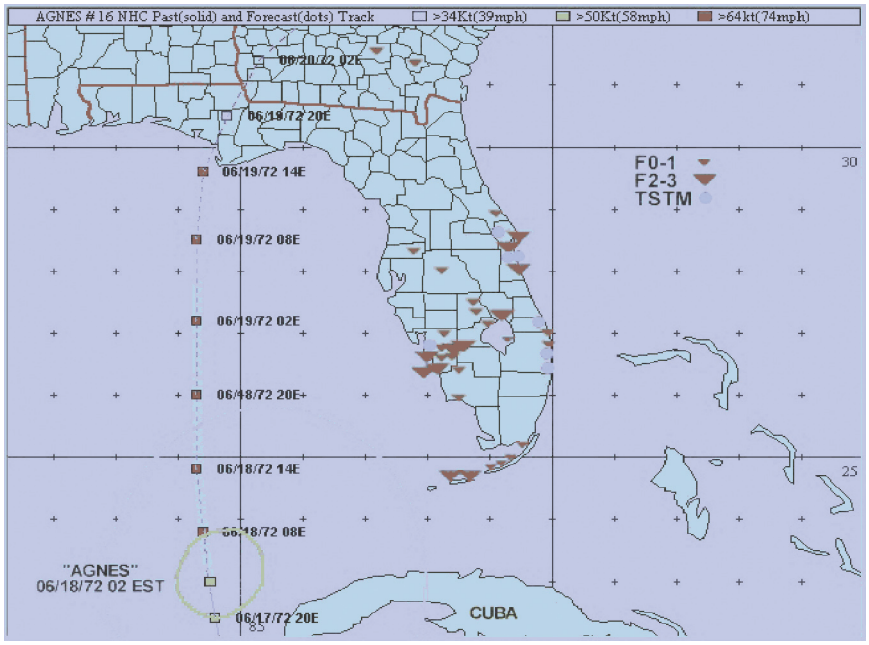

Figure 12-14. Plot of tornadoes by F-scale and severe thunderstorms of the Agnes outbreak. Agnes is shown at 0200 EDT, June 18, 1972, with wind field radii just before the first tornado report in the Keys. Six hourly positions are shown on the track. The heavily shaded part of the track marks the period when Agnes's rain bands were producing tornadoes (ref. 12-48).

Hurricane Alicia hit coastal Texas on August 15–21, 1983, spawning 29 tornadoes with 58-m/s (130-mph) winds. Damage was primarily in the Galveston and Houston areas and was estimated at $3 billion.

See figure 12-15 showing the track of Hurricane Beulah in September 1967 with its associated 115 tornado occurrences inland into Texas (ref. 12-47).

The Hurricane Katrina tornado outbreak occured across the eastern United States from August 29–31, 2005. The tornadoes spawned were mostly by the outer bands of Hurricane Katrina, or the remnants thereof. Numerous communities suffered damage of varying degrees from central Mississippi to Pennsylvania, with Georgia the hardest hit. There were 58 confirmed tornadoes in Georgia, Mississippi, Virginia, Pennsylvania, Alabama, and one isolated tornado in Florida 3 days before the main outbreak (ref. 12-49).

12.4.3 Tornadoes Generated From Exiting Hurricanes

Not only do tornadoes occur on and just after tropical cyclone landfall, but tropical cyclone remnants can produce tornadoes when exiting back to the sea. This phenomenon can pose a danger to life and property

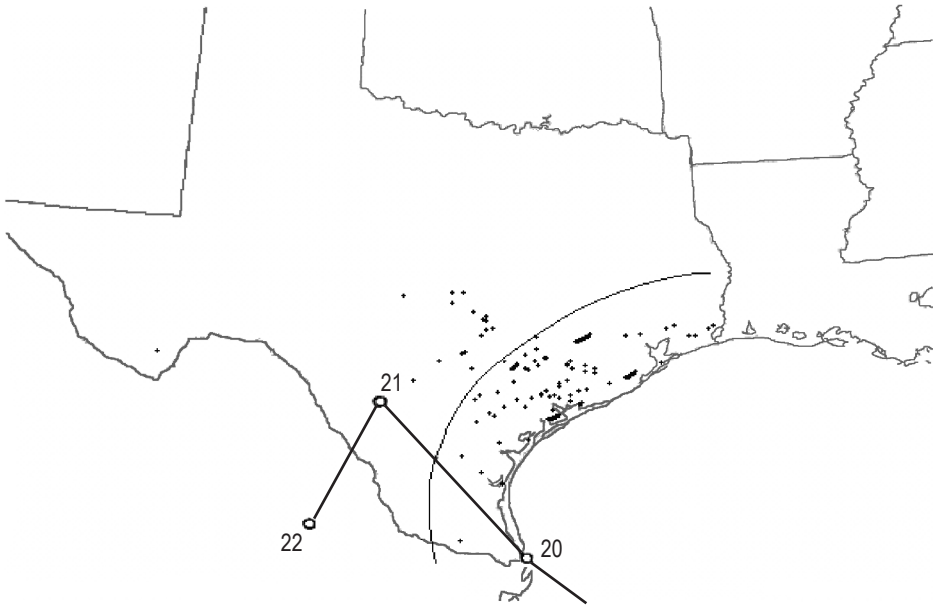

Figure 12-15. Track of Hurricane Beulah, September 20–22, 1967. Hollow circles indicate center of circulation at 0000 UTC on each day. Thin line denotes a distance of 185 km (100 nm) from shore. Major individual tornado reports are marked with small plus signs (ref. 12-47).

well after the hurricane has made landfall. See an example in figure 12-16 (ref. 12-50). Edwards studied this phenomenon and of the 22 total exiting tropical cyclones examined for the 42-yr study period from 1955–1998, only 8 (or 36 percent) spawned tornadoes during their exit phase. These included 6 hurricanes, 1 tropical storm, and 1 tropical depression that produced a total of 47 exiting tornadoes well after their initial landfall entry. The tropical cyclone storm maximum was 9, with a minimum of 3, and an average of 5.9. Six of the 8 tropical cyclones entered along the Gulf Coast, while the other 2 entered along the Atlantic coast in northeast Florida and in South Carolina. All storm tracks exited along the Atlantic coast in either northern North Carolina or in Virginia, while producing these 47 tornadoes in north-coastal Florida, and in Georgia, South Carolina, North Carolina, and Virginia. Some tornadoes developed well inland. See figure 12-17. Thirty-eight of the 47 tornadoes had F ratings, of which 50 percent were F1 and only16 percent were F2, with no F3–F5 tornado occurrences.

12.5 Other Similar Tornadic-Type Storm Events

12.5.1 Gustnado (Gust Front Tornado)

Definition: A relatively weak tornado associated with the thunderstorm outflow at the leading edge of a thunderstorm cell, often found along a gust front. A debris cloud or dust whirl may indicate the presence of a gustnado (ref. 12-51).

The average gustnado lasts a few seconds to a few minutes, although there can be several generations and simultaneous swarms. Most gustnadoes have the winds of an F0 or F1 tornado, and are commonly mistaken for tornadoes. However, unlike tornadoes, the rotating column of air in a gustnado usually does not extend all the way to the base of the thundercloud. Gustnadoes actually have more in common with whirlwinds, which include dust devils; i.e., whirlwinds that form due to superheated surface layers and stretched vorticity, most commonly

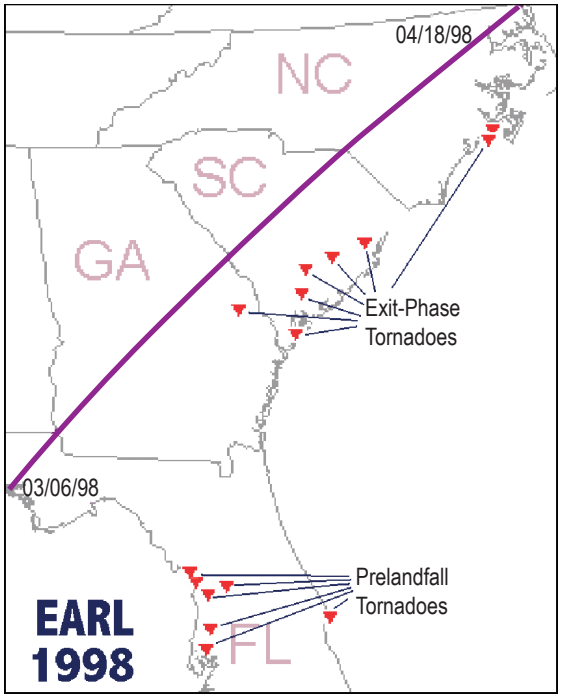

Figure 12-16. Prelandfall and exit-phase tornadoes generated from Hurricane Earl track in September 1998 (ref. 12-50).

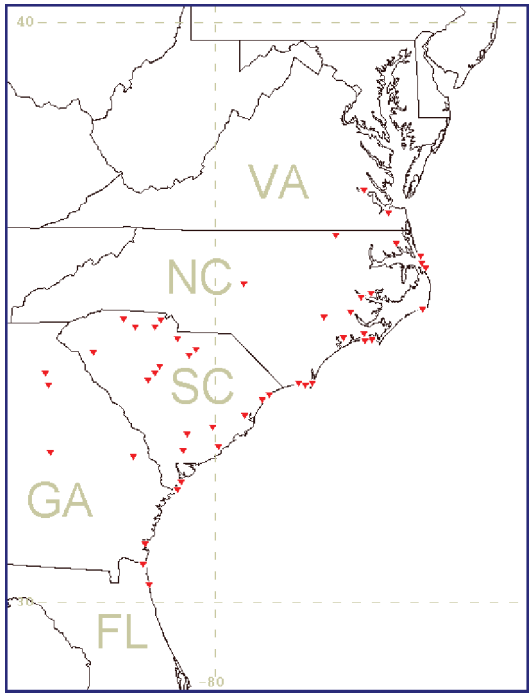

Figure 12-17. Map location of all 47 tropical cyclone exit tornadoes produced from 8 tropical cyclones from 1955 through 1998 (ref. 12-50).

on sunny, warm days with light winds. Gustnadoes are not considered true tornadoes—unless they connect the surface to the ambient cloud base—by most meteorologists and are not included in tornado statistics. Sometimes referred to as "spinup tornadoes," that term more correctly describes the rare tornadic gustnado that connects the surface to the ambient cloud base, or to relatively brief tornadoes associated with a mesovortex.

The most common setting for a gustnado is on the outflow boundary from a severe thunderstorm (26 m/s (58+ mph) winds). They are triggered by gust fronts (hence the name) in thunderstorms. The cool air in the gust front acts like a mesoscale cold front, as it slices under the warm air ahead of it, creating upward motions and turbulent interactions. The friction from this interaction creates spinning columns of air, or eddies, which can create a gustnado. (Picture an area of leaves swirling on a windy day, just on a much larger scale.)

In addition to forming on the leading edge of a thunderstorm, which in a supercell is the front-flank downdraft, gustnadoes are not uncommon in the rear-flank downdraft of supercell thunderstorms. This region often contains high vorticity air, and sometimes highly buoyant air, both of which are conducive to the formation of gustnadoes as well as tornadoes. Gustnadoes near the updraft-downdraft interface may evolve into bona fide tornadoes when ingested into a mesocyclone (ref. 12-52).

Gustnadoes have been associated with lines of thunderstorms, especially bow-echo structures, as well as with multicell thunderstorm clusters. Gustnadoes, like all tornadoes, are potentially dangerous to life and property. While most are very weak, some gustnadoes may reach F1 intensity, with winds as high as 49 m/s (110 mph). One such gustnado occurred on June 9, 1994, associated with bow echoes in a long line of thunderstorms which raced through southwest Tennessee. The gustnado was observed by an NWS meteorologist and storm spotters as it passed within 91 m (100 yd) of the Memphis NWS Forecast Office (ref. 12-53).

12.5.2 Landspout

Definition: A tornado; dust whirl (ref. 12-51). Bluestein in 1985 first used the term "landspout" to identify another type of nonsupercell tornado that has similarities to waterspouts. These tornadoes are not associated with the mesocyclone of a thunderstorm and are most common in the Plains states. Although typically thought of as the High Plains phenomenon, landspouts occur in other regions, including the Southern Plains and the Mississippi Valley. The higher number of landspouts in the Plains may be attributable to the fact that they occur in drier environments and therefore are easier to see (ref. 12-53).

Known officially as "dust-tube tornadoes" by the NWS, they form during the growth stage of convective clouds by the ingestion and tightening of boundary layer vorticity by the cumuliform tower's updraft. Landspouts most often occur in drier areas with high-based storms and considerable low-level instability. They generally are smaller and weaker than supercellular tornadoes, though many persist in excess of 15 min and some have produced F3 damage. Damage in the F1 category is not uncommon. Their appearance and generative mechanism are similar to that of waterspouts, usually taking the form of a translucent and highly laminar helical tube extending from cloud base to the ground. Like waterspouts, they are also technically considered tornadoes since they are defined by an intensely rotating column of air in contact with both the surface and a cumuliform cloud. Not all landspouts are visible, and many are first sighted as debris swirling at the surface before eventually filling in with condensation and dust (ref. 12-54). As with gustnadoes, landspouts do not usually form from mesocyclones or supercells. In fact, a large number of landspouts are observed in association with lines of cumulus congestus or towering cumulus clouds, often before precipitation is visible on radar. However, storm interceptors have noted the presence of landspouts in conjunction with supercell thunderstorms, sometimes at the same time as, but in a different part of the storm than a supercell tornado. Wall clouds are not usually observed with landspouts (ref. 12-53).

12.5.3 Waterspout

Definition: Usually a tornado-like rotating column of air (whirlwind) under a parent cumuliform cloud occurring over water, waterspouts are most common over tropical and subtropical waters and tend to dissipate upon reaching shore (ref. 12-51). However, under the right conditions, large waterspouts can move on shore and produce significant destruction. Typically, air and sea temperatures are in the 80s, with light surface winds. Waterspouts are usually 610 to 914 m (2,000 to 3,000 ft) high (to the parent cloudbase) and last between 10 and 15 min, but can persist up to 3 hr. In the 1970s, the AT-6 aircraft penetrated smaller waterspouts and found tangential winds ranging from 5 to 31 m/s (12 to 70 mph). Lidar measurements gave typical rotational velocities in funnels of 4 to 34 m/s (9 to 76 mph), at altitudes ranging from 95 m (312 ft) to cloudbase at 675 m (2,215 ft). Funnel diameters ranged from 6.6 to 90 m (21.7 to 295 ft) (ref. 12-55).

Waterspouts exist on the microscale, meaning their environment is <2 km (<1.2 mi) in width. While some waterspouts are strong (tornadic) like their land-based counterparts, most are much weaker and caused by different atmospheric dynamics. They normally develop in moisture-laden environments with little vertical wind shear along lines of convergence, such as land breezes, lake effect bands, lines of frictional convergence from nearby landmasses, or surface troughs. Waterspouts normally develop as their parent clouds are in the process of development, and it is theorized that they spin up as they move up the surface boundary from the horizontal shear near the surface, and then stretch upwards to the cloud once the low-level shear vortex aligns with a developing cumulus or thunderstorm. Weak tornadoes, known as landspouts, have been shown to develop in a similar manner. Waterspouts always form in the cloudline sections that have the most vigorous updrafts and growing cloud tops. An outbreak of over 66 waterspouts occurred in the Great Lakes in late September and early October 2003 along a lake-effect band. Their parent cloud can be as innocuous as a moderate cumulus, or as significant as a supercell.

Waterspouts have long been recognized as serious marine hazards. History is filled with examples of ships being destroyed or damaged by them. Stronger waterspouts are usually quite dangerous, posing threats to ships, planes, and swimmers. It is recommended to keep a considerable distance from these phenomena, and to always be on alert through special marine weather report warnings when waterspouts are likely or have been sighted over coastal waters, or tornado warnings when waterspouts move onshore.

Nontornadic waterspouts are waterspouts that are not associated with the rotating updraft of a supercell thunderstorm (also called fair-weather waterspouts) and are by far the most common type. Fair-weather waterspouts occur in coastal waters and are associated with dark, flat-bottomed, developing convective cumulus towers. They usually rate no higher than F0 on the Fujita scale, generally exhibiting winds <30 m/s (<67 mph). They are most frequently seen in tropical and subtropical climates, with upwards of 400 per year observed in the Florida Keys. They typically move slowly, if at all, since the cloud they are attached to is horizontally stationary, being formed by vertical convective action instead of the subduction/adduction interaction between colliding fronts. Fair-weather waterspouts are very similar in both appearance and mechanics to landspouts, and largely behave as such if they move ashore.

Tornadic waterspouts, also accurately referred to as “tornadoes over water,” are formed from mesocyclonic action in a manner essentially identical to traditional land-based tornadoes, but simply occurring over water. A tornado that travels from land to a body of water would also be considered a tornadic waterspout.

Since the vast majority of mesocyclonic thunderstorms occur in land-locked areas of the United States, true tornadic waterspouts are correspondingly rarer than their fair-weather counterparts. Like all tornadoes, their intensity is commensurate to the system that spawned them, but are generally limited in both power and lifespan by the disruptive thermodynamic and hydrodynamic effects the bodies of water tend to have on the complex mesocyclonic action needed to sustain a powerful tornado. Water is also a great deal heavier than the dirt, dust, and debris commonly ingested by a tornado.

Though the majority occurs in the tropics, they can seasonally appear in temperate areas throughout the world, and are common across the western coast of Europe as well as the British Isles and several areas of the Mediterranean and Baltic Sea. They are not restricted to saltwater; many have been reported on lakes and rivers, including all five Great Lakes. They are more frequent within 100 km (62 mi) from the coast than farther out at sea. Waterspouts are common along the southeast U.S. coast, especially off southern Florida and the Keys, and can occur over seas, bays, and lakes worldwide. Approximately 160 waterspouts currently are reported per year across Europe, with the Netherlands reporting the most at 60, followed by Spain and Italy at 25, and the United Kingdom at 15. They are most common in late summer. In the Northern Hemisphere, climatologies have pinpointed September as the prime month of formation (ref. 12-56). In the Florida Keys, climatology showed that the waterspout season runs from mid-May through September, with peaks in June and August and in late afternoons from building cumulus cloudlines (ref. 12-55).

12.5.4 Firewhirl/Pyrocumulonimbus

A firewhirl is a phenomenon in which a fire, under certain conditions—depending on air temperature and currents—acquires a vertical vorticity and forms a whirl, or a tornado-like effect of a vertically oriented rotating column of air. Firewhirls may be whirlwinds separated from the flames itself, either within or outside the burn area, or a vortex of flame.

Most of the largest firewhirls are spawned from wildfires. They form when a warm updraft and convergence from the wildfire are present. They are usually 10–60 m (30–200 ft) tall, a few meters (≈10 ft) wide, and last only a few minutes. However, some can be more than a kilometer (0.6 mi) tall, contain winds over 45 m/s (100 mph), and persist for more than 20 min (ref. 12-57). Firewhirls observed during prescribed burns also indicated that the atmosphere should have a superadiabatic lapse rate through the lower layer 90 to 120 m (300 to 400 ft or more), along with little or no wind, and clear skies (ref. 12-58).

On June 30, 2005, a long-lived firewhirl occurred over a wheat stubblefield prescribed burn in central Kansas. The fire front was ≈300 m (≈984 ft) wide at the time of the firewhirl development. It towered ≈200 m (≈655 ft) and lasted around 20 min, occurring in the vicinity of a slow-moving cold front that may have played an important role in the evolution, longevity, and strength of this fire-spawned vortex (ref. 12-59).

The Necedah NWR Wisconsin burn of August 21, 1970, produced firewhirls with the largest being ≈12 m (≈40 ft) in diameter and ≈760 m (≈2,500 ft) vertical. The Littlefork, Minnesota, burn of August 11, 1965, produced a fire whirlwind that was ≈30 m (100 ft) in diameter and several hundred feet high (ref. 12-58).

Pyrocumulus (pyro-Cu) and pyrocumulonimbus (pyro-Cb) clouds can result from extreme rising thermals (fire or industrial generated), and can even reach the lower stratosphere (9 km altitude). PyroCb can produce precipitation, hail, lightning, extreme winds at low-level, and even tornadoes.

12.5.5 Nontornadic Downburst-Type Severe Winds From Thunderstorms

Severe thunderstorms (also see sec. 12.7.1) can also produce nontornadic severe wind damage through the formation of downbursts, microbursts, and macrobursts. They have been responsible for airplane crashes during takeoff and landing, as well as overturning of boats on lakes, and other mishaps, such as fanning a forest fire into a raging inferno. Microburst winds—often mistaken as tornado damage—can flatten buildings and trees. Heatbursts are also a type of downburst but very rare and characterized by strong, even damaging, winds. One heatburst observed in Oklahoma in 1996 drove the temperature from 31 to 39 ºC (88 to 102 ºF) within 25 min, and produced wind gusts reaching 47 m/s (105 mph) within the 10-county Mesonet coverage area (ref. 12-60). All wind-related thunderstorm features are defined next (ref. 12-51).

12.5.5.1 Thunderstorm-Generated Severe Wind Definitions

Downburst—An exceptionally energetic downdraft that exits the base of a thunderstorm (not always severe) and spreads out at the Earth's surface as strong and gusty horizontal winds that may cause property damage. It may be accompanied by precipitation.

Downdraft—A term applied to the strong downward-flowing air current within a thunderstorm, which is usually associated with precipitation. An exceptionally strong downdraft can result in a downburst.

Gust front—The leading edge of a mass of relatively cool, gusty air that flows out of the base of a thunderstorm cloud (downdraft) and spreads along the ground well in advance of the parent thunderstorm cell; a mesoscale cold front, with cold temperatures in the advancing flow produced by evaporative cooling. A shelf cloud or roll cloud may accompany the gust front, as well as gustnadoes.

Gustnado (derived from gust front tornado)—A relatively weak tornado associated with the thunderstorm outflow at the leading edge of a thunderstorm cell, often found along a gust front. A debris cloud or dust whirl may indicate the presence of a gustnado.

Heatburst (also heat thunderstorm)—Localized, sudden increase in surface temperature associated with a thunderstorm, shower, or mesoscale convective system, often accompanied by extreme drying. The temperature jump can be so extreme that it is at times referred to as a "hot blast of air." It occurs in association with precipitation-driven downdrafts penetrating a shallow surface stable layer and reaching the ground (ref. 12-61).

Macroburst—A downburst (strong downdraft) that affects a path longer than 4 km (2.5 mi) and may persist for up to 30 min. Surface winds may reach 58 m/s (130 mph).

Microburst—An intense downburst that affects a path of 4 km (2.5 mi) or less and typically has a duration of <10 min; called a macroburst if path were >4 km (>2.5 mi). Microbursts may have winds reaching 78 m/s (174 mph). Depending upon the amount of precipitation in the vicinity, the microburst can be identified as a dry microburst or a wet microburst.

12.5.5.2 Kennedy Space Center Microbursts. Microbursts affect aviation and can also affect daily space operations at KSC. Exposed vehicles, such as the Space Shuttle, along with other facilities and equipment, can be toppled over from an unexpected microburst. Exposed workers on tall structures could also be endangered. Microbursts are considered the No. 2 weather hazard behind lightning at KSC (ref. 12-62).

Sanger analyzed 4 yr (1995–1998) of summertime (May–September) KSC/CCAS wind tower data to determine the frequency and statistics of microburst activity over the KSC area (ref. 12-62). His major findings indicate that a total of 282 microbursts—all wet microbursts—were observed during this 4-yr KSC summer period, which gave an average of 70.5 microbursts per summer season. Sixty-nine cases of microbursts (or ≈25 percent) occurred without accompanying lightning. Of the five summer months, June through August were the most prominent (72 percent) with July (30 percent) being dominant. The median microburst wind speed was 34 kt. The 5-min-averaged sustained wind speed, along with the peak gust (for cases with peaks ≥27 m/s (≥60 mph)), are also listed in table 12-19 in section 12.6.9.3. The strongest microburst wind speed gust measured (twice) was 46 m/s (103.6 mph). Out of the 282 microbursts observed, only 14 (or 5 percent) had peak winds ≥26 m/s (≥58 mph). However, there were a total of 131 microburst cases (or 46 percent) that met or exceeded 35 kt (18 m/s) (the warning criteria for KSC operations). Microburst winds at KSC can come from any direction, but the predominant direction is from the southeast through the west-northwest, with a maximum from the southwest. It is less probable for KSC to experience microburst winds from the east (80º to 100º). The most conductive time for microbursts is between 1600 UTC (12 p.m. EDT) and 2200 UTC (6 p.m. EDT), with the apex occurring

between 2000 UT (4 p.m.) and 2200 UT (6 p.m.). Ninety-nine total microbursts (or 35 percent) occurred during this 2-hr period. The spatial distribution for KSC microburst activity, as shown in figure 12-18, indicate that most KSC microburst activity can occur along the coastal area where the launch pads are located (ref. 12-62). Many measurements of KSC peak surface winds (most resulting from microburst activity) are presented in table 12-19 of section 12.6.9.3.

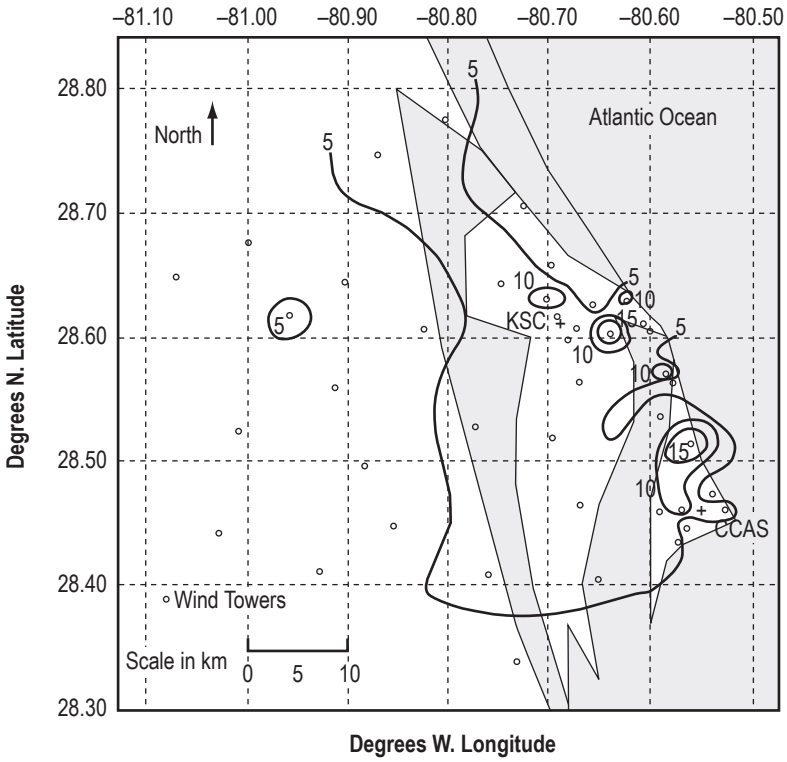

Figure 12-18. Spatial contour plot of 282 total microburst occurrences for 4 yr of summer months at KSC, Florida (ref. 12-62).

12.6 Hurricanes and Tropical Storms

A tropical cyclone is a generic term that can include a tropical disturbance, tropical depression, tropical storm, or hurricane (also called typhoon in the western Pacific) (ref. 12-51). The occurrence of hurricanes at KSC and other locations for the Eastern range is of concern to the space program because of high winds, associated storm surge and wave action, storm tide (storm surge with astronomical tide), precipitation flooding, and possible hurricane-generated tornadoes. (See sec. 12.4.) Also, because the range support for space operations is closed during passage or near approach of a hurricane. Damage can result from prolonged exposure to strong winds, since a structure may be damaged or destroyed due to fatigue of its parts. There also can be damage to structures (particularly power lines) sensitive to pronounced gusts in wind speeds (ref. 12-63). Tropical cyclones can produce widespread torrential rains, often in excess of 6 in, producing deadly and destructive floods that can trigger landslides and mud slides. Between 1970 and 1999, more people have been killed (59 percent) from freshwater flooding associated with landfalling tropical cyclones than from any other tropical cyclone weather hazard. Hurricane Andrew generated a 5.2-m (17-ft) storm tide in South Florida in 1992 (along with estimated wind gusts of 78 m/s (175 mph), whereas, Hurricane Katrina generated an 8.2-m (27-ft) tide in Mississippi (ref. 12-64).

A hurricane is a powerful, swirling storm that begins over a warm sea and requires a special set of natural environment conditions. The hurricane draws large amounts of heat and moisture from the sea. Hurricanes form in waters near the tropics, and then they move toward the poles. For a hurricane to form, there must be a warm layer of water at the top of the sea with a surface temperature >80 ºF (26.5 ºC). Warm sea water evaporates and is absorbed by the surrounding air. The warmer the ocean, the more water evaporates. The warm, moist air rises, lowering the atmospheric pressure of the air beneath. There must be little wind shear for a hurricane to develop; i.e., little difference in speed and direction between winds at upper and lower elevations. Uniform winds enable the warm inner core of the developing storm to stay intact. A low-pressure area must be more than 5º of latitude north or south of the equator in order to generate a hurricane. Hurricanes seldom occur closer to the equator. Tropical cyclones normally form within 25º of the equator, although some have formed as far away as 40º from the equator (ref. 12-65).

The winds of a hurricane swirl around a calm, central zone called the eye surrounded by a band of tall clouds called the eyewall. Surface pressure is lowest in the eye. The eye is usually 16–64 km (10–40 mi) in diameter and is free of rain and extensive clouds. In the eyewall, warm air spirals upward, and large horizontal changes in pressure create the hurricane's strongest winds. The speed of the winds in the eyewall is related to the diameter of the eye. Heavy rains fall from the eyewall and the bands of dense clouds that swirl around the eyewall. These bands, called rainbands, can produce more than 5 cm (2 in) of rain per hour. Hurricanes last an average of 3 to 14 days. A long-lived storm may wander 4,800 to 6,400 km (3,000 to 4,000 mi), typically moving over the sea at speeds of 4.5 to 9 m/s (10 to 20 mph). These winds can reach nearly 89 m/s (200 mph). Damaging winds may extend 400 km (250 mi) from the eye. Figure 12-19 illustrates the general wind flow structure around a typical Northern Hemisphere hurricane (ref. 12-65).

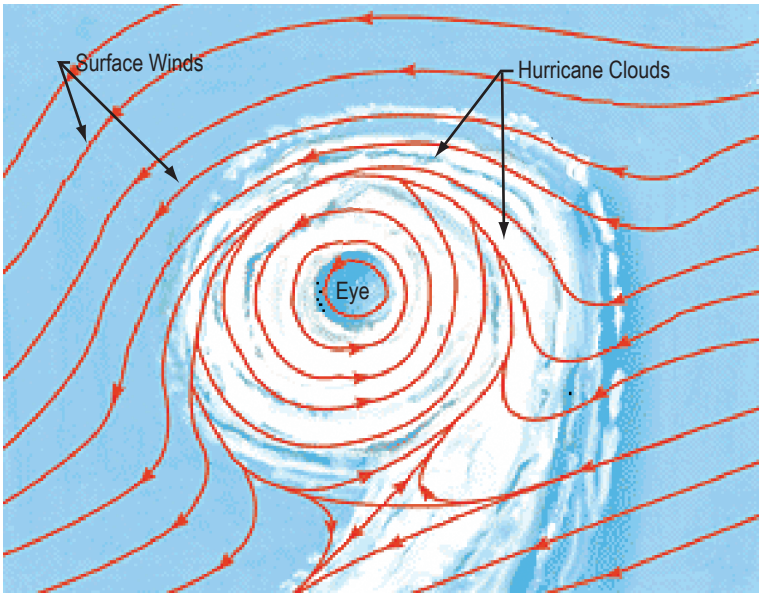

Figure 12-19. Hurricane wind flow on the ocean surface swirls counterclockwise around a calm eye in the Northern Hemisphere (ref. 12-65).

Figure 12-20 gives the world ocean areas where tropical cyclones normally form, their general movement, annual global percentage, and main months of activity. The historic tracks of nearly 150 yr of tropical cyclones are presented on the map, along with intensity, based on all storm tracks available from the NHC and the Joint Typhoon Warning Center through September 2006. Note that only ≈12 percent of all tropical cyclones develop

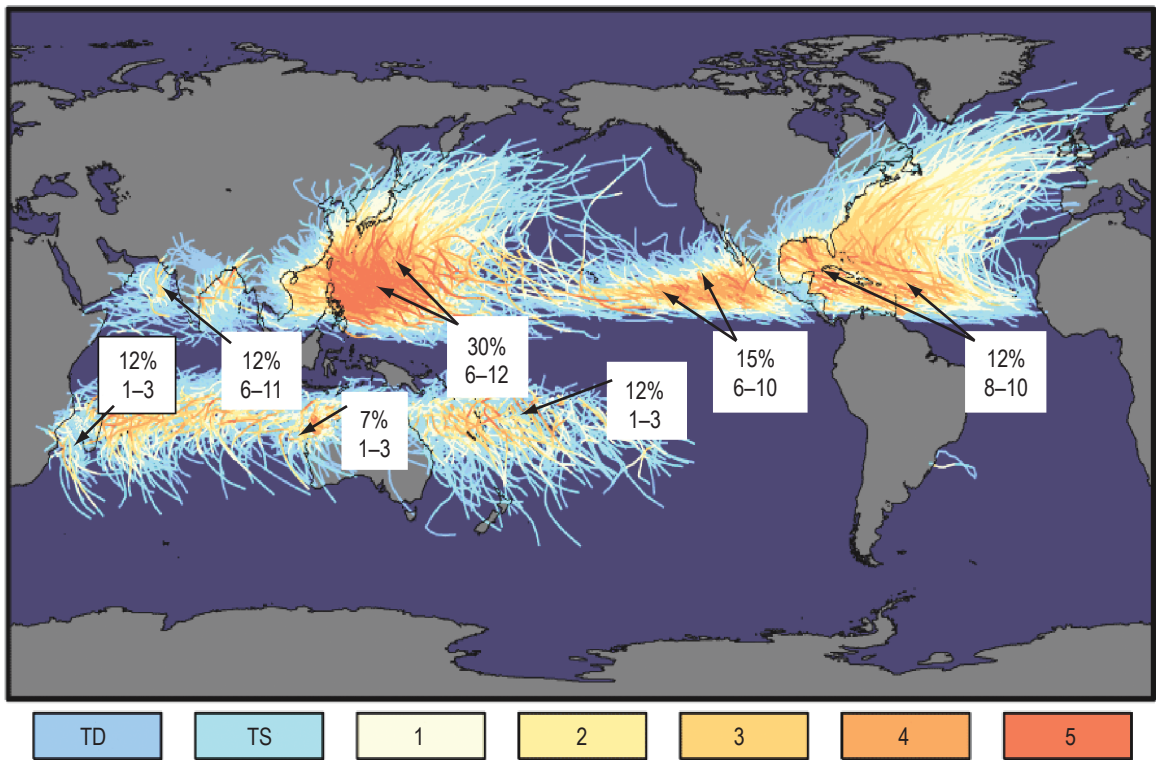

Figure 12-20. Typical global ocean areas where tropical cycones normally develop, their general movement, and all tracks and intensities plotted through 2006. Annual percentage of tropical cyclones and probable months of development are also given for each region (ref. 12-66).

in the Atlantic Ocean. Fifteen percent of all tropical cyclones develop in the eastern Pacific Ocean, 30 percent develop in the western Pacific Ocean, 24 percent in the Indian Ocean both north and south of the equator, and 12 percent develop in the southern Pacific Ocean. Essentially no tropical cyclones develop south of the equator in the Atlantic Ocean (ref. 12-66). Approximately 85 hurricanes, typhoons, and tropical cyclones occur in a year throughout the world.

On average each year, 11 tropical storms, 6 of which become hurricanes, develop over the Atlantic, Caribbean, or Gulf of Mexico. The U.S. coastline is normally struck five times by hurricanes, with two being major hurricanes, over a typical 3-yr span. The Atlantic hurricane season begins June 1 and ends November 30, while the East Pacific hurricane season runs from May 15 through November 30. Over other parts of the world, such as the western north Pacific, typhoons can occur year around (ref. 12-64).

This section of the Handbook will focus on the frequency and statistics of tropical cyclones (hurricanes, and/or tropical storms) for annual reference periods and certain monthly groupings, as a function of radial distances from KSC as well as information about tropical cyclones within the Gulf of Mexico and West Coast areas.

12.6.1 Launch Vehicle Hurricane Wind Fatigue Model

A problem can arise if a launch vehicle is exposed on the pad while being subjected to hurricane-force winds, and unable to be transported back to a sheltered area. The Shuttle design requirement for stay on the launch pad (unfueled) follows: “The integrated Space Shuttle System shall withstand predicted peak ground wind speed at the launch pad, up to and including 38.3 m/s (85.7 mph) at KSC from any azimuth” (ref. 12-67). Therefore,

Rockwell was requested by MSFC in October 1990 to define and develop a hurricane wind model for fatigue and fracture analysis, and to generate fatigue loads spectra at critical vehicle locations on the Space Shuttle. Measured wind data from the near passage of Hurricane Gladys in October 1968 were used to define such a model, and to generate the first hurricane fatigue loads spectra covering the prelaunch phase of the Shuttle (ref. 12-68). Rockwell indicated that during the period up to 1996, the prelaunch Shuttle duration on the pad has ranged from 14 to 161 days, with an average pad stay of 42 days. The highest wind speed recorded at KSC, prior to 1996, during a hurricane-associated gust was 45.5 m/s (101.7 mph). It was then determined that the hurricane model be developed that included a model consisting of 6 hr of buildup, with 1 hr of dwell time at the maximum wind speed of 38.3 m/s (85.7 mph), and then 6 hr of a decay period (ref. 12-68).

12.6.2 Hurricane Wind/Rain Damage to Space Vehicle's Thermal Protection System

Hurricane wind-driven rain can cause potential damage to the Shuttle orbiter's Thermal Protection System (TPS). Figure 12-21 gives the probable TPS Shuttle tile damage as a function of hurricane drop impact velocity (mph) and drop diameter (mm). The potential drop size from hurricane rains is about 5 to 7 mm (0.2 to 0.3 in) diameter. Therefore, no damage is expected with rain velocities <11 m/s (<25 mph) for 5-mm (0.2-in) drops and <16.5 m/s (<37 mph) for 7-mm (0.28-in) drops. Actual damage is expected with rain velocities >33 m/s (>75 mph) (5 mm (0.2 in)) and >50 m/s (>112 mph) (7 mm (0.28 in)). Damage is considered marginal between these two limits (J. Barneburg, NASA JSC, unpublished chart/memorandum).

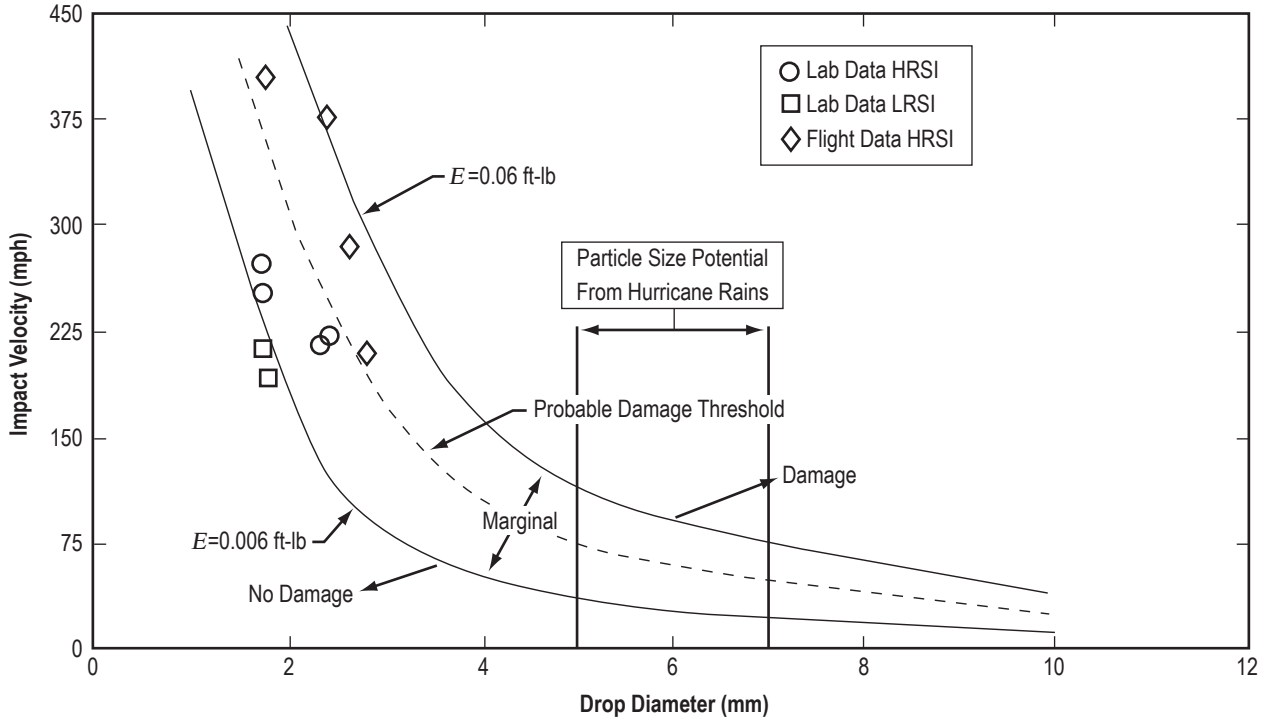

Figure 12-21. Shuttle orbiter tile damage potential from hurricane wind-driven rain (J. Barneburg, NASA JSC, unpublished chart/memorandum).

12.6.3 Tropical Cyclone Intensity

By definition, a hurricane is a severe tropical cyclone of tropical or subtropical origin with maximum sustained (1-min mean) surface winds >33 m/s (64 kt; 74 mph). A tropical storm is a tropical cyclone with sustained

winds between 17 and 32 m/s (34 and 63 kt; 39 and 73 mph). A tropical depression has maximum sustained winds of 16 m/s (33 kt; 38 mph) or less (ref. 12-51).

There is an established hurricane intensity scale for the Atlantic and Northeast Pacific basins that categorizes a hurricane's mean wind speed versus its severity to give an estimate of the potential flooding and property damage. It is called the Saffir-Simpson scale of hurricane intensity (refs. 12-69 and 12-70) and is presented in table 12-10. There is no upper limit for wind speed in hurricanes, but in the United States, maximum hurricane wind speeds of 85 m/s (165 kt; 190 mph) have been recorded in the Gulf of Mexico during Hurricane Camille in 1969 and Hurricane Allen in 1980. The most intense hurricane based on central pressure was Hurricane Wilma in 2005 that recorded an 882-mb (26.05-inHg) minimum pressure. The devastating Labor Day hurricane of 1935 in the Florida Keys recorded a 26.34-inHg (892-mb) pressure with winds probably well in excess of 72 m/s (160 mph) (ref. 12-71).

Table 12-10. Saffir-Simpson hurricane (tropical cyclone) intensity scale (contributed by ref. 12-70).

Saffir-Simpson Hurricane Category	Maximum Sustained Wind Speed			Minimum Central Pressure*		Storm Surge**		Damage Category
	(m/s)	(mph)	(kt)	(mb)	(inHg)	(m)	(ft)	
1	33–42	74–95	64–82	>980	>28.94	1–1.7	3–5	Minimal
2	43–49	96–110	83–95	979–965	28.91–28.50	1.8–2.6	6–8	Moderate
3	50–58	111–130	96–113	964–945	28.47–27.91	2.7–3.8	9–12	Extensive
4	59–69	131–155	114–135	944–920	27.88–27.17	3.9–5.6	13–18	Extreme
5	70+	156+	136+	<920	<27.17	5.7+	19+	Catastrophic
Tropical depression	<17	<39	<34	–	–	–	–	None or minimal
Tropical storm	18–32	39–73	35–63	–	–	–	–	Minimal

*Classification by central pressure was ended in the 1990s, and wind speed alone is now used. These estimates of the central pressure that accompany each category are for reference only.

**Surge values are for reference only. The actual storm surge experienced will depend on offshore bathymetry and onshore terrain and construction.

12.6.4 Hurricane Forecast Indices

NOAA uses a number of hurricane indices when making annual hurricane number and intensity forecasts. The measure of overall hurricane activity used by NOAA is called the Accumulate Cyclone Energy (ACE) index. The ACE index is essentially a wind energy index, and similar to the Hurricane Destruction Potential (HDP) index. The ACE is defined as the sum of the squares of a named storm's maximum sustained wind speed (in knots) for each 6-hr period of its existence, while they are at least tropical storm strength. It is applied to all named storms. Since this index represents a continuous spectrum of both system duration and intensity, it does not suffer from the discontinuities inherent in more widely used measures of activity such as the number of tropical storms, hurricanes, or major hurricanes.

Two other measures of overall activity, developed by Dr. William Gray (Colorado State University) are the HDP index and the Net Tropical Cyclone (NTC) index. These indices are correlated at ≈0.95 with the ACE index. NOAA uses the ACE index instead of the HDP index when making and verifying their seasonal outlooks because the ACE index includes the contribution from systems while at tropical storm strength, whereas the HDP index does not. The ACE index is used instead of the NTC index because it allows one to easily quantify activity occurring in different parts of the Atlantic basin, and because it does not suffer from resampling issues inherent in the mathematical formulation of the NTC index. NOAA uses the ACE index, in combination with the number

of named storms, hurricanes, and major hurricanes, to categorize North Atlantic hurricane seasons as being above normal, near normal, or below normal (ref. 12-72).

12.6.5 Atlantic Basin Annual Hurricane Statistics

The average, maximum, and minimum annual frequencies of tropical storms, hurricanes, and major hurricanes (category 3–5) for the Atlantic basin are presented in table 12-11 (refs. 12-70 and 12-73).

Table 12-11. Atlantic basin annual tropical cyclone occurrence statistics* through 2006 (refs. 12-70 and 12-73).

Category	Maximum No.	Minimum No.	1965–2006 Average No.
Named storms (wind ≥35 kt (40 mph, 18 m/s))	28 (2005)	4 (1983)	10.9
Hurricanes (wind ≥65 kt (75 mph, 33.4 m/s))	15 (2005)	2 (1982)	6.1
Major hurricanes (wind ≥95 kt (109 mph, 48.9 m/s))	8 (1950)	0 (many, 1994**)	2.3
U.S. landfalling named storms	9 (2004)	1 (many, 1991**)	3.6***
U.S. landfalling hurricanes	6† (1916, 1985, 2004)	0 (many, 2001**)	1.8‡
U.S. landfalling major hurricanes	4 (2005)	0 (many, 2003**)	0.6‡

*POR for entire Atlantic basin (1944–2006); POR for the U.S. coastline (1899–2006).
**The latest year with this number.
***T.M. Hall, Personal Communication, and reference 12-73.
†1886 is recorded as the most active hurricane season for the continental United States with seven landfalling hurricanes.
‡1851–2006 average (ref. 12-74).

12.6.6 General Hurricane Information, Models, and Statistics

Over the last few years the *NASA Earth Observatory News* (ref. 12-75) has complied various interesting hurricane facts. Some of these facts include items such as the following:

(1) NASA found intense lightning activity around a hurricane's eye during Hurricane Emily in July 2005 (6/23/2006 in issue of *NASA Earth Observatory News* (ref. 12-75)).

(2) The passing of hurricanes cools the entire Gulf of Mexico (2006) by up to 4 ºC (39 ºF) along the path and 1 ºC (34 ºF) over the entire Gulf.

(3) Thunderstorm Zeta formed on December 30, 2005, briefly reached hurricane status, and then dissipated on January 6, 2006, being the latest-forming storm and the first to ever survive so long in January (February 13, 2006).

(4) Dust may dampen a hurricane's fury (October 10, 2006).

(5) Hurricane Rita in 2005 indicated that rapid hurricane intensity changes can be caused by clouds outside the wall of the eye coming together to form a new eyewall (March 1, 2007).

(6) Researchers found that estimates of tropical storm counts prior to 1944 undercounted by only 1.2 storms/yr, not the 3 storms/yr as previously thought (ref. 12-76).

12.6.6.1 Typical Hurricane Energy/Cross Section. Dr. Greg Carbone and Eric Stevens of the University of South Carolina have developed a hurricane energy cross-sectional interactive program on the internet that allows the user to determine values of various meteorological parameters (atmospheric temperature, dewpoint, pressure, and wind) versus altitude and horizontal distance from the eye of a typical hurricane. Using figure 12-22, one can put a cursor over different parts of the storm (points A through M) to show the differences among these meteorological variables in the program on-line at <http://people.cas.sc.edu/carbone/modules/mods4car/tropcycl/pages/energy.html> (ref. 12-77).

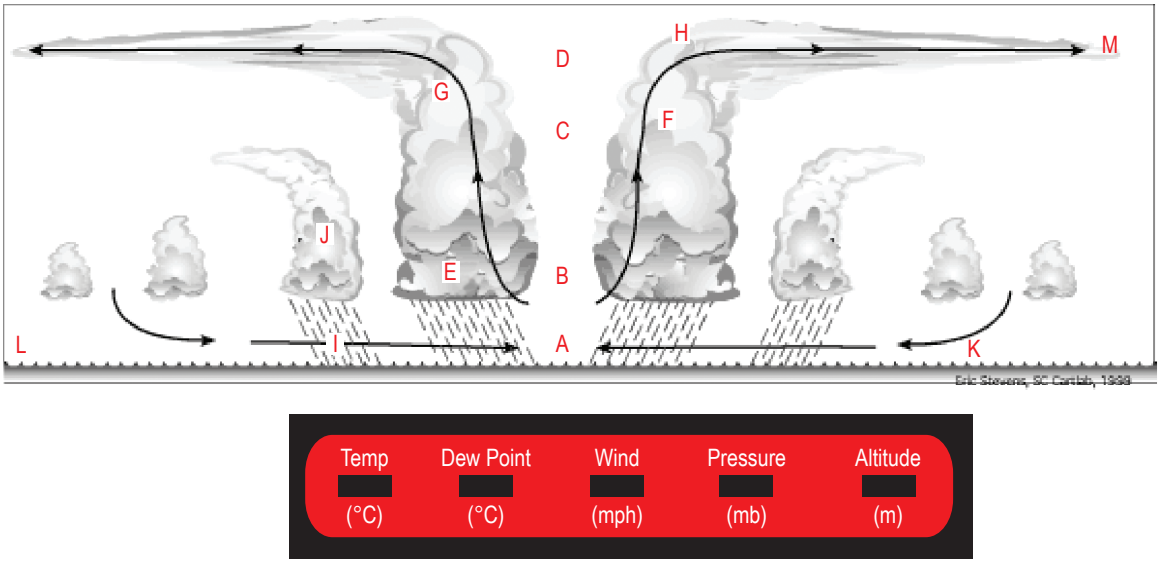

Figure 12-22. Graphic hurricane program indicating various meteorological values within a typical hurricane structure (ref. 12-77).

12.6.6.2 Hurricane Wind Relationships

12.6.6.2.1 Hurricane Circulation. Figure 12-23 shows the general wind circulation structure around a typical 52-m/s (100-kt) hurricane. Note the inward airflow into the center of the hurricane eye, and that the right front quadrant normally contains the strongest winds. Keim (ref. 12-79) indicates that recent studies suggest that for an "average" hurricane, hurricane-force winds extend forward and to the right of the eye about 50 to 100 km (31 to 62 mi) and 25 to 50 km (15.5 to 31 mi) to the left.

12.6.6.2.2 Hurricane Wind Speed Versus Pressure. Figure 12-24 shows the relationship between surface pressure and sustained wind speed for a number of tropical low-pressure systems. Tropical low-pressure systems are classified as hurricanes when their pressure is 989 mb (28.94 inHg) or lower, and sustained wind speeds are >119 km/hr (>74 mph) (ref. 12-80).

12.6.6.2.3 Estimating Hurricane Wind Speed and Vertical Variation. Hurricanes possess a relatively small, closed circulation of low pressure usually with dimensions between 500 and 1,000 km (311 and 621 mi)

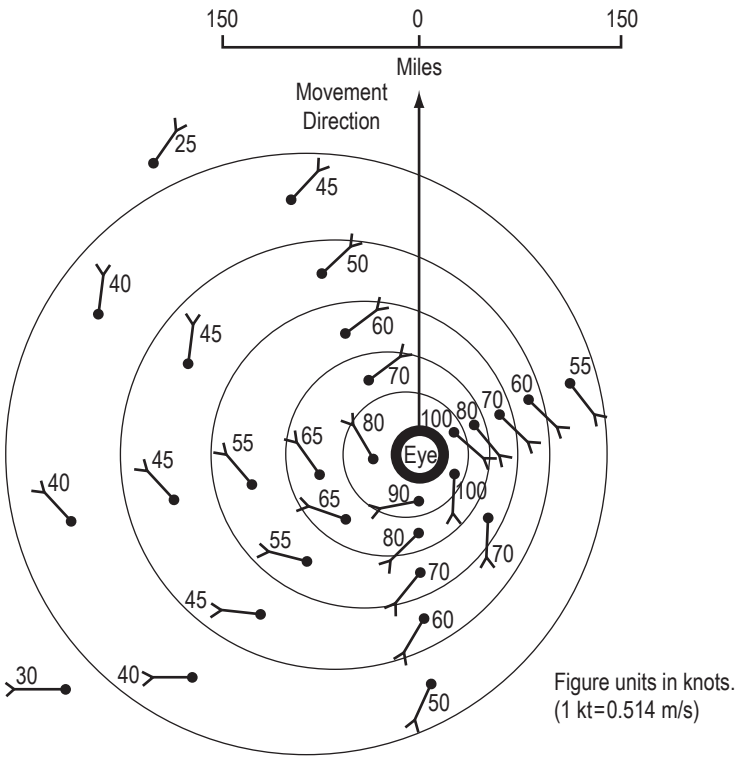

Figure 12-23. Wind circulation around a typical 52-m/s (100-kt) hurricane (ref. 12-78).

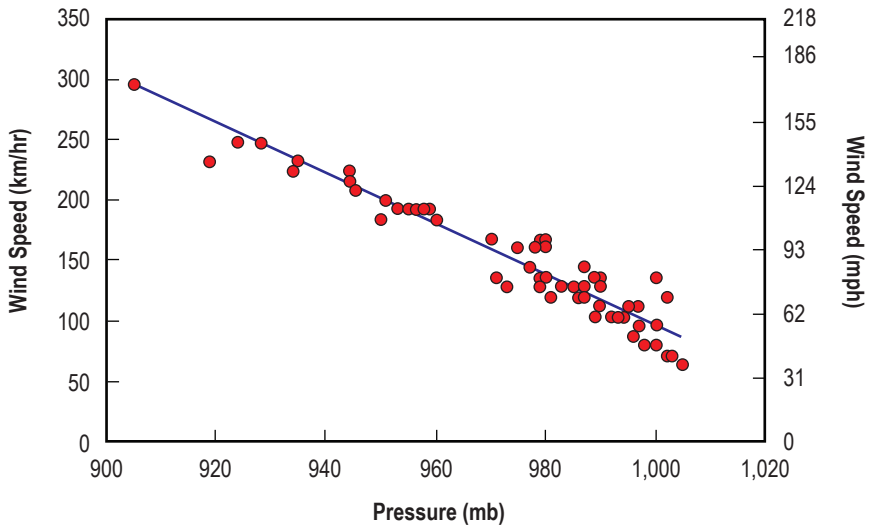

Figure 12-24. General relationship between hurricane surface pressure and sustained wind speed (ref. 12-80).

in diameter and within 1,524 m (5,000 ft) of the ocean surface. The hurricane's strongest winds are normally located ≈457 m (≈1,500 ft) above the sea surface with winds decreasing both above and below this level. The wind speeds being stronger below than above, which is a direct consequence of its warm-core structure (ref. 12-81). The top of the eyewall can extend up to 15,240 m (50,000 ft).

According to Hsu (ref. 12-82), a hurricane's wind speed and its vertical variation are important not only for maritime safety but also for wind loading and wave prediction:

$$U_{10} = 6.3\ (1{,}013 - P)^{0.5}\ , \tag{12.7}$$

and its limit is

$$U_{10\ \max} = 6.3\ (1{,}013 - P_0)^{0.5}\ , \tag{12.8}$$

where U_{10} (in m/s) is the wind speed at 10 m, P (in mb) is the pressure at a site in question, U_{10} (in m/s) is the maximum U_{10}, and P_0 is the hurricane's minimal sea level (central) pressure (in mb).

Note that the standard mean sea level pressure for 30° N. in July and 15° N. annual is 1,013 mb. An example to apply eqns. (12-7) and (12-8) follows: During Hurricane Lili (2002), buoy 42003 located ≈280 km to the east of the center recorded $P = 1011.1$ mb.

From eqn. (12-7), $U_{10} = 6.3(1{,}013 - 1{,}011.1)^{0.5} = 8.7$ m/s which is in good agreement with the measured value of 9.2 m/s at buoy 42003.

Also, since $P_0 = 956.1$ mb, from eqn. (12-8), $U_{10\ \max} = 6.3(1{,}013 - 956.1)0.5 = 47.5$ m/s, which is in excellent agreement with the measured value of 47.2 m/s at buoy 42001 near the eyewall.

The vertical variation of the wind speed is also important:

$$U_z / U_{10} = (z/10)^{0.125}\ . \tag{12.9}$$

According to Hsu (ref. 12-82), when U_{10} is >20 m/s, where U_z is the wind speed at height z other than 10 m,

$$U_{30\ \mathrm{m}} / U_{10\ \mathrm{m}} = (30/10)^{0.125} = 1.15\ . \tag{12.10}$$

For example, if the wind speed at 30 m is needed, then from eqn. (12.9) or U_{30} is ≈15 percent higher than U_{10}.

From eqn. (12.5), we conclude that

$$U_{10}\ (\text{in kt}) = 12.2\ (1{,}013 - P\ )^{0.5} \tag{12.11}$$

or

$$U_{10}\ (\text{in mph}) = 14.1\ (1{,}013 - P\ )^{0.5}\ , \tag{12.12}$$

where P is the pressure in millibars as before.

Figure 12-25 and table 12-12 present the graphical and tabular results of Franklin's (ref. 12-83) typical hurricane vertical eyewall wind profiles as measured via global positional system drop windsondes. Figure 12-25 shows the mean eyewall wind speed profile, where the wind at each level has been normalized by the sonde measured wind speed at 700 mb (20.67 inHg). The strongest winds in the eyewall are found near 500 m (1,640 ft) elevation; these are about 20 percent higher than the 700-mb (20.67-inHg) winds, owing to the warm-core nature of the tropical cyclone. For comparison, the mean profile for noneyewall sondes within 370 km (200 nmi)

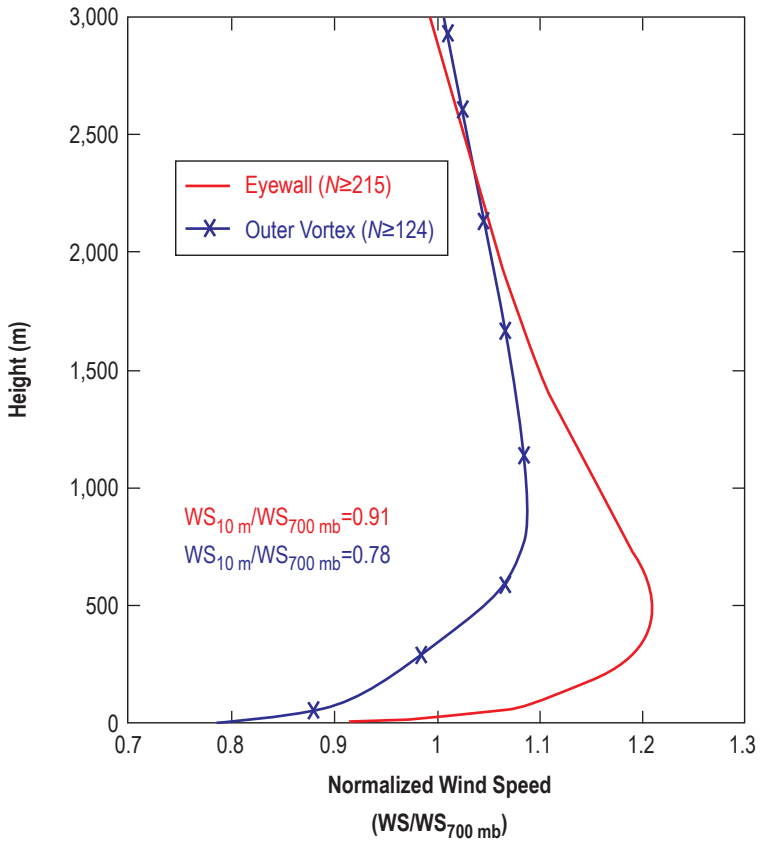

Figure 12-25. Mean wind speed profile (normalized by 700-mb (20.67-inHg) wind speed) for eyewall and outer vortex soundings (ref. 12-83).

of the cyclone center is also shown. In the outer part of the vortex, the low-level wind maximum is found at a somewhat higher elevation and is not as pronounced as in the eyewall. The ratio of the surface to 700-mb (20.67-inHg) wind (R_{700}) is 0.78 in the outer vortex and 0.91 in the eyewall. This study is based on a sample of 357 quality-controlled eyewall profiles from 17 hurricanes (1997–1999). A majority of these dropsonde releases were made from the 700-mb (20.67-inHg) level (≈3,050 m (≈10,000 ft)).

12.6.6.2.4 Estimating Hurricane Wind Gusts Over Land Relative to Sustained Winds Measured Over Water. The S-S scale for categorizing hurricane intensity and damage potential is associated with 1-min wind speeds. The ASCE-7 Standard (for structural engineering purposes) defines these 1-min speeds as measured at 10 m (33 ft) over open water. Simiu (ref. 12-84) related the 3-s wind gust ratio estimated over land to the 60-s sustained wind measured over water, and found that at 10 m (33 ft) above open water, it equals 1.03 using the power law model. However, Simiu indicated that the logarithmic law model gave ratios varying from 1.03 to 1.12, depending on the surface roughness over water. The ratio value 1.07 is reasonable to use for operational purposes; i.e., use ratio equation (12.13):

$$R = \frac{U_{3\,\mathrm{s}}^{\text{open terrain}}\left(10\,\mathrm{m}\right)}{U_{60\,\mathrm{s}}^{\text{open water}}\left(10\,\mathrm{m}\right)}\ , \tag{12.13}$$

where R is ratio.

Table 12-12. Mean hurricane eyewall wind variation with elevation (ref. 12-83).

Height		Wind (% of Surface)	Pressure Force (% of Surface)
(m)	(ft)		
10.0	33 (sfc)	100	100
15.2	50	103	106
30.5	100	108	151
45.7	150	111	123
61.0	200	115	132
76.2	250	117	137
91.4	300	119	142
121.9	400	121	146
152.4	500	123	151
182.9	600	125	156
228.6	750	128	164
304.8	1,000	131	172

12.6.6.2.5 Estimating Wind Decay After Landfall. Tropical cyclone winds weaken when the storm center moves across land (after landfall) as land surfaces provide much more resistance than comparatively smooth water surfaces, and also because the surface energy flux which fuels the storm is significantly reduced. The empirical model developed in 1995 by Kaplan and DeMaria (ref. 12-85) (as used by Froehlich (ref. 12-86)) is normally applied to estimate the maximum sustained surface wind as a storm moves inland. The model applies a simple two-parameter decay equation to the hurricane wind speed (V) (knots) at landfall, resulting in

$$V_t = 26.7 + (0.9V - 26.7)\, e^{-0.095t} - t\,(50 - t)\,(0.0109 \log_e D - 0.0503) \quad , \tag{12.14}$$

where

V_t = wind speed after landfall (knots)
V = initial landfall wind speed (knots)
t = time since landfall (hours)
D = distance the storm has advanced inland (kilometers).

Note: No adjustments are made to the storm forward speed (V_f).

Figure 12-26 shows graphically how tropical cyclone sustained winds rapidly decrease once a tropical cyclone reaches land. Hurricane sustained winds generally decrease at a relatively constant rate (approximately half the wind speed in the first 24 hr). Generally, the faster the forward speed of a landfalling hurricane, the further the inland penetration of hurricane force winds (ref. 12-87).

Figure 12-27 indicates the maximum inland extent of strong category 4 hurricane winds 64.4 m/s (144 mph) that approach the southeast United States from any direction, with a hurricane forward speed of 11.2 m/s (25 mph). This is one example of the interactive “Maximum Envelope of Winds” (MEOW) program. There are three menus, one for each of the regions—Gulf Coast, East Coast, and Northeast Coast. Within this program, click on the desired hurricane strength and it will link to the MEOW for hurricanes with various

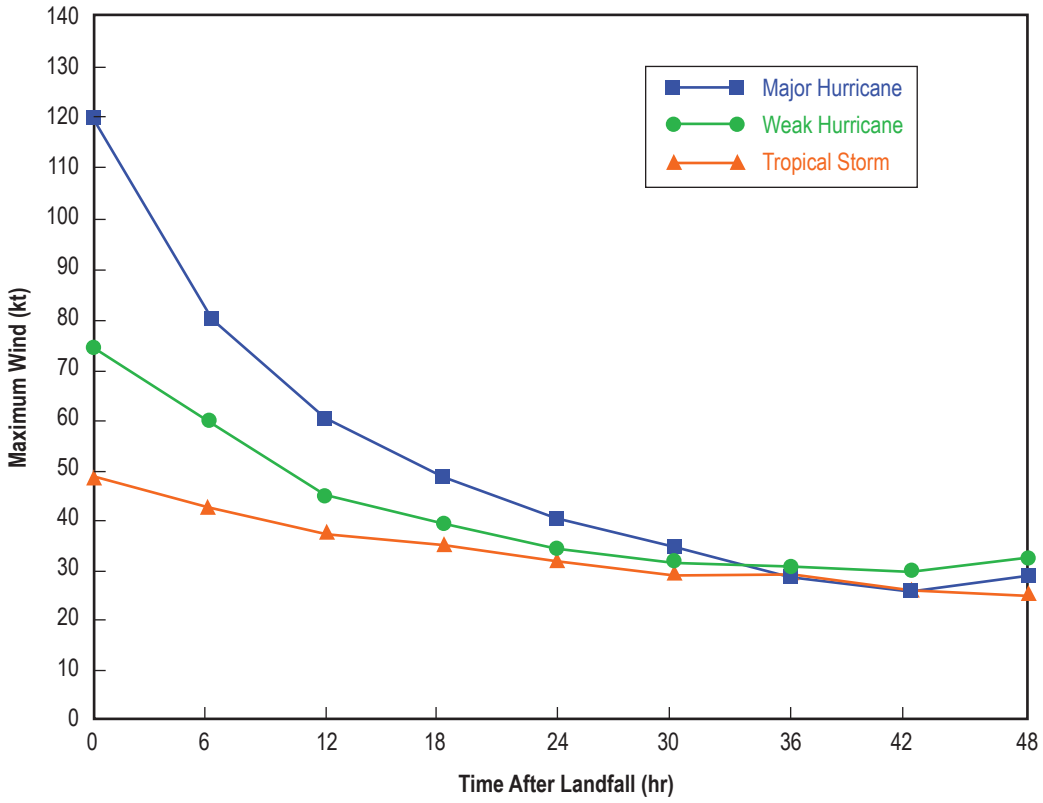

Figure 12-26. Tropical cyclone sustained winds decrease with time after landfall (NWC) (ref. 12-87).

forward speeds of 11, 9, 6, and 4 m/s (of 25, 20, 14, and 9 mph)). The inland wind model was developed by Kaplan and DeMaria (ref. 12-85). This model can be used for operational forecasting of the maximum winds of landfalling tropical cyclones. It can also be used to estimate the maximum inland penetration of hurricane-force winds (or any wind threshold) for a given initial storm intensity and forward storm motion. For further explanation, refer to references 12-85 and 12-88.

12.6.6.3 U.S. Hurricane Landfall Frequency. East Coast: Figure 12-28 gives all the hurricane strikes for the continental United States between 1950 and 2007, for all hurricane intensities (categories 1–5) (ref. 12-89).

12.6.6.4 Coastal U.S. Hurricane Return Periods. Average return periods, in years, are given in figure 12-29 for 45 key U.S. Gulf and Atlantic coastal city locations using the 105-yr tropical cyclone POR (1901–2005). These return periods were derived by dividing the 105-yr tropical cyclone record by the total number of tropical cyclone strikes at the various locations. Results for all tropical cyclones are represented by the inner tier, all hurricanes by the middle tier, and all major hurricanes (categories 3–5) in the outer tier. Location 4 represents Galveston, TX (JSC), locations 6–8 represent the lower Louisiana and Mississippi regions (Michoud/Stennis), location 23 represents Cocoa Beach, FL (KSC), and location 34 represents Virginia Beach, VA (Wallops Island) (ref. 12-79).

12.6.6.5 Tropical Cyclone Landfall Probability. Hall and Jewson (ref. 12-73) have verified that the distributions of annual tropical cyclone landfall counts are Poisson. To calculate a hurricane landfalling

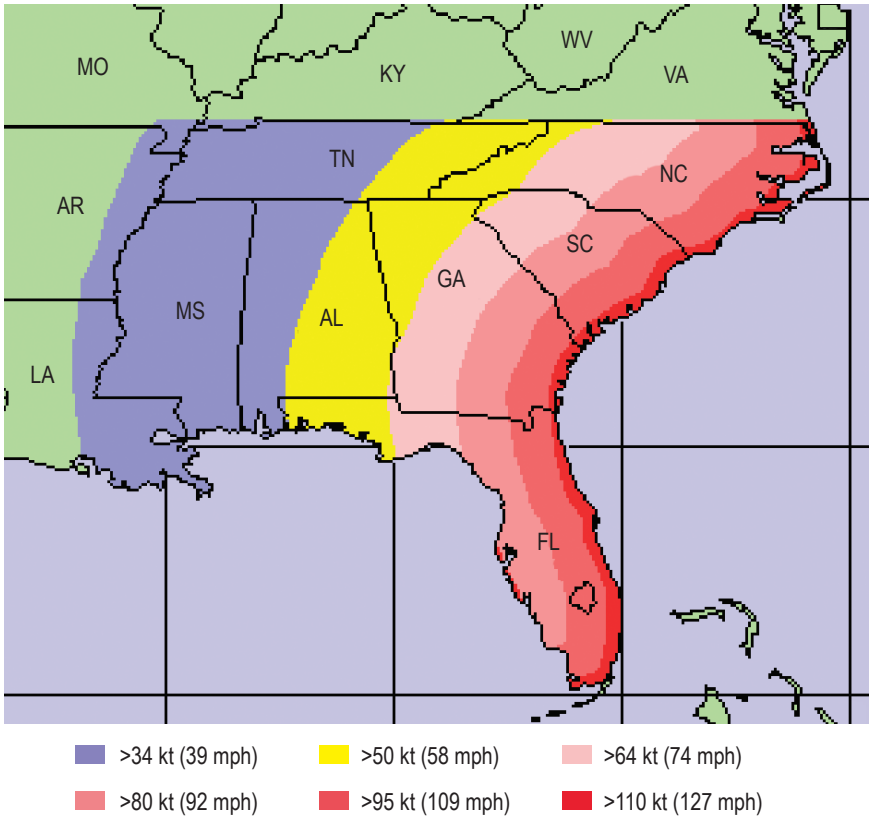

Figure 12-27. Maximum inland extent of winds for category 4 hurricanes approaching the Southeast from any direction with a forward speed of 11.2 m/s (25 mph) (ref. 12-88).

probability, it can be modeled as a Poisson process when resulting from a negative binomial distribution. Equation (12.15) can then be used. Given i landfalls in m years, the probability of n landfalls in a subsequent year can be expressed as follows:

$$f(n/i) = \{([i+n]!)/(i!n!)\} \times (m/[m+1])^{i+1} \times (1/[m+1]) \quad . \tag{12.15}$$

This expression reduces to a Poisson distribution when using large m and i.

A unique set of wind measurements were made by The University of Alabama in Huntsville's (UAH's) 915 MHz doppler wind profiler during the September 16, 2004, eyewall passage of Hurricane Ivan into Alabama. These results are presented in section 12.8.

12.6.7 Florida Hurricane Statistics

12.6.7.1 Major Hurricanes (Categories 3–5) Making Landfall in Florida. The years 1928–1965 (38 yr) saw 14 major hurricanes (≈1 per 3 yr) making landfall in Florida. However, during the period 1966–2003, only one major hurricane made landfall in Florida (one per 38 yr). Then, in 2004, four hurricanes (three major) all made landfall in Florida (ref. 12-90). Hurricane Charley was the strongest and costliest storm to hit the United States since Andrew in 1992. Jeanne was the first major (category 3 or higher) storm to make landfall on the east coast north of Palm Beach, FL, and south of the mouth of the Savannah River since 1899. The year 2005 was also

Figure 12-28. All category hurricane strikes (categories 1–5) for the continental United States between 1950 and 2007 (POR 57 yr) (ref. 12-89).

a very active hurricane season with four major hurricanes hitting the U.S. coast, including Wilma that made landfall from the Gulf, and Kartrina from the Atlantic, both coming into southern Florida. Between 1995 and 2006, the Atlantic hurricane seasonal activity has been hyperactive in 7 out of those 12 yr. Other noteworthy facts are: Thirty-six percent of all U.S. hurricanes hit Florida, and 76 percent of category 4 or higher hurricanes have hit either Florida or Texas (ref. 12-91).

The measured/estimated wind speeds of the 2004 tropical cyclones to make landfall in Florida are presented in table 12-13, along with the coastal extent of hurricane-force winds, the maximum storm surge, and the average rainfall. Figure 12-30 shows the ground track plot of the five 2004 tropical cyclones that made landfall in Florida.

12.6.7.2 Florida Hurricane Wind Probabilities. Figure 12-31 gives the frequency of Florida hurricanes with wind speeds ≥100 kt (≥51 m/s or ≥115 mph) as mapped in terms of the probability of occurrence during a 20-yr exposure period. These probabilistic estimates, based on a 106-yr POR, illustrate that hurricanes with 100-kt (51-m/s or 115-mph) winds occur more frequently in southern Florida, and gradually decrease in frequency towards northern Florida (ref. 12-96). Figure 12-32 presents the annual probability of Florida counties experiencing hurricane-force winds using a 97-yr POR. Brevard County, FL, (KSC) has an annual 10-percent probability. Since counties can vary in size, the results can be slightly biased (ref. 12-97).

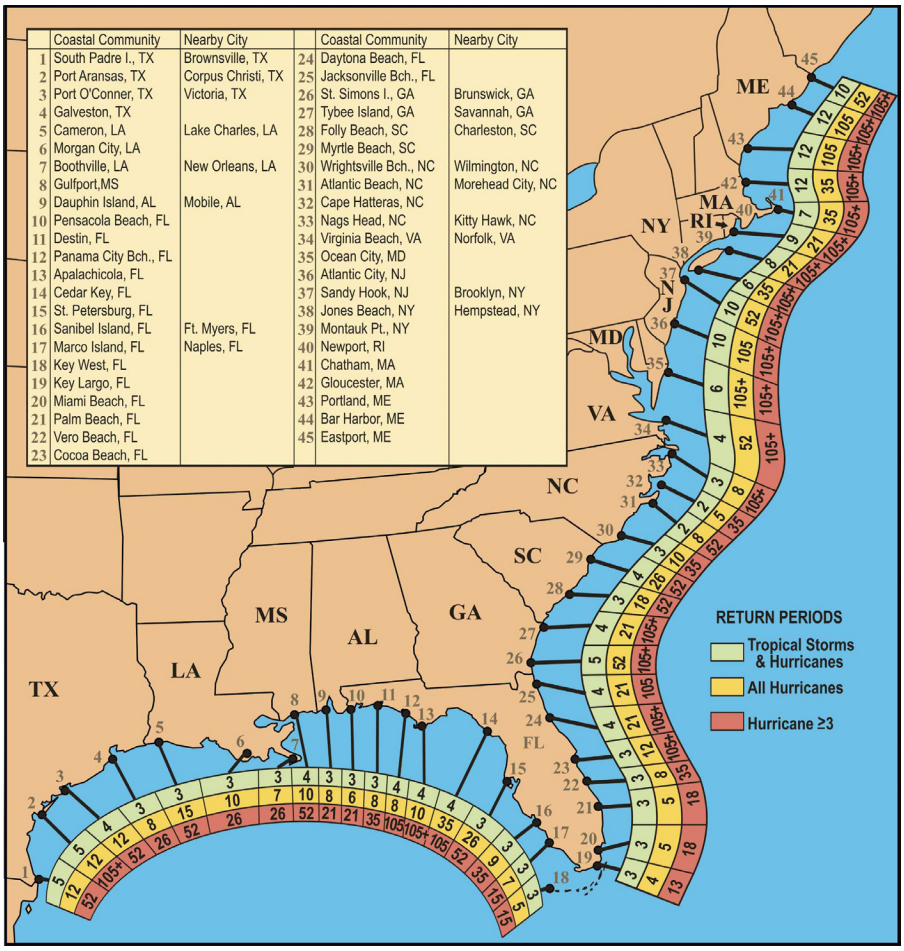

Figure 12-29. Average key city return periods for Gulf and Atlantic tropical storms, hurricanes, and severe hurricanes (categories 3–5), POR 1901–2005 (ref. 12-78).

Table 12-13. 2004 Florida tropical cyclone statistics at landfall (refs. 12-92 through 12-94).

Hurricane Name	Category	Date	Sustained Winds		Extent of Hurricane-Force Winds		Extent of Hurricane-Force Winds Right of Landfall		Maximum Storm Surge		Northwest Florida* Average Rainfall		South Florida* Average Rainfall	
			(m/s)	(mph)	(km)	(mi)	(km)	(mi)	(m)	(ft)	(cm)	(in)	(cm)	(in)
Bonnie	(TS)	Aug. 12	20.6	46	–	–	–	–	–	–	3.8–6.4	1.5–2.5	–	–
Charley	(4)	Aug. 13	67.1	150	54	34	35	22	2.5	8.2	–	–	8.4	3.3
Frances	(2)	Sept. 5	46.5	104	279	173	156	97	2.5	8.2	20–23	8–9	17.3	6.8
Ivan	(3)	Sept. 16	54.1	121	227	141	141	88	2.7	8.9	20–23	8–9	9.4	3.7
Jeanne	(3)	Sept. 26	54.1	121	253	157	179	111	1.8	5.9	15–18	6–7	14.2	5.6

*Average in watershed or river basin. Maximum could be close to double the average.

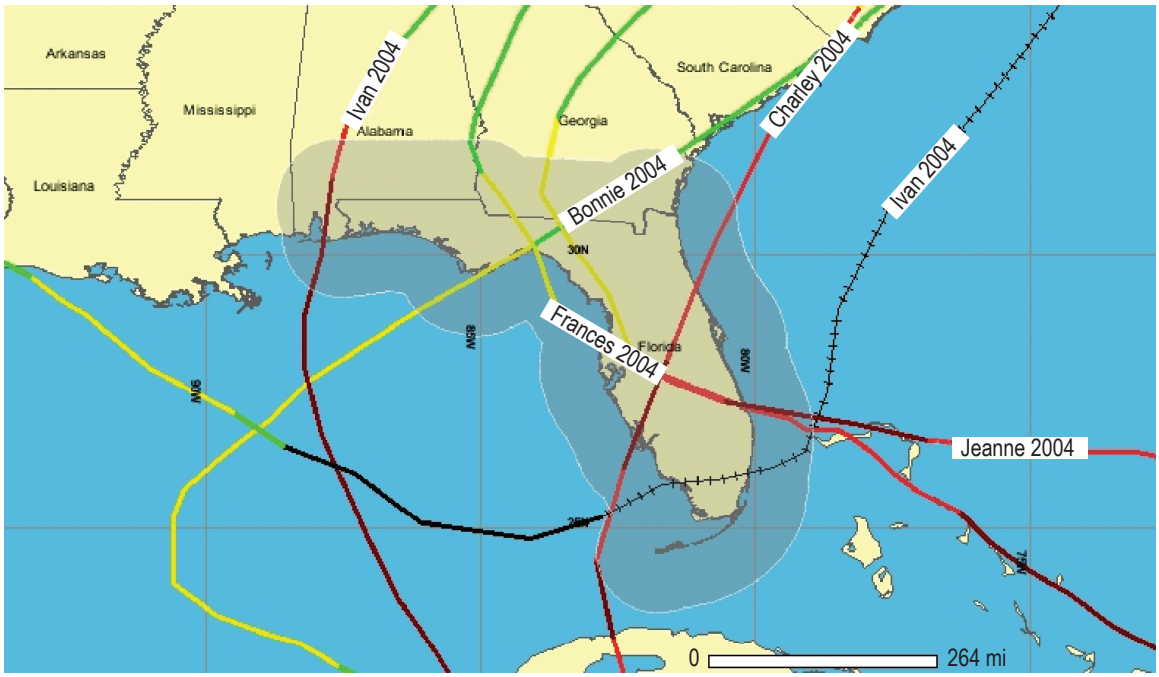

Figure 12-30. 2004 ground tracks of the five tropical cyclones that made landfall in Florida (ref. 12-95).

12.6.8 U.S. West Coast Hurricane Statistics

Normally, an average of ≈18 tropical storms form over the eastern Pacific Ocean each year with about half developing into hurricanes. Few of these storms ever hit U.S. land. A few do hit Mexico's west coast, and every few years a storm will brush Hawaii. The hurricane threat to the U.S. west coast NASA-associated facilities (California's VAFB, EAFB, and Dryden) is not a major concern since only one hurricane's winds in recorded history has ever been experienced on the west coast.

Hurricane-force winds hit California from San Diego to Los Angeles on October 2, 1858, while just missing making landfall (ref. 12-98). Since 1900, only four tropical cyclones have brought gale-force winds to the southwestern United States. A tropical storm made landfall near Long Beach in late September 1939 with 23-m/s (50-mph) winds. The remnants of Hurricane Joanne in 1972, of Hurricane Kathleen in 1976, and of Hurricane Nora in 1997 are the other three. A few tropical cyclones may hit the southern and central areas of the Baja, California peninsula, but they usually do not make landfall any further north. Usually only the remnants of a Pacific hurricane or tropical storm can affect California with extreme rainfall and flooding, mudslides, etc. There have been about 50 incidents of damage due to high wind and extreme rain throughout California from the influence of tropical cyclones since 1900 (ref. 12-99).

Figure 12-33 presents the tropical cyclones tracks that have approached within 370 km (200 nmi) of the VAFB area. Only six storms—one tropical storm, four tropical depressions, and one extratropical storm—occurring between 1972 through 2000 have come that close, with some tropical depressions making landfall in Southern California. Of these six storms, only one has come as close as 185 km (100 nmi) to VAFB (ref. 12-95). See table 12-14. These Pacific storms can also track into Arizona and New Mexico, as six storms, including one tropical storm, generated from Pacific tropical cyclones have come within 370 km (200 nmi) of Holloman AFB/WSMR, NM. The hurricane seasonal climatology for the Central Pacific during 1971–2005 is given in table 12-15 (ref. 12-100).

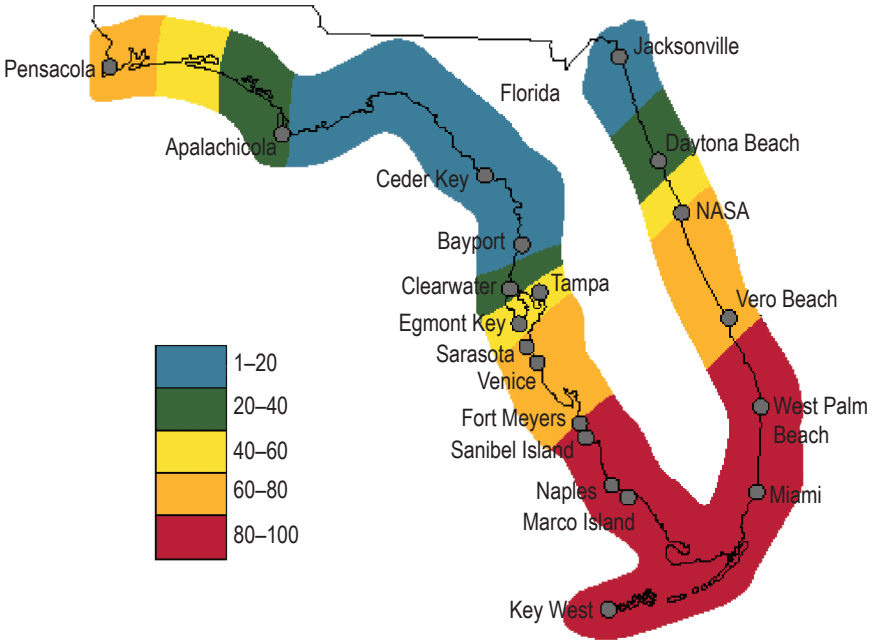

Figure 12-31. Florida 20-yr, 100-kt (51-m/s or 115-mph) wind probability (ref. 12-96).

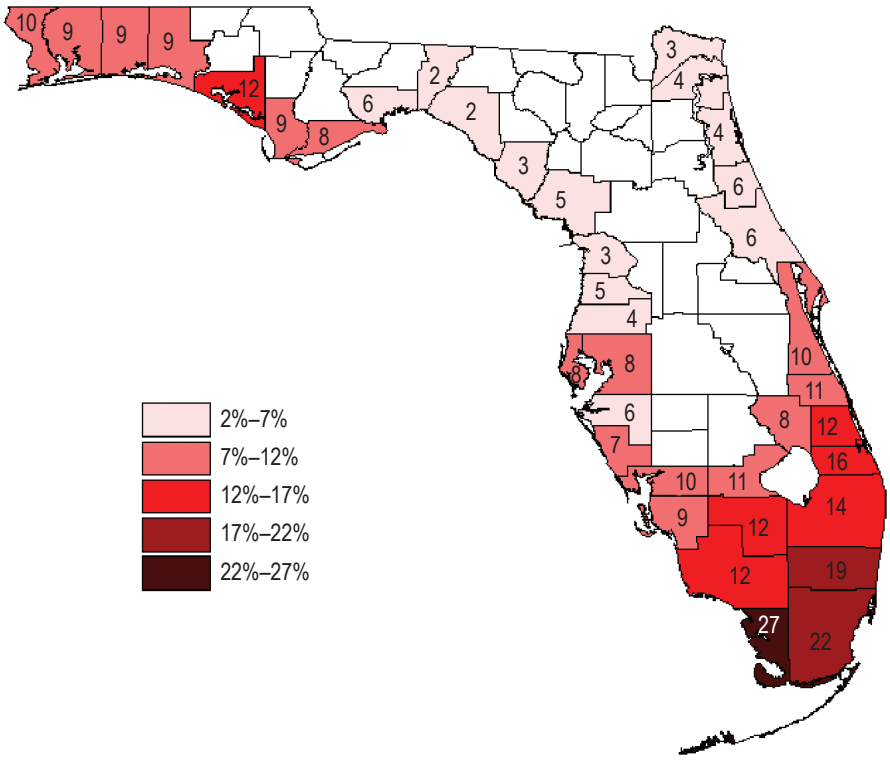

Figure 12-32. Annual probabilities of Florida counties experiencing hurricane-force winds from a hurricane (1900–1996) (ref. 12-97).

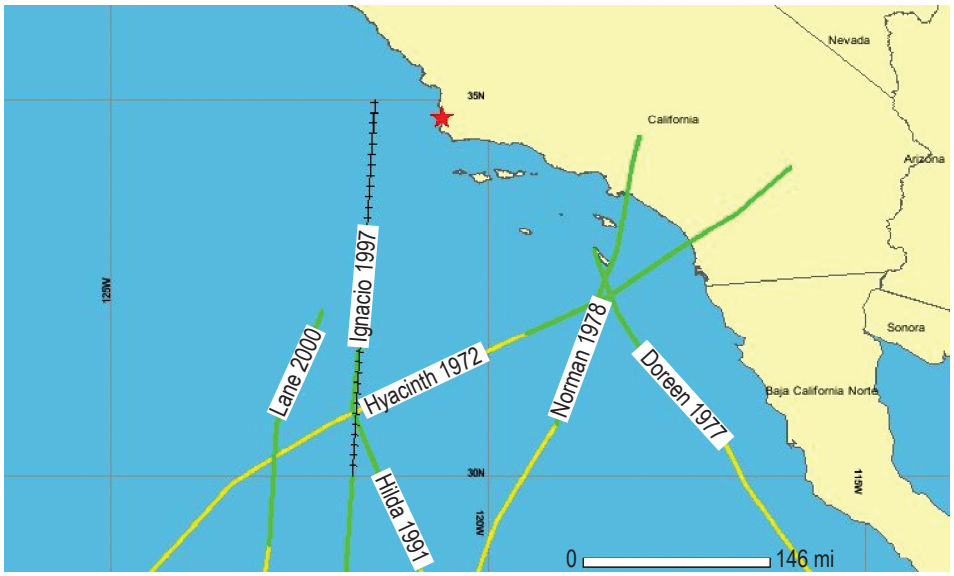

Figure 12-33. Six tropical cyclone tracks within 370 km (200 nmi) of VAFB, CA (ref. 12-95).

12.6.9 Tropical Cyclones Near NASA Installations

Table 12-14 gives the total annual number of tropical cyclones (tropical storms and hurricanes) that have passed within 93 km (50 nmi) of the eastern U.S. NASA Centers influenced by Atlantic and Gulf coast tropical storms. Table 12-14 also presents the number of Pacific-generated storms (extratropical, tropical depressions, and tropical storms) that have come within 370 km (200 nmi) of NASA-associated west coast installations.

12.6.9.1 Tropical Cyclone Frequency Near Kennedy Space Center, FL. Illustrated in figure 12-34 are the tracks of the 43 tropical cyclones (26 tropical storms and 17 hurricanes) that passed within 93 km (50 nmi) of KSC's pad 39A. These 156-yr (1851–2006) tropical cyclone statistics were obtained from the NOAA Coastal Service Center's Historical Hurricane Tracks Program (ref. 12-95).

Table 12-16 presents the total number of hurricanes and total number of tropical storms that historically have passed within 185 km (100 nmi) and 370 km (200 nmi) of KSC launch complex pad 39A over the last 156 yr (ref. 12-95). The data are presented by month and by storm intensity. The most active tropical cyclone months for KSC have been from August through October, which compose more than three-fourths of all hurricane categories listed in table 12-16. Tropical cyclones have been experienced near KSC as early as May and as late as December.

Although a hurricane's path may come within a radius of 185 km (100 nmi), the wind speeds observed at KSC are not always of hurricane speed. Hurricanes at distances >185 km (>100 nmi) from KSC can produce hurricane-force winds at KSC. The highest recorded KSC hurricane-associated wind gust speed was 45.5 m/s (88.4 kt or 101.7 mph) measured on top (96 m (315 ft)) of the LC34 service structure during Hurricane Dora on September 9, 1964. A simultaneous measurement of 42.4 m/s (94.8 mph) from the 21-m (69-ft) level, blockhouse location, was also recorded (ref. 12-101). See table 12-17.

Hurricanes downgraded to tropical storms, have also produced strong peak winds in the KSC area; i.e., peak speeds of 38.8 m/s (86.8 mph) at 150 m (492 ft) and 34.2 m/s (76.5 mph) at 18 m (59 ft) were recorded from downgraded Hurricane Abby in June 1968. In general, hurricanes approaching KSC from the east (from the sea)

Table 12-14. Number of tropical cyclone (tropical storm and hurricane) tracks within 93 km* (50 nmi*) or 370 km* (200 nmi*) of various NASA installations over 156 yr (1851–2006) (ref. 12-95).

NASA Locations (93-km (50-nmi) Radius)	Total No. of TSs	Hurricane Intensity					Total No. of Hurricanes	Total No. of TCs	Storm POR**
		No. of H1	No. of H2	No. of H3	No. of H4	No. of H5			
Langley, VA	30	4	1	1	0	0	6	36	1854–2004
Wallops, VA	28	3	2	1	0	0	6	34	1854–2004
Goddard, MD	10	0	1	0	0	0	1	11	1876–1955
Headquarters, DC	10	1	1	0	0	0	2	12	1876–1955
Glenn, OH	0	0	0	0	0	0	0	0	–
Kennedy, FL	26	10	4	3	0	0	17	43	1852–2006
Stennis, MS	24	9	3	5	1	1	19	43	1855–2005
Michoud, LA	22	10	4	3	2	1	20	42	1855–2005
Slidell, LA	25	9	3	4	1	1	18	43	1855–2005
Marshall, AL	8	0	0	0	0	0	0	8	1879–1995
Johnson, TX	19	12	2	2	4	0	20	39	1854–2003

NASA Locations (370-km (200-nmi) Radius)	Total No. of E***	Total No. of TDs	Total No. of TSs	Total No. H (1–5)		Total No. of Hurricanes	Total No. of TSs	Storm POR**
Ames, CA	1	1	0	0		0	2	1965–1997
JPL, CA	0	4	3	0		0	7	1959–1978
Dryden, CA	0	4	2	0		0	6	1963–1997
Holloman AFB, NM	1	4	1	0		0	6	1970–1992
VAFB, CA	1	4	1	0		0	6	1972–2000

*Eastern and Central U.S. NASA sites use 93-km (50-nmi) radius from site, while Western U.S. NASA sites use 370-km (200-nmi) radius from sites.
**The time range at site in which the storms have occurred over.
***E=extratropical type storm
Note: Holloman AFB also includes WSMR, NM, and NASA Dryden also includes EAFB, CA.

Table 12-15. Central Pacific tropical cyclone statistics (ref. 12-100).

Item	No. of Hurricanes	No. of Tropical Storms	No. of Tropical Depressions	Total No. of Tropical Cyclones
Total No. of storms	48	57	48	153
TC yearly average	1.4	1.6	1.4	4.4
Percent of all systems	31	36	33	100

will produce higher winds than those approaching KSC after crossing the peninsula of Florida (from the land). Hurricane David, September 1979, was the first hurricane to strike the Cape Canaveral area directly since 1926. The eastern edge of the eye passed within an estimated 2.4 km (1.5 mi) of the Space Shuttle runway. Hurricane David's peak wind speed of 34.5 m/s (77.2 mph) (measured at 10.4 m (34.1 ft)) exceeded the design launch peak wind speed profile of the Space Shuttle natural environment requirements for a 5-percent risk of exceeding a 10-m-level (33-ft-level) peak wind speed of 15.8 m/s (35.3 mph) for the windiest 1-hr exposure period (ref. 12-103).

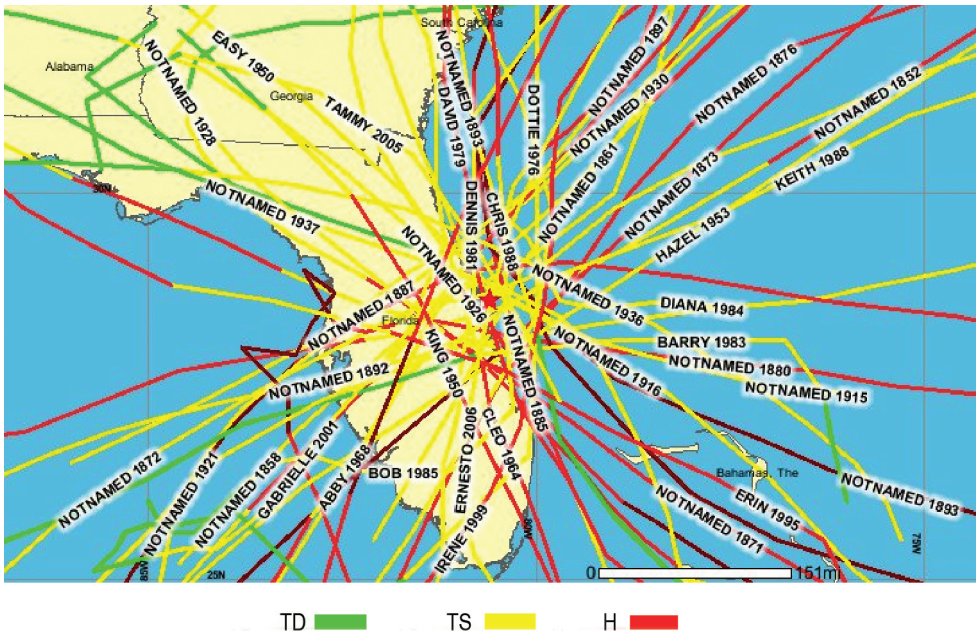

Figure 12-34. The 43 tropical cyclone tracks within 93 km (50 nmi) of KSC pad 39A between 1851 and 2006 (ref. 12-95).

Nonhurricane-associated peak winds at KSC have reached peak speeds equal to or even higher than those produced by hurricanes, as indicated in table 12-17.

As a typical example of what the horizontal hurricane wind field can look like coming into eastern Florida, the maximum surface winds of Hurricane Jeanne at landfall are graphically presented in the wind swath map shown in figure 12-35. Hurricane Jeanne arrived in Florida following a track from 101° and initially proceeded along that same direction across Florida. These data were prepared and provided by the Hurricane Research Division (HRD) at the Atlantic Oceanographic and Meteorological Laboratory of the NOAA (ref. 12-104).

12.6.9.2 Kennedy Space Center Hurricane Peak Winds. Table 12-17 presents some selected tropical cyclone wind and rain measurements that have impacted various KSC operations. The strongest measured hurricane wind speed in the KSC area was 45.5 m/s (101.7 mph) at the 96-m (315-ft) level AGL, on the LC34 service structure during passage of Hurricane Dora on September 9, 1964, with 42.4-m/s (94.8-mph) winds measured at the LC34 blockhouse at the 21-m (69-ft) level. Hurricane Frances, in September 2004, produced sustained winds at KSC >31 m/s (>70 mph) for 30 consecutive hours, and >22 m/s (>50 mph) for 36 hr. The greatest hurricane-produced total rainfall at KSC in recent years has been 34.5 cm (13.6 in) from Hurricane Wilma during October 2005. Hurricane King, in October 1950, produced 39.1 cm (15.4 in) of total rainfall at nearby Patrick AFB. For 45 days during 2004 (August 13–September 26), four hurricanes hit Florida in rapid succession. Three of those hurricanes hindered launch preparations.

Table 12-18 presents wind and rain measurements near NASA Gulf coast facilities (Stennis, Michoud, and Slidell) during the 2005 hurricane season, with Hurricane Katrina causing the most damage to these NASA sites (ref. 12-105).

Table 12-16. Number of hurricanes and tropical storms in a 156-yr period (1851–2006) within a 185-km (100-nmi)* and 370-km (200-nmi)* radius of KSC launch complex (LC) 39A* (ref. 12-95).

Month	Radius of KSC LC39A (km)	Radius of KSC LC39A (nmi)	Hurricane Intensity Category H1	H2	H3	H4	H5	Total No. of Hurricanes	Total No. of Tropical Storms
January	185	100	–	–	–	–	–	–	–
	(370)	(200)	(–)	(–)	(–)	(–)	(–)	(–)	(–)
February	185	100	–	–	–	–	–	–	–
	(370)	(200)	(–)	(–)	(–)	(–)	(–)	(–)	(–)
March	185	100	–	–	–	–	–	–	–
	(370)	(200)	(–)	(–)	(–)	(–)	(–)	(–)	(–)
April	185	100	–	–	–	–	–	–	–
	(370)	(200)	(–)	(–)	(–)	(–)	(–)	(–)	(–)
May	185	100	–	–	–	–	–	–	**2**
	(370)	(200)	(**2**)	(–)	(–)	(–)	(–)	(**2**)	**(3)**
June	185	100	**1**	–	–	–	–	**1**	**5**
	(370)	(200)	(**2**)	(**1**)	(**1**)	(–)	(–)	(**4**)	**(13)**
July	185	100	**1**	**1**	–	–	–	**2**	**8**
	(370)	(200)	(**6**)	(**1**)	(**1**)	(–)	(–)	(**8**)	**(12)**
August	185	100	**3**	**5**	**3**	**2**	–	**13**	**19**
	(370)	(200)	(**7**)	(**9**)	(**6**)	(**4**)	(–)	(**26**)	**(32)**
September	185	100	**3**	**4**	**5**	**2**	–	**14**	**24**
	(370)	(200)	(**10**)	(**6**)	(**8**)	(**8**)	(**2**)	(**34**)	**(50)**
October	185	100	**9**	**5**	**2**	**1**	–	**17**	**23**
	(370)	(200)	(**12**)	(**10**)	(**12**)	(**4**)	(–)	(**38**)	**(51)**
November	185	100	–	–	–	–	–	–	**4**
	(370)	(200)	(**3**)	(–)	(–)	(–)	(–)	(**3**)	**(7)**
December	185	100	**1**	–	–	–	–	**1**	**1**
	(370)	(200)	(–)	(**1**)	(–)	(–)	(–)	(**1**)	**(1)**
Annual	185	100	**18**	**15**	**10**	**5**	**0**	**48**	**86**
	(370)	(200)	(**42**)	(**28**)	(**28**)	(**16**)	(**2**)	(**116**)	**(170)**

*Top value in table pertains to 185-km (100-nmi) distance and bracketed value below pertains to 370-km (200-nmi) distance.

Note: There are occurrences of the lower hurricane intensities (or even tropical storm intensity) within the specified distance from KSC not indicated in this hurricane table, as the highest hurricane intensity (for the hurricane in question) was used to compile this table. Likewise, the tropical storm numbers may have included hurricane intensities somewhere else on their track within the specified distance from KSC; i.e., one storm track may include both a tropical storm track and a hurricane track, both within that specified distance from KSC.

12.6.9.3 Kennedy Space Center Nonhurricane Peak Winds. Table 12-19 presents selected peak winds measured at KSC during nonhurricane time periods. These peak winds can be caused by severe thunderstorms, squall lines, microbursts, etc. One of the strongest peak winds recorded was 46.3 m/s (103.6 mph) measured on the 9.1-m (30-ft) tower at KSC wind tower No. 512 on August 11, 1996. A microburst caused this wind gust. See subsection 12.5.5.2 for a further discussion of KSC microbursts.

Table 12-17. Selected Florida tropical cyclone/hurricane wind and rain measurements that impacted KSC operations (refs. 12-101 and 12-102).

Hurricane	Date	Sustained Wind Speed[a]		Peak Wind Speed[a]		Wind Speed Comments[a]	KSC Damage/Impact
		(m/s)	(mph)	(m/s)	(mph)		
Unnamed	Oct. 3–5, 1948	–	–	–	–	Hurricane winds at Cape[b]	–
King	Oct. 18, 1950	–	–	–	–	–	Patrick rain=39.1 cm (15.4 in)
Cleo[c]	Aug. 27, 1964	–	–	34.9	78	At 30 m (98 ft) LC37 S.S.	($360,000 from
Dora[c]	Sept. 9, 1964	–	–	42.5/45.5	95/101.7[d]	At BH 21 m (69 ft)/LC34 315 ft	both Cleo and Dora)
Alma	June 9, 1966	–	–	40.7	91	At 90 m (295-ft) tower No. 313	Caused rollback[e]
Abby	June 5, 1968	–	–	34.4/38.9	77/87	At 18.3-m (60-ft)/150-m (492-ft) tower No. 313	
Gladys	Oct. 19, 1968	–	–	29.1	65	At 90-m (295-ft) tower No. 313	Rainfall=31.8 cm (12.5 in)
Jane	Nov. 11, 1968	–	–	27.7	62	At 150-m (492-ft) tower No. 313	–
Jenny	Oct. 3, 1969	–	–	27.3	61	At 120-m (394-ft) tower No. 313	–
Tropical depression	Aug. 6, 1970	–	–	–	–	–	Moved into KSC
Agnes	June 19, 1972	–	–	30.4/32.6	68/73	At 39A 18.3 m (60 ft)/150 m (492 ft) No. 313	–
David[f]	Sept. 3–4, 1979	–	–	34.4	77	At 0.9-m (3-ft) level	$100,000 damage
T.S. Klaus	Oct. 9–10, 1990	–	–	–	–	–	Caused rollback
Erin	Aug. 2, 1995	–	–	37.1	83	At USAF wind tower	Caused rollback[g]
Bertha	July 11, 1996	–	–	–	–	–	Caused rollback
Fran	Sept. 5, 1996	–	–	–	–	–	Caused rollback
Floyd[h]	Sept. 15, 1999	29.5	66	40.7	91	At 9.1-m (30-ft) SLF tower	Some damage
Irene	Oct. 16, 1999	30.8	69	37.1	83	At 9.1-m (30-ft) SLF tower	Some damage[i]
Charley	Aug. 13, 2004	–/28.6	–/64[j]	38.9/38.4	87/86	At SLF/16.5-m (54-ft) tower No. 421	$700,000 damage
Frances[k]	Sept. 5, 2004	31.3	70[l]	42.0	94	At 9.1-m (30-ft) SLF tower	$100,000,000 damage
Ivan[m]	Sept. 16, 2004		–	–	–	–	Little damage[m]
Jeanne[n]	Sept. 26, 2004	24.1	54[o]	28.6	64	At surface	Some damage
Jeanne		30.4	68	41.6	93	At 150-m (492-ft) tower No. 313	–
Jeanne		36.7	82	41.6	93	At 160-m (525-ft) VAB level[p]	–
Jeanne		25.9	58	37.1	83	At 16.5-m (54-ft) tower No. 1007	–
Ophelia	Sept. 8, 2005	9.8/17.4	22/39	19.7/26.8	44/60	At SLF/tower No. 394	SLF rain= cm (2.8 in)
Wilma	Oct. 24, 2005	–/28.6	–/64	34.0/42.0	76/94	At SLF/39B 18.3-m (60-ft) tower	Minor damage[q]
TD Ernesto[r]	Aug. 30, 2006	–/–	–/–	19.7/25.0	44/56	At 39B 18.3-m (60-ft)/(150-m (492-ft) tower No. 313	Partial rollback

[a] The listed wind speeds were measured at or near the NASA KSC/Cape Canaveral area. Highest 2-min-averaged sustained winds and peak wind gust (most listed are probably 3-s average gust) are also included. The SLF has three 9.1-m (30-ft) wind towers.

[b] Reference 12-101.

[c] Cleo & Dora: Induced damage to LC39A, KSC Headquarters, and Hanger AFB. Delayed Gemini-Titan II launch.

[d] Reference 12-68.

[e] Alma: Caused the Saturn V 500-F dummy vehicle to be rolled back from pad 39A on June 8, 1966, due to the its influence. Sheets of rain and 27-m/s (60-mph) wind gusts hampered its journey back to the VAB.

[f] David: Produced tornado near VAB causing roof damage. Also water damage. David (cat. 2) moved inland 32 km (20 mi) south of Melbourne with 40-m/s (90-mph) winds and traveled north along the Indian River Lagoon to exit at New Smyrna Beach. It was the first hurricane to strike the Cape Canaveral area since the hurricane of 1926 (ref. 12-68). David spawned over 10 tornadoes while passing over the state, though causing no deaths or injuries.

[g] Erin: Produced some KSC damage. Total rainfall at Melbourne AP=27.4 cm (10.8 in). NASA Wallops Island rocket launch delayed 3 days due to Hurricane Erin.

[h] Floyd: Passed 195 km (121 mi) east of KSC and caused minor KSC damage, including VAB siding panels and pad 39B damage. Buoy 204 km (110 nmi) east-northeast of Cape Canaveral broke loose from its mooring in waves >15 m (>50 ft), with 36-m/s (80-mph) sustained winds and gusts >45 m/s (100 mph).

[i] Irene: Produced damage to buildings of light construction. VAB had minor damage with some siding panels blown off. Total rainfall=16.5 cm (6.5 in).
[j] Charley: Produced sustained winds at KSC >40 kt (>46 mph) for 5 hr. Total rainfall=6.6 cm (2.6 in).
[k] Frances: Removed 820 large siding panels from VAB south wall. Extensive damage. KSC closed for 11 days. Total rainfall=20.3 cm (8 in).
[l] Frances: Produced sustained winds at KSC >31 m/s (>70 mph) for 30 hr and >22 m/s (>50 mph) for 36 hr.
[m] Ivan: Did not affect KSC, as hurricane Ivan made Gulf landfall near the Alabama-Florida border with little or no damage at NASA Stennis, MS, and NASA Michoud, LA. Ivan also generated the largest ever-measured significant wave height (SWH) in the Gulf of Mexico by a buoy. Buoy No. 42040 recorded a SWH of 15.96 m (52.4 ft), which translates (a 1.8 factor) into a maximum wave height of ≈29 m (≈95 ft). Only two other U.S. buoy measurements exceed this value, with a 16.9-m (55.4-ft) SWH recorded in the south Gulf of Alaska during 1991 (ref. 12-103).
[n] Jeanne: Removed 25–30 more siding panels from VAB east wall. Jeanne's eye entered 98 km (61 mi) south of KSC. Total rainfall=7.6 cm (3 in).
[o] Jeanne: Produced sustained winds at KSC >22 m/s (>50 mph) for 21 hr.
[p] Jeanne: Measured atop VAB.
[q] Wilma: Produced sustained winds at KSC's pad 39B >18 m/s (>40 mph for over 9 hr, and >26 m/s (>58 mph) for over 5 hr. Also a tornado touched down briefly near the south entrance to KSC on north Merritt Island. Wilma slightly damaged a 61-m- (200-ft-) tall Atlas 5 rocket when the reinforced fabric door to the Vehicle Integration Facility at CC Complex 41 failed, causing minor damage to the rocket and GSE. Total rainfall=34.5 cm (13.6 in). Wilma also became the most intense Atlantic hurricane on record, in terms of barometric pressure, by registering a minimum central pressure of 26.05 inHg (882 mb).
[r] Ernesto: Postponed Atlantis launch. No damage to Shuttle Atlantis at pad 39B nor to Delta II at pad 17-B. Total rainfall=10.7 cm (4.2 in). Ernesto was downgraded to a tropical storm at landfall and tropical depression as it passed through Florida. Partial rollback occurred prior to Ernesto arrival. Ernesto emerged into the Atlantic Ocean near Cape Canaveral on August 31. Prior to the KSC arrival of Ernesto, pad 39B was also hit by one of the most powerful lightning bolts on record at KSC ≈100 kA on August 25, causing a launch delay.

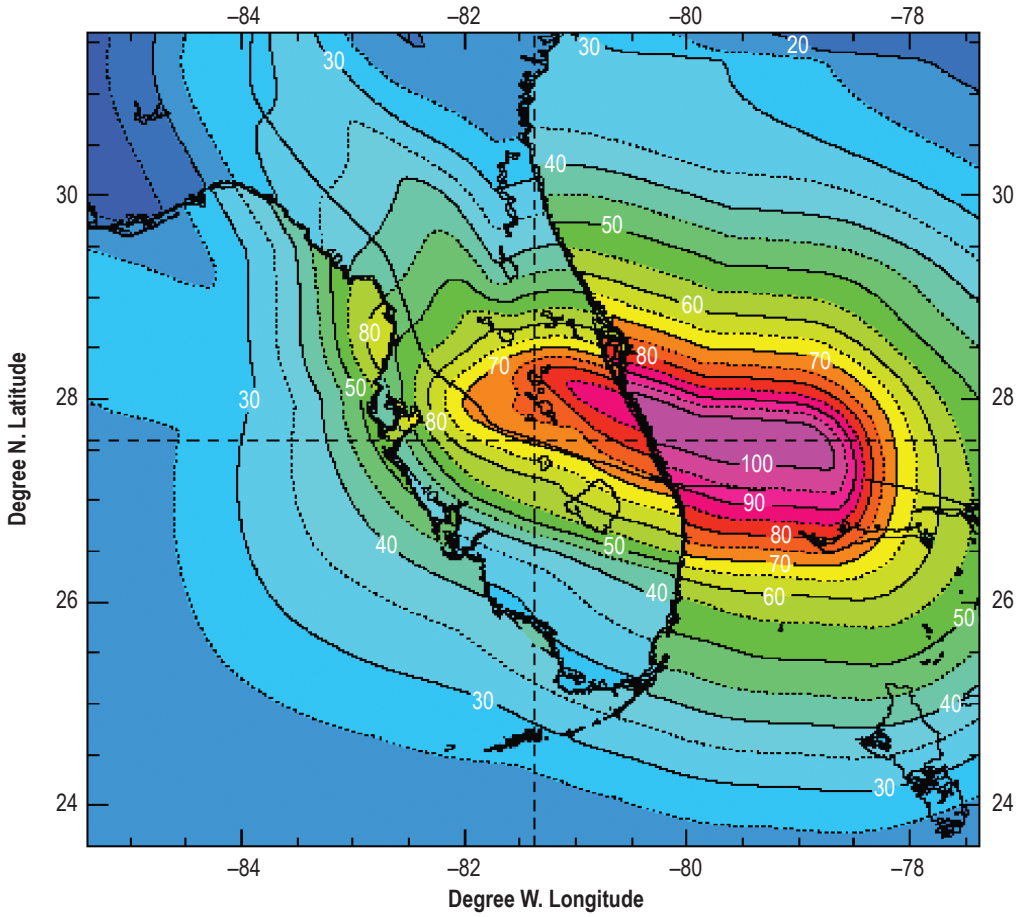

Figure 12-35. Hurricane Jeanne maximum surface wind field at landfall (in mph; 1 mph=0.45 m/s) (ref. 12-104).

Table 12-18. Weather statistics for the three major 2005 hurricanes that impacted the Gulf of Mexico region—Mississippi, Louisiana, and Texas (ref. 12-105).

Hurricane	Date	Sustained Wind Speed		Peak Wind Speed		Wind Speed Comments	NASA Damage/Impact
		(m/s)	(mph)	(m/s)	(mph)		
Cindy	July 6	–	–	–	–	At Stennis International Airport	Total rainfall =17.9 cm (7.05 in)
Katrina	Aug. 29	30.4	68	52.3	117	At 9.1-m (30-ft) tower, Stennis Airport	$600M SSC damage
Katrina	Aug. 29	31.3	70	44.7	100	At 9.1-m (30-ft) tower, Slidell Airport	Total rainfall =29.5 cm (11.6 in)
Katrina	Aug. 29	–	–	≈55	≈123	At gauge 2, Michoud	$500M MAF damage
Rita	Sept. 23	15.6	35	19.7	44	At Slidell, LA	–
Rita	Sept. 24	26.4	59	33.1	74	At Galveston Bay, TX	Minor JSC damage

At least four high-wind events took place over a span of 35 days while the STS-122 Shuttle vehicle was exposed on pad 39A. STS-122 had been on the pad 75 days since its rollout. These events occurred on December 21, 2007, and January 17, 20, and 25, 2008. The January 20 case had a maximum peak wind of 24.3 m/s (54 mph), with an associated 17.1 m/s (38 mph), 2-min moving average value. This high wind event duration lasted ≈2½ hr. However, the wind limit for the aft skirts is 20.6 m/s (46 mph), so there was no concern for the STS-122 solid rocket booster hardware. Between January 2000 and January 2008, there have been 23 pad-recorded high wind events for the 14 Shuttle missions with the orbiter on the pad. High wind events can occur regularly at KSC during any season.

12.6.9.4 Port Canaveral Hurricane Statistics. The Hurricane Havens Handbook (ref. 12-109) gives various tropical cyclone statistics and facts for the Port Canaveral, FL, site using the 112-yr hurricane POR (1886–1997). Figure 12-36 presents the various directions in which the 168 historical tropical storms and hurricanes passed within 333 km (180 nmi) of Port Canaveral at the closest point of approach (CPA). Note that 155 (92.3 percent) arrived from the four octants, southwest through south, southeast and into east, with the majority (37.5 percent) arriving into the southwest quadrant. Only 13 (7.7 percent) arrive from the four octants west though northwest, north into the northeast. Table 12-20 also presents this information, but by month, along with number of storm types and storm speed, mean values, etc. The average occurrence date for tropical cyclone arrival at Port Canaveral is September 6, while the median occurrence date is September 13. Figure 12-37 gives the probability (in percent) that a tropical storm or hurricane will pass within 333 km (180 nmi) of Port Canaveral (circle), and the approximate time (in days) to closest CPA during the peak tropical cyclone month of September (ref. 12-109). Various other Port Canaveral, Cape Kennedy, and Brevard County hurricane statistics are presented in reference 12-110.

12.6.9.5 Distribution of Kennedy Space Center Hurricane and Tropical Storm Frequencies. Knowing the mean number of tropical storms or hurricanes (events) per year that come within a given radius of KSC, without knowing other information, is of little use. Assuming the distribution of the number of tropical storms or hurricanes is a Poisson-type distribution, the mean number of events per year (or any reference period) can be used to completely define the Poisson distribution function as demonstrated below.

From figure 12-38, the probability of no event, $P(E_0,r)$, where r = radius, for the following can be read: (1) Tropical storms and hurricanes for annual reference periods, (2) tropical storms and hurricanes for July–August–September; and (3) tropical storms and hurricanes for July–August–September–October, versus radius (in kilometers) from KSC. To obtain the probability for one or more events, $P(E_1,r)$ from figure 12-38 the reader is required to subtract the $P(E_0,r)$, read from the abscissa, from unity; i.e., $[1-P(E_0,r)]=P(E_1,r)$. For example, the probability that no hurricane path (eye) will come within 556 km (300 nmi) of KSC in a year is 0.33

Table 12-19. Selected nonhurricane-induced peak wind cases measured at KSC (refs. 12-101, 12-106 through 12-108).

Cause*	Date	Peak Wind Speed (m/s)	Peak Wind Speed (mph)	Measurement Location**	KSC Damage/ Impact
Unknown	Jan. 22, 1966	26/33	58/73	At 18.3-m (60-ft) pad 39/150 m (492-ft) No. 313***	Unknown
Unknown	April 4, 1966	28.6	64	At 150-m (492-ft) tower No. 313***	Unknown
Unknown	Feb. 13, 1967	29.5	66	At 150-m (492-ft) tower No. 313	Unknown
Unknown	Feb. 29, 1968	27.3	61	At 150-m (492-ft) tower No. 313	Unknown
Unknown	Feb. 15, 1969	30.8	69	At 150-m (492-ft) tower No. 313	Unknown
Unknown	Feb. 3, 1970	30.4	68	At 150-m (492-ft) tower No. 313	Unknown
Unknown	March 5, 1970	29.1	65	At 150-m (492-ft) tower No. 313	Unknown
Microburst	Aug. 16, 1994	33.5	75†	At 9.1-m (30-ft) SLF tower‡	Unknown
Microburst	July 10, 1995	32.2	72	At 16.5-m (54-ft) tower No. 1007	Unknown
Microburst	Aug. 2 ,1995	27.7	62	At 49.4-m (162-ft) tower No. 1101	Unknown
Microburst	Aug. 24, 1995	28.2	63	At 16.5-m (54-ft) tower No. 19	Unknown
Microburst	May 31, 1996	27.3	61	At 62.2-m (204-ft) tower No. 61	Unknown
Microburst	Aug. 11, 1996	46.0	103	At 9.1-m (30-ft) tower No. 512	Unknown
Microburst	Aug. 15, 1996	46.0	103	At 9.1-m (30-ft) tower No. 513	Unknown
Microburst	March 29, 1997	30.0	67	At 9.1-m (30-ft) SLF tower	Unknown
Microburst	May 3, 1997	33.1	74	At 16.5-m (54-ft) tower No. 421	Unknown
Microburst	June 1, 1997	28.2	63	At 16.5-m (54-ft) tower No. 509	Unknown
Microburst	May 5, 1998	27.3	61	At 16.5-m (54-ft) tower No. 1007	Unknown
Microburst	July 6, 1998	28.2	63	At 16.5-m (54-ft) tower No. 1612	Unknown
Microburst	July 28, 1998	29.5	66	At 49.4-m (162-ft) tower No. 1101	Unknown
Thunderstorm	May 8, 1999	22.8	51	At 9.1-m (30-ft) SLF tower	Hail ET and orbiter/rollback
Unknown	Sept. 24, 2001	31.7	71	At 9.1-m (30-ft) SLF tower	Unknown
Unknown	March 17, 2003	30.0	67	At 9.1-m (30-ft) SLF tower	Unknown
Unknown	April 7, 2005	29.1	65	At 18.3-m (60-ft) pad tower	Unknown
Unknown	Sept. 19, 2006	28.2	63	At 9.1-m (30-ft) SLF tower	Unknown
Thunderstorm	Feb. 26, 2007	31.7	71	At pad 39A	Hail ET/rollback
Unknown	July 13, 2007	33.1	74	At 9.1-m (30-ft) SLF tower	Unknown

*Unknown causes are probably due to thunderstorm activity, although it was not indicated as that.
**KSC/SLF period of record: July 1995–December 2007. KSC tower No. 313 period of record: December 1, 1965–March 31, 1970. KSC/CCAS tower array period of record: May 1995–September 1998.
***Reference 12-101.
†Reference 12-106.
‡Reference 12-107.

[$P(E_0,r=300)=0.33$], and the probability that there will be one or more hurricanes within 556 km (300 nmi) of KSC in a year is 0.67 (1–0.33 = 0.67).

12.6.10 Nor'easters—A Major Severe Wind-Weather Mesoscale Storm System

Geer (ref. 12-51)—Northeaster (or nor'easter): A northeast wind (from a northeast direction), particularly a strong wind or gale; a northeast storm over the east coast of North America.

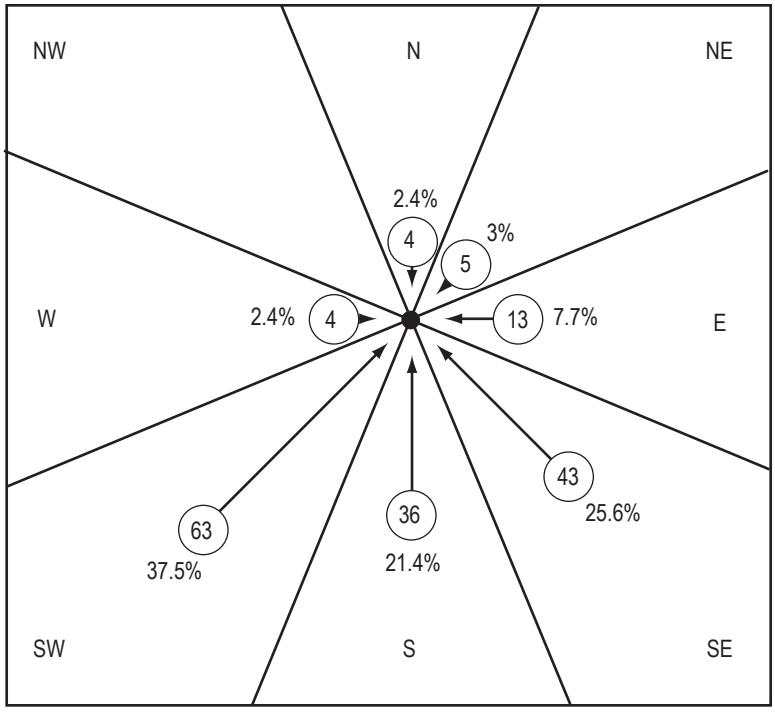

Figure 12-36. Direction of approach for all 168 tropical storms and hurricanes passing within 333 km (180 nmi) of Port Canaveral during the 112-yr period (1886–1997). The length of each arrow is proportional to the number of storms from that direction (ref. 12-109).

Table 12-20. Frequency and motion of the 168 tropical storms and hurricanes passing within 333 km (180 nmi) of Port Canaveral during the 112-yr period (1886–1997) (ref. 12-109).

Port Canaveral, Florida Tropical Cyclone Category	Month													Mean Occurrence Per Year	Mean Reoccurrence Interval Year
Month when TC was at CPA*	Jan	Feb	Mar	Apr	May	Jun	Jul	Aug	Sep	Oct	Nov	Dec	Ann	–	–
Total No. of TC passing within 333 km (180 nmi) of Port Canaveral	0	1	0	0	4	14	13	33	44	52	6	1	168	1.50	0.7
Total No. of hurricane intensity storms at CPA	0	0	0	0	1	3	5	13	18	19	1	0	60	0.54	1.9
Total No. of tropical storm intensity storms at CPA	0	1	0	0	3	11	8	20	26	33	5	1	108	0.96	1
Average heading (deg) toward which storms moving at CPA	–	**	–	–	**	030	345	322	359	025	020	**	002	–	–
Average storm speed at CPA (kt) (m/s) (mph)	–	**	–	–	**	17 8.7 19.6	11 5.7 12.7	11 5.7 12.7	12 6.2 13.8	16 8.2 18.4	17 8.7 19.6	**	14 7.2 16.1	–	–

*CPA=Closest point of approach.
**Indicates insufficient storms for average direction and speed computations.

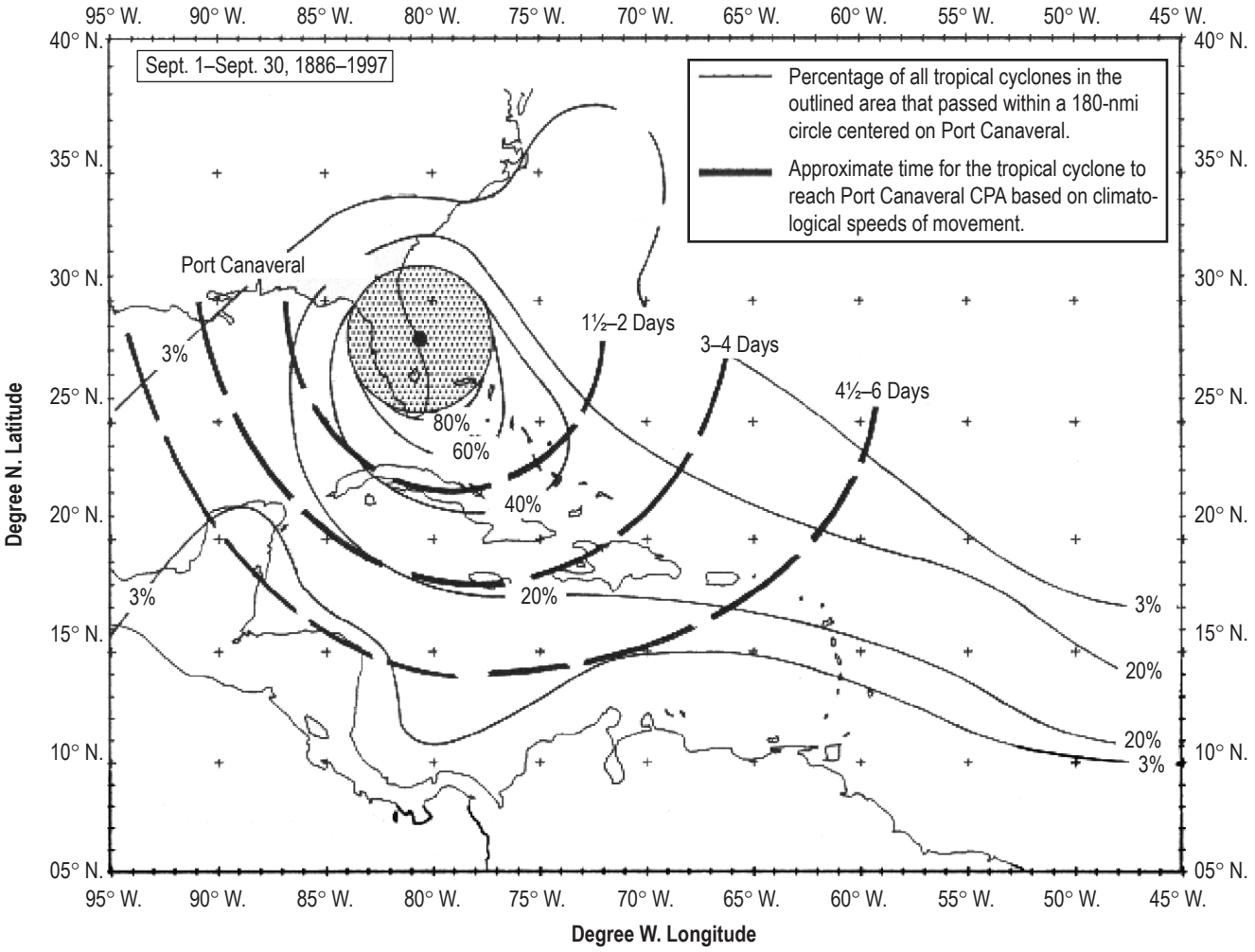

Figure 12-37. Probability that a tropical storm or hurricane will pass within 333 km (180 nmi) of Port Canaveral (circle), and approximate time to CPA during September (ref. 12-109).

Nor'easters are extratropical cyclonic storms that originate outside of the tropics. They are, like hurricanes, centers of low pressure with winds that circulate in a counterclockwise direction around the low pressure. Nor'easters originate in various locations and normally move along the east coast. They are called nor'easters because the cyclonic circulation causes winds to blow out of the northeast as the storms move up the coast. Nor'easters usually have winds less than hurricane strength, but they last several days and can create storm surges up to 7 m (23 ft) high (ref. 12-111).

During a single storm, the precipitation can range from a torrential downpour to a fine mist. Low temperatures and wind gusts up to 40 m/s (90 mph) are also associated with nor'easters. On very rare occasions, such as the North American blizzard of 2006, and a nor'easter in 1979, the center of the storm can even take on the circular shape more typical of a hurricane and have a small eye. The Atlantic coast, from northern Georgia northward up the coast, can suffer high winds, pounding surf, and extremely heavy rains during these storms. Nor'easters cause a significant amount of severe beach erosion in these areas, as well as flooding in the associated low-lying areas (ref. 12-112).

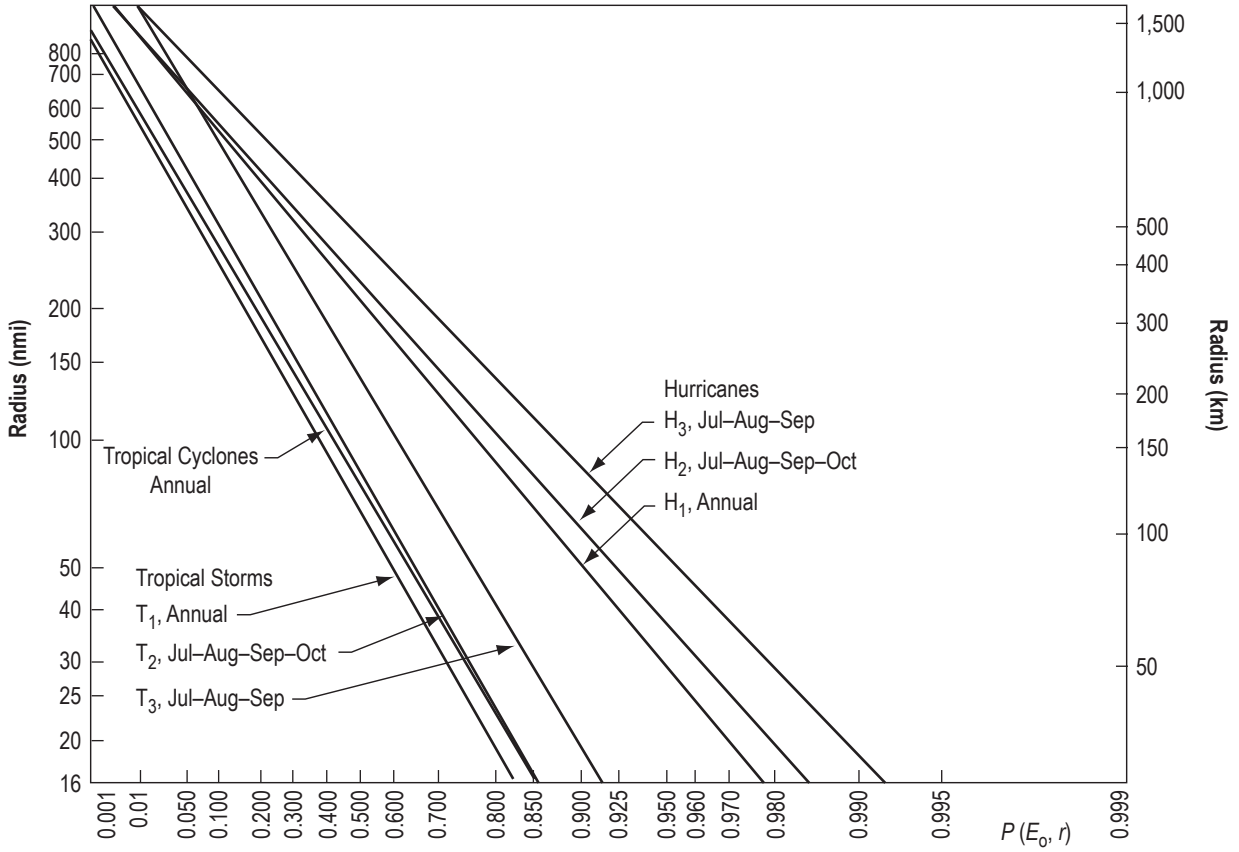

Figure 12-38. Probability of number of tropical storms or hurricanes for various reference periods versus various radii from KSC.

Nor'easters are among winter's most ferocious storms. These strong areas of low pressure often form either in the Gulf of Mexico or off the East Coast in the Atlantic Ocean. The low will then either move up the east coast into New England and the Atlantic provinces of Canada or out to sea (ref. 12-113).

12.7 Severe Weather (Wind, Hail, and Tornadoes)

Severe weather is any destructive weather phenomenon that can "pose a threat to life and property." This section addresses only severe weather related to wind, hail, and tornadoes. These phenomena can hamper various NASA plans, operations, and equipment. Besides hurricanes, squall lines, and severe thunderstorms, which can produce these severe weather events, the actual key individual severe weather parameters that can impact activities or damage equipment addressed here are damaging wind, large hail, and tornadoes. Lightning, hail, and flash flooding can also be damaging, and the reader is guided to those appropriate sections; i.e., lightning (sec. 9.5), hail (secs. 5.1.3.3 and 7.2.7), and flash flooding (sec. 13.2.2.4). Severe weather can also include phenomena such as ice storms (see sec. 7.4.2), blizzards, and heat waves.

This subsection contains some key severe and significant-severe weather occurrence maps for various sites of interest to NASA. The site occurrence maps for these three parameters are given in figures 12-39 and 12-40, and in table 12-21. The maps were taken from the NOAA Web site (ref. 12-114) that includes maps for numerous other locations across the United States. Nine sites included here are, Huntsville, AL (MSFC), Melbourne, FL (KSC), Houston/Galveston, TX (JSC), Vandenberg AFB (VAFB), Edwards AFB (EAFB and DFRC), Holloman

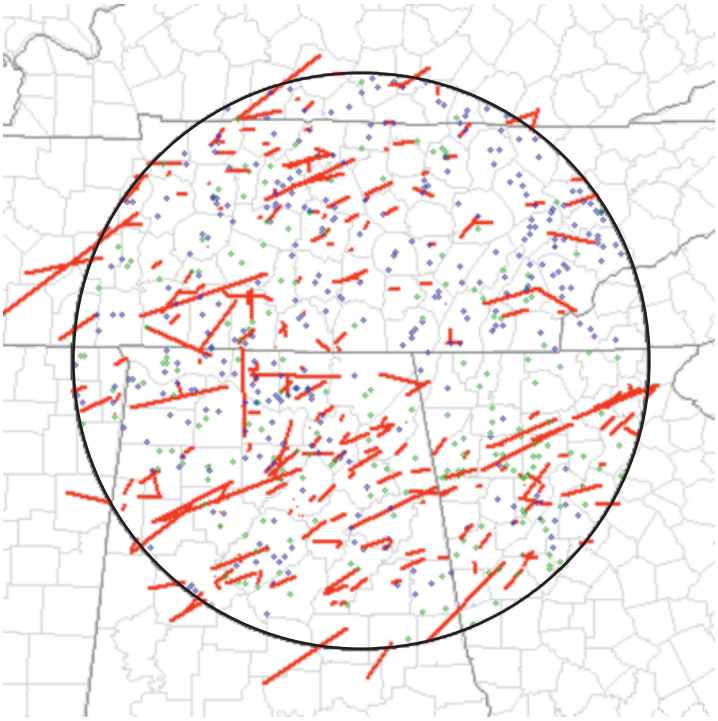

(a) Huntsville, AL (MSFC)

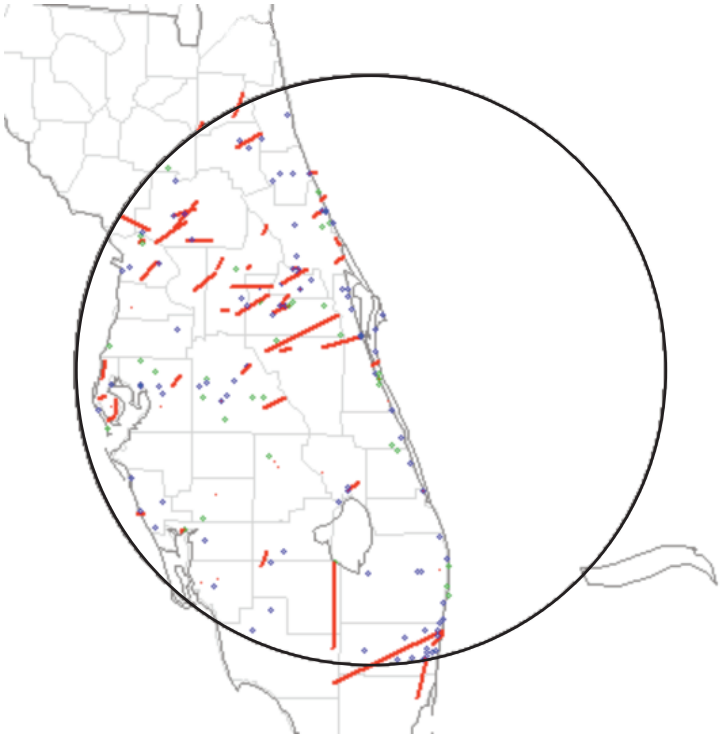

(b) Melbourne, FL (KSC)

Figure 12-39. Locations of significant-severe weather—wind, hail, and tornadoes—occurrences for (a) Huntsville, AL (MSFC),(b) Melbourne, FL (KSC), (c) Houston, TX (JSC), (d) New Orleans (Slidell), LA, (e) Cleveland, OH (GRC), and (f) Wakefield, VA (includes NASA Wallops), using a 124-nmi radius about the location during a 27-yr POR (1980–2006). Severe weather color code: blue—damaging wind, green—large hail, and red—tornadoes (ref. 12-114).

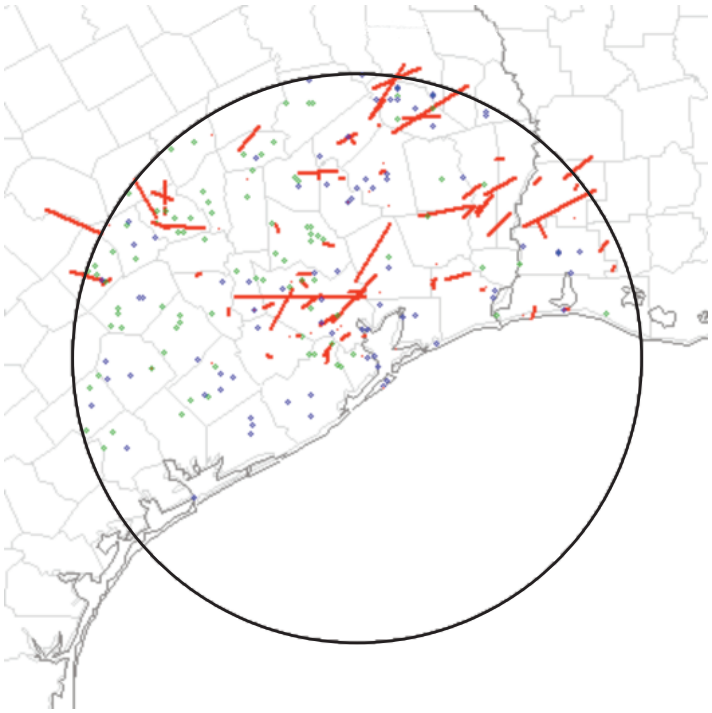

(c) Houston-Galveston, TX (JSC)

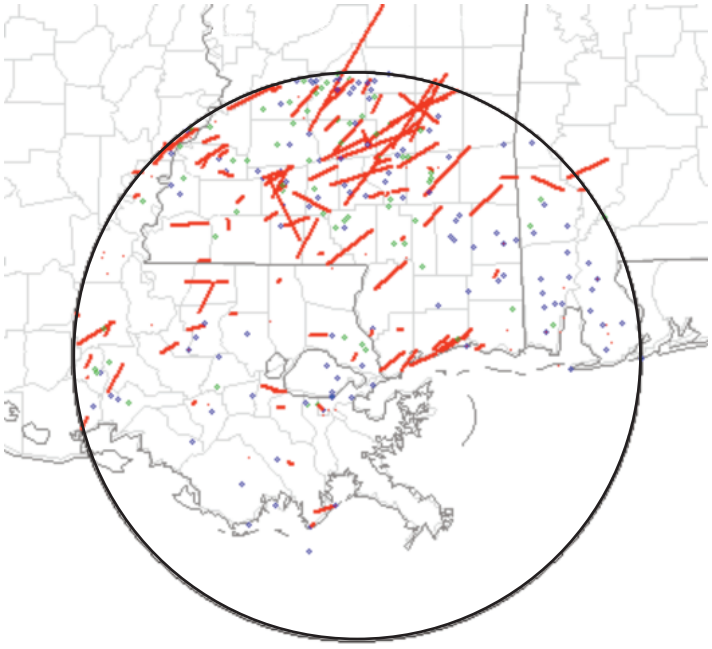

(d) New Orleans (Slidell), LA

Figure 12-39. Locations of significant-severe weather—wind, hail, and tornadoes—occurrences for (a) Huntsville, AL (MSFC),(b) Melbourne, FL (KSC), (c) Houston, TX (JSC), (d) New Orleans (Slidell), LA, (e) Cleveland, OH (GRC), and (f) Wakefield, VA (includes NASA Wallops), using a 124-nmi radius about the location during a 27-yr POR (1980–2006). Severe weather color code: blue—damaging wind, green—large hail, and red—tornadoes (ref. 12-114) (Continued).

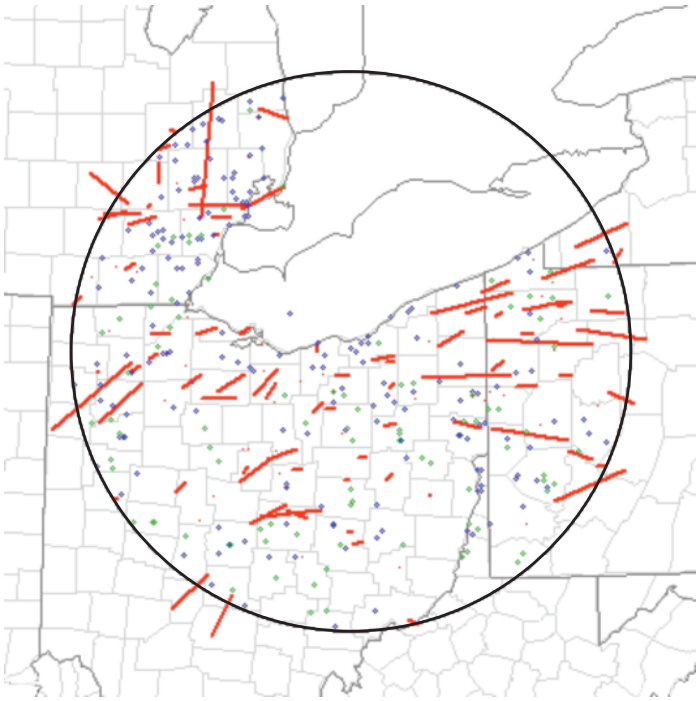

(e) Cleveland OH (GRC)

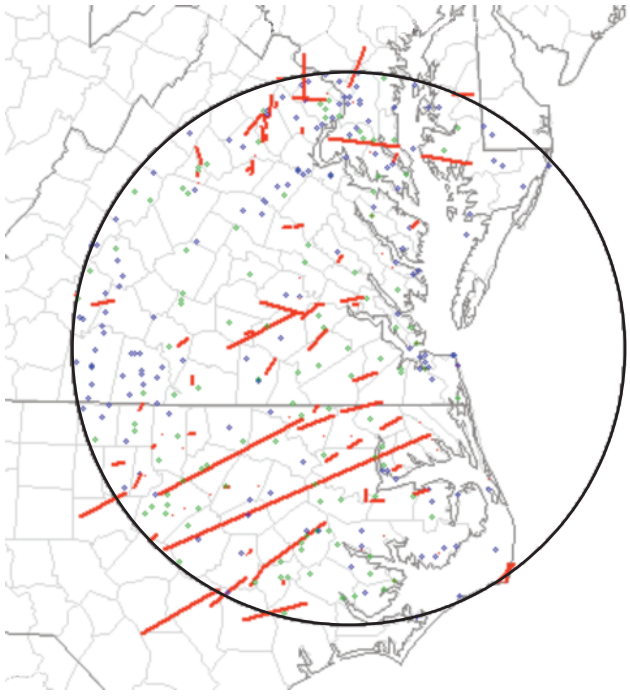

(f) Wakefield, VA (includes NASA Wallops)

Figure 12-39. Locations of significant-severe weather—wind, hail, and tornadoes—occurrences for (a) Huntsville, AL (MSFC),(b) Melbourne, FL (KSC), (c) Houston, TX (JSC), (d) New Orleans (Slidell), LA, (e) Cleveland, OH (GRC), and (f) Wakefield, VA (includes NASA Wallops), using a 124-nmi radius about the location during a 27-yr POR (1980–2006). Severe weather color code: blue—damaging wind, green—large hail, and red—tornadoes (ref. 12-114) (Continued).

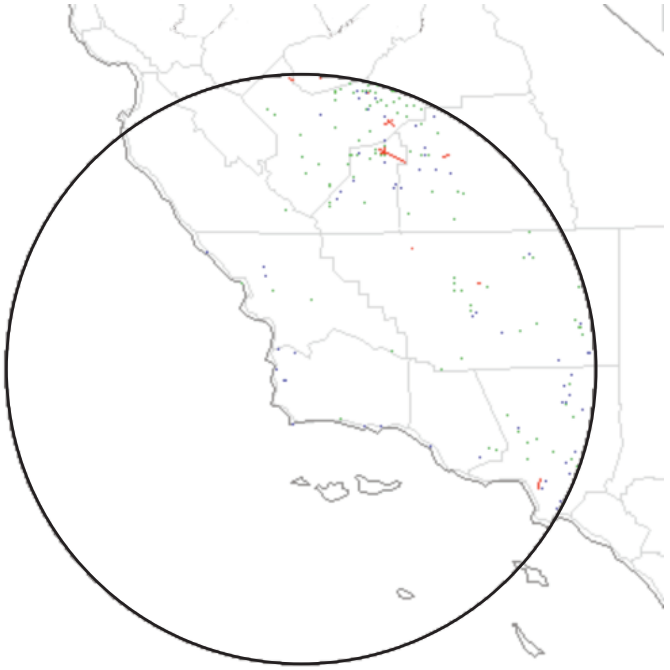

(a) Vandenberg AFB, CA

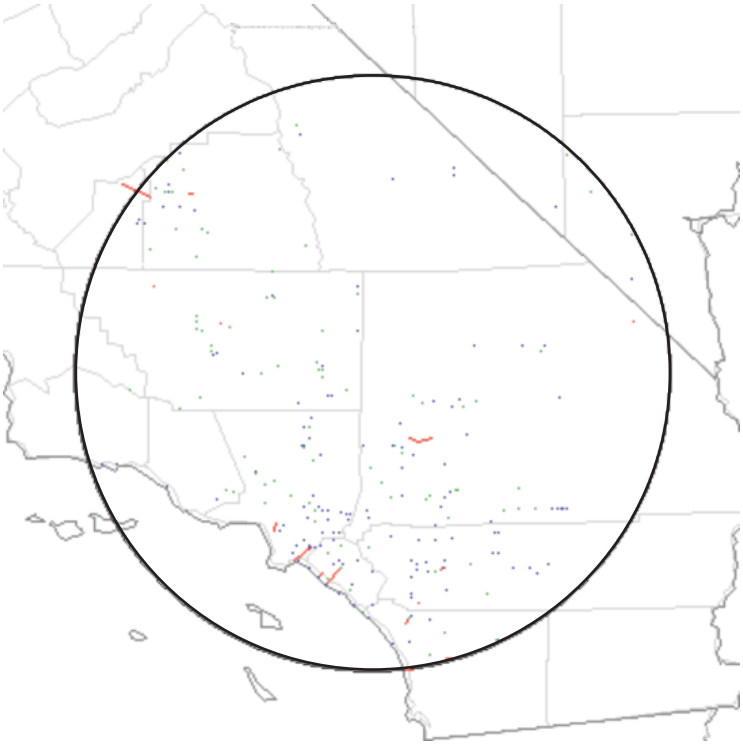

(b) Edwards AFB, CA

Figure 12-40. Locations of severe weather—wind, hail, and tornadoes—occurrences for Vandenberg, Edwards, and Holloman using a 124-nmi radius about the location during a 27-yr POR (1980–2006). Severe weather color code: blue—damaging wind, green—large hail, and red—tornadoes (ref. 12-114).

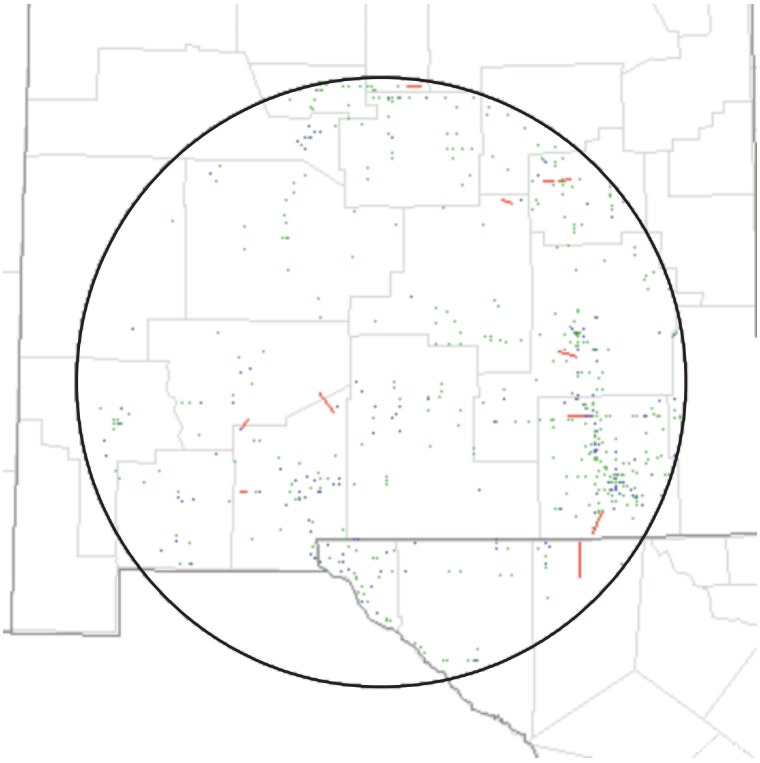

(c) Holloman AFB, NM

Figure 12-40. Locations of severe weather—wind, hail, and tornadoes—occurrences for Vandenberg, Edwards, and Holloman using a 124-nmi radius about the location during a 27-yr POR (1980–2006). Severe weather color code: blue—damaging wind, green—large hail, and red—tornadoes (ref. 12-114) (Continued).

Table 12-21. Occurrences of severe weather (all) and significant-severe (SigSev.) weather for nine NASA sites of interest, using a 124-nmi radius about the location during a 27-yr POR (1980–2006) (ref. 12-114).

Site	Hail All/SigSev.	Wind All/SigSev.	Tornadoes All/SigSev.
Huntsville	6,832/256	11,426/463	954/270
Melbourne	1,874/41	3,015/112	1,107/66
Houston	2,278/103	3,061/108	891/91
New Orleans	2,779/84	5,643/132	912/149
Cleveland	4,386/102	10,926/225	547/126
Wakefield*	3,101/145	6,538/184	694/104
Vandenberg	124/2	77/6	68/3
Edwards**	123/1	193/29	114/5
Holloman	754/61	321/37	118/4

*Includes Wallops.
**Also applies to NASA Dryden.

AFB (WSMR), New Orleans (Slidell), LA, Cleveland, OH (GRC), and Wakefield, VA (WFRC). Generally, the definition of severe weather and significant-severe weather for these three parameters are defined in table 12-22.

Table 12-22. Definitions of severe and significant-severe weather.

Event	Severe Weather	Significant-Severe Weather
Wind gusts	≥58 mph (≥26 m/s)	≥75 mph (≥33.5 m/s)
Hail	≥0.75-in diameter	≥2-in diameter
Tornado	Any	EF2 or stronger

Vandenberg, Edwards, and Holloman maps are presented for severe weather or greater (fig. 12-40), whereas all the other six sites are presented for significant-severe weather only (fig. 12-39). The map period of record is 37 yr (1980–2006), with 124 nmi (230 km or 143 mi) as the range radius for the respective site. The severe weather map color code is blue— damaging wind, green—large hail, and red—tornadoes.

Table 12-21 gives the number of occurrences of severe weather consisting of hail, wind, and tornadoes, and categorized as "all" and as "significant-severe" for the nine NASA sites. Table 12-21 uses a 124-nmi radius about the location and a 27-yr POR (1980–2006) (ref. 12-114).

12.7.1 Severe Thunderstorms and Their Effects (ref. 12-115)

Despite their small size, all thunderstorms are dangerous. Every thunderstorm produces lightning, which kills more people each year than tornadoes. Heavy rain from thunderstorms can lead to flash flooding. Strong winds, hail, and tornadoes are also dangers associated with some thunderstorms.

Thunderstorms affect relatively small areas when compared with hurricanes and winter storms. The typical thunderstorm is 15 mi in diameter and lasts an average of 20 to 30 min. Of the estimated 100,000 thunderstorms that occur each year in the United States, only about 10 percent are classified as severe. Thunderstorms may occur singly, in clusters, or in lines. Some of the most severe weather occurs when a single thunderstorm affects one location for an extended time. As indicated in section 12.7, the NWS considers a thunderstorm severe if it produces hail at least three-quarters of an inch in diameter, has winds of 58 mph or higher, or produces a tornado.

Lightning is a major threat during a thunderstorm. Lightning is very unpredictable, which increases the risk to individuals and property. In the United States, 75 to 100 people are killed each year by lightning. Lightning often strikes outside of heavy rain and may occur as far as 10 mi away from any rainfall. "Heat lightning" is actually lightning from a thunderstorm too far away for thunder to be heard.

Many strong thunderstorms produce hail. Large hail, or flying glass it may have broken, can injure people and animals. Hail can be smaller than a pea, or as large as a softball, and can be very destructive to automobiles, glass surfaces (skylights and windows), roofs, plants, and crops.

Downbursts and straight-line winds associated with thunderstorms can produce winds 100 to 150 mph, enough to flip cars, vans, and semi-trucks. The resulting damage can equal the damage of most tornadoes (ref. 12-115). Also see sections 12.5.5 and 12.6.9.3 dealing with downburst-type severe winds. The frequency of thunderstorms is presented in section 9.4.2.

12.8 Unique Wind Measurements of Hurricane Ivan Eyewall Passage

Presented in figure 12-41 is a unique set of wind speed/time plots of Hurricane Ivan's landfall measured by UAH's mobile 915 MHz doppler wind profiler in place just southeast of Foley, AL (at U.S. Navy Wolf Airfield, 6 mi from Orange Beach, AL, and 3 mi from the Gulf of Mexico) on September 16, 2004. Around 2 a.m. CDT on September 16 (0650Z), Hurricane Ivan made landfall on the U.S. mainland west of Gulf Shores, AL, between Jack Edwards Airport (south of Foley, AL) and Dauphin Island, as a category 3 hurricane. The eye of the hurricane at its closest to the profiler site was ≈7 mi to the west of the site. The UAH profiler sampled the eyewall as it was right in the wall of the storm edge. The east part of the hurricane eye moved over Foley, AL. The inset shows Mobile, AL, radar velocity data at 1:29 a.m. CDT—as Hurricane Ivan begins to make landfall between Dauphin Island and Jack Edwards airports, radar velocity data confirms wind speeds far in excess of 64 kt on shore. Later, the hurricane quickly weakened to tropical depression status as it turned to the northeast.

A maximum wind gust of 91 kt (105 mph) was measured by UAH at 3 m AGL, with sustained winds of ≈74 kt (≈85 mph). Prior to landfall, winds aloft from 105 m through 7 km altitude reached peak wind conditions of >83 kt (>96 mph) between ≈0300Z and ≈0530Z. Winds between ≈0.5 and ≈2 km altitude increased to >110 kt (>127 mph) between ≈0500 and ≈0630Z. Lighter winds were then measured between 0700Z and 0900Z. A wind directional reversal, from southeast to southwest, started at ≈0730Z and became southwesterly by ≈0800Z. Between 0900 and 1100, the winds again peaked before becoming light starting at ≈1330Z, out of the west-southwest. Winds within the first 3 km altitude then became light and variable.

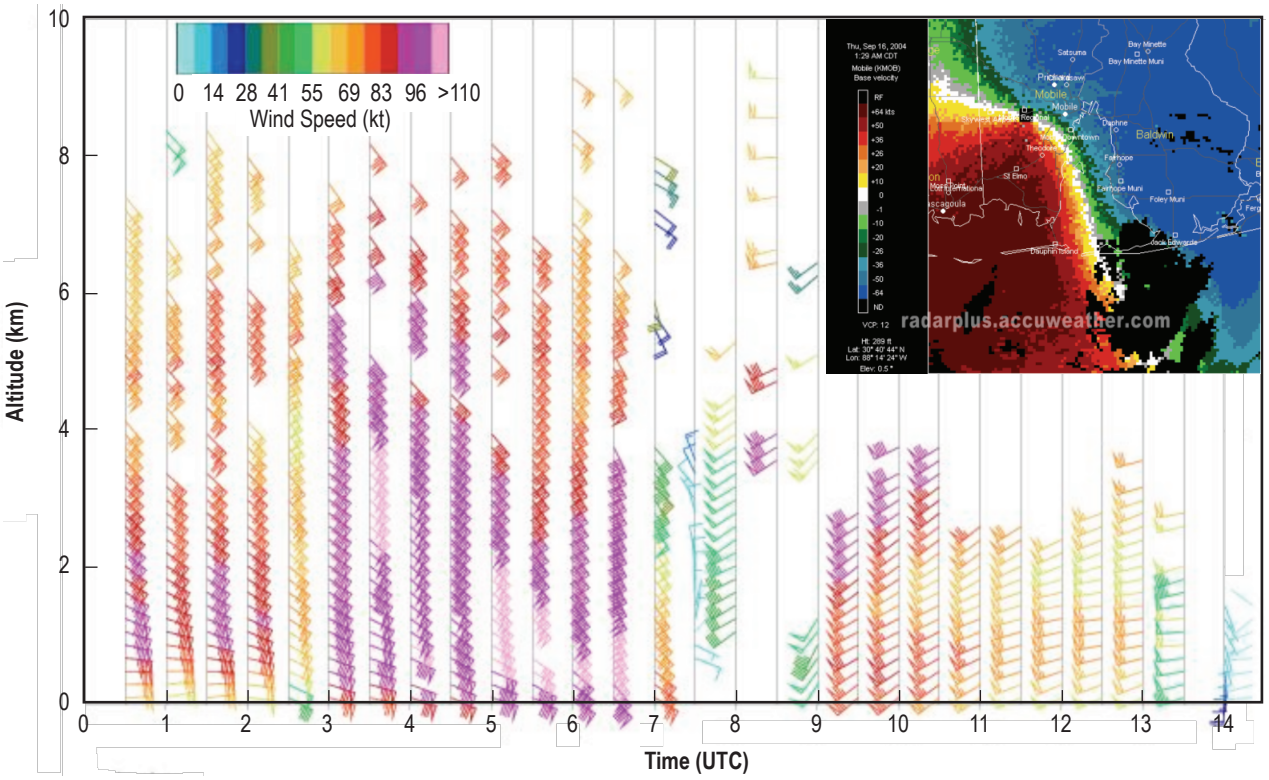

Figure 12-41. UAH doppler wind profiler sequential wind measurements taken during Hurricane Ivan landfall on September 16, 2004 (courtesy of D. Phillips, J. Walters, and K. Knupp) (refs. 12-116 and 12-117).

REFERENCES

12-1. "Design and Construction Guidance for Community Shelters," FEMA 361, Chapter 3: Characteristics of Tornadoes and Hurricanes, July 2000.

12-2. "Thunderstorms, Tornadoes, Lightning: Nature's Most Violent Storms," NOAA/NWS Brochure No. NOAA/PA 99050: ARC 1122, 1999.

12-3. "Tornado Forecasting and Warning," AMS Statement adopted by the AMS Council, October 8, 2004, *Bulletin of the American Meteorological Society*, Vol. 87, Issue 7, p. 972+, July 2006.

12-4. Fujita, T.T.: "U.S. Tornadoes, Part One, 70-Year Statistics," SMRP–RP No. 218, The University of Chicago, 1987.

12-5. FEMA: Tornado Activity in the United States, <http://www.fema.gov/plan/prevent/saferoom/tsfs02_torn_activity.shtm>, Accessed 2007.

12-6. "Tornado Climatology," NOAA, NCDC, Global Climate Monitoring, August 17, 2006, <http://www.ncdc.noaa.gov/oa/climate/severeweather/tornadoes.html>, Accessed 2007.

12-7. Sky-Fire, "Update Your Knowledge of Tornadoes and What They can do to our Environment," Sky Fire Productions, Inc., 2007, <http://sky-fire.tv/index.cgi/tornadoes.html#windowsdoors>, Accessed 2007.

12-8. Tatom, J.W.; and Giroir, M.J.: "Site Assessment of Tornado Threat (SATT 3.0) User's Manual," APT Research, Inc., Huntsville, AL, March 2002.

12-9. "A Guide to F-Scale Damage Assessment," NOAA/NWS, April 2003, <http://www.meted.ucar.edu/resource/wcm/ftp/FinalNWSF-scaleAssessmentGuide.pdf>, Accessed 2007.

12-10. Fujita, T.T.: "Workbook of Tornadoes and High Winds for Engineering Applications," *Res. Pap. 165, Satell. and Mesometeorol. Res. Proj.*, Univ. of Chicago, Chicago, IL, 142 pp., 1978.

12-11. Texas Tech University, "A Recommendation for an Enhanced Fujita Scale (EF-Scale): Submitted to the National Weather Service and Other Interested Users," Rev. 2, Wind Science and Engineering Center, October 10, 2006, <http://www.spc.noaa.gov/efscale/ef-ttu.pdf>, Accessed 2007.

12-12. "The Enhanced Fujita Scale (EF Scale)," NOAA, NWS, National Centers for Environmental Prediction, Storm Prediction Center Article, June 4, 2007, <http://www.spc.noaa.gov/efscale/>, Accessed 2007.

12-13. Meaden, G.T.; Terence, G.; Kochev, S.; et al.: "Comparing the Theoretical Versions of the Beaufort Scale, the T-Scale and the Fujita Scale," *Atmospheric Research*, Vol. 83, pp. 446–449, 2007.

12-14. McCarthy D.W.; and Schaefer, J.T.: "Tornado Trends Over the Past Thirty Years," POR: 1970–2002, Preprints, AMS 14th Conference on Applied Climatology, Seattle WA, January 10–15, 2004.

12-15. Ramsdell, J.V.; and Andrews, G.L.: "Tornado Climatology of the Contiguous United States," NUREG/CR–4461, Battelle-Pacific Northwest Laboratory, May 1986.

12-16. Tatom, F.B.: "Assessment of the Threat of Tornadoes in the Forty-Eight Contiguous United States Plus Hawaii for the Years 1950–2001," VT–EN–03–002, VorTek LLC, Huntsville, AL, March 2003.

12-17. Thom, H.C.S.: "Tornado Probabilities," *Monthly Weather Review*, Vol. 91, No. 10–12, pp. 730–736, October–December 1963.

12-18. NASA Technical Handbook: "Terrestrial Environment (Climatic) Criteria Handbook for Use in Aerospace Vehicle Development," *NASA-HDBK-1001*, August 11, 2000.

12-19. Johnson, D.L.; Pearson, S.D.; and Yung, S.: "Tornadic Weather Consideration for Various NASA Sites/Projects," *AIAA Paper 96–0396*, AIAA 34th Aerospace Sciences Meeting and Exhibit, Reno, NV, January 15–18, 1996.

12-20. Garinger, L.P.; and Knupp, K.R.: "Seasonal Tornado Climatology for the Southeastern United States, The Tornado: Its Structure, Dynamics, Prediction, and Hazards," C. Church (Ed.), *AGU Geophysical Monograph,* Vol. 79, pp. 445–452, 1993.

12-21. Vaughan, O.H.; and Vonnegut, B.: "Luminous Electrical Phenomena in Huntsville, Alabama, Tornadoes on April 3, 1974," *NASA–TM–X–73301*, Marshall Space Flight Center, AL, May 1976.

12-22. Wikipedia Contributors: "November 1989 Tornado Outbreak," *Wikipedia, the Free Encyclopedia*, March 16, 2008, <http://en.wikipedia.org/wiki/November_1989_Tornado_Outbreak>, Accessed March 18, 2008.

12-23. "Listing of Tornadoes That Have Occurred in Madison, AL County," National Weather Service Forecast Office, Huntsville, AL, November 20, 2006, <http://www.srh.noaa.gov/hun/tornadodatabase/tornado.php?type=county&name=MadisonAL>, Accessed 2007.

12-24. Hagemeyer, B.C.: "Peninsular Florida Tornado Outbreaks," *AMS Weather and Forecasting*, Vol. 12, pp. 399–427, September 1997.

12-25. NOAA, Brevard Co. FL Tornado Statistics, NOAA-NCDC, 2007, <http://www4.ncdc.noaa.gov/cgi-win/wwcgi.dll?wwevent~storms>, Accessed 2007.

12-26. "Central Florida Tornado Outbreak February 22–23, 1998," NOAA Service Assessment Report SA–1998, June 1998.

12-27. Driscoll, K.: "LIS and OTD Science Accomplishments," White Paper on Lightning Detection From Space, <http://thunder.msfc.nasa.gov/bookshelf/docs/white_paper_driscoll.html>, Accessed 2007.

12-28. "Spotting Tornadoes From Space," Science at NASA, May 1, 2000, <http://science.nasa.gov/headlines/y2000/ast01may_1m.htm>, Accessed 2007.

12-29. Liston, E.E.: "Chronology of KSC and KSC Related Events for 2001," *NASA/TM—2002–210267*, Kennedy Space Center, FL, February 2002.

12-30. Merceret F.: "Synthesis for June 24, 2001—ABFM," Presented on September 19, 2002, Summary, January 8, 2003, <http://www.mmm.ucar.edu/abfm/webpage/june2001/Synthesis/010624/010624_synth.html>, Accessed 2007.

12-31. "Tornado at Kennedy Space Center," Strikefish Blog, July 21, 2006, <http://blog.strikefish.com/blog/index.cfm?mode=entry&entry=91322EEB-1422-201A-558CD3B613E54BE8>, Accessed March 18, 2008.

12-32. Edwards, L.: "Spin, Spin, Spin," California Climate Watch, Western Regional Climate Center, Scripps Institution of Oceanography, California Energy Commission, February 2005, <http://www.calclim.dri.edu>, Accessed 2007.

12-33. "California Tornado Statistics," Golden Gate Weather Services, 2005, <http://ggweather.com/ca_tornado.htm>, Accessed 2007.

12-34. Curtis, L.: "Analysis of a Texas Tornado Outbreak Involving Three Modalities of Enhanced Tornadogenesis," Paper 3A.4, AMS 22nd Conference on Severe Local Storms, Hyannis, MA, October 4–8, 2004.

12-35. "November 17, 2003 Tornado Outbreak: Tornado Track Maps," NOAA-NWS Forecast Office, Houston/Galveston, Texas, February 6, 2006, <http://www.srh.noaa.gov/hgx/projects/nov17_03/trackmap.htm>, Accessed 2007.

12-36. "What are Some Tornadoes and Tornado Outbreaks That Have Impacted Southeast Texas?" NOAA-NWS Forecast Office, Houston/Galveston, TX, February 25, 2007, <http://www.srh.noaa.gov/hgx/severe/swa/tornadoes.htm>, Accessed 2007.

12-37. Doswell, C.A.; and Schultz, D.M.: "On the Use of Indices and Parameters in Forecasting Severe Storms," *Electronic J. Severe Storms Meteor.*, Vol. 1, No. 3, pp. 1–14, August 2006, <http://www.ejssm.org/ojs/index.php/ejssm/issue/archive>, Accessed 2007.

12-38. "Convective Season Environmental Parameters and Indices," NOAA-NWS Louisville, KY Weather Forecast Office, November 3, 2005, <http://www.crh.noaa.gov/lmk/soo/docu/indices.php>, Accessed 2007.

12-39. Johnson, D.L.: "A Stability Analysis of AVE-IV Severe Weather Soundings," *NASA TP–2045*, November 1982, Marshall Space Flight Center, AL, <http://ntrs.nasa.gov/archive/nasa/casi.ntrs.nasa.gov/19830006553_1983006553.pdf>, Accessed 2007.

12-40. Gentry, R.C.: "Genesis of Tornadoes Associated With Hurricanes," *Monthly Weather Review*, Vol. 111, pp. 1793–1805, September 1983.

12-41. Grazulis, T.; and McCaul, E.W.: "The Tornado Project," 2003, <http://www.tornadoproject.com/front.htm>, Accessed 2007.

12-42. "Hurricanes and Tornadoes," NOAA/NWS/CPHC, Central Pacific Hurricane Center, <http://www.prh.noaa.gov/cphc/pages/FAQ/Hurricanes_vs_tornadoes.php>, Accessed 2007.

12-43. "Hurricane Basics," NOAA, May 1999, <http://hurricanes.noaa.gov/pdf/hurricanebook.pdf>, Accessed 2007.

12-44. McCaul, E.W.: “Hurricane Tornadoes 2004,” AMS Paper J3.3, at AMS IMPACT: Weather 2004: Third Annual Users Conference, San Diego, CA, January 9–12, 2005.

12-45. McCaul, E.W.: “Severe Weather in Landfalling Hurricanes,” Joint NCAR/ASP, NOAA/HRD Colloquium on Hurricanes at Landfall, Boulder, CO, July 13–24, 1998.

12-46. McCaul, E.W.: “Buoyancy and Shear Characteristics of Hurricane-Tornado Environments,” *MWR*, Vol. 119, pp. 1954–1978, August 1991.

12-47. Verbout, S.M.; Schultz, D.M.; Leslie, L.M.; et al.: “Tornado Outbreaks Associated With Landfalling Hurricanes in the North Atlantic Basin: 1954–2004,” *Meteor. and Atmos. Phys.*, Vol. 97, No. 1–4, pp. 255–271, DOI: 10.1007/s00703–006–0256–x, March 14, 2007.

12-48. Hagemeyer, B.C.: “Thirty Years After Hurricane Agnes—The Forgotten Florida Tornado Disaster,” Paper 10A.6, 25th AMS Conference on Hurricanes and Tropical Meteorology, San Diego, CA, April 29–May 3, 2002.

12-49. Wikipedia Contributors: “Hurricane Katrina Tornado Outbreak,” *Wikipedia, the Free Encyclopedia*, August 1, 2007, <http://en.wikipedia.org/wiki/Hurricane_Katrina_tornado outbreak>, Accessed March 18, 2008.

12-50. Edwards, R.: “Tornado Production by Exiting Tropical Cyclones,” 23rd AMS Conference on Hurricanes and Tropical Meteorology, Dallas, TX, January 11–15, 1998.

12-51. Geer, I.W. (Ed.): “Glossary of Weather and Climate: With Related Oceanic and Hydrologic Terms,” *American Meteorological Society*, 272 pp.,1996.

12-52. Wikipedia Contributors: “Gustnado,” *Wikipedia, the Free Encyclopedia*, February 12, 2008, <http://en.wikipedia.org/wiki/Gustnado>, Accessed March 18, 2008.

12-53. Smith, R.: “Non-Supercell Tornadoes: A Review for Forecasters,” Technical Attachment, NWSFO Memphis, SR/SSD 96–8, February 15, 1996, <http://www.srh.noaa.gov/topics/attach/html/ssd96-8.htm>, Accessed 2008.

12-54. Wikipedia Contributors: “Landspout,” Wikipedia, the Free Encyclopedia, February 15, 1996, <http://en.wikipedia.org/wiki/Landspout>, Accessed March 18, 2008.

12-55. Golden, J.H.: “Chasing the Wet Whirlwind,” *Weatherwise*, Vol. 61, No. 1, pp.18–25, February 2008.

12-56. Wikipedia Contributors: “Waterspout,” *Wikipedia, the Free Encyclopedia*, March 10, 2008, <http://en.wikipedia.org/wiki/Waterspout>, Accessed March 18, 2008.

12-57. Wikipedia Contributors: “Fire Whirl,” *Wikipedia, the Free Encyclopedia*, March 10, 2008, <http://en.wikipedia.org/wiki/Fire_whirl>, Accessed March 18, 2008.

12-58. Haines, D.A.; and Updike, G.H.: “Fire Whirlwind Formation Over Flat Terrain,” USDA Forest Service, St. Paul, MN, Research Paper NC-71, 1971.

12-59. Umscheid, M.E.; Monteverdi, J.P.; and Davies, J.M.; “Photographs and Analysis of an Unusually Large and Long-Lived Firewhirl,” *E-Journal of Severe Storms Meteorology*, Vol. 1, No. 2, February 6, 2006.

12-60. Heidorn, K.C.: "For Strong Winds: Microbursts and Heatbursts," *The Weather Doctor*, July 1, 2005, <http://www.islandnet.com/~see/weather/storm/bursts.htm>, Accessed March 18, 2008.

12-61. *Glossary of Meteorology*, American Meteorological Society, 2nd Edition, p. 850, 2000.

12-62. Sanger, N.T.: "A Four-Year Summertime Microburst Climatology and Relationship Between Microburst and Cloud-to-Ground Lightning Flash Rate for the NASA Kennedy Space Center, Florida: 1995–1998, M.S. Thesis, Texas A&M University, August 1999.

12-63. Bunting W.F.; and B.E. Smith: "A Guide for Conducting Convective Windstorm Surveys," NOAA Technical Memorandum NWS SR–146, February 1993.

12-64. NOAA 2007: NOAA/FEMA, Hurricanes: Unleashing Nature's Fury: A Preparedness Guide, NOAA/PA 94050, Revised January 2007.

12-65. Barnes, G.: "Hurricane," With Illustration by B. Kerr, World Book Online Reference Center, 2005, World Book, Inc. <http://www.nasa.gov/worldbook/hurricane_worldbook_prt.htm>, Accessed 2007.

12-66. Earth Observatory News: "Historic Tropical Cyclone Tracks," 2007, <http://earthobservatory.nasa.gov/Newsroom/NewImages/images.php3?img_id=17447>, Accessed 2007.

12-67. NASA JSC Space Shuttle Document, "Natural Environment Design Requirements," Vol. X, Book 2, Appendix 10.10, paragraph 3.1.2.1.1.

12-68. Gupta, S.; and Ortasse, R.: "Definition of Hurricane Wind Environment for Space Shuttle Fatigue Loads," *AIAA–6/96–0395*, AIAA 34th Aerospace Sciences Meeting and Exhibit, Reno, NV, January 15–18, 1996.

12-69. "Storm Data With Annual Summaries," Department of Commerce/NOAA/NCDC Publication, Vol. 30, No. 12, December 1988.

12-70. Landsea, C.: "Frequently Asked Questions," NOAA-AOML-HRD, June 11, 2007, <http://www.aoml.noaa.gov/hrd/tcfaq/E11.html>, Accessed 2007.

12-71. Cerveny, R.S.; Lawrimore, J.; Edwards, R.; et al.: "Extreme Weather Records," *BAMS*, pp. 853–860, June 2007.

12-72. NOAA-NWS-CPC, "Background Information: The North Atlantic Hurricane Season," August 7, 2002, <http://www.cpc.ncep.noaa.gov/products/outlooks/hurricane2003/August/backgroundinformation.html>, Accessed 2007.

12-73. Hall, T.M.; and Jewson, S.: "SST and North American Tropical Cyclone Landfall: A Statistical Modeling Study," arXiv:0801.1013v1 [physics.ao-ph], February 2, 2008, <http://arxiv.org/PS_cache/arxiv/pdf/0801/0801.1013v1.pdf>, Accessed 2007.

12-74. Blake, E.S.: "The Deadliest, Costliest, and Most Intense United States Tropical Cyclones From 1851 to 2006 (and Other Frequently Requested Hurricane Facts)," NOAA Technical Memorandum-NWS TPC-5, April 2007.

12-75. NASA News, Earth Observatory, <http://earthobservatory.nasa.gov/Newsroom/>, 2006–2007, Accessed 2007.

12-76. "Counting Hurricanes," *Weatherwise*, Vol. 61, No. 1, pp. 11–12, January–February 2008.

12-77. Carbone, G.: "Tropical Cyclones: Energy/Cross Section," University of South Carolina, Dept. of Geography, <http://people.cas.sc.edu/carbone/modules/mods4car/tropcycl/pages/energy.html>, 1999.

12-78. <http://www.texasento.net/witch_storm.htm or http://deepcreekyachtclub.com/WebPage/images/WindDirectionHurricane.jpg>, Accessed 2007.

12-79. Keim, B.D.; Muller, R.A.; and Stone, G.W.: "Spatiotemporal Patterns and Return Periods of Tropical Storm and Hurricane Strikes from Texas to Maine," *Journal of Climate*, Vol. 20, Issue 14, pp. 3498–3509, July 2007.

12-80. Pidwirny, M.: "Fundamentals of Physical Geography," Chapter 7: Introduction to the Atmosphere; (u) Tropical Weather and Hurricanes, <http://www.physicalgeography.net/ http://www.physicalgeography.net/fundamentals/7u.html>, Accessed 2007.

12-81. Hart, R.: "Hurricanes: A Primer on Formation, Structure, Intensity Change and Frequency," George C. Marshall Institute Paper, May 1, 2006, <http://www.marshall.org/pdf/materials/409.pdf>, Accessed 2007.

12-82. Hsu, S.A.: "Estimating the Wind Speed During A Hurricane at Sea," *NOAA Mariners Weather Log*, Vol. 50, No. 3, 2 pp., December 2006.

12-83. Franklin, J.L.; Black, M.L.; and Valde, K.: "Eyewall Wind Profiles in Hurricanes Determined by GPS Dropwindsondes," 2000, <http://www.nhc.noaa.gov/aboutwindprofile.shtml>, Accessed 2007.

12-84. Simiu, E.; Vickery, P.; and Kareem, A.: "Relation Between Saffir-Simpson Hurricane Scale Wind Speeds and Peak 3-s Gust Speeds Over Open Terrain," *J. Structural Engineering*, Vol. 133, Issue 7, pp. 1043–1045, July 2007.

12-85. Kaplan, J.; and DeMaria, M.: "A Simple Empirical Model for Predicting the Decay of Tropical Cyclone Winds After Landfall," *J. App. Meteor.*, Vol. 34, No. 11, pp. 2499–2512, 1995.

12-86. Froehlich, D.C.: "User's Manual for FESWMS FLo2DH: Two-Dimensional Depth-averaged Flow and Sediment Transport Model—Release 3," Federal Highway Administration (DOT), Office of Research, Development, and Technology, Publication No. FHWA-RD-03-053, September 2002.

12-87. National Hurricane Center, <http://www.nhc.noaa.gov/HAW2/english/wind/wind_decay.shtml>, Accessed 2007.

12-88. National Hurricane Center, <http://www.nhc.noaa.gov/HAW2/english/wind/risk_areas.shtml>, Accessed 2007.

12-89. NOAA Satellite and Information Service, National Climatic Data Center, <http://www.ncdc.noaa.gov/img/climate/severeweather/hurricane2007.pdf>, Accessed 2007.

12-90. Gray, W.M.; PKlotzbach, .J.; and Thorson, W.: "Summary of 2004 Atlantic Tropical Cyclone Activity and Verification of Author's Seasonal and Monthly Forecasts," Colorado State University, Dept. of Atmospheric Science, November 19, 2004.

12-91. Hebert, P.J.; Jarrell, J.D.; and Mayfield, B.M.: "The Deadliest, Costliest and Most Intense United States Hurricanes of this Century (and Other Frequently Requested Hurricane Facts), NOAA, Technical Memorandum NWS-TPC-1, 30 pp., 1997.

12-92. Sallenger, A.H.; Stockdon, H.F.; Fauver, L.; et al.: "Hurricanes 2004: An Overview of Their Characteristics and Coastal Change," *Estuaries and Coasts*, Vol. 29, No. 6A, pp. 880–888, December 2006.

12-93. Verdi, R.J.: "Hydrologic Effects of the 2004 Hurricane Season in Northwest Florida," USGS Open-File Report 2005–1277, 18 pp., 2005.

12-94. Abtew, W.; and Huebner, R.S.: "Hydrologic Impact of the 2004 Hurricane Season on South Florida," Technical Paper ERA#431, 2006 ASCE/EWRI World Environmental and Water Resources Conference, Omaha NE, May 21–25, 2006.

12-95. "Historical Hurricane Tracks," NOAA Coastal Services Center, <http://maps.csc.noaa.gov/hurricanes/viewer.html>, Accessed 2007.

12-96. Barton, C.; and Nishencko, S.: "Natural Disasters—Forecasting Economic and Life Losses," USGS Coastal & Marine Geology Program, USGS Fact Sheet, December 18, 2003, <http://pubs.usgs.gov/fs/natural-disasters/index.html> or <http://pubs.usgs.gov/fs/natural-disasters/figures/fig7.html>, December 16, 2003, Accessed 2007.

12-97. Elsner, J.: "Hurricane Probabilities," April 23, 2004, <http://www.floridadisaster.org/bpr/Response/Plans/Nathaz/hurricanes/hurr_freq.htm> or <www.FloridaDisaster.org>, Accessed 2007.

12-98. Chenoweth, M.; and Landsea, C.: "The San Diego Hurricane of 2 October 1858," *Bull. Am.Meteor.Soc.*, Vol. 85, pp.1689–1697, November 2004.

12-99. Wikipedia Contributors: "List of California Hurricanes," *Wikipedia, the Free Encyclopedia,* <http://en.wikipedia.org/wiki/List_of_California_tropical_storms>, Accessed 2007.

12-100. NOAA/NWS/Central Pacific Hurricane Center, "Climatology of Tropical Cyclones in the Central Pacific Basin," 2007, <http://www.prh.noaa.gov/cphc/pages/climatology.php>, Accessed 2007.

12-101. Alexander, M.B.: "An Analysis of Maximum Horizontal Wind Speeds Recorded Since 1961 at Kennedy Space Center, Florida," *NASA TM–78177*, Marshall Space Flight Center, AL, May 1978.

12-102. Liston, E.E.: "Chronology of KSC and KSC Related Events for 2004," *NASA/TM—2005–211539*, Kennedy Space Center, FL, February 2005.

12-103. Alexander, M.B.: "Hurricane David Wind Velocities," NASA MSFC ES82 Memorandum for Record, September 20, 1979.

12-104. "Hurricane Frances & Hurricane Jeanne: Post-storm Beach Conditions and Coastal Impact Report With Recommendations for Recovery and Modifications of Beach Management Strategies," Florida Department of Environmental Protection, Division of Water Resource Management, Bureau of Beaches and Coastal Systems, October 2004. Graphic printed in <http://bcs.dep.state.fl.us/reports/franjean/Hurricanes_Frances_&_Jeanne/Full_Report/Full_Report.pdf> and in <http://bcs.dep.state.fl.us/reports/strmtide/jeanne.pdf>, Accessed 2007.

12-105. NOAA references: “Atlantic Hurricane Season of XXXX”, from various Monthly Weather Review articles published annually to document each year’s hurricane statistics for the U.S., authors from NOAA Tropical Prediction Center, National Hurricane Center, Miami FL, various hurricane years examined.

12-106. Wheeler, M.: “Verification and Implementation of Microburst Day Potential Index (MDPI) and Wind INDEX (WINDEX) Forecasting Tools at Cape Canaveral Air Station,” *CR–201354*, Kennedy Space Center, FL, 1996.

12-107. Grinter, K.K.: “KSC Online: Weather Status Reports—Climatological Report,” <www-pao.ksc.nasa.gov>, Accessed 2007.

12-108. Sanger, N.T.: “A Four-Year Summertime Microburst Climatology and Relationship Between Microburst and Cloud-to-Ground Lightning Flash Rate for the NASA Kennedy Space Center, Florida: 1995–1998,” M.S. Thesis, Texas A&M University, August 1999.

12-109. Englebretson, R.; Gilmore, R.; and Brand, S.: “Hurricane Havens Handbook, for the North Atlantic Ocean,” Naval Meteorology and Oceanography Command, Stennis Space Center, MS, NAVENVPREDRSCHFAC Technical Report TR 82-03, October 1999, <http://www.nrlmry.navy.mil/~cannon/tr8203nc/0start.htm>, Accessed 2007.

12-110. Johnson, D.; and Rawlins, M.A.: “Hurricane Properties for KSC and Mid-Florida Coastal Sites,” Paper 6.5, AMS 9th Conference on Aviation, Range and Aerospace Meteorology, Orlando FL, September 11–15, 2000.

12-111. Nelson, S.A.: Tulane University, EENS 204, Natural Disasters, Exceptional Weather (Part 2), <http://www.tulane.edu/~sanelson/geol204/exceptweath2.htm>, Accessed 2007.

12-112. Wikipedia Contributors: “Nor’easter,” *Wikipedia, the Free Encyclopedia*, <http://en.wikipedia.org/wiki/Nor’easter>, Accessed 2007.

12-113. The Weather Channel, <http://www.weather.com/encyclopedia/winter/noreast.html>, Accessed 2007.

12-114. “Online Severe Weather Climatology,” NOAA—NWS, Storm Prediction Center, <http://www.spc.noaa.gov/climo/online/rda/index.html>, October 2007.

12-115. “Severe Thunderstorm,” The Disaster Center, From: *Talking About Disaster: Guide for Standard Messages,* Produced by the National Disaster Education Coalition, Washington, DC, <http://www.disastercenter.com/guide/thunder.html>, 1999.

12-116. “UAH Storm Research Team Gets an Eyeful of Hurricane Ivan,” October 1, 2004, <http://urnet.uah.edu/News/read.asp?newsID=359>, The University of Alabama in Huntsville – News & Events, 2008.

12-117. “Hurricane Ivan Hits Florida and Floods East Coast, September 14–17, 2004,” <http://www.accuweather.com/adcbin/public/radarplus_gallery.asp?gallery=040916>.

Terrestrial Environment (Climatic) Criteria Guidelines for Use in Aerospace Vehicle Development, 2008 Revision

NASA/TM—2008–215633
December 2008

D.L. Johnson, Editor

Section 13: Geologic Hazards, Earth Properties, and Aerospace Vehicle Implications

TABLE OF CONTENTS

TABLE OF CONTENTS (Continued)

LIST OF FIGURES

LIST OF FIGURES (Continued)

LIST OF TABLES

LIST OF ACRONYMS

CATS	Consequences Assessment Tool Set
CGS	California Geological Survey
CRR	cyclic resistance ratio
CUSEC	Central United States Earthquake Consortium
EAFB	Edwards Air Force Base
EQ	earthquake
FEMA	Federal Emergency Management Agency
GSE	ground support equipment
IM	intensity measures
KSC	Kennedy Space Center
MCE	maximum credible earthquake
MDE	maximum design earthquake
MEOW	maximum envelope of water
MMI	Modified Mercalli Intensity (scale)
MOM	maximum of MEOW
MPE	maximum probable earthquake
NHC	National Hurricane Center
NOAA	National Oceanic and Atmospheric Administration
NUVEL-1	Northwestern University VELocity-1 (model)
NWS	National Weather Service
OBE	operating basis earthquake
PE	probability of exceedance
PGA	peak ground acceleration
PGD	peak ground displacement
PGV	peak ground velocity
PHA	peak horizontal acceleration
PHD	peak horizontal displacement
PHV	peak horizontal velocity
SLOSH	sea, lake, and overland surges from hurricanes
SPLASH	special program to list amplitudes of surges from hurricanes

LIST OF ACRONYMS (Continued)

SSV	Space Shuttle vehicle
USGS	U.S. Geological Survey
VAFB	Vandenberg Air Force Base
VEI	volcanic explosive index

NOMENCLATURE

A	fault area
A_h	design acceleration = 0.10+0.15 (h/h_t)
C	seismic force coefficient (no units)
C_s	soil constant (no units) = 2.25–0.125 $f_b \geq 1$
D	average static displacement
F	equivalent static lateral force applied at the center of gravity (in pounds)
F_b	allowable soil bearing value in kips per square foot (see Geophysical Investigation Supplement for VAFB Station Set V23 (VCR-77-067 of 20 January 1977) (1 kip = 1,000 lb))
$f(m)$	function on magnitude
G	rigidity modulus
$G_{\max}$	maximum shear moduli
H	height of equipment in building above building base
H_t	height of building
K	coefficient based on building type (no units)
M	Richter magnitude
M	moment magnitude
M_b	body wave magnitude
MF	magnification factor (no units)
M_L	local magnitude; maximum magnitude earthquake
M_o	seismic moment
M_s	surface wave magnitude
M_w	seismic moment scale
m_0	minimum magnitude
N	number of uniform stress cycles
n	number of years
p	particular value
q	probability
T	period of building (in seconds)
T_a	period of item under consideration (in seconds)
T_m	mean period
T_p	predominant period
T_v	pulse period

NOMENCLATURE (Continued)

W	weight
Z	seismic probability coefficient (no units), where $Z = 1.5$ for high-loss potential equipment (damages SSV element) and $Z = 1$ for low-loss potential equipment (damages GSE only)
Δ	distance from epicenter
μ	displacement amplitude

13. GEOLOGIC HAZARDS, EARTH PROPERTIES, AND AEROSPACE VEHICLE IMPLICATIONS

13.1 Introduction

The U.S. Geological Survey (USGS) Glossary of Geology (ref. 13-1) defines a geologic hazard as "a naturally occurring or manmade geologic condition that presents a risk or is a potential danger to life and property." Geologic hazards are a subset of natural hazards, as are atmospheric, hydrologic, and wildfire hazards. In this section, geologic hazards are discussed as they pertain to Vandenberg Air Force Base (VAFB), CA, Edwards Air Force Base (EAFB), and Cape Canaveral, FL. A section on seismic environment, prepared for Space Shuttle ground support equipment (GSE) design, is included, as well as the physical and dynamical properties and characteristics of the Earth, Sun, and planets within the solar system.

It should be noted that the contents of section 13 are intended to provide the aerospace vehicle facilities developer with the necessary background information to make informed engineering decisions relative to geological hazards that may affect the operational utility of an aerospace vehicle.

Section 13.7 provides a ready reference on the Earth's physical properties and dynamical characteristics.

13.2 Specific Hazards

Geologic hazards presented here include seismic (earthquakes), slope processes (debris avalanches, landslides, rockfalls, and submarine landslides), expanding ground, ground subsidence, tsunamis, seiches, storm surges, floods, and volcanic activity.

Seismic hazards can be further subdivided into areas of (1) fault ruptures, (2) ground shaking, (3) lateral spreading, (4) liquifaction, and (5) tsunamis and seiches, although seiches can also be wind driven. With the exception of flooding, purely hydrological or atmospheric hazards will not be presented in this section. Volcanic eruption hazards can include (1) mud, lava, and pyroclastic flows, (2) gases, (3) tephra (ash, cuiders, and lapilli), and (4) projectiles and lateral blasts.

13.2.1 Earthquakes

Seismology is defined as the study of earthquakes and the structure of the Earth by natural and artificial seismic (earthquake) waves (ref. 13-1). Earthquakes are due to sudden releases of tectonic stresses that result in relative movement of rocks on opposite sides of a fault plane, as well as shaking of the ground in areas near, and sometimes far from, the actual fault movement. Ground movement and shaking can trigger numerous other disasters, including landslides; liquefaction and sliding of unconsolidated sediments; destruction of buildings, dams, and roads; fires; tsunamis; seiches; changes in ground water level; and uplift or subsidence. They can also bring about far-reaching atmospheric pressure changes and sound waves and oscillations of the ionosphere (ref. 13-2).

The relative movement of different sections (plates) of the Earth's crust causes stresses to build up near the boundaries between them. Movement along faults, releasing seismic waves, takes place when the effective stresses exceed either the strength of the solid rock or the frictional resistance between rocks on either side of a preexisting break or fault. Since preexisting fault surfaces usually have lower strength than the surrounding rock, movement takes place along them.

13.2.1.1 Stress and Strain. Tectonic stress within the Earth is either compressional, tension, or shear, which can give reverse, normal, and strike-slip faults, respectively, or three orthogonal principal stress directions—maximum, middle, and minimum. The difference between maximum and minimum principal stress causes an earthquake. As stress builds up within the Earth, the rocks will gradually be deformed, or strained, and considerable elastic strain energy is released as seismic waves that radiate from the source, partly as heat.

Many microearthquakes take place along active faults, such as in parts of the San Andreas. But a greater number do not correspond to any known surface fault. Many of the earthquakes that are not associated with surface faults occur under folds—geologic structures formed when layered sediments are buckled upward in a broad arch called an anticline. The presence of an anticline reflects crustal compression as two moving tectonic plates collide, in the same way a carpet wrinkles when pushed across the floor. An unanswered question is whether these active folds conceal large faults, which could provide the sites for large shocks (ref. 13-3).

Earthquakes have proven to be one of the most disastrous and insurmountable geologic hazards. Buildings constructed to withstand them have crumbled under their forces (ref. 13-2). Prediction of earthquake likelihood, intensity, and timing for a given location has not yet proved reliable. Experience has shown that, to date, the best protection against earthquakes is identification of high-risk areas and avoidance of construction in them.

Definition of high-risk areas—a complicated process—includes mapping faults, dating movement on them to determine whether they are or might be still active, calculating theoretical maximum possible earthquake intensity for active faults, and predicting effects of possible earthquakes on sediments and rocks in the area. This information is then used to judge the safety of the area for construction.

13.2.1.2 Earthquake Ground Motions. An earthquake is a complex series of vibratory ground motions that emanate from a disturbance in the brittle zone of the Earth's crust (refs. 13-4 through 13-6). Earthquake motion can be considered in two parts:

(1) Transient vibrations (or dynamic deformation)—The movement during fault rupture produces a range of vibrations, or seismic waves, that radiate outward at frequencies <0.2 to 20 Hz (periods from ≈5 s down to ≈0.05 s), and at speeds, depending on the type of rock, usually in the range of 3 to 8 km/s for rocks within 30 km (19 mi) of the Earth's surface. The motions take the form of body waves that propagate in the interior of the Earth and surface waves that propagate along or near the surface of the Earth. Body waves are composed of compressional and shear waves; surface waves are composed of Rayleigh and Love waves. This motion can be measured as displacement, velocity, or acceleration. Dynamic deformation is essentially "sound waves" radiating from the earthquake as it ruptures, and comprises up to 10 percent of the energy dissipating immediately in the form of seismic waves. The mechanical properties of the rocks that seismic waves travel through quickly organize the waves into the two types of body waves. Compressional (or P-) waves (primary) travel faster at speeds between 1.5 and 8 km/s in the Earth's crust, and shake the ground in the direction they are propagating. Shear (or S-) waves (secondary) travel slower, usually 60 to 70 percent of the P-wave speed, and shake perpendicularly to the direction of propagation. Since the ratio between the average speeds of a P-wave and its following S-wave is quite constant, seismologists are able to get an estimate of the distance of the earthquake from the observation station. Multiply the S- minus P- time, in seconds, by the factor 8 km/s to get an approximate distance in kilometers.

(2) Permanent deformation—When an earthquake fault ruptures, static deformation and dynamic deformation take place. Static deformation is the permanent displacement of the ground across or near the fault, due to the event that takes up most of the energy released. Fault displacements vary from a few millimeters in small quakes to a few meters for large quakes, and the length of a rupture may vary from a few meters, to a few kilometers, to over 100 km for very large earthquakes.

13.2.1.2.1 Ground Motion Characteristics. The following are characteristics of ground motion:

- Ground motion is generally strongest in the vicinity of its source—near, or at, the fault rupture—with the severity of shaking diminishing with distance.

- The predominant periods of ground motion vibration generally trend toward longer periods as distance increases from the source. This is due to the attenuation of the higher frequency content of the wave train and spreading of the waves.

- Deep deposits of soft soils tend to produce ground surface motions having predominantly long-period characteristics and may greatly accentuate peak motions and their durations.

- Deposits of stiff soils or rock result in ground motions having predominantly short-period characteristics compared to softer materials.

13.2.1.3 Faults. A fault is characterized as a series of segments (or a single segment) that can either rupture individually or in groups. A fault zone is an area of numerous fractures. A fault segment is characterized by a length (or area), a probability density function describing the relative likelihood of the fault producing earthquakes of different magnitudes, and a long-term slip rate. By balancing the rate of seismic moment buildup on a fault (calculated from slip rate) with the rate of moment release (due to earthquakes), it is possible to derive the rate of occurrence of earthquake events on the fault. The measure of magnitude is moment magnitude. The minimum magnitude (m_0) of an earthquake along a fault delineates the minimum level of energy release expected to produce ground motions damaging to structures (usually ≈5.0). The largest magnitude earthquake depends on the largest possible fault area that could rupture in a single event and the stress drop. Use of a constant "stress drop"; i.e., average stress reduction across the rupture, allows magnitude to be described in terms of fault area (A) only. Since magnitude is correlated with area, characterization of probable rupture surfaces along major faults is best performed by assuming that faults are composed of segments (fault segmentation) that define the location and extent of future large earthquakes.

The area of a ruptured fault correlates with the earthquake magnitude as shown in table 13-1. The rupture displacement is typically ≈1/20,000 of the rupture length. The rupture velocity is ≈3 km/s, so the approximate rupture duration (s) is given by fault length (km) divided by 3.

Table 13-1. Typical fault rupture dimensions (ref. 13-5).

Magnitude (Mw)	Fault Area (km^2)	Rupture Dimensions (km×km)
4.0	1	1×1
5.0	10	3×3
6.0	100	10×10
7.0	1,000	30×30
8.0	10,000	50×200

13.2.1.4 Seismometer. The basic measurement of earthquake ground motion of engineering interest is the accelerogram record taken by special strong motion seismometers, which form a primary database for seismic load specifications. A seismometer can provide a record of two orthogonal horizontal components of motion and one vertical component of motion versus time. These are acceleration (cm/s^2), velocity (cm/s), and displacement (cm). The maximum values of peak ground displacement (PGD), peak ground velocity (PGV), and peak ground

acceleration (PGA) provide the most elementary and popular measures of an earthquake's severity. Duration of strong motion is also an important measure.

13.2.1.5 Response Spectrum. More engineering-related characterizations of ground motion can be determined in structural response analysis (modal analysis) by the "response spectrum" method. This spectrum can be used to describe the intensity and vibration frequency content of accelerograms at various levels of structural damping, but also spectra from several earthquake records can be normalized, averaged, and then scaled to predict future motion at a given site. Spectral acceleration (g), relative velocity (cm/s), and relative displacement (cm) can be calculated as a function of period for various percentages of damping.

13.2.1.6 Earthquake Peak Ground Acceleration. Seismic hazard assessments and PGA analyses or maps can be obtained by:

- A probabilistic approach, based on earthquake statistics and theory-guided numerical calculations.

- A deterministic approach, based on geology using rupture mechanisms and geometry; i.e., fault length, slip rate, rupture area, dip angle, depth, etc. The motions are not time dependent using this approach. Attenuation curves can then be applied to calculate the PGA.

Both approaches require ground motion attenuation models (or relationships). Probabilistic maps can be used for preliminary evaluations for risk analysis and for the design of ordinary and noncritical construction. The deterministic approach is more reliable and should be used for all final design of critical structures (ref. 13-4).

13.2.1.7 Earthquake Force. The force of an earthquake is normally given in terms of magnitude or intensity as defined below.

13.2.1.7.1 Earthquake Magnitude. The magnitude of an earthquake is a measure of the size of an earthquake related to the total strain energy released as measured in displacement amplitudes of seismic waves of certain periods and at certain distances from sources. Earthquake magnitude is a logarithmic measure of earthquake size. The most common magnitude scales include:

- Body wave magnitude (M_b)—Developed to measure the magnitude of deep focus earthquakes, which do not ordinarily set up detectable surface waves with long periods. It is measured as the common logarithm of displacement amplitude in micrometers of the P-wave with period near 1 s.

- Local magnitude (M_L)—Original magnitude definition by Richter and applies only to earthquakes having focal depths smaller than ≈30 km. It is measured as the common logarithm of the displacement amplitude (μ). Only used when seismographs are within 600 km (370 mi) of the earthquake.

- Surface wave magnitude (M_s)—Developed to measure the magnitude of shallow focus earthquakes at relatively long distances, and is measured as the common logarithm of the resultant of the maximum, mutually perpendicular horizontal displacement amplitudes, in microns of the 20-s-period surface waves.

- Richter magnitude (M)—Is usually M_L up to 5.0, M_s from 5.9 to 8.0, and M_w up to 8.3.

- Seismic moment (M_o)—Indirect measure of earthquake energy, and a direct function of rigidity modulus (G), area of fault movement (A), and average static displacement (D), in dyne cm units. $M_o = GAD$.

- Seismic moment scale (M_w)—Can be used over a wide range of magnitudes and distances. Defines magnitude based on the seismic moment:

$$M_w = 2/3 \log M_o - 10.7 \ . \quad (13.1)$$

13.2.1.7.2 Maximum Earthquake Definitions. The definitions for maximum earthquake are as follows:

- Maximum credible earthquake (MCE)—Largest earthquake that reasonably can be expected to occur. The MCE must be obtained by the deterministic method. The MCE is usually taken at a mean +1 standard deviation of recorded earthquake motions. This provides reasonable design conservatism by bracketing the spread of observed motions at the 84th percentile level. This is also referred to as maximum expectable earthquake.

- Maximum possible earthquake—Largest earthquake that can be postulated to occur (probable magnitude 8.7 to 9.5).

- Maximum probable earthquake (MPE)—Worst historic earthquake. It is an earthquake that can be obtained by a seismic probability calculation taken for a recurrence in a selected number of years; i.e., it produces the 100-yr recurrence earthquake, or maximum earthquake that may occur during the life of the structure at a specified probabilistic level of occurrence.

- Maximum design earthquake (MDE)—Level of ground motion at the structure site of concern; takes many factors—earthquake frequency/intensity, structure life, life/property hazard, political and economic constraints—into account. For a critical structure, the MDE is the same as the MCE and must be obtained by a deterministic procedure.

- Operating basis earthquake (OBE)—Earthquake for which the structure is designed to remain operational. The OBE is an engineering determination based on a probability or other estimation that the earthquake might happen during the life of a structure. Seismic probability can give a projected economic lifetime of the structure, commonly 29–40 yr for a nuclear plant, 50 yr for a commercial building, and 100–150 yr for a dam. However, there are huge error bands associated with this method.

13.2.1.7.3 Earthquake Intensity. Earthquake intensity is a subjective numerical guide that describes the effects of an earthquake on people, structures, and the Earth's surface at a site (shaking). Generally, earthquake intensity will decrease with distance from the source. The Modified Mercalli Intensity (MMI) scale of 1931 is the intensity scale used in the United States, with intensities indicated by Roman numerals from I to XII. See tables 13-2 and 13-3. See sections 13.2.1.8 and 13.2.1.9 on ShakeMap and SHAKE2000 models, respectively, regarding the potential of earthquake shaking as opposed to earthquake magnitude. More on earthquake intensity is provided in section 13.2.1.12 regarding Central and Eastern U.S. earthquakes.

Table 13-2. Relationship between earthquake magnitude and intensity.

Magnitude Class	Magnitude–Richter Scale	Intensity–Modified Mercalli Scale	Area Felt		Distance Felt		≈Equivalent TNT Energy* (≈tons)
			(≈km^2)	(≈mi^2)	(≈km)	(≈mi)	
Micro	1.0 – 3.0	I	–	–	–	–	–
Minor	3.0 – 3.9	II – III	1,940	750	24	15	–
Light	4.0* – 4.9	IV – V	7,770	3,000	48	30	1,010
Moderate	5.0* – 5.9	VI – VII	38,850	15,000	113	70	31,800
Strong	6.0* – 6.9	VII – VIII	129,500	50,000	200	125	1.01×10^6
Major	7.0* – 7.9	VIII or higher	–	–	–	–	3.18×10^7
Great	>8.0*	–	–	–	–	–	1.01×10^9
Great	9.0*	–	–	–	–	–	3.18×10^{10}

*Equivalent TNT energy is based on this magnitude.

An approximate relationship between earthquake magnitude and intensity, and other various characteristics is presented in table 13-2. Table 13-3 also presents intensities with associated velocities and accelerations as used in the USGS ShakeMap program.

Table 13-3. An adjusted MMI used in ShakeMap.

Instrumental Intensity	Acceleration (%g)	Velocity (cm/s)	Perceived Shaking	Potential Damage
I	<0.17	<0.1	Not felt	None
II, III	0.17–1.4	0.1–1.1	Weak	None
IV	1.4–3.9	1.1–3.4	Light	None
V	3.9–9.2	3.4–8.1	Moderate	Very light
VI	9.2–18	8.1–16	Strong	Light
VII	18–34	16–31	Very strong	Moderate
VIII	34–65	31–60	Severe	Moderate to heavy
IX	65–124	60–116	Violent	Heavy
X+	>124	>116	Extreme	Very heavy

13.2.1.8 ShakeMap. ShakeMap is a USGS agency tool that produces California computerized maps of the intensity of ground shaking, rather than the magnitude; i.e., the total amount of energy released, of the earthquake, and is valuable for emergency-response agencies. The USGS ShakeMap Web site is at <http://earthquake.usgs.gov/shakemap> (ref. 13-7). ShakeMap produces an estimated MMI Scale (I_{mm}) map from intensity I to X+ (from not being felt to extreme shaking). See table 13-3. In general, intensity decreases as one moves away from the fault. ShakeMap produces estimated ground motions using a predictive empirical attenuation relationship that allows the estimation of peak ground motions at a given distance and for an assumed magnitude. The relationship of Boore et al. (ref. 13-8) for peak and spectral acceleration, and that of Joyner and Boore (ref. 13-9) for peak velocity are used which gives average peak ground motion values. ShakeMap initially generates peak ground acceleration (%g) and velocity (cm/s) contoured maps, and then estimates an MMI map. Spectral response maps are also generated following earthquakes larger than magnitude 5.5, giving data useful for engineers determining how a structure will react to these ground motions in determining building code for design. A focal mechanism diagram indicating the direction of slip on the fault is also calculated from the polarity of the recorded P-wave's first motions. Finally, ShakeMap estimates the peak ground motions for scenario earthquakes by using the relationships mentioned above and receiving parametric data from the station network, including PGA, PGV, and peak response spectral amplitudes (at 0.3, 1, and 3 s)—all associated with rock sites. The amplitude at a location is then corrected for the exact site's soil conditions. The earthquake epicenter location does not have any effect on the resulting average peak ground motions, only on the location and dimensions of the fault matter.

One might think that earthquakes with similar magnitudes would produce similar shaking, but this is not always the case. The difference in earthquake focal depth can result in substantially different levels of shaking and damage. The 6.7 magnitude 1994 Northridge, CA, earthquake—with epicenter depth of only approximately 5 to 18 km (3 to 11 mi)—produced a shaking intensity of IX (violent), whereas the 6.8 magnitude Nisqually, WA, earthquake—with a depth of approximately 48 to 58 km (30 to 36 mi)—reached only VII (very strong) in terms of shaking.

13.2.1.9 SHAKE2000. SHAKE2000 is a Windows-based, user-friendly computer program for the one-dimensional analysis of geotechnical earthquake engineering problems that helps engineers and researchers with the analysis of site-specific response and evaluation of earthquake effects on soil deposits. See Web site <http://www.shake2000.com> (ref. 13-10). It can be a learning tool for students of geotechnical engineering, and can serve practitioners of geotechnical earthquake engineering as a scoping tool to provide a first approximation for

the dynamic response of a site. The solution of a particular problem requires use of realistic ground motions (loading), modeling site dynamics (response), and the interpretation and prediction of soil behavior subject to dynamic loading (analysis). SHAKE2000, developed to help the engineer address geotechnical aspects of earthquake engineering of a project site, includes the following:

- Numerous attenuation relationships for estimating peak horizontal acceleration and velocity with distance, and for the pseudoacceleration and pseudovelocity response spectra
- Design spectra
- Calculation of permanent slope displacements
- Estimating seismic hazard
- Estimating the maximum shear moduli (G_{max}) and computation of cyclic stress ratio
- Estimation of cyclic resistance ratio required to initiate liquefaction
- Calculation of settlement induced by earthquake shaking
- Obtaining the PGA
- A database of 2,500+ files of recorded and artificially-generated ground motions
- Generation of artificial acceleration records
- Computation of response spectra for a ground motion
- Evaluation of liquefaction-induced ground deformation
- Printing of output results for each graph in table form.

The output from SHAKE2000 provides the engineer with a suite of tools that facilitates the translation of the output from SHAKE2000 into predictions of liquefaction potential, and earthquake-induced displacements of a site and its ability to graphically display the results of the ground motion and other analyses. For example, values of peak acceleration are displayed versus depth; time history accelerations are displayed as values of acceleration versus time; attenuation relationships are displayed as a log-log graph of acceleration versus distance; etc. SHAKE2000 improvements are ongoing.

13.2.1.10 Earthquake Probability. Presented in figure 13-1 is a depiction of damaging earthquake potential occurring within the contiguous United States, as expressed in peak acceleration (%g) having a 10-percent probability of exceedance (90-percent probability of not being exceeded) in 50 yr (a return period of ≈500 yr). Peak horizontal ground acceleration is defined as the fastest measured change in speed for a particle at ground level that is moving horizontally due to an earthquake. This map is a suitable indicator of probabilistic earthquake hazards for general purposes, as this reflects the traditional values used in most building codes. Peak ground acceleration is a good index to determine hazards for short buildings.

Since USGS national earthquake (seismic) hazard maps are now produced for different probabilities and time periods, the choice to use depends on the users' needs. Bridge or dam builders would want longer periods of time and a smaller likelihood that shaking will be exceeded than a homebuilder would. Therefore, bridge designers would use a hazard map with a 2-percent chance of a given level of shaking being exceeded in 50 yr, while a homebuilder is likely to use a map with a 10-percent chance of being exceeded in 50 yr (ref. 13-12).

The older earthquake velocity maps provided longer period ground motion in the shaking demand for taller structures. Figure 13-2 presents the U.S. spectral acceleration for a 2-percent probability of exceedance during a 1-s period over 50 yr (≈2,500-yr return period). These replace velocity maps by providing a better long-period anchor for a uniform hazard spectrum.

Figure 13-3 presents a U.S. spectral acceleration map for a 2-percent probability exceedance that gives a short-period anchor for a design spectrum. Figures 13-1 through 13-3 (plus other geological probability maps) can all be obtained at the USGS Web site: <http://eqhazmaps.usgs.gov/html/us2002.html>.

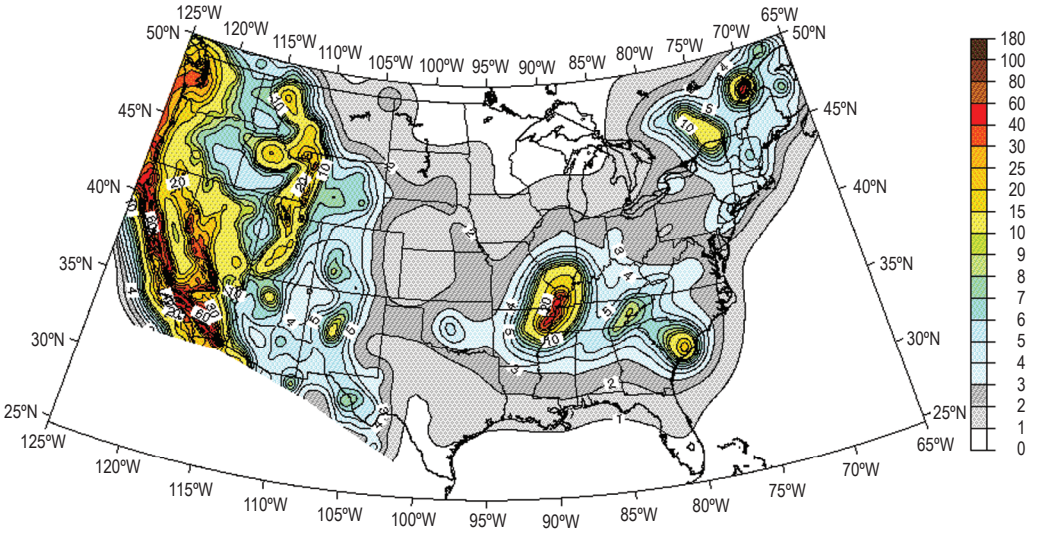

Figure 13-1. Earthquake peak acceleration (%g) with a 10-percent probability of exceedance in 50 yr within the contiguous United States (ref. 13-11).

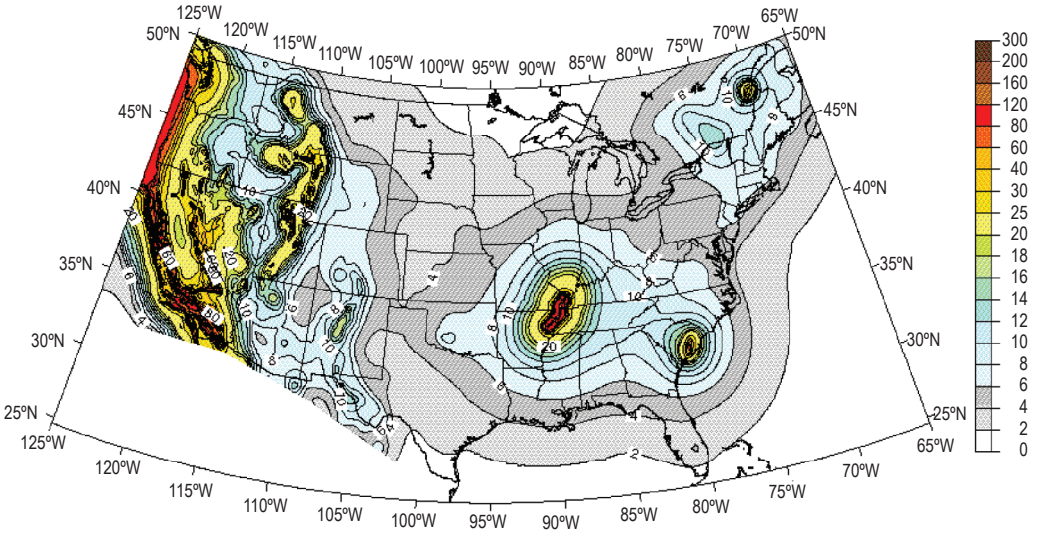

Figure 13-2. Earthquake 1-s spectral acceleration (%g) with 2-percent probability of exceedance in 50 yr within the contiguous United States (ref. 13-11).

The global tectonic activity map given in figure 13-4 presents plate boundaries and macroscale tectonic structures depicted at scale for both continental and oceanic crust. A representative sampling of volcanic hotspots are georegistered to known areas of recent volcanism (≈Holocene Epoch). Crustal motions at oceanic-spreading ridges are at a rate measured in centimeters per year derived from the Northwestern University VELocity-1 (NUVEL-1) model. This Digital World Tectonic Activity Map information is available (ref. 13-13). Also, a 200,855 global epicenter event map from 1963–1998, along with very long baseline interferometry crustal motion maps, are also available here.

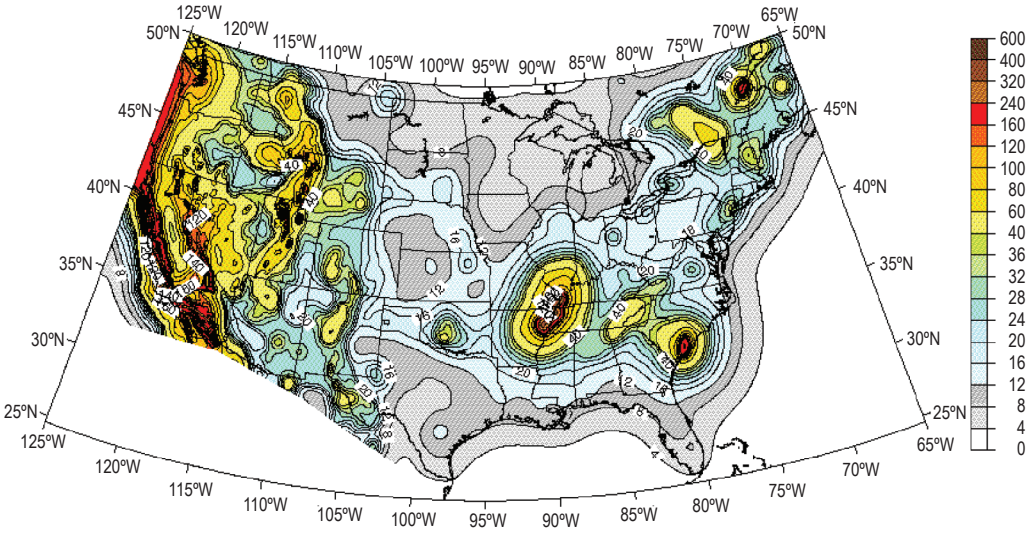

Figure 13-3. Earthquake 0.2-s spectral acceleration (%g) with 2-percent probability of exceedance in 50 yr within the contiguous United States (ref. 13-11).

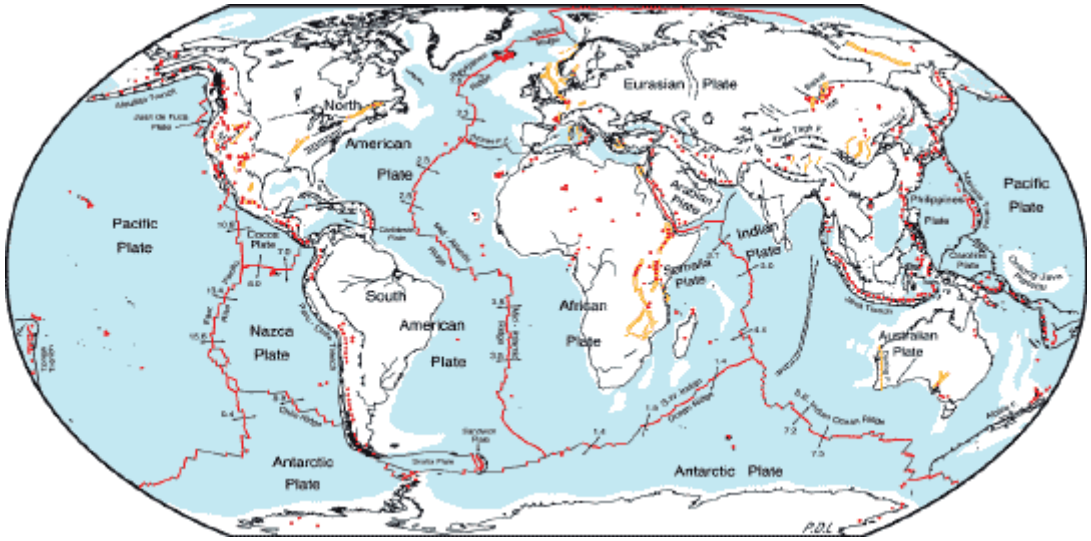

Figure 13-4. Global tectonic activity map (ref. 13-13).

U.S. velocity attenuation curves can be replaced by long-period spectral attenuation curves (fig. 13-5), and also U.S. acceleration attenuation curves can be replaced by short-period spectral attenuation curves (fig. 13-6). Figure 13-6 presents spectral acceleration curves for the 2- and 10-percent probability levels, pertaining to California, Western, and Central and Eastern United States, for high, moderate, and low seismology.

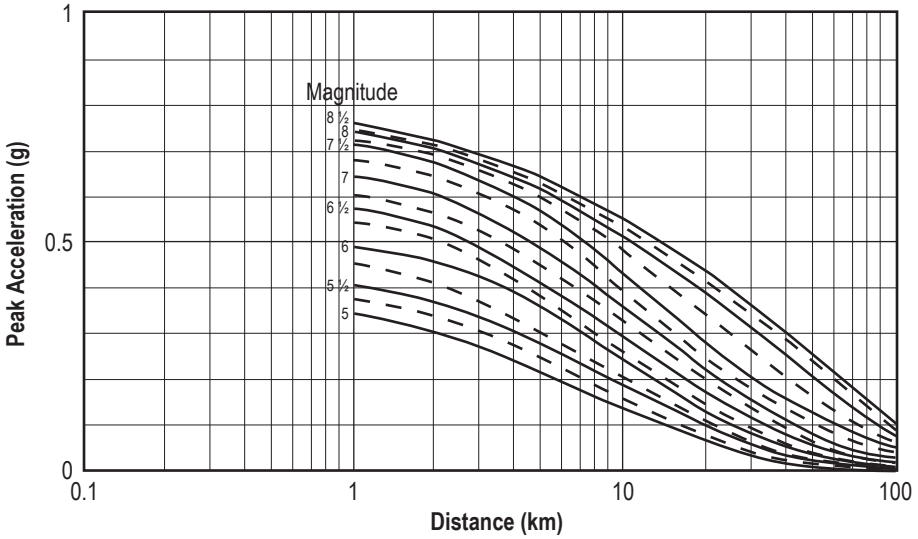

Figure 13-5. Earthquake attenuation curves (ref. 13-14).

Figure 13-7 presents the entire Northern Hemisphere hazard map of peak ground acceleration from Alaska (Kodiak Island) down through Central America. Global seismic hazard maps can be obtained from the GSHAP Web site at <http://seismo.ethz.ch/GSHAP/> (ref. 13-16).

13.2.1.11 California Earthquakes. Since sections 13.3 and 13.4 present and discuss earthquake and seismic activity potential related to EAFB and VAFB, it is appropriate that a brief general discussion on California earthquakes and predictions be given here.

Between 1912 and 1984 there have been 38 recorded southern California earthquakes with magnitudes of 6.0 or greater (ref. 13-18). Cousineau selectively lists 46 active and potentially active southern California faults which all have a maximum credible earthquake magnitude potential of 6.25 and higher. The San Andreas Fault poses the greatest hazard to a NASA site from the standpoint of accelerations or shaking intensity. Detailed geologic studies indicate that this fault is likely to generate the largest earthquake of any fault in southern California and such an event is imminent (ref. 13-18).

Cousineau presents the work of Krinitizsky and Chang (ref. 13-19) (fig. 13-8) in which western U.S. earthquakes have been analyzed relating intensity to epicentral distance over a range of earthquake magnitudes. Figure 13-9 presents the relationship between fault length (length of surface rupture) and earthquake magnitude, based on the work of Bonilla (ref. 13-20) and Greensfelder (ref. 13-21).

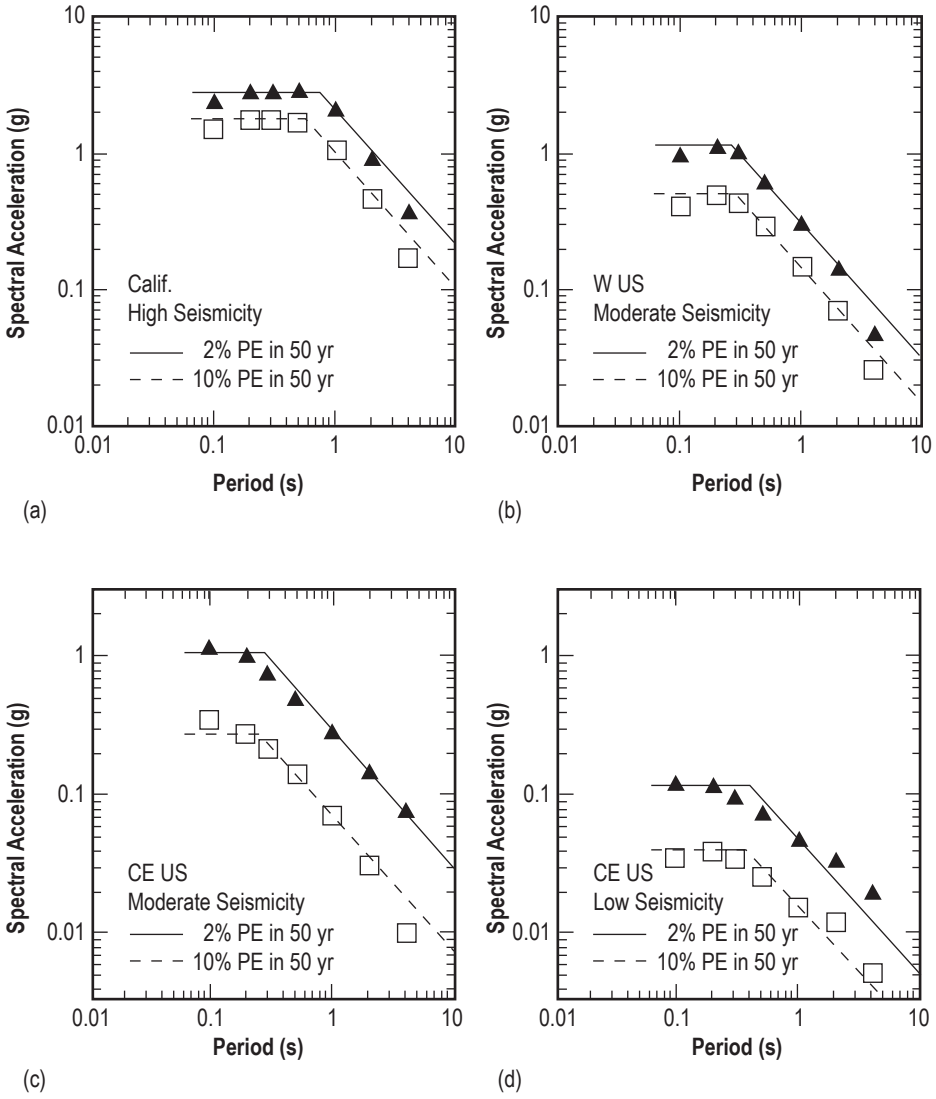

Figure 13-6. Spectral acceleration curves at 2- and 10-percent probability of exceedance levels in 50 yr in (a) California—high seismicity, (b) Western United States—moderate seismicity, (c) Central and Eastern United States—moderate seismicity, and (d) Central and Eastern United States—low seismicity (ref. 13-15).

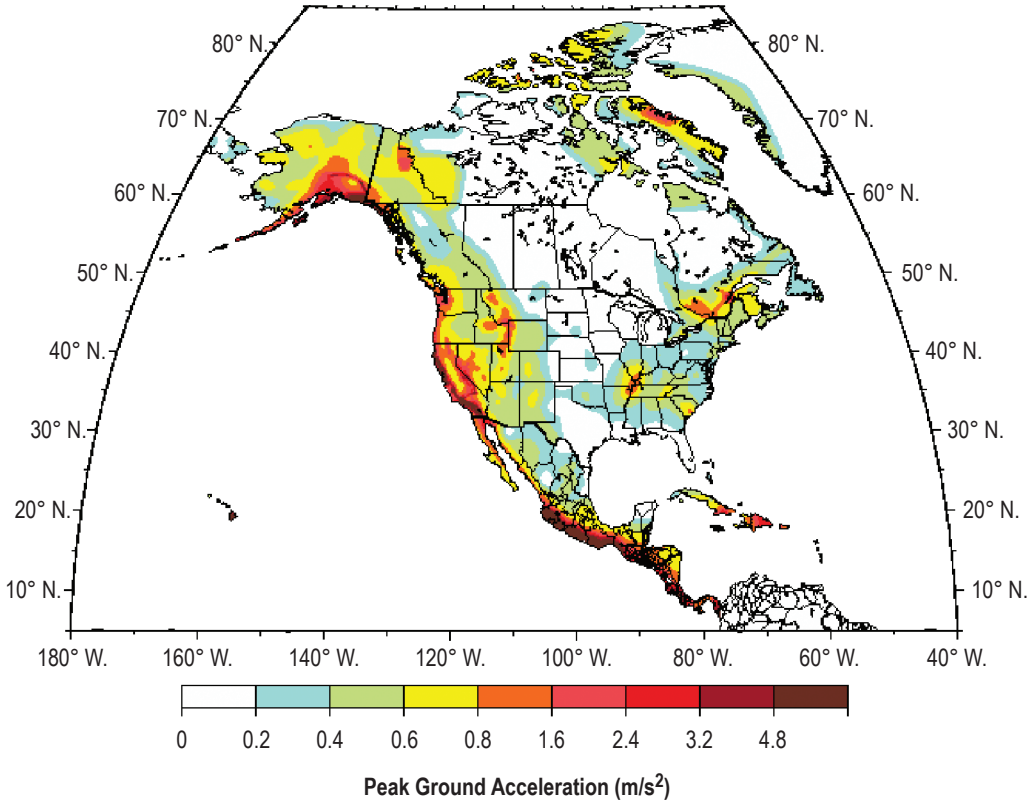

Figure 13-7. Seismic hazard map of North and Central America and the Caribbean. PGA with a 10-percent chance of exceedance in 50 yr (m/s^2) (ref. 13-17).

A seismic shaking hazard map (peak ground acceleration in %g) for California is presented in figure 13-10. It presents a 10-percent probability of being exceeded in 50 yr, based on the USGS/CGS Probabilistic Seismic Hazards Assessment Model of 2002/2003 at Web site <http://www.consrv.ca.gov/CGS/rghm/pshamap/pshamain.html> (ref. 13-22).

In U.S. Geological Survey Fact Sheet 039-03 (ref. 13-23), USGS and other scientists conclude that there is a 62-percent probability of at least one magnitude 6.7 or greater quake capable of causing widespread damage, striking the San Francisco Bay, CA, region from 2003 to 2032. See Web site <http://pubs.usgs.gov/fs/2003/fs039-03/fs039-3.pdf>.

13.2.1.12 Central and Eastern U.S. Earthquakes. Earthquakes in the Central and Eastern United States, although less frequent, are typically felt over a much broader region than in the Western United States, by as much as 10 times greater than a similar magnitude earthquake on the west coast. The Eastern United States is far from any plate boundaries, with no active faults reaching the surface. But probably numerous smaller or more deeply buried faults can remain undetected. However, as in most other areas east of the Rockies, the best guide to earthquake hazards in the seismic zone is the earthquakes themselves. Most historical Eastern and Central U.S. earthquakes consist mainly of intensity rather than magnitude measurements. The MMI scale—expressed in Roman numerals—is described in table 13-3.

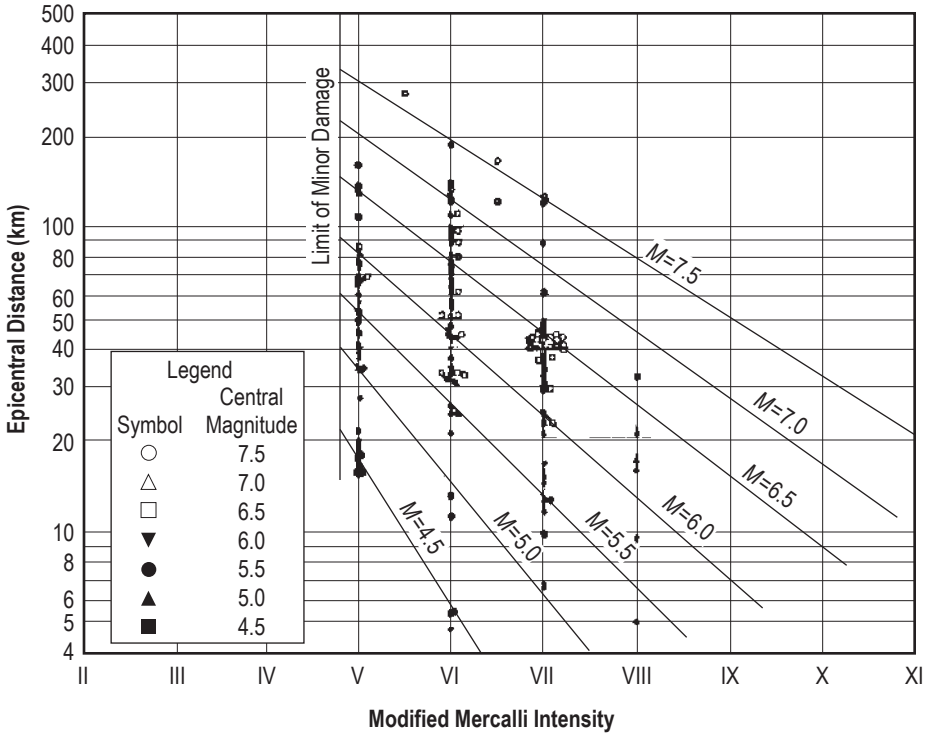

Figure 13-8. Intensity versus magnitude and epicentral distance (ref. 13-18).

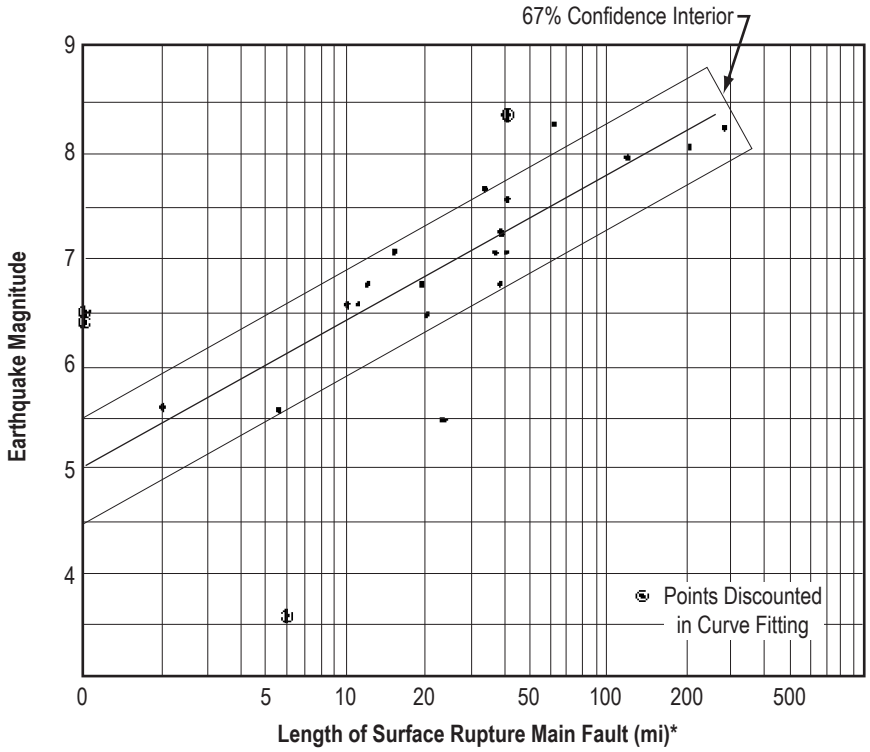

Figure 13-9. Earthquake magnitude versus fault rupture length (ref. 13-18) (*multiply miles by 1.609344 to get kilometers).

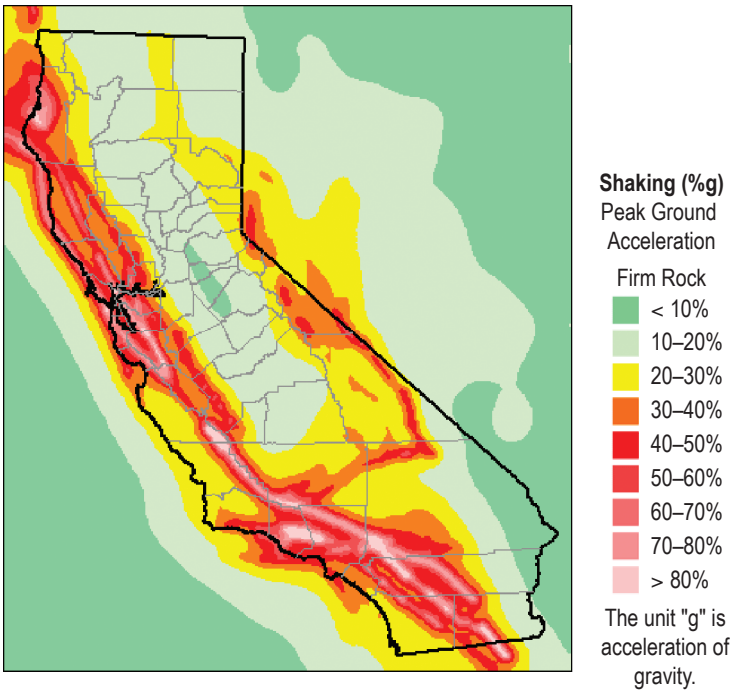

Figure 13-10. Seismic shaking hazard map (peak ground acceleration in %g) for California (ref. 13-22).

The earthquakes that occurred in the Mississippi Valley (New Madrid) in late 1811 and early 1812 rank as the largest known shocks, with the largest potential damage and felt areas known, since the settlement of America. An estimated area of 600,000 km^2 (232,000 mi^2) had potential damage of MMI ≥ level VII. The 1964 Alaskan earthquake yielded a similar damage area of about 210,000 to 250,000 km^2 (81,100 to 96,500 mi^2), while the 1906 San Francisco earthquake had an area with MMI ≥ level VII of ≈30,000 km^2.

Figures 13-1 through 13-3 also apply to the central and eastern portions of the United States. The Mississippi Valley region (1811–1812 M8.0 New Madrid) along with the South Carolina region (1886 M7.3 Charleston) earthquakes anchor the potentially most active seismic zones east of the Rockies. Figure 13-11 presents a Central United States Earthquake Consortium (CUSEC) map of the New Madrid seismic zone in which a hypothetical magnitude 8.0 (VIII) MMI earthquake would be felt intensity wise throughout this zone. A similar New Madrid magnitude map (from CUSEC) presenting earthquake peak ground acceleration (%g) with a 2-percent probability of exceedance in 50 yr is given in figure 13-12.

Analyzing and dating sand blow deposits around the New Madrid seismic zone has resulted in suggesting that major earthquakes of magnitude 7.0 or greater reoccur in this region approximately every 500 yr, with the last occurrence being in 1811–1812 (ref. 13-12). The New Madrid along with the Wabash Valley seismic zones constitutes the hotspots for Central United States earthquake potential.

Bakun, Johnston, and Hopper (ref. 13-24) constructed a model that estimates locations and magnitudes of earthquakes in Eastern North America from past MMIs. Their resultant equation relating MMI versus epicentral distance for any inputted magnitude is

$$\text{MMI} = 1.41 + 1.68 \times \mathbf{M} - 0.00345 \times \text{median } \Delta - 2.08\log(\text{median } \Delta) \quad , \tag{13.2}$$

where **M** is moment magnitude and Δ is the distance (km) from the epicenter.

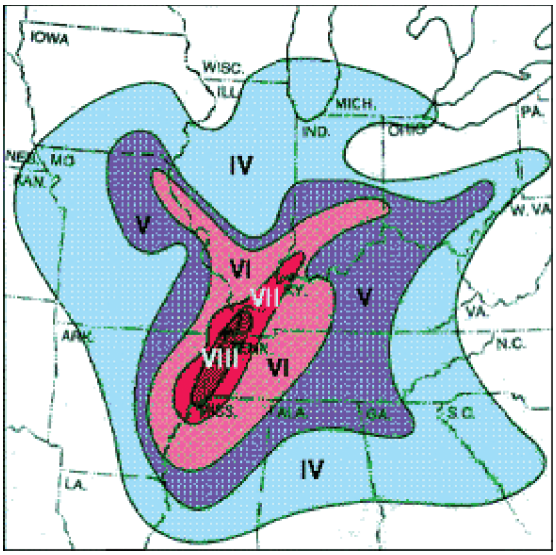

Figure 13-11. New Madrid seismic zone presenting a hypothetical MMI magnitude 8.0 (VIII) earthquake intensity pattern (Assoc. of CUSEC State Geologists).

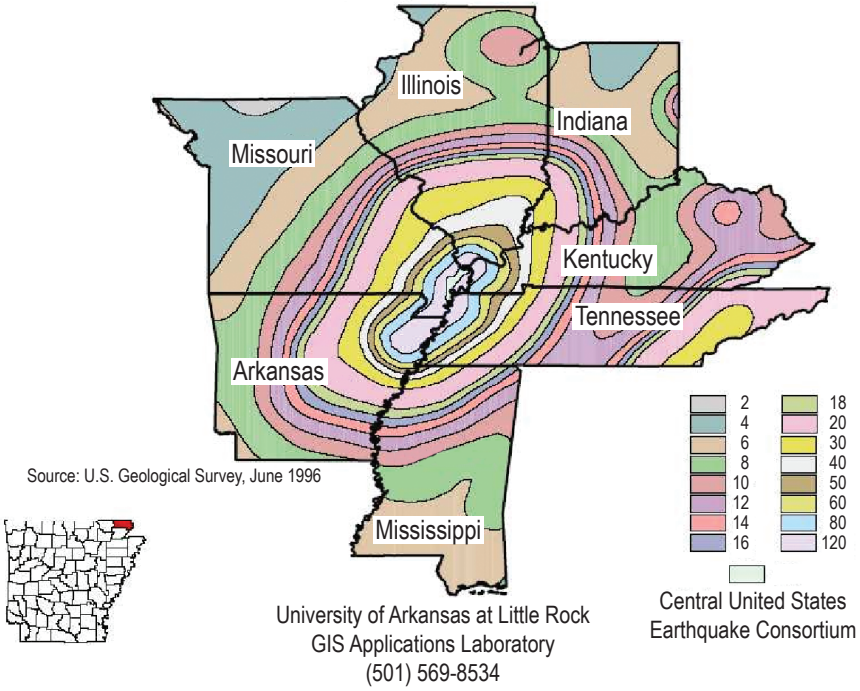

Figure 13-12. Peak ground acceleration (%g) with 2-percent probability of exceedance in 50 yr for seven CUSEC states (Assoc. of CUSEC State Geologists).

Therefore, Central and Eastern United States earthquake magnitudes can be estimated directly from MMI observations.

13.2.1.13 Evaluating Ground Motion Hazard

13.2.1.13.1 Ground Motion Attenuation Relations. The most commonly used ground motion intensity measure is spectral acceleration at a specific damping level (usually 5 percent) (ref. 13-25). Attenuation relations for this parameter are available for each of the three generally recognized tectonic regimes—active regions, subduction zones, and intraplate regions, with attenuation relations for active regions being the most abundant. Attenuation relationships are also available for other intensity measures, including peak horizontal velocity, vertical spectral acceleration, Arias intensity, duration-related parameters, and mean period. The response of many classes of structures is sensitive to more than one of these intensity measures, and hence requires a probabilistic representation of multiple intensity measures (IMs). Most all attenuation relations are derived from, or calibrated against, strong ground motion recordings. A number of IMs can be used to represent the amplitude, frequency content, or duration characteristics of earthquake accelerograms. The most widely used IM in earthquake engineering is spectral acceleration.

13.2.1.13.2 Amplitude Parameters. The accelerograms give acceleration with velocities and displacements obtained through time integration. Therefore, peak values of these three parameters can be obtained. The integration process tends to dilute high-frequency components of the motion and enhance low-frequency components. Therefore, peak horizontal acceleration (PHA) is a relatively high-frequency ground motion parameter, whereas peak horizontal velocity (PHV) and peak horizontal displacement (PHD) are more sensitive to mid- and low-range frequencies, respectively, although PHD has not been used extensively as a demand parameter.

13.2.1.13.3 Frequency Content Parameters. The frequency content of accelerograms is best measured with the use of spectra—either Fourier amplitude spectra or response spectra. Acceleration response spectra are widely used in structural engineering, as well as response spectral displacement and pseudovelocity. As an alternate to complete spectra, frequency content can also be approximately measured by individual period parameters, such as predominant period (T_p) and mean period (T_m). Pulse period (T_v) has been used for near-fault motions. Parameter T_m provides a reasonable single-parameter representation of ordinary (nonnear-fault) ground motions, whereas T_v provides a better representation of near-fault motions.

13.2.1.13.4 Duration Parameters. The duration of strong ground motion is related to the time for rupture to spread across the fault surface, and therefore is correlated to fault rupture area, which in turn is correlated to magnitude. Thereby, duration tends to scale with magnitude. Various duration measures are used, such as bracketed duration—the time between first and last exceedence of a threshold acceleration (usually 0.05 g). Significant duration is defined as the time interval across which a specified amount of energy in the accelerogram is dissipated. The equivalent number of uniform stress cycles (N) is sometimes substituted for duration and is obtained by counting a weighted number of cycles in an accelerogram, with the weighting factors being application dependent (ref. 13-25).

13.2.1.13.5 Magnitude-Area Scaling Relationships. Magnitude-area scaling relationships are used to relate the size of a ruptured fault segment (area) to the energy release from the event (magnitude). Since magnitude is also dependent on the average stress drop across the rupture, magnitude-area relations inherently also assume a constant stress drop. Mean magnitude-area relationships were developed (ref. 13-26) between moment magnitude and fault length (along strike), fault width (dimension down dip), and fault area—for all rupture mechanisms (strike-slip, reverse, and normal).

13.2.1.13.6 Earthquake Magnitude Versus Rupture Parameters. The relationships between moment magnitude (**M***)* (or M_w), surface rupture length, subsurface rupture length, rupture width, rupture area, and the maximum and average surface displacement (per event) can be obtained from the empirical relationships

developed by Wells and Coppersmith (ref. 13-26) in their analysis of 244 historic global earthquakes. Some of their relationships are presented in this section. Some findings include the following:

- The length of rupture at the surface is equal to ≈75 percent of the subsurface rupture length, with the ratio of surface rupture length to subsurface rupture length increasing with magnitude.

- The average surface displacement per event is approximately one-half the maximum surface displacement per event.

- The average subsurface displacement on the fault plane is less than the maximum surface displacement but more than the average surface displacement. Indicating that slip on the fault plane at depth is manifested by similar displacements at the surface. Log-linear regressions between earthquake magnitude with rupture area and both surface and subsurface rupture length are well correlated. Three of Wells and Coppersmith relationships correlating earthquake moment magnitude (M) with respect to surface rupture length, rupture area, and maximum displacement are presented in figure 13-13.

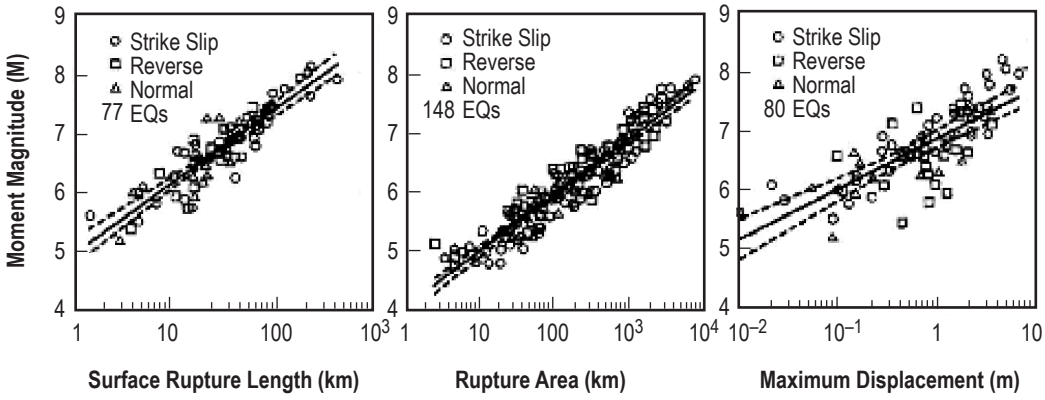

Figure 13-13. Relationships between earthquake moment magnitude and surface rupture length, rupture area, and maximum displacement. Short, dashed lines indicate 95-percent confidence interval (ref. 13-26).

13.2.1.13.7 Magnitude Recurrence Relations. Once the location and magnitude range for a seismic source have been identified, one characterizes the relative likelihood of different magnitude earthquakes on the fault, and the rate of occurrence of earthquakes. For a given fault, moment release must balance moment buildup, and release is proportional to slip rate (s), which is the long-term, time-averaged relative velocity of block movements on opposite sides of the fault. Characterizing magnitude recurrence relations involves (1) estimation of a probability density function on magnitude ($f(m)$), and (2) estimation of the rate of earthquake occurrence by one of the following:

- Earthquakes occur as a Poisson process—the event has no influence on the timing of future events.
- The earthquake releases stress on the fault and thus reduces the probability of future events.

13.2.1.13.8 Other Ground Motion Parameters. Other ground motion parameters besides spectral acceleration and PHA can affect the nonlinear response and performance of structures such as buildings and bridges. These other parameters include duration, mean period, PHV, and vertical ground motion parameters (for long-span

structures). For geotechnical structures, such parameters may include Arias intensity, duration, mean period, and equivalent number of uniform stress cycles.

13.2.1.13.9 Characteristics of Near-Fault Ground Motions. The near-fault zone is typically assumed to be within about 20–60 km from a ruptured fault, and ground motions are significantly influenced by the rupture mechanism. These factors result in ground motion effects, termed "rupture directivity" (forward or backward) and "fling step." Modeling rupture directivity effects is handled by (1) spectral acceleration, (2) duration and equivalent number of uniform stress cycles, (3) peak horizontal velocity, (4) pulse period, and (5) number of significant pulses. Fling step, being a result of a static ground displacement, is generally characterized by a unidirectional velocity pulse and a monotonic step in the displacement time history <http://nisee.berkeley.edu/library/PEER-200109/> (ref. 13-25).

13.2.2 Tsunamis, Seiches, Storm Surges, and Floods

13.2.2.1 Tsunamis. A tsunami is a rapidly moving ocean wave train, or series of waves, generated in a body of water by an impulsive disturbance that vertically displaces the water column. Tsunamis are also called seismic sea waves or Pacific-wide tsunamis when they are generated by submarine earthquakes (>7.5 magnitude on Richter scale) that suddenly elevate or lower portions of the sea floor. They can also be caused by underwater landslides (a slide or slump) producing a local tsunami. Other generation sources can be by submarine volcanic eruptions; by above-water rock, mud, lava, ice, and land slides; by nuclear explosions or other anthropogenic ways; and by the rare water impact of cosmic bodies, such as meteorites, comets, or asteroids.

The tsunami height is defined as the peak to trough excursion of the wave. The amplitude is half the height. Runup heights are based on the maximum height reached by the wave inland above sea level at the arrival time. Runup factor is the runup height divided by the deepwater wave amplitude. Inundation is the maximum land area covered (flooded) by water inland from the coastline (ref. 13-27). Areas at greatest risk are <8 m (<25 ft) above sea level and within 1.6 km (1 mi) of the shoreline (ref. 13-28).

Pacific-wide tsunamis can travel up to speeds of 800 km/hr (500 mph) and can cross an ocean in <1 day. Their wavelengths are long—more than 500 km (300 mi). Wave periods can vary from 5 to 90 min (ref. 13-29). Their amplitudes in deep water are small (<1 m), but as they approach a shoreline, their large volume of water piles up into sizable bore or breaking waves. Since the period of the wave remains constant as the wave velocity drops, the wave height greatly increases. The configuration of the shoreline and tidal and wind conditions can form waves over 10 m (33 ft) high. Runup heights can exceed 30 m (100 ft) (ref. 13-30).

The Pacific is by far the most active zone for tsunami generation, but tsunamis have been generated in the Caribbean and the Atlantic Ocean. The Caribbean has had 90 local tsunamis since 1498 (ref. 13-27). Over the last 100 yr, Caribbean tsunamis have occurred at the rate of one about every 3 yr (ref. 13-31). There have been 40 tsunamis affecting the Eastern United States since 1600 (ref. 13-32). Landslide-generated tsunamis are a significant serologic hazard in Pacific west coastal areas of Alaska, British Columbia, Washington, Oregon, and California where rapidly deposited sediments accumulate on steep underwater slopes. While the area's high seismicity often gives rise to tsunamigenic failures, many events have occurred in the absence of earthquakes (ref. 13-33). From 1992 through 1996, eight large earthquakes generated tsunamis with runup heights ranging from 5 to 30 m (16 to 100 ft) around the Pacific (ref. 13-34). Hawaii has the highest risk in the world, averaging one tsunami every year with a damaging occurrence every 7 yr. Hawaii has experienced 95 tsunamis over 175 yr (1813–1988), with 15 resulting in significant damage. Over the last 100 yr, only four local tsunamis have been generated, with only one (in 1868) being destructive with a runup of ≈20 m (≈65 ft) (ref. 13-35). From 1900 through 1999,

the 10-yr average number (104.3) of worldwide damaging and nondamaging tsunamis is 14.1 versus 90.2, respectively. Similar statistics for the U.S. Pacific coast since 1788 are 21 damaging and 42 nondamaging tsunamis (ref. 13-36).

In 1948, the U.S. Coast and Geodetic Survey team established the Pacific Tsunami Warning Center in Hawaii as a tsunami warning system for the Pacific Ocean, so the arrival of tsunamis from distant sources can now be anticipated by a few hours. In 1967, the West Coast and Alaska Tsunami Warning Center was established in Alaska. There is currently in place a real-time reporting of tsunamis by the Demonstration of Autonomous Rendezvous Technology network of buoys telemetering tsunami data via a global positioning system to geostationary satellite and then to the National Oceanic and Atmospheric Administration's (NOAA's) Tsunami Warning Centers in Alaska and Hawaii, and to the NOAA/Pacific Marine Environmental Laboratory. Prediction of wave height at a specific location, or how many successive waves there will be, is not currently possible.

13.2.2.2 Seiches. A seiche (meaning sloshing) is a long surface wavelength (standing wave) occurring in an enclosed or partially enclosed body of water, when the water surface is disturbed as a result of seismic or atmospheric disturbances. Periodic long waves generated will slosh (oscillate) back and forth across this basin. Its period can vary from a few minutes to several hours and is very dependent on the dimensions and depth of the basin, pond, lake, river, gulf, harbor, reservoir, or bay (ref. 13-37). This includes partially enclosed arms of the sea (bay). Seiches are commonly small in amplitude and are not noticeable. When a large-scale disturbance takes place, however, larger amplitude waves result and can continue to be reflected back and forth across the body of water for hours or days. Disturbances include rapid changes in atmospheric pressure, weather fronts, and shifts in the direction of strong winds. Large seiches can be caused when tsunamis arrive in bays, or when earthquakes and large slope movements initiate them in an enclosed body of water. Seiches can also cause the piling up of water at one end of a lake or bay, given proper steady wind conditions acting on a large fetch area. (See storm surge below.) When the wind dies, the building high water surges back and creates a wave that heads for the opposite shore. Strong winds cause small seiches (<1 ft high) on the Great Lakes almost every day. Seiches on the Great Lakes can reach in excess of 3 m (10 ft) (ref. 13-38). Near enclosed bodies of water, investigation of possible damaging seiche activity should be considered as a part of earthquake and slope movement studies.

13.2.2.3 Storm Surges. Storm surges, or storm rise, are temporary rises in water level caused by wind setup, wave setup, and air pressure drop (ref. 13-37). As a general rule of thumb, a 30-mb drop in surface pressure—from say 1,000 to 970 mb—results in a 0.3-m (1-ft) increase in the ocean level (ref. 13-39). Storm winds blowing across miles of open water also drag water towards the downwind shore, causing a buildup. They produce flooding on ocean coasts as well as on Great Lakes coasts. A lake storm surge may last all day and typically rises about as fast as the on-shore wind speed rises and typically lasts as long as the strong winds are blowing on shore. Great Lakes differences of up to 4.6 m (15 ft) from one end of the basin to the other have been measured (ref. 13-38). An edge wave—a special case of a storm rise—occurs rarely on the Great Lakes, generated by the passage of a damaging thunderstorm or derecho squall line (ref. 13-38).

An oceanic coastal storm or hurricane can cause a coastal storm surge. A hurricane-caused storm surge can produce a large dome of water often 80 to 160 km (50 to 100 mi) wide, which can raise sea levels on ocean coasts by 3 to 9 m (10 to 30 ft) near where it makes landfall. The surge duration can last several hours. It simply pushes water toward the shore by the force of the winds swirling around the storm. The right front quadrant of an Atlantic or Gulf hurricane or tropical storm typically contains the strongest winds and, therefore, the highest storm surge. The maximum surge normally occurs 16 to 32 km (10 to 20 mi) to the right of the eye.

The stronger the hurricane and the shallower the offshore water, the higher the surge will be. Also, the storm surge can be greater due to superimposed waves, and if the storm comes in at high tide (ref. 13-40). Inland surge penetration will be a function of the height and duration of the surge and the slope of the land with its obstacles (ref. 13-41). A storm surge is normally defined as the elevation of water generated by a hurricane above or below the normal astronomical tide. Whereas, a storm tide is the total elevation, including the astronomical tide, above or below a standard datum (ref. 13-40). NOAA/National Weather Service (NWS) forecasters use the Sea, Lake, and Overland Surges from Hurricanes (SLOSH) diagnostic model to simulate storm surge fairly accurately (ref. 3-40). The hurricane's track, size, and intensity are specified, and the SLOSH model wind field is produced which gives surface stresses, ultimately producing inland flooding at various coastal locations. The NOAA/National Hurricane Center (NHC) runs SLOSH diagnostics for 34 Atlantic and Gulf Basins, from Maine to Mexico, along with four Pacific Basins. Each hurricane computed can then indicate the amount of land area that would be expected to be inundated with water from the Maximum Envelope of Water (MEOW) model or the maximum of MEOW (MOM) program (ref. 13-42). Figure 13-14 presents a SPLASH-SLOSH (Special Program to List Amplitudes of Surges from Hurricanes-Sea, Lake, and Overland Surges from Hurricanes) nomogram for peak surge on the open coast by inputting pressure drop; i.e., ambient pressure surrounding the hurricane less its central pressure—and the radius of maximum winds—a 10-min average at 10-m (33-ft) elevation, an indicator of hurricane size. This surge nomogram is valid only for a standard basin and a stationary, standard hurricane over water (ref. 13-40). Correction factors would have to be applied for a nonstandard hurricane or basin configuration. See Jelesnianski and Holland (ref. 13-40) for proper correction factors. The Melbourne, FL, NOAA/NWS has produced The Florida Hurricane Surge Atlas, which depicts the storm surge threat along Florida's east coast for three categories of hurricanes; <http://www.srh.noaa.gov/mlb/atlas.html> (ref. 13-43). SAIC has developed the Consequences Assessment Tool Set (CATS) that calculates hazards including storm surge, earthquakes, hurricanes, and various type releases into the environment. CATS contains a hurricane storm surge module which utilizes SLOSH and MEOW. See section 12 for more information on hurricanes and their effects.

13.2.2.4 Floods. The USGS defines a flood as: An overflow of water onto lands that are used or usable by man and not normally covered by water (ref. 13-1). Floods have two essential characteristics: (1) The inundation of land is temporary and (2) the land is adjacent to and inundated by overflow from a river, stream, lake, or ocean (ref. 13-44). Statistically, streams will equal or exceed the mean annual flood once every 2.33 yr (ref. 13-45). Flooding can be generally classified three ways—river flood (from heavy rains or melting snow), coastal flood (from tsunamis/tropical storms/hurricanes), and urban flood (urbanization increases runoff). Flooding is a longer term event (up to a week or more), whereas flash flooding normally occurs within minutes to 6 hr of the rain event. Floods are natural, recurring events that become a problem only when they compete with man for the floodplain or flood channel. Rare catastrophic floods, in which water flows above and beyond the floodplains, may have disastrous consequences. Since the weight or density of water is 1,000 kg/m^3 (62.4 lb/ft^3) and flood water typically flows downstream at 3 to 6 m/s (6 to 12 mph), this results in ≈230 kg (≈500 lb) of lateral force against an object the size of a vehicle for each foot the water rises. The water's momentum is transferred to the object. The total flow of water in a river is also proportional to the depth of the river cubed. So if a storm causes a river to be twice as deep as normal, with steady flow, the flow rate will be eight times normal. Rapidly rising water from a flash flood can reach heights of 9 m (30 ft) or more. Flash flood-producing rains can also trigger catastrophic mud slides (ref. 13-46). Historically, catastrophic floods have resulted in loss of life and enormous property destruction. Initially, the greater-than-normal volumes of water, moving at abnormal velocities, are able to erode the land very quickly, picking up large volumes of sediment and debris. As the water and its debris continue downstream, large amounts of material, including manmade objects, are picked up or covered. Floods and flash floods normally occur as a result of cloudbursts, strong thunderstorms, extended rain, heavy rains from hurricanes/tropical storms, and/or rapid snowmelt accompanied by rapid runoff. Natural dams, such as those caused by landslides, as well as manmade dams, result in flooding of land upstream. Disastrous floods may also occur as a result of a sudden release of large amounts of water by ice-jam release or from dam failures.

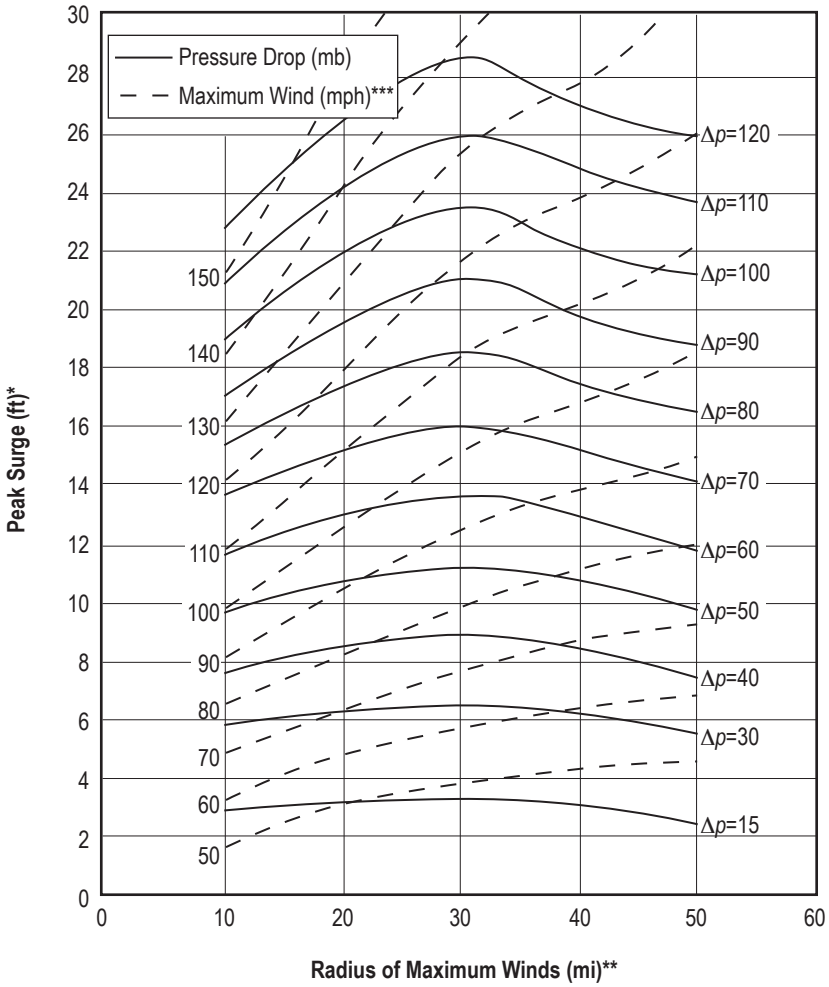

Figure 13-14. Peak surge nomogram on the open coast for a standard hurricane across a standard basin. Pressure drop and radius of maximum winds are input (*multiply feet by 3.048 to get meters, **multiply miles by 1.609344 to get kilometers, and ***multiply mph by 0.44704 to get meters per second) (ref. 13-40).

Floods are normally expressed by federal and state agencies as a 100-yr flood which has a 1 percent (1 in 100) chance of being equaled or exceeded in any given year. Table 13-4 presents the definition for various year floods. Note that water volume increases as the probability decreases. The use of the term "*n* flood year" has caused problems with the public. The term does not mean that a flood occurs every *n* years, but that it has a chance of 1/*n* of occurring in any one year (ref. 13-47).

The Ergonomics and Safety Research Institute and the Federal Emergency Management Agency (FEMA) offer a Web site <http://www.esri.com/hazards/makemap.html> on which an online hazard map can be constructed for most U.S. sites of interest. The hazards include earthquakes, hurricanes, tornadoes, hailstorms, windstorms, and flood hazard areas (refs. 13-8 and 13-48). Their flood hazard map includes 100- or 500-yr floods resulting from any kind of inland or coastal flooding. FEMA also offers Bulletin 17B, *Guidelines for Determining Flood Flow Frequency* in PDF format from their Web site: <http://www.fema.gov/mit/tsd/dl_flow.htm> (ref. 13-49). The guide only describes the data and procedures for computing flood flow frequency curves where stream gauging records of sufficient length are available.

Table 13-4. Definition and description of various year floods (ref. 13-47).

Flood Probabilities for Any One Year			
Year Flood	Probability	Percent	Flows
500	0.002	0.2	Extreme
100	0.010	1	Heavy to extreme
50	0.020	2	Moderate
25	0.040	4	Light to moderate
10	0.100	10	Light
5	0.200	20	Mild

Equation (13) can be used to compute the probability (q) that a flood (or a rainstorm) equal to or larger than a particular value will occur in the next n years (ref. 13-50):

$$q = 1 - (1 - p)^n \quad . \tag{13.3}$$

For example, every year there is a 20-percent chance of having a 5-yr flood. Therefore, to calculate the probability of this 5-yr flood recurring within the next 10 yr, $n=10$ and $p=0.2$, resulting in a probability of $q=0.89$.

Several approaches have been used to avoid the damaging effects of floods. All the approaches make use of flood predictability from stream flow records and historical flooding recurrences. Flood hazard maps are compiled as various areas and assigned risk factors. The type of approach used to reduce flood damage will depend on the calculated or assumed risk:

- Avoidance of high-risk areas for construction activities.
- Detention or delay of runoff in smaller tributaries at higher reaches of the watershed.
- Modification of the lower reaches of rivers, where flood plain inundation is expected, by channels and levees.

13.2.3 Slope Movement Processes

Slope movement processes, also called landslide types and processes, are the types of mass movement of soil or rock on slopes. The term landslide includes a wide range of ground movement, such as rockfalls, deep failure of slopes, mudflows, earth slump, shallow debris flows, and other types of mass movement. These types of mass movement are generally classified according to the combination of types of materials; e.g., earth, debris, or rock, and type of movement; e.g., falls, topples, slides, lateral spreads, flows, and complex—a combination of one or more types. Although gravity acting on an oversteepened slope is the primary reason for a landslide, there are other contributing factors:

- Erosion by rivers, glaciers, or ocean waves create oversteepened slopes.
- Rock and soil slopes are weakened through saturation by snowmelt or heavy rains.
- Earthquakes create stresses that make weak slopes fail.
- Earthquakes of magnitude 4.0 or greater can trigger landslides.
- Volcanic eruptions produce loose ash deposits, heavy rain, and debris flows.

- Excess weight from accumulating rain or snow, stockpiling of rock or ore, waste piles, or man-made structures may stress slopes and other structures to fail.

Slope material that becomes saturated with water may develop a debris flow or mudflow. The resulting slurry of rock and mud may pick up trees, houses, and cars, thus blocking bridges and tributaries causing flooding along its path.

Landslides occur in every state and U.S. territory. The Appalachian Mountains, the Rocky Mountains, the Pacific coastal ranges, and some parts of Alaska and Hawaii have severe landslide problems. The USGS continues to produce landslide susceptibility maps for many areas of the United States. See figure 13-15 for a USGS overview map summary of landslide potential—susceptibility and incidence—in the conterminous United States (ref. 13-51). This map can be called up in whole or in sections, at the following Web site: <http://landslides.usgs.gov/html_files/landslides/nationalmap/national.html>.

The map displays both the incidence of landslides and the susceptibility of the land surface to landslides. Classifications regarding incidence are high, medium, or low landslide incidence: (1) High incidence is having >15 percent of their area involved in landsliding (red), (2) medium incidence is having between 15 and 1.5 percent (gold), and (3) low incidence is having <1.5 percent (tan). These same percentages also are applied to the three categories of landslide susceptibility. For example, a high susceptibility area would exhibit some movement over 15 percent or more of its surface area in response to widespread artificial cutting or high precipitation. The three susceptibility categories are (1) high susceptibility with moderate incidence of landsliding (pale red), (2) high susceptibility combined with low landslide incidence (brown), and (3) moderate suscepitibility combined with low landslide incidence (green).

Mass processes range from imperceptible slow creep to landslides, rockfalls, and mudflows that can travel more than 100 m/s (320 ft/s). Mass movements are often seasonal or periodic, but they may be catastrophic or spasmodic. The nature of slope instabilities and resultant downslope transferences depend on:

- Type and structure of materials, including composition, size of their particles, degree of consolidation, and structural discontinuities—cleavages, bedding, contacts, fractures, etc.

- Geomorphic setting, including climate, vegetation, shape and degree of slope, and slope orientation.

- Triggering mechanisms, external factors which upset the delicate balance that maintains slope stability. These mechanisms include natural and man-caused activities, such as earthquakes; explosions; addition of excessive fluids, especially water; and alteration of hillslope configuration—undercutting, etc.

Table 13-5 describes various types of mass movements. Several forms of mass movement hazards are depicted in figure 13-16 (ref. 13-53).

Factors causing slope movement processes are:

- Wedging and prying: By plant roots; swaying of trees and bushes in wind; expansion of freezing water and hydrostatic pressure of water in joints and cracks; diurnal, annual, irregular expansion due to heating; expansion due to wetting; animal activity. Filling and closing of cracks and voids caused by: Burrowing of animals; decay of plant roots and other organic matter; gullying or undercutting by streams; removal of soluble rocks and minerals; erosion of fine particles by sheet wash and rills; downslope mass movement; shrinkage due to drying or cooling. Increase in load: addition of material upslope; rainfall, snow, or ice; traffic of vehicles or animals; tectonic, meteorological, or animal disturbance.

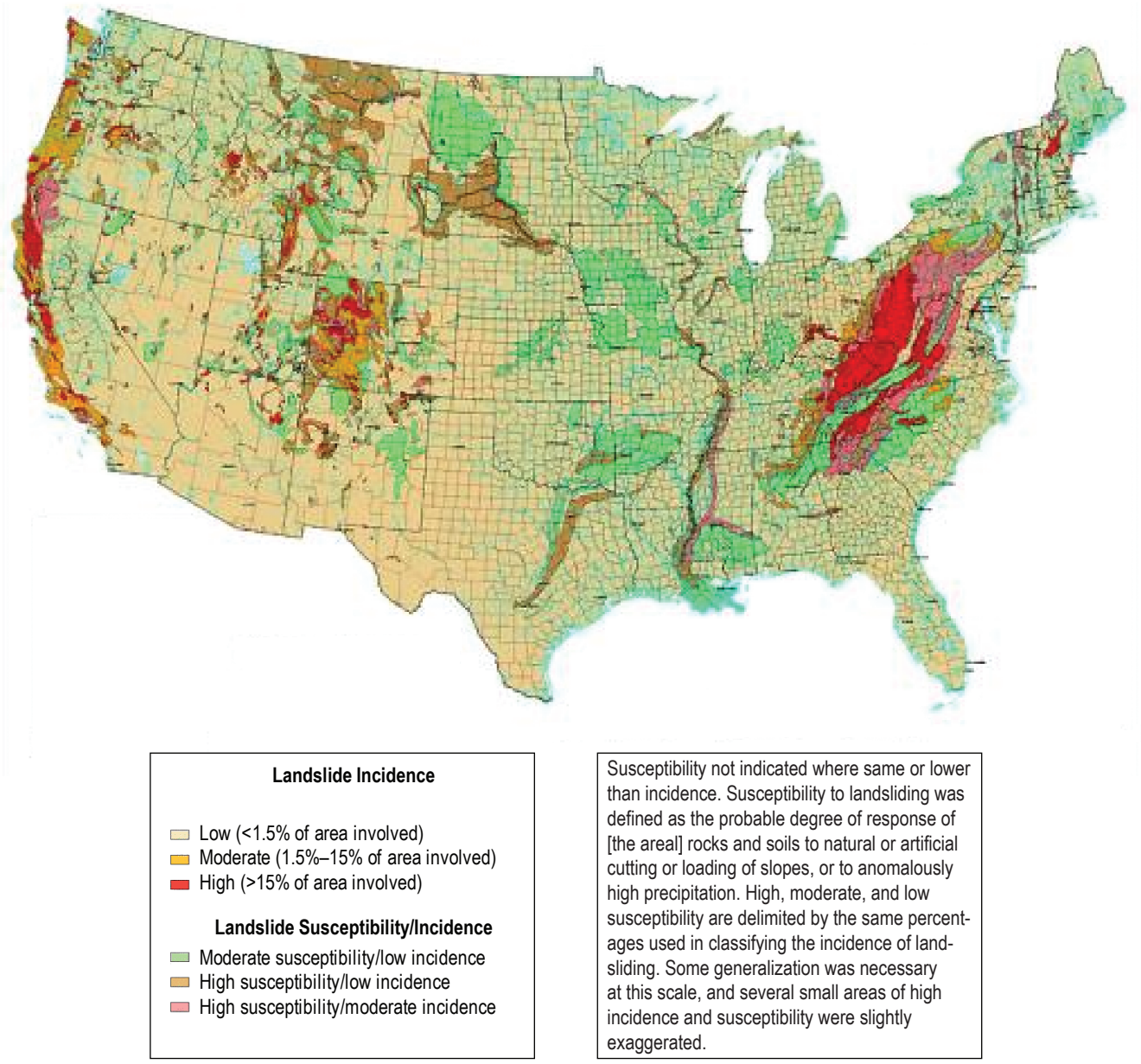

Figure 13-15. USGS landslide overview map of the conterminous United States showing landslide, susceptibility, and incidence (ref. 13-51).

- Reduction in internal friction due to excessive amounts of water in the soil mass. May start as slide; causes similar to landslides.

- Removal of support: Oversteepening of natural or artificial slopes by erosion; outflow, compaction, softening, burning out, solution, chemical alteration of subadjacent layer; disappearance of buttress against slope, such as ice front. Overloading: By other mass-movement processes; by rain, snow, ice, and saturation; overburden in excavation. Reduction if internal friction and cohesion: By surface and ground water, oil seeps, chemical alteration by weathering. Wedging and prying: As in creep. Earth movement: Produced by earthquakes; storms, traffic

Table 13-5. Slope movement processes.

Movement		Composition of Mass and Process			
Kind	Rate	Material Dry or With Minor Ice or Water	Material and Water	Material and Ice	Favoring Conditions
Creep	Very slow	Soil creep	Rock creep Talus creep	Solifluction	Unconsolidated sediment or structurally modified rock. Bedded or alternate resistant and weak beds. Rock broken by fractures, joints, etc. Slight to steep slopes. High daily and annual temperature ranges; high frequency of freeze and thaw; alternate abundant rainfall and dry periods. Balance of vegetation to inhibit runoff but not to anchor movable mass.
Flowage	Slow to rapid		Earth flow Mudflow Debris avalanche	Debris avalanche	Unconsolidated materials, weathering products; poorly consolidated rock. Alternate permeable and impermeable layers; fine-textured sediment on bedrock. Beds dipping from slight to steeper angles; beds fractured to induce water in cracks. Scarps and steep slopes well gullied. Alpine, humid temperature, semiarid climate. Absence of good vegetative cover such as forest.
Sliding	Slow to very rapid	Slump Debris slide Debris fall	Rockslide Rockfall		Inherently weak, poorly cemented rocks; unconsolidated sediments. One or more massive beds overlying weak beds; presence of one or more permeable beds; alternate competent and incompetent layers. Steep or moderate dips of rock structures; badly fractured rock; internal deforming stress unrelieved; undrained lenses of porous material. Scarps or steep slopes. Lack of retaining vegetation.
Subsidence	Slow to very rapid		Subsidence		Soluble rocks; fluent clays or quicksand; unconsolidated sediments or poorly lithified rocks; materials rich in organic matter, water, or oil. Permeable unconsolidated beds over fluent layers. Rocks crushed, fractured, faulted, jointed inducing good water circulation. Level or gently sloping surface.

Compiled and modified from Sharpe (ref. 13-52), by permission.

of vehicles and animals; drilling, blasting, gunfire, Earth strains due to temperature and atmospheric pressure and tidal pull.

- Removal of support of adjacent layers: By solution or chemical alteration; by outflow of fluent material; by natural or artificial excavation; by compaction caused by natural or artificial overloading; by reduction of internal friction; by desiccation. Earth movement: By warping; by natural or artificially-induced vibrations. Overloading: Natural or artificial.

Although some problem areas can be detected by examining aerial photos, infrared photography, and topographic maps, potential-use areas should be examined onsite by competent engineering geologists and/or geotechnical engineers. Since the physical cause of many landslides cannot be removed, geologic investigations, good engineering practices, and effective enforcement of land use management regulations can reduce landslide hazards.

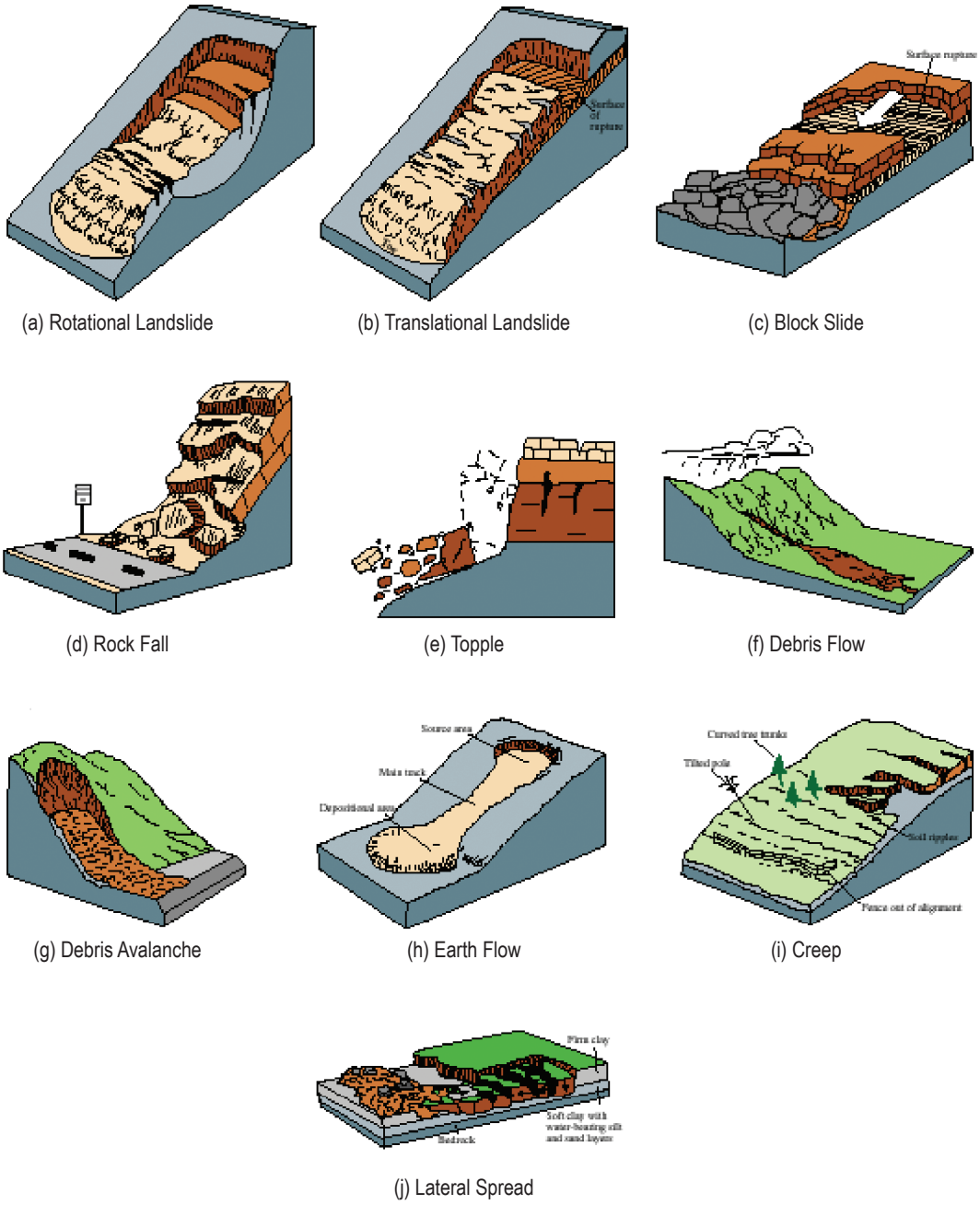

Figure 13-16. Illustrations of slope movement processes (ref. 13-53).

Historically, several methods of prevention and control of slope processes have been used with varying degrees of success. They are:

- Avoidance of problem areas.
- Water control—drains, surface water diversions.
- Excavations—slope reduction, unloading, terracing, total removal of slides.
- Restraining structures—walls, piles, bolts, grout, nets.
- Planting—effective only in controlling shallow, small-scale slope processes.

Many new techniques for identifying regional landslide potential and susceptibility have been recently developed that employ geographic information system technology (ref. 13-54). Likewise, the state of the art with respect to identifying hazards from seismically-induced landsliding has advanced significantly in the past several decades. Graphical relationships between earthquake magnitude and distance for different types of landslides have been developed (ref. 13-55), while another method was developed for producing digital probabilistic seismic landslide hazard maps (ref. 13-56).

13.2.4 Volcanic Hazards—Aerospace Operational Risks

Volcanoes are violent, chaotic phenomena. The principal hazards are: (1) large particles: local debris footprint, (2) ash: regional/subcontinental fallout footprint, (3) gas/aerosol: (tenuous) global coverage possible, and (4) lightning: mostly local but regional effects possible. Volcanic eruption and the associated plume can potentially pose a serious hazard to flight vehicle operations. However, cataclysmic eruptions are rare and dispersal radii are small compared to a vehicle's flight path. There is a very low probability of both KSC and EAFB decent trajectories being in-plume simultaneously.

Volcanic eruptions do not adhere to deterministic schedules; although there are some general trends, chaos reigns. Seismic monitoring provides some advance warning, but the timeframe is limited and uncertain. The most dangerous eruptions are infrequent, but also the most difficult to predict with any accuracy. Even with advance warning, effects are difficult to predict with any operational confidence.

Insofar as aerospace vehicle development and operations are concerned, volcanic hazards do not constitute a design problem except as related to facilities in earthquake-prone areas. However, with respect to operations, they do constitute a risk due to the transport of volcanic byproducts down wind in the troposphere and lower stratosphere. Thus, the information in this section provides an overview of potential aerospace operational risks associated with volcanic eruptions. Specific volcanic information is presented in subsections 13.2.5.3 through 13.2.5.9. Volcanic hazards fall into two categories—hazards near the volcanic activity and hazards distant from it (refs. 13-15 and 13-16).

13.2.4.1 Hazards Near Volcanic Activity. Within a few tens of miles of a volcanic center, hazards include lava flows, nues ardentes (hot ash flows) and poisonous gases, ash falls and bombs, earthquakes, debris, and mud flows (lahars):

(1) Lava flows vary a great deal in viscosity, depending on their chemistry and temperature. They can be up to 10 m (33 ft) thick, traveling 1 m/hr, or they can form a sheet as thin as 1 m (3.3 ft) which travels up to 50 km/hr (30 mph).

(2) Nues ardentes are heavier than air, gas-borne flows of incandescent volcanic ash released during explosive volcanic eruptions. Temperatures in the flows reach 800 °C, and the gases that carry them may be poisonous. These flows, though gas-borne, are extremely dense. Their physical force is great enough to snap large trees and destroy strong buildings.

(3) Ashfalls in the immediate vicinity of a volcano can be up to a few tens of meters deep and very hot. Near the eruption center they may contain sizable volcanic bombs of solid or solidifying rock, as well as pebble-sized fragments of pumice. They may give off gases for some time.

(4) Earthquakes usually accompany volcanic activity and often trigger debris flows and mud flows. (See sec. 13.2.1.)

(5) Debris and mud flows form from the unconsolidated material that makes up the flanks of active stratovolcanoes. The material becomes unstable because of the doming of the volcano, rapid melting of snow by hot ash or lava, and/or percolation of hot volcanic gases through snow masses. Volcanic mud and debris flows have been known to travel 80 km at speeds of several tens of kilometers per hour. Some flows from major volcanoes contain on the order of 2 to 4 km^3 of material. In addition to downstream damage, volcano-caused landslides can cause instability at their point of origin. When a large volume of material is removed suddenly from the flank or summit of an active volcano, pressure is released and an eruption may be triggered.

(6) Lightning may be associated with the eruption of a volcano. Electrification is typically caused by friction between rising ash particles and falling condensed gases. Lightning is more evident in the lower magnitude volcanic eruptions. It typically occurs in the immediate vicinity of the eruption but may travel many kilometers. Ash is highly conductive when wet; thus, electrical effects can propagate farther downwind.

13.2.4.2 Hazards Distant From Volcanic Activity. Far from volcanic centers, volcanic ash and tsunamis can still be serious hazards.

(1) An ashfall's total volume depends on the size of the eruption that brought it about. Its distribution depends on the elevation reached by the volcanic cloud and on wind conditions at the time of the eruption. A sizable ashfall can damage areas several hundred kilometers from the eruption site. Fine ash, if it reaches the stratosphere, can remain there for months or years, affecting climate by reducing insolation. See section 10 concerning aerosols in the atmosphere.

(2) Tsunamis can be caused by submarine volcanic explosions and debris slides, which can travel thousands of kilometers from the volcanism that caused them. They endanger life and all coastal construction within 40 m (130 ft) of sea level. (See sec. 13.2.2.)

When considering volcanic hazards, it is important to realize that volcanism is sporadic in any area. A volcanic area that has been inactive throughout historic times may reawaken to violent activity in a few days or weeks, or it may remain inactive for centuries into the future. Earthquakes, almost always felt or recorded several days or weeks before volcanic activity commences, serve as a warning of impending danger. Once volcanism commences, danger is greatest within a few tens of kilometers of the eruption. The effects of volcanism can be catastrophic, especially since volcanoes are virtually uncontrollable by man. Important constructions should not be located in the immediate vicinity of active or dormant volcanoes, or in areas likely to be affected by distant volcanism.

13.2.4.3 Volcanic Eruptions. Eighty percent of the Earth's surface is of volcanic origin (ref. 13-57). Volcanoes erupt under water as well as above water. There are four main types of volcanoes: (1) Cinder cones, built of lava fragments; (2) composite cones or strato-volcanoes, built of alternating layers of lava flows, volcanic ash, and ash; (3) shield volcanoes, built almost entirely of very fluid lava flows; and (4) lava domes, built of viscous or pasty lava extruded like toothpaste from a tube (ref. 13-58). Figure 13-17 illustrates the basic components and potential destructive hazard elements relating to a volcanic eruption (ref. 13-59).

There are ≈500 active volcanoes currently on Earth. The United States ranks third in the world with regard to historical active volcanoes (ref. 13-57). Active volcanism in the United States is presently confined to the Hawaiian Islands, the Aleutian Islands, the Alaska Peninsula, and the Pacific Cascade Mountain Range, all influenced by the ring-of-fire region about the Pacific Ocean. The Cascade Range volcanoes erupt about once or twice per century, and seven have erupted since our first U.S. Independence Day. Alaska has ≈80 major volcanic areas, with one or two eruptions per year since 1900 (ref. 13-57).

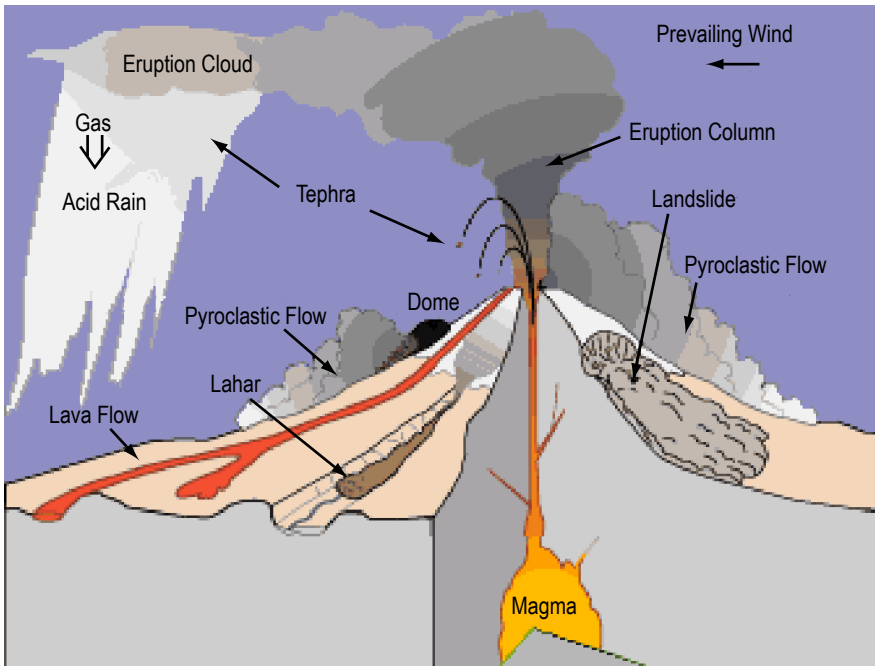

Figure 13-17. Volcanic natural hazards illustrated that are typical of western U.S. and Alaskan volcanoes (ref. 13-59).

13.2.4.4 Volcanic Explosive Index. The volcanic explosive index (VEI) is a noncomprehensive scale (0 to 8) used for volcanic eruptions that was developed by Newhall and Self (ref. 13-60). It is based on volume of erupted pyroclastic material—tephra, ashfall, pyroclastic flows; eruption column height; eruption duration; and qualitative descriptive terms. Each number represents an approximate factor of 10 increase in explosivity. Since 1400 AD, the 1815 Tambora Indonesia eruption has been the only one assigned a VEI of 7, with a volume in excess of 100 km^3. The 1980 Mount St. Helens was classified as a VEI of 5, with an erupted volume of ≈1 km^3. The largest explosive eruption occurred at Yellowstone (≈600,000 yr ago) with a VEI of 8, and a volume of ≈1,000 km^3 (240 mi^3) of material (ref. 13-61). The older Tsuya classification index of 1955 (ranging from I to IX) is also based on the volume of ejecta, but assuming pyroclastic flows. Table 13-6 presents the VEI details.

13.2.4.5 Alaskan Volcanoes. The largest eruption on Earth during the 20th century occurred at the Novarupta Volcano, Alaska, on June 6, 1912, which also created the Katmai caldera—a volcanic depression. The ash cloud reached an altitude of 20 mi and within 4 hr ash began to fall on Kodiak, 100 mi to the southeast. The eruption ended on June 9 with sulfurous ash falling on Vancouver, BC, and Seattle, WA. The next day the cloud passed over Virginia and by June 17, reached Algeria, Africa.

Alaskan volcanoes today present a greater threat to aviation on the west coast of the United States than do the volcanoes of the Cascade Range in the Pacific Northwest. Within 805 km (500 mi) of Anchorage, volcanologists have identified at least seven deposits of volcanic ash younger than 4,000 yr that approach or exceed the volume of ash ejected by Novarupta in 1912. Of the numerous volcanoes scattered across southern Alaska, at least 10 are capable of exploding at the scale of the 1912-scale eruption.

Explosive eruptions are best compared by recalculating the amount of erupted volcanic materials, such as ash and pumice, in terms of the original volume of molten rock (magma) released. On this basis, the 12.5 km^3 (3 mi^3) of magma erupted from Novarupta in 1912 was 30 times greater than the volume of magma released in the 1980 eruption of Mount St. Helens 0.4 km^3 (0.1 mi^3). The 1991 eruption of Mount Pinatubo, the second

Table 13-6. Volcanic explosive index (ref. 13-60).

VEI	Description	Plume Height	Volume Ejected	Duration	Tropospheric Injection	Stratospheric Injection	Occurrence	Total Eruption*	Example
0	Nonexplosive	<100 m	>1,000 m^3	Variable	Negligible	None	Daily	699	Kilauea (1983 on)
1	Small	100–1,000 m	>10,000 m^3	<1 hr	Minor	None	Daily	845	Nyiragongo (1982)
2	Moderate	1–5 km	>1,000,000 m^3	1–6 hr	Moderate	None	Weekly	3,477	Colima (1991)
3	Moderate-large	3–15 km	>10,000,000 m^3	1–12 hr	Substantial	Possible	Yearly	869	Galeras (1924)
4	Large	10–25 km	>0.1 km^3	1–12 hr	Substantial	Definite	≥10 yr	278	Sakura-Jima (1914)
5	Very large	>25 km	>1 km^3	6–12 hr	Substantial	Significant	≥100 yr	84	Villarrica (1810)
6	Very large	>25 km	>10 km^3	>12 hr	Substantial	Significant	≥100 yr	39	Vesuvius (79 AD)
7	Very large	>25 km	>100 km^3	>12 hr	Substantial	Significant	≥1,000 yr	4	Tambora (1812)
8	Very large	>25 km	>1,000 km^3	>12 hr	Substantial	Significant	≥10,000 yr	0	Yellowstone (≈2 mil)

*Total eruptions, given this VEI value, over the past 10,000 years through 1994 (source: Global Volcanism Program of the Smithsonian Institution).

largest in the world during the 20th century, was less than half the size of Novarupta's eruption 5.0 km^3 (1.2 mi^3) (ref. 13-62).

13.2.4.6 Cascade Range—Mount St. Helens. On May 18, 1980, at 08:30 a.m. LT, Mount St. Helens in Washington State erupted seconds after a 5.1 magnitude earthquake. The north flank of Mount St. Helens began to collapse, unleashing a powerful, laterally-directed blast. This collapse produced a rockslide-debris avalanche of 0.5 mi^3 (2.1 km^3), the world's largest in historical time. Within 10 min of the eruption onset, the interaction of hot volcanic ejecta with snow- and ice-triggered lahars (volcanic mudflows) that caused widespread flooding and extensive damage. Lasting <5 min, the lateral blast traveled at speeds of up to 998 km/hr (620 mph), extending out as far as 600 km (373 mi) and devastating 596 km^2 (230 mi^2) of land north of the volcano. Ash fallout from the eruption affected eastern Washington and neighboring states, and drifted across the country in 3 days and ultimately circled the globe in ≈2 wk (ref. 13-58).

Mount St. Helens produced an estimated minimum volume of 1.1 km^3 of uncompacted tephra on May 18, of which an estimated volume of 0.20–0.25 km^3 was solid rock. This relates to a total mass of $\approx 4.9 \times 10^{14}$ g. Mount St. Helens produced a total of 183.4 million m^2 (≈219.4 million yd^2) of erupted material from May 1980 through October 1980, with ≈540 million tons of ash, with a total volume of 1.25 km^3 (0.3 mi^3) that fell over 57,000 km^2 (22,000 mi^2) on Washington, Idaho, and Montana. Most of the ash fell within 300 mi of the mountain, and the size of ash particles decrease exponentially with increasing distance from the volcano. Most downwind ash was <0.001 mm in diameter. The average uncompacted dry bulk density for the downwind ash was ≈0.45 g/cm^3. Figure 13-18 presents a timeline of the ash plume growth characteristics for the Mount St. Helens eruption. The plume rose at ≈1,500 m/min (≈5,000 ft/min) and by 0900 LT, the vertical plume peaked out at 27 km altitude. At 0945 LT, the plume front was 135 km from the eruption site. At 1200 LT, the front was 400 km away. By the morning of May 19, the plume front was located at midcontinent, and by May 21 it had arrived at the U.S. east coast. The diffuse plume cloud encircled the Earth, and by early June, made its U.S. west coast arrival.

Figure 13-19 shows the fallout pattern downwind of Mount St. Helens (ref. 13-64).

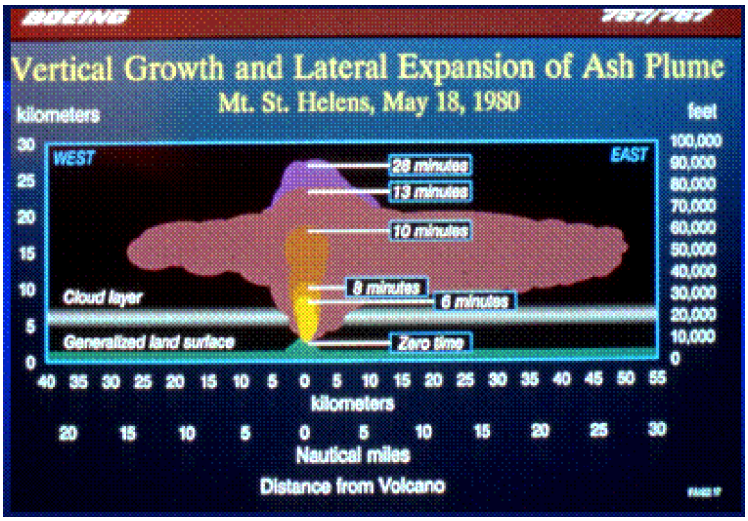

Figure 13-18. Mount St. Helens vertical and lateral ash plume growth (ref. 13-63).

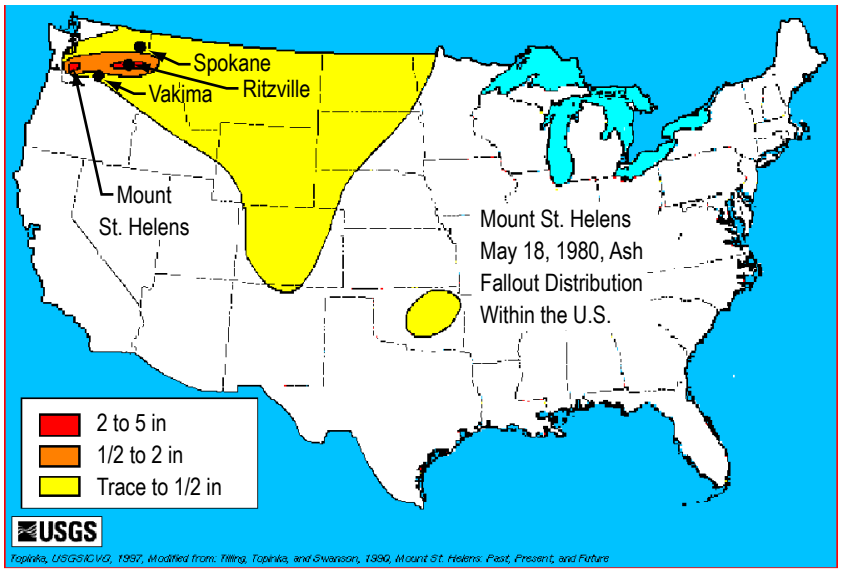

Figure 13-19. Mount St. Helens May 18, 1980, ash fallout distribution and thickness within the United States (ref. 13-64).

Figure 13-20 gives the mean Mount St. Helen's ash particle diameter as a function of distance from the eruption (ref. 13-65). The maximum thickness of ash fall from Mount St. Helens was ≈18 cm, all within 40 km of the mountain, as shown in figure 13-21. Figure 13-21 also gives the measured tephra compacted thicknesses for three other historical Cascade Range volcanic eruptions. It has been estimated that the original fall thicknesses for the three may have been twice as great (ref. 13-66).

13.2.4.7 General Volcanic Statistics. A comparison of Mount St. Helens and Mount Pinatubo ashfall deposits (total volume) with the ancient Yellowstone eruption is given in figure 13-22 (ref. 13-67). This figure gives a general indication for the total volume erupted versus its frequency of occurrence.

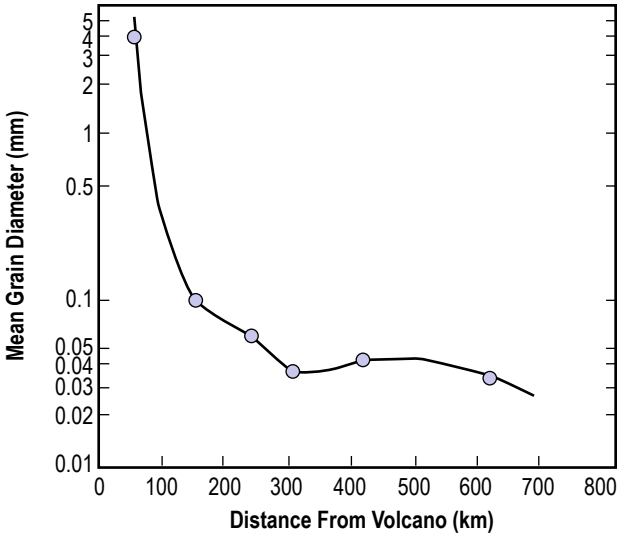

Figure 13-20. Mean diameter of ash particles that fell to the ground downwind of Mount St. Helens on May 18, 1980 (ref. 13-65).

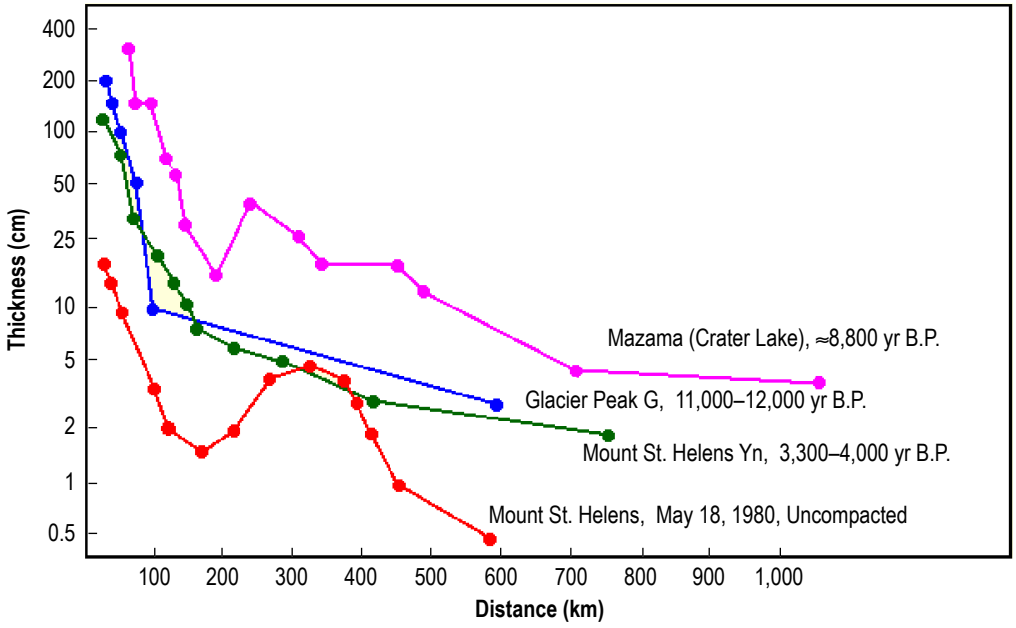

Figure 13-21. Plot of tephra-fall thickness versus distance from vent for several Cascade Range volcanoes (ref. 13-66).

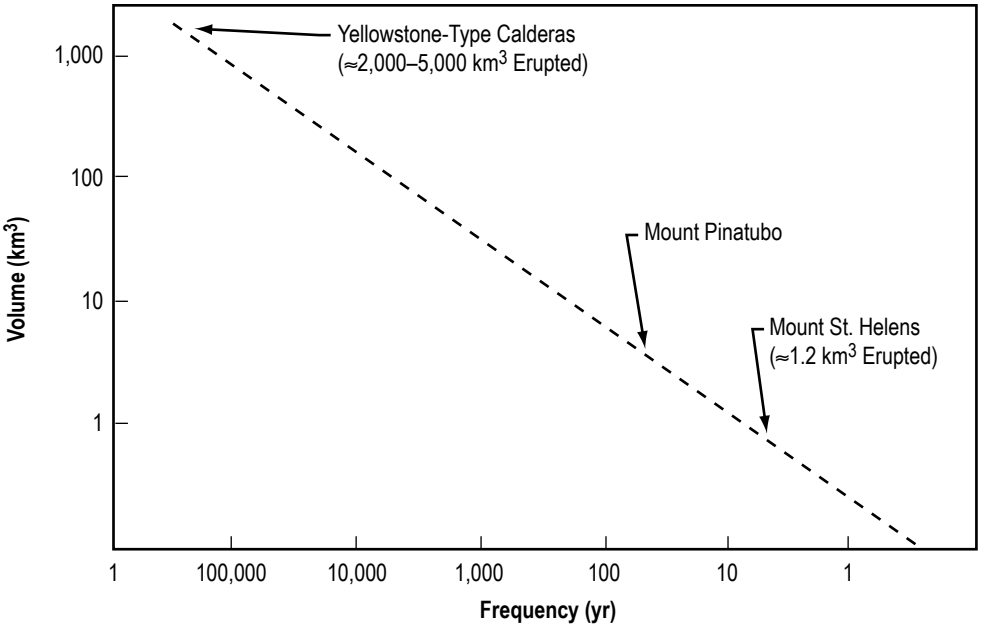

Figure 13-22. Estimated volume of ash-fall deposits as a function of frequency as shown for three historical volcanic eruptions (ref. 13-67).

Table 13-7 gives approximate volcanic material fallout rates versus particle size (ref. 13-68), while table 13-8 presents the approximate density of the various individual ash particles (ref. 13-65).

Table 13-7. General volcanic plume fallout rates (ref. 13-68).*

Particle Diameter (μm)	Fallout Rate (km/hr)	Particle Time to Reach the Ground **
>50	≈0.8	≈11.5 hr
10	≈0.01	≈290 hr
1	≈0.0003	≈3.3 yr

*Rough estimate, assuming laminar flow and high-latitude atmospheric conditions.
**From ≈10-km altitude.

Table 13-8. Density of individual ash particles (from Shipley and Sarna-Wojcicki, 1982) (ref. 13-65).*

Type of Ash Particle	Density of Particle (g/cm3)
Pumice fragments	0.70–1.20
Volcanic glass shards	2.35–2.45
Crystals and minerals	2.70–3.30
Other rock fragments	2.60–3.20

*Dry bulk ash densities ranging from 0.50 to 1.50 g/cm3.
Wet bulk ash densities ranging from 1 to 2 g/cm3.

Figure 13-23a shows how the total height of rise of the column and the neutral buoyancy height of the column vary with the mass eruption rate for three different initial temperatures. In this graph, it can be seen that the rate of increase of column height decreases once it passes through the tropopause (11-km tropopause assumed here). This is because the temperature begins to increase with height in the stratosphere, causing the atmosphere to become much more stratified. It can also be seen that, because hotter columns generate more buoyancy, they tend to rise higher. Figure 13-23b presents calculations using this model of the ascent height and neutral buoyancy height of a volcanic thermal ash cloud. Calculations are for three different initial temperatures as a function of the initial mass of the thermal cloud. The results are qualitatively similar to those in figure 13-23a, which describe maintained eruption columns (ref. 13-69).

Figure 13-24 presents a plot of the probability of an injection of various metric tons of volcanic matter into the stratosphere as a function of waiting time in years (ref. 13-70).

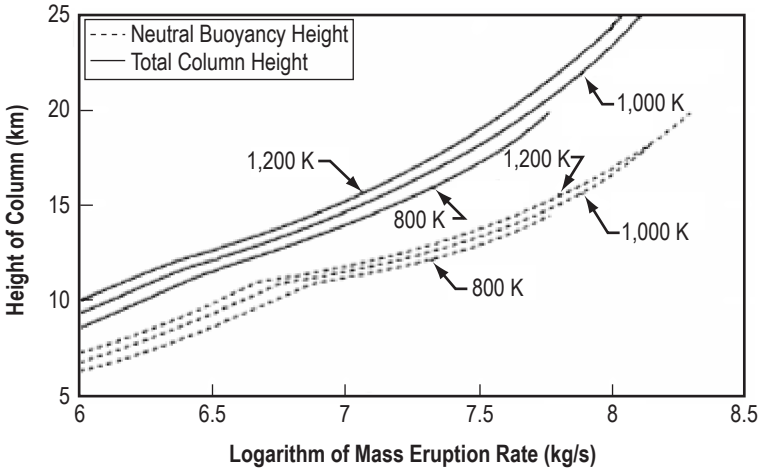

Figure 13-23a. Calculations of neutral buoyancy height and total column height as a function of erupted mass flux. Curves are given for three eruption temperatures (800 K, 1,000 K, and 1,200 K) (ref. 13-69).

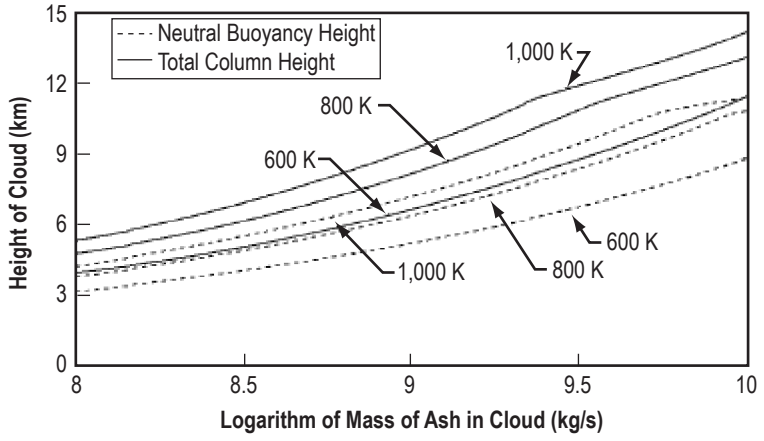

Figure 13-23b. Calculations of neutral buoyancy height and total column height as a function of erupted mass. Curves are given for three eruption temperatures (600 K, 800 K, and 1,000 K) (ref. 13-69).

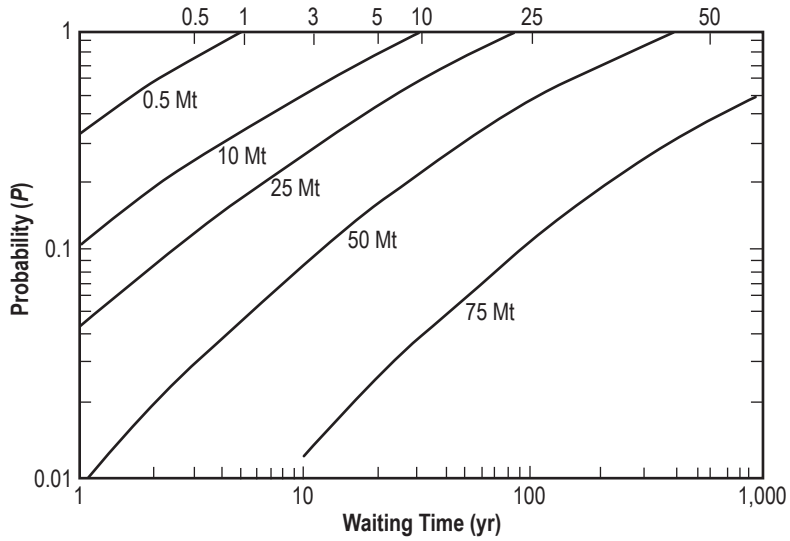

Figure 13-24. The probability (*P*) that a volcanic eruption will inject (add) a given quantity of matter (in metric tons (Mt) into the stratosphere (ref. 13-70).

13.2.4.8 Volcanic Ash Particle Sizes. Tephra is a general term for fragments of volcanic rock, lava, and glass fragments. Such fragments range in size from <2,000 μm (ash) to >1 m in diameter (ref. 13-71). Very small ash particles can be <1 μm across. Volcanic ash is hard, does not dissolve in water, is extremely abrasive and mildly corrosive, and conducts electricity when wet (ref. 13-65). Volcanic ash normally contains sulfuric acid (H_2SO_4), as ice/water droplets within the cloud combined with the smaller ash particles as the cloud disperses over time. A nascent (initial) volcanic eruption cloud consists of large ash particles (0.1–100 μm) with short residence times and a highly variable vertical distribution. The dispersed (older than ≈12 hr) volcanic clouds consist largely of smaller sulfuric acid-coated particles (≤0.1 μm) with long residence times and a relatively uniform vertical distribution (ref. 13-72).

13.2.4.9 Largest Eruptions on Earth. One of the largest volcanic eruptions that has ever occurred on Earth is the Yellowstone eruption that occurred ≈2.2 million years ago. It produced ≈2,500 km^3 (≈600 mi^3) of ash, which was ≈2,500 times more ash than Mount St. Helens produced in 1980 (ref. 13-73). The area it covered was ≈15,500 km^2 (6,000 mi^2).

Based on all previous known eruptions with a VEI of 8, Mason, Pyle, and Openheimer have compiled and analyzed the size and frequency of these largest known eruptions. They have computed and concluded that there is at least a 75-percent probability of one M8 eruption occurring within the next million years, while there is a 1-percent chance of an M8 eruption occurring within the next 460–7,200 years (ref. 13-74).

13.2.5 Expanding Ground

Expanding ground is caused by freezing and/or expansive soil or anhydrous expansion—without freezing—of moisture in the ground or by rock components that expand when wet. Expansive soils are found throughout the United States. The soil can increase its volume as much as 1,000 percent if it is allowed to. The actual expansion depends upon the amount of water available and the overburden on the soil. The process of expansion is generally slow. The heaving force can cause serious damages to foundations and structures.

When water freezes, its volume increases by ≈9 percent. When water in fine-grained, unconsolidated material freezes, additional water from the atmosphere and from the unfrozen ground below slowly adds to the already frozen mass. Eventually, lenses of ice build up, lifting the soil above them. In areas where winters are cold and moist, or where day-night temperatures differ markedly, freezing and thawing may cause marked dislocation of surface and near-surface materials. Some clays contain minerals that increase in volume upon wetting and decrease in volume upon drying. The most common of these minerals is anhydrite—from the montomorillonite clay group. Problems with expansive clays and the rocks and soil in which they occur are most frequently encountered in arid or semiarid areas with strong seasonal changes in soil moisture.

Expansive clays are particularly associated with volcanically-derived materials. Shales containing clays of the montomorillonite group, including bentonite derived from volcanic ash, commonly swell 25 to 50 percent in volume (ref. 13-75). Such swelling results from chemical attraction of water molecules and their subsequent incorporation between submicroscopic, platelike clay molecules. As more water becomes available, it infiltrates between the clay plates and, with freezing, pushes them farther apart. Similarly, hydration of the mineral anhydrite induces a chemical change, causing 40-percent expansion and altering the anhydrite to the mineral gypsum.

These large increases in volume upon freezing or hydration, and associated decreases in volume with thawing or drying, can be very destructive. Volume increases of only 3 percent are considered to be potentially damaging and require specially designed foundations. James and Holtz (ref. 13-76) report that shrinking and swelling damage to foundations, roads, and pipelines in the United States amounts to more than twice the dollar value of damage incurred by floods, hurricanes, tornadoes, and earthquakes combined.

Onsite inspection by a competent soil engineer or engineering geologist can pinpoint potential clay-expansion problems. Engineering soil tests are required to evaluate the extent and severity of the problem at construction sites.

Installation of well-designed drainage systems using chemical treatment, or complete removal of expansive materials, may lessen the potential damage from expansive ground.

13.2.6 Ground Subsidence

Ground subsidence is characterized by the downward movement of surface material, caused by natural phenomena, such as removal of underground fluid, consolidation, burning of coal seams, or dissolution of underground materials. It may also be caused by man's removal or compaction of Earth materials.

Ground subsidence is generally a relatively slow process; it has been known to continue for many decades. Usually the result is broad warping and flexing, with some cracking, and offset at the ground surface. If the process causing subsidence persists, the surface may suddenly collapse. Foundation failures, ruptures of pipe and utility lines, dam collapses, salt water invasion, and disruption of roads and canals have all been directly attributable to ground subsidence.

Potential causes for ground subsidence include:

- Removal of solids—Removal of the solid subsurface support base involves mining; natural or human solution of carbonate and other easily soluble minerals, including salt and sulfur; and underground burning of organic beds. Cavern collapse is the most catastrophic result. Alternatives to avoiding such areas for heavy loads include subsurface backfilling, cement-grouting, and installation of underground support pillars.

- Withdrawal of fluids—Subsidence due to withdrawal of fluids, including gas, oil, and water, is the most common type of man-caused regional ground subsidence. As fluids are removed, and fluid pressure within

the aquifer or reservoir rock is reduced, the aquifer skeleton must bear an increased grain-to-grain load. In permeable media, the increase in effective stress and subsequent compaction is immediate. Increasing percentages of clays in the aquifer cause the adjustment to take place more slowly. In extreme cases, subsidence of more than 7 m over a 60-yr period has been directly attributed to the withdrawal of water and/or petroleum. Injection of fluids back into the aquifer might arrest the subsidence.

- Oxidation of organic beds—Oxidation of organic beds, such as layers of peat, and resultant breakdown of support structures have been known to follow the drainage of peat bogs. Raising the water table can inhibit this oxidation.

- Application of surface loads—Compaction due to surface loading alone commonly results in only minor ground subsidence. However, application of surface loads may trigger more severe subsidence when added to already weakened substratum conditions.

- Hydrocompaction—Wetting of some clays in moisture-deficient, low-density soils can lead to weakening of clay bonds which support soil voids, and ultimately to the collapse of internal soil structure and compaction. Hydrocompaction commonly occurs in wind-deposited silts and fine-grained colluvial soils that have a high clay content. Some areas near the south and west borders of the San Joaquin Valley dropped 1.5 to 5 m in the early 20th century after application of water. Drainage installations and replacement of the offending clay-bearing materials are modifications used to circumvent potential hydrocompaction problems.

- Tectonic movements—These movements include earthquakes and man-made explosions which directly cause reordering and subsidence, and which commonly cause additional ground subsidence in already unstable areas. Some materials, such as quick clays and quicksands, lose all their cohesive strength and acquire the properties of a liquid upon being violently disturbed. Such materials can flow and envelope buildings constructed on them.

- Liquefaction—When loose, saturated soils are subjected to cyclic or impact loads, they tend to compact, thereby developing excess pore water pressures which may in turn result in complete loss of interparticle friction in the soil mass. Such a state is called liquefaction. A liquefied soil behaves like a fluid and cannot carry any shear loads. As a result, buildings can sink into a liquefied ground mass, earth slopes cannot be sustained, dams and bridges may collapse, or large landslides may occur. Liquefaction is a common phenomenon during earthquakes and can also be triggered by strong explosions, pile driving, wave action, etc.

Ground subsidence is commonly caused by a combination of factors. Geologic conditions that are favorable for liquefaction include the presence of mines, soluble or flammable materials, oil, water or gas, windblown soils, fluent clays or quicksand, faults or fractured rocks, and good water circulation. It is imperative to recognize these potential problems *before* construction commences and to take corrective measures where they are called for.

13.2.7 Volcanic Hazards

Volcanic hazards fall into two categories—hazards near the volcanic activity and hazards distant from it (refs. 13-77 and 13-78).

13.2.7.1 Hazards Near Volcanic Activity. Within a few tens of miles of a volcanic center, hazards include lava flows, nuées ardentes (hot ash flows) and poisonous gases, ash falls and bombs, earthquakes, debris, and mudflows:

- Some lava flows are much more dangerous to man than others. Lava flows vary a great deal in viscosity, depending on their chemistry and temperature. They can be up to 10 m thick, traveling a meter per hour,

or they can form a sheet as thin as 1 m that travels up to 50 km/hr. The latter have been the most hazardous to man in the past. A trained geologist can predict, to some extent, the type of flow most likely to occur in a given volcanic area. If fast fluid flows are likely, guiding levees can be built to shunt them away from populous or otherwise valuable areas.

- Nuées ardentes are heavier than air, gas-borne flows of incandescent volcanic ash released during explosive volcanic eruptions. Temperatures in the flows reach 800 °C (1,470 °F), and the gases that carry them may be poisonous. These flows, though gas borne, are extremely dense. Their physical force is great enough to snap large trees and crumble strong buildings. It was a nuée ardent from Mt. Pelée that devastated St. Pierre, Martinique, in 1902, completely destroying the town and killing an estimated 40,000 people. Hot, dense, poisonous gases can also be emitted without ash.

- Ashfalls in the immediate vicinity of a volcano can be up to a few tens of meters deep and very hot. Near the eruption center they may contain sizable volcanic bombs of solid or solidifying rock, as well as pebble-sized fragments of pumice. They may release gases for some time.

- Earthquakes (sec. 13.2.1) usually accompany volcanic activity and often trigger debris flows and mudflows.

- Debris flows and mudflows form from the unconsolidated material that makes up the flanks of active strato-volcanoes. The material becomes unstable because of doming of the volcano, rapid melting of snow by hot ash or lava, and/or percolation of hot volcanic gases through snow masses. Volcanic mud and debris flows have been known to travel 80 km at speeds of several tens of kilometers per hour. Some flows from major volcanoes contain on the order of 2 to 4 km^3 of material. Dams in the paths of mudflow may break and contribute to the volume of flows that overtop them. In some places where mudslide hazard has been recognized, dams have been built and reservoirs kept empty to absorb them. In addition to downstream damage, volcano-caused land-slides can cause instability at their point of origin. When a large volume of material is removed suddenly from the flank or summit of an active volcano, pressure is released and an eruption may be triggered—as in the May 18, 1980, eruption of Mount St. Helens.

13.2.7.2 Hazards Distant From Volcanic Activity. Far from volcanic centers, volcanic ash and tsunamis can still be serious hazards:

- An ashfall's total volume depends on the size of the eruption that brought it about. Its distribution depends on the elevation reached by the volcanic cloud and on wind conditions at the time of the eruption. A sizable ashfall can damage areas several hundred kilometers from the eruption site. Ash is detrimental to human health and damaging to mechanical equipment. It reduces visibility if there is wind or traffic, and must be removed from buildings and pavement. Fine ash, if it reaches the stratosphere, may remain there for months or years, affecting climate by reducing insolation. See section 10 concerning aerosols in the atmosphere.

- Tsunamis (sec. 13.2.2.1) can be caused by submarine volcanic explosions and debris slides, which can travel thousands of kilometers from the volcanism that caused them. They endanger life and all coastal construction within 12 m of sea level.

When considering volcanic hazards, it is important to realize that volcanism is sporadic. A volcanic area that has been inactive throughout historic times may reawaken to violent activity in a few days or weeks, or it may remain inactive for centuries into the future. Earthquakes, almost always felt or recorded several days or weeks before activity commences, serve as a warning of impending danger. Once volcanism commences, danger is greatest within a few tens of kilometers of the eruption. The effects of volcanism can easily be catastrophic,

especially since volcanoes are virtually uncontrollable by man. Important constructions should not be located in the immediate vicinity of active or dormant volcanoes, or in areas likely to be affected by distant volcanism.

13.2.8 Other Hazards

Geologic hazards, such as avalanches and other snow and ice processes, do not influence the three areas (VAFB, EAFB, and KSC) concerned and are not discussed here.

13.2.9 Conclusions

A word should be added to the preceding description of geologic hazards. Many of those described occur suddenly, while others take place over a long period of time. Almost all of these hazardous events are normal geologic processes and should be expected to occur from time to time. We have learned to predict and control some of these processes, but for others, the best we can do is study the likelihood of their occurrence in different areas and avoid building where danger is great.

13.3 Geology and Geologic Hazards at Edwards Air Force Base, California

13.3.1 Geology

EAFB is covered by rock materials of three distinct age groups (ref. 13-79). The oldest rocks are pre-Tertiary (pre-65 million years ago) granite instrusive and metamorphic units (I_g in fig. 13-25). These rocks are similar in age and composition to the Sierra Nevada Batholith. They form most of the ridges and hills within the EAFB boundaries.

Minor amounts of Tertiary Age rocks (3 to 65 million years old) are exposed at EAFB (T_{vi} in fig. 13-25). Most of these are dikes and sills of fine-grained rock. A few volcanic flows and pyroclastics, with interbedded sediments, crop out along the eastern boundary of the base. Some bentonite layers occur within the sedimentary units. Although the dikes and sills form stable slopes, some of the slopes covered by the pyroclastic and sedimentary interbeds are unstable.

Most of the terrain within the boundaries of EAFB is covered with thick units of Quaternary and Recent (3 million years old) unconsolidated and weakly consolidated materials, including alluvial sand and gravel (Q_a in fig. 13-25), beach dunes and bars (also Q_a), playa clays (Q_c), windblown sands (Q_{cs}), and older, partly consolidated gravels (Q_f). These deposits generally occupy areas of low relief.

Alluvial sand and gravel, deposited by the action of flowing water, form channel and fan deposits. Wave-deposited bars and wind-deposited dunes occur along the northern shore of Rogers Lake. Minor clay balls occur in the wave-deposited bars. Windblown sand forms small dunes elsewhere within the base, and also covers parts of the desert floor with a thick veneer of sand.

The playa clays are mudflat facies of the alluvium. They are hard when dry but become soft and sticky when wet. Studies by Droste (ref. 13-80) found that playa clays from Rogers Lake consist of 40 to 50 percent montmorillonite and 40 to 50 percent illite. Clays from Rosamond Lake consist of 20 to 30 percent montmorillonite, 50 percent illite, and 20 to 30 percent chlorite. Although in the desert climate where thorough wetting of the playas is rare, these high montmorillonite clays are subject to severe swelling and shrinking, which should be considered when planning construction activities near the dry lake beds.

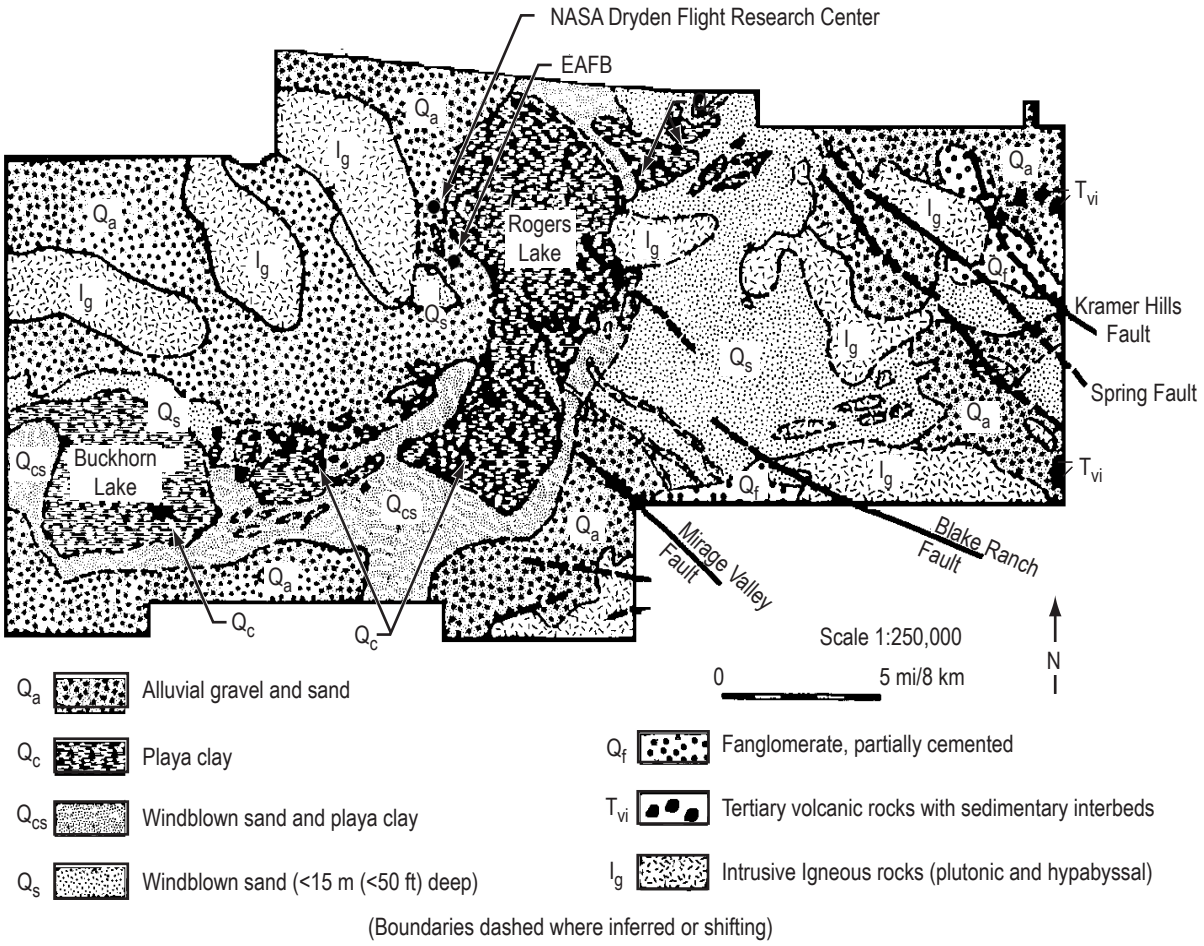

Figure 13-25. Geology of EAFB, CA (ref. 13-79).

Several high-angle, northwest-trending faults have been mapped in the southern and eastern parts of the EAFB. They have small displacements and seem to edge granitic domal features. The faults are inactive at present.

13.3.2 Geologic Hazards

The following subsections describe the general locations of potential geologic hazards that exist at EAFB (fig. 13-26). Onsite investigations and engineering properties tests are recommended on a location-by-location basis before initiation of any construction activities.

13.3.2.1 Earthquakes. There were no recorded earthquakes with epicenter magnitude of 4.0 or greater at EAFB or within 40 km (25 mi) of it between 1910 and the present (refs. 13-81 and 13-82). The base is located on a relatively stable wedge between the San Andreas and Garlock Faults, both of which are <64 km (<40 mi) from the base. The proximity of these major active faults indicates regional tectonic instability. However, the known faults mapped in the eastern and southern parts of EAFB seem to be inactive, and earthquake hazards are judged to be negligible.

The likelihood of surface fault rupture at the EAFB, NASA Dryden Flight Research Center site, is considered to be very remote. However, it cannot be dismissed completely because it is unknown if any buried faults

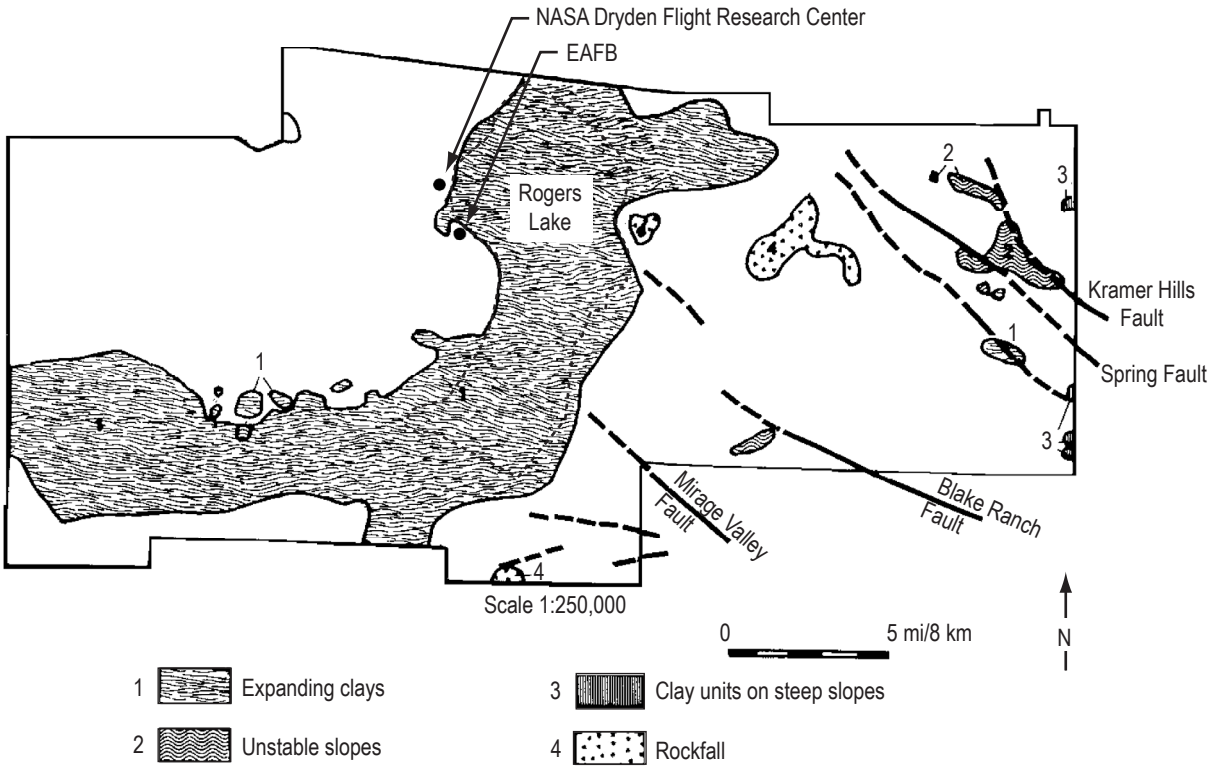

Figure 13-26. Geological hazards of EAFB, CA.

underlie the site that may belong to the group of Mojave block faults. Another risk—albeit a low one—is the possibility of sympathetic movement, including fault rupture extending to the ground surface, of these possible underlying faults in response to large motions from a great earthquake on the San Andreas Fault (ref. 13-18).

It is recommended that facilities that are to be constructed on EAFB be evaluated for their resistance to the two following earthquakes (ref. 13-18):

- A magnitude 8.5 event on the nearest approach of the San Andreas Fault ≈47 km (≈29 mi) would impose an acceleration of 0.40 g on the site with a bracketed duration of 40 s. It is suggested that a scaled trace of the N21E component of the Taft accelerogram of the 1952 Kern County Earthquake is an adequate model.

- A near-field magnitude 4.5 event from a Mojave Block Fault would impose an acceleration of 0.20 g at the site with a short bracketed duration of 6 s. It is suggested that the unscaled trace of the Lake Hughes No. 4 S69E component from the San Fernando Valley Earthquake of 1971 be used as an appropriate model.

13.3.2.2 Slope Processes. All of EAFB lies within an area designated as 1 by Radbruch and Crowther (ref. 13-83). This designation identifies areas in California that have the lowest number and volume of landslides per given area. Hilly parts within a unit 1 area may experience landslides, but because of the overall low to moderate relief, few problems from slope processes are expected. Some hazards may exist on steep, gravel-covered slopes. The fanglomerate units that form steep slopes in the Kramer Hills, near Jackrabbit Hill, and elsewhere on the Base should be considered susceptible to mass movement. Slopes covered by Tertiary pyroclastics and interbedded sedimentary layers along the eastern boundary are potentially hazardous. Rockfall problems may exist at the bases of granite cliffs.

13.3.2.3 Flooding. Except for very local flash flooding, no flood hazards are likely. Flash flooding may turn playas into shallow, temporary lakes.

13.3.2.4 Expanding Ground. Careful examination of the engineering properties of the playa clays should precede construction activities. The high montmorillonite content of these clays leads to swelling and shrinking when they are alternately wet and dry. Similar caution should be exercised when dealing with the Tertiary pyroclastics and their sedimentary interbeds.

13.3.2.5 Subsidence. Localized subsidence may occur near old mine diggings. There is also the possibility of hydrocompaction in playa clays.

13.3.3 Conclusions

EAFB, though mostly underlain by granite, is 65 percent covered by Pleistocene and Recent unconsolidated sand, clay, and gravel. Despite the proximity of major active faults, seismic risk is low. Slopes are generally <10 percent, so geologic hazards resulting from slope processes are localized and probably restricted to steep slopes consisting of weakly consolidated fanglomerate.

Approximately 30 percent of EAFB is covered by unconsolidated clay-rich material. The clays include a high proportion of montmorillonite and are susceptible to expansion and shrinking. However, the low precipitation of the Mojave Desert region greatly reduces the potential for such problems.

In summary, EAFB is located in a geologically low-risk area.

13.4 Geology and Geologic Hazards at Vandenberg Air Force Base, California

13.4.1 Introduction

Land use planning for VAFB should take into account the possible danger from earthquakes, seismic waves, slope instability, floods, and burning ground. Volcanism, expanding clays and rocks, and subsidence are not expected to interfere with activities on VAFB.

13.4.2 Geology

Figure 13-27 is a geologic map of the VAFB area. The oldest rocks on VAFB, found in its northwest end, are Franciscan mafic and ultramafic igneous rocks and the sedimentary Knoxville Formation of Jurassic Age. The remaining rocks, which cover the greater part of VAFB, are much younger, ranging in age from Oligocene to Recent. Oligocene poorly consolidated nonmarine sediments crop out near the older rocks. Miocene diatomaceous earth underlies the rest of VAFB and is overlain extensively by younger sediments. At most of its outcroppings, the diatomaceous earth is soft, lightweight, and porous, but resistant to weathering. It contains abundant water-soluble salts that form an efflorescence on outcrops. This rock is a source and a reservoir for gas, oil, and tar, which have been removed in oilfields north and east of VAFB. Pliocene to Recent sediments are generally unconsolidated fine to coarse sand and conglomerate. These sediments form terraces, fill valley bottoms, and are piled into extensive sand dunes near the coast. Sediments of the Pliocene Age contain hydrocarbons of Miocene derivation. Pliocene and older rocks have been extensively folded and locally faulted, probably as they were compressed during western drift of the continent (ref. 13-84).

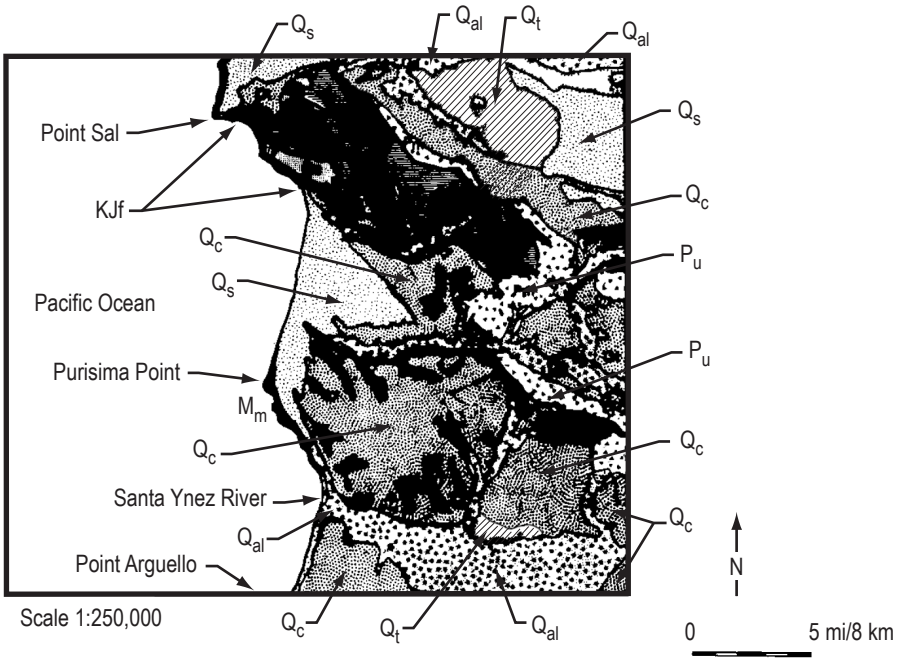

Q_{al}		Recent alluvium, horizontally stratified, identical in places to Q_t
Q_s		Recent dune sand, mobile near shore, partly anchored by vegetating inland
Q_c		Pleistocene nonmarine sedimentary deposits; terraces, unconsolidated gravel
P_u		Upper Pliocene marine sedimentary rocks
Q_t		Quaternary nonmarine terrace deposits; river and stream terrace deposits
M_u		Upper Miocene marine sedimentary rocks
M_m		Middle Miocene marine sedimentary rocks
ϕ_c		Oligocene nonmarine sedimentary rocks
J_k		Jurassic Knoxville Formation; shale, sandstone, conglomerate
KJf_v		Franciscan volcanic and matavolcanic rocks

*Note: Much of the "black" areas are either M_m, M_u, J_k, or KJf_v.

Figure 13-27. Geology of VAFB area (ref. 13-84).

13.4.3 Geologic Hazards

Sections 13.4.3.1 through 13.4.3.7 describe general locations of potential geologic hazards that exist at VAFB (fig. 13-28). Onsite investigations and engineering properties tests are recommended on a location by location basis before initiation of any construction activities.

13.4.3.1 Earthquakes. Although no recent fault scarps are known on VAFB, earthquakes pose an ever-present threat to it. VAFB is in one of the most earthquake-prone parts of the country. Between 1910 and 1971, five earthquakes with a magnitude between 4.0 and 4.9 had foci within 5 km (3 mi) of VAFB (ref. 13-85). See figure 13-29 for a depiction of earthquake epicenters around VAFB. Ground shaking has been

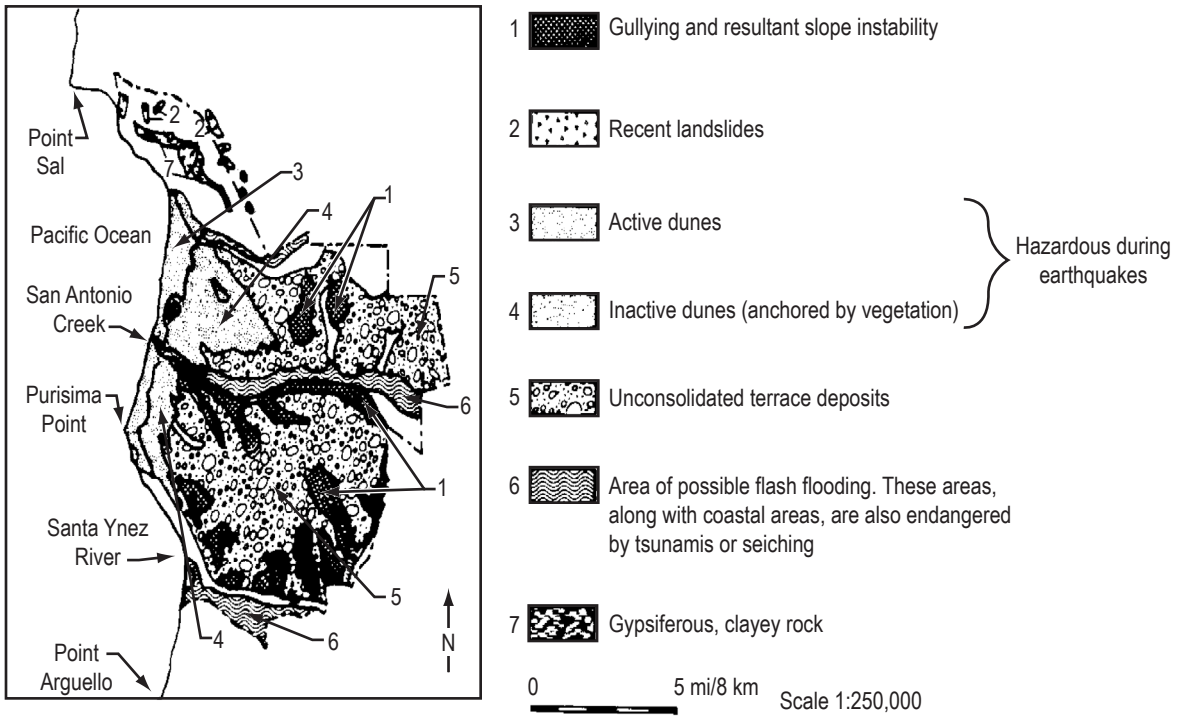

Figure 13-28. Geology hazards of VAFB area.

felt on the Base during many other earthquakes. Although usually of short duration, such shaking can trigger building collapse, water waves and flooding, slope movements, and/or release of flammable gases. Earthquakes are a definite hazard at VAFB.

VAFB is situated in one of the more seismically active regions of the United States and is characterized by a number of fault systems capable of generating major earthquakes. VAFB is located between two physiographic regions—the Transverse Ranges Province at the south and the Coastal Ranges in the north.

Battis (ref. 13-86) presents a statistical and nonstatistical approach in predicting maximum credible earthquakes and associated ground motion attenuation for VAFB. Battes' statistical hazard analysis, based on the historic earthquake (epicenter data) catalogue for a regional seismic risk study, gave 11 significant source regions identified within a 500-km (310 mi) radius of VAFB. Estimates of the maximum magnitude earthquake (M_L) possible from each source region gave results ranging from an M_L maximum of 6.1 (from the Coastal Ranges) to an 8.25 (from the Nevada Fault Zone). Maximum ground motion attenuation—acceleration, velocity, and displacement—levels were calculated at the Point Arguello site (SLC6) and are shown in figure 13-30.

Battis also presented a nonstatistical approach in predicting maximum magnitude earthquakes and ground motion. The majority of the faults within 50 km and faults with quaternary displacements within 100 km of Point Arguello gave maximum credible earthquakes between 6.75 (Santa Rosa Island Fault) and 8.5 M_L (San Andreas Fault zone). Table 13-9 presents these maximum credible earthquake potentials using Battis' calculation of maximum displacements at the Point Arguello site (at the 90-percent confidence level). The Hosgri and San Andreas Fault zones produce the maximum credible ground motions possible for Point Arguello.

However, it is felt that the majority of faults very near VAFB have maximum credible earthquake potentials of between 6.0 and 6.5 M_L. In actuality, from 1932 to 1975 there have been 135 earthquakes with magnitudes

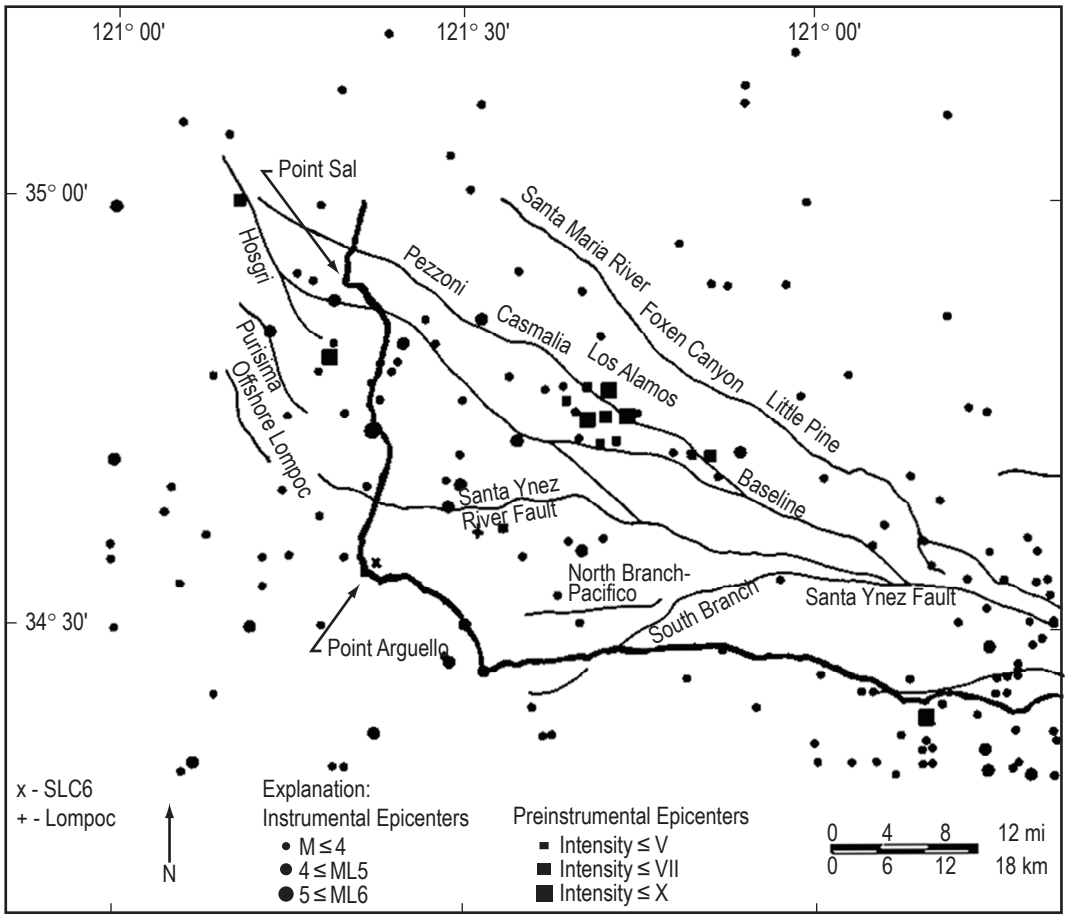

Figure 13-29. VAFB area and Western Santa Barbara County, CA, earthquake epicenters (ref. 13-86).

between 2.5 to 4.9 M_L within 50 km of Point Arguello. The largest recent event to affect the VAFB region was the 1927 Lompoc earthquake with a reported magnitude of 7.3 M_L (MMI IX), with its epicenter appearing to lie on an off-shore fault west of Point Arguello (ref. 13-86). Figure 13-29 presents a plot of these earthquake epicenters that have occurred in western Santa Barbara County, CA. Battis' work indicates that VAFB should experience an MMI of V somewhat less than once a year, which agrees with historical data.

13.4.3.2 Tsunamis and Seiches. Seismic water waves (tsunamis) must be considered a threat all along the shore of the Pacific Ocean. Land within 12 m of sea level is in the tsunami danger zone. (Actually, few documented tsunamis have reached that height.) Fresh-water dams should be examined to determine their strength should seiching take place. Areas on VAFB that could be affected by tsunamis or by seiching are given in figure 13-28.

13.4.3.3 Slope Processes. The potential for slow or fast slope changes exists in several parts of VAFB, described later and illustrated in figure 13-28:

- Gullying is cutting away diatomaceous earth around the edges of Burton Mesa and San Antonio Terrace. This slow, almost continuous process has formed very steep slopes that would be unstable in a strong earthquake.

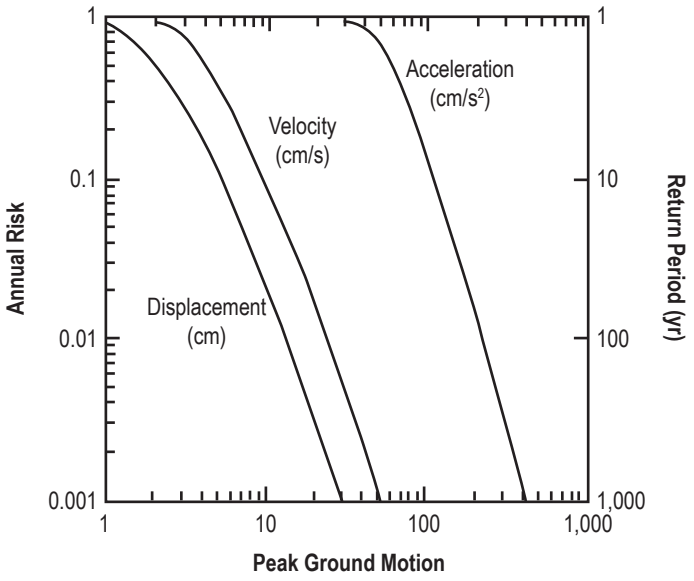

Figure 13-30. Annual seismic risk curves for peak ground motions at VAFB (SLC6)—given at the 90-percent confidence level and based on Battis' statistical method (ref. 13-86).

Table 13-9. Major faults near VAFB and associated maximum credible earthquakes and ground motions (90-percent confidence level) at Point Arguello site (based on nonstatistical method of Battis (ref. 13-86)).

Fault	Maximum Credible Earthquake (M_L)	Maximum Credible Ground Motions at Point Arguello*,**		
		Acceleration (cm/s^2)	Velocity (cm/s)	Displacement (cm)
San Andreas Fault zone	8.5	387.2	91.4	64.6
Hosgri Fault zone	7.5	678.6	110.8	54.3
Big Pine Fault	7.5			
Santa Ynez Fault	7.5			
Rinconada Fault	7.5			
Nacimiento Fault zone	7.0			
Santa Cruz Island Fault	6.75			
Santa Rosa Island Fault	6.75			

*Point Arguello and Point Sal are at the extremes of maximum credible ground motion for this area. Therefore, at the Point Sal site (Hosgri Fault zone), the maximum acceleration, velocity, and displacement values of 1,288.8 cm/s^2, 200.2 cm/s, and 83.8 cm, respectively, are possible.

**Other fault ground motion statistics were not available from ref. 13-86.

- Several large landslides have occurred in the Casmalia Hills, in or near the north end of the Base. Surface material there is obviously unstable and should be examined carefully onsite before any construction.

- Roughly one quarter of VAFB is covered by recent sand dunes. Though much of the dune area is anchored by vegetation, including windbreaks at the landward edge of the dunefield, sand blasting should be expected on San Antonio Terrace and Burton Mesa during times of high winds. (See sec. 2 on winds.)

- Although their surfaces are flat and nearly level, San Antonio Terrace and Burton Mesa are likely to be strongly affected by earthquake-induced surface movements because of the thick layer of unconsolidated sand and gravel terrace deposits that cover them. Shaking is highly amplified by thick, loose material, and buildings or other constructions on such material are at risk, especially if they are several stories high.

13.4.3.4 Floods. Three flood plain systems exist on VAFB; from north to south they are Shuman Canyon, San Antonio Valley, and Santa Ynez Valley. All three should be considered possible sites for flash flooding, especially since during times when their rivers are dry, dune and bar sand partially block their outlets to the ocean. In addition, small dams in the Santa Ynez drainage basin could break and cause flooding during an earthquake.

13.4.3.5 Volcanic Hazards. No volcanic hazards are expected to affect this area, although tsunamis caused by distant volcanism are an always-present danger. (See sec. 13.4.3.2.)

13.4.3.6 Expanding Clays and Rocks. Expanding clays and rocks are not a major hazard on most of the Base. Several hundred feet of gypsiferous, clayey, alkaline shale are present in the Casmalia Hills and should be avoided when locating construction sites.

13.4.3.7 Subsidence. Burning of hydrocarbon-rich layers of diatomaceous earth is well documented in historic time in the Casmalia Hills area. Burnt ground has been encountered to depths as great as 300 m (1,000 ft) in nearby oil wells (ref. 13-87). Red, hard, vesicular, scoriaceous rock (clinker) results from this burning. However, no change in the volume of the burnt rock has been documented. Burning itself poses a threat, as it is next to impossible to stop once it has been started—by lightning or man.

13.4.4 Conclusions

Numerous potential geologic hazards exist within VAFB. Earthquakes occur from time to time and could set off other dangerous events. Tsunamis caused by remote earthquakes or volcanism could affect the area of the base whose altitude is within 12 m of sea level. Seiching may pose a danger to small dams on VAFB. Widespread slope and surface instability is likely in the event of a strong earthquake. Blowing sand at times reduces the usefulness of some areas. Flash floods are possible in the valleys during rainy seasons. In some areas, hydrocarbon-soaked rocks have been known to catch fire. Use of different areas of VAFB should take these hazards into account. True, the surface of VAFB is stable until rare, hazard-causing events occur. But if they do, extensive destruction is possible.

13.5 Geology and Geologic Hazards at Cape Canaveral and Kennedy Space Center, Florida

13.5.1 Introduction and Geology

Cape Canaveral, on the eastern coast of the Florida peninsula, covers an expanse of barrier bars, swamps, and lagoons between the Atlantic Ocean and the mainland. The entire Kennedy Space Center (KSC) lies within 8 m of sea level. Surficial deposits on KSC are roughly 30 m of Miocene to Recent shelly sand and clay and medium-to-fine-grained sand and silt (ref. 13-88) (fig. 13-31). These sediments overlie Eocene limestone and dolomite.

13.5.2 Geologic Hazards at Cape Canaveral and Kennedy Space Center

13.5.2.1 Earthquakes. Earthquakes are extremely unlikely in this area of the United States and should not be considered a hazard.

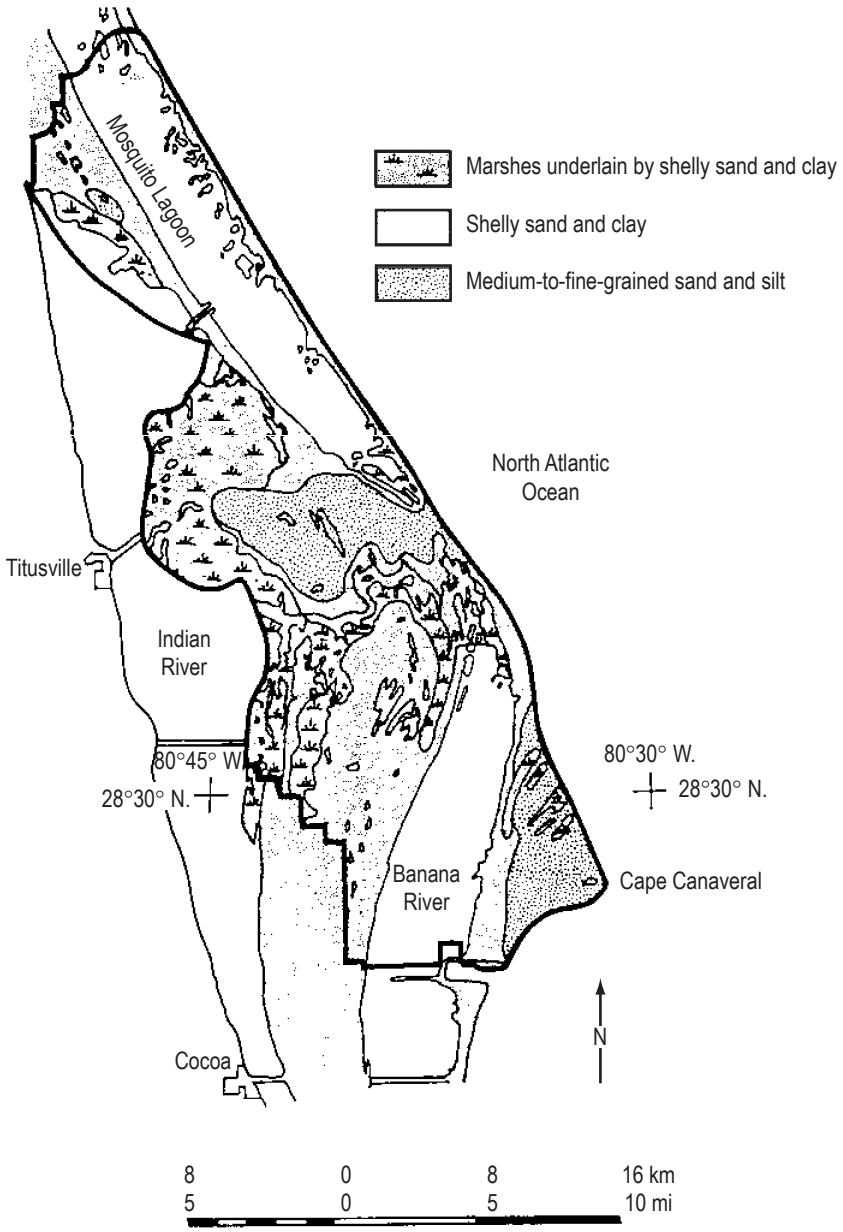

Figure 13-31. Geology of Cape Canaveral, FL.

13.5.2.2 Tsunamis and Seiches. Sea waves (tsunamis) induced by earthquakes and/or volcanism elsewhere could be a hazard to the entire KSC because of its low elevation. However, tsunamis are not common in the Atlantic Ocean and, although not impossible, are considered unlikely. Nor are the lagoons and rivers likely to develop seiches.

13.5.2.3 Slope Stability. The lack of topographic relief on Cape Canaveral and KSC means slope stability is not a problem there.

13.5.2.4 Floods. Flooding could be a hazard to KSC if high water is brought about by hurricane winds. (See secs. 2 and 12 on wind and severe weather, respectively.)

13.5.2.5 Volcanic Hazards. Volcanism near Cape Canaveral is unknown in recent time. The only volcanic hazards to the Cape are tsunamis caused by distant volcanism.

13.5.2.6 Expanding Soils and Rocks. Expanding soils and rocks are not a hazard to KSC because of the high sand content of sediments and the consistently high humidity.

13.5.2.7 Subsidence and Uplift. Drilling results indicate the presence of caverns in the limestone and dolomite units that underlie KSC (ref. 13-88); therefore, there is potential for eventual caving. There is no apparent evidence of karst topography in the KSC area, nor is collapse expected in the foreseeable future. However, test drilling should always precede building location and construction.

13.5.3 Conclusions

Cape Canaveral/KSC is a low-risk area for geologic hazards. Only flooding due to hurricanes or seismically-induced waves is considered to be of possible importance. Crucial structures that would not survive high water should be protected by dikes.

13.6 Seismic Environment for Ground Support Equipment (VAFB and EAFB)

GSE, which may be subjected to a high-risk potential seismic environment (principally at VAFB and to a lesser degree EAFB), should be designed considering the geologic hazards defined in this section. The following are recommendations to consider during the design process.

13.6.1 Ground Support Equipment Categories and Recommendations

For seismic purposes, two categories of GSE have been established:

(1) Equipment that can inflict structural damage on space vehicle elements during and after a seismic event by its operation or by its failure to operate.

(2) Equipment located in close proximity to space vehicle elements that can cause major structural damage due to support failure or physical contact with the integrated space vehicle elements.

All GSE elements should remain integrally constrained in their packages. The equipment should not be allowed to separate from the unit and become missiles. This recommendation does not include equipment that is already separated from space vehicle elements by strong physical barriers, such as walls or enclosures sufficient to prevent equipment contact with space vehicle elements.

13.6.2 Types of Design Analyses for Ground Support Equipment

Recommendations for typical dynamic or static analyses follow.

13.6.2.1 Dynamic Analysis. A rigorous dynamic analysis should be made to demonstrate that the equipment and its supporting mechanism/structure will withstand—without collapse or excessive deflection—the design loads induced in the system by a major seismic event. The effect of such an event on the system can be determined using the GSE design response spectra for major seismic events at VAFB, shown in figure 13-32. The design loads should equal the root-sum-square of the modal responses, where natural frequencies are determined

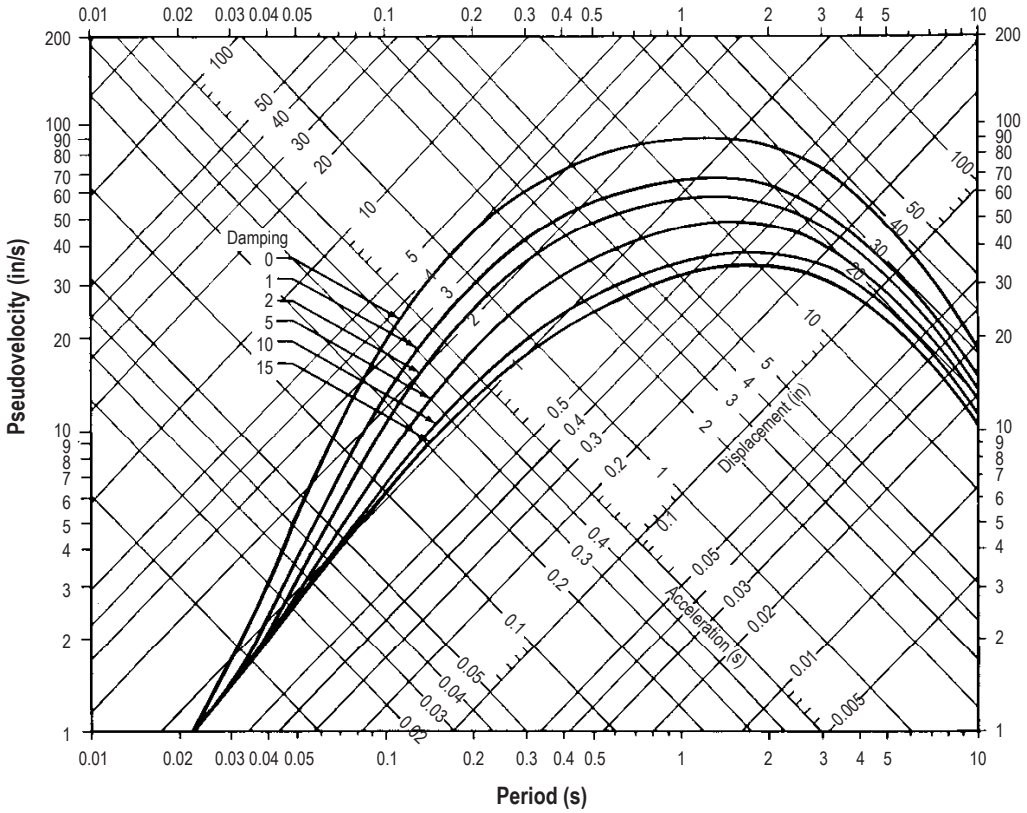

Note: Spectra are for horizontal response; for vertical response, multiply the acceleration ordinate by 2/3. Maximum credible earthquake for maximum probable earthquake; i.e., 10-percent probability of exceedance for 20-yr structural life, multiply acceleration by 0.4.

Figure 13-32. 0.70E elastic design spectra for strongest potential vibratory ground motion.

by modal analysis and whose damping values are estimated by damping analysis, or by similarity to structures whose damping has been measured under actual or simulated earthquake motion.

13.6.2.2 Static Analysis. The following criteria are recommendations for designing GSE for seismic resistance:

- GSE weighing <45 kg (<100 lb) should have restraints to resist a horizontal force of ×1.5 equipment weight from any direction applied to its center of gravity.

- For GSE weighing between 45 and 450 kg (100 and 1,000 lb), the following equation can be used to determine the recommended restraints:

$$F = ZKCW\,, \tag{13.4}$$

where

F = equivalent static lateral force (in pounds) applied at the center of gravity
Z = seismic probability coefficient (no units), where $Z = 1.5$ for high-loss potential equipment (damages SSV element), $Z = 1$ for low-loss potential equipment (damages GSE only)

C = seismic force coefficient (no units)
K = coefficient based on building type (no units)
W = weight (in pounds) of item under consideration.

C may be calculated using equation (13.5):

$$C = (C_s)\,(A_h)\,(MF)\ , \tag{13.5}$$

where

C_s = soil constant (no units) = $2.25 - 0.125\,f_b \geq 1$
f_b = allowable soil-bearing value (in kips/ft^2) (See Geophysical Investigation Supplement for VAFB Station Set V23 (VCR-77-067 of 20 January 1977) (1 kip = 1,000 lb) (ref. 13-89)
A_h = design acceleration = $0.10 + 0.15\,(h/h_t)$
h = height of equipment in building above building base
h_t = height of building
MF = magnification factor (no units):

$$MF = \frac{1}{\sqrt{\left[1-\left(T_a\,/\,T\right)^2\right]^2 + \left[0.04\,T_{a/T}\right]^2}}\ , \tag{13.6}$$

where

T_a = period of item under consideration (in seconds)
T = period of building (in seconds).

(For the graphical solution to equation (13.6), see figures 13-33 and 13-34.)

The building characteristic constants for the mobile service tower, the payload changeout room, and the access tower are shown in table 13-10. For equipment in contact with the soil, buried in the soil, or supported by footings, pedestals, or slaps supported by soil, use the following coefficients: $K = 1.00$ and $C = 0.15$.

Also recommended is that items weighing >450 kg (>1,000 lb) be subjected to dynamic analysis. Items weighing >450 kg (>1,000 lb) and having a ratio of 4:1 or greater between structural strength of tiedown and limit load, as defined in paragraph 2, are exempt from dynamic analysis.

Equipment that is to be in use for <8 hr in close proximity to or supporting SSV elements is exempt from these requirements. Equipment that is mounted on casters or wheels should have lockable casters/wheels and be rigidly tied to primary or substantial secondary structure.

13.7 Earth's Properties

The physical properties and dynamical characteristics of the Earth along with the Sun and the other major and minor planets within our solar system are presented in table 13-11. This is given to provide a ready reference on the Earth's physical properties and dynamical characteristics (ref. 13-90).

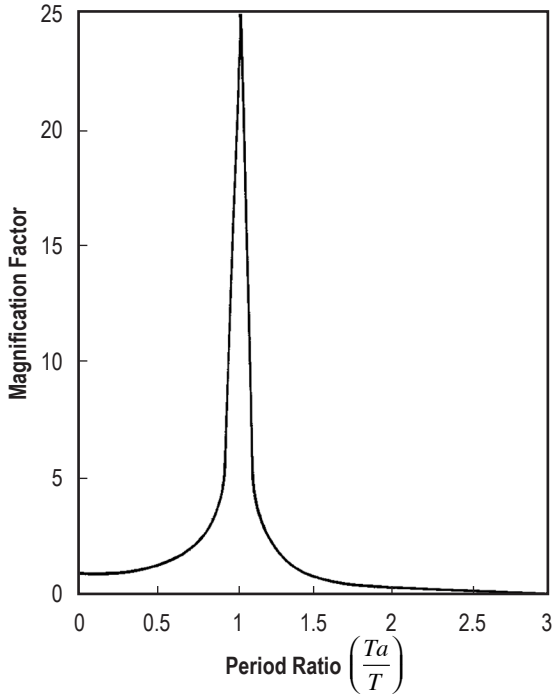

Figure 13-33. 0–25 magnification factor (MF) versus period ratio.

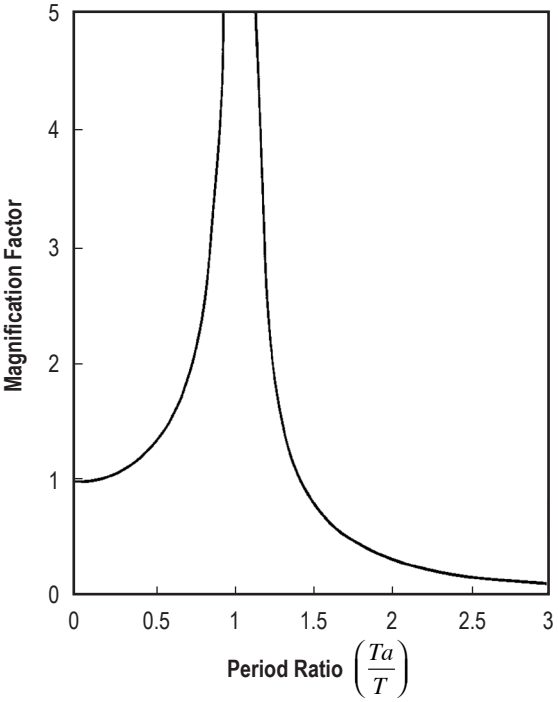

Figure 13-34. 0–5 magnification factor (MF) versus period ratio.

Table 13-10. Building characteristic constants.

	Building Type Coefficient (*K*) (unitless)	Height of Equipment in Building (*h*)		Period of Building (*T*)* (in s)
		(ft)	(m)	
Mobile service tower	0.8	275	84	1.23
Payload changeout room	0.8	160	49	0.93
Access tower	0.8	192	59	0.61

*Building period is the inverse of the building frequency.

Table 13-11. Physical properties and dynamical characteristics of the Earth, Sun, and other planets.

Physical Properties	Sun	Mercury	Venus	Earth	Mars	Ceres	Jupiter	Saturn	Uranus	Neptune	Pluto	Eris
Equatorial radius (km)	6.96E+05	2439.7	6051.8	6378.136	3397	474	71492	60268	25559	24766	1151	~1400
Flattening	0	0	0	0.003352813	0.006476306	0	0.06487	0.09796	0.02293	0.0171	0	–
g polar (m/s)	274	3.701	8.87	9.832186369	3.69	0.28	27.01	12.14	9.19	11.41	0.655	–
g equatorial (m/s)	274	3.701	8.87	9.780326772	3.69	0.28	23.12	8.96	8.69	11	0.655	–
g_0 (m/s)	274	3.701	8.87	9.82022	3.69	0.28	24.79	10.44	8.87	11.15	0.655	–
GM (km^3/s^2)	13271243994	22032.09	324858.63	398600.44	42828.3	63.2	126686537	37931284.5	7793947	6835107	870	–
Mass (kg)	1.9891E+30	3.302E+23	4.8685E+24	5.9736E+24	6.4185E+23	9.4715E+20	1.8986E+27	5.68461E+26	8.6832E+25	1.0243E+26	1.314E+22	–
Mass ratio (GM Sun/GM planet)	–	6.0236E+6	4.0852E+05	3.3295E+05	3.0987E+06	2.0999E+09	1.0473E+03	3.4979E+03	2.2903E+04	1.9412E+04	1.3500E+08	–
Density (gm/cm^3)	1.408	5.427	5.204	5.515	3.933	–	1.326	0.687	1.318	1.638	1.75	–
Mean temperature (K)	5778 (photosphere)	442.5	735	270	210	–	165 (1 bar)	134 (1 bar)	76 (1 bar)	72 (1 bar)	37.5	–
Geometric albedo	–	0.106	0.65	0.367	0.15	0.1132	0.52	0.47	0.51	0.41	0.3	–
Solar constant (W/m^2)	6.3180E+07	9936.9	2613.9	1367.6	589.2	178.7776775	50.5	15.04	3.71	1.47	0.89	0.295962975
Dynamical Characteristics	**Sun**	**Mercury**	**Venus**	**Earth**	**Mars**	**Ceres**	**Jupiter**	**Saturn**	**Uranus**	**Neptune**	**Pluto**	**2003 UB313**
Semimajor axis (AU)	–	0.38709893	0.72333199	1.00000011	1.52366231	2.765813554	5.20336301	9.53707032	19.1912639	30.0689635	39.48168677	67.97682158
Eccentricity	–	0.20563069	0.00677323	0.01671022	0.09341233	0.078561009	0.04839266	0.0541506	0.04716771	0.00858587	0.24880766	0.436581589
Inclination (degrees)	–	7.00487	3.39471	0.00005	1.85061	10.6069597	1.3053	2.48446	0.76986	1.76917	17.14175	43.83410933
Escape velocity (km/s^2)	617.7	4.435	10.361	11.186	5.027	0.45061632	59.5	35.5	21.3	23.5	1.3	–
Mean orbit velocity (km/s)	–	47.8725	35.0214	29.7859	24.1309	17.9091	13.0697	9.6624	5.4778 (6.81)	5.43	4.947	3.6125
Sidereal day (hr)	609.12	1407.5088	–5832.5	23.93419	24.62	9.08	9.894	10.61	17.14	16.7	–	–
Mean solar day (d)	–	175.9421	116.749	1.002738	1.03E+00	–	–	–	–	–	6.38675	–
Sidereal period (yr)	–	0.2408445	0.6151826	1.0000174	1.88081578	4.59984	11.856523	29.423519	83.747407	163.72321	248.0208	560.46627
Sidereal period (days)	–	87.968435	224.695434	365.25636	686.98	1680.12	4330.60	10746.94	30588.74	59799.9	90589.596	204710.30
Obliquity to orbit (degrees)	7.25 (ecliptic)	~0.1	177.3	23.45	25.19	–	3.12	26.73	97.86	29.56	122.53	–
Pole (RA in deg. J2000)	286.13	281.01	272.76	0	317.681	–	268.05	40.589	357.311	299.36	313.02	–
Pole (DEC in deg. J2000)	63.87	61.45	67.16	90	52.881	–	64.49	83.537	–15.175	43.46	9.09	–
Dipole tilt (deg)	–	169	–	11.3	–	–	9.6	0	58.6	47	–	–
Dipole offset (r_p)	–	–	–	0.0725	–	–	0.131	0.04	0.3	0.55	–	–
Magnetic moment (gauss R_p^3)	–	0.0033	–	0.61	$<10^{-4}$	–	4.28	0.21	0.228	0.133	–	–

E+30 = 10^{30}

REFERENCES

13-1. Neuendorf, K.K.E.; Mehl, Jr., J.P.; and Jackson, J.A.: *Glossary of Geology*, 5th Edition, American Geological Institute, 2005.

13-2. Van Dorn, W.G.: "Source Mechanism of the Tsunami of March 28, 1964," *Proc. 9th Alaska Coastal Engineering Conference*, Lisbon, ASCE, pp. 166–190, 1964.

13-3. Stein, R.S.; and Yeats, R.S.: "Hidden Earthquakes," *Scientific American*, Vol. 260, pp. 48–57, June 1989.

13-4. Krinitzsky, E.L.: "State-of-the-Art for Assessing Earthquake Hazards in the United States, Report 29, Selection of Earthquake Ground Motions for Engineering," Technical Report S-73-1, U.S. Army Corps of Engineers Waterways Experiment Station, Vicksburg, MS, July 1995.

13-5. "Basic Seismology–Earthquake Size–Fault Dimensions," Seismology Research Centre, Australia, <http://www.seis.com.au>, 2006.

13-6. Louie, J.: "Seismic Deformation," University of Nevada Reno Seismological Laboratory, <http://www.seismo,unr.edu/ftp/pub/louie/class/100/seismic-waves.html>, October 7, 1996.

13-7. USGS Earthquake Hazards Program, ShakeMaps, <http://earthquake.usgs.gov/shakemap>, 2006.

13-8. Boore, D.M.; Joyner, W.B.; and Fumal, T.E.: "Equations for Estimating Horizontal Response Spectra and Peak Accelerations From Western North American Earthquakes: A Summary of Recent Work," *Seism. Res. Lett.*, Vol. 68, No. 1, pp. 128–153, 1997.

13-9. Joyner, W.B.; and Boore, D.M.: "Measurement, Characterization, and Prediction of Strong Ground Motion," in *Proceedings of Conf. on Earthq. Eng. & Soil Dyn. II,* Geotechnical Vision, Am. Soc. Civil Eng., Park City, Utah, Geotechnical Special Publication 20, pp. 43–102, June 27–30, 1988.

13-10. SHAKE2000, A Computer Program for the 1-D Analysis of Geotechnical Earthquake Engineering Problems, <http://www.shake2000.com>, 2006.

13-11. USGS Earthquake Hazards Program, "2002 USGS National Seismic Hazard Maps, Conterminous United States, Revised April 2003," <http://earthquake.usgs.gov/research/hazmaps/products_data/2002/us2002.php>.

13-12. USGS, "Earthquake Hazard in the Heart of the Homeland," U.S. Geological Survey Fact Sheet: FS-131-02, U.S. Dept. of the Interior, October 2002.

13-13. O'Carroll, C.: "New Global Digital Tectonic Activity Map of the Earth Produced," NASA News Archive, Earth Observatory, Release No. 99-16, 5 November 1999.

13-14. Mualchin, L.; and Jones, A.L.: "Peak Acceleration From Maximum Credible Earthquakes in California," California Department of Conservation, Division of Mines and Geology Open-file Report 92–01, 1992.

13-15. Power, M.S.; Chiou, S.-J.; and Mayes, R.L.: "National Representation of Seismic Hazard and Ground Motion for Highway Facilities," in *Research Progress and Accomplishments: 1997–1999*, From Multidisciplinary Center for Earthquake Engineering Research – University of Buffalo, State University of New York, pp. 69–78, July 1999.

13-16. Global Seismic Hazard Map, <http://seismo.ethz.ch/GSHAP/>, January 14, 2000.

13-17. Shedlock, K.M.: "Seismic Hazard Map of North and Central America and the Caribbean," *Annali di Geofisica*, Vol. 42, No. 6, pp. 1225–1230, December 1999.

13-18. Cousineau, R.D.; Crook, Jr., R.; and Leeds, D.J.: "Investigation of Seismicity and Related Effects at NASA Ames-Dryden Flight Research Facility, Computer Center, Edwards, California," *NASA CR–170415*, November 1985.

13-19. Krinitizsky, E.L.; and Chang, F.K.: "State-of-the-Art for Assessing Earthquake Hazards in the United States, Specifying Peak Motions for Design Earthquakes," Corps of Engineers, Waterways Experiment Station, Misc. Paper S-73-1, Report 7, 34 pp., 1977.

13-20. Bonilla, M.G.: "Surface Faulting and Related Effects," In *Earthquake Engineering*, R.L. Wiegel (ed.), Prentice-Hall, Englewood Cliffs, NJ, pp. 47–74, 1970.

13-21. Greensfelder, R.W.: "Map of Maximum Bedrock Acceleration From Earthquakes in California," California Division of Mines and Geology, Map Sheet 23, 1974.

13-22. USGS/CGS Probabilistic Seismic Hazards Assessment Model of 2002/2003, <http://www.consrv.ca.gov/CGS/rghm/pshamap/pshamain.html>, Accessed 2007.

13-23. USGS Fact Sheet FS-039-03, "Is a Powerful Quake Likely to Strike in the Next 30 Years?" U.S. Dept. of the Interior, U.S. Geological Survey, <http://pubs.usga.gov/fs/2003/fs039-03/fs039-03.pdf>, 2003.

13-24. Bakun, W.H.; Johnston, A.C.; and Hopper, M.G.: "Estimating Locations and Magnitudes of Earthquakes in Eastern North America from Modified Mercalli Intensities," *Bull. Seismol. Soc. Am.*, Vol. 93, No. 1, pp. 190–202, February 2003.

13-25. Stewart, J.P.; Chiou, S.J.; Bray, J.D.; et al.: "Ground Motion Evaluation Procedures for Performance-Based Design," PEER Report 2001/09, Pacific Earthquake Engineering Research Center, College of Engineering, University of California, Berkeley, September 2001.

13-26. Wells, D.L.; and Coppersmith, K.J.: "New Empirical Relationships Among Magnitude, Rupture Length, Rupture Width, Rupture Area, and Surface Displacement," *Bull. Seismol. Soc. Am.*, Vol. 84, No. 4, pp. 974–1002, August 1994.

13-27. Lander, J.F.: "Two Decades of Global Tsunamis: 1982–2002," *Science of Tsuknami Hazards*, Vol. 21, No. 1, pp. 3–8, 2003.

13-28. "Tsunami," FEMA, <http://www.fema.gov/hazard/tsunami/index.shtm>, April 2006.

13-29. "Frequently Asked Questions About Tsunamis-Tsunamic: The Great Waves," NOAA National Weather Service – International Tsunami Information Center, <http://ioc3.unesco.org/itic/categories.php?category_no=137>, 10C Brochure 2006-2, April 2006.

13-30. Garrison, T.S.: *Tsunami, Seiches, and Tides*, 4th Ed., Brooks/Cole Publishing Co., Chapter 11, pp. 259–287, 2002.

13-31. Lander, J.F.; Whiteside, L.S.; and Lockridge, P.A.: "A Brief History of Tsunamis in the Caribbean Sea," *Science of Tsunami Hazards*, Vol. 20, No. 2, pp. 57–64, 2002.

13-32. Lockridge, P.A.; Whiteside, L.S.: and Lander, J.F.: "Tsunamis and Tsunami-like Waves of the Eastern United States," *Science of Tsunami Hazards*, Vol. 20, No. 3, pp. 120–125, 2002.

13-33. Bornhold, B.D.; Thomson, R.E.; Rabinovich, A.B.; et al.: "Risk of Landslide-Generated Tsunamis for the Coast of British Columbia and Alaska," *Proc. 54th Canadian Geotechnical Conference*, Calgary, Alberta, pp. 1450–1454, September 16–19, 2001.

13-34. Synolakis, C.E.; McCarthy, D.; Titov, V.V.; and Borrero, J.: "Evaluating the Tsunami Risk in California," in California and the World Ocean '97, *Proc. Conference American Society of Civil Engineers*, San Diego, CA, Vol. 2, pp. 1225–1236, March 24–27, 1997.

13-35. "Seismic Hazards: Tsunamis," Oahu Civil Defense Agency, City and County of Honolulu, State of Hawaii, pp. 9-1 to 9-11, <http://www.mothernature-hawaii.com/files/honolulu_planning-13.pdf>, 2003.

13-36. "Tsunami Statistics," on NOAA-NWS West Coast & Alaska Tsunami Warning Center, <http://wcatwc.arh.noaa.gov/tsustats.pdf>, source of data: National Geophysical Data Center, NOAA, 2000.

13-37. "Engineering and Design: Tidal Hydraulics – Engineer Manual," EM 1110-2-1607, Dept. of the Army, U.S. Army Corps of Engineers, Chapter 2 Definition and Forcing Functions of Estuaries, Section IV Seiche, pp. 2–12, March 15, 1991.

13-38. "Storm Surges, Seiches and Edge Waves," University of Wisconsin Sea Grant, <http://seagrant.wisc.edu>, April 30, 2002.

13-39. Sobien, D.A.; and Paxton, C.H.: " A Primer on Coastal Flood Forecasting," Technical Attachment, NOAA SR/SSD 98-2, NWSO Tampa Bay Area, FL, January 15, 1998.

13-40. Jelesnianski, C.P.; and Holland, G.J.: "Global Guide to Tropical Cyclone Forecasting: Chapter 4: The Habitation Layer," Section 4.2 Storm Surges, Bureau of Meteorology Research Centre, Commonwealth of Australia, <http://www.bom.gov.au/bmrc/pubs/tcguide/ch4/ch4_2.htm>, 2006**.**

13-41. Oliver, J.: "The Tropical Cyclone Surge," In *Natural Hazards and Reinsurance – 1989*, J. Oliver and N. Britton (eds.), Proceedings of Sterling Office College, Lidcombe, NSW: Cumberland College of Health Sciences (Australia), 1989.

13-42. "Hurricane Storm Surge Risk Analysis: Description of Hurricane Storm Surge Inundation Data," Alabama Coastal Hazards Assessment – Coastal Risk Management, as part of NOAA Coastal Services Center, <http://www.csc.noaa.gov>, 2006.

13-43. The Florida Hurricane Surge Atlas, <http://www.srh.nasa.gov/mlb/atlas.html>, April 12, 2006.

13-44. USGS Water Science Glossary of Terms, USGS Water Science for Schools: <http://ga.water.usgs.gov/edu/dictionary.html>, September 1, 2005.

13-45. Leopold, L.B.; Wolman, M.G.; and Miller, J.P.: "Fluvial Processes in Geomorphology," W.H. Freeman and Co., San Francisco, CA, 522 pp., 1964.

13-46. "Flash Floods and Floods. The Awesome Power!" A Preparedness Guide, U.S. Dept of Commerce – NOAA/NWS, Brochure No. NOAA/PA 92050: ARC 4493, July 1992.

13-47. "What is a 5 Year Flood Event? (The answer isn't simple…)", U.S. Army Corps of Engineers – Walla District, <http://www.nww.usace.army.mil/html/offices/op/em/5yrflood.htm>, February 16, 2006.

13-48. ESRI/FEMA Hazard Map, <http://www.esri.com/hazards/makemap.html>, March 22, 2006.

13-49. FEMA Bulletin 17B, "Guidelines for Determining Flood Flow Frequency," <http://www.fema.gov/mit/tsd/dl_flow.htm>, IACWD, 1982.

13-50. Dunne, T.; and Leopold, L.B.: *Water in Environmental Planning*, W.H. Freeman and Co., San Francisco, CA, 1978.

13-51. Godt, J.W.: Digital Compilation of Landslide Overview Map of the Conterminous United States: U.S. Geological Survey Open-File Report 97-289, <http://landslides.usgs.gov/html_files/landslides/nationalmap/national.html>, 1997.

13-52. Sharpe, C.F.S.: *Landsides and Related Phenomena*, Columbia University Press, New York, p. 137, 1938.

13-53. Highland, L.; and Johnson, M.: "Landslide Types and Processes," Dept. of the Interior – USGS Fact Sheet 2004-3072, July 2004.

13-54. Montgomery, D.R.; and Dietrich, W.E.: "A Physically-Based Model for Topographic Control on Shallow Landsliding," *Water Resources Research*, Vol. 30, No. 4, pp. 1153–1171, 1994.

13-55. Keefer, D.K.: "Landslides Caused by Earthquakes," *Geological Society of America Bulletin*, Vol. 95, pp. 406–421, 1984.

13-56. Jibson, R.W.; Harp, E.L.; and Michael, J.A.: "A Method for Producing Digital Probabilistic Seismic Landslide Hazard Maps: An Example from the Los Angeles, California, Area," U.S. Geological Survey Open-File Report 98-113, <http://geohazards.cr.usgs.gov/pubs/ofr/98-113/ofr98-113.html>, 1998.

13-57. USGS, "Miscellaneous Volcanic Facts," USGS/Cascades Volcano Observatory, Vancouver, WA, <http://vulcan.wr.usgs.gov/LivingWith/VolcanicFacts/misc_volcanic_facts.html>, 2006.

13-58. "Volcanic Activity," Volcanic Activity Forum/Weather Almanac/Vol. 1, <http://www.weatherexplained.com/Vol-1/Volcanic-Activity.html>, 2006.

13-59. USGS, "What Are Volcano Hazards?," USGS Fact Sheet 002–97, revised July 2004.

13-60. Newhall, C.G.; and Self, S.: "An Estimate of Explosive Magnitude for Historical Volcanism," *JGR*, Vol. 87, No. C2, pp. 1231–1238, February 20, 1982.

13-61. USGS, "VEI – Photo Glossary of Volcano Terms," Volcano Hazards Program – Reducing Volcanic Risk, <http://volcanoes.usgs.gov/Products/Pglossary/vei.html>, November 8, 2001.

13-62. USGS, “Can Another Great Volcanic Eruption Happen in Alaska?,” USGS Fact Sheet 075-98, 2004.

13-63. Kessinger, C.; Tsvi, T.; Herzegh, P.; et al.: Oceanic Weather Product Development Team Presentation at 2005 NASA ASAP Science Review Meeting, Boulder CO, April 13–14, 2005.

13-64. USGS, “Mount St. Helens, Washington, May 18, 1980, Ash Fallout Distribution Within the U.S.,” <http://vulcan.wr.usgs.gov/Volcanoes/MSH/Maps/may18_ashmap.html>, 1990.

13-65. U.S. Geological Survey, Menlo Park, California, “Volcanic Ash: Effects & Mitigation Strategies,” <http://volcanoes.usgs.gov/ash/properties.html>, March 21, 2005.

13-66. USGS, “Cascade Range Volcanoes – Thickness vs. Distance of Select Cascade Range Tephras,” <http://vulcan.wr.usgs.gov/Volcanoes/Cascades/Hazards/tephra_plot_distance.html>, November 26, 2002.

13-67. Williams, S.; Watkins, A.; De Grey, L.; and Yalcin, K.: “Environmental Geology – Geol 406/506: Module 6 – Volcanoes,” Idaho State University, Department of Geosciences, <http://wapi.isu.edu/envgeo/EG6_volcano/volcanoes.htm>, August 23, 2004.

13-68. Bluth, G.J.S.; and Rose, W.I.: “Removal Processes of Volcanic Ash Particles From the Atmosphere,” Michigan Tech, Geological and Mining Engineering and Sciences, In *Proceedings of the Second International Conference on Volcanic Ash and Aviation Safety*, Alexandria, VA, June 21–24, 2004.

13-69. Woods, A.W.; and Kienle, J.: “The Injection of Volcanic Ash Into the Atmosphere,” In *Proceedings of the 1st International Symposium on Volcanic Ash and Aviation Safety* , Casadevall, T.J. (ed.), USGS Bulletin, 2047, pp. 101–106, 1994.

13-70. Rosen, J.; and Vladimir, A.I.: “Stratospheric Aerosols—Chapter 4,” In *Aerosol Effects on Climate*, S.G. Jennings (ed), University of Arizona Press, 304 pp., 1993.

13-71. USGS, “Tephra: Volcanic Rock and Glass Fragments,” Volcano Hazards Program, <http://volcanoes.usgs.gov/Hazards/What/Tephra/tephra.html>, December 23, 1999.

13-72. Vermote, E.; Vibert, S.; Kilcoyne, H.; et al.: “Suspended Matter: Visible/Infrared Imager/Radiometer Suite Algorithm Theoretical Basis Document,” Version 5, Raytheon Systems Co., NPOESS/VHRS, SBRS Document No. Y2390, March 2002.

13-73. “What is the Largest Eruption Ever?,” North Dakota Space Grant Consortium, <http://volcano.und.edu/vwdocs/frequent_questions/top_101/Interesting/Interesting6.html>, 2006.

13-74. Mason, B.G.; Pyle, D.M.; and Oppenheimer, C.: “The Size and Frequency of the Largest Explosive Eruptions on Earth,” *Bull. Volcanol*., Vol. 66, pp. 735–748, DOI 10.1007/s00445-004-0355-9, 2004.

13-75. Rogers, W.P.: “Guidelines and Criteria for Identification and Land Use Controls of Geologic Hazard and Mineral Resource Areas,” *Colo. Geol. Survey Special Publ*., No. 6, pp. 68–76, 1974.

13-76. James, Jr., D.E.; and Holtz, W.G.: “Expansive Soils—The Hidden Disaster,” *Civil Eng*., Vol. 43, No. 8, pp. 49–51, August 1973.

13-77. Mullineaux, D.R.: “Preliminary Map of Volcanic Hazards in the Conterminous United States,” U.S. Geological Survey, Misc. Field Inv. MF-786, scale 1:7,500,000, 1976.

13-78. Bolt, B.A.; Horn, W.L.; Macdonald, G.A.; and Scott, R.E.: *Geologic Hazards: New York*, Chapter on Evaluation of Volcanic Hazards, Springer-Verlag, 328 pp., 1975.

13-79. Dibblee, Jr., T.W.: “Geology of the Rogers Lake and Kramer Quadrangle,” U.S. Geol. Survey Bull. 1089-B, pp. 73–139, 1960.

13-80. Droste, J.B.: “Clay Minerals in the Playa Sediments of the Mojave Desert, California,” California Division of Mines and Geology Special Report 69, 19 pp., 1961.

13-81. Mortan, D.M.: “Geologic Hazards in Southwestern San Bernardino County, California,” California Division of Mines and Geological Special Report 113, 1976.

13-82. Real, C.R.; Toppozada, T.R.; and Parke, D.L.: “Earthquake Epicenter Map of California, 1900–1974,” California Dept. of Conservation, Division of Mines and Geology, MS 39, 1978.

13-83. Radbruch, D.H.; and Crowther, K.C.: Maps Showing Areas of Estimated Relative Amounts of Landslides in California, U.S. Geol. Survey Misc. Geol. Inv. Map 747, scale 1:1,000,000, 1973.

13-84. Jennings, C.W.: Santa Maria Sheet, Geologic Map of California, California Division of Mines, 1:125,000, 1959.

13-85. Fife, D.L.; Rodgers, D.A.; Chase, D.W.; et al.: “Geologic Hazards in Southwestern San Bernardino County, CA,” California Division of Mines and Geology Special Report 113, Plate 7, Earthquake Epicenters in Southern California, 1910–1917, 40 pp., 1976.

13-86. Battis, J.C.: Seismic Hazards Estimation Study for Vandenberg AFB, AFGL-TR-79-0277, AFSIG No. 418, November 14, 1979.

13-87. Arnold, R.; and Anderson, R.: “Geology and Oil Resources of the Santa Maria Oil District, Santa Barbara County, California,” U.S. Geol. Survey Bull. 322, Map (1:125,000), 1907.

13-88. Scott, T.M.: Orlando Sheet, Environmental Geology Series, Florida Geol. Survey MS 85, 1978.

13-89. Geophysical Investigation Supplement for VAFB Station Set V23 (VCR-77-067), January 20, 1977.

13-90. The Extra-Terrestrial Space Environment–A Reference Chart, JPL 400-1281, NASA Jet Propulsion Laboratory, September 6, 2006.

Terrestrial Environment (Climatic) Criteria Guidelines for Use in Aerospace Vehicle Development, 2008 Revision

NASA/TM—2008–215633
December 2008

D.L. Johnson, Editor

Section 14: Sea State

TABLE OF CONTENTS

LIST OF FIGURES

LIST OF TABLES

LIST OF ACRONYMNS

CDF	cumulative distribution function
CD–ROM	compact disk–read only memory
CPC	Climate Prediction Center
ERS–1	European Remote-Sensing Satellite No. 1 (launched July 1991)
GEOSAT	Geodetic Satellite (a U.S. Navy satellite that provided unclassified sea surface height data from November 1986 to January 1990)
KSC	Kennedy Space Center
NOAA	National Oceanic and Atmospheric Administration
SST	sea surface temperature
TOPEX	Topography experiment (for Ocean Circulation—unflown NASA precursor mission to TOPEX/Poseidon)
TOPEX/Poseidon	Joint U.S.-French satellite launched in 1992 to track changes in sea level height with radar altimeters
VAFB	Vandenberg Air Force Base
WOCE	World Ocean Circulation experiment

NOMENCLATURE

A	area
f_p	spectral peak frequency
g	acceleration of gravity
H	wave height
$H_{1/10}$	average of the highest one-tenth of waves
H_s	significant wave height
H_s^N	significant wave height expected to be exceeded once every N years
L	wave length
N	number of waves
P	probability
$P(x)$	exceedence probability
T	total number of hindcasts
T^*	total number of hindcasts that met the stated criteria
T_m	mean wave period
T_p	spectral peak wave period
t	exposure time
U_{10}	wind speed measured at a reference height of 10 m
W_s	wind speed
x	fetch
α	wave slope
ε	nondimensional variable
θ	angle
θ_{wave}	mean wave direction
θ_{wind}	wind wave direction
μ	exceedence probability
ν	nondimensional variable
σ	variance of the wave record
χ	nondimensional variable

14. SEA STATE

14.1 Introduction

Knowledge of sea state characteristics and probabilities is important in aerospace vehicle design and trade studies, to the development of detailed design specifications, in mission planning, and in support of operations. For example, Space Transportation System design and operations utilized sea state information in the recovery and tow back of the solid rocket boosters. In that instance, sea state information was specifically required only in the Atlantic Ocean recovery area adjacent to Kennedy Space Center (KSC). Other aerospace vehicle applications may require sea state information at various locations around the world. Water recovery of any spacecraft will require detail design and operational consideration using sea state information.

In deep water, sea state is determined by the mean wind speed, the fetch (x)—the distance over which it blows, and the duration of wind over open water.

Within the last decade, the availability of oceanic data from satellites, such as the GEOSAT, TOPEX/Poseidon, and ERS–1, coupled with computer model data, has made possible the means of providing selected sea state characteristics and probabilities. This has been possible on a more or less global basis in a way that was previously impossible with only land-/sea-based wind and wave measurements. Capitalizing on these technology advances, a global wind/wave atlas has been developed (I.R. Young, Personal Communication, 2003) and recorded on CD–ROM for NASA. Utilizing commercially available MATLAB® software, the CD–ROM can be used by NASA Marshall Space Flight Center personnel to calculate and plot historical sea state characteristics and statistical distributions for nearly any designated latitude and longitude ocean location. These parameters include mean monthly wave height, mean monthly wind speed, wave height exceedance, wind speed exceedance, mean monthly spectral peak period, mean monthly spectral mean period, spectral peak period exceedance, spectral mean period exceedance, mean monthly wave duration, mean monthly wind direction, and extreme wave heights for nearly any designated latitude and longitude ocean location. It should be noted that this CD–ROM uses longitudes measured east rather than west. Therefore, the location of the Eastern Range is specified as 29° N., 285° E. and the location of Vandenberg Air Force Base (VAFB) as 31° N., 237° E. Examples of program output are provided later in this section.

Section 14 contains general information on global ocean surface currents, the definition and determination of wave height, and the use of exposure time. Sea state data calculated with selected probability results are given. This is followed by wave height and wind speed durations and interval statistics, as well as selected atmospheric observations for KSC recovery areas. Finally, global ocean temperature and salinity statistics are presented.

14.2 Ocean Surface Currents

Ocean currents transport sea water from one location in the ocean to another. They also transport momentum; chemicals, such as salts, oxygen, and carbon dioxide; biological species, such as plankton and fish; and any objects purposely or inadvertently inserted into the ocean. Knowledge of ocean currents is important to marine navigation, to dispersal of pollutants, and for aerospace applications, such as search and rescue at sea or recovery of space-borne objects. Ocean currents are composed of both surface currents and subsurface currents. Since subsurface currents are primarily driven by differences in the density of the sea water, they generally travel at much slower speeds—two to three orders of magnitude slower—than surface flows and are typically of less

interest to aerospace applications. Ocean surface currents are primarily driven by the atmospheric wind above the surface waters. Frictional stress at the interface between the ocean and the wind causes the water to move in the direction of the wind. Steady winds cause the sea surface to slope as water is piled up in the direction of the wind. The maximum difference in water surface height is typically ≈1 m in 100 km. Water then flows from the region of higher water height to the region of lower water height. The Coriolis force, which results from the Earth's rotation, causes the current to move to the right of the pressure gradient path in the Northern Hemisphere and to the left in the Southern Hemisphere. In the ocean, at the small scale, water flows from high to low pressure—the pressure gradient force, but for large-scale motion, the Earth's rotation leads to flow along lines of constant pressure—isopleths. Water flows that are controlled by a balance between the pressure gradient force and the Coriolis deflection result in currents called geostrophic currents that flow along isopleths. Large-scale, mid-latitude ocean flow is an approximate geostrophic current. On a global scale, large ocean currents are constrained by the continents that border the three major oceanic basins. Continental borders cause these currents to develop large-scale, almost closed, circular patterns called gyres. These gyres actually result from a combination of wind forcing, buoyancy forcing, and the Coriolis acceleration. Since the Coriolis acceleration varies with latitude, gyre circulations are not symmetric, and the ocean surface flow on the western boundaries of a gyre is generally stronger. Figure 14-1 is a simplified illustration of the major ocean surface currents of the world (ref. 14-1; M. Pidwirny, Personal Communication, 2003).

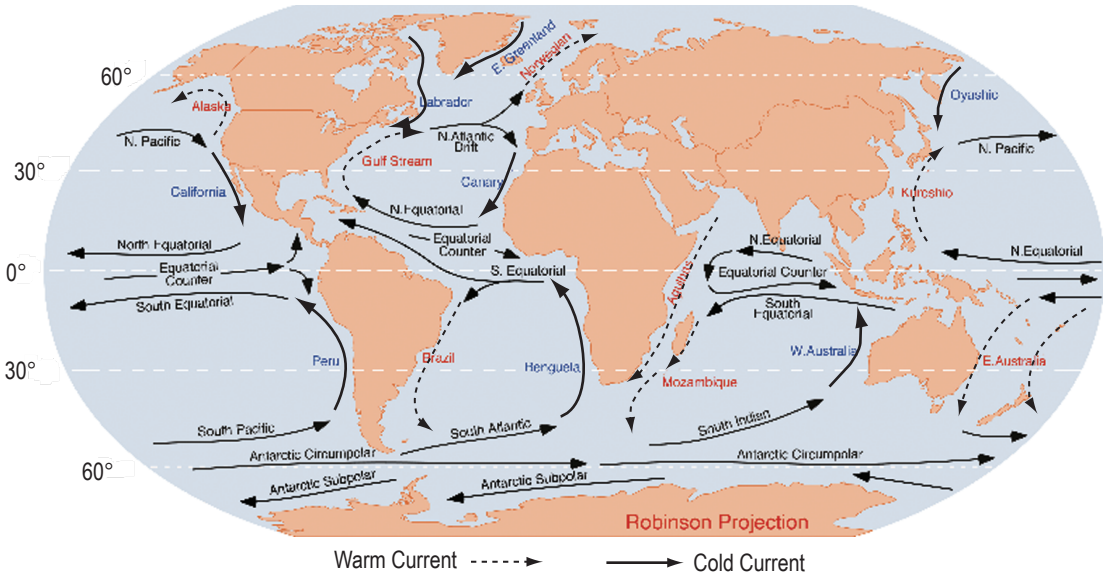

Figure 14-1. Major ocean surface currents of the world—dashed arrows indicate warm currents, while cold currents are displayed with solid arrows (ref. 14-1).

On either side of the equator, in all ocean basins, there are two west-flowing currents—the north and south equatorial. These currents move between 3 and 6 km/day and usually extend 100 to 200 m in depth below the ocean surface. The equatorial counter current, which flows toward the east, is a partial return of water carried westward by the north and south equatorial currents. During El Niño years, this current intensifies in the Pacific Ocean.

Flowing from the equator to high latitudes are the western boundary currents. These warm-water currents have specific names associated with their location: North Atlantic—Gulf Stream, North Pacific—Kuroshio, South Atlantic—Brazil, South Pacific—East Australia, and Indian Ocean—Agulhas. Each of these currents is

a generally narrow, jet-like flow that travels at speeds between 40 and 120 km/day. Western boundary currents are the deepest ocean surface flows, usually extending 1,000 m below the ocean surface. The largest and most prominent of the western boundary currents is the Gulf Stream in the North Atlantic Ocean. The volume transport of the Gulf Stream is ≈55 million m^3/s (or 55 Sverdrups (Sv)); 1 Sv = 10^6 m^3 s^{-1}. Figure 14-2 is a National Oceanic and Atmospheric Administration (NOAA) satellite image of the Gulf Stream which shows temperature differentials of the ocean water off the coast of the eastern United States (J. Bosch, Personal Communication, 2003). The component of the Gulf Stream that flows through the Florida Straits is called the Florida current. The near-surface current speed off the coast of Florida is typically 2 m/s (4 kt). The Florida current's mean northward transport is ≈30 Sv. This is more than the total flow of all the rivers in the world combined. For comparison, the Mississippi River is ≈0.02 Sv. The width of the Florida current is ≈80 km at 27° N. and 120 km at 29° N. As the Florida current is joined by other northward-flowing currents, the volume transport of the Gulf Stream increases to ≈85 Sv near Cape Hatteras, NC. The annual mean surface currents in the recovery areas off KSC and VAFB (with sigmas) are given in table 14-1.

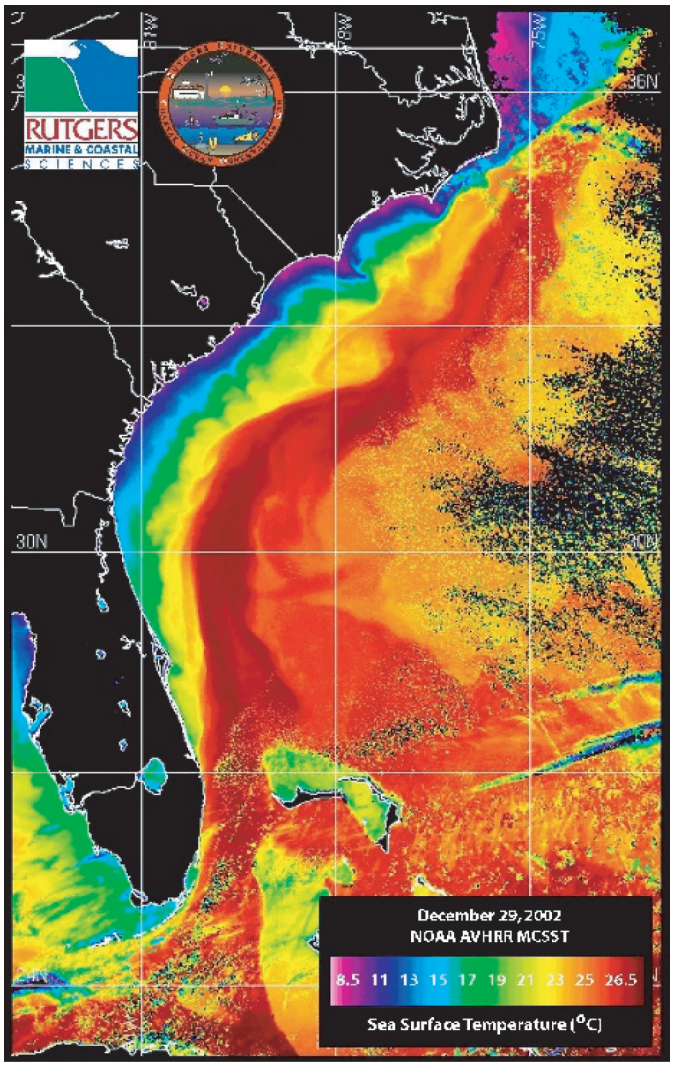

Figure 14-2. This satellite image of the Gulf Stream shows the temperature differential of the ocean water off the eastern coast of the United States. The warmer water—red thermal image—of the current is a good indicator of the path it takes on its journey north (J. Bosch, Personal Communication, 2003).

Table 14-1. KSC and VAFB recovery area annual mean surface currents and standard deviations (ref. 14-2).

Site	Recovery Area	Mean		Standard Deviation	
		(m/s)	(kt)	(m/s)	(kt)
KSC	B	0.4	0.8	0.7	1.27
KSC	A	1.3	2.5	0.6	1.25
VAFB	All	0.3	0.54	0.3	0.56

Flowing from high latitudes toward the equator are the eastern boundary currents. These cold-water currents also have specific names associated with their location: North Atlantic—Canary, North Pacific—California, South Atlantic—Benguela, South Pacific—Peru, and Indian Ocean—West Australia. All of these currents are generally broad, shallow moving flows that travel at speeds between 3 and 7 km/day.

In the Northern Hemisphere, the east-flowing North Pacific current and North Atlantic drift move the waters of western boundary currents to the starting points of the eastern boundary currents. The South Pacific current, South Atlantic current, and South Indian current provide the same function in the Southern Hemisphere. These currents are associated with the Antarctic circumpolar current—west wind drift. Because of the absence of landmass at this latitude zone, the Antarctic circumpolar current flows in continuous fashion around Antarctica and only provides a partial return of water to the three Southern Hemispheric ocean basins.

Another driving mechanism for ocean flow, in addition to water density gradients and atmospheric winds, is the ocean tides generated by the Moon and Sun. For open ocean currents, the contribution to the flow from this source is generally considered noise. However, in coastal areas, tidal flow is usually the dominant flow component. Therefore, tidal forecasts are very important for many marine applications, such as shipping, but less important for most aerospace applications.

General information on ocean currents is available from NOAA's National Ocean Data Center at <http://www.nodc.noaa.gov>. Satellite graphics and other data can be found at <http://wwwo2c.nesdis.noaa.gov>.

The most ambitious oceanographic experiment undertaken to date was the internationally conducted World Ocean Circulation Experiment (WOCE) from 1990 through 1998. In addition to global observations from satellites, conventional in situ physical and chemical observations were made throughout the world's oceans by ≈30 nations. Global numerical ocean models are still being developed and refined to assimilate these measurements. As of calendar year 2004, analyses, interpretation, modeling, and data synthesis activities continue. A four-volume WOCE atlas series, called the definitive Hydrographic Atlas of the World's Oceans, is being prepared. Each atlas will be devoted to one of the four major oceans—Southern, Pacific, Atlantic, and Indian.

14.3 Determination of Significant Wave Height

Any observation of the ocean wave field will show that individual waves differ in height—distance from the crest to trough, and period—time between successive crests. In order to conveniently depict the wave field, representative values for these quantities are typically used. The wave height is often described in terms of the significant wave height (H_s) or $H_{1/3}$, defined as the average of the highest one-third of the waves in any record. Typically, H_s also corresponds to the value that would be visually estimated by an experienced observer. The individual waves in the record typically follow a Rayleigh probability distribution, and based on this assumption,

it is possible to relate other representative wave height estimates to H_s. As an example, $H_{1/10}$, the average of the highest one-tenth of waves, can be related to H_s by the relationship (ref. 14-3)

$$H_{1/10} = 1.27\, H_s \ . \tag{14.1}$$

The wave period is typically represented by the peak spectral wave period (T_p) or the spectral peak frequency (f_p): $f_p = 1/T_p$, which is the period associated with the most energetic waves in any record. Again, this value is typically the same as that estimated from visual observations.

For wind-generated waves, as opposed to remotely generated swell, values of H_s and T_p are a function of the wind speed (U_{10})—typically measured at a reference height of 10 m (33 ft), and the fetch (x), or distance over water that the wind has blown.

For fetch-limited growth, the wind blows perpendicular, but away from an infinitely long coastline. Fetch is measured offshore in the direction of the wind; and for a constant wind speed, the wave field develops as a function of fetch.

These quantities are typically expressed in terms of the following nondimensional variables:

$$\varepsilon = \frac{\sigma^2 g^2}{U_{10}^4} \ , \tag{14.2}$$

$$\nu = \frac{f_p U_{10}}{g} \ , \tag{14.3}$$

and

$$\chi = \frac{gx}{U_{10}^2} \ . \tag{14.4}$$

In the above relationships, σ is the variance of the wave record, $H_s = 4\sigma$, and g is the acceleration of gravity. Based on extensive data, the wave field can be described (ref. 14-4) by the following two expressions:

$$\varepsilon = \min \begin{cases} (7.5 \pm 2) \times 10^{-7}\, \chi^{0.8} \\ (3.6 \pm 0.9) \times 10^{-3} \end{cases} \tag{14.5}$$

and

$$\nu = \max \begin{cases} (2 \pm 0.3)\, \chi^{-0.25} \\ (0.13 \pm 0.02) \end{cases} \ . \tag{14.6}$$

These relationships are shown in figure 14-3.

As can be seen by the plateau region of figure 14-3, growth ceases at large values of fetch (x). In this region, the wave height and period are no longer a function of the fetch. Such conditions are typically termed

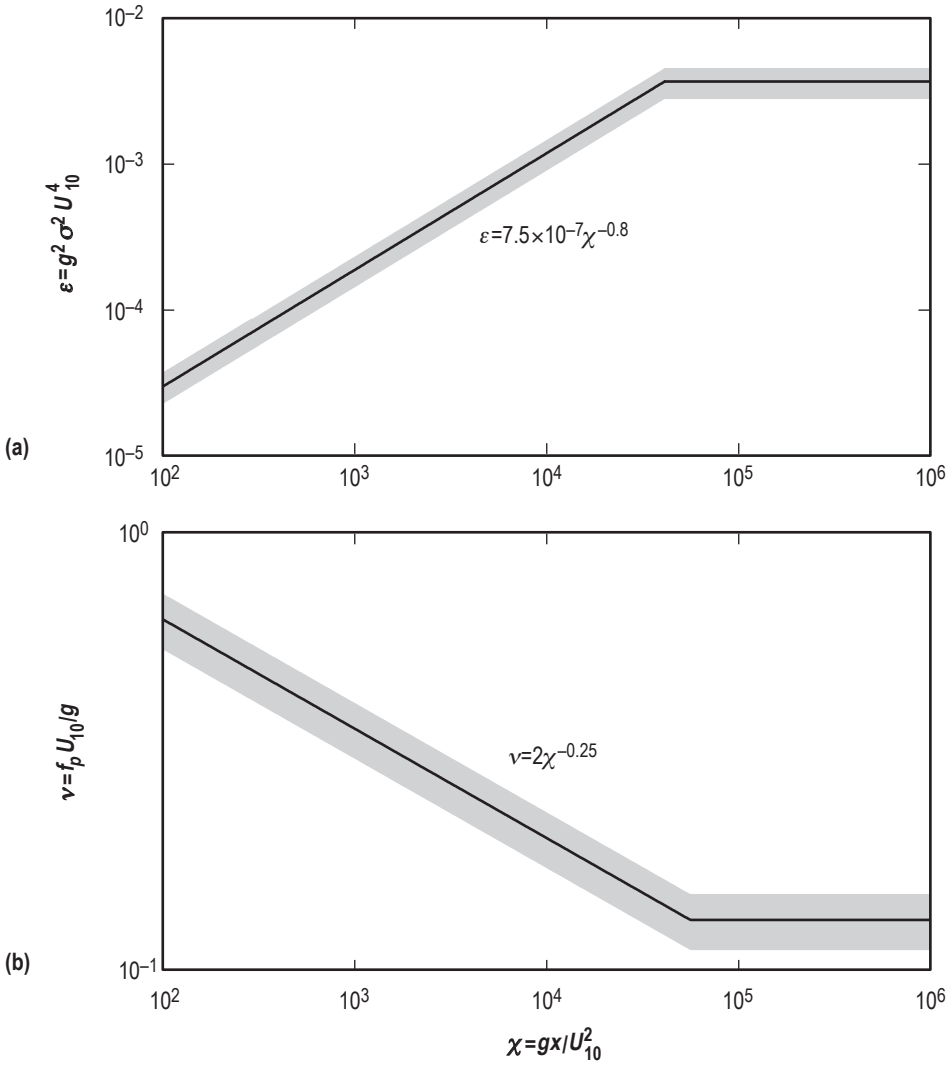

Figure 14-3. Wave height and period growth laws are given by (a) equation (14.5) and (b) equation (14.6). The shaded region shows the typical variation between various experimental data sets and provides a representation of the accuracy of the relationships (ref. 14-4).

"fully developed"; this limit is called the Pierson-Moskowitz limit (ref. 14-5). Rearrangement of this asymptotic limit, as defined by equation (14.5), yields

$$H_s = 2.46 \times 10^{-2} U_{10}^2 \ , \tag{14.7}$$

where H_s has units of meters and U_{10} units of meters per second. Equation (14.7) is shown in figure 14-4, along with the corresponding values of $H_{1/10}$ from equation (14.1).

As an example of the application of the above relationships to wave forecasting, consider a case with a wind speed $U_{10} = 10$ m/s at a location $x = 40$ km offshore.

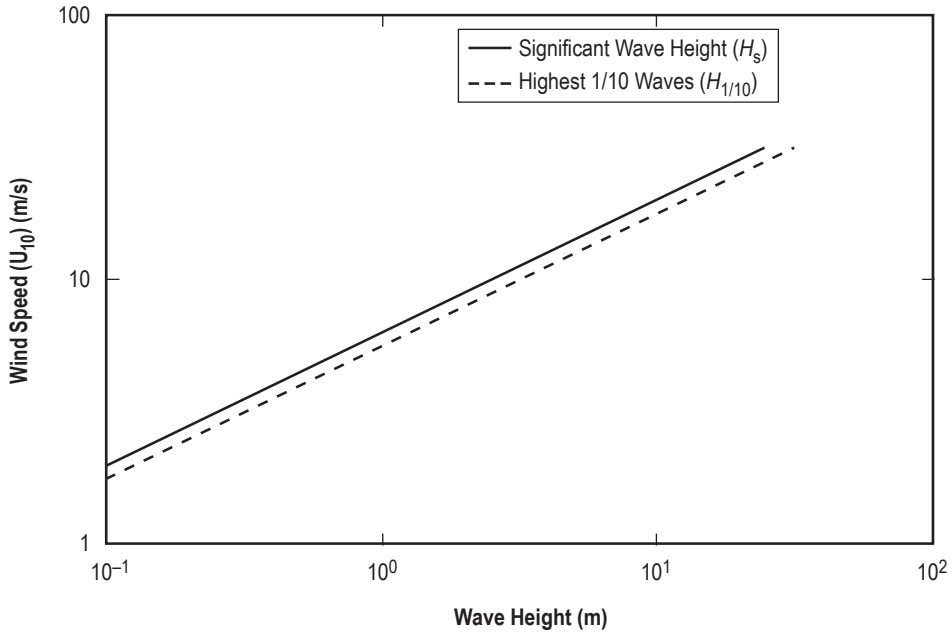

Figure 14-4. Development of the significant wave height (H_s) and average of the highest one-tenth of waves ($H_{1/10}$) as a function of wind speed (U_{10}) for fully developed asymptotic growth conditions.

From equation (14.4),

$$\chi = \frac{gx}{U_{10}^2} = \frac{9.81 \times 40 \times 10^3}{10^2} = 3{,}924 \ , \tag{14.8}$$

and hence from equation (14.5),

$$\varepsilon = 7.5 \times 10^{-7} \times (3{,}924)^{0.8} = 5.62 \times 10^{-4} \ . \tag{14.9}$$

Therefore, from equation (14.2),

$$\frac{\sigma^2 g^2}{U_{10}^4} = 5.62 \times 10^{-4}$$

$$\sigma^2 = \frac{5.62 \times 10^{-4} \times 10^4}{9.81^2} = 5.84 \times 10^{-2} \, \mathrm{m}^2$$

$$H_s = 4\sigma = 4\sqrt{5.84 \times 10^{-2}}$$

$$H_s = 0.97 \ \mathrm{m} \, . \tag{14.10}$$

The value $H_s = 0.97$ m is significantly less than the fully developed value of 2.45 m that would be determined from the upper bound in figure 14-4 or from equation (14.7) for waves developing under unlimited fetch conditions.

The peak wave period can be calculated for this case in a similar fashion. From equation (14.6),

$$\nu = 2 \times (3{,}924)^{-0.25} = 0.26 \ . \tag{14.11}$$

From equation (14.3),

$$\frac{f_p U_{10}}{g} = 0.26$$

$$f_p = \frac{0.26 \times 9.81}{10} = 0.25 \text{Hz}$$

$$T_p = 1 / f_p = 3.95 \text{ s} \ . \tag{14.12}$$

Again, this value is significantly less than the value of $T_p = 7.81$ s, which would be calculated from the fully developed limit in equation (14.6).

The distribution of wave heights versus wind speed, from equation (14.7) or figure 14-4, at any given instant is applicable to aerospace vehicle water entry. Other operations; e.g., afloat, secure, tow-back recovery, where some considerable time interval is involved must take into account their exposure time as described below.

14.4 Exposure Time

Quantities such as H_s or $H_{1/10}$ represent average values of wave height. In any given record, individual wave heights will be both greater and less than these values. For a wave field that is not changing with time, the largest individual wave that one could expect to encounter will increase with the length of the record involved. For a vehicle floating in the ocean, the maximum wave height likely to be encountered will increase with exposure time.

Two main classes of gravity waves exist in the ocean; i.e., wind wave (or wind sea) and swell. Wind sea refers to young, growing waves interacting with local wind, while swell deals with waves generated elsewhere and then propagating over distances.

Following Longuet-Higgins (ref. 14-6), individual waves within a wind sea, as opposed to remotely generated swell, follow a Rayleigh probability distribution. Based on this probability distribution,

$$H_{\max} = \frac{H_s}{\sqrt{2}} \left\{ \ln \left[\frac{N}{\ln \left(\frac{1}{1-\mu} \right)} \right] \right\}^{1/2} \ , \tag{14.13}$$

at least one wave with a height of $H_{\max}$ or greater will be encountered with a probability of exceedence (μ), in a record of N waves. In the application of equation (14.13), consider the case examined previously, where $H_s = 0.97$ m, $T_p = 3.95$ s, the vehicle is exposed for a period of 5 hr, and the aim is to calculate the value of wave height that one would expect to be encountered or exceeded with a risk of 5 percent.

When $t=5$ hr, the value of N becomes

$$N = \frac{t}{T} = \frac{5 \times 3,600}{3.95} = 4,557 \ . \tag{14.14}$$

Substitution into equation (14.13) yields

$$H_{\max} = \frac{0.97}{\sqrt{2}} \left\{ \ln \left[\frac{4,557}{\ln\left(\frac{1}{1-0.05}\right)} \right] \right\}^{1/2}$$

$$H_{\max} = 2.32 \, \text{m} \ . \tag{14.15}$$

Therefore, in a period of 5 hr, there is a 5-percent risk that at least one wave of 2.32 m or greater in height will be encountered in this sea state 3 example.

For fully developed conditions, equation (14.13) can be expressed in graphical form (see fig. 14-5). Table 14-2 presents the international meteorological codes for the state of the sea as used in figure 14-5.

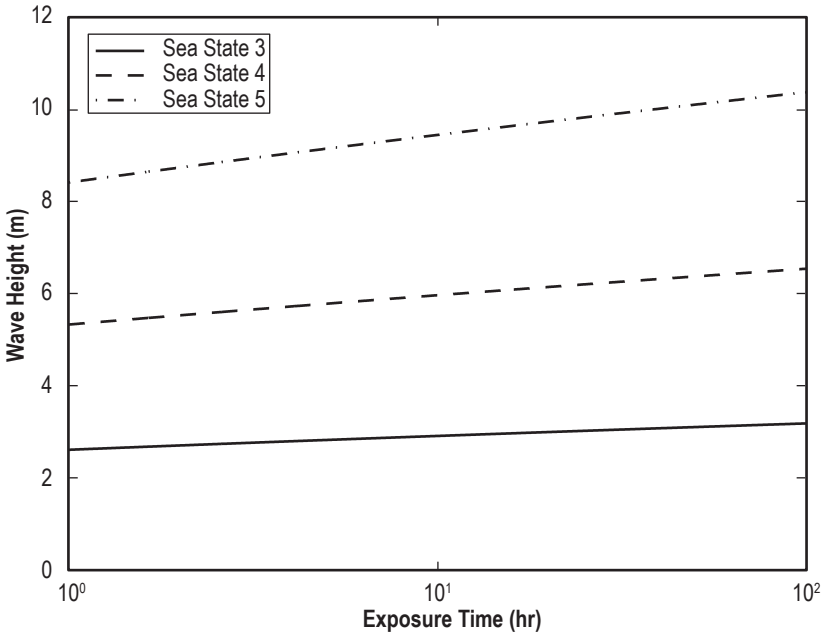

Figure 14-5. Five-percent risk ocean wave height versus exposure time for sea states 3 ($H_s=1.25$ m), 4 ($H_s=2.5$ m), and 5 ($H_s=4$ m). Fully developed conditions remain for duration of growth conditions.

As noted, figure 14-5 assumes fully developed conditions to determine N as a function of exposure time (t). Application to other wind sea cases will, however, yield results of reasonable accuracy. From figure 14-5, an exposure for 1 hr in sea state code 3 entails a 5-percent risk of encountering at least one wave >2.6 m high. Likewise, a 48-hr exposure at a 5-percent risk would give 3.2 m.

Table 14-2. International meteorological codes—state of sea.

Sea State Code	Descriptive Terms	$H_{1/3}$ of Waves	
		(m)	(ft)
0	Calm (glassy)	0	0
1	Calm (rippled)	0–0.1	0–0.33
2	Smooth (wavelets)	0.1–0.5	0.33–1.6
3	Slight	0.5–1.25	1.6–4.1
4	Moderate	1.25–2.5	4.1–8.2
5	Rough	2.5–4	8.2–13.1
6	Very rough	4–6	13.1–19.7
7	High	6–9	19.7–29.5
8	Very high	9–14	29.5–45.9
9	Phenomenal	Over 14	Over 45.9

Note: Exact bounding height is assigned to lower code; e.g., a height of 4 m is coded 5.

14.5 Sea State Data Used

In order to understand the sea state conditions that can be encountered in vehicle ocean recovery areas off KSC, VAFB, Kodiak Island, or any other locations, it is necessary to combine data from a number of sources. For the present analysis, three basic sources are used. Data from the global database of Young (ref. 14-4) has been used for the bulk of the analysis. This data set consists of satellite altimeter observations of H_s and U_{10}, together with numerical model values for T_p, mean wave period (T_m), mean wave direction (θ_{wave}), and mean wind direction (θ_{wind}). The satellite data are from 10 yr of observations by the GEOSAT, TOPEX/Poseidon, and ERS–1 satellites. The model data are from the European Centre for Medium Range Weather Forecasting with implementation of the global wave analysis model.

The data set from Young (ref. 14-4) does not provide information about the duration or interval of sea state exposure. For this information, the published results from NASA–HDBK–1001 (ref. 14-2), corrected for consistency with the altimeter data from Young (ref. 14-4), have been utilized. As indicated by Johnson (ref. 14-2), the U.S. Navy Hindcast Spectral Ocean Wave Model data used for that analysis underestimates wind speed and wave height, but is the only known source for duration/interval statistics. Note that the time an episode persists above a given threshold is arbitrarily referred to as duration of the event. The times between episodes have been termed intervals.

Figure 14-6 is a global contour plot example of mean monthly wave height in meters for January. Figure 14-7 is another global plot example of mean wave direction for August with arrows indicating wave direction of travel. These two figures are just examples of the output available from the Sea State Atlas/ CD–ROM (I.E. Young, Personal Communication, 2003).

14.6 Sea State Data Results for Kennedy Space Center and Vandenberg Air Force Base

14.6.1 Wave Height, Period, and Direction, Including Wind Speed and Direction

Various mean monthly values of sea state parameters at KSC and VAFB, as well as a location in the North Atlantic, are given in tables 14-3 through 14-5. For both wind direction and wave direction, the meteorological convention “coming from” is used. For example, wind or a wave coming from the east is represented by a direction of 90°. Figure 14-8 illustrates the key recovery areas and grid points around KSC and VAFB. In section 14.6, the grid points K and V are representative of KSC and VAFB, respectively.

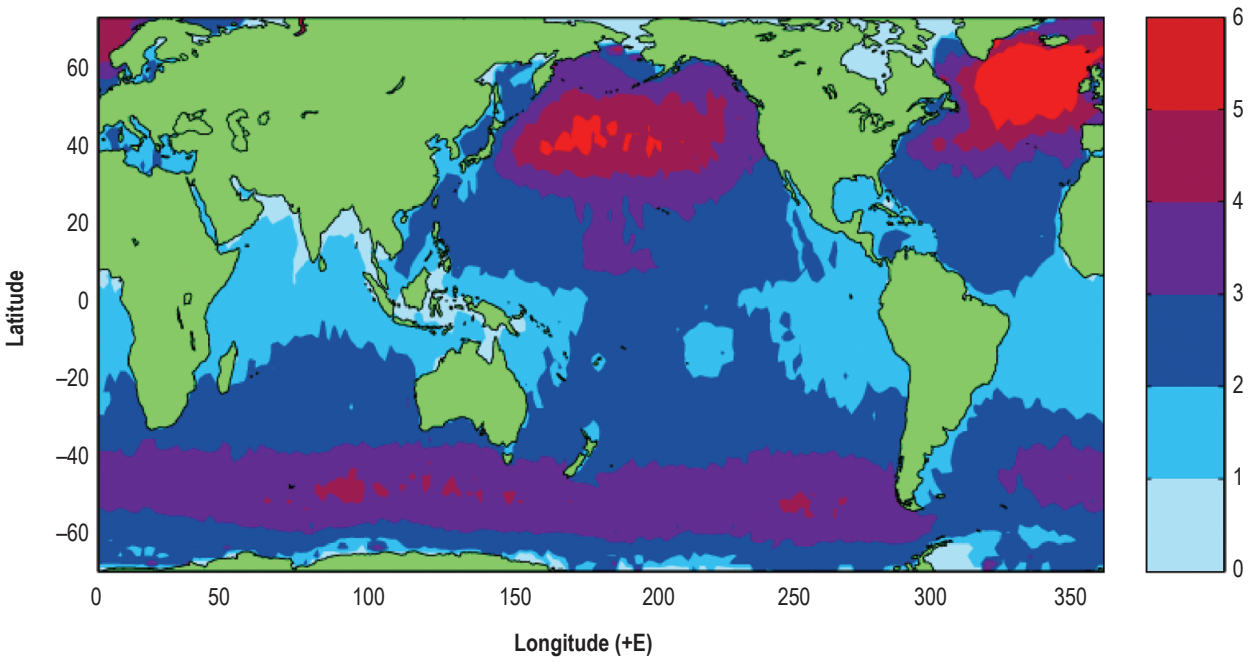

Figure 14-6. Global contour plot of mean significant wave height (H_s) in meters for January. Note that longitudes are measured east rather than west. The darker (red) areas depict regions with wave height of >5 m (I.R. Young, Personal Communication, 2003).

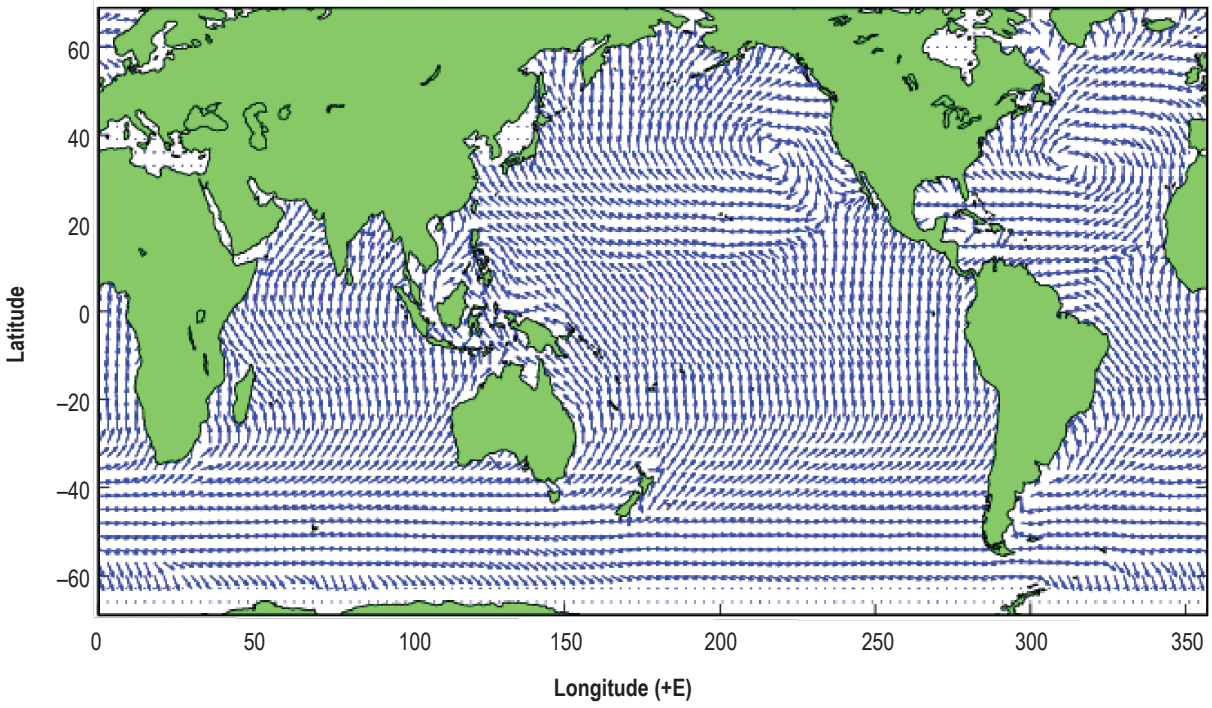

Figure 14-7. Global plot of mean wave direction for August. Arrows indicate direction of wave travel. Longitudes are measured east rather than west (I.R. Young, Personal Communication, 2003).

Table 14-3. Mean monthly sea state statistics at KSC. Data are taken for a point centered at 29° N., 75° W. (I.R. Young, Personal Communication, 2003).

Month	H_s (m)	T_p (s)	T_m (s)	U_{10} (m/s)	θ_{wind} (deg)	θ_{wave} (deg)
J	2.28	8.27	7.28	8.15	259	62
F	2.13	7.85	6.99	7.71	259	359
M	2.23	8.08	7.06	7.59	265	25
A	1.67	7.66	6.49	6.61	277	86
M	1.42	7.82	6.64	4.89	273	86
J	1.11	7.06	6.21	4.25	252	125
J	0.95	7.21	6.05	4.25	231	139
A	1.33	7.72	6.62	4.74	215	113
S	1.38	8.45	7.15	4.85	97	92
O	2.12	8.54	7.33	6.9	171	73
N	1.89	8.32	7.16	7.25	237	65
D	2.34	8.75	7.63	8.32	262	26

Table 14-4. Mean monthly sea state statistics at VAFB. Data are taken for a point centered at 31° N., 123° W. (I.R. Young, Personal Communication, 2003).

Month	H_s (m)	T_p (s)	T_m (s)	U_{10} (m/s)	θ_{wind} (deg)	θ_{wave} (deg)
J	2.98	12.33	10.08	6.28	333	297
F	2.57	12.86	10.31	6.4	323	289
M	2.71	12.46	9.81	6.97	328	298
A	2.27	11.59	9.19	5.9	331	314
M	2.28	10.96	8.82	6.48	333	300
J	2.18	9.97	8.5	6.83	326	311
J	1.96	10.31	8.73	5.44	344	295
A	1.93	10.25	8.63	5.99	318	297
S	1.96	10.66	8.78	5.15	326	298
O	1.97	11.8	9.57	5.2	328	295
N	2.62	12.27	9.64	6.77	346	315
D	3.17	13.31	10.45	6.73	331	312

Table 14-5. Mean monthly sea state statistics in North Atlantic. Data are taken for a point centered at 51° N., 43° W. (I.R. Young, Personal Communication, 2003).

Month	H_s (m)	T_p (s)	T_m (s)	U_{10} (m/s)	θ_{wind} (deg)	θ_{wave} (deg)
J	5.73	11.15	9.82	15.07	251	280
F	5.49	10.91	9.59	14.43	255	249
M	4.40	10.61	9.22	11.94	253	269
A	3.65	10.09	8.81	11.53	264	347
M	2.61	9.06	7.89	9.18	251	49
J	2.43	8.50	7.48	8.24	245	236
J	2.18	8.07	7.04	7.46	252	242
A	2.24	8.00	7.06	7.98	270	249
S	3.35	8.99	7.84	11.46	257	275
O	3.29	9.88	8.44	10.83	271	329
N	4.96	10.72	9.39	14.28	248	284
D	5.15	11.41	10.00	14.14	250	280

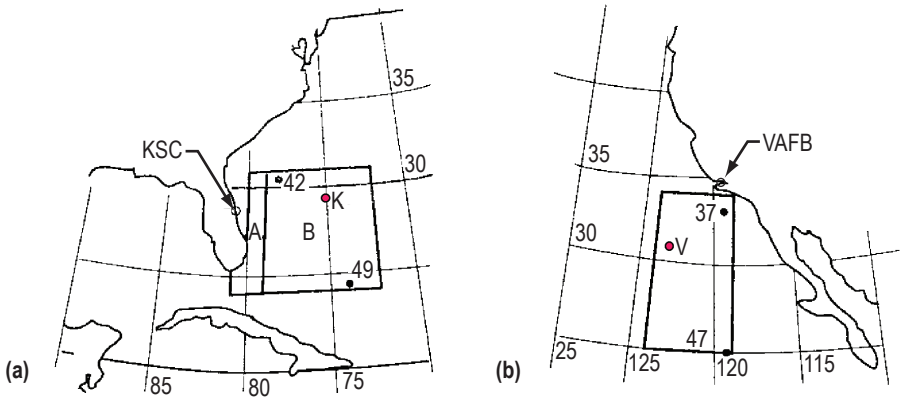

Figure 14-8. Booster recovery areas for (a) KSC and (b) VAFB, includes special Gulf Stream current areas (*A*) and wave/wind duration grid points. Special representative KSC (K at 29° N., 75° W.) and VAFB (V at 32° N., 123° W.) grid points are also shown.

Examination of the results in tables 14-3 through 14-5 shows that ocean wave characteristics near the two NASA launch sites are quite different. VAFB has larger wave heights and longer wave periods, indicating that the wave climate is largely dominated by Pacific Ocean swell entering the region. In contrast, the wave climate at KSC is more dominated by locally generated wind sea. The values of mean wave direction also confirm this result, with the mean wave direction at VAFB being consistently from north and west. In contrast, the wave direction at KSC is more variable ranging between north and east. The North Atlantic site exhibits more extreme sea conditions than either KSC or VAFB.

Wave slopes for KSC and VAFB (table 14-6) were calculated along the wind direction after assuming a Gaussian distribution in a fully developed sea. Local significant wave heights were used in these calculations. The wave slope (α) is normally defined as the ratio of wave height (H) over the wave length (L). Therefore, wave slope can be expressed either as a numeric value (ratio) or as an angle (θ). The arctan of the ratio equals the angle θ.

Table 14-6. Monthly KSC and VAFB recovery area wave slopes (5-percent risk), in degrees—calculated from significant wave heights (ref. 14-2).

Site	Risk of Exceeding (%)	J (deg)	F (deg)	M (deg)	A (deg)	M (deg)	J (deg)	J (deg)	A (deg)	S (deg)	O (deg)	N (deg)	D (deg)	Average (deg)
KSC	5	11	12	11	10	10	10	10	9	11	11	11	11	10
VAFB	5	10	10	10	10	11	11	10	10	10	10	10	11	10

KSC and VAFB recovery area mean annual surface currents with their standard deviations were presented in table 14-1.

14.6.2 Probability of Exceedence

For various sea states, the probability of exceedence ($P(x)$) of the various parameters is defined as the probability of that parametric value x being exceeded in magnitude. Annual—averaged over all months—values

of the probability of exceedence for the parameters H_s, U_{10}, T_p, and T_m at KSC, VAFB, and the North Atlantic are shown in figures 14-9 through 14-11, respectively.

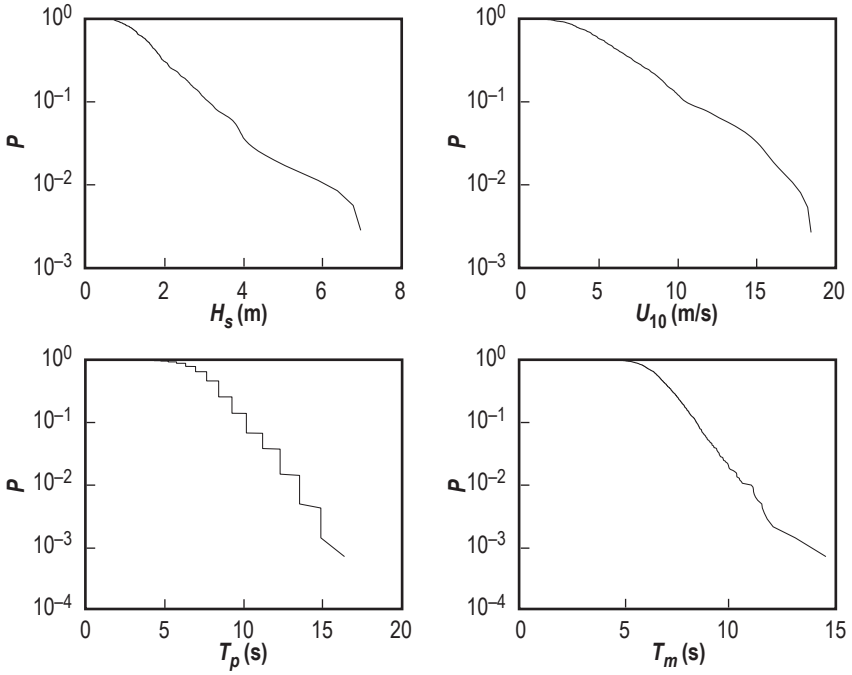

Figure 14-9. Annual exceedence probabilities at KSC. Data are taken for a point centered at 29° N., 75° W. (I.R. Young, Personal Communication, 2003).

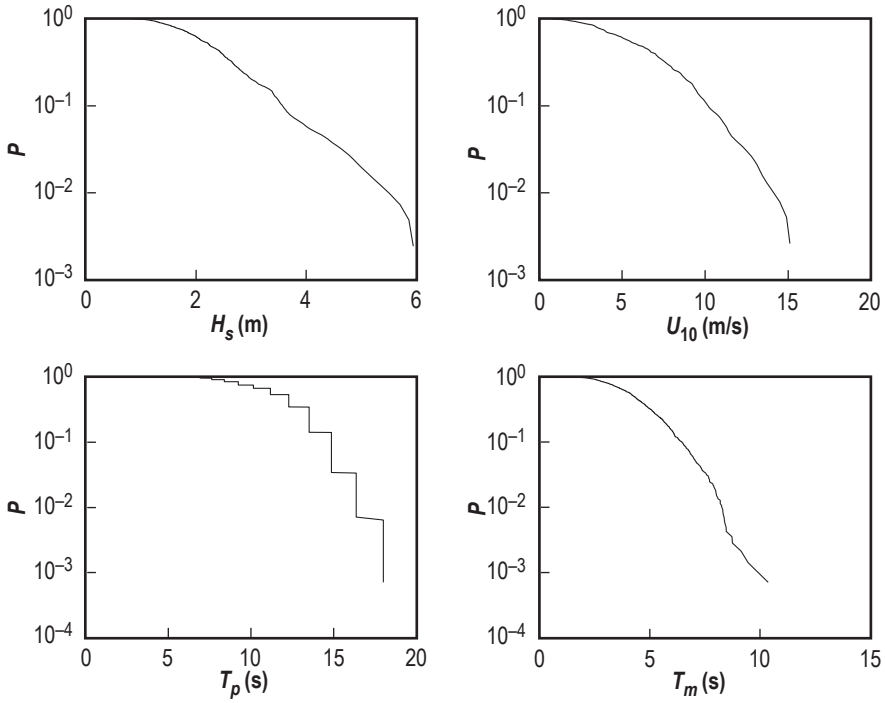

Figure 14-10. Annual exceedence probabilities at VAFB. Data are taken for a point centered at 31° N., 123° W. (I.R. Young, Personal Communication, 2003).

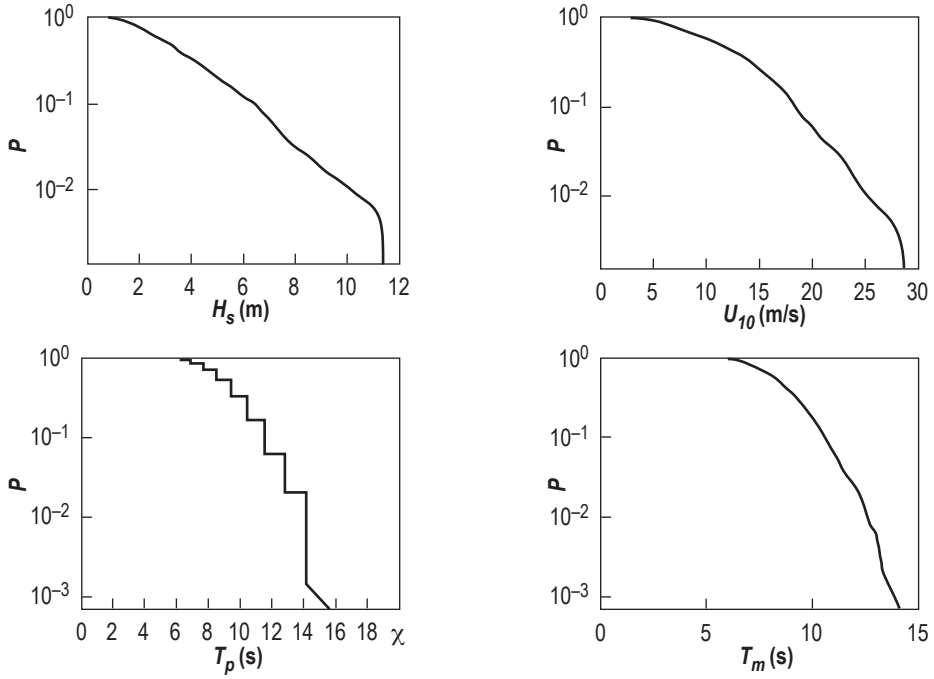

Figure 14-11. Annual exceedence probabilities at the North Atlantic site. Data are taken for a point centered at 51.5° N., 42.7° W.

Exceedence probabilities can also be produced on a monthly basis for H_s. These values are shown in table 14-7 for KSC and VAFB. Insufficient data are available to produce reliable monthly exceedence probabilities for the other parameters.

Table 14-7. Monthly exceedence probabilities of H_s at KSC, VAFB, and the North Atlantic site. H_s is the significant wave height in meters. KSC at 29° N., 75° W.; VAFB at 31° N., 123° W.; and North Atlantic at 51.5° N., 42.7° W. (I.R. Young, Personal Communication, 2003).

	KSC			VAFB			North Atlantic		
Month	H_s at 5%	H_s at 25%	H_s at 50%	H_s at 5%	H_s at 25%	H_s at 50%	H_s at 5%	H_s at 25%	H_s at 50%
J	5.01	2.85	2.11	5.18	3.53	2.80	11.72	7.48	5.34
F	4.68	2.66	1.97	4.46	3.04	2.42	11.23	7.17	5.11
M	4.90	2.79	2.07	4.71	3.21	2.55	9.00	5.75	4.10
A	3.67	2.09	1.55	3.94	2.69	2.13	7.46	4.77	3.40
M	3.12	1.77	1.32	3.96	2.70	2.14	5.34	3.41	2.43
J	2.44	1.39	1.03	3.79	2.58	2.05	4.97	3.17	2.26
J	2.09	1.19	0.88	3.40	2.32	1.84	4.46	2.85	2.03
A	2.92	1.66	1.23	3.35	2.28	1.81	4.58	2.93	2.09
S	3.03	1.72	1.28	3.40	2.32	1.84	6.85	4.38	3.12
O	4.66	2.65	1.96	3.42	2.33	1.85	6.73	4.30	3.06
N	4.16	2.36	1.75	4.55	3.10	2.46	10.14	6.48	4.62
D	5.14	2.92	2.17	5.51	3.75	2.98	10.53	6.73	4.80

14.6.3 Extreme Wave Height Values

Extreme values of wave height can also be estimated from the satellite database described earlier. The value H_S^N is the extreme value of significant wave height expected to be exceeded once every N years. For typical engineering design applications, N is usually set at either 50 or 100 yr.

In order to estimate the extreme wave height from a record collected over a finite time, the following steps are usually applied:

(1) Extract a series representing observed maxima from the H_s database.
(2) Rank the series of maxima.
(3) Assign cumulative distribution functions (CDFs) to individual maxima.
(4) Fit statistical distributions or models to the series of maxima and their CDFs.
(5) Apply tests to assess goodness of fit.
(6) Compute the extreme H_s values with a prescribed return period.

For the present application, the process described by Alves and Young (ref. 14-7) has been applied. This method involves fitting a Fisher-Tippet type 1 distribution to the data. Application of this approach to the KSC, VAFB, and North Atlantic sites of interest yields the results shown in table 14-8—applying a 2×2 deg resolution.

Table 14-8. Extreme values of significant wave height at VAFB, KSC, and the North Atlantic for 50- and 100-yr periods. The uncertainty values represent 95-percent confidence intervals on the estimated extreme wave height. KSC at 29° N., 75° W.; VAFB at 31° N., 123° W.; and North Atlantic location of 51.5° N., 42.7° W. (I.R. Young, Personal Communication, 2003).

Significant Wave Height (m)	VAFB	KSC	North Atlantic
H_s^{50}	10.57±0.69	10.52±0.76	21.33±1.61
H_s^{100}	11.07±0.80	11.06±0.88	22.41±1.86

14.7 Kennedy Space Center Atmospheric Conditions

Climatological information applicable to the KSC recovery area is given in table 14-9 (ref. 14-8). These values, developed from observations made at 00, 06, 12, and 18 GMT by ships passing through the area, show the percent frequency of the indicated atmospheric condition. For example, off KSC in January, the sky cover is 0, 1/8, or 2/8 (≤2/8) on 20.3 percent of the observations. The sky is completely covered (8/8) on 20.8 percent of the observations. The similar table for the VAFB recovery area can be obtained by downloading table 14-9 of Johnson (ref. 14-9) at <http://trs.nis.nasa.gov>.

Additional climatic and sea state statistics for these two areas can be found in references 14-10 and 14-11. Also, the U.S. Navy Fleet Numerical METROC Detachment at Asheville, NC, Web site at <http://navy.ncdc.noaa.gov/products/publications.html>, offers wind, wave, and atmospheric climate studies and atlases for the world's oceans. This includes the U.S. coastal areas of KSC and VAFB for the Atlantic (No. 1–Caribbean, Florida Coastal, and Southwest Atlantic: Vol. 3, and No. 2–North Atlantic (MCA): Vol. 1); and the Pacific (No. 1–Near Coastal Zone, Southern California (MCA): Vol. 2, and No. 2–North Pacific Ocean (MCA): Vol. 2).

Table 14-9. KSC recovery area atmospheric conditions (ref. 14-9).

Percent Frequency of Occurrence											
	Visibility		Total Precipitation*		Sky Cover (fraction)			Wind Speed			
										Mean	
Month	≤2 nm	≥10 nm	(cm)	(in)	0–2/8	8/8	Mean**	≤10 kt ≤5.1 m/s	≥17 kt ≥8.7 m/s	m/s†	kt†
J	1.3	89.4	10.2	4.0	20.3	20.8	0.62	29.0	35.8	7.8	15.2
F	1.9	88.4	11.4	4.5	21.3	22.1	0.62	29.9	39.2	8.2	15.9
M	0.5	88.6	6.6	2.6	26.5	19.2	0.58	30.0	37.9	7.8	15.2
A	1.0	89.6	3.3	1.3	36.2	9.6	0.47	34.4	30.6	7.2	14.0
M	0.9	88.7	5.6	2.2	37.5	12.7	0.47	48.2	18.6	6.1	11.9
J	2.4	86.2	11.4	4.5	24.2	17.2	0.57	49.7	17.8	6.1	11.9
J	1.3	92.0	9.7	3.8	30.8	12.4	0.52	50.6	14.6	5.9	11.5
A	1.1	90.0	11.4	4.5	22.5	11.8	0.55	57.6	13.4	5.8	11.2
S	2.2	87.3	12.4	4.9	25.4	16.2	0.56	50.6	19.1	6.2	12.0
O	0.6	90.6	5.8	2.3	28.5	13.7	0.53	36.5	28.7	7.0	13.6
N	1.1	92.7	8.6	3.4	28.7	11.6	0.53	33.8	33.2	7.6	14.7
D	0.9	92.7	5.3	2.1	29.0	14.3	0.56	41.3	28.6	7.6	14.7

*Total precipitation values are expressed in inches, not in percent.
**Mean sky cover is expressed in one-hundredths of the sky being covered.
†Mean wind speed values are expressed in knots and m/s, not in percent.

14.8 Wave Height and Wind Speed Durations and Intervals

The time an episode of significant wave height or wind speed persists above a given threshold is referred to as a duration of the event. The time between two episodes is termed an interval. The length of time an episode is likely to last once it has begun is important to aerospace applications such as launch operations, rescue, and recovery.

The Atlas data set of Young (I.R. Young, Personal Communication, 2003) does not provide information on duration or interval tables of wind and wave conditions. However, the U.S. Navy has compiled a historical data set in the form of wind and wave climatology called the "U.S. Navy Hindcast Spectral Ocean Wave Model Climatic Atlases" for both the North Atlantic Ocean (ref. 14-12) and the North Pacific Ocean (ref. 14-13). Duration and interval tables are provided for various grid points across the oceans at various months of the year. Information on the construction and use of these tables, including examples of their applications, are provided in the Navy atlases. A subset of these tables for KSC and VAFB and a brief description of their use was also provided in the NASA–HDBK–1001 published in August 2000 (ref. 14-2). Since these tables are rather voluminous and have not been updated since their inclusion in the NASA–HDBK–1001, they are not duplicated here. Note that, as indicated in NASA–HDBK–1001 (ref. 14-2), the Spectral Ocean Wave Model underestimates wind speed and wave height near U.S. east coast areas. However, the Spectral Ocean Wave Model is the only known source for duration/interval statistics.

The following duration and interval tables of wave height and wind speed, taken from the U.S. Navy Hind-cast Spectral Ocean Wave Model Climatic Atlas (ref. 14-12), are given for one Atlantic Ocean sequence No. 42 (grid point No. 222-1) (located at lat. 30.4° N., long. 77.9° W.) near Cape Canaveral, FL. Even though these Navy statistics are given at grid points, they are representative of surrounding areas. Also, interpolation may be used for areas between grid points. Consult reference 14-12 for various other Atlantic areas, and reference 14-13 for other areas in the Pacific Ocean. The Atlantic Ocean database of 20 yr was considered large enough to produce reliable monthly statistics, whereas, the Pacific Ocean tables present only seasonal results. The Pacific

Ocean duration and interval tables are not presented in this document, but can be obtained by season from Johnson (ref. 14-9) at <http://trs.nis.nasa.gov>.

Atlantic Ocean duration and interval tables were published for only 4 mo—January, April, July, and October—to represent winter, spring, summer, and fall, respectively. A summary table also includes all the hindcasts. Episodes of durations—continuous hours or days—of events and episodes of intervals—continuous hours or days—between events were tallied for various thresholds. These tables give an indication of how long an episode is likely to last once it has begun. For convenience, the time an episode persisted above a given threshold is arbitrarily referred to as a duration of the event. The times inbetween episodes have been termed intervals.

14.8.1 Duration and Interval Tables

Table 14-10 gives the legends for the KSC duration and interval tables. Table 14-11 presents KSC wind speed durations by mid-season months. Wind speed intervals for KSC are in table 14-12. Tables 14-13 and 14-14 present the KSC wave height duration and interval statistics, respectively.

14.8.2 Duration and Interval Table Examples

When answering questions using the duration and interval tables, it is important to distinguish between questions that require the use of the number of episodes and those that require the number of hindcasts. Hindcasting involves analyzing past, measured site data in order to arrive at a data climatology for that site. Answers for questions regarding the percentage of time at or above, or below, certain thresholds require the use of the number of hindcasts. On the other hand, questions concerned with the percentage of episodes at or above, or below, certain thresholds demand the use of episode frequencies, where a 1-day episode or a 60-day episode will each count as one episode.

The following four examples illustrate applications of the duration and interval tables:

- Question 1: Of all the events with wind speeds (W_s) ≥ 22 kt at grid point 42 in January (table 14-11), what percentage had durations of longer than 1 day?
  - Answer: Consult table 14-11. The number of events or episodes of $W_s \geq 22$ kt (from TE column) is 72. The number of events of wind speeds ≥22 kt lasting more than 1 day is $2+1+2+1+1=7$. The percentage of events of wind speed ≥22 kt lasting more than 1 day is then $7 \div 72 \times 100 = 9.7$ percent.

- Question 2: What percentage of the time during January at Atlantic grid point No. 42 can waves ≥9 ft (≥2.7 m) be expected to persist longer than 24 hr?
  - Answer: This problem involves computations using hindcasts from the monthly duration table (table 14-13) rather than episodes from the duration table, since we are answering a question regarding the percentage of time. The solution can be found by computing the joint percentage as follows: percent of waves ≥9 ft times percent of ≥9-ft waves that persist longer than 24 hr. Note that the percent of ≥9-ft waves that lasted <24 hr plus the percent of ≥9-ft waves that lasted ≥24 hr is 100 percent, so we can compute whichever is easier and subtract from 100 percent, if necessary. Percentages are used because of the difference between T and T^* caused by missing data.

    Step (1): Compute the percent of ≥9-ft waves that lasted >24 hr (table 14-15). In this example, it will be easier to find the percent for ≤24 hr then subtract from 100 percent to obtain the percent required. This requires the calculation of the total number of hindcasts meeting this criterion.

Table 14-10. Legends for wind and wave height duration and interval tables.

WIND SPEED DURATIONS-MONTHLY SEASONAL

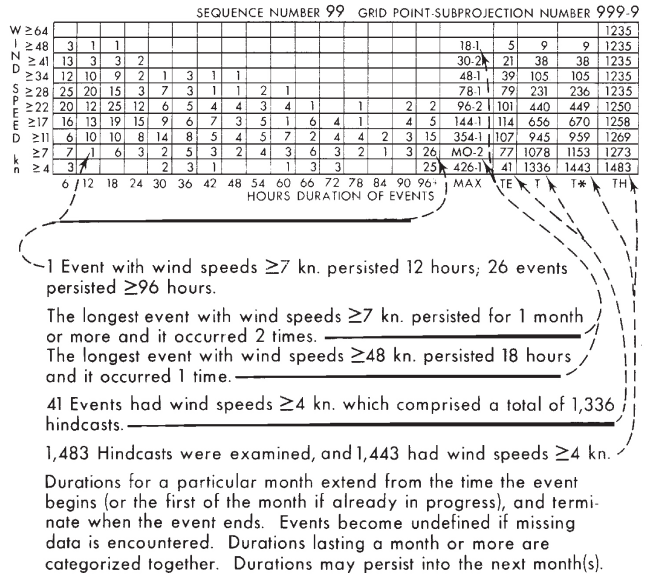

WIND SPEED INTERVALS- MONTHLY SEASONAL

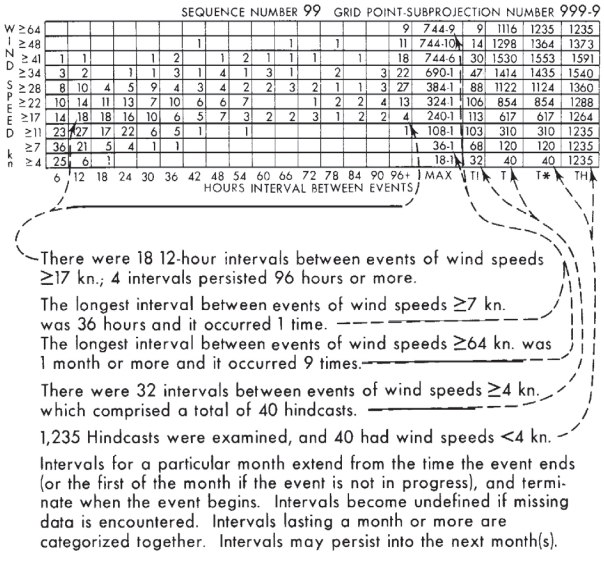

WAVE HEIGHT DURATIONS-MONTHLY SEASONAL

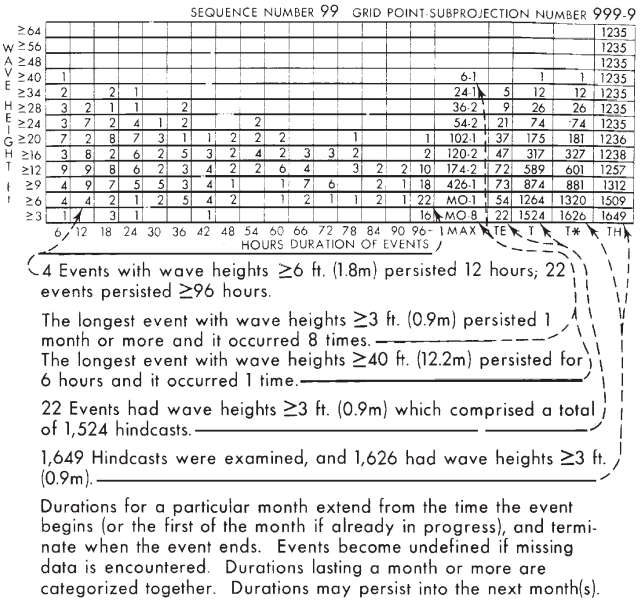

WAVE HEIGHT INTERVALS- MONTHLY SEASONAL

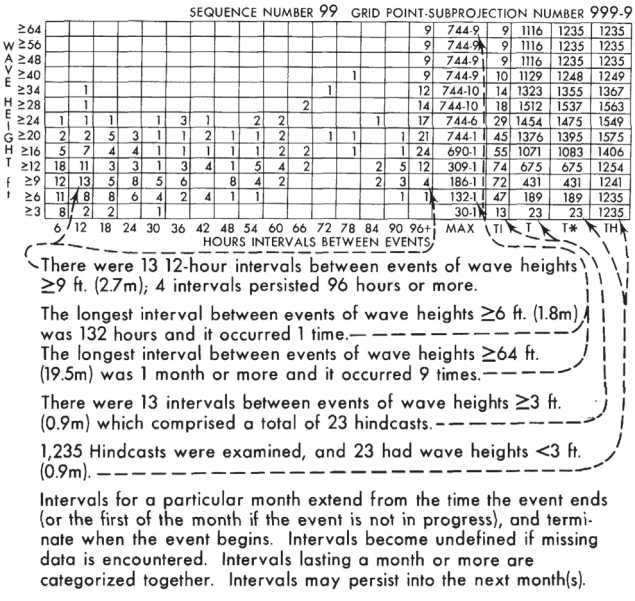

Abbreviations

MAX:	Maximum duration or interval, followed by the number of occurrences	TH:	Total number of hindcasts examined
TE or TI:	Total number of events or intervals	MO:	Month
T:	Total number of hindcasts included in TE or TI	SEA:	Season
T*:	Total number of hindcasts that met the stated criteria		

Table 14-11. KSC wind speed durations, Atlantic grid point 42: 30.4° N., 77.9° W.

January

Wind Speed (kt)	6	12	18	24	30	36	42	48	54	60	66	72	78	84	90	96+	MAX	TE	T	Tx	TH
											42						222-1				
≥64																					2439
≥48	1																6-1	1	1		2439
≥41			2														18-2	2	3		2439
≥34	1		2														18-2	3	7		2439
≥28	6	2	1	3			1										42-1	13	32		2439
≥22	34	21	8	2		2	1	2	1				1				78-1	72	165		2439
≥17	62	30	23	23	11	8	6	3	3	1	1		1			1	96-1	173	529		2439
≥11	28	19	23	23	18	15	14	13	12	9	3	9	2			14	198-1	202	1293	1301	2463
≥7	22	21	14	18	20	5	13	8	13	10	5	3	7	8	3	34	306-1	204	1949	2005	2602
≥4	19	5	2	7	12	2	7	7	2	6	6	3	2	4	8	49	408-1	148	2272	2390	2666
	6	12	18	24	30	36	42	48	54	60	66	72	78	84	90	96+	MAX	TE	T	Tx	TH

Duration of Events (hr)

April

Wind Speed (kt)	6	12	18	24	30	36	42	48	54	60	66	72	78	84	90	96+	MAX	TE	T	Tx	TH
											42						222-1				
≥64																					2399
≥48																					2399
≥41																					2399
≥34	3																6-3	3	3	3	2399
≥28	8	4	2	1													24-1	15	26	26	2399
≥22	19	10	10	6		1											36-1	46	99	99	2399
≥17	37	21	23	11	13	4	2		2	1							60-1	114	323	323	2404
≥11	57	30	25	24	13	18	16	12	6	6	4	3	1	1	1	8	192-1	225	1080	1080	2427
≥7	29	17	14	16	16	12	9	5	13	10	8	7	6	8	3	32	246-1	205	1773	1799	2458
≥4	16	11	4	4	5	5	6	5	7	8	5	7	1	4	2	58	378-1	148	2241	2269	2548
	6	12	18	24	30	36	42	48	54	60	66	72	78	84	90	96+	MAX	TE	T	Tx	TH

Duration of Events (hr)

July

Wind Speed (kt)	6	12	18	24	30	36	42	48	54	60	66	72	78	84	90	96+	MAX	TE	T	Tx	TH
											42						222-1				
≥64																					2477
≥48																					2477
≥41																					2477
≥34																					2477
≥28																					2477
≥22	2																6-2	2	2	2	2477
≥17	9	5	2	2	11	2											36-2	21	50	52	2477
≥11	34	11	7	7	4	8	7	4	3	4		1		1		1	162-1	92	374	383	2477
≥7	62	37	13	12	7	13	6	6	3	7	3	3	4	6	5	12	306-1	199	1091	1113	2517
≥4	49	18	7	7	7	12	3	7	3	5	4	5	5	3	3	42	372-1	180	1971	2043	2639
	6	12	18	24	30	36	42	48	54	60	66	72	78	84	90	96+	MAX	TE	T	Tx	TH

Duration of Events (hr)

October

Wind Speed (kt)	6	12	18	24	30	36	42	48	54	60	66	72	78	84	90	96+	MAX	TE	T	Tx	TH
											42						222-1				
≥64																					2418
≥48																					2418
≥41																					2418
≥34	1				1												30-1	2	6	6	2418
≥28	3	2	1	3	2	1								1			84-1	13	52	52	2420
≥22	7	9	7	1	2	3		3		1					1	2	108-1	36	161	161	2425
≥17	34	14	8	4	5	7	4	4	5		4		1	1		6	192-1	97	469	469	2440
≥11	28	14	11	9	7	3	7	4	7	6	4	3	2	5	3	25	270-1	138	1196	1203	2466
≥7	32	12	11	9	10	11	4	4	5	9	6	5	3		3	39	306-1	463	1766	1776	2530
≥4	9	8	4	6	3	4	6	6	5	3	4	3	5		4	56	MO-2	126	2607	2618	2926
	6	12	18	24	30	36	42	48	54	60	66	72	78	84	90	96+	MAX	TE	T	Tx	TH

Duration of Events (hr)

Table 14-12. KSC wind speed intervals, Atlantic grid point 42: 30.4° N., 77.9° W.

January

Wind Speed (kt)	6	12	18	24	30	36	42	48	54	60	66	72	78	84	90	96+	MAX	TE	T	Tx	TH
											42						222-1				
≥64																17	744-17	17	2108	2469	2439
≥48																18	744-17	18	2171	2532	2439
≥41										1						18	744-16	19	2169	2530	2439
≥34										1						19	744-14	20	2183	2544	2439
≥28								1								28	744-11	29	2577	2784	2439
≥22	2	2	7	2	3		2	1	3		4	2	1		4	57	744-1	84	2565	2654	2439
≥17	31	17	15	4	8	7	9	6	2	14	6	6	5	3	6	43	456-1	182	2001	2083	2439
≥11	32	27	23	21	19	13	15	8	7	3	4	6	3	5	2	13	174-1	201	1194	1229	2463
≥7	54	54	33	17	12	5	3	5	2		2	1	2	1		2	138-1	193	615	329	2602
≥4	73	33	10	10	3	2	3		2								54-1	136	275	278	2666

Duration of Events (hr)

April

Wind Speed (kt)	6	12	18	24	30	36	42	48	54	60	66	72	78	84	90	96+	MAX	TE	T	Tx	TH
											42						222-1				
≥64																19	720-19	19	2280	2399	2399
≥48																19	720-19	19	2280	2399	2399
≥41																19	720-19	19	2280	2399	2399
≥34				1						1						20	720-19	22	2328	2447	2450
≥28	1		2						1	1	2					27	720-20	34	2705	2747	2773
≥22	3	3		2	1	1	1	3	4	3		3				41	720-14	65	3147	3170	3269
≥17	5	13	7	4	5	7	4	9	7	3	1		2	4	1	52	720-3	124	2679	2702	3020
≥11	39	35	20	18	21	17	10	10	5	6	4	8	4	2	5	22	288-1	226	1505	1508	2560
≥7	59	42	31	16	13	15	8	6	2	1	2	1		2	2	1	96-1	201	695	695	2435
≥4	65	34	17	7	6	6	1										42-1	136	285	285	2405

Duration of Events (hr)

July

Wind Speed (kt)	6	12	18	24	30	36	42	48	54	60	66	72	78	84	90	96+	MAX	TE	T	Tx	TH
											42						222-1				
≥64																17	744-17	17	2108	2477	2477
≥48																17	744-17	17	2108	2477	2477
≥41																17	744-17	17	2108	2477	2477
≥34																17	744-17	17	2108	2477	2477
≥28																17	744-17	17	2108	2477	2477
≥22																18	744-17	18	2224	2593	2595
≥17		4	1									1				32	744-16	38	2890	3108	3160
≥11	13	5	3	3	5	3	2	5	1	2	4	1		4	2	53	636-1	108	2505	2559	2942
≥7	54	27	14	6	9	10	10	5	9	9	1	5	2	3	3	32	180-2	202	1446	1468	2541
≥4	72	21	16	18	3	10	9	5	4	3	2	3	5	1	1	3	120-1	171	620	622	2503

Duration of Events (hr)

October

Wind Speed (kt)	6	12	18	24	30	36	42	48	54	60	66	72	78	84	90	96+	MAX	TE	T	Tx	TH
											42						222-1				
≥64																18	744-18	18	2232	2474	2474
≥48																18	744-18	18	2232	2474	2474
≥41																18	744-18	18	2232	2474	2474
≥34																20	744-17	20	2258	2477	2483
≥28	3		1							2						24	744-15	30	2456	2674	2724
≥22	4	1		2	1	1		1	1	1	1			1		37	744-6	51	2570	2759	2913
≥17	9	5	10	4	1	3	6	2	2	2	4	2	2		2	56	744-1	110	2094	2155	2602
≥11	31	10	11	9	13	7	5	8	3	5	5	5	4	4	1	22	402-1	143	1262	1312	2467
≥7	33	22	19	11	18	9	7	9	6	3	5	1		4		5	144-1	152	745	759	2423
≥4	37	31	16	10	5	3	2	2		1	2			1			84-1	110	306	310	2420

Duration of Events (hr)

Table 14-13. KSC wave height duration, Atlantic grid point 42: 30.4° N., 77.9° W.

January

Wave Height (ft)	6	12	18	24	30	36	42	48	54	60	66	72	78	84	90	96+	MAX	TE	T	Tx	TH
											42						222-1				
≥64																					2439
≥56																					2439
≥48																					2439
≥40																					2439
≥34																					2439
≥28	1																6-1	1	1	1	2439
≥24	1		1														18-1	2	4	4	2439
≥20			1		1												30-1	2	8	8	2439
≥16	1				1	1	1		1								54-1	5	28	28	2439
≥12	6	3			1				1	2	1						66-1	14	57	57	2439
≥9	8	10	5	3	3		1		2		2			1	1		90-1	36	146	146	2439
≥6	31	23	17	11	11	11	5	6		2	1	3		1		6	174-1	128	575	575	2450
≥3	24	13	8	13	9	13	7	9	7	6	6	3	6	1	2	34	414-1	161	1665	1684	2607

Duration of Events (hr)

April

Wave Height (ft)	6	12	18	24	30	36	42	48	54	60	66	72	78	84	90	96+	MAX	TE	T	Tx	TH
											42						222-1				
≥64																					
≥56																					
≥48																					
≥40																					2399
≥34																					2399
≥28																					2399
≥24																					2399
≥20																					2399
≥16																					2399
≥12						1											36-1	2	9	9	2399
≥9	7	6	1		2	1	1										42-1	21	54	54	2399
≥6	30	11	416	9	6	2	5	1		1	3	1				2	138-1	87	319	319	2409
≥3	26	24	24	14	7	12	13	11	8	3	5	2	2	1	4	20	288-1	176	1280	1281	2453

Duration of Events (hr)

July

Wave Height (ft)	6	12	18	24	30	36	42	48	54	60	66	72	78	84	90	96+	MAX	TE	T	Tx	TH
											42						222-1				
≥64																					
≥56																					
≥48																					
≥40																					2477
≥34																					2477
≥28																					2477
≥24																					2477
≥20																					2477
≥16																					2477
≥12	1																6-1	1	1	1	2477
≥9	1	1				1											36-1	3	9	9	2477
≥6	3	4	1	1		1					1						66-1	11	35	35	2477
≥3	36	13	12	8	6	10	3	8	4	5	1	1		4	2	7	186-1	120	656	664	2477

Duration of Events (hr)

October

Wave Height (ft)	6	12	18	24	30	36	42	48	54	60	66	72	78	84	90	96+	MAX	TE	T	Tx	TH
											42						222-1				
≥64																					
≥56																					
≥48																					
≥40																					2418
≥34																					2418
≥28																					2418
≥24		1															12-1	1	2	2	2418
≥20							1										42-1	1	7	7	2418
≥16	1	1	1						1								54-1	4	15	15	2418
≥12	5	1	1	2	3	2								1	1	2	108-2	18	110	110	2423
≥9	9	2	3	3		1	2	1	3	2	1	1				6	180-1	34	253	253	2428
≥6	13	6	5	3	1	4	5	2	1	3	3	2	2	1	1	19	216-1	70	703	703	2462
≥3	14	8	7	9	5	2	5	5	1	2		3	4		1	40	618-1	107	1646	1646	2594

Duration of Events (hr)

Table 14-14. KSC wave height intervals, Atlantic grid point 42: 30.4° N., 77.9° W.

January

Wave Height (ft)	6	12	18	24	30	36	42	48	54	60	66	72	78	84	90	96+	MAX	TE	T	Tx	TH
											42						222-1				
≥64																17	744-17	17	2108	2469	2469
≥56																17	744-17	17	2108	2469	2469
≥48																17	744-17	17	2108	2469	2469
≥40																17	744-17	17	2108	2469	2469
≥34																17	744-17	17	2108	2469	2469
≥28																18	744-17	18	2171	2532	2533
≥24												1				18	744-17	19	2182	2543	2547
≥20											1					18	744-17	19	2181	2542	2550
≥16	1								1							19	744-15	21	2179	2540	2568
≥12	1							1								26	744-14	28	2527	2737	2794
≥9					2	1	1	1				1				43	744-6	49	2525	2622	2768
≥6	21	12	3	6	5	2	3	3	2	8	5	2	3	1	5	53	522-1	134	1988	2066	2630
≥3	30	20	18	12	14	11	6	9	4	4	3	2	5	3	2	13	150-1	156	935	956	2472

Duration of Events (hr)

April

Wave Height (ft)	6	12	18	24	30	36	42	48	54	60	66	72	78	84	90	96+	MAX	TE	T	Tx	TH
											42						222-1				
≥64																19	720-19	19	2280	2339	2399
≥56																19	720-19	19	2280	2339	2399
≥48																19	720-19	19	2280	2339	2399
≥40																19	720-19	19	2280	2339	2399
≥34																19	720-19	19	2280	2339	2399
≥28																19	720-19	19	2280	2339	2399
≥24																19	720-19	19	2280	2339	2399
≥20																19	720-19	19	2280	2339	2399
≥16																19	720-19	19	2280	2339	2339
≥12																21	720-19	21	2280	2499	2508
≥9	2	2		1			1			1				1		29	720-17	37	2739	2780	2834
≥6	11	2	2	3	3	4	2	3	3	8	3	2	4		2	45	720-6	97	2765	2788	3097
≥3	29	21	16	15	9	12	10	5	9	8	4	4	5	2	5	20	276-1	174	1292	1293	2520

Duration of Events (hr)

July

Wave Height (ft)	6	12	18	24	30	36	42	48	54	60	66	72	78	84	90	96+	MAX	TE	T	Tx	TH
											42						222-1				
≥64																17	744-17	17	2108	2477	2477
≥56																17	744-17	17	2108	2477	2477
≥48																17	744-17	17	2108	2477	2477
≥40																17	744-17	17	2108	2477	2477
≥34																17	744-17	17	2108	2477	2477
≥28																17	744-17	17	2108	2477	2477
≥24																17	744-17	17	2108	2477	2477
≥20																17	744-17	17	2108	2477	2477
≥16																17	744-17	17	2108	2477	2477
≥12								1								17	744-17	18	2116	2485	2486
≥9	1															18	744-17	20	2166	2535	254
≥6			1		1									1		24	744-15	26	2628	3043	3078
≥3	20	6	5	4	5	6	7	5	4	5	3	4	4	3	2	48	690-1	131	2167	2241	2905

Duration of Events (hr)

October

Wave Height (ft)	6	12	18	24	30	36	42	48	54	60	66	72	78	84	90	96+	MAX	TE	T	Tx	TH
											42						222-1				
≥64																18	744-18	18	2232	2474	2474
≥56																18	744-18	18	2232	2474	2474
≥48																18	744-18	18	2232	2474	2474
≥40																18	744-18	18	2232	2474	2474
≥34																18	744-18	18	2232	2474	2474
≥28																18	744-18	18	2232	2474	2474
≥24																19	744-18	19	2253	2472	2474
≥20																19	744-18	19	2250	2467	2474
≥16	1													1		20	744-17	22	2337	2553	2568
≥12	2		2		1					1						28	744-14	34	2601	2815	2920
≥9	1			2			1			2	1					42	744-7	49	2690	2876	3119
≥6	6	6	2	1	3	4	2	3		2	3	1	1	2	4	42	744-1	82	1886	1980	2639
≥3	16	10	8	5	8	3	2	9	5	4	3	5	2	1	2	17	318-1	100	955	995	2465

Duration of Events (hr)

Table 14-15. Procedure for computing the percent of ≥9-ft waves lasting >24 hr.

Duration (hr)	Hindcasts Per Event		Frequency (From Table)		Hindcasts ≥9 ft (≥2.7 m) Lasting ≤24 hr
6	1	×	8	=	8
12	2	×	10	=	20
18	3	×	5	=	15
24	4	×	3	=	12
					Total 55

Thus, the percent of ≥9-ft waves that lasted ≤24 hr is $(55 \div 146) \times 100 = 37.7$ percent. The percent of ≥9-ft waves lasting >24 hr is 100 percent – 37.7 percent = 62.3 percent.

Step (2): Percent of waves ≥9 ft is $(T^*/TH) \times 100$ or $(146 \div 2{,}439) \times 100 = 6$ percent.

Step (3): The answer is 62.3 percent × 6 percent = 3.7 percent.

- Question 3: Suppose a certain operation to be conducted in April near grid point No. 42 requires that the significant wave height must remain <9 ft for at least 24 hr. What is the climatological probability that the operation can be conducted successfully?

  – Answer: This problem involves the use of the wave height interval tables, since we want intervals between wave heights ≥9 ft. The number of intervals between events of waves ≥9 ft is 37 (from the TI column of the interval table (table 14-14)). The number of intervals between events (episodes) of wave heights ≥9 ft lasting ≤24 hr is $2 + 2 + 0 + 1 = 5$. The percentage of intervals between waves ≥9 ft lasting ≤24 hr is thus $(5 \div 37) \times 100 = 13.5$ percent. In other words, 13.5 percent of all the episodes with waves <9 ft persisted 24 hr or less, and the percentage of <9-ft wave episodes lasting >24 hr is 100 percent –13.5 percent = 86.5 percent. Thus, the climatological probability that the operation can successfully be conducted is 86.5 percent.

- Question 4: What percentage of the time can significant wave heights <9 ft be expected to persist longer than 2 days in April at Atlantic grid point No. 42?

  – Answer: This problem requires the use of hindcast frequencies from the interval table (table 14-14) for April. Proceed following the steps outlined in question 2.

  Step (1). Compute the percent of <9-ft waves that lasted >2 days (table 14-16). This requires estimation of the total number of hindcasts meeting this criterion. Estimation is necessary because beyond 1 day, the 0.25-day resolution of the hindcasts is lost in the summary process, so we must approximate the average number of hindcasts per interval. Since the 1- to 2-day interval includes episodes consisting of 1.25, 1.5, 1.75, and 2 days; i.e., 5, 6, 7, and 8 hindcasts, the average hindcasts per interval is 6.5. In this example, it will be easier and more accurate to find the percent for ≤2 days, then subtract from 100, to obtain the percent required.

  Thus, the percent of <9-ft waves that lasted <2 days is $(16.5 \div 2{,}739) \times 100 = 0.6$ percent. The percent of <9-ft waves that lasted >2 days is 100 percent – 0.6 percent = 99.4 percent.

  Step (2). The percent of waves <9 ft is $(T^*/TH) \times 100$ or $(2{,}780 \div 2{,}834) \times 100 = 98.1$ percent.

  Step (3). The answer is 99.4 percent × 98.1 percent = 97.5 percent.

Table 14-16. Procedure for computing the percent of <9-ft waves lasting >2 days.

Interval (day)	Hindcasts Per Interval		Frequency (From Table)		Hindcasts ≥9 ft (≥2.7 m) Lasting ≤2 Days
0.25	1	×	2	=	2
0.50	2	×	2	=	4
0.75	3	×	0	=	0
1	4	×	1	=	4
1–2	6.5	×	1	=	6.5
					Total 16.5

14.9 Ocean Temperature and Salinity

Physical properties of sea water depend primarily on salinity and temperature. Differences in salinity and/or temperature throughout the ocean cause density differences that drive subsurface water masses. These subsurface water mass movements are called thermohaline currents.

Salinity is defined as the total amount of solid material in grams contained in 1 kg of sea water when carbonate has been converted to oxide, bromine and iodine replaced by chlorine, and all organic material completely oxidized. While coastal waters can exhibit a wide range of salinity as a result of fresh-water runoff, most of the world's ocean water lies in the narrow salinity range of 33.8 to 36.8 gm of dissolved salts per kilogram of sea water. The North Atlantic is the most saline of the world's oceans, having a mean salinity of 35.09 compared to the global average of 34.72. At a given temperature and pressure, sea water is denser than fresh water.

Temperature in the ocean varies widely, both horizontally and with depth. Maximum values of ≈32 °C are recorded at the surface in the Persian Gulf in summer. The lowest possible values of about –2 °C—the usual minimum freezing point of sea water—occur in polar regions. Fresh water reaches maximum density at 4 °C and then expands—becomes less dense—as it cools to 0 °C and freezes. This is why fresh-water ponds in cold climates convectively turn over every season. Saltwater, on the other hand, continues to become denser as it cools to its freezing point. However, when saltwater freezes, the salt impurities, primarily composed of sodium chloride molecules, are not easily incorporated into the ice crystal lattice structure so the newly formed ice is composed primarily of fresh water. The solution rejected when sea water freezes is even higher in salt content, even denser, and has an even lower freezing point than the original solution. The greatest changes in density of sea water occur at the surface where density is decreased by precipitation, water runoff from land surfaces, melting ice, and heating. Density is increased by formation of sea ice, cooling, and by evaporation. The greatest increase in density occurs in polar regions, where the water is cold and great quantities of ice form. This cold, dense polar water sinks and spreads to lower latitudes via thermohaline currents.

At depths of more than a couple hundred meters below the surface of the ocean, the temperature and salinity of water normally change very slowly. When it does change rapidly, it is because a new water mass—with new salinity and temperature values—advects into, and displaces the original water from that location. Since both temperature and salinity are conservative properties of a fluid; i.e., changed mainly by advection, the movement of a water mass can be traced by its temperature and salinity. Water masses are often characterized by their region of origin and their relative depth. Four depths, beginning at the surface and extending to the ocean bottom, are used: surface, intermediate, deep, and bottom.

The greatest known depth of ocean water is 11,524 m in the Marianas Trench in the Pacific. The average ocean depth worldwide is 3,795 m. By way of comparison, the highest land on Earth—Mount Everest—is 8,840 m and the average height of land is 840 m above sea level. Approximately 23 percent of the ocean is shallower than 3,000 m, ≈76 percent is between 3,000 and 6,000 m, and a little more than 1 percent is deeper than 6,000 m. About 77 percent of the world ocean volume is colder than 4 °C, with salinities in the relatively narrow range of 34.1 to 35.1 g of dissolved salts per kilogram of sea water.

Maximum, mean, and minimum water temperatures for 3-mo periods from the surface to depths of 50 m for the KSC ocean area is given in table 14-17 (ref. 14-14). A similar table for VAFB can be obtained by downloading table 14-6 of *NASA–TM–4511* at <http://trs.nis.nasa.gov> (ref. 14-9).

Table 14-17. Ocean temperatures (°C)* in the KSC recovery area (ref. 14-14).

Depth		January to March			April to June			July to September			October to December		
(m)	(ft)	Max.	Mean	Min.	Max.	Mean	Min.	Max.	Mean	Min.	Max.	Mean	Min.
0	0	26	23	16	29	26	21	31	29	27	29	26	19
10	33	26	23	16	29	26	20	30	29	26	29	26	19
20	66	26	23	17	29	26	19	30	28	23	29	26	20
30	98	26	23	16	28	26	17	29	28	21	29	26	21
50	164	26	23	17	28	25	17	29	27	19	28	26	22

*$T_{°F} = T_{°C}\left(\frac{9}{5}\right) + 32$

Figure 14-12 presents four global plots of mean sea surface temperature (SST) for selected months—January, April, July, and October—representative of the four seasons. These images and those for the other months are provided by NOAA's Climate Prediction Center (CPC) from their Web site at <http://www.cpc.noaa.gov/products/predictions/30day/SSTs/sst_clim.html>. These images are monthly means from the base period 1971–2000. This sea surface temperature climatology is constructed using the method of Reynolds and Smith (ref. 14-15) and Smith and Reynolds (ref. 14-16). This climatology is built from two intermediate climatologies: a 2° SST climatology developed from in situ data for the period 1971–2000 and a 1° SST climatology for the period 1982–2000 which incorporates satellite data and is derived from the second version optimum interpolation SST analysis.

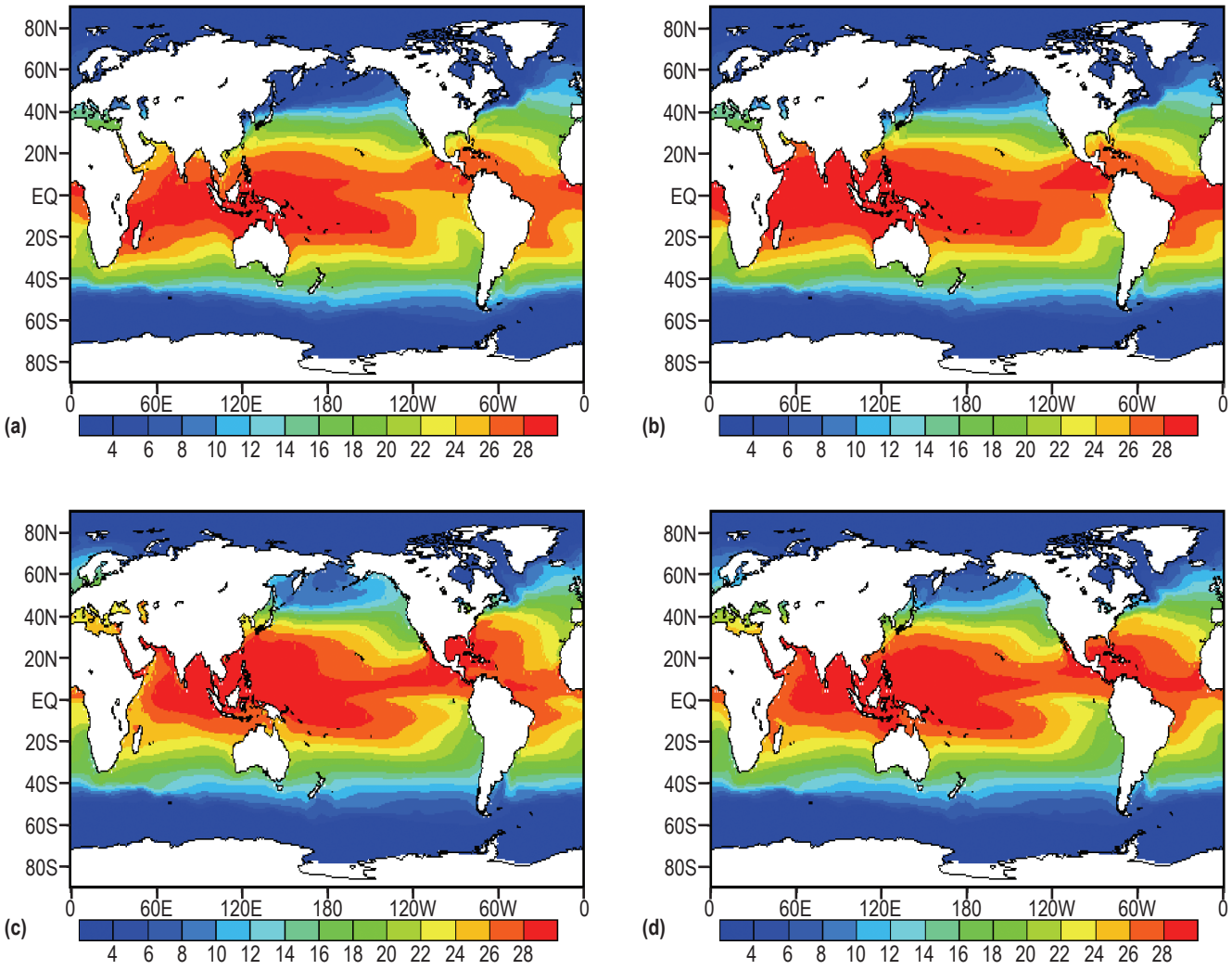

Figure 14-12. Global plots of monthly mean SST from the base period 1971–2000 for (a) January, (b) April, (c) July, and (d) October. Temperatures are in °C as indicated by color from cold blue (<4 °C) to warm red (>28 °C). Images are from NOAA's Climate Prediction Center Web site.

REFERENCES

14-1. "Fundamentals of Physical Geography," <http://www.geog.ouc.bc.ca/physgeog/>, copyright 1996–2000, Cited 2005.

14-2. Johnson, D.L. (ed.): "Terrestrial Environment (Climatic) Criteria Handbook for Use in Aerospace Vehicle Development," NASA–HDBK–1001, August 2000, based on *NASA TM–4511*, August 1993.

14-3. Goda, Y.: *Random Seas and Design of Maritime Structures*, 2nd Edition, Advanced Series on Ocean Engineering, Vol. 15, World Scientific Publishing, 443 pp., 2000.

14-4. Young, I.R.: "Seasonal Variability of the Global Ocean Wind and Wave Climate," *International Journal of Climatology*, Vol. 19, pp. 931–950, 1999.

14-5. Pierson, W.J.; and Moskowitz, L.: "A Proposed Spectral Form for Fully Developed Wind Seas Based on the Similarity Theory of S.A. Kitaigorodskii," *J. Geophys. Res.*, Vol. 69, pp. 5181–5190, 1964.

14-6. Longuet-Higgins, M.S.: "On the Statistical Distributions of Sea Waves," *J. Marine Res.*, Vol. 11, No. 3, pp. 245–265, 1952.

14-7. Alves, J.H.; and Young, I.R.: "Extreme Significant Wave Heights From Combined Satellite Altimeter Data," *Proc. 27th International Conference on Coastal Engineering*, Sydney, Australia, pp. 1064–1077, 2000.

14-8. "Summary of Synoptic Meteorological Observations," North American Coast Marine Areas, Vol. 4, No. AD707701; Vol. 7, No. AD709055; and Vol. 8, No. AD710771, U.S. Naval Weather Service Command, Washington, DC, May 1970.

14-9. Johnson, D.L. (ed.): "Terrestrial Environment (Climatic) Criteria Guidelines for Use in Aerospace Vehicle Development, 1993 Revision," *NASA–TM–4511*, <http://trs.nis.nasa.gov>, August 1993.

14-10. "U.S. Navy Climatic Study of the Caribbean Sea and Gulf of Mexico, Vol. 3," Naval Oceanography Command Detachment, Asheville, NC, July 1986.

14-11. "Climatology of California Coastal Waters," Fleet Weather Central NAS, Alameda, CA, July 1972.

14-12. "U.S. Navy Hindcast Spectral Ocean Wave Model Climatic Atlas: North Atlantic Ocean," NAVAIR 50–1C–538, Naval Oceanography Command Detachment, Asheville, NC, October 1983.

14-13. "U.S. Navy Hindcast Spectral Ocean Wave Model Climatic Atlas: North Pacific Ocean," NAVAIR 50–1C–539, Naval Oceanography Command Detachment, Asheville, NC, March 1985.

14-14. Churgin, J.; and Halminski, S.J.: "Temperature, Salinity, Oxygen, and Phosphate in the Waters Off United States," Key to Oceanographic Records, Documentation No. 2, Vol. 2, Gulf of Mexico, National Oceanographic Data Center, March 1974.

14-15. Reynolds, R.W.; and Smith, T.M.: "A High Resolution Global Sea Surface Temperature Climatology," *J. Climate*, Vol. 8, pp. 1572–1583, 1995.

14-16. Smith, T.M.; and Reynolds, R.W.: "A High Resolution Global Sea Surface Temperature Climatology for the 1961–90 Base Period," *J. Climate*, Vol. 11, pp. 3320–3323, 1998.

Terrestrial Environment (Climatic) Criteria Guidelines for Use in Aerospace Vehicle Development, 2008 Revision

NASA/TM—2008–215633
December 2008

D.L. Johnson, Editor

Section 15: Mission Analysis, Prelaunch Monitoring, and Flight Evaluation

TABLE OF CONTENTS

LIST OF FIGURES

LIST OF TABLES

LIST OF ACRONYMS

DOL	day of launch
DRWP	Doppler radar wind profiler
EST	eastern standard time
FPS-16	Fixed Ground Radar Search-16
KSC	Kennedy Space Center
LST	local standard time
MFFG	median filter/first guess
MSFC	Marshall Space Flight Center
RF	radio frequency
RMS	root mean square
SRB	solid rocket booster
STS	Space Transportation System
USAF	United States Air Force

NOMENCLATURE

P	probability
T	total time

15. MISSION ANALYSIS, PRELAUNCH MONITORING, AND FLIGHT EVALUATION

General weather and especially wind information is useful in the following three general cases of mission analysis:

(1) Mission planning—Since this activity will normally take place well in advance of the mission, the statistical attributes of the wind are used.

(2) Prelaunch operations—Although wind statistics are useful at the beginning of this period, the emphasis is placed upon forecasting and especially wind monitoring for inflight ascent wind loads relative to design capabilities of the vehicle.

(3) Postflight evaluation—The effect of the observed winds on the flight is analyzed and evaluated.

15.1 Mission Planning

Many factors enter into the planning of a mission. One of these factors is the risk of launch delay due to atmospheric constraints associated with the various operational conditions established for a vehicle. These also apply to landing delay risks where applicable. The following sections address and provide examples of how wind and other atmospheric statistics can be utilized by a mission planner and how the combined atmospheric constraints associated with thunderstorms, precipitation, visibility, cloud ceiling, and winds might be used in tradeoff analyses relative to launch and landing risks. The examples shown in figures 15-1 and 15-2 were developed using the Atmospheric Parametric Risk Analysis Program developed by NASA Marshall Space Flight Center (MSFC). Additional information on the program and its application can be obtained from the Natural Environments Branch, Engineering Directorate, NASA Marshall Space Flight Center, Marshall Space Flight Center, AL 35812.

15.1.1 Wind Statistics and Mission Planning

From wind climatology, the optimum time—month and time of day—and place to conduct the operation can be identified. Missions with severe wind constraints may have such a low probability of success that the risk is unacceptable. Feasibility studies based on wind statistics can identify these problem areas and answer questions such as, “Is the mission feasible as planned?” and “If the probable risk of mission delay or failure is unacceptably high, can it be reduced by rescheduling to a lighter wind period?”

Examples in the following paragraphs illustrate the use of the many wind statistics available to the mission planner.

If it is necessary to remove the ground wind loads damper from a large launch vehicle for a number of hours, and this operation must be scheduled some days in advance, the well-known diurnal ground wind variation should be considered for this problem. If, for example, 10.3 m/s (20 kt) were the critical wind speed, there is a 1-percent risk at 0600 EST, but a 13-percent risk at 1500 EST, in July. Obviously, the midday period in the summer should be avoided for this operation. Since these probability values apply to 1-hr exposure periods, it is important to recognize that the wind risk depends not only on wind speed but also on exposure time. From figure 15-3, the risk in percentage associated with a 15.4-m/s (30-kt) wind at 10 m (33 ft) in February at Kennedy Space Center (KSC) can be obtained for various exposure times. The upper curve shows the risk increasing from

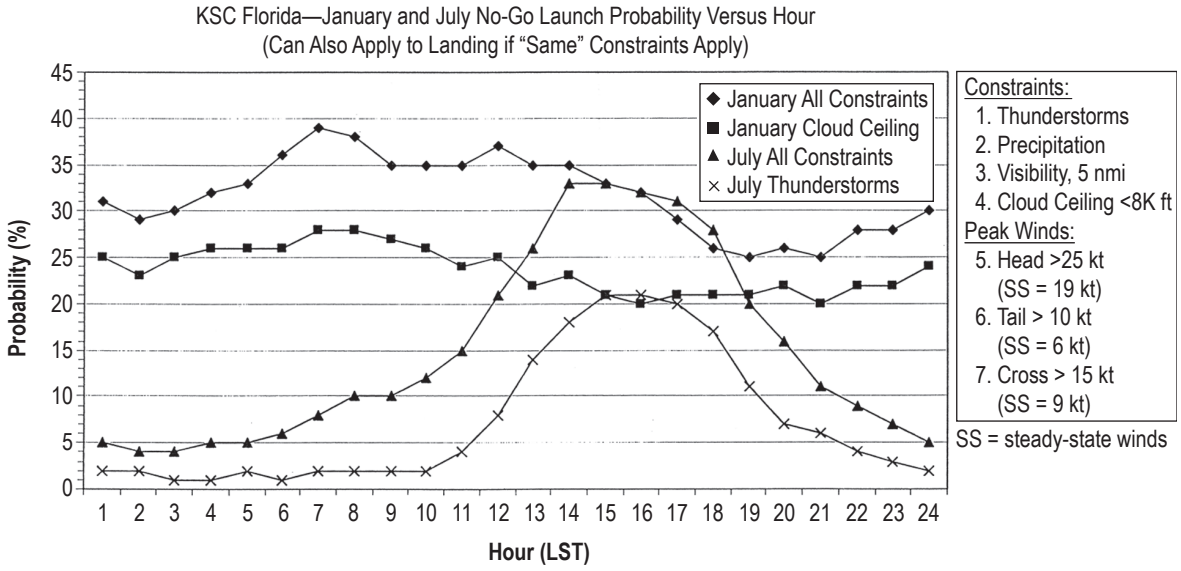

Figure 15-1. Mission analysis, KSC—launch example (used with permission of Wiley Larson, Space Launch and Transportation Systems, USAF Academy).

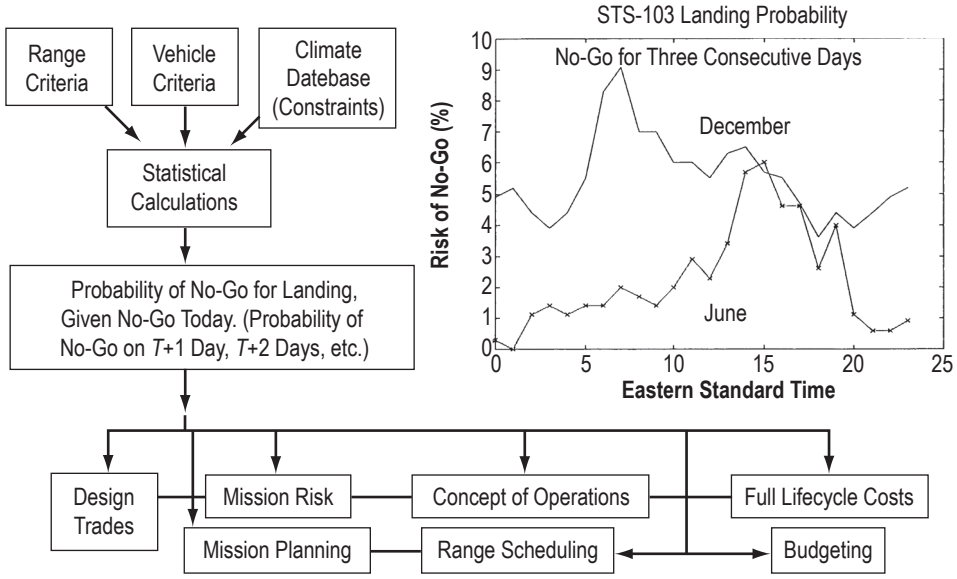

Figure 15-2. Mission analysis trades—landing example (used with permission of Wiley Larson, Space Launch and Transportation Systems, USAF Academy).

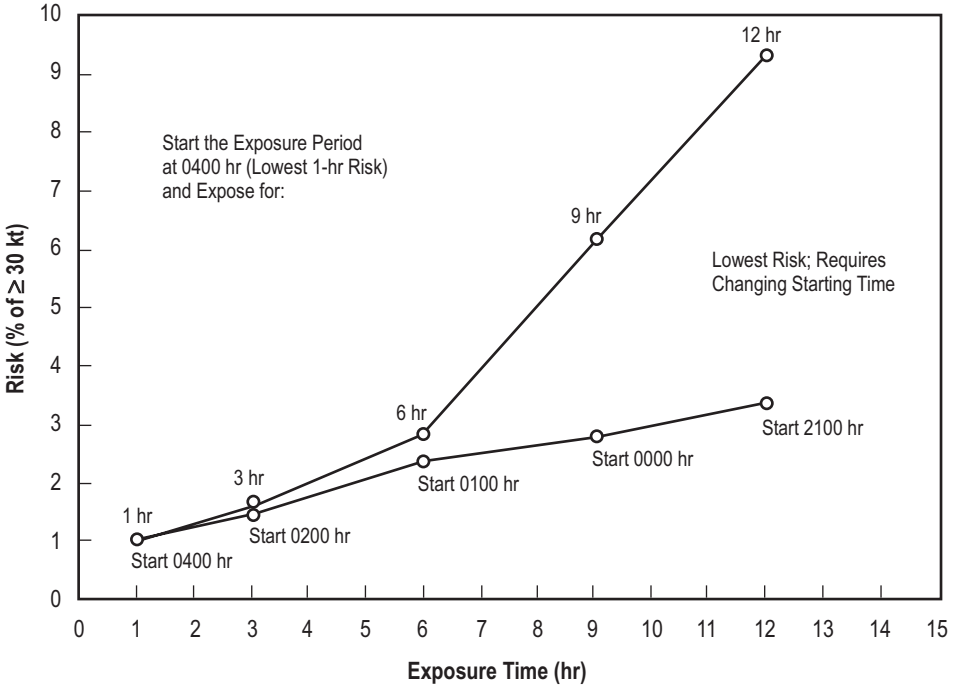

Figure 15-3. Example of wind risk for various exposure times.

1 percent for 1-hr exposure starting at 0400 EST to 9.3 percent for 12-hr exposure starting at 0400 EST. In this case, the exposure period extends through the high-risk part of the day. The lower curve illustrates the minimum risk associated with each exposure period. The lowest risk, of course, can be realized if the starting times are changed to avoid the windy portion of the day. Although there is no space here for the tabulation, wind risk probabilities by month and starting hour for exposure periods from 1 hr to 365 days are available upon request.

When winds aloft are considered for mission planning purposes, again the first step might be to acquire general climatological information on the area of concern. From figure 15-4, it is readily apparent that for KSC, most strong winds occur during winter in the 10- to 15-km (32,800- to 49,200-ft) altitude region. This applies also to nearly all midlatitude locations. It is also true that these strong winds have a westerly component.

Next, the mission analyst might ask if a particular mission is feasible. If, for example, the flight is to take place in January and 10- to 15-km-altitude winds ≥50 m/s are critical, the probability of favorable winds on any given day in January is 0.496. With such a low probability of success, this mission may not be feasible. But, to continue the example, if it is necessary that continuously favorable winds exist for 3 days (perhaps for a dual launch), the probability of success will decrease to 0.256. Obviously, an alternate mission schedule must be planned or else the scheduled space vehicle must be provided additional capability through redesign.

Perhaps the vehicle can remain on the pad in a state of near readiness, awaiting launch for several days. In this case, it would be desirable to know that the probability of occurrence of at least one favorable wind speed; e.g., in a 4-day period, is 0.813. If greater flexibility of operation is desired, one might require four favorable opportunities in 4 days; this probability is 0.550. Now, if consecutive favorable opportunities are required; e.g., four consecutive favorable opportunities in eight periods, the probability of success will be somewhat lower (0.431).

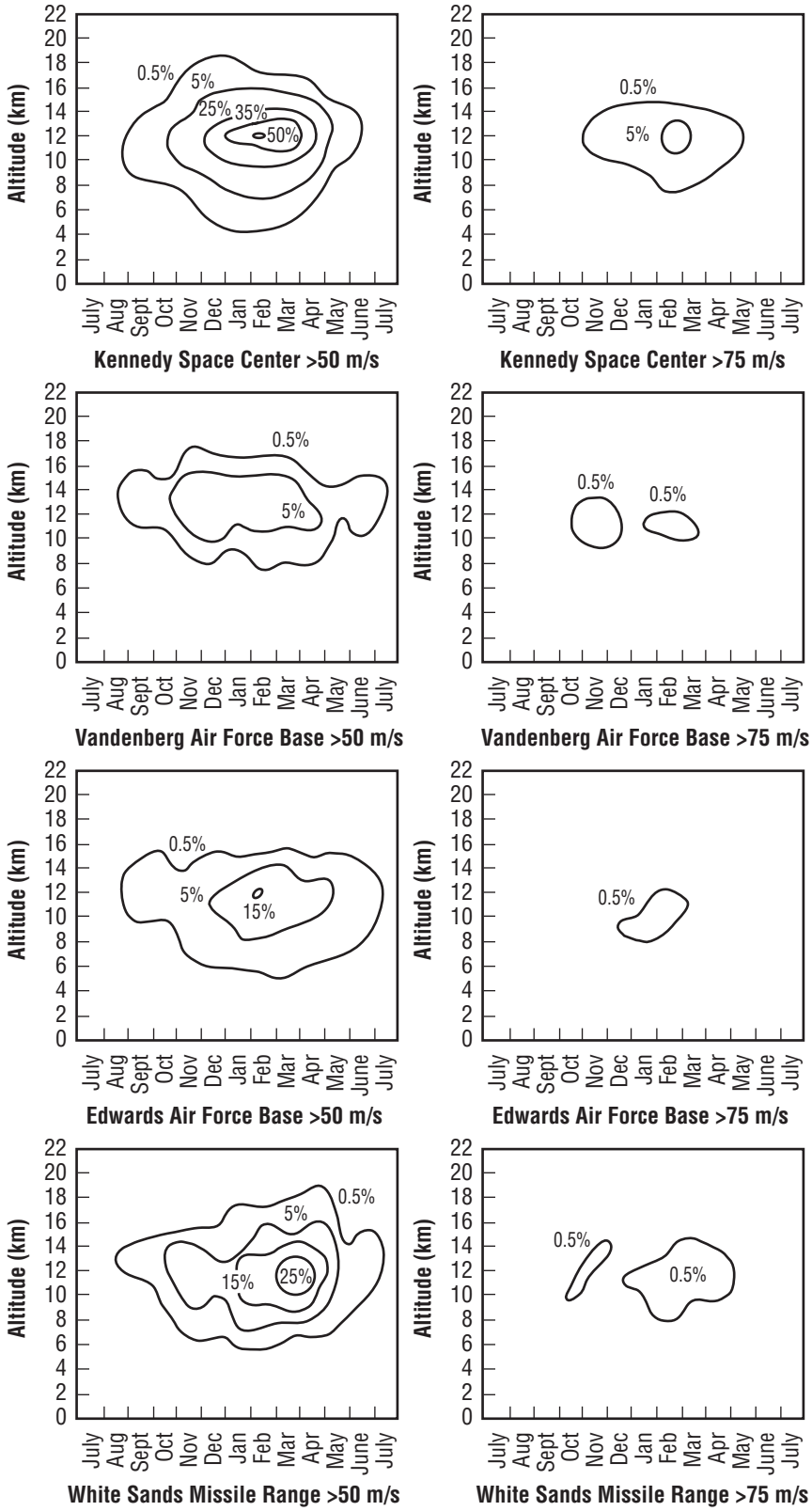

Figure 15-4. Frequency of scalar wind speed exceeding given wind speed as a function of altitude for stations indicated.

The mission planner might also gain some useful information from the persistence of the wind aloft within the 10- to 15-km-altitude region. The probability of winds <50 m/s on any day in January is 0.496. But if a wind speed <50 m/s does occur, then the probability that the next observed wind 12 hr later would be <50 m/s is 0.82, a rather dramatic change. Furthermore, if the wind continues below 50 m/s for five observations, the probability that it will remain there for one more 12-hr period is 0.92.

As the time of the operation approaches *T*–4 to *T*–1 days, the conditional probability statements assume a more significant role. At this point, since the winds will usually be monitored, the appropriate conditional probability value can be identified and used to greater advantage.

The preceding examples are intended to illustrate the type of analysis that can be accomplished to provide objective data for program decisions using the NASA MSFC Atmosphere Parametric Risk Analysis Program. This may best be accomplished by a close working relationship between the analyst and those concerned with the decision for the flight program.

15.1.2 Atmosphere Parameters and Mission Planning

The launch of a vehicle depends upon, among other factors, the condition of the atmosphere (weather) relative to the constraints established for operation of the vehicle. These constraints are based on the specified atmospheric conditions/requirements for the design of the vehicle, desired operational conditions for test and deployment of the vehicle, and degree of risk the launch control officer wishes to assume relative to ability to see (camera coverage, etc.) the vehicle during launch and ascent, etc.

Figure 15-1 is an example of the no-go launch probability versus hour for January and July at KSC. These no-go launch probabilities are calculated using the NASA MSFC Atmosphere Parametric Risk Analysis Program based on constraints associated with not launching within or near a thunderstorm, when precipitation is occurring, with visibility <5 mi and a cloud ceiling (>0.5 cloud cover) <8,000 ft and associated peak ground wind constraints as noted in figure 15-1. The figure illustrates the January no-go launch probability versus hour for all constraints and for only cloud ceiling. For July, the no-go launch probability is given relative to all constraints and for only thunderstorms. It is readily apparent that, relative to these atmospheric constraints, all hours produce about the same no-go launch probabilities. Whereas for July, the afternoon and early evening hours constitute a significant impact for launch probability relative to the late evening and morning hours. For other sites and atmospheric constraints, the no-go launch probability conditions can vary significantly from those in this example.

Figure 15-2 provides a similar example for selected atmospheric constraints relative to the probability of no-go for landing at the indicated hour, given a no-go today, for 3 consecutive days. In addition, for this particular figure, the various factors involved in landing probability analyses and the many interface aspects of the analyses relative to the decision process are illustrated. This is also applicable to the no-go launch probability analyses example in figure 15-1.

15.1.3 In-Flight Winds Exceedance Probabilities

The probability of in-flight winds exceeding or not exceeding some critical speed for a specified time duration may be of considerable importance in mission planning, and in many cases, more information than just the occurrence of critical winds is desired. If a dual launch is planned, with the second vehicle being launched

1 to 3 days after the first, and if the launch opportunity extends over a 10-day period, what is the probability that winds below (or above) critical levels will last for the entire 10 days? What is the probability of 2 or 3 consecutive days of favorable winds in the 10-day period? Suppose the winds are favorable on the scheduled launch day, but the mission is delayed for other reasons. Now, what is the probability that the winds will remain favorable for 3 or 4 more days? Answers to these questions could also be used for certain mission analyses studies involving specific vehicles prepared for a given mission and launch window. A body of statistics is available from MSFC's Environments Group that can be used to answer these and possibly other related questions. An example of the kind of wind persistence statistics that are available is given in figure 15-5. This figure gives the probability of the maximum wind speed in the 10- to 15-km region being less than, equal to, or greater than 50 and 75 m/s for various multiples of 12 hr for the month of January. Thus, for example, there is approximately an 18-percent chance that the wind speed will be ≥50 m/s for 10 consecutive 12-hr periods in January. The random series is plotted as p^k, for k = 1,2,…, 12-hr periods.

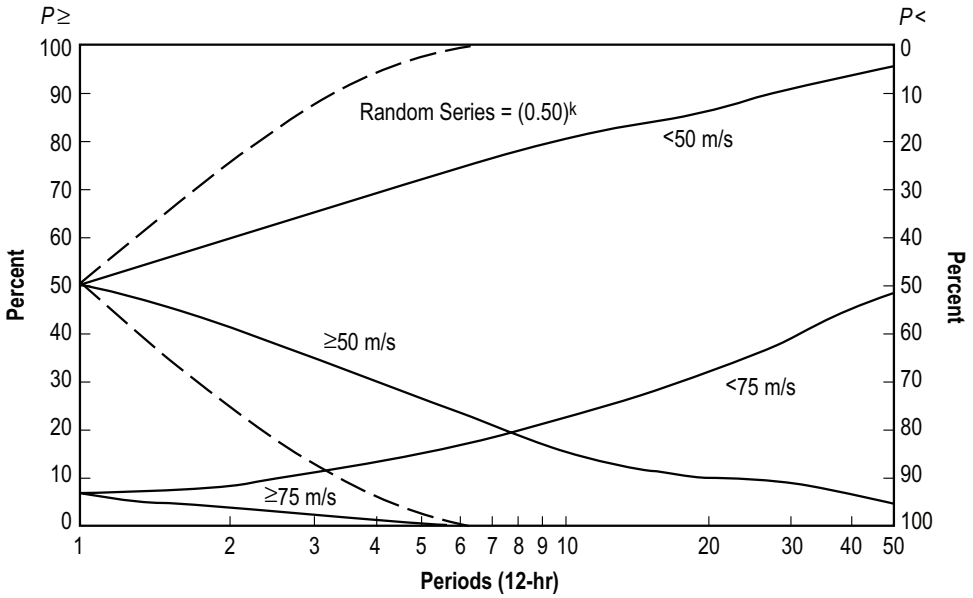

Figure 15-5. Probability of the maximum wind speed in the 10- to 15-km layer being less than, equal to, or greater than specified values for k consecutive 12-hr periods during January at KSC.

15.2 Prelaunch Wind Monitoring

15.2.1 Introduction

In-flight winds constitute a major atmospheric parameter in aerospace vehicle and missile design. A frequency content of the wind profile near the bending mode frequencies or wind shear with the characteristics of a step input may exceed the vehicle's structural capabilities, especially on forward locations of the vehicle. Wind profiles with high speeds and shears exert high structural loads at all stations on a large space vehicle, and when the influences of bending dynamics are high, even a profile with low speeds and high shears can create large loads (ref. 15-1).

Because of the possibility of launch into unknown winds, operational missile systems must accept some in-flight loss risk in exchange for a rapid-launch capability. But research and development missiles, and space vehicles in particular, cost so much that the overall success of a flight outweighs the consideration of launch delays caused by excessive in-flight wind loads. If the exact wind profile could be known in advance, it would be a relatively simple task to decide on the launch date and time. However, there is little hope of accurately forecasting the detailed wind profile far into the future.

Over the years, these situations have increasingly put emphasis on prelaunch monitoring of in-flight winds. Today, prelaunch and profile determination techniques essentially preclude the risk of launching a space vehicle or research and development missile into an in-flight wind condition that would cause it to fail.

The day of launch (DOL) prelaunch winds aloft monitoring by the MSFC Natural Environments Branch follows the Shuttle operations plan outlined in reference 15-2.

15.2.2 FPS-16 Radar/Jimsphere Wind Monitoring System

The development and operational deployment of the FPS-16 radar/Jimsphere system (ref. 15-3) significantly minimizes vehicle failure risks when properly integrated into a flight simulation program. The Jimsphere sensor (a 2-m-diameter aluminized mylar spherical constant volume balloon with roughness elements on its surface), when tracked with the FPS-16 or other radar with equal tracking capability, provides a very accurate "all weather" detailed wind profile measurement. See figure 15-6. FPS-16 radar is available at all national test ranges.

In general, the system provides a wind profile measurement from the surface to an altitude of 17 km in slightly <1 hr, a vertical spatial frequency resolution of 1 cycle per 200 m, and a root mean square (RMS) error of ≈0.5 m/s or less for wind velocities averaged over 50-m intervals. The resolution of these data permits calculating the structural loads associated with the first bending mode and generally the second mode of missiles and space vehicles during the critical, high dynamic pressure phase of flight. This provides better than an order of magnitude accuracy improvement over the conventional rawinsonde wind profile measurement system.

By employing the appropriate data transmission resources, a detailed wind profile from the FPS-16 radar can be ready for input to the vehicle's flight simulation program within a few minutes after tracking of the Jimsphere. The flight simulation program provides flexibility relative to vehicle dynamics and other parameters in order to make maximum use of detailed wind profiles.

If very critical wind conditions exist and the mission requirement dictates a maximum effort to launch with provision for last-minute termination of the operation, then a contingency plan that will provide essentially real-time wind profile and flight simulation data may be employed. This is done while the Jimsphere balloon is still in flight.

An example of the FPS-16 radar/Jimsphere system data—the November 8 and 9, 1967, sequence observed during prelaunch activities for the first Apollo/Saturn-V test flight, AS-501—is shown in figure 15-7. Reference 15-4 contains additional sequential Jimsphere wind profile sets for KSC and Point Mugu, CA, respectively. The persistence over a period of 1 hr of some small-scale features in the wind profile structure, as well as the rather distinct changes that developed in the profiles over a period of a few hours, is evident.

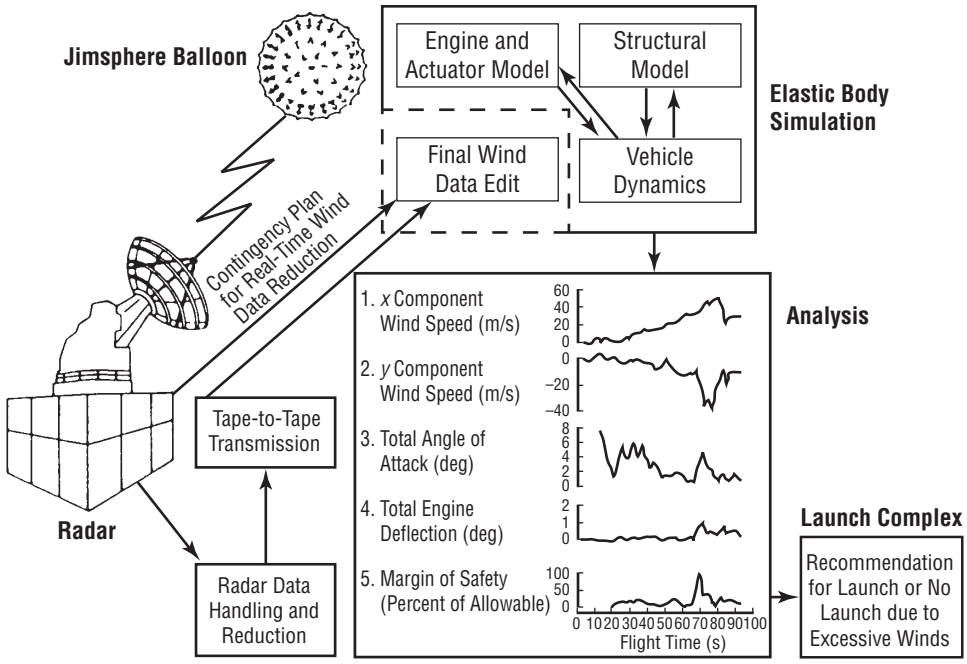

Figure 15-6. Operation of the FPS-16 radar/Jimsphere system.

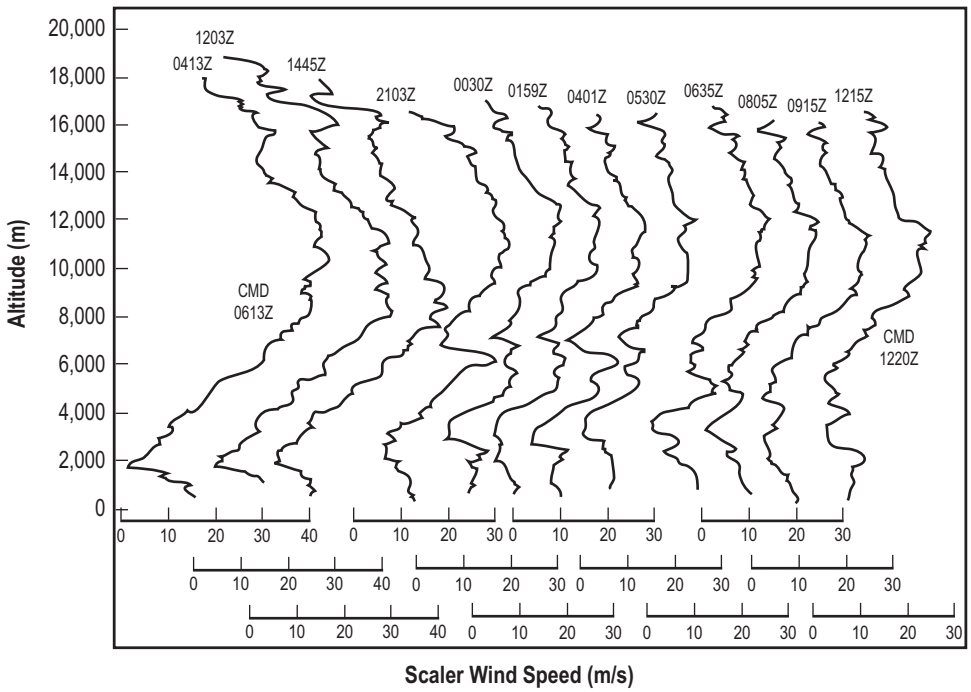

Note: Times between Jimsphere measurements not constant; Jimsphere balloon rise time to 10 km/50 min.

Figure 15-7. Examples of the FPS-16 radar/Jimsphere system data, November 8–9, 1967.

The FPS-16 radar/Jimsphere system (fig. 15-6) was routinely used in the prelaunch monitoring of NASA's Apollo/Saturn and the Space Shuttle flights as part of the Launch System Evaluation Team responsibilities. The wind profile data were transmitted to Johnson Space Center and MSFC, and the flight simulation results were sent to the launch complex at KSC.

An FPS-16 radar/Jimsphere operational measurement program capability exists at all the national test ranges to obtain detailed wind profile data for use in space vehicle and missile response studies, airplane turbulence analysis, atmospheric turbulence investigations, and mesometeorological studies. Sequential measurements similar to those made in support of a Saturn-V launch shown here—of 8 to 10 Jimsphere wind profiles ≈1 hr apart—were made on at least 1 day per month for each location. Single profile measurements were also made daily at KSC.

15.2.3 50-MHz Doppler Radar Wind Profiler

In 1990, KSC installed a vertically pointing 50-MHz Doppler radar wind profiler (DRWP) to evaluate its applicability in measuring upper-level winds in support of space launch operations. An attractive feature of the DRWP, when compared with a radar-tracked Jimsphere, is the ability to continuously monitor upper atmospheric winds. This is particularly important for aerospace vehicles as wind structures in the upper atmosphere exhibit a large spectrum of vertical wavelengths that range on time scales from seconds to days. A description of the DRWP system and studies performed using the system follow.

The DRWP transmits pulses of radio frequency (RF) energy at a nominal frequency of 49.25 MHz, corresponding to a free space wavelength of 6.085 m. The transmitted pulse length is 160 μs with a beam width of 2.9°. The antenna transmits one vertical beam to measure the vertical wind field and two oblique beams inclined 15° from the vertical and oriented at 45° and 135° from due north to determine the u and v wind components (ref. 15-5). Signal return to the receiver comes from a predetermined sample volume of the atmosphere, which is defined by the transmitted pulse length and beam width. In its operational support configuration, the instrument samples the atmosphere at 150-m levels, or gates, beginning with the first gate at ≈2 km, up to 18.6 km. With the implementation of current algorithms (see below), the cycle time to produce wind profiles for u and v is 3 min (ref. 15-5).

A detailed description of the KSC profiler and its data reduction algorithm may be found in Schumann et al. (ref. 15-5). The resolution of the instrument is discussed by Merceret (ref. 15-6), but the actual resolution of the instruments is believed to be better than the average of 500 m (1,600 ft) reported. When the effect of atmospheric decorrelation (refs. 15-6 and 15-7) is accounted for, the data selected at 150 intervals has an effective resolution of 300 m (1,000 ft) (Nyquist limit).

Transient interference signals are an inherent problem when receiving RF waves through the atmosphere (ref. 15-8). Signal processing methods to eliminate the effects of atmospheric "noise" have received considerable research attention after the DRWP installation. Currently, the DRWP incorporates a median filter/first guess (MFFG) algorithm to reduce the effects of transient interference signals (ref. 15-9). The MFFG applies a running temporal median filter (usually a three-point filter) to successive frequency spectra from the oblique beams. Vertical velocities are excluded from the algorithm technique and are not used in the derivation of horizontal velocities (ref. 15-5). After filtering the frequency spectrum, a predefined window, based on the antecedent radial velocity, is chosen to constrain the search for the spectral peak. The spectral peak within the constraining window represents the radial velocity. By selecting a first-guess window, persistent interference signals are eliminated from the

computation of the radial velocity. Based on algorithm development by Schumann et al. (ref. 15-5), the first-guess window is normally set to 12 frequency bins or about ±1.5 m/s.

Constraining the first-guess window does not always mean that all spurious signals will be filtered out of the frequency spectrum. Therefore, the MFFG applies an integration window after calculating the spectral moments from the frequency spectrum. Within the integration window, a maximum difference between the signal peak and lowest signal level above the noise limit is included in the integration. This spectral averaging further reduces effects from spurious noise and better defines the peak in the power spectrum.

To evaluate the DRWP MFFG algorithm's ability to monitor the prelaunch wind environment, comparison studies were conducted based on wind velocity measurements from the DRWP and Jimsphere (refs. 15-5 and 15-9). The studies focused on the relative performance of horizontal velocity component measurements made by the DRWP as compared to time-proximate Jimsphere measurements. Due to the differing vertical resolutions between the two methods, the Jimsphere velocity components were converted to DRWP component velocities along the profiler's oblique beam's azimuths and then interpolated to the DRWP reporting altitudes (150-m levels). Another limitation to the study is that the DRWP samples the atmosphere above the antenna, whereas the Jimsphere follows the winds as it ascends, therefore sampling at different spatial locations with altitude. Comparisons were made from tests performed in the summer and winter seasons to capture differing atmospheric wind conditions. Quantitative analysis consisted of calculating the RMS difference between the Jimsphere and DRWP. From the summer and winter season profiles, the RMS difference between the Jimsphere and DRWP was 1.7 and 2.2 m/s, respectively (ref. 15-5). The RMS differences were also dependent on the velocity magnitude as RMS values rose steadily with altitude to a maximum at the jet steam level.

Since DOL loads analysis is a function of slowly varying (mean) and rapidly varying (turbulent) wind characteristics, the persistence of wind features has been studied through the use of measured wind pairs at discrete time intervals to identify the spectral boundary between mean and turbulent wind features. Various studies have utilized DRWP- and Jimsphere-measured wind pairs to identify slowly varying and turbulent wind features (refs. 15-5 through 15-7). The methodology of extracting these features from an altitude-dependent profile is to perform spectral analysis on the pairs.

A wind component profile can be thought of as multiple spectral components in various vertical wavelengths representing an individual signal. Contained within a sample wind profile are fine structures (turbulence/gusts) superimposed over a general trend (mean wind). Figure 15-6 shows example profiles made by the Jimsphere at discrete times.

Quantifying the temporal persistence of wind features from two time-varying profiles requires converting the data to a frequency domain and performing a cross-spectrum analysis. A product of the cross spectrum is the coherency spectrum, which measures the correlation between the two signals; e.g., profiles, at each wavelength (ref. 15-5). The square of the coherency can range between zero and 1 and is analogous to the square of the correlation coefficient, except that the coherency is a function of wavelength (ref. 15-5). For a pair of points at a given wavelength, coherence-squared values approaching 1 are highly correlated, whereas values approaching zero are uncorrelated. Highly correlated pairs represent persistent wind components (slowly varying winds) while uncorrelated pairs are characteristic of turbulent wind components (rapidly varying winds).

In the studies by Merceret and Spiekermann et al. (refs. 15-6 and 15-7), a coherence-squared value of 0.5 represented the spectral boundary between persistent and nonpersistent wind features. The lag times of

wind pairs ranged from 5 min to 2 hr. A general conclusion from the studies showed that as the lag times between measured pairs increased, the spectral boundary between slowly and rapidly varying wind components increased. For example, wind components with a vertical wave number of ≈0.002 m^{-1} (wavelength of ≈500 m) are coherently resolved for a lag time of 5 min (ref. 15-6). However, at 2 hr, the wind components with a vertical wave number of ≈0.00066 m^{-1} (wavelength of ≈1,500 m) were coherently resolved (ref. 15-7).

The DRWP was originally intended to replace the Jimsphere system for use in the derivation of trajectory and loads analysis in addition to monitoring upper-level winds in support of Shuttle launches. Concern over the selection of the incorrect database when performing DOL load updates, and the cost to build a second database from DRWP measurements, resulted in the Space Shuttle Program office canceling the attempt to certify the DRWP to perform DOL Shuttle loads analysis (ref. 15-9). For DOL Shuttle support, the DRWP is used to provide persistence observations and compare with the general signature of the Jimsphere profiles.

15.3 Postflight Evaluation

15.3.1 Introduction

Because of the variable effects of the atmosphere on a large aerospace vehicle at launch and during flight, various meteorological parameters are measured at the time of each vehicle launch, including wind and thermodynamic data at the Earth's surface and up to an altitude of at least 36 km. To make the data available, meteorological tapes are prepared, presentations made at flight evaluation meetings, memoranda of data tabulations prepared and distributed, and a summary written. Reference 15-11 for Space Shuttle STS-1 is an example of one of the reports with an atmospheric section.

15.3.2 Meteorological Data Profiles

Shortly after the launch of each aerospace vehicle under the cognizance of MSFC, a meteorological ascent data profile was prepared by combining the FPS-16 radar/Jimsphere wind profile data and the rawinsonde wind profile and thermodynamic data (temperature, pressure, and humidity) observed as near the vehicle launch time as feasible. This was done under the supervision of MSFC's Earth Science and Applications Division. The meteorological data were normally available within 3 days after launch time and provided data to ≈36 km (≈120,000 ft). In the meteorological data profile, thermodynamic and wind data limit above the measured data are given by the range reference atmosphere (ref. 15-12) and the global reference atmosphere model (ref. 15-13) values. To prevent unnatural jumps in the data when the two types are merged, the data were carefully examined to pick the best altitude for the merging, and a ramping procedure was employed. The meteorological data profiles were made available to all Government and contractor groups for their use in the space vehicle launch and flight evaluation. This provides a consistent set of data for all evaluation studies and ensures the best available information of the state of the atmosphere during launch. For Space Shuttle launches, a solid rocket booster (SRB) descent meteorological data tape was constructed using rawinsonde data taken from a ship stationed near the SRB impact site. Twenty parameters of data were included in the meteorological data tape at 100-ft increments of altitude. (Altitude increments of 100 ft were chosen to provide maximum engineering utilization for use of the available atmospheric data and do not necessarily represent the attainable response frequency of the measurements.) Table 15-1 presents the parametric format of the *L*–0 atmospheric data profile that is assembled for flight evaluation after each MSFC-associated vehicle launch.

Pad winds and thermodynamic data were measured and recorded at different heights above the launch pad starting several hours before launch time. Reference 15-14 summarizes atmospheric data observations for 155 flights of MSFC-related launches. Records and summary reports are maintained on the atmospheric parameters for MSFC-sponsored vehicle test flights conducted at KSC. Requests for summaries of these atmospheric data or related questions on specific topics should be directed to the Natural Environments Branch, NASA Marshall Space Flight Center, Marshall Space Flight Center, AL 35812.

Table 15-1. Format of meteorological data profile.

Word	Symbol	Description	Units
1	LAT	Latitude	deg, +N
2	LON	Longitude	deg, +E to 360°
3	FLAG	0 = Measured data 1 = Modeled data 2 = Combined measured and modeled data	
4	—	Spare	
5	ALT	Geometric altitude	ft
6	WS	Horizontal wind speed	ft/s
7	WD	Directional horizontal wind is coming from relative to true north, north being 0°, increasing positively clockwise	deg
8	TE	Ambient temperature	°C
9	PR	Ambient pressure	mb
10	D	Ambient density	gm/m^3
11	DW	Dewpoint	°C
12	TEU	Ambient temperature systematic uncertainty	°C
13	PRU	Ambient pressure systematic uncertainty	mb
14	DU	Ambient density systematic uncertainty	gm/m^3
15	HWSUS	Horizontal wind speed systematic uncertainty	ft/s
16	HWSUN	Horizontal wind speed noise or fluctuation uncertainty	ft/s
17	VWSUN	Vertical wind speed noise or fluctuation uncertainty	ft/s
18	HWDUS	Horizontal wind direction systematic uncertainty	deg
19	HWDUN	Horizontal wind direction noise or fluctuation uncertainty	deg
20		Spare	

REFERENCES

15-1. Ryan, R.S.; Scoggins, J.R.; and King, A.W.: "Use of Wind Shears in the Design of Aerospace Vehicles," *J. Spacecraft and Rockets*, Vol. 4, No. 11, pp. 1526–1532, November 1967.

15-2. "MSFC Environments Group (ED44) Terrestrial and Planetary Environments Team Space Shuttle Program Flight Operations Support Baseline," ED44–MNL–001 B, ED: August 12, 2003.

15-3. Vaughan, W.W.: "New Wind Monitoring System Protects R and D Launches," *J. Astronautics and Aeronautics*, Vol. 6, No. 12, pp. 41–43, December 1968.

15-4. Johnson, D.L.; and Vaughan, W.W.: "Sequential High Resolution Wind Profile Measurements," *NASA TP–1354*, Marshall Space Flight Center, AL, December 1978.

15-5. Schumann, R.S.; Taylor, G.E.; Merceret, F.J.; and Wilfong, T.L.: "Performance Characteristics of the Kennedy Space Center 50-MHz Doppler Radar Wind Profiler Using the Median Filter/First Guess Data Reduction Algorithm," *J. Atmos. and Oceanic Tech.*, Vol. 16, No. 5, pp. 532–549, May 1999.

15-6. Merceret, F.J.: The Coherence Time of Mid-Tropospheric Wind Features as a Function of Vertical Scale From 300 m to 2 km, *J. Appl. Meteor.*, Vol. 39, pp. 2409–2420, 2000.

15-7. Spiekerman, C.E.; Sako, B.H.; and Kabe, A.M.: Identifying Slowly Varying and Turbulent Wind Features for Flight Loads Analysis, *J. Spacecraft and Rockets*, Vol. 37, pp. 426–433, 2000.

15-8. Weber, B.L.; and Wuertz, D.B.: "Comparison of Rawinsonde and Wind Profiler Measurements," *J. Atmos. and Oceanic Tech.*, Vol. 7, No. 2, pp. 157–174, 1990.

15-9. Wilfong, T.L.; Smith, S.A.; and Creasey, R.L.: "High Temporal Resolution Velocity Estimates From a Wind Profiler," *J. Spacecraft and Rockets*, Vol. 30, No. 3, pp. 348–354, May–June 1993.

15-10. NASA Letter WE2–93–078, Use of Doppler Radar Wind Profiler for Launch Support, September 28, 1993.

15-11. Johnson, D.L.; Jasper, G.; and Brown, S.C.: "Atmospheric Environment for Space Shuttle (STS–1) Launch," *NASA TM–82436*, Marshall Space Flight Center, AL, July 1981.

15-12. IRIG Document No. 104-63, Range Reference Atmosphere Documents Published by Secretariat, Range Commander's Council, White Sands Missile Range, NM, April 1963.

15-13. Justus, C.G.; Alyea, F.N.; Cunnold, D.M.; Jeffries, W.R., III; and Johnson, D.L.: "The NASA/MSFC Global Reference Atmospheric Model—1990 Version (GRAM–90); Part I Technical/Users Manual," *NASA TM–4268*, Marshall Space Flight Center, AL, April 1991.

15-14. Johnson, D.L.: "Summary of Atmospheric Data Observations for 155 Flights of MSFC/ABMA Related Aerospace Vehicles," *NASA TM X–64796*, Marshall Space Flight Center, AL, December 1973.

Terrestrial Environment (Climatic) Criteria Guidelines for Use in Aerospace Vehicle Development, 2008 Revision

NASA/TM—2008–215633
December 2008

D.L. Johnson, Editor

Section 16: Conversion Units

TABLE OF CONTENTS

LIST OF TABLES

16. CONVERSION UNITS

16.1 Physical Constants and Conversion Factors

Section 16.1 lists the preferred metric units, alternative units, and conversion factors for a number of commonly used quantities in the aerospace industry. The selection presented, while not intended to be restrictive, will prove helpful in presenting values of quantities in an identical manner in similar contexts within the industry. The NASA directive for using the SI (metric) system in NASA programs is given in NASA Policy Directive 8010.2E.

The preferred metric units, alternative units, and conversion factors in table 16-1 are grouped according to the following categories:

1. Space and Time
2. Mass
3. Force
4. Mechanics
5. Flow
6. Thermodynamics
7. Electricity and Magnetism
8. Light
9. Acoustics

Tables 16-2 through 16-6, respectively, list SI base units, supplementary units, derived units, acceptable non-SI units, standard prefixes, and definition for selected physical constants and non-SI units.

When the preferred unit appears without a prefix, multiples of that unit per table 16-5 may be used as necessary at the user's discretion. When a prefix appears with the unit, it is the preferred prefix. When the prefix is left to the user's discretion, however, units shall be consistent within any given document.

The conversion factors given are exact, unless the last digit is underlined. The level of error is 0.1 percent or less.

A quick and easy on-line units conversion Web site is available at **<http://www.onlineconversion.com>**.

Table 16-1. Preferred metric units.

	Quantity	Preferred Metric Unit	Alternative Units	Conversion Factors
1. Space and Time				
1.1	Time	s (second)	min (minute) hr (hour) d (day)	
1.2	Plane angle	rad (radian)	° (degree) ' (minute) " (second)	
1.3	Solid angle	sr (steradian)		
1.4	Length	mm (millimeter)		1 in = 2.54 cm = 25.4 mm 1 ft = 0.3048 m = 304.8 mm 1 yd = 0.9144 m = 914.4 mm
1.4.1	Distance	km (kilometer)	nautical mile	1 statute mile = 1.609 344 km 1 nautical mile (US) = 1.852 km
1.4.2	Distance	m (meter)		1 in = 2.54 cm = 25.4 mm 1 ft = 0.3048 m = 304.8 mm 1 yd = 0.9144 m = 914.4 mm
1.4.3	Visibility	km (kilometer)		1 statute mile = 1.609 344 km
1.4.4	Altitude	m (meter)		1 ft = 0.3048 m
1.4.5	Vibration amplitude	mm (millimeter)		1 in = 25.4 mm
1.4.6	Porosity; surface texture; thickness of surface coating	µm (micrometer)		1 microinch = 0.0254 µm
1.5	Area	m^2 (square meter)		1 in^2 = 645.16 mm^2 = 6.4516 cm^2 1 ft^2 = 0.092 903 04 m^2 1 acre = 0.4047 hectare 1 sq. mile = 2.590 km^2
1.6	Volume	m^3 (cubic meter)		1 in^3 = 16 387.064 mm^3 1 ft^3 = 0.028 316 847 m^3 1 yd^3 = 0.764 554 86 m^3 1 gal (dry) = 0.004 405 m^3
1.6.1	Fluid tank; water heating tank; high pressure oxygen	L (liter)	m^3 (cubic meter)	1 ft^3 = 28.317 L 1 gal (liquid) = 3.785 412 L 1 fl oz = 29.573 53 cm^3

Table 16-1. Preferred metric units (Continued).

	Quantity	Preferred Metric Unit	Alternative Units	Conversion Factors
		2. Mass		
2.1	Mass	kg (kilogram)		1 oz (avoir) = 28.349 52 g 1 lb (avoir) = 0.453 592 37 kg 1 long ton (2,240 lb) = 1016.047 kg 1 short ton (2,000 lb) = 907.1847 kg 1 long ton = 1.016 047 metric ton 1 short ton = 0.907 185 metric ton
2.1.1	Gross mass; payload	kg (kilogram)	t (tonne)	
2.1.2	Hoisting provision	kg (kilogram)	t (tonne)	
2.1.3	Cargo capacity	kg (kilogram)	t (tonne)	
2.1.4	Fuel capacity (gravimetric)	kg (kilogram)	t (tonne)	
2.2	Linear density	kg/m (kilogram per meter)		1 lb/ft = 1.488 16 kg/m 1 lb/yd = 0.496 055 kg/m
2.3	Density, concentration	kg/m^3 (kilogram per cubic meter)	g/L (gram per liter)	1 lb/in^3 = 27 679.9 kg/m^3 1 lb/ft^3 = 16.018 46 kg/m^3 1 short ton/yd^3 = 1186.5526 kg/m^3 1 lb/gal = 119.8264 kg/m^3 1 oz/gal = 8.489 152 kg/m^3
2.3.1	Air density	kg/m^3 (kilogram per cubic meter)		1 $slug/ft^3$ = 515.379 kg/m^3
2.3.2	Cargo density	kg/m^3 (kilogram per cubic meter)	t/m^3 (tonne per cubic meter)	
2.3.3	Gas density	kg/m^3 (kilogram per cubic meter)		
2.3.4	Liquid density	kg/m^3 (kilogram per cubic meter)	g/L (gram per liter)	
2.4	Ambient humidity	mg/g (milligram per gram)		
2.5	Balance moment	kg m (kilogram meter)	g mm (gram millimeter)	
2.6	Moment of inertia	kg m^2 (kilogram square meter)		1 lb in^2 = 0.000 292 64 kg m^2 1 lb ft^2 = 0.031 140 kg m^2
2.7	Momentum	kg m/s (kilogram meter per second)		1 lb ft/s= 0.138 255 kg m/s
2.8	Moment of momentum	kg m^2/s (kilogram square meter per second)		1 lb ft^2/s = 0.042 140 kg m^2/s
2.9	Floor loading	kg/m^2 (kilogram per square meter)	t/m^2 (tonne per square meter)	
2.10	Wing loading	kg/m^2 (kilogram per square meter)	t/m^2 (tonne per square meter)	

Table 16-1. Preferred metric units (Continued).

	Quantity	Preferred Metric Unit	Alternative Units	Conversion Factors
		3. Force		
3.1	Force	N (newton)		1 lbf = 4.448 222 N
3.1.1	Handle operating load	N (newton)		
3.1.2	Jet and rocket engine thrust	kN (kilonewton)		
3.1.3	Rocket engine total impulse	N s (newton second)		
3.1.4	Rocket engine specific impulse	N s/kg (newton second per kilogram)		
3.2	Vacuum	Pa (pascal)		
3.3	Pressure	kPa (kilopascal)		1 psi = 6.894 757 kPa 1 in H_2O (39.2 °F) = 0.249 08 kPa 1 in H_2O (60 °F) = 0.248 84 kPa 1 in Hg (32 °F) = 3.386 39 kPa 1 in Hg (60 °F) = 3.376 85 kPa
3.3.1	Air pressure (general)	kPa (kilopascal)		1 atmos (std) = 101.325 kPa
3.3.2	Air pressure (meteorological)	kPa (kilopascal)		1 torr = 133.322 Pa = 0.133 32 kPa
3.3.3	Hydraulic pressure	kPa (kilopascal)		1 psi = 6.894 757 kPa
3.4	Stress	mPa (megapascal)		1 ksi = 6.894 757 mPa
3.4.1	Elastic limit; proportional limit; endurance limit	mPa (megapascal)		
3.4.2	Modulus of elasticity; Young's modulus; modulus of rigidity	mPa (megapascal)		10^6 psi = 6894.757 mPa
3.5	Fracture toughness	mPa · $m^{1/2}$ (megapascal $meter^{1/2}$)		1 ksi $in^{1/2}$ = 1.098 843 mPa · $m^{1/2}$
3.6	Strain energy per unit volume	J/m^3 (joule per cubic meter)		
3.7	Torque; moment of force	N m (newton-meter)		1 in lbf = 0.112 984 8 N m
3.8	Bending moment	N m (newton-meter)		1 in lbf = 1.355 818 N m
3.9	Bending moment per unit length; torque per unit length	N m/m (newton-meter per meter)		1 lbf ft/in = 53.378 66 N m/m 1 lbf in/in = 4.428 222 N m/m
3.10	Stiffness	N/m (newton per meter)		1 lbf/in = 175.127 N/m
3.11	Surface tension	mN/m (milli-newton per meter)		

Table 16-1. Preferred metric units (Continued).

	Quantity	Preferred Metric Unit	Alternative Units	Conversion Factors
		4. Mechanics		
4.1	Section modulus	cm^3 (cubic centimeter)		1 in^3 = 16.387 064 cm^3 1 in^4 = 41.623 1 cm^4
4.2	Second moment of area	cm^4		
4.3	Frequency	Hz (hertz)		
4.4	Rotational frequency	r/s (revolutions per second)	r/min (revolutions per minute)	
4.4.1	Rotational speed	r/min (revolutions per minute)		
4.5	Angular velocity	rad/s (radian per second)		
4.5.1	Rate of trim	°s (degree per second)		
4.6	Angular acceleration	rad/s^2 (radian per $second^2$)		
4.7	Velocity	m/s (meter per second)	km/hr (kilometer per hour)	1 ft/s = 0.304 8 m/s 1 mile/hour = 1.609 344 km/hr
4.7.1	Air speed	km/hr (kilometer per hour)		1 knot (US) = 1.8532 km/hr
4.7.2	Land speed	km/hr (kilometer per hour)		1 mile/hour = 1.609 344 km/hr
4.7.3	Wind speed	km/hr (kilometer per hour)	m/s	1 mile/hour = 1.609 344 km/hr
4.7.4	Vertical speed	m/s (meter per second)		1 ft/s = 0.3048 m/s 1 ft/min = 0.005 08 m/s
4.8	Linear acceleration	m/s^2 (meter per $second^2$)		
4.9	Energy; work	J (joule)		1 ft lb/f = 1.355 818 J 1 hp H = 2.6845 mJ 1 kw H = 3.6 mJ
4.9.1	Kinetic energy absorbed by brakes	mJ (megajoule)		
4.10	Impact	J/m^2 (joule per square meter)		
4.11	Power	W (watt)		
4.11.1	Shaft power; equivalent shaft power	kW (kilowatt)		

Table 16-1. Preferred metric units (Continued).

	Quantity	Preferred Metric Unit	Alternative Units	Conversion Factors
		5. Flow		
5.1	Mass flow	kg/s (kilogram per second)		1 lb/hr = 0.000 125 998 kg/s 1 lb/min = 0.007 56 kg/s 1 lb/s = 0.453 59 kg/s
5.2	Gas flow	kg/s (kilogram per second)		
5.2.1	Ventilation air	g/s (gram per second)		
5.2.2	Gas leakage	m^3/min (cubic meter per minute)		
5.2.3	Engine airflow	kg/s (kilogram per second)		
5.3	Liquid flow (gravimetric)	g/s (gram per second)		1 lb/min = 7.560 g/s
5.3.1	Fuel flow	g/s (gram per second)	kg/hr (kilogram per hour)	1 lb/hour = 0.4536 kg/hr 1 lb/s = 453.6 g/s
5.3.2	Fuel tank filling rate (gravimetric)	kg/min (kilogram per minute)		1 lb/min = 0.4536 kg/min
5.3.3	Fuel consumption	kg/hr (kilogram per hour)		1 lb/hour = 0.4536 kg/hr
5.3.4	Oil flow	L/min (liter per minute)		
5.4	Liquid flow (volumetric)	cm^3/s (cubic centimeter per second)	L/s (liter per second)	1 in^3/min = 0.273 cm^3/s 1 U.S. gal/min = 0.063 08 L/s
5.4.1	Pump capacity; fuel tank filling rate (volumetric)	L/min (liter per minute)		1 U.S. gal/min = 3.785 L/min
5.4.2	Oil leakage	cm^3/min (cubic centimeter per minute)		1 in^3/min = 16.39 cm^3/min
5.5	Viscosity (dynamic)	mPa s (millipascal second)		1 lb/ft s = 1.488 164 Pa s 1 lbf s/ft^2 = 47.880 26 Pa s
5.6	Viscosity (kinematic)	mm^2/s (square millimeter per second)		1 ft^2/s = 92 903 mm^2/s

Table 16-1. Preferred metric units (Continued).

	Quantity	Preferred Metric Unit	Alternative Units	Conversion Factors
		6. Thermodynamics		
6.1	Temperature	K (kelvin)	°C (° Celsius)	°C = (°F – 32)/1.8 K = °C + 273.15
6.1.1	Standard day temperature; ambient temperature	°C (° Celsius)		
6.2	Coefficient of linear expansion	K^{-1} ($kelvin^{-1}$)	$°C^{-1}$ ($°Celsius^{-1}$)	
6.3	Quantity of heat	J (joule)		1 Btu (60 °F) = 1.05468 kJ
6.4	Heat flow per unit area	J/m^2 (joule per square meter)		
6.5	Heat flow rate	kW (kilowatt)		1 Btu/hr = 0.293 071 W
6.5.1	Heat rate	mJ/(kW hr) (megajoule per kilowatt hour)		1 Btu/(hp hr) = 1.415 kJ/(kW hr)
6.6	Density of heat flow rate	W/m^2 (watt per square meter)		1 Btu/(h ft^2) = 3.154 59 W/m^2
6.7	Thermal conductivity	W/(m K) (watt per meter kelvin)		1 Btu–in/ft^2.hr °F = 0.144 23 W/(m K)
6.8	Thermal conductance	$W/(m^2$ K) (watt per square meter kelvin)		1 Btu/(ft^2.hr °F) = 5.678 26 $W/(m^2$ K)
6.9	Coefficient of heat transfer	$W/(m^2$ K) (watt per square meter kelvin)		
6.10	Thermal diffusivity	mm^2/s (square millimeter per second)		
6.11	Thermal resistivity	m K/W (meter kelvin per watt)		
6.12	Thermal resistance	m^2 K/W (square meter kelvin per watt)		
6.13	Heat capacity	kJ/K (kilojoule per kelvin)		
6.14	Specific heat capacity	kJ/(kg K) (kilojoule per kilogram kelvin)		1 Btu/(lb °F) = 4.1868 kJ/(kg K)
6.14.1	Specific heat	kJ/(kg K) (kilojoule per kilogram kelvin)		
6.15	Entropy	kJ/K (kilojoule per kelvin)		1 Btu/°R = 1.8991 kJ/K
6.16	Specific entropy	kJ/(kg K) (kilojoule per kilogram kelvin)		1 Btu/(lb °R) = 4.1868 kJ/(kg K)
6.17	Gas constant	J/(kg K) (joule per kilogram kelvin)		1 ft lb/(lb °F) = 5.382 J/(kg K)
6.17.1	Molar gas constant	J/(mol K) (joule per mole kelvin)		R_o = 8.3143 J/(mol K)
6.18	Specific energy	J/kg (joule per kilogram)		
6.18.1	Heating value; enthalpy	mJ/kg (megajoule per kilogram)		1 Btu/lb = 2326 J/kg
6.19	Specific latent heat	J/kg (joule per kilogram)		

Table 16-1. Preferred metric units (Continued).

	Quantity	Preferred Metric Unit	Alternative Units	Conversion Factors
7. Electricity and Magnetism				
7.1	Electric current	A (ampere)		
7.2	Current density	A/m^2 (ampere per square meter)		1 A/in^2 = 1.550 kA/m^2
7.3	Dielectric strength	V/mm (volt per millimeter)		
7.4	Electric potential	V (volt)		
7.5	Electric field strength	V/m (volt per meter)		
7.6	Power	W (watt)		1 hp (550 ft lbf/s) = 0.7457 kW 1 hp (metric) = 0.7355 kW 1 hp (electric) = 0.746 kW
7.7	Power (apparent)	VA (volt ampere)		
7.8	Electric resistance; impedance; modulus of impedance; reactance	Ω (ohm)		
7.9	Resistivity	Ωm (ohm meter)		
7.10	Conductance; admittance; modulus of admittance; susceptance	S (siemens)		
7.11	Conductivity	S/m (siemens per meter)		
7.12	Quantity of electricity	C (coulomb)		1 Ah = 3,600.0 C
7.13	Electric capacitance	F (farad)		
7.14	Permittivity	F/mm (farad per millimeter)		
7.15	Self inductance; mutual inductance	H (henry)		
7.16	Permeance	H (henry)		
7.17	Reluctance	H^{-1} (henry^{-1})		
7.18	Permeability	H/m (henry per meter)		
7.19	Magnetic flux	Wb (weber)		1 maxwell = 0.01 μWb
7.20	Magnetic flux density	T (tesla)		1 gauss = 0.1 MT
7.21	Magnetic field strength	A/m (ampere per meter)		1 oersted = 1,000/4π A/M
7.22	Electromagnetic moment; magnetic moment	A m^2 (ampere square meter)		
7.23	Electric dipole moment	(coulomb meter)		
8. Light				
8.1	Luminous intensity	cd (candela)		
8.2	Luminous flux	lm (lumen)		
8.3	Luminous exitance	lm/m^2 (lumen per square meter)		
8.4	Illuminance	lx (lux)		
8.4.1	Cabin illumination	lx (lux)		1 ft candle = 10.764 lx
8.5	Luminance	cd/m^2 (candela per square meter)		1 foot lambert = 3.426 26 cd/m^2 1 lambert = 3183.1 cd/m^2

Table 16-1. Preferred metric units (Continued).

	Quantity	Preferred Metric Unit	Alternative Units	Conversion Factors
9. Acoustics				
9.1	Noise level; sound level	dB (decibel)		
9.2	Period; periodic time	s (second)		
9.3	Frequency	Hz (hertz)		
9.4	Wavelength	m (meter)		
9.5	Mass density	kg/m^3 (kilogram per cubic meter)		
9.6	Static pressure, instantaneous sound pressure	Pa (pascal)		
9.7	Instantaneous sound particle velocity	m/s (meter per second)		
9.8	Instantaneous volume velocity	m^3/s (cubic meter per second)		
9.9	Velocity of sound	m/s (meter per second)		
9.10	Sound energy flux; sound power	W (watt)		
9.11	Sound intensity	W/m^2 (watt per square meter)		
9.12	Specific acoustic impedance	Pa s/m (pascal second per meter)		
9.13	Acoustic impedance	Pa s/m^3 (pascal second per cubic meter)		
9.14	Mechanical impedance	N s/m (newton second per meter)		

Table 16-2. SI base and supplementary units.

Quantity	Name	Symbol
Base Units		
Length	meter	m
Mass	kilogram	kg
Time	second	s
Electric current	ampere	A
Thermodynamic temperature	kelvin	K
Amount of substance	mole	mol
Luminous intensity	candela	cd
Supplementary Units		
Plane angle	radian	rad
Solid angle	steradian	sr

Table 16-3. SI derived units.

Quantity	Name	Symbol	Derivation
Frequency	hertz	Hz	1 Hz = 1 s^{-1}
Force	newton	N	1 N = 1 kg m/s^2
Pressure; stress	pascal	Pa	1 Pa = 1 N/m^2
Energy; work; quantity of heat	joule	J	1 J = 1 N m
Power	watt	W	1 W = 1 J/s
Electric charge; quantity of electricity	coulomb	C	1 C = 1 A s
Electric potential; electromotive force	volt	V	1 V = 1 W/A
Electric capacitance	farad	F	1 F = 1 A s/V
Electric resistance	ohm	Ω	1Ω = 1 V/A
Electric conductance	siemens	S	1 S = 1 A/V
Magnetic flux	weber	Wb	1 Wb = 1 V s
Magnetic flux density; magnetic induction	tesla	t	1 t = 1 V s/m^2
Inductance	Henry	H	1 hr = 1 V s/A
Luminous flux	lumen	lm	1 lm = 1 cd sr
Illuminance	lux	lx	1 lx = 1 lm/m^2

Table 16-4. Non-SI units accepted for use with SI.

Quantity	Name	Symbol	Definition
Time	minute	min	1 min = 60 s
	hour	hr	1 hr = 60 min = 3,600 s
	day	d	1 d = 24 hr = 86,400 s
	week	wk	1 wk = 7 d
	month	mo	1 mo
	year	yr	1 yr = 365.26 days
Plane angle	degree	°	1°= (π/180) rad
	minute	'	1' = (1/60) °
	second	"	1" = (1/60)'
Volume	liter	L	1 L = 1 dm^3 = 10^{-3} m^3
Area	hectare	ha	1 ha = 1 hm^2 = 10^4 m^2
Pressure	bar	Bar	1 Bar = 10^5 Pa
Energy	kilowatt-hour	kWhr	1 kWhr = 3.6 mJ
Temperature	degree Celsius	°C	
Mass	metric ton	t	1 t = 10^3 kg

Table 16-5. Prefixes for SI units.

Factor by Which the Unit Is Multiplied	Prefix		Factor by Which the Unit is Multiplied	Prefix	
	Name	Symbol		Name	Symbol
10^{18}	exa	E	10^{-1}	deci*	d
10^{15}	peta	P	10^{-2}	centi	c
10^{12}	tera	T	10^{-3}	milli	m
10^9	giga	G	10^{-6}	micro	μ
10^6	mega	M	10^{-9}	nano	n
10^3	kilo	k	10^{-12}	pico	p
10^2	hecto*	h	10^{-15}	femto	f
10^1	deka*	da	10^{-18}	atto	a

* To be avoided where possible

Table 16-6. SI definitions for selected physical constants and non-SI units.

Unit	SI Equivalent
Angstrom unit (Å)	10^{-10} meter
Micron (μ)	10^{-6} meter
Light year	9.460 55×10^{12} kilometer
Speed of light	299,792.4580±0.0012 kilometer per second
Speed of sound (sea level, 15 °C US76)	340.294 meter per second
Gravitational constant (G_N)	9.806 65 newton-meter/kilogram-$second^2$
Centistoke	10^{-6} square meter/second

BIBLIOGRAPHY

International Standard ISO 1000, Third Edition, Amendment 1, 1998, "SI Units and Recommendations or the Use of Their Multiples and of Certain Other Units," Reference Number: ISO 1000:1992/Amd.:1998(E), International Organization for Standards, Geneva, Switzerland, 1992.

ISO, "SI Guide—International System of Units," English Edition 2, International Organization for Standardization, 2008.

List, R.J.: *Smithsonian Meteorological Tables—Sixth Revised Edition*, Smithsonian Misc. Collections, Vol. 114, Smithsonian Inst. Press, Washington, DC, Fifth Reprint, 1984.

Mechtly, E.A.: "The International System of Units: Physical Constants and Conversion Factors," *NASA SP-7012*, Second Revision, NASA, Washington DC, 1973.

NASA Policy Directive 8010.2E, "Use of the SI (Metric) System of Measurement in NASA Programs," <http://standards.nasa.gov>.

Online conversion site containing thousands of conversions for quick online use, <http://www.onlineconversion.com/>.

SI Guide - International System of Units, International Organization for Standards, Central Secretariat, Geneva, Switzerland, 2008.

Taylor, B.N.: "Guide for the Use of the International System of Units (SI)," U.S. Department of Commerce, National Institute of Standards and Technology, NIST Special Publication 811, <http://physics.nist.gov/Pubs/SP811/appenB8.html>, 1995 Edition.

Taylor, B.N.: "The International System of Units (SI)," U.S Department of Commerce, National Institute of Standard and Technology, NIST Special Publication 330, <http://physics.nist.gov/Pubs/SP330/sp330.pdf>, 2001 Edition.

REPORT DOCUMENTATION PAGE

Form Approved
OMB No. 0704-0188

PLEASE DO NOT RETURN YOUR FORM TO THE ABOVE ADDRESS.

1. REPORT DATE *(DD-MM-YYYY)*	2. REPORT TYPE	3. DATES COVERED *(From - To)*
01–12–2008	Technical Memorandum	

4. TITLE AND SUBTITLE

Terrestrial Environment (Climatic) Criteria Guidelines for Use in Aerospace Vehicle Development, 2008 Revision

5a. CONTRACT NUMBER

5b. GRANT NUMBER

5c. PROGRAM ELEMENT NUMBER

6. AUTHOR(S)

D.L. Johnson, Editor

5d. PROJECT NUMBER

5e. TASK NUMBER

5f. WORK UNIT NUMBER

7. PERFORMING ORGANIZATION NAME(S) AND ADDRESS(ES)

George C. Marshall Space Flight Center
Marshall Space Flight Center, AL 35812

8. PERFORMING ORGANIZATION REPORT NUMBER

M–1247

9. SPONSORING/MONITORING AGENCY NAME(S) AND ADDRESS(ES)

National Aeronautics and Space Administration
Washington, DC 20546–0001

10. SPONSORING/MONITOR'S ACRONYM(S)

11. SPONSORING/MONITORING REPORT NUMBER

NASA/TM—2008– 215633

12. DISTRIBUTION/AVAILABILITY STATEMENT

Unclassified-Unlimited
Subject Category 46
Availability: NASA CASI (443–757–5802)

13. SUPPLEMENTARY NOTES

Prepared for the Spacecraft & Vehicle Systems Department, Engineering Directorate

14. ABSTRACT

This document provides guidelines for the terrestrial environment that are specifically applicable in the development of design requirements/specifications for NASA aerospace vehicles, payloads, and associated ground support equipment. The primary geographic areas encompassed are the John F. Kennedy Space Center, FL; Vandenberg AFB, CA; Edwards AFB, CA; Michoud Assembly Facility, New Orleans, LA; John C. Stennis Space Center, MS; Lyndon B. Johnson Space Center, Houston, TX; George C. Marshall Space Flight Center, Huntsville, AL; and the White Sands Missile Range, NM. This document presents the latest available information on the terrestrial environment applicable to the design and operations of aerospace vehicles and supersedes information presented in NASA-HDBK-1001 and *TM X-64589*, *TM X-64757*, *TM-78118*, *TM-82473*, and *TM-4511*. Information is included on winds, atmospheric thermodynamic models, radiation, humidity, precipitation, severe weather, sea state, lightning, atmospheric chemistry, seismic criteria, and a model to predict atmospheric dispersion of aerospace engine exhaust cloud rise and growth. In addition, a section has been included to provide information on the general distribution of natural environmental extremes in the conterminous United States, and world-wide, that may be needed to specify design criteria in the transportation of space vehicle subsystems and components. A section on atmospheric attenuation has been added since measurements by sensors on certain Earth orbital experiment missions are influenced by the Earth's atmosphere. There is also a section on mission analysis, prelaunch monitoring, and flight evaluation as related to the terrestrial environment inputs. The information in these guidelines is recommended for use in the development of aerospace vehicle and related equipment design and associated operational criteria, unless otherwise stated in contract work specifications. The terrestrial environmental data in these guidelines are primarily limited to information below 90 km altitude.

15. SUBJECT TERMS

environment criteria, terrestrial environment, surface extremes, wind, temperature, humidity, precipitation, density, pressure, atmospheric electricity, cloud cover, control systems, geology, sea state, severe storms, constituents, radiation, diffusion, models

16. SECURITY CLASSIFICATION OF:			17. LIMITATION OF ABSTRACT	18. NUMBER OF PAGES	19a. NAME OF RESPONSIBLE PERSON
a. REPORT	b. ABSTRACT	c. THIS PAGE			STI Help Desk E-mail: help@sti.nasa.gov
U	U	U	UU	856	19b. TELEPHONE NUMBER *(Include area code)* STI Help Desk: 443–757–5802

National Aeronautics and
Space Administration
IS20
George C. Marshall Space Flight Center
Marshall Space Flight Center, Alabama
35812